NEW MEXICO DEPARTMENT OF TRANSPORTATION

RESEARCH BUREAU

Innovation in Transportation

Feasibility Analysis of Ultra High Performance Concrete for Prestressed Concrete Bridge Applications – Phase IV

Prepared by:
New Mexico State University
Department of Civil Engineering
Las Cruces, NM

May 2022

Prepared for:
New Mexico
Department of Transportation
Research.Bureau@state.nm.us
http://NMDOTResearch.com

In Cooperation with:
The US Department of Transportation
Federal Highway Administration

Final Report
NM09MCS-01

MAY 2022

PROJECT NO. NM09MSC-01

FEASIBILITY ANALYSIS OF ULTRA HIGH PERFORMANCE CONCRETE FOR PRESTRESSED CONCRETE BRIDGE APPLICATIONS

PHASE IV

Final Report
May 2022

Report Submitted to:

Research Bureau
New Mexico Department of Transportation
7500B Pan American Freeway NE
PO Box 94690
Albuquerque, NM 87199-4690
(505) 841-9145

Prepared by:

Brad D. Weldon
David V. Jáuregui
Craig M. Newtson
Mark P. Manning
Jordan Varbel

Department of Civil Engineering
New Mexico State University
PO Box 30001, MSC 3CE
Las Cruces, NM 88003



USDOT FHWA SUMMARY PAGE

1. Report No. NM09MSC-01	2. Government Accession No.	3. Recipient's Catalog No.
4. Title and Subtitle Feasibility Analysis of Ultra High Performance Concrete for Prestressed Concrete Bridge Applications – Phase IV		5. Report Data 6. Performing Organization Code
7. Author(s): Brad D. Weldon, David V. Jáuregui, and Craig M. Newtson		8. Performing Organization Report No.
7. Performing Organization Name and Address New Mexico State University Box 30001, MSC 3CE Las Cruces, NM 88003		
12. Sponsoring Agency Name and Address NMDOT Research Bureau 7500B Pan American Freeway PO Box 94690 Albuquerque, NM 87199-4690		13. Type of Report and Period Covered Final Report July 1 – May 2022 14. Sponsoring Agency Code
15. Supplementary Notes		
16. Abstract		
17. Key Words ultra high performance concrete; UHPC; prestressed bridge design	18. Distribution Statement Available from NMDOT Research Bureau	

19. Security Classification (of this report)	20. Security Classification (of this page)	21. No. of pages	22. Price
Form DOT F 1700.7 (8-72)			

PREFACE

The broad objective of this research program is to investigate the feasibility and limitations of Ultra High Performance Concrete (UHPC) for prestressed concrete bridge applications in New Mexico. UHPC is an emerging material technology in which concrete develops very high compressive strengths and exhibits improved tensile strength and toughness. Through the findings of a comprehensive literature and historical application review and trial designs and cost analyses on typical prestressed concrete bridges using UHPC, it was determined that UHPC could potentially benefit design, construction, maintenance, and the lifespan of structures. Optimized mixture proportions and a curing regimen for an UHPC that uses materials local to New Mexico were developed that meet the strength and durability design requirements of the NMDOT. The creep and shrinkage behavior of the local UHPC has been investigated and Special Provisions have been developed for the implementation of UHPC in bridge design. To verify the design and behavior of UHPC girders large scale flexural tests were conducted. Bridge 9706, a two simple-span structure, was recently constructed. One span of the bridge used UHPC and the other used high performance concrete (HPC). In the current work, Bridge 9706 is being tested and monitored to investigate the performance of UHPC compared to HPC. Using the data gathered from the bridge, analytical models are being developed to further investigate the behavior Bridge 9706. Finally, new applications for UHPC are being investigated.

NOTICE

The United States government and the State of New Mexico do not endorse products or manufacturers. Trade or manufactures' names appear herein solely because they are considered essential to the object of this report. This information is available in alternative accessible formats. To obtain an alternative format, contact the NMDOT Research Bureau, 7500B Pan American Freeway NE, PO Box 94690, Albuquerque, NM 87199-4690, (505) 841-9145.

DISCLAIMER

This report presents the results of research conducted by the authors and does not necessarily represent the views of the New Mexico Department of Transportation. This report does not constitute a standard or specification.

THIS PAGE INTENTIONALLY LEFT BLANK

ABSTRACT

Phase IV was a continuation of a project to implement Ultra High Performance Concrete (UHPC) in precast, prestressed bridge girders in New Mexico. In Phase I of this research, case studies were conducted to investigate the advantages of implementing UHPC in bridge superstructure design. Due to the benefits that UHPC offers, this feasibility study resulted in recommendations to move forward with the development of mixture proportions for UHPC produced from materials local to New Mexico (Phase II). The UHPC mixture proportions developed in Phase II incorporated fine angular sand with a No. 4 top size, silica fume, fly ash, and elevated curing temperatures for both wet and dry cure periods. These mixture proportions and curing practices were optimized to produce UHPC that is economical and producible in New Mexico for implementation into prestressed concrete bridge design. Additionally, the durability of the optimized mixture for resistance to alkali-silica reaction, freezing and thawing, and delayed ettringite formation was established and the results demonstrate that the UHPC has excellent durability properties. Phase III included investigations on the creep and shrinkage behavior of these UHPC mixture proportions as well as conducting full scale flexural tests on UHPC bridge girders. UHPC using local materials was introduced into a local precast plant and Special Provisions were developed for casting UHPC girders. Bridge 9706 was recently constructed and incorporated the use of UHPC. In the current phase of the research, Bridge 9706 will be load tested and monitored to investigate the performance of UHPC under loads. Using the results of the load tests, an analytical model will be developed and used to further investigate the bridge behavior under different loading scenarios. Additional uses of UHPC will be investigated, including field studies, and the mixture proportions will be further optimized. Finally, to disseminate the knowledge base of UHPC to a wide community, a UHPC Symposium was held.

THIS PAGE INTENTIONALLY LEFT BLANK

TABLE OF CONTENTS

PREFACE iv

ABSTRACT vi

TABLE OF CONTENTS viii

FIGURES xx

TABLES lv

Notation ..... **Error! Bookmark not defined.**

Units & Conversions lxix

LAYOUT OF REPORT 1

INTRODUCTION AND BACKGROUND 3

i. Measured Material Properties and General Testing Procedures 7

i.i Compressive Strength 7

i.ii Unit Weight 9

i.iii Modulus of Rupture 10

i.iv Modulus of Elasticity 12

TASK 1: MONITORING OF BRIDGE 9706 15

1.1 NM Bridge No. 9706 15

1.1.1 Bridge Design 15

1.1.2 Girder Design 18

1.1.3 Girder Production 26

1.1.4 Superstructure Construction 34

1.1.5 Completed Structure 38

1.2 Field Testing 41

1.2.1.1 Truck Loads and Load Paths 41
1.3 Preparatory Calculations 49
1.3.1 Available and Expected Strain 49
1.3.2 Composite and Non-Composite Neutral Axis 51
1.3.3 Available Shear Strength 52
1.3.4 Live Load Distribution Factors 53
1.3.4.1 Live Load Distribution Factor for Moment 53
1.3.4.2 Live Load Distribution Factor for Shear 54
1.3.5 Summary 55
1.3.5.1 Available and Expected Strain Results 55
1.3.5.2 Composite and Non-Composite Neutral Axis Results 59
1.3.5.3 Available Shear Strength Results 62
1.3.5.4 Live Load Distribution Factor Results 62
1.4 BDI ST350 Strain Transducers 63
1.4.1 Digital Image Correlation 67
1.5 Diagnostic Load Testing 74
1.5.1 Truck Paths and Phases 74
1.5.2 Diagnostic Test Results 76
1.5.2.1 Maximum Strain 76
1.5.2.2 Transverse Strain Distribution 81
1.5.2.3 Composite and Non-Composite Neutral Axis Behavior 85
1.5.3 UHPC and HPC Diagnostic Test Comparison 91
1.5.3.1 Comparison of Strain Behavior 91

1.5.3.2 Comparison of Actual and Expected Strain 93
1.5.3.3 Comparison of Neutral Axis Behavior 94
1.6 Proof Load Testing 95
1.6.1 Proof Test Load Paths 95
1.6.2 Proof Test 1 Results 97
1.6.2.1 Maximum Strain 97
1.6.2.2 Transverse Strain Distribution 105
1.6.2.3 Composite and Non-Composite Neutral Axis Behavior 108
1.6.3 UHPC and HPC Proof Test 1 Comparison 113
1.6.3.1 Comparison of Strain Behavior 113
1.6.3.2 Comparison of Actual and Expected Strain 115
1.6.3.3 Comparison of Neutral Axis Behavior 117
1.6.3.4 Diagnostic and Proof Test Comparisons and Conclusions 118
1.6.3.5 Strain Behavior 118
1.6.4 Induced Moment 122
1.6.5 Neutral Axis Behavior. 125
1.6.6 Calculated Live Load Distribution 127
1.6.7 Impact Factor 130
1.7 Proof Test 3 131
1.7.1 PT3 Results 131
1.7.1.1 Maximum Strains 131
1.7.1.1.1 Comparison of Strain Behavior 138
1.7.1.1.2 DIC Results 139

1.7.1.1.2.1 Analysis of Displacements Using ARAMIS 139
1.7.1.1.2.2 Experimental Testing Results for Vertical Displacement 141
1.7.1.1.2.2.1 Performance of HPC Span 141
1.7.1.1.2.2.2 Performance of UHPC Span 150
1.8 Vibrating Wire Strain Data 162
1.8.1 Vibrating Wire Strain Gauges 162
1.8.2 Naming Convention 164
1.8.3 Sensor Arrangements 165
1.8.3.1 Location Measurements 166
1.8.3.1.1 UHPC Span 168
1.8.3.1.2 HPC Span 172
1.8.4 Sensor Installation 176
1.8.5 Initial Data 182
1.8.5.1 Curing Temperatures 182
1.8.5.2 Prestressing Forces 185
1.8.5.2.1 Measured Prestressing Forces 185
1.8.6 Material Properties 193
1.8.6.1 Compressive Strength 194
1.8.6.2 Unit Weight 196
1.8.6.3 Modulus of Rupture 198
1.8.7 Batch Results 200
1.8.7.1.1 UB1 201
1.8.7.1.2 UB2 205

1.8.7.1.3 UB3 210
1.8.7.1.4 UB4 215
1.8.7.1.5 HB1 220
1.8.7.1.6 HB2 225
1.8.7.1.7 HB3 229
1.8.7.1.8 HB4 234
1.8.8 Strain Comparisons 239
1.8.8.1 Single Truck Loading 243
1.8.8.2 Double Truck Loading 258
1.8.8.3 Triple Truck Loading 270
1.8.8.4 Single Truck Back-to-Back Loading 280
1.8.8.5 Double Truck Back-to-Back Loading 292
1.8.9 Summary of Maximum Strains 305
Task 2: BRIDGE 9706 ANALYTICAL MODEL 312
Task 3: UHPC SYMPOSIUM 327
Task 4: MIXTURE PROPORTION OPTIMIZATION 331
4.1 Mixture Proportion Investigation 331
4.2 Time-Dependent Strength Gain of Nonproprietary UHPC 341
4.2.1 Mixture Proportions 341
4.2.2 Laboratory Production of UHPC 342
4.2.3 Measured Material Properties 343
4.2.3.1 Compressive Strength 343
4.2.3.2 Unit Weight 344

4.2.3.3 Modulus of Rupture 345
4.2.3.4 Modulus of Elasticity 346
4.2.4 Strength Gain of UHPC Using Thermal Curing 348
4.2.4.1 Thermal Curing Regimen 348
4.2.4.2 Curing Temperatures 349
4.2.4.3 Compressive Strength 354
4.2.4.4 Unit Weight 357
4.2.4.5 Modulus of Rupture 358
4.2.4.6 Modulus of Elasticity 361
4.2.4.7 Batch Results for UHPC Using Thermal Curing Regimen 363
4.2.4.7.1 Batch TC1 363
4.2.4.7.2 Batch TC2 365
4.2.4.7.3 Batch TC3 366
4.2.4.7.4 Batch TC4 367
4.2.4.7.5 Batch TC5 369
4.2.4.7.6 Batch TC6 371
4.2.4.7.7 Batch TC7 373
4.2.4.7.8 Batch TC8 375
4.2.4.7.9 Batch TC9 377
4.2.4.7.10 Batch TC10 379
4.2.4.7.11 Batch TC11 381
4.2.4.7.12 Batch TC12 383
4.2.4.7.13 Batch TC13 385

4.2.4.7.14 Batch TC14 387
4.2.4.7.15 Batch TC15 389
4.2.5 Strength Gain of UHPC Using Ambient Curing 391
4.2.5.1 Ambient Curing Regimen 391
4.2.5.2 Curing Temperatures 392
4.2.5.3 Compressive Strength 398
4.2.5.4 Unit Weight 401
4.2.5.5 Modulus of Rupture 402
4.2.5.6 Modulus of Elasticity 404
4.2.5.7 Batch Results for UHPC Using Ambient Curing Regimen 406
4.2.5.7.1 Batch AC1 406
4.2.5.7.2 Batch AC2 408
4.2.5.7.3 Batch AC3 409
4.2.5.7.4 Batch AC4 411
4.2.5.7.5 Batch AC5 413
4.2.5.7.6 Batch AC6 415
4.2.5.7.7 Batch AC7 417
4.2.5.7.8 Batch AC8 419
4.2.5.7.9 Batch AC9 421
4.2.5.7.10 Batch AC10 423
4.2.6 Comparison of Results and Property Interactions 425
4.2.6.1 Compressive Strength 425
4.2.6.1.1 Initial Set Data 427

4.2.6.2 Unit Weight 430
4.2.6.3 Modulus of Rupture 431
4.2.6.4 Modulus of Elasticity 434
4.2.6.5 Evaluation of Curing Regimens 437
4.3 Chemical Analysis of UHPC 441
4.3.1 X-Ray Diffraction (XRD) 441
4.3.2 Brunauer, Emmett and Teller Testing Procedure 443
4.3.3 Scanning Electron Microscope Testing Procedure 447
4.4 Direct Tension Tests 448
4.4.1 Objective 448
4.4.2 Specimen Design 449
4.4.3 Test Setup and Instrumentation 450
4.4.4 Preliminary direct tension results 451
Task 5:IDENTIFY POTENTIAL ADDITIONAL USES OF UHPC 455
5.1 Joint Applications 455
5.1.1 Design of Test Specimens 457
5.1.2 Test Set-up and Instrumentation 462
5.1.3 Material 466
5.1.4 Mixture Proportions 467
5.1.5 Preparation of Test Compressive Strength Specimens 468
5.1.6 Preparation of Box Girder Top Slab 468
5.1.7 Curing Regimen 472
5.1.8 Compressive Strength Test 472

5.1.9 Flexural Strength Test 474
5.1.10 Experimental Results 475
5.1.10.1 Specimen 1 476
5.1.10.2 Specimen 2 491
5.1.10.3 Specimen 3 506
5.1.10.4 Specimen 4 512
5.1.10.5 Specimen 5 524
5.1.10.6 Specimen 6 528
5.1.10.7 Cyclic Test Comparison 539
5.1.10.8 Failure Test Comparison 541
5.1.11 Conclusions and Limitations 543
5.2 UHPC Shear Keys in Concrete Bridges 546
5.2.1 Full-Scale Experimental Methods 547
5.2.1.1 Flexural Test Set-Up and Instrumentation 549
5.2.1.2 Shear Testing Set-Up and Instrumentation 555
5.2.1.3 Grouting Materials 561
5.2.1.4 Grouting Methods 562
5.2.1.5 Flexural Loading 565
5.2.1.6 Shear Loading 569
5.2.1.7 Casting and Curing 570
5.2.2 Material Property Test Results 571
5.2.3 Cyclic Testing 573
5.2.3.1 Cyclic Loading 1 574

5.2.3.1.1 Vertical Deflection Behavior 574
5.2.3.1.2 Transverse Deflection Behavior 577
5.2.3.2 Cyclic Loading 2 579
5.2.3.2.1 Vertical Deflection Behavior 579
5.2.3.2.2 Transverse Deflection Behavior 582
5.2.3.3 Cyclic Loading 3 584
5.2.3.3.1 Vertical Deflection Behavior 584
5.2.3.4 Cyclic Loading 4 586
5.2.3.4.1 Vertical Deflection Behavior 586
5.2.3.4.2 Transverse Deflection Behavior 589
5.2.3.5 Comparison of Flexural Cyclic Loading 591
5.2.3.5.1 Vertical Deflection Behavior 591
5.2.3.5.2 Transverse Deflection Behavior 594
5.2.3.6 Cyclic Loading 5 595
5.2.3.6.1 Vertical Deflection Behavior 595
5.2.3.6.2 Rotation 597
5.2.3.7 Cyclic Loading 6 598
5.2.3.7.1.1 Vertical Deflection Behavior 598
5.2.3.7.1.2 Transverse Deflection Behavior 602
5.2.3.8 Comparison of Shear Cyclic Loading 604
5.2.3.8.1 Vertical Deflection Behavior 604
5.2.4 Ultimate Loading 606
5.2.4.1 Flexural Testing Results 606

5.2.4.1.1 Vertical Deflection Behavior 606
5.2.4.1.2 Transverse Deflection Behavior 611
5.2.4.2 Shear Testing Results 614
5.2.4.2.1 Vertical Deflection Behavior 614
5.2.4.2.2 Transverse Deflection Behavior 617
5.2.5 Moment Distribution Factors 619
5.2.6 Shear Distribution Factor 620
5.2.7 Summary 621
5.2.8 Conclusions 622
5.2.8.1 Flexural Testing 622
5.2.8.2 Shear Testing 623
5.3 UHPC and NSC Composite Beams 624
5.3.1 Mixture Proportions 624
5.3.2 Preliminary Specimen Design 625
5.3.3 Test Setup and Instrumentation 628
5.3.4 Preliminary Results 632
5.4 UHPC As an Overlay Material 642
5.4.1 Mixture Proportions 643
5.4.2 UHPC 643
5.4.3 NSC 645
5.4.4 Measured Material Properties 646
5.4.4.1 Compressive Strength 646
5.4.4.2 Modulus of Elasticity 647

5.4.4.3 Modulus of Rupture 648
5.4.4.4 Longer-Term Shrinkage 649
5.4.4.5 Tensile Test of Mild Reinforcement 651
5.4.5 Design Selection 654
5.4.6 Instrumentation for Data Acquisition 655
5.4.6.1 Dataloggers 655
5.4.6.2 Strain Gauges 657
5.4.6.3 Vibrating Wire Strain Gauges (VWSG) 658
5.4.7 Specimen Production 659
5.4.7.1 NSC Slabs 659
5.4.7.2 UHPC Overlays 661
5.4.8 Tests Setup and Instrumentation 664
5.4.8.1 Strain Measurement 664
5.4.8.2 Flexural Test 665
5.4.8.3 Digital Image Correlation 669
5.4.9 RESULTS 671
5.4.9.1 Vibrating Wire Strain Gauges 671
5.4.10 Flexural Testing Results 696
5.4.10.1 Cyclic Load Testing 697
5.4.10.2 Ultimate Load Testing 712
5.4.11 Conclusions 734
REFERENCES 737

FIGURES

Figure 1.1: A 4.0 in. (100 mm) UHPC cube specimen prior to testing using a 1000-kip (4450 kN) capacity compression machine. 8

Figure 1.2: Weighing a 4.0 in. (100 mm) UHPC cube specimen for calculation of unit weight. .. 9

Figure 1.3: Photos showing (a) front and (b) back view of the modulus of rupture test setup..... 10

Figure 1.4: Four-point bending test setup for small-scale modulus of rupture beam specimens . 11

Figure 1.5: UHPC cylinder specimen with modulus of elasticity testing apparatus (prior to testing). 12

Figure 1.6: NM Bridge No. 9706 crossing the La Union Main Canal, State Road 186, Anthony, NM. 16

Figure 1.7: Transverse section detail for Bridge No 9706. 17

Figure 1.8: Cross-sectional detail for UHPC interior design section for Bridge No 9706 (a) near girder centerline, (b) at centerline post-tensioning, and (c) at girder ends. 19

Figure 1.9: Cross-sectional detail for UHPC exterior design section for Bridge No 9706 (a) near girder centerline, (b) at centerline post-tensioning, and (c) at girder ends. 20

Figure 1.10: Reinforcement elevation detail for UHPC design section for Bridge No 9706. 21

Figure 1.11: Cross-sectional detail for HPC interior design section for Bridge No 9706 (a) near girder centerline, (b) at centerline post-tensioning, and (c) at girder ends. 22

Figure 1.12: Cross-sectional detail for HPC exterior design section for Bridge No 9706 (a) near girder centerline, (b) at centerline post-tensioning, and (c) at girder ends. 23

Figure 1.13: Reinforcement elevation detail for HPC design section for Bridge No 9706. 24

Figure 1.14: (a) Studded steel shoe (bearing) plates embedded at girder ends and (b) ducts for pier end dowel “pinned” connection (pier end exit ducts for VWSG cables also pictured). 25

Figure 1.15: Channel girder formwork (a) before and (b) after installation of reinforcement. 27
Figure 1.16: Coreslab® Structures (Albuquerque), Inc. (a) batching facility and (b) view inside 3.0 yd^3 (2.30 m^3) concrete mixer. 28
Figure 1.17: Batch plant mixing process: (a) Dry mixing stage, (b) manual addition of HRWRA, (c and d) continued mixing of concrete until (e) desired consistency was achieved, and (f) manual addition of steel fibers. 29
Figure 1.18: NMSU graduate researchers checking sensor installation prior to concrete placement during channel girder production for NM Bridge No. 9706 30
Figure 1.19: Channel girder production for Bridge No. 9706: (a) concrete mixing in batch plant; (b) placement of concrete by auger fed delivery; (c) vibrating concrete for consolidation; (d) finishing of girder surface; (e) removing girder from formwork after strand release; (f) completed channel girders. 31
Figure 1.20: Channel girder production for Bridge No. 9706: (a) concrete mixing in batch plant; (b) placement of concrete by auger fed delivery; (c) vibrating concrete for consolidation; (d) finishing of girder surface; (e) removing girder from formwork after strand release; (f) completed channel girders. 32
Figure 1.21: Channel girder production for Bridge No. 9706: (a) concrete mixing in batch plant; (b) placement of concrete by auger fed delivery; (c) vibrating concrete for consolidation; (d) finishing of girder surface; (e) removing girder from formwork after strand release; (f) attaching sensors of completed channel girders to temporary data acquisition unit. 33
Figure 1.22: Construction of NM Bridge No. 9706 superstructure: Placement of UHPC girders (a) U-3 and (b) U-5. 35

Figure 1.23: Construction of NM Bridge No. 9706 superstructure: (a) placement of HPC girder H-8 and (b) view of channel girders after placement. 36
Figure 1.24: Photos of (a) deck reinforcement and mechanical bridge paver and (b) finishing of deck surface during concrete placement. 37
Figure 1.25: Nameplate of NM Bridge No. 9706. 38
Figure 1.26: NM Bridge No. 9706: View of (a) south bridge face and (b) north bridge face. 39
Figure 1.27: NM Bridge No. 9706: View of (a) east bound NM 186 and (b) stepped central pier. 40
Figure 1.28: Load Paths 1 through 6 for field testing of NM Bridge No. 9706. 45
Figure 1.29: Load Paths 7 through 9 for field testing of NM Bridge No. 9706. 46
Figure 1.30: Load Path 10 for field testing of NM Bridge No. 9706. 47
Figure 1.31: Locations of load stations for incremental load paths. 48
Figure 1.32: LRFD live load distribution superstructure type (h). 53
Figure 1.33: BDI Structural Testing System II. 63
Figure 1.34: BDI strain transducers linked collection boxes with connected strain transducers. 64
Figure 1.35: Attached BDI strain transducers on the stem and on the bottom of girder stems for girder H-2 and H-3. 64
Figure 1.36: BDI strain transducers. 65
Figure 1.37: BDI strain transducers linked collection boxes with connected strain transducers. 65
Figure 1.38: BDI acquisition system and laptop computer arrangement. 66
Figure 1.39: BDI instrumentation for typical girder cross section. 66
Figure 1.40: BDI instrumentation layout for bridge cross section. 67

Figure 1.41: Stochastic white chalk grid pattern and DIC cameras set up at the north face of the exterior girder H-1. 68
Figure 1.42: Stochastic black marker grid pattern on the bottom of UHPC girder legs for girder U-2 and U-3..... 68
Figure 1.43: FASTEC IL5 System for monitoring exterior girder of UHPC span..... 70
Figure 1.44: FASTEC HiSpec1 System for monitoring exterior girder of HPC span..... 70
Figure 1.45: View of GoPro Hero + System for monitoring exterior girder of HPC span from (a) behind cameras and (b) in front of cameras..... 70
Figure 1.46: View of GoPro Hero 4 System for monitoring exterior girder of HPC span from (a) behind cameras and (b) in front of cameras..... 71
Figure 1.47: 2M System for monitoring an interior girder of UHPC span..... 71
Figure 1.48: 2M System for monitoring an interior girder of HPC span..... 71
Figure 1.49:Side view of Bridge No. 9706 showing 4 DIC systems..... 72
Figure 1.50: Command station with computer systems running DIC cameras. 72
Figure 1.51: Locations of each DIC camera system for monitoring of Bridge No. 9706. 73
Figure 1.52: Photographs from diagnostic load test of Bridge 9706. 75
Figure 1.53: Location of strain gauges on adjacent girders measuring load distribution. 81
Figure 1.54: Diagnostic Test – Transverse strain girders H-1 and H-2, Single Path 1..... 82
Figure 1.55: Diagnostic Test – Transverse strain girders H-2 and H-3, Single Path 1..... 82
Figure 1.56: Diagnostic Test – Transverse strain girders U-1 and U-2, Single Path 1..... 83
Figure 1.57: Diagnostic Test – Transverse strain girders U-2 and U-3, Single Path 1..... 83
Figure 1.58: Girder cross section: Strain profile..... 85
Figure 1.59: Diagnostic Test – Girder U-2, Single Path 1..... 87

Figure 1.60: Diagnostic Test – Girder U-2, Single Path 2. 87
Figure 1.61: Diagnostic Test – Girder U-3, Single Path 1. 88
Figure 1.62: Diagnostic Test – Girder U-3, Single Path 2. 88
Figure 1.63: Diagnostic Test – Girder H-2, Single Path 1. 89
Figure 1.64: Diagnostic Test – Girder H-2, Single Path 2. 89
Figure 1.65: Diagnostic Test – Girder H-3, Single Path 1. 90
Figure 1.66. Diagnostic Test – Girder H-3, Single Path 2. 90
Figure 1.67: PT1: Transverse strain UHPC girders 1 and 2, single path 1. 105
Figure 1.68: PT1: Transverse strain UHPC girders 2 and 3, single path 2. 106
Figure 1.69: PT1: Transverse strain HPC girders 1 and 2, single path 1. 106
Figure 1.70: PT1: Transverse strain HPC girders 2 and 3, single path 2. 107
Figure 1.71: PT1 – Girder U-2, Single Path 1. 109
Figure 1.72: PT1 – Girder U-2, Single Path 2. 109
Figure 1.73: PT1 – Girder U-3, Single Path 1. 110
Figure 1.74: PT1 – Girder U-3, Single Path 2. 110
Figure 1.75: PT1 – Girder H-2, Single Path 1. 111
Figure 1.76: PT1 – Girder H-2, Single Path 2. 111
Figure 1.77: PT1 – Girder H-3, Single Path 1. 112
Figure 1.78: PT1–Girder H-3, Single Path 2. 112
Figure 1.79: Y Displacement of an UHPC beam obtained from ARAMIS. 139
Figure 1.80: Vertical displacement value of a UHPC beam under Single Truck loading on path along a line segments shown in Figure 12 (NOTE: 1 in. = 25.4 mm). 140

Figure 1.81: Displacement versus rear axle placement for an exterior HPC beams for Single Truck loading measured by the HiSpec1 system (NOTE: 1 in. = 25.4 mm). 142
Figure 1.82: Displacement versus centerline location of rear axle placement for an exterior HPC beams for Single Truck Back-To-Back loading measured by the HiSpec1 system (NOTE: 1 in. = 25.4 mm). 143
Figure 1.83: Displacement versus centerline location of rear axle placement for an exterior HPC beams for Triple Truck loading measured by the HiSpec1 system (NOTE: 1 in. = 25.4 mm). 144
Figure 1.84: Displacement versus rear axle placement for an exterior HPC beams for Single Truck loading along Path 1 measured by the GoPro Hero+ system (NOTE: 1 in. = 25.4 mm). 146
Figure 1.85: Displacement versus rear axle placement for an exterior HPC beams for Single Truck loading along Path 2 measured by the GoPro Hero+ system (NOTE: 1 in. = 25.4 mm). 147
Figure 1.86: Displacement versus rear axle placement for an exterior HPC beams for Single Truck loading along Path 3 measured by the GoPro Hero+ system (NOTE: 1 in. = 25.4 mm). 148
Figure 1.87: Comparison of vertical displacement versus rear axle placement for the exterior HPC beams for Single Truck loading along Path 3 (NOTE: 1 in. = 25.4 mm). 149
Figure 1.88: Displacement versus rear axle placement for an exterior UHPC beams for Single Truck loading measured by the IL5 system (NOTE: 1 in. = 25.4 mm). 151
Figure 1.89: Displacement verus rear axle placement for an exterior UHPC beams for Single Truck loading along Path 1 measured by the GoPro Hero 3 system (NOTE: 1 in. = 25.4 mm). 153
Figure 1.90: Displacement versus rear axle placement for an exterior UHPC beams for Single Truck loading along Path 2 measured by the GoPro Hero 3 system (NOTE: 1 in. = 25.4 mm). 154
Figure 1.91: Displacement versus rear axle placement for an exterior UHPC beams for Single Truck loading along Path 3 measured by the GoPro Hero 3 system (NOTE: 1 in. = 25.4 mm). 155

Figure 1.92: Comparison of vertical displacement vs rear axle placement for the exterior HPC beams for Single Truck loading along Path 3 (NOTE: 1 in. = 25.4 mm). 156
Figure 1.93: Comparison of vertical displacement versus rear axle placement for the exterior beams monitored by the IL5 (dashed lines) and HiSpec1 (solid lines) systems under Single Truck loading (NOTE: 1 in. = 25.4 mm), ... 157
Figure 1.94: Displacement versus rear axle placement for an interior UHPC beams for Single Truck loading along paths 1-6 measured by the 2M system (NOTE: 1 in. = 25.4 mm). 158
Figure 1.95: Comparison of vertical displacement versus rear axle placement for beams monitored by the IL5 (solid lines) and 2M (dashed lines) systems under single truck loading (NOTE: 1 in. = 25.4 mm) 160
Figure 1.96: Roctest Ltd. model EM-5 vibrating wire strain gauge 163
Figure 1.97: EM gauges installed (a) in stem above prestressing strands and (b) in flange region 163
Figure 1.98: Roctest Ltd. SM-5 series vibrating wire strain gauges: (a) model SM-5A and (b) model SM-5B with attachable embedment anchors. 164
Figure 1.99: Naming convention used for VWSGs in NM Bridge No. 9706. 164
Figure 1.100: Location of cross-sectional VWSG arrangements in NM Bridge No. 9706. 165
Figure 1.101: Cross-sectional VWSG arrangements. 166
Figure 1.102: VWSG installation schematics for (a) longitudinal and (b) cross-sectional location measurements. 167
Figure 1.103: Protective encasement sequence for SM gauges: (a) gauge and embedment anchors inserted in wood template; (b) application of dense insulating foam; (c) hardened foam encasement; (d) SM gauge foam encasement cut to final shape. 177

Figure 1.104: Installation of encased SM gauges to interior vertical face of girder stem formwork as viewed from (a) above and (b) down the face of the stem. 178
Figure 1.105: Basic wiring schematic for VWSGs in NM Bridge No. 9706. 179
Figure 1.106: Final sensor/equipment installation: (a) Drilling of threaded inserts to support (b) weatherproof enclosures; (c) embedded VWSGs after foam removal and (d) installation of protective PVC channel; (e) view of completed sensor installation and wiring running to (f) Roctest Ltd. RT-MUX 16/32 signal multiplexer. 180
Figure 1.107: Data acquisition equipment for Bridge No. 9706: Weatherproof enclosures housing (a) datalogger with backup power supply and power regulator, and (b) main power supply with solar charge controller..... 181
Figure 1.108:. Cast aluminum pole on cantilever pier extension supporting (a) datalogger and power supply enclosures and (b) solar panels..... 181
Figure 1.109: Concrete core temperatures during curing of UHPC girders for Bridge No. 9706. 183
Figure 1.110: Concrete core temperatures during curing of HPC girders for Bridge No. 9706. 184
Figure 1.111: Frequency data from gauge U-3-EM-M-N beginning at the time of girder casting. 186
Figure 1.112: (a) Tensioned prestressing strands laced through channel girder formwork and (b) cut strands after prestress transfer. 187
Figure 1.113: Prestressing force calculated for gauge U-3-EM-M-N beginning at transfer. 188
Figure 1.114: (a) Auger delivery truck provides concrete to NMSU graduate researchers preparing representative (b) cube, (c) cylinder, and (d) prism specimens during channel girder fabrication for testing material properties..... 193

Figure 1.115: Exterior girder H-8 being crane lifted (a) from casting bed after precast fabrication and (b) placed into position during construction of NM Bridge No. 9706. 200
Figure 1.116: Concrete core temperatures during curing for U-6. 202
Figure 1.117: Concrete core temperatures during curing for U-7. 202
Figure 1.118: VWSG frequency data for U-6 beginning at the time of girder casting..... 203
Figure 1.119: VWSG frequency data for U-7 beginning at the time of girder casting..... 203
Figure 1.120: VWSG prestressing force for U-6 beginning at transfer. 204
Figure 1.121: VWSG prestressing force for U-7 beginning at transfer. 204
Figure 1.122: Concrete core temperatures during curing for U-2. 206
Figure 1.123: Concrete core temperatures during curing for U-5. 206
Figure 1.124: VWSG frequency data for U-2 beginning at the time of girder casting..... 207
Figure 1.125: VWSG frequency data for U-5 beginning at the time of girder casting..... 207
Figure 1.126: VWSG prestressing force for U-2 beginning at transfer. 208
Figure 1.127: VWSG prestressing force for U-5 beginning at transfer. 208
Figure 1.128: Concrete core temperatures during curing for U-1. 211
Figure 1.129: Concrete core temperatures during curing for U-4. 211
Figure 1.130: VWSG frequency data for U-1 beginning at the time of girder casting..... 212
Figure 1.131: VWSG frequency data for U-4 beginning at the time of girder casting..... 212
Figure 1.132: VWSG prestressing force for U-1 beginning at transfer. 213
Figure 1.133: VWSG prestressing force for U-4 beginning at transfer. 213
Figure 1.134: Concrete core temperatures during curing for U-3. 216
Figure 1.135: Concrete core temperatures during curing for U-8. 217
Figure 1.136: VWSG frequency data for U-3 beginning at the time of girder casting..... 217

Figure 1.137: VWSG frequency data for U-8 beginning at the time of girder casting..... 218
Figure 1.138: VWSG prestressing force for U-3 beginning at transfer..... 218
Figure 1.139: VWSG prestressing force for U-8 beginning at transfer..... 219
Figure 1.140: Concrete core temperatures during curing for H-1. 221
Figure 1.141: Concrete core temperatures during curing for H-4. 221
Figure 1.142: VWSG frequency data for H-1 beginning at the time of girder casting..... 222
Figure 1.143: VWSG frequency data for H-4 beginning at the time of girder casting..... 222
Figure 1.144: VWSG prestressing force for H-1 beginning at transfer..... 223
Figure 1.145: VWSG prestressing force for H-4 beginning at transfer..... 223
Figure 1.146: Concrete core temperatures during curing for H-7. 226
Figure 1.147: Concrete core temperatures during curing for H-8. 226
Figure 1.148: VWSG frequency data for H-7 beginning at the time of girder casting..... 227
Figure 1.149: VWSG frequency data for H-8 beginning at the time of girder casting..... 227
Figure 1.150: VWSG prestressing force for H-7 beginning at transfer..... 228
Figure 1.151: VWSG prestressing force for H-8 beginning at transfer..... 228
Figure 1.152: Concrete core temperatures during curing for H-3. 230
Figure 1.153: Concrete core temperatures during curing for H-6. 230
Figure 1.154: VWSG frequency data for H-3 beginning at the time of girder casting..... 231
Figure 1.155: VWSG frequency data for H-6 beginning at the time of girder casting..... 231
Figure 1.156: VWSG prestressing force for H-3 beginning at transfer..... 232
Figure 1.157: VWSG prestressing force for H-6 beginning at transfer..... 232
Figure 1.158: Concrete core temperatures during curing for H-2. 235
Figure 1.159: Concrete core temperatures during curing for H-5. 235

Figure 1.160: VWSG frequency data for H-2 beginning at the time of girder casting..... 236
Figure 1.161: VWSG frequency data for H-5 beginning at the time of girder casting..... 236
Figure 1.162: VWSG prestressing force for H-2 beginning at transfer. 237
Figure 1.163: VWSG prestressing force for H-5 beginning at transfer. 237
Figure 1.164: Sample plot showing the transverse strain profile for the UHPC span during Diagnostic Test under single truck loading for Paths 1-6. 241
Figure 1.165: Sample plot showing selected midspan strains measured for single truck loading during the Diagnostic Test for (a) Path 2 in girders U-3/H-3 and (b) Path 5 for girders U-6/H-6. 242
Figure 1.166: Path 1 single truck loading during field testing of Bridge No. 9706..... 243
Figure 1.167: UHPC and HPC transverse strain profiles for ST load Paths 1-6: Diagnostic Test (a and b) and Proof Test 1 (c and d). 249
Figure 1.168: UHPC and HPC transverse strain profiles for ST load Paths 1-6: Proof Test 2 (a and b) and Proof Test 3 (c and d). 250
Figure 1.169: Comparison of transverse strain profiles of each load test for ST load Paths 1 and 6 for the (a) UHPC span and (b) HPC span. 251
Figure 1.170: Strains for ST loading during DT0 for U-3/H-3 (a) Path 1, (b) Path 2, (c) Path 3, and U-6/H-6 (d) Path 6, (e) Path 5, (f) Path 4..... 252
Figure 1.171: Strains for ST loading during PT1 for U-3/H-3 (a) Path 1, (b) Path 2, (c) Path 3, and U-6/H-6 (d) Path 6, (e) Path 5, (f) Path 4..... 253
Figure 1.172: Strains for ST loading during PT2 for U-3/H-3 (a) Path 1, (b) Path 2, (c) Path 3, and U-6/H-6 (d) Path 6, (e) Path 5, (f) Path 4..... 254

Figure 1.173: Strains for ST loading during PT3 for U-3/H-3 (a) Path 1, (b) Path 2, (c) Path 3, and U-6/H-6 (d) Path 6, (e) Path 5, (f) Path 4..... 255
Figure 1.174: Comparison of strains for girder Lines 3 and 6 under ST loading for DT0 (a and b) and PT1 (c and d). 256
Figure 1.175: Comparison of strains for girder Lines 3 and 6 under ST loading for PT2 (a and b) and PT3 (c and d). 257
Figure 1.176: Double truck loading during field testing of Bridge No. 9706. 258
Figure 1.177: UHPC and HPC transverse strain profiles for DT load Paths 7-8: Diagnostic Test (a and b) and Proof Test 1 (c and d)..... 263
Figure 1.178: UHPC and HPC transverse strain profiles for DT load Paths 7-8 for Proof Test 3. 264
Figure 1.179: Comparison of transverse strain profiles of each load test for DT load Paths 7 and 8 for the (a) UHPC span and (b) HPC span. 265
Figure 1.180: Strains for DT loading during DT0 for U-3/H-3 (a) Path 7, (b) Path 8, (c) Path 9, and U-6/H-6 (d) Path 7, (e) Path 8, (f) Path 9..... 266
Figure 1.181: Strains for DT loading during PT1 for U-3/H-3 (a) Path 7 and (b) Path 8, and U-6/H-6 (c) Path 7 and (d) Path 8. 267
Figure 1.182: Strains for DT loading during PT3 for U-3/H-3 (a) Path 7 and (b) Path 8, and U-6/H-6 (c) Path 7 and (d) Path 8. 268
Figure 1.183: Comparison of strains for girder Lines 3 and 6 under DT loading: DT0 (a and b), PT1 (c and d), and PT3 (e and f)..... 269
Figure 1.184: Path 10 triple truck load configuration during field testing of NM Bridge No. 9706: (a) Aligned prior to loading and (b) positioned over the bridge central pier. 271

Figure 1.185: UHPC and HPC transverse strain profiles for TT load Path 10: Diagnostic Test (a and b) and Proof Test 1 (c and d). 273
Figure 1.186: UHPC and HPC transverse strain profiles for TT load Path 10 for Proof Test 3. 274
Figure 1.187: Comparison of transverse strain profiles of each load test for TT load Path 10 (Pass 2) for the (a) UHPC span and (b) HPC span. 275
Figure 1.188: Strains for TT loading during PT1 for U-3/H-3 Path 10 (a) Pass 1 and (b) Pass 2, and U-6/H-6 Path 10 (c) Pass 1 and (d) Pass 2. 276
Figure 1.189: Strains for TT loading during PT2 for U-3/H-3 Path 10 (a) Pass 1 and (b) Pass 2, and U-6/H-6 Path 10 (c) Pass 1 and (d) Pass 2. 277
Figure 1.190: Strains for TT loading during PT3 for U-3/H-3 Path 10 (a) Pass 1 and (b) Pass 2, and U-6/H-6 Path 10 (c) Pass 1 and (d) Pass 2. 278
Figure 1.191: Comparison of strains for girder Lines 3 and 6 under TT Path 10 (Pass 2) loading: PT1 (a and b), PT2 (c and d), and PT3 (e and f). 279
Figure 1.192: Single truck back-to-back load configuration for field testing of Bridge No. 9706. 280
Figure 1.193: UHPC and HPC transverse strain profiles for STBB load Paths 1-6: Proof Test 1 (a and b) and Proof Test 2 (c and d). 285
Figure 1.194: UHPC and HPC transverse strain profiles for STBB load Paths 1-6 for Proof Test 3. 286
Figure 1.195: Comparison of transverse strain profiles of each load test for STBB load Paths 1-6 for the (a) UHPC span and (b) HPC span. 287
Figure 1.196: Strains for STBB loading during PT1 for U-3/H-3 (a) Path 1, (b) Path 2, (c) Path 3, and U-6/H-6 (d) Path 6, (e) Path 5, (f) Path 4. 288

Figure 1.197: Strains for STBB loading during PT2 for U-3/H-3 (a) Path 1, (b) Path 2, (c) Path 3, and U-6/H-6 (d) Path 6, (e) Path 5, (f) Path 4. 289
Figure 1.198: Strains during PT3 STBB loading for U-3/H-3 (a) Path 1, (b) Path 2, (c) Path 3, and U-6/H-6 (d) Path 6, (e) Path 5, (f) Path 4 290
Figure 1.199: Comparison of strains for girder Lines 3 and 6 under STBB loading: PT1 (a and b), PT2 (c and d), and PT3 (e and f) 291
Figure 1.200: Double truck back-to-back load configuration for field testing of Bridge No. 9706. 292
Figure 1.201: Drone aerial view of NM Bridge No. 9706 field testing: Path 7 DTBB load centered over HPC midspan load station 293
Figure 1.202: Arrangement of trucks during DTBB loading of NM Bridge No. 9706. 294
Figure 1.203: UHPC and HPC transverse strain profiles for DTBB load Paths 7-8: Proof Test 1 (a and b) and Proof Test 2 (c and d) 298
Figure 1.204: UHPC and HPC transverse strain profiles for DTBB load Paths 7-8 for Proof Test 3 299
Figure 1.205: Comparison of transverse strain profiles of each load test for DTBB load Paths 7 and 8 for the (a) UHPC span and (b) HPC span. 300
Figure 1.206: Strains for DTBB loading during PT1 for U-3/H-3 (a) Path 7, (b) Path 8, (c) Path 9, and U-6/H-6 (d) Path 7, (e) Path 8, (f) Path 9. 301
Figure 1.207: Strains for DTBB loading during PT2 for U-3/H-3 (a) Path 7 and (b) Path 8, and U-6/H-6 (c) Path 7 and (d) Path 8. 302
Figure 1.208: Strains during PT3 DTBB loading for U-3/H-3 (a) Path 7 and (b) Path 8, and U-6/H-6 (c) Path 7 and (d) Path 8. 303

Figure 1.209: Comparison of strains for girder Lines 3 and 6 under DTBB loading: PT1 (a and b), PT2 (c and d), and PT3 (e and f)..... 304
Figure 2.1: Bridge cross-section with solid element..... 313
Figure 2.2: Strand locations on the bridge girders..... 314
Figure 2.3: 3-D view of bridge using solid element..... 315
Figure 2.4: Bridge side view and different girder depth..... 316
Figure 2.5: Bridge at Z=0 (bottom elevation)..... 316
Figure 2.6: Bridge at Z=20 in. (508 mm) (top elevation)..... 316
Figure 2.7: Design Truck specifications used for model..... 317
Figure 2.8: UHPC girders comparison for Single Truck moving load Path 1..... 321
Figure 2.9: UHPC girders comparison for Single Truck moving load Path 2..... 321
Figure 2.10: UHPC girders comparison for Single Truck moving load Path 3..... 322
Figure 2.11: UHPC girders comparison for Single Truck moving load Path 6..... 322
Figure 2.12: HPC girders comparison for Single Truck moving load Path 1..... 323
Figure 2.13: HPC girders comparison for Single Truck moving load Path 2..... 323
Figure 2.14: HPC girders comparison for Single Truck moving load Path 3..... 324
Figure 2.15: HPC girders comparison for Single Truck moving load Path 4..... 324
Figure 3.1: UHPC Symposium Save-the-Date Announcement..... 328
Figure 3.2: Pictures from the UHPC Symposium..... 328
Figure 4.1 Slump Flow Test measurements for (a) slump and (b) spread..... 332
Figure 4.2: Batch naming convention for nonproprietary UHPC strength gain studies..... 341
Figure 4.3: Laboratory mixing process for nonproprietary UHPC strength gain studies..... 342

Figure 4.4: Laboratory thermal curing regimen for investigation of nonproprietary UHPC time-dependent strength gain. 348
Figure 4.5: Core temperatures for batch TC13 during initial 24 hours after casting. 350
Figure 4.6: Core temperatures for batch TC14 during initial 24 hours after casting. 350
Figure 4.7: Core temperatures for batch TC15 during initial 24 hours after casting. 351
Figure 4.8: Core temperatures for batch TC13 during 7-day thermal curing regimen. 352
Figure 4.9: Core temperatures for batch TC14 during 7-day thermal curing regimen. 352
Figure 4.10: Core temperatures for batch TC15 during 7-day thermal curing regimen. 353
Figure 4.11: Compressive strength gain of 4.0 in (100 mm) UHPC cube specimens produced using the thermal curing regimen during the first seven days after casting. 356
Figure 4.12: Compressive strengths of 4.0 in (100 mm) UHPC cube specimens produced using thermal curing up to 365 days after casting. 356
Figure 4.13: Modulus of rupture strength gain of UHPC prism specimens produced using the thermal curing regimen during the first seven days after casting. 360
Figure 4.14: Modulus of rupture strengths of UHPC prism specimens produced using thermal curing up to 365 days after casting. 360
Figure 4.15: Modulus of elasticity strengths of UHPC cylinder specimens for the thermal curing regimen up to 365 days after casting. 362
Figure 4.16: Laboratory ambient curing regimen for investigation of nonproprietary UHPC time-dependent strength gain. 391
Figure 4.17: Core temperatures for batch AC6 during initial 24 hours after casting. 393
Figure 4.18: Core temperatures for batch AC7 during initial 24 hours after casting. 393
Figure 4.19: Core temperatures for batch AC9 during initial 24 hours after casting. 394

Figure 4.20: Core temperatures for batch AC10 during initial 24 hours after casting. 394
Figure 4.21: Core temperatures for batch AC6 during 7-day ambient curing regimen. 395
Figure 4.22: Core temperatures for batch AC8 during 7-day ambient curing regimen. 396
Figure 4.23: Core temperatures for batch AC9 during 7-day ambient curing regimen. 396
Figure 4.24: Core temperatures for batch AC10 during 7-day ambient curing regimen. 397
Figure 4.25: Compressive strength gain of 4.0 in (100 mm) UHPC cube specimens produced using the ambient curing regimen during the first seven days after casting. 400
Figure 4.26: Compressive strengths of 4.0 in (100 mm) UHPC cube specimens produced using the ambient curing regimen up to 365 days after casting. 400
Figure 4.27: Modulus of rupture strength gain of UHPC prism specimens produced using the ambient curing regimen during the first seven days after casting. 403
Figure 4.28: Modulus of rupture strengths of UHPC prism specimens produced using ambient curing up to 365 days after casting. 403
Figure 4.29: Modulus of elasticity strengths of UHPC cylinder specimens for the ambient curing regimen up to 365 days after casting. 405
Figure 4.30: Comparison of compressive strength results from 4.0 in (100 mm) UHPC cube specimens for thermal and ambient curing regimens. 426
Figure 4.31: Average compressive strengths from 4.0 in (100 mm) UHPC cube specimens for thermal and ambient curing regimens. 426
Figure 4.32: Compressive strength gain of thermal cured 4.0 in (100 mm) UHPC cube specimens during initial 24 hours after casting from Giesler (2014) initial set study. 428
Figure 4.33: Compressive strength gain of thermal cured 4.0 in (100 mm) UHPC cube specimens during the 7-day thermal curing regimen from Giesler (2014) initial set study. 428

Figure 4.34: Combined results for compressive strength gain of 4.0 in (100 mm) UHPC cube specimens from Giesler (2014) initial set study and TC specimens. 429
Figure 4.35: Compressive strength versus unit weight for 4.0 in. (100 mm) UHPC cube specimens for thermal and ambient curing regimens. 430
Figure 4.36: Comparison of modulus of rupture strength gain of UHPC prism specimens for thermal and ambient curing regimens. 432
Figure 4.37: Average modulus of rupture strength of UHPC prism specimens for thermal and ambient curing regimens. 432
Figure 4.38: UHPC modulus of rupture versus compressive strength for thermal and ambient curing regimens. 433
Figure 4.39: Comparison of modulus of elasticity strength gain of UHPC cylinder specimens for thermal and ambient curing regimens. 435
Figure 4.40: Average modulus of elasticity strength of UHPC cylinder specimens for thermal and ambient curing regimens. 435
Figure 4.41: UHPC modulus of elasticity versus compressive strength for thermal and ambient curing regimens. 436
Figure 4.42: Combined results for compressive strength gain of 4.0 in (100 mm) UHPC cube specimens from Giesler (2014) initial set study and TC specimens versus core temperatures during initial 24 hours after casting. 437
Figure 4.43: Combined results for compressive strength gain of 4.0 in (100 mm) UHPC cube specimens from Giesler (2014) initial set study and TC specimens versus core temperatures during 7-day thermal curing regimen. 438

Figure 4.44: Compressive strength gain of 4.0 in (100 mm) UHPC cube specimens versus core temperatures during 7-day ambient curing regimen. 439
Figure 4.45: Average compressive strength and modulus of rupture results for TC and AC specimens normalized to 7-day target strengths. 440
Figure 4.46: XRD test preparation – (a) crushing and griding; (b) powder collection; (c) electronic mortal and pastel; (d) sample containment. 442
Figure 4.47: Adsorption process and subsequent calculations of BET Testing (Gas Absorption Analysis Brochure, 2001). 445
Figure 4.48: BET Testing - (a) ASAP 2050; (b) test tube filled with sample; 446
Figure 4.49: Direct tension specimens. 449
Figure 4.50: Direct tension dog-bone specimen – (a) dimensions; (b) mold. 450
Figure 4.51: Direct tension specimen being loaded (with extensometer). 451
Figure 5.1 Basic joint geometries. 457
Figure 5.2 Typical NMDOT box girder cross-section. 459
Figure 5.3 Typical NMDOT staggered bar lap detail. 459
Figure 5.4 NMDOT box girder joint lap splice cross section. 460
Figure 5.5 NMDOT box girder joint cross-sections with UHPC (a) before joint grinded flat, (b) after joint grinded down smooth. 460
Figure 5.6 Modified top flange of NMDOT box girder cross-section. 461
Figure 5.7: North view of test setup. 463
Figure 5.8: East view of test setup. 464
Figure 5.9: Top and bottom view of test setup. 465
Figure 5.10: Slab formwork. 468

Figure 5.11: Casting of the slabs..... 469
Figure 5.12: Specimen No. 1 slab prior to casting and curing of the joint. 469
Figure 5.13: View of experimental joint (a) prior to casting and (b) during casting. 470
Figure 5.14: Specimen No. 1 testing setup. 471
Figure 5.15: UHPC prism at failure under flexural test. 474
Figure 5.16: Specimen No. 1- cyclic test load versus vertical deflection (SP 0). 477
Figure 5.17: Specimen No. 1- cyclic test load versus vertical deflection (SP 1). 477
Figure 5.18: Specimen No. 1- cyclic test load versus vertical deflection (SP 2). 478
Figure 5.19: Specimen No. 1- cyclic test load versus vertical deflection (SP 4). 478
Figure 5.20: Specimen No. 1- cyclic test load versus vertical deflection (SP 5). 479
Figure 5.21: Specimen No. 1- cyclic test load versus vertical deflection (SP 7). 479
Figure 5.22: Specimen No. 1- cyclic test load versus transverse deflection (LVDT 2). 480
Figure 5.23: Specimen No. 1- cyclic test load versus transverse deflection (LVDT 3). 480
Figure 5.24: Specimen No. 1- cyclic test load versus transverse deflection (LVDT 4). 481
Figure 5.25: Specimen No. 1- cyclic test load versus transverse deflection (LVDT 5). 481
Figure 5.26: Specimen No. 1- cyclic test load versus transverse deflection (LVDT 6). 482
Figure 5.27: Specimen No. 1- cyclic test load versus transverse deflection (LVDT 7). 482
Figure 5.28: Specimen No. 1- cyclic test load versus transverse deflection (LVDT 8). 483
Figure 5.29: Specimen No. 1- cyclic test load versus transverse deflection (LVDT 9). 483
Figure 5.30: Specimen No. 1- cyclic test load versus rotation (Tiltmeter 1). 484
Figure 5.31: Specimen No. 1- cyclic test load versus rotation (Tiltmeter 2). 484
Figure 5.32: Specimen No. 1- cyclic test load versus rotation (Tiltmeter 4). 485
Figure 5.33: Specimen No. 1- cyclic test load versus rotation (Tiltmeter 5). 485

Figure 5.34: Specimen No. 1- failure test load versus vertical deflection. 487
Figure 5.35: Specimen No. 1- failure test load versus transverse deflection. 488
Figure 5.36: Specimen No. 1- initial separation at bond of joint. 489
Figure 5.37: Specimen No. 1- failure at south face. 489
Figure 5.38: Specimen No. 1- failure at north face 490
Figure 5.39: Specimen No. 2- cyclic test load versus vertical deflection (SP 0). 492
Figure 5.40: Specimen No. 2- cyclic test load versus vertical deflection (SP 1). 492
Figure 5.41: Specimen No. 2- cyclic test load versus vertical deflection (SP 2). 493
Figure 5.42: Specimen No. 2- cyclic test load versus vertical deflection (SP 4). 493
Figure 5.43: Specimen No. 2- cyclic test load versus vertical deflection (SP 5). 494
Figure 5.44: Specimen No. 2- cyclic test load versus vertical deflection (SP 7). 494
Figure 5.45: Specimen No. 2- cyclic test load versus transverse deflection (LVDT 2). 495
Figure 5.46: Specimen No. 2- cyclic test load versus transverse deflection (LVDT 3). 495
Figure 5.47: Specimen No. 2- cyclic test load versus transverse deflection (LVDT 4). 496
Figure 5.48: Specimen No. 2- cyclic test load versus transverse deflection (LVDT 5). 496
Figure 5.49: Specimen No. 2- cyclic test load versus transverse deflection (LVDT 6). 497
Figure 5.50: Specimen No. 2- cyclic test load versus transverse deflection (LVDT 7). 497
Figure 5.51: Specimen No. 2- cyclic test load versus transverse deflection (LVDT 8). 498
Figure 5.52: Specimen No. 2- cyclic test load versus transverse deflection (LVDT 9). 498
Figure 5.53: Specimen No. 1- cyclic test load versus rotation (Tiltmeter 1). 499
Figure 5.54: Specimen No. 1- cyclic test load versus rotation (Tiltmeter 2). 499
Figure 5.55: Specimen No. 1- cyclic test load versus rotation (Tiltmeter 4). 500
Figure 5.56: Specimen No. 1- cyclic test load versus rotation (Tiltmeter 5). 500

Figure 5.57: Specimen No. 2- failure test load versus vertical deflection. 502
Figure 5.58: Specimen No. 2- failure test load versus transverse deflection. 503
Figure 5.59: Specimen No. 2- initial separation at bond of joint 504
Figure 5.60: Specimen No. 2- failure at south face. 504
Figure 5.61: Specimen No. 2- failure at north face 505
Figure 5.62: Specimen No. 3- failure test load versus vertical deflection. 507
Figure 5.63: Specimen No. 3- failure test load versus transverse deflection. 508
Figure 5.64: Specimen No. 3- initial separation at south face bond of joint. 509
Figure 5.65: Specimen No. 3- initial separation at top side bond of joint. 509
Figure 5.66: Specimen No. 3- initial cracking of the slab specimen. 510
Figure 5.67: Specimen No.3- failure at south face. 510
Figure 5.68: Specimen No. 3- failure at north face 511
Figure 5.69: Specimen No. 4- cyclic test load versus vertical deflection (SP 0). 513
Figure 5.70: Specimen No. 4- cyclic test load versus vertical deflection (SP 1). 513
Figure 5.71: Specimen No. 4- cyclic test load versus vertical deflection (SP 2). 514
Figure 5.72: Specimen No. 4- cyclic test load versus vertical deflection (SP 4). 514
Figure 5.73: Specimen No. 4- cyclic test load versus vertical deflection (SP 7). 515
Figure 5.74: Specimen No. 4- cyclic test load versus transverse deflection (LVDT 2). 515
Figure 5.75: Specimen No. 4- cyclic test load versus transverse deflection (LVDT 3). 516
Figure 5.76: Specimen No. 4- cyclic test load versus transverse deflection (LVDT 4). 516
Figure 5.77: Specimen No. 4- cyclic test load versus transverse deflection (LVDT 5). 517
Figure 5.78: Specimen No. 4- cyclic test load versus transverse deflection (LVDT 6). 517
Figure 5.79: Specimen No. 4- cyclic test load versus transverse deflection (LVDT 7). 518

Figure 5.80: Specimen No. 4- cyclic test load versus transverse deflection (LVDT 8). 518

Figure 5.81: Specimen No. 4- cyclic test load versus transverse deflection (LVDT 9). 519

Figure 5.82: Specimen No. 4- failure test load versus vertical deflection. 520

Figure 5.83: Specimen No. 4- failure test load versus transverse deflection..... 521

Figure 5.84: Specimen No. 4- initial separation at bond of joint. 522

Figure 5.85: Specimen No. 4- failure at south face. 522

Figure 5.86: Specimen No. 4- failure at north face..... 523

Figure 5.87: Specimen No. 4- failure of overall system. 523

Figure 5.88: Specimen No. 5- failure test load versus vertical deflection (SP 1). 524

Figure 5.89: Specimen No. 5- self weight cracking at south face. 525

Figure 5.90: Specimen No. 5- self weight cracking at top side. 526

Figure 5.91: Specimen No. 5- failure at south face. 526

Figure 5.92: Specimen No. 5- failure of overall system. 527

Figure 5.93: Specimen No. 6- cyclic test load versus vertical deflection (SP 0)..... 529

Figure 5.94: Specimen No. 6- cyclic test load versus vertical deflection (SP 1)..... 529

Figure 5.95: Specimen No. 6- cyclic test load versus vertical deflection (SP 2)..... 530

Figure 5.96: Specimen No. 6- cyclic test load versus vertical deflection (SP 4)..... 530

Figure 5.97: Specimen No. 6- cyclic test load versus vertical deflection (SP 7)..... 531

Figure 5.98: Specimen No. 6 - cyclic test load versus transverse deflection (LVDT 2). 531

Figure 5.99: Specimen No. 6 - cyclic test load versus transverse deflection (LVDT 3). 532

Figure 5.100: Specimen No. 6 - cyclic test load versus transverse deflection (LVDT 4). 532

Figure 5.101: Specimen No. 6 - cyclic test load versus transverse deflection (LVDT 5). 533

Figure 5.102: Specimen No. 6 - cyclic test load versus transverse deflection (LVDT 6). 533

Figure 5.103: Specimen No. 6 - cyclic test load versus transverse deflection (LVDT 7). 534
Figure 5.104: Specimen No. 6 - cyclic test load versus transverse deflection (LVDT 8). 534
Figure 5.105: Specimen No. 6 - cyclic test load versus transverse deflection (LVDT 9). 535
Figure 5.106: Specimen No. 6- failure test load versus vertical deflection. 536
Figure 5.107: Specimen No. 6- failure test load versus transverse deflection. 537
Figure 5.108: Specimen No. 6- failure at south face 538
Figure 5.109: Bridge 5296 girder cross-section (a) reinforced concrete channel girder cross-section (b) shear key detail. 548
Figure 5.110: Profile view of two-girder system flexural test set-up and instrumentation. 551
Figure 5.111: Plan view of two-girder system flexural test set-up and instrumentation. 552
Figure 5.112: Profile view of single girder system flexural test set-up and instrumentation. 553
Figure 5.113: Plan view of single girder system flexural test set-up and instrumentation. 554
Figure 5.114: Profile view of two- girder system shear test set-up and instrumentation. 556
Figure 5.115: Plan view of two-girder system shear test set-up and instrumentation. 557
Figure 5.116: Profile view of single girder system shear test set-up and instrumentation. 559
Figure 5.117: Plan view of single girder system flexural test set-up and instrumentation. 560
Figure 5.118: Bundle of steel fibers used in UHPC mix design. 562
Figure 5.119: Grouting of shear key with UHPC (a) use of trowel to place UHPC in top opening of shear key, (b) pencil vibrator being used to consolidate UHPC within shear keyway..... 564
Figure 5.120 (AASHTO 2012): Characteristics of HS20 design truck. 565
Figure 5.121: Load versus deflection of east and west girders during ultimate loading. 568
Figure 5.122:Load versus vertical deflection of east and west adjacent girders for CL1 for (a) exterior stem of the east girder and interior stem of the west girder at mid-span, (b) interior stem

of each girder at mid-span, (c) interior stem of each girder at the first quarter point of span, and (c) interior stem of each girder at third quarter point of span. 575
Figure 5.123: Transverse view of vertical deflection of adjacent girders during CL1 at 1.0 kip (4.45 kN) intervals. 576
Figure 5.124: Load versus transverse deflection of shear key joint during CL1 at (a) first quarter point of span, (b) mid-span, and (c) third quarter point of span. 578
Figure 5.125: Load versus vertical deflection of east and west adjacent girders for CL2 for (a) exterior stem of the east girder and interior stem of the west girder at mid-span, (b) interior stem of each girder at mid-span, (c) interior stem of each girder at the first quarter point of span, and (c) interior stem of each girder at third quarter point of span. 580
Figure 5.126: Transverse view of vertical deflection of adjacent girders during CL2 at every 1.0 kip (4.45 kN). 581
Figure 5.127: Load versus transverse deflection of shear key joint during CL2 for (a) first quarter point of span, (b) mid-span, and (c) third quarter point of span. 583
Figure 5.128: Load versus vertical deflection of single girder for CL3 at (a) mid-span, (b) first quarter point of span, and (c) third quarter point of span. 585
Figure 5.129: Load versus vertical deflection of east and west adjacent girders for CL4 for (a) exterior stem of the east girder and interior stem of the west girder at mid-span, (b) interior stem of each girder at mid-span, (c) interior stem of each girder at the first quarter point of span, and (c) interior stem of each girder at third quarter point of span. 587
Figure 5.130: Transverse view of vertical deflection of adjacent girders during CL4 at every 1.0 kip (4.45 kN). 588

Figure 5.131: Load versus transverse deflection of shear key joint during CL4 at (a) first quarter point of span, (b) mid-span, and (c) third quarter point of span. 590
Figure 5.132: Comparison of load versus vertical mid-span deflection of adjacent girders for (a) exterior stem of east girder, (b) interior stem of east girder at mid-span, and (c) interior stem of west girder. 592
Figure 5.133: Transverse view comparison of vertical deflection of adjacent girders during cyclic loading at every 1.0 kip (4.47 kN). 593
Figure 5.134: Comparison of load versus transverse deflection of the shear key during cyclic loading at (a) first quarter point of span, (b) mid-span, and (c) third quarter point of span. 594
Figure 5.135: Load versus vertical deflection of single girder for CL5 at (a) first quarter point of span, (b) midspan and (c) third quarter point of span. 596
Figure 5.136: Load versus rotation of single girder during CL5. 597
Figure 5.137: Load versus deflection of adjacent girders for CL6 for (a) interior stem of each girder at midspan, and (b) exterior stem of each girder at midspan. 599
Figure 5.138: Load versus deflection of adjacent girders for CL6 at (a) interior stem of each girder at first quarter-point of span, and (b) interior stem of each girder at third quarter point of span, and (c) centerline of four-point loading. 600
Figure 5.139: Transverse view of vertical deflection of adjacent girders during CL6 at every 1.0 kip (4.45 kN). 601
Figure 5.140: Load versus transverse deflection of shear key joint during CL6 at (a) first quarter point of span, (b) mid-span, (c) third quarter point of span, and (d) centerline of four-point loading. 603

Figure 5.141: Comparison of load versus vertical deflection of CL5 and CL6 at (a) exterior stem of east girder at midspan, (b) interior stem of east girder at mid-span, (c) interior stem of east girder at first quarter point of span, and (d) interior stem of east girder at third quarter point of span. 605
Figure 5.142: Load versus vertical deflection of east and west adjacent girders for ultimate loading for (a) exterior stem of the east girder and interior stem of the west girder at mid-span, (b) interior stem of each girder at mid-span, (c) interior stem of each girder at the first quarter point of span, and (c) interior stem of each girder at third quarter point of span. 607
Figure 5.143: Transverse view of vertical deflection of adjacent girders during ultimate loading at 5.0 kip (4.45 kN) intervals. 608
Figure 5.144: Load versus vertical deflection of east and west adjacent girders during final 100 cycles for (a) exterior stem of the east girder and interior stem of the west girder at mid-span, (b) interior stem of each girder at mid-span, (c) interior stem of each girder at the first quarter point of span, and (c) interior stem of each girder at third quarter point of span. 609
Figure 5.145: Transverse view of vertical deflection of adjacent girders during final 100 cycles at every 1.0 kip (4.45 kN). 610
Figure 5.146: Load versus transverse deflection of shear key joint during ultimate loading at (a) first quarter point of span, (b) mid-span, and (c) third quarter point of span. 612
Figure 5.147: Load versus transverse deflection of shear key joint during final 100 cycle at (a) first quarter point of span, (b) mid-span, and (c) third quarter point of span. 613
Figure 5.148: Load versus vertical deflection of east and west adjacent girders for ultimate shear loading at (a) interior stem of each girder at midspan and (b) exterior stem of each girder at midspan. 614

Figure 5.149:Load versus deflection behavior of adjacent girders for ultimate shear loading for (a) interior stem of each girder at the first quarter point of span, and (b) interior stem of each girder at third quarter point of span, and (c) centerline of four-point loading. 615
Figure 5.150: Transverse view of vertical deflection of adjacent girders during CL6 at every 10.0 kip (44.5 kN). 616
Figure 5.151: Load versus transverse deflection of shear key joint during ultimate shear loading at (a) first quarter point of span, (b) mid-span, (c) third quarter point of span, and (d) centerline of four-point loading. 618
Figure 5.152: Composite beam design for tests (040919) and (062719). 626
Figure 5.153: Composite beam design for tests (040919) and (062719). 626
Figure 5.154: NSC beam design tested with 24 in. composite beams. 626
Figure 5.155: Composite beam design for tests (080519) and (102419). 626
Figure 5.156: Composite beam design for tests (081219) and (101719). 627
Figure 5.157: Composite beam design for test (082219). 627
Figure 5.158: NSC beam design tested with 30 in. unreinforced composite beams. 627
Figure 5.159: NSC beam design tested with 30 in. reinforced composite beams. 627
Figure 5.160: Instrumentation set up for NSC beams. 628
Figure 5.161: Instrumentation set up for beams with 1 in. of UHPC at the bottom. 629
Figure 5.162: Instrumentation set up for beams with 1 in. of UHPC at the bottom and at the top. 629
Figure 5.163: Test set-up for NSC beams. 630
Figure 5.164: Test set-up for beams with 1in. of UHPC at the bottom. 630
Figure 5.165: Test set-up for beams with 1 in. of UHPC at the bottom and at the top. 631

Figure 5.166: Load vs deflection for plot for tests (040919) – (a) NSC beam, (b) First composite beam, (c) Second composite beam..... 633
Figure 5.167: Load vs deflection for plot for tests (051719) – (a) First composite beam, (b) Second composite beam. 634
Figure 5.168: Load vs deflection for plot for tests (062619) – (a) NSC beam, (b) First composite beam, (c) Second composite beam..... 635
Figure 5.169: Load vs deflection for plot for tests (062719) – (a) NSC beam, (b) First composite beam, (c) Second composite beam..... 636
Figure 5.170: Load vs deflection plot for tests (080519) – (a) NSC beam, (b) First composite beam, (c) Second composite beam. 637
Figure 5.171: Load vs deflection for plot for tests (081219) – (a) NSC beam, (b) First composite beam, (c) Second composite beam..... 638
Figure 5.172: Load vs deflection for plot for tests (082219) – (a) NSC beam, (b) First composite beam, (c) Second composite beam..... 639
Figure 5.173: Load vs deflection plot for tests (101719) – (a) NSC beam, (b) First composite beam, (c) Second composite beam. 640
Figure 5.174: Load vs deflection for plot for tests (102419) – (a) NSC beam, (b) First composite beam, (c) Second composite beam..... 641
Figure 5.175: Photos of comparator measurements for long-term shrinkage procedure..... 649
Figure 5.176: UHPC longer term shrinkage data..... 650
Figure 5.177: Steel tension test on a No. 3 (No. 10) rebar. 651
Figure 5.178: Stress-strain behavior No. 3 (No. 10) rebar..... 653
Figure 5.178: Stress-strain behavior No. 4 (No. 13) rebar..... 653

Figure 5.179: Dataloggers – (a) CR3000 Micrologger®, (b) CR6, and (c) CR6-WIFI. 656
Figure 5.180: Types of sensors – (a) materials used to attached strain gauges; (b) surface preparation of rebar; (c) strain gauge; (d) placing of strain gauges on reinforcement. 657
Figure 5.181: Vibrating Wire Strain Gauges – (a) VWSGs attached to the rebar before reinforcement mesh production: and (b) location of VWSGs at midspan of slab on top and bottom of the rebar. 658
Figure 5.182: Slab design and location of sensors (VWSG and SG). 660
Figure 5.183: Preparation of slabs – (a) formwork and sensors; (b) placement of NSC substrate; (c) final view of slabs after surface finished. 660
Figure 5.184: Texturizing slabs surface – (a) Procedure used with air hammers and (b) final texturized surface. 661
Figure 5.185: Construction of UHPC overlay – (a) saturated surface with exposed aggregates before UHPC application; (b) application of UHPC with workable consistency; (c) surface finished for UHPC deck overlay. 663
Figure 5.186: Strain setup test – (a) materials that were used for the test setup (b) colocation of plastic with grease between the slab and the cubes. 664
Figure 5.187: Construction of UHPC overlay – (a) saturated surface with exposed aggregates before UHPC application; (b) application of UHPC with workable consistency; (c) surface finished for UHPC deck overlay. 666
Figure 5.188: Flexural test setup. 667
Figure 5.189: Flexural test instrumentation plan. 668
Figure 5.190: Location 1 of application of DIC (right side of the slab). 670
Figure 5.191: Location 2 of application of DIC (top face west side). 670

Figure 5.192: Temperature in Las Cruces, NM. 672
Figure 5.193: Temperature changes in Slab 1. 672
Figure 5.194: Temperature changes in Slab 2. 673
Figure 5.195: Temperature changes in Slab 3. 673
Figure 5.196: Temperature changes in Slab 4. 674
Figure 5.197: Temperature changes in Slab 5. 674
Figure 5.198: Temperature changes in Slab 6. 675
Figure 5.199: Temperature changes in Slab 7 675
Figure 5.200: Temperature changes in Slab 8 676
Figure 5.201: Temperature changes in Slab 9 676
Figure 5.202: Strain versus time in Slab 1. 677
Figure 5.203: Strain versus time in Slab 2. 678
Figure 5.204: Strain versus time in Slab 3. 678
Figure 5.205: Strain versus time in Slab 4. 679
Figure 5.206: Strain versus time in Slab 5. 679
Figure 5.207: Strain versus time in Slab 6. 680
Figure 5.208: Strain versus time in Slab 7. 680
Figure 5.209: Strain versus time in Slab 8. 681
Figure 5.210: Strain versus time in Slab 9. 681
Figure 5.211: Average shrinkage versus time for all slabs. 684
Figure 5.212: Strain versus time due to UHPC deck overlay. 685
Figure 5.213: Strain versus time due to UHPC only in Slab 1. 686
Figure 5.214: Strain versus time due to UHPC only in Slab 3. 686

Figure 5.215: Strain versus time due to UHPC only in Slab 4. 687
Figure 5.216: Strain versus time due to UHPC only in Slab 5. 687
Figure 5.217: Strain versus time due to UHPC only in Slab 6. 688
Figure 5.218: Strain versus time due to UHPC only in Slab 7. 688
Figure 5.219: Strain versus time due to UHPC only in Slab 8. 689
Figure 5.220: Strain versus time due to UHPC only in Slab 9. 689
Figure 5.221: Neutral axis height Slab 1. 690
Figure 5.222: Neutral axis height Slab 3. 691
Figure 5.223: Neutral axis height Slab 4. 691
Figure 5.224: Neutral axis height Slab 5. 692
Figure 5.225: Neutral axis height Slab 6. 692
Figure 5.226: Neutral axis height Slab 7. 693
Figure 5.227: Neutral axis height Slab 8. 693
Figure 5.228: Neutral axis height Slab 8. 694
Figure 5.229: Load versus deflection Slab 2. 697
Figure 5.230: Load versus deflection Slab 3. 698
Figure 5.231: Load versus deflection Slab 4 (load applied perpendicular to direction of slope during casting of UHPC). 698
Figure 5.232: Load versus deflection Slab 4 (load applied parallel to direction of slope during casting UHPC). 699
Figure 5.233: Load versus deflection Slab 5. 699
Figure 5.234: Load versus deflection Slab 6. 700
Figure 5.235: Load versus deflection Slab 7. 700

Figure 5.236: Load versus deflection Slab 8. 701
Figure 5.237: Load versus deflection Slab 9. 701
Figure 5.238: Load versus deformation Slab 2. 702
Figure 5.239: Load versus deformation Slab 3. 702
Figure 5.240: Load versus deformation Slab 4 (load applied perpendicular to direction of slope during casting of UHPC). 703
Figure 5.241: Load versus deformation Slab 4 (load applied parallel to direction of slope during casting of UHPC). 703
Figure 5.242: Load versus deformation Slab 5. 704
Figure 5.243: Load versus deformation Slab 6. 704
Figure 5.244: Load versus deformation Slab 7. 705
Figure 5.245: Load versus deformation Slab 8. 705
Figure 5.246: Load versus deformation Slab 9. 706
Figure 5.247: Moment curvature behavior Slab 2. 706
Figure 5.248: Moment curvature behavior Slab 3. 707
Figure 5.249: Moment curvature behavior Slab 4 (load applied perpendicular to direction of slope during casting of UHPC). 707
Figure 5.250: Moment curvature behavior Slab 4 (load applied parallel to direction of slope during casting of UHPC). 708
Figure 5.251: Moment curvature behavior Slab 5. 708
Figure 5.252: Moment curvature behavior Slab 6. 709
Figure 5.253: Moment curvature behavior Slab 7. 709
Figure 5.254: Moment curvature behavior Slab 8. 710

Figure 5.255: Load versus deflection Slab 1. 712
Figure 5.256: Load versus deflection Slab 2. 713
Figure 5.257: Load versus deflection Slab 3. 713
Figure 5.258: Load versus deflection Slab 4. 714
Figure 5.259: Load versus deflection Slab 5. 714
Figure 5.260: Load versus deflection Slab 6. 715
Figure 5.261: Load versus deflection Slab 7. 715
Figure 5.262: Load versus deflection Slab 8. 716
Figure 5.263: Load versus deflection Slab 9. 716
Figure 5.264: Load versus deformation Slab 1. 717
Figure 5.265: Load versus deformation Slab 2. 717
Figure 5.266: Load versus deformation Slab 3. 718
Figure 5.267: Load versus deformation Slab 4. 718
Figure 5.268: Load versus deformation Slab 5. 719
Figure 5.269: Load versus deformation Slab 6. 719
Figure 5.270: Load versus deformation Slab 7. 720
Figure 5.271: Load versus deformation Slab 8. 720
Figure 5.272: Load versus deformation Slab 9. 721
Figure 5.273: Moment curvature behavior Slab 1. 721
Figure 5.274: Moment curvature behavior Slab 2. 722
Figure 5.275: Moment curvature behavior Slab 3. 722
Figure 5.276: Moment curvature behavior Slab 4. 723
Figure 5.277: Moment curvature behavior Slab 5. 723

Figure 5.278: Moment curvature behavior Slab 6. 724

Figure 5.279: Moment curvature behavior Slab 7. 724

Figure 5.280: Moment curvature behavior Slab 8. 725

Figure 5.281: Moment curvature behavior Slab 9. 725

Figure 5.282: Final deformation of Slab 1 – (a) South side view and (b) bottom view. 727

Figure 5.283: Final deformation of Slab 2 – (a) South side view and (b) bottom view. 728

Figure 5.284: Vertical displacements of the top of the slab (9100 lb [40.5 kN]). 729

Figure 5.285: Vertical displacement of the top of the slab (DIC only) 729

Figure 5.286: Bending strains at top of the slab (8900 lb [39.6 kN]). 730

Figure 5.287: Bending Strains in Slab – (a) at 4500 lb (20 kN), (b) at 5000 lb (22 kN), (c) at 5500 lb (24.5 kN), (d) at 6000 lb (26.7 kN) in cycle 1, (e) at 6000 lb (26.7 kN) in cycle 2, (f) at 6000 lb (26.7 kN) in cycle 3, (g) at 6000 lb (26.7 kN) going to failure..... 731

Figure 5.288: Vertical displacement on side of the slab. 732

Figure 5.289: Vertical displacement on side of the slab (DIC only). 732

Figure 5.290: Longitudinal strains on side of slab. 733

Figure 5.291: Displacement of sections along slab edge. 733

TABLES

Table 1.1: Girder Production Schedule for NM Bridge No. 9706. 26

Table 1.2: Schedule of Load Tests Conducted on Bridge No. 9706 41

Table 1.3: Truck Weights for Diagnostic Test of NM Bridge No. 9706 42

Table 1.4: Truck Weights for Proof Test 1of NM Bridge No. 9706 42

Table 1.5: Truck Weights for Proof Test 2 of NM Bridge No. 9706 43

Table 1.6: Truck Weights for Proof Test 3 of NM Bridge No. 9706 43

Table 1.7: UHPC Available Strain Parameters 56

Table 1.8: HPC Available Strain Parameter 57

Table 1.9: Expected Strain with AASHTO Distribution Factors 58

Table 1.10: Expected Strain with Distribution Factor of 1 58

Table 1.11: UHPC Interior Girder – Transformed Moment of Inertia 60

Table 1.12: HPC Exterior Girder – Transformed Moment of Inertia 60

Table 1.13: HPC Interior Girder – Transformed Moment of Inertia 61

Table 1.14: UHPC and HPC Shear Capacity 62

Table 1.15: RISA Live Load Distribution Factors 62

Table 1.16: RISA Live Load Distribution Factors 62

Table 1.17: Camera Systems Used for DIC Monitoring 69

Table 1.18: Maximum Diagnostic Strain: UHPC Single Moving Truck Load 76

Table 1.19: Maximum Diagnostic Strain – HPC Single Moving Truck Load 77

Table 1.20: Maximum Diagnostic Strain – UHPC Double Moving Truck Load 77

Table 1.21: Maximum Diagnostic Strain – HPC Double Moving Truck Load 78

Table 1.22: Maximum Diagnostic Strain – UHPC Single Incremental Truck Load 78

Table 1.23: Maximum Diagnostic Strain – HPC Single Incremental Truck Load 79

Table 1.24: Maximum Diagnostic Strain – UHPC Double Incremental Truck Load 80

Table 1.25: Maximum Diagnostic Strain – HPC Double Incremental Truck Load 80

Table 1.26: Diagnostic Test – UHPC Average Neutral Axis 86

Table 1.27: Diagnostic Test – HPC Average Neutral Axis 86

Table 1.28: Diagnostic Test – Expected Versus Measured Strain 93

Table 1.29: Proof Testing Sequence 96

Table 1.30: PT1: Maximum Strain – UHPC Span Single Moving Truck Load 97

Table 1.31: PT1: Maximum Strain – HPC Span Single Moving Truck Load 98

Table 1.32. Maximum PT1 Strain – UHPC Double Moving Truck Load 98

Table 1.33. Maximum PT1 Strain – HPC Double Moving Truck Load 99

Table 1.34. Maximum PT1 Strain – UHPC Single Incremental Truck Load 99

Table 1.35. Maximum PT1 Strain – HPC Single Incremental Truck Load 100

Table 1.36. Maximum PT1 Strain – UHPC Double Incremental Truck Load 100

Table 1.37. Maximum PT1 Strain – HPC Double Incremental Truck Load 101

Table 1.38. Maximum PT1 Strain – UHPC Triple Incremental Truck Load 101

Table 1.39. Maximum PT1 Strain – HPC Triple Incremental Truck Load 102

Table 1.40. Maximum PT1 Strain – UHPC Single Back-To-Back Incremental Truck Load 102

Table 1.41. Maximum PT1 Strain – HPC Single Back-To-Back Incremental Truck Load 103

Table 1.42. Maximum PT1 Strain – UHPC Double Back-To-Back Incremental Truck Load... 103

Table 1.43. Maximum PT1 strain – HPC Double Back-To-Back Incremental Truck Load 104

Table 1.44: PT1: UHPC Average Neutral Axis 108

Table 1.45: PT1: HPC Average Neutral Axis 108

Table 1.46: PT1 – Expected Versus Measured Strain 116

Table 1.47. Maximum Measured Strains for DT0 and PT1 121

Table 1.48. Overall Maximum Measured Strains for DT0 and PT1 121

Table 1.49. Average Truck Weights for DT0 and PT1..... 122

Table 1.50. DT0 – Induced Moment..... 123

Table 1.51. PT1 – Induced Moment 124

Table 1.52: DT0 and PT1: Average HPC Neutral Axis..... 125

Table 1.53: DT0 and PT1: Average UHPC Neutral Axis..... 126

Table 1.54: DT0 and PT1 – One Lane Loaded Calculated Distribution Factor 127

Table 1.55: DT0 and PT1 – Two Lanes Loaded Calculated Distribution Factors 128

Table 1.56: DT0 and PT1 – Single and Double Back-To-Back Lane Loaded Calculated Distribution Factors 128

Table 1.57: DT0 and PT1 – Three Lanes Loaded Calculated Distribution Factors 129

Table 1.58: PT1 – UHPC Single Moving Truck Load 130

Table 1.59: PT3 Maximum Strain – UHPC Span Single Moving Truck Load 132

Table 1.60: PT3 Maximum Strain – HPC Span Single Moving Truck Load 132

Table 1.61. PT3 Maximum Strain – UHPC Single Incremental Truck Load..... 133

Table 1.62. PT3 Maximum Strain – HPC Single Incremental Truck Load..... 133

Table 1.63: PT3: Maximum Strain – UHPC Single Back-To-Back Incremental Truck Load... 134

Table 1.64: PT3 Maximum Strain – HPC Single Back-To-Back Incremental Truck Load..... 134

Table 1.65. PT3 Maximum Strain – UHPC Double Incremental Truck Load 135

Table 1.66. PT3 Maximum Strain – HPC Double Incremental Truck Load 135

Table 1.67. PT3 Maximum Strain – UHPC Double Back-To-Back Incremental Truck Load... 136

Table 1.68. PT3 Maximum Strain – HPC Double Back-To-Back Incremental Truck Load..... 136

Table 1.69. PT3 Maximum Strain – UHPC Triple Incremental Truck Load 137

Table 1.70. PT3 Maximum Strain – HPC Triple Incremental Truck Load 137

Table 1.71: Numerical Data for Vertical Displacements Corresponding to Figure 1.81 142

Table 1.72: Numerical Data for Vertical Displacements Corresponding to Figure 1.82 143

Table 1.73: Numerical Data for Vertical Displacements Corresponding to Figure 1.83 144

Table 1.74: Numerical Data for Vertical Displacements Corresponding to Figure 1.84 146

Table 1.75: Numerical Data for Vertical Displacements Corresponding to Figure 1.85 147

Table 1.76: Numerical Data for Vertical Displacements Corresponding to Figure 1.86 148

Table 1.77: Numerical data values for the vertical displacements corresponding to Figure 1.87 149

Table 1.78: Numerical Data for Vertical Displacements Corresponding To Figure 1.88 151

Table 1.79: Numerical Data for Vertical Displacements Corresponding To Figure 1.89 153

Table 1.80: Numerical Data for Vertical Displacements Corresponding To Figure 1.90 154

Table 1.81: Numerical Data for Vertical Displacements Corresponding To Figure 1.91 155

Table 1.82: Numerical Data for Vertical Displacements Corresponding To Figure 1.92 156

Table 1.83: Numerical Data for Vertical Displacements Corresponding To Figure 1.93 157

Table 1.84: Numerical Data for Vertical Displacements Corresponding To Figure 1.94(..... 159

Table 1.85: Numerical Data for Vertical Displacements Corresponding To Figure 1.95 161

Table 1.86: VWSGs Location Measurements for Girder U-1 168

Table 1.87: VWSGs Location Measurements for Girder U-2 168

Table 1.88: VWSGs Location Measurements for Girder U-3 169

Table 1.89: VWSGs Location Measurements for Girder U-4 169

Table 1.90: VWSGs Location Measurements for Girder U-5 170
Table 1.91: VWSGs Location Measurements for Girder U-6 170
Table 1.92: VWSGs Location Measurements for Girder U-7 171
Table 1.93: VWSGs Location Measurements for Girder U-8 171
Table 1.94: VWSGs Location Measurements for Girder H-1 172
Table 1.95: VWSGs Location Measurements for Girder H-2 172
Table 1.96: VWSGs Location Measurements for Girder H-3 173
Table 1.97: VWSGs Location Measurements for Girder H-4 173
Table 1.98: VWSGs Location Measurements for Girder H-4 174
Table 1.99: VWSGs Location Measurements for Girder H-6 174
Table 1.100: VWSGs Location Measurements for Girder H-7 175
Table 1.101: VWSGs Location Measurements for Girder H-8 175
Table 1.102: Dates of Casting and Strand Release for NM Bridge No. 9706 Girders 182
Table 1.103: Summary of AASHTO Estimated Prestress Losses for NM Bridge No. 9706 185
Table 1.104: Summary of AASHTO Estimated Prestress Forces for NM Bridge No. 9706 185
Table 1.105: Summary of Initial Prestressing Forces Calculated from Midspan VWSG Data for the Channel Girders of NM Bridge No. 9706 190
Table 1.106: Comparison of AASHTO Estimated Prestress Forces and Measured Prestress Forces from VWSG Data for NM Bridge No. 9706 191
Table 1.107: Summary of Compressive Strength Results for the UHPC Span of NM Bridge No. 9706 195
Table 1.108: Summary of Compressive Strength Results for the HPC Span of NM Bridge No. 9706 195

Table 1.109: Summary of Unit Weight Results for the UHPC Span of NM Bridge No. 9706 .. 197
Table 1.110: Summary of Unit Weight Results for the HPC Span of NM Bridge No. 9706 197
Table 1.111: Summary of Modulus of Rupture Results for UHPC Span of NM Bridge No. 9706 198
Table 1.112: Summary of Modulus of Rupture Results for HPC Span of NM Bridge No. 9706 199
Table 1.113: Compressive Strength Results for Batch UB1 201
Table 1.114: Unit Weight Results for Batch UB1 201
Table 1.115: Initial Prestressing Forces Calculated for Batch UB1 204
Table 1.116: Compressive Strength Results for Batch UB2 205
Table 1.117: Unit Weight Results for Batch UB2 205
Table 1.118: Initial Prestressing Forces Calculated for Batch UB2 209
Table 1.119: Compressive Strength Results for Batch UB3 210
Table 1.120: Unit Weight Results for Batch UB3 210
Table 1.121: Initial Prestressing Forces Calculated for Batch UB3 214
Table 1.122: Compressive Strength Results for Batch UB4 215
Table 1.123: Unit Weight Results for Batch UB4 216
Table 1.124: Initial Prestressing Forces Calculated for Batch UB4 219
Table 1.125: Compressive Strength Results for Batch HB1 220
Table 1.126: Unit Weight Results for Batch HB1 220
Table 1.127: Initial Prestressing Forces Calculated for Batch HB1 224
Table 1.128: Compressive Strength Results for Batch HB2 225
Table 1.129: Unit Weight Results for Batch HB2 225

Table 1.130: Initial Prestressing Forces Calculated for Batch HB2 228
Table 1.131: Compressive Strength Results for Batch HB3..... 229
Table 1.132: Unit Weight Results for Batch HB3 229
Table 1.133: Initial Prestressing Forces Calculated for Batch HB3 233
Table 1.134: Compressive Strength Results for Batch HB4..... 234
Table 1.135: Unit Weight Results for Batch HB4 234
Table 1.136: Initial Prestressing Forces Calculated for Batch HB4 238
Table 1.137: Sample Table Showing Comparisons of Maximum Measured Strains for Single Truck Loading During Diagnostic Test..... 240
Table 1.138: Summary of Maximum Measured Strains Under ST Loading for DT0..... 245
Table 1.139: Summary of Maximum Measured Strains Under ST Loading for PT1..... 246
Table 1.140: Summary of Maximum Measured Strains Under ST Loading for PT2..... 247
Table 1.141: Summary of Maximum Measured Strains Under ST Loading for PT3..... 248
Table 1.142: Summary of Maximum Measured Strains Under DT Loading for DT0 260
Table 1.143: Summary of Maximum Measured Strains Under DT Loading for PT1 261
Table 1.144: Summary of Maximum Measured Strains Under DT Loading for PT3 262
Table 1.145: Summary of Maximum Measured Strains Under TT Loading During Proof Testing. 272
Table 1.146: Summary of Maximum Measured Strains Under STBB Loading for PT1 282
Table 1.147: Summary of Maximum Measured Strains Under STBB Loading for PT2 283
Table 1.148: Summary of Maximum Measured Strains Under STBB Loading for PT3 284
Table 1.149: Summary of Maximum Measured Strains Under DTBB Loading for PT1..... 295
Table 1.150: Summary of Maximum Measured Strains Under DTBB Loading for PT2..... 296

Table 1.151: Summary of Maximum Measured Strains Under DTBB Loading for PT3..... 297

Table 1.152: Comparison of Expected and Measured Strains for Field Testing of NM Bridge No. 9706..... 306

Table 2.1. Path1 Preliminary Results..... 318

Table 2.2. Path 4 Preliminary Results..... 319

Table 2.3. Path 6 Preliminary Results..... 320

Table 4.1: Workability Summary 333

Table 4.2: Compressive Strength Summary 334

Table 4.3: Chemical Admixture Variation Dosages 335

Table 4.4: Compressive Strength Results for Different Chemical Admixtures..... 336

Table 4.5: Results for Varying Steel Fiber Contents 337

Table 4.6: Flexural Strength Results for Increasing Steel Fiber Content 337

Table 4.7: Summarized Results for Use of Polyethylene Fibers 338

Table 4.8: Flexural Strength Results for Ambient Polyethylene Fiber Reinforced UHPC 338

Table 4.9: Summary Results for New USA-Made Steel Fibers (0.15-50/50-1700)..... 339

Table 4.10: Summary Results for New USA-Made Steel Fibers (0.14-50/50-1700)..... 339

Table 4.11: Summary Results for New USA-Made Steel Fibers (0.16-50/50-1700)..... 340

Table 4.12: Summary Results for New USA-Made Steel Fibers (0.145-37.5/62.5-1600)..... 340

Table 4.13: Mixture Proportions for 1.25 ft^3 (0.035 m^3) Batch of Nonproprietary UHPC 341

Table 4.14: Summary of Compressive Strength Results for UHPC Produced Using Thermal Curing 355

Table 4.15: Summary of Unit Weight Results for UHPC Produced Using Thermal Curing 357

Table 4.16: Summary of Modulus of Rupture Results for UHPC Produced Using Thermal Curing 359
Table 4.17: Summary of Modulus of Elasticity Results for UHPC Produced Using Thermal Curing 361
Table 4.18: Unit Weight Results for Batch TC1 363
Table 4.19: Compressive Strength Results for Batch TC1 363
Table 4.20: Modulus of Rupture Results for Batch TC1 364
Table 4.21: Unit Weight Results for Batch TC2 365
Table 4.22: Compressive Strength Results for Batch TC2 365
Table 4.23: Modulus of Rupture Results for Batch TC2 365
Table 4.24: Unit Weight Results for Batch TC3 366
Table 4.25: Compressive Strength Results for Batch TC3 366
Table 4.26: Modulus of Rupture Results for Batch TC3 366
Table 4.27: Unit Weight Results for Batch TC4 367
Table 4.28: Compressive Strength Results for Batch TC4 367
Table 4.29: Modulus of Rupture Results for Batch TC4 368
Table 4.30: Unit Weight Results for Batch TC5 369
Table 4.31: Compressive Strength Results for Batch TC5 369
Table 4.32: Modulus of Rupture Results for Batch TC5 370
Table 4.33: Unit Weight Results for Batch TC6 371
Table 4.34: Compressive Strength Results for Batch TC6 371
Table 4.35: Modulus of Rupture Results for Batch TC6 372
Table 4.36: Unit Weight Results for Batch TC7 373

Table 4.37: Compressive Strength Results for Batch TC7 373
Table 4.38: Modulus of Rupture Results for Batch TC7 374
Table 4.39: Unit Weight Results for Batch TC8 375
Table 4.40: Compressive Strength Results for Batch TC8 375
Table 4.41: Modulus of Rupture Results for Batch TC8 376
Table 4.42: Unit Weight Results for Batch TC9 377
Table 4.43: Compressive Strength Results for Batch TC9 377
Table 4.44: Modulus of Rupture Results for Batch TC9 378
Table 4.45: Unit Weight Results for Batch TC10 379
Table 4.46: Compressive Strength Results for Batch TC10 379
Table 4.47: Modulus of Rupture Results for Batch TC10 380
Table 4.48: Unit Weight Results for Batch TC11 381
Table 4.49: Compressive Strength Results for Batch TC11 381
Table 4.50: Modulus of Rupture Results for Batch TC11 382
Table 4.51: Unit Weight Results for Batch TC12 383
Table 4.52: Compressive Strength Results for Batch TC12 383
Table 4.53: Modulus of Rupture Results for Batch TC12 384
Table 4.54: Unit Weight Results for Batch TC13 385
Table 4.55: Compressive Strength Results for Batch TC13 385
Table 4.56: Modulus of Rupture Results for Batch TC13 386
Table 4.57: Unit Weight Results for Batch TC14 387
Table 4.58: Compressive Strength Results for Batch TC14 387
Table 4.59: Modulus of Elasticity Results for Batch TC14 388

Table 4.60: Unit Weight Results for Batch TC15 389
Table 4.61: Compressive Strength Results for Batch TC15 389
Table 4.62: Modulus of Elasticity Results for Batch TC15 390
Table 4.63: Summary of Compressive Strength Results for UHPC Produced Using Ambient Curing 399
Table 4.64: Summary of Unit Weight Results for UHPC Produced Using Ambient Curing 401
Table 4.65: Summary of Modulus of Rupture Results for UHPC Produced Using Ambient Curing 402
Table 4.66: Summary of Modulus of Elasticity Results for UHPC Produced Using Ambient Curing 404
Table 4.67: Unit Weight Results for Batch AC1 406
Table 4.68: Compressive Strength Results for Batch AC1 406
Table 4.69: Modulus of Rupture Results for Batch AC1 407
Table 4.70: Unit Weight Results for Batch AC2 408
Table 4.71: Compressive Strength Results for Batch AC2 408
Table 4.72: Modulus of Rupture Results for Batch AC2 408
Table 4.73: Unit Weight Results for Batch AC3 409
Table 4.74: Compressive Strength Results for Batch AC3 409
Table 4.75: Modulus of Rupture Results for Batch AC3 410
Table 4.76: Unit Weight Results for Batch AC4 411
Table 4.77: Compressive Strength Results for Batch AC4 411
Table 4.78: Modulus of Rupture Results for Batch AC4 412
Table 4.79: Unit Weight Results for Batch AC5 413

Table 4.80: Compressive Strength Results for Batch AC5 413
Table 4.81: Modulus of Rupture Results for Batch AC5 414
Table 4.82: Unit Weight Results for Batch AC6 415
Table 4.83: Compressive Strength Results for Batch AC6 415
Table 4.84: Modulus of Rupture Results for Batch AC6 416
Table 4.85: Unit Weight Results for Batch AC7 417
Table 4.86: Compressive Strength Results for Batch AC7 417
Table 4.87: Modulus of Rupture Results for Batch AC7 418
Table 4.88: Unit Weight Results for Batch AC8 419
Table 4.89: Compressive Strength Results for Batch AC8 419
Table 4.90: Modulus of Rupture Results for Batch AC8 420
Table 4.91: Unit Weight Results for Batch AC9 421
Table 4.92: Compressive Strength Results for Batch AC9 421
Table 4.93: Modulus of Elasticity Results for Batch AC9 422
Table 4.94: Unit Weight Results for Batch AC10 423
Table 4.95: Compressive Strength Results for Batch AC10 423
Table 4.96: Modulus of Elasticity Results for Batch AC10 424
Table 4.97: Preliminary UHPC Mix Proportions (Yields 1 ft^3) 448
Table 4.98: Preliminary Direct Tension Results 452
Table 5.1: Chemical and Physical Properties of Cementitious Material (Alvarez, 2019). 466
Table 5.2: UHPC Mixture Proportions 467
Table 5.3: Comparison of Average Compressive Strengths for Full-Scale Specimens (NWC) 472
Table 5.4: Comparison of Average Compressive Strengths for Joint Specimens (UHPC) 472

Table 5.5: Comparison of Average Compressive Strengths for Joint Specimens (Non-Shrink Grout) 473
Table 5.6: Flexural Strengths for Joint Specimens (UHPC) 474
Table 5.7: Cyclic Test Measured Data Summary. 540
Table 5.8: Failure Test Measured Data Summary. 542
Table 5.9: Nonproprietary UHPC Mix Design 561
Table 5.10: US Spec NA non-shrink grout mixture proportions 561
Table 5.11: Summary of Deflection Criteria for Cyclic Loading 566
Table 5.12: Load criteria for shear testing 569
Table 5.13: Compressive strength results for UHPC and US Spec NA 571
Table 5.14: Average compressive strengths of UHPC and US Spec NA 572
Table 5.15: Modulus of elasticity results of UHPC and US Spec NA 572
Table 5.16: Moment Distribution Factors of CL1, CL2, and CL4 619
Table 5.17: Change In Moment Distribution Factors for CL1, CL2 and CL4 Between Cycle 1 and Cycle 100 619
Table 5.18: Summary of Maximum Load-Deflection Behavior for Adjacent Girders 621
Table 5.19 Ultra High Performance Concrete Mixture Proportions 624
Table 5.20 Normal Strength Concrete Mixture Proportions 624
Table 5.21 Mixture Proportions of UHPC with 1.5% of Steel Fibers 644
Table 5.22 Mixture Proportions of UHPC with 2.0% of Steel Fibers 644
Table 5.23 Mixture Proportions of UHPC with 3.0% of Steel Fibers 644
Table 5.24 Mixture Proportions of NSC 645
Table 5.25 Compressive Strengths of NSC and UHPC Specimens 646

Table 5.26 Modulus of Elasticity for NSC and UHPC Specimens..... 647

Table 5.27 Flexural performance and modulus of rupture for NSC and UHPC specimens..... 648

Table 5.28 Stress-strain behavior steel reinforcement..... 652

Table 5.29 Characteristics of Specimens..... 654

Table 5.30 Results of Macrotexture Depth Using Volumetric Technique 662

Table 5.31 Shear Stress Range at Interface 695

UNITS & CONVERSIONS

US CUSTOMARY					SI
LENGTH					
inches	1 in	=	25.4	mm	millimeters
feet	1 ft	=	0.3048	m	meters
yards	1 yd	=	0.914	m	meters
AREA					
square inches	1 $in.^2$	=	645.2	mm^2	square millimeters
square inches	1 ft^2	=	0.0929	m^2	square meters
VOLUME					
fluid ounces	1 fl oz	=	29.57	mL	milliliters
gallons	1 gal	=	3.785	L	liters
cubic feet	1 ft^3	=	0.028	m^3	cubic meters
cubic yards	1 yd^3	=	0.765	m^3	cubic meters
MASS					
ounces	1 oz	=	28.35	g	grams
pound (mass)	1 lb	=	0.454	kg	kilograms
FORCE OR STRESS					
pound (force)	1 lb	=	4.45	N	newtons
kilopound (force)	1 kip, k	=	4.45	kN	kilonewtons
pounds per square inch	1 psi	=	0.00689	MPa	megapascals
kilopounds per square inch	1 ksi	=	6.89	MPa	megapascals
			0.00689	GPa	gigapascal
TEMPERATURE					
Fahrenheit (°F)	T(°*C*)	=	[T(°*F*) – 32] ÷ 1.8		Celsius (°C)
	T(°*F*)	=	1.8T(°*C*) + 32		
ADDITIONAL CONVERSIONS					
kilopound (force)-feet	1 kip-ft	=	1.3558	kN-m	kilonewton-meters
kilopounds (force) per feet	1 kips/ft	=	0.0138	kg/m	kilograms per meter
pound (mass) per cubic feet	1 lb/ft^3	=	16.02	kg/m^3	kilograms per cubic meter
pound (mass) per cubic yard	1 lb/yd^3	=	0.593	kg/m^3	kilograms per cubic meter
gallons per cubic yard	1 gal/yd^3	=	4.95	L/m^3	liters per cubic meter

ounces per cubic yard	1 oz/yd^3	=	0.03868	L/m^3	liters per cubic meter
radians per inch	1 rad/in.	=	0.03937	rad/mm	radians/mm

NOTE: Conversion factors are often approximate.
(SI) International System of Units

THIS PAGE INTENTIONALLY LEFT BLANK

LAYOUT OF REPORT

This report covers the fourth phase of research conducted for the New Mexico Department of Transportation, Transportation Research Bureau investigating the use of Ultra High Performance Concrete (UHPC) in prestressed concrete bridge design. This report is broken into the following parts: (1) Introduction and Background; (2) Task 1: Monitoring of Bridge 9706; (3) Task 2: Bridge Analytical Model; (4) Task 3: UHPC Symposium; (5) Task 4: Mixture Proportion Optimization; (6) Task 5: Potential Additional Uses of UHPC; and (7) Task 6: Field Implementation Studies.

THIS PAGE INTETIONALLY LEFT BLANK

INTRODUCTION AND BACKGROUND

Ultra High Performance Concrete (UHPC) is a material that exhibits exceptional strength and durability properties that have led to its use in a variety of structural applications. The dense microstructure of UHPC is achieved through an optimized packing density resulting in a material that is nearly impermeable and very strong in compression. High strength steel fibers are added to provide ductility to the material. The high strength of the material makes it possible to reduce the member size and/or the number of members in a design. UHPC also has excellent durability properties, and, in the form of prestressed bridge components, it has been projected to have a design life of up to 180 years (Ahlborn et al. 2008a). All these factors lead to lower project costs associated with labor, material quantities, and replacement and/or repairs.

In Phase I of this project, the feasibility of incorporating UHPC into bridge design was evaluated (Taylor et al. 2013, Weldon et al. 2012). Two existing bridges in Southern New Mexico were chosen to be evaluated by redesigning the bridges with UHPC. Three bridge configurations were evaluated in the study: single span, two-span continuous, and three-span continuous structures. All of the existing bridges were designed and constructed using High Performance Concrete [HPC, 9500 psi (65.5 MPa)] girders and followed the American Association of State Highway and Transportation Officials (AASHTO) Standard Specification. Modified Load Factor Design and Load Resistance Factor Design procedures were used to redesign the existing bridges with UHPC by considering the compressive strength, modulus of rupture, and modulus of elasticity of UHPC. These redesigned UHPC bridges were then compared to the existing designs to evaluate the benefits of using the new material (Weldon et al. 2012). It was shown that the use of UHPC in bridge design could lead to smaller girder sizes and fewer girder lines. This, in addition to the exceptional durability of UHPC, could lead to bridge designs that utilize less material and have a longer lifespan than current designs. Overall, UHPC presents many benefits for use in the structural engineering spectrum, particularly in bridge design. When compared with a typical bridge design using conventional concrete, material quantities are reduced, construction time is saved, and a more durable, longer lasting design is achieved. Despite the many advantages of UHPC, widespread implementation in the United States has been slow due to a lack of design code provisions, high material costs, and lack of industry familiarization with the material.

UHPC provides many advanced properties that make it a desirable construction material for a variety of applications. These benefits, however, come at a relatively high cost when compared with conventional concrete. Commercially available UHPC products typically use high quality constituents that drive up the cost of the material. Furthermore, these products have to be shipped long distances further increasing the cost. In Phase II of this project, UHPC mixture proportions using local materials were developed at NMSU (Weldon et al. 2012). This mixture utilizes a 0.14 water-to-cementitious material ratio, locally obtained sand, and Class F fly ash. A locally available Type I/II cement and commercially available silica fume, High Range Water Reducing Admixture (HRWRA), and steel fibers are used. To implement this material in practice,

it was necessary to provide recommendations that incorporate the advanced qualities of UHPC in design, which was the focus of Phase III.

In Phase III of this study, the creep and shrinkage of UHPC using material local to New Mexico was investigated. Before UHPC was incorporated into prestressed concrete girders in New Mexico, it was necessary to have a fundamental understanding of the creep and shrinkage behavior of the UHPC mixture developed using local materials. Due to the removal of large aggregate and a heated curing regimen, the shrinkage and creep behavior is different than normal or high strength concretes. Additionally, due to the strict mixing and curing procedures and mixture proportions required to achieve the enhanced properties of UHPC, an approved Special Provision for Prestressed Concrete Members Using Fiber Reinforced Ultra High Performance Concrete Section 518-C was developed for the production of the girders for Bridge 9706.

To ensure the behavior of UHPC in structural design, two full-scale prestressed concrete girder specimens were cast, cured, and tested in flexure. One girder was design with HPC and the second with UHPC. Both girders were tested in longitudinal and transverse flexure. The results from these tests provided an experimental background for the implementation of this material. The results from these tests demonstrated the superior behavior of UHPC compared with HPC. Through the mixing, casting, and curing of these girders, UHPC was successfully implemented in a local precast facility with no modifications to current practices.

Finally, in Phase III, in collaboration with the Technical Panel, an instrumentation and data acquisition plans for the collection of information necessary to evaluate the performance of UHPC and HPC in the field was developed. The instrumentation will be used during the current phase (Phase IV) and potential subsequent phases to conduct short and long term studies on the behavior and performance of the bridge. The instrumentation and data acquisition plans were developed to perform a comparative study between HPC and UHPC and be used to investigate the long term performance of the bridge. During Phase III, all embedded instrumentation, including vibrating wire strain gauges and fiber optic sensors, were installed during the casting of the bridge girders. During the first quarter of Phase IV, Bridge 9706 was constructed in Anthony, NM and currently all sensors have been placed in the field. The diagnostic load test was conducted on March 30, 2017 and proof load test is tentatively planned for October 2017.

Phase IV will continue to investigate the behavior of UHPC and explore new applications for the use of the advanced material. The following six tasks have been identified for Phase IV of this research project:

Task 1: Monitoring of Bridge 9706

Following the construction of Bridge 9706, a diagnostic and proof load test will be conducted on the bridge. This information will serve to establish the baseline behavior of the bridge. To monitor the behavior and durability properties of the bridge, load tests will be conducted approximately 1 year following the initial load test and again approximately 3 years from the initial load test. The data collected will provide information related to the performance of the UHPC and HPC spans (for purposes of comparison), and additional data for the lifecycle cost analysis. Data will be collected using the internal and embedded sensors, supplemented by external additional gauges. During the load tests of Bridge 9706, the NMSU research team will require support from the NMDOT District 1 Office in the form of traffic control and/or bridge access equipment (e.g., man lifts, working platforms). NMDOT will provide access to the bridges, traffic control, and weighted trucks as needed for each bridge.

Data will be collected from the bridge instrumentation system approximately once a quarter. The data will be used for the continuous monitoring of Bridge 9706 and aid in the development of analytical models (Task 2). Additionally, the system will be examined for proper working conditions and maintained and repaired as needed (within budget constraints) during the site visits.

Task 2: Bridge 9706 Analytical Model

Based on the collected data from the load tests, an analytical model of Bridge 9706 will be developed. The analytical model will be used to investigate the behavior of the bridge under various loading scenarios that will help to improve design, construction, and evaluation procedures. It will also be used to identify important changes in behavior over time.

Task 3: UHPC Symposium

A symposium will be arranged to help provide additional information to researchers, design engineers, and precasters on the use of UHPC in design and construction. The Transportation Engineering Conference and/or Pavement Engineering Conference will be target venues for the symposium to disseminate information to a wide and diverse audience. A site visit to Bridge 9706 will be arranged for interested parties as well as a hands-on demonstration of UHPC.

Task 4: Mixture Proportion Optimization

The mixture proportions will be continued to be optimized for ingredients, curing, and different uses. New technologies (e.g., admixtures) have become available that could be introduced into the mixture proportions to improve strengths and durability while reducing the heating curing and / or the curing duration. Furthermore, as new uses of UHPC become apparent, the effect of different material constituents on the mixture proportions and how to optimize them for performance, economy, and casting / curing methods will be investigated.

Task 5: Identify Potential Additional Uses of UHPC

Working with the Technical Panel, additional uses of UHPC for the State will be identified. Uses such as cast-in-place field joints, precast applications (e.g., deck panels), substructures, and deck overlays will be investigated. Additionally, new applications for the use of UHPC in the rehabilitation of bridges will be studied.

Task 6: Field Implementation Studies

Laboratory and field studies on the potential uses of cast-in-place UHPC will be conducted to determine strength and durability properties, best practices for mixing and placing, and curing requirements. Investigations on the material properties and durability properties of UHPC with and without the steam and dry heat curing regimen will be conducted. Working with ready mix companies, field application studies and large-scale batching of UHPC will be examined for cast-in-place applications.

i. Measured Material Properties and General Testing Procedures

i.i Compressive Strength

Evaluation of compressive strength was primarily conducted according to British Standards Institution (BSI) specification BS 1881 Part 116 using 4.0 in. (100 mm) cube specimens (BSI, 1983). The use of cube specimens was due to the much larger compressive strengths exhibited by UHPC and to avoid difficult end preparation for cylinder specimens. First, the use of unbonded neoprene end caps as specified by ASTM C1231 (2015) is limited to lower strength concretes. Similarly, sulfur capping as specified by ASTM C617 (2015) is ineffective for expected compressive strengths upwards of 18 ksi (124 MPa). End grinding, though effective for UHPC, is a time-consuming process and requires specialized equipment. Cube specimens eliminate the need for specimen end preparation. Furthermore, 4.0 in. (100 mm) cube specimens have been shown to exhibit highly comparable strengths to 3.0 in. (76 mm) and 4.0 in. (102 mm) diameter cylinder specimens (Graybeal, 2015).

To measure compressive strength, cube specimens were placed between high-yield steel auxiliary platens to evenly distribute load. The auxiliary platens were lightly oiled to reduce lateral confinement and load was applied using a 1000-kip (4450 kN) capacity compression machine (Figure 1.1). Due to the much higher compressive strengths exhibited by UHPC, an increased load rate of 9000 psi/min (62.0 MPa/min), shown to provide accurate results for UHPCs while avoiding extended testing times (Graybeal, 2015), was employed for all compressive strength samples. It is noted that the nominal 4.0 in. dimension of the cubes, expressed herein for simplicity, corresponds to 101.6 mm. The cube specimen molds are designed for testing according to British Standards using the nominal dimension of 100 mm, or 3.937 in. However, the area of the cube specimens was calculated using the 4.0 in. (101.6 mm) nominal dimension, thus providing a conservative calculation of compressive strength.

When using cylinder specimens, testing was conducted according to ASTM C39 (2018). Cylinder specimen sizes were limited to nominal diameter to length measurements 4.0 x 8.0 in. (100 x 203 mm). UHPC cylinder specimens were prepared by fixed-end grinding and tested using the increased load rate of 9000 psi/min (62.0 MPa/min) previously described from Graybeal (2015). Non-UHPC specimens were equipped with unbonded neoprene end caps and tested at the standard load rate of 2100 psi/min (14.5 MPa/min) specified by ASTM C39 (2018).



Figure 1.1: A 4.0 in. (100 mm) UHPC cube specimen prior to testing using a 1000-kip (4450 kN) capacity compression machine.

i.ii Unit Weight

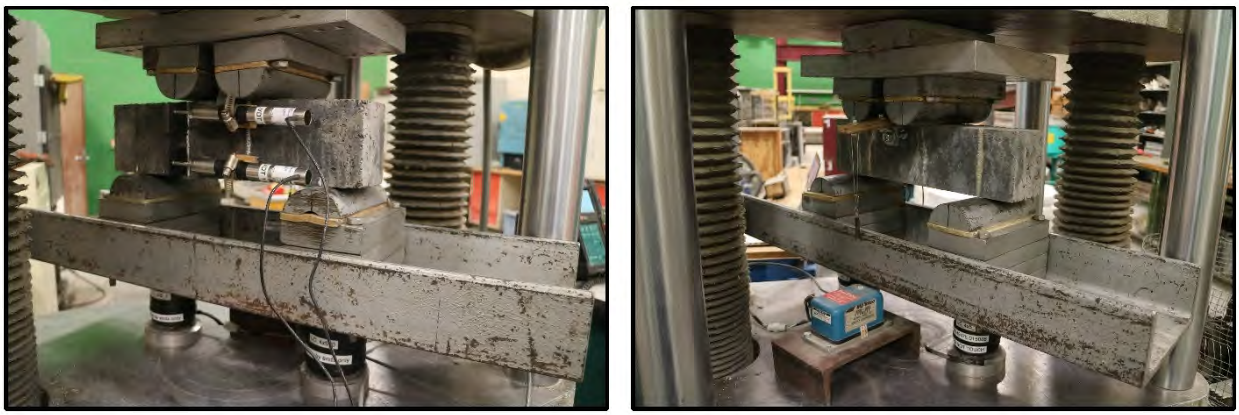
The unit weight of UHPC for the research presented in this document was quantified using 4.0 in. (100 mm) cube specimens produced for evaluation of compressive strength. Specimens were weighed immediately prior to testing (Figure 1.2), and the weight divided by the nominal volume of the specimen mold. It is noted that the nominal 4.0 in. dimension of the cubes, expressed herein for simplicity, corresponds to 101.6 mm. The cube specimen molds were designed for testing according to British Standards using the nominal dimension of 100 mm, or 3.937 in. So as not to underestimate the unit weight of the specimens, the value 3.937 in. (100 mm) was used for the calculation of nominal specimen volume.



Figure 1.2: Weighing a 4.0 in. (100 mm) UHPC cube specimen for calculation of unit weight.

i.iii Modulus of Rupture

Evaluation of modulus of rupture strength, defined herein as the flexural stress corresponding to first cracking, was accomplished by testing small-scale beam specimens in four-point bending based on ASTM C1609 (2019; Figure 1.3 and Figure 1.4). Specimens were 16 in. (406 mm) in length, with a 3 x 4 in. (76 x 102 mm) cross section. The beam rests on two semi-circular end supports located 2.0 in. (51 mm) from each end of the beam, resulting in a 12.0 in. (305 mm) clear span. The two load points were spaced 4.0 in. (102 mm) apart and equidistant from beam midspan, creating a pure moment region. Load cells centered below each end support capture applied force. Vertical deflection was measured by a string potentiometer attached at midspan to a removeable yoke. Two linear variable differential transformers (LVDTs) were fixed to the vertical face of the beam with the point of rotation centered below one load point. Reaction supports (steel angles) were fixed directly below the opposite load point, creating a 4.0 in. (102 mm) gauge length between the load points. The LVDTs recorded the compressive and tensile deformations induced by bending, facilitating the calculation of beam curvature. The occurrence of first cracking was identified by analysis of LVDT deformation data.



(a) (b)

Figure 1.3: Photos showing (a) front view and (b) back view of the modulus of rupture test setup.

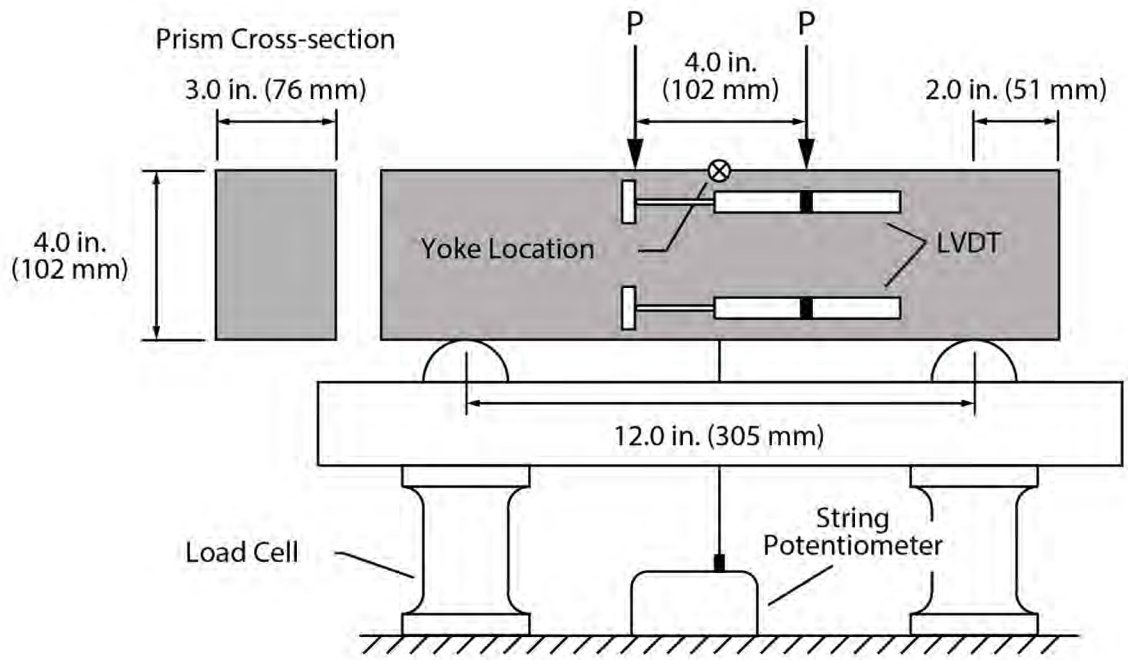


Figure 1.4: Four-point bending test setup for small-scale modulus of rupture beam specimens

i.iv Modulus of Elasticity

Modulus of elasticity (Young's modulus) is the mechanical property that characterizes the linear-elastic relationship between stress and strain prior to inelastic behavior and is important in avoiding permanent deformation while achieving serviceability and economy in design. Evaluation of the modulus of elasticity was performed according to ASTM C469 (2014) using cylinder specimens with nominal diameter to length measurements of 4.0 x 8.0 in. (102 x 203 mm). Specimens were fit with a standard unbonded three-yoke combination compressometer/extensometer and tested using a 1000-kip (4450 kN) capacity compression machine. Vertical and lateral deformations were measured using digital indicator gauges accurate to 0.00005 in. (0.00127 mm). Due to the much higher compressive strengths exhibited by UHPC, an increased load rate of 9000 psi/min (62.0 MPa/min), shown to provide accurate results for UHPCs while avoiding extended testing times (Graybeal 2006b, 2015), was employed for all modulus of elasticity samples.

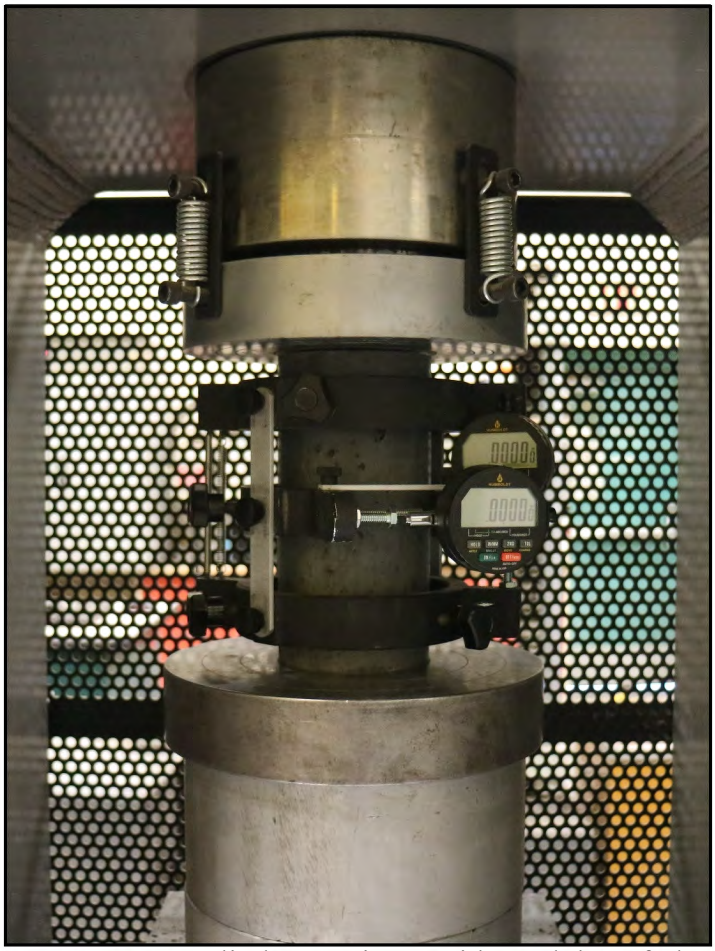


Figure 1.5: UHPC cylinder specimen with modulus of elasticity testing apparatus (prior to testing).

THIS PAGE INTETIONALLY LEFT BLANK

Task 1: Monitoring of Bridge 9706

TASK 1: MONITORING OF BRIDGE 9706

Research programs at NMSU regarding the development and implementation of nonproprietary UHPC recently culminated in the first deployment of UHPC for New Mexico highway infrastructure. Successfully completed in March 2017, NM Bridge No. 9706 replaced the structurally deficient Bridge No. 5296 along State Road 186 (or NM 186; also known as West Ohara Road) crossing the La Union Main Canal in Anthony, NM (Figure 1.6). The bridge superstructure was designed to incorporate one span using high performance concrete [HPC, 9.5 ksi (66.0 MPa)] typical of current NM bridge design, and the second span using the nonproprietary UHPC [21.0 ksi (145 MPa)] developed with local materials and high-strength steel fibers. Embedded thermal and strain-based instrumentation were installed in each girder prior to casting, facilitating direct comparative analyses of the two types of concrete.

As one of the main objectives of the research programs at NMSU regarding nonproprietary UHPC, monitoring and field testing of NM Bridge No. 9706 was conducted to quantify the response of the structure under a variety of load conditions and evaluate the comparative behavior and performance of the two spans. The following subsections provide an overview of the design and construction of NM Bridge No. 9706.

1.1 NM Bridge No. 9706

1.1.1 Bridge Design

The superstructure of New Mexico Bridge No. 9706 consists of two 25.0 ft (7.62 m) simply supported spans. As detailed in Figure 1.7, eight precast-prestressed concrete channel girders per span, oriented at an 18° skew, support two design lanes and provide a rail-to-rail width of 30.0 ft (9.14 m) [32.0 ft (9.75 m) out-to-out]. The east span was designed with high performance concrete [HPC; 9.5 ksi (66.0 MPa)] typical of current NM bridge designs and mild steel reinforcement. The west span was designed with the nonproprietary UHPC [21.0 ksi (145 MPa)] mixture proportions developed at NMSU consisting of primarily of local materials and high-strength steel fibers. Girders were post-tensioned through adjacent stems at midspan with high-strength threaded steel rods and shear keyways filled with 5.0 ksi (35 MPa) non-shrink grout. A 5.0 in. (127 mm) cast-in-place concrete deck [4.0 ksi (28.0 MPa)] reinforced with a single mat of No. 5 (No. 16) mild steel bars would serve as the riding surface. The substructure consisted of cast-in-place abutment caps with wingwalls and a central pier, each supported by five concrete-filled driven pipe piles, providing a 2% transverse grade from the peak at centerline of the roadway and a stepped pier cap designed to accommodate the necessary elevation of each span based on girder depth.



Figure 1.6: NM Bridge No. 9706 crossing the La Union Main Canal, State Road 186, Anthony, NM.

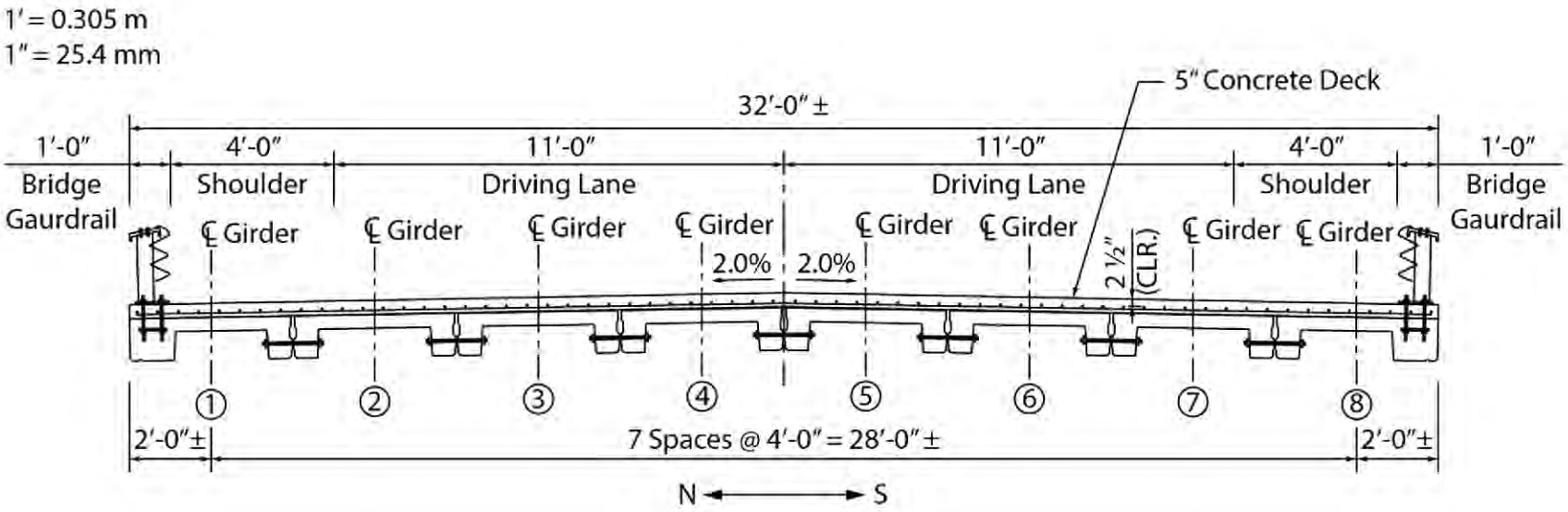


Figure 1.7: Transverse section detail for Bridge No 9706.

1.1.2 Girder Design

The interior and exterior girder design sections for both spans of NM Bridge No. 9706 (UHPC and HPC) are presented in Figure 1.8 through Figure 1.13. The typical interior design section (Figure 1.8 and Figure 1.11) was 48.0 in. (1220 mm) wide, with flange depth of 4 in. (102 mm) and minimum stem width of 7.0 in. (178 mm). A 0.50 in. (12.7 mm) taper was provided on the inner face of each stem to facilitate shear keys and provide adequate reinforcement clear cover. The outer stem of exterior design sections (Figure 1.9 and Figure 1.12) was increased to a minimum width of 13.0 in. (330 mm) due to larger moment distribution factors for exterior girders and to accommodate the installation and added loads of bridge railing.

Referring to Figure 1.10 and Figure 1.13, each girder was pretensioned with twelve fully-bonded 270 ksi (1860 MPa), 0.60 in. (15.2 mm) diameter, seven-wire low-relaxation strands. Strands were placed in three levels, six per stem, and tensioned to a total jacking force of approximately 527 kips (2345 kN). The advanced compressive strength of UHPC required significantly less area to resist compressive and bending stresses due to pretensioning, resulting in a design section depth of 12.5 in. (318 mm) and 10% reduction in cross-sectional area compared to the HPC design. Due to lower compressive strength, the depth of the HPC section had to be increased to 15.0 in. (381 mm) to ensure adequate resistance to compressive stresses developed after release of prestressing strands. The central pier and abutments were designed to accommodate the necessary elevation of each span for the structure.

Mild steel with a yield strength of 60.0 ksi (414 MPa) was used for all conventional reinforcement. Longitudinal reinforcement in the flange region consisted of nine No. 4 (No. 13) bars spaced at 5 in. on-center. Transverse flange reinforcement [No. 6 (No. 19) bars] and shear stirrups [No. 4 (No. 13)] were spaced at 6.0 in. (152 mm) on-center over the first 26.0 in. (610 mm) at girder ends within the anchorage zones and strand transfer length, then increased to 8.0 in. (203 mm) on-center over the remaining girder length. The vertical U-shaped shear stirrups were placed in pairs with the inverted upper stirrups extending 2.5 in. (64 mm) above the top surface of the girder to serve as horizontal interface shear reinforcement for the cast-in-place composite concrete deck.

Studded steel shoe plates [8.0 x 18.0 in. (203 x 457 mm)] were embedded at girder ends for bearing, two per end as shown in Figure 1.14-a. Vertical ducts were embedded at pier ends only to facilitate dowel bar “pinned” connections at the central pier cap (Figure 1.14-b), and horizontal ducts were embedded in all interior stems for lateral post-tensioning of adjacent stems at midspan using high-strength steel tie-rods. Lastly, polyvinyl chloride (PVC) exit ducts for sensor cables were embedded at pier ends as seen in both photos of Figure 1.14.

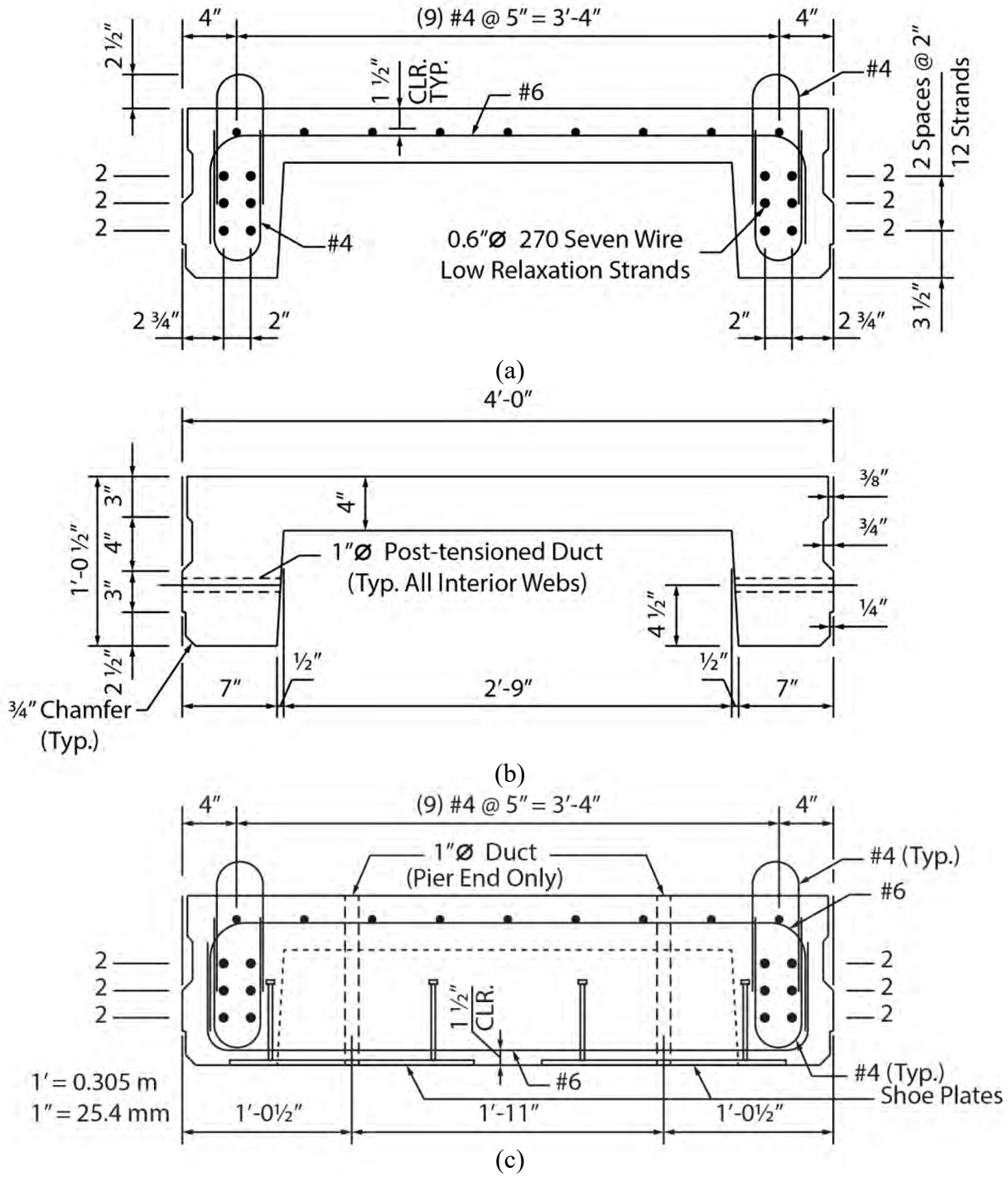


Figure 1.8: Cross-sectional detail for UHPC interior design section for Bridge No 9706 (a) near girder centerline, (b) at centerline post-tensioning, and (c) at girder ends.

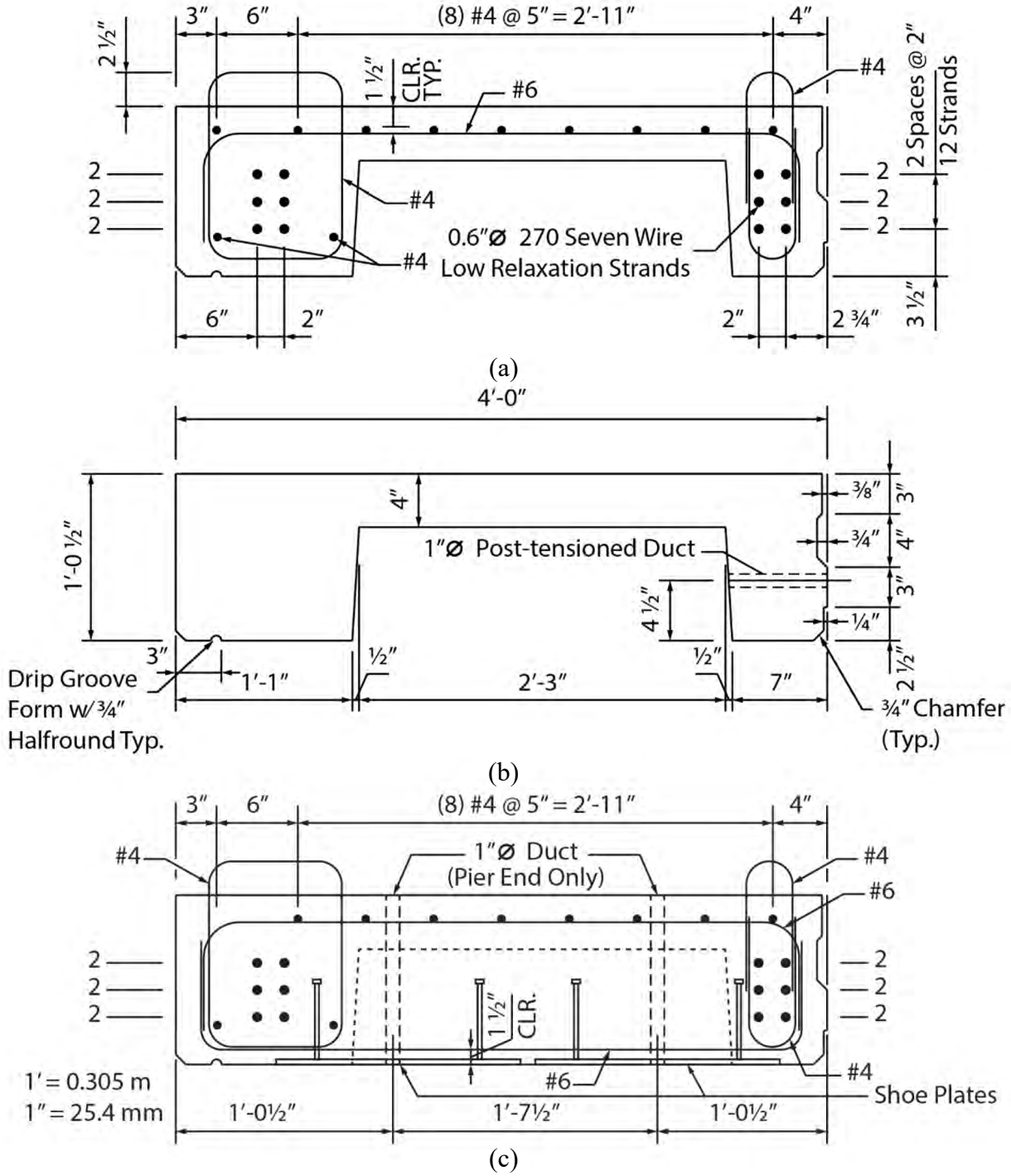


Figure 1.9: Cross-sectional detail for UHPC exterior design section for Bridge No 9706 (a) near girder centerline, (b) at centerline post-tensioning, and (c) at girder ends.

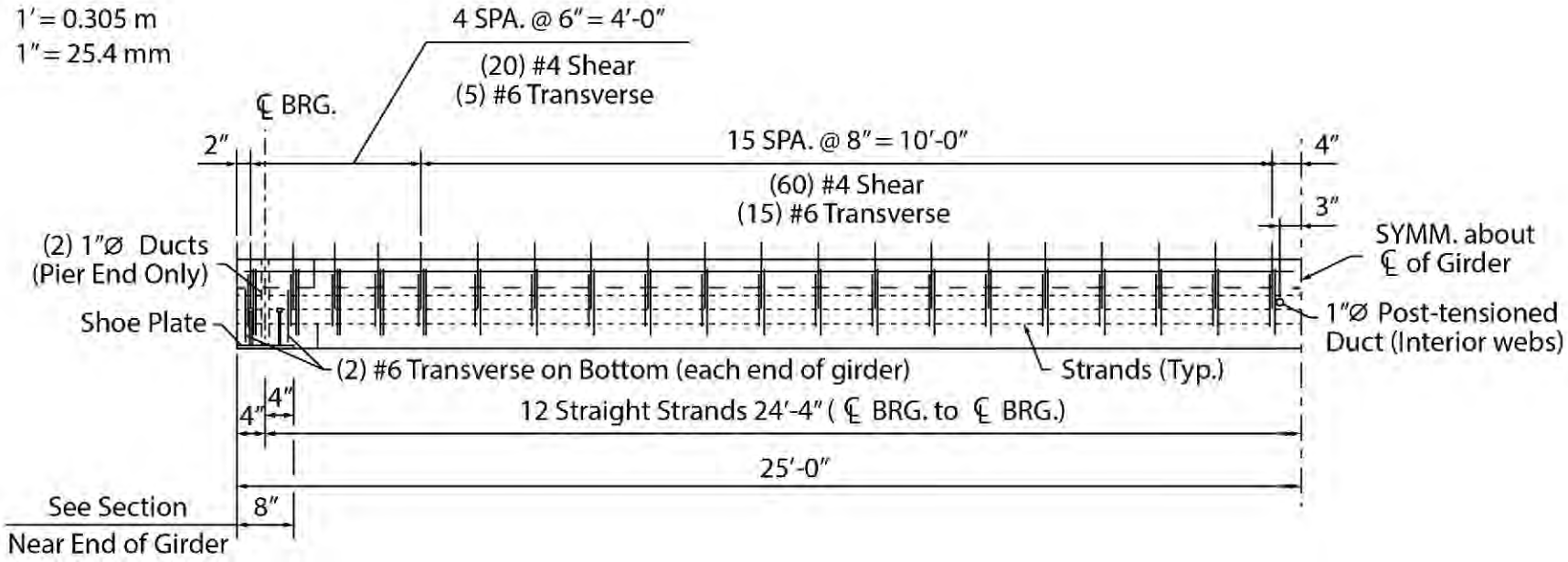


Figure 1.10: Reinforcement elevation detail for UHPC design section for Bridge No 9706.

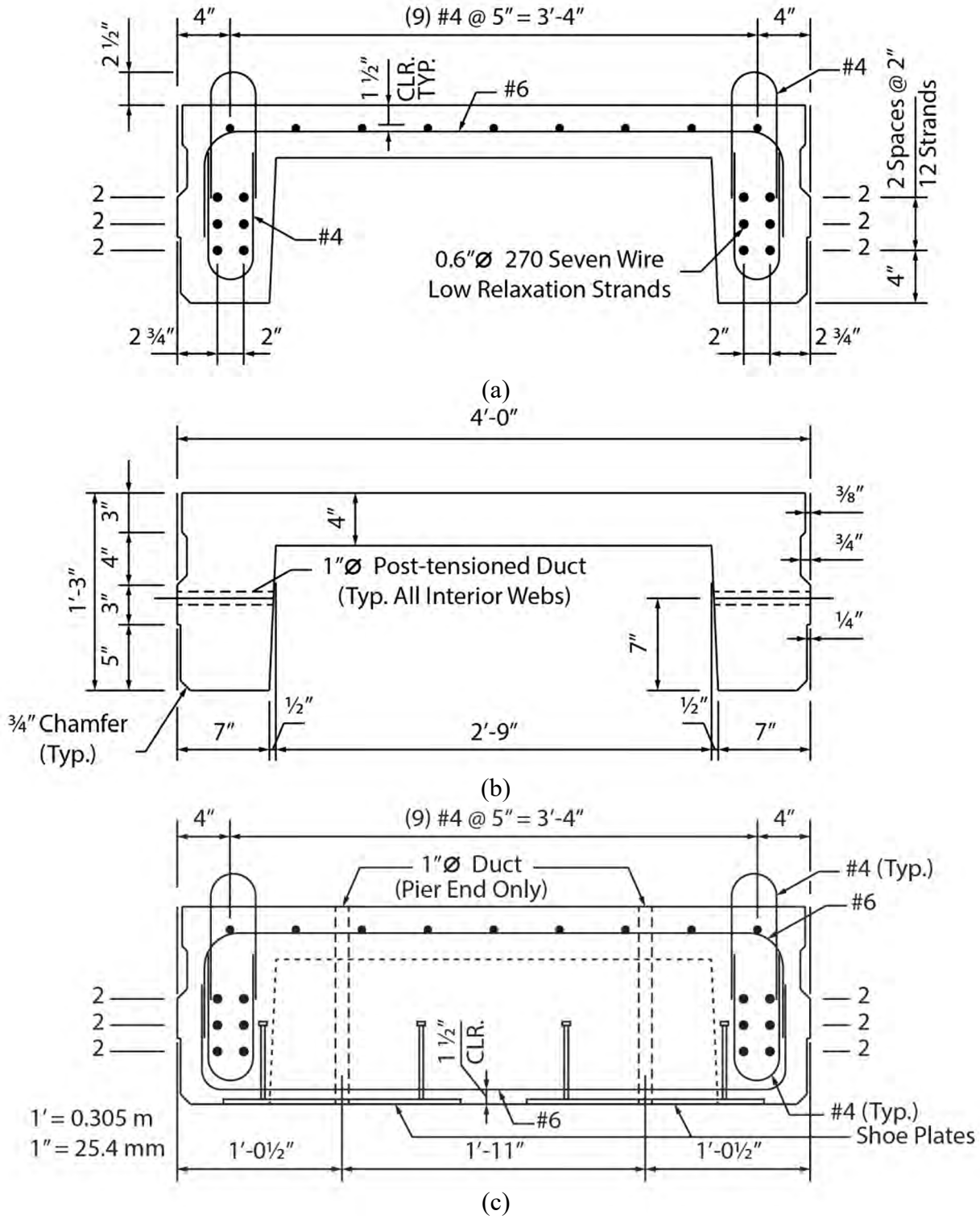


Figure 1.11: Cross-sectional detail for HPC interior design section for Bridge No 9706 (a) near girder centerline, (b) at centerline post-tensioning, and (c) at girder ends.

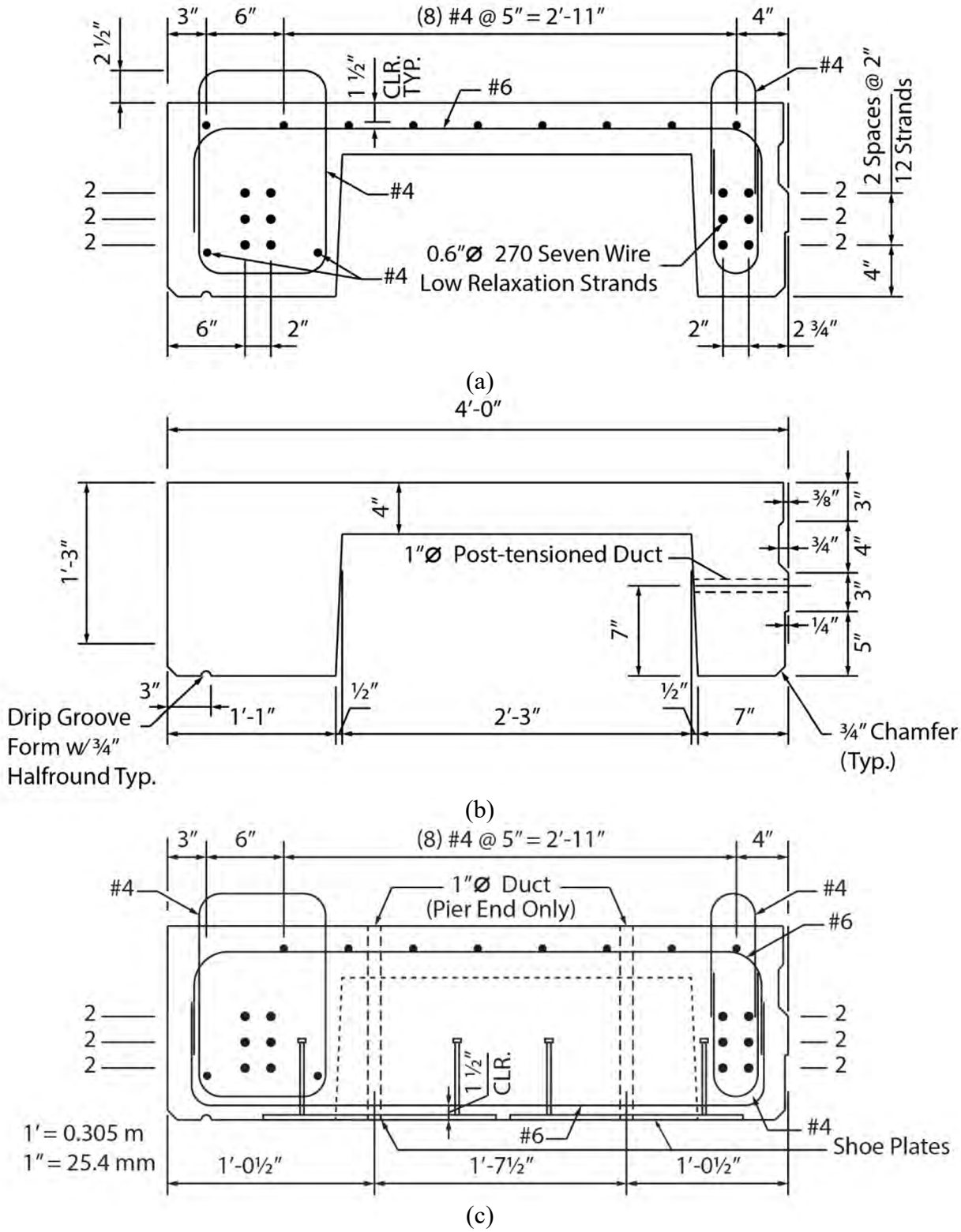


Figure 1.12: Cross-sectional detail for HPC exterior design section for Bridge No 9706 (a) near girder centerline, (b) at centerline post-tensioning, and (c) at girder ends.

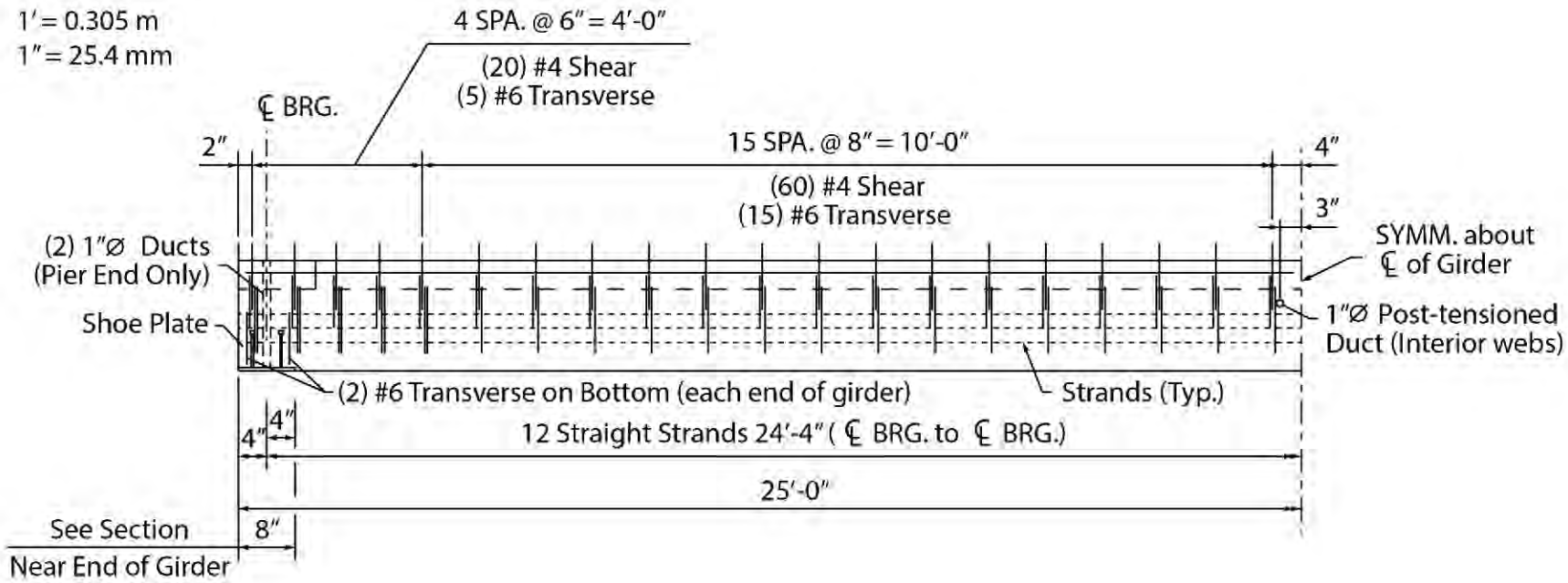
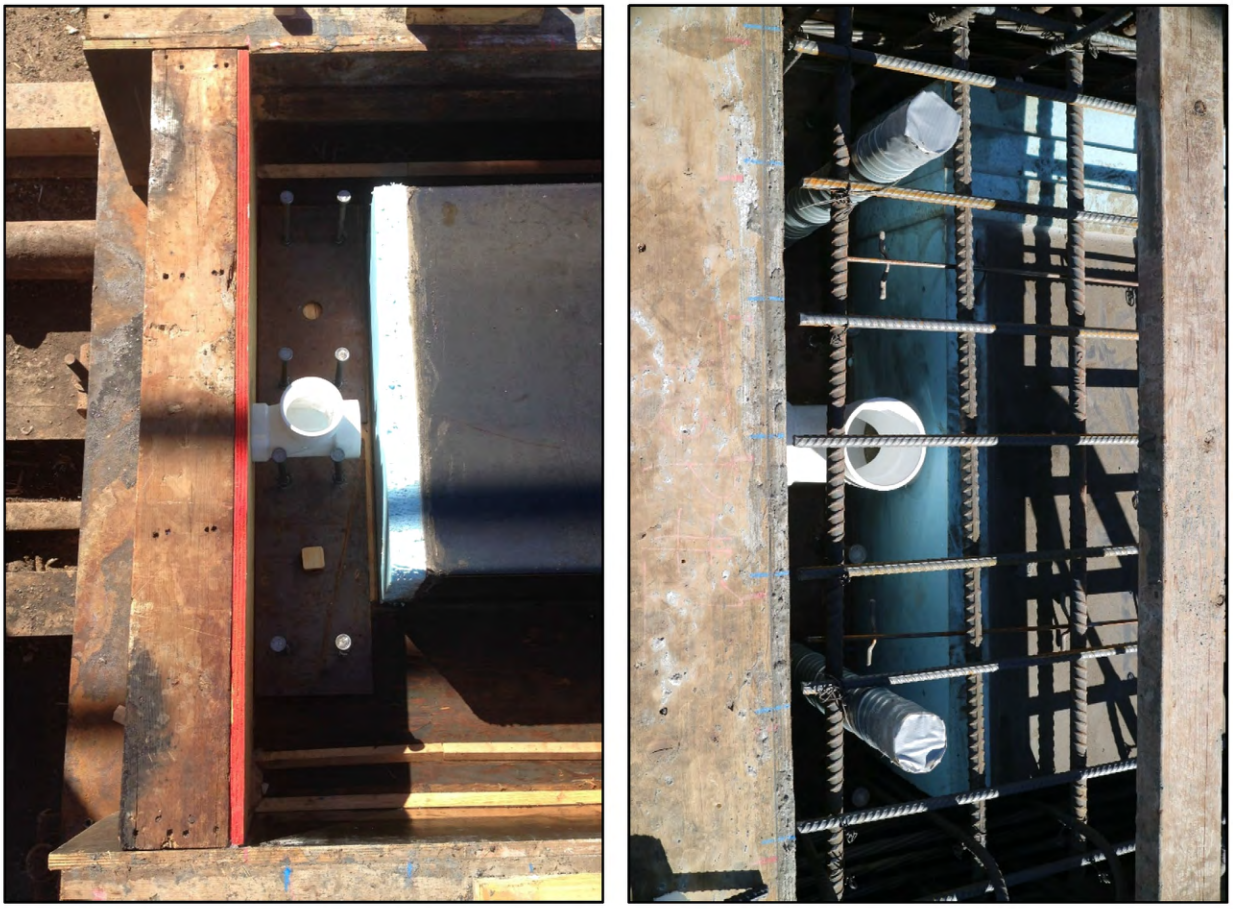


Figure 1.13: Reinforcement elevation detail for HPC design section for Bridge No 9706.



(a) (b)

Figure 1.14: (a) Studded steel shoe (bearing) plates embedded at girder ends and (b) ducts for pier end dowel “pinned” connection (pier end exit ducts for VWSG cables also pictured).

1.1.3 Girder Production

Production of the precast-prestressed channel girders for NM Bridge No. 9706 was conducted during fall 2016 at Coreslab® Structures (Albuquerque), Inc. in Albuquerque, NM, USA. The production schedule for each batch of two girders is provided in Table 1.1.

Table 1.1: Girder Production Schedule for NM Bridge No. 9706.

Batch Name	Girders Cast		Casting Day	Casting Date
UB1	U-6	U-7	Monday	08/22/16
UB2	U-2	U-5	Thursday	09/22/16
UB3	U-1	U-4	Friday	10/07/16
UB4	U-3	U-8	Saturday	10/22/16
HB1	H-1	H-4	Friday	11/04/16
HB2	H-7	H-8	Friday	11/11/16
HB3	H-3	H-6	Friday	11/18/16
HB4	H-2	H-5	Friday	12/02/16

As the girders were cast in pairs, two forms were constructed and aligned end to end as shown in Figure 1.15-a. Prestressing strands were then laced through both forms and stressed between abutments, and mild steel reinforcement was tied into place (Figure 1.15-b).

Concrete mixing was then conducted at the Coreslab® batching facility pictured in Figure 1.16-a and detailed in Figure 1.17. Equipped with twin 3.0 yd^3 (2.30 m^3) capacity concrete mixers, the automated batching system controlled the addition of cementitious materials and water to produce 1.5 yd^3 (1.15 m^3) batches. Because the HRWRA used for this UHPC differed from the products in use at the precast plant, it was added manually so as not to disrupt other batch plant operations. Additionally, to avoid loss of material associated with wind and vibrations during conveyor belt addition, high-strength steel fibers were also added manually during UHPC production.



(a) (b)

Figure 1.15: Channel girder formwork (a) before and (b) after installation of reinforcement.



(a) (b)

Figure 1.16: Coreslab® Structures (Albuquerque), Inc. (a) batching facility and (b) view inside 3.0 yd^3 (2.30 m^3) concrete mixer.

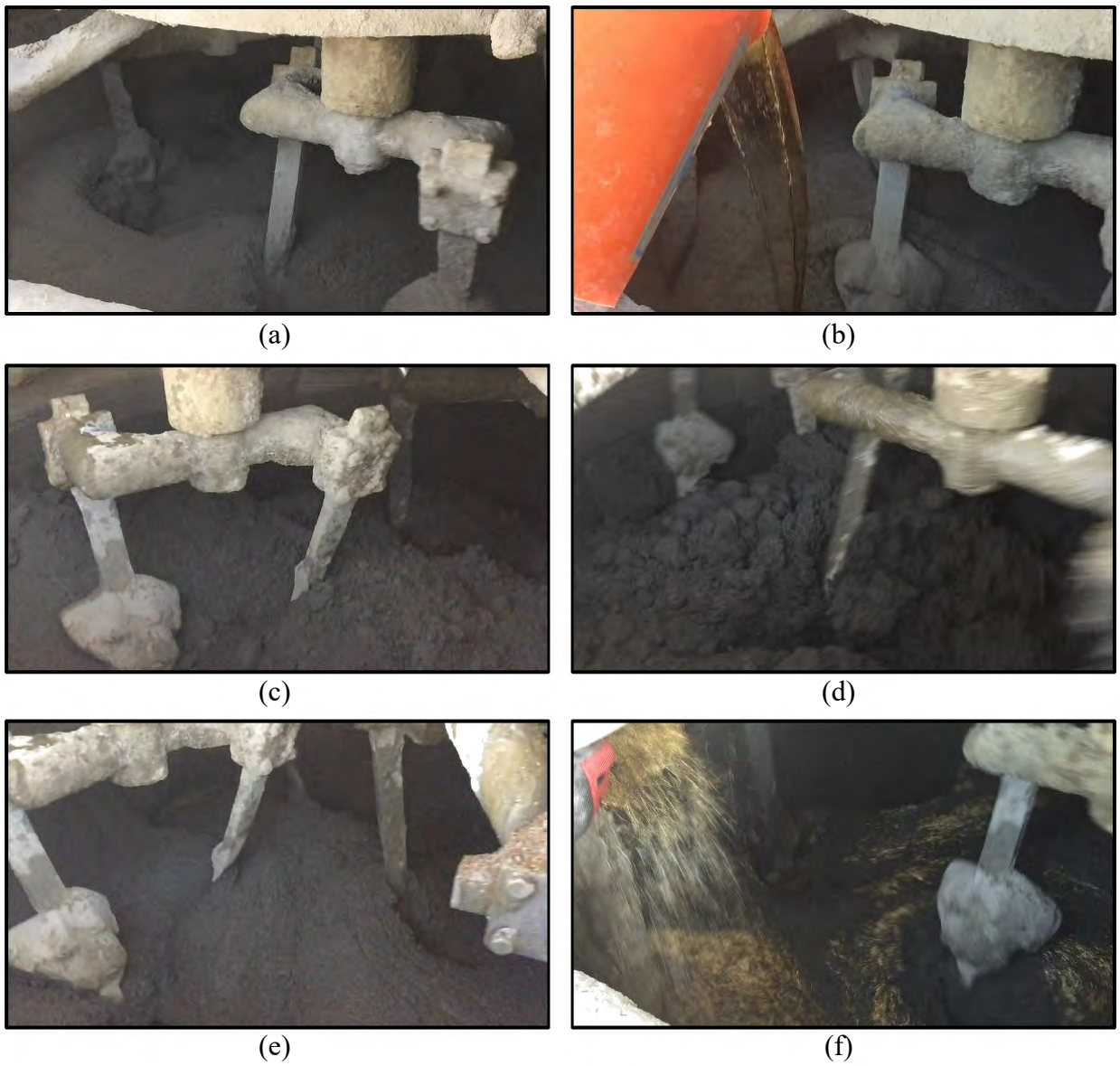


Figure 1.17: Batch plant mixing process: (a) Dry mixing stage, (b) manual addition of HRWRA, (c and d) continued mixing of concrete until (e) desired consistency was achieved, and (f) manual addition of steel fibers.

Several photos during girder production are provided in Figure 1.18 though Figure 1.21. Concrete was transported from the batching facility and placed in outdoor casting beds via auger delivery trucks and a layer casting method was used to promote favorable fiber orientation. Casting beds were vibrated, and manual concrete vibrators were also used to aid proper consolidation of concrete. After finishing of the top surface, the girders were covered with an insulated tarp and steam cured at a target temperature of 175°F (80°C) for a minimum of 18 hours for HPC and up to 7 days or more for UHPC. Prestressing strands were cut after adequate compressive strengths were verified by cylinder and/or cube testing. After removal from formwork, the channel girders were placed in the precast plant yard to await transport to the bridge construction site.



Figure 1.18: NMSU graduate researchers checking sensor installation prior to concrete placement during channel girder production for NM Bridge No. 9706 .



(a)



(b)

Figure 1.19: Channel girder production for Bridge No. 9706: (a) concrete mixing in batch plant; (b) placement of concrete by auger fed delivery; (c) vibrating concrete for consolidation; (d) finishing of girder surface; (e) removing girder from formwork after strand release; (f) completed channel girders.



(a)



(b)

Figure 1.20: Channel girder production for Bridge No. 9706: (a) concrete mixing in batch plant; (b) placement of concrete by auger fed delivery; (c) vibrating concrete for consolidation; (d) finishing of girder surface; (e) removing girder from formwork after strand release; (f) completed channel girders.



(a)



(b)

Figure 1.21: Channel girder production for Bridge No. 9706: (a) concrete mixing in batch plant; (b) placement of concrete by auger fed delivery; (c) vibrating concrete for consolidation; (d) finishing of girder surface; (e) removing girder from formwork after strand release; (f) attaching sensors of completed channel girders to temporary data acquisition unit.

1.1.4 Superstructure Construction

Demolition and removal of the existing Bridge No. 5296 along NM 186 in Anthony, NM, USA, was conducted in fall 2016 and construction of Bridge No. 9706 began immediately following. After completion of the bridge substructure, the channel girders were transported from the precast plant in Albuquerque, NM, USA, to the construction site and erected on January 31, 2017. Beginning with the UHPC (east) span, each girder was lifted by crane and positioned on the central pier cap and end abutments as shown in Figure 1.22 and Figure 1.23. Girders were supported under each haunch (at central pier and abutments) by two 16 x 6.75 in. (406 x 172 mm) elastomeric bearing pads spaced at 24 in. (610 mm) on-center. The girders were laterally tied at longitudinal midspan using 0.75 in. (19 mm) diameter high-strength steel post-tensioned rods through adjacent stems. Shear keys were filled with non-shrink grout and cast-in-place diaphragms were added at the pier cap and end abutments. On February 16, 2017, a 5.0 in. (127 mm) cast-in-place deck [4.0 ksi (28.0 MPa)] reinforced with a single mat of No. 5 (No. 16) mild steel reinforcement was placed on top of the girders (Figure 1.24).



(a)



(b)

Figure 1.22: Construction of NM Bridge No. 9706 superstructure: Placement of UHPC girders (a) U-3 and (b) U-5.



(a)



(b)

Figure 1.23: Construction of NM Bridge No. 9706 superstructure: (a) placement of HPC girder H-8 and (b) view of channel girders after placement.



(a)



(b)

Figure 1.24: Photos of (a) deck reinforcement and mechanical bridge paver and (b) finishing of deck surface during concrete placement.

1.1.5 Completed Structure

Construction of NM Bridge No. 9706 was completed opened to traffic in March 2017. Photos of the bridge nameplate and completed structure are provided in Figure 1.25 and Figure 1.27. A small cantilever was designed to extend from the north end of the central pier cap to support a standard aluminum pole (Figure 1.27-a), and the central pier and abutments were designed to accommodate the necessary elevation of each span for the structure based on the depth of the girder design sections (Figure 1.27-b). Additionally, the pole supports the enclosures for the datalogger and solar panel power supply used for long-term data acquisition of strain sensors installed in the bridge girders.



Figure 1.25: Nameplate of NM Bridge No. 9706.



(a)



(b)

Figure 1.26: NM Bridge No. 9706: View of (a) south bridge face and (b) north bridge face.



(a)



(b)

Figure 1.27: NM Bridge No. 9706: View of (a) east bound NM 186 and (b) stepped central pier.

1.2 Field Testing

Field testing was conducted to quantify the structural response of NM Bridge No. 9706 under various load conditions and investigate the comparative behavior and performance of the UHPC and HPC spans. Working with NMDOT, an experimental testing plan for evaluating the structural behavior of Bridge No. 9706 was developed by researchers at NMSU (Kennedy 2018, Alahmari et al., 2019). An initial diagnostic test was conducted after construction of Bridge No. 9706 and consisted of monitoring strains at pre-determined locations to quantify bridge behavior under known, tandem-axle truck loads applied to various load paths. Preparatory calculations were performed to establish available moment and strain capacities of the bridge girders and used to monitor the measured strains during load testing to prevent damage to the structure. Load paths for the diagnostic test were conducted to investigate strain behavior and load distribution between adjacent girders, establish critical load paths for proof testing, and provide comparative analyses of the initial behavioral response of the UHPC and HPC spans.

Having identified critical load paths (see following Section 1.2.1.1) via the diagnostic test, proof tests were then conducted with the intent of maximizing truck loads to induce maximum strains. The first proof test was performed approximately one year later to observe any possible changes in the behavior of the bridge throughout the first year of service and followed yearly by two additional proof tests. The schedule of load tests conducted on Bridge No. 9706 is provided in Table 1.2.

Table 1.2: Schedule of Load Tests Conducted on Bridge No. 9706

Test Name	Test Date(s)
Diagnostic Test (DT0)	30 March 2017
Proof Test 1 (PT1)	29-31 January 2018
Proof Test 2 (PT2)	27-28 February 2019
Proof Test 3 (PT3)	26-28 February 2020

1.2.1.1 Truck Loads and Load Paths

Field testing of NM Bridge No. 9706 was conducted using NMDOT standard 10 yd^3 tandem-axle dump trucks. Prior to each test, NMDOT reported the weight of each truck as measured at a local weight station. Table 1.3 through Table 1.6 summarize the reported weight of front and rear tandem axles and total truck weight for each load test. Because the trucks for PT2 were loaded with saturated sand, the truck loads changed day to day due to moisture loss. Table 1.4 provides the daily average axle and total weight, the daily percent difference in total truck weight from the first day of testing, and the average axle (front and back) and average total weight of all trucks used. During PT3, Truck 1 spilled a small amount of gravel and had to be weighed a second time.

Table 1.3: Truck Weights for Diagnostic Test of NM Bridge No. 9706

Truck No.	Front Single kips (kN)	Rear Tandem kips (kN)	Total kips (kN)
1	15.7 (69.8)	46.8 (208)	62.5 (278)
2	14.1 (62.7)	46.6 (207)	60.8 (270)
Average	14.9 (66.3)	46.7 (208)	61.7 (274)

Table 1.4: Truck Weights for Proof Test 1of NM Bridge No. 9706

Truck No.	Date	Front Single kips (kN)	Rear Tandem kips (kN)	Total kips (kN)	% Diff.
1	01/28/18	15.7 (69.8)	47.9 (213)	63.6 (283)	--
	01/29/18	15.7 (69.8)	47.7 (212)	63.4 (282)	0.31
	01/30/18	15.7 (69.8)	47.3 (210)	62.9 (280)	1.10
	Average	15.7 (69.8)	47.6 (212)	63.3 (282)	
2	01/28/18	15.6 (69.4)	48.4 (215)	63.9 (284)	--
	01/29/18	15.3 (68.1)	47.8 (213)	63.1 (281)	1.25
	01/30/18	15.3 (68.1)	47.8 (213)	63.0 (280)	1.41
	Average	15.4 (68.5)	48.0 (214)	63.3 (282)	
3	01/28/18	14.6 (64.9)	48.6 (216)	63.2 (281)	--
	01/29/18	14.4 (64.1)	47.8 (213)	62.2 (277)	1.58
	Average	14.5 (64.5)	48.2 (214)	62.7 (279)	
4	01/28/18	17.0 (75.6)	47.7 (212)	64.7 (288)	--
	01/29/18	16.9 (75.2)	47.2 (210)	64.0 (285)	1.08
	Average	17.0 (75.4)	47.5 (211)	64.4 (286)	
	Average	15.6 (69.5)	47.8 (213)	63.4 (282)	

Table 1.5: Truck Weights for Proof Test 2 of NM Bridge No. 9706

Truck No.	Front Single kips (kN)	Rear Tandem kips (kN)	Total kips (kN)
1	16.6 (73.8)	52.0 (231)	68.6 (305)
2	15.9 (70.9)	51.7 (230)	67.6 (301)
3	14.3 (63.8)	50.7 (225)	65.0 (289)
4	17.0 (75.4)	51.0 (227)	67.9 (302)
Average	16.0 (71.0)	51.3 (228)	67.3 (299)

Table 1.6: Truck Weights for Proof Test 3 of NM Bridge No. 9706

Truck No.	Date	Front Single kips (kN)	Rear Tandem kips (kN)	Total kips (kN)	% Diff.
1	02/26/20	16.1 (71.6)	55.9 (249)	72.0 (320)	-
	02/28/20	16.2 (72.2)	55.1 (245)	71.3 (317)	0.92
	Average	16.2 (71.9)	55.5 (247)	71.7 (319)	
2	02/26/20	15.9 (70.9)	56.1 (250)	72.0 (320)	
3	02/26/20	14.4 (64.1)	56.3 (251)	70.7 (315)	
4	02/26/20	16.4 (72.8)	55.9 (249)	72.2 (321)	
	Average	15.8 (70.3)	55.9 (248)	71.7 (319)	

Truck load paths were established for the diagnostic and proof tests based on the NMDOT Bridge Procedures and Design Guide (NMDOT, 2018) and the bridge geometry (Kennedy, 2018; Alahmari et al., 2019). Load paths were first characterized by the number and configuration of trucks loads. Between one and four trucks were used to apply the following truck load configurations: single truck (ST), double truck side-by-side (DT), triple truck side-by-side (TT), single truck back-to-back (STBB), and double truck back-to-back (DTBB). The desired truck configuration would then travel longitudinally across the bridge from east to west, thereby beginning on the UHPC span, and ending on the HPC span. A total of ten truck paths were used for field testing. ST and STBB load configurations were conducted using Paths 1 through 6 (Figure 1.28). DT and DTBB load configurations were conducted using Paths 7, 8, and 9 (Figure 1.29). Lastly, TT load configuration used Path 10 (Figure 1.30).

Each load path was also characterized by one of three types of load cases: slow-moving load, fast-moving load, or incremental load. Moving loads consisted of the truck load(s) traversing the desired load path at approximately 5 mph (slow-moving) or 45-55 mph (fast-moving). Incremental loading consisted of the truck load(s) traversing the desired load path incrementally, placing either the front or back axle at pre-marked positions, or stations, located longitudinally along the bridge spans for extended periods. Figure 1.31 illustrates the typical load stations, located at longitudinal quarter and midpoint locations of each span. Due the length of the VWSG data

collection interval, which requires a minimum of two minutes due to the large number of sensors installed in the two spans of Bridge No. 9706, only incremental load paths are adequately captured by VWSGs. Therefore, only the results of incremental load paths are presented and discussed in this document.

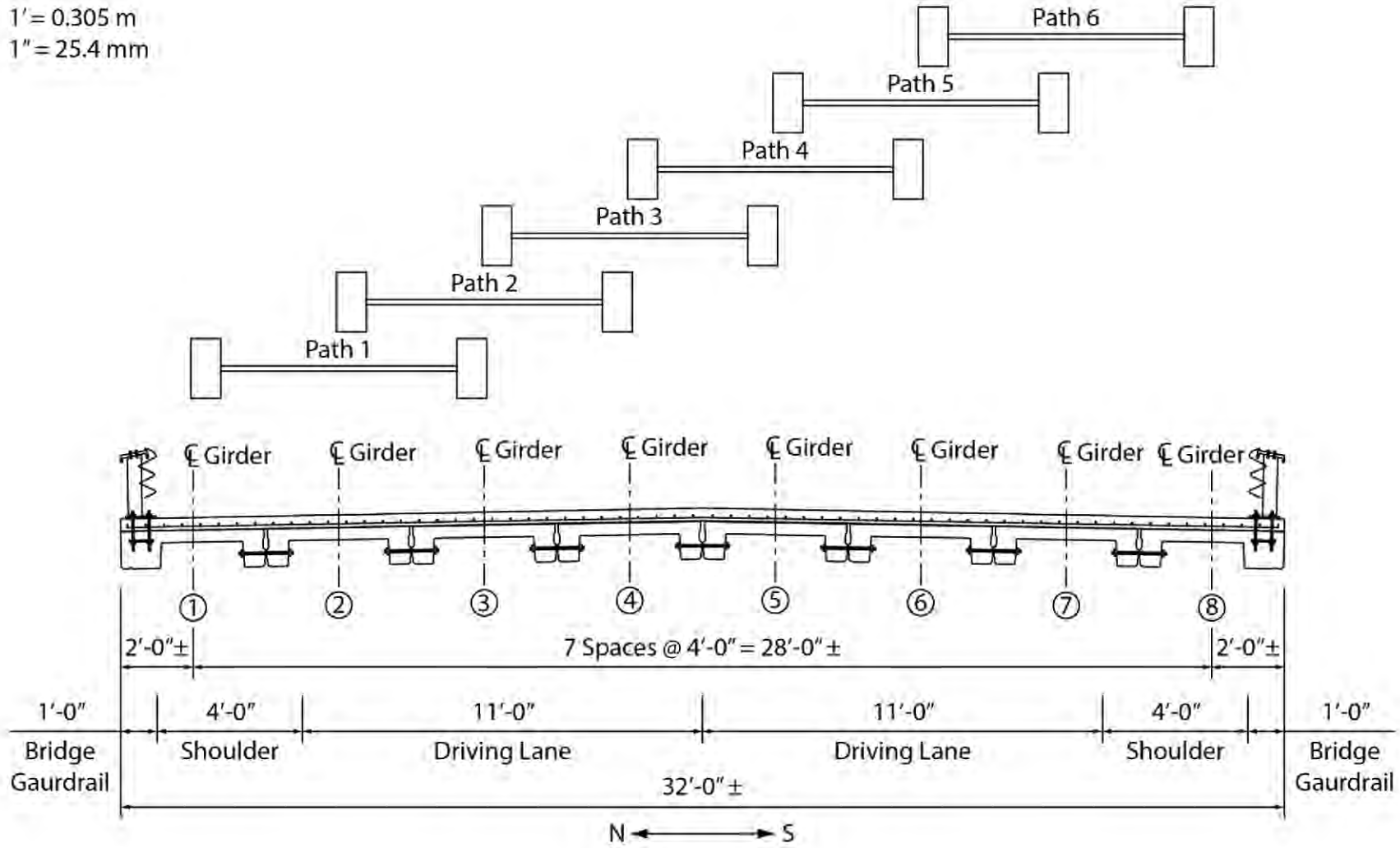


Figure 1.28: Load Paths 1 through 6 for field testing of NM Bridge No. 9706.

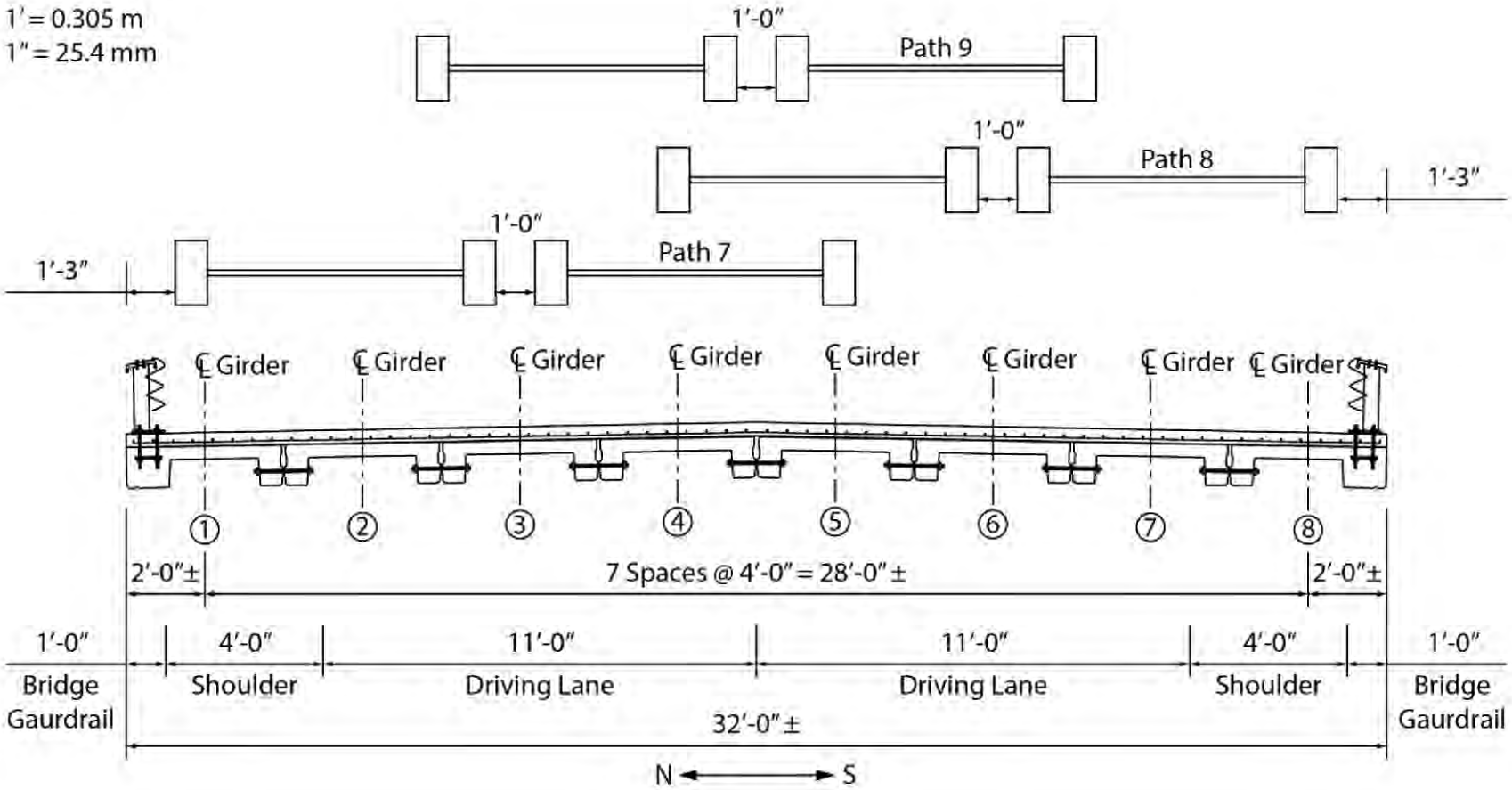


Figure 1.29: Load Paths 7 through 9 for field testing of NM Bridge No. 9706.

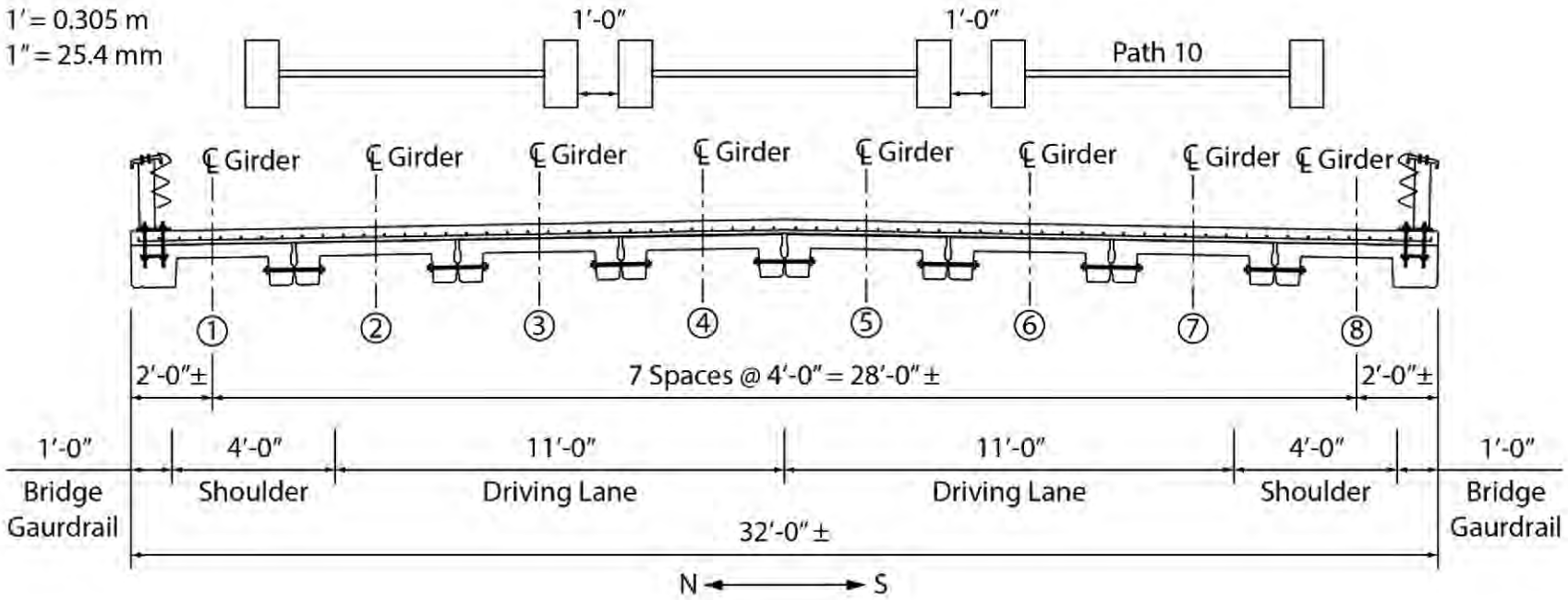


Figure 1.30: Load Path 10 for field testing of NM Bridge No. 9706.

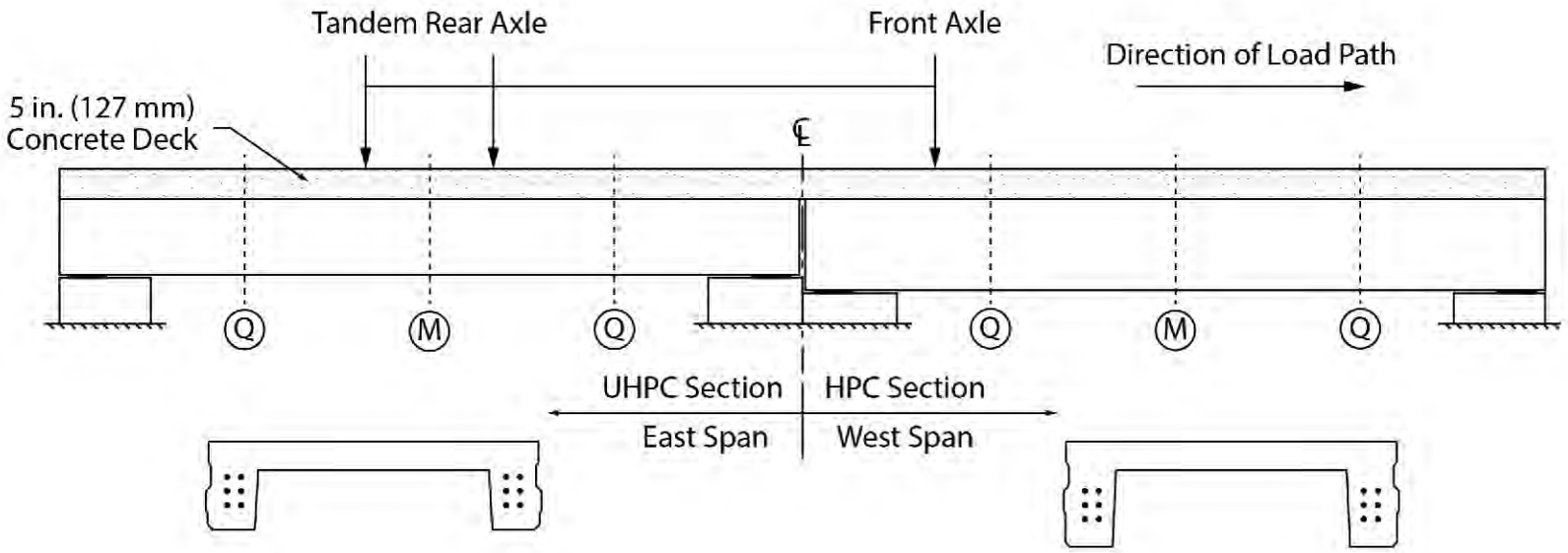


Figure 1.31: Locations of load stations for incremental load paths.

1.3 Preparatory Calculations

Estimations of the capacity, as well as an analysis of the expected behavior of the UHPC and HPC girders ensure that one, the diagnostic and proof tests do not damage the bridge, and two, the behavior of the bridge is accurately predicted. Presented in the following sections are preparatory calculations for available and expected strains, composite and non-composite neutral axis, available shear strength, and determination of live load distribution factors for moment and shear.

1.3.1 Available and Expected Strain

The available strain capacities of the beams should be computed and continuously monitored during load testing to prevent damage to the bridge. To obtain the available moment, the beam cracking moment is first calculated based on the construction method of the bridge: non-composite or composite. Once the cracking moment is found, the dead load moments are subtracted to determine the available moment capacity the beam can resist before cracking. To convert available moment to available strain, the moment is divided by the product of the section modulus and the design modulus of elasticity. The beam moment and strain equations are given in Equations 1.1 through 1.3:

$$M_{available,non-comp} = S_b * \left[P_e * \left(\frac{1}{A} + \frac{e}{S_b}\right) + f_{cr}\right] - M_{DL} \qquad 1.1$$

Where f_{cr} is the modulus of rupture, M_{DL} is the dead load moment, and P_e is the effective prestress determined from AASHTO LRFD Bridge Design Specifications (2012).

$$M_{available,comp} = S_c * \left[P_e * \left(\frac{1}{A} + \frac{e}{S_{nc}}\right) + f_{cr}\right] - M_{dnc} * \left(\frac{S_c}{S_{nc}}\right) - M_{dc} \qquad 1.2$$

Where S_c, S_{nc}, M_{dc}, and M_{dnc} are the composite and non-composite section moduli and the composite and non-composite dead load moments, respectively. Note that the moment due to the non-composite dead load is multiplied by the ratio of the composite section modulus to the non-composite section modulus. This accounts for the effect of the induced moment of the width of transformed deck per girder in addition to the induced moment of the self-weight of each girder. For non-composite and composite behavior, the available strain capacity for the beam is computed as:

$$\varepsilon_{available} = \frac{M_{available}}{S * E_{design}} \qquad 1.3$$

where S is the section modulus and E_{design} is the concrete elastic modulus. Equations 1.4 and 1.5 are used to calculate the design modulus of elasticity for UHPC and HPC:

$$E_{design,UHPC} = 46.2\sqrt{f'_{c-UHPC}} \quad 1.4$$

$$E_{design,HPC} = 33000 * w_{conc-HPC}{}^{1.5}\sqrt{f'_{c-HPC}} \quad 1.5$$

Where $f'_{c\,(UHPC)}$ is the compressive strength of UHPC [21 ksi (144.8 MPa)], $w_{conc\text{-}HPC}$ is the unit weight of HPC (150 lb/ft^3 [kn/m^3]) and $f'_{c\,(HPC)}$ is the compressive strength of HPC [9.5 ksi (66.5 MPa)].

For comparison to the available moment and strain capacities calculated from Equations 1.1 through 1.3, the total midspan moment should be calculated under the diagnostic test truck loading. The total moment should then be multiplied by the design-based distribution derived through applicable guidelines of the AASHTO (2012), and the "upper bound" distribution factor that represents the worst-case scenario for live load distribution between the girders (e.g., distribution factor of one). These two factors provide the range of beam moments possible under the diagnostic and proof test truck load and should not exceed the available moment computed using by Equation 1.1 or 1.2.

The expected strains for UHPC and HPC were computed using Equations 1.6 and 1.7 below:

$$\text{Expected Strain (Int.) } \mu\varepsilon = \frac{DF_{INT} * \text{ Truck Moment (k} - \text{ft)} * 12\ \left(\frac{\text{in}}{\text{ft}}\right)}{Sc * \text{ E(beam)}} \quad 1.6$$

$$\text{Expected Strain (Ext.) } \mu\varepsilon = \frac{DF_{EXT}}{DF_{INT}} * \text{ Expected Strain (Ext)} \quad 1.7$$

Where DF_{INT} is the calculated AASHTO distribution factor for an interior girder, and DF_{EXT} is the calculated ASSHTO distribution factor for an exterior girder.

An evaluation of the calculated live load distribution factors is found in Section 1.3.4. A summary for available versus expected strain for exterior and interior UHPC and HPC girders can be found in Section 1.3.5.4.

1.3.2 Composite and Non-Composite Neutral Axis

Girders are designed for three major stages. The first stage is when the girders are erected. The second stage is the placing of the concrete deck slab. The third stage is applying the live loads to the finished structure. The internal stresses accumulate in the girder from each stage of design. Prestressed concrete girders are designed where the prestress compression and bending moment are countered by the dead weight of the girder. The added dead loads and live load subsequently will cause a tension in the bottom fiber nearly equal to the induced prestress compression. The design allows the girder to remain in total compression.

The neutral axis is the location along the depth of the cross-section of the girder that separates the area under compressive strain from area in tensile strain during loading. The non-composite neutral axis for the girders is determined by the centroid of the section. The composite neutral axis is determined by calculating the effective width of each girder and a transformed area. A comparison is made of the calculated non-composite and composite neutral axis to the measured non-composite and composite neutral axis, to determine the efficiency of the concrete deck and girder interaction. The composite and non-composite neutral axis is computed using Equation 1.8:

$$\bar{y} = \frac{\Sigma\, y_i A_i}{\Sigma\, A_i} \qquad 1.8$$

Where A_i for the non-composite neutral axis is the cross-sectional area for the girder only, and A_i for the composite neutral axis is the summation of the area of the girder and the transformed concrete deck. Equation 1.9 for the transformed concrete deck area is computed as:

$$A_{t\,(Deck)} = w_{t(Deck)} * t_{Deck} \qquad 1.9$$

where $w_{t\,(Deck)}$ is the transformed deck with and t_{Deck} is the thickness of the concrete deck. Equation 1.10 for the transformed deck width is computed as:

$$w_{t(Deck)} = n/S \qquad 1.10$$

where n is the modular ratio of the modulus of elasticity of the girder divided by the modulus of elasticity of the deck, and S is center to center beam spacing.

1.3.3 Available Shear Strength

Before the test was executed, a shear check was conducted to ensure that the truck loads will not crack the bridge beams in shear. The shear capacity is evaluated using the Equations 1.11 and 1.12:

$$V_{ci} = 0.6\sqrt{f'_c}\, b'd + V_d + \frac{V_i M_{cr}}{M_{max}} \qquad 1.11$$

$$V_{ci} = \left(3.5\sqrt{f'_c}\, 0.3f_{pc}\right) b'd + V_p \qquad 1.12$$

Where f'_c is the concrete compressive strength; f_{pc} is the compressive concrete stress after all losses at beam centroid; b' is the beam web width; d is the distance from the compression face to the centroid of the tension reinforcement (not less than 80% of overall beam depth); V_p is the vertical component of the effective prestressing force; V_i is the design shear load; V_d is the non-composite dead shear load; M_{cr} is the concrete cracking moment; and M_{max} is the maximum design shear load. The lesser of Equations 1.11 and 1.12 controls the capacity for each girder in shear.

1.3.4 Live Load Distribution Factors

Design live loads are used during the design of a new bridge, reconstruction or rehabilitation design. Design truck loads are not legal loads. Generally, design axle loads are more severe than legal axle loads to ensure adequate factors of safety. In the calculation of bending moments and shear for longitudinal girders, the lateral distribution should be selected in accordance to current AASHTO LRFD Bridge Design Specifications.

1.3.4.1 Live Load Distribution Factor for Moment

AASHTO LRFD Bridge Design Specifications, Table 4.6.2.2.1-1 Common Deck Superstructures Covered in Articles 4.6.2.2.2 and 4.6.2.2.3, defines a list of superstructure types. Bridge 9706 falls under type (h): Precast Concrete Channel Sections with Shear Keys with a cast-in-place concrete overlay, shown in Figure 1.32. However, Bridge 9706 has an integral composite deck instead of the listed cast-in-place concrete overlay. The scope of the defining superstructure is still applicable, but the calculated live load distribution factors is conservative.

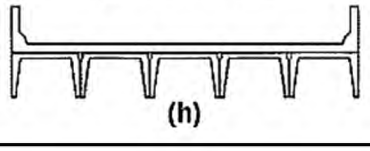
Supporting Components	Type Of Deck	Typical Cross-Section
Precast Concrete Channel Sections with Shear Keys	Cast-in-place concrete overlay	 (h)

Figure 1.32: LRFD live load distribution superstructure type (h).

Table 4.6.2.2.2b-1 Distribution of Live Load Per Lane for Moment in Interior Beams (AASHTO, 2012) defines the equation applicable based on the corresponding superstructure type. For type (h), precast concrete channel sections, the distribution factor for moment in interior beams calculated based on Equations 1.13 through 1.17 as follows:

$$\mathrm{DF(int)} = \mathrm{S/D} \qquad 1.13$$

Where S is the center-to-center spacing of adjacent girders, and D is the width of the distribution lane (ft), which is dependent upon the following equations:

When,

$$\mathrm{C} = \mathrm{K}\left(\frac{\mathrm{W}}{\mathrm{L}}\right) \leq \mathrm{K} \text{ use: (Eq. 2.11)} \qquad 1.14$$

$$\mathrm{D} = 11.5 - \mathrm{N_L} + 1.4\mathrm{N_L}(1.02\mathrm{C})^2 \qquad 1.15$$

When, $\mathrm{C} \leq \mathrm{N_L}$

$$D = 11.5 - N_L \quad (1.16)$$

When $C > 5$,

$$K = \frac{\sqrt{((1+\mu)I)}}{J} \quad (1.17)$$

where, C is the stiffness parameter, K is the effective length factor in plane of bending, W is the edge-to-edge width of the bridge (ft), L is the span length of the bridge (ft), N_L is the number of design lanes, μ is Poisson's ratio, I is the moment of inertia (in^4), and J is the St. Venant torsional inertia (in^4).

Table 4.6.2.2.2d-1 Distribution of Live Load Per Lane for Moment in Exterior Beams (AASHTO, 2012) defines the equation applicable based on the corresponding superstructure type. For type (h) the distribution factor, regardless of lanes loaded is calculated by the Lever Rule.

1.3.4.2 Live Load Distribution Factor for Shear

AASHTO (2012) Table 4.6.2.2.3a-1 and Table 4.6.2.2.3b-1, Distribution of Live Load Per Lane for Shear in Interior Beams and Exterior Beams, respectively, define the equation applicable based on the corresponding superstructure type. For type (h) the distribution factor, regardless of lanes loaded is calculated by the Lever Rule.

1.3.5 Summary

Table 1.7 through Table 1.10 reflect the preparatory calculations and the respective results for available and expected strains, composite and non-composite neutral axis, and lastly, live load distribution factors for moment and shear.

1.3.5.1 Available and Expected Strain Results

Following preparatory computational procedures outlined in the preceding sections, Table 1.7 and Table 1.8 summarize the calculations for available strain. Table 1.9 and Table 1.10 summarize calculations for expected strain. Table 1.9 illustrates the expected values of strain based on the design bending moment, for one and two lanes loaded, with the corresponding live load distribution factors outlined in the AASHTO LRFD Bridge Design Specifications and Section 1.3.4 illustrates the expected values of strain based on the design moment, for one and two lanes loaded, with the corresponding live load distribution factor of 1. These two factors provide the range of beam moments possible under the diagnostic and proof test truck load and should not exceed the available strain, corresponding to each appropriate girder, computed in Table 1.7 and Table 1.8.

Table 1.7: UHPC Available Strain Parameters

Variable	Average	Exterior	Interior
k	0.8	0.8	0.8
f_{pi} [ksi (MPa)]	218.295 (1505.2)	219.0 (1506.0)	217.62 (1500.3)
Number of Strands	12.0	12.0	12.0
Area per strand [in^2 (mm^2)]	0.22 (129.0)	0.22 (129.0)	0.22 (129.0)
P_e [kips (kN)]	460.4 (2046)	463.3 (2060.9)	457.6 (2035.5)
S_c [in^3 (mm^3)]	1029.3 (1.686 e^7)	1160.7 (1.90 e^7)	897.9 (1.47 e^7)
S_{nc} [in^3 (mm^3)]	548.0 (8.96 e^6)	627 (1.0 e^7)	468.8 (7.7 e^6)
A [in^2 (mm^2)]	333.6 (2.2 e^5)	361.5 (2.3 e^5)	305.75 (2.0 e^5)
e [in. (mm)]	2.3 (58.4)	2.0 (52)	2.6 (66.0)
f'_c girder [psi (MPa)]	21000 (144.8)	21000 (144.8)	21000 (144.8)
f'_c deck [psi (MPa)]	4000 (27.6)	4000 (27.6)	4000 (27.6)
f_{cr} [ksi (MPa)]	0.9 (6.2)	0.9 (6.2)	0.9 (6.2)
M_{dnc} [kip-ft (kN-m)]	46.7 (63.3)	48.9 (66.3)	44.4 (60.2)
M_{dc} [kip-ft (kN-m)]	2.0 (2.7)	3.9 (5.3)	0
$M_{available}$ [kip-ft (kN-m)]	270.5 (366.7)	259.6 (352.0)	281.4 (381.5)
Available Strain using effective flange width of [48 in. (mm)]	471.0 με	400.8 με	561.7 με

Table 1.8: HPC Available Strain Parameter

Variable	Average	Exterior	Interior
k	0.8	0.8	0.8
f_{pi} [ksi (MPa)]	217.89 (1502)	218.4 (1505.8)	217.4 (1498.9)
Number of Strands	12.0	12.0	12.0
Area per strand [in^2 (mm^2)]	0.22 (129.0)	0.22 (129.0)	0.22 (129.0)
P_e [kips (kN)]	458.7 (2040.4)	461.0 (2050.6)	456.5 (2030.6)
S_c [in^3 (mm^3)]	1328.5 (2.2 e^7)	1511.5 (2.5 e^7)	1145.5 (1.9 e^7)
S_{nc} [in^3 (mm^3)]	789.0 (1.3 e^7)	903.6 (1.5 e^7)	674.4 (1.1 e^7)
A [in^2 (mm^2)]	376.8 (2.4 e^5)	412.4 (2.7 e^5)	341.1 (2.0 e^5)
e [in. (mm)]	3.3 (83.8)	3.0 (76.2)	3.6 (92.6)
f'_c girder [psi (MPa)]	9500 (65.5)	9500 (65.5)	9500 (65.5)
f'_c deck [psi (MPa)]	4000 (27.6)	4000 (27.6)	4000 (27.6)
f_{cr} [ksi (MPa)]	0.6 (4.1)	0.6 (4.1)	0.6 (4.1)
M_{dnc} [kip-ft (kN-m)]	50.2 (68.1)	53.1 (72.0)	47.3 (64.1)
M_{dc} [kip-ft (kN-m)]	2.0 (2.7)	3.9 (5.3)	0
$M_{available}$ [kip-ft (kN-m)]	326.2 (442.3)	312.9 (424.2)	338.9 (459.5)
Available Strain using effective flange width of [48 in. (mm)]	498.6 με	420.4 με	600.7 με

Table 1.9: Expected Strain with AASHTO Distribution Factors

Truck Loading	Expected Strain	
	UHPC in./in. (mm/mm)	HPC in./in. (mm/mm)
Interior (Single)	101.0	89.7
Exterior (Single)	103.0	91.5
Interior (Double)	134.7	119.6
Exterior (Double)	137.3	122.0
Interior (Triple)	138.9	123.3
Exterior (Triple)	141.6	125.8
Interior Back-to-Back (Single)	126.3	112.1
Exterior Back-to-Back (Single)	128.7	114.3
Interior Back-to-Back (Double)	151.5	134.6
Exterior Back-to-Back (Double)	154.5	137.2

Table 1.10: Expected Strain with Distribution Factor of 1

Truck Loading	Expected Strain	
	UHPC in./in. (mm/mm)	HPC in./in. (mm/mm)
Interior (Single)	239.5	212.7
Exterior (Single)	239.5	212.7
Interior (Double)	319.4	283.7
Exterior (Double)	319.4	283.7
Interior (Triple)	329.4	292.5
Exterior (Triple)	329.4	292.5
Interior Back-to-Back (Single)	299.4	265.9
Exterior Back-to-Back (Single)	299.4	265.9
Interior Back-to-Back (Double)	359.3	319.1
Exterior Back-to-Back (Double)	359.3	319.1

1.3.5.2 Composite and Non-Composite Neutral Axis Results

The procedural computations of the composite and non-composite neutral axis are found in Section 1.3.2. The calculated composite and non-composite neutral axis for UHPC and HPC girder are found in Table 1.11 through Table 1.13 where y_{bc} is the location of the theoretical composite neutral axis taken from the bottom of the girder, y_{tc} is the location of the theoretical composite neutral axis taken from the top of the slab, y_{bnc} is the location of the theoretical non-composite neutral axis taken from the bottom of the girder, and y_{tnc} is the theoretical location of the non-composite neutral axis taken from the top of the girder.

Table 1.11: UHPC Interior Girder – Transformed Moment of Inertia

	Area, in^2, (mm^2)	y_b, in., (mm)	A_{yb}, in^3, (mm^3)	$A(y_{bc}-y_b)^2$, in^3, (mm^3)	I, in^4, (mm^4)	$I+A(y_{bc}-y_b)]^2$, in^4, (mm^4)
Beam	305.8 (1.97 e^5)	8.1 (205.7)	2474.5 (4.1 e^7)	1402.8 (2.3 e^7)	3794.4 (1.6 e^9)	5197.2 (2.2 e^9)
Deck	137.4 (8.9 e^4)	15.0 (381)	2061.7 (3.4 e^7)	3120.5 (5.1 e^7)	873.1 (3.6 e^8)	3993.5 (1.7 e^9)
Sum	443.2 (2.9 e^5)	-	4536.3 (7.5 e^7)	-	-	9190.7 (3.8 e^9)
y_{bc}, in. (mm)		10.2 (259.1)				
y_{tc}, in. (mm))]		7.3 (185.4)				
y_{bnc}, in. (mm)		8.1 (205.74)				
yt_{nc}, in. (mm))		4.4 (111.8)				

Table 1.12: HPC Exterior Girder – Transformed Moment of Inertia

	Area, in^2, (mm^2)	y_b, in., (mm)	A_{yb}, in^3, (mm^3)	$A(y_{bc}-y_b)^2$, in^3, (mm^3)	I, in^4, (mm^4)	$I+A(y_{bc}-y_b)]^2$, in^4, (mm^4)
Beam	412.4 (2.7 e^5)	9.0 (228.6)	3701.4 (6.1 e^7)	2252.1 (3.7 e^7)	8109.8 (3.3 e^9)	10361.9 (4.3 e^9)
Deck	155.7 (1.0 e^5)	17.5 (444.5)	2725.3 (4.5 e^7)	5964.4 (9.8 e^7)	770.6 (3.2 e^7)	6734.9 (2.9 e^9)
Sum	568.2 (3.7 e^5)	-	6426.7 (1.1 e^8)	-	-	17096.8 (7.1 e^9)
y_{bc}, in. (mm)		11.3 (287.0)				
y_{tc}, in. (mm)		8.7 (221.0)				
y_{bnc}, in. (mm)		9.0 (228.6)				
yt_{nc}, in. (mm)		6.0 (152.4)				

Table 1.13: HPC Interior Girder – Transformed Moment of Inertia

	Area, in^2, (mm^2)	y_b, in., (mm)	A_{yb}, in^3, (mm^3)	$A(y_{bc}-y_b)^2$, in^3, (mm^3)	I, in^4, (mm^4)	$I+A(y_{bc}-y_b)]^2$, in^4, (mm^4)
Beam	341.1 (2.2 e^5)	9.6 (243)	3290.8 (5.4 e^7)	2066.7 (3.4 e^7)	6506.2 (2.7 e^9)	8572.9 (3.6 e^9)
Deck	155.7 (1.0 e^5)	17.5 (444.5)	2725.3 (4.5 e^7)	4527.0 (7.4 e^7)	770.6 (3.2 e^7)	5297.6 (2.2 e^9)
Sum	496.9 (3.2 e^5)	-	6016.1 (9.9 e^8)	-	-	13870.5 (5.8 e^9)
y_{bc}, in. (mm)		12.1 (307.3)				
y_{tc}, in. (mm)		7.9 (200.7)				
y_{bnc}, in. (mm)		9.6 (243.8)				
yt_{nc}, in. (mm)		5.4 (137.2)				

1.3.5.3 Available Shear Strength Results

Table 1.14 summarizes the shear capacity for UHPC and HPC girders under the design truck load. The results from using Eq. 2.8 are less than results using Eqs. 2.7 and 2.8 therefore controls the capacity of UHPC and HPC girders.

Table 1.14: UHPC and HPC Shear Capacity

	Shear Capacity, kips (kN)	
Girder	Eq. 2.7	Eq. 2.8
UHPC Int.	71.8 (319.4)	211.9 (942.6)
UHPC Ext.	70.6 (314.0)	211.9 (942.6)
HPC Int.	79.5 (353.6)	124.4 (553.4)
HPC Ext.	78.3 (348.3)	124.4 (553.4)

1.3.5.4 Live Load Distribution Factor Results

AASHTO LRFD Bridge Design Specifications outlines the procedure of determining live load distribution factors for moment and shear. Summarized in Section 1.3.4, distribution factors for single or multiple lanes loaded were computed and shown in Table 1.15. Distribution factors for three loaded are shown in Table 1.16.

Table 1.15: RISA Live Load Distribution Factors

Girder	Moment	Shear
UHPC Int.	0.42	0.43
UHPC Ext.	0.43	0.43
HPC Int.	0.42	0.43
HPC Ext.	0.43	0.43

Table 1.16: RISA Live Load Distribution Factors

Girder	Moment	Shear
UHPC Int.	0.45	0.58
UHPC Ext.	0.58	0.58
HPC Int.	0.45	0.58
HPC Ext.	0.58	0.58

1.4 BDI ST350 Strain Transducers

Bridge 9706 was instrumented with 36 external BDI ST350 strain transducers located at midspan for both UHPC and HPC bridge spans. Four BDI strain transducers can be connected to a single BDI-STS unit. BDI-STS units are connected in series with one cable running from the computer / power supply to the BDI-STS receiver. BDI strain transducers are used in conjunction the Structural Testing System by Bridge Diagnostics, Inc. (BDI-STS) which has been designed for preforming live-load tests. WinSTS Software allows for adjustment of sampling rates, test durations, and the automatic transducer balancing. Recorded measurements are stored in ASCII file format and can be displayed during the test. The Structural Testing System II is provided in Figure 1.33.



Figure 1.33: BDI Structural Testing System II.

BDI strain transducers were attached directly to the UHPC and HPC girders prior to the diagnostic and proof bridge test. A power grinder was used to remove any surface roughness on the concrete girders. This ensures a sufficient bond between the strain transducers and the bridge girders with the application of an adhesive. A two-part adhesive compound, Loctite 410 adhesive gel and Loctite SF 712 activator spray, was used to attach the strain transducers. The pictures of strain transducers and test setup during the diagnostic and proof bridge test are provided in Figure 1.34 and Figure 1.36 . Pictures of the BDI connection boxes are provided in Figure 1.37. The data acquisition system and laptop arrangement are provided in Figure 1.38.



Figure 1.34: BDI strain transducers linked collection boxes with connected strain transducers.



Figure 1.35: Attached BDI strain transducers on the stem and on the bottom of girder stems for girder H-2 and H-3.



Figure 1.36: BDI strain transducers.



Figure 1.37: BDI strain transducers linked collection boxes with connected strain transducers.



Figure 1.38: BDI acquisition system and laptop computer arrangement

The BDI structural testing system was used to measure compressive and tensile strain for the UHPC and HPC girders during a diagnostic and proof test. The system has a total of 36 channels of which, all 36 were used for strain measurement for the diagnostic and proof test. The girder and stem gauges are numbered from north to south and labeled corresponding by notation. (N/S – North Leg / South Leg, B/L – Gauge placement on bottom or at mid-height of the stem, G# - Indicates the girder number.) Figure 1.39 shows the instrumentation layout for the bridge cross section. Figure 1.40 shows the instrumentation layout for the girder cross section.

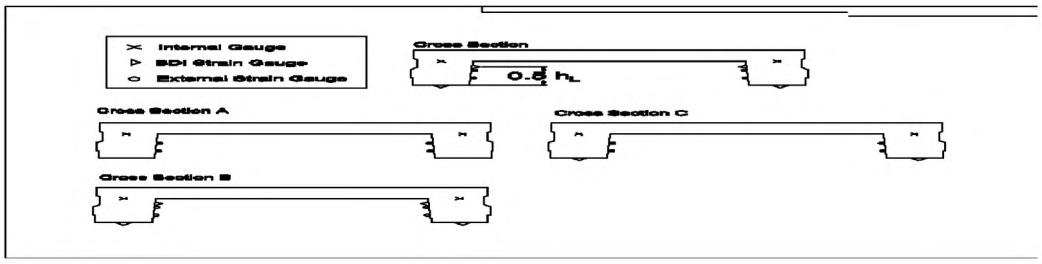


Figure 1.39: BDI instrumentation for typical girder cross section.

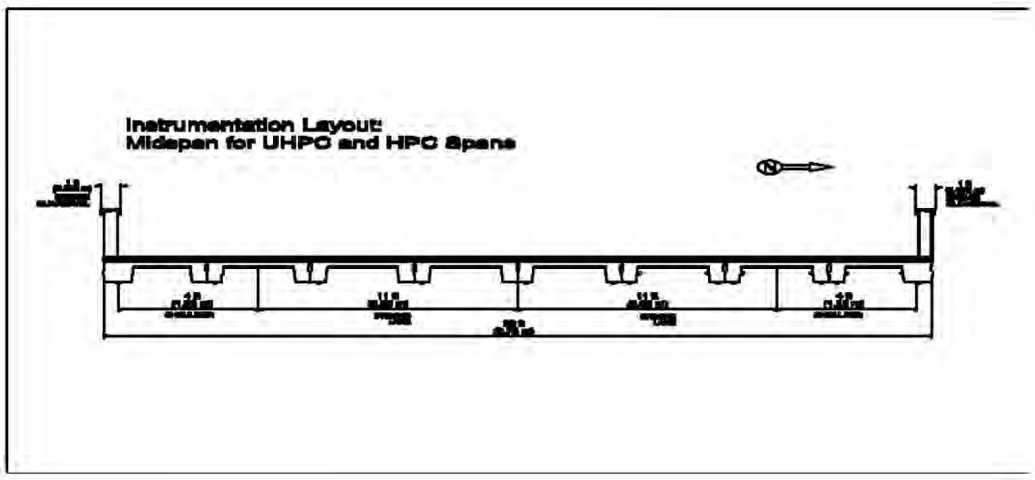


Figure 1.40: BDI instrumentation layout for bridge cross section.

1.4.1 Digital Image Correlation

The presence of high strength steel fibers in UHPC creates a dynamic between concrete-reinforcement interfaces. As tensile strain is developed, steel fibers are engaged, bridging micro-cracks throughout the UHPC bridge girders and distributing tensile stress and slowing the propagation of macro-cracks prior to fiber pullout. Strain gauges are limited to the point of application or by instrument gauge lengths. Advancements in digital image technology provide alternative methods for capturing a range of parameters during structural testing. This is particularly useful for application to UHPC containing steel fibers, as digital image correlation (DIC) may be applied to capture a larger field of strain deformation, deflections, and track the progression of potential crack development.

Through the application of photogrammetric location principles and image correlation techniques, DIC may provide a comprehensive strain profile (McGinnis 2012). High resolution cameras are placed such that their relative position and orientation with respect to one another is fixed and known. A stochastic grid pattern is marked on the surface of the specimen with adequate contrast from which thousands of unique correlation areas, referred to as facets, are defined across the imaging area. These facets are tracked through each sequential pair of images as the specimen develops strain and deformation.

While traditional instrumentation provided ample information regarding the bridge behavior, digital image correlation (DIC) was applied to capture discrete UHPC and HPC bridge girder behaviors, providing a more comprehensive strain profile. DIC was applied at midspan to the east and west exterior faces for UHPC and HPC spans, as well as at midspan on the bottom of girder legs. The exterior face of bridge spans are marked with white chalk, and the bottom of girders are marked with a black marker to form grid pattern as seen in Figure 1.41 and Figure 1.42. Multiple sets of cameras were utilized to capture strain deformation, deflections, and potential

crack development throughout the load testing of the bridge. The non-orthogonal grid is intentionally randomized to identify locations on the surface and facilitate the monitoring of deformations.



Figure 1.41: Stochastic white chalk grid pattern and DIC cameras set up at the north face of the exterior girder H-1.



Figure 1.42: Stochastic black marker grid pattern on the bottom of UHPC girder legs for girder U-2 and U-3.

A total of eight Digital Image Correlation (DIC) sensor systems were deployed at various locations of the bridge. Four 3D and four 2D DIC systems were positioned at the mid-span of both fascia girders and one of the interior girders for each span. For this testing, the DIC sensors were used to measure surface strains and displacements. A pattern used to capture these measurements was drawn on the surface of the girder using chalk. The surface strains captured will be compared to measurements obtained from BDI strain transducers placed at the same location in a later report. A limitation of most experimental load testing is the ability to capture in-situ displacement measurements due to the limitations in mounting the sensors directly to the bridge element. Traditional displacement sensors like Linear Variable Displacement Transducers (LVDTs) and String Potentiometers (String Pots) only allow for displacements to be measured at a single point. The DIC system allows for the cameras to be positioned away from the element which allows for a full field view of displacement readings and is not limited to a single point measurement.

The camera systems used for this testing included: The FASTEC IL5 and FASTEC HiSpec1 high speed digital cameras, a 2M ARAMIS system, DMK monochrome industrial cameras from The Imaging Source, 2 GoPro Hero + cameras and 2 GoPro Hero 3 cameras. Table 1.17 outlines the camera systems used on the two different spans, their location, their normal (perpendicular) distance to the bridge girder surface and whether the system was used as a 2D or 3D system. Each of the testing systems that were deployed are shown in Figure 1.43 through Figure 1.48.

Table 1.17: Camera Systems Used for DIC Monitoring

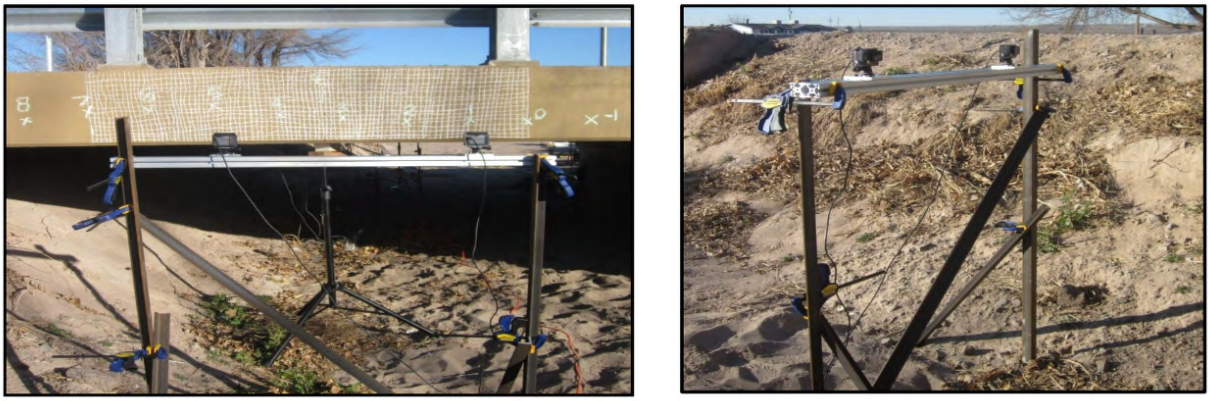
	Camera System	2D or 3D DIC	Sensor Location	Normal Distance from Camera to Beam Surface
HPC	HiSpec1	3D	Exterior Girder	2.82 m (9.25 ft.)
	Go Pro Hero +	2D	Exterior Girder	Approximately 3 m (9.84 ft)
	Go Pro Hero +	2D	Exterior Girder	Approximately 3 m (9.84 ft)
	DMK	3D	Interior Girder	1.32 m (4.33 ft.)
UHPC	IL5	3D	Exterior Girder	3.02 m (9.92 ft.)
	Go Pro Hero 3	2D	Exterior Girder	Approximately 3 m (9.84 ft)
	Go Pro Hero 3	2D	Exterior Girder	Approximately 3 m (9.84 ft)
	2M	3D	Interior Girder	1.04 m (3.42 ft.)



Figure 1.43: FASTEC IL5 System for monitoring exterior girder of UHPC span.

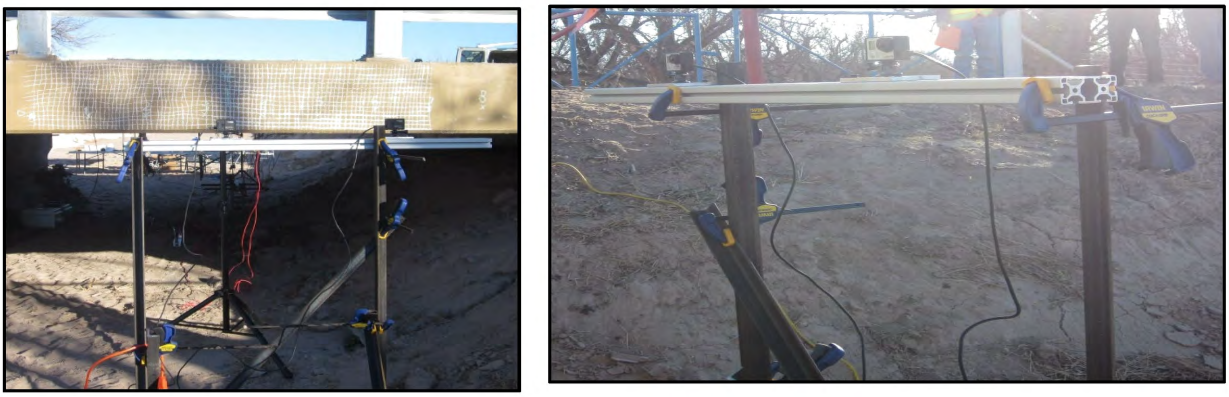


Figure 1.44: FASTEC HiSpec1 System for monitoring exterior girder of HPC span.



(a) (b)

Figure 1.45: View of GoPro Hero + System for monitoring exterior girder of HPC span from (a) behind cameras and (b) in front of cameras.



(a) (b)

Figure 1.46: View of GoPro Hero 4 System for monitoring exterior girder of HPC span from (a) behind cameras and (b) in front of cameras.



Figure 1.47: 2M System for monitoring an interior girder of UHPC span.



Figure 1.48: 2M System for monitoring an interior girder of HPC span.

The sensors monitoring the fascia were mounted on custom designed frames made from L2x2x1/4" angle iron and quick grips to create a frame that would not only support the weight of the camera system but was also rigid enough to keep the cameras from swaying as a result of any wind. Example of this frame system are seen in Figure 1.43 through Figure 1.46. Figure 1.49and Figure 1.50 show the location of the four 3D DIC systems as well as the command station where the camera systems were controlled. Figure 1.45, Figure 1.46 and Figure 1.50 show examples of the chalk patterning used for DIC. Figure 1.51 illustrates the location of each DIC system using a plan view of the bridge.

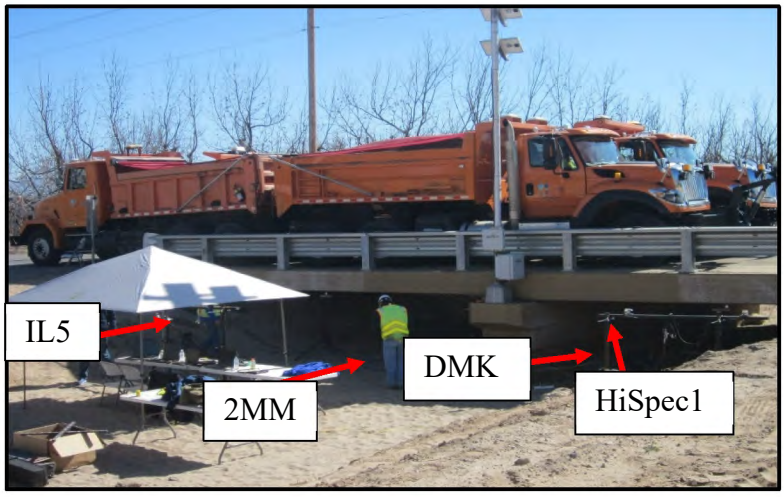


Figure 1.49:Side view of Bridge No. 9706 showing 4 DIC systems.

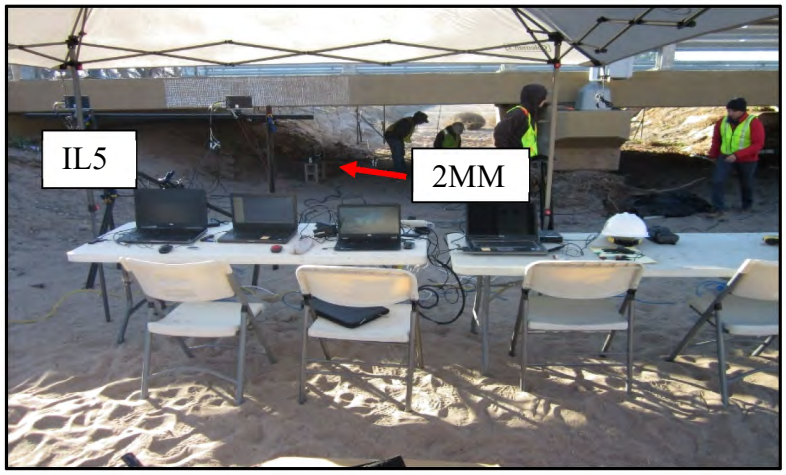


Figure 1.50: Command station with computer systems running DIC cameras.

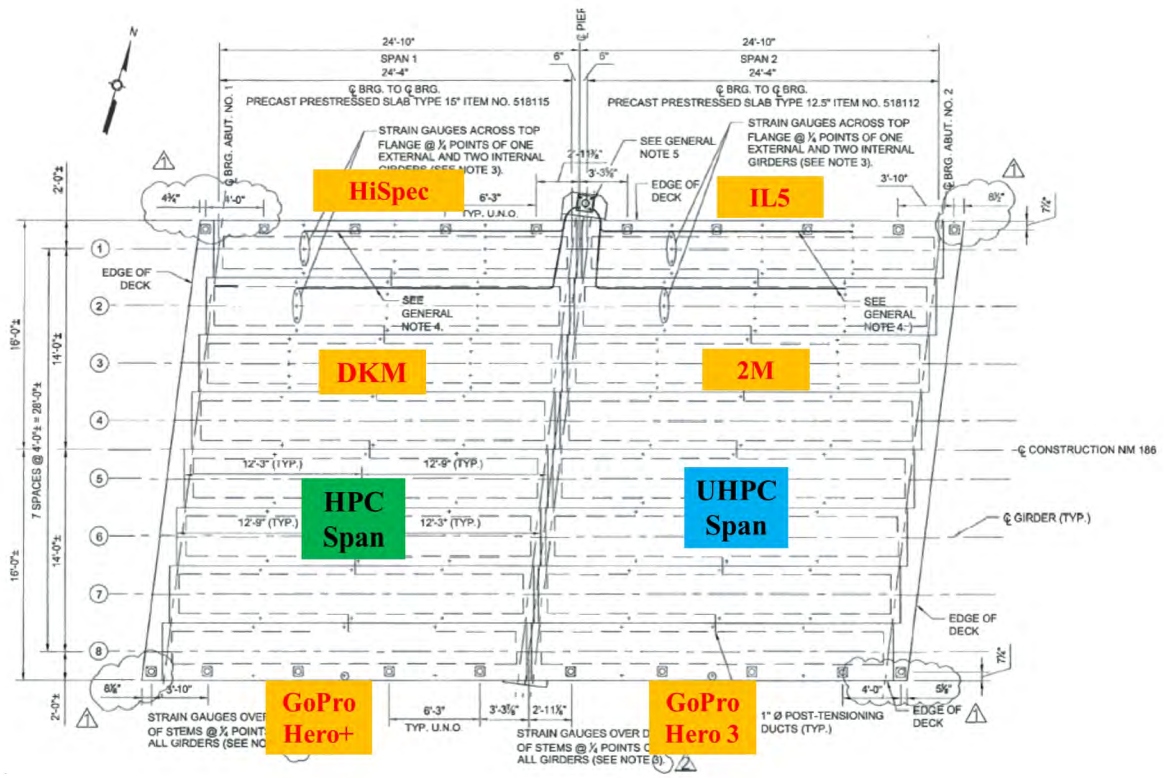


Figure 1.51: Locations of each DIC camera system for monitoring of Bridge No. 9706.

1.5 Diagnostic Load Testing

A diagnostic test was used to gain a better understanding of the bridge behavior before the proof test. The magnitude of the total truck load applied on the bridge in a diagnostic test should be smaller than the target proof load due to the uncertainties in the bridge response. In a proof test, load trucks, weighing around 60 kips (267 kN), are typically used to maximize the load experienced on the bridge by applying multiple load trucks during a specific load path encompassed within the complete proof load test. In contrast, the diagnostic test applies similar loads, however, truck load paths are not applied to maximize load but to compare strain behavior, ensure effective load distribution between adjacent girders for Bridge 9706, and to compare initial behavioral response between the UHPC and HPC spans, of which both are designed to have comparable flexural capacities.

On March 30th, 2017 the diagnostic test was performed on Bridge 9706. The diagnostic test consisted of a pre-test encompassed of a few slow-moving truck load paths to calibrate the BDI Strain Transducers and ensure strain values matched closely to the expected strain values calculated in Section 2.21. The day before, March 29, 2017, 36 external BDI Strain Transducers were attached as shown in the instrumentation layout in Section 1.4. Load paths were established to ensure effective load distribution between adjacent girders, and to compare initial behavioral response between the UHPC span and HPC span. Load paths were designed to isolate individual girders with specific load paths and to determine the load distribution symmetry of the bridge.

1.5.1 Truck Paths and Phases

Truck load paths using NMDOT 10 yd^3 trucks were used for the diagnostic test. Based on bridge geometry, rail to rail dimensions, and NMDOT Bridge Procedures and Design Guide 3.1.3.2 (2018), 9 truck load paths were designed for the diagnostic. Each load path was characterized by the number of trucks used and the type of load.

All load paths were repeated twice to ensure similar results and behavior. The load test started with a single truck placed in different transverse paths. In general, the trucks were either centered along a particular beam or between two beams. Each truck load sequence began with paths that were placed 9 in. (228 mm) from either the south or north guardrail. The direction of truck load paths for the diagnostic were applied progressing west. All truck load paths started on the East UHPC proceeding longitudinally to the West HPC span.

Throughout the diagnostic, the strain at the bottom of the beams at midspan were monitored so the loading could be halted, if necessary, before exceeding the available strain capacity. Trucks were applied to the bridge during the diagnostic test as either a moving load or incremental load. Moving loads are characterized by applying the truck through load paths at 5 mph. The incremental loads are characterized by applying the truck at pre-marked positions, or stations, longitudinally across the bridge.

The diagnostic test was conducted in two sequences with two loading phases for each sequence. Sequence 1.a designates the first phase of Sequence 1 which was comprised of applying a single 10 yd^3 truck as a slow-moving load sequentially through six single truck load paths shown

in (see Figure 1.28, Section 1.2.1.1). Each of the six single truck load paths were repeated to adequately confirm consistent behavior. Sequence 1.b designates the second phase of Sequence 1 which was comprised of applying two 10 yd^3 trucks side-by-side as a slow-moving load through three double truck moving load paths (Figure 1.29, Section 1.2.1.1).

Sequence 2.a designates the first phase of Sequence 2 which consisted of a single 10 yd^3 truck applied as an incremental load for a limited number of critical single truck load paths at both end points, quarter points and mid-span locations for both UHPC and HPC spans. Lastly, Sequence 2.b designates the second phase of sequence 2 which consisted of two 10 yd^3 trucks side-by-side applied as an incremental load for limited number of critical double truck load paths at matching locations as Sequence 2.a. Likewise, each single incremental load path and side-by-side incremental load path for sequence 2 were repeated. Each load path was designed to demonstrate three main characteristics: maximum strain for each individual girder, transverse strain distribution between UHPC and HPC girders, and behavior symmetry of the bridge.

Furthermore, Two NMDOT load trucks were used weighing on average 61.2 kips (274 kN) completing a total of 30 load paths that were performed during the diagnostic test. Table 1.3 shows the axle weights of the 10 cubic trucks used for the diagnostic test. Figure 1.52 shows pictures of the diagnostic load test.



Figure 1.52: Photographs from diagnostic load test of Bridge 9706.

1.5.2 Diagnostic Test Results

The results of the diagnostic test include the maximum strain for each load path and the representing strain transducer and the location on the UHPC span and HPC span. Additionally, the diagnostic test results are used to illustrate the effectiveness of the shear keys to distribute load evenly across adjacent girder. BDI Strain Transducers placed on adjacent girder legs demonstrate the ability for the girders to transfer loads across the span. The results were also used to calculate the neutral axis location. The experimentally determined neutral axis location was compared to the calculated non-composite and composite neutral axis to determine if composite action between the deck and girders was established. Finally, comparisons were made between the UHPC span and the HPC span. A summary is provided comparing maximum strains for single and double trucks, with slow-moving and incremental load paths, as well as the location of the neutral axis during various load paths.

1.5.2.1 Maximum Strain

Strains are continuously monitored and recorded through the 36 BDI Strain Transducers. Table 1.18 through Table 1.25 show the maximum recorded strain measurements for each BDI Strain Transducer for each load path on the UHPC span and HPC span. The overall maximum value of recorded strain, for each load path on each span, is indicated in bold.

Table 1.18: Maximum Diagnostic Strain: UHPC Single Moving Truck Load

	Maximum Strain: με, in./in. (mm/mm)					
Gauge Location	Path 1	Path 2	Path 3	Path 4	Path 5	Path 6
UHPC NBG1	80.7	47.4	19.2	8.4	4.2	3.28
UHPC SBG1	87.9	61.8	27.9	16.9	9.2	6.87
UHPC NBG2	81.0	61.3	29.0	19.2	7.0	5.62
UHPC SBG2	67.0	63.2	41.5	28.9	12.5	10.13
UHPC NBG3	66.1	64.7	48.0	32.1	14.9	13.51
UHPC SBG3	60.5	65.5	64.0	51.1	27.8	25.78
UHPC NBG4	54.2	54.7	60.0	54.2	31.7	24.47
UHPC SBG4	45.2	47.5	66.0	69.2	55.8	47.54
UHPC SBG5	21.4	22.8	47.0	62.9	60.1	62.38
UHPC SBG6	12.5	11.6	28.2	44.4	64.2	71.16
UHPC SBG7	4.7	4.7	13.7	25.0	45.8	86.42
UHPC SBG8	1.9	1.5	5.3	17.8	31.8	85.34

Table 1.19: Maximum Diagnostic Strain – HPC Single Moving Truck Load

Maximum Strain: με, in./in. (mm/mm)						
Gauge Location	Path 1	Path 2	Path 3	Path 4	Path 5	Path 6
HPC NBG1	73.7	37.5	11.8	5.9	1.8	2.36
HPC SBG1	76.0	50.3	19.2	13.5	5.7	5.69
HPC NBG2	78.0	60.1	27.7	17.3	6.5	7.18
HPC SBG2	69.8	72.3	44.8	29.4	14.7	14.72
HPC NBG3	66.8	68.1	44.2	30.4	15.7	12.86
HPC SBG3	56.0	60.8	62.7	49.9	29.9	24.49
HPC NBG4	55.9	61.0	65.1	54.7	34.6	26.08
HPC SBG4	49.3	52.7	74.9	73.0	59.9	53.67
HPC SBG5	24.6	29.5	57.2	71.5	74.3	72.74
HPC SBG6	9.4	11.5	27.5	42.7	69.9	77.35
HPC SBG7	2.3	5.2	13.1	22.0	42.6	77.76
HPC SBG8	-1.8	2.7	7.2	10.3	24.7	77.98

Table 1.20: Maximum Diagnostic Strain – UHPC Double Moving Truck Load

Maximum Strain: με, in./in. (mm/mm)			
Gauge Location	Path 7	Path 8	Path 9
UHPC NBG1	97.1	56.3	53.9
UHPC SBG1	113.5	72.3	71.0
UHPC NBG2	106.8	74.5	74.0
UHPC SBG2	98.4	70.9	84.9
UHPC NBG3	104.3	70.3	85.7
UHPC SBG3	105.6	75.4	98.7
UHPC NBG4	99.3	66.2	96.0
UHPC SBG4	97.4	96.9	113.1
UHPC SBG5	75.0	106.1	93.6
UHPC SBG6	43.4	110.0	74.9
UHPC SBG7	24.6	106.3	53.4
UHPC SBG8	12.1	95.0	34.7

Table 1.21: Maximum Diagnostic Strain – HPC Double Moving Truck Load

Maximum Strain: με, in./in. (mm/mm)			
Gauge Location	Path 7	Path 8	Path 9
HPC NBG1	86.1	49.8	60.8
HPC SBG1	91.9	61.7	70.6
HPC NBG2	103.5	71.8	82.2
HPC SBG2	110.7	78.7	89.6
HPC NBG3	108.6	72.5	88.5
HPC SBG3	98.3	73.5	93.5
HPC NBG4	99.0	67.9	99.6
HPC SBG4	97.7	98.9	121.1
HPC SBG5	73.1	125.6	108.8
HPC SBG6	67.4	114.5	77.7
HPC SBG7	39.4	92.3	45.4
HPC SBG8	24.7	83.4	29.6

Table 1.22: Maximum Diagnostic Strain – UHPC Single Incremental Truck Load

Maximum Strain: με, in./in. (mm/mm)						
Gauge Location	Path 1	Path 2	Path 3	Path 4	Path 5	Path 6
UHPC NBG1	84.4	35.7	10.3	6.6	9.4	2.35
UHPC SBG1	93.4	52.2	20.1	9.6	5.5	2.75
UHPC NBG2	84.8	50.1	21.1	12.6	9.4	0.94
UHPC SBG2	68.0	58.4	36.7	24.1	9.2	5.31
UHPC NBG3	68.0	53.1	40.5	26.1	15.8	7.92
UHPC SBG3	41.2	53.6	63.0	48.1	29.3	24.29
UHPC NBG4	35.0	45.6	57.1	50.9	31.2	25.91
UHPC SBG4	19.9	30.0	62.8	65.5	54.5	48.92
UHPC SBG5	3.3	14.9	43.8	62.4	63.3	58.66
UHPC SBG6	0.0	6.5	23.1	36.0	68.9	75.79
UHPC SBG7	3.8	5.7	8.0	19.4	52.0	89.73
UHPC SBG8	1.9	4.3	5.8	13.0	49.7	73.28

Table 1.23: Maximum Diagnostic Strain – HPC Single Incremental Truck Load

	Maximum Strain: με, in./in. (mm/mm)					
Gauge Location	Path 1	Path 2	Path 3	Path 4	Path 5	Path 6
HPC NBG1	72.6	18.0	21.8	15.9	3.2	10.62
HPC SBG1	70.0	37.1	30.2	24.2	2.4	12.27
HPC NBG2	71.8	39.2	32.3	33.3	2.3	9.14
HPC SBG2	57.0	41.0	47.4	45.8	7.7	8.64
HPC NBG3	50.5	38.3	48.3	46.4	4.7	9.1
HPC SBG3	37.9	39.4	62.0	66.2	23.5	27.04
HPC NBG4	33.3	33.6	62.2	71.0	25.1	25.77
HPC SBG4	27.2	35.9	66.5	78.6	49.6	54.29
HPC SBG5	2.8	5.3	65.0	84.2	71.5	73.05
HPC SBG6	1.6	-0.3	25.6	50.8	50.5	73.61
HPC SBG7	5.2	2.3	20.6	31.9	30.0	71.67
HPC SBG8	9.0	8.1	17.5	21.1	28.7	68.57

Table 1.24: Maximum Diagnostic Strain – UHPC Double Incremental Truck Load

Maximum Strain: με, in./in. (mm/mm)		
Gauge Location	Path 7	Path 8
UHPC NBG1	101.0	46.0
UHPC SBG1	125.0	62.7
UHPC NBG2	117.0	67.4
UHPC SBG2	115.0	70.4
UHPC NBG3	116.0	73.1
UHPC SBG3	114.0	76.4
UHPC NBG4	105.0	76.8
UHPC SBG4	105.0	99.7
UHPC SBG5	75.0	102.0
UHPC SBG6	68.9	113.0
UHPC SBG7	61.4	113.0
UHPC SBG8	44.4	95.9

Table 1.25: Maximum Diagnostic Strain – HPC Double Incremental Truck Load

Maximum Strain: με, in./in. (mm/mm)		
Gauge Location	Path 7	Path 8
HPC NBG1	100.0	48.1
HPC SBG1	110.0	60.20
HPC NBG2	124.0	70.5
HPC SBG2	126.0	77.4
HPC NBG3	120.0	74.7
HPC SBG3	112.0	70.0
HPC NBG4	114.0	78.6
HPC SBG4	111.0	106.0
HPC SBG5	92.6	142.0
HPC SBG6	78.6	118.0
HPC SBG7	55.3	99.3
HPC SBG8	41.7	90.1

1.5.2.2 Transverse Strain Distribution

BDI Strain Transducers placed were placed both on the bottom of channel girder legs and at mid-height on the stem located at midspan for both the UHPC span and the HPC span. BDI Strain Transducers placed at mid-height on adjacent channel girder legs, as shown in Figure 1.53, demonstrate the effectiveness to distribute load across the width of the span. Similar values in recorded strain validate that both girders were working together to support the truck loads.

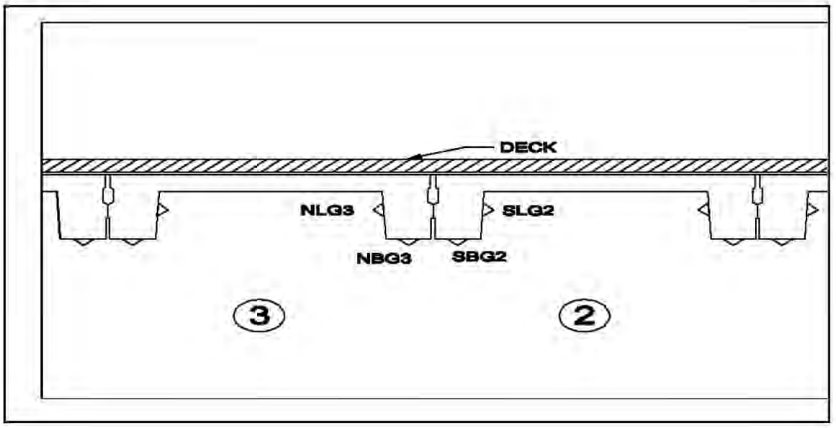


Figure 1.53: Location of strain gauges on adjacent girders measuring load distribution.

For the diagnostic test, transverse strain distribution was analyzed using the BDI Strain Transducers placed on adjacent girders. Figure 1.54 through Figure 1.57 show the measured transverse strain diagrams for UHPC and HPC girders 1 and 2 as well as UHPC and HPC girders 2 and 3. For Figure 1.54 through Figure 1.57, the x-axis measuring time is arbitrary and does not represented the interval time in other figures presented.

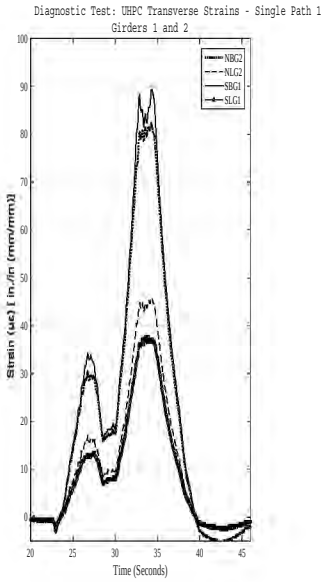


Figure 1.54: Diagnostic Test – Transverse strain girders H-1 and H-2, Single Path 1.

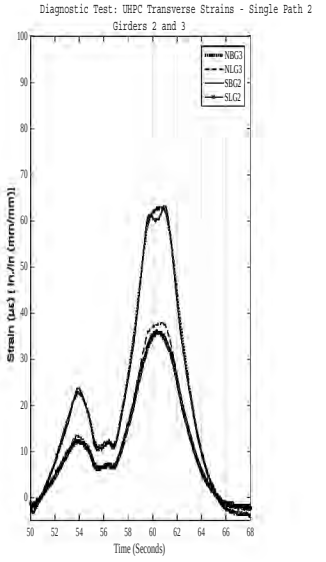


Figure 1.55: Diagnostic Test – Transverse strain girders H-2 and H-3, Single Path 1.

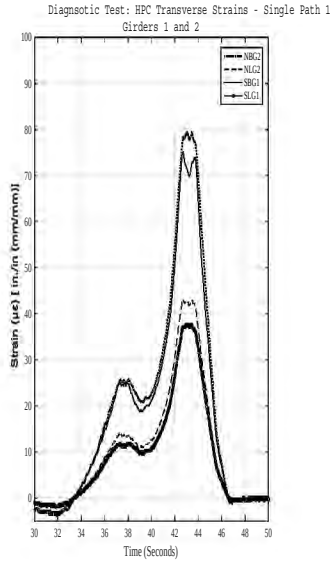


Figure 1.56: Diagnostic Test – Transverse strain girders U-1 and U-2, Single Path 1.

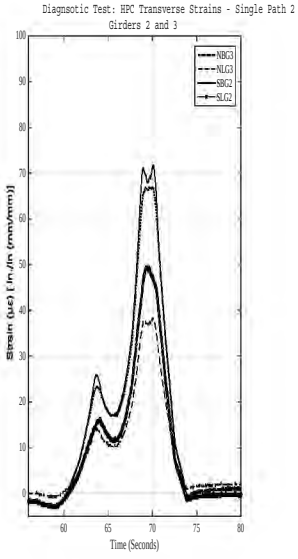


Figure 1.57: Diagnostic Test – Transverse strain girders U-2 and U-3, Single Path 1.

Based on the diagnostic transverse strain results, shown in Figure 1.54 through Figure 1.57, the BDI Strain Transducers placed on the bottom of each girder leg measured higher values of tensile strain, as expected. The BDI Strain Transducers placed on adjacent girder legs at mid-height experience a lower value of recorded strain. Gauges on the bottom of girder stems, as well as gauges placed at mid-height of girder legs, show similar recorded values of strain across adjacent girders. This indicates that the truck load is being distributed evenly during the diagnostic test.

It is important to note that the maximum strain shown depends on the placement of the load truck tire during each load path. For single truck path 1, the load truck tire was closer to NBG3 and NLG3, compared to SBG2 and SLG2. For this reason, maximum strains are measured by gauges on the North stem of girder 3, with slightly lower values of measured strain for gauges on the South stem of girder 3. A similar occurrence was observed for single path 2. The load truck tire is closer to the gauges placed on the South stem of girder 2 and therefore have higher measured strains than the strains measured by the gauges on the North stem of girder 2.

1.5.2.3 Composite and Non-Composite Neutral Axis Behavior

A comparison was made between the calculated non-composite and composite neutral axis locations. The measured composite neutral axis was determined by assuming a linear strain profile using the measured strains at different heights along the same vertical plane of the stem of the girder. The shear stirrups in the UHPC and HPC girders were design to extend 2 ½ in. (63.5 mm) out of the top of girders. The deck was cast on top of the girders and the shear stirrups were designed to be developed into the deck to create a composite superstructure. The location of the neutral axis depends on relative stiffness and overall size of each material section. The neutral axis for a non-composite girder will be lower in the cross-section than to the neutral axis of a composite girder. The deck increases the total area above the girder, rising the neutral axis.

To determine the measured neutral axis, two values of strain are needed within the same vertical plane. Strain compatibilty was used to determine the neutral axis under various loads using Eqaution 1.18 below, where $\mu\varepsilon_{(GB)}$ is the strain measured at the BDI Strain Transducer placed on the bottom of the girder leg, $\mu\varepsilon_{(GS)}$ is the strain measured at the BDI Strain Transducer placed at mid-height on the girder leg, and d_{gauge} is the distance between bottom and mid-height stem gauges, as shown in Figure 1.58.

$$\text{n.a.} = \frac{\mu\varepsilon\,(G_B)}{\mu\epsilon(G_B) - \mu\epsilon(G_S)} * d_{gauge} \qquad 1.18$$

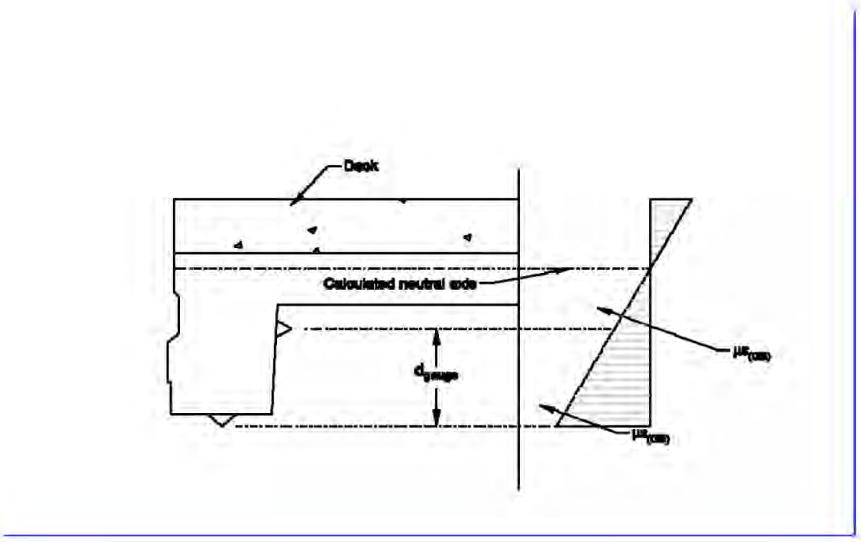


Figure 1.58: Girder cross section: Strain profile.

Average neutral axis results for the diagnostic test for girder 2 and girder 3 are presented in Table 1.26 and Table 1.27. The neutral axis is measured from the bottom of the UHPC and HPC girder. The location of the neutral axes for UHPC and HPC girder 2 and girder 3 during the diagnostic test are shown in Figure 1.59 through Figure 1.66. For each figure, the measured, average neutral axis between north and south stems, and composite and non-composite neutral axes are shown for comparison.

Table 1.26: Diagnostic Test – UHPC Average Neutral Axis

	Average Neutral Axis, in. (mm)	
Load Path	G2	G3
Path 1	9.5 (241.3)	9.5 (241.3)
Path 2	9.5 (241.4)	9.0 (228.6)
Path 3	9.6 (243.8)	9.2 (233.7)
Path 4	9.5 (241.3)	8.7 (221.0)
Path 5	8.3 (210.8)	8.1 (205.7)
Path 6	8.2 (208.3)	8.1 (205.7)

Table 1.27: Diagnostic Test – HPC Average Neutral Axis

	Average Neutral Axis, in. (mm)	
Load Path	G2	G3
Path 1	13.3 (337.8)	13.2 (335.3)
Path 2	12.9 (327.7)	12.7 (322.6)
Path 3	13.8 (250.5)	13.3 (337.8)
Path 4	12.1 (307.3)	13.9 (253.1)
Path 5	14.2 (360.7)	13.1 (332.7)
Path 6	12.4 (315.0)	13.4 (340.4)

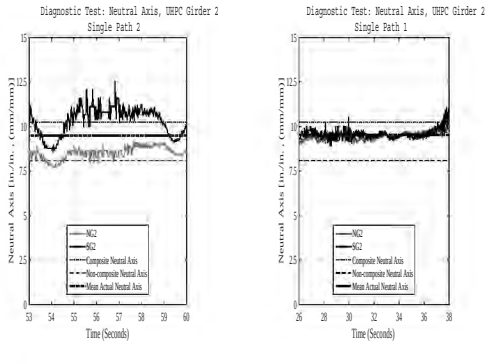


Figure 1.59: Diagnostic Test – Girder U-2, Single Path 1.

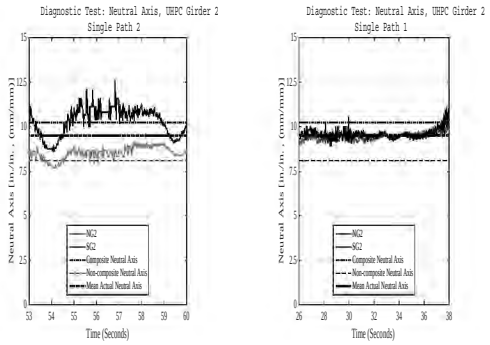


Figure 1.60: Diagnostic Test – Girder U-2, Single Path 2.

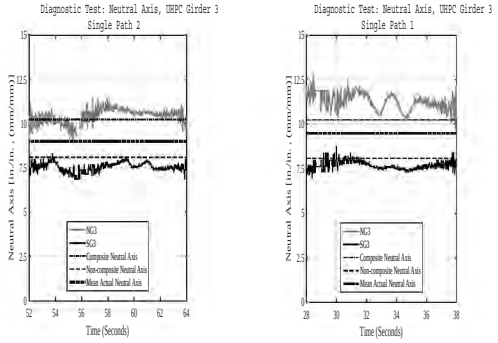


Figure 1.61: Diagnostic Test – Girder U-3, Single Path 1.

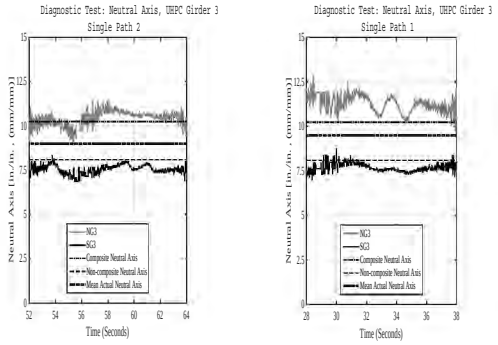


Figure 1.62: Diagnostic Test – Girder U-3, Single Path 2.

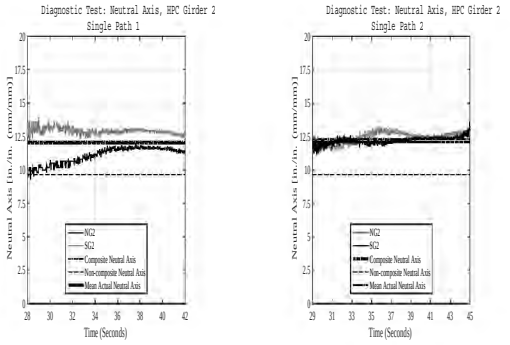


Figure 1.63: Diagnostic Test – Girder H-2, Single Path 1.

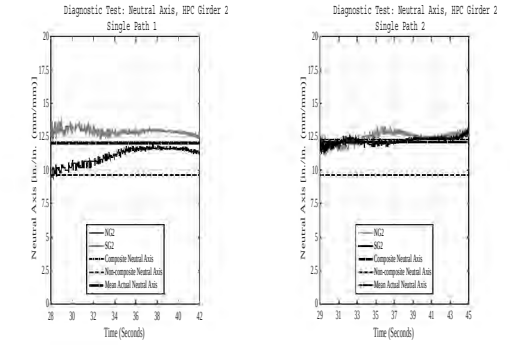


Figure 1.64: Diagnostic Test – Girder H-2, Single Path 2.

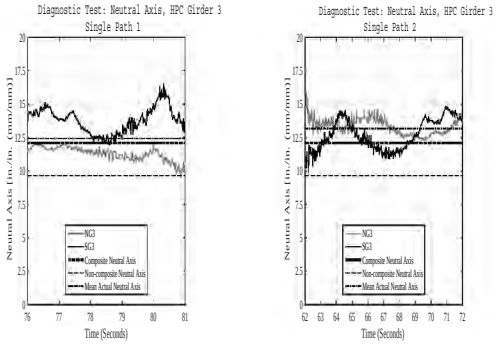


Figure 1.65: Diagnostic Test – Girder H-3, Single Path 1.

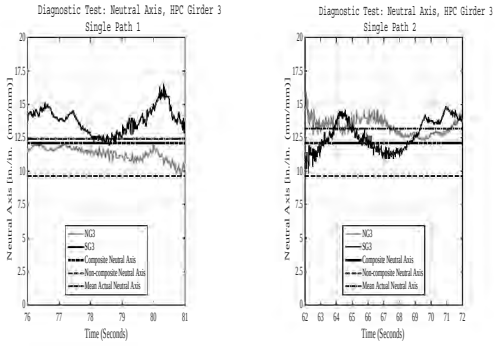


Figure 1.66. Diagnostic Test – Girder H-3, Single Path 2.

1.5.3 UHPC and HPC Diagnostic Test Comparison

1.5.3.1 Comparison of Strain Behavior

The largest measured strains for sequence 1.a, (moving single truck load test) of the UHPC span, were 87.9 με and 86 με during single paths 1 and 6, respectively (Table 1.18). For the HPC span, the largest measured strains were 78 με and 77.98 με during path 1 and path 6, respectively (Table 1.19).

In sequence 1.b (moving double truck load test) the largest measured strains for the UHPC span were 113.5 με and 110 με for paths 7 and 8, see (Table 1.20). For the HPC span, the largest measured strains were 125.6 με and 121 με during double truck load paths 8 and 9 (Table 1.21).

For sequence 2.a (incremental single truck load test) the largest recorded strains for the UHPC span were 102.5 με and 89 με for paths 1 and 6, see (Table 1.22). For the HPC span, the largest recorded strains were 84.5 με and 84.2 με during paths 1 and 4 (Table 1.23).

Lastly, in sequence 2.b, (incremental moving truck load test) the largest recorded strains for the UHPC span were 116 με for path 7 (Table 1.24). For the HPC span, the largest recorded strain was 142 με during path 8 (Table 1.25).

Overall, comparing strains between the UHPC span and the HPC span for all diagnostic sequences a few conclusions can be made:

- The measured strains for the incremental single truck load test during the diagnostic test were, on average 6% higher than the slow-moving single truck load tests, for the UHPC and HPC spans, respectively. Incremental load paths are designed to stop at specific stations along the bridge for a period of time. Compared to the moving load, incremental truck loads measure more precise values of measured strain because they are stationary at maximum moment regions. The moving truck load doesn't allow for the maximum tensile strain to develop due to the speed of loading. Higher values of measured strains are expected for the incremental load tests in comparison to the moving load tests.
- Overall, strains measured by the single moving and incremental load tests, during the diagnostic test, in the UHPC span measured approximately 9% higher than strains recorded in the HPC span. The maximum strains for the UHPC span occurred in either girder 2 or 7. The HPC girders have a larger cross-sectional area in comparison to the UHPC girders. Although the UHPC and HPC girders were designed to have the same capacity, UHPC girders measured higher values of strain due to the reduced cross-sectional properties when a single load truck was used.
- The measured strains by the incremental double truck load tests were, on average, 7% higher than the slow-moving double truck load tests for the UHPC and HPC spans. As expected, the incremental truck loads measure more precise values of measured strain because they are stationary at maximum moment regions.
    - Between incremental and moving single truck load tests a percent difference of 6% was calculated. For incremental and moving double truck load tests, a percent difference of 7% was calculated. Results reflect that with an increase of total load, the percent increase between incremental and moving load tests remained similar.

- Overall, strains measured in the HPC span are approximately 5% higher than strains measured in the UHPC span. For incremental and moving double truck loads paths, the HPC girders measured higher values of strain, however, during the incremental and moving single truck load paths, the UHPC girders measured higher values of strain. On average, UHPC and HPC girder show closer values of measured strain when two load trucks were used. UHPC girders showed to distributed load better than HPC girder for sequence 1.b and 2.b. The maximum strain occurred in HPC girder 5. It is important to note the largest measured diagnostic test strain of 127.0 με occurred during the incremental double truck load test.

1.5.3.2 Comparison of Actual and Expected Strain

An evaluation of the maximum measured diagnostic test strains to the expected strains are tabulated in Table 1.28. The percent difference between the expected strains to the recorded diagnostic strains are also shown.

Overall, the measured strain profile for UHPC and HPC matched well with theoretical beam behavior, indicating the analytical method of behavior predictions to be accurate and valid for the UHPC and HPC bridge girders. Expected strains display slightly higher strains during the diagnostic test. AASHTO specifications and the designed RISA models used to calculate the expected strains show to be conservative compared to the measured strain.

Table 1.28: Diagnostic Test – Expected Versus Measured Strain

Load Test		UHPC Strain με, in./in. (mm/mm)	HPC Strain με, in./in. (mm/mm)
Interior (Single)	expected	101.0	89.7
	measured	89.7	84.24
	% difference	-11%	-6%
Exterior (Single)	expected	103.0	91.5
	measured	93.37	77.98
	% difference	-9%	-15%
Interior (Double)	expected	134.7	119.6
	measured	117.0	127.0
	% difference	-13%	6%
Exterior (Double)	expected	137.3	122.0
	measured	125.00	110.0
	% difference	-9%	-10%

1.5.3.3 Comparison of Neutral Axis Behavior

Overall, comparing the measured neutral axis between UHPC and HPC girder 2 and girder 3, a few conclusions can be made.

- The theoretical non-composite neutral axis measured from the bottom of the interior UHPC girder is 8.1 in. (205.8 mm) and for an interior HPC girder is 9.6 in. (243.4 mm). The increase in height between the theoretical non-composite and composite neutral axis for UHPC and HPC girders is due to the placement of a 5 in. (127 mm) concrete deck.
- The theoretical composite neutral axis measured from the bottom of the interior UHPC girder is 10.2 in. (259.1 mm) and for an interior HPC girder is 12.1 in. (307.3 mm).
- The average measured neutral axis measured from the bottom of the UHPC girder 2 during the diagnostic test was approximately 9.1 in. (230.6 mm). The average measured neutral axis for UHPC girder 3 during the diagnostic test was approximately 8.8 in. (223.5 mm).
    - The mean neutral axis for UHPC girder 2 is approximately 1.1 in. (27.9 mm) below the theoretical composite neutral axis, and 1 in. (25.4 mm) above the theoretical non-composite neutral axis.
    - The measured neutral axis for UHPC girder 3 is approximately 1.4 in. (35.6 mm) below the theoretical composite neutral axis, and 0.7 in. (17.8 mm) above the theoretical non-composite neutral axis.
- The average measured neutral axis for HPC girder 2 during the diagnostic test was approximately 13.1 in. (330.2 mm). The average measured neutral axis for HPC girder 3, during the diagnostic test, is approximately 13.2 in. (335.3 mm).
    - The measured neutral axis for HPC girder 2 was approximately 1 in. (25.4 mm) above the theoretical composite neutral axis.
    - The measured neutral axis for HPC girder 3 was approximately 1.1 in. (27.9 mm) above the theoretical composite neutral axis.
        - Diagnostic test results lend that the HPC girder 2 and girder 3 exhibit composite behavior. The measured neutral axis is located above the calculated theoretical neutral axis therefore it can be concluded that the deck and HPC girders are acting jointly.

1.6 Proof Load Testing

Based on the critical paths determined from the diagnostic test, the proof test was planned and conducted with the goal of applying the largest load possible to the bridge without exceeding the available moment. The bridge behavior under proof truck loading should be monitored carefully via strain measurements. For the proof test, the test vehicles were loaded to the maximum weight (i.e., between 62 and 64 kips) and positioned along the critical paths producing the largest girder strains. Because UHPC and HPC girder were loaded more heavily than the diagnostic test, the applied proof load tests, especially critical truck load tests were monitored carefully to ensure measured strains did not exceed the expected or available strains. Furthermore, starting at the abutments, the trucks were positioned at different longitudinal stations (shown in **Error! Reference source not found.** through **Error! Reference source not found.**).

On January 29-31, 2018 the first proof test was performed on Bridge 9706, nine months following the completion of the diagnostic test. The proof test consisted of a preliminary slow-moving and incremental truck load paths to calibrate the BDI Strain Transducers. These preliminary loads were conducted at the beginning of each of the three days of proof testing. The proof test also included a repeat of all the diagnostic load paths completed in May 2017. These strain results were used for comparison to the diagnostic test results. Finally, the proof test was load paths that maximized the total load applied to each span were applied, specifically, side-by-side, and back-to-back load paths with double and triple load trucks were used to load the bridge.

The day before, January 28, 2018, 36 external BDI Strain Transducers were attached similarly to the instrumentation layout as the diagnostic test. Additionally, the UHPC and HPC spans were instrumented with D.I.C. systems each of the three days of testing. Four NMDOT trucks, weighing on average 63.5 kips (282 kN), were used to complete a total of 61 load paths over the three days of testing.

For proof tests, an effort was made to maximize the moment for three loading conditions: single lane loaded (one truck or two trucks, back-to-back); two lanes loaded (four trucks, back-to-back and side-by-side); and multiple lanes loaded (two and/or three trucks, side-by-side).

1.6.1 Proof Test Load Paths

In similar fashion to the diagnostic test, the proof test consisted of four sequences. Sequence 1 consists of two testing phases. Sequence 1.A designates the first phase of Sequence 1, which was comprised of applying a single 10 yd^3 truck as a slow-moving load sequentially through three preliminary single truck load paths (see Figure 1.28, Section 1.2.1.1). Sequence 1.B designates the second phase of Sequence 1 which consists of applying a slow-moving load through three preliminary double truck load paths (Figure 1.29, Section 1.2.1.1). All three paths were repeated during the proof test for redundancy.

Sequence 2 of the proof test is a full repeat of Diagnostic Test: Sequence 1. Single and double, slow-moving truck loads are applied as Sequence 2.A and Sequence 2.B, respectively, for the proof test. This allows for direct comparison of strain behavior and results between the diagnostic and proof test.

Sequence 3 is comprised of three testing phases. Sequence 3A designates the first phase of Sequence 3 which is comprised of applying a single 10 yd^3 truck as an incremental load through six single truck load paths shown in **Error! Reference source not found.**. All six single truck load paths for Sequence 3.A were repeated. Sequence 3.B designates the second phases of Sequence 3 which is comprised of an incremental double truck load applied for three double truck load paths. Again, all three double truck loads were repeated during the proof test. Lastly, Sequence 3.C designates the third phase of Sequence 3. Sequence 3.C is comprised of an incremental triple truck load applied for one triple truck load path shown in **Error! Reference source not found.**. The single, triple truck load path was likewise repeated.

Sequence 4 is comprised of two testing phases that mirrors diagnostic test, Sequence 2. Sequence 4 entails applying back-to-back single and double truck loads. Load trucks are situated along each load path such that each truck's back axles are approximately 3 ft (0.91 m) apart such that the back-to-back distance between truck ends is less than 6 in. (152 mm). Each end of the load trucks extended 1.5 ft (0.46 m) past the back axel.

Critical proof load paths are defined by load paths which maximize the total load on the bridge for critical load paths and key locations on the bridge, such as shear and mid-span zones. Critical proof load paths were determined by the diagnostic truck load paths that caused the maximum strain behavior, and 3D RISA analysis of the induced moments of multiple truck loads on the bridge. Incremental double and triple truck load paths, as well as back-to-back incremental single and double truck load paths are regarded as critical proof load paths. Refer to Table 1.29 for proof test sequencing. An asterisk placed besides a sequence in Table 1.29 signifies a critical load path.

Table 1.29: Proof Testing Sequence

Sequence 1.A Prelim. Single Moving Truck Load
Sequence 1.B Prelim. Double Moving Truck Load
Sequence 2.A Single Moving Truck Load
Sequence 2.B Double Moving Truck Load
Sequence 3.A Single Incremental Truck Load
Sequence 3.B* Double Incremental Truck Load
Sequence 3.C* Triple Incremental Truck Load
Sequence 4.A* Single Back-to-Back Truck Load
Sequence 4.B* Double Back-to-Back Truck Load

*critical proof load paths

1.6.2 Proof Test 1 Results

The results Proof Test 1 (PT1) include the maximum strain for each preliminary load path, repeated diagnostic load paths, and proof load paths. Additionally, the PT1 results were used to illustrate the effectiveness of the shear keys to distribute load evenly across adjacent girders. BDI Strain Transducers placed on adjacent girder legs demonstrate the ability for the girders to transfer load across the span. The results were also used to calculate the neutral axis location. The experimentally determined neutral axis location was compared to the theoretical non-composite and composite neutral axis to determine if composite action between the deck and girders was established. Finally, comparisons were made between the UHPC span and the HPC span.

1.6.2.1 Maximum Strain

Strains were continuously monitored and recorded throughout PT1. Table 1.30 through Table 1.43 show the maximum measured strain for each BDI Strain Transducer for each respective load path on the UHPC span and HPC span. The overall maximum value of recorded strain, for each load path on each span, is indicated in bold.

Table 1.30: PT1: Maximum Strain – UHPC Span Single Moving Truck Load

Maximum Strain: με, in./in. (mm/mm)						
Gauge Location	Path 1	Path 2	Path 3	Path 4	Path 5	Path 6
UHPC NBG1	75.98	48.31	21.11	12.20	2.81	8.44
UHPC SBG1	86.51	59.96	32.96	16.48	8.70	8.70
UHPC NBG2	81.48	67.43	35.12	17.33	8.90	9.83
UHPC SBG2	65.60	67.53	43.41	22.67	12.06	12.06
UHPC NBG3	69.86	72.65	53.09	33.07	14.44	19.09
UHPC SBG3	51.07	70.90	73.38	49.08	29.75	26.77
UHPC NBG4	46.54	68.61	69.57	56.61	31.67	30.23
UHPC SBG4	28.15	53.08	76.61	74.31	56.31	49.38
UHPC SBG5	14.43	25.14	48.41	72.16	67.50	66.57
UHPC SBG6	5.55	13.86	29.58	53.14	73.94	76.71
UHPC SBG7	1.89	6.14	16.53	34.95	68.48	94.45
UHPC SBG8	1.93	5.30	11.09	21.21	47.73	81.00

Table 1.31: PT1: Maximum Strain – HPC Span Single Moving Truck Load

Maximum Strain: με, in./in. (mm/mm)						
Gauge Location	Path 1	Path 2	Path 3	Path 4	Path 5	Path 6
HPC NBG1	71.96	47.78	17.11	9.44	2.36	0.88
HPC SBG1	78.12	56.57	24.24	13.47	4.49	2.10
HPC NBG2	90.73	72.13	33.94	16.32	7.83	3.92
HPC SBG2	77.12	81.93	53.44	30.08	16.32	8.64
HPC NBG3	69.97	74.68	52.40	29.81	16.00	8.47
HPC SBG3	60.43	77.93	79.20	54.71	32.12	17.81
HPC NBG4	48.71	69.45	72.59	54.68	33.31	15.71
HPC SBG4	34.01	54.91	79.88	78.00	60.53	31.83
HPC SBG5	13.68	30.46	64.03	89.21	84.86	65.59
HPC SBG6	4.06	14.35	31.50	51.15	82.03	86.71
HPC SBG7	0.00	5.62	16.40	25.77	48.72	83.39
HPC SBG8	0.00	1.79	8.96	12.10	33.61	77.53

Table 1.32. Maximum PT1 Strain – UHPC Double Moving Truck Load

Maximum Strain: με, in./in. (mm/mm)			
Gauge Location	Path 7	Path 8	Path 9
UHPC NBG1	98.03	15.01	48.31
UHPC SBG1	107.10	20.60	67.74
UHPC NBG2	108.20	24.82	72.58
UHPC SBG2	95.98	32.80	77.17
UHPC NBG3	113.60	43.78	91.28
UHPC SBG3	108.10	68.92	82.30
UHPC NBG4	115.10	77.25	101.20
UHPC SBG4	107.10	99.69	103.80
UHPC SBG5	83.33	107.10	91.71
UHPC SBG6	54.53	114.60	89.65
UHPC SBG7	30.23	120.00	74.15
UHPC SBG8	13.98	97.87	44.84

Table 1.33. Maximum PT1 Strain – HPC Double Moving Truck Load

Maximum Strain: με, in./in. (mm/mm)			
Gauge Location	Path 7	Path 8	Path 9
HPC NBG1	84.35	12.68	45.42
HPC SBG1	93.09	19.46	56.57
HPC NBG2	115.90	28.72	72.78
HPC SBG2	113.90	44.80	94.09
HPC NBG3	107.30	44.87	83.78
HPC SBG3	124.00	77.29	76.97
HPC NBG4	109.40	75.42	92.71
HPC SBG4	117.90	102.30	106.40
HPC SBG5	101.60	125.60	115.90
HPC SBG6	56.46	124.80	93.57
HPC SBG7	25.77	102.60	59.49
HPC SBG8	13.44	95.90	44.81

Table 1.34. Maximum PT1 Strain – UHPC Single Incremental Truck Load

Maximum Strain: με, in./in. (mm/mm)						
Gauge Location	Path 1	Path 2	Path 3	Path 4	Path 5	Path 6
UHPC NBG1	84.43	53.47	25.80	9.38	7.51	2.81
UHPC SBG1	97.04	72.32	40.28	15.10	10.07	5.49
UHPC NBG2	95.99	81.01	42.14	15.45	11.71	5.15
UHPC SBG2	72.83	70.90	48.71	22.67	16.40	3.86
UHPC NBG3	80.57	82.43	63.80	25.61	20.49	6.05
UHPC SBG3	55.53	76.85	83.79	46.11	31.24	12.40
UHPC NBG4	47.50	74.37	75.81	50.86	35.02	16.31
UHPC SBG4	32.77	53.08	86.30	79.38	64.15	30.00
UHPC SBG5	15.36	27.00	54.93	68.90	74.48	51.67
UHPC SBG6	11.09	17.56	38.36	55.92	83.18	84.10
UHPC SBG7	10.39	13.70	25.97	38.25	65.64	99.18
UHPC SBG8	7.23	2.89	20.73	23.62	36.64	89.68

Table 1.35. Maximum PT1 Strain – HPC Single Incremental Truck Load

Maximum Strain: με, in./in. (mm/mm)						
Gauge Location	Path 1	Path 2	Path 3	Path 4	Path 5	Path 6
HPC NBG1	63.41	60.75	16.22	14.45	9.14	7.96
HPC SBG1	65.55	72.14	26.94	15.56	9.88	7.78
HPC NBG2	63.97	92.04	30.35	18.93	11.10	8.16
HPC SBG2	57.28	90.57	50.88	27.84	18.56	11.52
HPC NBG3	52.40	81.27	52.71	30.12	21.02	9.73
HPC SBG3	27.04	87.79	77.29	51.53	39.76	20.67
HPC NBG4	19.17	71.97	70.71	50.91	37.71	19.80
HPC SBG4	1.56	60.53	83.00	80.50	67.08	37.44
HPC SBG5	3.73	37.00	86.41	96.36	89.21	71.18
HPC SBG6	0.62	36.00	53.65	81.72	84.53	94.82
HPC SBG7	1.41	35.00	33.73	46.38	55.75	93.22
HPC SBG8	1.79	34.00	28.23	34.06	41.23	96.80

Table 1.36. Maximum PT1 Strain – UHPC Double Incremental Truck Load

Maximum Strain: με, in./in. (mm/mm)			
Gauge Location	Path 7	Path 8	Path 9
UHPC NBG1	78.80	21.11	78.80
UHPC SBG1	102.10	27.46	102.10
UHPC NBG2	99.74	34.18	99.74
UHPC SBG2	84.41	40.03	84.41
UHPC NBG3	98.73	52.16	98.73
UHPC SBG3	105.10	75.36	105.10
UHPC NBG4	108.40	88.28	108.40
UHPC SBG4	108.90	103.40	108.90
UHPC SBG5	86.59	108.50	86.59
UHPC SBG6	64.70	102.60	64.70
UHPC SBG7	59.98	125.60	59.98
UHPC SBG8	64.12	118.60	64.12

Table 1.37. Maximum PT1 Strain – HPC Double Incremental Truck Load

Maximum Strain: με, in./in. (mm/mm)		
Gauge Location	Path 7	Path 8
HPC NBG1	88.48	29.79
HPC SBG1	98.48	36.82
HPC NBG2	120.80	53.52
HPC SBG2	121.00	68.80
HPC NBG3	115.20	68.09
HPC SBG3	127.40	109.10
HPC NBG4	120.00	105.00
HPC SBG4	126.10	127.00
HPC SBG5	110.00	129.00
HPC SBG6	69.87	122.20
HPC SBG7	42.16	119.90
HPC SBG8	30.47	104.60

Table 1.38. Maximum PT1 Strain – UHPC Triple Incremental Truck Load

Maximum Strain: με, in./in. (mm/mm)		
Gauge Location	Path 10.1	Path 10.2
UHPC NBG1	Path 10.1	Path 10.2
UHPC SBG1	77.86	91.93
UHPC NBG2	92.00	96.58
UHPC SBG2	87.56	92.72
UHPC NBG3	73.31	76.21
UHPC SBG3	86.16	92.68
UHPC NBG4	93.21	99.66
UHPC SBG4	97.88	103.20
UHPC SBG5	101.50	104.30
UHPC SBG6	103.80	101.50
UHPC SBG7	122.00	116.90
UHPC SBG8	127.50	121.40

Table 1.39. Maximum PT1 Strain – HPC Triple Incremental Truck Load

Maximum Strain: με, in./in. (mm/mm)		
Gauge Location	Path 10.1	Path 10.2
HPC NBG1	69.07	65.18
HPC SBG1	79.37	77.82
HPC NBG2	93.20	84.2
HPC SBG2	96.50	90.25
HPC NBG3	110.10	83.46
HPC SBG3	111.40	100.8
HPC NBG4	94.10	85.16
HPC SBG4	116.7	103
HPC SBG5	127.3	121.5
HPC SBG6	120.4	105.7
HPC SBG7	99.50	90.88
HPC SBG8	97.90	78.43

Table 1.40. Maximum PT1 Strain – UHPC Single Back-To-Back Incremental Truck Load

Maximum Strain: με, in./in. (mm/mm)						
Gauge Location	Path 1	Path 2	Path 3	Path 4	Path 5	Path 6
UHPC NBG1	110.2	70.83	26.74	23.45	11.73	19.7
UHPC SBG1	101.6	75.07	40.74	32.04	13.27	19.22
UHPC NBG2	107.2	81.01	39.33	33.25	16.39	18.73
UHPC SBG2	80.55	72.35	53.06	42.44	20.26	19.78
UHPC NBG3	87.56	83.36	69.39	54.96	27.48	20.49
UHPC SBG3	65.45	73.38	82.8	77.84	42.14	27.27
UHPC NBG4	59.49	75.33	84.44	79.64	46.06	29.75
UHPC SBG4	42.92	57.23	84.56	101.1	71.07	48.46
UHPC SBG5	19.09	27.01	54.04	89.38	83.33	75.42
UHPC SBG6	7.394	15.25	37.89	74.4	84.57	99.82
UHPC SBG7	1.417	7.084	18.89	56.2	83.59	120.4
UHPC SBG8	2.893	3.375	11.57	41.46	58.34	104.6

Table 1.41. Maximum PT1 Strain – HPC Single Back-To-Back Incremental Truck Load

Maximum Strain: με, in./in. (mm/mm)						
Gauge Location	Path 1	Path 2	Path 3	Path 4	Path 5	Path 6
HPC NBG1	82.28	42.47	10.03	17.4	8.258	12.09
HPC SBG1	78.72	55.07	23.95	23.65	11.97	10.48
HPC NBG2	89.75	65.27	27.41	30.03	14.69	17.30
HPC SBG2	77.76	74.24	52.16	44.48	25.28	16.96
HPC NBG3	68.09	69.66	50.52	42.99	24.47	20.08
HPC SBG3	52.48	62.66	69.02	73.47	46.76	32.76
HPC NBG4	41.17	50.91	62.22	68.51	44.94	33.31
HPC SBG4	29.33	47.11	73.32	95.48	77.38	56.16
HPC SBG5	7.46	37.30	59.06	99.47	103.2	93.25
HPC SBG6	0.62	6.86	26.51	75.80	91.7	109.5
HPC SBG7	-0.94	0.94	6.09	48.72	64.18	101.7
HPC SBG8	-1.78	-0.45	1.79	34.96	49.30	119.5

Table 1.42. Maximum PT1 Strain – UHPC Double Back-To-Back Incremental Truck Load

Maximum Strain: με, in./in. (mm/mm)			
Gauge Location	Path 7	Path 8	Path 9
UHPC NBG1	145.9	35.2	74.6
UHPC SBG1	148.3	46.2	90.1
UHPC NBG2	153.6	52.9	93.6
UHPC SBG2	127.3	62.7	98.9
UHPC NBG3	150	81.04	117.4
UHPC SBG3	143.3	105.1	131.4
UHPC NBG4	140.6	110.8	132.9
UHPC SBG4	136.1	142.1	140.8
UHPC SBG5	87.98	135.9	116.8
UHPC SBG6	66.54	146.5	94.3
UHPC SBG7	39.67	135.5	83.1
UHPC SBG8	14.46	107	59.3

Table 1.43. Maximum PT1 strain – HPC Double Back-To-Back Incremental Truck Load

Maximum Strain: με, in./in. (mm/mm)			
Gauge Location	Path 7	Path 8	Path 9
HPC NBG1	114.7	31.6	64.6
HPC SBG1	112.5	42.2	74.8
HPC NBG2	134.5	60.4	95.6
HPC SBG2	139.8	78.7	115.2
HPC NBG3	129.6	74.4	106.7
HPC SBG3	143.1	110.1	134.2
HPC NBG4	124.4	102.8	121.0
HPC SBG4	138.2	144.8	145.4
HPC SBG5	116.9	145.0	144.2
HPC SBG6	79.9	151.6	105.4
HPC SBG7	51.1	121.8	78.7
HPC SBG8	33.2	129.5	66.3

1.6.2.2 Transverse Strain Distribution

BDI Strain Transducers placed were placed both on the bottom of channel girder legs and on the stem, at mid-height on the stem at midspan for both the UHPC span and the HPC span. BDI Strain Transducers placed on adjacent channel girder legs demonstrate the effectiveness to distribute load across the width of the span. Similar values in recorded strain indicate that both girders were working to support the truck loads. For PT1, girders 1, 2, and 3 for each span were analyzed for transverse strain distribution. Figure 1.67 through Figure 1.70 show the transverse strain diagrams for UHPC and HPC girders 1, 2 and 3.

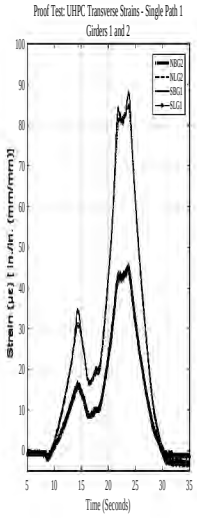


Figure 1.67: PT1: Transverse strain UHPC girders 1 and 2, single path 1.

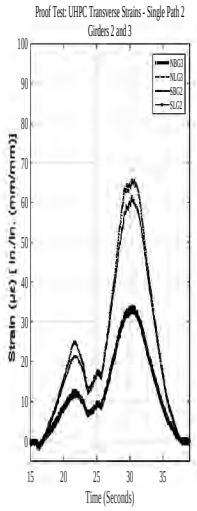


Figure 1.68: PT1: Transverse strain UHPC girders 2 and 3, single path 2.

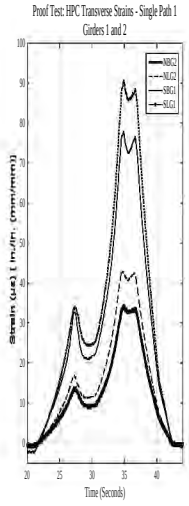


Figure 1.69: PT1: Transverse strain HPC girders 1 and 2, single path 1.

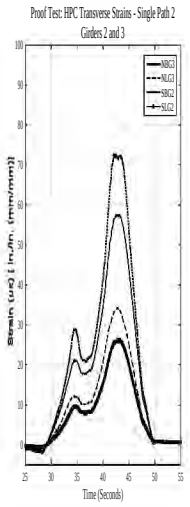


Figure 1.70: PT1: Transverse strain HPC girders 2 and 3, single path 2.

The PT1 transverse strain results show that BDI Strain Transducers placed on the bottom of each girder leg experience larger values of tensile strain. The measured strain at mid-height of the leg was smaller. Gauges on the bottom of girder stems, as well as gauges placed at mid-height of girder legs, show similar recorded values of strain across adjacent girders. This indicates that the truck load was being distributed during the proof test.

It is important to note that the maximum strain shown depends on the placement of the load truck tire during each load path. For single truck path 1, the truck tire was closer to gauges NBG3 and NLG3, than gauges SBG2 and SLG2. For this reason, maximum strains are recorded by gauges on the North section of girder 3, followed by slightly lower values of measured strain for gauges on the South leg of girder 3 for single truck paths 1. A similar occurrence was observed for single path 2. The truck tire was closer to the gauges placed on the South leg of girder 2 and therefore have higher measured strains than the strains measured by the gauges on the North stem of girder 2.

1.6.2.3 Composite and Non-Composite Neutral Axis Behavior

A comparison was made between the calculated non-composite and composite neutral axis locations. The measured composite neutral axis was determined by assuming a linear strain profile using the measured strains at different heights along the same vertical plane of the stem of the girder. The shear stirrups in the UHPC and HPC girders were designed to extend 2 ½ in. (63.5 mm) out of the top the girders. The deck was cast on top of the girder and the shear stirrups were designed to be cast into the deck to create a composite superstructure. The location of the neutral axis depends on relative stiffness and overall size of each material section. The neutral axis for a non-composite girder will be lower in the cross section then in comparison to the neutral axis of a composite girder. The deck increases the total area above the girder, raising the neutral axis.

Average neutral axis results for PT1 for girder 2 and girder 3 are presented in Table 1.44 and Table 1.45. The neutral axis is measured from the bottom of the UHPC and HPC girder. The location of the neutral axes for UHPC and HPC girder 2 and girder 3 during the diagnostic test are shown in Figure 1.71 through Figure 1.78 For each figure, the measured, average neutral axis between north and south stems, and composite and non-composite neutral axes are shown for comparison.

Table 1.44: PT1: UHPC Average Neutral Axis

	Average Neutral Axis, in. (mm)	
Load Path	G2	G3
Path 1	8.9 (226.1)	8.9 (226.1)
Path 2	8.6 (218.4)	8.9 (226.1)
Path 3	8.9 (226.1)	9.1 (231.1)
Path 4	8.6 (218.4)	8.6 (218.4)
Path 5	9.6 (243.8)	9.6 (243.8)
Path 6	8.4 (213.4)	8.5 (215.9)

Table 1.45: PT1: HPC Average Neutral Axis

	Average Neutral Axis, in. (mm)	
Load Path	G2	G3
Path 1	13.7 (347.9)	12.9 (327.7)
Path 2	12.4 (314.9)	13.1 (332.7)
Path 3	11.4 (298.6)	12.9 (327.7)
Path 4	11.7 (297.2)	12.1 (307.3)
Path 5	13.2 (335.3)	13.9 (353.1)
Path 6	12.5 (317.5)	14.9 (378.5)

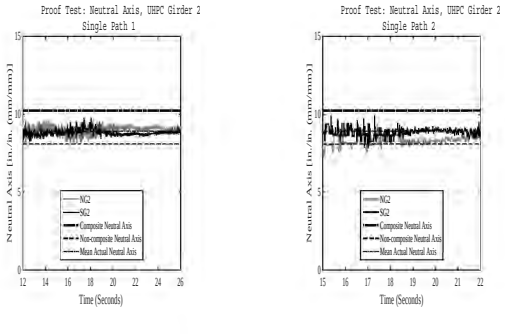


Figure 1.71: PT1 – Girder U-2, Single Path 1.

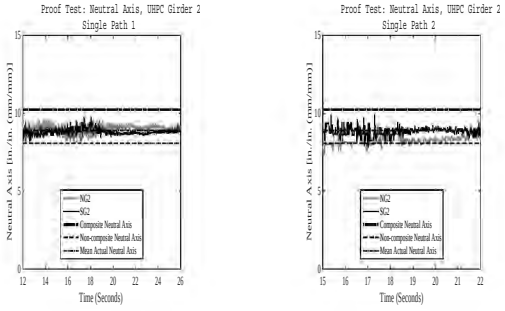


Figure 1.72: PT1 – Girder U-2, Single Path 2.

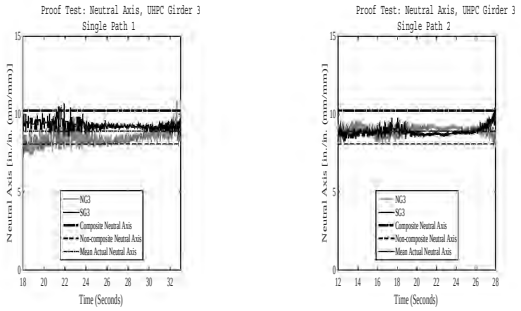


Figure 1.73: PT1 – Girder U-3, Single Path 1.

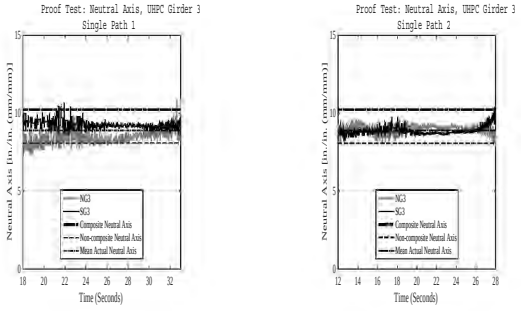


Figure 1.74: PT1 – Girder U-3, Single Path 2.

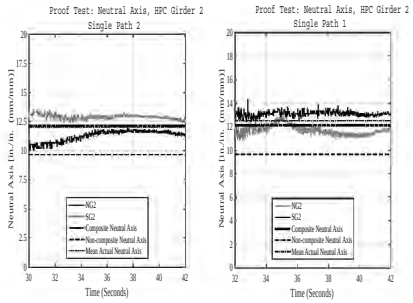


Figure 1.75: PT1 – Girder H-2, Single Path 1.

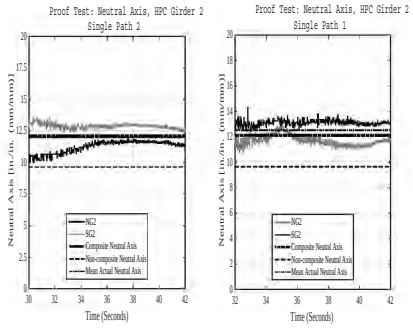


Figure 1.76: PT1 – Girder H-2, Single Path 2.

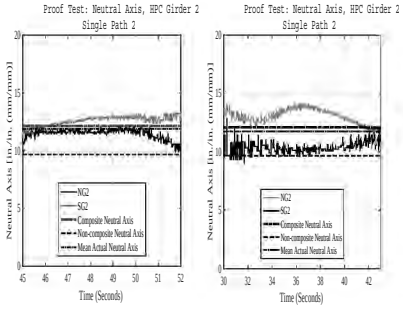


Figure 1.77: PT1 – Girder H-3, Single Path 1.

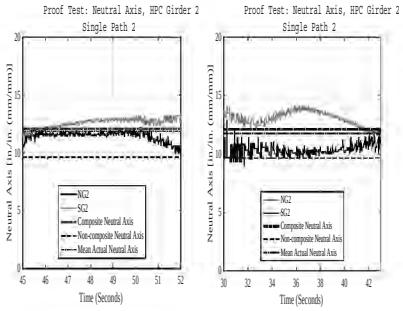


Figure 1.78: PT1–Girder H-3, Single Path 2.

1.6.3 UHPC and HPC Proof Test 1 Comparison

1.6.3.1 Comparison of Strain Behavior

The largest measured strains for sequences 1.A and 2.A, (moving single truck load tests) of the UHPC span were 97.5 με and 86.5 με during path 6 and path 1, respectively. For the HPC span, the largest measured strains recorded were 90.7 με and 89.2 με during single truck paths 1 and 4, respectively. In sequence 1.B and 2.B, (moving double truck load tests) the largest measured strains for the UHPC span were 120 με and 113 με, during path 8 and path 7. For the HPC, the largest measured strains were 125 με and 118 με during path 8 and path 7.

For sequence 3.A, (incremental single truck load tests) the largest measured strains for the UHPC span were 99 με and 97 με during path 6 and path 1. For the HPC span the largest strains were 96 με and 94 με during path 4 and path 6. For sequence 3.B (incremental double truck load tests) the largest measured strains for the UHPC span were 126 με and 109 με during path 8 and path 7. For the HPC span, the largest measured strains were 152 με and 134 με during path 8 and path 7. Finally, for sequence 3.C, (triple incremental truck load) the largest measured strain for the UHPC span were 127.5 με for path 10. For the HPC span, the largest measured strain was 152. 3 με for path 10.

To conclude, for sequence 4.A, (incremental back-to-back single truck load tests) the largest measured strains for the UHPC span were 120 με and 110 με for path 6 and path 1. For the HPC span, the largest measured strains were 112.5 με and 103.2 με. For sequence 4.B, (double incremental back-to back truck load path) the largest measured strains for the UHPC span were 146.5 με and 153.6 με during path 7 and path 8. For the HPC span, the largest measured strains were of 166 με and 145 με during path 8 and path 9.

Overall, comparing strains between the UHPC span and the HPC span for all (both load tests) diagnostic sequences a few conclusions can be made:

- The measured strains during the incremental single truck load tests during PT1 were, on average, 5.5 % higher than the slow-moving single truck load tests, for the UHPC and HPC spans, respectively. Incremental load tests are designed to stop at specific stations along the bridge for a period of time. Compared to the moving load, incremental truck loads measure more precise values of measured strain because they are stationary at maximum moment regions. The moving truck load does not allow for the maximum tensile strain to develop due to the speed of loading. Higher values of measured strains are expected for the incremental load tests in comparison to the moving load tests.
    - Overall, for single truck load tests during PT1, strains recorded in the UHPC span measured approximately 3.4% higher than strains recorded in the HPC span. The maximum strains for the UHPC span occurred in either girder 2 or 7. The HPC girders have a larger cross-sectional area in comparison to the UHPC girders. Although the UHPC and HPC girders were designed to have the same capacity, UHPC girders measured higher values of strain due to the reduced cross-sectional properties when a single load truck was used.

- Measured strains during incremental double truck load tests during PT1 were, on average, 4% higher than strains recorded during the slow-moving double truck loads for the UHPC and HPC spans, respectively.
    - Between incremental and moving single truck load tests a percent difference of 5.5% was calculated. For incremental and moving double truck load tests, a percent difference of 4% was calculated. Results reflect that with an increase of total load, the percent increase between incremental and moving load tests remained similar.
    - Overall, between PT1 sequences 1.A and 3.B, the HPC span measured approximately 3 % higher strains than the UHPC span. For incremental and moving double truck loads paths, the HPC girders measured higher values of strain, however, during the incremental and moving single truck load paths, the UHPC girders measured higher values of strain. On average, UHPC and HPC girder show closer values of measured strain when two load trucks were used. The maximum strain occurred in HPC girder 5. It is noted the largest measured strain for the first three proof test sequences of 129 με occurred during the incremental double truck load test.
- The recorded strains for the incremental triple truck loads were, on average, 1.5% higher than the incremental double truck load tests, and 25% higher than the incremental single truck loads for the UHPC and HPC spans. It is important to note, results show that incremental double truck load tests and triple incremental load tests did not have a large increase in strain, despite the increase in overall truck load. The increase in induced moment between three and two trucks did not significantly increase the expected strain due to the load being distributed across the bridge.
    - Overall, between PT1 sequences 3.C and 3.B the HPC span measured approximately 1.4% higher strains than the UHPC span. Maximum strains occurred most often in interior girders 3 and 5
- The measured strains for the back-to-back double truck load tests were, on average, 22% higher than the back-to back single truck load tests for the UHPC and HPC spans. Maximum strains occurred most often in girders 3 and 5.
    - Overall, between PT1 sequences 4.A and 4.B the UHPC span measured approximately 1.9% higher strains than the HPC span. Maximum strains occurred most often in interior girders 2 and 7 by single back-to-back tests, and girders 3 and 5 by double back-to-back load test. Results show that as the bridge is more uniformly loaded, the percent difference in measured strain between the HPC and UHPC spans are more similar.

1.6.3.2 Comparison of Actual and Expected Strain

An evaluation of the maximum measured PT1 strains to the expected strains are tabulated in Table 1.46. The percent difference between the expected strain to the measured strains are also shown.

Overall, the measured strain for UHPC and HPC matched well with expected beam strains, indicating the analytical method to be a good estimate for the UHPC and HPC bridge girders. On average, AASHTO specifications and the RISA models used to calculate the expected strains are shown to be conservative compared to the measured strain.

Table 1.46: PT1 – Expected Versus Measured Strain

Load Test		UHPC Strain με, in./in. (mm/mm)	HPC Strain με, in./in. (mm/mm)
Interior (Single)	expected	101.0	89.7
	measured	96.0	96.36
	% difference	-5%	7%
Exterior (Single)	expected	103.0	91.5
	measured	99.18	96.8
	% difference	-4%	6%
Interior (Double)	expected	134.7	119.6
	measured	125.6	129.0
	% difference	-7%	8%
Exterior (Double)	expected	137.3	122.0
	measured	107.10	104.6
	% difference	-22%	-14%
Interior (Triple)	expected	138.9	123.3
	measured	127.5	127.3
	% difference	-8%	3%
Exterior (Triple)	expected	141.6	125.8
	measured	107	97.9
	% difference	-24%	-22%
Interior Back-to-Back (Single)	expected	126.3	112.1
	measured	120.4	109.5
	% difference	-5%	-2%
Exterior Back-to-Back (Single)	expected	128.7	114.3
	measured	110.2	112.5
	% difference	-14%	-2%
Interior Back-to-Back (Double)	expected	151.5	134.6
	measured	153.6	151.6
	% difference	1%	13%
Exterior Back-to-Back (Double)	expected	154.5	137.2
	measured	148.3	129.5
	% difference	-4%	-6%

1.6.3.3 Comparison of Neutral Axis Behavior

Overall, comparing the actual neutral axis between UHPC and HPC girder 2 and girder 3, a few conclusions can be made.

- The theoretical non-composite neutral axis measured from the bottom of the interior UHPC girder is 8.1 in. (205.8 mm) and for an interior HPC girder is 9.6 in. (243.4 mm).
- The theoretical composite neutral axis, measured from the bottom of the girder, for an interior UHPC girder is 10.2 in. (259.1 mm) and for an interior HPC girder is 12.1 in. (307.3 mm).
- The average measured neutral axis, measured from the bottom of the UHPC girder 2, during the proof test, is approximately 8.8 in. (223.5 mm). The average measured neutral axis for UHPC girder 3, during the proof test, is approximately 8.9 in. (226.7 mm).
    - The mean neutral axis for UHPC girder 2 is approximately 1.4 in. (35.7 mm) below the theoretical composite neutral axis, and 0.7 in. (17.8) above the theoretical composite neutral axis
    - The mean neutral axis for UHPC girder 3 is approximately 1.3 in. (33.0 mm) below the theoretical composite neutral axis and 0.8 in. (20.3) above the non-composite neutral axis.
        - Proof Test 1 results lend that the UHPC girder 2 and girder 3 exhibit some composite behavior. The actual neutral axis is located between both the calculated theoretical neutral axis and non-composite neutral axis. Therefore, the deck and UHPC girders are acting together, however, there are differences between expected and measured neutral axis behavior. The differences could be for several reasons including assumptions of UHPC material properties, the size of effective deck width, and locations and vertical distance of strain transducers.

- The average measured neutral axis for HPC girder 2 during the diagnostic test was approximately 10.5 in. (330.2 mm). The average measured neutral axis for HPC girder 3 during the diagnostic test was approximately 11.42 in. (290.1 mm).
    - The mean neutral axis for HPC girder 2 is approximately 0.37 in. (9.40 mm) above the theoretical composite neutral axis.
    - The mean neutral axis for HPC girder 3 is approximately 1.2 in. (30.5 mm) above the theoretical composite neutral axis.
        - Proof Test 1 results lend that the HPC girder 2 and girder 3 exhibit composite behavior. The measured neutral axis is located above the calculated theoretical neutral and therefore it can be concluded that the deck and HPC girders are acting jointly

1.6.3.4 Diagnostic and Proof Test Comparisons and Conclusions

This section discusses the results and comparison between the Diagnostic Test (DT0) and Proof Test 1 (PT1) of Bridge 9706. Furthermore, the analysis consists of an evaluation of the differences in maximum strain, the induced moment and shear during the diagnostic and proof load tests, determination of non-composite and composite behavior, as well as the overall load distribution efficiency.

1.6.3.5 Strain Behavior

Both DT0 and PT1 for Bridge 9706 produced tensile strains that were continuously measured during testing by BDI Strain Transducers and other embedded sensors. DT0 took place on March 30, 2017 and was comprised of only single and double truck load paths, with maximum strains provided in Table 1.18 through Table 1.25. PT1 took place nine months after the diagnostic test on January 29 through January 31, 2018 and was comprised of single, double, and triple truck load paths, with maximum strains provided in Table 1.30 through Table 1.43.

The following analysis compares differences in values and locations of maximum recorded strains between the diagnostic test and proof test. Table 1.48 shows each truck load test, for DT0 and PT1, along with the corresponding maximum recorded strain. The first four sets of tests were repeated during PT1. However, the last three sets of tests were PT1 specific truck load paths.

Overall, the measured maximum for UHPC and HPC for both the diagnostic test and proof test were similar.

- On average for DT0 the UHPC span measured higher values of tensile strain compared to the HPC span.
    - For interior girders, the HPC span measured strains 1.2% higher than the UHPC span.
    - For exterior girders, the UHPC span measured strains 14.2% higher than the HPC span.
- For PT1, the UHPC span measured higher values of strain.
    - For interior girders the UHPC span measured strains 1% higher than the HPC span.
    - For exterior girders the UHPC span measured strains 3.3% higher than the HPC span.
- For incremental and moving single truck load tests, the UHPC span measured larger values of strain. During DT0 the UHPC span measured values of strain 9% higher than the HPC span. However, for the repeat of the incremental and moving single truck load tests during PT1, the UHPC span measured strain 3.4% higher than the HPC span. Comparing the single truck paths for DT0 and PT1, the percent difference between the UHPC and HPC spans decreased. Results reflect that the UHPC span measured proportionally less strain in comparison to the strain measured for the HPC under heavier loads.
    - The diagnostic and proof test results showed that the UHPC span generally measured higher strains than the HPC span when loaded with a single truck. Single truck load paths were designed to isolate individual girders. The decrease in cross-

sectional area for the UHPC girder compared to the HPC girder may account for the larger strains measured in the UHPC span.

  - During DT0, the maximum measured strains for the UHPC and HPC spans did not exceed the expected strains by the single truck load tests. During PT1, the UHPC span did not exceed the expected strains by the single truck load tests, however the measured proof strains for the HPC span did exceed the expected strain.
  - For DT0 the HPC span was 10.5% lower than the expected strain, and for the PT1 the HPC span was 6.5% above the expected strain. The increase in strain was anticipated between tests due to the additional truck loads applied during the proof test. Furthermore, expected strains are based on the designed truck load paths. Actual placement of the truck during testing did not always match the designed load path placement due to truck-to-truck clearance and normal movement during slow-moving load tests.

- The HPC span measured slightly higher larger values of tensile strain for double moving truck load paths and double incremental double truck moving load paths during the diagnostic and proof test. During DT0 the HPC span measured values of strain 9% higher than the UHPC span. During PT1 the HPC span measured values of strain 2.4% higher than the UHPC span.
  - During the diagnostic and proof test the maximum measured strains for the UHPC spans did not exceed the expected strains by the double truck load tests. During the diagnostic and proof test, the measured strains for the exterior HPC girder did not exceed the expected strains, but the interior HPC girder did exceed the expected strains by double truck loading.
  - For DT0 the exterior HPC exterior girder was 10% lower than the expected strain, and the interior HPC girder was 6% above the expected strain. For PT1 the exterior HPC girder was 14% lower than the expected strain, and the interior HPC girder was 8% above the expected strain.
  - Results show that UHPC girders distributed load more effectively than the HPC girder during the double truck loads for the diagnostic and proof test. Results also reflect that the expected strains for the HPC girders were not as conservative as the expected strains for the exterior girder.
- Overall, the calculated expected strains resulting from LRFD specifications and RISA models show conservative values compared to the measured strains.
  - The expected strains for the UHPC span during DT0 were 11% larger than the measured strains. The expected strains for the UHPC span during PT1 were 9% larger than the measured strains. An increase in measured strain was expected however expected strains results are conservative for diagnostic and proof tests.
  - The expected strains for the HPC span during DT0 were 6% larger than the measured strains. The expected strains for the HPC span during PT1 were on average 0.30% larger than the measured strains. The measured strains for the HPC

interior girders during PT1 exceeded the expected strains for single, double, triple, single back-to-back, and double back-to-back truck load tests. The measured strains for the specific truck load tests listed previously exceeded the expected strain by 7%.

- The calculated expected strains were conservative for the UHPC span for DT0 and PT1.
- The calculated expected strains were conservative for the HPC span during DT0 but did not represent the measured behavior as well during PT1.
- On average, the strains recorded during PT1 were approximately 6% higher than the strains recorded during DT0.
- Typically, the maximum measured strains during PT1 were experienced by the UHPC span. However, the percent difference in measured strains between the UHPC and HPC spans were 2.2%.
- Interior girder 5 and girder 2, on average, experienced the highest values of strain. This occurred when multiple truck loads were placed side-by-side and back-to-back.
- Exterior girder 1 and girder 7 experienced the highest values of strain for single truck load tests over each span.

Table 1.47. Maximum Measured Strains for DT0 and PT1

Test	Maximum Strain (με)	Girder
DT0: UHPC Single Moving Truck Load	87.9	UHPC SBG1
DT0: HPC Single Moving Truck Load	78.0	HPC NBG2
PT1: UHPC Single Moving Truck Load	94.5	UHPC SBG7
PT1: HPC Single Moving Truck Load	90.7	HPC NBG2
DT0: UHPC Double Moving Truck Load	113.5	UHPC SBG1
DT0: HPC Double Moving Truck Load	125.6	HPC SBG5
PT1: UHPC Double Moving Truck Load	120.0	UHPC SBG7
PT1: HPC Double Moving Truck Load	125.6	HPC SBG5
DT0: UHPC Single Incremental Truck Load	93.4	UHPC SBG1
DT0: HPC Single Incremental Truck Load	84.2	HPC SBG6
PT1: UHPC Single Incremental Truck Load	99.2	UHPC SBG7
PT1: HPC Single Incremental Truck Load	96.8	HPC SBG6
DT0: UHPC Double Incremental Truck Load	125.0	UHPC SBG1
DT0: HPC Double Incremental Truck Load	127.0	HPC SBG5
PT1: UHPC Double Incremental Truck Load	125.6	UHPC SBG7
PT1: HPC Double Incremental Truck Load	129.0	HPC SBG5
PT1: UHPC Triple Incremental Truck Load	127.5	UHPC SBG7
PT1: HPC Triple Incremental Truck Load	127.3	UHPC SBG5
PT1: UHPC Single Back-to-Back Truck Load	120.4	UHPC SBG7
PT1: HPC Single Back-to-Back Truck Load	119.5	UHPC SBG8
PT1: UHPC Double Back-to-Back Truck Load	153.6	UHPC NBG2
PT1: HPC Double Back-to-Back Truck Load	151.6	UHPC SBG6

Table 1.48. Overall Maximum Measured Strains for DT0 and PT1

Overall Maximum UHPC Strain (με)	153.6
Overall Maximum HPC Strain (με)	151.6
Average % Difference (Span)	4.9%
Average % Difference (Load Tests)	5.9%

1.6.4 Induced Moment

Like the comparison of expected and recorded strain, the analysis of the induced truck load moments during the diagnostic and proof load tests reflects strain behavior for the UHPC and HPC spans. Table 1.49 compares average diagnostic and proof test truck weights, and the percent difference between tests. The PT1 truck loads weighed on average 3% more than DT0. Table 1.50 and Table 1.51 provide the expected and actual measured truck moments, as well as the moment capacity for reference during the diagnostic and proof test.

Overall, the expect and measured truck moments maximum for the UHPC and HPC spans, for both the diagnostic test and proof test, were similar. The measured and expected moments show the same behavior of the measured and expected strains.

Table 1.49. Average Truck Weights for DT0 and PT1

		Axle Weight, kips (kN)		
Test	Truck Number	Front Single	Rear Tandem	Total
DT0	50729	15.7 (70)	46.8 (209)	62.5 (279)
	31444	14.1 (63)	46.6 (208)	60.8 (271)
	Average	14.9 (66.3)	46.7 (207.7)	61.6 (274.1)
PT1	50729	15.7 (69.8)	47.6 (211.7)	63.6 (281.5)
	51190	15.3 (68)	48.0 (213.5)	63.6 (218.5)
	31444	14.4 (64)	48.2 (214.4)	62.6 (278.5)
	37589	16.9 (75)	47.8 (212.6)	64.7 (287.8)
	Average	15.6 (69.4)	47.9 (213.1)	63.5 (282.5)
% Difference		4.5%	2.5%	3.0%

Table 1.50. DT0 – Induced Moment

Diagnostic Behavior Stage		UHPC – Moment, kip-ft (kN-m)	HPC – Moment, kip-ft (kN-m)
Interior (Single)	expected	50.6 (68.6)	44.9 (60.9)
	measured	45.0 (61.0)	42.2 (57.2)
	capacity	281.4 (381.5)	338.9 (459.5)
Exterior (Single)	expected	51.6 (69.9)	45.8 (62.1)
	measured	46.8 (63.5)	39.1 (53.0)
	capacity	259.6 (351.9)	312.9 (424.2)
Interior (Double)	expected	67.5 (91.5)	59.9 (81.2)
	measured	58.6 (79.5)	63.6 (86.2)
	capacity	281.4 (381.5)	338.9 (459.5)
Exterior (Double)	expected	68.8 (93.3)	61.1 (82.8)
	measured	62.6 (84.9)	55.1 (74.7)
	capacity	259.6 (351.9)	312.9 (424.2)

Table 1.51. PT1 – Induced Moment

		UHPC – Moment, kip-ft (kN-m)	HPC – Moment, kip-ft (kN-m)
Interior (Single)	expected	50.6 (68.6)	44.9 (60.9)
	measured	48.1 (65.2)	48.3 (65.5)
	capacity	281.4 (381.5)	338.9 (459.5)
Exterior (Single)	expected	51.6, (69.9)	45.8 (62.1)
	measured	49.7 (67.4)	48.5 (65.8)
	capacity	259.6 (351.9)	312.9 (424.2)
Interior (Double)	expected	67.5 (91.5)	59.9 (81.2)
	measured	62.9 (85.3)	64.6 (87.6)
	capacity	281.4 (381.5)	338.9 (459.5)
Exterior (Double)	expected	68.8 (93.3)	61.1 (82.8)
	measured	53.7 (72.8)	52.4 (71.0)
	capacity	259.6 (351.9)	312.9 (424.2)
Interior (Triple)	expected	69.6 (94.4)	61.8 (83.8)
	measured	63.9 (86.6)	63.8 (86.5)
	capacity	281.4 (381.5)	338.9 (459.5)
Exterior (Triple)	expected	71.0 (96.3)	63.0 (85.4)
	measured	53.6 (72.7)	49.0 (65.4)
	capacity	259.6 (351.9)	312.9 (424.2)
Interior Back-to-Back (Single)	expected	63.2 (85.7)	56.2 (76.2)
	measured	60.3 (81.8)	54.9 (74.4)
	capacity	281.4 (381.5)	338.9 (459.5)
Exterior Back-to-Back (Single)	expected	64.5 (87.4)	57.3 (77.7)
	measured	55.2 (74.8)	56.4 (76.5)
	capacity	259.6 (351.9)	312.9 (424.2)
Interior Back-to-Back (Double)	expected	75.9 (102.9)	67.4 (91.4)
	measured	77.0 (104.4)	75.9 (102.9)
	capacity	281.4 (381.5)	338.9 (459.5)
Exterior Back-to-Back (Double)	expected	77.4 (104.9)	68.7 (93.1)
	measured	74.3 (100.7)	64.9 (88.0)
	capacity	259.6 (351.9)	312.9 (424.2)

1.6.5 Neutral Axis Behavior.

An evaluation was made by comparing the measured neutral axis for UHPC and HPC girders. Table 1.52 and Table 1.53 provides the average measured neutral axis for UHPC and HPC girders 2 and 3, for the diagnostic test and proof test, with comparison to the theoretical non-composite and composite neutral axis.

Overall, the measured neutral axis for the UHPC and HPC for both DT0 and PT1 were similar.

- The average neutral axis for UHPC girder 2 and girder 3 matched well between DT0 and PT1. The location of the measured neutral axis fell between the theoretical composite and non-composite neutral axis.
- Further investigation of the modulus of elasticity for UHPC is needed to more accurately determine the neutral axis behavior for UHPC girders.
- The measured neutral axis for HPC girder 2 and girder 3 matched well between DT0 and PT1. The location of the measured neutral axis for girder 2 and girder 3 were above the theoretical composite neutral axis. The measured neutral axes for HPC girder 2 and girder 3 for DT0 are approximately 1.06 in. (26.9 mm) higher than the theoretical composite neutral axes. The measured neutral axes for HPC girder 2 and girder 3 for PT1 are approximately 0.78 in. (19.8 mm) higher than the theoretical composite neutral axes.
    - DT0 and PT1display composite behavior for HPC girder 2 and girder 3.

Table 1.52: DT0 and PT1: Average HPC Neutral Axis

HPC Average Neutral Axis, in. (mm)		
DT0	HPC G2	13.11 (332.99)
	HPC G3	13.23 (336.04)
PT1	HPC G2	12.48 (317.00)
	HPC G3	13.30 (337.82)
% Difference	2%	
Theoretical non-composite neutral axis	9.65 (254.11)	
Theoretical composite neutral axis	12.11 (307.59)	

Table 1.53: DT0 and PT1: Average UHPC Neutral Axis

UHPC Average Neutral Axis, in. (mm)		
DT0	HPC G2	9.09 (230.88)
	HPC G3	8.76 (222.50)
PT1	HPC G2	8.83 (224.28)
	HPC G3	8.92 (226.57)
% Difference	1%	
Theoretical non-composite neutral axis	8.09 (205.49)	
Theoretical composite neutral axis	10.24 (260.10)	

1.6.6 Calculated Live Load Distribution

AASHTO LRFD Bridge Design Specifications defines the calculated live load distribution factors provided in Table 1.9 and Table 1.10. Following AASHTO LRFD Bridge Design Specifications; Table 4.6.2.2.1-1 Common Deck Superstructures Covered in Articles 4.6.2.2.2 and 4.6.2.2.3, Bridge 9706 falls under type (h): Precast Concrete Channel Sections with Shear Keys with a Cast-in-place concrete overlay. The measure live load distribution factors shown in Table 1.54 through Table 1.57 are for one, two, and three lanes loaded, as well as single back-to-back, and double back-to-back lanes loaded. The measured live load distribution factors matched well with the calculated AASHTO live load distribution factors. Distribution factors for exterior girders are slightly larger than interior girders. Distribution factors for one and two lanes loaded are similar, verifying the AASHTO assumption that distribution factors for interior girders are similar regardless of lanes loaded. For back-to-back lanes loaded, exterior and interior girders see a slight increase in distribution factors. The more uniformly the bridge is loaded, the distribution factors for all girders approaches 0.5.

Table 1.54: DT0 and PT1 – One Lane Loaded Calculated Distribution Factor

Actual Live Load Distribution Factors DT0: Two Lanes Loaded				Actual Live Load Distribution Factors PT1: Two Lanes Loaded			
UHPC Gauge Location	DF	HPC Gauge Location	DF	UHPC Gauge Location	DF	HPC Gauge Location	DF
NBG1	0.47	NBG1	0.44	NBG1	0.61	NBG1	0.55
SBG1	0.44	SBG1	0.42	SBG1	0.55	SBG1	0.55
NBG2	0.42	NBG2	0.40	NBG2	0.53	NBG2	0.53
SBG2	0.41	SBG2	0.40	SBG2	0.47	SBG2	0.45
NBG3	0.40	NBG3	0.40	NBG3	0.46	NBG3	0.45
SBG3	0.38	SBG3	0.37	SBG3	0.42	SBG3	0.45
NBG4	0.38	NBG4	0.37	NBG4	0.39	NBG4	0.39
SBG4	0.36	SBG4	0.37	SBG4	0.34	SBG4	0.36
SBG5	0.38	SBG5	0.37	SBG5	0.38	SBG5	0.37
SBG6	0.43	SBG6	0.42	SBG6	0.44	SBG6	0.45
SBG7	0.47	SBG7	0.44	SBG7	0.50	SBG7	0.51
SBG8	0.47	SBG8	0.44	SBG8	0.52	SBG8	0.52

Table 1.55: DT0 and PT1 – Two Lanes Loaded Calculated Distribution Factors

Actual Live Load Distribution Factors DT0: Two Lanes Loaded				Actual Live Load Distribution Factors PT1: Two Lanes Loaded			
UHPC Gauge Location	DF	HPC Gauge Location	DF	UHPC Gauge Location	DF	HPC Gauge Location	DF
NBG1	0.45	NBG1	0.50	NBG1	0.46	NBG1	0.48
SBG1	0.48	SBG1	0.45	SBG1	0.41	SBG1	0.44
NBG2	0.47	NBG2	0.40	NBG2	0.48	NBG2	0.45
SBG2	0.37	SBG2	0.43	SBG2	0.31	SBG2	0.35
NBG3	0.38	NBG3	0.40	NBG3	0.49	NBG3	0.48
SBG3	0.39	SBG3	0.39	SBG3	0.27	SBG3	0.29
NBG4	0.36	NBG4	0.42	NBG4	0.45	NBG4	0.43
SBG4	0.41	SBG4	0.47	SBG4	0.25	SBG4	0.25
SBG5	0.37	SBG5	0.50	SBG5	0.44	SBG5	0.57
SBG6	0.45	SBG6	0.46	SBG6	0.30	SBG6	0.32
SBG7	0.49	SBG7	0.46	SBG7	0.43	SBG7	0.43
SBG8	0.51	SBG8	0.46	SBG8	0.42	SBG8	0.43

Table 1.56: DT0 and PT1 – Single and Double Back-To-Back Lane Loaded Calculated Distribution Factors

Actual Live Load Distribution Factors DT0: Two Lanes Loaded				Actual Live Load Distribution Factors PT1: Two Lanes Loaded			
UHPC Gauge Location	DF	HPC Gauge Location	DF	UHPC Gauge Location	DF	HPC Gauge Location	DF
NBG1	0.42	NBG1	0.48	NBG1	0.57	NBG1	0.54
SBG1	0.36	SBG1	0.39	SBG1	0.52	SBG1	0.49
NBG2	0.48	NBG2	0.39	NBG2	0.51	NBG2	0.46
SBG2	0.28	SBG2	0.44	SBG2	0.44	SBG2	0.42
NBG3	0.49	NBG3	0.41	NBG3	0.43	NBG3	0.42
SBG3	0.22	SBG3	0.44	SBG3	0.38	SBG3	0.37
NBG4	0.50	NBG4	0.41	NBG4	0.37	NBG4	0.36
SBG4	0.25	SBG4	0.57	SBG4	0.34	SBG4	0.34
SBG5	0.53	SBG5	0.61	SBG5	0.40	SBG5	0.36
SBG6	0.31	SBG6	0.65	SBG6	0.48	SBG6	0.45
SBG7	0.71	SBG7	0.60	SBG7	0.52	SBG7	0.48
SBG8	0.47	SBG8	0.67	SBG8	0.59	SBG8	0.57

Table 1.57: DT0 and PT1 – Three Lanes Loaded Calculated Distribution Factors

Actual Live Load Distribution Factors DT0: Two Lanes Loaded			
UHPC Gauge Location	DF	HPC Gauge Location	DF
NBG1	0.54	NBG1	0.54
SBG1	0.51	SBG1	0.51
NBG2	0.51	NBG2	0.51
SBG2	0.51	SBG2	0.51
NBG3	0.52	NBG3	0.52
SBG3	0.52	SBG3	0.52
NBG4	0.51	NBG4	0.51
SBG4	0.51	SBG4	0.51
SBG5	0.51	SBG5	0.51
SBG6	0.51	SBG6	0.51
SBG7	0.51	SBG7	0.51
SBG8	0.52	SBG8	0.52

1.6.7 Impact Factor

For highway bridges, the dynamic response amplitude is a function of several factors. Such factors include, but are not limited to bridge span, type (continuous or simple span), number of girders, slab stiffness, bridge damping, deck roughness, vehicle mass, vehicle velocity, damping, number of axles, suspension system, vertical velocity upon entering the bridge, probability of coincidence of maximum load and maximum impact, and position of load relative to a girder (Hwang and Nowak 1991). To simplify this dynamic behavior, the AASHTO specifications provides an impact factor that is to be no greater than 0.3. AASHTO has developed Equation 1.19 shown below to increase the live load to account of the dynamic behavior and sway of vehicles, where L is the length of the span in feet.

$$I = \frac{50}{L + 125} \leq 0.3 \qquad 1.19$$

The theoretical impact factor was calculated to be 0.33, which is greater than 0.3, and therefore controlled by an impact factor of 0.3. During the proof test, a single load truck was driven over the bridge at 5 mph and again at approximately 55 mph. The measured strains, as well as the calculated impact factor, for the slow and fast-moving truck load are provided in Table 1.58.

Table 1.58: PT1 – UHPC Single Moving Truck Load

	Strain (με)		
Gauge Location	Path 2	Path 2*	I
UHPC NBG1	48.3	65.67	0.26
UHPC SBG1	60.0	79.18	0.24
UHPC NBG2	67.4	84.76	0.20
UHPC SBG2	67.5	93.57	0.28
UHPC NBG3	72.7	102.9	0.29
UHPC SBG3	70.9	101.6	0.30
UHPC NBG4	68.6	101.2	0.32
UHPC SBG4	53.1	76.61	0.31
UHPC SBG5	25.1	39.1	0.36
UHPC SBG6	13.9	19.87	0.30
UHPC SBG7	6.1	12.28	0.50
UHPC SBG8	5.3	5.303	0.00

Path 2 designates the slow-moving truck load and Path 2 * designates the fast-moving truck load. The calculated impact factor is shown with an overall average impact factor of 28%. The measure factor of 0.28 is similar to the controlling AASHTO impact factor value of 0.30.

1.7 Proof Test 3

Proof Test 3 (PT3) was conducted in early 2020 on Bridge 9706, in Anthony, New Mexico. The test was performed on 26th, 27th and 28th of February 2020. The goal of this test was to better understand the behavior of the materials and compare with previous load tests. The day before the test, 36 strain transducers were attached to the bridge to measure the tensile strain during the loading. Similar instrumentation and location with the previous load tests to have a direct comparison. There were four trucks used for PT3. The weight of the trucks, loaded with dry rocks/sand, are provided in Table 1.6 (Section 1.2.1.1). The load paths were designed to maximize the tensile strains on the bridge to investigate the behavior of the new materials (UHPC) verses (HPC) materials. Single truck moving, single truck incremental moving, double truck side-by-side, single truck back-to-back incremental moving, double trucks back-to-back, and triple trucks side-by-side, were used during the load test with various positions on the bridge. Similar load paths configurations to previous load tests were applied.

1.7.1 PT3 Results

The results of PT3 include the maximum strain, transferred strains between adjacent girders, impact factor, and comparison between the UHPC and HPC.

1.7.1.1 Maximum Strains

Strains were monitored during PT3 to ensure no damage happened to the bridge or exceeding the available moment. Strain results presented for each path are the maximum for that path. The overall maximum strain for each path is indicated in bold. Six paths for single moving, six paths for single incremental moving, two paths for double truck side-by-side, six paths for single back-to-back incremental moving, two paths for double back-to-back incremental moving, and one path for triple trucks side-by-side incremental moving. Each path was repeated twice to ensure the accuracy of the behavior and ensure the strain transducers recording properly. Table 1.59 through Table 1.70 are presented the maximum strain for each path with the respective strain transducers. An analysis of the behavior and discussion of the results is found in the following section.

Table 1.59: PT3 Maximum Strain – UHPC Span Single Moving Truck Load

Maximum Strain: με, in./in. (mm/mm)						
Gauge Location	Path 1	Path 2	Path 3	Path 4	Path 5	Path 6
UHPC NBG1	113	56	29	11	5	2
UHPC SBG1	121	75	42	18	9	4
UHPC NBG2	109	74	43	19	8	4
UHPC SBG2	89	85	57	26	13	5
UHPC NBG3	94	91	68	34	17	7
UHPC SBG3	61	88	92	57	30	13
UHPC NBG4	47	72	76	53	29	13
UHPC SBG4	32	62	86	81	54	28
UHPC SBG5	16	37	64	88	87	58
UHPC SBG6	8	21	39	64	91	95
UHPC SBG7	4	10	22	39	76	109
UHPC SBG8	1.4	5	13	20	47	91

Table 1.60: PT3 Maximum Strain – HPC Span Single Moving Truck Load

Maximum Strain: με, in./in. (mm/mm)						
Gauge Location	Path 1	Path 2	Path 3	Path 4	Path 5	Path 6
HPC NBG1	104	50	23	9	3	1
HPC SBG1	122	76	40	17	7	2
HPC NBG2	108	75	41	18	8	3
HPC SBG2	109	105	74	37	17	6
HPC NBG3	85	82	62	31	14	5
HPC SBG3	59	83	83	58	32	15
HPC NBG4	61	97	97	73	40	19
HPC SBG4	30	64	95	95	61	31
HPC SBG5	16	37	67	105	104	71
HPC SBG6	5	15	31	67	100	104
HPC SBG7	1	6	15	36	72	111
HPC SBG8	0.45	2	8	19	50	106

Table 1.61. PT3 Maximum Strain – UHPC Single Incremental Truck Load

Maximum Strain: με, in./in. (mm/mm)						
Gauge Location	Path 1	Path 2	Path 3	Path 4	Path 5	Path 6
UHPC NBG1	110	57	19	5	3	3
UHPC SBG1	123	76	35	9	5	4
UHPC NBG2	110	74	35	9	5	4
UHPC SBG2	94	83	50	18	8	4
UHPC NBG3	99	85	60	24	12	7
UHPC SBG3	65	84	82	47	27	11
UHPC NBG4	48	67	69	45	28	12
UHPC SBG4	35	49	79	77	54	24
UHPC SBG5	19	26	56	83	81	55
UHPC SBG6	12	14	37	64	88	93
UHPC SBG7	7	13	29	46	72	110
UHPC SBG8	2	8	16	31	51	94

Table 1.62. PT3 Maximum Strain – HPC Single Incremental Truck Load

Maximum Strain: με, in./in. (mm/mm)						
Gauge Location	Path 1	Path 2	Path 3	Path 4	Path 5	Path 6
HPC NBG1	111	61	20	5	14	1
HPC SBG1	124	87	36	6	13	1
HPC NBG2	111	86	39	6	16	2
HPC SBG2	111	110	71	22	22	3
HPC NBG3	84	86	58	18	20	2
HPC SBG3	61	87	82	48	36	4
HPC NBG4	61	96	95	62	45	7
HPC SBG4	35	60	85	75	70	22
HPC SBG5	21	34	60	88	112	67
HPC SBG6	18	15	26	48	104	105
HPC SBG7	22	13	11	26	74	123
HPC SBG8	26	14	10	17	57	121

Table 1.63: PT3: Maximum Strain – UHPC Single Back-To-Back Incremental Truck Load

	Maximum Strain: με, in./in. (mm/mm)					
Gauge Location	Path 1	Path 2	Path 3	Path 4	Path 5	Path 6
UHPC NBG1	130	87	42	20	12	5
UHPC SBG1	132	102	57	29	15	7
UHPC NBG2	125	101	57	29	15	8
UHPC SBG2	104	105	68	39	20	10
UHPC NBG3	103	114	78	47	26	13
UHPC SBG3	82	108	93	68	45	21
UHPC NBG4	62	83	79	59	41	21
UHPC SBG4	51	78	85	77	68	40
UHPC SBG5	30	51	69	83	95	72
UHPC SBG6	18	32	46	71	91	98
UHPC SBG7	17	21	23	47	83	119
UHPC SBG8	15	25	10	24	58	113

Table 1.64: PT3 Maximum Strain – HPC Single Back-To-Back Incremental Truck Load

	Maximum Strain: με, in./in. (mm/mm)					
Gauge Location	Path 1	Path 2	Path 3	Path 4	Path 5	Path 6
HPC NBG1	140	86	32	13	6	2
HPC SBG1	146	107	53	22	10	2
HPC NBG2	138	102	55	26	9	2
HPC SBG2	138	126	83	49	21	4
HPC NBG3	102	101	67	43	17	3
HPC SBG3	85	96	90	72	39	11
HPC NBG4	92	110	104	85	51	16
HPC SBG4	57	81	93	100	76	33
HPC SBG5	37	54	70	113	114	86
HPC SBG6	22	29	35	75	97	118
HPC SBG7	21	21	19	45	75	145
HPC SBG8	26	23	16	25	53	173

Table 1.65. PT3 Maximum Strain – UHPC Double Incremental Truck Load

Maximum Strain: με, in./in. (mm/mm)		
Gauge Location	Path 7	Path 8
UHPC NBG1	120	10
UHPC SBG1	135	20
UHPC NBG2	131	18
UHPC SBG2	126	29
UHPC NBG3	137	35
UHPC SBG3	129	62
UHPC NBG4	106	57
UHPC SBG4	108	91
UHPC SBG5	87	123
UHPC SBG6	57	138
UHPC SBG7	39	134
UHPC SBG8	35	104

Table 1.66. PT3 Maximum Strain – HPC Double Incremental Truck Load

Maximum Strain: με, in./in. (mm/mm)		
Gauge Location	Path 7	Path 8
HPC NBG1	136	16
HPC SBG1	163	26
HPC NBG2	152	29
HPC SBG2	183	53
HPC NBG3	142	45
HPC SBG3	149	81
HPC NBG4	164	100
HPC SBG4	127	121
HPC SBG5	96	173
HPC SBG6	47	166
HPC SBG7	25	156
HPC SBG8	20	149

Table 1.67. PT3 Maximum Strain – UHPC Double Back-To-Back Incremental Truck Load

Maximum Strain: με, in./in. (mm/mm)		
Gauge Location	Path 7	Path 8
UHPC NBG1	157	36
UHPC SBG1	179	47
UHPC NBG2	167	47
UHPC SBG2	150	62
UHPC NBG3	163	73
UHPC SBG3	157	110
UHPC NBG4	127	99
UHPC SBG4	121	137
UHPC SBG5	90	179
UHPC SBG6	57	185
UHPC SBG7	30	187
UHPC SBG8	13	147

Table 1.68. PT3 Maximum Strain – HPC Double Back-To-Back Incremental Truck Load

Maximum Strain: με, in./in. (mm/mm)		
Gauge Location	Path 7	Path 8
HPC NBG1	140	14
HPC SBG1	173	28
HPC NBG2	162	35
HPC SBG2	192	61
HPC NBG3	142	56
HPC SBG3	146	88
HPC NBG4	167	111
HPC SBG4	132	137
HPC SBG5	94	194
HPC SBG6	41	187
HPC SBG7	4	181
HPC SBG8	4	181

Table 1.69. PT3 Maximum Strain – UHPC Triple Incremental Truck Load

Maximum Strain: με, in./in. (mm/mm)	
Gauge Location	Path 7
UHPC NBG1	102
UHPC SBG1	120
UHPC NBG2	113
UHPC SBG2	112
UHPC NBG3	126
UHPC SBG3	145
UHPC NBG4	120
UHPC SBG4	132
UHPC SBG5	147
UHPC SBG6	133
UHPC SBG7	123
UHPC SBG8	80

Table 1.70. PT3 Maximum Strain – HPC Triple Incremental Truck Load

Maximum Strain: με, in./in. (mm/mm)	
Gauge Location	Path 7
HPC NBG1	113
HPC SBG1	146
HPC NBG2	137
HPC SBG2	171
HPC NBG3	134
HPC SBG3	149
HPC NBG4	174
HPC SBG4	161
HPC SBG5	182
HPC SBG6	153
HPC SBG7	130
HPC SBG8	101

1.7.1.1.1 Comparison of Strain Behavior

From the measured strain, a few conclusions can be drawn:

- According to single truck moving paths, the overall maximum measured strain for UHPC was 121 με, and for HPC was 122 με. These occurred during path 1 on the exterior girders, which was expected. The UHPC and HPC measured similar strain during single truck moving load.
- According to single truck incremental moving, the overall maximum measured strain for UHPC was 123 με, and for HPC was 124 με. Also, these occurred during path 1 on the exterior girders, which was expected.
- According to single back-to-back incremental moving, the maximum measured strain for UHPC was 132 με, and for HPC 173 με. These occurred during path 1 and path 6 on the exterior girders as expected.
- According to double back-to-back incremental moving, the maximum measured strain for UHPC was 179 με, and for HPC 194 με.
- According to triple trucks side-by-side incremental moving, the maximum measured strain for UHPC was 147 με, and for HPC 182 με.
- Based on the maximum measured strain for each path, the HPC span measured higher strain compared to UHPC for the majority of the tests.
- Additionally, the UHPC shows better gain of strength after three years of construction, faster than HPC.

Overall, the measured strain did not exceed the available calculated strain based on AASHTO Design Specifications.

1.7.1.1.2 DIC Results

1.7.1.1.2.1 Analysis of Displacements Using ARAMIS

The ARAMIS software program, a DIC platform from GOM, was used in processing the images from the camera systems to obtain the displacements at the locations monitored. For each test, an image was taken prior to loading on the bridge to obtain a reference, or baseline measurement. An image, or stage, was also taken each time the truck stopped on the bridge. The images from the test were then input into ARAMIS and processed to obtain a full field of displacements over the patterned area. Figure 1.79 is an example of the ARAMIS output for vertical displacement in mm for an exterior girder for one particular stage of a test. Because the displacements are computed for the entire field of the pattern there is a lot of flexibility in where to take the displacement measurement. A line segment through the center of the measurement field was established and the vertical displacements across that line for a particular stage were output from the ARAMIS program similar to what is shown in Figure 1.80. The displacement readings across that line segment were then averaged to obtain a single vertical displacement value at the monitored location. This approach was completed for all displacement readings that follow in the next sections of the report.

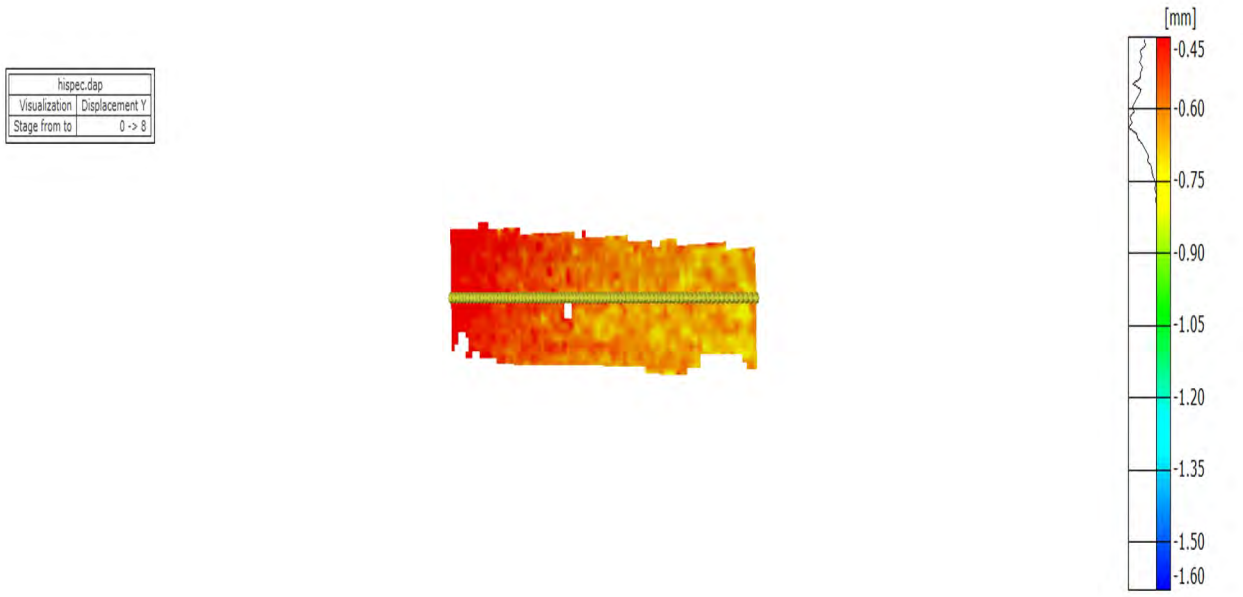


Figure 1.79: Y Displacement of an UHPC beam obtained from ARAMIS.

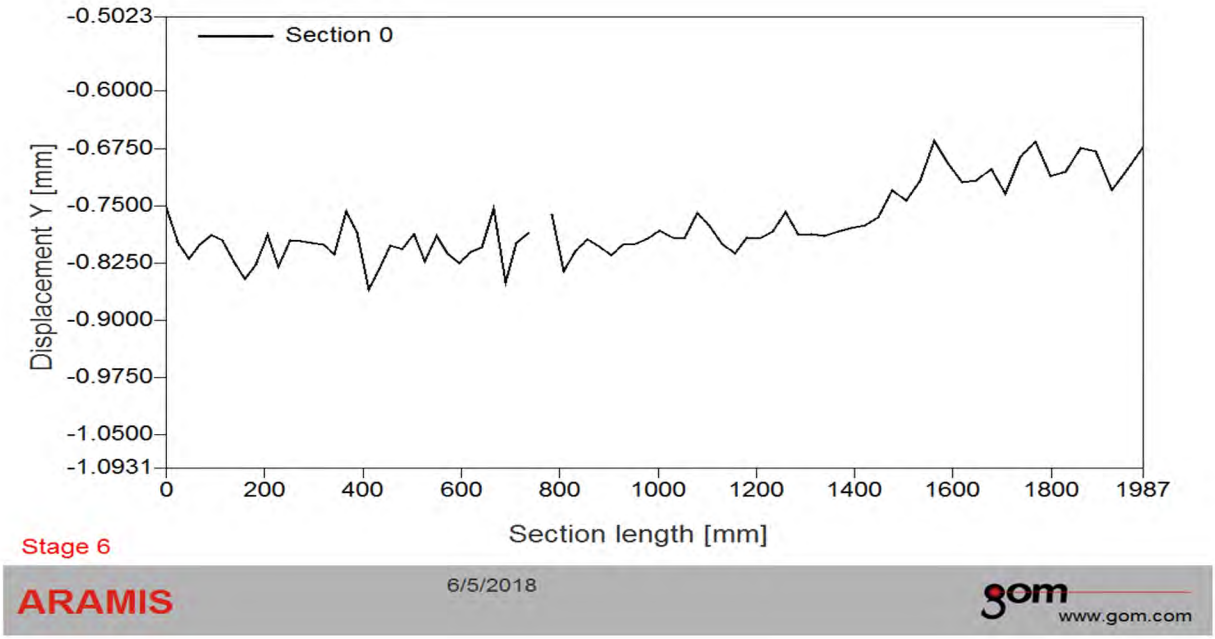


Figure 1.80: Vertical displacement value of a UHPC beam under Single Truck loading on path along a line segments shown in Figure 12 (NOTE: 1 in. = 25.4 mm).

1.7.1.1.2.2 Experimental Testing Results for Vertical Displacement

1.7.1.1.2.2.1 Performance of HPC Span

The HPC span was monitored using the HiSpec1, and GoPro Hero + systems at the mid-span of the fascia girders and the DMK system at the mid-span of an interior girder. Upon completion of testing, it was determined that none of the images from the DMK system were able to be used successfully in determining displacements. Therefore, no data from the DMK system will be presented in this report. Additionally, it should be noted that some stages were not captured and as a result some displacement values are missing from the influence line plots of vertical displacement. A negative displacement indicates downward deflection while a positive displacement would mean the element moved upward. The rear axle placement is in relation to the start of the UHPC span.

The HiSpec1 camera system monitored the behavior of an exterior girder on the HPC span of the bridge. The influence line plots for vertical displacement of a single H-Truck on the bridge for paths 1-6 are presented in Figure 1.81 with the corresponding numerical values in Table 1.71. It is noted that path 1 is closest to the HiSpec1 system while path 6 is farthest away. As expected, the greatest response is when the truck is moving along path 1 and the rear axle is directly over the location of the measured field. The peak vertical displacement for this test run is 1.2 mm (0.05 in.). It is interesting to note that when the truck is running along path 3 there appears to be some twisting in the bridge with the exterior girder moving slightly upward 0.47 mm (0.02 in.). This upward motion is present but faint for paths 5 and 6. The data from path 2 seems to suggest some continuity between the two spans as there is a slight downward movement on the HPC side when the truck is on the UHPC span.

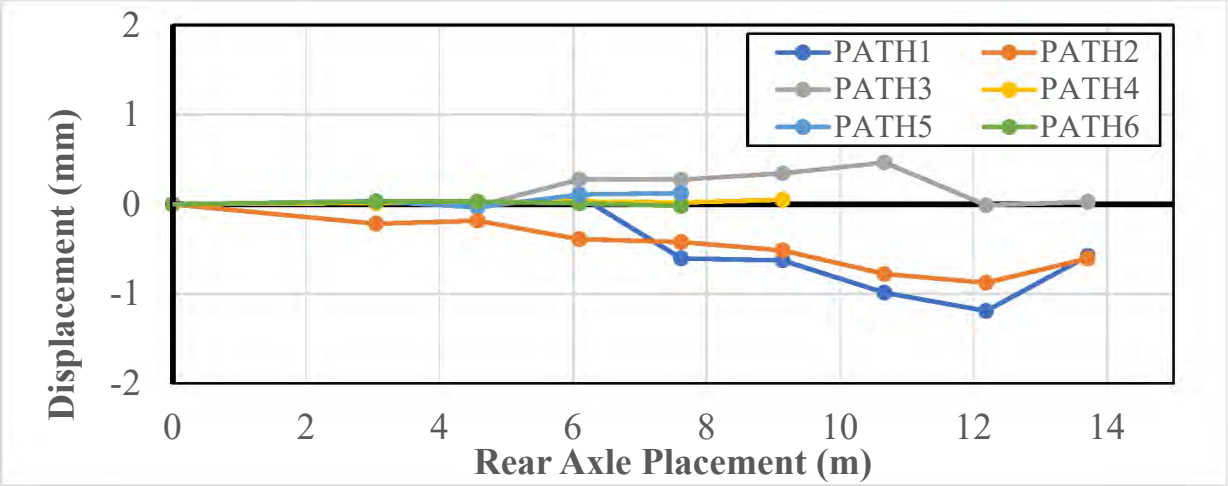


Figure 1.81: Displacement versus rear axle placement for an exterior HPC beams for Single Truck loading measured by the HiSpec1 system (NOTE: 1 in. = 25.4 mm).

Table 1.71: Numerical Data for Vertical Displacements Corresponding to Figure 1.81

Rear Axle Location (m)	PATH 1 (mm)	PATH 2 (mm)	PATH 3 (mm)	PATH 4 (mm)	PATH 5 (mm)	PATH 6 (mm)
0	0	0	0	0	0	0
3.048	0.0339	-0.216	0.034	0.0151	0.0338	0.0315
4.572	-0.0234	-0.183	-0.0153	0.0288	-0.034	0.0311
6.096	0.0949	-0.388	0.278	0.0334	0.109	0.00885
7.62	-0.604	-0.421	0.276	0.0198	0.126	-0.0165
9.144	-0.627	-0.514	0.345	0.0503		
10.668	-0.986	-0.776	0.467			
12.192	-1.19	-0.875	-0.0109			
13.716	-0.576	-0.603	0.0272			

NOTE: 3.28 ft. = 1 m

Data for vertical displacements captured from the HiSpec1 system due to the back-to-back truck configuration is shown for paths 2, 3, 5 and 6 in Figure 1.82. Data was only captured for this system when the centerline of the two rear truck axles were on the UHPC span. For each path, there appears to be a minimal downward displacement at the mid-span of the HPC exterior girder when the vehicles are on the UHPC span. However, when the centerline of the two axles are positioned on the HPC span there is more vertical displacement, up to 1.35 mm (0.053 in.) and the displacement is greatest when the trucks are closest to the sensor.

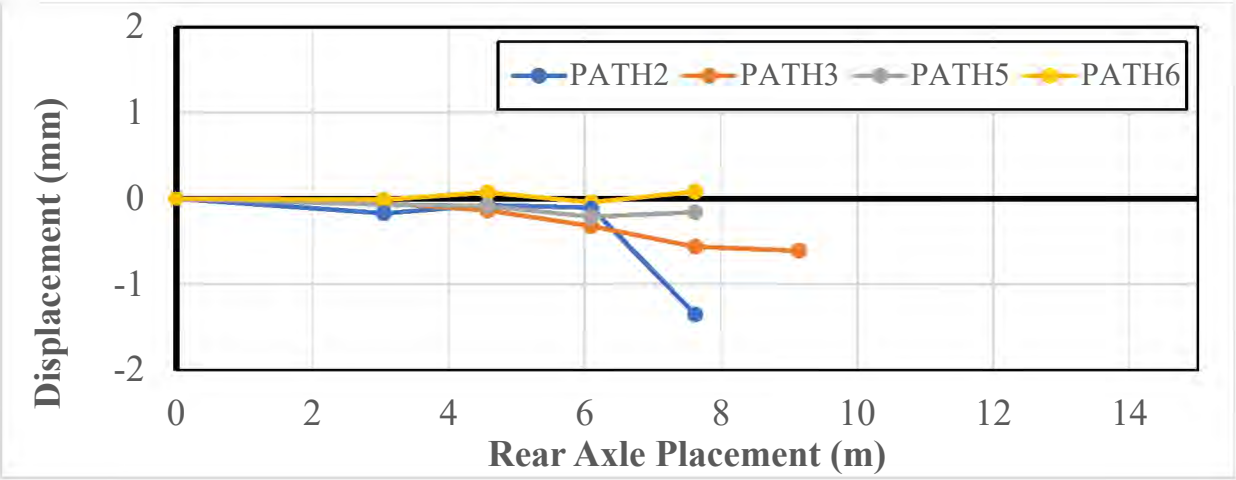


Figure 1.82: Displacement versus centerline location of rear axle placement for an exterior HPC beams for Single Truck Back-To-Back loading measured by the HiSpec1 system (NOTE: 1 in. = 25.4 mm).

Table 1.72: Numerical Data for Vertical Displacements Corresponding to Figure 1.82

Center Location of Rear Axles (m)	PATH 2 (mm)	PATH 3 (mm)	PATH 5 (mm)	PATH 6 (mm)
0	0	0	0	0
3.048	-0.169	-0.051	-0.0682	-0.0112
4.572	-0.0741	-0.135	-0.0847	0.0742
6.096	-0.103	-0.319	-0.211	-0.0399
7.62	-1.35	-0.56	-0.156	0.0828
9.144		-0.608		

NOTE: 3.28 ft. = 1 m

Three trucks were positioned side-by-side-by-side to maximize the transverse load across the bridge spans. Displacements were computed from the images gathered with the HiSpec1 system and reported in Figure 1.83 and Table 1.73. The data shows that as the trucks are on the UHPC span there is some slight upward displacement on the UHPC side. When the trucks transition to the UHPC span the displacements are downward with a maximum of 0.65 mm (0.026 in.) when the axles are near the mid-span. This again suggests some continuity between the UPHC and HPC spans.

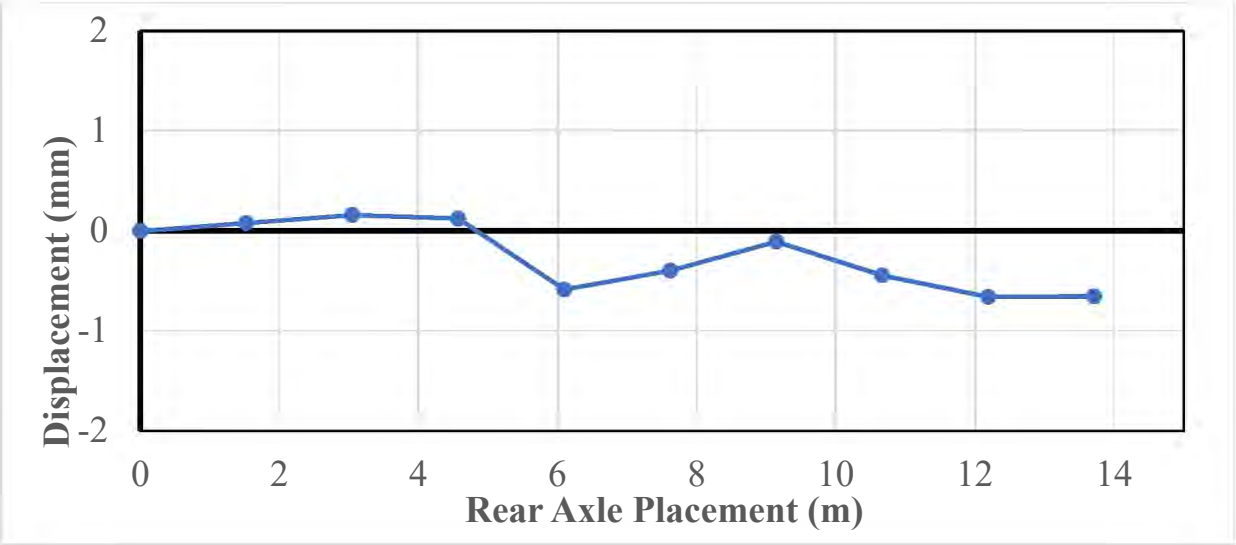


Figure 1.83: Displacement versus centerline location of rear axle placement for an exterior HPC beams for Triple Truck loading measured by the HiSpec1 system (NOTE: 1 in. = 25.4 mm).

Table 1.73: Numerical Data for Vertical Displacements Corresponding to Figure 1.83

Center Location of Rear Axles (m)	Vertical Displacement (mm)
0	0
1.524	0.080180332
3.048	0.16
4.572	0.124996108
6.096	-0.584978157
7.62	-0.396649023
9.144	-0.106802757
10.668	-0.443748364
12.192	-0.65889513
13.716	-0.653352452

NOTE: 3.28 ft. = 1 m

The GoPro Hero+ was used as two separate cameras capturing the same field of view on the exterior girder opposite of the HiSpec1 cameras. Since the cameras were run separately, the images were processed using 2D DIC analysis. To verify both sets of images were capturing the same, or nearly the same, displacements, the results were compared then averaged. An example of the response for a single truck along paths 1, 2 and 3 can be found in Figure 1.84 through Figure 1.86 and Table 1.74 through Table 1.76, respectively. As seen, the vertical displacements from both cameras are nearly identical. Similar to what was seen with the exterior girder on the opposite side of the bridge, measured by the HiSpec1 system, very little vertical displacement is seen when the truck is farthest away from the sensor. Additionally, path 3 loading near the centerline of the bridge is producing an upward displacement on the girder. A plot comparing the influence line for vertical displacements at the mid-span of both exterior girders on the HPC span is seen in Figure 1.87 and Table 1.77.

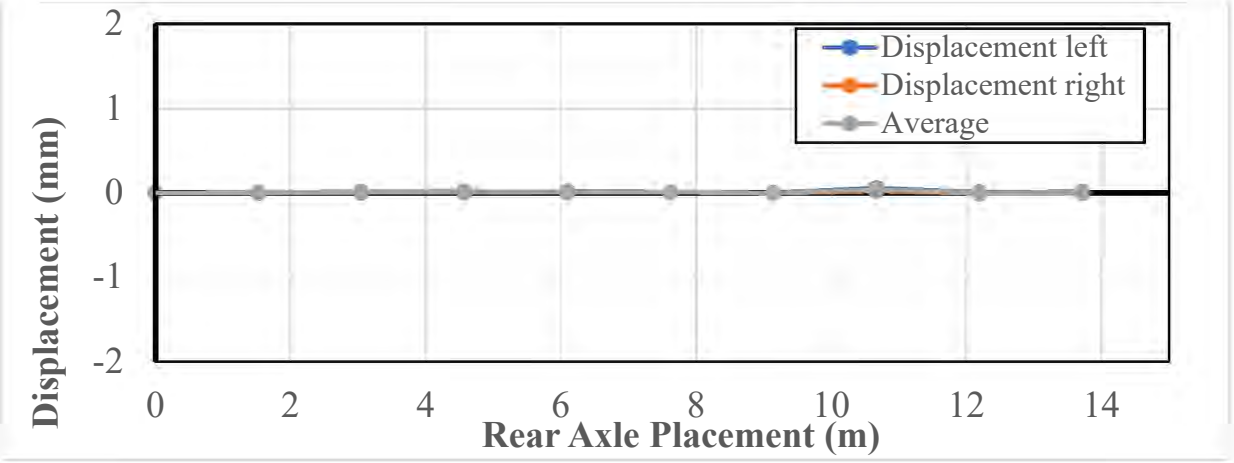


Figure 1.84: Displacement versus rear axle placement for an exterior HPC beams for Single Truck loading along Path 1 measured by the GoPro Hero+ system (NOTE: 1 in. = 25.4 mm).

Table 1.74: Numerical Data for Vertical Displacements Corresponding to Figure 1.84

Center Location of Rear Axles (m)	Left Camera Vertical Displacement (mm)	Right Camera Vertical Displacement (mm)	Average Vertical Displacement (mm)
0	0	0	0
1.524	-0.002638719	0.004110348	0.000736
3.048	0.004267249	0.013641659	0.008954
4.572	0.005959781	0.01775422	0.011857
6.096	0.015700000	0.004362149	0.010031
7.62	0.007556735	0.006619496	0.007088
9.144	-0.00095938	-0.005879161	-0.00342
10.668	0.053762897	0.02170369	0.037733
12.192	0.005853638	-0.007496007	-0.00082
13.716	0.011879036	-0.003482845	0.004198

NOTE: 3.28 ft. = 1 m

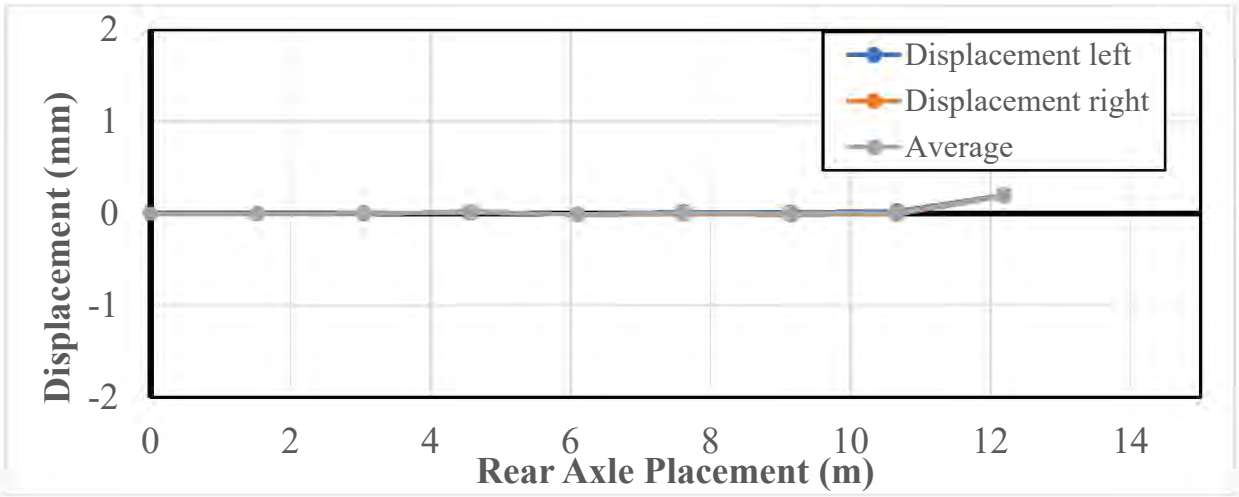


Figure 1.85: Displacement versus rear axle placement for an exterior HPC beams for Single Truck loading along Path 2 measured by the GoPro Hero+ system (NOTE: 1 in. = 25.4 mm).

Table 1.75: Numerical Data for Vertical Displacements Corresponding to Figure 1.85

Center Location of Rear Axles (m)	Left Camera Vertical Displacement (mm)	Right Camera Vertical Displacement (mm)	Average Vertical Displacement (mm)
0	0	0	0
1.524	-0.001593585	-0.004730382	-0.00316
3.048	0.007089307	-0.004982084	0.001054
4.572	0.011694644	0.023623258	0.017659
6.096	-0.007681889	-0.011506529	-0.00959
7.62	0.018082812	-0.003553649	0.007265
9.144	1.32E-02	-0.009013342	0.002106
10.668	0.026272766	-0.003339391	0.011467
12.192	0.203481349	0.194218064	0.19885
0	0	0	0

NOTE: 3.28 ft. = 1 m

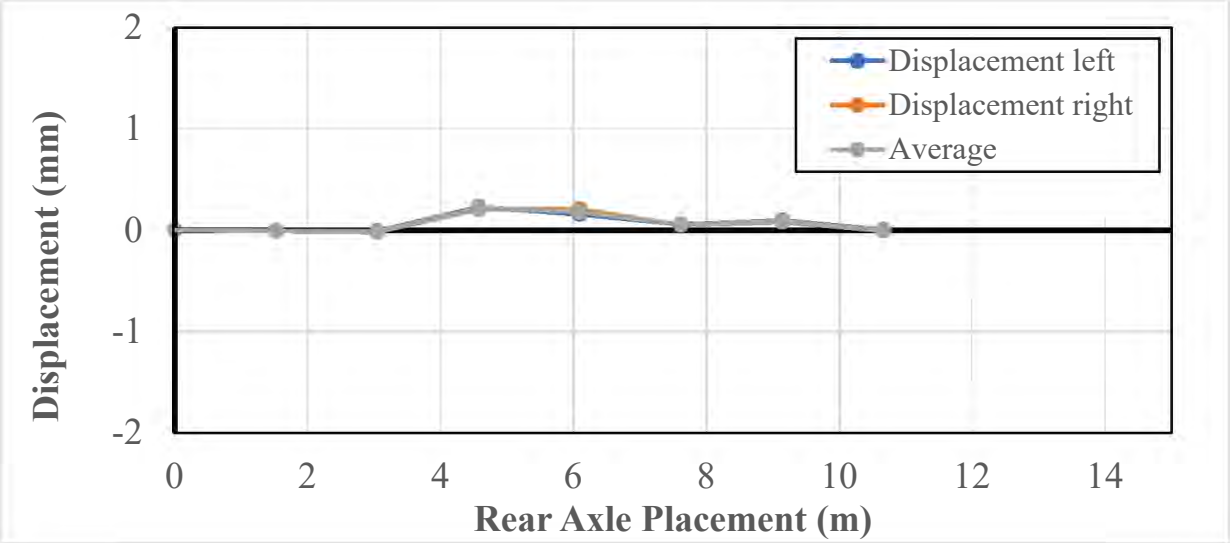


Figure 1.86: Displacement versus rear axle placement for an exterior HPC beams for Single Truck loading along Path 3 measured by the GoPro Hero+ system (NOTE: 1 in. = 25.4 mm).

Table 1.76: Numerical Data for Vertical Displacements Corresponding to Figure 1.86

Center Location of Rear Axles (m)	Left Camera Vertical Displacement (mm)	Right Camera Vertical Displacement (mm)	Average Vertical Displacement (mm)
0	0	0	0
1.524	-0.00402347	-0.007952247	-0.00599
3.048	-0.007513774	-0.016435751	-0.01197
4.572	0.228155738	0.207392453	0.217774
6.096	0.158985037	0.20680541	0.182895
7.62	0.057572937	0.050342027	0.053957
9.144	0.097095394	0.083378007	0.090237
10.668	0.005867367	-0.006080053	-0.00011

NOTE: 3.28 ft. = 1 m

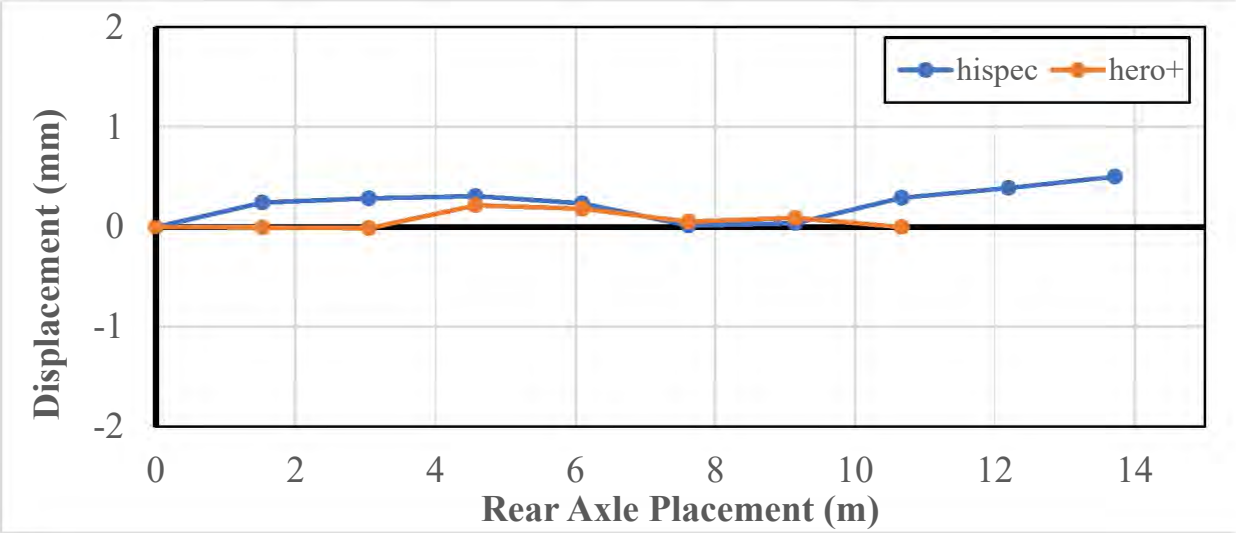


Figure 1.87: Comparison of vertical displacement versus rear axle placement for the exterior HPC beams for Single Truck loading along Path 3 (NOTE: 1 in. = 25.4 mm).

Table 1.77: Numerical data values for the vertical displacements corresponding to Figure 1.87

Center Location of Rear Axles (m)	Vertical Displacement from HiSpec1 System (mm)	Vertical Displacement from GoPro Hero+ System (mm)
0	0	0
1.524	0.244	-0.005987858
3.048	0.286	-0.011974763
4.572	0.308	0.217774096
6.096	0.236	0.182895223
7.62	0.0132	0.053957482
9.144	0.038	0.0902367
10.668	0.293	-0.000106343
12.192	0.39	
13.716	0.504	

NOTE: 3.28 ft. = 1 m

1.7.1.1.2.2.2 Performance of UHPC Span

The UHPC span was monitored using the IL5, and GoPro Hero 3 systems at the mid-span of the fascia girders and the 2M system at the mid-span of an interior girder. It should be noted that some stages were not captured and as a result some displacement values are missing from the influence line plots of vertical displacement. A negative displacement indicates downward deflection while a positive displacement would mean the element moved upward. The rear axle placement is in relation to the start of the UHPC span.

The IL5 camera system monitored the behavior of an exterior girder on the UHPC span of the bridge. The influence line plots for vertical displacement of a single H-Truck on the bridge for paths 1-6 are presented in Figure 1.88 and Table 1.78. It is noted that path 1 is closest to the IL5 system while path 3 is closer to the centerline of the bridge. For paths 1 and 2 as the truck enters on the bridge the displacements at the mid-span begin to increase. As expected, the greatest response is when the truck is moving along path 1 and smallest for paths 3, 5 and 6. The peak vertical displacement for this test run is approximately 1 mm (0.04 in.). When the truck is running along paths 3-6 there appears to be some twisting in the bridge with the exterior girder moving very slight upward with a maximum displacement of 0.43 mm (0.017 in.). This is slightly lower than what was seen for the HPC span. The data from path 1 seems to suggest some continuity between the two spans as there is a slight upward movement on the UHPC side when the truck is on the HPC span.

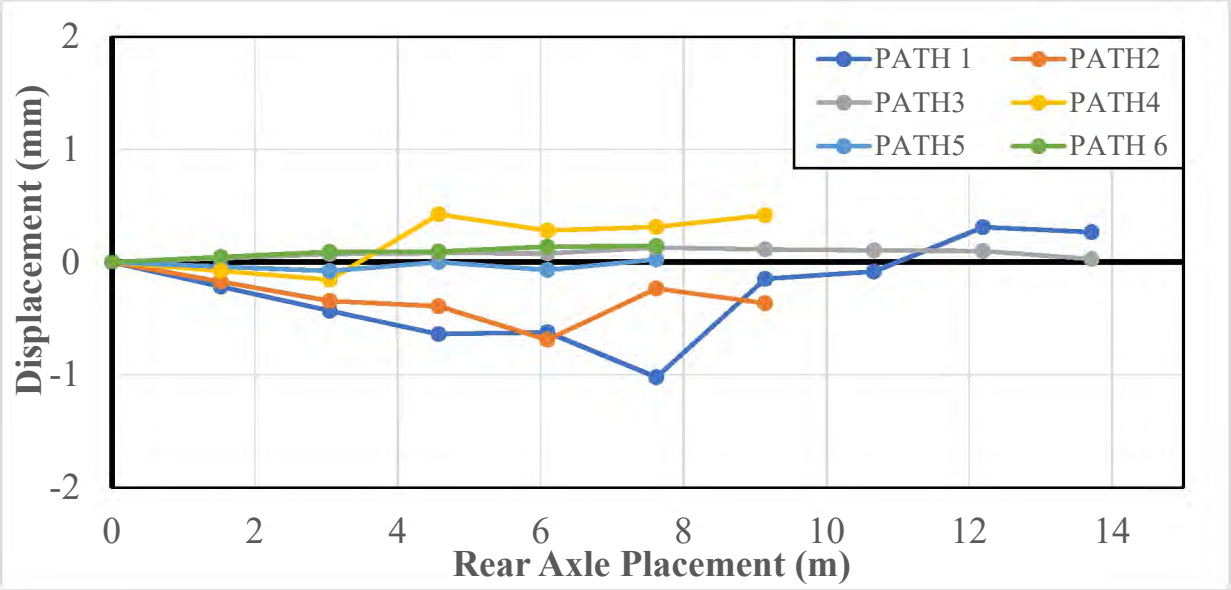


Figure 1.88: Displacement versus rear axle placement for an exterior UHPC beams for Single Truck loading measured by the IL5 system (NOTE: 1 in. = 25.4 mm).

Table 1.78: Numerical Data for Vertical Displacements Corresponding To Figure 1.88

Rear Axle Location (m)	PATH 1 (mm)	PATH 2 (mm)	PATH 3 (mm)	PATH 4 (mm)	PATH 5 (mm)	PATH 6 (mm)
0	0	0	0	0	0	0
1.524	-0.215	-0.1715	0.0361	-0.0769	-0.03916	0.0463835
3.048	-0.43	-0.343	0.0722	-0.15381	-0.07832	0.092767
4.572	-0.638	-0.39	0.0817	0.425234	0.001695	0.0949137
6.096	-0.62	-0.687	0.0787	0.282311	-0.06844	0.1377856
7.62	-1.02	-0.233	0.13	0.312833	0.026139	0.1447496
9.144	-0.147	-0.363	0.114	0.418648		
10.668	-0.0824		0.105			
12.192	0.311		0.0995			
13.716	0.267		0.0293			

NOTE: 3.28 ft. = 1 m

The GoPro Hero 3 was used as was used as two separate cameras capturing the same field of view on the exterior girder opposite of the IL5 cameras. Since the cameras were run separately, the images were processed using 2D DIC analysis. To verify both sets of images were capturing the same, or nearly the same, displacements, the results were compared then averaged. An example of the response for a single truck along paths 1, 2 and 3 can be found in Figure 1.89 through Figure 1.91 and Table 1.79 through Table 1.81, respectively. As seen, the vertical displacements from both cameras are nearly identical. Since all three paths are not near the girder monitored by the GoPro Hero 3 sensors, the displacement values are very small. For path 3, the closest of the 3 paths to the cameras, the displacements are greatest and are downward as the truck moves across the entire bridge. Very little upward movement is seen for paths 1 and 2. A plot comparing the influence line for vertical displacements at the mid-span of both exterior on the UHPC span is seen in Figure 26. This data suggests that there is a very slight upward movement on the girder monitored with the IL5 when the truck is positioned along path 3 compared to the girder monitored by the GoPro Hero 3. Comparing Figure 1.87 and Figure 1.92 it also appears that both spans are shedding the load.

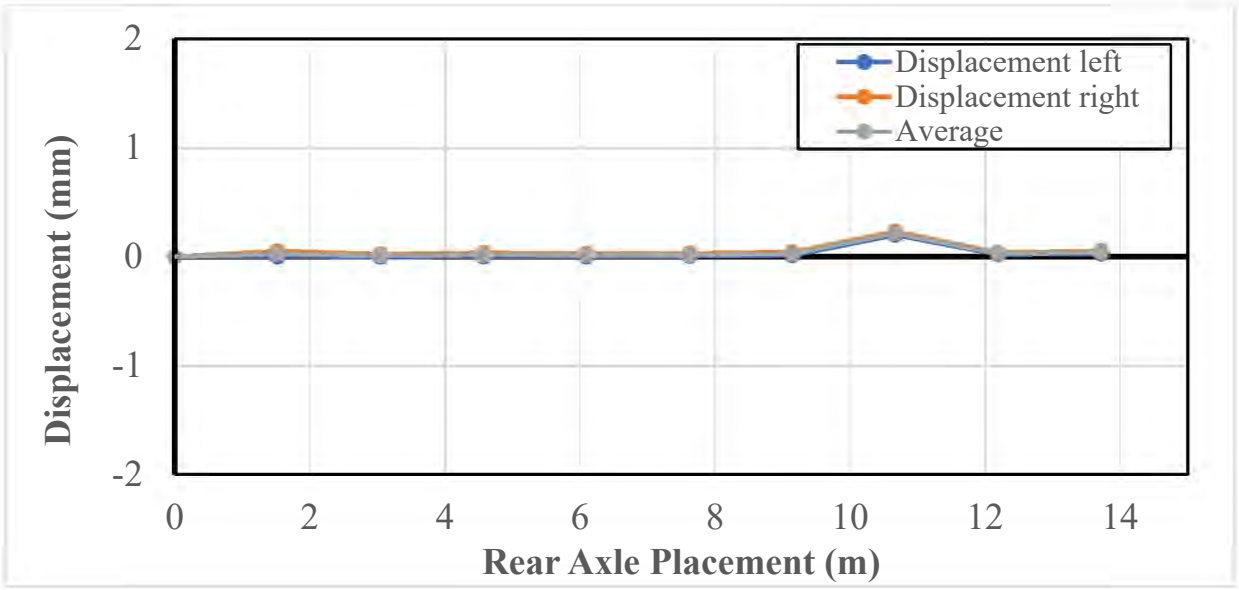


Figure 1.89: Displacement verus rear axle placement for an exterior UHPC beams for Single Truck loading along Path 1 measured by the GoPro Hero 3 system (NOTE: 1 in. = 25.4 mm).

Table 1.79: Numerical Data for Vertical Displacements Corresponding To Figure 1.89

Center Location of Rear Axles (m)	Left Camera Vertical Displacement (mm)	Right Camera Vertical Displacement (mm)	Average Vertical Displacement (mm)
0	0	0	0
1.524	-0.000122259	0.049705844	0.024792
3.048	-0.002613383	0.023791464	0.010589
4.572	0.00056299	0.033678129	0.017121
6.096	0.000540478	0.028586615	0.014564
7.62	0.004800415	0.028736819	0.016769
9.144	0.01186678	0.042935278	0.027401
10.668	0.200571311	0.231778707	0.216175
12.192	0.019647429	0.037084896	0.028366
13.716	0.027824569	0.052008794	0.039917

NOTE: 3.28 ft. = 1 m

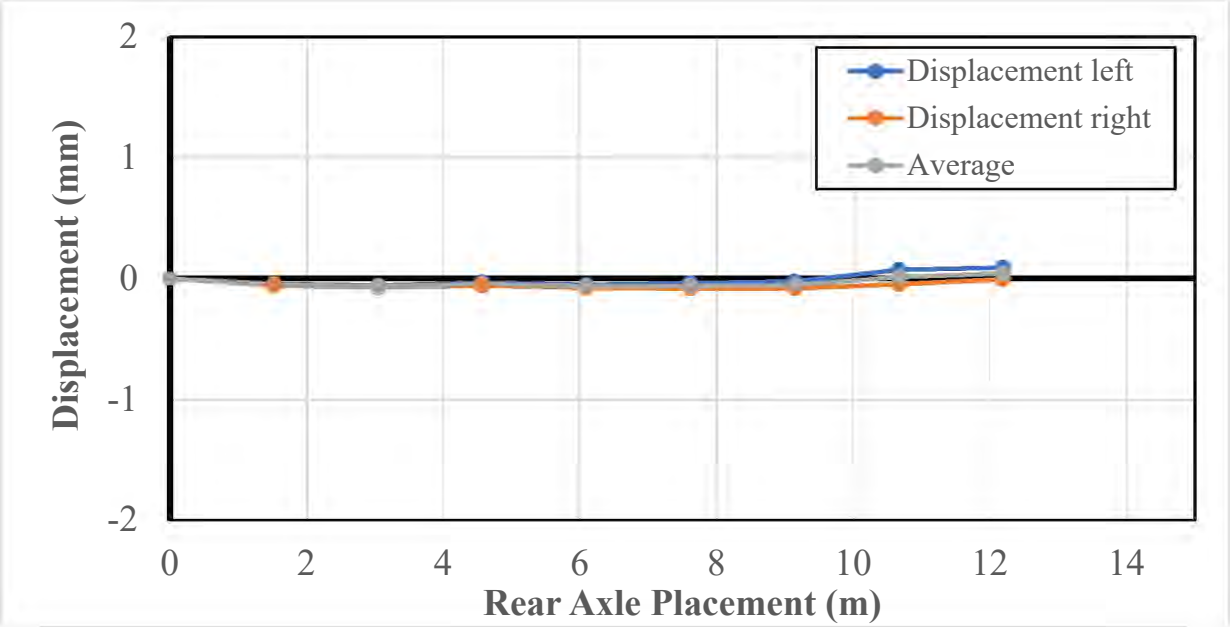


Figure 1.90: Displacement versus rear axle placement for an exterior UHPC beams for Single Truck loading along Path 2 measured by the GoPro Hero 3 system (NOTE: 1 in. = 25.4 mm).

Table 1.80: Numerical Data for Vertical Displacements Corresponding To Figure 1.90

Center Location of Rear Axles (m)	Left Camera Vertical Displacement (mm)	Right Camera Vertical Displacement (mm)	Average Vertical Displacement (mm)
0	0	0	0
1.524	-0.04399257	-0.056771312	-0.050381941
3.048	-0.05797841	-0.074315364	-0.066146887
4.572	-0.031385274	-0.057592424	-0.044488849
6.096	-0.051116342	-0.076817069	-0.063966705
7.62	-0.038670475	-0.081130752	-0.059900613
9.144	-0.024063064	-0.081414123	-0.052738594
10.668	0.072378207	-0.046000684	0.013188761
12.192	0.091242714	-0.004942359	0.043150177

NOTE: 3.28 ft. = 1 m

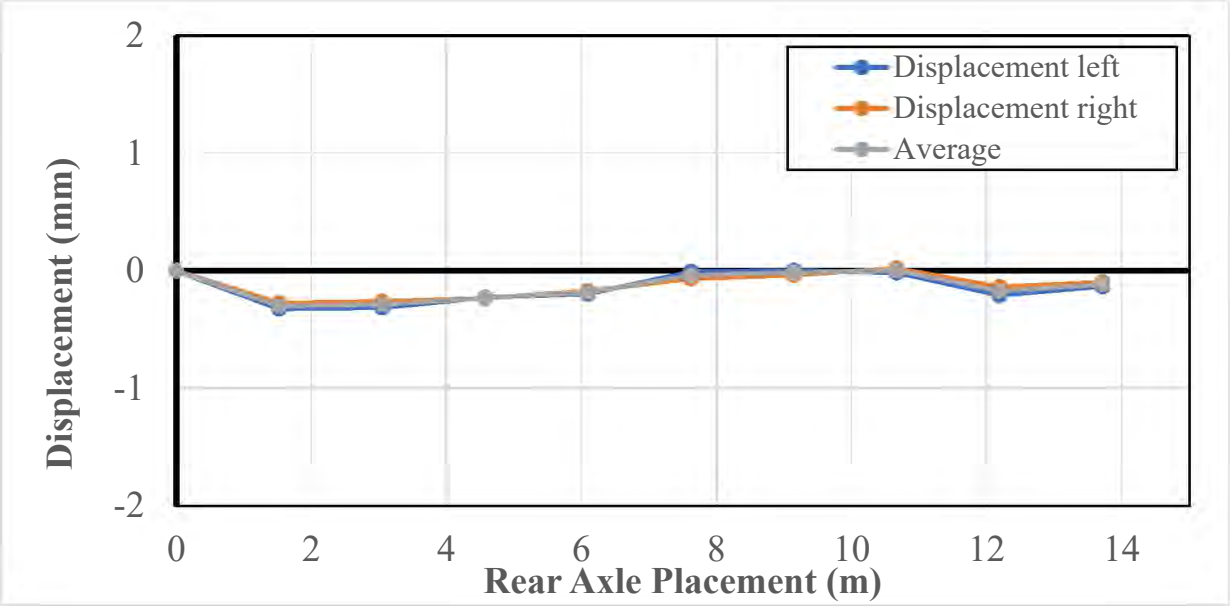


Figure 1.91: Displacement versus rear axle placement for an exterior UHPC beams for Single Truck loading along Path 3 measured by the GoPro Hero 3 system (NOTE: 1 in. = 25.4 mm).

Table 1.81: Numerical Data for Vertical Displacements Corresponding To Figure 1.91

Center Location of Rear Axles (m)	Left Camera Vertical Displacement (mm)	Right Camera Vertical Displacement (mm)	Average Vertical Displacement (mm)
0	0	0	0
1.524	-0.323084595	-0.272006241	-0.29754542
3.048	-0.313029402	-0.260213537	-0.28662147
4.572	-0.226957521	-0.233740699	-0.23034911
6.096	-0.195202237	-0.170685587	-0.18294391
7.62	-0.007616019	-0.065558102	-0.03658706
9.144	0.002531499	-0.036127108	-0.0167978
10.668	-0.014838934	0.021998921	0.003579993
12.192	-0.207333387	-0.136997686	-0.17216554
13.716	-0.132852812	-0.097200983	-0.1150269

NOTE: 3.28 ft. = 1 m

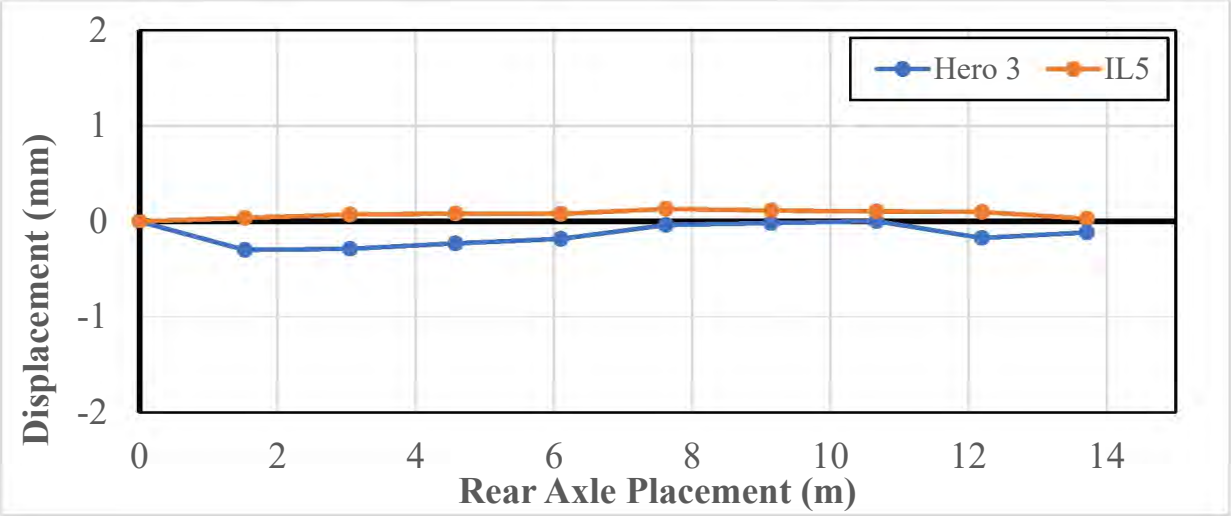


Figure 1.92: Comparison of vertical displacement vs rear axle placement for the exterior HPC beams for Single Truck loading along Path 3 (NOTE: 1 in. = 25.4 mm).

Table 1.82: Numerical Data for Vertical Displacements Corresponding To Figure 1.92

Center Location of Rear Axles (m)	Vertical Displacement from HiSpec1 System (mm)	Vertical Displacement from GoPro Hero+ System (mm)
0	0	0
1.524	-0.297545418	0.0361
3.048	-0.286621469	0.0722
4.572	-0.23034911	0.0817
6.096	-0.182943912	0.0787
7.62	-0.036587061	0.13
9.144	-0.016797804	0.114
10.668	0.003579993	0.105
12.192	-0.172165536	0.0995
13.716	-0.115026898	0.0293

NOTE: 3.28 ft. = 1 m

A comparison of vertical displacement was completed at the mid-span of the exterior girders monitored by the IL5 and HiSpec1 systems for a single vehicle on paths 1-3. The results for this are shown in Figure 1.93 with the corresponding numerical values in Table 1.83. The dashed and solid lines correspond to the IL5 and HiSpec1 systems respectively. For both beams the maximum downward vertical displacements occur when the truck is along path 1. This maximum value is 1.02 mm (0.04 in.) and 1.19 mm (0.047 in.) for the UHPC and HPC spans respectively. Path 3 produces an upward movement of the exterior girder for both spans with the larger result on the HPC span. While comparing the values for displacement for UHPC and HPC beams at similar stages and under similar loading stages, the displacement value of HPC beams are comparatively higher than the UHPC beams.

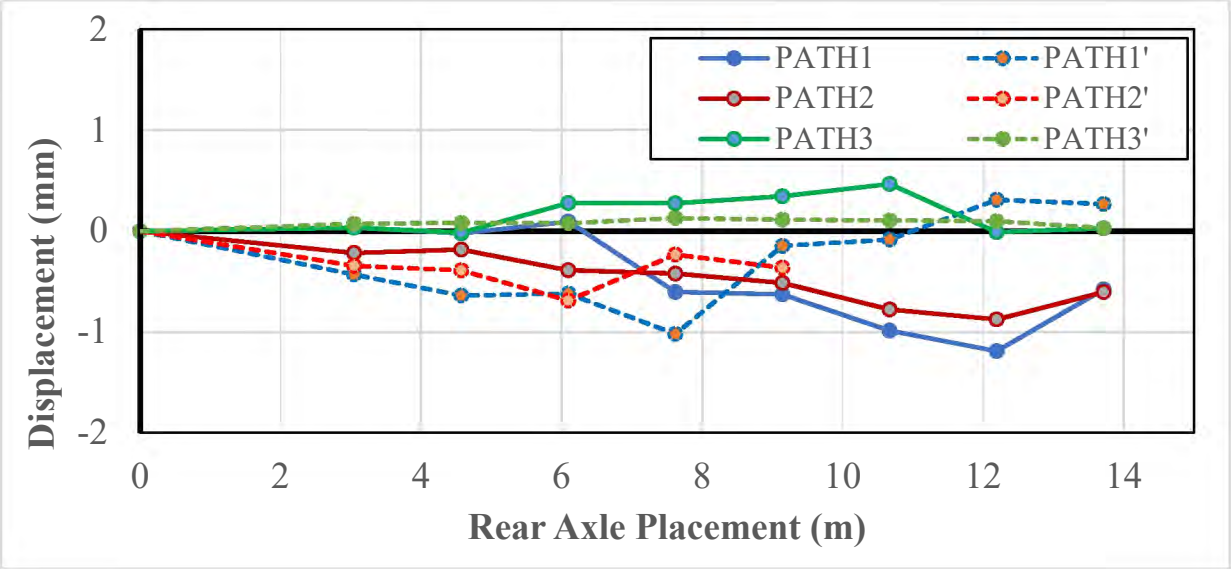


Figure 1.93: Comparison of vertical displacement versus rear axle placement for the exterior beams monitored by the IL5 (dashed lines) and HiSpec1 (solid lines) systems under Single Truck loading (NOTE: 1 in. = 25.4 mm),

Table 1.83: Numerical Data for Vertical Displacements Corresponding To Figure 1.93

Center Location of Rear Axles (m)	PATH 1 HiSpec1 Vert. Disp. (mm)	PATH 1' IL5Vert. Disp. (mm)	PATH 2 HiSpec1 Vert. Disp. (mm)	PATH 2' IL5 Vert. Disp. (mm)	PATH 3 HiSpec1 Vert. Disp. (mm)	PATH 3' IL5 Vert. Disp. (mm)
0	0	0	0	0	0	0
3.048	0.0339	-0.43	-0.216	-0.343	0.034	0.0722
4.572	-0.0234	-0.638	-0.183	-0.39	-0.0153	0.0817
6.096	0.0949	-0.62	-0.388	-0.687	0.278	0.0787
7.62	-0.604	-1.02	-0.421	-0.233	0.276	0.13
9.144	-0.627	-0.147	-0.514	-0.363	0.345	0.114
10.668	-0.986	-0.0824	-0.776		0.467	0.105
12.192	-1.19	0.311	-0.875		-0.0109	0.0995
13.716	-0.576	0.267	-0.603		0.0272	0.0293

NOTE: 3.28 ft. = 1 m

The 2M system was near the mid-span of an interior girder on the UHPC span of the bridge. Figure 1.94 and Table 15 depict the vertical displacements as a single truck passes over paths 1-6. For each influence line the vertical displacement is in the downward direction as expected. The largest displacement occurs for paths 1 and 2 with a maximum displacement of 1.7 mm (0.07 in.). The displacements are smallest for paths 5 and 6 which are farthest from the monitored location. Very small amounts of displacement are seen at this location when the vehicle is positioned on the HPC span of the bridge. While they are small, there does appear to be some interaction between the two spans.

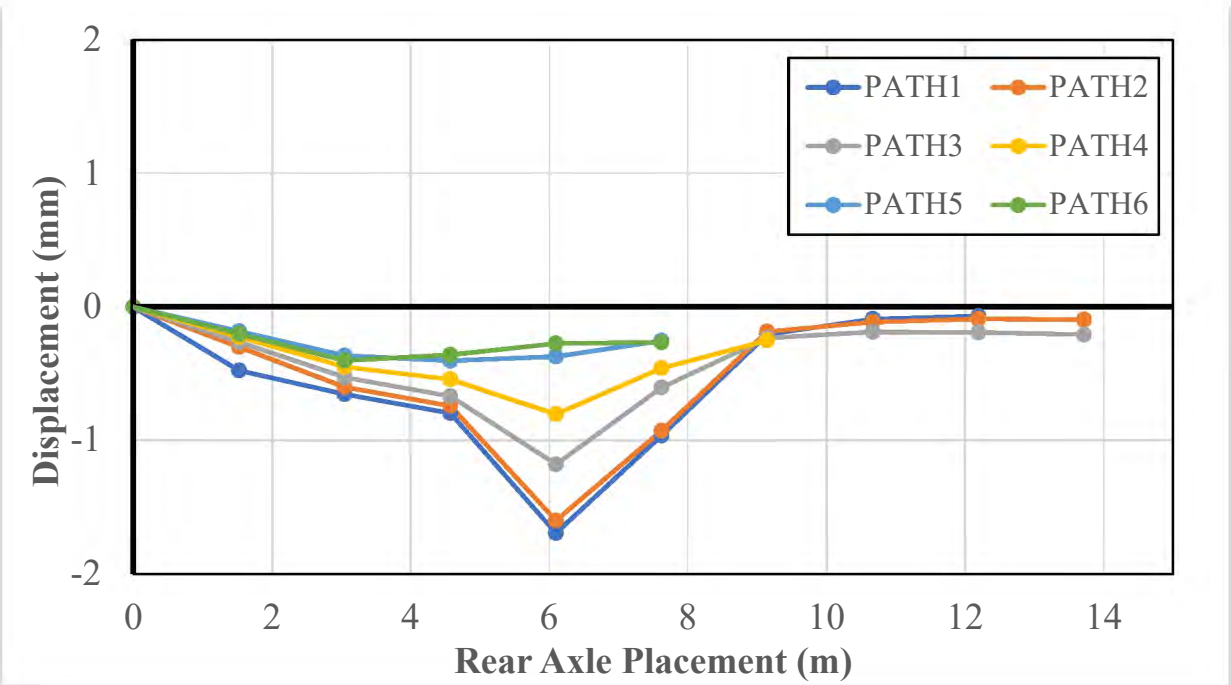


Figure 1.94: Displacement versus rear axle placement for an interior UHPC beams for Single Truck loading along paths 1-6 measured by the 2M system (NOTE: 1 in. = 25.4 mm).

Table 1.84: Numerical Data for Vertical Displacements Corresponding To Figure 1.94(

Rear Axle Location (m)	PATH 1 (mm)	PATH 2 (mm)	PATH 3 (mm)	PATH 4 (mm)	PATH 5 (mm)	PATH 6 (mm)
0	0	0	0	0	0	0
1.524	-0.47611	-0.29954	-0.26366	-0.224	-0.18207	-0.201
3.048	-0.65278	-0.59908	-0.52732	-0.44799	-0.36414	-0.402
4.572	-0.79429	-0.74122	-0.66743	-0.54134	-0.4022	-0.35892
6.096	-1.69298	-1.59879	-1.17877	-0.80367	-0.37115	-0.27376
7.62	-0.96249	-0.9267	-0.60335	-0.45845	-0.25334	-0.2643
9.144	-0.2051	-0.18447	-0.23237	-0.25041		
10.668	-0.08933	-0.11286	-0.18711			
12.192	-0.06834	-0.09031	-0.19044			
13.716		-0.09513	-0.20781			

NOTE: 3.28 ft. = 1 m

The IL5 and 2M systems were compared for testing in paths 1-3 for a single truck loading and shown in Figure 1.95 and Table 1.85. The data indicates higher vertical displacement measured by the 2M system towards the center of the bridge compared to that measured by the IL5 on the exterior. It was expected that the exterior girder should have higher displacements than an interior girder because the loading is near the exterior. Path 2 on the other hand is more directly over the location of the 2M system so that should have higher displacement. A possible reason for the lower displacements on the exterior girder are the result from a stiffer cross-section compared to an interior beam. More investigation into this finding needs to be completed before any conclusions can be drawn.

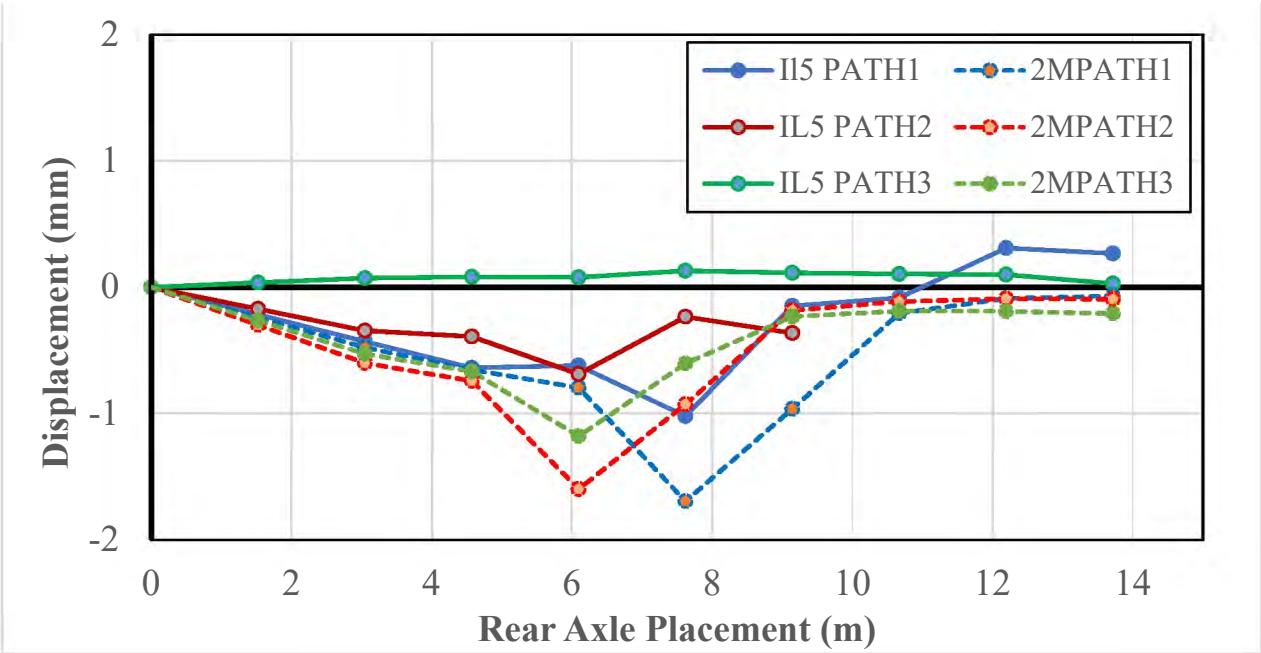


Figure 1.95: Comparison of vertical displacement versus rear axle placement for beams monitored by the IL5 (solid lines) and 2M (dashed lines) systems under single truck loading (NOTE: 1 in. = 25.4 mm)

Table 1.85: Numerical Data for Vertical Displacements Corresponding To Figure 1.95

Center Location Rear Axles (m)	IL5 PATH 1 Disp. (mm)	2M PATH 1 Disp. (mm)	IL5 PATH 2 Disp. (mm)	2M PATH 2 Disp. (mm)	IL5 PATH 3 Disp. (mm)	2M PATH 3 Disp. (mm)
0	0	0	0	0	0	0
1.524	-0.215	-0.238057	-0.1715	-0.2995395	0.0361	-0.2636576
3.048	-0.43	-0.4761139	-0.343	-0.5990790	0.0722	-0.5273152
4.572	-0.638	-0.6527754	-0.39	-0.7412191	0.0817	-0.6674349
6.096	-0.62	-0.7942945	-0.687	-1.5987940	0.0787	-1.1787692
7.62	-1.02	-1.6929848	-0.233	-0.9266969	0.13	-0.6033512
9.144	-0.147	-0.9624898	-0.363	-0.1844734	0.114	-0.2323686
10.668	-0.0824	-0.2050996		-0.1128629	0.105	-0.1871089
12.192	0.311	-0.089333		-0.0903123	0.0995	-0.1904354
13.716	0.267	-0.068345		-0.0951303	0.0293	-0.2078125

NOTE: 3.28 ft. = 1 m

1.8 Vibrating Wire Strain Data

Monitoring of NM Bridge No. 9706 was also conducted using vibrating wire strain gauges (VWSGs). Embedded in each girder prior to casting, VWSGs facilitated thermal and strain-based measurements and provided the unique opportunity for direct comparative analyses of the two types of concrete. The following sections presents the results of bridge girder monitoring including curing temperatures during precast production, measured material properties (compressive strength, unit weight, and modulus of rupture), initial prestress forces, and strain measurements during field testing of NM Bridge No. 9706.

1.8.1 Vibrating Wire Strain Gauges

Vibrating wire strain gauges (VWSG) provide strain measurement by means of the vibrating wire principle (Simon et al., 2015). A tensioned wire, housed in a protected shell and suspended between end blocks, produces a resonant frequency when excited by an electromagnetic coil which can be directly related to strain caused by prestress transfer, temperature changes, creep and shrinkage, vehicular loads, etc. As the end blocks of the sensor move relative to one another, changes in frequency can be converted to strain based on material and geometric properties of the gauge. The calculated strain corresponds to the position (depth) of the gauge and can be related to the level of the prestressing tendons.

Each VWSG is equipped with an integral high-temperature thermistor. A thermally sensitive electrical resistor, a thermistor exhibits a precise and predictable change in resistance proportional to fluctuations in temperature (Omega, 2018b). Resistance (ohms) is transformed to temperature (degrees Celsius) using the Steinhart-Hart equation (Equation 1.20), an empirical formula determined to be the most accurate mathematical expression for the resistance-temperature relationship of a thermistor (Steinhart and Hart, 1968).

$$T(°C) = \frac{1}{A + BLnR_T + CLn^3R_T} - 273.2 \qquad 1.20$$

The coefficients A, B and C are found by taking the resistance of the thermistor at three temperatures, entering each of the known resistance and temperature values into Equation 1.20, and solving the three equations simultaneously. The term LnR_T represents the natural logarithm of the measured resistance of the thermistor measured in ohms.

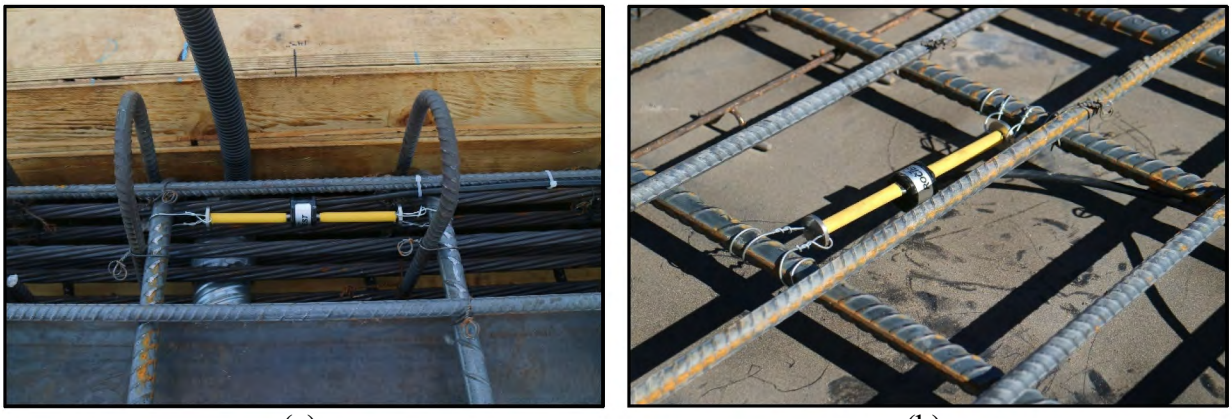
After careful consideration of the available instrumentation options, two types of vibrating wire strain gauges (VWSGs) produced by Roctest Ltd. were installed in the girders of NM Bridge No. 9706. The first type was the model EM-5 embedded VWSG (Roctest Ltd., 2017a), referred to herein as an EM gauge and pictured in Figure 1.96. Measuring approximately 6.5 in. (165 mm) long, EM gauges were suspended between adjacent transverse mild steel reinforcement bars using rebar tie-wire (Figure 1.97) and embedded within the girder concrete. The sensor cables were fastened to longitudinal reinforcement down the length of the girder and exited the girder at the pier end haunch through an embedded PVC duct. EM gauges were connected to a data logger

immediately following placement of concrete and collected strain and temperature data continuously throughout curing.

The second sensor type was the SM-5 series surface mounting VWSG (Roctest Ltd., 2017b). Identical in size and function to the type EM gauge, the SM gauge is meant to be externally attached, or surface mounted, and remain accessible during the sensor service life. Referred to herein as an SM gauge, this sensor was available in two models which differ in mechanical support, the SM-5A (Figure 1.98-a) and SM-5B (Figure 1.98-b). The anchor blocks of the SM-5A were attached to the interior face of the girder stems using an epoxy adhesive after final construction of the bridge (-a), whereas the anchor blocks of the SM-5B were welded to a short rebar length that was embedded in the girder concrete (-b).

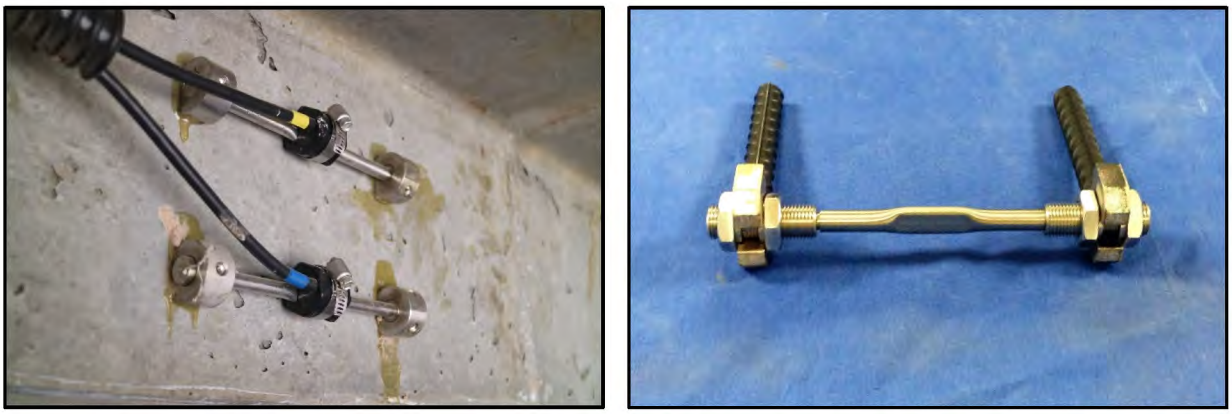


Figure 1.96: Roctest Ltd. model EM-5 vibrating wire strain gauge



(a) (b)

Figure 1.97: EM gauges installed (a) in stem above prestressing strands and (b) in flange region



(a) (b)

Figure 1.98: Roctest Ltd. SM-5 series vibrating wire strain gauges: (a) model SM-5A and (b) model SM-5B with attachable embedment anchors.

1.8.2 Naming Convention

The naming convention used for VWSGs is provided in Figure 1.99. The first two characters referencing concrete type and girder line (girder lines shown in Figure 1.100) will be used herein to refer to individual girders (e.g., girder 7 of the UHPC span is designated U-7).

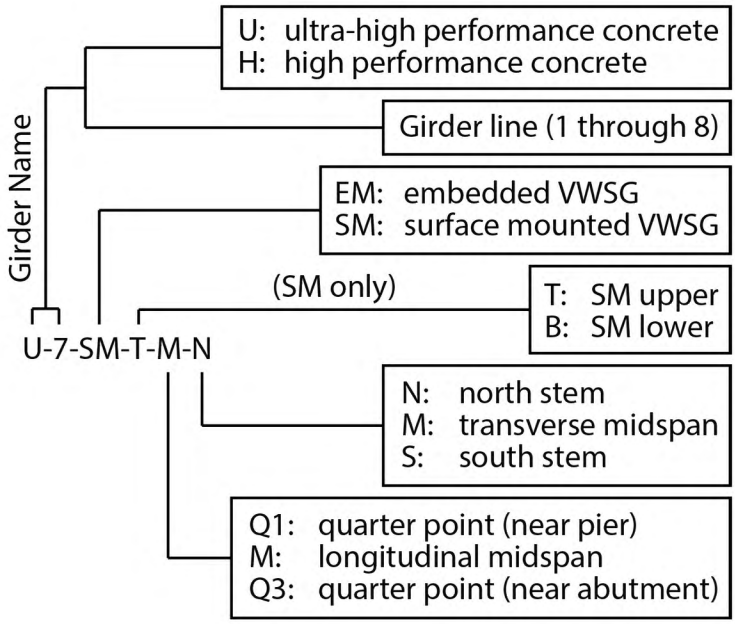


Figure 1.99: Naming convention used for VWSGs in NM Bridge No. 9706.

1.8.3 Sensor Arrangements

The approximate locations summarized in Figure 1.100 correspond to the two cross-sectional arrangements used for placement of VWSGs shown in Figure 1.101. Placed at longitudinal quarter point and/or midspan locations, each arrangement provided between two and six EM gauges directly embedded within the girder concrete and an additional four to eight SM gauges attached to embedded anchors on the inside face of each stem. Installation of the gauges is detailed in Section 1.8.4.

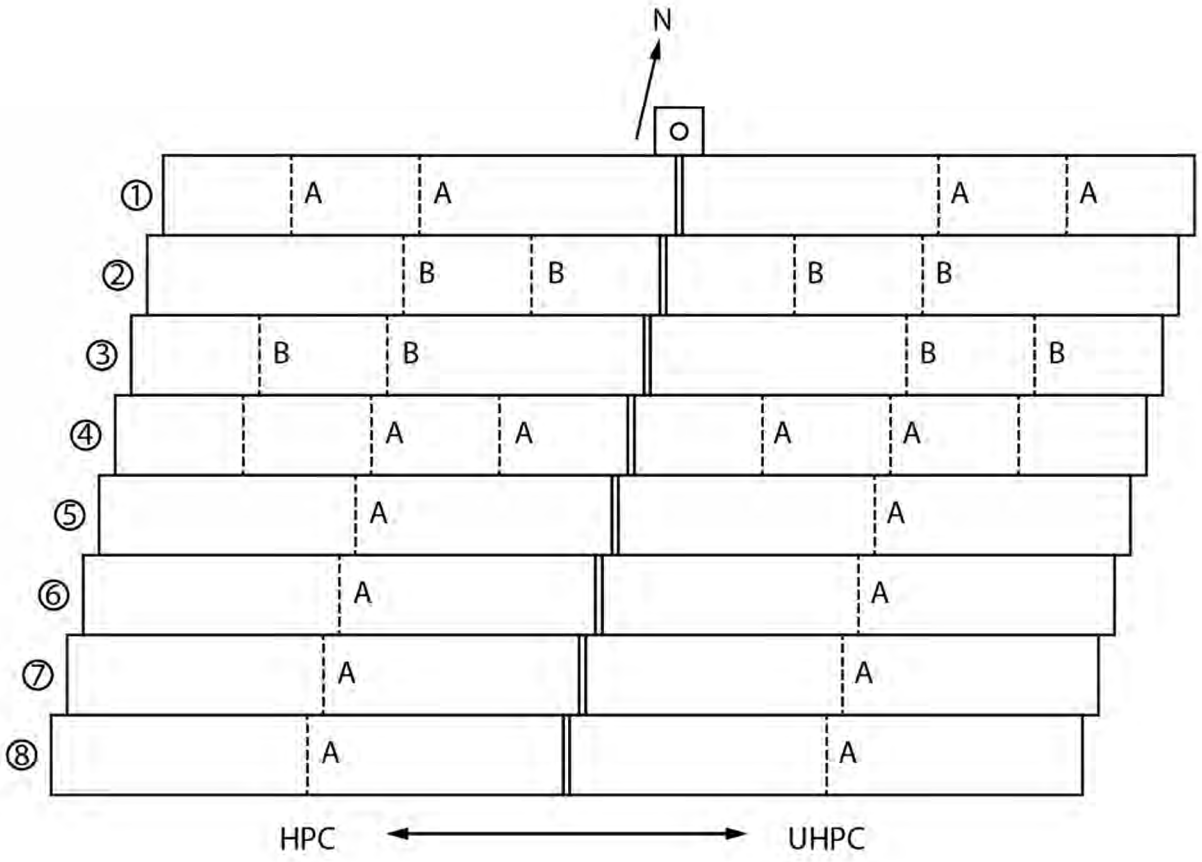


Figure 1.100: Location of cross-sectional VWSG arrangements in NM Bridge No. 9706.

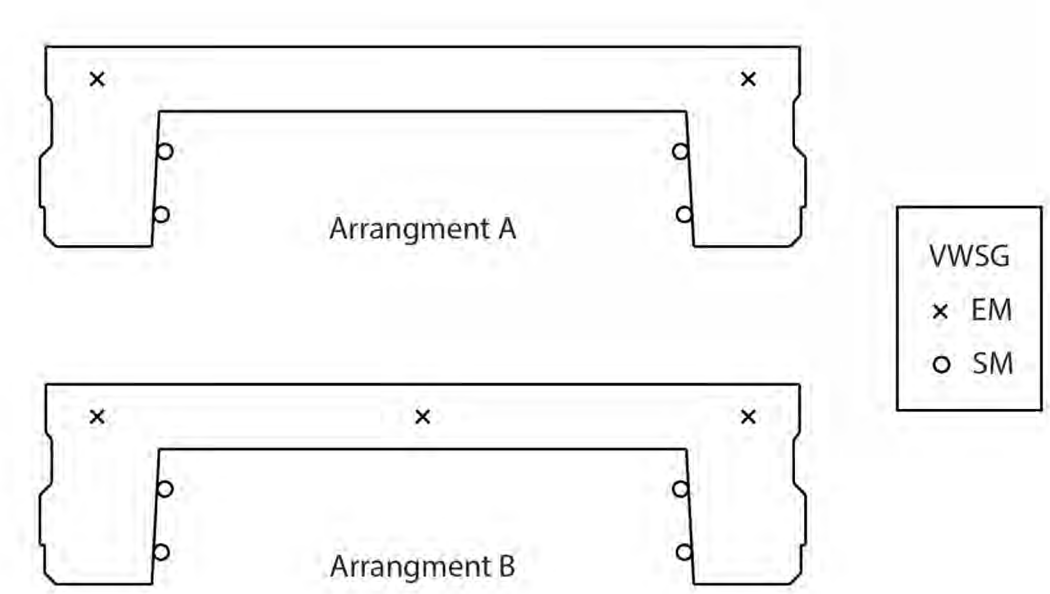
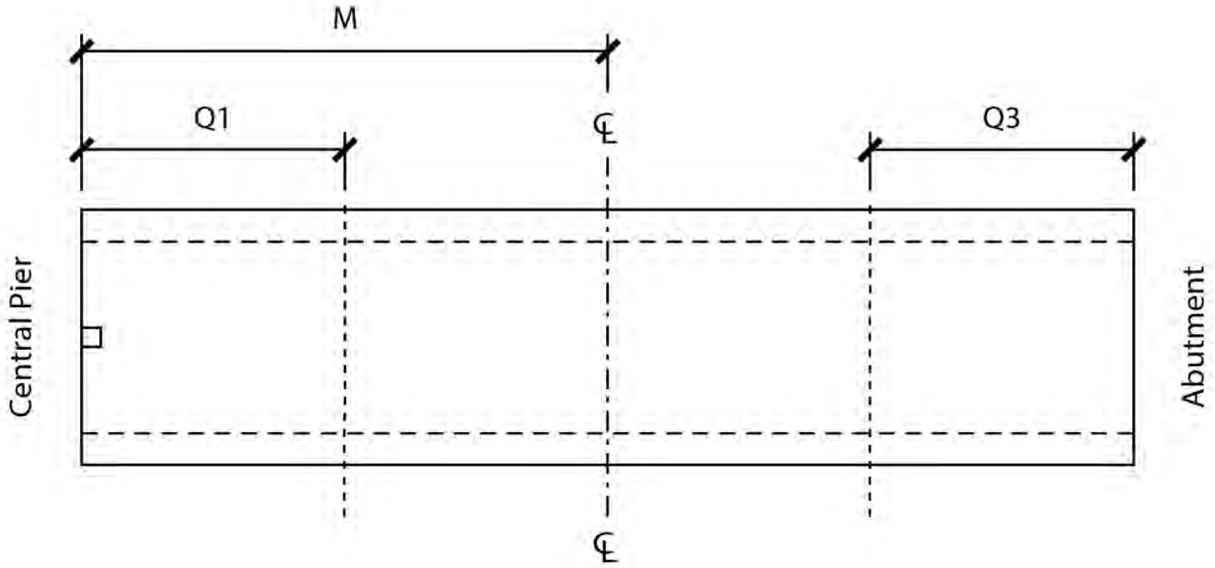


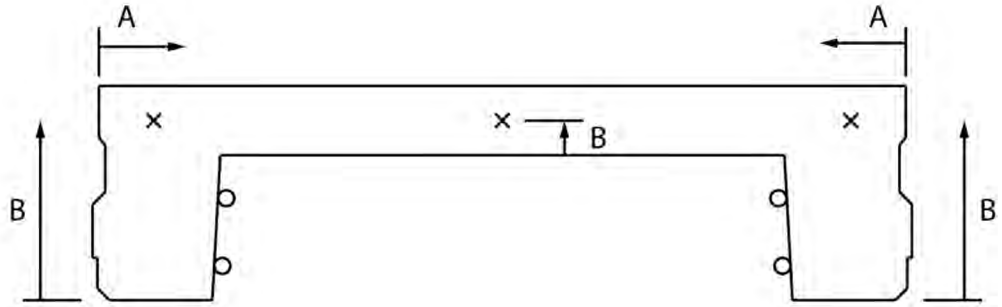
Figure 1.101: Cross-sectional VWSG arrangements.

1.8.3.1 Location Measurements

Location measurements were recorded for each VWSG during sensor installation. The installation schematics in Figure 1.102 are provided as visual references accompanying the sensor location measurements summarized for each girder in Table 1.94 through Table 1.93. Longitudinal measurements (Figure 1.102-a) to sensors placed at Q1 and M locations were taken from the end of the girder at the central pier, and from the end of the girder at the abutment for sensors placed at Q3. Cross-sectional measurements (Figure 1.102-b) consisted of the transverse measurement, A, and depth measurement, B. Transverse measurements were typically taken from the closest edge of the girder form, and depth was measured from the bottom of the stem to the sensor level. For EM gauges placed in the flange at transverse midspan in girder Lines 2 and 3 using sensor arrangement B (Figure 1.101), the transverse measurement was taken from the south edge of the girder, and the depth was measured from the bottom of the flange.



(a)



(b)

Figure 1.102: VWSG installation schematics for (a) longitudinal and (b) cross-sectional location measurements.

1.8.3.1.1 UHPC Span

Table 1.86: VWSGs Location Measurements for Girder U-1

Gauge Name	Location Measurements			
	M	Q3	A	B
	in.(mm)	in.(mm)	in.(mm)	in.(mm)
U-1-EM-M-N	157 (3988)	--	6.0 (152)	9.75 (248)
U-1-SM-T-M-N	148 (3759)	--	--	6.0 (152)
U-1-SM-B-M-N	148 (3759)	--	--	2.75 (70)
U-1-EM-M-S	157 (3975)	--	3.50 (89)	8.50 (216)
U-1-SM-T-M-S	148 (3759)	--	--	5.25 (133)
U-1-SM-B-M-S	148 (3759)	--	--	2.50 (64)
U-1-EM-Q3-N	--	75.5 (1918)	7.0 (178)	9.50 (241)
U-1-SM-T-Q3-N	--	216 (5486)	--	6.25 (159)
U-1-SM-B-Q3-N	--	216 (5486)	--	2.50 (64)
U-1-EM-Q3-S	--	75.0 (1905)	3.50 (89)	8.75 (222)
U-1-SM-T-Q3-S	--	216 (5486)	--	5.25 (133)
U-1-SM-B-Q3-S	--	216 (5486)	--	2.25 (57)

(--) not applicable

Table 1.87: VWSGs Location Measurements for Girder U-2

Gauge Name	Location Measurements			
	Q1	M	A	B
	in.(mm)	in.(mm)	in.(mm)	in.(mm)
U-2-EM-Q1-N	77.5 (1969)	--	5.25 (133)	9.0 (229)
U-2-SM-T-Q1-N	70.0 (1778)	--	--	6.50 (165)
U-2-SM-B-Q1-N	70.0 (1778)	--	--	2.75 (70)
U-2-EM-Q1-M*	77.0 (1956)	--	21.0 (533)	1.50 (38)
U-2-EM-Q1-S	77.0 (1956)	--	5.50 (140)	9.0 (229)
U-2-SM-T-Q1-S	69.0 (1753)	--	--	6.50 (165)
U-2-SM-B-Q1-S	69.0 (1753)	--	--	3.25 (83)
U-2-EM-M-N	--	142 (3607)	5.50 (140)	10.0 (254)
U-2-SM-T-M-N	--	133 (3378)	--	6.50 (165)
U-2-SM-B-M-N	--	133 (3378)	--	2.50 (64)
U-2-EM-M-M*	--	151 (3835)	26.0 (660)	1.50 (38)
U-2-EM-M-S	--	150 (3810)	3.0 (76)	10.0 (254)
U-2-SM-T-M-S	--	143 (3632)	--	6.75 (171)
U-2-SM-B-M-S	--	143 (3632)	--	3.0 (76)

NOTE: * Measurement A taken from south edge and B measured from bottom of flange
(--) not applicable

Table 1.88: VWSGs Location Measurements for Girder U-3

Gauge Name	Location Measurements			
	M	Q3	A	B
	in.(mm)	in.(mm)	in.(mm)	in.(mm)
U-3-EM-M-N	160 (4051)	--	4.0 (102)	9.25 (235)
U-3-SM-T-M-N	151 (3835)	--	--	4.75 (121)
U-3-SM-B-M-N	151 (3835)	--	--	2.25 (57)
U-3-EM-M-M*	160 (4051)	--	23.5 (597)	1.0 (25)
U-3-EM-M-S	159 (4045)	--	3.50 (89)	9.0 (229)
U-3-SM-T-M-S	151 (3835)	--	--	5.0 (127)
U-3-SM-B-M-S	151 (3835)	--	--	2.75 (70)
U-3-EM-Q3-N	--	79.3 (2013)	4.0 (102)	8.75 (222)
U-3-SM-T-Q3-N	--	214 (5436)	--	4.75 (121)
U-3-SM-B-Q3-N	--	214 (5436)	--	2.50 (64)
U-3-EM-Q3-M*	--	79.3 (2013)	24.0 (610)	1.0 (25)
U-3-EM-Q3-S	--	79.8 (2026)	3.25 (83)	9.0 (229)
U-3-SM-T-Q3-S	--	212 (5385)	--	5.25 (133)
U-3-SM-B-Q3-S	--	212 (5385)	--	2.75 (70)

NOTE: * Measurement A taken from south edge and B measured from bottom of flange
(--) not applicable

Table 1.89: VWSGs Location Measurements for Girder U-4

Gauge Name	Location Measurements			
	Q1	M	A	B
	in.(mm)	in.(mm)	in.(mm)	in.(mm)
U-4-EM-Q1-N	72.5 (1842)	--	3.50 (89)	9.75 (248)
U-4-SM-T-Q1-N	63.0 (1600)	--	--	5.75 (146)
U-4-SM-B-Q1-N	63.0 (1600)	--	--	2.75 (70)
U-4-EM-Q1-S	72.5 (1842)	--	4.25 (108)	9.75 (248)
U-4-SM-T-Q1-S	63.0 (1600)	--	--	6.75 (171)
U-4-SM-B-Q1-S	63.0 (1600)	--	--	2.75 (70)
U-4-EM-M-N	--	143 (3632)	4.0 (102)	9.50 (241)
U-4-SM-T-M-N	--	134 (3404)	--	6.0 (152)
U-4-SM-B-M-N	--	134 (3404)	--	2.0 (51)
U-4-EM-M-S	--	163 (4128)	4.0 (102)	9.50 (241)
U-4-SM-T-M-S	--	158 (4013)	--	6.75 (171)
U-4-SM-B-M-S	--	158 (4013)	--	2.75 (70)

(--) not applicable

Table 1.90: VWSGs Location Measurements for Girder U-5

Gauge Name	Location Measurements		
	M	A	B
	in.(mm)	in.(mm)	in.(mm)
U-5-EM-M-N	143 (3620)	4.0 (102)	9.50 (241)
U-5-SM-T-M-N	134 (3404)	--	6.75 (171)
U-5-SM-B-M-N	134 (3404)	--	2.50 (64)
U-5-EM-M-S	140 (3556)	3.0 (76)	9.50 (241)
U-5-SM-T-M-S	131 (3327)	--	6.75 (171)
U-5-SM-B-M-S	131 (3327)	--	3.25 (83)

(--) not applicable

Table 1.91: VWSGs Location Measurements for Girder U-6

Gauge Name	Location Measurements		
	M	A	B
	in.(mm)	in.(mm)	in.(mm)
U-6-EM-M-N	143 (3620)	4.25 (108)	10.0 (254)
U-6-SM-T-M-N	154 (3912)	--	5.50 (140)
U-6-SM-B-M-N	154 (3912)	--	2.50 (64)
U-6-EM-M-S	143 (3632)	4.50 (114)	10.0 (254)
U-6-SM-T-M-S	149 (3785)	--	6.0 (152)
U-6-SM-B-M-S	149 (3785)	--	2.25 (57)

(--) not applicable

Table 1.92: VWSGs Location Measurements for Girder U-7

Gauge Name	Location Measurements		
	M	A	B
	in.(mm)	in.(mm)	in.(mm)
U-7-EM-M-N	151 (3823)	5.0 (127)	10.0 (254)
U-7-SM-T-M-N	154 (3912)	--	6.50 (165)
U-7-SM-B-M-N	154 (3912)	--	2.75 (70)
U-7-EM-M-S	149 (3791)	4.25 (108)	10.0 (254)
U-7-SM-T-M-S	149 (3785)	--	6.0 (152)
U-7-SM-B-M-S	149 (3785)	--	2.50 (64)

(--) not applicable

Table 1.93: VWSGs Location Measurements for Girder U-8

Gauge Name	Location Measurements		
	M	A	B
	in.(mm)	in.(mm)	in.(mm)
U-8-EM-M-N	146 (3696)	3.5 (89)	9.0 (229)
U-8-SM-T-M-N	138 (3505)	--	5.25 (133)
U-8-SM-B-M-N	138 (3505)	--	3.50 (89)
U-8-EM-M-S	145 (3670)	6.75 (171)	8.50 (216)
U-8-SM-T-M-S	138 (3505)	--	6.0 (152)
U-8-SM-B-M-S	138 (3505)	--	3.25 (83)

(--) not applicable

1.8.3.1.2 HPC Span

Table 1.94: VWSGs Location Measurements for Girder H-1

Gauge Name	Location Measurements			
	M	Q3	A	B
	in.(mm)	in.(mm)	in.(mm)	in.(mm)
H-1-EM-M-N	145 (3683)	--	6.25 (159)	11.25 (286)
H-1-SM-T-M-N	140 (3556)	--	--	7.0 (178)
H-1-SM-B-M-N	140 (3556)	--	--	3.50 (89)
H-1-EM-M-S	148 (3747)	--	3.50 (89)	11.5 (292)
H-1-SM-T-M-S	137 (3480)	--	--	7.0 (178)
H-1-SM-B-M-S	137 (3480)	--	--	3.50 (89)
H-1-EM-Q3-N	--	80.0 (2032)	5.50 (140)	11.5 (292)
H-1-SM-T-Q3-N	--	214 (5436)	--	7.50 (191)
H-1-SM-B-Q3-N	--	214 (5436)	--	3.50 (89)
H-1-EM-Q3-S	--	75.0 (1905)	3.75 (95)	11.0 (279)
H-1-SM-T-Q3-S	--	212 (5385)	--	7.50 (191)
H-1-SM-B-Q3-S	--	212 (5385)	--	3.50 (89)

(--) not applicable

Table 1.95: VWSGs Location Measurements for Girder H-2

Gauge Name	Location Measurements			
	Q1	M	A	B
	in.(mm)	in.(mm)	in.(mm)	in.(mm)
H-2-EM-Q1-N	159 (4032)	--	3.50 (89)	11.25 (286)
H-2-SM-T-Q1-N	78.0 (1981)	--	--	7.25 (184)
H-2-SM-B-Q1-N	78.0 (1981)	--	--	3.75 (95)
H-2-EM-Q1-M*	159 (4032)	--	24.5 (622)	1.75 (44)
H-2-EM-Q1-S	158 (4013)	--	4.0 (102)	11.0 (279)
H-2-SM-T-Q1-S	77.0 (1956)	--	--	7.25 (184)
H-2-SM-B-Q1-S	77.0 (1956)	--	--	3.50 (89)
H-2-EM-M-N	--	168 (4261)	4.0 (102)	11.0 (279)
H-2-SM-T-M-N	--	160 (4064)	--	7.25 (184)
H-2-SM-B-M-N	--	160 (4064)	--	1.75 (44)
H-2-EM-M-M*	--	167 (4242)	20.5 (521)	1.50 (38)
H-2-EM-M-S	--	167 (4235)	4.5 (114)	11.0 (279)
H-2-SM-T-M-S	--	158 (4013)	--	7.25 (184)
H-2-SM-B-M-S	--	158 (4013)	--	3.25 (83)

NOTE: * Measurement A taken from south edge and B measured from bottom of flange
(--) not applicable

Table 1.96: VWSGs Location Measurements for Girder H-3

Gauge Name	Location Measurements			
	M	Q3	A	B
	in.(mm)	in.(mm)	in.(mm)	in.(mm)
H-3-EM-M-N	167 (4242)	--	3.25 (83)	11.25 (286)
H-3-SM-T-M-N	159 (4039)	--	--	7.50 (191)
H-3-SM-B-M-N	159 (4039)	--	--	3.50 (89)
H-3-EM-M-M*	167 (4242)	--	22.0 (559)	1.50 (38)
H-3-EM-M-S	167 (4229)	--	4.0 (102)	11.5 (292)
H-3-SM-T-M-S	158 (4013)	--	--	8.25 (210)
H-3-SM-B-M-S	158 (4013)	--	--	2.50 (64)
H-3-EM-Q3-N	--	86.0 (2184)	4.50 (114)	12.0 (305)
H-3-SM-T-Q3-N	--	207 (5258)	--	7.0 (178)
H-3-SM-B-Q3-N	--	207 (5258)	--	3.0 (76)
H-3-EM-Q3-M*	--	87.0 (2210)	22.0 (559)	1.0 (25)
H-3-EM-Q3-S	--	87.5 (2223)	4.0 (102)	11.25 (286)
H-3-SM-T-Q3-S	--	205 (5207)	--	8.0 (203)
H-3-SM-B-Q3-S	--	205 (5207)	--	3.25 (83)

NOTE: * Measurement A taken from south edge and B measured from bottom of flange
(--) not applicable

Table 1.97: VWSGs Location Measurements for Girder H-4

Gauge Name	Location Measurements			
	Q1	M	A	B
	in.(mm)	in.(mm)	in.(mm)	in.(mm)
H-4-EM-Q1-N	87.0 (2210)	--	4.0 (102)	11.25 (286)
H-4-SM-T-Q1-N	77.0 (1956)	--	--	7.0 (178)
H-4-SM-B-Q1-N	77.0 (1956)	--	--	3.50 (89)
H-4-EM-Q1-S	87.0 (2210)	--	3.0 (76)	10.25 (260)
H-4-SM-T-Q1-S	77.0 (1956)	--	--	7.25 (184)
H-4-SM-B-Q1-S	77.0 (1956)	--	--	5.0 (127)
H-4-EM-M-N	--	134 (3404)	4.0 (102)	11.25 (286)
H-4-SM-T-M-N	--	125 (3175)	--	7.50 (191)
H-4-SM-B-M-N	--	125 (3175)	--	3.50 (89)
H-4-EM-M-S	--	133 (3378)	3.0 (76)	11.0 (279)
H-4-SM-T-M-S	--	125 (3175)	--	7.0 (178)
H-4-SM-B-M-S	--	125 (3175)	--	3.25 (83)

(--) not applicable

Table 1.98: VWSGs Location Measurements for Girder H-4

Gauge Name	Location Measurements		
	M	A	B
	in.(mm)	in.(mm)	in.(mm)
H-5-EM-M-N	167 (4235)	3.50 (89)	11.0 (279)
H-5-SM-T-M-N	158 (4013)	--	7.50 (191)
H-5-SM-B-M-N	158 (4013)	--	3.25 (83)
H-5-EM-M-S	166 (4223)	4.0 (102)	11.25 (286)
H-5-SM-T-M-S	158 (4013)	--	7.0 (178)
H-5-SM-B-M-S	158 (4013)	--	3.25 (83)

(--) not applicable

Table 1.99: VWSGs Location Measurements for Girder H-6

Gauge Name	Location Measurements		
	M	A	B
	in.(mm)	in.(mm)	in.(mm)
H-6-EM-M-N	143 (3620)	3.50 (89)	10.75 (273)
H-6-SM-T-M-N	133 (3378)	--	8.50 (216)
H-6-SM-B-M-N	132 (3353)	--	3.25 (83)
H-6-EM-M-S	143 (3620)	3.75 (95)	11.0 (279)
H-6-SM-T-M-S	131 (3327)	--	7.75 (197)
H-6-SM-B-M-S	131 (3327)	--	3.0 (76)

(--) not applicable

Table 1.100: VWSGs Location Measurements for Girder H-7

Gauge Name	Location Measurements		
	M	A	B
	in.(mm)	in.(mm)	in.(mm)
H-7-EM-M-N	159 (4039)	4.0 (102)	10.5 (267)
H-7-SM-T-M-N	150 (3810)	--	7.50 (191)
H-7-SM-B-M-N	150 (3810)	--	3.25 (83)
H-7-EM-M-S	166 (4216)	4.50 (114)	11.0 (279)
H-7-SM-T-M-S	157 (3988)	--	7.25 (184)
H-7-SM-B-M-S	157 (3988)	--	3.25 (83)

(--) not applicable

Table 1.101: VWSGs Location Measurements for Girder H-8

Gauge Name	Location Measurements		
	M	A	B
	in.(mm)	in.(mm)	in.(mm)
H-8-EM-M-N	166 (4216)	4.0 (102)	11.0 (279)
H-8-SM-T-M-N	156 (3962)	--	7.25 (184)
H-8-SM-B-M-N	156 (3962)	--	3.50 (89)
H-8-EM-M-S	145 (3683)	7.50 (191)	11.5 (292)
H-8-SM-T-M-S	136 (3454)	--	7.75 (197)
H-8-SM-B-M-S	136 (3454)	--	3.0 (76)

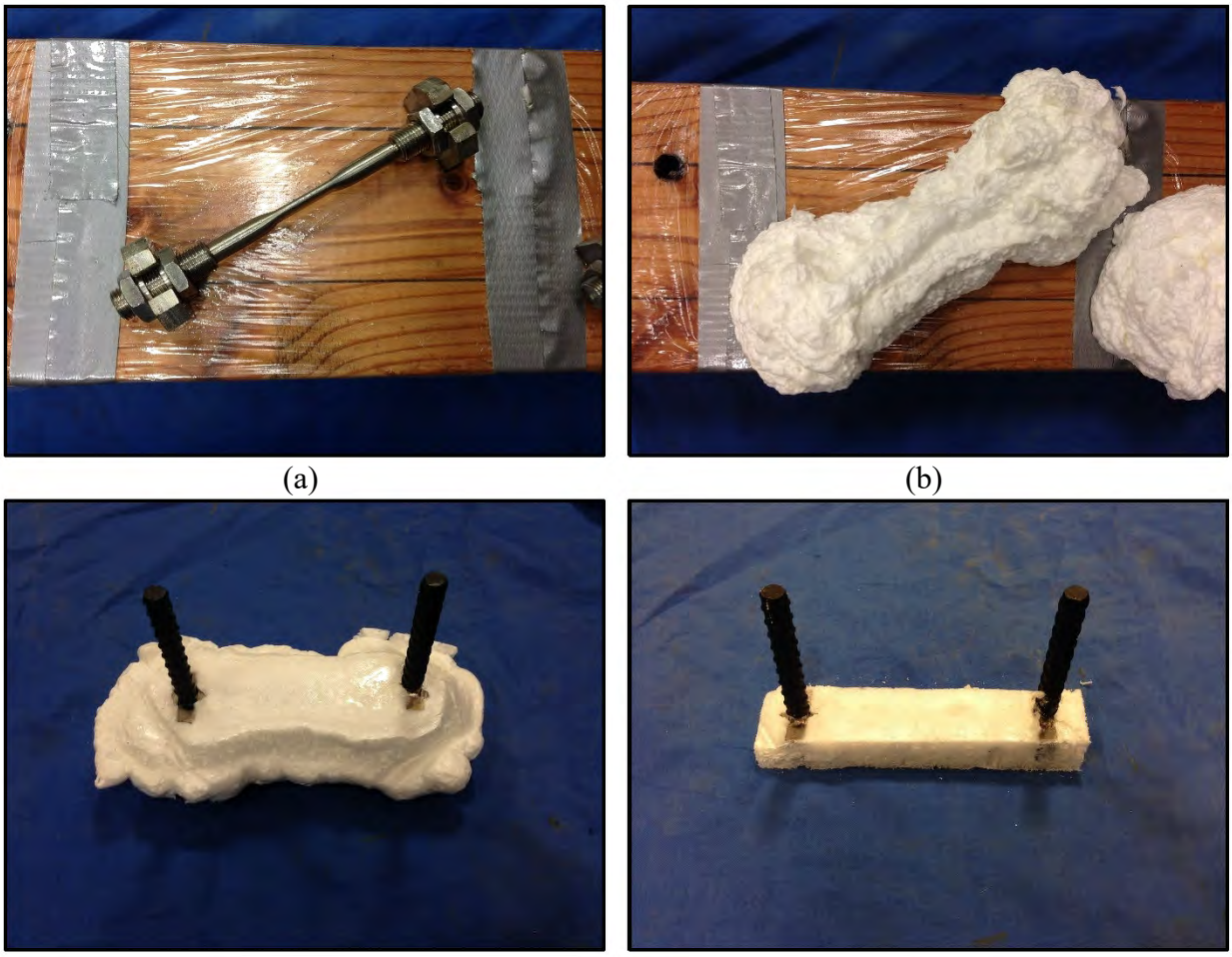
(--) not applicable

1.8.4 Sensor Installation

Requiring diligent planning and preparation, the installation of over 150 individual sensors in the girders of NM Bridge No. 9706 was executed in three phases. First, VWSGs acquired from Roctest Ltd. were prepared for embedment and transported from the SSMTL at NMSU to the precast plant at Coreslab® Structures (Albuquerque), Inc. There NMSU graduate researchers carefully installed the sensors prior to casting of each batch of prestressed channel girders and set up temporary data acquisition equipment for collection of initial data (e.g., concrete core temperatures during curing, strain measurements at prestress transfer). Lastly, installation of permanent data acquisition equipment, sensor connections, and protective coverings was conducted after construction of the bridge. When completed, over $70,000 of instrumentation and equipment was installed for monitoring of NM Bridge No. 9706. The following provides a detailed account of the VWSG preparation and installation process.

The primary SM gauge used was the model SM-5B and required advanced preparation to encase the SM gauges in protective foam prior to installation and casting of the bridge girders. First, a wood template was prepared with holes drilled approximately 5.0 in. (127 mm) apart and covered with non-stick plastic wrap (Figure 1.103-a). The gauge and attached embedment anchors were placed in the template and covered with polyurethane-based dense insulating foam (Figure 1.103-b). The foam was misted with water to enhance the curing process and allowed to sit for approximately four to six hours until fully hardened. The encased sensor was then removed from the template and cut to shape (Figure 1.103-c and -d). The resulting foam encasement measured approximately 1.0 x 0.75 x 6.0 in. (25 x 19 x 152 mm).

The encased SM gauges were then installed in the girders prior to casting as shown in Figure 1.104. Mounting tape was applied to the backside of the foam casing and pressed against the steel form on the inner wall of the girder stem. Corresponding to each location where an EM gauge was installed, two SM gauges were placed between the three levels of prestressing strands. The foam casing was later removed after construction of Bridge No 9706.



(a) (b)

(c) (d)

Figure 1.103: Protective encasement sequence for SM gauges: (a) gauge and embedment anchors inserted in wood template; (b) application of dense insulating foam; (c) hardened foam encasement; (d) SM gauge foam encasement cut to final shape.



(a) (b)

Figure 1.104: Installation of encased SM gauges to interior vertical face of girder stem formwork as viewed from (a) above and (b) down the face of the stem.

Following construction of Bridge No. 9706, the installation of permanent sensor monitoring equipment was conducted in March 2017. The schematic in Figure 1.105 illustrates the basic wiring plan for the bridge monitoring equipment. Cables (shown in black) ran from each sensor to Roctest Ltd. RT-MUX 16/32 signal multiplexers located at the central pier (Roctest Ltd., 2017c). Additional cabling (shown in gray) ran to a Campbell® Scientific, Inc. CR6 Measurement and Control Datalogger on the north end of the central pier (CSI, 2020a).

Because the maximum number of VWSGs in a single girder was limited to 14, only one multiplexer (capable of supporting 16 sensors) was need under each girder. However, only six VWSGs were installed in each girder of Lines 5–8, totaling 24 sensors in the final four girders of each span. To simplify installation, two multiplexers were installed under girders H-5 and U-5 (as shown in Figure 1.105), providing support for the sensors in Lines 5–8.

Shown in Figure 1.106-a and b, weatherproof enclosures were installed on the underside of girder Lines 1–5 to house each multiplexer. An impact drill was used to bore small holes into the bottom face of the girders, and the enclosures were fastened into place using threaded inserts.

The foam surrounding SM gauges installed in the stems of each girder was manually removed and cables were attached to the exposed sensors (Figure 1.106-c). A protective PVC channel was then fixed over the exposed gauge with high-strength adhesive (Figure 1.106-d), and the ends of the channel were filled with foam sealant. The cables were threaded through

weatherproof corrugated tubing running the length of the girder to the enclosures and wired into the multiplexers (Figure 1.106-e and f). The corrugated tubing was attached to the stem wall using perforated hangar straps and hammer-set nail drive concrete anchors inserted into small, drilled holes. Cables from embedded gauges (exiting the girders through embedded PVC ducts) were likewise passed through corrugated tubing to the enclosure.

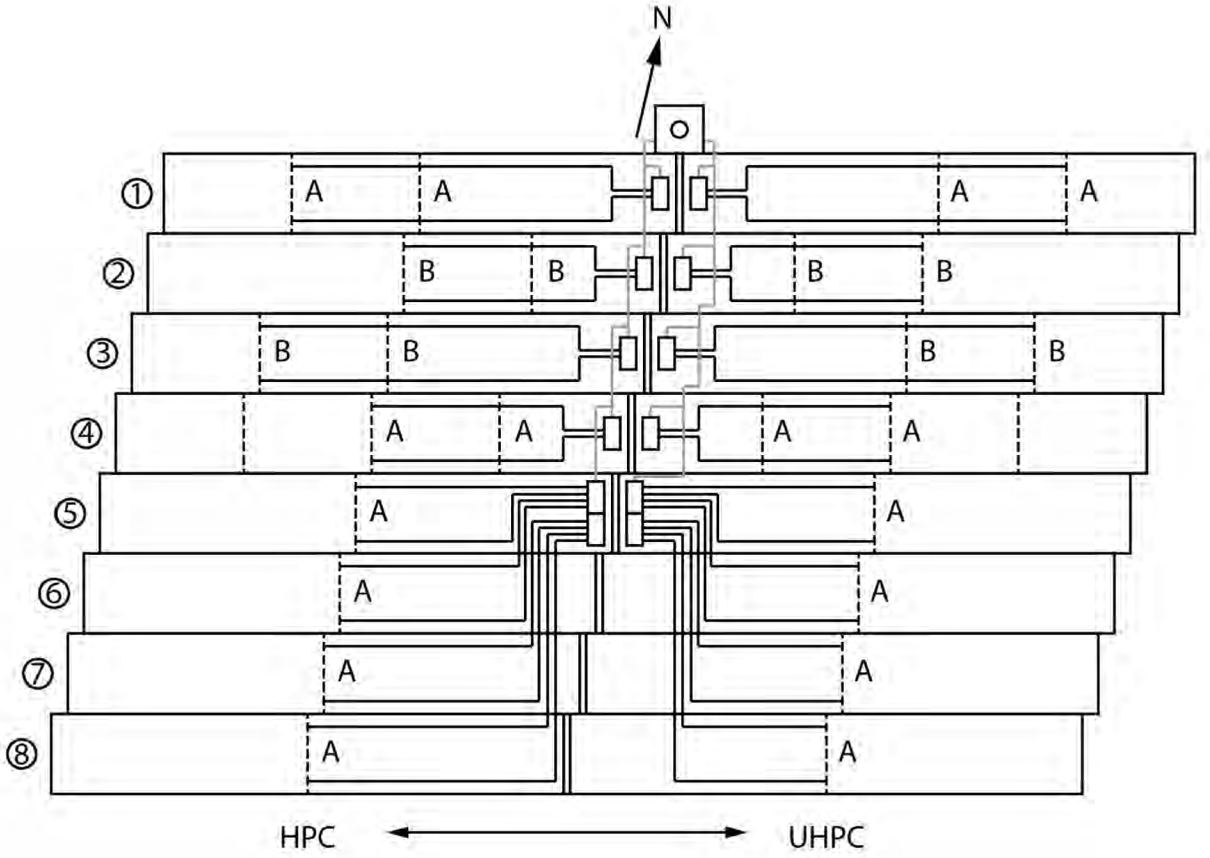


Figure 1.105: Basic wiring schematic for VWSGs in NM Bridge No. 9706.

The multiplexers were wired in series beginning at girder U-1 and ending at the multiplexers under girder H-5. The multiplexer under girder U-1 was then wired by cable directly to a CR6 datalogger (CSI, 2020a). The datalogger, an emergency 12-volt battery supply, and the system power regulator were housed in a weatherproof enclosure (Figure 1.107-a) like those used for the multiplexers. A separate, smaller enclosure housed two 12-volt batteries, that would serve as the main power supply, and a solar charge controller (Figure 1.107-b). Both batteries and two solar panels were wired to the solar charge controller, supplying uninterrupted power to the datalogger, and facilitating continuous data collection. The datalogger and battery enclosures and solar panels were attached to a standard cast aluminum pole installed on the small cantilever extension of the pier cap as shown in Figure 1.108.

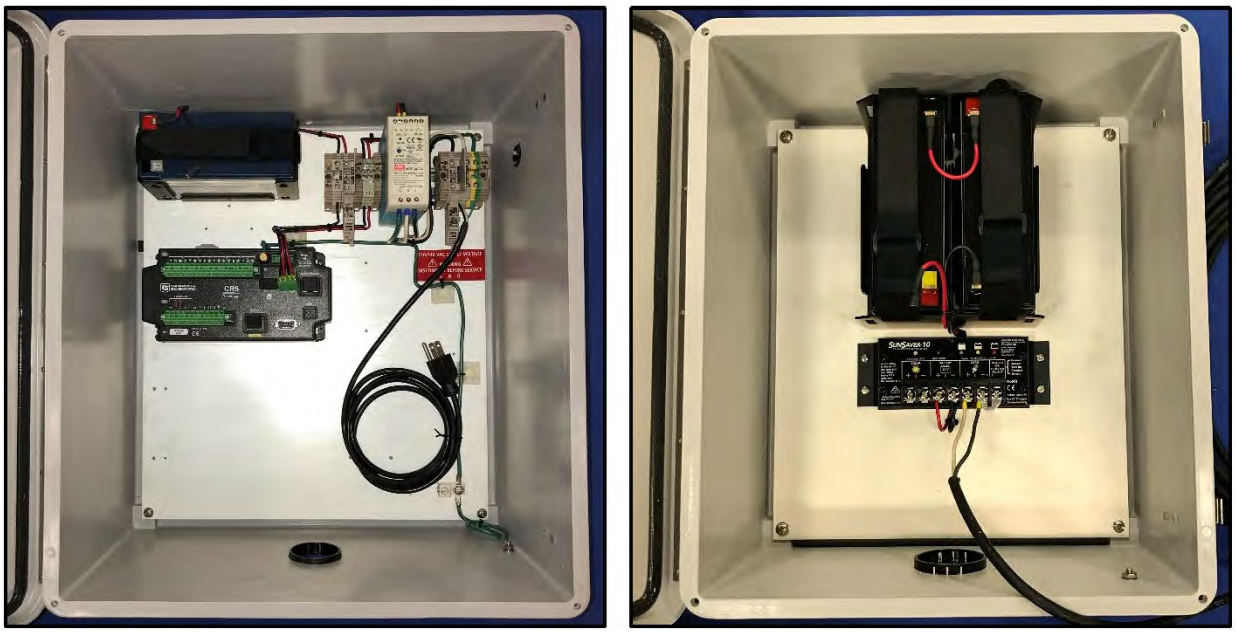


(a) (b)

(c) (d)

(e) (f)

Figure 1.106: Final sensor/equipment installation: (a) Drilling of threaded inserts to support (b) weatherproof enclosures; (c) embedded VWSGs after foam removal and (d) installation of protective PVC channel; (e) view of completed sensor installation and wiring running to (f) Roctest Ltd. RT-MUX 16/32 signal multiplexer.



(a) (b)

Figure 1.107: Data acquisition equipment for Bridge No. 9706: Weatherproof enclosures housing (a) datalogger with backup power supply and power regulator, and (b) main power supply with solar charge controller.



(a) (b)

Figure 1.108:. Cast aluminum pole on cantilever pier extension supporting (a) datalogger and power supply enclosures and (b) solar panels.

1.8.5 Initial Data

The following sections discuss initial temperature and strain data collected for the prestressed channel girders of Bridge No. 9706 during curing and at prestress transfer. Table 1.102 below provides the dates of casting and prestress strand release for each girder.

Table 1.102: Dates of Casting and Strand Release for NM Bridge No. 9706 Girders

Batch	Girders		Casting		Release	
Name	Cast		Day	Date	Day	Date
UB1	U-6	U-7	Monday	08/22/16	Monday	08/29/16
UB2	U-2	U-5	Thursday	09/22/16	Thursday	09/29/16
UB3	U-1	U-4	Friday	10/07/16	Saturday	10/15/16
UB4	U-3	U-8	Saturday	10/22/16	Monday	10/31/16
HB1	H-1	H-4	Friday	11/04/16	Monday	11/07/16
HB2	H-7	H-8	Friday	11/11/16	Monday	11/14/16
HB3	H-3	H-6	Friday	11/18/16	Monday	11/21/16
HB4	H-2	H-5	Friday	12/02/16	Friday	12/23/16

1.8.5.1 Curing Temperatures

Concrete core temperatures were recorded by internal thermistors within embedded VWSGs in each girder. Beginning immediately prior to placement of girder concrete, temperature data was collected throughout the curing process. Temperatures were relatively similar regardless of the individual sensor locations, therefore core temperatures for each girder were averaged and presented in Figure 1.109 and Figure 1.110 for UHPC and HPC, respectively. Typically cast near the end of the work week, steam treatment of the prestressed girders commenced immediately after casting and average concrete core temperatures typically peaked between approximately 150-185°F (65-85°C). The concrete core temperatures recorded by all sensors for each girder are provided in the Batch Results of Section 1.8.7.

Typically cast near the end of the work week (see Table 1.102), steam treatment of the UHPC girders commenced immediately after placement and finishing of the concrete. Steam was applied for approximately 12 hours after casting, then suspended to allow for initial set of the UHPC, thus the decline in temperatures after day 1. After initial set, steam treatment resumed until adequate transfer strengths were achieved. Measured concrete core temperatures during curing often fell below the target steam temperature of 175°F (80°C). Additional challenges during curing included steam bed malfunctions, power outages, and low ambient temperatures at the outdoor precast facility. For U-2 and U-5 (see also Figure 1.122 and Figure 1.123), data ends abruptly at Day 7 because sensors were disconnected after strand release and not reconnected to a datalogger until a later date. For U-6 and U-7 (see also Figure 1.116 and Figure 1.117), loss of power to the datalogger resulted in no data collection after Day 4.

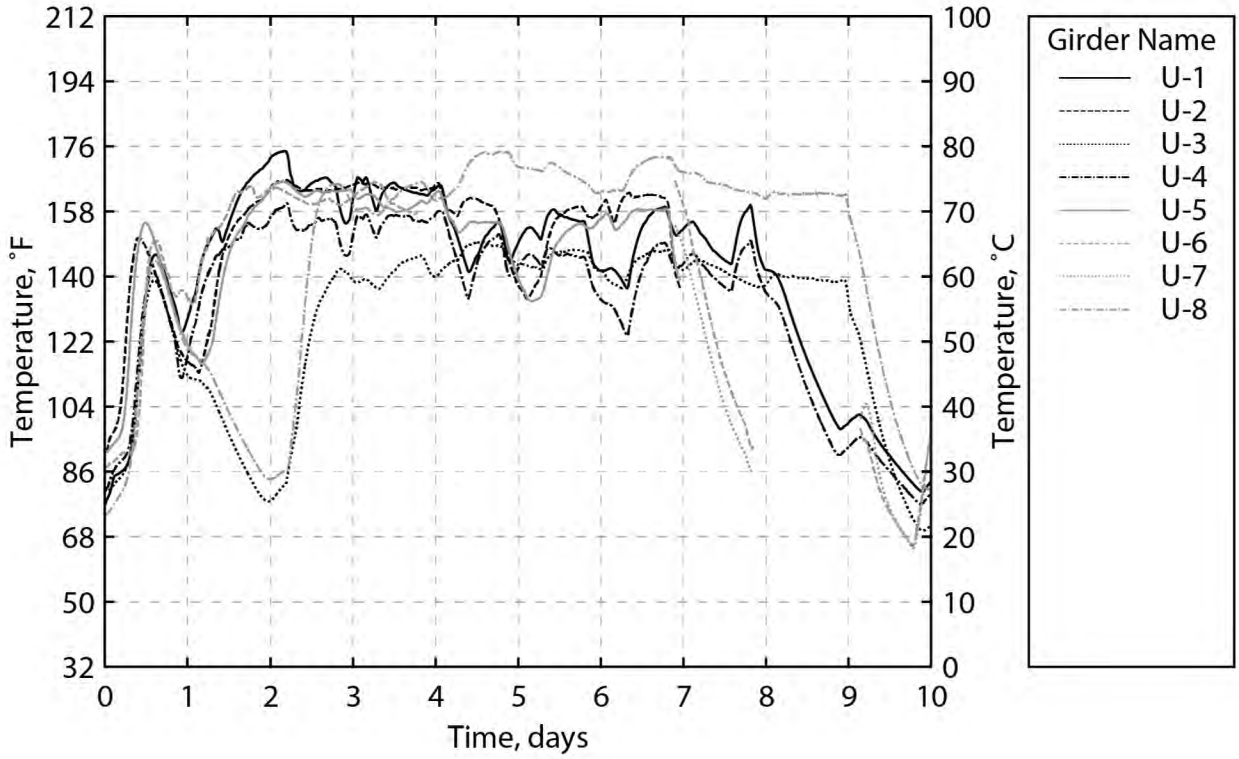


Figure 1.109: Concrete core temperatures during curing of UHPC girders for Bridge No. 9706.

Steam treatment of HPC girders commenced immediately after finishing of the concrete surface and continued for approximately 18 hours after casting. As was the case for the UHPC girders, measured temperatures often fell below the 175°F (80°C) target temperature for steam curing due to various factors such as steam bed malfunctions, power outages, and low ambient temperatures at the outdoor precast facility. In the case of girders H-1, H-4, H-7, and H-8 (see also Figure 1.140, Figure 1.141, Figure 1.146, and Figure 1.147), data ends abruptly at Day 7 because the sensors were disconnected after strand release and not reconnected to a datalogger until a later date.

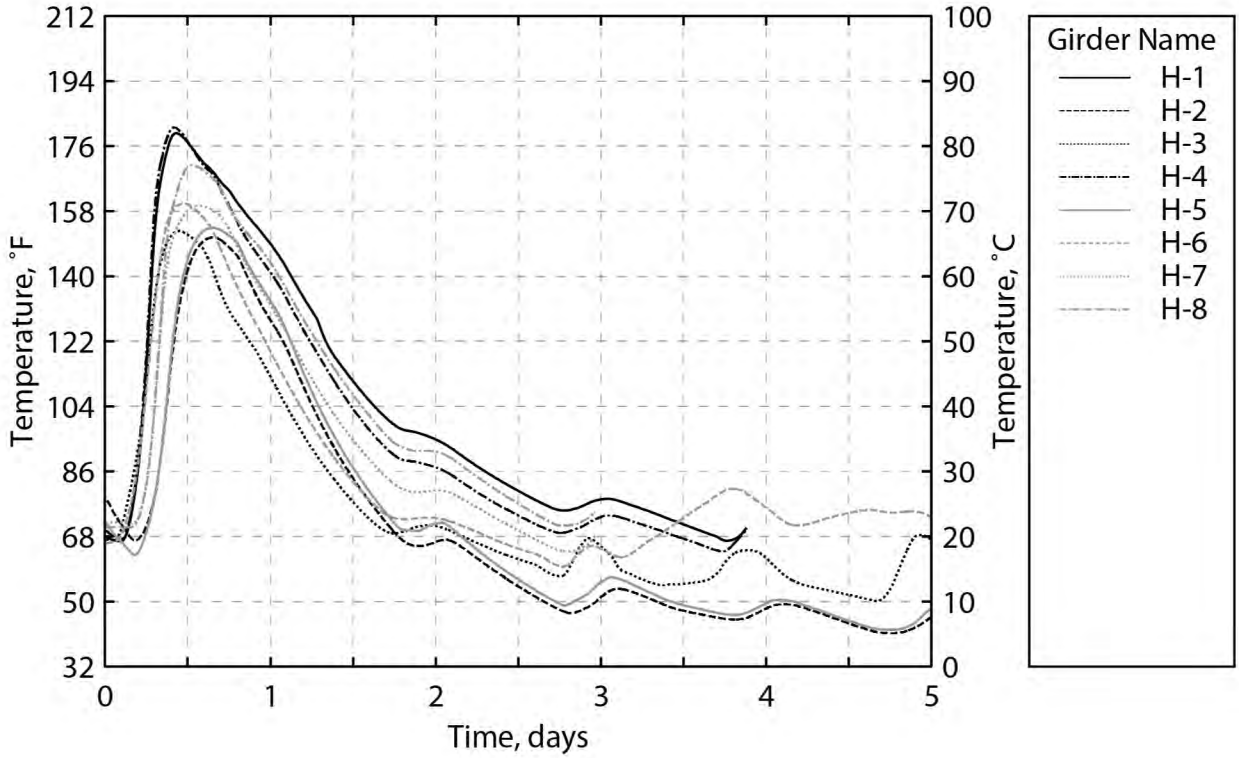


Figure 1.110: Concrete core temperatures during curing of HPC girders for Bridge No. 9706.

1.8.5.2 Prestressing Forces

Measurement of strain developed due to prestressing was facilitated by VWSG technology embedded in the channel girders of Bridge No. 9706. This data was used to calculate corresponding prestressing forces and compared to estimated prestressing forces and losses according to. AASHTO LRFD (2012) provisions were used to calculate estimated prestress losses and forces for both the interior and exterior type U and H channel girder design sections of NM Bridge No. 9706. These values are summarized in Table 1.103 and Table 1.104.

Table 1.103: Summary of AASHTO Estimated Prestress Losses for NM Bridge No. 9706

Prestress Loss	U Section		H Section	
	Interior	Exterior	Interior	Exterior
	ksi (MPa)	ksi (MPa)	ksi (MPa)	ksi (MPa)
Elastic shortening	10.4 (71.4)	7.7 (53.1)	11.5 (79.4)	8.4 (58.1)
Shrinkage	11.0 (75.8)	11.0 (75.8)	11.0 (75.8)	11.0 (75.8)
Creep	28.1 (194)	20.9 (144)	27.8 (192)	20.2 (139)
Strand relaxation	2.4 (16.6)	3.2 (21.8)	2.3 (15.8)	3.1 (21.5)
Total Losses	51.9 (358)	42.7 (295)	52.6 (363)	42.8 (295)

Table 1.104: Summary of AASHTO Estimated Prestress Forces for NM Bridge No. 9706

Prestress Force	U Section		H Section	
	Interior	Exterior	Interior	Exterior
	kips (kN)	kips (kN)	kips (kN)	kips (kN)
Jacking, P_j	527.3 (2346)	527.3 (2346)	527.3 (2346)	527.3 (2346)
Initial, P_i	500.3 (2226)	507.3 (2256)	497.3 (2212)	505.4 (2248)
Effective, P_e	392.1 (1744)	416.1 (1851)	390.4 (1736)	415.9 (1850)

1.8.5.2.1 Measured Prestressing Forces

VWSG data was used to monitor concrete strain development for the prestressed channel girders of Bridge No. 9706 during precast fabrication. Suspended between adjacent transverse mild steel reinforcement bars using rebar tie-wire (see Figure 1.97) and embedded within the girder concrete, data from EM type gauges was collected beginning immediately before girder casting until after prestress transfer. The raw data produced by VWSGs is a resonant frequency which can be directly related to strain. As an example, Figure 1.111 provides the frequency data collected from a VWSG located in the north stem at midspan of girder U-3 (gauge U-3-EM-M-N) beginning at the time of girder casting.

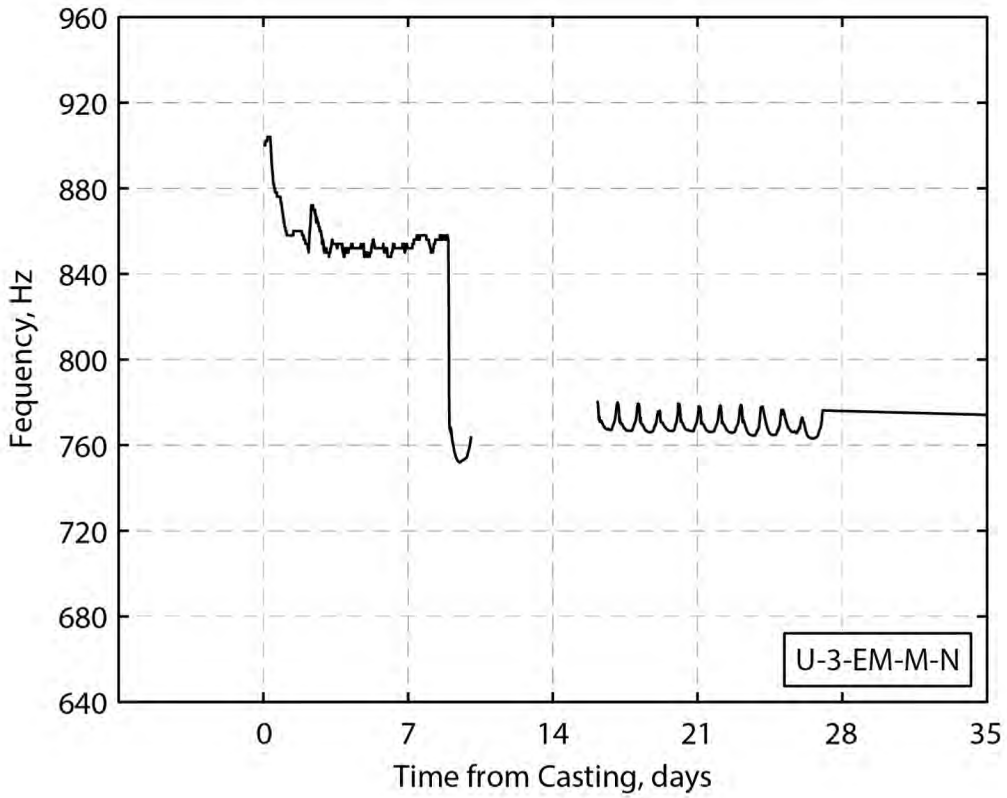


Figure 1.111: Frequency data from gauge U-3-EM-M-N beginning at the time of girder casting.

Release of prestressing strands results in shortening of the tensioned vibrating wire and is registered as a decrease in frequency. This is evident in Figure 1.111 for girder U-3 (part of batch UB4), which measured a dramatic decrease in frequency from approximately 810 to 760 Hz corresponding to the time of prestress transfer approximately nine days after casting (see production schedule in Table 1.102). The gaps in data in Figure 1.111 were due to disconnection of the gauges for movement of the girder after release of prestress strands and/or loss of power to the datalogger.

Frequency, f (Hz), was converted to strain, ε_{vwsg}, using Equation 1.21 where K is the manufacturer supplied EM gauge constant (Roctest Ltd., 2017a).

$$\varepsilon_{vwsg} = K\left(\frac{f^2}{1000}\right) \quad (\mu\varepsilon) \tag{1.21}$$

The calculated strain must then be corrected to account for temperature fluctuations and the resulting differential thermal expansion of the steel wire and surrounding concrete. Thus, Equation 1.22 was used to calculate real strain, $\varepsilon_{vwsg,r}$ (Roctest Ltd., 2017a).

$$\varepsilon_{vwsg,r} = \varepsilon_{vwsg} + (\alpha - \eta\beta)(T_1 - T_0) \quad (\mu\varepsilon) \tag{1.22}$$

In the equation above the thermal expansion coefficient of the vibrating wire, α, was provided by the manufacturer as 6.39×10^{-6} in./in./°F (11.5×10^{-6} mm/mm/°C; Roctest Ltd., 2017a). The thermal expansion coefficient of concrete, β, was taken as 8.33 $\times10^{-6}$ in./in./°F (15.0 $\times10^{-6}$ mm/mm/°C) for UHPC (Graybeal 2006a), and 5.78 $\times10^{-6}$ in./in./°F (10.4 $\times10^{-6}$ mm/mm/°C) for HPC. The value η is a freedom factor for the surrounding material (taken as 1 because confinement of the gauge allows no movement but the strain imposed by the concrete mass), and T_0 and T_1 represent the initial and final thermistor temperature measurements, respectively (Roctest Ltd., 2017a; see also Section 1.8).

Strain was then used to calculate the initial prestressing force after prestress transfer. However, the strain calculated using Equations 1.21 and 1.22 corresponds to the position (depth) of the gauge within the girder. Using Equation 1.23, this strain was related to the depth of the prestressing tendons and converted to prestressing force, P_{vwsg}.

$$P_{vwsg} = \frac{\varepsilon_{vwsg,r}E_c + \dfrac{M_o\left(e - d_{vwsg}\right)}{I_t}}{\dfrac{1}{A_t} + \dfrac{e\left(e - d_{vwsg}\right)}{I_t}} \quad \text{kips (kN)} \tag{1.23}$$

Equation 1.23 above includes the modulus of elasticity of concrete, E_c [ksi (GPa)], distance between the VWSG and the centroid of the prestressing strands, d_{vwsg} [in. (mm)], moment due to member self-weight, M_o [kip-ft (N-m)], eccentricity of the centroid of the prestressing strands from the centroid of the member, e [in. (mm)], the area moment of inertia and cross-sectional area of the transformed section, I_t [in.^{4} (mm^4)] and A_t [in.^{2} (mm^2)].



(a) (b)

Figure 1.112: (a) Tensioned prestressing strands laced through channel girder formwork and (b) cut strands after prestress transfer.

Because VWSGs cannot capture the jacking force applied to prestressing tendons, instantaneous prestress losses due to elastic shortening cannot be calculated. However, data proved effective in monitoring prestress transfer and provided estimates of initial prestressing forces, P_i [kips (kN)]. Using data from all EM-5 VWSGs, prestressing forces were calculated beginning immediately prior to prestress transfer. For gauge U-3-EM-M-N shown in Figure 1.113, the immediate jump in prestress force corresponds to the decrease in frequency at prestress transfer previously noted in Figure 1.111.

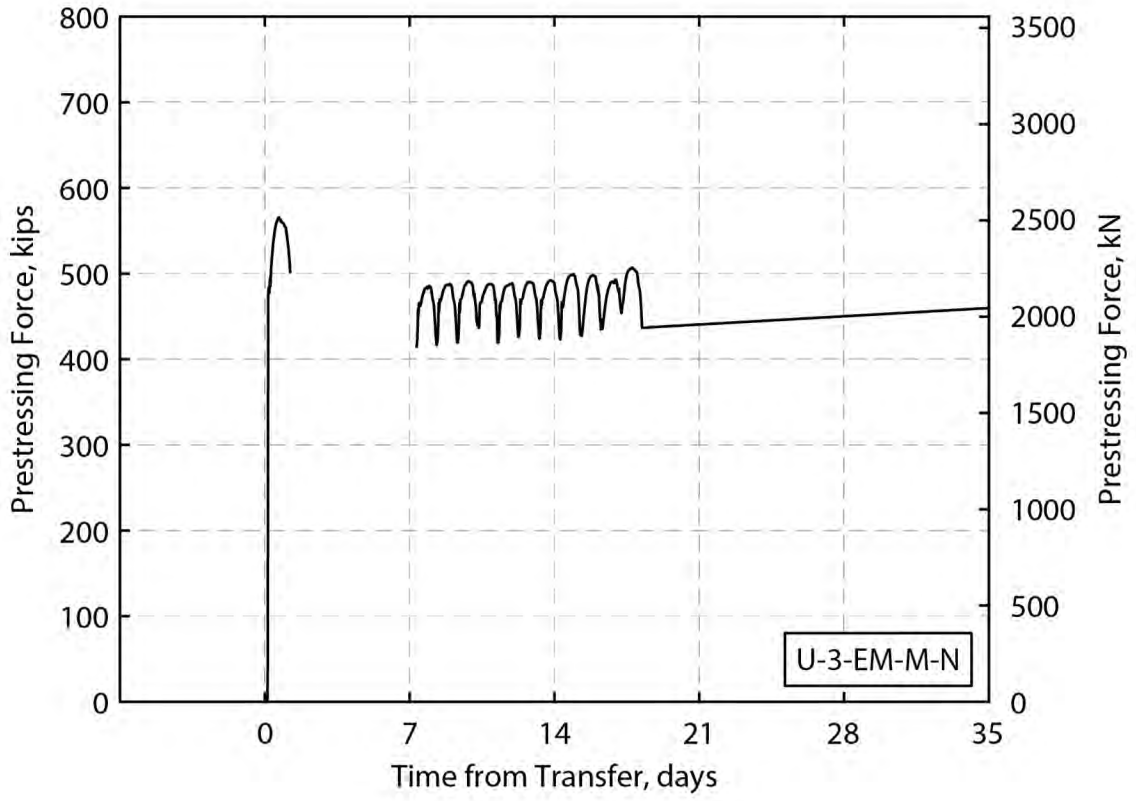


Figure 1.113: Prestressing force calculated for gauge U-3-EM-M-N beginning at transfer.

Table 1.105 summarizes the initial prestressing forces for each girder of NM Bridge No 9706 at both the north and south stem midspan locations. The average midspan initial prestress force, P_{VW}, is presented along with ratios to the design jacking force, P_j, and the AASHTO estimated initial prestressing force, P_i. Girder batch designations are also provided next to each girder name for comparison of batch specific data. Additionally, Table 1.106 compares the AASHTO estimated initial prestress forces are compared to the average initial prestress forces measured at midspan for interior and exterior type U and H channel girders. Data for all EM gauges including plotted frequencies, prestressing forces, and calculated initial prestressing forces are provided in the Batch Results of Section 1.8.7.

The following observations were made with respect to the prestressing forces calculated from VWSG measurements.

- Values for P_{VW} were generally within a reasonable range of the target jacking force of 527.3 kips (2346 kN). Though several values exceed P_j, it should be noted design of the channel girder permitted overstressing of the prestressing tendons to 46.8 kips (208 kN), or a total jacking force of 561.6 kips (2498 kN), to offset seating losses.
- Smaller calculated forces (and thus less strain) in the north stem of girders U-1 and H-1 and the south stem of girders U-8 and H-8 are indicative of the increased stem exterior stem of edge girder.
- For the UHPC span, the average initial prestressing force was 466.6 kips (2075 kN) with a standard deviation of 64.1 kips (285 kN). For the HPC span, this comparative value was 496.3 kips (2208kN) with a standard deviation of 89.0 kips (396 kN).
- Batch specific values typically compared well, increasing general confidence in the VWSG data.

Table 1.105: Summary of Initial Prestressing Forces Calculated from Midspan VWSG Data for the Channel Girders of NM Bridge No. 9706

Batch	Girder Name	Stem	P_{vwsg} kips (kN)	P_{VW} kips (kN)	$\frac{P_{VW}}{P_j}$	$\frac{P_{VW}}{P_i}$
(UB3)	U-1	N	348.5 (1550)	453.2 (2016)	0.86	0.89
		S	557.8 (2481)			
(HB1)	H-1	N	346.6 (1542)	449.7 (2000)	0.85	0.89
		S	552.7 (2459)			
(UB2)	U-2	N	--	543.7 (2419)	1.03	1.09
		S	543.7 (2419)			
(HB4)	H-2	N	480.9 (2139)	481.0 (2140)	0.91	0.97
		S	481.1 (2140)			
(UB4)	U-3	N	500.5 (2226)	518.3 (2305)	0.98	1.04
		S	536.1 (2385)			
(HB3)	H-3	N	555.5 (2471)	528.7 (2352)	1.00	1.06
		S	501.9 (2232)			
(UB3)	U-4	N	429.2 (1909)	435.4 (1937)	0.83	0.87
		S	441.5 (1964)			
(HB1)	H-4	N	585.7 (2605)	572.0 (2544)	1.08	1.15
		S	558.2 (2483)			
(UB2)	U-5	N	510.2 (2269)	520.3 (2315)	0.99	1.04
		S	530.5 (2360)			
(HB4)	H-5	N	527.2 (2345)	477.9 (2126)	0.91	0.96
		S	428.5 (1906)			
(UB1)	U-6	N	395.9 (1761)	395.2 (1758)	0.75	0.79
		S	394.4 (1755)			
(HB3)	H-6	N	509.8 (2268)	464.3 (2065)	0.88	0.93
		S	418.7 (1862)			
(UB1)	U-7	N	404.6 (1800)	428.4 (1906)	0.81	0.86
		S	452.3 (2012)			
(HB2)	H-7	N	553.8 (2463)	538.9 (2397)	1.02	1.08
		S	524.0 (2331)			
(UB4)	U-8	N	526.3 (2341)	476.5 (2120)	0.90	0.94
		S	426.6 (1898)			
(HB2)	H-8	N	640.4 (2848)	457.8 (2037)	0.87	0.91
		S	275.3 (1225)			

(--) no data

Table 1.106: Comparison of AASHTO Estimated Prestress Forces and Measured Prestress Forces from VWSG Data for NM Bridge No. 9706

Prestressing Force	U Section		H Section	
	Interior	Exterior	Interior	Exterior
	kips (kN)	kips (kN)	kips (kN)	kips (kN)
AASHTO, P_i	500.3 (2226)	507.3 (2256)	497.3 (2212)	505.4 (2248)
Measured, P_{VW}	467.2 (2078)	464.8 (2068)	510.5 (2271)	453.7 (2018)
Difference (%)	6.85	8.73	-2.61	10.77

- Measured P_{VW} for interior and exterior type girders fell below the AASHTO estimated values except for interior H section girders. However, percent differences for each section type were within approximately 10% of the AASHTO estimated initial prestressing forces.
- Measured P_{VW} for UHPC interior and exterior girders were comparable, whereas greater variability was exhibited for the two HPC section types. However, loss of power to the datalogger occurred during prestress transfer for batch UB1 (girders U-6 and U-7), and the calculation of initial prestressing forces was affected. When discounting the values for these two girders, the average prestressing force for the remaining interior girders increases to 498.8 kips (2219 MPa).
- It is important to consider that prestressing forces typically vary along the length of the structure due to several factors including but not limited to friction losses and variation of geometrical and/or mechanical properties of the cross-section at different points. The error for the measured forces is considered acceptable and provides a starting point for the purpose of long-term monitoring of prestress losses.
- It should be further noted that although some error in the data was expected (and variability between north and south stem locations), the magnitude of initial prestressing forces could be highly sensitive with respect to the selected value corresponding to maximum transfer, often exhibiting a significant increase or decrease in magnitude from just one measurement to the next.

The following are several factors that affected the collection of VWSG data, during and/or after fabrication, and the calculation of prestress forces for the individual girders.

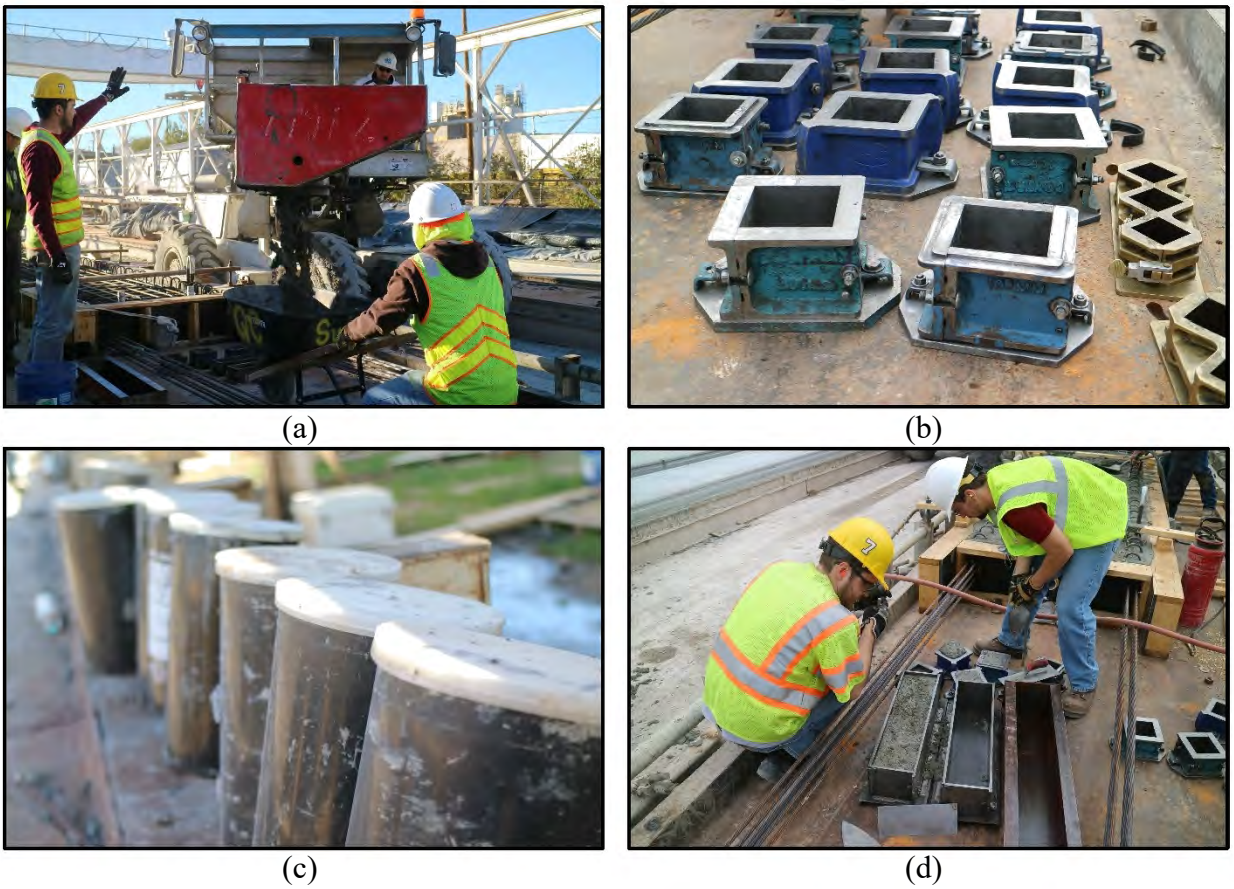
- Available peripherals limited the sensor capacity of the temporary dataloggers used for data acquisition during girder fabrication. Only 32 sensors could be monitored at one time, though a total of 56 EM-5 gauges were embedded in the channel girders.
- Physical distance and cable lengths from the girders to the datalogger, with respect to the placement of the girders in the precast yard after fabrication, limited the ability of some sensors to be monitored while awaiting transport to the bridge location.

- Other factors affecting data collection included power failures at the precast plant, accidental disconnection of sensors and/or datalogger power supply, and premature disconnection of sensors after prestress transfer (i.e., release of prestress strands) and/or failure to reconnect sensors to the datalogger in a timely manner after girder movement from casting bed to precast yard.

Finally, whereas VWSG measurements were effective in identifying the effects of prestress transfer, continued monitoring would theoretically facilitate the calculation of effective prestress under the assumption that subsequent decreases in frequency were directly related to time-dependent prestress losses. Because of the (often large) gaps in VWSG data, particularly those occurring immediately after prestress transfer, the accuracy of calculated effective prestress forces would be questionable and would require some form of validation. Additionally, unexplained "drift" in the data was identified beginning after connection of the sensors to the permanent data acquisition equipment. While this did not affect the ability to isolate discrete changes in strain during field testing of NM Bridge No 9706, the cause of the drift must be discovered before additional analyses of prestressing forces can be performed. Therefore, effective prestressing forces were not calculated for the girders.

1.8.6 Material Properties

Specimens were produced with each batch of prestressed girders for Bridge No. 9706 and cured alongside the girders during steam treatment to provide representative samples for testing material properties (Figure 1.114). Specimens included cubes and cylinders for evaluating compressive strength and unit weight, prisms for determining modulus of rupture. A minimum of two compressive strength samples for each batch were tested after curing to confirm adequate transfer strength for release of prestressing strands. After prestress transfer, remaining samples were placed in a wet room until they could be transported to the NMSU SSMTL to be tested at future dates. Results are provided in the following sections.



(a) (b) (c) (d)

Figure 1.114: (a) Auger delivery truck provides concrete to NMSU graduate researchers preparing representative (b) cube, (c) cylinder, and (d) prism specimens during channel girder fabrication for testing material properties.

1.8.6.1 Compressive Strength

Evaluation of compressive strength (f_c) was evaluated using 4.0 in. (100 mm) UHPC cube specimens as outlined in Section i.i. Table 1.107 and Table 1.108 provide a summary of the batch results for the UHPC and HPC spans, respectively. The top section of each table summarizes batch specific data. Columns 2–6 provide the daily average compressive strength for each batch at seven and 28 days after casting, and for the day of each load test conducted on Bridge No. 9706 (DT0, PT1, PT2, and PT3). Due to the limited number of remaining test specimens and because additional load testing of Bridge No. 9706 may continue for several years, only two samples were tested at the time of PT2 and PT3 to ensure that specimens will be available for testing at future dates. Compressive strength results are presented for each batch in Section 1.8.7.

Columns 7 and 8 provide additional batch specific data. Because 7-day strengths were typically lower than the target design strengths for both types of concrete, column 7 provides the average compressive strength for all samples tested at 28 days or older, and column 8 provides the standard deviation of strengths for each batch. Lastly, span specific data in the bottom two rows of each table include daily average compressive strength and standard deviation based on all samples tested for all batches (i.e. the entire span).

As detailed in Section 1.8.5.1, several challenges affected the curing of UHPC test specimens. Batch average compressive strengths at seven days typically fell below the 21.0 ksi (145 MPa) target strength, but still well above the design transfer strength. It was also assumed that the small specimen sizes were more greatly affected by the adverse conditions. Design strength was met by all UHPC batches at 28 days after casting, and strengths continued to increase over time. HPC specimens achieved design transfer strength for all batches at seven days and exceeded the 9.5 ksi (66.0 MPa) design strength at 28 days.

Table 1.107: Summary of Compressive Strength Results for the UHPC Span of NM Bridge No. 9706

	Batch	$f_{c,avg}$, ksi (MPa)						Average*	Std. Dev.
	Name	7-day†	28-day	DT0	PT1	PT2	PT3	ksi (MPa)	ksi (MPa)
Batch Data	UB1	18.0 (124)	21.0 (145)	2.35 (16.2)	19.0 (131)	22.0 (152)	22.9 (158)	21.0 (145)	2.35 (16.2)
	UB2	17.5 (121)	22.1 (152)	2.28 (15.7)	22.7 (156)			22.1 (152)	2.28 (15.7)
	UB3	20.1 (139)	21.9 (151)	1.88 (13.0)	21.9 (151)			22.1 (153)	1.93 (13.3)
	UB4	19.6 (135)	21.1 (146)	1.44 (9.93)	20.2 (139)			21.2 (146)	1.43 (9.86)
Span Data	Average	18.8 (130)	20.7 (143)	22.8 (157)	20.9 (144)	22.0 (152)	22.9 (158)		
	Std. Dev.	1.52 (10.5)	1.12 (7.73)	1.23 (8.50)	1.86 (12.8)	0.434 (2.99)	1.308 (9.02)		

(DT0) diagnostic test; (PT1) proof test 1; (PT2) proof test 2; (PT3) proof load test 3
(†) specimen ages varied between 7–10 days; (*) batch average for specimens of minimum 28 days or older
NOTE: Results based on 4.0 in. (100 mm) cube specimens.

Table 1.108: Summary of Compressive Strength Results for the HPC Span of NM Bridge No. 9706

	Batch	$f_{c,avg}$, ksi (MPa)						Average*	Std. Dev.
	Name	7-day†	28-day	DT0	PT1	PT2	PT3	ksi (MPa)	ksi (MPa)
Batch Data	UB1	7.06 (48.7)	12.6 (87.0)	9.23 (63.6)	8.80 (60.7)	10.7 (73.7)	9.6 (66.0)	10.1 (69.8)	1.89 (13.0)
	UB2	7.21 (49.7)	11.5 (79.3)	10.1 (69.9)	10.1 (69.6)			10.5 (72.6)	1.31 (9.00)
	UB3	7.06 (48.7)	9.90 (68.3)	8.34 (57.5)	7.53 (51.9)			8.6 (59.2)	1.15 (7.94)
	UB4	7.39 (50.9)	13.3 (91.7)	13.7 (94.2)	12.2 (83.9)			13.0 (89.9)	2.32 (16.0)
Span Data	Average	7.18 (49.5)	11.8 (81.6)	10.3 (71.3)	9.65 (66.5)	10.7 (73.7)	9.6 (66.0)		
	Std. Dev.	0.158 (1.09)	1.39 (9.59)	2.23 (15.3)	1.93 (13.3)	0.547 (3.77)	0.180 (1.24)		

(DT0) diagnostic test; (PT1) proof test 1; (PT2) proof test 2; (PT3) proof load test 3
(†) specimen ages varied between 7–10 days; (*) batch average for specimens of minimum 28 days or older
NOTE: Results based on 4.0 in. (100 mm) cube specimens.

1.8.6.2 Unit Weight

The 4.0 in. (100 mm) cube specimens produced for evaluation of compressive strength were weighed before testing to determine the unit weight (w_c) of both types of concrete used for the prestressed girders of NM Bridge No. 9706. It is noted that the nominal 4.0 in. dimension of the cubes, expressed herein for simplicity, corresponds to 101.6 mm. The cube specimen molds were designed for testing according to British Standards using the nominal dimension of 100 mm, or 3.937 in. So as not to underestimate the unit weight of the specimens, the value 3.937 in. (100 mm) was used for the calculation of nominal specimen volume.
Unit weight results are presented for each batch in Section 1.8.7.

Unit weight results for the UHPC and HPC spans are summarized in Table 1.109 and Table 1.110. The top section of each table summarizes batch specific data including daily average unit weight and overall average unit weight and standard deviation. Unit weight data was collected for the day of each load test conducted on Bridge No. 9706 (DT0, PT1, PT2, and PT3). Testing at seven days was conducted by NMDOT or Coreslab® Structures (Albuquerque), Inc., and no data was reported for unit weight. All remaining specimens were tested at the NMSU SSMTL, though no data was collected at 28 days. Due to the limited number of remaining test specimens and because additional load testing of Bridge No. 9706 will continue for several years, only two samples were tested at the time of Proof Test 2 (PT2) to ensure that specimens will be available for testing at future dates. The last two columns (column 7 and 8) provide batch average unit weight and standard deviation, and the bottom two rows of each table correspond to span specific data. The daily average unit weight and standard deviation presented in these rows is based on all samples tested for all batches (i.e., the entire span).

The typical average unit weight for UHPC batches was approximately 150 lb/ft^3 (2403 kg/m^3). For HPC batches these values were generally lower, closer to 140 lb/ft^3 (2243 kg/m^3). However, specimens measured for unit weight do not account for mild steel reinforcement present in all girders.

Table 1.109: Summary of Unit Weight Results for the UHPC Span of NM Bridge No. 9706

	Batch	$w_{c,avg}$, lb/ft^3 (kg/m^3)						Average	Std. Dev.
	Name	7-day†	28-day	DT0	PT1	PT2	PT3	lb/ft^3 (kg/m^3)	lb/ft^3 (kg/m^3)
Batch Data	UB1	--	151.6 (2429)	151.7 (2429)	151.6 (2429)	151.4 (2426)	148.8 (2384)	151.6 (2429)	1.61 (25.7)
	UB2	--	--	150.1 (2405)	152.4 (2441)			151.3 (2423)	2.07 (33.2)
	UB3	--	--	148.3 (2375)	149.2 (2390)			150.2 (2407)	2.36 (37.9)
	UB4	--	--	139.5 (2234)	146.6 (2349)			148.1 (2373)	1.95 (31.29)
Span Data	Average	--	151.6 (2429)	147.4 (2361)	150.0 (2402)	151.4 (2426)	148.8 (2384)		
	Std. Dev.	--	0.601 (9.62)	1.99 (31.86)	3.20 (51.2)	0.160 (2.57)	2.042 (32.7)		

(DT0) diagnostic load test; (PT1) proof load test 1; (PT2) proof load test 2; (PT3) proof load test 3
(†) specimen ages varied between 7–10 days
NOTE: Results based on 4.0 in. (100 mm) cube specimens.

Table 1.110: Summary of Unit Weight Results for the HPC Span of NM Bridge No. 9706

	Batch	$w_{c,avg}$, lb/ft3 (kg/m3)						Average	Std. Dev.
	Name	7-day†	28-day	DT0	PT1	PT2	PT3	lb/ft3 (kg/m3)	lb/ft3 (kg/m3)
Batch Data	UB1	--	--	139.5 (2234)	140.9 (2257)	10.7 (73.7)	139.4 (2233)	140.3 (2248)	2.34 (37.5)
	UB2	--	--	138.0 (2211)	134.5 (2155)			137.3 (2199)	2.66 (42.6)
	UB3	--	--	135.3 (2168)	133.2 (2134)			134.3 (2151)	2.38 (38.2)
	UB4	--	--	148.6 (2380)	144.2 (2309)			146.4 (2344)	4.33 (69.36)
Span Data	Average	--	--	140.3 (2248)	138.2 (2214)	140.4 (2249)	139.4 (2233)		
	Std. Dev.	--	--	5.62 (89.96)	5.53 (88.5)	1.32 (21.2)	3.12 (50.0)		

(DT0) diagnostic load test; (PT1) proof load test 1; (PT2) proof load test 2; (PT3) proof load test
(†) specimen ages varied between 7–10 days
NOTE: Results based on 4.0 in. (100 mm) cube specimens.

1.8.6.3 Modulus of Rupture

Modulus of rupture strength, defined herein as the flexural stress corresponding to first cracking, was evaluated for these investigations using 16.0 x 3.0 x 4.0 in. (406 x 76 x 102 mm) beam specimens as outlined in Section i.iii. Representative samples were cast with each batch of prestressed girders for NM Bridge No. 9706 for determining modulus of rupture strength (f_r) and were cured alongside the girders, remaining on the casting bed during steam treatment. Unfortunately, several UHPC specimens were lost due to several factors including lack of available forms, damage during curing or transportation, and freezing. No specimens from batches UB1 and UB4 were available for testing.

The results of modulus of rupture testing are provided in Table 1.111 and Table 1.112 for UHPC and HPC, respectively. All specimens were tested at the NMSU SSMTL on Friday, April 7, 2017, approximately one week after the Diagnostic Test was conducted on Bridge No. 9706. The top section of each table summarizes batch specific data including specimen strengths and batch average strength and standard deviation. The last two rows provide overall average modulus of rupture strength and standard deviation based on all samples tested for the span.

Modulus of rupture strength for all UHPC specimens provided an average value of 1054 psi (7.27 MPa). In comparison, HPC modulus of rupture was approximately have this value, with an average strength of 514 psi (3.54 MPa).

Table 1.111: Summary of Modulus of Rupture Results for UHPC Span of NM Bridge No. 9706

	Batch Name	Specimen No.	f_r psi (MPa)	Average psi (MPa)	Std. Dev. psi (MPa)
Batch Data	UB2	1	1100 (7.58)		
		2	1113 (7.67)		
		3	875 (6.03)	1029 (7.10)	133.7 (0.922)
	UB3	4	1100 (7.58)		
		5	1088 (7.50)		
		6	1050 (7.24)	1079 (7.44)	26.0 (0.179)
Span Data		Average	1054 (7.27)		
		Std. Dev.	82.5 (0.569)		

NOTE: Results based on 16.0 x 3.0 x 4.0 in. (406 x 76 x 102 mm) beam specimens.

Table 1.112: Summary of Modulus of Rupture Results for HPC Span of NM Bridge No. 9706

	Batch Name	Specimen No.	f_r psi (MPa)	Average psi (MPa)	Std. Dev. psi (MPa)
Batch Data	HB1	1	563 (3.88)		
		2	438 (3.02)	500 (3.45)	88.4 (0.609)
	HB2	3	525 (3.62)		
		4	563 (3.88)	544 (3.75)	26.5 (0.183)
	HB3	5	525 (3.62)		
		6	438 (3.02)	481 (3.32)	61.9 (0.427)
	HB4	7	500 (3.45)		
		8	563 (3.88)	531 (3.66)	44.2 (0.305)
Span Data		Average	514 (3.54)		
		Std. Dev.	52.4 (0.361)		

NOTE: Results based on 16.0 x 3.0 x 4.0 in. (406 x 76 x 102 mm) beam specimens.

1.8.7 Batch Results

The following sections provide additional data and information for each batch of girders produced for Bridge No. 9706 including curing temperatures, measured VWSG frequency and prestressing forces, and measured material properties. The dates of casting and prestress transfer (see Table 1.102 of Section 0) are reiterated for each batch, and some additional commentary is provided for clarification when necessary.

Complete datasets of compressive strength and unit weight include the superscript characters (^{DT0}), (^{PT1}), (^{PT2}), and (^{PT3}) to denote the specimen age at the time of the Diagnostic Test (March, 2017), Proof Test 1 (January, 2018), Proof Test 2 (February, 2019), and Proof Test 3 (February, 2020). Specimen results reported by Coreslab® Structures (Albuquerque), Inc. are denoted by an asterisk, (*). All other specimens were tested at the NMSU SSMTL. It should be noted that due to the limited number of remaining test specimens and because additional load testing of Bridge No. 9706 will continue for several years, only two samples were tested at the time of PT2 and PT3 to ensure that specimens will be available for testing at future dates.



(a) (b)

Figure 1.115: Exterior girder H-8 being crane lifted (a) from casting bed after precast fabrication and (b) placed into position during construction of NM Bridge No. 9706.

1.8.7.1.1 UB1

Batch UB1 consisted of girders U-6 and U-7 and was cast on Monday, August 22, 2016. Prestressing strands were cut on Monday, August 29, 2016, seven days after casting.

Table 1.113: Compressive Strength Results for Batch UB1

Age	Specimen		f_c	Average	Std. Dev.
days	No.	Type	ksi (MPa)	ksi (MPa)	ksi (MPa)
7	1*	cube	16.7 (115.4)		
	2*	cube	20.2 (139.4)		
	3	cube	16.3 (112.2)		
	4	cube	19.5 (134.2)		
	5	cube	17.4 (119.8)	18.0 (124.2)	1.73 (12.0)
28	6	cube	20.6 (142.0)		
	7	cube	22.7 (156.5)	21.7 (149.3)	1.48 (10.2)
232^{DT0}	8	cube	22.2 (153.0)		
	9	cube	22.4 (154.3)	22.3 (153.6)	0.133 (0.914)
528^{PT1}	10	cube	17.4 (119.9)		
	11	cube	20.5 (141.6)	19.0 (130.8)	2.22 (15.3)
Average			19.6 (135.3)		2.35 (16.2)

(*) specimen prepared by Coreslab® Structures (Albuquerque), Inc.
(--) no data/not applicable

Table 1.114: Unit Weight Results for Batch UB1

Age	Specimen		Weight	w_c	Average	Std. Dev
days	No.	Type	lb (kg)	lb/ft^3 (kg/m^3)	lb/ft^3 (kg/m^3)	lb/ft^3 (kg/m^3)
7	1*	cube	--	--		
	2*	cube	--	--		
	3	cube	--	--		
	4	cube	--	--		
	5	cube	--	--	--	--
28	6	cube	5.34 (2.42)	151.2 (2422)		
	7	cube	5.37 (2.44)	152.1 (2436)	151.6 (2429)	0.601 (9.62)
232^{DT0}	8	cube	5.30 (2.40)	150.1 (2405)		
	9	cube	5.41 (2.45)	153.2 (2454)	151.7 (2429)	2.16 (34.6)
528^{PT1}	10	cube	5.28 (2.40)	149.6 (2397)		
	11	cube	5.42 (2.46)	153.6 (2460)	151.6 (2429)	2.80 (44.9)
Average			5.36 (2.43)	151.6 (2429)		1.61 (25.7)

(*) specimen prepared by Coreslab® Structures (Albuquerque), Inc.
(--) no data/not applicable

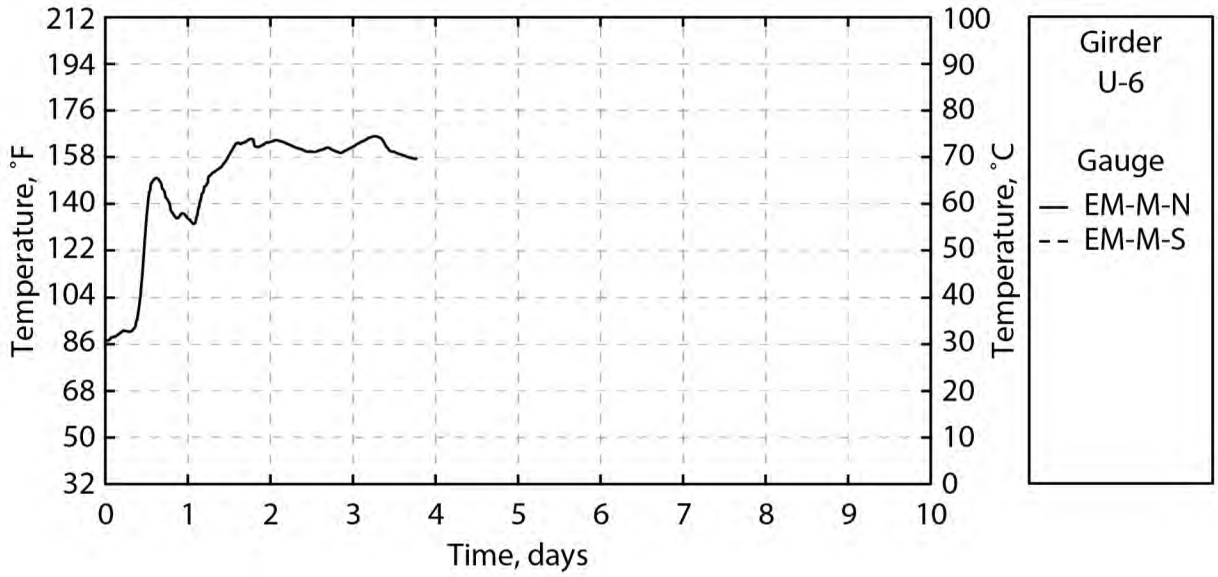


Figure 1.116: Concrete core temperatures during curing for U-6.

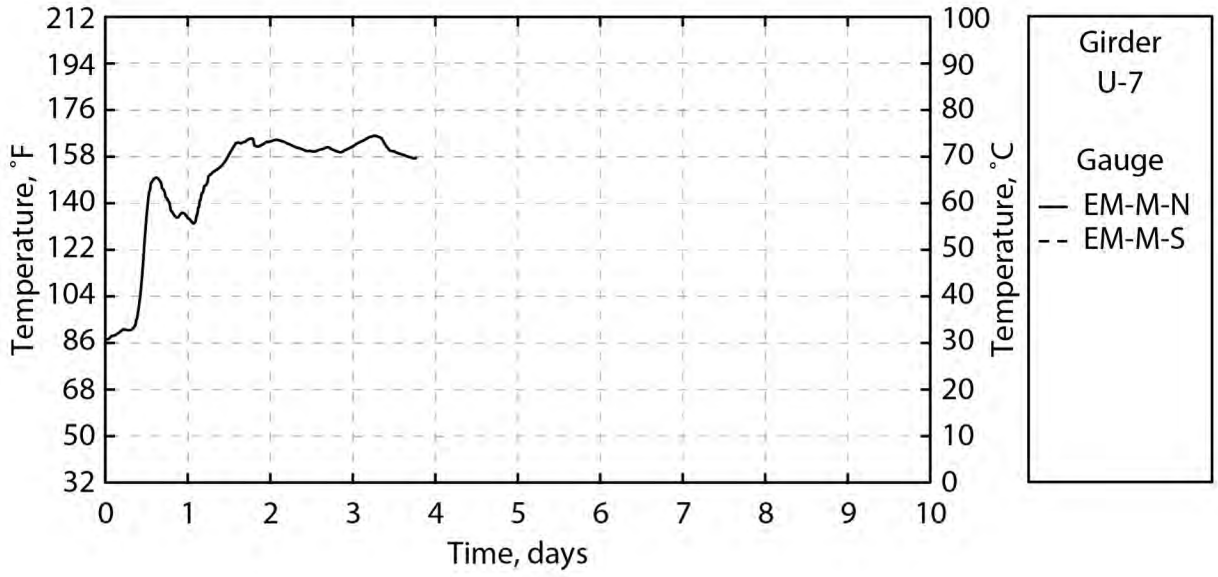


Figure 1.117: Concrete core temperatures during curing for U-7.

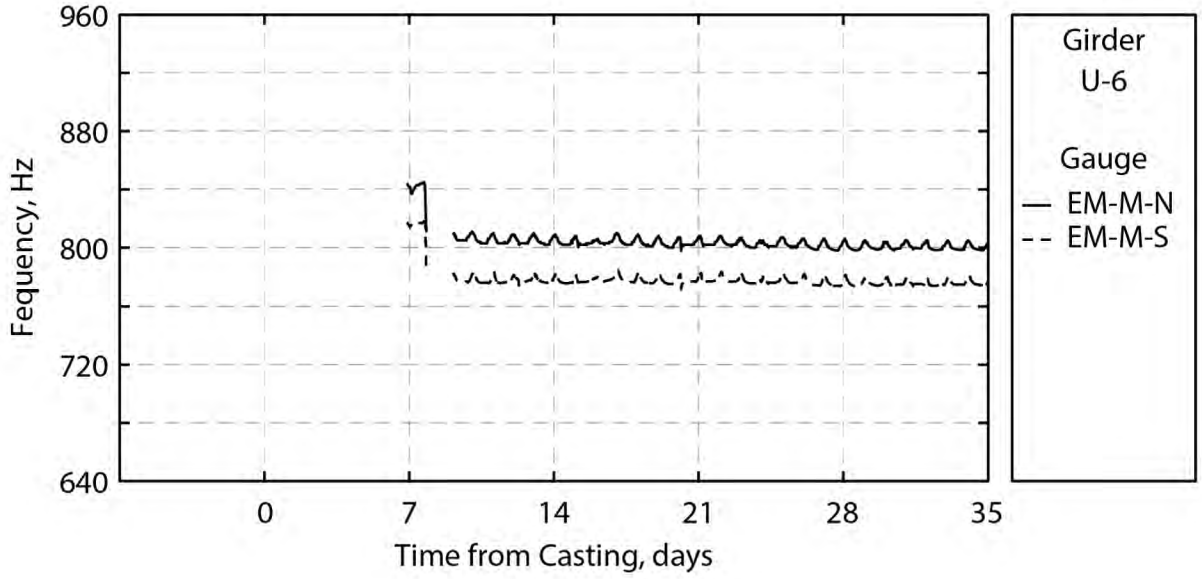


Figure 1.118: VWSG frequency data for U-6 beginning at the time of girder casting.

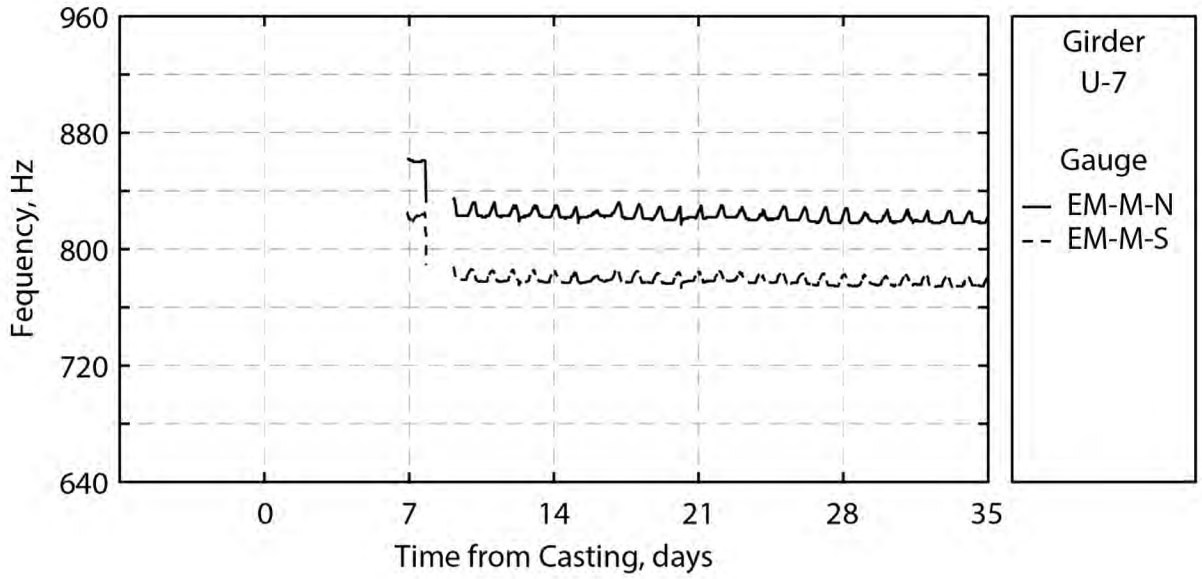


Figure 1.119: VWSG frequency data for U-7 beginning at the time of girder casting.

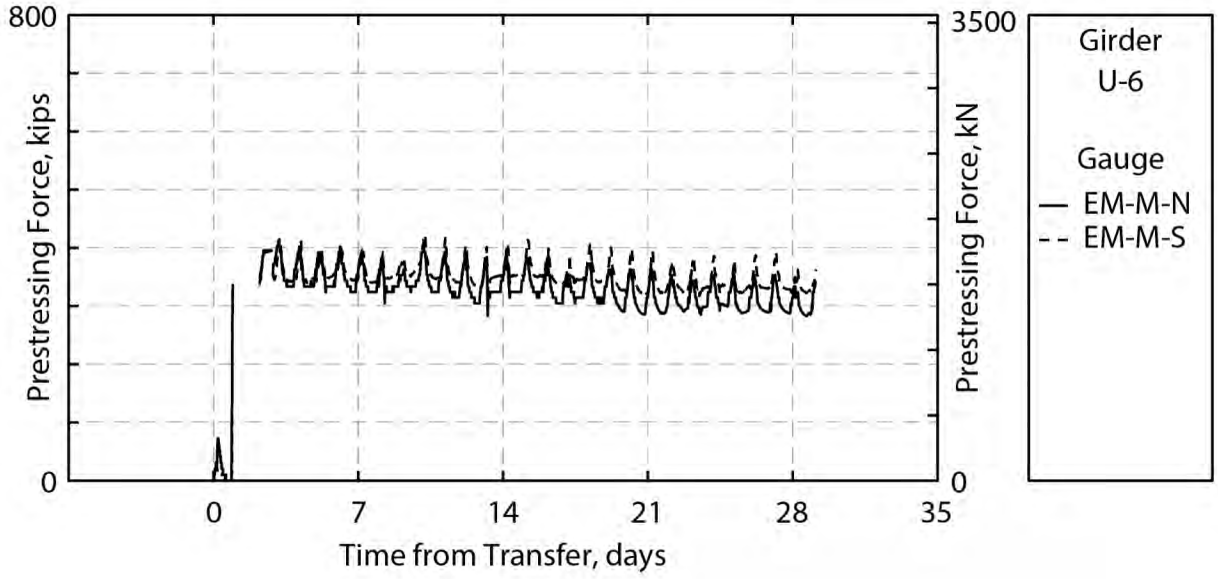


Figure 1.120: VWSG prestressing force for U-6 beginning at transfer.

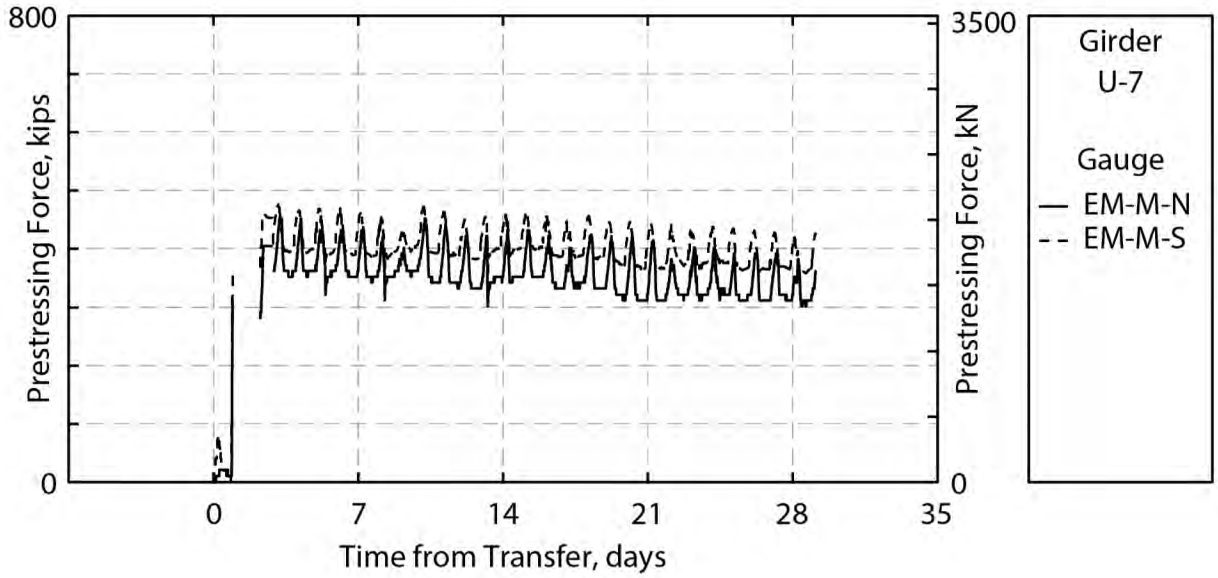


Figure 1.121: VWSG prestressing force for U-7 beginning at transfer.

Table 1.115: Initial Prestressing Forces Calculated for Batch UB1

Gauge Name	P_i kips (kN)
U-6-EM-M-N	395.9 (1761)
U-6-EM-M-S	394.4 (1755)
U-7-EM-M-N	404.6 (1800)
U-7-EM-M-S	452.3 (2012)

(--) no data

1.8.7.1.2 UB2

Batch UB2 consisted of girders U-2 and U-5 and was cast on Thursday, September 22, 2016. Prestressing strands were cut on Thursday, September 29, 2016, seven days after casting.

Table 1.116: Compressive Strength Results for Batch UB2

Age	Specimen		f_c	Average	Std. Dev.
days	No.	Type	ksi (MPa)	ksi (MPa)	ksi (MPa)
7	1*	cube	17.6 (121)		
	2*	cube	17.4 (120)	17.5 (121)	0.141 (0.975)
28	3	cube	20.9 (144)		
	4	cube	20.4 (141)	20.7 (142)	0.354 (2.44)
201^{DT0}	5	cube	23.7 (163)		
	6	cube	22.0 (152)	22.8 (158)	1.19 (8.23)
497^{PT1}	7	cube	23.5 (162)		
	8	cube	21.9 (151)	22.7 (156)	1.15 (7.93)
893^{PT2}	9	cube	22.3 (154)	22.3 (154)	--
Average			21.1 (145)		2.28 (15.7)

(*) specimen prepared by Coreslab® Structures (Albuquerque), Inc.
(--) no data/not applicable

Table 1.117: Unit Weight Results for Batch UB2

Age	Specimen		Weight	w_c	Average	Std. Dev
days	No.	Type	lb (kg)	lb/ft^3 (kg/m^3)	lb/ft^3 (kg/m^3)	lb/ft^3 (kg/m^3)
7	1*	cube	--	--		
	2*	cube	--	--	--	--
28	3	cube	--	--		
	4	cube	--	--	--	--
201^{DT0}	5	cube	5.25 (2.38)	148.8 (2383)		
	6	cube	5.35 (2.43)	151.5 (2427)	150.1 (2405)	1.92 (30.8)
497^{PT1}	7	cube	5.45 (2.47)	154.4 (2474)		
	8	cube	5.31 (2.41)	150.4 (2409)	152.4 (2441)	2.88 (46.2)
893^{PT2}	9	cube	5.34 (2.42)	151.3 (2424)	151.3 (2424)	--
Average			5.34 (2.42)	151.3 (2423)		2.07 (33.2)

(*) specimen prepared by Coreslab® Structures (Albuquerque), Inc.
(--) no data/not applicable

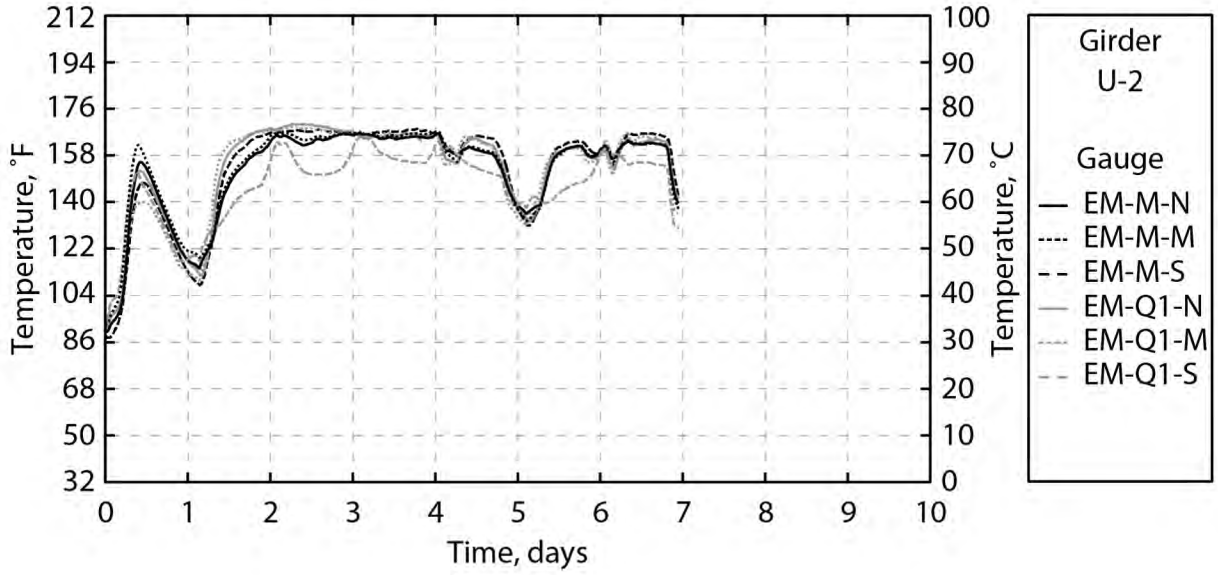


Figure 1.122: Concrete core temperatures during curing for U-2.

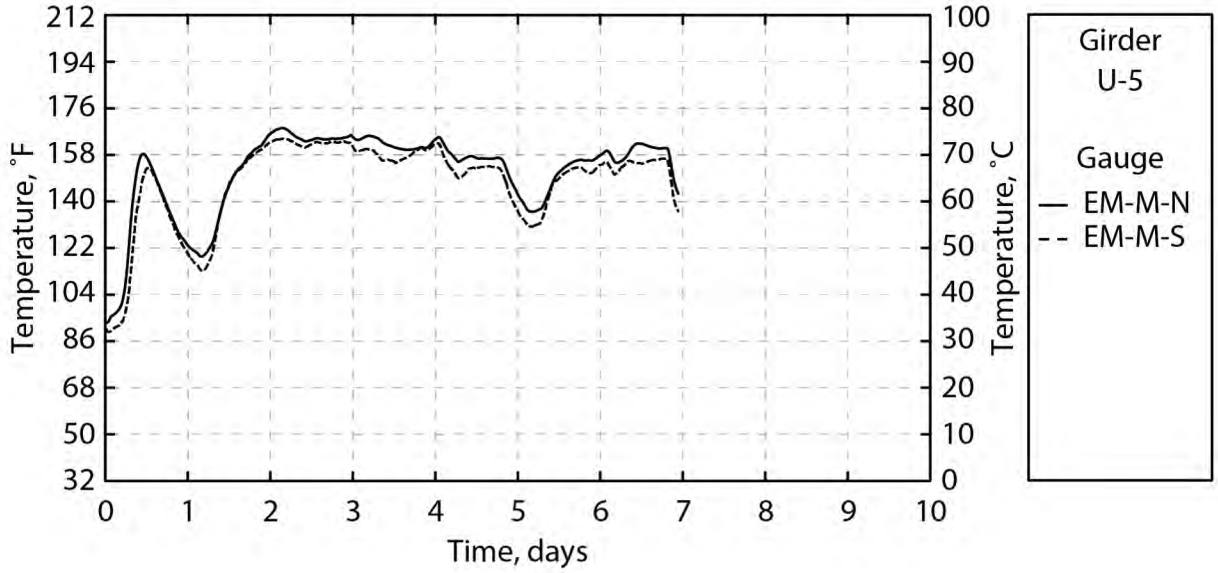


Figure 1.123: Concrete core temperatures during curing for U-5.

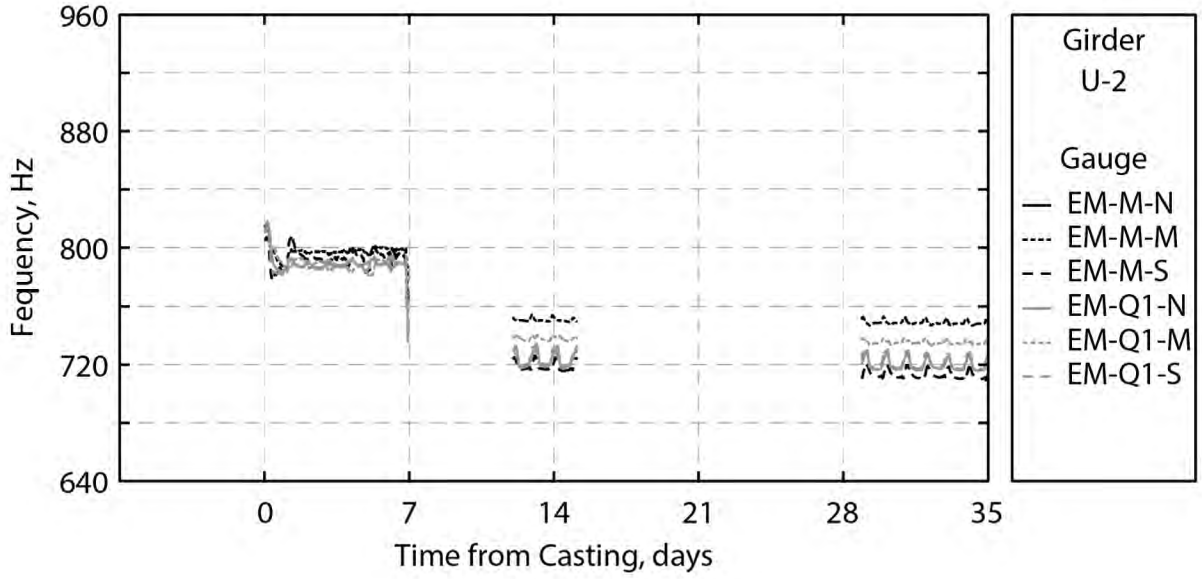


Figure 1.124: VWSG frequency data for U-2 beginning at the time of girder casting.

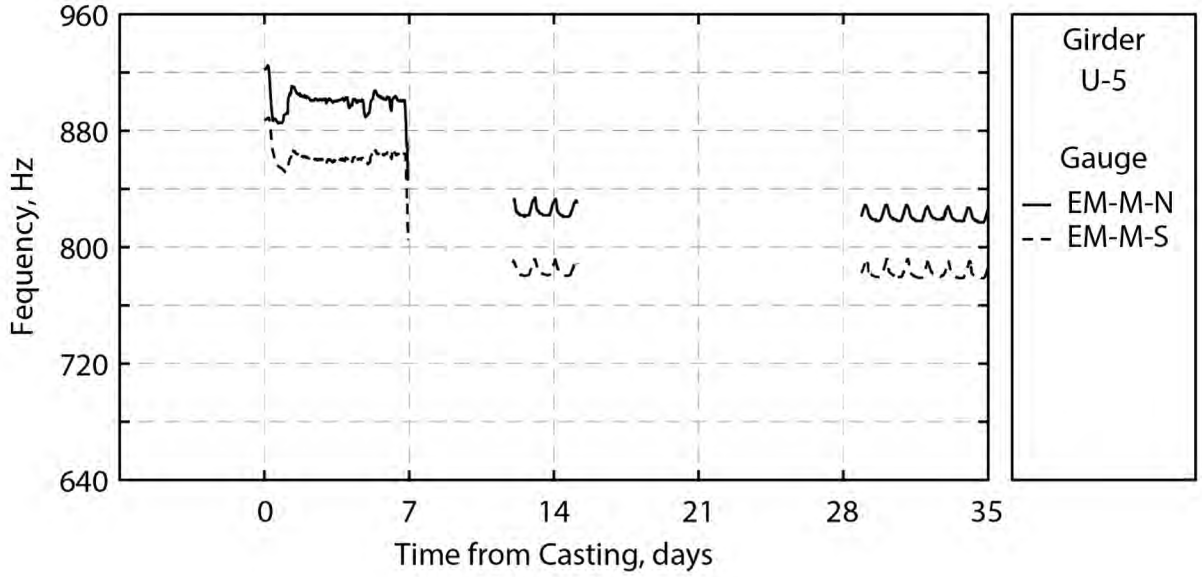


Figure 1.125: VWSG frequency data for U-5 beginning at the time of girder casting.

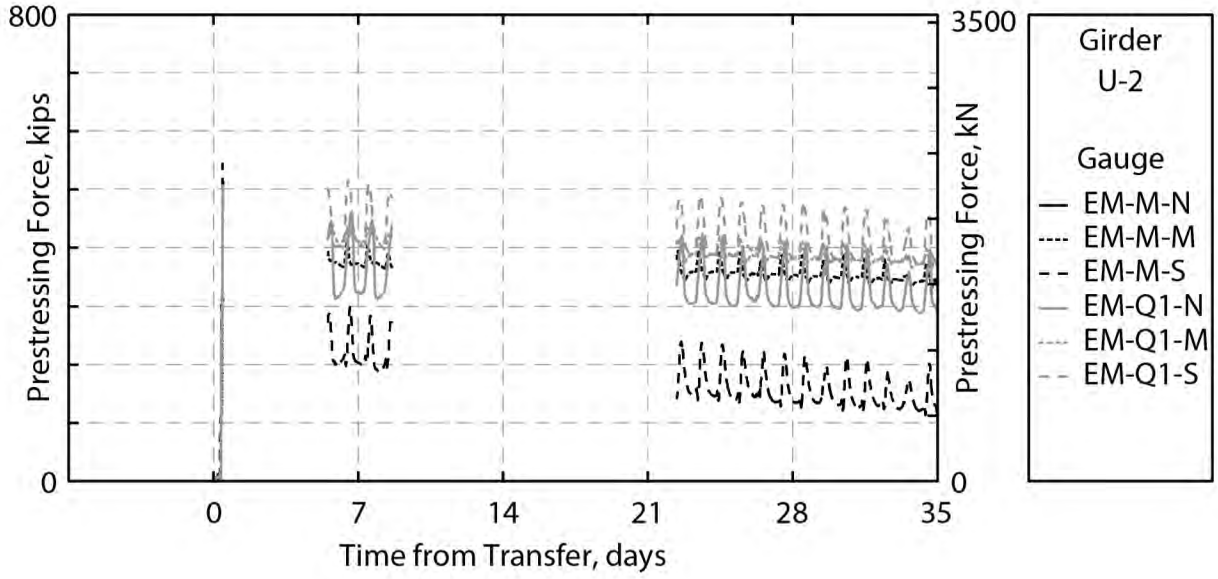


Figure 1.126: VWSG prestressing force for U-2 beginning at transfer.

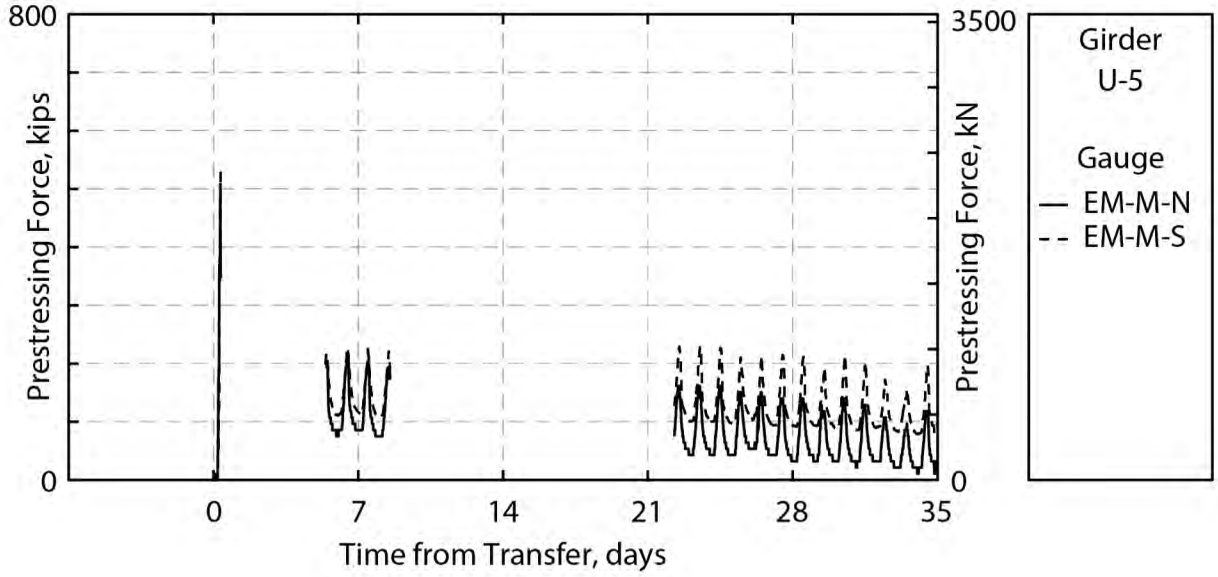


Figure 1.127: VWSG prestressing force for U-5 beginning at transfer.

Table 1.118: Initial Prestressing Forces Calculated for Batch UB2

Gauge Name	P_i kips (kN)
U-2-EM-Q1-N	508.2 (2260)
U-2-EM-Q1-M	463.9 (2063)
U-2-EM-Q1-S	539.8 (2401)
U-2-EM-M-N	--
U-2-EM-M-M	437.4 (1946)
U-2-EM-M-S	543.7 (2419)
U-5-EM-M-N	510.2 (2269)
U-5-EM-M-S	530.5 (2360)

(--) no data

1.8.7.1.3 UB3

Batch UB3 consisted of girders U-1 and U-4 and was cast on Friday, October 7, 2016. Prestressing strands were cut on Saturday, October 15, 2016, eight days after casting.

Table 1.119: Compressive Strength Results for Batch UB3

Age	Specimen		f_c	Average	Std. Dev.
days	No.	Type	ksi (MPa)	ksi (MPa)	ksi (MPa)
7	1	cube	20.3 (140)		
	2	cube	19.9 (137)	20.1 (139)	0.269 (1.85)
28	3	cube	18.9 (130)		
	4	cube	20.6 (142)	19.7 (136)	1.22 (8.39)
186^{DT0}	5	cube	23.8 (164)		
	6	cube	24.1 (166)	24.0 (165)	0.221 (1.52)
482^{PT1}	7	cube	21.3 (147)		
	8	cube	22.5 (155)	21.9 (151)	0.861 (5.93)
1242^{PT3}	9	cube	23.8 (164)	23.8 (164)	--
Average			21.7 (150)		1.93 (13.3)

(--) no data/not applicable

Table 1.120: Unit Weight Results for Batch UB3

Age	Specimen		Weight	w_c	Average	Std. Dev
days	No.	Type	lb (kg)	lb/ft^3 (kg/m^3)	lb/ft^3 (kg/m^3)	lb/ft^3 (kg/m^3)
7	1	cube	--	--		
	2	cube	--	--	--	--
28	3	cube	--	--		
	4	cube	--	--	--	--
186^{DT0}	5	cube	5.29 (2.40)	149.9 (2401)		
	6	cube	5.39 (2.44)	152.6 (2444)	151.2 (2423)	1.88 (30.1)
482^{PT1}	7	cube	5.17 (2.35)	146.5 (2347)		
	8	cube	5.37 (2.43)	151.9 (2434)	149.2 (2390)	3.84 (61.6)
1242^{PT3}	9	cube	5.31 (2.41)	150.2 (2407)	150.2 (2407)	--
Average			5.31 (2.41)	150.2 (2407)		2.36 (37.9)

(--) no data/not applicable

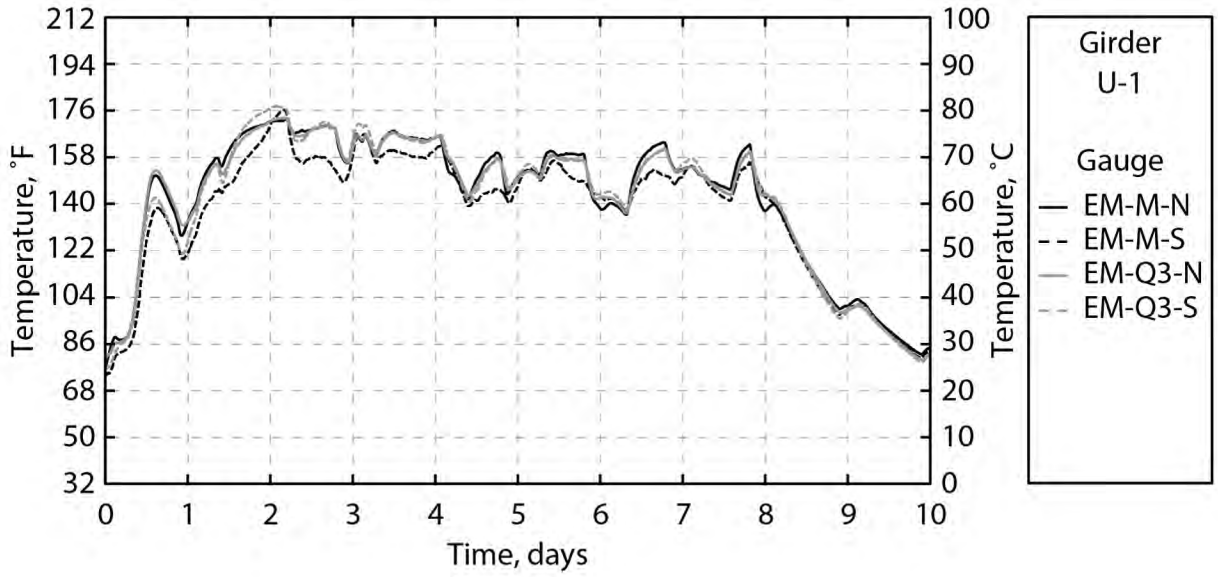


Figure 1.128: Concrete core temperatures during curing for U-1.

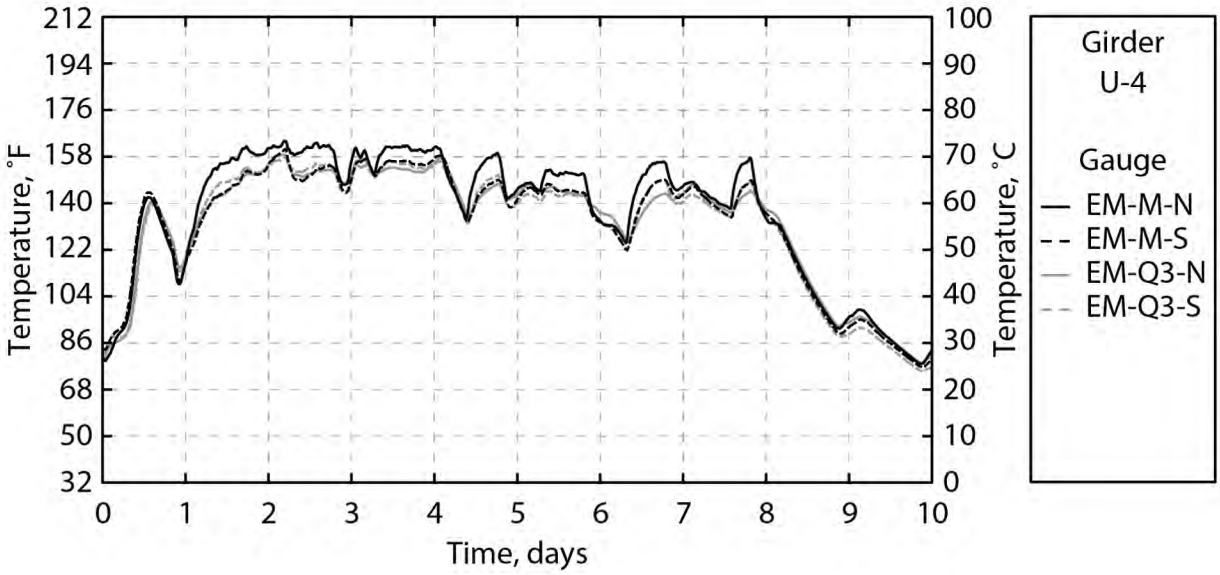


Figure 1.129: Concrete core temperatures during curing for U-4.

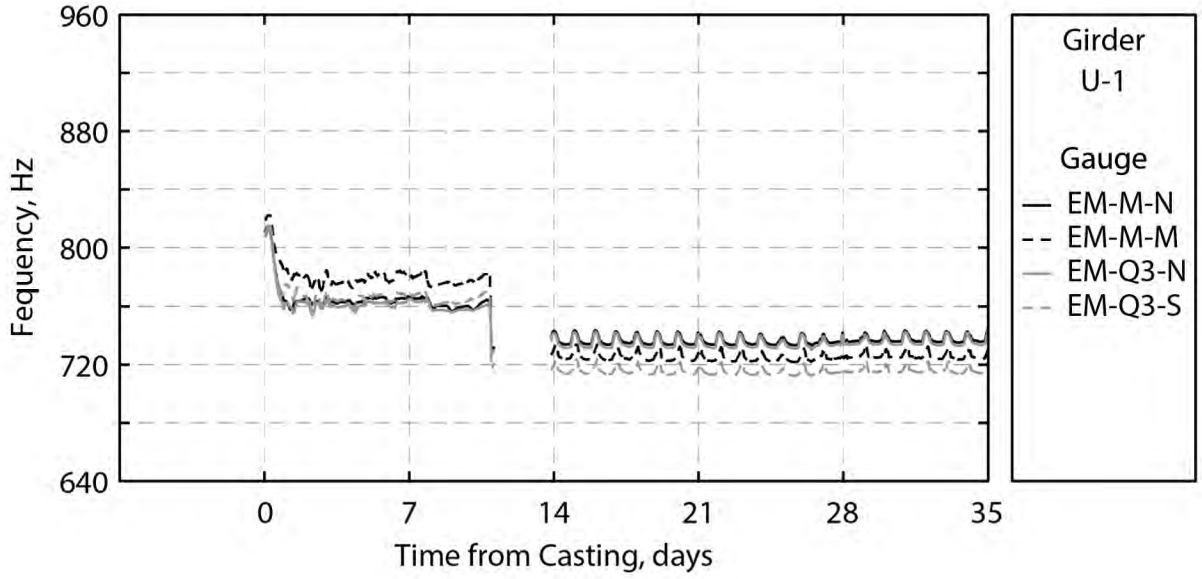


Figure 1.130: VWSG frequency data for U-1 beginning at the time of girder casting.

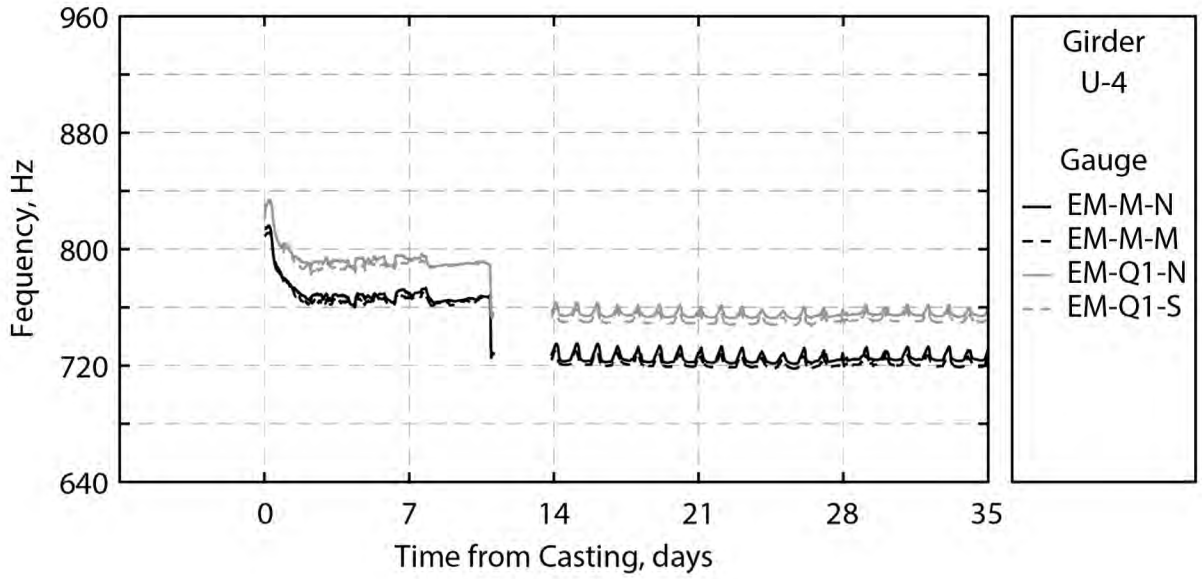


Figure 1.131: VWSG frequency data for U-4 beginning at the time of girder casting.

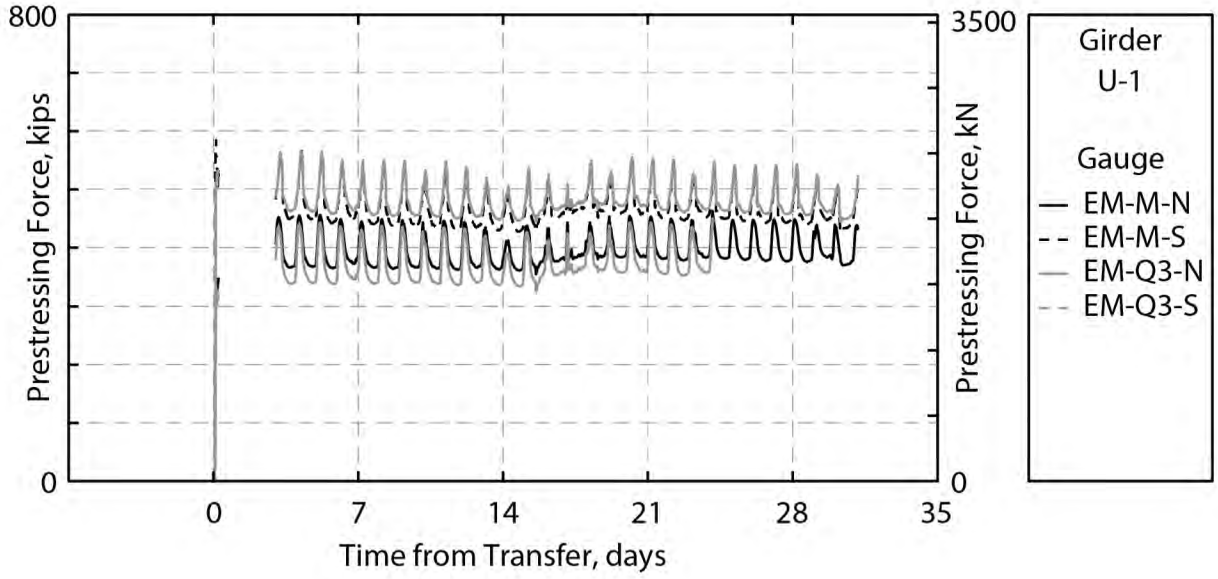


Figure 1.132: VWSG prestressing force for U-1 beginning at transfer.

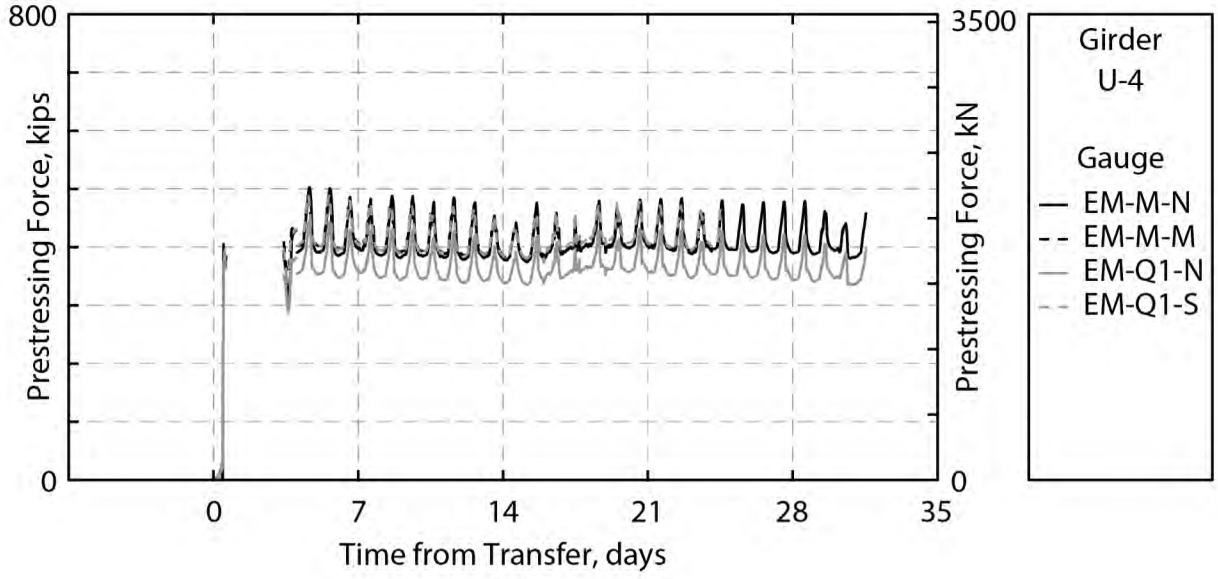


Figure 1.133: VWSG prestressing force for U-4 beginning at transfer.

Table 1.121: Initial Prestressing Forces Calculated for Batch UB3

Gauge Name	P_i kips (kN)
U-1-EM-M-N	348.5 (1550)
U-1-EM-M-S	557.8 (2481)
U-1-EM-Q3-N	328.2 (1460)
U-1-EM-Q3-S	528.1 (2349)
U-4-EM-Q1-N	381.8 (1699)
U-4-EM-Q1-S	430.2 (1914)
U-4-EM-M-N	429.2 (1909)
U-4-EM-M-S	441.5 (1964)

(--) no data

1.8.7.1.4 UB4

Batch UB4 consisted of girders U-3 and U-8 and was cast on Saturday, October 22, 2016. Because steam treatment was interrupted by a power failure (see Figure 1.134 and Figure 1.135), release of prestressing strands was delayed to provide adequate curing time until Monday, October 31, 2016, nine days after casting.

Table 1.122: Compressive Strength Results for Batch UB4

Age	Specimen		f_c	Average	Std. Dev.
days	No.	Type	ksi (MPa)	ksi (MPa)	ksi (MPa)
7	1*	cube	18.7 (129)		
	2*	cube	18.8 (130)	18.8 (129)	0.071 (0.488)
11	3	cube	20.6 (142)		
	4	cube	20.4 (141)	20.5 (141)	0.141 (0.98)
28	5	cube	19.9 (137)		
	6	cube	21.4 (148)	20.7 (142)	1.05 (7.26)
171^{DT0}	7	cube	20.6 (142)		
	8	cube	23.9 (165)	22.3 (153)	2.30 (15.8)
467^{PT1}	9	cube	19.7 (136)		
	10	cube	20.6 (142)	20.2 (139)	0.619 (4.27)
863^{PT2}	11	cube	21.7 (150)	21.7 (150)	--
1227^{PT3}	12	cube	22.0 (151)	22.0 (151)	--
Average			20.7 (143)		1.43 (9.86)

(*) specimen prepared by Coreslab® Structures (Albuquerque), Inc.
(--) no data/not applicable

Table 1.123: Unit Weight Results for Batch UB4

Age	Specimen		Weight	w_c	Average	Std. Dev
days	No.	Type	lb (kg)	lb/ft^3 (kg/m^3)	lb/ft^3 (kg/m^3)	lb/ft^3 (kg/m^3)
7	1*	cube	--	--		
	2*	cube	--	--	--	--
11	3	cube	--	--		
	4	cube	--	--	--	--
28	5	cube	--	--		
	6	cube	--	--	--	--
171^{DT0}	7	cube	5.20 (2.36)	147.2 (2359)		
	8	cube	5.27 (2.39)	149.3 (2392)	148.3 (2375)	1.48 (23.7)
467^{PT1}	9	cube	5.18 (2.35)	146.6 (2349)		
	10	cube	5.18 (2.35)	146.6 (2349)	146.6 (2349)	0.00 (0.0)
863^{PT2}	11	cube	5.35 (2.43)	151.6 (2428)	151.6 (2428)	--
1227^{P3}	12	cube	5.20 (2.36)	147.4 (2360)	147.4 (2360)	--
Average			5.23 (2.37)	148.1 (2373)		1.95 (31.3)

(*) specimen prepared by Coreslab® Structures (Albuquerque), Inc.
(--) no data/not applicable

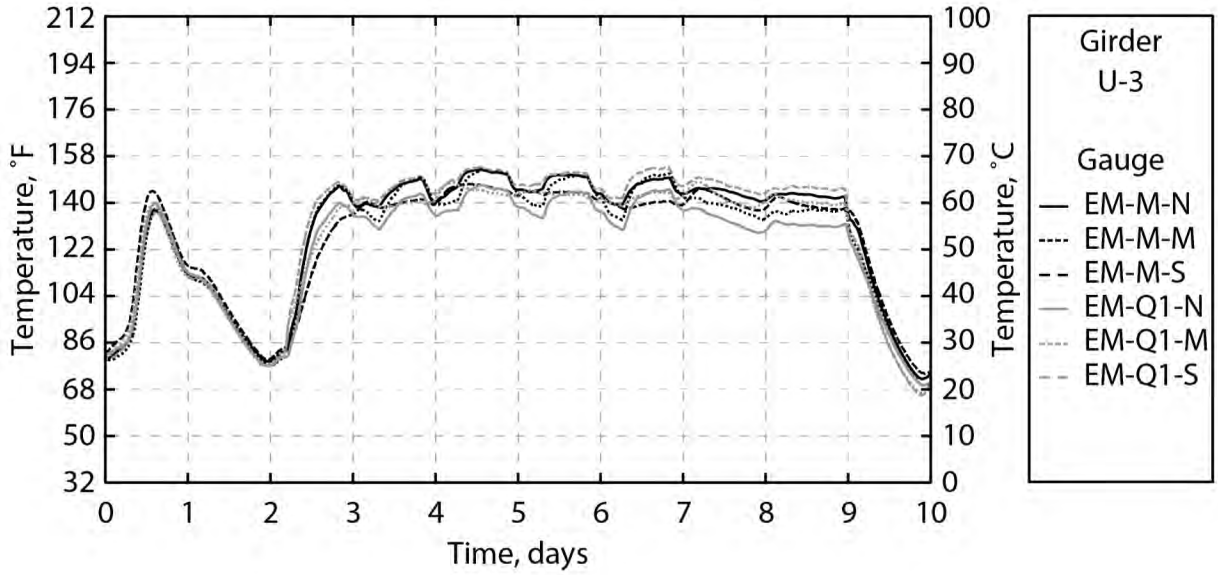


Figure 1.134: Concrete core temperatures during curing for U-3.

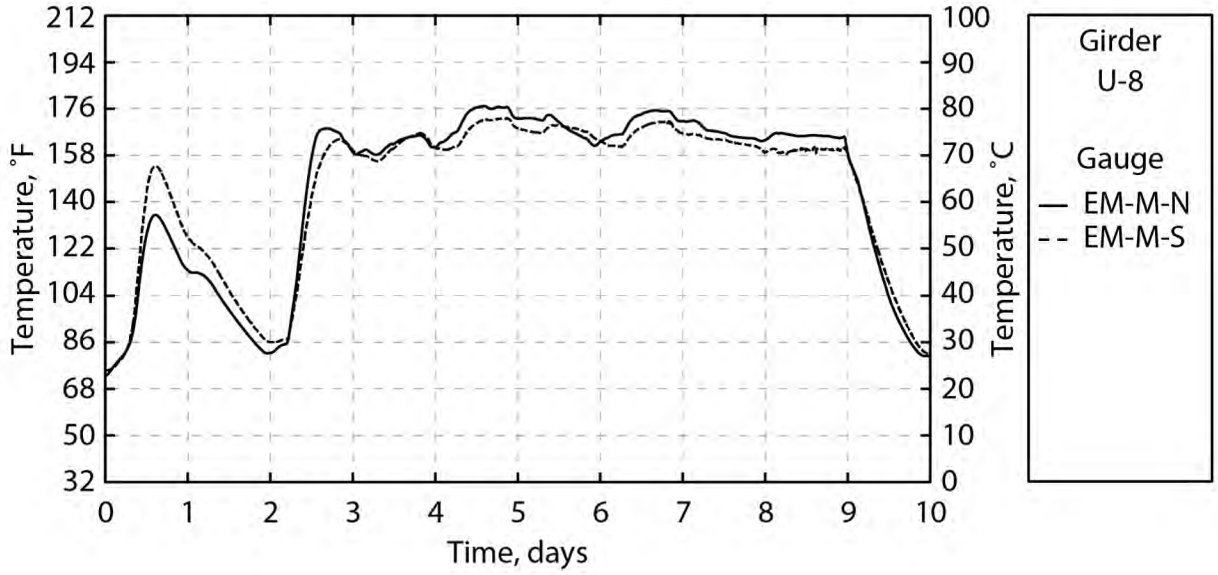


Figure 1.135: Concrete core temperatures during curing for U-8.

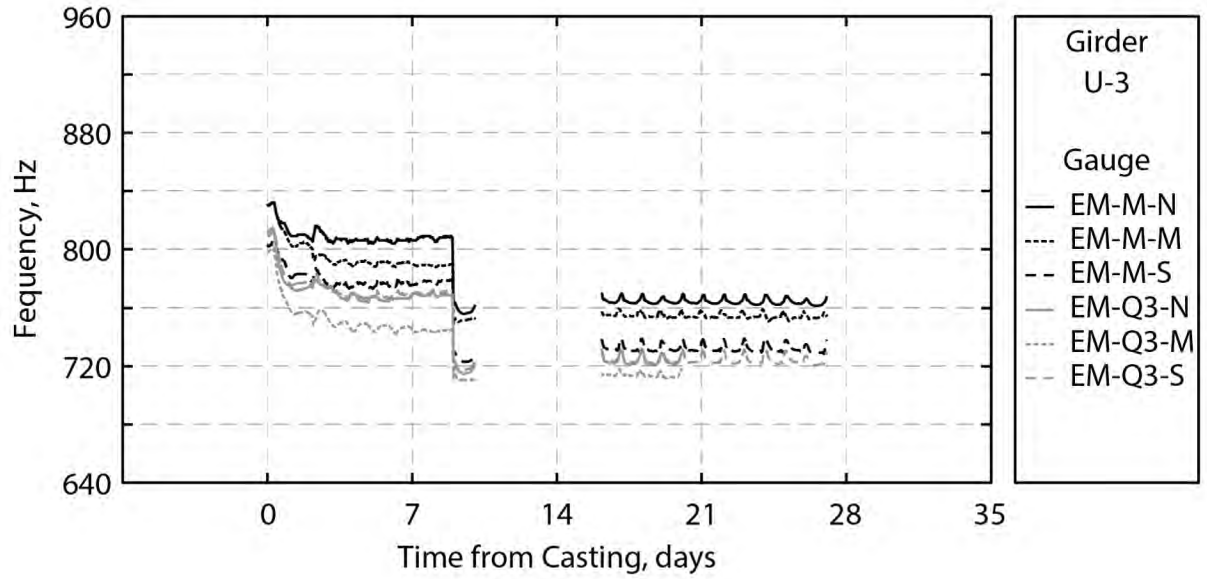


Figure 1.136: VWSG frequency data for U-3 beginning at the time of girder casting.

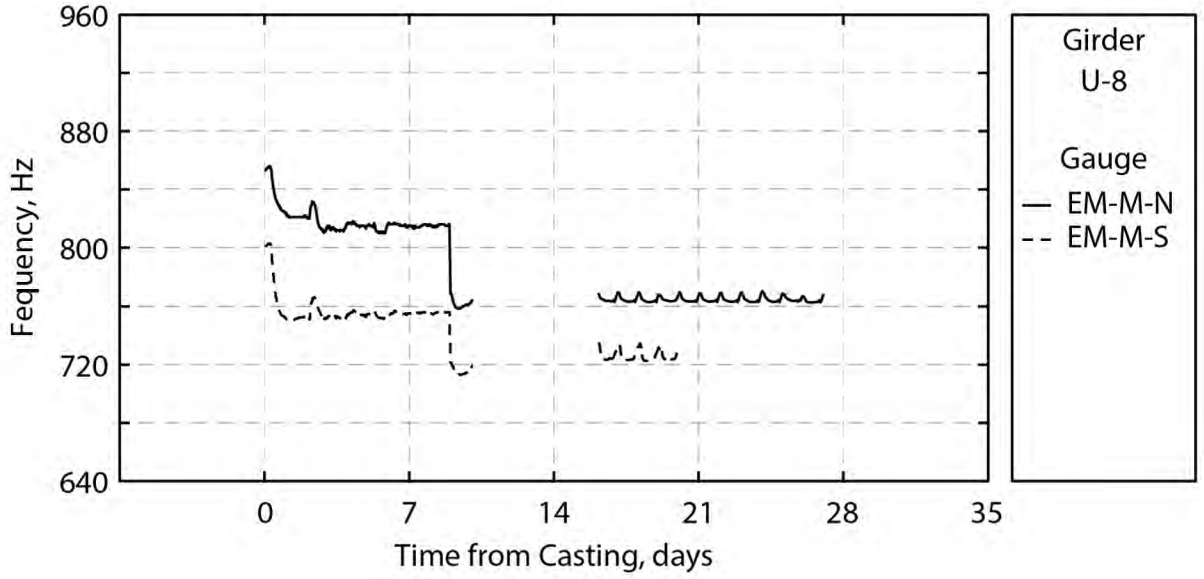


Figure 1.137: VWSG frequency data for U-8 beginning at the time of girder casting.

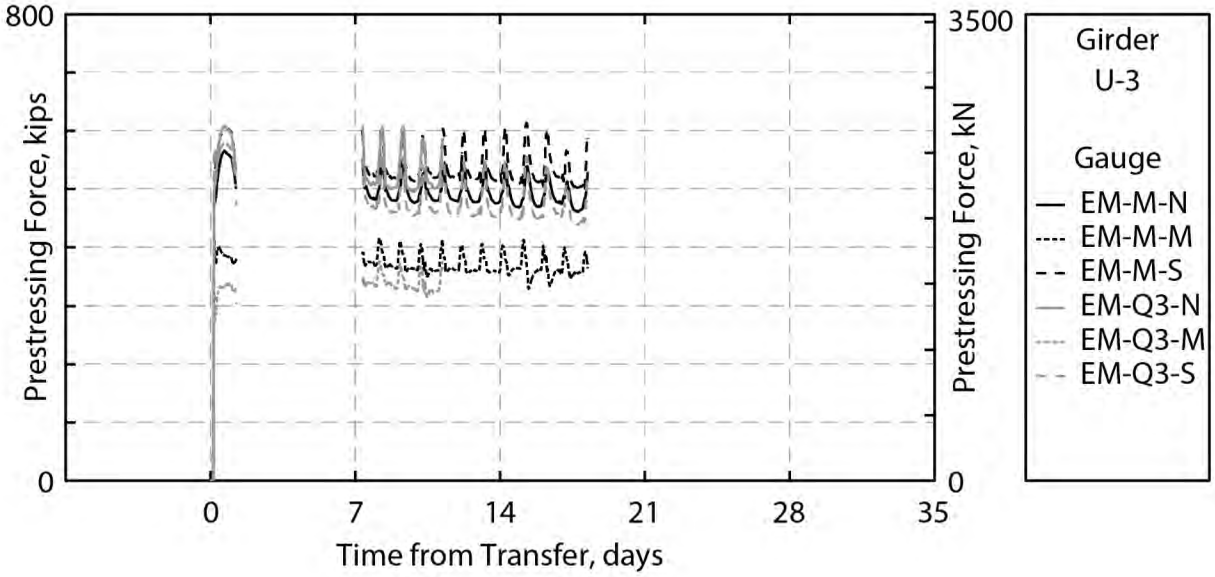


Figure 1.138: VWSG prestressing force for U-3 beginning at transfer.

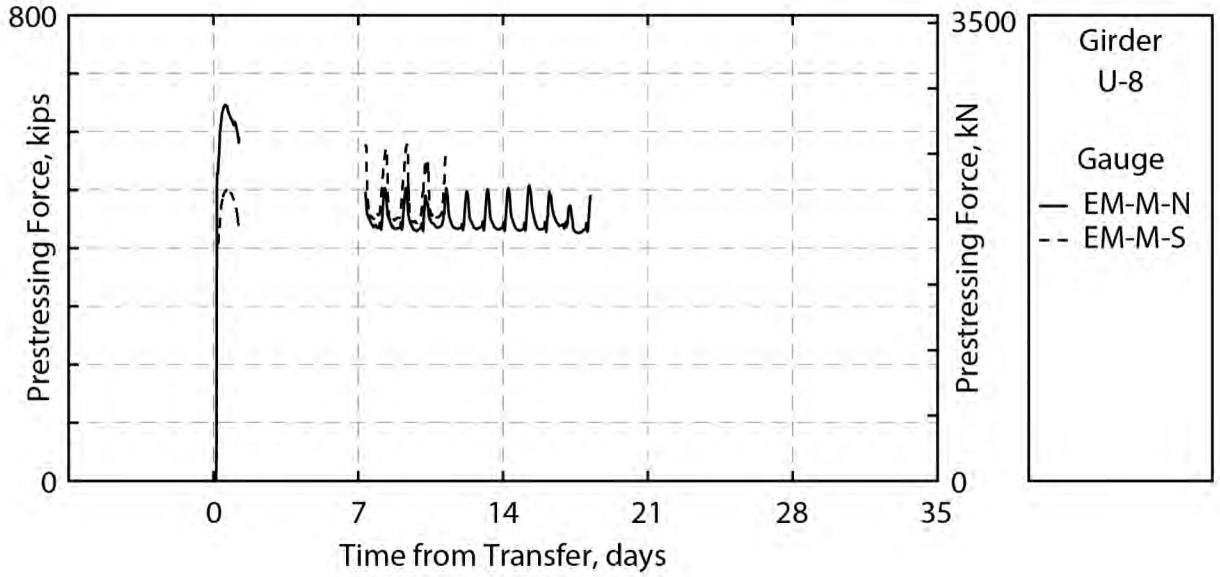


Figure 1.139: VWSG prestressing force for U-8 beginning at transfer.

Table 1.124: Initial Prestressing Forces Calculated for Batch UB4

Gauge Name	P_i kips (kN)
U-3-EM-M-N	500.5 (2226)
U-3-EM-M-M	381.0 (1695)
U-3-EM-M-S	536.1 (2385)
U-3-EM-Q3-N	528.6 (2352)
U-3-EM-Q3-M	333.5 (1483)
U-3-EM-Q3-S	504.7 (2245)
U-8-EM-M-N	526.3 (2341)
U-8-EM-M-S	426.6 (1898)

(--) no data

1.8.7.1.5 HB1

Batch HB1 consisted of girders H-1 and H-4 and was cast on Friday, November 4, 2016. Although the earliest specimen age as reported by Coreslab® was seven days, analysis of strain data shows that prestressing strands were cut on Monday, November 7, 2016, three days after casting.

Table 1.125: Compressive Strength Results for Batch HB1

Age	Specimen		f_c	Average	Std. Dev.
days	No.	Type	ksi (MPa)	ksi (MPa)	ksi (MPa)
7	1*	cylinder	7.1 (48.7)	7.1 (48.7)	--
32	2*	cylinder	12.6 (87.0)		
	3*	cylinder	12.6 (87.0)	12.6 (87.0)	0.008 (0.052)
158^{DT0}	4	cube	8.2 (56.6)		
	5	cube	10.2 (70.6)	9.2 (63.6)	1.43 (9.87)
454^{PT1}	6	cube	8.9 (61.3)		
	7	cube	8.7 (60.0)	8.8 (60.7)	0.136 (0.936)
850^{PT2}	8	cube	10.3 (71.0)	10.3 (71.0)	--
1214^{PT3}	9	cube	9.5 (65.2)	9.5 (65.2)	--
Average			9.8 (67.5)		1.89 (13.0)

(*) specimen prepared by Coreslab® Structures (Albuquerque), Inc.
(--) no data/not applicable

Table 1.126: Unit Weight Results for Batch HB1

Age	Specimen		Weight	w_c	Average	Std. Dev
days	No.	Type	lb (kg)	lb/ft^3 (kg/m^3)	lb/ft^3 (kg/m^3)	lb/ft^3 (kg/m^3)
7	1*	cylinder	--	--	--	--
32	2*	cylinder	--	--		
	3*	cylinder	--	--	--	--
158^{DT0}	4	cube	4.81 (2.18)	136.1 (2180)		
	5	cube	5.04 (2.29)	142.8 (2288)	139.5 (2234)	4.77 (76.3)
454^{PT1}	6	cube	4.98 (2.26)	141.1 (2261)		
	7	cube	4.97 (2.25)	140.7 (2253)	140.9 (2257)	0.320 (5.13)
850^{PT2}	8	cube	4.93 (2.23)	139.5 (2234)	139.5 (2234.4)	--
1214^{PT3}	9	cube	5.00 (2.27)	141.6 (2269)	141.6 (2268.9)	--
Average			4.96 (2.25)	140.3 (2248)		2.34 (37.5)

(*) specimen prepared by Coreslab® Structures (Albuquerque), Inc.
(--) no data/not applicable

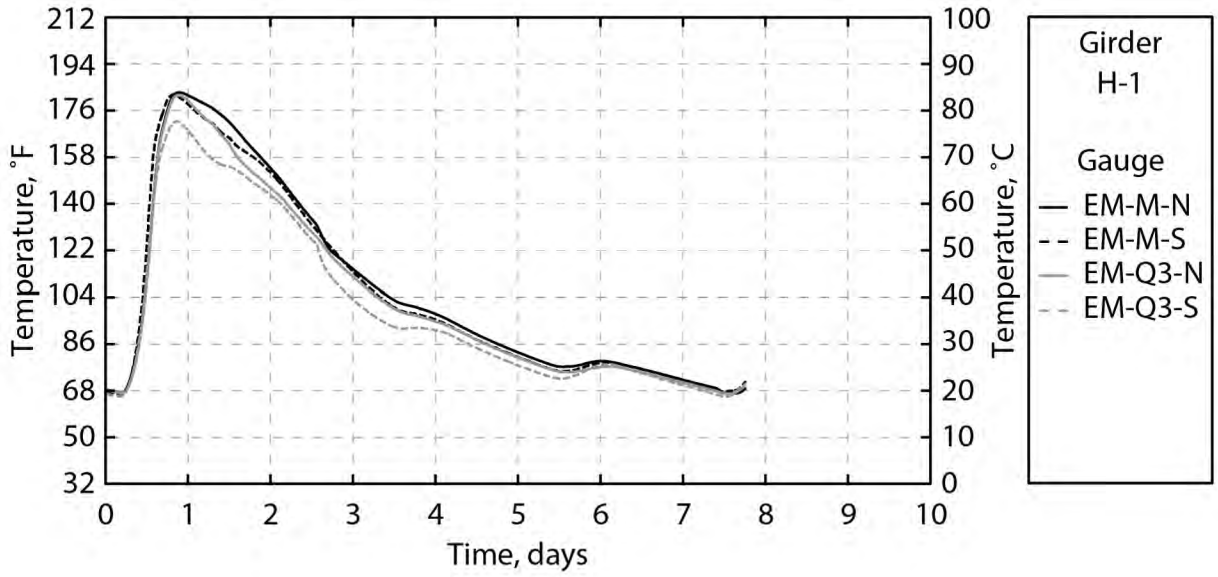


Figure 1.140: Concrete core temperatures during curing for H-1.

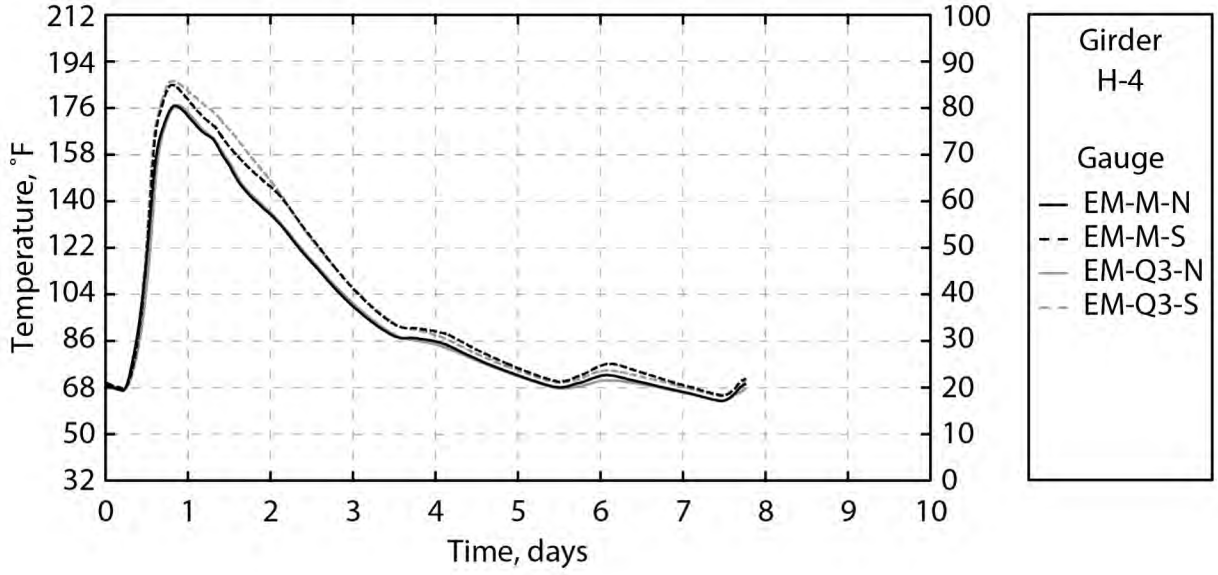


Figure 1.141: Concrete core temperatures during curing for H-4.

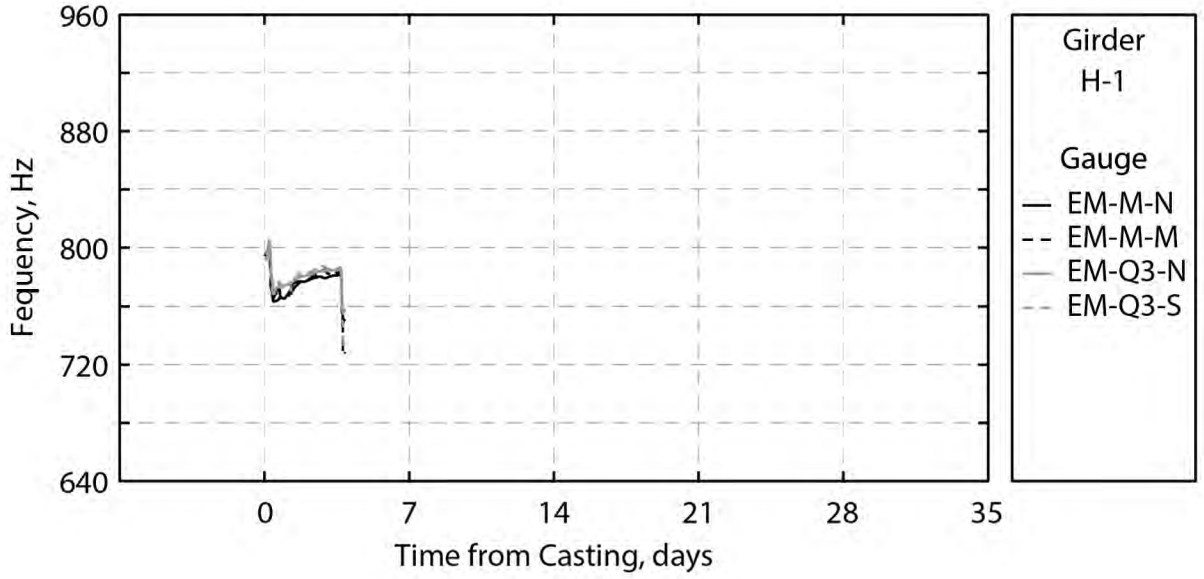


Figure 1.142: VWSG frequency data for H-1 beginning at the time of girder casting.

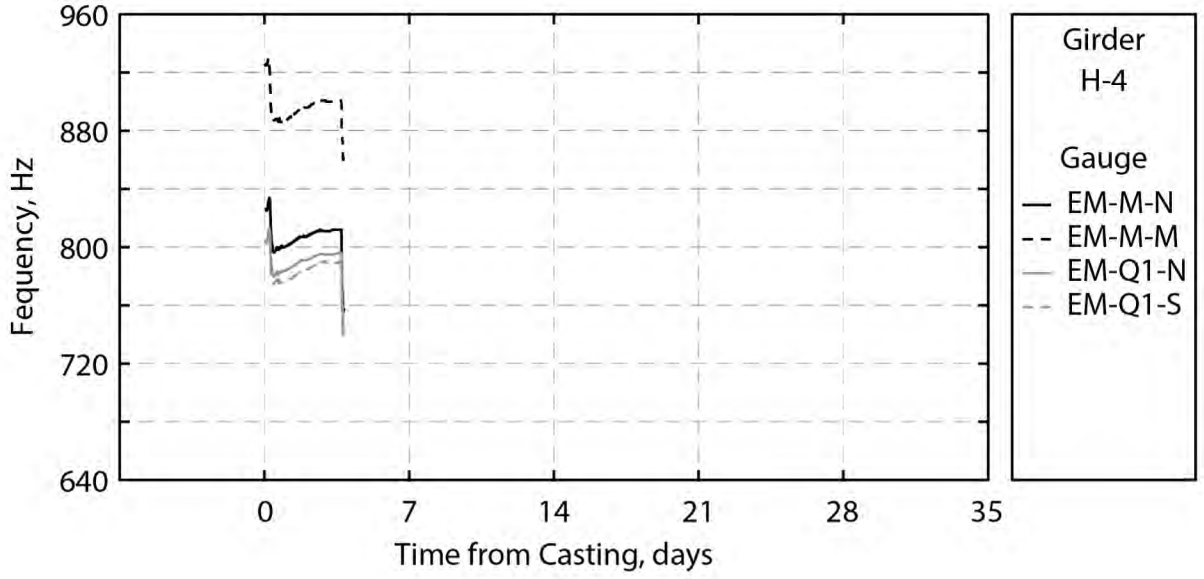


Figure 1.143: VWSG frequency data for H-4 beginning at the time of girder casting.

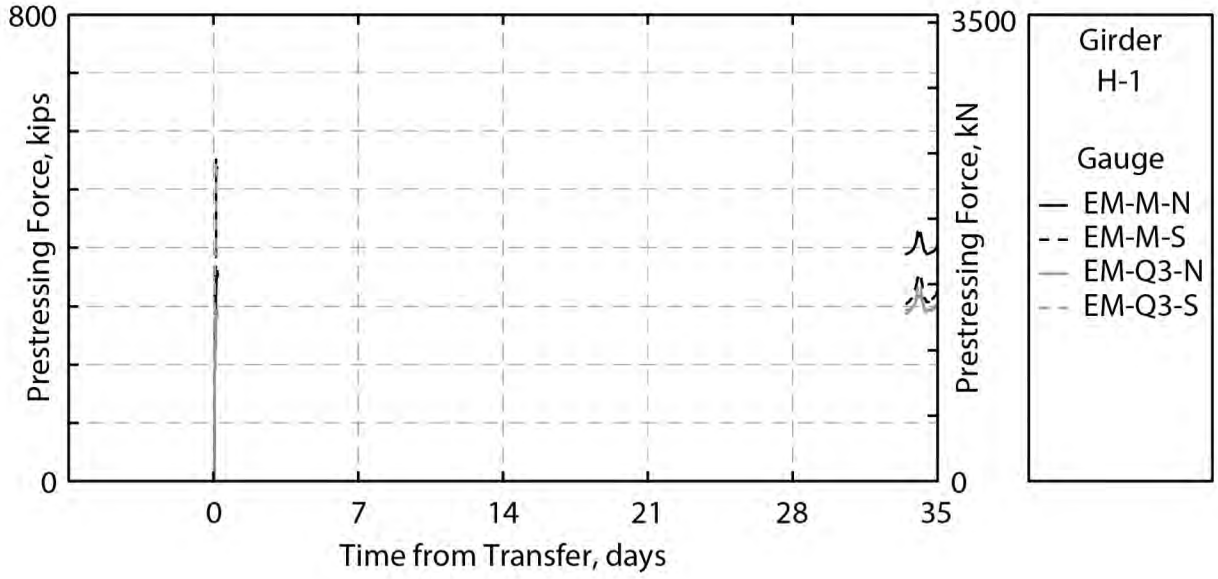


Figure 1.144: VWSG prestressing force for H-1 beginning at transfer.

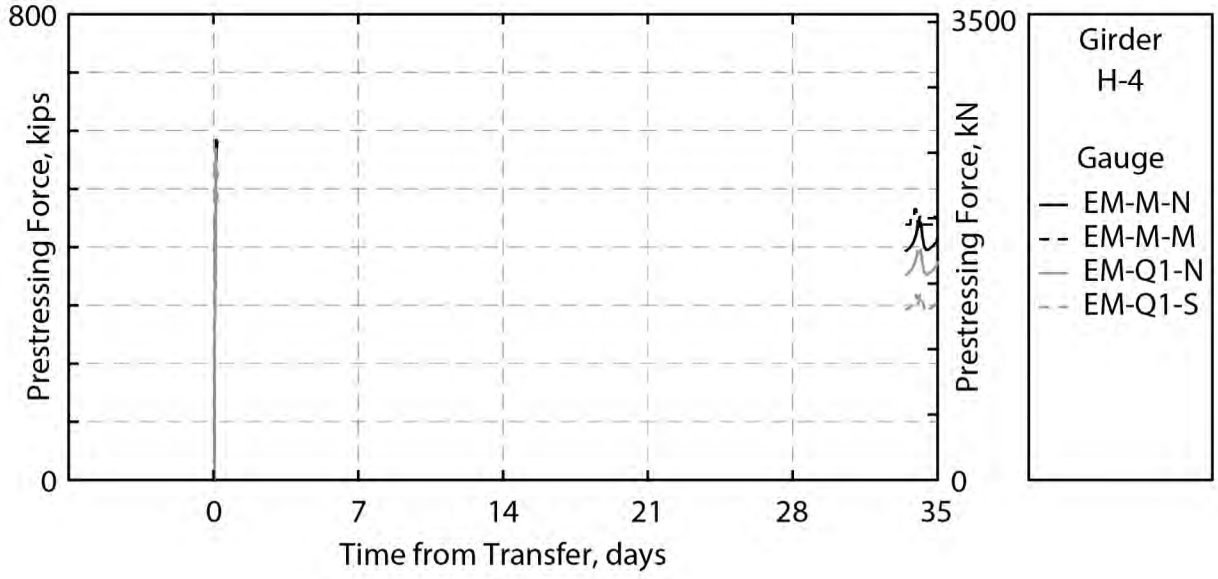


Figure 1.145: VWSG prestressing force for H-4 beginning at transfer.

Table 1.127: Initial Prestressing Forces Calculated for Batch HB1

Gauge Name	P_i kips (kN)
H-1-EM-M-N	346.6 (1542)
H-1-EM-M-S	552.7 (2459)
H-1-EM-Q3-N	290.8 (1294)
H-1-EM-Q3-S	559.2 (2487)
H-4-EM-Q1-N	547.5 (2435)
H-4-EM-Q1-S	509.3 (2266)
H-4-EM-M-N	585.7 (2605)
H-4-EM-M-S	558.2 (2483)

(--) no data

1.8.7.1.6 HB2

Batch HB2 consisted of girders H-7 and H-8 and was cast on Friday, November 11, 2016. Although the earliest specimen age as reported by Coreslab® was seven days, analysis of strain data shows that prestressing strands were cut on Monday, November 14, 2016, three days after casting.

Table 1.128: Compressive Strength Results for Batch HB2

Age	Specimen		f_c	Average	Std. Dev.
days	No.	Type	ksi (MPa)	ksi (MPa)	ksi (MPa)
7	1*	cylinder	7.2 (49.7)	7.2 (49.7)	--
28	2*	cylinder	11.2 (77.2)		
	3*	cylinder	11.8 (81.3)	11.5 (79.3)	0.425 (2.93)
151^{DT0}	4	cube	10.1 (69.7)		
	5	cube	10.2 (70.1)	10.1 (69.9)	0.044 (0.305)
447^{PT1}	6	cube	10.4 (71.6)		
	7	cube	9.8 (67.7)	10.1 (69.6)	0.393 (2.71)
843^{PT2}	8	cube	11.1 (76.3)	11.1 (76.3)	--
1207^{PT3}	9	cube	9.7 (66.9)	9.7 (66.9)	--
Average			10.2 (70)		1.31 (9.00)

(*) specimen prepared by Coreslab® Structures (Albuquerque), Inc.
(--) no data/not applicable

Table 1.129: Unit Weight Results for Batch HB2

Age	Specimen		Weight	w_c	Average	Std. Dev
days	No.	Type	lb (kg)	lb/ft^3 (kg/m^3)	lb/ft^3 (kg/m^3)	lb/ft^3 (kg/m^3)
7	1*	cylinder	--	--	--	--
28	2*	cylinder	--	--		
	3*	cylinder	--	--	--	--
151^{DT0}	4	cube	4.89 (2.22)	138.5 (2218)		
	5	cube	4.86 (2.20)	137.6 (2204)	138.0 (2211)	0.601 (9.62)
447^{PT1}	6	cube	4.79 (2.17)	135.6 (2172)		
	7	cube	4.71 (2.14)	133.5 (2138)	134.5 (2155)	1.48 (23.7)
843^{PT2}	8	cube	4.99 (2.26)	141.4 (2264)	141.4 (2264)	--
1207^{PT3}	9	cube	4.85 (2.20)	137.2 (2198)	137.2 (2198)	--
Average			4.85 (2.20)	137.3 (2199)		2.66 (42.6)

(*) specimen prepared by Coreslab® Structures (Albuquerque), Inc.
(--) no data/not applicable

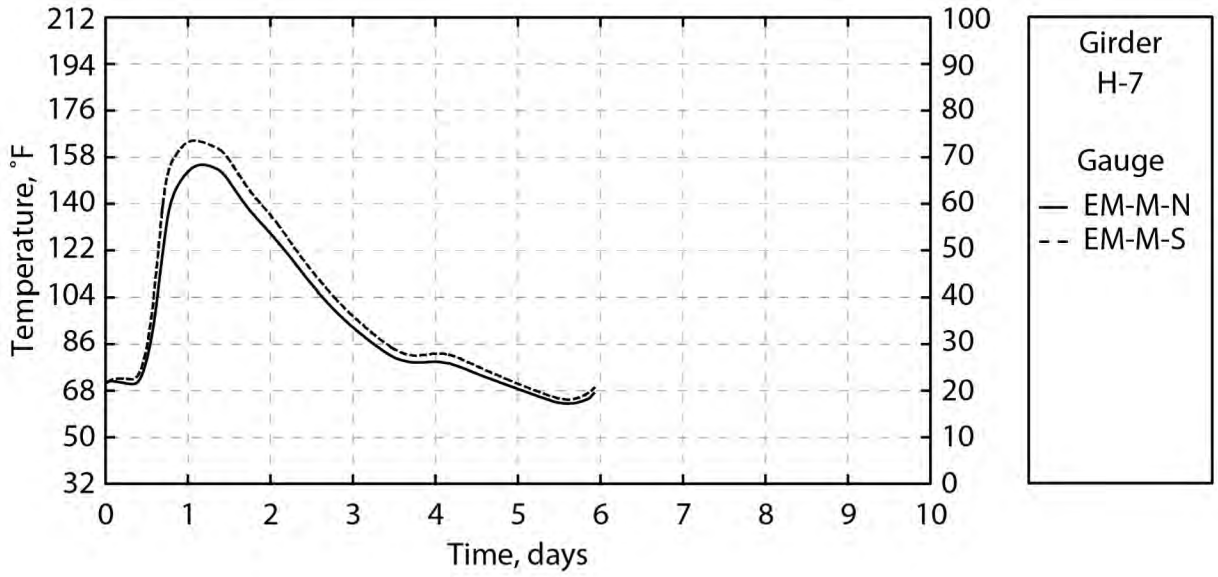


Figure 1.146: Concrete core temperatures during curing for H-7.

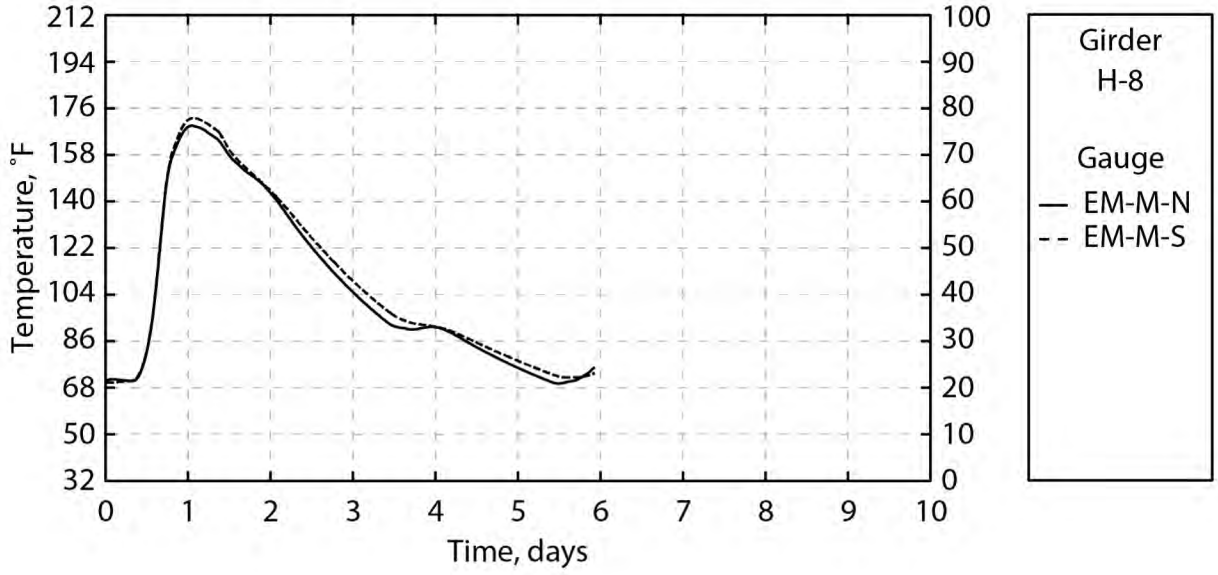


Figure 1.147: Concrete core temperatures during curing for H-8.

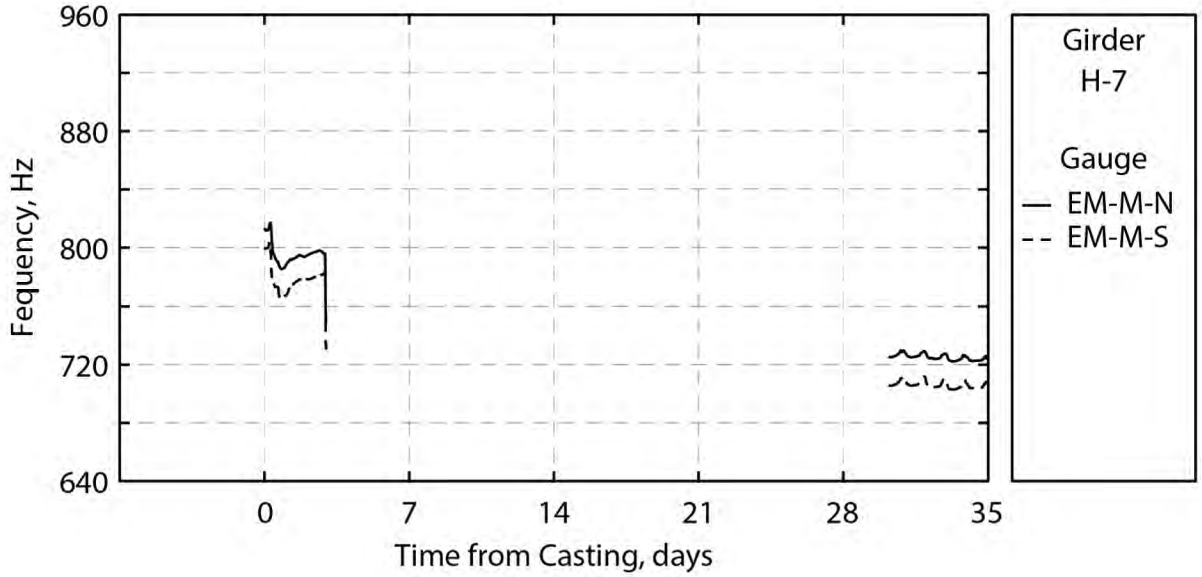


Figure 1.148: VWSG frequency data for H-7 beginning at the time of girder casting.

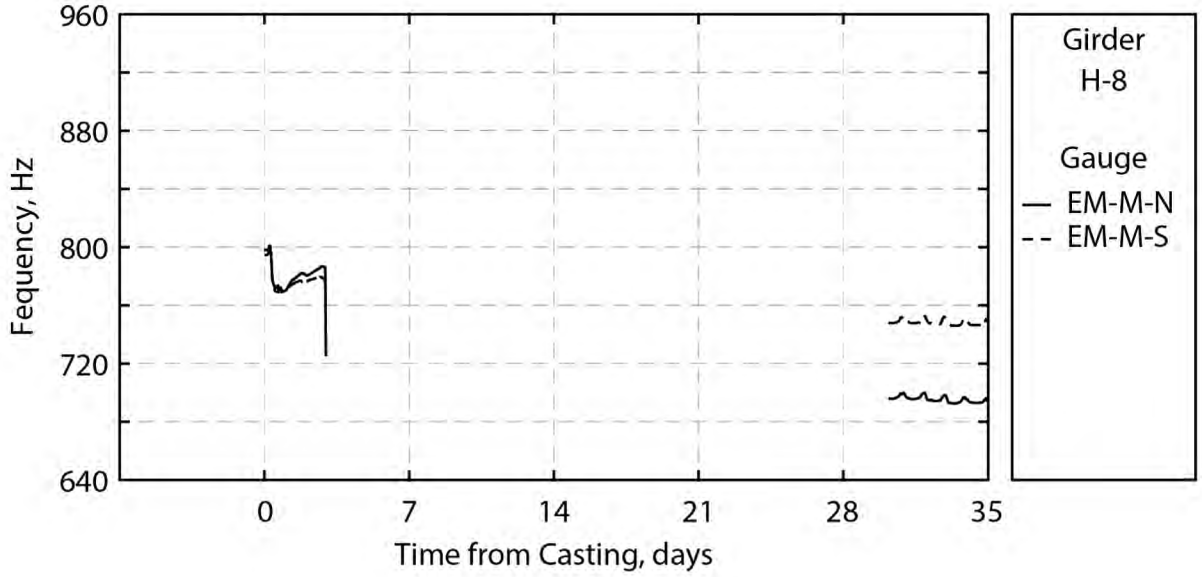


Figure 1.149: VWSG frequency data for H-8 beginning at the time of girder casting.

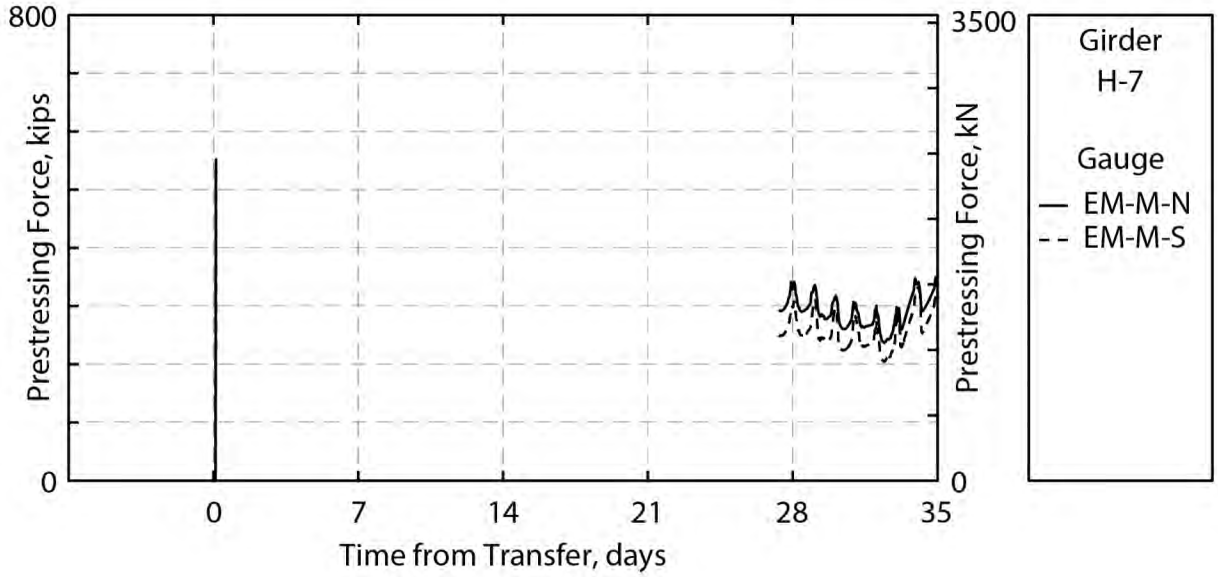


Figure 1.150: VWSG prestressing force for H-7 beginning at transfer.

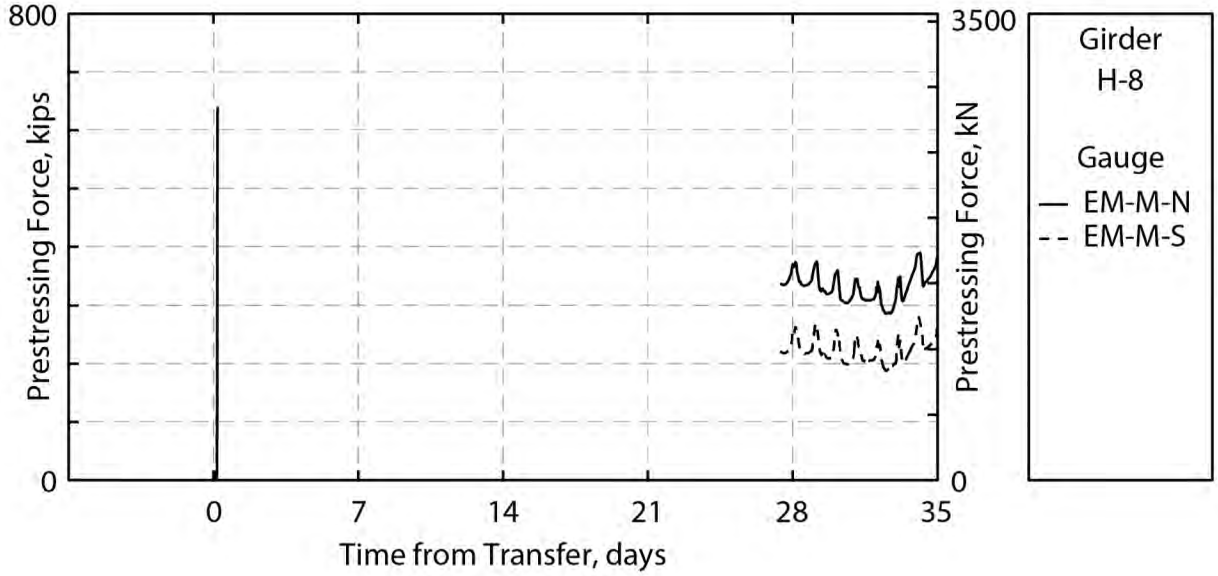


Figure 1.151: VWSG prestressing force for H-8 beginning at transfer.

Table 1.130: Initial Prestressing Forces Calculated for Batch HB2

Gauge Name	P_i kips (kN)
H-7-EM-M-N	553.8 (2463)
H-7-EM-M-S	524.0 (2331)
H-8-EM-M-N	640.4 (2848)
H-8-EM-M-S	275.3 (1225)

(--) no data

1.8.7.1.7 HB3

Batch HB3 consisted of girders H-3 and H-6 and was cast on Friday, November 18, 2016. Although the earliest specimen age as reported by Coreslab® was seven days, analysis of strain data shows that prestressing strands were cut on Monday, November 21, 2016, three days after casting.

Table 1.131: Compressive Strength Results for Batch HB3

Age	Specimen		f_c	Average	Std. Dev.
days	No.	Type	ksi (MPa)	ksi (MPa)	ksi (MPa)
7	1*	cylinder	7.1 (48.7)	7.1 (48.7)	--
28	2*	cylinder	9.8 (67.9)		
	3*	cylinder	10.0 (68.7)	9.9 (68.3)	0.080 (0.553)
144^{DT0}	4	cube	8.2 (56.5)		
	5	cube	8.5 (58.5)	8.3 (57.5)	0.203 (1.40)
440^{PT1}	6	cube	7.7 (53.1)		
	7	cube	7.3 (50.6)	7.5 (51.9)	0.255 (1.76)
Average			8.4 (58)		1.15 (7.94)

(*) specimen prepared by Coreslab® Structures (Albuquerque), Inc.
(--) no data/not applicable

Table 1.132: Unit Weight Results for Batch HB3

Age	Specimen		Weight	w_c	Average	Std. Dev
days	No.	Type	lb (kg)	lb/ft^3 (kg/m^3)	lb/ft^3 (kg/m^3)	lb/ft^3 (kg/m^3)
7	1*	cylinder	--	--	--	--
28	2*	cylinder	--	--		
	3*	cylinder	--	--	--	--
144^{DT0}	4	cube	4.79 (2.17)	135.6 (2172)		
	5	cube	4.77 (2.16)	135.1 (2164)	135.3 (2168)	0.360 (5.77)
440^{PT1}	6	cube	4.62 (2.09)	130.7 (2094)		
	7	cube	4.79 (2.17)	135.7 (2174)	133.2 (2134)	3.52 (56.4)
Average			4.74 (2.15)	134.3 (2151)		2.38 (38.2)

(*) specimen prepared by Coreslab® Structures (Albuquerque), Inc.
(--) no data/not applicable

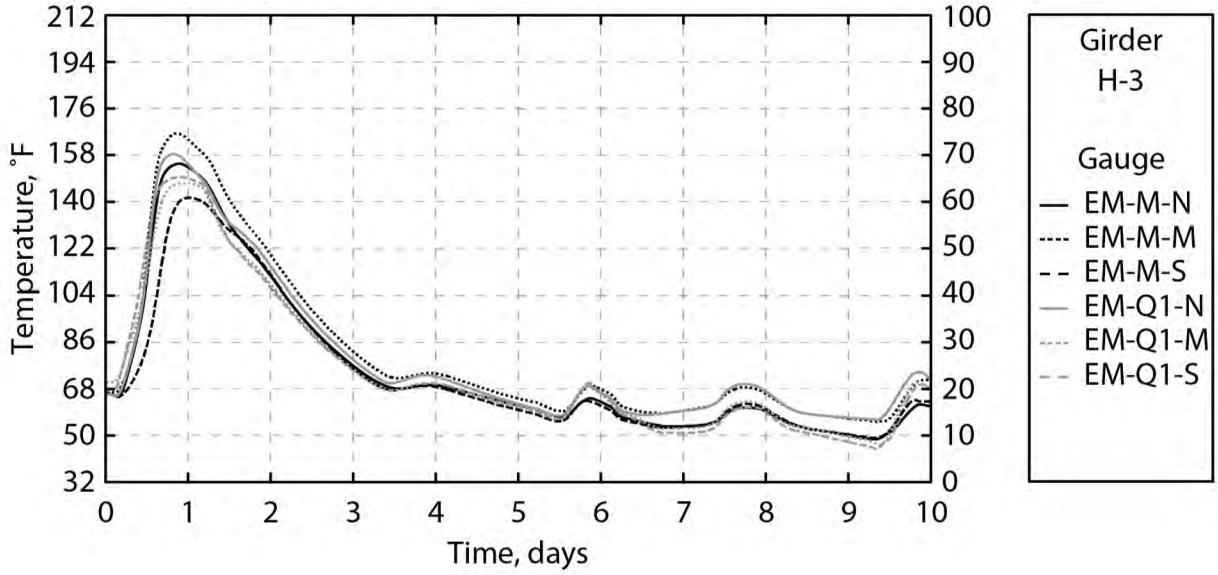


Figure 1.152: Concrete core temperatures during curing for H-3.

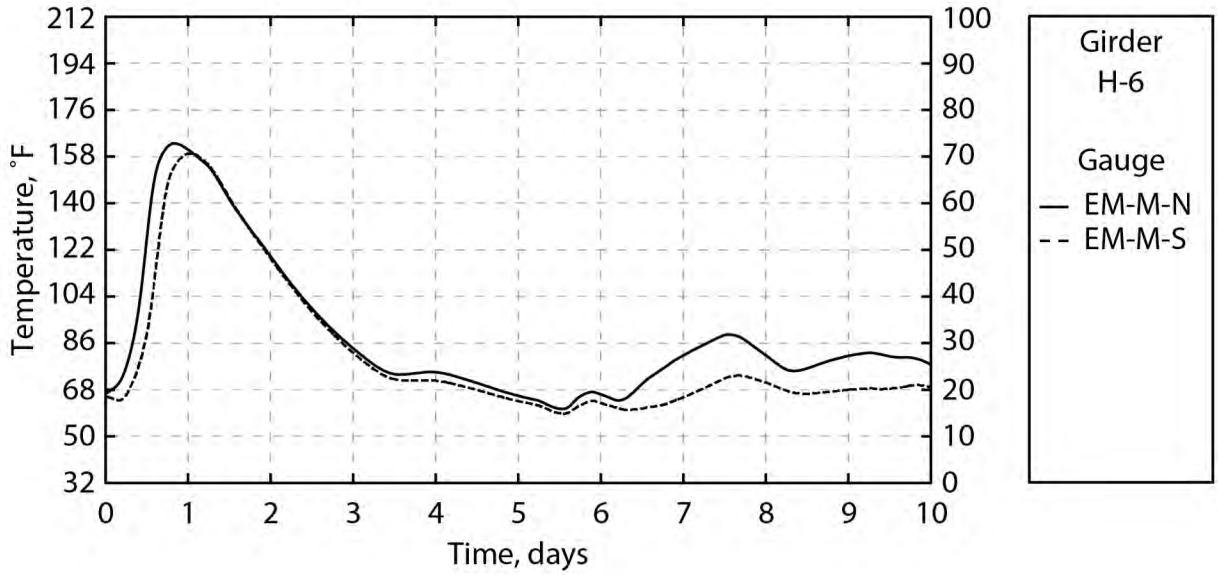


Figure 1.153: Concrete core temperatures during curing for H-6.

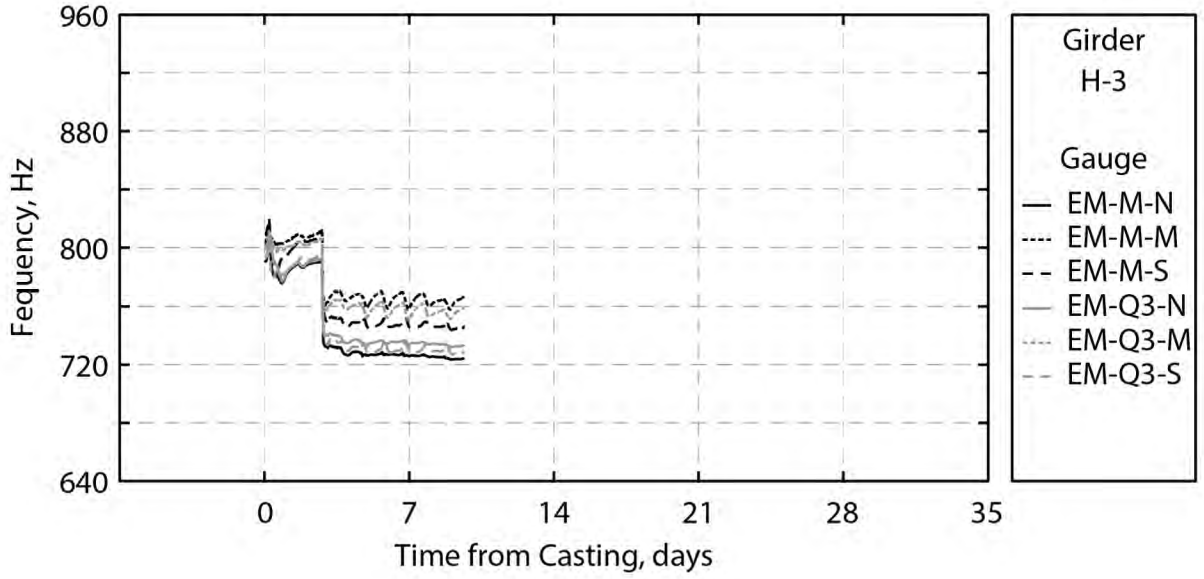


Figure 1.154: VWSG frequency data for H-3 beginning at the time of girder casting.

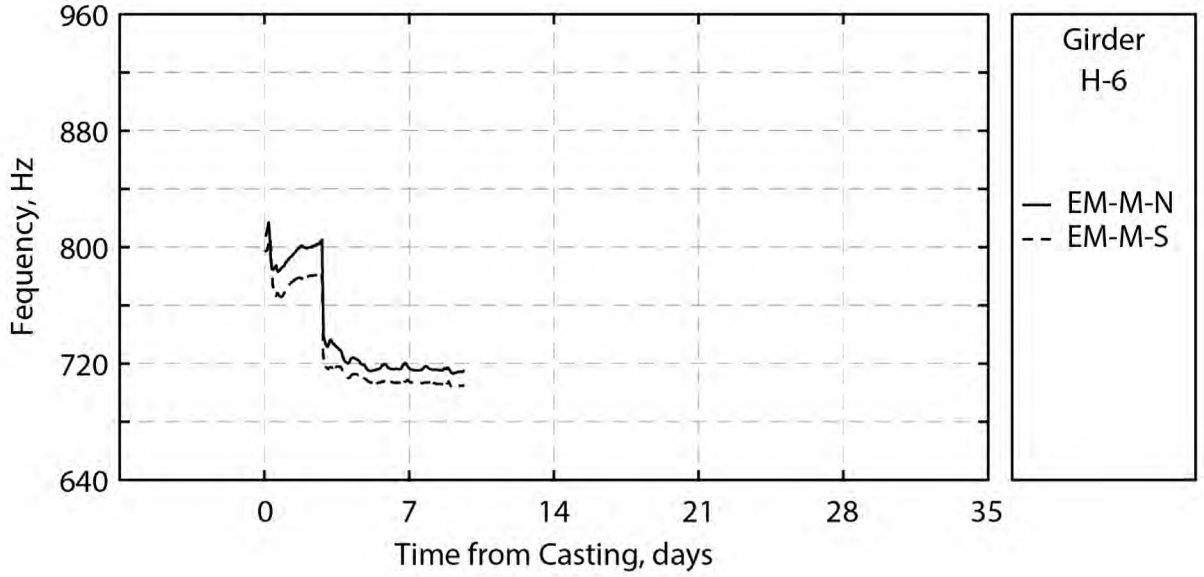


Figure 1.155: VWSG frequency data for H-6 beginning at the time of girder casting.

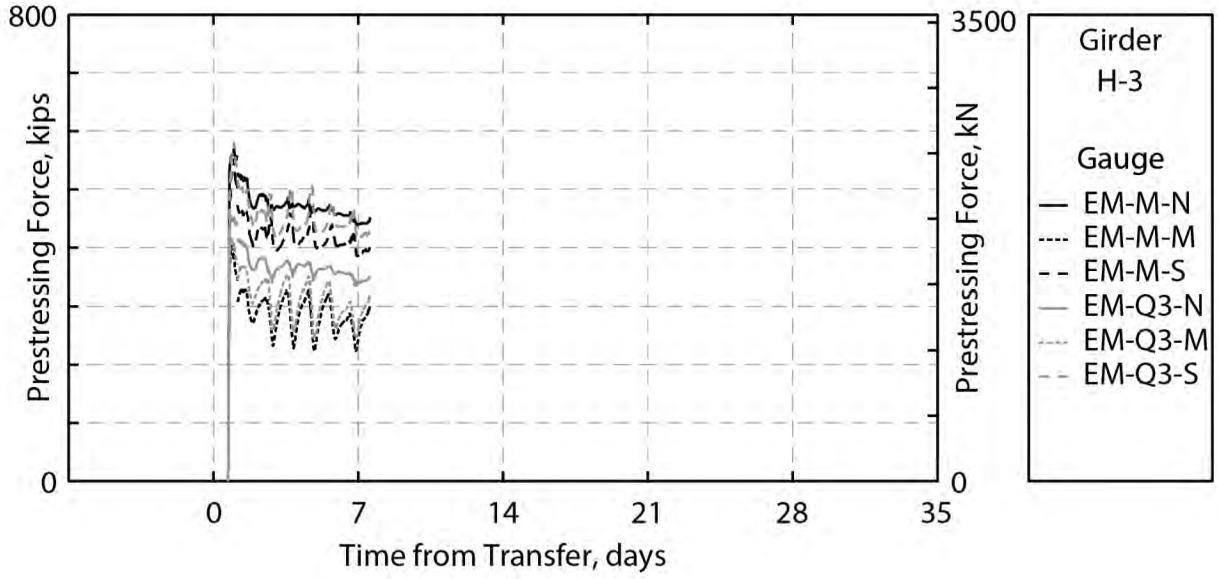


Figure 1.156: VWSG prestressing force for H-3 beginning at transfer.

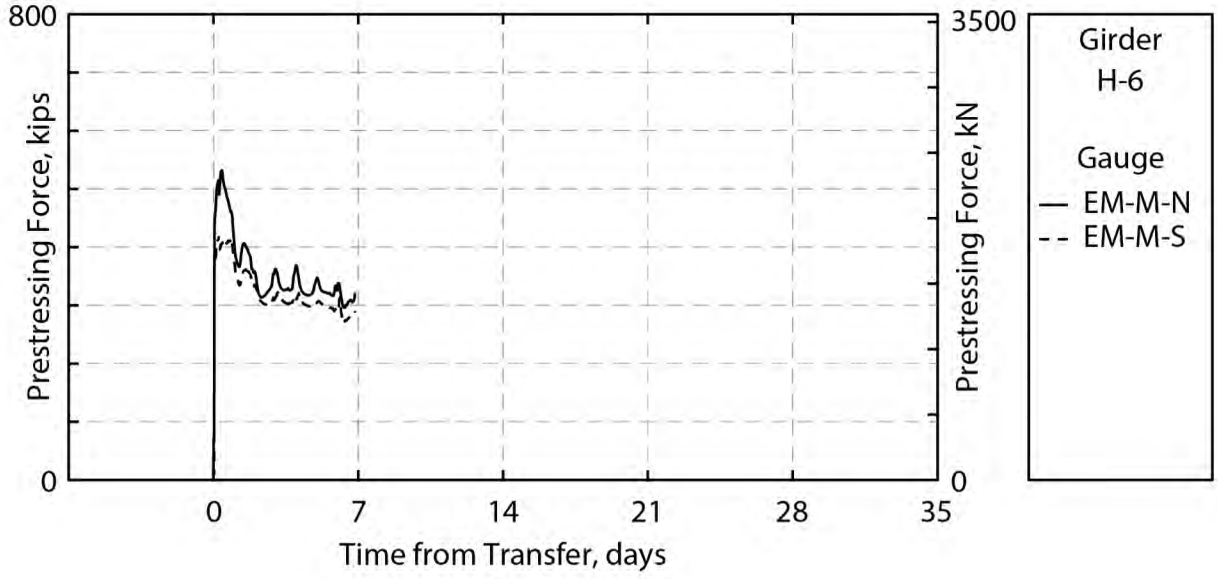


Figure 1.157: VWSG prestressing force for H-6 beginning at transfer.

Table 1.133: Initial Prestressing Forces Calculated for Batch HB3

Gauge Name	P_i kips (kN)
H-3-EM-M-N	555.5 (2471)
H-3-EM-M-M	343.5 (1528)
H-3-EM-M-S	501.9 (2232)
H-3-EM-Q3-N	441.4 (1964)
H-3-EM-Q3-M	370.4 (1647)
H-3-EM-Q3-S	538.1 (2394)
H-6-EM-M-N	509.8 (2268)
H-6-EM-M-S	418.7 (1862)

(--) no data

1.8.7.1.8 HB4

Batch HB4 consisted of girders H-2 and H-5 and was cast on Friday, December 2, 2016. The date of prestress transfer for Batch HB4 was not reported by Coreslab®, however, analysis of VWSG data shows that prestressing strands were cut on Friday, December 23, 2016, a total of 21 days after casting. No explanation was available for the delay, and the situation represented no detriment to the girders.

Table 1.134: Compressive Strength Results for Batch HB4

Age	Specimen		f_c	Average	Std. Dev.
days	No.	Type	ksi (MPa)	ksi (MPa)	ksi (MPa)
7	1*	cylinder	7.4 (50.9)	7.4 (50.9)	--
28	2*	cylinder	13.1 (90.3)		
	3*	cylinder	13.5 (93.2)	13.3 (91.7)	0.294 (2.03)
130^{DT0}	4	cube	13.8 (94.8)		
	5	cube	13.6 (93.5)	13.7 (94.2)	0.133 (0.91)
426^{PT1}	6	cube	13.3 (91.5)		
	7	cube	11.1 (76.3)	12.2 (83.9)	1.56 (10.8)
Average			12.2 (84)		2.32 (16.0)

(*) specimen prepared by Coreslab® Structures (Albuquerque), Inc.
(--) no data/not applicable

Table 1.135: Unit Weight Results for Batch HB4

Age	Specimen		Weight	w_c	Average	Std. Dev
days	No.	Type	lb (kg)	lb/ft^3 (kg/m^3)	lb/ft^3 (kg/m^3)	lb/ft^3 (kg/m^3)
7	1*	cylinder	--	--	--	--
28	2*	cylinder	--	--		
	3*	cylinder	--	--	--	--
130^{DT0}	4	cube	5.23 (2.37)	148.1 (2372)		
	5	cube	5.26 (2.39)	149.0 (2387)	148.6 (2380)	0.641 (10.3)
426^{PT1}	6	cube	5.24 (2.38)	148.4 (2378)		
	7	cube	4.94 (2.24)	139.9 (2241)	144.2 (2309)	6.05 (96.9)
Average			5.17 (2.34)	146.4 (2344)		4.33 (69.4)

(*) specimen prepared by Coreslab® Structures (Albuquerque), Inc.
(--) no data/not applicable

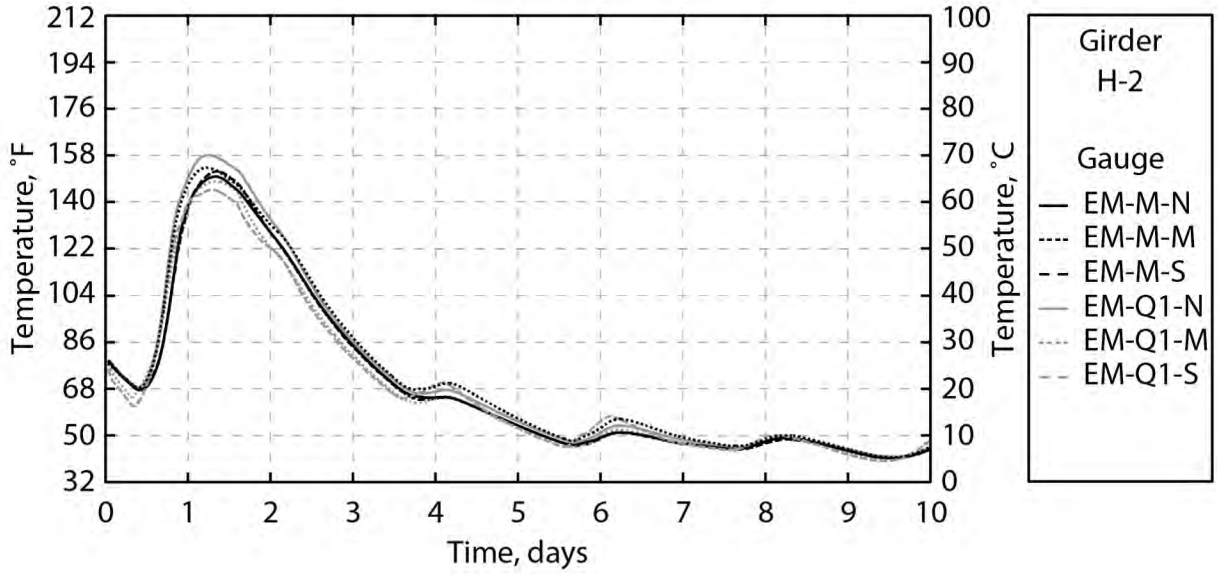


Figure 1.158: Concrete core temperatures during curing for H-2.

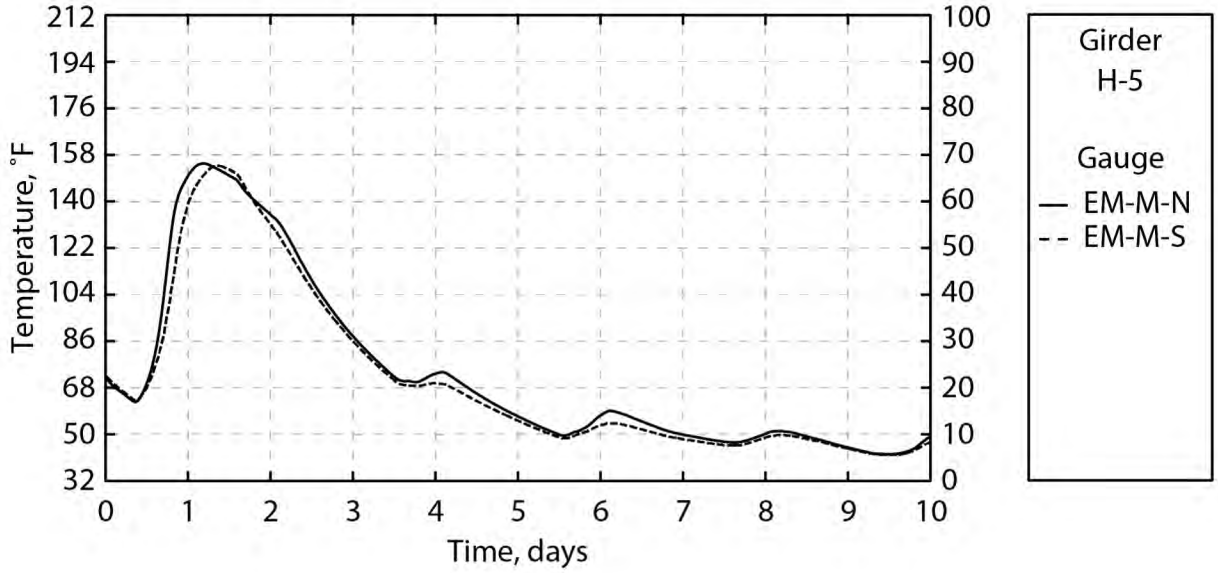


Figure 1.159: Concrete core temperatures during curing for H-5.

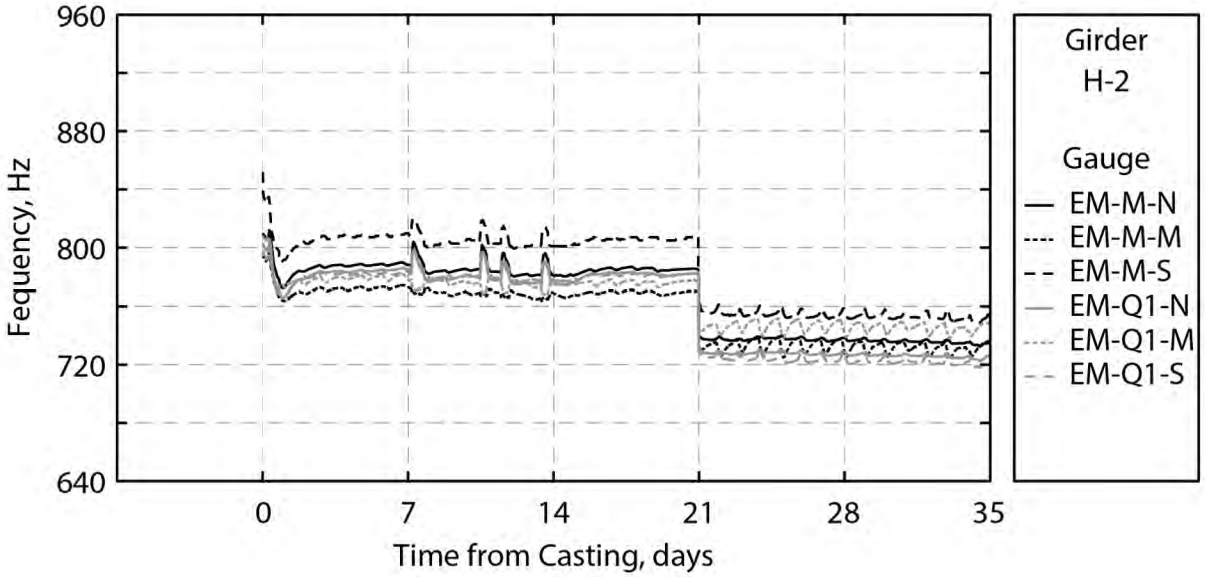


Figure 1.160: VWSG frequency data for H-2 beginning at the time of girder casting.

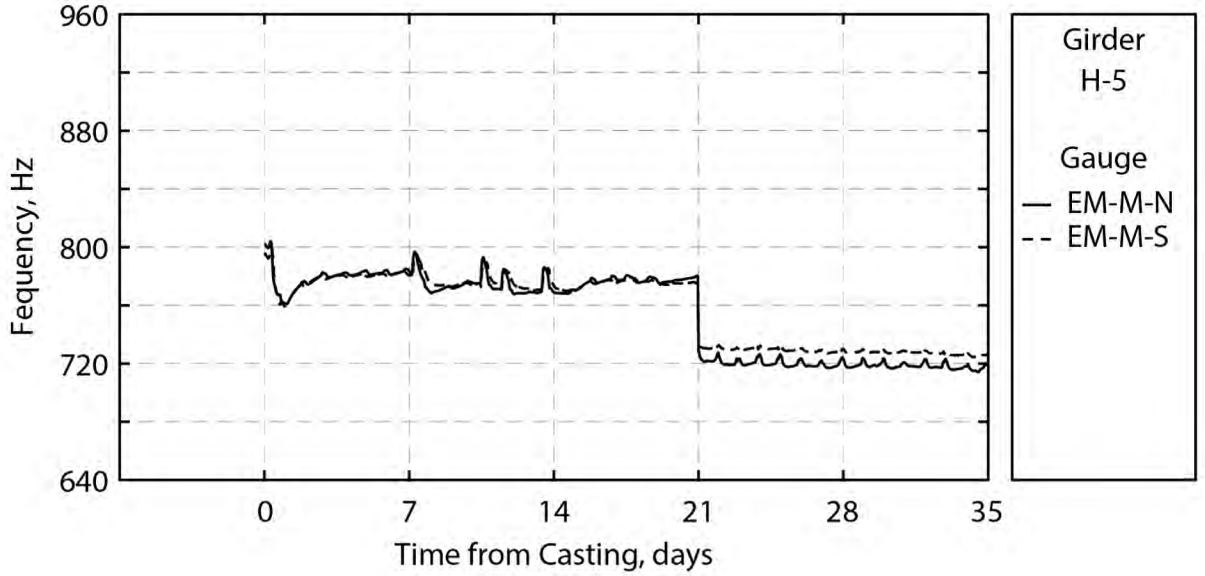


Figure 1.161: VWSG frequency data for H-5 beginning at the time of girder casting.

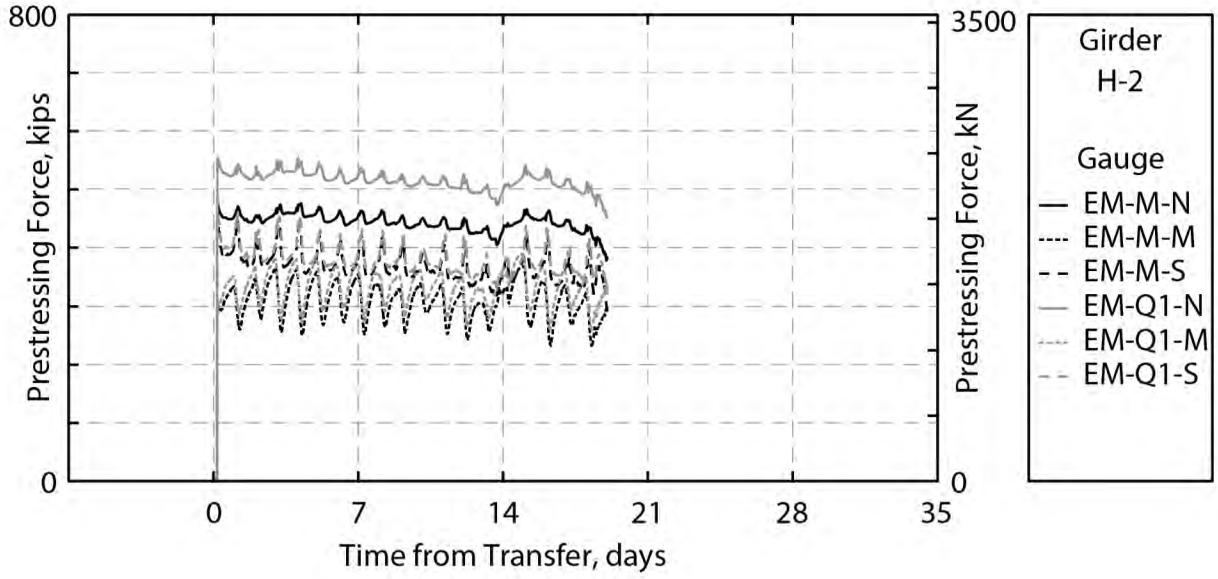


Figure 1.162: VWSG prestressing force for H-2 beginning at transfer.

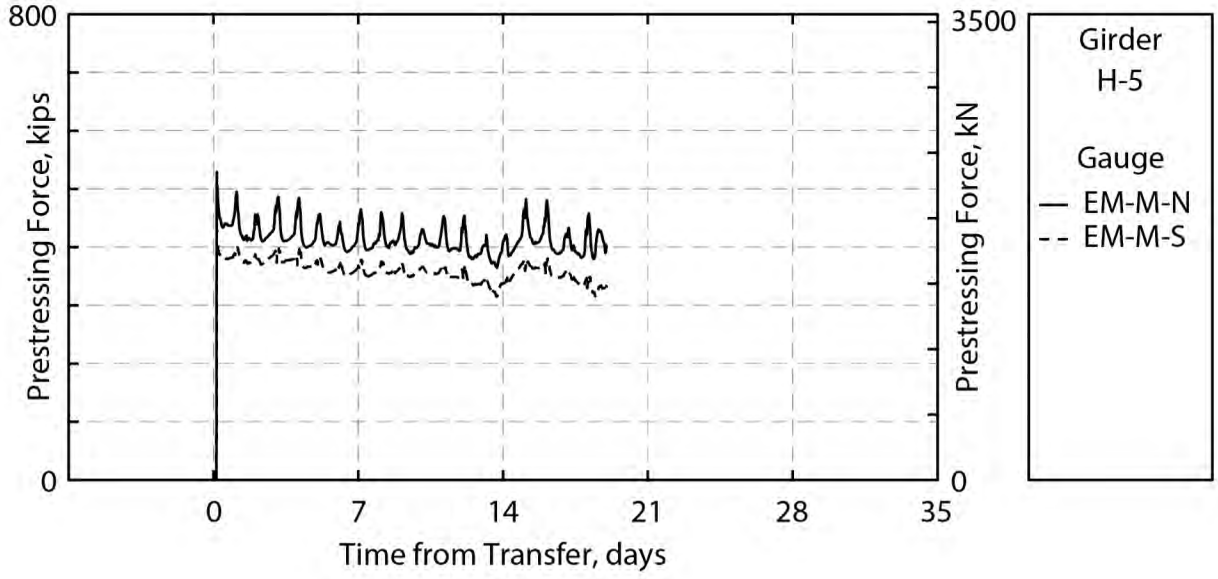


Figure 1.163: VWSG prestressing force for H-5 beginning at transfer.

Table 1.136: Initial Prestressing Forces Calculated for Batch HB4

Gauge Name	P_i kips (kN)
H-2-EM-Q1-N	554.3 (2466)
H-2-EM-Q1-M	314.2 (1398)
H-2-EM-Q1-S	506.3 (2252)
H-2-EM-M-N	480.9 (2139)
H-2-EM-M-M	327.9 (1459)
H-2-EM-M-S	481.1 (2140)
H-5-EM-M-N	527.2 (2345)
H-5-EM-M-S	428.5 (1906)

(--) no data

1.8.8 Strain Comparisons

Strain data presented in this chapter are displayed in three formats for the purpose of comparison. First, field testing strain results are condensed into tables like the sample shown in Table 1.137. These tables summarize the maximum strains measured in each girder for a specified load test for all load path of a selected load condition (e.g., single truck loading) and provide multiple means of comparing strain behavior during testing.

Column data corresponding to each load path can be used to compare symmetry of each span (e.g., trends in strain magnitude for Path 1 contrast those for Path 6) and between spans (e.g., strains for Path 1 are greater in magnitude for girder Lines 1 and 2 and decrease in magnitude toward girder Line 8 for both the UHPC and HPC span), whereas row data provides an indication of the individual girder behavior for each load path (e.g., strains for girder U-2 are largest during Path 1 when the truck load is positioned directly above that girder and minimized for Path 6). Rows are intentionally arranged to facilitate direct comparison of strains for each girder line of the two spans (e.g., comparing the magnitude of strains measured in girders U-2 and H-2), and row data can be used to compare the symmetry of behavior for individual girders or girder lines (e.g., trends in strain magnitude for girder Line 2 contrast those for girder Line 7).

Lastly, formatting and markers are used to denote table information. A shaded background indicates larger comparative strain in the HPC girder of a given girder line (e.g., strain for Path 1 loading is greater for girder H-1 in comparison to U-1). Instances in which reported strains for U and H girders are NOT directly comparable based on the sensor location (i.e., midspan or quarter-point location and depth of placement within the girder stem) are indicated by *italic* font (e.g., because data from the lower midspan sensors in H-4 were unavailable, the values reported in Table 1.137 are not directly comparable to the values for U-4). Values displayed in **bold** font represent the overall maximum strains measured among exterior girders (i.e., Lines 1 and 8) and interior girders (i.e., Lines 2–7) for the truck load configuration (e.g., overall maximum strain for exterior girders occurred in U-1 and H-1, and for interior girders occurred in U-2 and H-2). The superscript character (‡) denotes the maximum strain measured for a given girder (e.g., the maximum strain for girder U-2 occurred under Path 1 loading). The superscript character (†) denotes the maximum strain measured in each span for a given load path (e.g., the maximum strains under Path 1 loading occurred in girder U-2 for the UHPC span and girder H-1 for the HPC span).

The next format used for strain comparisons is shown in Figure 1.164. In this type of plot, a transverse strain profile is created for the span (either UHPC or HPC) by plotting the strain data from sensors located nearest to the bottom of the girder stem at midspan of each girder at the approximate time when the maximum strains occurred in the span for each load path, such as the path data presented in the columns of Table 1.137. In the sample Figure 1.164, strain profiles are created using this method for single truck (ST) loading of Paths 1–6 during the Diagnostic Test (DT0). These transverse strain profiles are used to compare the strain behavior between each span and the symmetry for load paths during individual tests, as well as to compare the behaviors between tests.

Table 1.137: Sample Table Showing Comparisons of Maximum Measured Strains for Single Truck Loading During Diagnostic Test

	Strain (με)					
Girder	Path 1	Path 2	Path 3	Path 4	Path 5	Path 6
U-1	76.30‡	34.70	21.50	9.30	6.60	8.70
H-1	†103.10‡	†78.30	37.40	21.20	9.00	6.40
U-2	†84.41‡	53.99	35.75	21.83	11.37	8.07
H-2	92.21‡	66.73	54.69	26.96	16.45	6.96
U-3	66.78‡	†55.93	39.23	28.31	12.98	9.01
H-3	55.25	60.82	†75.49‡	†51.33	36.32	14.02
U-4	36.28	50.16	†62.48‡	†53.21	46.81	24.41
H-4	40.94	41.76	57.64‡	33.81	26.21	15.09
U-5	21.45	32.63	56.67	40.34	†63.66‡	51.73
H-5	24.80	48.28	75.39	47.70	75.42‡	55.00
U-6	12.32	11.58	28.10	39.64	56.20	65.87‡
H-6	14.35	12.97	49.28	33.99	†76.49	79.81‡
U-7	8.49	7.40	16.24	31.48	49.58	†75.41‡
H-7	7.75	8.18	23.86	22.58	53.49	†85.10‡
U-8	10.28	9.48	8.48	5.98	11.55	19.92‡
H-8	7.10	7.40	13.90	12.80	38.40	81.20‡

NOTE: Shaded background indicates larger comparative strain in HPC girder.
Bold indicates maximum strain for span among exterior and interior girders.
Italic indicates strain values NOT directly comparable based on sensor location and/or depth.
(‡) maximum strain for individual girder
(†) span maximum strain for Path

Transverse strain profiles should be treated as an approximate "envelope" of strain for the corresponding load path because strain data was not always available from sensors located nearest to the bottom of the girder stem at each midspan location (due to either temporary or permanent sensor malfunction). Furthermore, because the transverse strain profiles were created for a single moment in time during each path duration that corresponded closest to the maximum strain in all girders, there are instances in which the maximum strain for individual girders is not accurately depicted in the figure. Data points corresponding to the location of properly functioning sensors are simply connected linearly to provide a reasonable estimate of strain and may not reflect the true strain development at a given point in the span cross-section. It should be noted that data for girder U-8 is omitted from all transverse strain profile figures for purposes of clarity. Though data was available from the gauges in girder U-8, the validity of the data is questionable as consistently negligible strain (typically measuring less than 10 με) suggest permanent gauge malfunction.

Lastly, strains measured by selected individual VWSGs are also presented for the duration of selected load paths, such as in the sample plot in Figure 1.165. Once again, the sensors/data presented in figures of this type are those located at the lowest point in the girder cross-section at

the north and south midspan location, designated by EB-M-N and/or EB-M-S. Although these gauges do not always correspond exactly to the data in the tables previously discussed, they were chosen for comparison because (1) maximum strains were often measured at these locations and (2) because it provided a consistent comparison of strain data with respect to both the depth and symmetry of sensor locations. Furthermore, comparisons are primarily made between girder Line 3 (i.e., girders U-3 and H-3) and Line 6 (i.e., girders U-6 and H-6), located opposite of one another in the span cross-section, and for opposing load paths (e.g., Paths 1 and 6, Paths 2 and 5, Paths 3 and 4, and Paths 7 and 8).

With respect to the date in Figure 1.165, the gauges located in UHPC girders U-3 and U-6 (black lines) register larger strain at the beginning of the path due to the placement of the truck, which began each load path by loading the UHPC span first. As the path duration continues and the truck load moves onto the HPC span, measured strains eventually increases in the gauges located in girders H-3 and H-6 (gray lines)

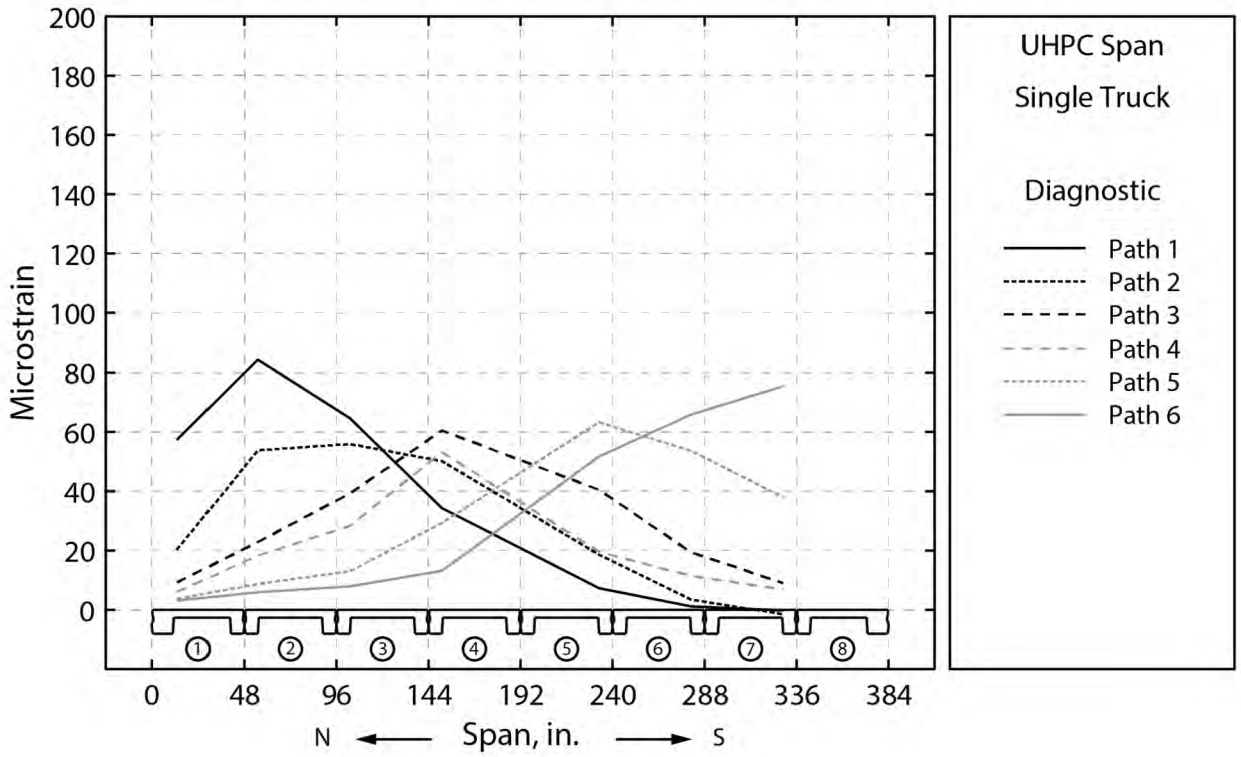


Figure 1.164: Sample plot showing the transverse strain profile for the UHPC span during Diagnostic Test under single truck loading for Paths 1-6.

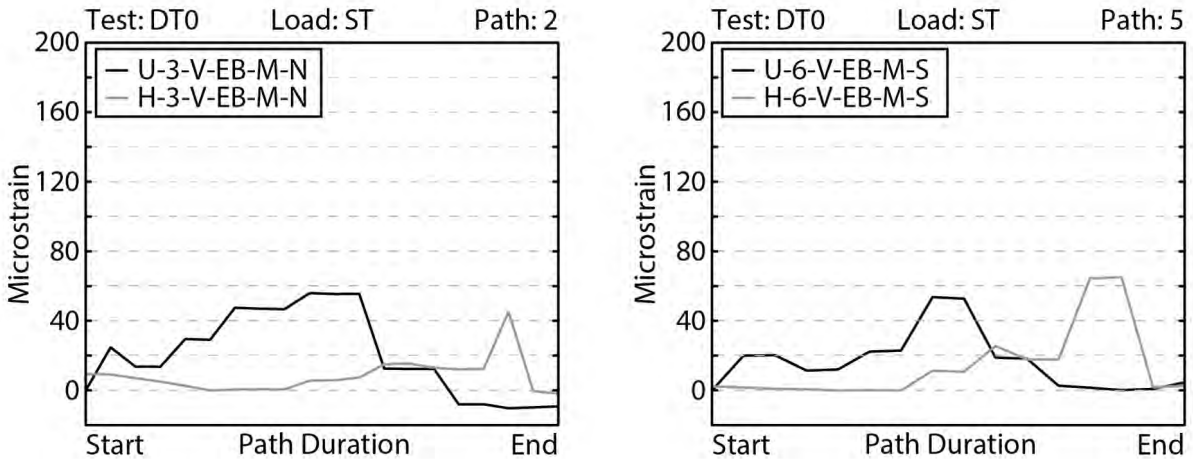


Figure 1.165: Sample plot showing selected midspan strains measured for single truck loading during the Diagnostic Test for (a) Path 2 in girders U-3/H-3 and (b) Path 5 for girders U-6/H-6.

1.8.8.1 Single Truck Loading

The maximum strains measured in each girder for all single truck (ST) load paths conducted during the four load tests are summarized in Table 1.138 through Table 1.141. To further illustrate the behavior of Bridge No. 9706 during field testing, the UHPC and HPC span transverse strain profiles for ST loading during each of the four load test are presented in Figure 1.167 and Figure 1.168, and direct comparisons of Paths 1 and 6 for each span during the four tests are provided in Figure 1.169. Next, strains measured in girder Line 3 and Line 6 for ST loading are presented in Figure 1.170 for the Diagnostic Test (DT0), Figure 1.171 for Proof Test 1 (PT1), Figure 1.172 for Proof Test 2 (PT2), and Figure 1.173 for Proof Test 3 (PT3). The data plots within the figure are arranged purposefully to provide a visual juxtaposition of the strain behavior for the opposing girder lines (i.e., Lines 3 and 6) and path loadings (i.e., Paths 1 and 6, Paths 2 and 5, Paths 3 and 4). Lastly, Figure 1.174 and Figure 1.175 provide direct comparisons of ST loading for girder Line 3–Path 1 and Line 6–Path 6 for each of the four load tests.



Figure 1.166: Path 1 single truck loading during field testing of Bridge No. 9706.

Comparing the strain data presented in the tables and figures for ST loading of NM Bridge No. 9706, the following observations were made:

- Maximum strains were generally greater for the HPC span during DT0. During subsequent proof tests, strains for Paths 1–3 tended to be larger for UHPC girders toward the middle and south end of the transverse span, and in HPC girders toward the north end of the transverse span for Paths 4–6.
  NOTE: As denoted by *italic* font in Table 1.138 through Table 1.141, data was unavailable from lower midspan sensors for girders H-4 during all load tests, and for H-7 during the three proof tests. Therefore, the reported values may not accurately reflect maximum strains for those girders, and it is conceivable that strains may have been greater in the HPC girders.
- Maximum overall strains for both the spans were measured when truck loads were nearest to each edge of the transverse span during Path 1 (Figure 1.166) and Path 6.
- Strains in both the UHPC and HPC span tended to be larger toward the north edge, and overall maximum strains measured in exterior girders typically occurred in girders U-1 and H-1 (except for PT3, in which maximum strain for the HPC span occurred H-8).
- As the truck paths moved further away from the edge of each span, the magnitude of strains typically decreased, indicating better distribution between adjacent girders.
- For interior girders, maximum strains consistently occurred in girders U-2 and H-2, further indicating greater strain was developed to the north side of each span.
- As illustrated in the transverse strain profiles of Figure 1.167 and Figure 1.168, maximum strains for Path 1–3 and sometimes 4 were often larger in the UHPC span for girders U-4 and U-5 for each of the three proof tests.
- The largest strains measured in girders U-3 and H-3 for ST loading typically occurred for Path 1, while the largest strains in girders U-6 and H-6 occurred under Path 6.
- For girders U-3 and U-6, strains were often similar in magnitude for the opposing load paths, while larger variance in strain magnitude was exhibited for girders H-3 and H-6.
- The magnitude of measured strains remained relatively consistent from year to year for both the UHPC and HPC spans, typically within an approximate range of ±20 με across all four load tests. Considering the variation in truck loads from each test (see reported truck loads in Section 1.2.1.1), the magnitude of measured strains from year to year for both the UHPC and HPC spans are within a reasonable range.
- A greater degree of strain symmetry was typically exhibited for the opposing girder lines and path loadings of the UHPC span.

Table 1.138: Summary of Maximum Measured Strains Under ST Loading for DT0

Girder	Strain (με)					
	Path 1	Path 2	Path 3	Path 4	Path 5	Path 6
U-1	76.30‡	34.70	21.50	9.30	6.60	8.70
H-1	†103.10‡	†78.30	37.40	21.20	9.00	6.40
U-2	†84.41‡	53.99	35.75	21.83	11.37	8.07
H-2	92.21‡	66.73	54.69	26.96	16.45	6.96
U-3	66.78‡	†55.93	39.23	28.31	12.98	9.01
H-3	55.25	60.82	†75.49‡	†51.33	36.32	14.02
U-4	36.28	50.16	†62.48‡	†53.21	46.81	24.41
H-4	40.94	41.76	57.64‡	33.81	26.21	15.09
U-5	21.45	32.63	56.67	40.34	†63.66‡	51.73
H-5	24.80	48.28	75.39	47.70	75.42‡	55.00
U-6	12.32	11.58	28.10	39.64	56.20	65.87‡
H-6	14.35	12.97	49.28	33.99	†76.49	79.81‡
U-7	8.49	7.40	16.24	31.48	49.58	†75.41‡
H-7	7.75	8.18	23.86	22.58	53.49	†85.10‡
U-8	10.28	9.48	8.48	5.98	11.55	19.92‡
H-8	7.10	7.40	13.90	12.80	38.40	81.20‡

NOTE: Shaded background indicates larger comparative strain in HPC girder.
Bold indicates maximum strain for span among exterior and interior girders.
Italic indicates strain values NOT directly comparable based on sensor location and/or depth.
(‡) maximum strain for individual girder
(†) span maximum strain for Path

Table 1.139: Summary of Maximum Measured Strains Under ST Loading for PT1

Girder	Strain (με)					
	Path 1	Path 2	Path 3	Path 4	Path 5	Path 6
U-1	65.70‡	40.00	12.50	6.80	4.80	4.00
H-1	†106.66‡	75.06	33.87	9.15	9.99	3.40
U-2	†84.25‡	†66.60	45.10	16.15	12.07	7.00
H-2	88.42‡	†78.69	54.22	13.31	15.92	5.80
U-3	60.46	61.11‡	40.52	22.89	15.03	5.92
H-3	71.28‡	71.10	†62.23	13.90	24.49	38.97
U-4	44.49	63.82	69.33‡	†64.07	52.63	26.86
H-4	33.39	44.81	47.84‡	†34.46	23.69	9.83
U-5	60.99	38.72	†70.36	49.38	†71.64‡	53.82
H-5	14.38	23.02	52.62	26.14	73.57‡	57.66
U-6	17.47	21.88	42.81	53.66	63.37	68.57‡
H-6	8.26	26.04	28.22	24.46	†73.58	87.76‡
U-7	10.38	14.98	27.19	37.53	54.21	†69.88‡
H-7	7.52	9.43	19.46	16.79	41.51	57.63‡
U-8	13.48	8.45	7.15	6.73	10.78	20.99‡
H-8	8.48	6.83	18.11	18.92	43.05	†89.29‡

NOTE: Shaded background indicates larger comparative strain in HPC girder.
Bold indicates maximum strain for span among exterior and interior girders.
Italic indicates strain values NOT directly comparable based on sensor location and/or depth.
(‡) maximum strain for individual girder
(†) span maximum strain for Path

Table 1.140: Summary of Maximum Measured Strains Under ST Loading for PT2

Girder	Strain (με)					
	Path 1	Path 2	Path 3	Path 4	Path 5	Path 6
U-1	85.70‡	39.50	16.80	10.80	4.80	3.80
H-1	†115.13‡	72.00	22.73	11.15	5.49	5.19
U-2	†95.35‡	†70.86	44.08	21.20	8.93	6.07
H-2	96.72‡	83.87	52.10	27.47	9.75	5.99
U-3	74.59‡	69.71	49.61	24.45	11.83	6.08
H-3	72.70	†73.78‡	41.47	30.61	14.62	8.81
U-4	44.87	68.94	†74.23‡	66.40	44.02	28.62
H-4	33.28	49.06	52.27‡	44.83	25.03	12.67
U-5	20.54	45.53	71.35	†72.62‡	†67.67	56.86
H-5	13.03	25.39	†55.43	†77.81	80.86‡	70.12
U-6	9.34	16.89	44.75	51.91	67.04	†73.53‡
H-6	6.88	13.26	30.24	40.89	†84.64	†92.64‡
U-7	7.14	8.60	27.19	34.34	63.15	73.09‡
H-7	7.60	8.81	19.06	27.50	52.03	63.94‡
U-8	10.92	6.21	9.31	12.49	14.39	20.68‡
H-8	8.62	6.73	13.89	19.06	54.39	90.27‡

NOTE: Shaded background indicates larger comparative strain in HPC girder.
Bold indicates maximum strain for span among exterior and interior girders.
Italic indicates strain values NOT directly comparable based on sensor location and/or depth.
(‡) maximum strain for individual girder
(†) span maximum strain for Path

Table 1.141: Summary of Maximum Measured Strains Under ST Loading for PT3

Girder	Strain (με)					
	Path 1	Path 2	Path 3	Path 4	Path 5	Path 6
U-1	89.70‡	45.90	16.90	7.20	5.90	5.20
H-1	99.17‡	58.31	26.94	11.65	5.99	4.64
U-2	†102.84‡	74.40	47.26	21.10	11.75	12.02
H-2	†108.81‡	†87.89	†64.92	33.35	12.33	5.36
U-3	80.48‡	†77.85	52.13	25.39	12.03	5.66
H-3	75.76‡	74.59	48.73	34.62	17.65	7.70
U-4	49.61	70.16	†76.84‡	71.40	48.31	24.88
H-4	32.76	51.33	54.95‡	45.32	28.11	11.27
U-5	22.68	43.77	72.51	†81.70‡	75.04	55.43
H-5	13.18	25.67	50.22	†86.30	89.24‡	62.02
U-6	9.40	21.12	43.63	68.33	†75.08	78.39‡
H-6	7.47	13.44	27.85	55.44	†91.46	101.45‡
U-7	6.72	16.16	32.61	50.81	69.22	†89.59‡
H-7	9.08	10.29	19.36	34.83	52.65	71.49‡
U-8	11.59	12.99	11.27	9.05	16.04	25.99‡
H-8	8.75	10.17	12.78	27.60	56.22	†105.98‡

NOTE: Shaded background indicates larger comparative strain in HPC girder.
Bold indicates maximum strain for span among exterior and interior girders.
Italic indicates strain values NOT directly comparable based on sensor location and/or depth.
(‡) maximum strain for individual girder
(†) span maximum strain for Path

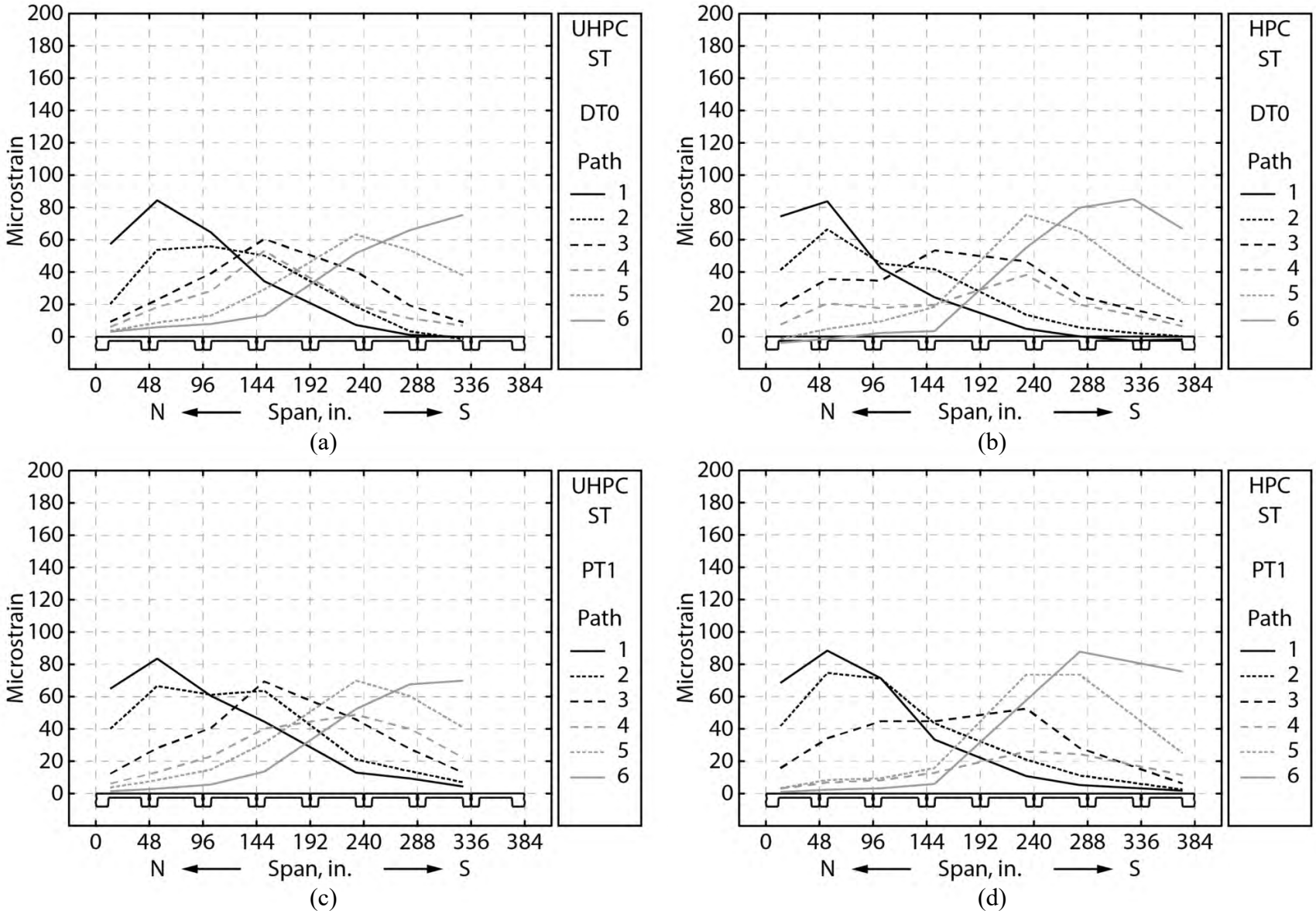


Figure 1.167: UHPC and HPC transverse strain profiles for ST load Paths 1-6: Diagnostic Test (a and b) and Proof Test 1 (c and d).

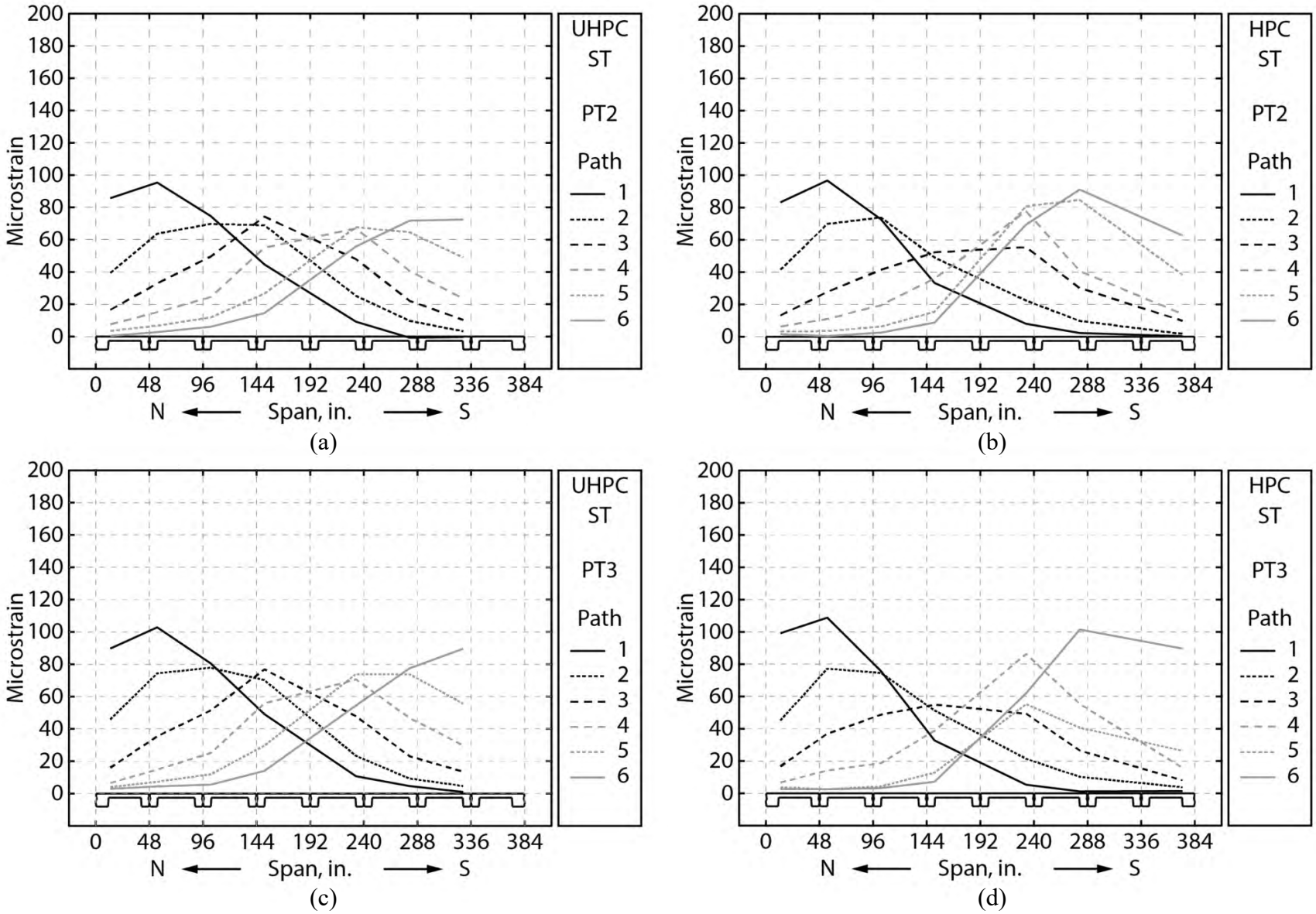


Figure 1.168: UHPC and HPC transverse strain profiles for ST load Paths 1-6: Proof Test 2 (a and b) and Proof Test 3 (c and d).

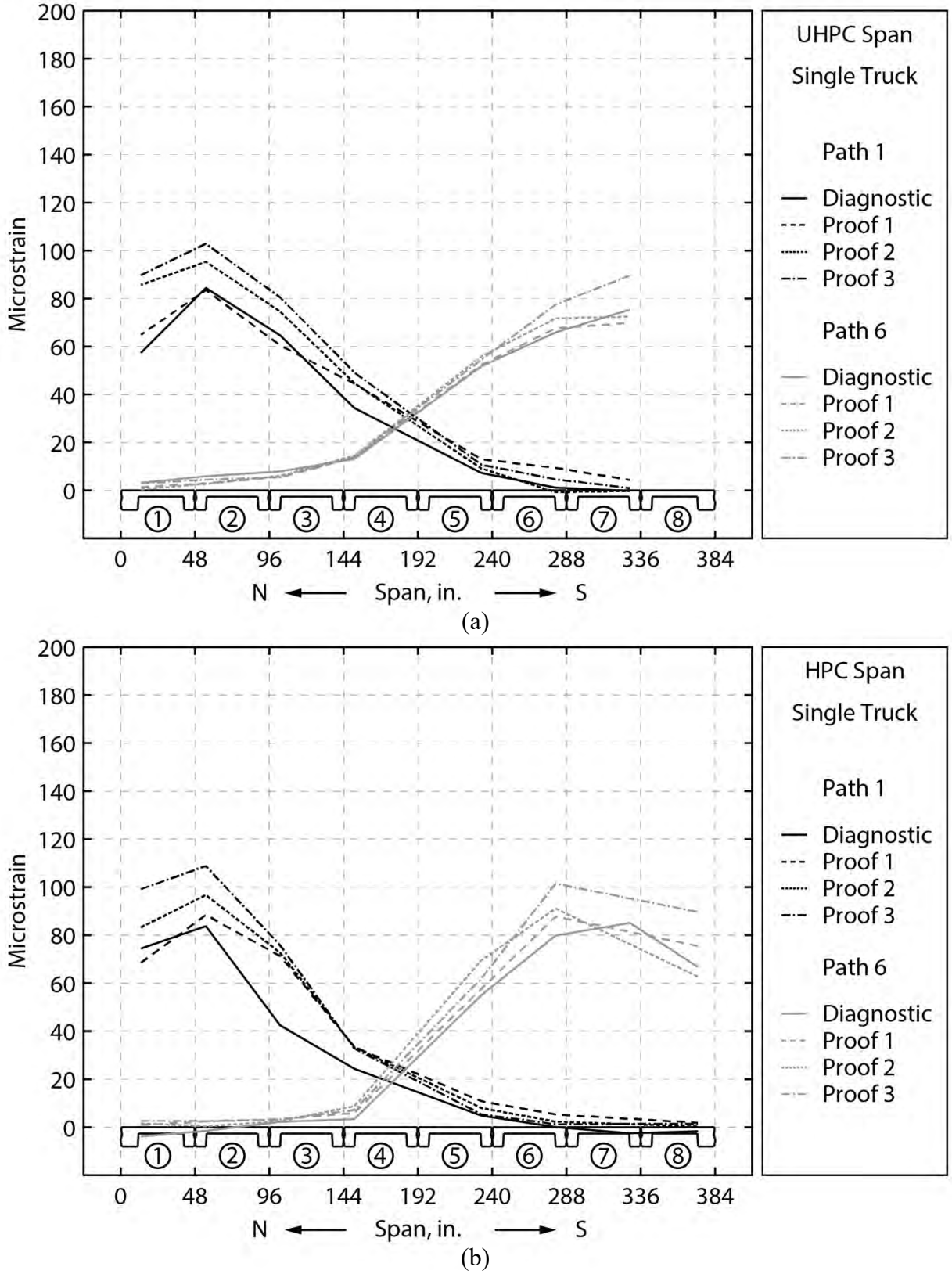


Figure 1.169: Comparison of transverse strain profiles of each load test for ST load Paths 1 and 6 for the (a) UHPC span and (b) HPC span.

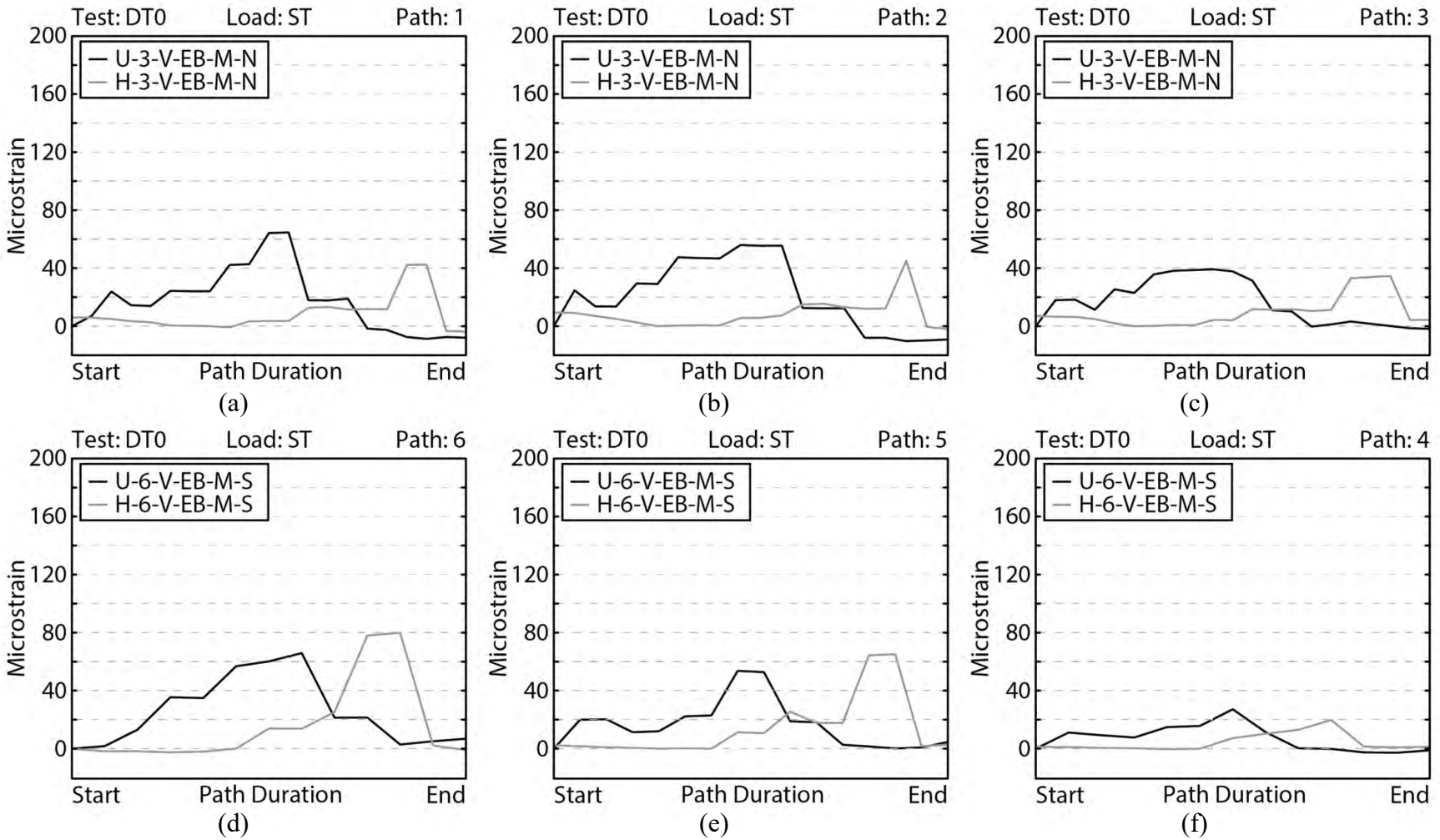


Figure 1.170: Strains for ST loading during DT0 for U-3/H-3 (a) Path 1, (b) Path 2, (c) Path 3, and U-6/H-6 (d) Path 6, (e) Path 5, (f) Path 4.

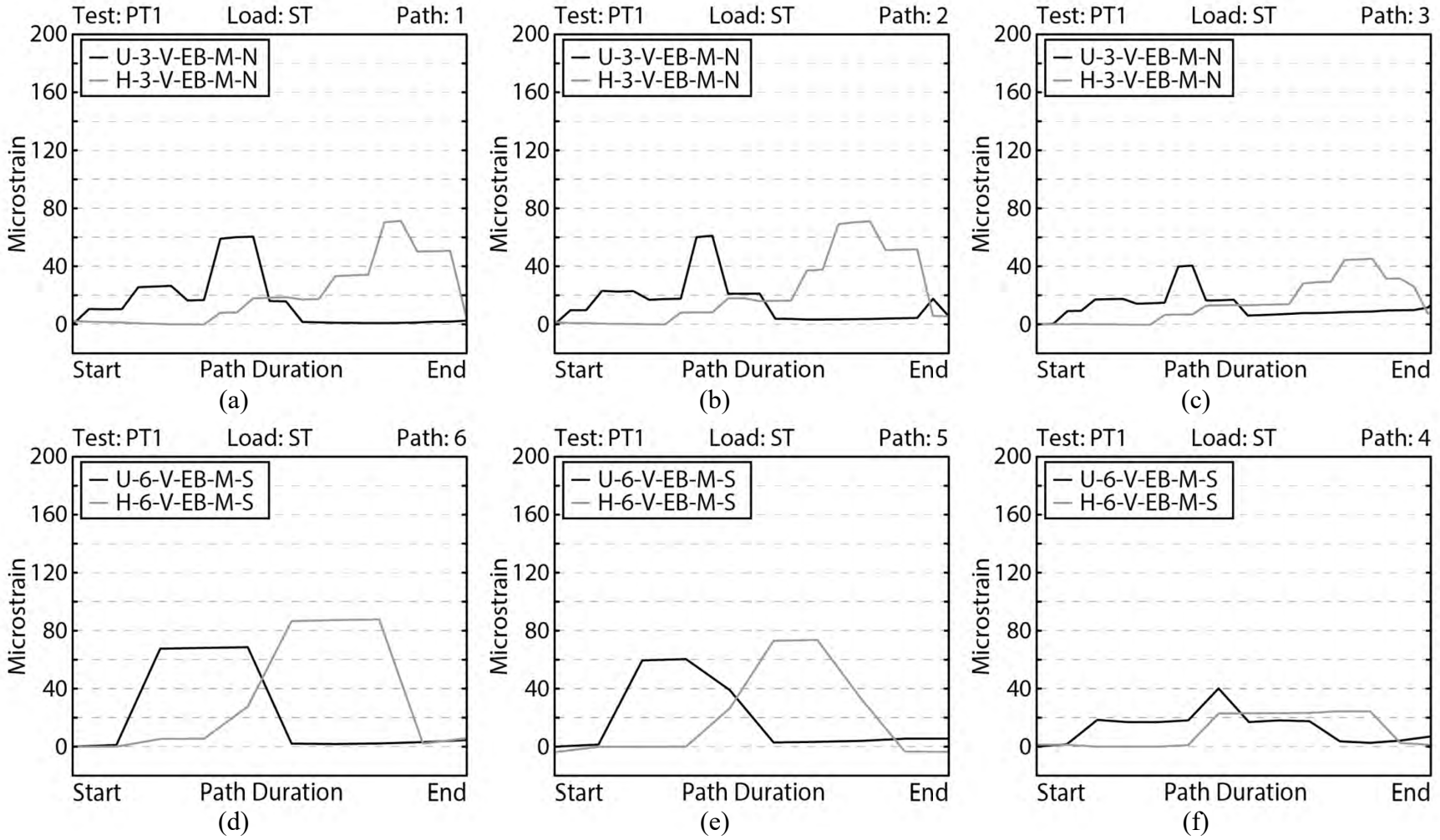


Figure 1.171: Strains for ST loading during PT1 for U-3/H-3 (a) Path 1, (b) Path 2, (c) Path 3, and U-6/H-6 (d) Path 6, (e) Path 5, (f) Path 4.

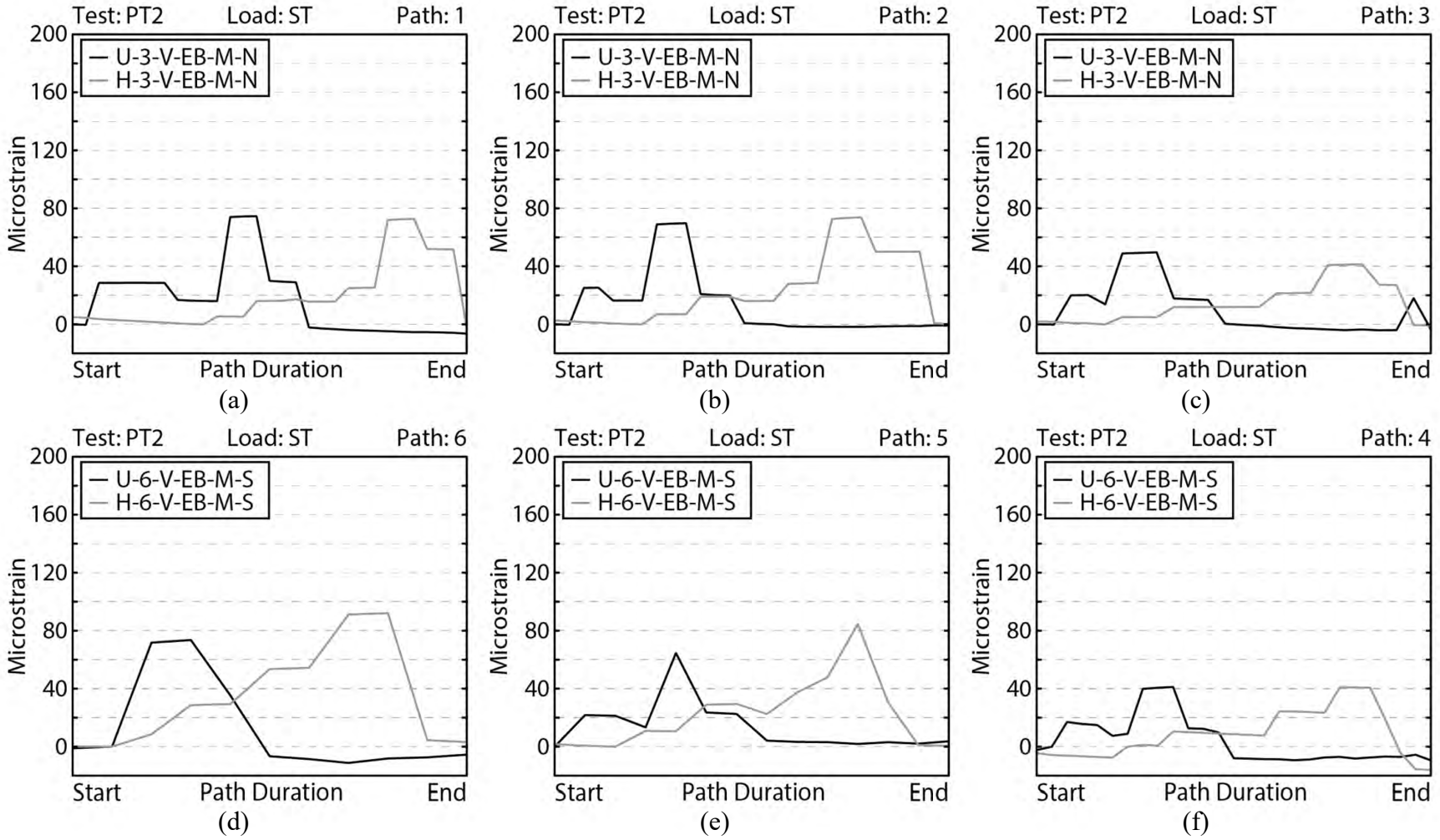


Figure 1.172: Strains for ST loading during PT2 for U-3/H-3 (a) Path 1, (b) Path 2, (c) Path 3, and U-6/H-6 (d) Path 6, (e) Path 5, (f) Path 4.

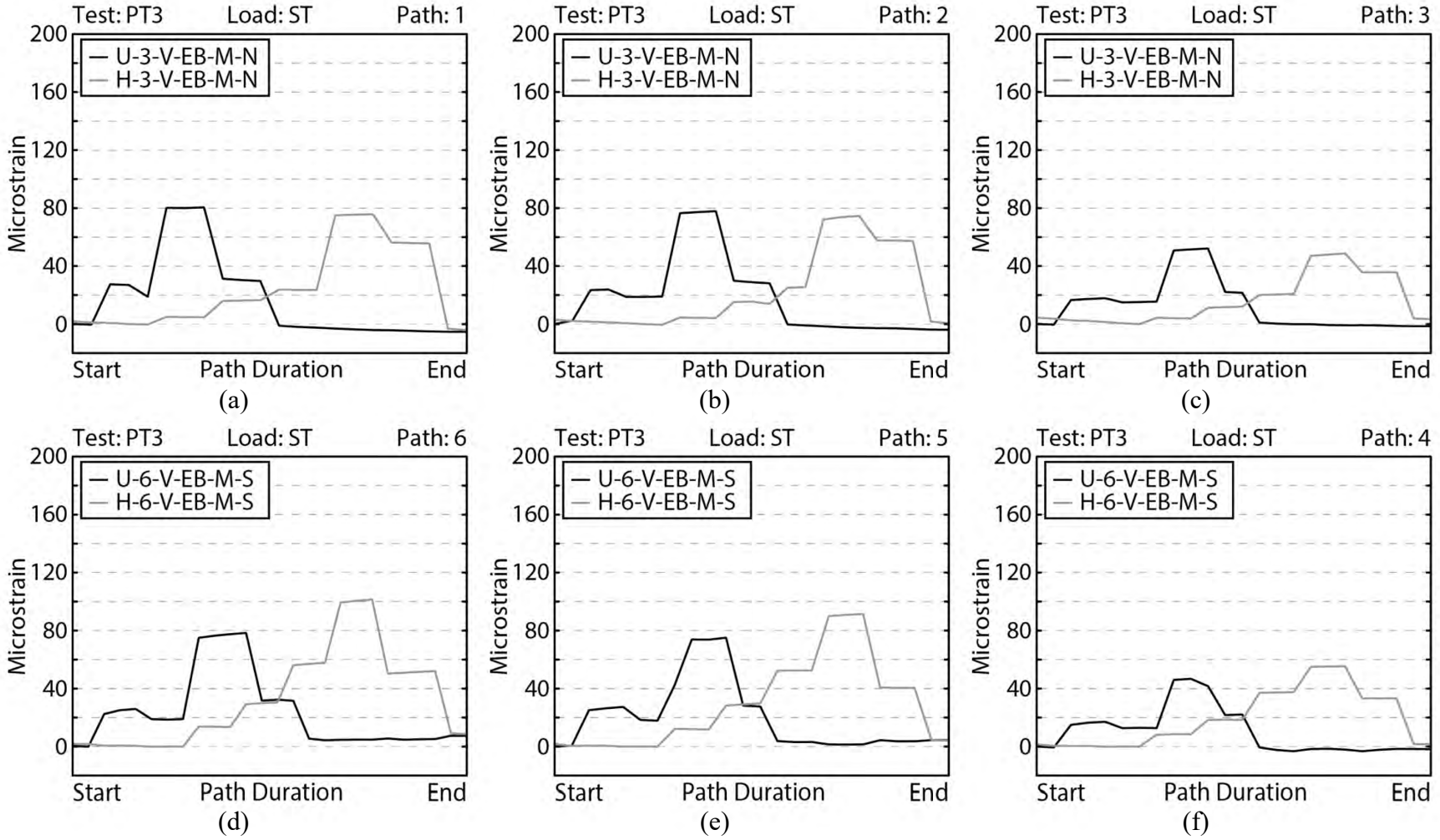


Figure 1.173: Strains for ST loading during PT3 for U-3/H-3 (a) Path 1, (b) Path 2, (c) Path 3, and U-6/H-6 (d) Path 6, (e) Path 5, (f) Path 4.

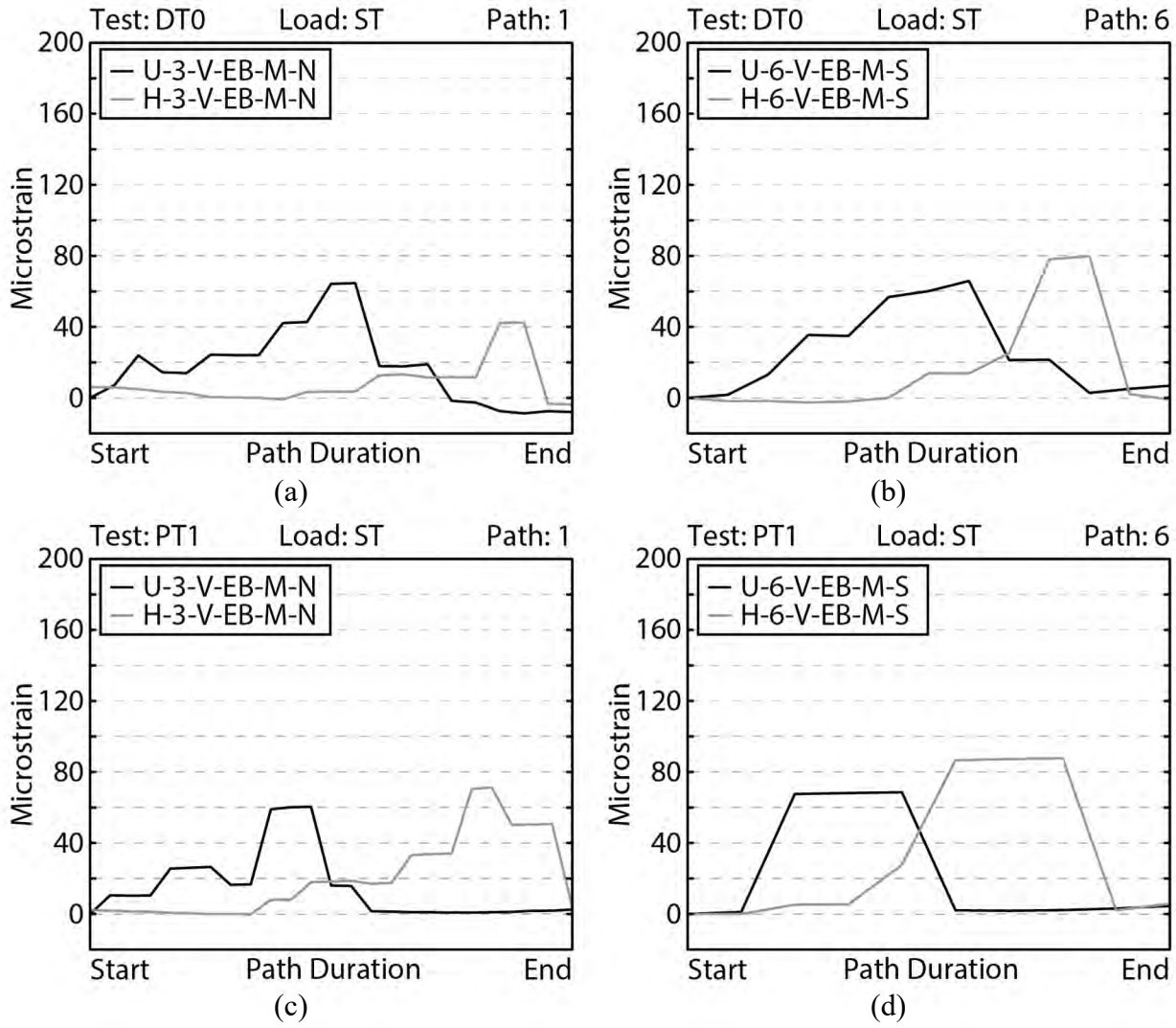


Figure 1.174: Comparison of strains for girder Lines 3 and 6 under ST loading for DT0 (a and b) and PT1 (c and d).

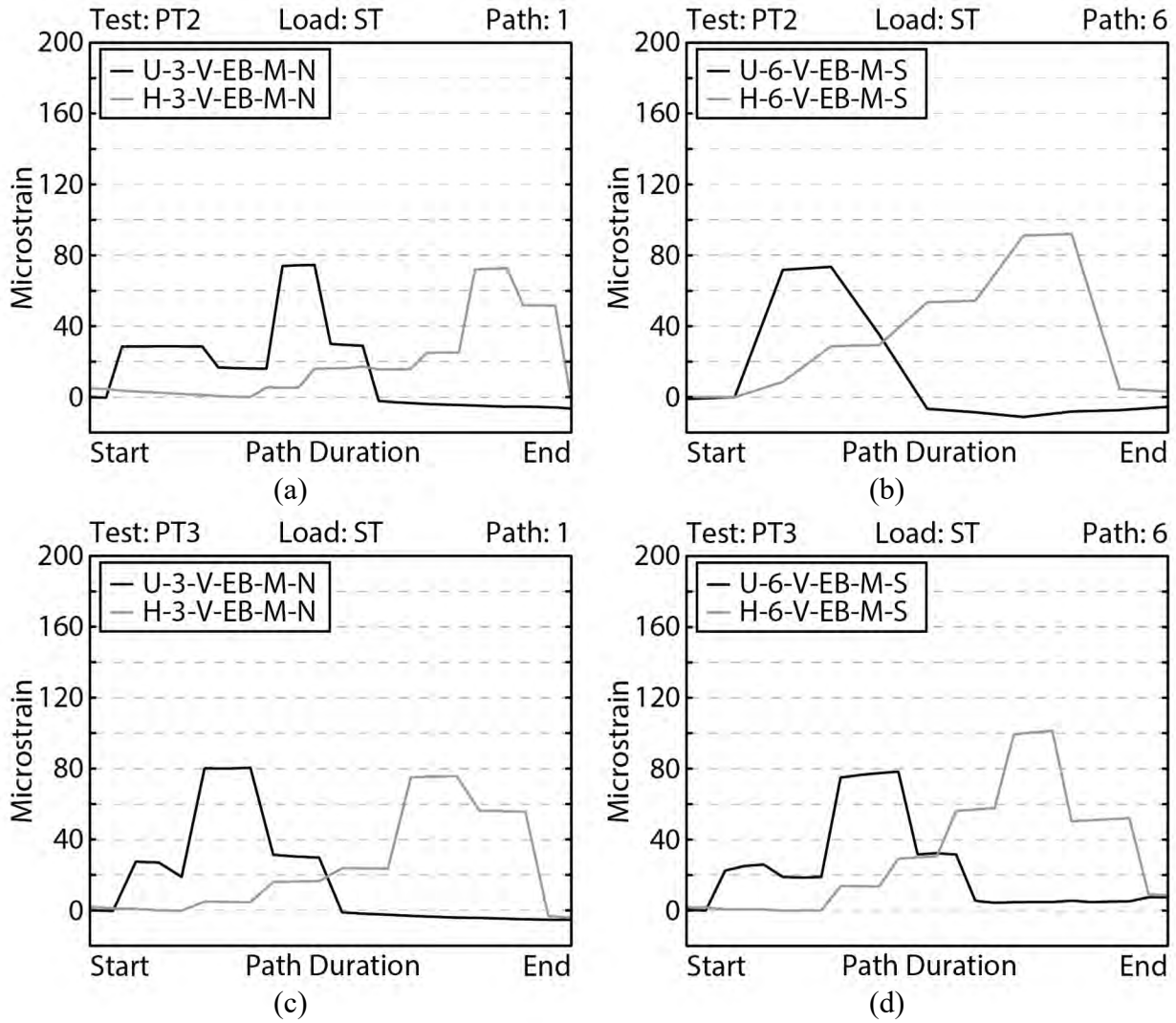


Figure 1.175: Comparison of strains for girder Lines 3 and 6 under ST loading for PT2 (a and b) and PT3 (c and d).

1.8.8.2 Double Truck Loading

The maximum strains measured in each girder for all double truck (DT) load paths conducted during DT0, PT1, and PT3 are summarized in Table 1.142 through Table 1.144 (DT loading was not conducted for PT2). To further illustrate the behavior of Bridge No. 9706 during field testing, the UHPC and HPC span transverse strain profiles for DT loading during each load test are presented in Figure 1.177 and Figure 1.178, and direct comparison of Paths 7 and 8 for each span during the three tests in which DT loading was conducted are provided Figure 1.179. Next, strains measured in girder Line 3 and Line 6 for DT loading are presented in Figure 1.180 for DT0, Figure 1.181 for PT1, and Figure 1.182 for PT3. The data plots within the figure are arranged purposefully to provide a visual juxtaposition of the strain behavior for the opposing girder lines (i.e., Lines 3 and 6) and path loadings (i.e., Paths 7 and 8). Lastly, Figure 1.183 provides direct comparisons of DT loading for girder Line 3–Path 7 and Line 6–Path 8 for each of the load tests.

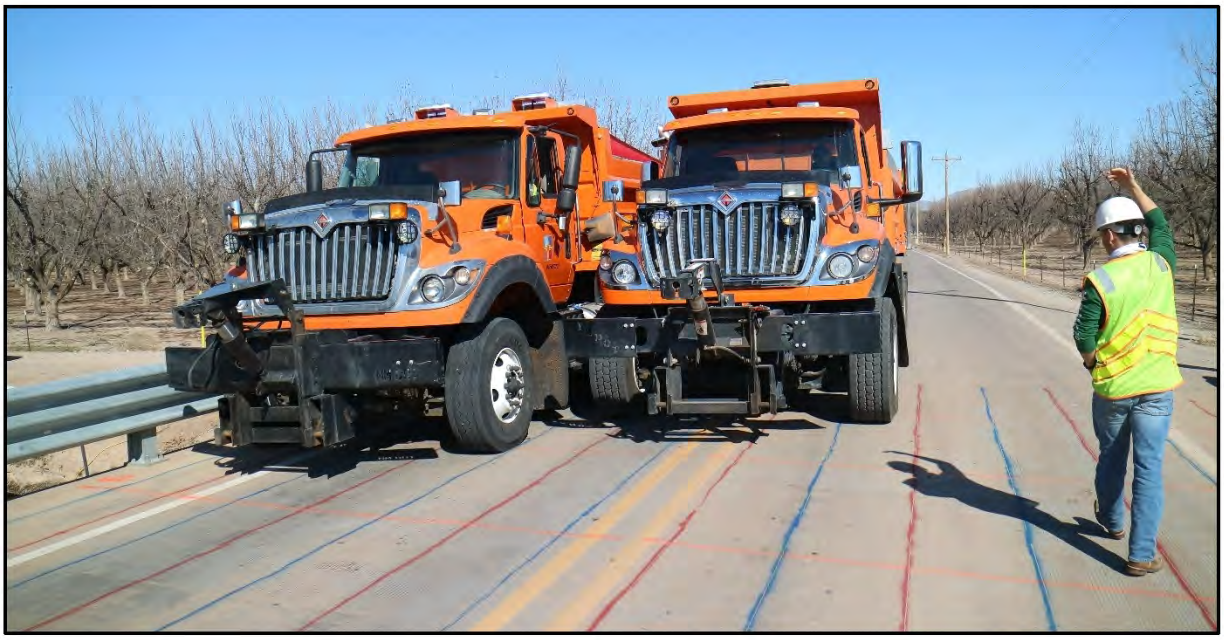


Figure 1.176: Double truck loading during field testing of Bridge No. 9706.

Comparing the strain data presented in the tables and figures for DT loading of NM Bridge No. 9706, the following observations were made:

- Load Paths 7, 8, and 9 were conducted for DT loading during DT0. However, it was determined that Path 9 only produced maximum strain in three girders (H-4, H-5, and U-5), and the magnitude of those strains were comparable to the strains for Paths 7 and 8. Therefore, Path 9 was not conducted during subsequent load testing.
- Maximum strains were generally greater for the HPC span during DT0, with only strains in girder U-4 surpassing the comparative strain of H-4. During subsequent proof tests, maximum strains in the UHPC span were greater for girder Lines 4–6 under Path 7, and for Lines 4 and 6 under Path 8.
  NOTE: As denoted by *italic* font in Table 1.142 through Table 1.144, data was unavailable from lower midspan sensors for girders H-4 and H-7. Therefore, the reported values may not accurately reflect maximum strains for those girders, and it is conceivable that strains may have been greater in the HPC girders.
- Maximum overall strains among exterior girders generally occurred in girder Line 1 for both the UHPC and HPC, except for PT3 in which the maximum strain for the HPC span occurred in H-8. The location of overall maximum strains among interior girders was more variable. Maximum strains for interior girders in both the UHPC and HPC spans occurred in girder Line 2 for DT0, and in Line 5 for PT1. For PT3, maximum interior girder strains occurred in girders U-2 and H-6.
- Strains were expectedly maximized on the north end of the transverse span under Path 7, and on the south end under Path 8.
- Both the UHPC and HPC spans exhibited relatively symmetric strain behavior for double truck loading. However, strains in the UHPC span tended to be larger toward the north end of the transverse span, while strains in the HPC span tended to be larger toward the south end.
- Comparing the strains during PT1 and PT3 for Path 7 and 8 in Figure 1.181 and Figure 1.182, and accounting for the expected changes of magnitude due to heavier truck loads during PT3, the strain behaviors exhibited by each girder are nearly identical between the two test which occurred two years apart. Furthermore, girder Lines 3 and 6 exhibit highly symmetric strain behaviors for both the UHPC and HPC spans under DT loading.
- Considering the variation in truck loads from each test (see reported truck loads in Section 1.2.1.1), the magnitude of measured strains from year to year for both the UHPC and HPC spans are within a reasonable range.

Table 1.142: Summary of Maximum Measured Strains Under DT Loading for DT0

Girder	Strain (με)		
	Path 7	Path 8	Path 9
U-1	†140.20‡	14.40	79.00
H-1	†140.30‡	27.50	84.70
U-2	114.68‡	32.06	74.44
H-2	120.88‡	42.45	93.94
U-3	109.15‡	39.07	73.09
H-3	116.20‡	76.45	116.81
U-4	108.76‡	83.99	97.05
H-4	85.68	51.36	91.93‡
U-5	94.80	†102.35	†106.43‡
H-5	97.03	119.58	†123.53‡
U-6	56.57	93.30‡	73.44
H-6	77.27	†125.20‡	115.35
U-7	36.20	90.35‡	60.87
H-7	37.52	115.32‡	72.81
U-8	6.89	22.40‡	11.69
H-8	21.80	108.30‡	45.50

NOTE: Shaded background indicates larger comparative strain in HPC girder.
Bold indicates maximum strain for span among exterior and interior girders.
Italic indicates strain values NOT directly comparable based on sensor location and/or depth.
(‡) maximum strain for individual girder
(†) span maximum strain for Path

Table 1.143: Summary of Maximum Measured Strains Under DT Loading for PT1

Girder	Strain (με)	
	Path 7	Path 8
U-1	71.80‡	11.50
H-1	†129.95‡	35.44
U-2	†104.51‡	37.15
H-2	118.76‡	57.27
U-3	92.44‡	37.44
H-3	113.68‡	73.60
U-4	103.48‡	73.60
H-4	69.79‡	52.83
U-5	97.05	†105.95‡
H-5	94.62	†130.48‡
U-6	63.52	88.15‡
H-6	56.28	125.22‡
U-7	50.99	81.77‡
H-7	33.74	71.14‡
U-8	7.00	25.46‡
H-8	32.46	108.24‡

NOTE: Shaded background indicates larger comparative strain in HPC girder.
Bold indicates maximum strain for span among exterior and interior girders.
Italic indicates strain values NOT directly comparable based on sensor location and/or depth.
(‡) maximum strain for individual girder
(†) span maximum strain for Path

Table 1.144: Summary of Maximum Measured Strains Under DT Loading for PT3

Girder	Strain (με)	
	Path 7	Path 8
U-1	96.60‡	10.90
H-1	115.11‡	21.87
U-2	†129.40‡	31.16
H-2	†149.62‡	46.48
U-3	122.26‡	34.55
H-3	147.43‡	42.86
U-4	128.82‡	85.45
H-4	87.82‡	56.81
U-5	105.06	†122.22‡
H-5	73.98	145.92‡
U-6	64.77	118.56‡
H-6	39.08	†154.96‡
U-7	42.04	117.07‡
H-7	25.34	88.44‡
U-8	6.32	37.26‡
H-8	19.67	134.15‡

NOTE: Shaded background indicates larger comparative strain in HPC girder.
Bold indicates maximum strain for span among exterior and interior girders.
Italic indicates strain values NOT directly comparable based on sensor location and/or depth.
(‡) maximum strain for individual girder
(†) span maximum strain for Path

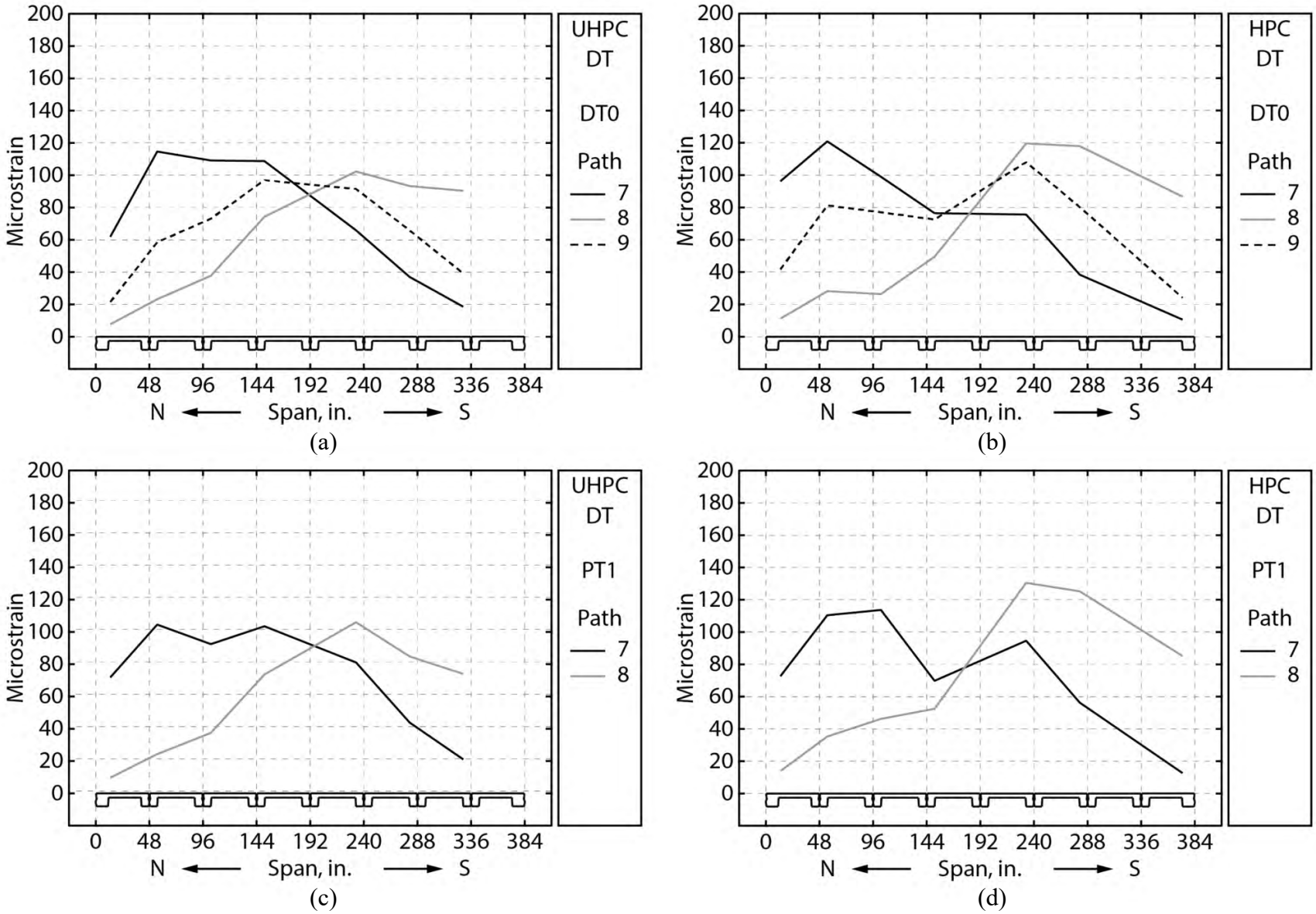


Figure 1.177: UHPC and HPC transverse strain profiles for DT load Paths 7-8: Diagnostic Test (a and b) and Proof Test 1 (c and d).

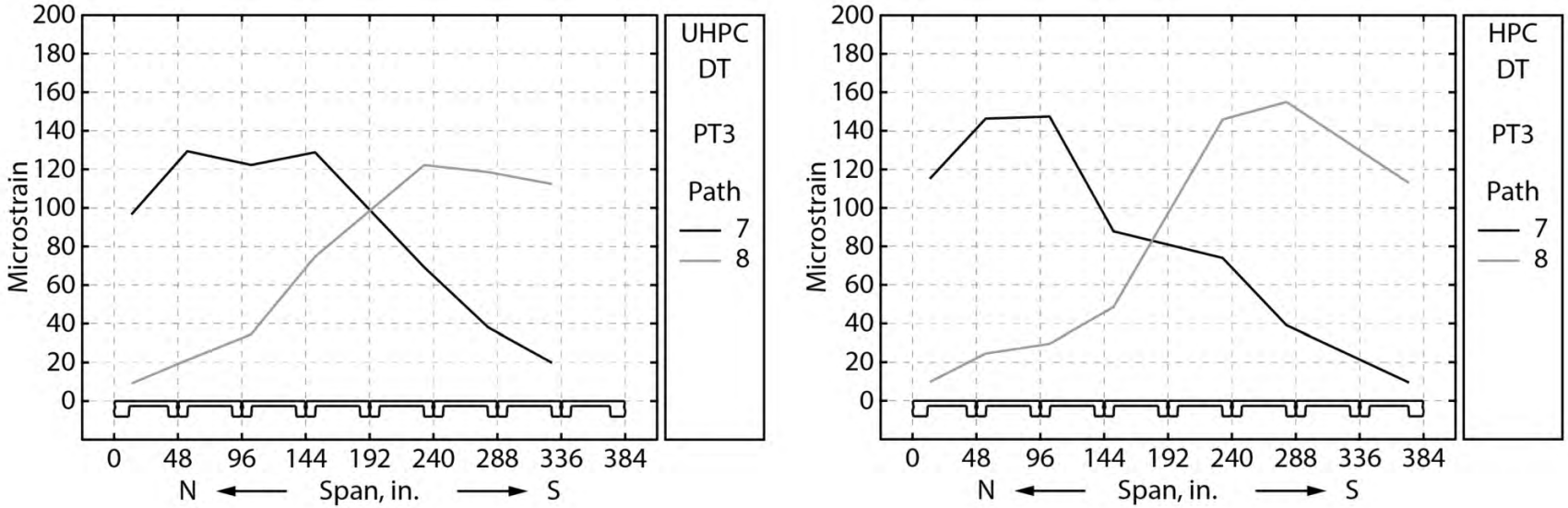


Figure 1.178: UHPC and HPC transverse strain profiles for DT load Paths 7-8 for Proof Test 3.

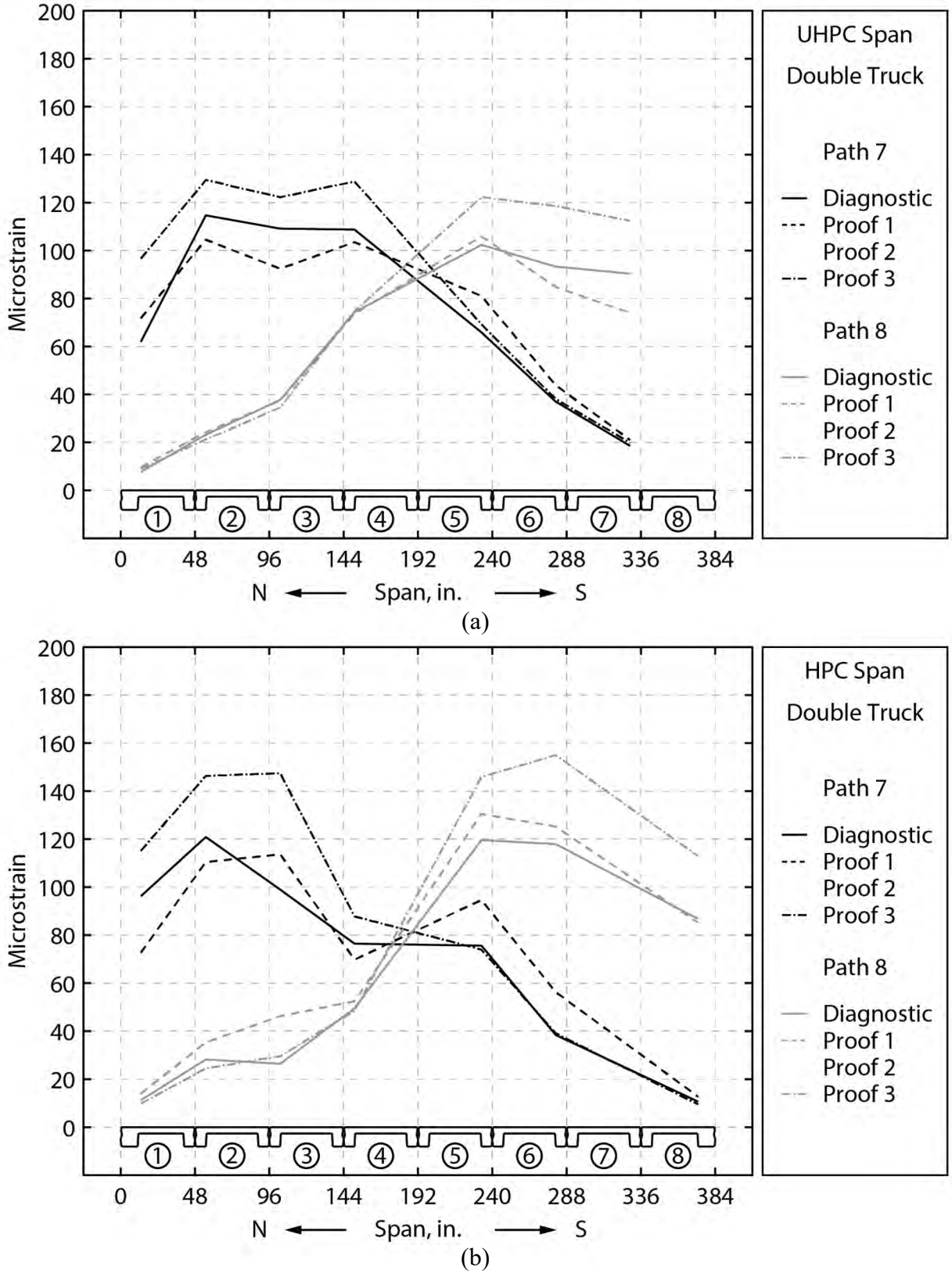


Figure 1.179: Comparison of transverse strain profiles of each load test for DT load Paths 7 and 8 for the (a) UHPC span and (b) HPC span.

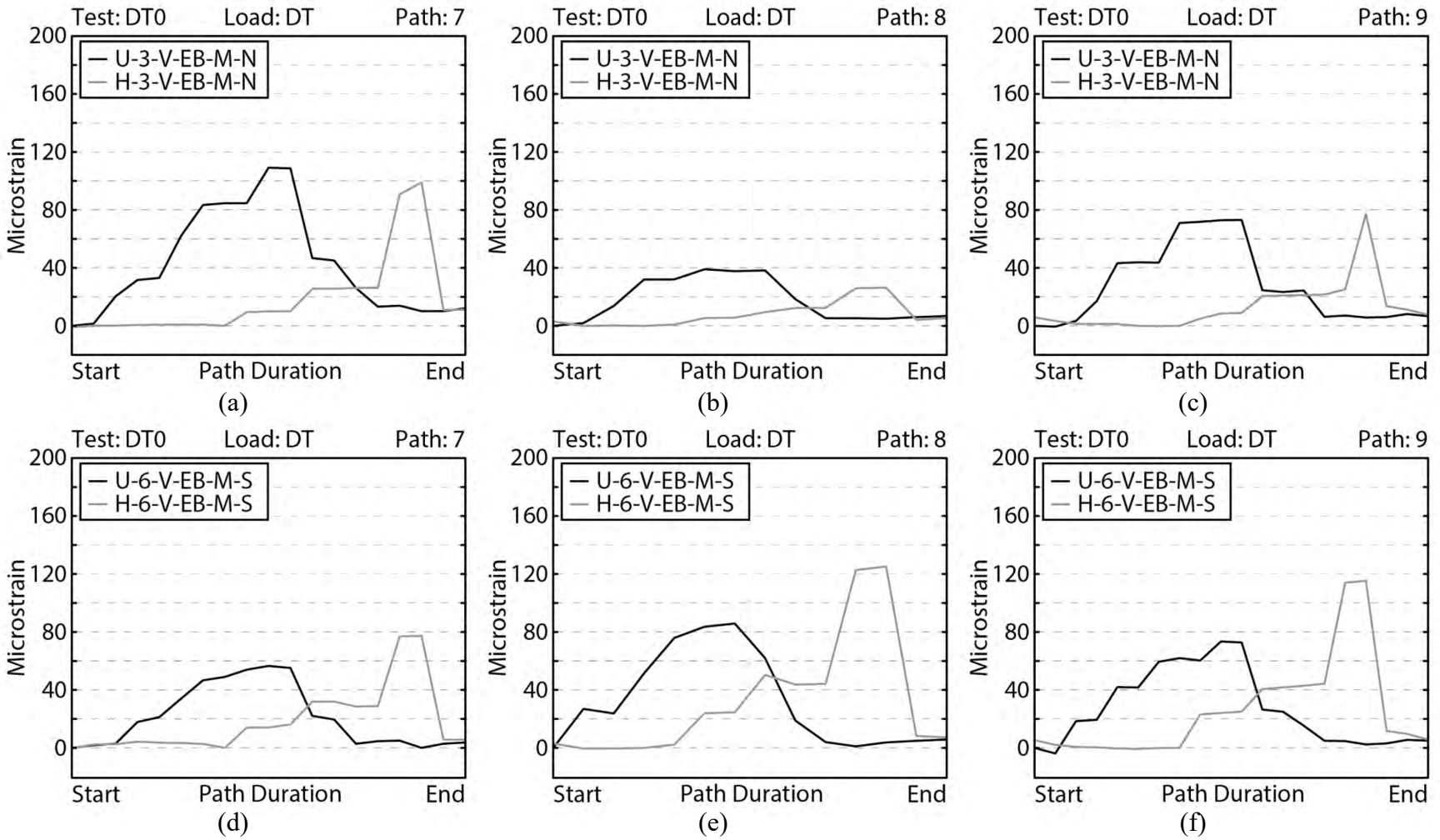


Figure 1.180: Strains for DT loading during DT0 for U-3/H-3 (a) Path 7, (b) Path 8, (c) Path 9, and U-6/H-6 (d) Path 7, (e) Path 8, (f) Path 9.

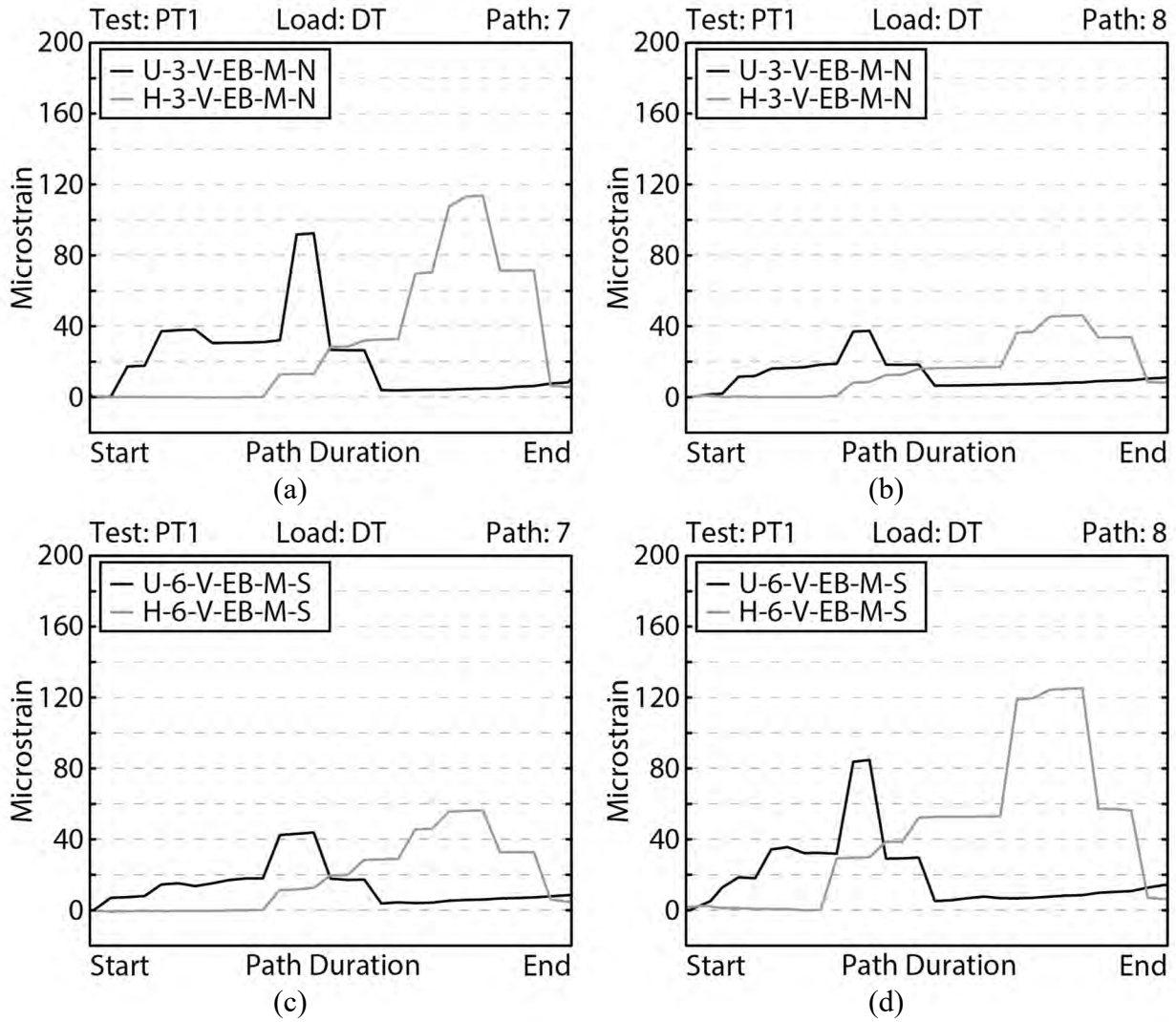


Figure 1.181: Strains for DT loading during PT1 for U-3/H-3 (a) Path 7 and (b) Path 8, and U-6/H-6 (c) Path 7 and (d) Path 8.

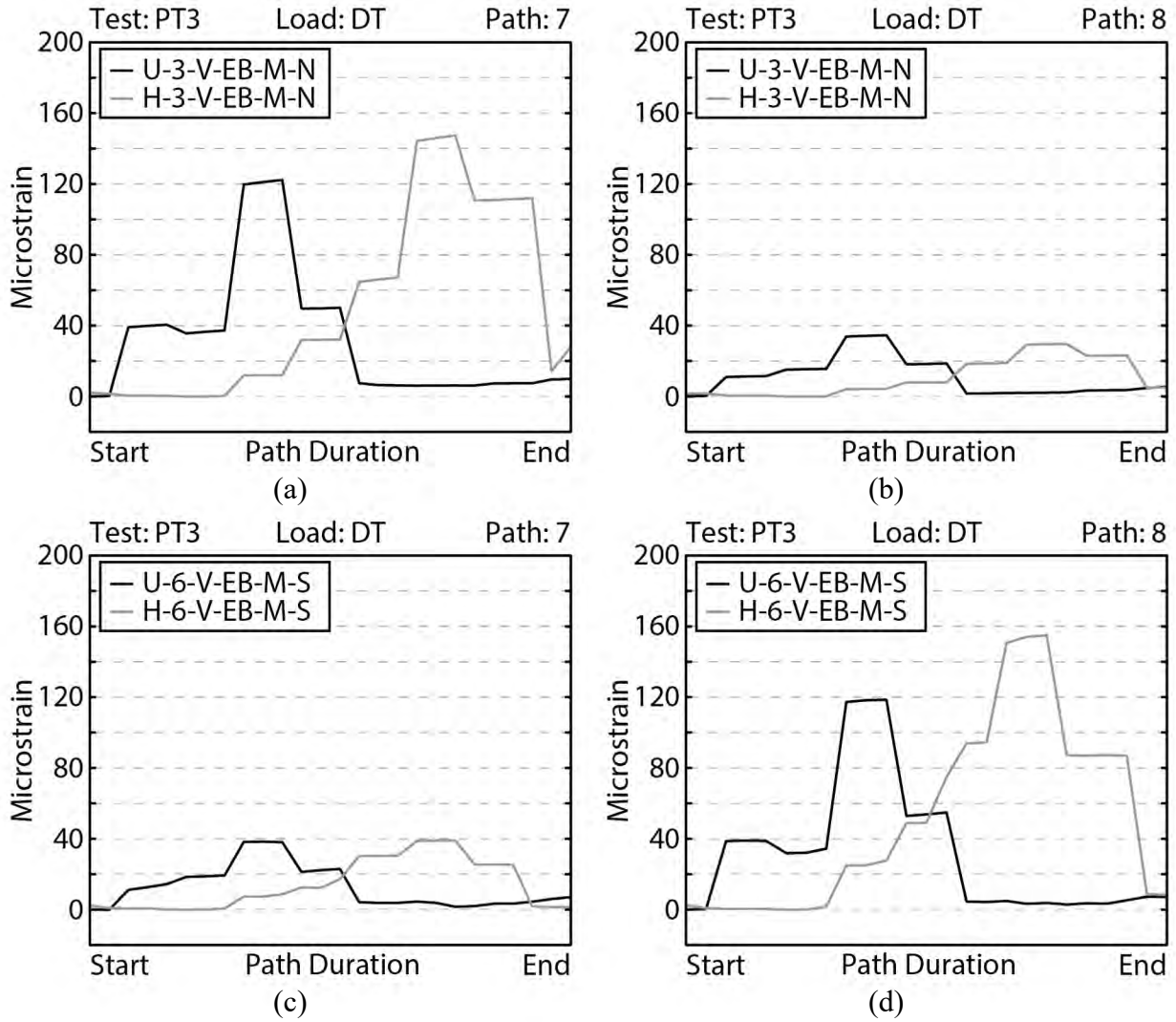


Figure 1.182: Strains for DT loading during PT3 for U-3/H-3 (a) Path 7 and (b) Path 8, and U-6/H-6 (c) Path 7 and (d) Path 8.

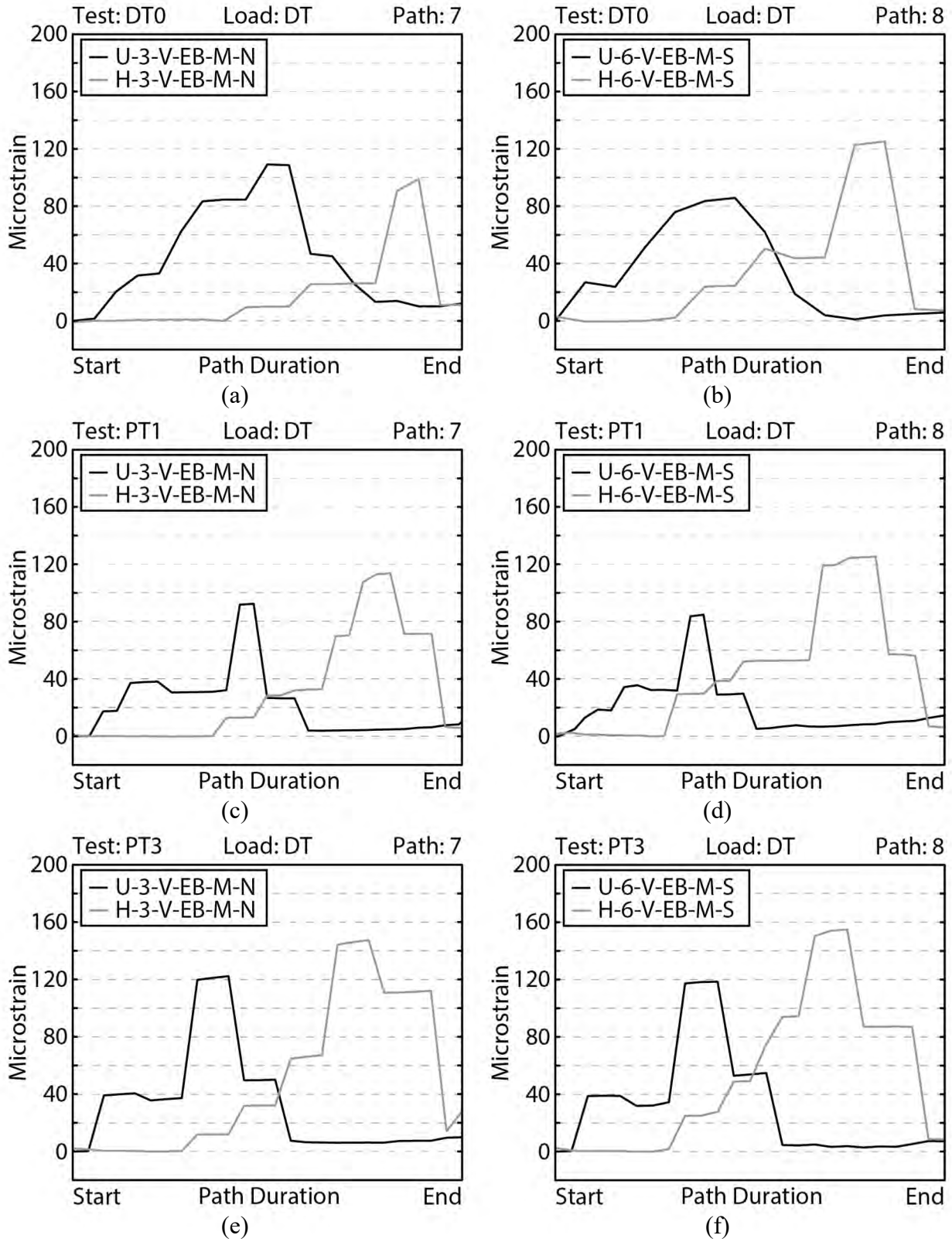


Figure 1.183: Comparison of strains for girder Lines 3 and 6 under DT loading: DT0 (a and b), PT1 (c and d), and PT3 (e and f).

1.8.8.3 Triple Truck Loading

The maximum strains measured in each girder for all triple truck (TT) load paths conducted during the three proof tests are summarized in Table 1.145. To further illustrate the behavior of Bridge No. 9706 during field testing, the UHPC and HPC span transverse strain profiles for TT loading during each load test are presented in Figure 1.185 and Figure 1.186, and direct comparison of Path 10 (Pass 2) for each span during the three proof tests are provided in Figure 1.187. Next, strains measured in girder Line 3 and Line 6 for TT loading are presented in Figure 1.188 for PT1, Figure 1.189 for PT2, and Figure 1.190 for PT3. Lastly, Figure 1.191 provides direct comparisons of Line 3 and Line 6 under TT Path 10 (Pass 2) loading during the three proof tests.

Comparing the strain data presented in the tables and figures for TT loading of NM Bridge No. 9706, the following observations were made:

- Strains were consistently greater in the HPC span for all girder lines except for Line 4 and Line 7 under Path 10 triple truck loading. **NOTE:** As denoted by *italic* font in Table 1.145, data was unavailable from lower midspan sensors for girders H-4 and H-7. Therefore, the reported values may not accurately reflect maximum strains for those girders, and it is conceivable that strains may have been greater in the HPC girders.
- Although trucks were always placed to provide as much consistency between load paths and tests, Path 10 loading required precise truck placement due to the tight spacing of three trucks across the width of the bridge (as shown in Figure 1.184), and so Path 10 triple truck loading was the easiest load configuration to replicate, both from one pass to another and between tests.
- Maximum strains exhibited by both spans of Bridge No. 9706 generally increased during each subsequent proof test as a result of increasing truck loads. However, placement of the trucks resulted in highly consistent strain behaviors in both spans of Bridge No. 9706.
- Maximum overall strains among exterior girders generally occurred in girder Line 1 for both the UHPC and HPC, except for PT3 in which the maximum strain for the HPC span occurred in H-8.
- Strains among interior girders during TT loading were expectedly maximized in girder Lines 4, 5, and 6.
- Triple truck loading was always repeated during each load test (PT1, PT2, and PT3), and was typically conducted on separate days. Still, Figure 1.185 through Figure 1.186 illustrate the highly consistent results for Path 10 from one pass to another. Similarly, Figure 1.187 illustrates the consistency of strain behavior for Path 10 for each proof test.
- Direct comparisons of TT loading in Figure 1.191 for opposing girder Lines 3 and 6 illustrates strain development over the duration of Path 10 loading. The strain behaviors during PT2 (Figure 1.191-b and -d) are visually dissimilar to the other proof tests because the trucks were stopped at fewer load stations due to time constraints. However, strain behaviors are very similar between PT1 and PT3, and the magnitudes of strain for each test show an increasing trend corresponding to the increase in average truck weight for each successive load test.



(a)



(b)

Figure 1.184: Path 10 triple truck load configuration during field testing of NM Bridge No. 9706: (a) Aligned prior to loading and (b) positioned over the bridge central pier.

Table 1.145: Summary of Maximum Measured Strains Under TT Loading During Proof Testing.

Girder	Strain (με)		
	Path 10		
	PT1	PT2	PT3
U-1	71.70	88.60	92.10
H-1	136.62	147.40	113.77
U-2	103.35	119.20	127.58
H-2	120.36	140.16	151.66
U-3	91.08	113.88	121.30
H-3	113.68	137.35	149.03
U-4	112.81	130.98	†144.09
H-4	79.95	91.01	100.55
U-5	†122.04	†134.51	144.07
H-5	138.73	†156.00	†159.59
U-6	90.82	111.14	120.00
H-6	†138.80	150.60	144.02
U-7	84.53	99.55	104.80
H-7	83.67	85.11	85.14
U-8	28.01	28.00	31.20
H-8	113.82	116.94	116.40

NOTE: Shaded background indicates larger comparative strain in HPC girder.
Bold indicates maximum strain for span among exterior and interior girders.
Italic indicates strain values NOT directly comparable based on sensor location and/or depth.
(‡) maximum strain for individual girder
(†) span maximum strain for Path

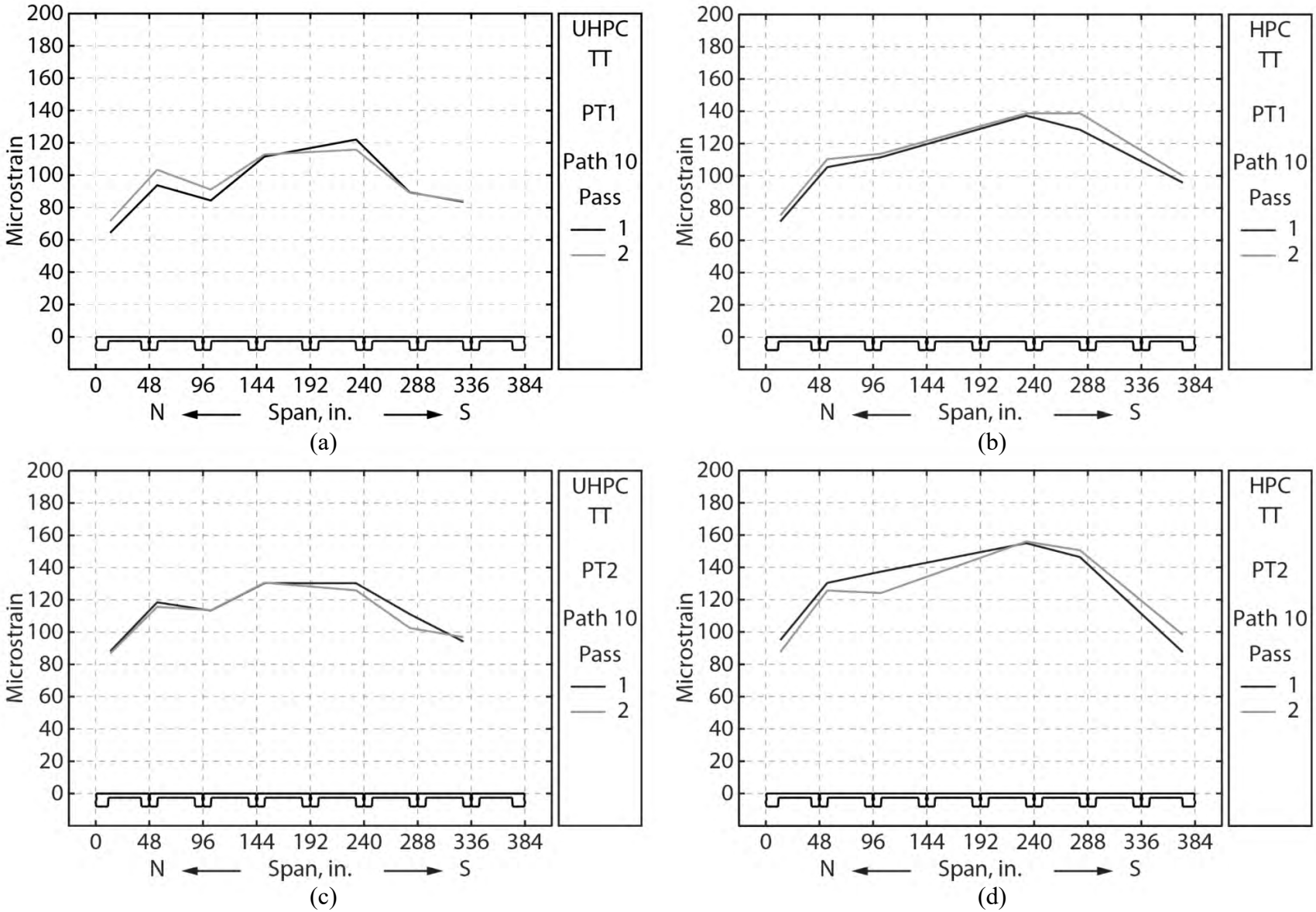


Figure 1.185: UHPC and HPC transverse strain profiles for TT load Path 10: Diagnostic Test (a and b) and Proof Test 1 (c and d).

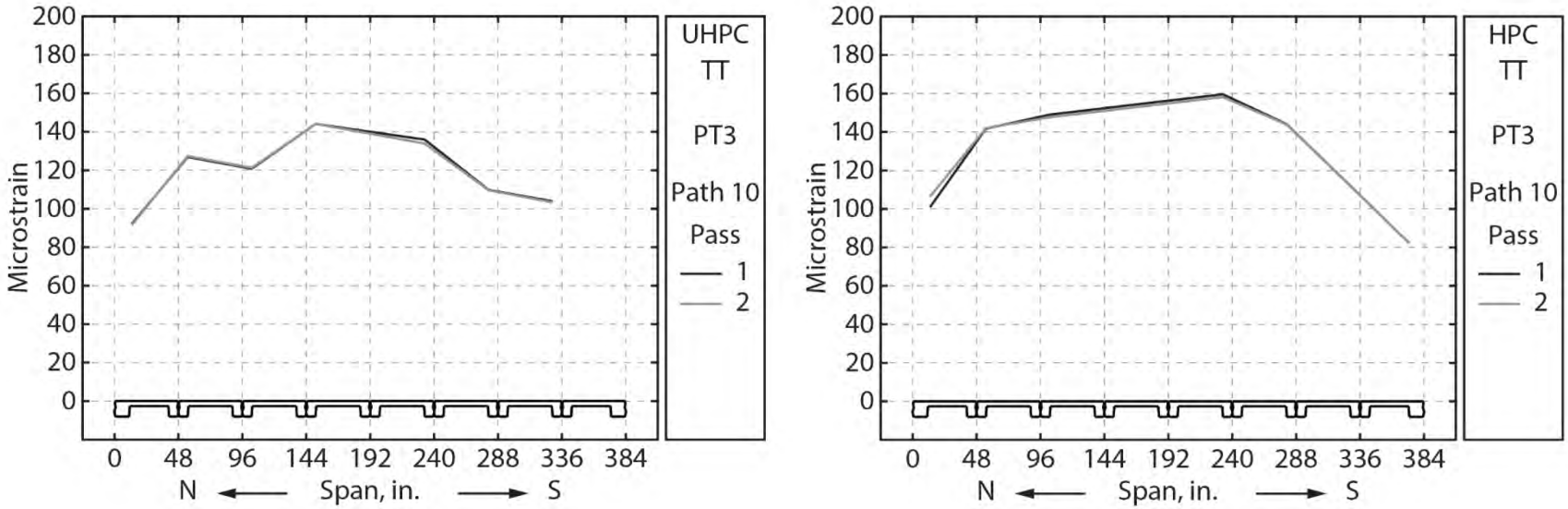


Figure 1.186: UHPC and HPC transverse strain profiles for TT load Path 10 for Proof Test 3.

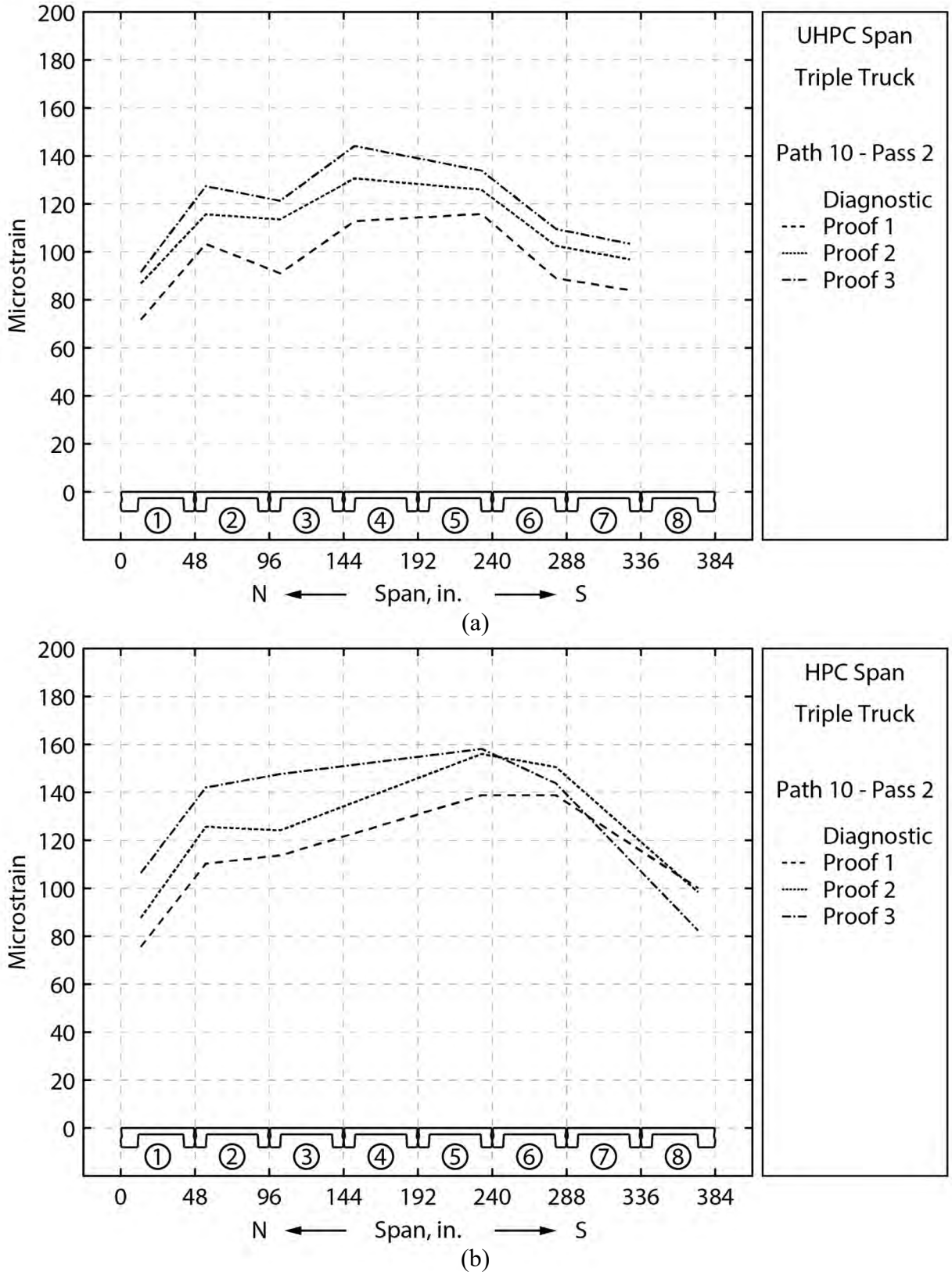


Figure 1.187: Comparison of transverse strain profiles of each load test for TT load Path 10 (Pass 2) for the (a) UHPC span and (b) HPC span.

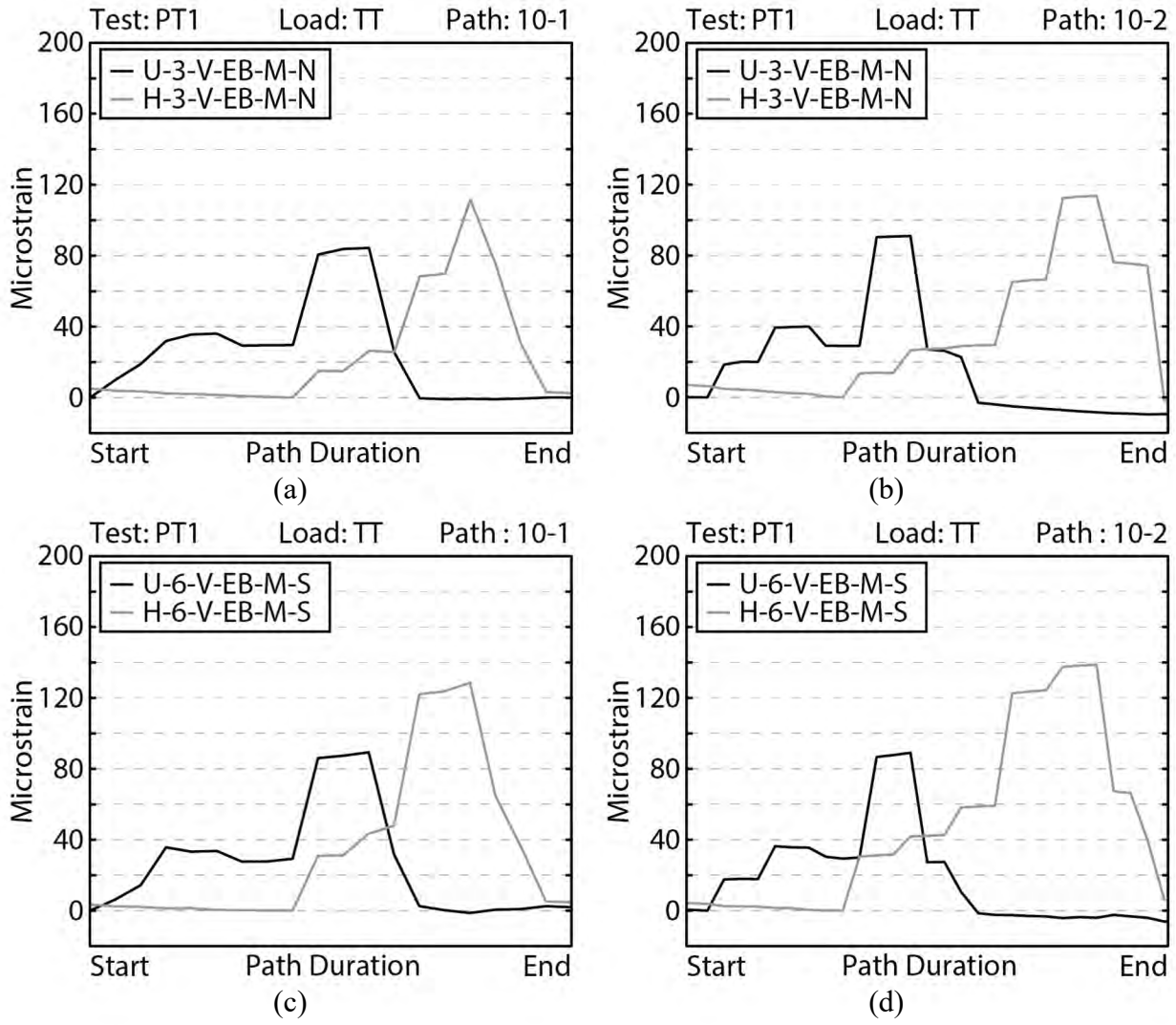


Figure 1.188: Strains for TT loading during PT1 for U-3/H-3 Path 10 (a) Pass 1 and (b) Pass 2, and U-6/H-6 Path 10 (c) Pass 1 and (d) Pass 2.

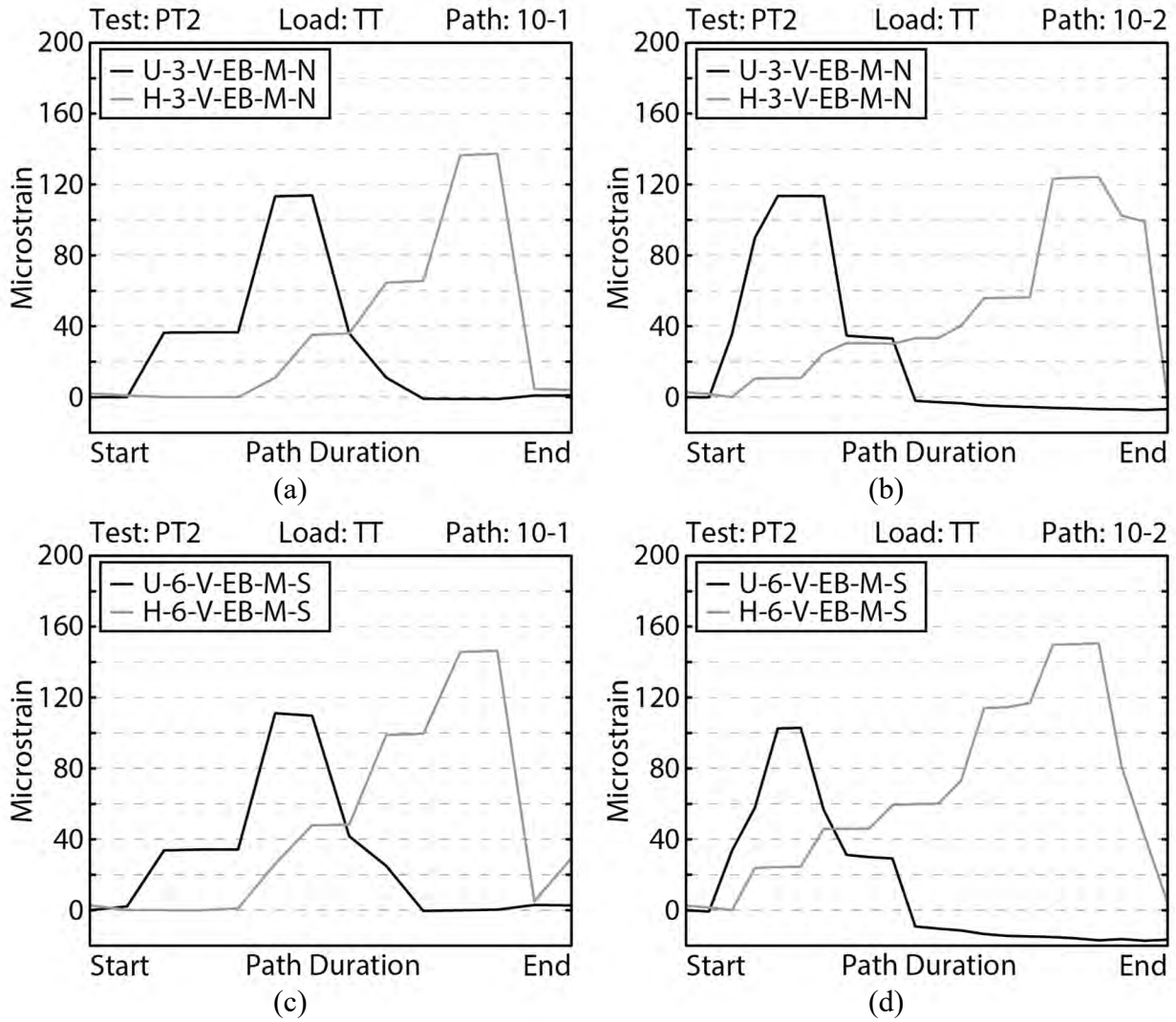


Figure 1.189: Strains for TT loading during PT2 for U-3/H-3 Path 10 (a) Pass 1 and (b) Pass 2, and U-6/H-6 Path 10 (c) Pass 1 and (d) Pass 2.

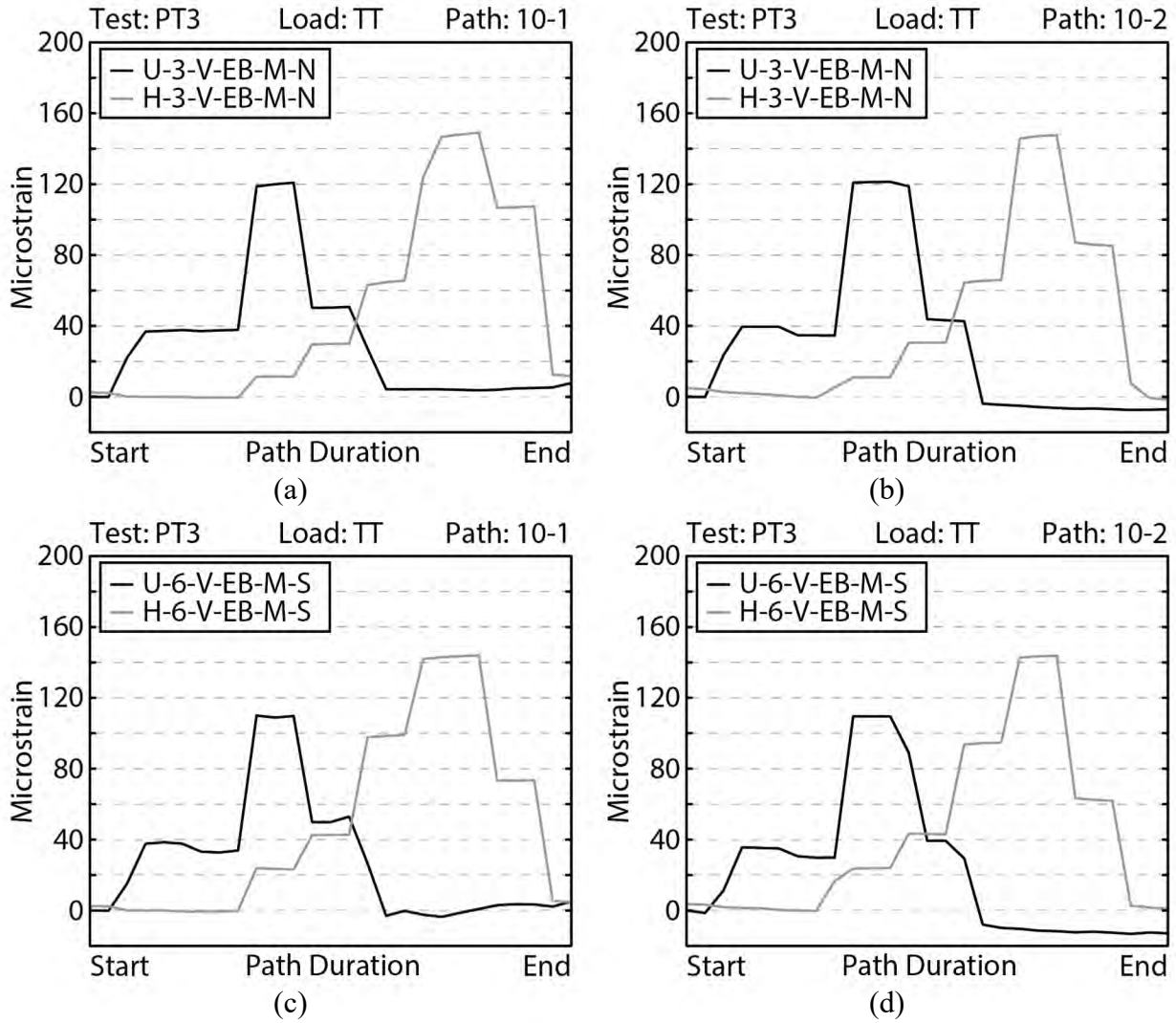


Figure 1.190: Strains for TT loading during PT3 for U-3/H-3 Path 10 (a) Pass 1 and (b) Pass 2, and U-6/H-6 Path 10 (c) Pass 1 and (d) Pass 2.

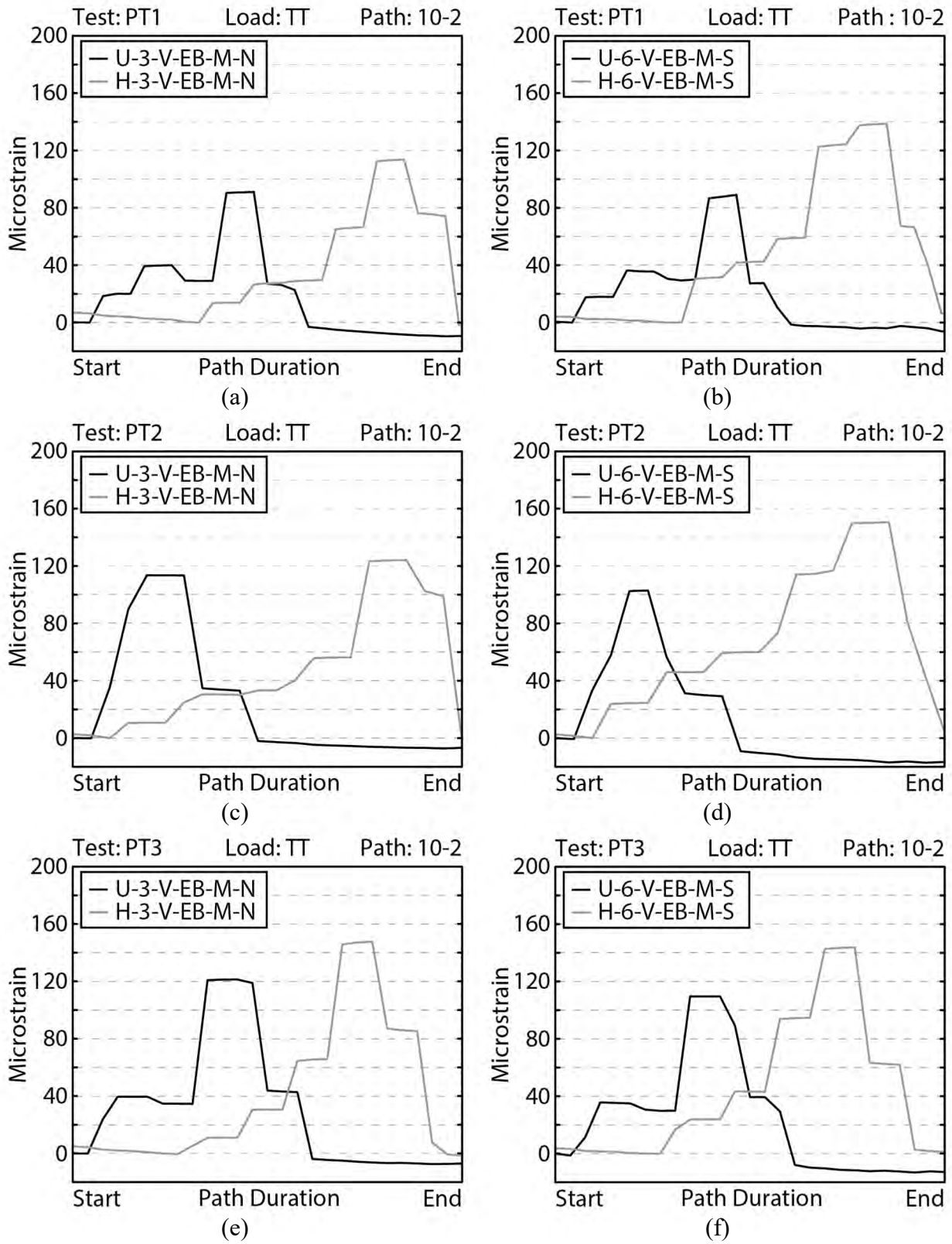


Figure 1.191: Comparison of strains for girder Lines 3 and 6 under TT Path 10 (Pass 2) loading: PT1 (a and b), PT2 (c and d), and PT3 (e and f).

1.8.8.4 Single Truck Back-to-Back Loading

The maximum strains measured in each girder for all single truck back-to-back (STBB) load paths conducted during the three proof tests are summarized in Table 1.146 through Table 1.148. To further illustrate the behavior of Bridge No. 9706 during field testing, the UHPC and HPC span transverse strain profiles for STBB loading during each of the three proof tests are presented in Figure 1.193 and Figure 1.194, and direct comparison of Paths 1 and 6 for each span during the three proof tests are provided in Figure 1.195. Next, strains measured in girder Line 3 and Line 6 for STBB loading are presented in Figure 1.196 for PT1, Figure 1.197 for PT2, and Figure 1.198 for PT3. The data plots within the figure are arranged purposefully to provide a visual juxtaposition of the strain behavior for the opposing girder lines (i.e., Lines 3 and 6) and path loadings (i.e., Paths 1 and 6, Paths 2 and 5, Paths 3 and 4). Lastly, Figure 1.199 provides direct comparisons of STBB loading for girder Line 3–Path 1 and Line 6–Path 6 during the three proof tests.



Figure 1.192: Single truck back-to-back load configuration for field testing of Bridge No. 9706.

Comparing the strain data presented in the tables and figures for STBB loading of NM Bridge No. 9706, the following observations were made:

- Strain behaviors exhibited by both spans were similar to the behavior for ST loading previously discussed in Section 1.8.8.1, as expected considering the same paths were conducted for both configurations.
- Load stations (see Figure 1.31, Section 1.2.1.1) during STBB loading were selected to maximize load based on placement of the heavier back axles of the trucks, and fewer stations were used for STBB load paths in comparison to ST, DT, or TT loadings.

- Maximum strains were often greater in the UHPC span for girder Lines 4–7 under Paths 1–3 (U-4 and U-7 were often larger for all ST paths). The remaining girder lines/path loadings exhibited larger maximum strains in the HPC span.
  NOTE: As denoted by *italic* font in Table 1.146 through Table 1.148, data was unavailable from lower midspan sensors for girder H-4 during all load tests, and for H-7 during the three proof tests. Therefore, the reported values may not accurately reflect maximum strains for those girders, and it is conceivable that strains may have been greater in the HPC girders.
- Maximum overall strains for both the UHPC and HPC were measured when truck loads were nearest to each edge of the transverse span during Path 1 and Path 6.
- Strains in the UHPC span tended to be larger toward the north edge, and overall maximum strains among exterior and interior girders consistently occurred in U-1 and U-2, respectively.
- Strains in the HPC span tended to be slightly larger toward the south edge, but overall maximum strains for each proof test varied, occurring in both exterior girders H-1 and H-8, and in H-2 and H-6 for interior girders.
- Though strains were typically between 10–30 με greater, both the consistency and symmetry of the transverse strain profiles in Figure 1.193 through Figure 1.195 were similar to those exhibited during ST loading.
- Whereas side-by-side load configuration (i.e., ST, DT, and TT) resulted in an imbalanced position of load (lighter front axle and heavier back axle), placement of the back-to-back trucks created a more symmetric load placement (see Figure 1.192) and less variation in strain magnitude while the load was present on each girder/span as illustrated for girder Lines 3 and 6 in Figure 1.196 through Figure 1.198 .
- The number of load stations (and path duration) was sometimes reduced based on time constraints, resulting in strange looking behavior such as for Line 6-Path 4, 5, and 6 during PT2 (Figure 1.197).
- Though more uniform and larger in magnitude than for ST loading, the maximum strains under STBB loads were less than for DT and TT loading due to the greater distribution of load with respect to the sensor locations in comparison to the side-by-side configurations. Despite increasing truck loads with each successive test, strains in girder Lines 3 and 6 did not change greatly between tests, within approximately ±20 με for the data shown.
- The magnitude of measured strains remained relatively consistent from year to year for both spans, typically within an approximate range of ±20 με across all three proof tests. Considering the variation in truck loads from each test (see truck loads in Section 1.2.1.1), the changes in measured strains for both spans are within a reasonable range.

Table 1.146: Summary of Maximum Measured Strains Under STBB Loading for PT1

Girder	Strain (με)					
	Path 1	Path 2	Path 3	Path 4	Path 5	Path 6
U-1	88.70‡	52.50	20.70	11.50	7.00	4.80
H-1	†135.93‡	†97.14	44.86	28.45	14.99	7.84
U-2	†100.45‡	75.49	54.13	37.20	16.48	7.78
H-2	103.17‡	85.92	65.72	48.43	24.61	11.83
U-3	78.38‡	75.35	59.10	41.38	21.65	8.94
H-3	79.17‡	76.60	†71.29	60.43	36.46	20.23
U-4	60.52	†78.03	†76.59	79.42‡	63.09	39.83
H-4	44.70	54.76	60.59‡	49.41	37.32	16.26
U-5	38.38	55.94	72.48	†82.52‡	†82.16	69.57
H-5	19.01	29.48	60.43	†87.83	94.14‡	76.07
U-6	17.38	22.92	47.66	71.98	72.31	†82.65‡
H-6	8.30	15.26	36.32	70.31	†101.63	†106.73‡
U-7	9.59	9.94	30.35	52.74	58.52	84.83‡
H-7	8.79	14.32	24.54	40.13	49.86	68.71‡
U-8	7.34	11.09	11.38	8.92	15.95	24.39‡
H-8	11.83	12.14	14.55	43.86	65.01	98.19‡

NOTE: Shaded background indicates larger comparative strain in HPC girder.
Bold indicates maximum strain for span among exterior and interior girders.
Italic indicates strain values NOT directly comparable based on sensor location and/or depth.
(‡) maximum strain for individual girder
(†) span maximum strain for Path

Table 1.147: Summary of Maximum Measured Strains Under STBB Loading for PT2

Girder	Strain (με)					
	Path 1	Path 2	Path 3	Path 4	Path 5	Path 6
U-1	99.50‡	62.60	24.60	11.10	8.80	2.90
H-1	97.29‡	77.06	36.06	20.78	7.76	5.32
U-2	†103.01‡	†86.40	57.22	29.61	12.19	6.44
H-2	†111.67‡	†100.83	71.18	43.77	12.76	10.30
U-3	82.24‡	80.98	61.95	35.77	17.91	8.82
H-3	99.03‡	97.96	63.78	36.13	14.10	11.73
U-4	65.02	79.64	†86.44‡	76.61	57.11	41.41
H-4	46.67	55.73	58.70‡	47.22	22.55	16.45
U-5	35.81	55.04	81.95‡	†80.36	75.78	68.80
H-5	23.14	35.14	†73.38	†87.30‡	85.67	80.85
U-6	22.04	39.48	54.21	70.28	†76.47‡	†75.73
H-6	11.48	18.61	45.50	63.30	†95.48	†118.90‡
U-7	14.27	24.38	36.10	54.80	62.68	70.95‡
H-7	8.32	13.39	29.57	34.87	59.85	71.76‡
U-8	5.35	4.08	5.77	10.06	14.59	20.88‡
H-8	5.43	9.65	24.89	27.89	85.22	107.74‡

NOTE: Shaded background indicates larger comparative strain in HPC girder.
Bold indicates maximum strain for span among exterior and interior girders.
Italic indicates strain values NOT directly comparable based on sensor location and/or depth.
(‡) maximum strain for individual girder
(†) span maximum strain for Path

Table 1.148: Summary of Maximum Measured Strains Under STBB Loading for PT3

Girder	Strain (με)					
	Path 1	Path 2	Path 3	Path 4	Path 5	Path 6
U-1	109.30‡	66.10	28.80	12.30	6.50	4.70
H-1	116.47‡	80.55	41.68	18.40	7.78	5.59
U-2	†119.00‡	†89.66	64.10	33.29	14.27	11.70
H-2	†128.01‡	†104.90	†76.22	44.78	18.34	8.38
U-3	87.93	88.36‡	62.59	37.25	19.18	8.37
H-3	100.42	100.67‡	63.82	40.69	23.78	11.20
U-4	66.02	87.12	88.20‡	77.04	58.88	36.90
H-4	41.41	57.03	60.53‡	54.15	39.42	15.40
U-5	34.99	62.81	†89.36‡	†88.62	†80.49	67.74
H-5	18.28	37.41	58.10	†96.58	†102.36‡	78.54
U-6	19.77	33.34	53.98	64.72	76.09	83.63‡
H-6	9.41	18.99	32.00	68.78	95.99	115.88‡
U-7	14.22	20.19	33.64	50.47	67.54	†94.23‡
H-7	11.44	12.97	22.81	43.72	57.75	81.09‡
U-8	11.89	13.39	7.81	10.20	19.01	29.90‡
H-8	12.37	13.66	12.39	35.85	72.20	†119.35‡

NOTE: Shaded background indicates larger comparative strain in HPC girder.
Bold indicates maximum strain for span among exterior and interior girders.
Italic indicates strain values NOT directly comparable based on sensor location and/or depth.
(‡) maximum strain for individual girder
(†) span maximum strain for Path

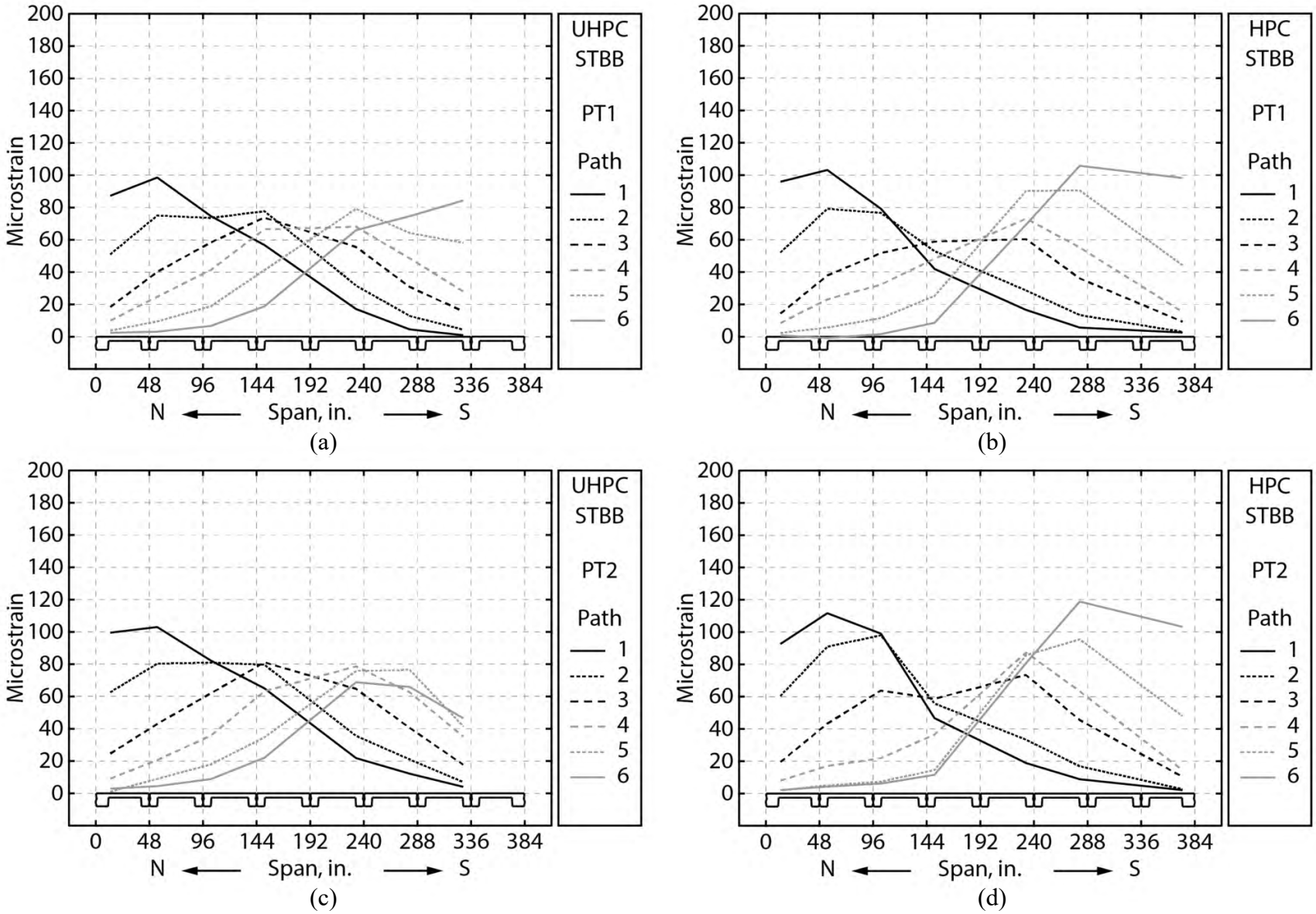


Figure 1.193: UHPC and HPC transverse strain profiles for STBB load Paths 1-6: Proof Test 1 (a and b) and Proof Test 2 (c and d).

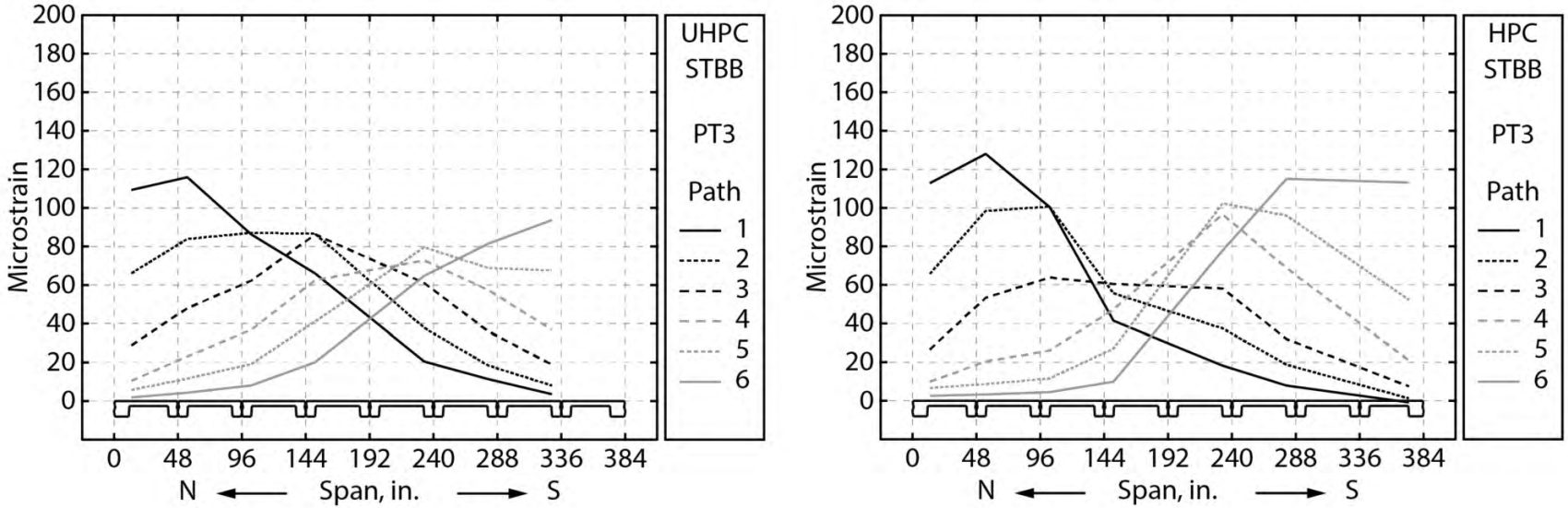


Figure 1.194: UHPC and HPC transverse strain profiles for STBB load Paths 1-6 for Proof Test 3.

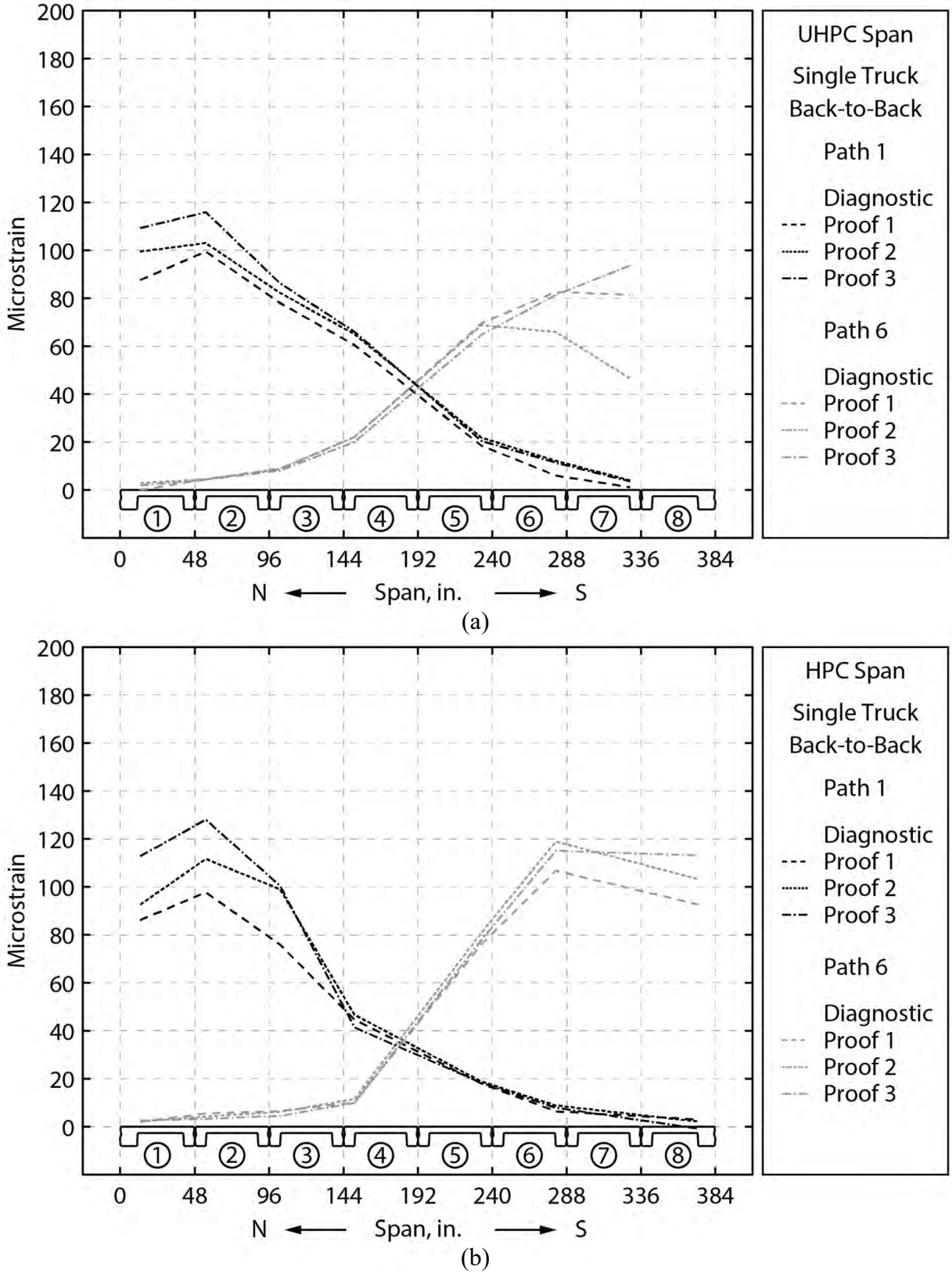


Figure 1.195: Comparison of transverse strain profiles of each load test for STBB load Paths 1-6 for the (a) UHPC span and (b) HPC span.

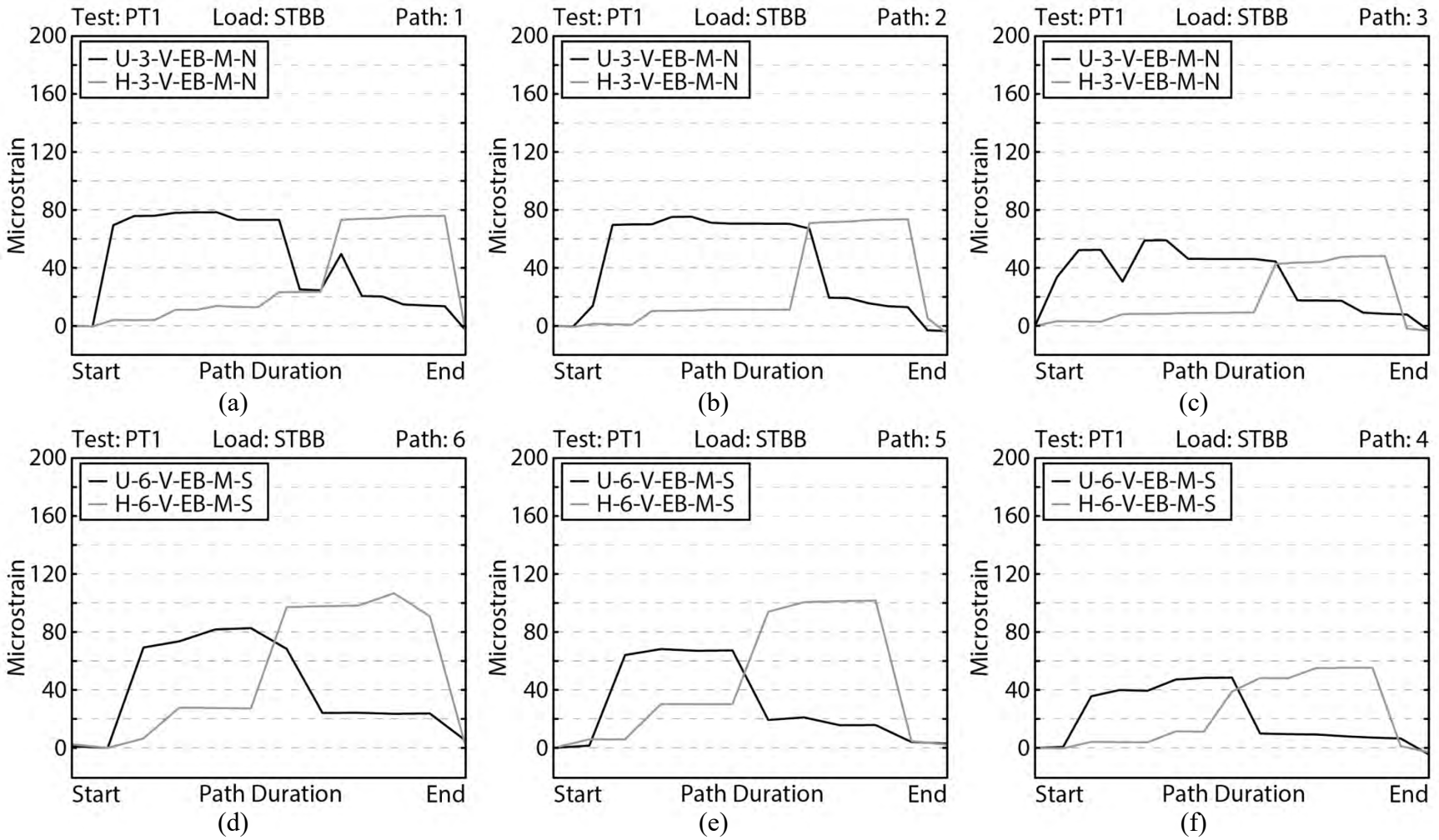


Figure 1.196: Strains for STBB loading during PT1 for U-3/H-3 (a) Path 1, (b) Path 2, (c) Path 3, and U-6/H-6 (d) Path 6, (e) Path 5, (f) Path 4.

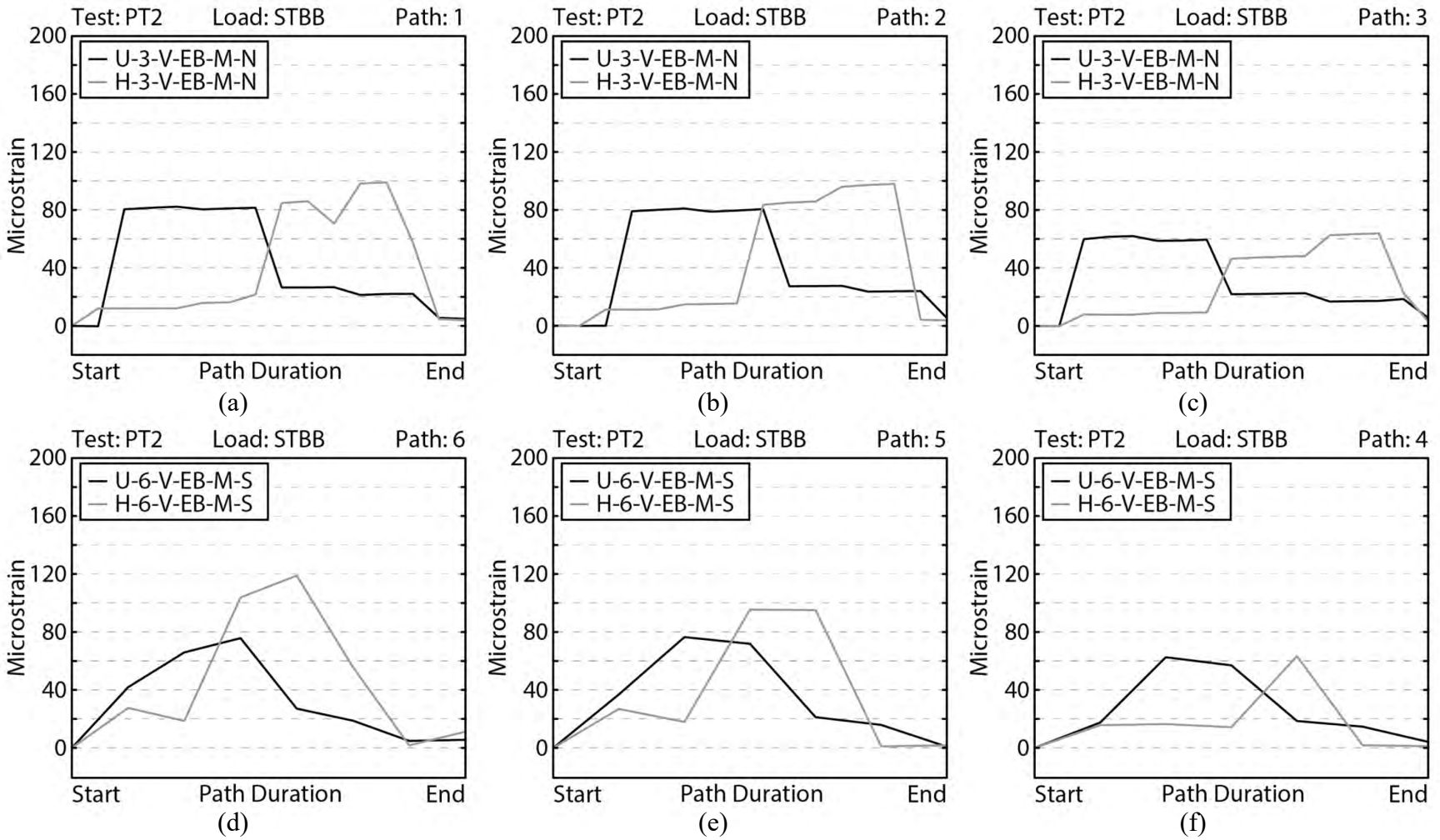


Figure 1.197: Strains for STBB loading during PT2 for U-3/H-3 (a) Path 1, (b) Path 2, (c) Path 3, and U-6/H-6 (d) Path 6, (e) Path 5, (f) Path 4.

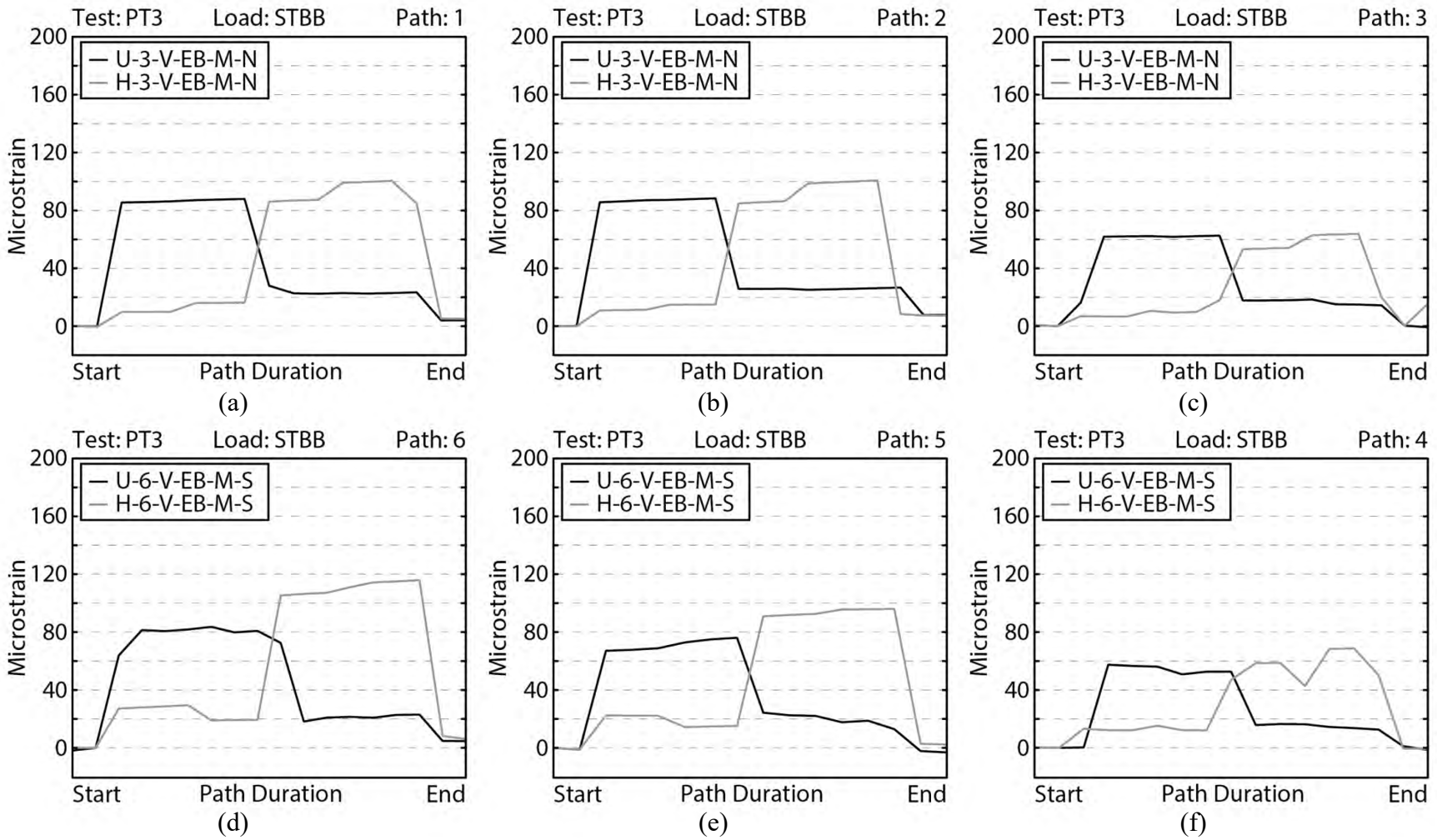


Figure 1.198: Strains during PT3 STBB loading for U-3/H-3 (a) Path 1, (b) Path 2, (c) Path 3, and U-6/H-6 (d) Path 6, (e) Path 5, (f) Path 4.

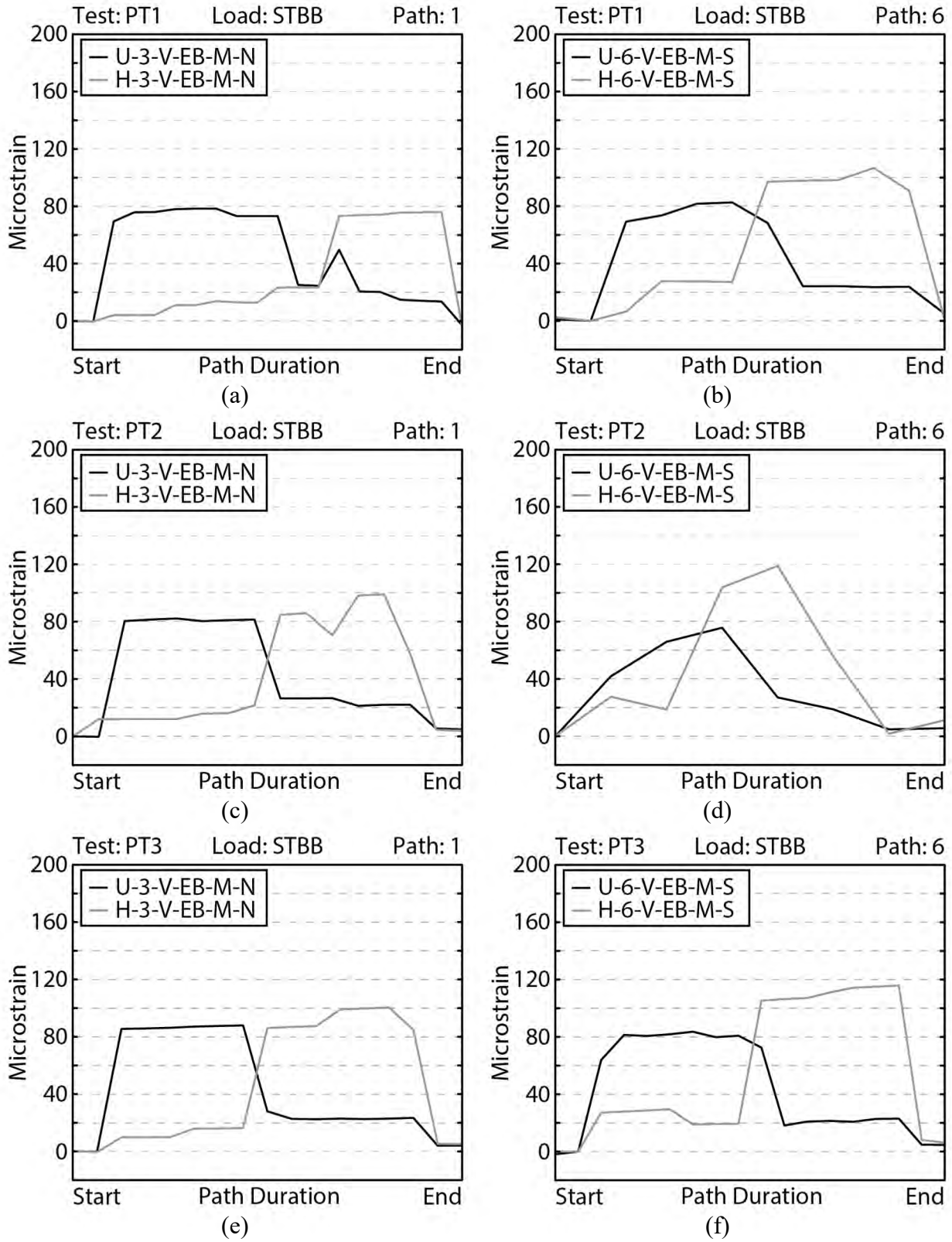


Figure 1.199: Comparison of strains for girder Lines 3 and 6 under STBB loading: PT1 (a and b), PT2 (c and d), and PT3 (e and f).

1.8.8.5 Double Truck Back-to-Back Loading

The maximum strains measured in each girder for all double truck back-to-back (DTBB) load paths conducted during the four load tests are summarized in Table 1.149 through Table 1.151. To further illustrate the behavior of Bridge No. 9706 during field testing, the UHPC and HPC span transverse strain profiles for DTBB loading during each of the three proof tests are presented in Figure 1.203 and Figure 1.204, and direct comparison of Paths 7 and 8 for each span during the three proof tests are provided in Figure 1.205. Next, strains measured in girder Line 3 and Line 6 for STBB loading are presented in Figure 1.206 for PT1, Figure 1.207 for PT2, and Figure 1.208 for PT3. The data plots within the figure are arranged purposefully to provide a visual juxtaposition of the strain behavior for the opposing girder lines (i.e., Lines 3 and 6) and path loadings (i.e., Paths 7 and 8). Lastly, Figure 1.209 provides direct comparisons of DTBB loading for girder Line 3–Path 7 and Line 6–Path 8 during the three proof tests.



Figure 1.200: Double truck back-to-back load configuration for field testing of Bridge No. 9706.



Figure 1.201: Drone aerial view of NM Bridge No. 9706 field testing: Path 7 DTBB load centered over HPC midspan load station.

Comparing the strain data presented in the tables and figures for DTBB loading of NM Bridge No. 9706, the following observations were made:

- Like the STBB configuration, DTBB provides a symmetrical arrangement of axle loads (shown in Figure 1.200), and the use of four trucks maximized the total load placed on the bridge. Load stations during DTBB loading were also selected to maximize load based on placement of the heavier back axles of the trucks.
- Load Paths 7, 8, and 9 (see Figure 1.29, Section 1.2.1.1) were conducted for DTBB loading during PT1. However, it was determined that Path 9 did not produce maximum strains for DTBB loading, and therefore Path 9 was not conducted during subsequent load testing. Strains were expectedly maximized on the north end of the transverse span under Path 7, and on the south end under Path 8.
- Maximum strains were consistently greater in the HPC span for girder Lines 1–3 and 7 for both Path 7 and 8, and in Lines 5 and 6 for Path 8. Conversely, maximum strains were consistently greater in the UHPC span were greater for girder Lines 4–6 under Path 7, and for Lines 4 and 6 under Path 8.

  NOTE: As denoted by *italic* font in Table 1.149 through Table 1.151, data was unavailable from lower midspan sensors for girders H-4 and H-7. Therefore, the reported values may not accurately reflect maximum strains for those girders, and it is conceivable that strains may have been greater in the HPC girders.
- Maximum strains overall strains among exterior girders consistently occurred in girder U-1 for the UHPC span, but varied between test for the HPC span, occurring in either H-1 and

H-8. The location of overall maximum measured strains among interior girders varied for both the UHPC and HPC spans between each proof test, but consistently occurred in either girder Line 2 or 6.

- Both UHPC and HPC spans exhibited relatively symmetric strain behavior for DTBB loading.
- The transverse strain profiles of Figure 1.205 indicate an increase in strain development for the UHPC span during PT3 as compared to PT2. However, maximum strains in the UHPC span remained below 160 με for all three proof tests, whereas strains in the HPC span exceeded 160 με for each proof test.
- Figure 1.206 through Figure 1.208 illustrate the relatively symmetric strains (both in magnitude and behavior) measured for the opposing girder lines and load paths, maximized for girder Line 3 under Path 7 (placed to the north side of the span width), and for girder Line 6 under Path 8 (placed to the south side of the span width).
- The general strain behaviors exhibited by each girder line are nearly identical for the three proof tests, and in magnitude between PT2 and PT3. Note that strains during PT2 and PT3 are expectedly larger than exhibited for PT1 due to the heavier truck loads.
- The sometimes sharp decreases in measured strains during the path duration were due to the movement of the trucks (Figure 1.202), which often required several minutes to arrange over the next load station and resulted in momentary decrease of strain at the particular gauge location.



Figure 1.202: Arrangement of trucks during DTBB loading of NM Bridge No. 9706.

Table 1.149: Summary of Maximum Measured Strains Under DTBB Loading for PT1

Girder	Strain (με)		
	Path 7	Path 8	Path 9
U-1	113.80‡	19.20	58.60
H-1	†174.25‡	52.39	104.66
U-2	†138.32‡	59.61	97.02
H-2	145.47‡	75.70	113.41
U-3	130.67‡	62.39	104.03
H-3	146.99‡	97.85	109.10
U-4	128.61‡	117.51	128.04
H-4	95.72‡	73.33	83.06
U-5	117.55	†128.87‡	†128.09
H-5	95.67	145.24‡	†130.31
U-6	75.43	121.14‡	103.02
H-6	65.84	†149.51‡	110.12
U-7	53.28	109.47‡	74.86
H-7	42.83	83.34‡	60.18
U-8	10.12	29.33‡	15.79
H-8	35.87	114.33‡	70.84

NOTE: Shaded background indicates larger comparative strain in HPC girder.
Bold indicates maximum strain for span among exterior and interior girders.
Italic indicates strain values NOT directly comparable based on sensor location and/or depth.
(‡) maximum strain for individual girder
(†) span maximum strain for Path

Table 1.150: Summary of Maximum Measured Strains Under DTBB Loading for PT2

Girder	Strain (με)	
	Path 7	Path 8
U-1	126.20‡	17.80
H-1	†195.95‡	32.36
U-2	†149.90‡	45.67
H-2	170.57‡	65.45
U-3	147.10‡	50.70
H-3	175.87‡	53.42
U-4	137.67‡	120.16
H-4	100.72‡	77.35
U-5	115.76	149.65‡
H-5	100.26	165.93‡
U-6	82.15	†150.26‡
H-6	61.73	†185.49‡
U-7	59.10	136.68‡
H-7	42.02	110.69‡
U-8	16.71	35.98‡
H-8	35.59	161.24‡

NOTE: Shaded background indicates larger comparative strain in HPC girder.
Bold indicates maximum strain for span among exterior and interior girders.
Italic indicates strain values NOT directly comparable based on sensor location and/or depth.
(‡) maximum strain for individual girder
(†) span maximum strain for Path

Table 1.151: Summary of Maximum Measured Strains Under DTBB Loading for PT3

Girder	Strain (με)	
	Path 7	Path 8
U-1	139.60‡	19.50
H-1	140.04‡	27.47
U-2	†156.44‡	44.28
H-2	171.83‡	62.48
U-3	149.14‡	52.55
H-3	†176.07‡	51.89
U-4	138.74‡	116.99
H-4	100.99‡	77.35
U-5	116.05	141.45‡
H-5	90.17	170.35‡
U-6	71.59	†150.38‡
H-6	54.73	†185.60‡
U-7	46.13	144.26‡
H-7	36.24	115.06‡
U-8	17.60	50.96‡
H-8	23.87	160.36‡

NOTE: Shaded background indicates larger comparative strain in HPC girder.
Bold indicates maximum strain for span among exterior and interior girders.
Italic indicates strain values NOT directly comparable based on sensor location and/or depth.
(‡) maximum strain for individual girder
(†) span maximum strain for Path

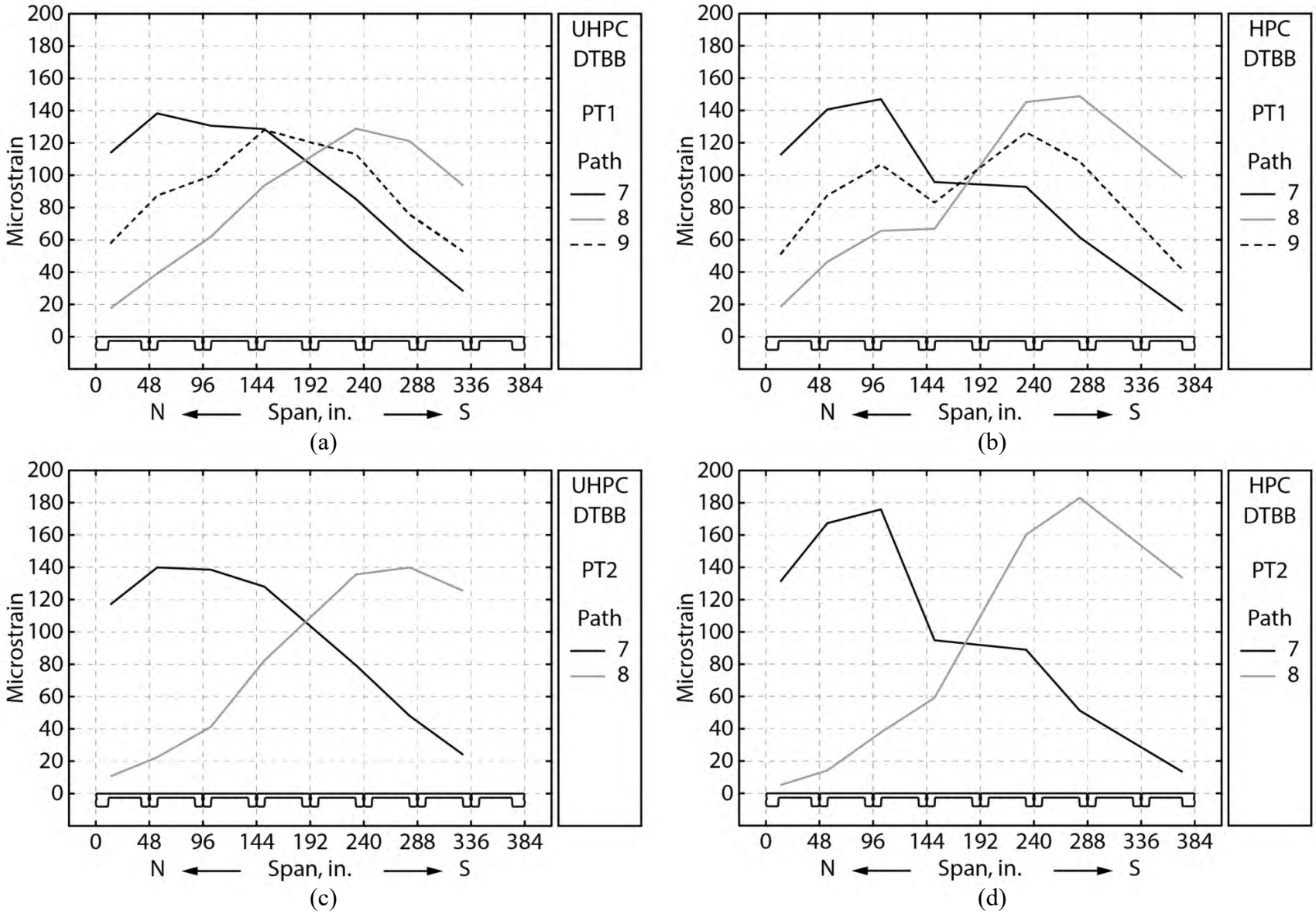


Figure 1.203: UHPC and HPC transverse strain profiles for DTBB load Paths 7-8: Proof Test 1 (a and b) and Proof Test 2 (c and d).

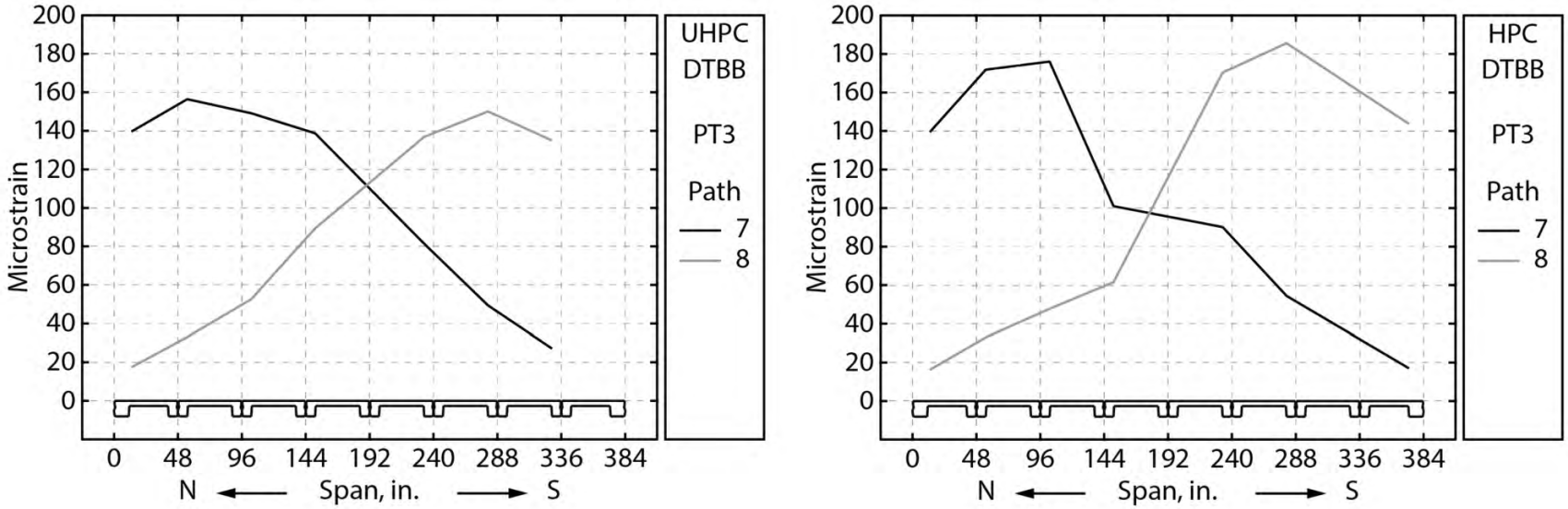


Figure 1.204: UHPC and HPC transverse strain profiles for DTBB load Paths 7-8 for Proof Test 3.

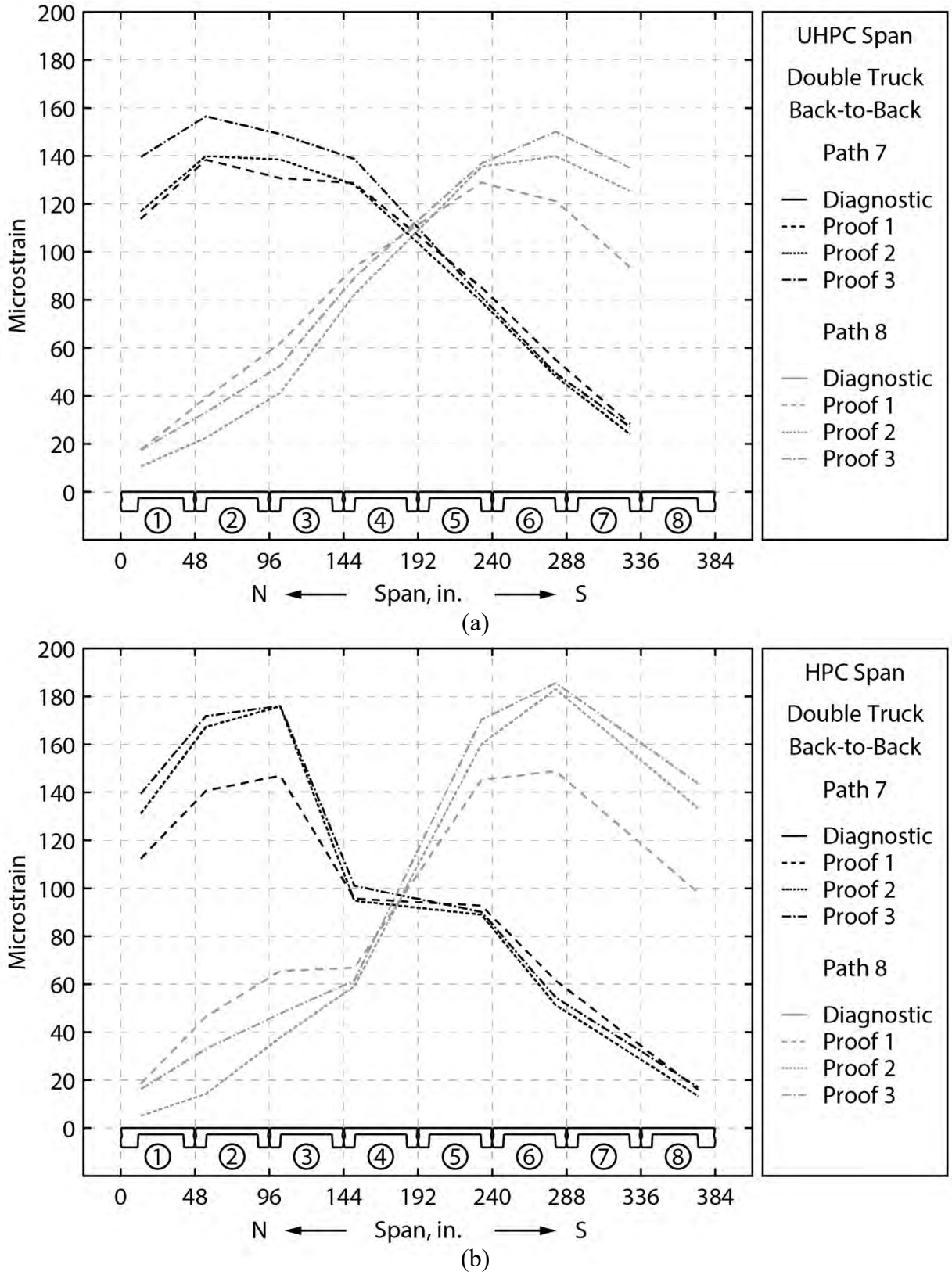


Figure 1.205: Comparison of transverse strain profiles of each load test for DTBB load Paths 7 and 8 for the (a) UHPC span and (b) HPC span.

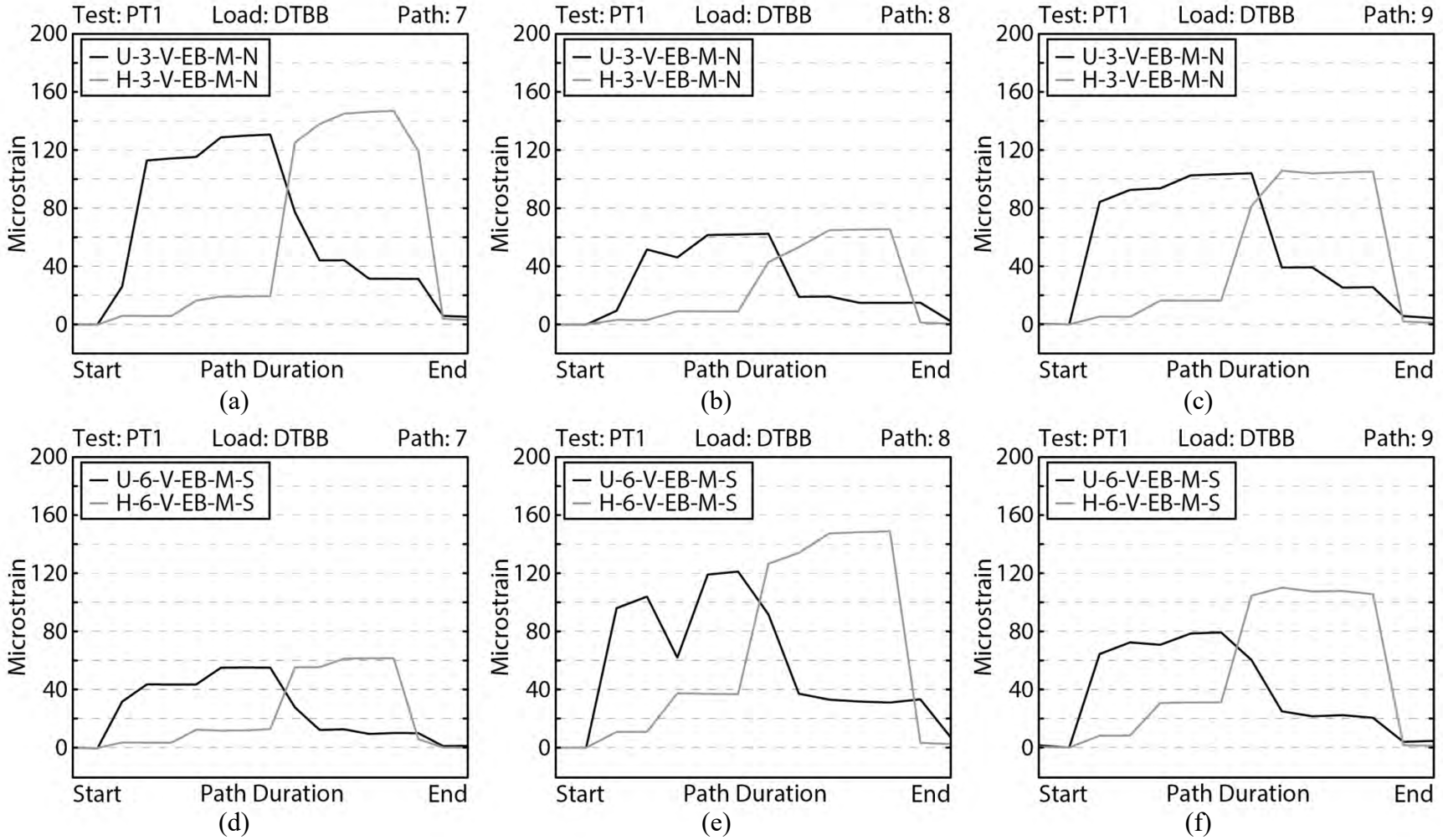


Figure 1.206: Strains for DTBB loading during PT1 for U-3/H-3 (a) Path 7, (b) Path 8, (c) Path 9, and U-6/H-6 (d) Path 7, (e) Path 8, (f) Path 9.

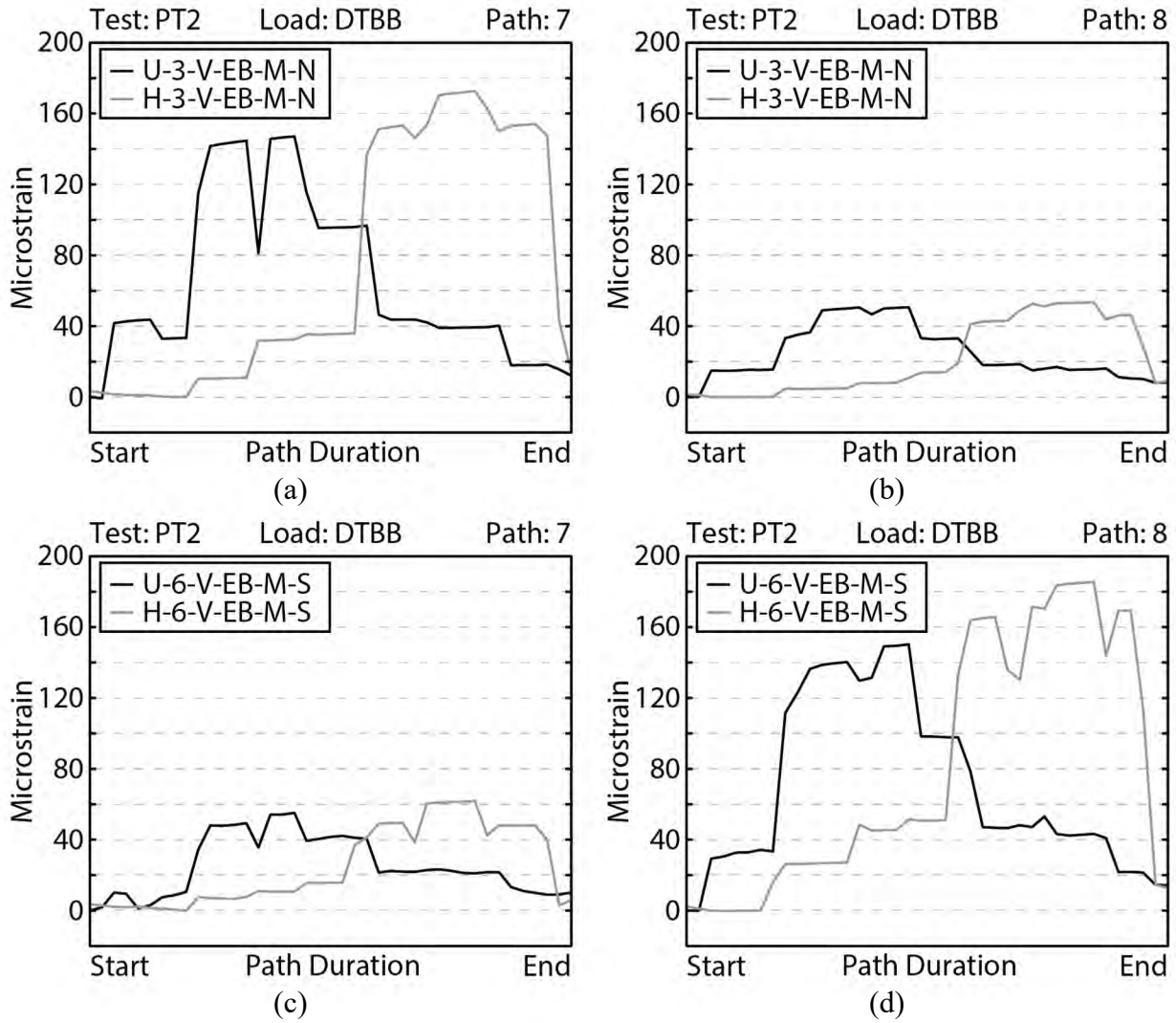


Figure 1.207: Strains for DTBB loading during PT2 for U-3/H-3 (a) Path 7 and (b) Path 8, and U-6/H-6 (c) Path 7 and (d) Path 8.

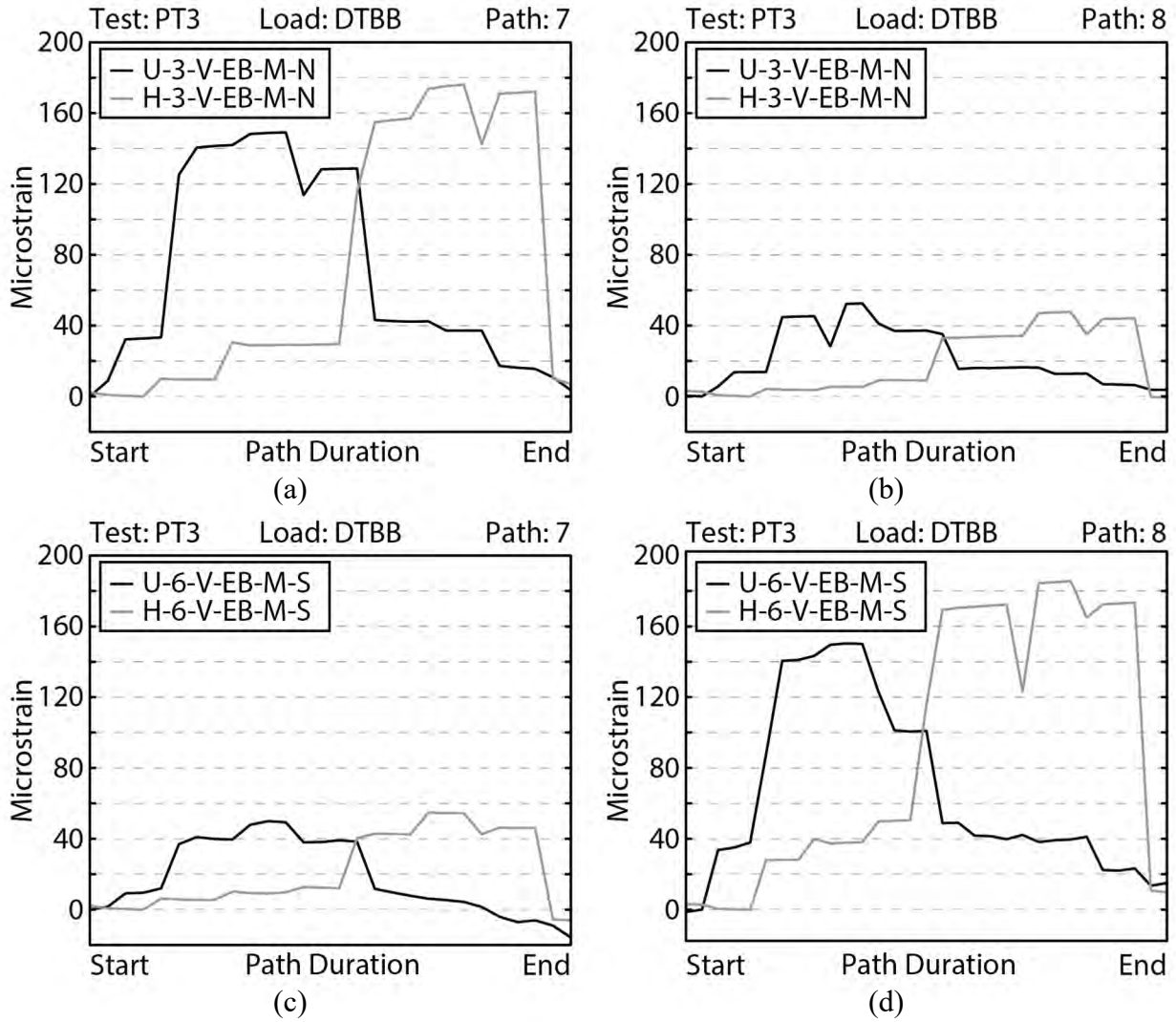


Figure 1.208: Strains during PT3 DTBB loading for U-3/H-3 (a) Path 7 and (b) Path 8, and U-6/H-6 (c) Path 7 and (d) Path 8.

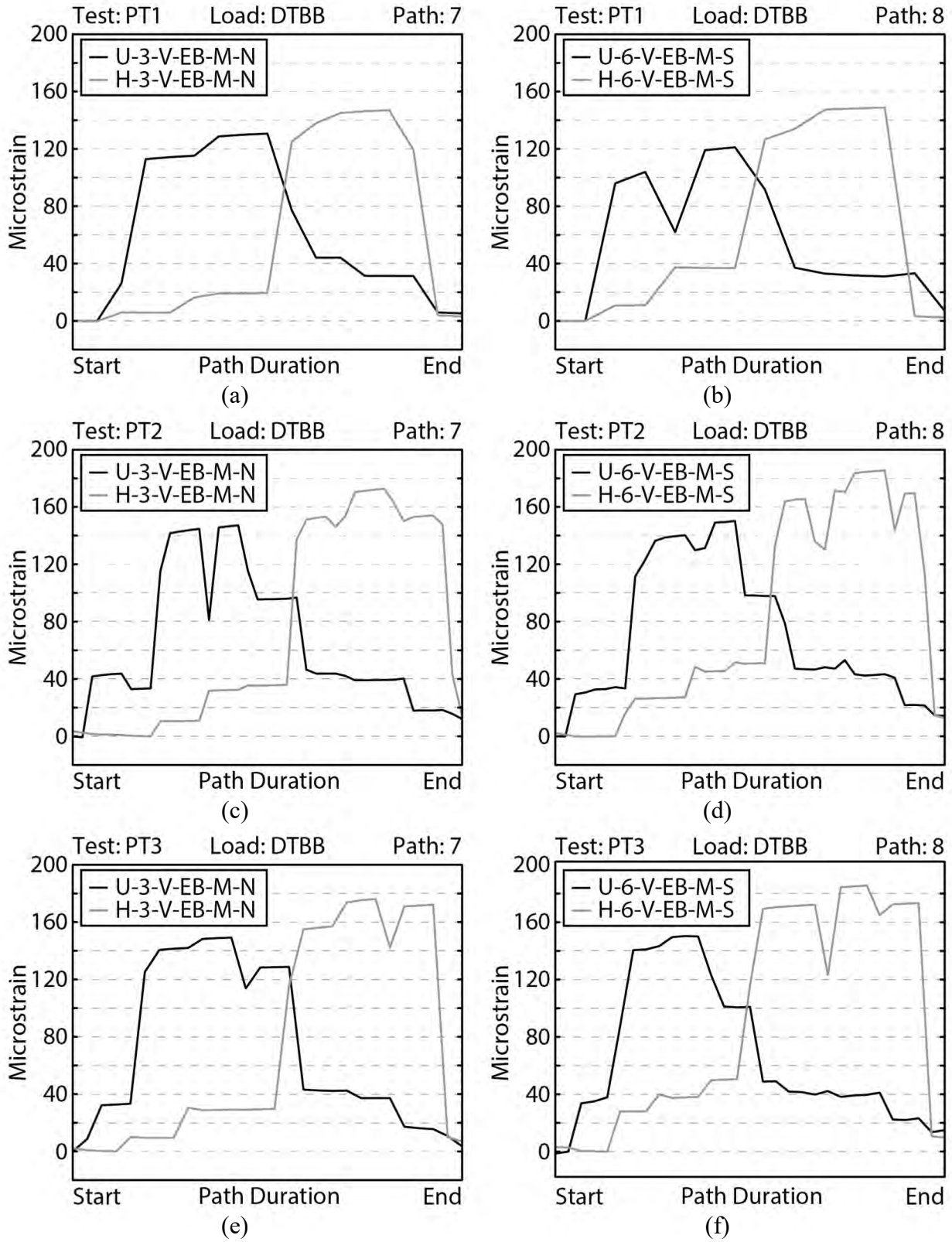


Figure 1.209: Comparison of strains for girder Lines 3 and 6 under DTBB loading: PT1 (a and b), PT2 (c and d), and PT3 (e and f).

1.8.9 Summary of Maximum Strains

The volume of available strain data from field testing of NM Bridge No. 9706 offers no shortage of means for comparing the behavior and performance of the two bridge spans and concrete types. While the previous section (and sub-sections) of this chapter attempted to provide a more in-depth summary of the results for each truck load configuration, the results of field testing are condensed to a more succinct representation in the following discussion.

Expected strains for each truck load configuration were calculated for UHPC and HPC girders for the desired distribution factor, DF (based on interior or exterior girder and number of lanes loaded). The expected strains for AASHTO DFs are presented in Table 1.152, calculated based on the maximum measured truck load(s) used for PT1 (because average truck loads for PT2 and PT3 increased in comparison to PT1), thus providing a "lower bound" for expected strains during proof testing of Bridge No. 9706. Conversely, expected strains calculated using a DF equal to one provide an "upper bound" representing the worst-case scenario for live load distribution between girders. Also provided beside each value (placed in parentheses) is the ratio of the given strain to the AASHTO DF strain.

Table 1.152 further presents the maximum strains measured among interior and exterior girders during each load test for the various truck load configurations. Like the tables presented in Section 1.8.8, formatting and markers are used to denote information for. A shaded background indicates larger comparative strain in the HPC span. Values displayed in **bold** font represent the overall maximum strains measured across all load tests among exterior and interior girders of each span for the given truck load configuration. For Table 1.152, the superscript character (†) denotes the overall maximum strain measured in each span for the given truck load configuration (regardless of whether it occurred for interior or exterior girders).

Due to the placement of truck loads and the fact that the outer stem of exterior girders was larger, it would be reasonable to expect greater strains in the smaller interior stem of exterior girders. This was typically the case for HPC exterior girders, where maximum strains were measured at the lower midspan gauge location in the southward stem of girder H-1, and in the northward stem of H-8. However, strain development in the UHPC span was often greater toward the north edge of the span, and data was unavailable from the lower midspan gauge in the southward (interior) stem for girder U-1. Strains measured for UHPC exterior girders and displayed in Table 1.152 using *italic* font indicate that the data is from the northward (exterior) stem of U-1 and are not directly comparable to the HPC exterior strain based on the location of the sensor.

Table 1.152: Comparison of Expected and Measured Strains for Field Testing of NM Bridge No. 9706

Truck Load	Girder Type		Expected Strain (με)		Maximum Measured Strain (με)							
			AASHTO DF	DF = 1	DT0		PT1		PT2		PT3	
ST	Int.	U	111	326 (2.94)	84	(0.76)	84	(0.76)	95	(0.86)	†103	(0.93)
	Int.	H	95	280 (2.95)	92	(0.97)	88	(0.93)	97	(1.02)	109	(1.15)
	Ext.	U	133	222 (1.67)	76	(0.57)	66	(0.49)	86	(0.64)	90	(0.67)
	Ext.	H	112	187 (1.67)	103	(0.92)	107	(0.95)	†115	(1.03)	106	(0.95)
DT	Int.	U	174	326 (1.87)	115	(0.66)	106	(0.61)	--	--	129	(0.74)
	Int.	H	150	280 (1.87)	125	(0.83)	130	(0.87)	--	--	†155	(1.03)
	Ext.	U	133	222 (1.67)	†140	(1.05)	72	(0.54)	--	--	97	(0.73)
	Ext.	H	112	187 (1.67)	140	(1.25)	130	(1.16)	--	--	134	(1.20)
TT	Int.	U	171	326 (1.91)	--	--	122	(0.71)	135	(0.79)	†144	(0.84)
	Int.	H	147	280 (1.90)	--	--	139	(0.94)	156	(1.06)	†160	(1.09)
	Ext.	U	133	222 (1.67)	--	--	72	(0.54)	89	(0.67)	92	(0.69)
	Ext.	H	112	187 (1.67)	--	--	137	(1.22)	147	(1.32)	116	(1.04)
STBB	Int.	U	127	373 (2.94)	--	--	100	(0.79)	103	(0.81)	†119	(0.94)
	Int.	H	109	320 (2.94)	--	--	107	(0.98)	119	(1.09)	128	(1.17)
	Ext.	U	152	253 (1.66)	--	--	89	(0.58)	100	(0.65)	109	(0.72)
	Ext.	H	128	214 (1.67)	--	--	†136	(1.06)	108	(0.84)	119	(0.93)
DTBB	Int.	U	199	373 (1.87)	--	--	138	(0.70)	150	(0.76)	†156	(0.79)
	Int.	H	171	320 (1.87)	--	--	150	(0.87)	185	(1.08)	186	(1.09)
	Ext.	U	152	253 (1.66)	--	--	114	(0.75)	126	(0.83)	140	(0.92)
	Ext.	H	128	214 (1.67)	--	--	174	(1.36)	†196	(1.53)	160	(1.25)

NOTE: Shaded background indicates larger comparative strain in HPC girder.
Values in parentheses ( ) represent the ratio of the reported strain to the AASHTO DF strain.
Bold indicates overall maximum strain for span among exterior and interior girders.
Italic indicates U and H strain values are NOT directly comparable based on sensor location and/or depth.
(†) span maximum strain for truck load configuration
(--) no data/not available

Comparing the strain data presented in Table 1.152 for field testing of Bridge No. 9706, the following observations were made:

- Two important details should be highlighted with respect to both the expected and measured strains. First, consider the expected strains calculated for the two spans. Although the design modulus of elasticity for UHPC was greater than that of HPC (ratio for elastic moduli was approximately 1.13), the cross-sectional area of the UHPC girders were approximately 10% smaller than the HPC girders, with ratios for the respective section moduli (UHPC-to-HPC) of 0.7 for interior girders and 0.75 for exterior girders. Not surprisingly, expected strains calculated for both interior and exterior UHPC girders were consistently larger than those for HPC girders.
- Results of field testing were markedly different to the calculated expected strains. As indicated by the shaded background, maximum measured strains during each load test were consistently greater in magnitude for the HPC span, regardless of truck load configuration. The difference in maximum measured strains between the UHPC and HPC spans tended to increase with greater truck loads.
- Across all load tests and tuck configurations, the maximum strain recorded in the UHPC span was 157 με in girder U-2 for DTBB Path 7 loading during PT3. For the HPC span, strains upwards of 160 με were measured during each load test (under DTBB loading), with a maximum strain of 196 με in girder H-1 for DTBB Path 7 loading during PT2.
- For the UHPC span, only one maximum measured strain exceeded the AASHTO DF expected strain (calculated based on PT1 truck loads and placement). Under DT loading during DT0, the maximum strain value among UHPC exterior girders was measured as 140 με to produce a ratio of 1.05 with respect to the AASHTO DF expected strain.
- The maximum measured strains for UHPC interior and exterior girders of 157 με (U-2 for DTBB Path 7 during PT3) and 140 με (U-1 for DT Path 7 during DT0). When compared to the available strain for UHPC girders, calculated as 455 με for interior girders and 369 με for exterior girders, respectively, the maximum percentage of the available strain exhausted for the UHPC span was approximately 35% for interior girders and 38% for exterior girders.
- For the HPC span, the largest strain ratio with respect to the AASHTO DF expected strain was 1.53, corresponding to the 196 με measured in girder H-1 for DTBB Path 7 during PT2 (the overall maximum strain during all field testing of Bridge No. 9706).
- The maximum measured strains for HPC interior and exterior girders of 186 με (H-6 for DTBB Path 8 during PT3) and 196 με (H-1 for DTBB Path 7 during PT2). When compared to the available strain for HPC girders, calculated as 483 με for interior girders and 389 με for exterior girders, respectively, the maximum percentage of the available strain exhausted for the HPC span was approximately 39% for interior girders and 50% for exterior girders.
- Overall, the measured strains for the UHPC span girders were typically lower than the expected behavior as calculated for the truck loads of PT1, even for the heavier tuck loads

during PT2 and PT3 (apart from the exterior girder strain for DT loading during DT0). These findings indicate that the UHPC span exhibited better than expected live load distribution, and the design-based load distribution factors calculated for the UHPC girders were conservative.

Construction of NM Bridge No. 9706 marked the first deployment of UHPC for New Mexico highway infrastructure, and perhaps the first structural application of a nonproprietary UHPC in the United States. Successfully completed in March 2017, the two-span bridge superstructure was designed to incorporate precast-prestressed concrete channel shaped bridge girders from two types of concrete: one span from HPC [9.5 ksi (66.0 MPa)] typical of current NM bridge design, and the second span from nonproprietary UHPC [21.0 ksi (145 MPa)] developed at NMSU using primarily local materials and steel fiber reinforcement.

Thermal and strain-based instrumentation embedded in each girder during production provided the capability for direct comparative analyses of behavior and performance of the two types of concrete. Concrete core temperatures were monitored during girder fabrication to evaluate the precast curing regimens, and strain data was analyzed to evaluate the transfer of prestressing forces.

Following construction of Bridge No. 9706, multiple field tests were conducted to quantify the response of the structure under various load conditions and investigate the comparative strain behaviors of the two spans. An initial diagnostic test established baseline strain behavior for each span, evaluated load distribution between adjacent girders, and identified critical load paths. Subsequent proof tests were performed approximately one year apart to further evaluate the structure and observe any changes in bridge behavior. Load paths for proof testing were characterized by the number and configuration of trucks loads and consisted of monitoring strain under static loads at incremental quarter-point and midspan locations for each span. Between one and four tandem-axle trucks arranged in various configurations were used to apply ten load paths established with the intent of maximizing induced strains.

The following conclusions and recommendations are based on monitoring and field-testing data from VWSG instrumentation for NM Bridge No. 9706.

- Expected strains calculated for UHPC girders (interior and exterior) were consistently larger than those for the larger HPC girders. However, maximum measured strains during each load test were consistently greater in magnitude for the HPC span, regardless of truck load configuration, and the difference in maximum measured strain between the spans tended to increase with greater truck loads.
- The contrast in expected and measured strains during field testing for the UHPC and HPC spans may suggest the modulus of elasticity value, calculated using Equation (Graybeal, 2006b; see Section **Error! Reference source not found.**) used for calculating available and expected strains was conservative for the nonproprietary UHPC. A value more representative of this unique UHPC would in fact increase the available and expected strain

for the U section girders, making the contrast in strain behavior between the two spans even more apparent.

- For ST loading, the maximum strains recorded across all load tests was approximately 103 με in girder U-2 (Path 1 of PT3), and 115 με in girder H-1 (Path 1 of PT2). Strains were largest when truck loads were nearest to each edge of the transverse span and typically decreased as the truck paths moved toward the middle of the span, indicating better distribution between adjacent girders.
- Both the UHPC and HPC spans exhibited relatively symmetric strain behavior for double truck loading. maximum strains recorded across all load tests for DT loading were approximately 140 με in girder U-1 (Path 7 of DT0), and 155 με in H-6 (Path 8 of PT3).
- Triple truck load Path 10 was conducted twice during each proof test of Bridge No. 9706, and strain behavior exhibited by both spans was highly consistent and relatively symmetric, both between Pass 1 and 2 of each test and year to year between tests (though strains generally increased during each subsequent proof test as a result of increasing truck loads). For TT loading, the maximum strains recorded across all load tests were approximately 144 με in girder U-4 (Path 10-Pass2 of PT3), and 160 με in girder H-5 (Path 10-Pass1 of PT3).
- Though typically between 10–30 με greater, both the consistency and symmetry of strain behaviors under STBB loading were similar to the results of ST loading. For STBB loading, the maximum strains recorded across all load tests were approximately 119 με in girder U-2 (Path 1 of PT3), and 136 με in girder H-1 (Path 1 of PT1).
- The four-truck configuration for DTBB loading maximized the total load placed on the bridge and expectedly maximized the measured strains and behaviors in comparison to all other configurations. Both the UHPC and HPC spans exhibited relatively symmetric strain behavior for DTBB loading. While strains among exterior girders consistently occurred in girder U-1 for the UHPC span, the locations varied between test for the HPC span between H-1 and H-8, and among interior girders varied for both the UHPC and HPC spans between each proof test, but consistently occurred in either girder Line 2 or 6.
- For DTBB loading, the overall maximum strain recorded in the UHPC span across all load tests was approximately 157 με in girder U-2 (Path 7 of PT3). For the HPC span, strains upwards of 160 με were measured during each load test, with a maximum overall strain of approximately 196 με in girder H-1 (Path 7 of PT2).
- Across all load tests and load configurations, strains in the UHPC span tended to be higher to north side of the span, whereas the HPC span exhibited more variable in comparison. This could possibly be indicative of the connection between girder U-2 through U-4. During construction of NM Bridge No. 9706, a production flaw was encountered in girder U-3. The post-tensioning ducts cast into interior stems were mistakenly embedded at the wrong depth in U-3, and thus did not align with the ducts of adjacent girders U-2 and U-4.

THIS PAGE INTETIONALLY LEFT BLANK

Task 2: Bridge 9706 Analytical Model

TASK 2: BRIDGE 9706 ANALYTICAL MODEL

New Mexico Bridge No. 9706 was constructed with two simple spans with a normal strength cast-in-place concrete deck. Each span consists of eight prestressed channel girders. The first span girders were constructed with high performance concrete (HPC) and the second span girders constructed with ultra-high performance concrete (UHPC). Computers and Structures, Inc. developed a software, CsiBridge that has bridge features and terminologies. This software was used to model the superstructure of Bridge No. 9706. The software does not have an existing template containing the unique channel shape of the prestressed girders used for Bridge No. 9706. Therefore, the girders were modeled using solid elements to create the cross-section of the beams and model its behavior. Each material is modeled using different material properties that are defined in the model. The design compressive strength used for the deck was 4 ksi (28 MPa). For UHPC and HPC, the design compressive strength used in the model was 21 and 9.5 ksi (145 and 65.5 MPa), respectively. The modulus of elasticity of UHPC materials was estimated based on Equation **Error! Reference source not found.** developed by Graybeal (2006b). The modulus of elasticity for the normal concrete and HPC materials was calculated based on Equation **Error! Reference source not found.** provided by ACI 318-code.

The UHPC and HPC girders and the cast-in-place concrete deck were modeled using solid element. Also, solid elements were used to model the deck on top of the girders. Solid element is an eight-node element based upon an isoparametric formulation, which include nine optional incompatible bending modes that improve bending behavior (Computer and Structural Inc., 2017). The solid element model began by drawing area element that meet the cross-section required. The area was then converted to solid elements. The solid elements for each section were then incremented at 6 in. (152 mm) in the longitudinal direction. This results in a small mesh in the longitudinal direction of the bridge. The cross-section mesh also was generated automatically due to the non-uniform cross-section of the girders. Figure 2.1presents the cross-section used for this model.

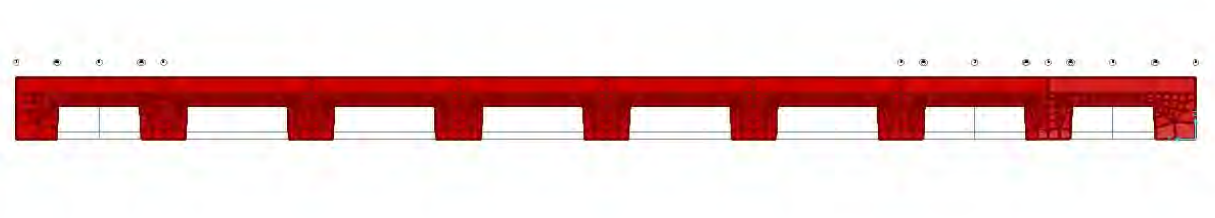


Figure 2.1: Bridge cross-section with solid element.

The prestressed was modeled using tendon elements having a diameter 0.6 in. The tendon parameters used were prestressed type with material defined by A722 Gr150 Type II. Figure 2.2 shows the strand locations along the bridge girders.

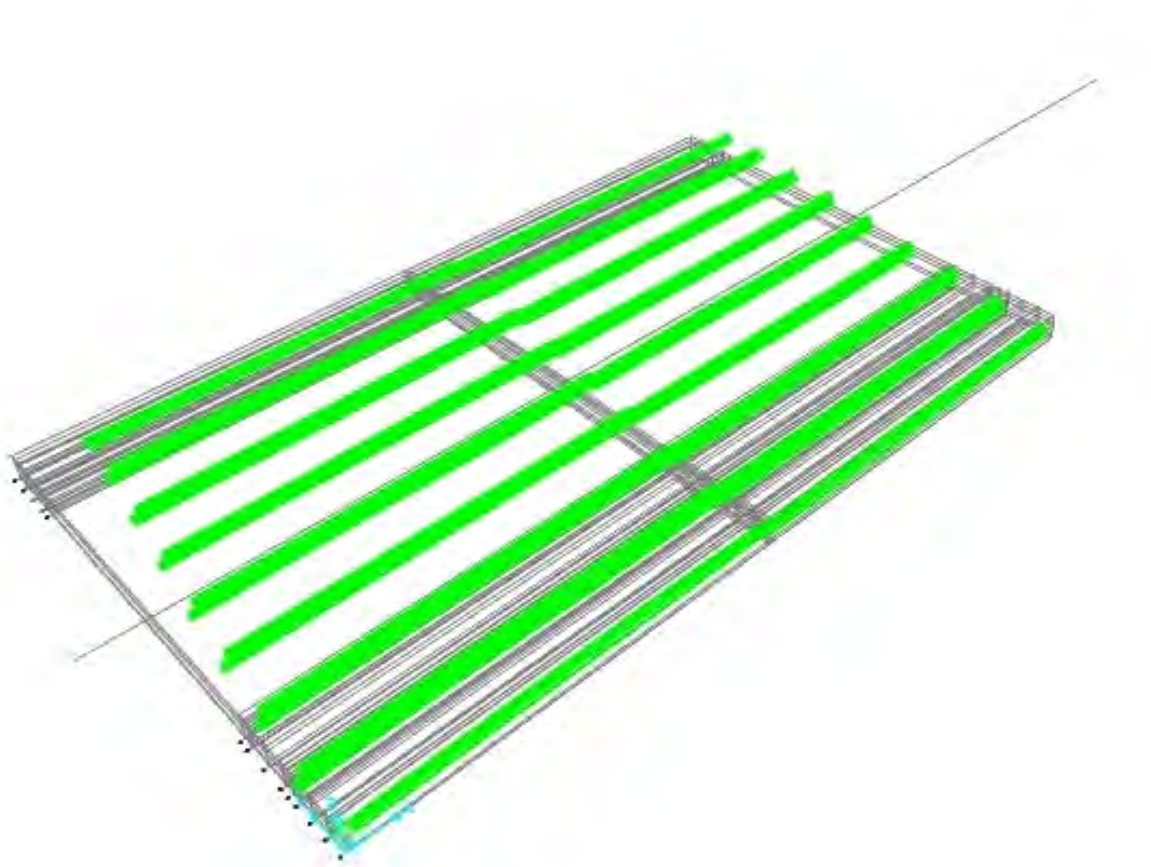


Figure 2.2: Strand locations on the bridge girders.

The supports were model using joint supports. These joint supports were assigned at each node underneath of the girder solid elements. Roller supports were used at each end of the span, and pin support used at the pier location. Supports, girders, deck, and prestressed are combined and imbedded together presenting the whole model as shown in Figures 3, 4, 5 and 6.

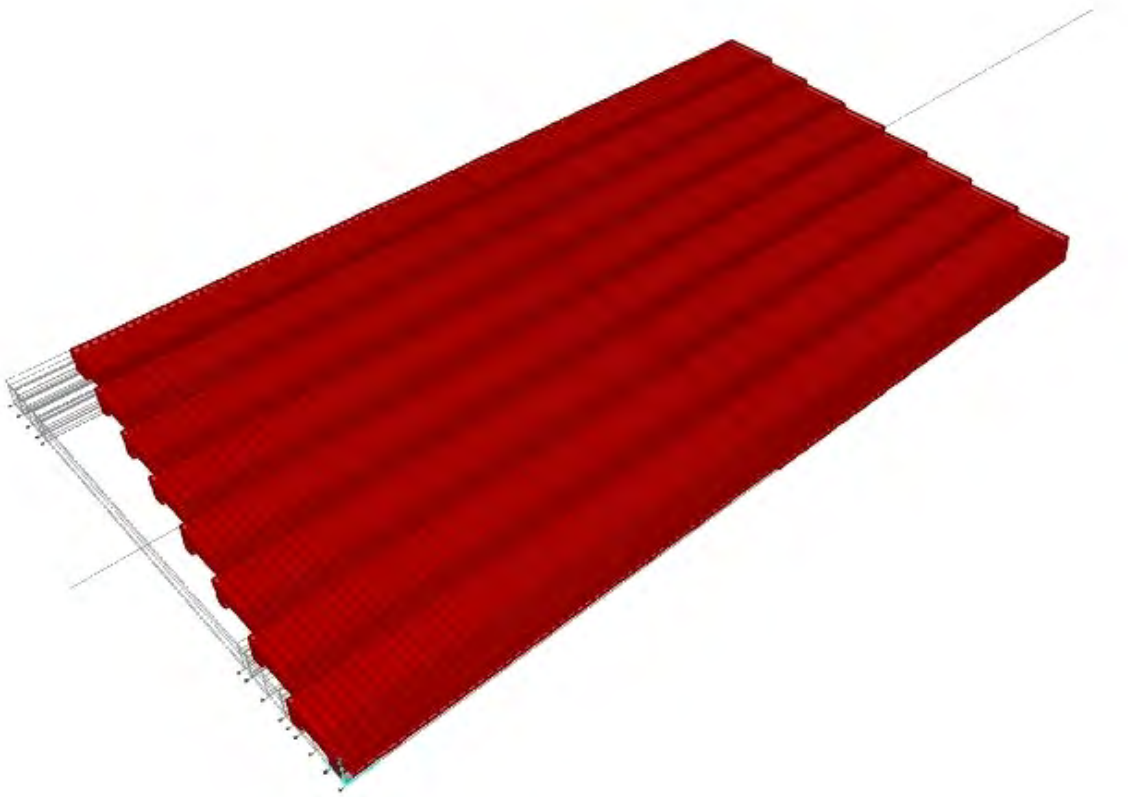


Figure 2.3: 3-D view of bridge using solid element.

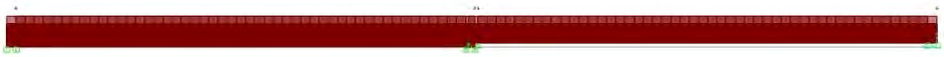


Figure 2.4: Bridge side view and different girder depth.



Figure 2.5: Bridge at Z=0 (bottom elevation).

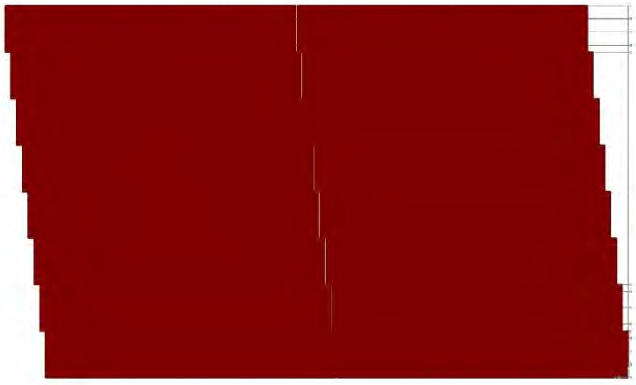


Figure 2.6: Bridge at Z=20 in. (508 mm) (top elevation).

The trucks load model began with defining the lane or path in which the truck travel across the bridge. For each path, there is a lane modeled corresponding to that specific path. Applying the width of the truck to the width of the lane, and lane length was along with superstructure length. The truck load was modeled using dimensions and loads provided from the field load tests. The design type of the truck was vehicle live with vertical load at front axle and back axle. Front axle loads consisted of two point loads with a total load 15.66 kips (70 kN). Back axle load consisted of four-point load spaced at 4.5 ft (1.4 m) with total load of 46.82 kips (208 kN). Figure 6 shows the truck designed for this model.



Figure 2.7: Design Truck specifications used for model.

Table 2.1 through Table 2.3 provide a comparison between the preliminary analytical results from the finite element model and the results measured during the field load test. Gauges were attached to the girders to measure the strain during the load tests. Analytical results were taken at approximately the same location as the strain gauge locations. To know where those gauges attached, sample letters used to identify their location. For example, UHPC NBG1, is ultra-high-performance concrete, north, bottom, girder number one, and so on. Proof and diagnostic load test results are donated by P and D for each path, respectively. Model results also are shown under model column. A single truck load was applied on Path 1 for a moving truck in this model for comparison with measured results from proof and diagnostic test. The results are presented in Table 2.1. It is noted that only one truck was used for the model at this time – a second truck model with be developed with the weights from the Proof load test in the future.

Table 2.1. Path1 Preliminary Results

Gauge Location	Path 1(moving) P*	Path 1(moving) D*	Path 1(moving) Model
UHPC NBG1	76.0	80.7	92.9
UHPC SBG1	86.5	87.9	83.3
UHPC NBG2	81.5	81.0	81.3
UHPC SBG2	65.6	67.0	70.0
UHPC NBG3	69.9	66.1	67.7
UHPC SBG3	51.1	60.5	45.5
UHPC NBG4	46.5	54.2	44.5
UHPC SBG4	28.2	45.2	26.7
UHPC SBG5	14.4	21.4	13.8
UHPC SBG6	5.5	12.5	5.1
UHPC SBG7	1.9	4.7	0.3
UHPC SBG8	1.9	1.9	0.3
Gauge Location	Path 1(moving) P	Path 1(moving) D	Path 1(moving) Model
HPC NBG1	72.0	73.7	93.2
HPC SBG1	78.1	76.0	79.3
HPC NBG2	90.7	78.0	81.4
HPC SBG2	77.1	69.8	66.7
HPC NBG3	70.0	66.8	68.1
HPC SBG3	60.4	56.0	44.9
HPC NBG4	48.7	55.9	46.7
HPC SBG4	34.0	49.3	26.0
HPC SBG5	13.7	24.6	13.5
HPC SBG6	4.1	9.4	4.8
HPC SBG7	0.0	2.3	0.1
HPC SBG8	0.0	-1.8	0.4

Additionally, a single moving truck load was applied on Paths 4 and 6 in the model for comparison with measured results from the proof and diagnostic tests. Results are presented in Table 2.2 and Table 2.3.

Table 2.2. Path 4 Preliminary Results

Gauge Location	Path 4(moving) P	Path 4(moving) D	Path 4 (moving) Model
UHPC NBG1	12.2	8.4	13.3
UHPC SBG1	16.5	16.9	21.0
UHPC NBG2	17.3	19.2	20.0
UHPC SBG2	22.7	28.9	31.2
UHPC NBG3	33.1	32.1	29.6
UHPC SBG3	49.1	51.1	41.4
UHPC NBG4	56.6	54.2	40.8
UHPC SBG4	74.3	69.2	50.0
UHPC SBG5	72.2	62.9	49.9
UHPC SBG6	53.1	44.4	42.4
UHPC SBG7	35.0	25.0	30.8
UHPC SBG8	21.2	17.8	22.6
Gauge Location	Path 4(moving) P	Path 4(moving) D	Path 4 (moving) Model
HPC NBG1	9.4	5.9	10.2
HPC SBG1	13.5	13.5	17.7
HPC NBG2	16.3	17.3	17.4
HPC SBG2	30.1	29.4	29.1
HPC NBG3	29.8	30.4	28.9
HPC SBG3	54.7	49.9	42.2
HPC NBG4	54.7	54.7	42.2
HPC SBG4	78.0	73.0	51.9
HPC SBG5	89.2	71.5	52.5
HPC SBG6	51.2	42.7	44.6
HPC SBG7	25.8	22.0	33.1
HPC SBG8	12.1	10.3	24.1

Table 2.3. Path 6 Preliminary Results

Gauge Location	Path 6 (moving) P	Path 6 (moving) D	Path 6 (moving) Model
UHPC NBG1	8.4	3.3	0.4
UHPC SBG1	8.7	6.9	0.5
UHPC NBG2	9.8	5.6	0.1
UHPC SBG2	12.1	10.1	6.6
UHPC NBG3	19.1	13.5	5.9
UHPC SBG3	26.8	25.8	15.5
UHPC NBG4	30.2	24.5	14.7
UHPC SBG4	49.4	47.5	28.4
UHPC SBG5	66.6	62.4	45.8
UHPC SBG6	76.7	71.2	66.5
UHPC SBG7	94.5	86.4	76.2
UHPC SBG8	81.0	85.3	86.7
Gauge Location	Path 6 (moving) P	Path 6 (moving) D	Path 6 (moving) Model
HPC NBG1	0.9	2.4	0.0
HPC SBG1	2.1	5.7	0.0
HPC NBG2	3.9	7.2	0.0
HPC SBG2	8.6	14.7	5.0
HPC NBG3	8.5	12.9	4.6
HPC SBG3	17.8	24.5	13.9
HPC NBG4	15.7	26.1	13.5
HPC SBG4	31.8	53.7	27.1
HPC SBG5	65.6	72.7	46.4
HPC SBG6	86.7	77.4	68.8
HPC SBG7	83.4	77.8	81.4
HPC SBG8	77.5	78.0	93.1

Figures 3.8 – 3.15 compare the analytical model and the experiment results from the 2rd proof load test. The figures show the results from the single truck moving load for paths 1, 2, 3, and 6. The results are in good agreement between the analytical model and the experiment results for the paths illustrated.

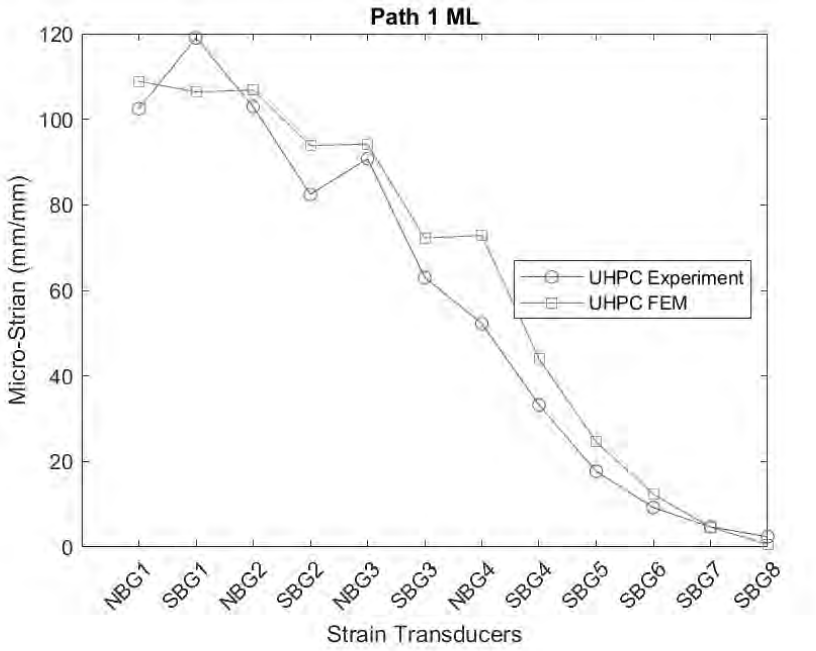


Figure 2.8: UHPC girders comparison for Single Truck moving load Path 1.

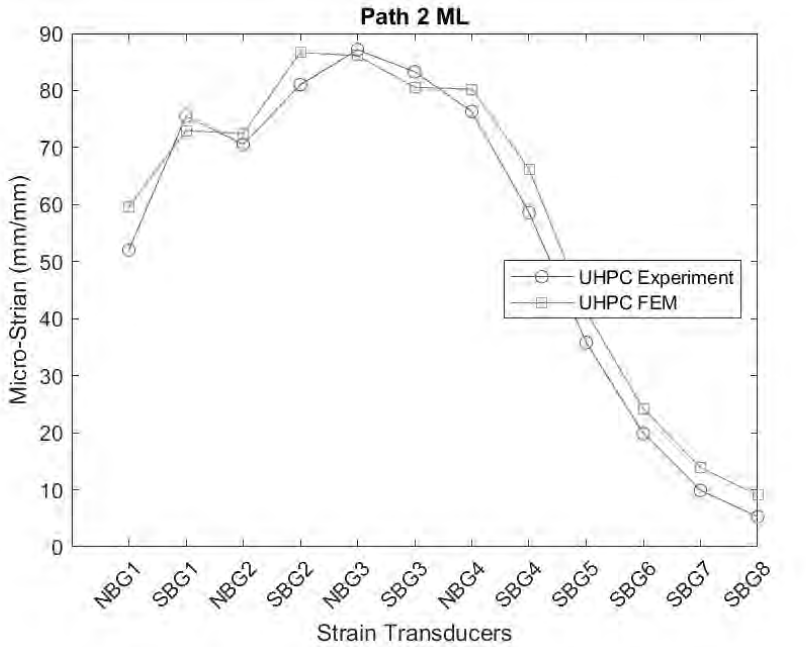


Figure 2.9: UHPC girders comparison for Single Truck moving load Path 2.

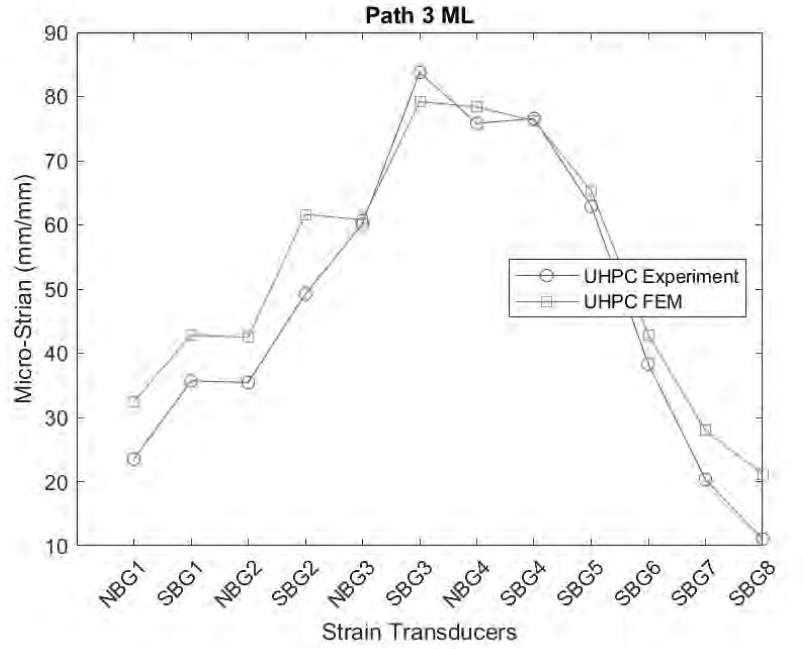


Figure 2.10: UHPC girders comparison for Single Truck moving load Path 3.

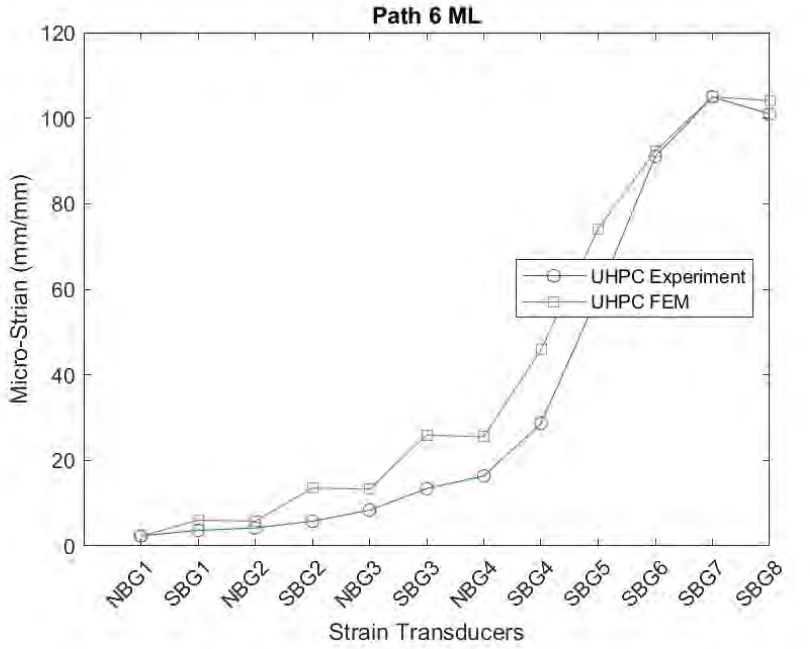


Figure 2.11: UHPC girders comparison for Single Truck moving load Path 6.

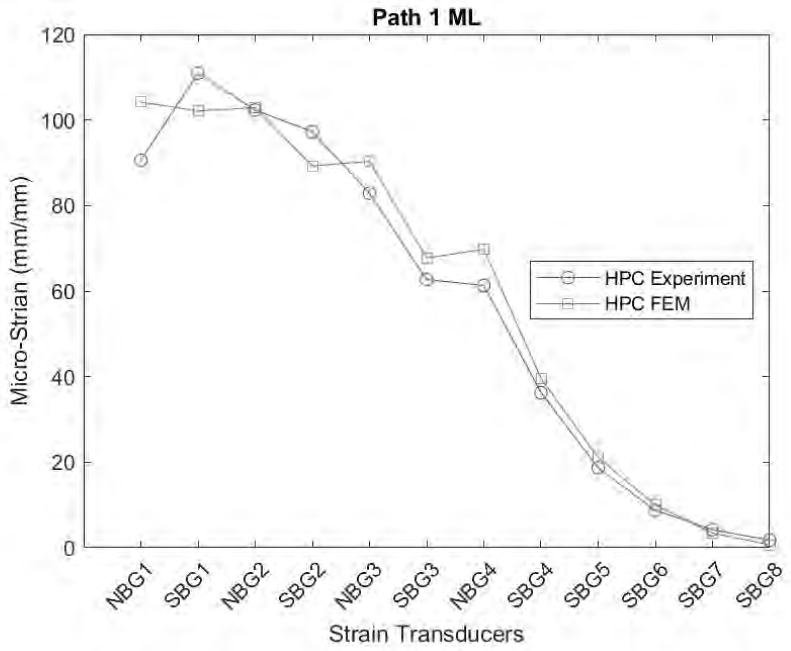


Figure 2.12: HPC girders comparison for Single Truck moving load Path 1.

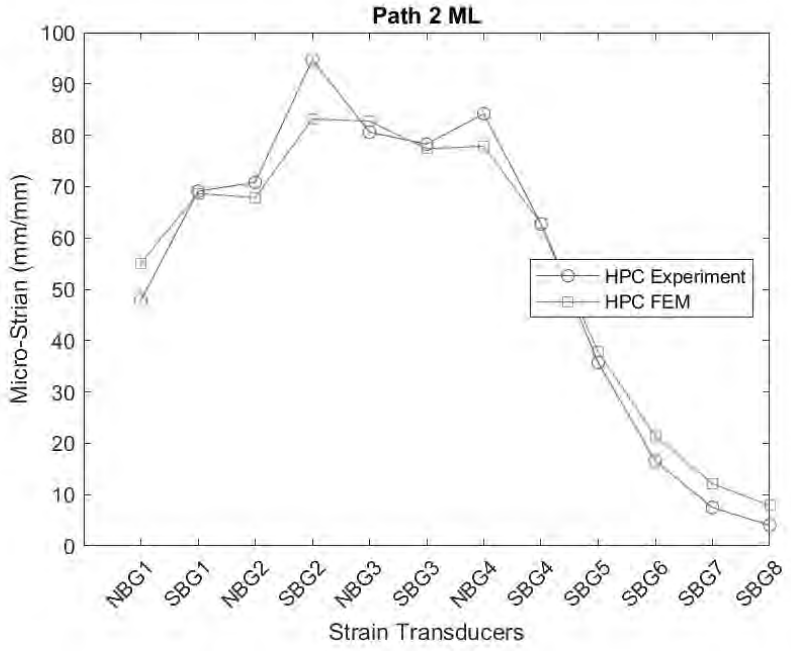


Figure 2.13: HPC girders comparison for Single Truck moving load Path 2.

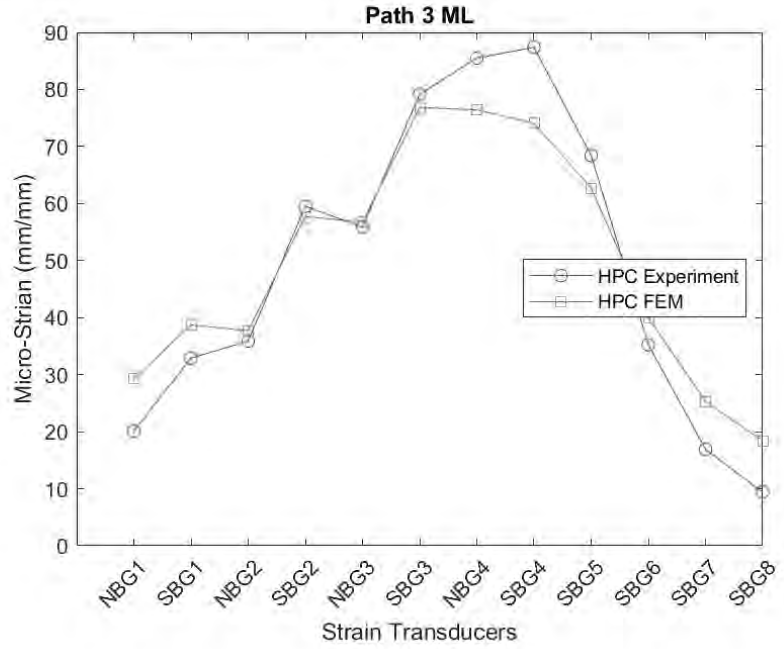


Figure 2.14: HPC girders comparison for Single Truck moving load Path 3.

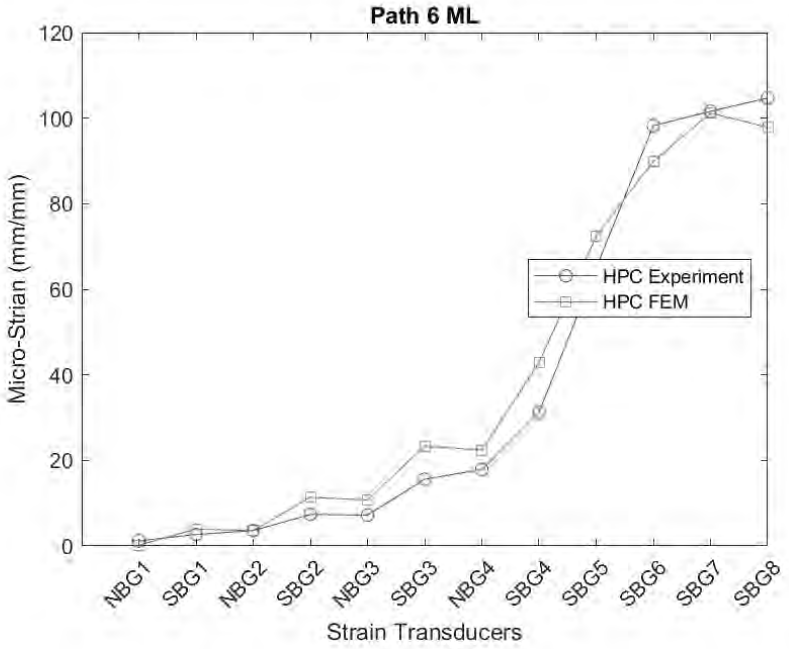


Figure 2.15: HPC girders comparison for Single Truck moving load Path 4.

THIS PAGE INTETIONALLY LEFT BLANK

Task 3: UHPC Symposium

TASK 3: UHPC SYMPOSIUM

The UHPC Symposium was held on April 17 – 18, 2018. The first session was 1:00-5:00 pm on April 17. The second session was 8:00 am – 12:00 pm on April 18. The sessions consisted of presentations and hands-on demonstrations held at the NMSU Structural Systems and Material Testing Laboratory (SSMTL). Over 30 people attended the symposium including members of the NMDOT, contractors, designers, researchers, and ready-mix companies. The list of presentations and speakers is provided below. Additionally, the save the date and a few pictures from the symposium are shown in Figure 3.1 and Figure 3.2.

List of presentation and speakers:

April 17, 2018

Introduction –Lakshmi Reddi, Dean of the College of Engineering, NMSU; David Jauregui, Department Head, Civil Engineering, NMSU
What is UHPC? – Brad Weldon, NMSU
Upcoming NMDOT UHPC Projects – Kathy Crowell, NMDOT
Research at NMSU – Feasibility to Implementation – Craig Newtson, NMSU
Large Scale Testing – Michael J. McGinnis, University of Texas at Tyler
Designing with UHPC – Danton Beam, HDR; Ben Najera, NMDOT
Implementation in a Precast Plant – Mark Manning, NMSU
Construction and Load Testing of Bridge 9706 – Mark Manning, Chris Kennedy, and Alain Cuaron (NMSU)
UHPC Projects in New Mexico – Kathy Crowell (NMDOT)

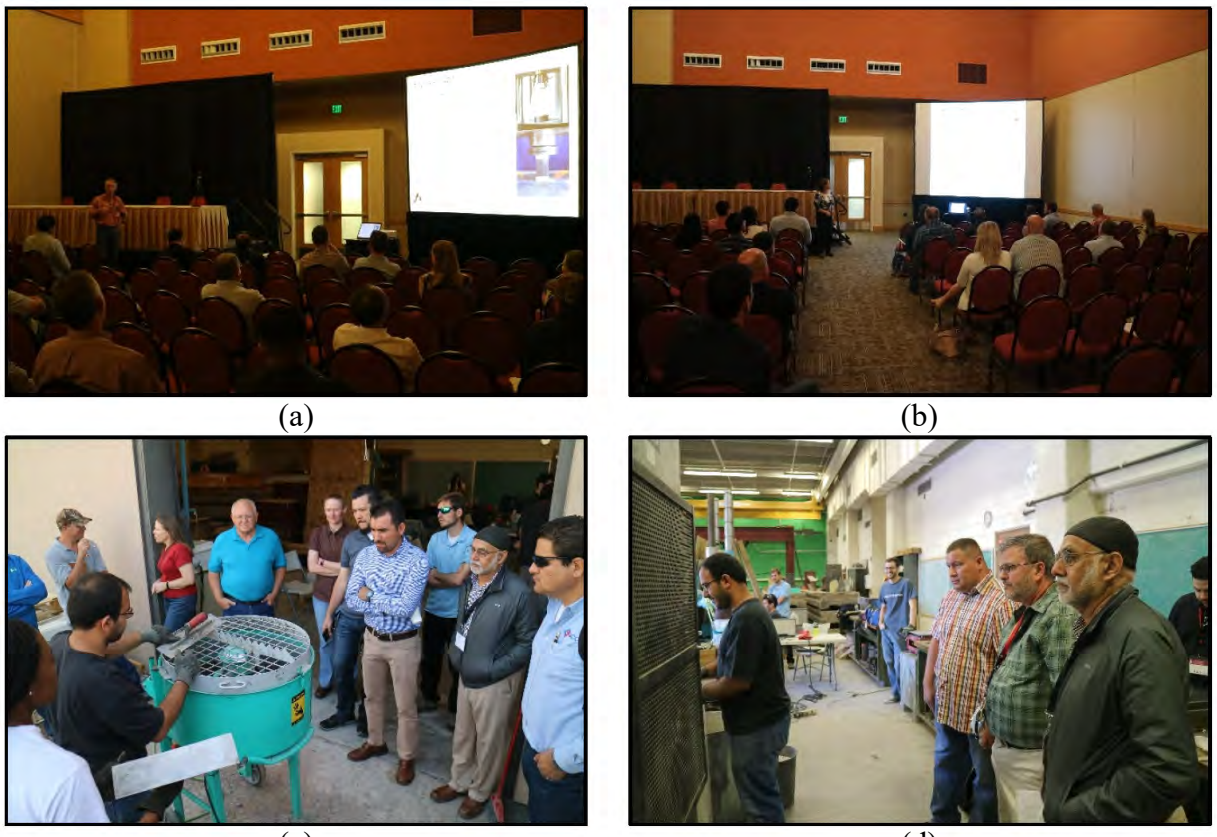
April 18, 2018

Introduction – Brad Weldon, NMSU
Overlay Project – TranSET, Craig Newtson, NMSU; Kathy Crowell, NMDOT

Hands on demonstration: mixing, casting, and testing led by NMSU graduate students at the SSMTL.



Figure 3.1: UHPC Symposium Save-the-Date Announcement.



(a) (b)

(c) (d)

Figure 3.2: Pictures from the UHPC Symposium.

THIS PAGE INTETIONALLY LEFT BLANK

Task 4: Mixture Proportion Optimization

TASK 4: MIXTURE PROPORTION OPTIMIZATION

Numerous batches of UHPC have been cast and tested at NMSU to investigate the effects of different mixture constituents on the strength characteristics and workability of the unique concrete. UHPC is typically produced with a lower water to cementitious materials (w/cm) ratio when compared to a normal concrete mixture. Additionally, UHPC typically does not use coarse aggregate. Both factors affect the workability of concrete. Workability describes how easily fresh concrete can be mixed, placed, consolidated, and finished. Workability is an important property of concrete because it relates to strength, quality, appearance, and labor cost. This property is significant in construction so that it can be handled, placed, compacted, and finished easily without any loss of homogeneity. Due to the low w/cm ratio of UHPC, HRWRA are used to increase the workability. The workability and compressive strength were investigated by modifying the mixture proportions, measuring slump and flow, and measuring compressive strengths.

4.1 Mixture Proportion Investigation

Currently, ten different UHPC mixture proportions have been cast. During the casting of each batch, the slump and / or flow of each mixture was measured. The mixture proportions varied different constituents to identify their influence on strength and workability. A slump and spread test were performed on each batch according to ASTM C143 and ASTM C1611, respectively. In conjunction with the slump and spread tests, compressive strength of the UHPC was measured at 7- and 28-days following BS 1881 for the compressive strength testing of cube specimens.

The baseline mixture proportions had 37.5% fly ash and 62.5% silica fume as the supplemental cementitious materials (the original mixture proportions developed). As the study progressed, the fly ash and silica fume were changed to a ratio of 50/50. The sand content was then varied at 1900 lb, 1700 lb, and 1500 lb. Finally, the w/cm ratio was varied at 0.14, 0.15, and 0.16.

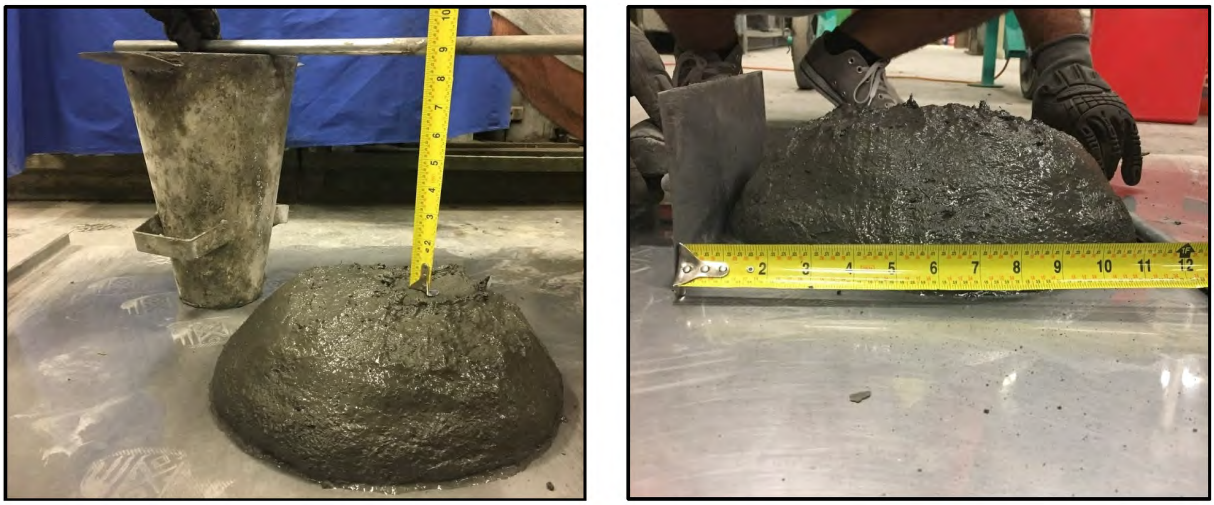
Each of the mixes had the same constituents, therefore had a consistent mixing procedure. All constituents were weighed and measured to the specified amounts. The dry material was added to the mixer with the sand first, followed by the cement, fly ash, and silica fume and mixed for 30 seconds. Next, the water was added followed by the HRWRA. The batch was mixed until a visible sheen appeared on the surface of the mixture, at this point the mixer was reversed to ensure a thorough mix. After 3 minutes, the steel fibers were added and mixed for another 3 minutes. After mixing, slump and spread tests were conducted.

The slump and spread tests performed on each batch were in accordance with ASTM C143 and ASTM C1611, respectively, by using a standard slump cone of 12-inch height, 8-inch base diameter, and 4-inch opening diameter. The slump cone was placed over a stainless-steel base plate, with the 4-inch opening diameter facing top. The UHPC was scooped into the cone in 1/3 volume increments allowing 25 rods in a circular motion in between scoops. When the cone was filled to the top and rodded, it was troweled flush with the brim of the slump cone. Slowly, and in a straight single motion the cone was pulled directly up allowing the UHPC to slump and spread, measurements were then taken using a tape measure. For the slump measurement, the slump cone

was inverted (placed with the 8 inch base diameter facing top) and a rod was placed flush with the top of the slump cone. The tape measurement was taken from the center of the top of the UHPC mixture to the bottom of the rod (Figure 4.1a).

The spread of the UHPC was determined by taking three measurements of the bottom of the UHPC mixture: from the left to the right, front to back, and on a diagonal axis (Figure 4.1b). After the slump and spread were recorded the UHPC mixture was placed back into the mixer and mixed for 45 seconds. Lastly, 2 in. and 4 in. cube molds were filled with the UHPC mixtures for each batch. The UHPC was cured in ambient conditions and compression strength tests were conducted at 7 and 28 days.

Table 4.1 provides the spread and slump measurements (inches), the average spread (inches), and the total mixing time (min). Table 4.2 provides the average compressive strength (psi) for both 2 in. and 4 in. cubes, both at 7 and 28 days of ambient curing.



(a) (b)

Figure 4.1 Slump Flow Test measurements for (a) slump and (b) spread.

Table 4.1: Workability Summary

Mixture		Spread (in.)	Slump (in.)	Avg. Spread (in.)	Mix Time (min)
0.14 w/cm[1] ratio	FA37.5 SF62.5 1900	8.25 8.0 8.25	N/A	8.17	20
0.14 w/cm ratio	FA50 SF50 1900	9.5 9.75 10.0	N/A	9.75	18
0.14 w/cm ratio	FA50 SF50 1700	8.0 8.0 8.0	N/A	8.00	32
0.14 w/cm ratio	FA50 SF50 1500	8.0 8.0 8.0	N/A	8.00	30
0.15 w/cm ratio	FA50 SF50 1900	8.0 8.0 8.25	3.5	8.08	20
0.15 w/cm ratio	FA50 SF50 1700	9.75 9.75 10.0	N/A	9.83	16
0.15 w/cm ratio	FA50 SF50 1500	8.25 8.25 8.0	2	8.17	20
0.16 w/cm ratio	FA50 SF50 1900	8.5 8.5 8.75	2.25	8.58	21.5
0.16 w/cm ratio	FA50 SF50 1700	9.0 9.5 10.0	5.5	9.50	18
0.16 w/cm ratio	FA50 SF50 1500	9.5 9.5 10.0	6.5	9.67	16

[1] w/cm ratio, percent fly ash to silica fume (supplemental cementitious materials)

Table 4.2: Compressive Strength Summary

Mixture		$f_{c,7\text{-day}}$[2] (psi)		$f_{c,28\text{-day}}$[3] (psi)	
		2 in. Cubes	4 in. Cubes	2 in. Cubes	4 in. Cubes
0.14 w/cm[1] ratio	37.5 FA - 62.5 SF 1900 lb sand	-	-	15913.75	17413.33
	50 FA - 50 SF 1900 lb sand	-	-	17077.5	17076.27
	50 FA - 50 SF 1700 lb sand	-	-	16759.58	17396.7
	50 FA - 50 SF 1500 lb sand	16270	15157.2	18647.5	17650.65
0.15 w/cm ratio	50 FA - 50 SF 1900 lb sand	16146.67	15043.45	19320	18275.95
	50 FA - 50 SF 1700 lb sand	15777.5	14875.65	18876.67	17592.2
	50 FA - 50 SF 1500 lb sand	17598.13	15334.7	20095.5	17693.45
0.16 w/cm ratio	50 FA - 50 SF 1900 lb sand	16013.13	14546.9	18210	18562.5
	50 FA - 50 SF 1700 lb sand	17166.25	14055.35	20260.5	17271.9
	50 FA - 50 SF 1500 lb sand	16200	13613.1	19666.5	16889.05

[1] w/cm ratio, percent fly ash to silica fume (supplemental cementitious materials)
[2] 7 - day compressive strength
[3] 28 - day compressive strength

In an attempt to improve the workability and strength of UHPC, the use of different types of chemical admixtures was investigated. MasterGlenium 3030 was the HRWRA initially used, then three additional chemical admixtures were analyzed: MasterGlenium 7700, MasterGlenium 7920, and MasterSet DELVO. All MasterGlenium admixtures are HRWRAs, and MasterSet DELVO is a water-reducing and retarder. Prior to this, Mixture 0.15 w/cm – 50FA/50SF – 1700 lb sand was selected for further investigation based on workability and strength. Therefore, this served as the baseline for the new mixtures containing the different types of HRWRAs. Table 4.3 presents the different types of HRWRAs and the dosages used. The MasterGlenium admixtures dosage was 86.8 fl. oz. per 100 lb (5,658 ml per 100 kg) of cement, and the DELVO admixture dosage was 1 fl. oz. per 100 lb (65 ml per 100 kg) of cement.

Table 4.3: Chemical Admixture Variation Dosages

Mixture	Chemical Admixture	HRWRA, gal/yd^3 (L/m^3)	DELVO, gal/yd^3 (L/m^3)
0.15w/cm – 50FA/50SF – 1700 lb sand	7700	9.00 (44.6)	-
	7700	7.50 (37.1)	-
	7920	9.00 (44.6)	-
	7700 + DELVO	9.00 (44.6)	0.107 (0.530)

Results obtained from the effect of chemical admixture variation are summarized in Table 4.4. Table 4.4 provides the compressive strengths of both 2-inch (51-mm) and 4-inch (100-mm) cube specimens at 1, 3, 7, and 28 days of ambient curing.

Table 4.4: Compressive Strength Results for Different Chemical Admixtures

Chemical Admixture and Dosage	Specimens	Avg. Compressive Strength, psi [MPa]			
		1-Day	3-Day	7-Day	28-Day
7700 HRWRA (9.0 gal/yd^3) [44.6 L/m^3]	2-in. (51-mm)	4340 [29.9]	10,650 [73.4]	12,930 [89.9]	16,190 [111.6]
	3.94-in. (100-mm)	3960 [27.3]	10,130 [69.8]	12,450 [85.9]	14,430 [99.5]
7700 HRWRA (7.5 gal/yd^3) [37.1 L/m^3]	2-in. (51-mm)	5400 [37.3]	10,640 [73.4]	12,500 [86.2]	15,650 [1] [107.9] [1]
	3.94-in. (100-mm)	4890 [33.7]	10,370 [71.5]	11,120 [76.7]	13,990 [1] [96.5] [1]
7920 HRWRA (9.0 gal/yd^3) [44.6 L/m^3]	2-in. (51-mm)	664 [4.57]	6630 [45.7]	9050 [62.4]	12,200 [2] [84.1] [2]
	3.94-in. (100-mm)	329 [2.26]	6520 [45.0]	9780 [67.4]	12,650 [2] [87.2] [2]
7700 HRWRA (9.0 gal/yd^3) [44.6 L/m^3] + DELVO	2-in. (51-mm)	4800 [33.1]	10,500 [72.4]	12,600 [86.9]	14,730 [101.5]
	3.94-in. (100-mm)	5030 [34.7]	10,090 [69.6]	12,240 [84.4]	14,290 [98.5]

[1] 32 – day compressive strength
[2] 24 – day compresseive strength

The next part of the mixture proportion investigation was to look into the effect of increasing the steel fiber reinforcement. Steel fiber percent variations were analyzed in terms of workability, compressive and flexural strengths. Percentages started with 0% fibers, then increased to 1%, 1.5%, 2%, and 3% by volume. These fiber variations started with Mixture 0.14 w/cm ratio – 50FA/50SF – 1900 lb sand at 0% fibers, then moved to a mixture with an increased w/cm ratio of 0.145. Sand content was also decreased from 1900 to 1500 lb/yd^3. This w/cm ratio was increased to provide better workability of the UHPC, since at higher steel fiber dosages the workability goes down. Therefore, increasing to 3% by volume of steel fibers will affect the workability. The mixture proportions were also modified to isolate the effect of the steel fiber content in UHPC. The average seven-day compressive strength results at ambient and heat curing regimens are presented in Table 4.5.

Table 4.5: Results for Varying Steel Fiber Contents

Fiber Percent (%)	Slump, in. [mm]	Avg. Spread, in. [mm]	Curing Regimen	Avg. 7-Day Compressive Strength, psi [MPa]	
				2-in. (51-mm) Cubes	3.94-in.(100-mm) Cubes
Mixture 0.14 w/cm – 50FA/50SF – 1900 lb sand					
0	3.00 [76.2]	9.08 [231]	Ambient	12,410 [85.5]	11,330 [78.2]
			Heat Cured	18,795 [129.6]	15,830 [109.1]
Mixture 0.145 w/cm – 50FA/50SF – 1500 lb sand					
1	9.50 [241]	16.3 [414]	Ambient	13,190 [90.9]	12,700 [87.6]
			Heat Cured	20,310 [140.0]	18,000 [124.1]
1.5	8.00 [203]	11.9 [302]	Ambient	12,160 [83.9]	12,850 [88.6]
			Heat Cured	23,540 [162.3]	20,920 [144.2]
2	8.75 [222]	12.8 [325]	Ambient	13,590 [93.7]	14,230 [98.1]
			Heat Cured	24,700 [170.3]	20,330 [140.1]
3	6.50 [165]	10.5 [267]	Ambient	-	-
			Heat Cured	25.830 [178.1]	21,300 [146.9]

To further analyze the effect of steel fiber percent in UHPC, flexural strengths in terms of MOR of the fiber-reinforced batches were also analyzed. Flexural testing was conducted on specimens after 28 days of ambient curing. Batch 1 (0.14 w/cm – 50FA/50SF – 1900 lb sand) was not fiber-reinforced; therefore, was not included for flexural testing. The average moment and MOR results from flexural strength tests are summarized in Table 4.6.

Table 4.6: Flexural Strength Results for Increasing Steel Fiber Content

Batch No.	Fiber Percent (%)	Avg. Moment, lb-in [N-m]	Avg. MOR, psi [MPa]
1	1	12,860 [1454]	1610 [11.1]
2	1.5	14,380 [1625]	1800 [12.4]
3	2	14,760 [1668]	1850 [12.7]
4	3	14,550 [1644]	1820 [12.5]

The investigation progressed by focusing on the fiber reinforcement of UHPC and by implementing poly-based fibers to the mixtures. Mixtures consisted of 1.5% by volume of 2 in. (51 mm) and 0.5 in. (13 mm) polyethylene fibers with specific gravities of 0.92 and 0.91, respectively. Three mixtures were tested to see the strength of the different UHPC mixtures. For

the first mixture, steel fibers and polyethylene fibers were split evenly by volume; meaning that 0.75% by volume was 0.5 in. (13 mm) steel fibers and the remaining 0.75% was 2 in. (51 mm) polyethylene fibers. The second mixture consisted of the same mixture proportions as the first, but instead of 2 in. (51 mm) polyethylene fibers, 0.5 in. (13 mm) polyethylene fibers were used. Lastly, the third mixture contained 0.5 in. (13 mm) polyethylene fibers only. The effects of polyethylene fibers on compressive strength are presented in Table 4.7. Both ambient and heat curing regimens were used to evaluate the effect of heat curing on poly-based fibers.

Table 4.7: Summarized Results for Use of Polyethylene Fibers

	Mixture	Polyethylene Fiber Length, in. [mm]	Slump, in. [mm]	Avg. Spread, in. [mm]	Avg. Compressive Strength, psi [MPa] 4.0 in. (100 mm) Cubes 7-Day	28-Day
UHPC Under Ambient Curing						
1	50stl/50poly	2.0 [51]	5.00 [127]	11.0 [279]	13,290 [91.7]	15,490 [106.8]
2	50stl/50poly	0.5 [13]	4.25 [108]	9.67 [246]	13,720 [94.6]	17,850 [123.0]
3	All Poly	0.5 [13]	2.75 [69.9]	9.00 [229]	12,890 [88.8]	15,250 [105.1]
UHPC Under Heat Curing						
1	50stl/50poly	2.0 [51]	4.00 [102]	9.50 [241]	19,500 [134.4]	18,640 [128.5]
2	50stl/50poly	0.5 [13]	3.50 [88.9]	9.00 [229]	18,800 [129.6]	19,330 [133.3]
3	All Poly	0.5 [13]	2.25 [57.1]	8.42 [214]	17,330 [119.5]	17,100 [117.9]

Again, to further investigate the effect of polyethylene fibers in UHPC, flexural strengths in terms of MOR were also analyzed. Flexural testing was conducted on specimens after 28 days under ambient curing. The average moment and MOR results from flexural strength tests are summarized in Table 4.8.

Table 4.8: Flexural Strength Results for Ambient Polyethylene Fiber Reinforced UHPC

	Mixture	Polyethylene Fiber Length, in. [mm]	Avg. Moment, lb-in [N-m]	Avg. MOR, psi [MPa]
1	50stl/50poly	2.0 [51]	12,720 [1438]	1590 [11.0]
2	50stl/50poly	0.5 [13]	11,090 [1253]	1390 [9.56]
3	All Poly	0.5 [13]	10,410 [1176]	1300 [8.97]
4	All Steel	0.5 [13]	11,930 [1348]	1490 [10.3]

Currently, new USA-made steel fibers of 0.5 in. (51mm) in length were introduced to investigate its effect on the UHPC. Table 4.9 presents the compressive strengths at 1, 3, 7, 14, 21, and 28 days under both ambient and heat curing regimens by using Mixture 0.15 w/cm – 50FA/50SF – 1700 lb sand. As the study progresses, further changes to the mixture proportions are being conducted, such as decreasing and increasing the w/cm ratio to 0.14 and 0.16, respectively, the results of which are provided in Table 4.10 and Table 4.11.

Table 4.9: Summary Results for New USA-Made Steel Fibers (0.15-50/50-1700)

Slump, in. [mm]	Avg. Spread, in. [mm]	Curing Regimen	4 in. (100 mm) Cube Avg. Compressive Strength, psi [MPa]		
			1-Day	3-Day	7-Day
8.75 [222]	13.7 [348]	Ambient	7020 [48.4]	10,580 [72.9]	12,090 [83.3]
		Heat Cured	-	15,030 [103.6]	15,870 [109.4]
Slump, in. [mm]	Avg. Spread, in. [mm]	Curing Regimen	14-Day	21-Day	28-Day
7.75 [197]	11.6 [295]	Ambient	14,020 [96.1]	15,610 [107.6]	13,990 [96.4]
		Heat Cured	15,960 [110.1]	16,660 [114.9]	15,470 [106.6]

Table 4.10: Summary Results for New USA-Made Steel Fibers (0.14-50/50-1700)

Slump, in. [mm]	Avg. Spread, in. [mm]	Curing Regimen	4 in Cube Avg. Compressive Strength, psi [MPa]		
			1-Day	3-Day	7-Day
6.75 [171]	10.9 [277]	Ambient	6730 [46.4]	10,670 [73.6]	12,360 [85.2]
		Heat Cured	-	17,370 [119.8]	16,430 [113.3]
Slump, in. [mm]	Avg. Spread, in. [mm]	Curing Regimen	14-Day	21-Day	28-Day
4.75 [121]	9.33 [237]	Ambient	12,460 [85.9]	13,940 [96.1]	13,440 [92.7]
		Heat Cured	14,650 [101.0]	16,660 [114.9]	16,810 [115.9]

Table 4.11: Summary Results for New USA-Made Steel Fibers (0.16-50/50-1700)

Slump, in. [mm]	Avg. Spread, in. [mm]	Curing Regimen	4 in Cube Avg. Compressive Strength, psi [MPa]		
			1-Day	3-Day	7-Day
8.75 [222]	15.1 [384]	Ambient	5260 [36.3]	9830 [67.8]	10,240 [70.6]
		Heat Cured	-	14,480 [99.8]	15,840 [109.2]
Slump, in. [mm]	Avg. Spread, in. [mm]	Curing Regimen	14-Day	21-Day	28-Day
8.50 [216]	13.3 [338]	Ambient	10,420 [71.8]	12,530 [86.4]	10,300 [71.0]
		Heat Cured	14,410 [99.4]	15,130 [104.3]	14,500 [100.0]

Additional optimization of the mixture proportions needed to be done since no compressive strengths reached the 17,000 psi (120 MPa) required minimum stated by ASTM. As a result, Mixture 0.145 w/cm – 50FA/50SF – 1600 lb sand was introduced. As the study progresses, further changes to the mixture proportions might be performed. Table 4.12 presents the compressive strengths at 1, 3, 7, 14, 21, and 28 days under both ambient and heat curing regimens.

Table 4.12: Summary Results for New USA-Made Steel Fibers (0.145-37.5/62.5-1600)

Slump, in. [mm]	Avg. Spread, in. [mm]	Curing Regimen	4 in Cube Avg. Compressive Strength, psi [MPa]		
			1-Day	3-Day	7-Day
4.50 [114]	9.42 [239]	Ambient	5770 [39.8]	9430 [65.0]	8170 [56.3]
		Heat Cured	-	12,630 [87.1]	13,370 [92.2]
Slump, in. [mm]	Avg. Spread, in. [mm]	Curing Regimen	14-Day	21-Day	28-Day
5.75 [146]	10.0 [254]	Ambient	9850 [67.9]	10,680 [73.6]	10,150 [70.0]
		Heat Cured	16,040 [110.6]	15,070 [103.9]	13,550 [93.4]

4.2 Time-Dependent Strength Gain of Nonproprietary UHPC

A series of parallel studies were conducted to investigate the early-age and long-term strength gain of the UHPC mixture proportions developed at NMSU. These studies included analyses of compressive strength, unit weight, modulus of rupture, and modulus of elasticity for UHPC specimens produced under laboratory conditions and using two curing regimens. Concrete core temperatures were also monitored to evaluate the efficiency of the laboratory curing regimens and the effects of curing on time-dependent strength gain. Furthermore, the relationships between compressive strength and the other measured material properties were evaluated to characterize these interactions for this unique UHPC.

4.2.1 Mixture Proportions

The results of the investigations presented in the following sections use the batch naming convention provided in Figure 4.2. All batches tested and presented for these studies were produced based on the standard mixture proportions shown in Table 4.13. The mixture proportions are calculated using a w/cm ratio of 0.140, volumetric fiber content of 1.50%, and must be adjusted for sand moisture content and absorption.

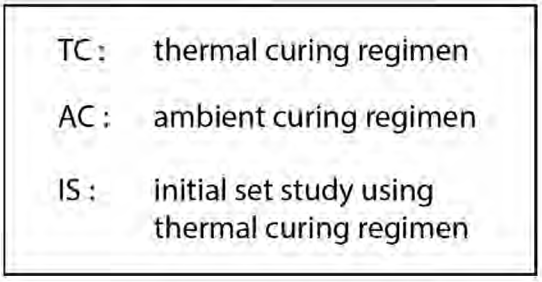


Figure 4.2: Batch naming convention for nonproprietary UHPC strength gain studies.

Table 4.13: Mixture Proportions for 1.25 ft^3 (0.035 m^3) Batch of Nonproprietary UHPC

Material	Quantity	
Sand	85.0 lb	(38.5 kg)
Type I/II Portland Cement	60.6 lb	(27.5 kg)
Silica Fume	9.47 lb	(4.30 kg)
Class F Fly Ash	5.68 lb	(2.58 kg)
Water (w/cm = 0.140)	10.6 lb	(4.81 kg)
High-Range Water-reducing Admixture	50.7 fl oz	(1499 mL)
High Strength Steel Fibers (volumetric content of 1.50%)	9.19 lb	(4.17 kg)

NOTE: Values based on aggregates at oven-dry conditions and must be adjusted for moisture content and absorption.

4.2.2 Laboratory Production of UHPC

Production of UHPC for the time-dependent strength gain studies was conducted at the Structural Systems and Materials Testing Laboratory (SSMTL) at NMSU. Mixing was performed using a 4.25 ft^3 (0.120 m^3) portable vertical shaft mixer, with a typical batch size of 1.25 ft^3 (0.035 m^3). The mixing process remained consistent across all batches, regardless of the curing regimen to be employed, and followed the sequence shown in Figure 4.3. Mixture proportions were weighed, and the mixing process began with only dry granular and cementitious materials. Oven-dried sand was thoroughly mixed with cement, silica fume, and fly ash for approximately 30 seconds before water and a high-range water-reducing admixture (HRWRA) were added simultaneously. Mixing was continued until proper consistency was achieved, at which time high-strength steel fibers were added at a volumetric content of 1.5%. Mixing times were generally consistent for each batch, though some variation occurred depending ambient conditions in the laboratory. Steel molds were prepared with a light coating of oil and placed on a vibrating table during placement of concrete to ensure consolidation. After the concrete had been properly finished, the molds were covered with plastic to prevent loss of moisture and remained at ambient conditions for 24 hours. The two curing regimens used for these strength gain studies are detailed in Section 4.2.4.1 and Section 4.2.5.1, respectively.

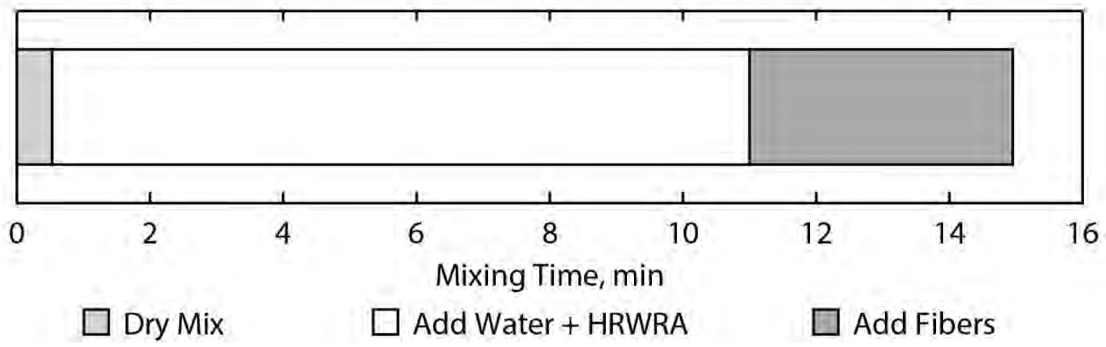


Figure 4.3: Laboratory mixing process for nonproprietary UHPC strength gain studies.

4.2.3 Measured Material Properties

4.2.3.1 Compressive Strength

The compressive strengths (f_c) for the UHPC developed at NMSU using local materials have been well documented for several variations of mixture proportions and curing regimens (Allena, 2010; Allena and Newtson, 2011; Lyell, 2011, Muro-Villanueva, 2012; Muro-Villanueva et al., 2013; Weldon et al., 2012; Guaderrama and Weldon, 2013, Visage, 2013; Giesler, 2014; Giesler et al., 2018; Visage et al., 2019). Specimens tested by Visage (2013) and Guaderrama and Weldon (2013) exhibited relatively linear compressive behavior prior to failure, as opposed to the traditional parabolic stress-strain curve exhibited by conventional concretes, which was consistent with results of previous research conducted on proprietary UHPC (Graybeal, 2006b). Furthermore, failure of UHPC specimens was typically observed to be sudden and forceful, particularly in the absence of fiber reinforcement. When fibers were included, redistribution of load across microcracks at the fiber-concrete interface produced audible indication of cracking before eventual specimen failure.

The most relevant data (conducted on specimens produced using the same or similar mixture proportions, fiber type and content, and curing regimen) from Giesler (2014), Manning (2015), Giesler et al. (2016), Manning et al. (2016), and Giesler et al. (2018) indicated compressive strengths typically range from 18.0 ksi (124 MPa) to 24.0 ksi (166 MPa). The previous studies also indicated that UHPC produced using thermal curing gains nearly all its compressive strength within the first week during the curing phase (see Section 4.2.4.1 for discussion of thermal curing regimen). Therefore, the reference age for compressive strength is typically taken as 7 days after casting for UHPC rather than the standard 28 days used for conventional concretes.

The development of compressive strength (f_c) was evaluated for these investigations using 4.0 in. (100 mm) UHPC cube specimens as outlined in Section i.i.

4.2.3.2 Unit Weight

Due to the variability of constituent materials (e.g., aggregate properties, type and content of fiber reinforcement, supplementary cementitious materials, etc.) and curing regimens for UHPCs, it is important to quantify the unit weight (w_c) of UHPC and assess its potential impact on design. AASHTO (2017) provides Equation 4.1 for the unit weight of concretes with compressive strength (f'_c) between 5.0 ksi (34.5 MPa) and 15.0 ksi (103.4 MPa). Assuming UHPC with an average compressive strength of 20.0 ksi (138 MPa), the resulting unit weight is calculated as 160 lb/ft^3 (2563 kg/m^3).

$$w_c = 0.140 + 0.001f'_c \text{ ksi} \qquad 4.1$$

$$w_c = 2240 + 2.32f'_c \text{ MPa}$$

The unit weight of the proprietary UHPC Ductal® has been shown to fall between 150 lb/ft^3 (2400 kg/m^3) and 160 lb/ft^3 (2500 kg/m^3) when subjected to various curing regimens (Graybeal, 2006b). Furthermore, unit weight was observed to increase with increasing compressive strength (Graybeal, 2006b). Though slightly conservative, this unit weight as calculated by AASHTO is not significantly larger than the results observed by Graybeal (2006b).

Previous research has shown the unit weight of the nonproprietary UHPC developed at NMSU and used in this research to correspond closely to NSC (Weldon et al., 2012, Giesler, 2014). Giesler (2014) reported the average unit weight of 4.0 in. (100 mm) UHPC cubes increased from 145.0 lb/ft^3 (2322 kg/m^3) without fiber reinforcement to 150.4 lb/ft^3 (2409 kg/m^3) when fibers were provided at a volumetric content of 1.50%. Even with the addition of fiber reinforcement increasing UHPC unit weights by approximately 5.0 lb/ft^3 (80.1 kg/m^3), the unit weight of this UHPC fell below AASHTO predictions.

The unit weight of UHPC for the research presented in this document was quantified using 4.0 in. (100 mm) cube specimens as outlined in Section i.ii.

4.2.3.3 Modulus of Rupture

While the ultimate flexural-tensile strength of UHPC is primarily a function of fiber reinforcement (based on fiber size, content, and orientation), fibers cannot contribute to flexural-tensile capacities until after initial cracking of the surrounding concrete, allowing tensile forces to be transferred into the crack-bridging fibers. The initial flexural-tensile cracking of UHPC has little to do with fiber reinforcement and is not unlike traditionally reinforced concrete. Research at NMSU previously established the modulus of rupture strength (f_r) for the UHPC mixture proportions similar to those used in this research as approximately 1.30 ksi (9.0 MPa) (Visage et al., 2019). However, the sampling size from that research for specimens with the same mixture proportions (particularly the fiber type and content) used in this study was limited and further verification of the results is required.

Regarding the relationship between modulus of rupture and compressive strength, various formulae have been developed to predict the interaction of the two material properties. AASHTO (2017) provides Equation 4.2 for calculating the modulus of rupture (f_r) of general use normal strength concretes with compressive strengths (f'_c) up to 15 ksi (103 MPa). AASHTO further notes that this material property is sensitive to constituent materials and curing regimens.

$$f_r = 0.24\sqrt{f'_c} \text{ ksi} \qquad 4.2$$
$$f_r = 0.63\sqrt{f'_c} \text{ MPa}$$

Graybeal (2006b) evaluated the tensile strength and behavior of UHPC in a parametric study using specimens produced with varied curing regimens and with various cross-sectional geometries, including flexural prisms like those used for this research. Several testing techniques were applied, with the combined results yielding an average tensile cracking strength of approximately 1.30 ksi (9.0 MPa) for thermally treated specimens and 0.90 ksi (6.20 MPa) for untreated specimens. Comparing these results with the compressive strength results from the same report, Equation 4.3 was developed to approximate the tensile cracking strength of UHPC for a given compressive strength (f'_c) (Graybeal, 2006b). The linear multiplier, x, is specified as 7.8 for thermally treated UHPC and 6.7 for untreated UHPC when using English units (psi) [0.65 and 0.55 for SI units (MPa)].

$$f_{ct} = x\sqrt{f'_c} \text{ psi (MPa)} \qquad 4.3$$

Due to varying constituent materials (e.g., aggregate properties, type and content of fiber reinforcement, supplementary cementitious materials, etc.) and curing regimens, it is necessary to determine if these equations are applicable to the UHPC mixture proportions developed at NMSU.

Modulus of rupture strength, defined herein as the flexural stress corresponding to first cracking, was evaluated for these investigations using 16.0 x 3.0 x 4.0 in. (406 x 76 x 102 mm) beam specimens as outlined in Section i.iii.

4.2.3.4 Modulus of Elasticity

Modulus of elasticity (Young's modulus) is the mechanical property that characterizes the linear-elastic relationship between stress and strain prior to inelastic behavior and is important in avoiding permanent deformation while achieving serviceability and economy in design. Design codes such as AASHTO LRFD (2017, Equation 4.4) and ACI 318 (2019, Equation 4.5) provide equations for calculating the modulus of elasticity (E) as a function of the square root of the ultimate compressive strength (f'_c) multiplied by a scalar factor, and are considered valid for concrete compressive strengths up to 15 ksi (103 MPa). In Equation 4.4, the unit weight of concrete (w_c) is in lb/ft^3 (kg/m^3).

$$E = 33 w_c^{1.5} \sqrt{f'_c} \quad \text{(psi)}$$
$$E = 0.043 w_c^{1.5} \sqrt{f'_c} \quad \text{(MPa)} \qquad 4.4$$

$$E = 57000 \sqrt{f'_c} \quad \text{(psi)}$$
$$E = 4700 \sqrt{f'_c} \quad \text{(MPa)} \qquad 4.5$$

For concretes with compressive strengths exceeding 15.0 ksi (103 MPa), such as UHPC, modified equations to more accurately represent linear-elastic behavior are required. Several relationships for determining the modulus of elasticity of UHPC have been developed and are discussed briefly here. The first, Equation 4.6, was developed by the Association Française de Génie Civil and Service d'Études Techniques des Routes et Autoroutes (AFGC-SETRA, 2002), is a function of compressive strength after thermal treatment (f'_{ATT}). Equation 4.6 has been previously verified by Ahlborn et al. (2011) using cylindrical specimen prepared using various thermal curing regimens.

$$E = 26200 \sqrt[3]{f'_{ATT}} \quad \text{(psi)}$$
$$E = 9500 \sqrt[3]{f'_{ATT}} \quad \text{(MPa)} \qquad 4.6$$

The second equation (Equation 4.7) is the result of material characterization studies conducted by Graybeal (2006b). This equation, recommended for UHPC with compressive strengths between 4.0 and 28.0 ksi (28 to 193 MPa), was developed to estimate the modulus of elasticity regardless of curing method.

$$E = 46200 \sqrt{f'_c} \quad \text{(psi)}$$
$$E = 3840 \sqrt{f'_c} \quad \text{(MPa)} \qquad 4.7$$

The last equation (Equation 4.8) was yielded by additional research by Graybeal and Stone (2012) conducted on rapid-strengthening UHPC for use in field-cast connections. The results found that for the specific formulation of UHPC being used in the study, the modulus of elasticity was largely independent of curing temperature and was found to be predictable as a function of compressive strengths between 14.0 and 26.0 ksi (97 to 179 GPa).

$$E = 49000\sqrt{f_c'} \text{ (psi)} \qquad 4.8$$
$$E = 4070\sqrt{f_c'} \text{ (MPa)}$$

The modulus of elasticity for UHPC developed at NMSU using local materials was previously investigated by Guaderrama and Weldon (2013). The parametric study evaluated several batches with varying fiber types, fine aggregate content, and moisture content. A batch of six, 4.0 in. (100 mm) cube specimens were produced with mixture proportions [including steel fibers with an ultimate tensile strength of 375 ksi (2586 MPa)] and subjected to thermal curing similar to the UHPC used for this research. The faces of each specimen were instrumented with surface bonded gauges to capture strain development under compressive loading.

The results provided average compressive strength of 22.4 ksi (155 MPa) an average modulus of elasticity of 5845 ksi (40.3 GPa) at an ultimate strain value of 0.0035. When compared to the methods of prediction previously discussed, it was clear that the equations overestimated the modulus of elasticity for the unique UHPC. However, because the sample size was so small, further testing is necessary to determine if these equations are applicable to the UHPC mixture proportions developed at NMSU.

The long-term modulus of elasticity (E_c) was evaluated for these investigations using 4.0 in. x 8.0 in. (102 mm x 203 mm) cylinder specimens as outlined in Section i.iv.

4.2.4 Strength Gain of UHPC Using Thermal Curing

4.2.4.1 Thermal Curing Regimen

The primary curing regimen used to investigate strength gain of this unique UHPC was a thermal curing regimen illustrated by Figure 4.4. After production and placement of UHPC as discussed in Section 4.2.2, concrete molds were covered with plastic to prevent loss of moisture and facilitate hydration and remained at ambient temperatures for 24 hours. Specimens were then demolded, submerged in water, and placed in an industrial oven set to a temperature of 203°F (95°C) for a period of four days. Following the wet curing stage, the concrete was removed from the water bath and remained in the oven for an additional two days of dry curing at 203°F (95°C). After completion of the 7-day curing regimen, specimens remained at ambient laboratory conditions until testing.

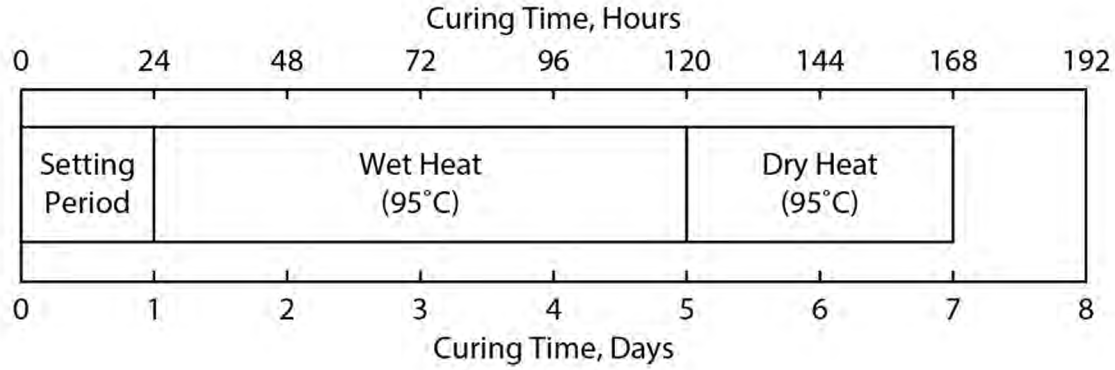


Figure 4.4: Laboratory thermal curing regimen for investigation of nonproprietary UHPC time-dependent strength gain.

4.2.4.2 Curing Temperatures

Concrete core temperatures were monitored using Type-T thermocouples placed directly in the center of 4.0 in. (100 mm) cube specimens and monitored throughout the curing process and over extended periods thereafter. Thermocouple voltage resistance measurements were collected every 30 seconds and averaged over 5-minute intervals, then converted to temperature and recorded by a Campbell® Scientific CR23X Micrologger® (CSI, 2020b). In addition to concrete core temperatures, a reference thermocouple was placed adjacent to the instrumented cube specimen to record the external control temperature and serve to evaluate whether the ambient conditions underwent any fluctuations, and whether the internal temperatures of the cubes were able to reach the same temperature as the external heat source. Temperature data is presented here for three separate batches of UHPC produced using the thermal curing regimen discussed in the previous section. Each figure presented displays the temperatures recorded by the control thermocouple (placed adjacent to the cube to monitor the external temperatures surrounding the specimen), the core temperature of the cube specimen, and an idealized target curing temperature throughout the curing regimen.

During the first 24 hours after casting the concrete exhibited temperature fluctuations due to both changes in the ambient laboratory conditions, particularly the cyclic effects of the air-conditioning system, as well as the hydration reaction of the concrete (Figure 4.5 through Figure 4.7). Specimen core temperatures followed a similar trend to the external temperature recorded by the control thermocouple for the first seven to nine hours after casting, after which the heat of hydration caused an increase in the specimen core temperature. Hydration temperatures in larger specimens would typically cause a more noticeable difference between the magnitude of core and external temperatures, however, the small size of the cube specimens mitigated this effect.

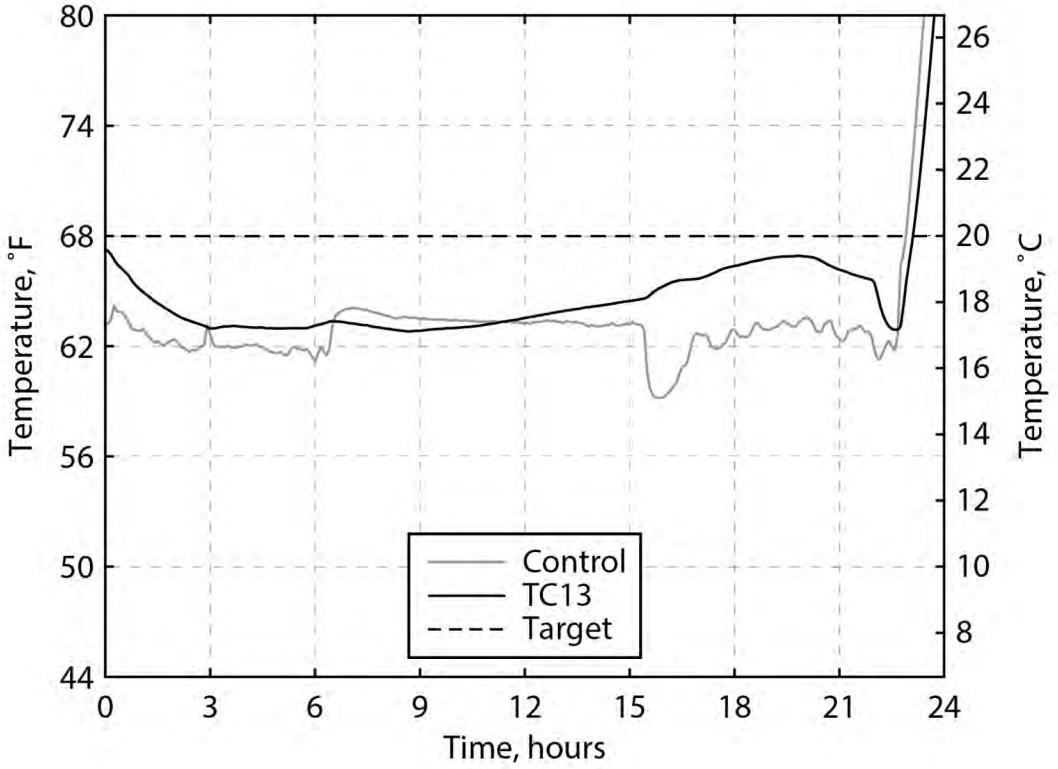


Figure 4.5: Core temperatures for batch TC13 during initial 24 hours after casting.

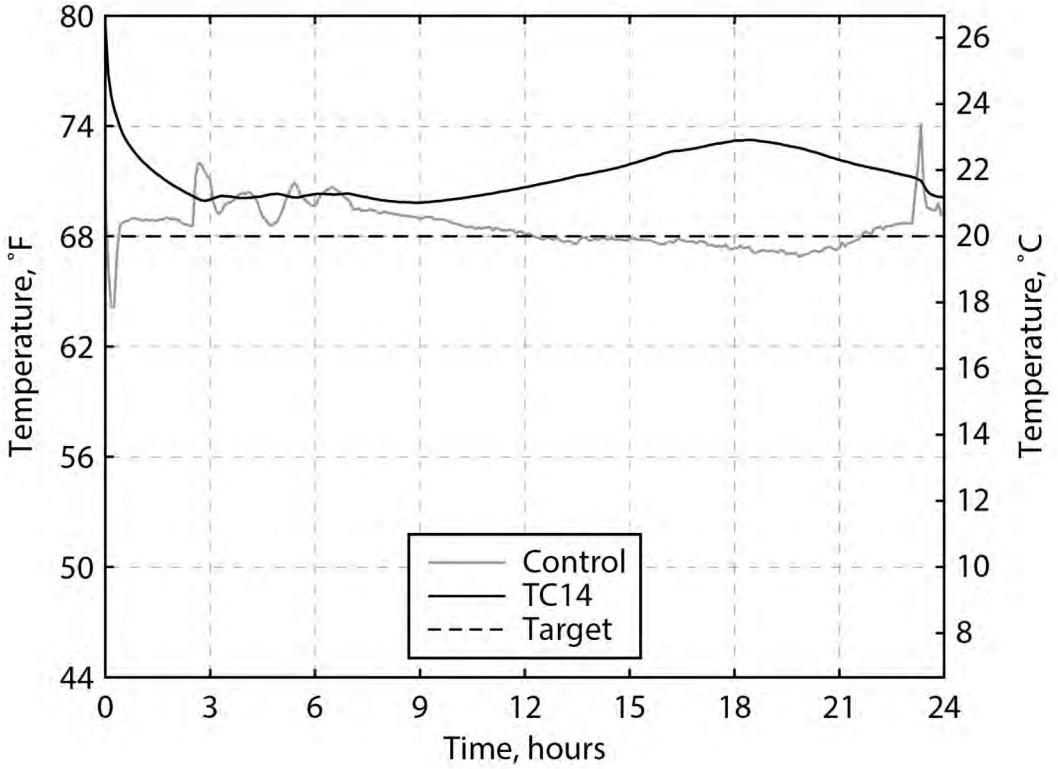


Figure 4.6: Core temperatures for batch TC14 during initial 24 hours after casting.

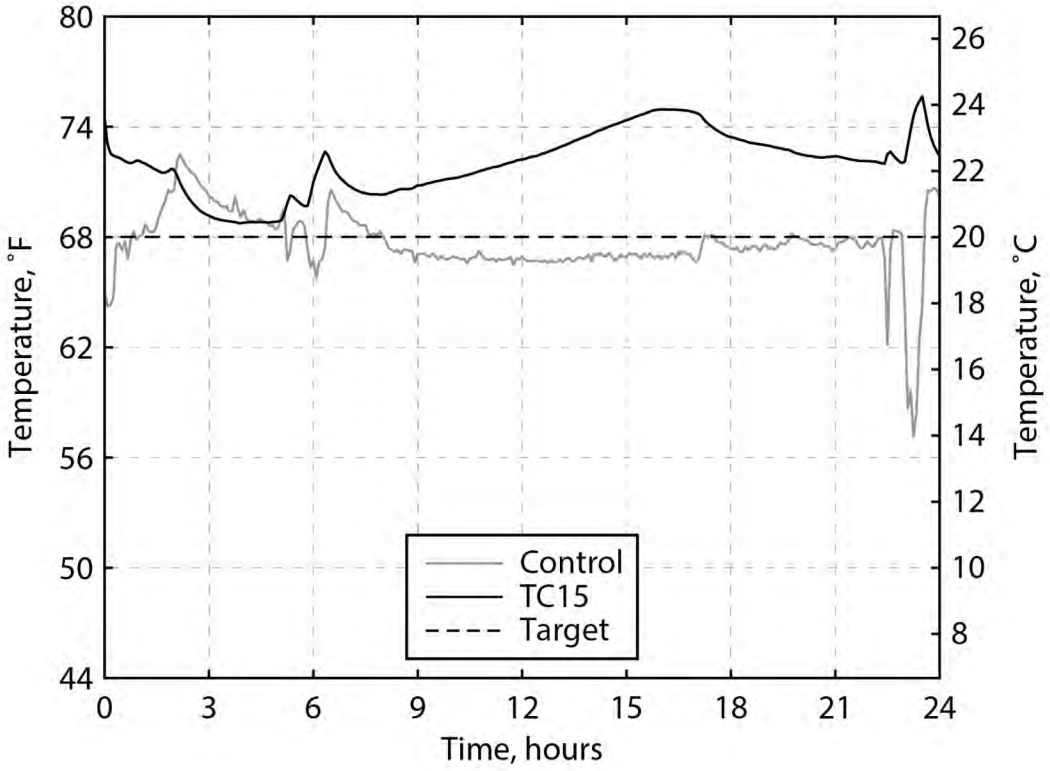


Figure 4.7: Core temperatures for batch TC15 during initial 24 hours after casting.

Curing temperatures throughout the seven-day thermal curing regimen for each batch are provided in Figure 4.8 through Figure 4.10. After the specimens were submerged in water and placed in the oven, approximately six hours were required to approach the target curing temperature of 203°F (95°C). Specimen core temperatures were generally within 10°F (5°C) of the target temperature during the wet curing phase between days one to five. Temperature fluctuations during this time were due to the oven doors being periodically opened to check current water levels and add water as necessary to keep specimens submerged. The sizeable drop at day 5 occurs when the water was drained from the container to begin the dry heat phase. Core temperatures between days five to seven were slightly closer to the target temperature. After completion of the thermal curing regimen the specimens were removed from the oven and remained at ambient laboratory conditions until tested.

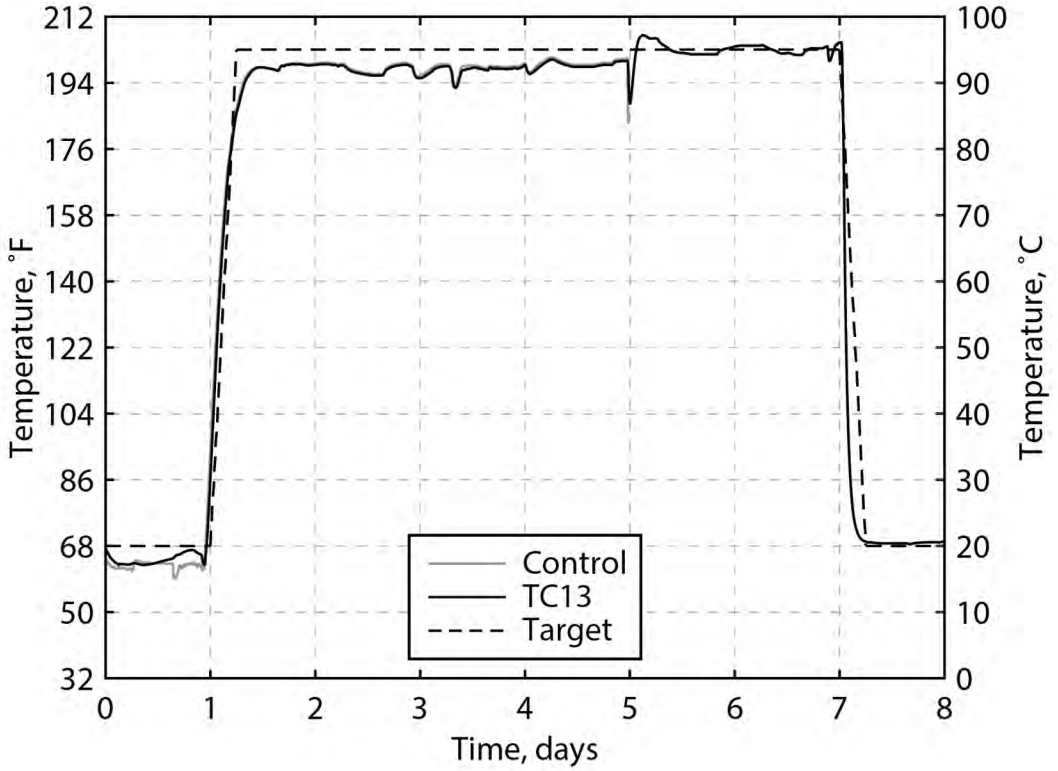


Figure 4.8: Core temperatures for batch TC13 during 7-day thermal curing regimen.

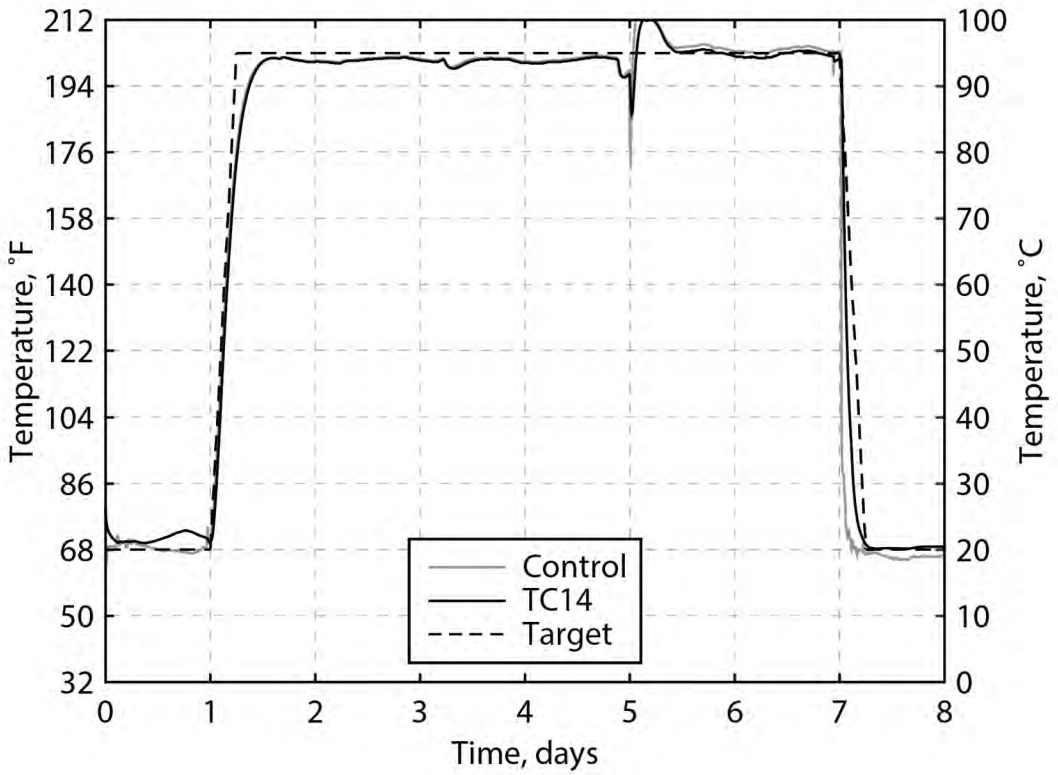


Figure 4.9: Core temperatures for batch TC14 during 7-day thermal curing regimen.

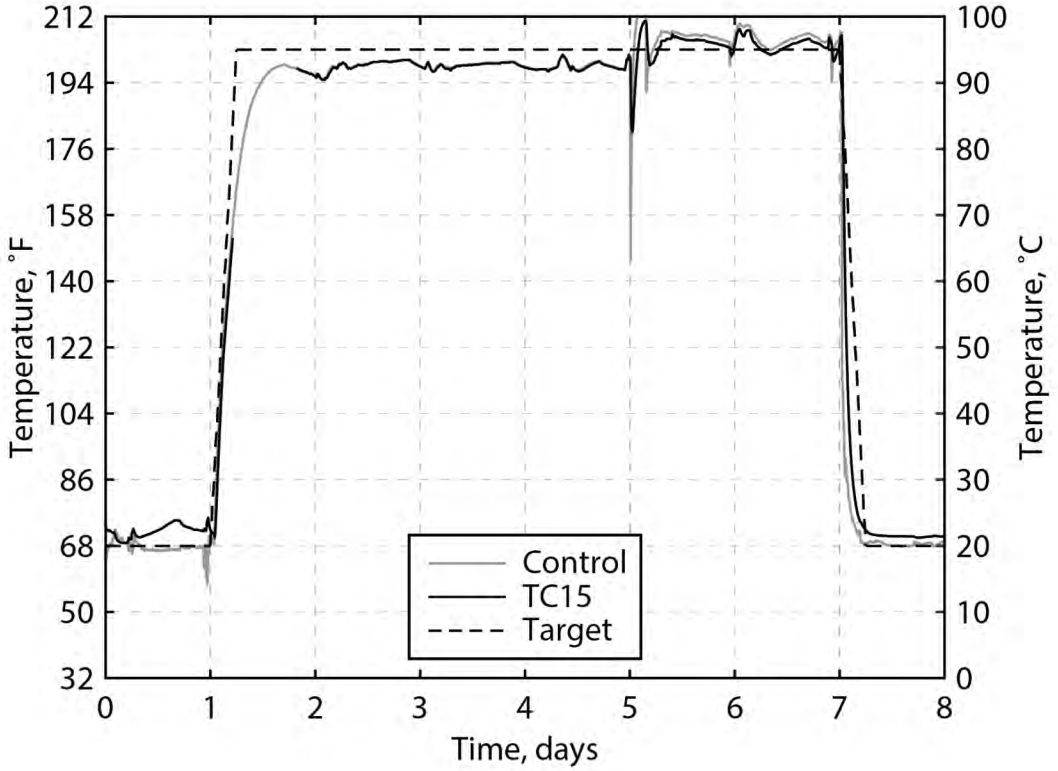


Figure 4.10: Core temperatures for batch TC15 during 7-day thermal curing regimen.

4.2.4.3 Compressive Strength

The development of compressive strength (f_c) was evaluated for the thermal curing regimen using 4.0 in. (100 mm) UHPC cube specimens as outlined in Section i.i. Early-age strength gain was investigated by testing specimens at 24-hour intervals during the seven-day curing period after casting (Figure 4.11). Beginning at seven days after casting, long-term strength gain was monitored by testing specimens at 7-, 14-, or 28-day intervals. Compressive strength results for UHPC produced with thermal curing are summarized based on specimen age at testing in Table 4.14, and data up to 365 days after casting are presented in Figure 4.12.

As seen in Table 4.14 and Figure 4.11, compressive strengths approaching 8.0 ksi (55 MPa) were recorded at 24 hours after casting. Then, after initiation of the wet thermal curing phase at elevated temperatures, strengths increased dramatically between 24 and 48 hours to upwards of 18 ksi (124 MPa). As the curing regimen progressed, day-to-day increases in strength were much smaller as the specimens approach the 7-day mark, typically peaking around 20 ksi (138 MPa). With an average 7-day compressive strength for all batches found to be 20.8 ksi (143 MPa), it was observed that the UHPC specimens typically developed approximately 90% of their 7-day strength within the first 48 hours after casting when using the thermal curing regimen. Following the first week, compressive strengths remained relatively constant through 365 days after casting (Figure 4.12). Outliers in the dataset can most likely be attributed to imperfections in cube specimens. The compressive strength results for each batch produced using the thermal curing regimen are presented in Section 4.2.4.7.

Table 4.14: Summary of Compressive Strength Results for UHPC Produced Using Thermal Curing

Age days	Specimen Count	$f_{c,avg}$ ksi (MPa)	Std. Dev. ksi (MPa)
1	4	7.78 (53.6)	0.30 (2.06)
2	4	18.4 (127)	0.20 (1.38)
3	4	19.4 (134)	0.94 (6.52)
4	4	19.0 (131)	0.90 (6.21)
5	6	20.7 (143)	0.73 (5.06)
6	6	20.4 (141)	0.89 (6.11)
7	30	20.8 (143)	1.01 (6.99)
14	6	22.0 (152)	1.13 (7.81)
21	6	22.9 (158)	1.11 (7.63)
28	8	20.4 (141)	1.68 (11.6)
42	6	21.3 (147)	0.72 (4.97)
56	8	21.3 (147)	1.41 (9.71)
84	6	21.0 (145)	0.93 (6.43)
112	4	19.6 (135)	0.46 (3.14)
138	2	18.5 (128)	0.11 (0.73)
168	2	21.5 (149)	0.62 (4.30)
182	2	22.3 (154)	0.54 (3.72)
186	2	21.0 (145)	0.69 (4.76)
365	12	21.7 (150)	1.46 (10.1)

NOTE: Results based on 4.0 in. (100 mm) cube specimens.

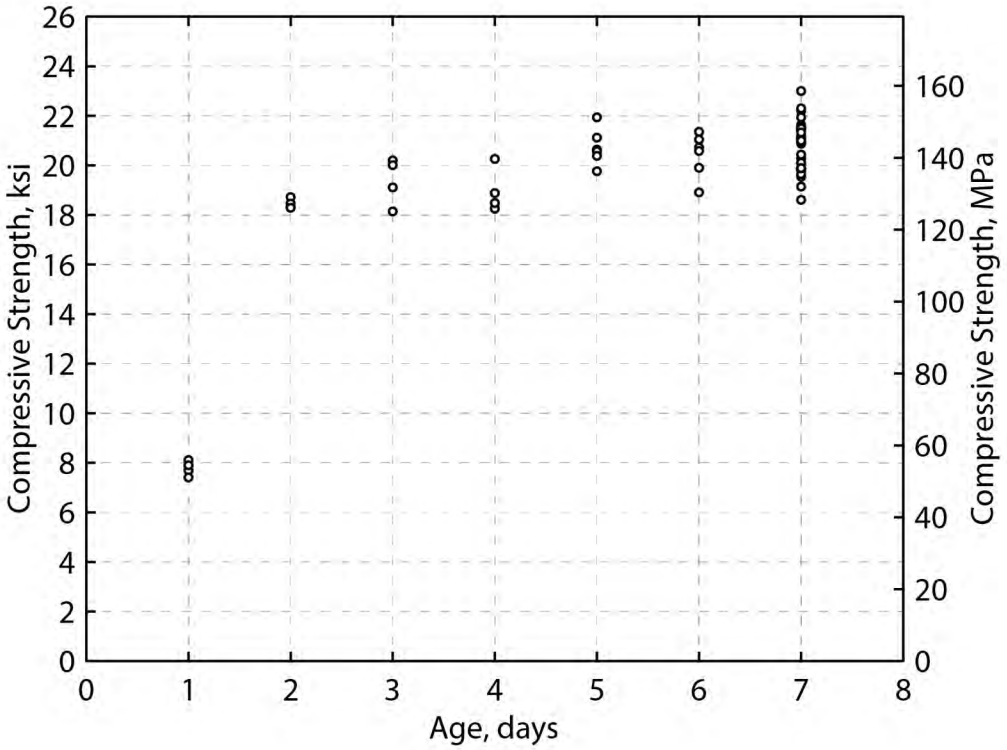


Figure 4.11: Compressive strength gain of 4.0 in (100 mm) UHPC cube specimens produced using the thermal curing regimen during the first seven days after casting.

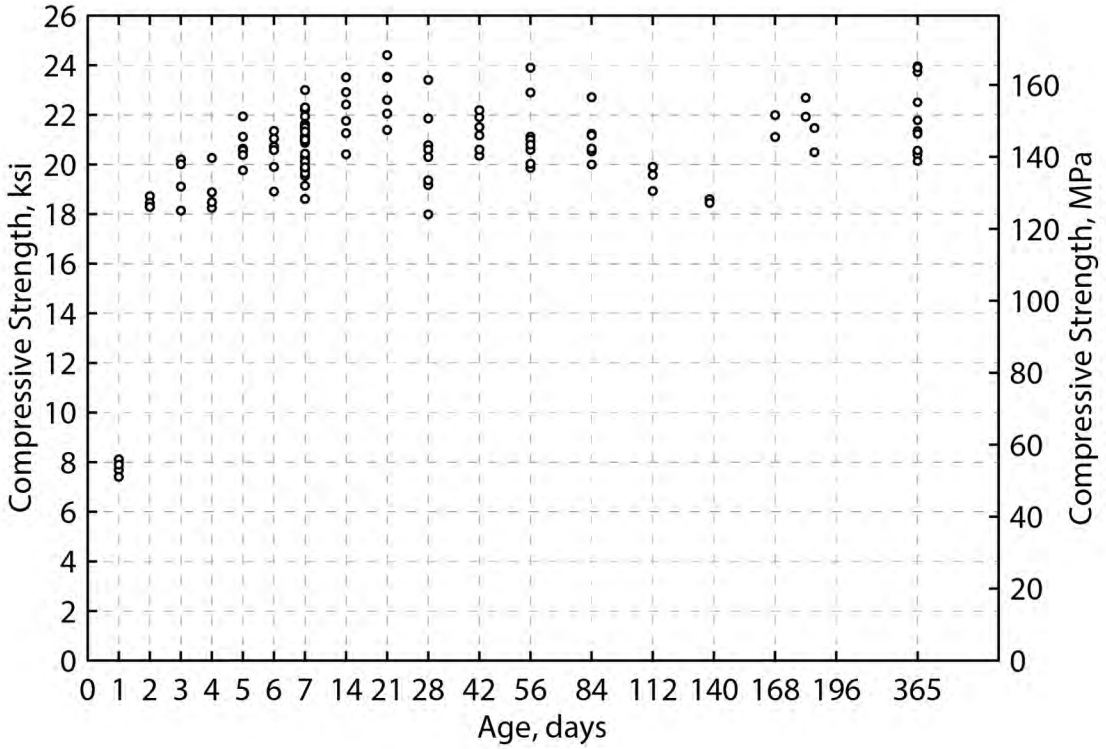


Figure 4.12: Compressive strengths of 4.0 in (100 mm) UHPC cube specimens produced using thermal curing up to 365 days after casting.

4.2.4.4 Unit Weight

The 4.0 in. (100 mm) cube specimens produced for evaluation of compressive strength were additionally used to determine the unit weight (w_c) of UHPC as outlined in Section i.ii. Specimens were weighed immediately prior to testing, and the average unit weight for all batches produced using the thermal curing regimen was 149.8 lb/ft^3 (2399 kg/m^3). The unit weight results for UHPC produced using the thermal curing regimen are summarized based on specimen age at testing in Table 4.15 below and presented for each batch in Section 4.2.4.7.

Table 4.15: Summary of Unit Weight Results for UHPC Produced Using Thermal Curing

Age days	Specimen Count	$w_{c,avg}$ lb/ft^3 (kg/m^3)	Std. Dev. lb/ft^3 (kg/m^3)
1	4	149.1 (2389)	0.38 (6.03)
2	4	150.5 (2411)	1.01 (16.1)
3	4	150.3 (2408)	1.25 (20.0)
4	4	150.3 (2407)	0.91 (14.5)
5	6	150.6 (2412)	0.83 (13.3)
6	6	150.0 (2403)	0.79 (12.7)
7	30	149.4 (2394)	1.49 (23.9)
14	6	150.7 (2413)	1.22 (19.6)
21	6	150.6 (2413)	0.87 (14.0)
28	8	149.8 (2399)	2.03 (32.5)
42	6	150.4 (2410)	1.36 (21.8)
56	8	149.9 (2402)	0.68 (11.0)
84	6	150.2 (2406)	1.65 (26.4)
112	4	149.5 (2395)	1.36 (21.7)
182	2	149.3 (2392)	0.36 (5.77)
186	2	146.4 (2346)	0.42 (6.74)
365	12	149.2 (2391)	1.46 (23.4)

NOTE: Results based on 4.0 in. (100 mm) cube specimens.

4.2.4.5 Modulus of Rupture

The development of modulus of rupture (f_r), defined here as the flexural stress corresponding to first cracking of the specimen, was evaluated for the thermal curing regimen using 16.0 x 3.0 x 4.0 in. (406 x 76 x 102 mm) UHPC prism specimens as outlined in Section i.iii. To evaluate early-age modulus of rupture strength gain, the prism specimens were tested at 24-hour intervals through completion of the seven-day thermal curing regimen (Figure 4.13). Beginning at seven days after casting, long-term modulus of rupture strength gain was monitored by testing specimens at 7-, 14-, or 28-day intervals. Modulus of rupture strength results for UHPC produced using the thermal curing regimen are summarized based on specimen age at testing in Table 4.16, and data up to 365 days after casting are presented in Figure 4.14.

Analysis of LVDT deformation data to determine the occurrence of first cracking indicated the modulus of rupture was near fully developed within approximately two to four days after concrete placement when thermal curing has been applied. An average 7-day modulus of rupture for all batches was found to be 1203 psi (8.30 MPa). The long-term results of Figure 4.14 indicate the modulus of rupture remains relatively constant as the concrete ages. The modulus of rupture strength results for each batch produced using the thermal curing regimen are presented in Section 4.2.4.7.

Table 4.16: Summary of Modulus of Rupture Results for UHPC Produced Using Thermal Curing

Age days	Specimen Count	$f_{r,avg}$ psi (MPa)	Std. Dev. psi (MPa)
1	3	502.1 (3.46)	56.7 (0.39)
2	4	1131 (7.80)	21.7 (0.15)
3	4	1197 (8.25)	52.4 (0.36)
4	4	1089 (7.51)	118.4 (0.82)
5	6	1168 (8.05)	117.8 (0.81)
6	6	1205 (8.31)	140.7 (0.97)
7	26	1203 (8.30)	107.6 (0.74)
14	4	1172 (8.08)	32.6 (0.22)
21	4	1165 (8.04)	102.8 (0.71)
28	6	1265 (8.72)	102.6 (0.71)
42	4	1158 (7.99)	66.2 (0.46)
56	6	1232 (8.50)	116.6 (0.80)
84	4	1270 (8.75)	53.9 (0.37)
113	2	1179 (8.13)	177.7 (1.22)
138	2	1105 (7.62)	58.3 (0.40)
182	2	1069 (7.37)	185.6 (1.28)
186	2	971.9 (6.70)	137.0 (0.94)
365	6	1138 (7.85)	149.3 (1.03)

NOTE: Results based on 16.0 x 3.0 x 4.0 in. (406 x 76 x 102 mm) beam specimens.

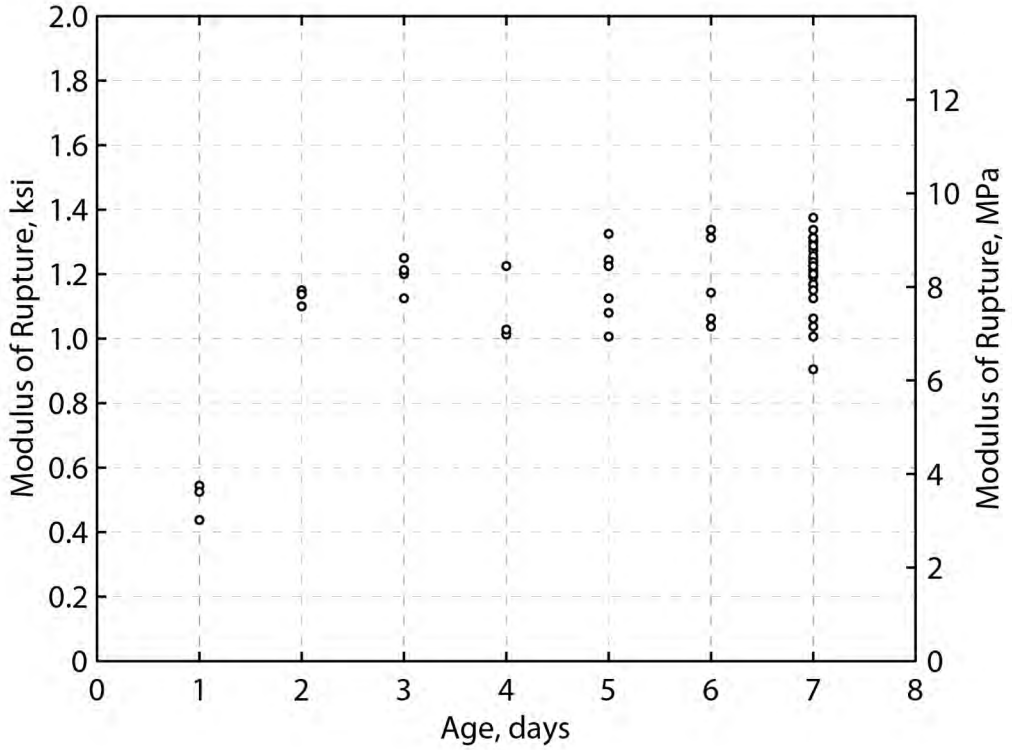


Figure 4.13: Modulus of rupture strength gain of UHPC prism specimens produced using the thermal curing regimen during the first seven days after casting.

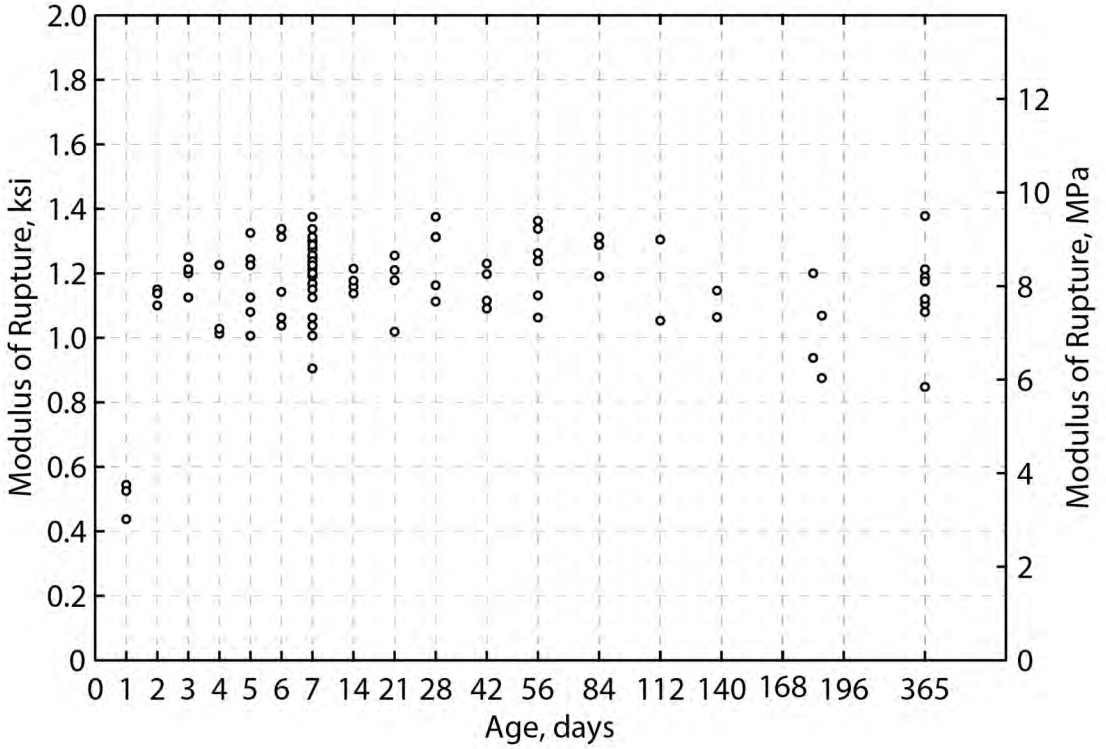


Figure 4.14: Modulus of rupture strengths of UHPC prism specimens produced using thermal curing up to 365 days after casting.

4.2.4.6 Modulus of Elasticity

The long-term modulus of elasticity (E_c) of UHPC produced with thermal curing was mapped by testing 4.0 in. x 8.0 in. (102 mm x 203 mm) cylinder specimens at 7-, 14-, or 28-day intervals as outlined in Section i.iv. Results of testing are summarized in Table 4.17 and presented in Figure 5.4 up to 365 days after casting. Initial specimens were tested at the end of the seven-day thermal curing regimen, with an average value of 5853 ksi (40.4 GPa), and subsequent values remain relatively constant as the concrete ages. Some variance in the results is expected due to the non-homogenous nature of concrete and can also be the result of imperfections in the specimen geometry or batch/specimen strength. The modulus of elasticity results for UHPC produced using the thermal curing regimen are summarized based on specimen age at testing in Table 4.17 below and presented for each batch in Section 4.2.4.7.

Table 4.17: Summary of Modulus of Elasticity Results for UHPC Produced Using Thermal Curing

Age days	Specimen Count	$E_{c,avg}$ ksi (GPa)	Std. Dev. ksi (GPa)
7	4	5853 (40.4)	78.6 (0.54)
14	2	5830 (40.2)	154 (1.06)
21	2	5835 (40.2)	78.0 (0.54)
28	2	5899 (40.7)	237 (1.63)
42	2	6069 (41.8)	333 (2.29)
56	2	6021 (41.5)	160 (1.10)
84	2	5727 (39.5)	206 (1.42)
112	2	6101 (42.1)	360 (2.48)
168	2	6441 (44.4)	646 (4.46)
365	3	6207 (42.8)	234 (1.61)

NOTE: Results based on 4.0 x 8.0 in. (102 x 203 mm) cylinder specimens.

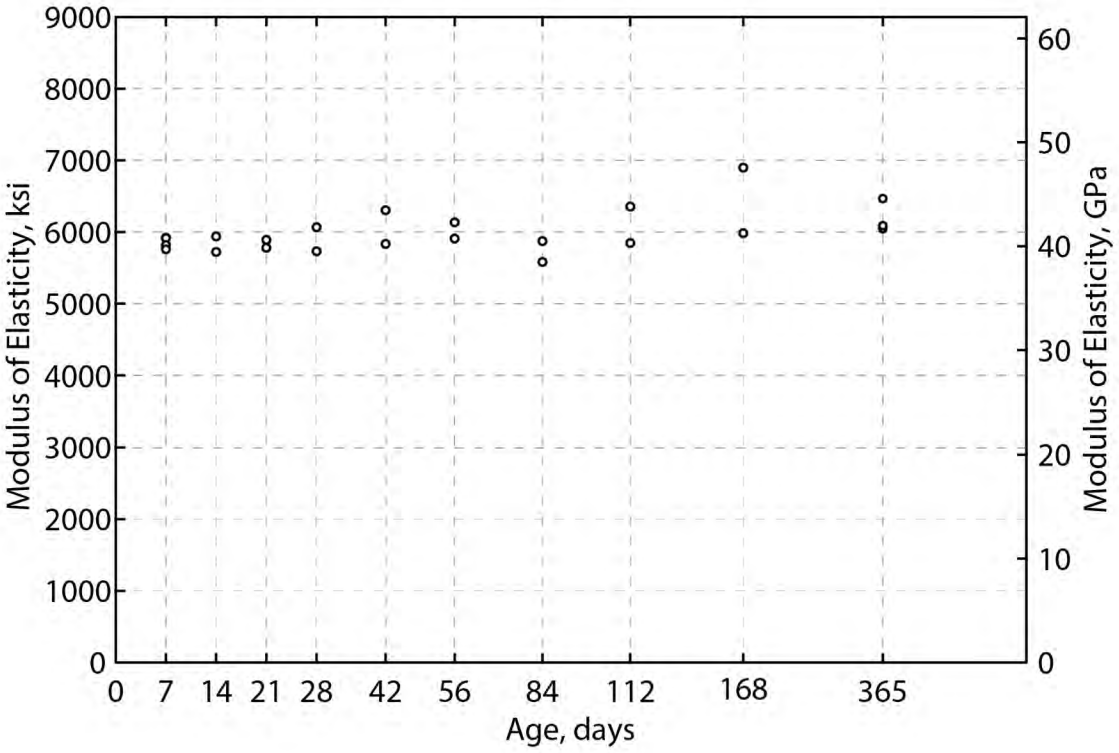


Figure 4.15: Modulus of elasticity strengths of UHPC cylinder specimens for the thermal curing regimen up to 365 days after casting.

4.2.4.7 Batch Results for UHPC Using Thermal Curing Regimen

Data is presented in the following sections for each batch of UHPC produced using the thermal curing regimen.

4.2.4.7.1 Batch TC1

Table 4.18: Unit Weight Results for Batch TC1

Specimen No.	Age days	Weight lb (kg)	w_c lb/ft^3 (kg/m^3)	Average lb/ft^3 (kg/m^3)	Std. Dev. lb/ft^3 (kg/m^3)
1	7	5.14 (2.33)	145.4 (2330)		
2	7	5.17 (2.35)	146.5 (2347)	146.0 (2338)	0.761 (12.2)
3	186	5.18 (2.35)	146.7 (2351)		
4	186	5.16 (2.34)	146.1 (2341)	146.4 (2346)	0.420 (6.74)
5	363	5.18 (2.35)	146.6 (2349)		
6	363	5.22 (2.37)	147.7 (2366)	147.2 (2357)	0.761 (12.2)
	Average	5.17 (2.35)	146.5 (2347)		
	Std. Dev.	0.026 (0.012)	0.744 (11.9)		

NOTE: Results based on 4.0 in. (100 mm) cube specimens.

Table 4.19: Compressive Strength Results for Batch TC1

Specimen No.	Age days	f_c ksi (MPa)	Average ksi (MPa)	Std. Dev. ksi (MPa)
1	7	21.0 (145)		
2	7	19.9 (137)	20.4 (141)	0.784 (5.41)
3	186	20.5 (141)		
4	186	21.5 (148)	21.0 (145)	0.691 (4.76)
5	363	21.2 (146)		
6	363	21.8 (150)	21.5 (148)	0.368 (2.54)
	Average	21.0 (145)		
	Std. Dev.	0.683 (4.71)		

NOTE: Results based on 4.0 in. (100 mm) cube specimens.

Table 4.20: Modulus of Rupture Results for Batch TC1

Specimen No.	Age days	f_r psi (MPa)	Average psi (MPa)	Std. Dev. psi (MPa)
1	7	1200 (8.27)		
2	7	1150 (7.93)	1175 (8.10)	35.4 (0.244)
3	186	875 (6.03)		
4	186	1069 (7.37)	972 (6.70)	137 (0.945)
5	363	1080 (7.45)		
6	363	1175 (8.10)	1128 (7.77)	67.2 (0.463)
	Average	1091 (7.53)		
	Std. Dev.	118 (0.814)		

NOTE: Results based on 4.0 x 8.0 in. (102 x 203 mm) cylinder specimens.

4.2.4.7.2 Batch TC2

Table 4.21: Unit Weight Results for Batch TC2

Specimen No.	Age days	Weight lb (kg)	w_c lb/ft^3 (kg/m^3)	Average lb/ft^3 (kg/m^3)	Std. Dev. lb/ft^3 (kg/m^3)
1	7	5.22 (2.37)	147.9 (2369)		
2	7	5.29 (2.40)	149.8 (2400)	148.8 (2384)	1.36 (21.8)
3	182	5.27 (2.39)	149.1 (2388)		
4	182	5.28 (2.40)	149.6 (2396)	149.3 (2392)	0.360 (5.77)
5	362	5.30 (2.40)	150.0 (2403)		
6	362	5.21 (2.36)	147.4 (2361)	148.7 (2382)	1.84 (29.5)
	Average	5.26 (2.39)	149.0 (2386)		
	Std. Dev.	0.038 (0.017)	1.08 (17.3)		

NOTE: Results based on 4.0 in. (100 mm) cube specimens.

Table 4.22: Compressive Strength Results for Batch TC2

Specimen No.	Age days	f_c ksi (MPa)	Average ksi (MPa)	Std. Dev. ksi (MPa)
1	7	21.3 (147)		
2	7	20.1 (139)	20.7 (143)	0.862 (5.94)
3	182	21.9 (151)		
4	182	22.7 (156)	22.3 (154)	0.540 (3.72)
5	362	23.9 (165)		
6	362	21.4 (147)	22.6 (156)	1.79 (12.3)
	Average	21.9 (151)		
	Std. Dev.	1.30 (8.96)		

NOTE: Results based on 4.0 in. (100 mm) cube specimens.

Table 4.23: Modulus of Rupture Results for Batch TC2

Specimen No.	Age days	f_r psi (MPa)	Average psi (MPa)	Std. Dev. psi (MPa)
1	7	1313 (9.05)		
2	7	1288 (8.88)	1300 (8.96)	17.7 (0.122)
3	182	938 (6.46)		
4	182	1200 (8.27)	1069 (7.37)	186 (1.28)
5	362	1213 (8.36)		
6	362	1189 (8.20)	1201 (8.28)	16.8 (0.116)
	Average	1190 (8.20)		
	Std. Dev.	133 (0.919)		

NOTE: Results based on 4.0 x 8.0 in. (102 x 203 mm) cylinder specimens.

4.2.4.7.3 Batch TC3

Table 4.24: Unit Weight Results for Batch TC3

Specimen No.	Age days	Weight lb (kg)	w_c lb/ft^3 (kg/m^3)	Average lb/ft^3 (kg/m^3)	Std. Dev. lb/ft^3 (kg/m^3)
1	5	5.36 (2.43)	151.6 (2429)		
2	5	5.34 (2.42)	151.2 (2422)	151.4 (2426)	0.300 (4.81)
3	6	5.31 (2.41)	150.4 (2409)		
4	6	5.27 (2.39)	149.1 (2389)	149.7 (2399)	0.881 (14.1)
5	7	5.31 (2.41)	150.3 (2408)		
6	7	5.35 (2.43)	151.6 (2428)	150.9 (2418)	0.881 (14.1)
	Average	5.32 (2.41)	150.7 (2414)		
	Std. Dev.	0.034 (0.015)	0.964 (15.4)		

NOTE: Results based on 4.0 in. (100 mm) cube specimens.

Table 4.25: Compressive Strength Results for Batch TC3

Specimen No.	Age days	f_c ksi (MPa)	Average ksi (MPa)	Std. Dev. ksi (MPa)
1	5	21.9 (151)		
2	5	20.4 (141)	21.2 (146)	1.10 (7.58)
3	6	18.9 (130)		
4	6	21.0 (145)	20.0 (138)	1.51 (10.41)
5	7	21.5 (148)		
6	7	20.4 (141)	21.0 (145)	0.749 (5.16)
	Average	20.7 (143)		
	Std. Dev.	1.06 (7.33)		

NOTE: Results based on 4.0 in. (100 mm) cube specimens.

Table 4.26: Modulus of Rupture Results for Batch TC3

Specimen No.	Age days	f_r psi (MPa)	Average psi (MPa)	Std. Dev. psi (MPa)
1	5	1006 (6.94)		
2	5	1125 (7.76)	1066 (7.35)	84.0 (0.579)
3	6	1338 (9.22)		
4	6	1313 (9.05)	1325 (9.14)	17.7 (0.122)
5	7	1300 (8.96)		
6	7	1375 (9.48)	1338 (9.22)	53.0 (0.366)
	Average	1243 (8.57)		
	Std. Dev.	145 (1.00)		

NOTE: Results based on 4.0 x 8.0 in. (102 x 203 mm) cylinder specimens.

4.2.4.7.4 Batch TC4

Table 4.27: Unit Weight Results for Batch TC4

Specimen No.	Age days	Weight lb (kg)	w_c lb/ft^3 (kg/m^3)	Average lb/ft^3 (kg/m^3)	Std. Dev. lb/ft^3 (kg/m^3)
1	7	5.27 (2.39)	149.1 (2389)		
2	7	5.33 (2.42)	151.0 (2419)	150.1 (2404)	1.36 (21.8)
3	55	5.27 (2.39)	149.3 (2391)		
4	55	5.27 (2.39)	149.3 (2392)	149.3 (2392)	0.040 (0.641)
5	83	5.30 (2.40)	150.1 (2405)		
6	83	5.25 (2.38)	148.7 (2382)	149.4 (2394)	1.00 (16.0)
7	365	5.28 (2.39)	149.5 (2395)		
8	365	5.28 (2.39)	149.4 (2393)	149.5 (2394)	0.080 (1.3)
	Average	5.28 (2.40)	149.6 (2396)		
	Std. Dev.	0.025 (0.011)	0.715 (11.5)		

NOTE: Results based on 4.0 in. (100 mm) cube specimens.

Table 4.28: Compressive Strength Results for Batch TC4

Specimen No.	Age days	f_c ksi (MPa)	Average ksi (MPa)	Std. Dev. ksi (MPa)
1	7	20.1 (139)		
2	7	19.1 (132)	19.6 (135)	0.674 (4.65)
3	55	21.0 (145)		
4	55	20.8 (143)	20.9 (144)	0.141 (0.975)
5	83	20.0 (138)		
6	83	20.6 (142)	20.3 (140)	0.453 (3.12)
7	365	20.6 (142)		
8	365	20.1 (139)	20.3 (140)	0.314 (2.16)
	Average	20.3 (140)		
	Std. Dev.	0.589 (4.06)		

NOTE: Results based on 4.0 in. (100 mm) cube specimens.

Table 4.29: Modulus of Rupture Results for Batch TC4

Specimen No.	Age days	f_r psi (MPa)	Average psi (MPa)	Std. Dev. psi (MPa)
1	7	1006 (6.94)		
2	7	1038 (7.15)	1022 (7.05)	22.1 (0.152)
3	55	1063 (7.33)		
4	55	1238 (8.53)	1150 (7.93)	124 (0.853)
5	83	1288 (8.88)		
6	83	1313 (9.05)	1300 (8.96)	17.7 (0.122)
7	365	1338 (9.22)		
8	365	1363 (9.39)	1350 (9.31)	17.7 (0.122)
	Average	1157 (7.98)		
	Std. Dev.	137 (0.943)		

NOTE: Results based on 4.0 x 8.0 in. (102 x 203 mm) cylinder specimens.

4.2.4.7.5 Batch TC5

Table 4.30: Unit Weight Results for Batch TC5

Specimen No.	Age days	Weight lb (kg)	w_c lb/ft^3 (kg/m^3)	Average lb/ft^3 (kg/m^3)	Std. Dev. lb/ft^3 (kg/m^3)
1	7	5.34 (2.42)	151.3 (2423)		
2	7	5.31 (2.41)	150.4 (2409)	150.8 (2416)	0.641 (10.3)
3	28	5.30 (2.40)	150.1 (2405)		
4	28	5.31 (2.41)	150.4 (2409)	150.2 (2407)	0.160 (2.57)
5	55	5.32 (2.41)	150.6 (2412)		
6	55	5.33 (2.42)	150.9 (2417)	150.7 (2414)	0.200 (3.21)
7	365	5.27 (2.39)	149.2 (2390)		
8	365	5.28 (2.40)	149.6 (2396)	149.4 (2393)	0.000 (0.00)
	Average	5.31 (2.41)	150.3 (2408)		
	Std. Dev.	0.023 (0.011)	0.661 (10.6)		

NOTE: Results based on 4.0 in. (100 mm) cube specimens.

Table 4.31: Compressive Strength Results for Batch TC5

Specimen No.	Age days	f_c ksi (MPa)	Average ksi (MPa)	Std. Dev. ksi (MPa)
1	7	21.4 (148)		
2	7	21.1 (145)	21.3 (147)	0.212 (1.46)
3	28	20.6 (142)		
4	28	20.3 (140)	20.5 (141)	0.212 (1.46)
5	55	19.9 (137)		
6	55	20.0 (138)	19.9 (138)	0.120 (0.829)
7	365	20.5 (141)		
8	365	20.4 (141)	20.5 (141)	0.092 (0.634)
	Average	20.5 (142)		
	Std. Dev.	0.515 (3.55)		

NOTE: Results based on 4.0 in. (100 mm) cube specimens.

Table 4.32: Modulus of Rupture Results for Batch TC5

Specimen No.	Age days	f_r psi (MPa)	Average psi (MPa)	Std. Dev. psi (MPa)
1	7	1238 (8.53)		
2	7	1225 (8.45)	1231 (8.49)	8.84 (0.061)
3	28	1375 (9.48)		
4	28	1313 (9.05)	1344 (9.26)	44.2 (0.305)
5	55	1263 (8.70)		
6	55	1338 (9.22)	1300 (8.96)	53.0 (0.366)
7	365	1413 (9.74)		
8	365	1488 (10.3)	1450 (10.0)	53.0 (0.366)
	Average	1292 (8.91)		
	Std. Dev.	59.5 (0.410)		

NOTE: Results based on 4.0 x 8.0 in. (102 x 203 mm) cylinder specimens.

4.2.4.7.6 Batch TC6

Table 4.33: Unit Weight Results for Batch TC6

Specimen No.	Age days	Weight lb (kg)	w_c lb/ft^3 (kg/m^3)	Average lb/ft^3 (kg/m^3)	Std. Dev. lb/ft^3 (kg/m^3)
1	7	5.23 (2.37)	148.2 (2373)		
2	7	5.23 (2.37)	148.0 (2370)	148.1 (2372)	0.120 (1.92)
3	28	5.21 (2.37)	147.6 (2365)		
4	28	5.24 (2.38)	148.4 (2377)	148.0 (2371)	0.521 (8.34)
5	85	5.25 (2.38)	148.8 (2383)		
6	85	5.26 (2.39)	149.1 (2388)	148.9 (2385)	0.200 (3.21)
7	138	5.12 (2.32)	144.9 (2321)		
8	138	5.24 (2.38)	148.3 (2375)	146.6 (2348)	2.36 (37.8)
	Average	5.22 (2.37)	147.9 (2369)		
	Std. Dev.	0.045 (0.020)	1.280 (20.5)		

NOTE: Results based on 4.0 in. (100 mm) cube specimens.

Table 4.34: Compressive Strength Results for Batch TC6

Specimen No.	Age days	f_c ksi (MPa)	Average ksi (MPa)	Std. Dev. ksi (MPa)
1	7	19.9 (137)		
2	7	18.6 (128)	19.2 (133)	0.898 (6.19)
3	28	18.0 (124)		
4	28	19.4 (133)	18.7 (129)	0.969 (6.68)
5	85	21.2 (146)		
6	85	20.5 (142)	20.8 (144)	0.457 (3.15)
7	138	18.6 (128)		
8	138	18.5 (127)	18.5 (128)	0.106 (0.731)
	Average	19.3 (133)		
	Std. Dev.	1.12 (7.71)		

NOTE: Results based on 4.0 in. (100 mm) cube specimens.

Table 4.35: Modulus of Rupture Results for Batch TC6

Specimen No.	Age days	f_r psi (MPa)	Average psi (MPa)	Std. Dev. psi (MPa)
1	7	1256 (8.66)		
2	7	1125 (7.76)	1191 (8.21)	92.8 (0.640)
3	28	1313 (9.05)		
4	28	1163 (8.02)	1238 (8.53)	106 (0.731)
5	85	1191 (8.21)		
6	85	1288 (8.88)	1239 (8.54)	68.5 (0.472)
7	138	1064 (7.33)		
8	138	1146 (7.90)	1105 (7.62)	58.3 (0.402)
	Average	1193 (8.23)		
	Std. Dev.	85.9 (0.592)		

NOTE: Results based on 4.0 x 8.0 in. (102 x 203 mm) cylinder specimens.

4.2.4.7.7 Batch TC7

Table 4.36: Unit Weight Results for Batch TC7

Specimen No.	Age days	Weight lb (kg)	w_c lb/ft^3 (kg/m^3)	Average lb/ft^3 (kg/m^3)	Std. Dev. lb/ft^3 (kg/m^3)
1	7	5.23 (2.37)	148.2 (2374)		
2	7	5.32 (2.41)	150.5 (2411)	149.4 (2393)	1.64 (26.3)
3	28	5.18 (2.35)	146.7 (2351)		
4	28	5.31 (2.41)	150.3 (2408)	148.5 (2379)	2.52 (40.4)
5	56	5.27 (2.39)	149.3 (2392)		
6	56	5.27 (2.39)	149.3 (2391)	149.3 (2392)	0.040 (0.641)
7	113	5.23 (2.37)	148.2 (2374)		
8	113	5.26 (2.39)	148.9 (2386)	148.6 (2380)	0.521 (8.34)
	Average	5.26 (2.39)	148.9 (2386)		
	Std. Dev.	0.043 (0.020)	1.23 (19.7)		

NOTE: Results based on 4.0 in. (100 mm) cube specimens.

Table 4.37: Compressive Strength Results for Batch TC7

Specimen No.	Age days	f_c ksi (MPa)	Average ksi (MPa)	Std. Dev. ksi (MPa)
1	7	19.7 (135)		
2	7	21.5 (148)	20.6 (142)	1.31 (9.02)
3	28	19.2 (132)		
4	28	21.9 (151)	20.5 (141)	1.90 (13.1)
5	56	21.1 (146)		
6	56	20.6 (142)	20.9 (144)	0.375 (2.58)
7	113	19.6 (135)		
8	113	18.9 (131)	19.3 (133)	0.457 (3.15)
	Average	20.3 (140)		
	Std. Dev.	1.11 (7.69)		

NOTE: Results based on 4.0 in. (100 mm) cube specimens.

Table 4.38: Modulus of Rupture Results for Batch TC7

Specimen No.	Age days	f_r psi (MPa)	Average psi (MPa)	Std. Dev. psi (MPa)
1	7	1213 (8.36)		
2	7	1250 (8.62)	1231 (8.49)	26.5 (0.183)
3	28	1313 (9.05)		
4	28	1113 (7.67)	1213 (8.36)	141 (0.975)
5	56	1363 (9.39)		
6	56	1131 (7.80)	1247 (8.60)	164 (1.13)
7	113	1053 (7.26)		
8	113	1304 (8.99)	1179 (8.13)	178 (1.22)
	Average	1217 (8.39)		
	Std. Dev.	110 (0.756)		

NOTE: Results based on 4.0 x 8.0 in. (102 x 203 mm) cylinder specimens.

4.2.4.7.8 Batch TC8

Table 4.39: Unit Weight Results for Batch TC8

Specimen No.	Age days	Weight lb (kg)	w_c lb/ft^3 (kg/m^3)	Average lb/ft^3 (kg/m^3)	Std. Dev. lb/ft^3 (kg/m^3)
1	1	5.28 (2.39)	149.5 (2395)		
2	1	5.25 (2.38)	148.7 (2381)	149.1 (2388)	0.601 (9.62)
3	2	5.32 (2.41)	150.7 (2414)		
4	2	5.26 (2.39)	149.1 (2388)	149.9 (2401)	1.16 (18.6)
5	3	5.27 (2.39)	149.2 (2390)		
6	3	5.28 (2.39)	149.5 (2394)	149.3 (2392)	0.200 (3.21)
7	7	5.28 (2.39)	149.5 (2395)		
8	7	5.33 (2.42)	151.0 (2419)	150.3 (2407)	1.08 (17.3)
	Average	5.28 (2.40)	149.6 (2397)		
	Std. Dev.	0.029 (0.013)	0.817 (13.1)		

NOTE: Results based on 4.0 in. (100 mm) cube specimens.

Table 4.40: Compressive Strength Results for Batch TC8

Specimen No.	Age days	f_c ksi (MPa)	Average ksi (MPa)	Std. Dev. ksi (MPa)
1	1	7.9 (54)		
2	1	7.4 (51)	7.7 (53)	0.346 (2.39)
3	2	18.5 (127)		
4	2	18.3 (126)	18.4 (127)	0.120 (0.829)
5	3	19.1 (132)		
6	3	18.1 (125)	18.6 (128)	0.686 (4.73)
7	7	19.5 (135)		
8	7	21.0 (145)	20.3 (140)	1.02 (7.02)
	Average	16.2 (112)		
	Std. Dev.	5.37 (37.0)		

NOTE: Results based on 4.0 in. (100 mm) cube specimens.

Table 4.41: Modulus of Rupture Results for Batch TC8

Specimen No.	Age days	f_r psi (MPa)	Average psi (MPa)	Std. Dev. psi (MPa)
1	1	813 (5.60)		
2	1	763 (5.26)	788 (5.43)	35.4 (0.244)
3	2	1150 (7.93)		
4	2	1138 (7.84)	1144 (7.89)	8.84 (0.061)
5	3	1213 (8.36)		
6	3	1125 (7.76)	1169 (8.06)	61.9 (0.427)
7	7	1275 (8.79)		
8	7	1313 (9.05)	1294 (8.92)	26.5 (0.183)
	Average	1098 (7.57)		
	Std. Dev.	203 (1.40)		

NOTE: Results based on 4.0 x 8.0 in. (102 x 203 mm) cylinder specimens.

4.2.4.7.9 Batch TC9

Table 4.42: Unit Weight Results for Batch TC9

Specimen No.	Age days	Weight lb (kg)	w_c lb/ft^3 (kg/m^3)	Average lb/ft^3 (kg/m^3)	Std. Dev. lb/ft^3 (kg/m^3)
1	4	5.32 (2.41)	150.6 (2413)		
2	4	5.34 (2.42)	151.3 (2424)	151.0 (2419)	0.481 (7.70)
3	5	5.33 (2.42)	150.9 (2418)		
4	5	5.31 (2.41)	150.5 (2410)	150.7 (2414)	0.320 (5.13)
5	6	5.33 (2.42)	151.0 (2419)		
6	6	5.29 (2.40)	149.8 (2400)	150.4 (2409)	0.841 (13.5)
7	7	5.27 (2.39)	149.2 (2390)		
8	7	5.18 (2.35)	146.8 (2351)	148.0 (2371)	1.72 (27.6)
	Average	5.30 (2.40)	150.0 (2403)		
	Std. Dev.	0.052 (0.024)	1.47 (23.6)		

NOTE: Results based on 4.0 in. (100 mm) cube specimens.

Table 4.43: Compressive Strength Results for Batch TC9

Specimen No.	Age days	f_c ksi (MPa)	Average ksi (MPa)	Std. Dev. ksi (MPa)
1	4	18.3 (126)		
2	4	18.5 (127)	18.4 (127)	0.163 (1.12)
3	5	20.6 (142)		
4	5	21.1 (146)	20.8 (144)	0.389 (2.68)
5	6	20.7 (143)		
6	6	20.6 (142)	20.7 (142)	0.099 (0.683)
7	7	21.5 (149)		
8	7	21.2 (146)	21.4 (147)	0.262 (1.80)
	Average	20.3 (140)		
	Std. Dev.	1.24 (8.57)		

NOTE: Results based on 4.0 in. (100 mm) cube specimens.

Table 4.44: Modulus of Rupture Results for Batch TC9

Specimen No.	Age days	f_r psi (MPa)	Average psi (MPa)	Std. Dev. psi (MPa)
1	4	1225 (8.45)		
2	4	--	1225 (8.45)	--
3	5	1225 (8.45)		
4	5	1325 (9.14)	1275 (8.79)	70.7 (0.488)
5	6	1038 (7.15)		
6	6	1338 (9.22)	1188 (8.19)	212 (1.46)
7	7	1225 (8.45)		
8	7	1250 (8.62)	1238 (8.53)	17.7 (0.122)
	Average	1232 (8.50)		
	Std. Dev.	98.4 (0.678)		

NOTE: Results based on 4.0 x 8.0 in. (102 x 203 mm) cylinder specimens.
(--) no data/not applicable

4.2.4.7.10 Batch TC10

Table 4.45: Unit Weight Results for Batch TC10

Specimen No.	Age days	Weight lb (kg)	w_c lb/ft^3 (kg/m^3)	Average lb/ft^3 (kg/m^3)	Std. Dev. lb/ft^3 (kg/m^3)
1	1	5.27 (2.39)	149.3 (2392)		
2	1	5.26 (2.39)	149.0 (2387)	149.2 (2390)	0.240 (3.85)
3	2	5.34 (2.42)	151.2 (2421)		
4	2	5.34 (2.42)	151.2 (2422)	151.2 (2422)	0.040 (0.641)
5	3	5.36 (2.43)	151.8 (2432)		
6	3	5.33 (2.42)	150.9 (2417)	151.4 (2424)	0.681 (10.9)
7	7	5.27 (2.39)	149.3 (2392)		
8	7	5.26 (2.39)	149.1 (2388)	149.2 (2390)	0.200 (3.21)
	Average	5.31 (2.41)	150.2 (2406)		
	Std. Dev.	0.041 (0.018)	1.15 (18.4)		

NOTE: Results based on 4.0 in. (100 mm) cube specimens.

Table 4.46: Compressive Strength Results for Batch TC10

Specimen No.	Age days	f_c ksi (MPa)	Average ksi (MPa)	Std. Dev. ksi (MPa)
1	1	8.1 (56)		
2	1	7.7 (53)	7.9 (54)	0.297 (2.05)
3	2	18.3 (126)		
4	2	18.7 (129)	18.5 (128)	0.297 (2.05)
5	3	20.2 (139)		
6	3	20.0 (138)	20.1 (139)	0.134 (0.93)
7	7	20.3 (140)		
8	7	21.0 (145)	20.6 (142)	0.474 (3.27)
	Average	16.8 (116)		
	Std. Dev.	5.55 (38.3)		

NOTE: Results based on 4.0 in. (100 mm) cube specimens.

Table 4.47: Modulus of Rupture Results for Batch TC10

Specimen No.	Age days	f_r psi (MPa)	Average psi (MPa)	Std. Dev. psi (MPa)
1	1	1000 (6.89)		
2	1	900 (6.21)	950 (6.55)	70.7 (0.488)
3	2	1138 (7.84)		
4	2	1100 (7.58)	1119 (7.71)	26.5 (0.183)
5	3	1200 (8.27)		
6	3	1250 (8.62)	1225 (8.45)	35.4 (0.244)
7	7	1338 (9.22)		
8	7	1225 (8.45)	1281 (8.83)	79.5 (0.548)
	Average	1144 (7.89)		
	Std. Dev.	142 (0.977)		

NOTE: Results based on 4.0 x 8.0 in. (102 x 203 mm) cylinder specimens.

4.2.4.7.11 Batch TC11

Table 4.48: Unit Weight Results for Batch TC11

Specimen No.	Age days	Weight lb (kg)	w_c lb/ft^3 (kg/m^3)	Average lb/ft^3 (kg/m^3)	Std. Dev. lb/ft^3 (kg/m^3)
1	4	5.27 (2.39)	149.2 (2390)		
2	4	5.29 (2.40)	149.9 (2401)	149.6 (2396)	0.481 (7.70)
3	5	5.28 (2.39)	149.5 (2394)		
4	5	5.29 (2.40)	149.9 (2400)	149.7 (2397)	0.280 (4.49)
5	6	5.26 (2.39)	149.1 (2388)		
6	6	5.32 (2.41)	150.6 (2412)	149.8 (2400)	1.08 (17.3)
7	7	5.27 (2.39)	149.2 (2390)		
8	7	5.29 (2.40)	149.7 (2399)	149.5 (2394)	0.400 (6.41)
	Average	5.28 (2.40)	149.6 (2397)		
	Std. Dev.	0.018 (0.008)	0.505 (8.09)		

NOTE: Results based on 4.0 in. (100 mm) cube specimens.

Table 4.49: Compressive Strength Results for Batch TC11

Specimen No.	Age days	f_c ksi (MPa)	Average ksi (MPa)	Std. Dev. ksi (MPa)
1	4	18.9 (130)		
2	4	20.3 (140)	19.6 (135)	0.976 (6.73)
3	5	20.6 (142)		
4	5	19.8 (136)	20.2 (139)	0.615 (4.24)
5	6	21.4 (147)		
6	6	19.9 (137)	20.6 (142)	1.03 (7.07)
7	7	21.6 (149)		
8	7	21.9 (151)	21.8 (150)	0.217 (1.50)
	Average	20.5 (142)		
	Std. Dev.	1.05 (7.21)		

NOTE: Results based on 4.0 in. (100 mm) cube specimens.

Table 4.50: Modulus of Rupture Results for Batch TC11

Specimen No.	Age days	f_r psi (MPa)	Average psi (MPa)	Std. Dev. psi (MPa)
1	4	1013 (6.98)		
2	4	1028 (7.09)	1020 (7.03)	11.0 (0.076)
3	5	1244 (8.58)		
4	5	1080 (7.45)	1162 (8.01)	115.8 (0.798)
5	6	1143 (7.88)		
6	6	1063 (7.33)	1103 (7.60)	56.6 (0.390)
7	7	1063 (7.33)		
8	7	1191 (8.21)	1127 (7.77)	91.0 (0.628)
	Average	1103 (7.60)		
	Std. Dev.	81.7 (0.564)		

NOTE: Results based on 4.0 x 8.0 in. (102 x 203 mm) cylinder specimens.

4.2.4.7.12 Batch TC12

Table 4.51: Unit Weight Results for Batch TC12

Specimen No.	Age days	Weight lb (kg)	w_c lb/ft^3 (kg/m^3)	Average lb/ft^3 (kg/m^3)	Std. Dev. lb/ft^3 (kg/m^3)
1	7	5.26 (2.38)	148.9 (2385)		
2	7	5.29 (2.40)	149.8 (2400)	149.3 (2392)	0.641 (10.3)
3	14	5.32 (2.41)	150.6 (2412)		
4	14	5.35 (2.43)	151.5 (2427)	151.0 (2419)	0.641 (10.3)
5	21	5.32 (2.41)	150.7 (2414)		
6	21	5.30 (2.40)	150.1 (2405)	150.4 (2409)	0.400 (6.41)
7	42	5.30 (2.40)	150.1 (2404)		
8	42	5.24 (2.38)	148.4 (2377)	149.2 (2390)	1.20 (19.2)
	Average	5.30 (2.40)	150.0 (2403)		
	Std. Dev.	0.035 (0.016)	1.00 (16.0)		

NOTE: Results based on 4.0 in. (100 mm) cube specimens.

Table 4.52: Compressive Strength Results for Batch TC12

Specimen No.	Age days	f_c ksi (MPa)	Average ksi (MPa)	Std. Dev. ksi (MPa)
1	7	19.9 (137)		
2	7	19.8 (137)	19.8 (137)	0.044 (0.302)
3	14	22.4 (155)		
4	14	23.5 (162)	23.0 (158)	0.777 (5.36)
5	21	22.0 (152)		
6	21	21.4 (147)	21.7 (150)	0.464 (3.20)
7	42	22.2 (153)		
8	42	20.6 (142)	21.4 (147)	1.12 (7.72)
	Average	21.5 (148)		
	Std. Dev.	1.31 (9.04)		

NOTE: Results based on 4.0 in. (100 mm) cube specimens.

Table 4.53: Modulus of Rupture Results for Batch TC12

Specimen No.	Age days	f_r psi (MPa)	Average psi (MPa)	Std. Dev. psi (MPa)
1	7	905 (6.24)		
2	7	1194 (8.23)	1050 (7.24)	205 (1.41)
3	14	1138 (7.84)		
4	14	1214 (8.37)	1176 (8.11)	54.4 (0.375)
5	21	1255 (8.65)		
6	21	1210 (8.34)	1233 (8.50)	31.8 (0.219)
7	42	1198 (8.26)		
8	42	1230 (8.48)	1214 (8.37)	23.0 (0.158)
	Average	1168 (8.05)		
	Std. Dev.	111 (0.769)		

NOTE: Results based on 4.0 x 8.0 in. (102 x 203 mm) cylinder specimens.

4.2.4.7.13 Batch TC13

Table 4.54: Unit Weight Results for Batch TC13

Specimen No.	Age days	Weight lb (kg)	w_c lb/ft^3 (kg/m^3)	Average lb/ft^3 (kg/m^3)	Std. Dev. lb/ft^3 (kg/m^3)
1	7	5.33 (2.42)	151.0 (2419)		
2	7	5.28 (2.39)	149.5 (2394)	150.2 (2406)	1.08 (17.3)
3	14	5.30 (2.40)	150.1 (2405)		
4	14	5.26 (2.39)	149.1 (2388)	149.6 (2396)	0.761 (12.2)
5	21	5.34 (2.42)	151.3 (2423)		
6	21	5.27 (2.39)	149.2 (2390)	150.2 (2407)	1.44 (23.1)
7	42	5.29 (2.40)	149.8 (2400)		
8	42	5.34 (2.42)	151.2 (2422)	150.5 (2411)	1.00 (16.0)
	Average	5.30 (2.41)	150.1 (2405)		
	Std. Dev.	0.032 (0.014)	0.904 (14.5)		

NOTE: Results based on 4.0 in. (100 mm) cube specimens.

Table 4.55: Compressive Strength Results for Batch TC13

Specimen No.	Age days	f_c ksi (MPa)	Average ksi (MPa)	Std. Dev. ksi (MPa)
1	7	20.9 (144)		
2	7	19.9 (137)	20.4 (140)	0.717 (4.94)
3	14	21.3 (147)		
4	14	21.8 (150)	21.5 (148)	0.352 (2.43)
5	21	23.5 (162)		
6	21	22.6 (156)	23.1 (159)	0.636 (4.39)
7	42	20.4 (140)		
8	42	21.2 (146)	20.8 (143)	0.580 (4.00)
	Average	21.4 (148)		
	Std. Dev.	1.18 (8.15)		

NOTE: Results based on 4.0 in. (100 mm) cube specimens.

Table 4.56: Modulus of Rupture Results for Batch TC13

Specimen No.	Age days	f_r psi (MPa)	Average psi (MPa)	Std. Dev. psi (MPa)
1	7	1166 (8.04)		
2	7	1169 (8.06)	1168 (8.05)	1.77 (0.012)
3	14	1159 (7.99)		
4	14	1177 (8.11)	1168 (8.05)	12.8 (0.088)
5	21	1178 (8.12)		
6	21	1019 (7.02)	1098 (7.57)	113 (0.777)
7	42	1091 (7.52)		
8	42	1115 (7.69)	1103 (7.60)	17.2 (0.119)
	Average	1134 (7.82)		
	Std. Dev.	56.3 (0.388)		

NOTE: Results based on 4.0 x 8.0 in. (102 x 203 mm) cylinder specimens.

4.2.4.7.14 Batch TC14

Table 4.57: Unit Weight Results for Batch TC14

Specimen No.	Age days	Weight lb (kg)	w_c lb/ft^3 (kg/m^3)	Average lb/ft^3 (kg/m^3)	Std. Dev. lb/ft^3 (kg/m^3)
1	7	5.31 (2.41)	150.3 (2408)		
2	7	5.30 (2.40)	150.0 (2403)	150.2 (2405)	0.200 (3.21)
3	56	5.30 (2.41)	150.2 (2406)		
4	56	5.32 (2.41)	150.5 (2411)	150.4 (2409)	0.240 (3.85)
5	84	5.37 (2.44)	152.1 (2436)		
6	84	5.38 (2.44)	152.3 (2440)	152.2 (2438)	0.200 (3.21)
7	112	5.28 (2.40)	149.6 (2396)		
8	112	5.35 (2.42)	151.4 (2425)	150.5 (2410)	1.28 (20.5)
9	168	5.29 (2.40)	149.9 (2401)		
10	168	5.29 (2.40)	149.7 (2398)	149.8 (2400)	0.160 (2.57)
11	359	5.30 (2.40)	150.1 (2405)		
12	359	5.25 (2.38)	148.7 (2381)	149.4 (2393)	1.04 (16.7)
	Average	5.31 (2.41)	150.4 (2409)		
	Std. Dev.	0.037 (0.017)	1.06 (16.9)		

NOTE: Results based on 4.0 in. (100 mm) cube specimens.

Table 4.58: Compressive Strength Results for Batch TC14

Specimen No.	Age days	f_c ksi (MPa)	Average ksi (MPa)	Std. Dev. ksi (MPa)
1	7	22.3 (154)		
2	7	21.1 (145)	21.7 (150)	0.849 (5.85)
3	56	23.9 (165)		
4	56	22.9 (158)	23.4 (161)	0.707 (4.88)
5	84	21.2 (146)		
6	84	22.7 (157)	22.0 (151)	1.04 (7.17)
7	112	19.9 (137)		
8	112	19.9 (137)	19.9 (137)	0.009 (0.06)
9	168	21.1 (146)		
10	168	22.0 (152)	21.5 (149)	0.624 (4.30)
11	359	22.5 (155)		
12	359	20.5 (142)	21.5 (148)	1.39 (9.58)
	Average	21.7 (149)		
	Std. Dev.	1.25 (8.6)		

NOTE: Results based on 4.0 in. (100 mm) cube specimens.

Table 4.59: Modulus of Elasticity Results for Batch TC14

Specimen No.	Age days	E_c ksi (GPa)	Average ksi (GPa)	Std. Dev. ksi (GPa)
1	7	5818 (40.1)		
2	7	5759 (39.7)	5788 (39.9)	41.8 (0.288)
3	56	6134 (42.3)		
4	56	5908 (40.7)	6021 (41.5)	160 (1.10)
5	84	5872 (40.5)		
6	84	5582 (38.5)	5727 (39.5)	206 (1.42)
7	112	5846 (40.3)		
8	112	6355 (43.8)	6101 (42.1)	360 (2.48)
9	168	6898 (47.6)		
10	168	5984 (41.3)	6441 (44.4)	646 (4.46)
11	365	6476 (44.6)		
12	365	--	6476 (44.6)	--
	Average	6057 (41.8)		
	Std. Dev.	382 (2.63)		

NOTE: Results based on 4.0 x 8.0 in. (102 x 203 mm) cylinder specimens.

4.2.4.7.15 Batch TC15

Table 4.60: Unit Weight Results for Batch TC15

Specimen No.	Age days	Weight lb (kg)	w_c lb/ft^3 (kg/m^3)	Average lb/ft^3 (kg/m^3)	Std. Dev. lb/ft^3 (kg/m^3)
1	7	5.33 (2.42)	150.9 (2417)		
2	7	5.34 (2.42)	151.1 (2420)	151.0 (2419)	0.160 (2.57)
3	14	5.30 (2.40)	150.1 (2405)		
4	14	5.39 (2.44)	152.6 (2444)	151.4 (2424)	1.72 (27.6)
5	21	5.36 (2.43)	151.7 (2430)		
6	21	5.32 (2.41)	150.7 (2414)	151.2 (2422)	0.721 (11.5)
7	28	5.38 (2.44)	152.5 (2442)		
8	28	5.37 (2.44)	152.1 (2436)	152.3 (2439)	0.280 (4.49)
9	42	5.32 (2.41)	150.7 (2414)		
10	42	5.38 (2.44)	152.4 (2441)	151.6 (2428)	1.20 (19.2)
11	365	5.34 (2.42)	151.2 (2422)		
12	365	5.35 (2.43)	151.5 (2427)	151.4 (2424)	0.20 (3.2)
	Average	5.35 (2.43)	151.5 (2426)		
	Std. Dev.	0.028 (0.013)	0.797 (12.8)		

NOTE: Results based on 4.0 in. (100 mm) cube specimens.

Table 4.61: Compressive Strength Results for Batch TC15

Specimen No.	Age days	f_c ksi (MPa)	Average ksi (MPa)	Std. Dev. ksi (MPa)
1	7	22.2 (153)		
2	7	23.0 (159)	22.6 (156)	0.566 (3.90)
3	14	20.4 (141)		
4	14	22.9 (158)	21.7 (149)	1.77 (12.2)
5	21	24.4 (168)		
6	21	23.5 (162)	24.0 (165)	0.622 (4.29)
7	28	23.4 (161)		
8	28	20.8 (143)	22.1 (152)	1.86 (12.82)
9	42	21.5 (148)		
10	42	21.9 (151)	21.7 (150)	0.282 (1.95)
11	365	23.7 (164)		
12	365	24.0 (165)	23.9 (164)	0.165 (1.14)
	Average	22.6 (156)		
	Std. Dev.	1.28 (8.85)		

NOTE: Results based on 4.0 in. (100 mm) cube specimens.

Table 4.62: Modulus of Elasticity Results for Batch TC15

Specimen No.	Age days	E_c ksi (GPa)	Average ksi (GPa)	Std. Dev. ksi (GPa)
1	7	5921 (40.8)		
2	7	5915 (40.8)	5918 (40.8)	4.20 (0.029)
3	14	5722 (39.4)		
4	14	5939 (40.9)	5830 (40.2)	154 (1.06)
5	21	5890 (40.6)		
6	21	5780 (39.9)	5835 (40.2)	78.0 (0.538)
7	28	5731 (39.5)		
8	28	6066 (41.8)	5899 (40.7)	237 (1.63)
9	42	5834 (40.2)		
10	42	6304 (43.5)	6069 (41.8)	333 (2.29)
11	365	6055 (41.7)		
12	365	6089 (42.0)	6072 (41.9)	24 (0.17)
	Average	5937 (40.9)		
	Std. Dev.	169 (1.17)		

NOTE: Results based on 4.0 x 8.0 in. (102 x 203 mm) cylinder specimens.

4.2.5 Strength Gain of UHPC Using Ambient Curing

4.2.5.1 Ambient Curing Regimen

The secondary curing regimen used to investigate strength gain of this unique UHPC was an ambient curing regimen illustrated by Figure 4.16. After production and placement of UHPC as discussed in Section 4.2.2, the concrete molds were covered with plastic to prevent loss of moisture and facilitate hydration and remained at ambient temperatures for 24 hours. Specimens were then demolded and moist cured in a wet room for 72 hours. Following this period of moist curing, the ambient curing regimen was complete, and the specimens remained at ambient laboratory conditions until testing. For comparison to the heat curing regimen, which typically developed full strength after seven days, the effective end of the curing regimen was at seven days after casting. The three-day moist curing period was chosen as a compromise between a conservative laboratory approach and an economic field approach and may be optimized based on the results of these strength gain studies and further investigation into field applications.

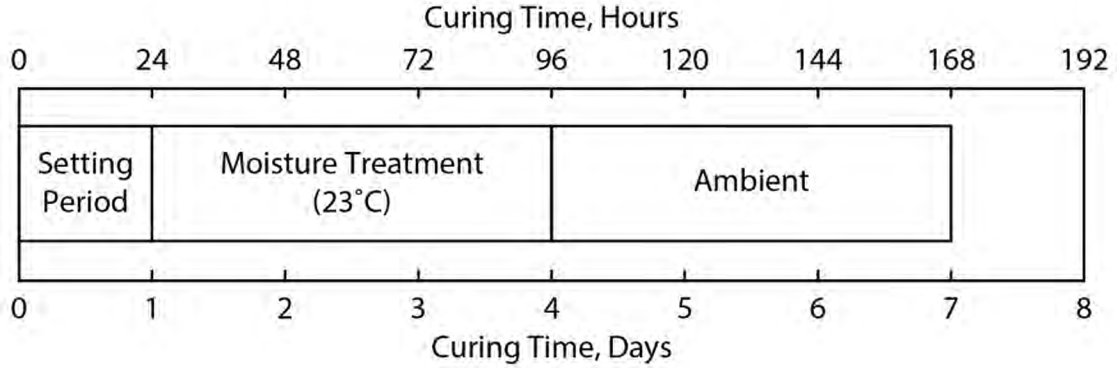


Figure 4.16: Laboratory ambient curing regimen for investigation of nonproprietary UHPC time-dependent strength gain.

4.2.5.2 Curing Temperatures

Concrete core temperatures were monitored using Type-T thermocouples placed directly in the center of 4.0 in. (100 mm) cube specimens and monitored throughout the curing process and over extended periods thereafter. Thermocouple voltage resistance measurements were collected every 30 seconds and averaged over 5-minute intervals, then converted to temperature and recorded by a Campbell® Scientific CR23X Micrologger® (CSI, 2020b). In addition to concrete core temperatures, a reference thermocouple was placed adjacent to the instrumented cube specimen to record the external control temperature and serve to evaluate the surrounding conditions and how they may have affected the internal temperatures of the cubes. Temperature data is presented here for four separate batches of UHPC produced using the ambient curing regimen discussed in Section 4.2.5.1. Each figure presented displays the temperatures recorded by the control thermocouple (placed adjacent to the cube to monitor the external temperatures surrounding the specimen), the core temperature of the cube specimen throughout the curing regimen, and an idealized target temperature based on typical laboratory temperatures.

During the first 24 hours after casting the concrete exhibited temperature fluctuations due to both changes in the ambient laboratory conditions, particularly the cyclic effects of the air-conditioning or heating system, as well as the hydration reaction of the concrete (Figure 4.17 through Figure 4.20). Specimen core temperatures followed a similar trend to the external temperature recorded by the control thermocouple for the first seven to nine hours after casting, after which the heat of hydration caused an increase in the specimen core temperature. Hydration temperatures in larger specimens would typically cause a more noticeable difference between the magnitude of core and external temperatures, however, the small size of the cube specimens mitigated this effect.

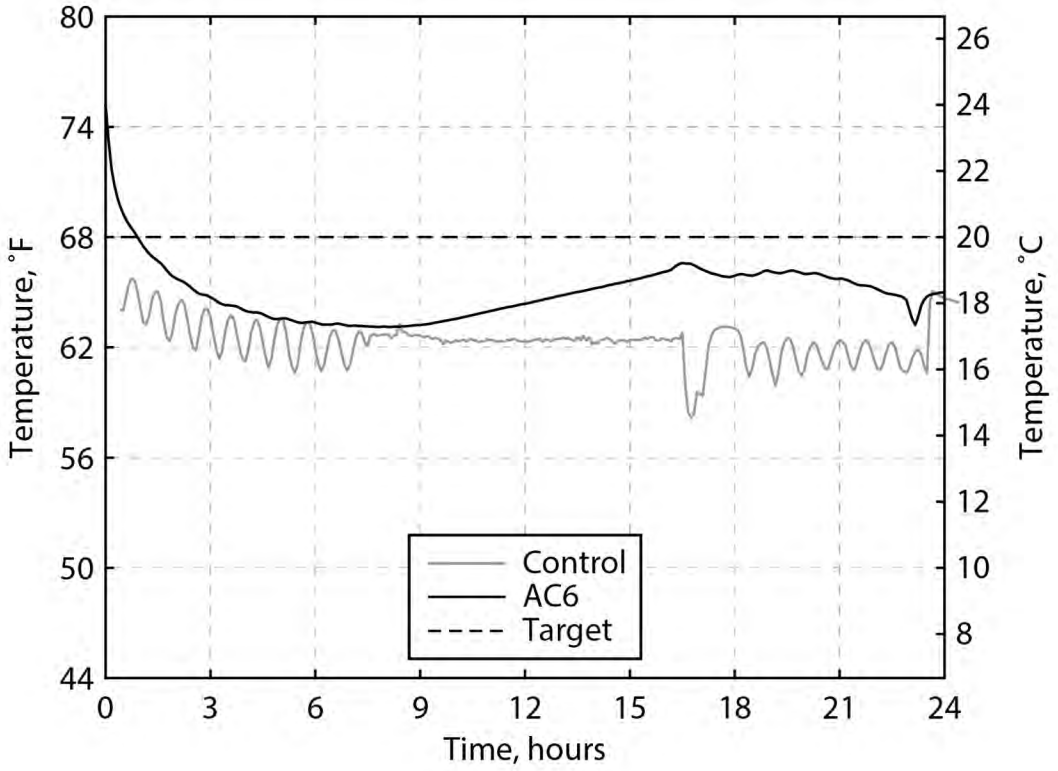


Figure 4.17: Core temperatures for batch AC6 during initial 24 hours after casting.

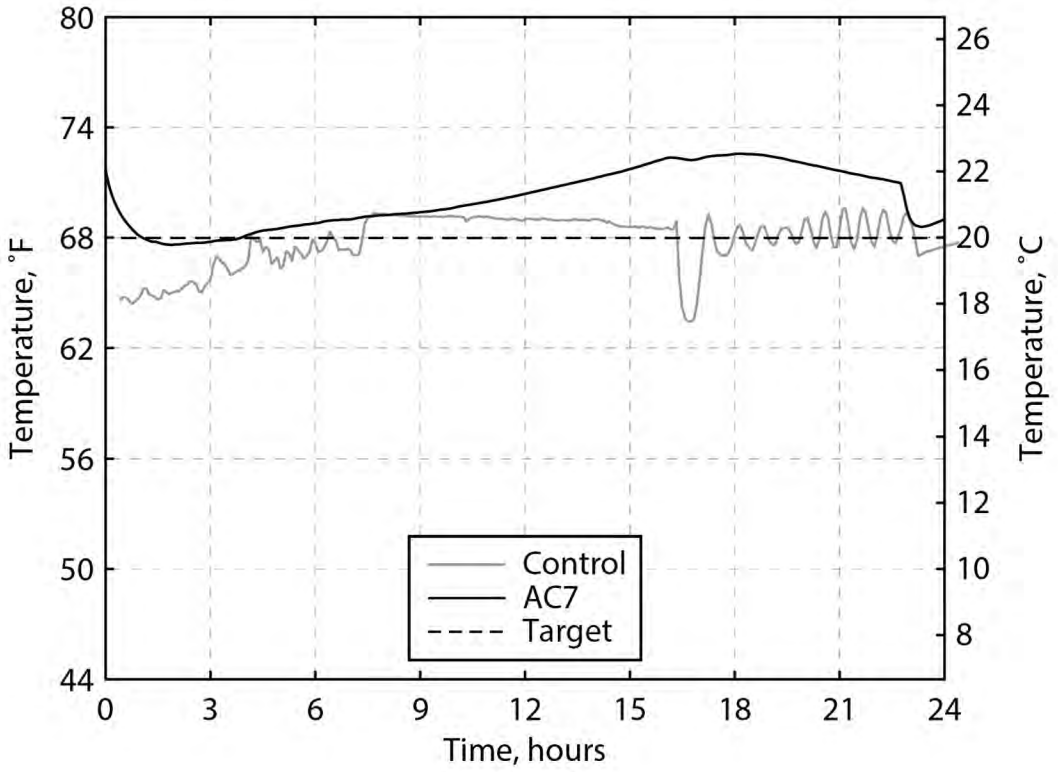


Figure 4.18: Core temperatures for batch AC7 during initial 24 hours after casting.

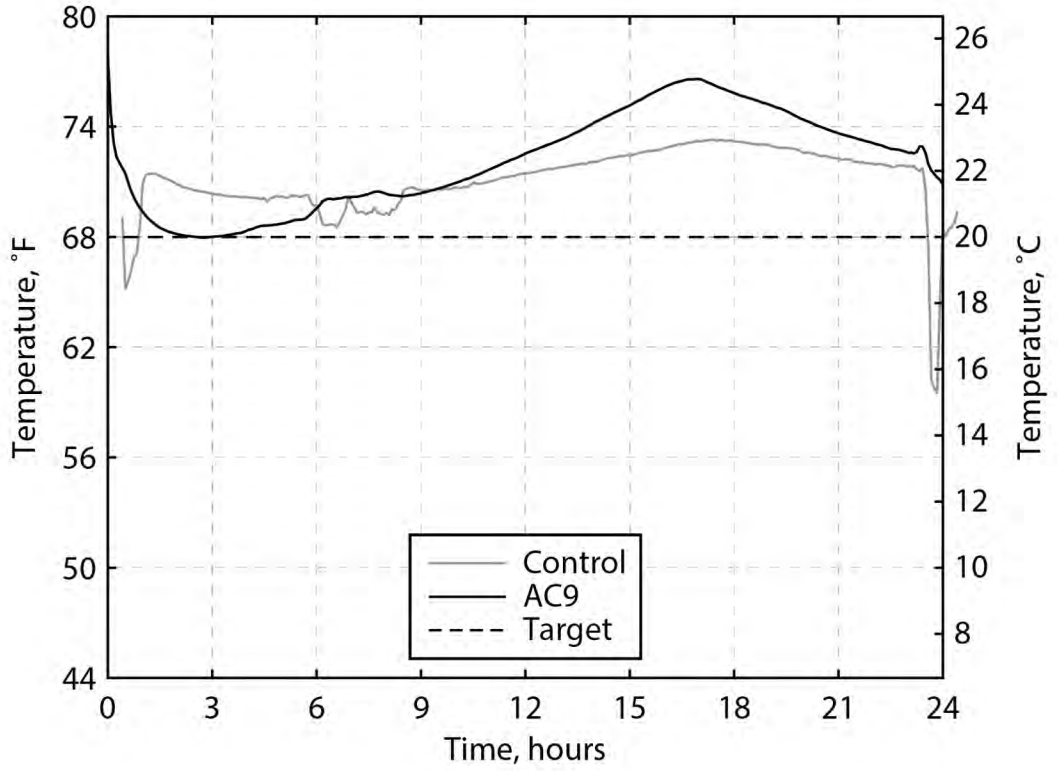


Figure 4.19: Core temperatures for batch AC9 during initial 24 hours after casting.

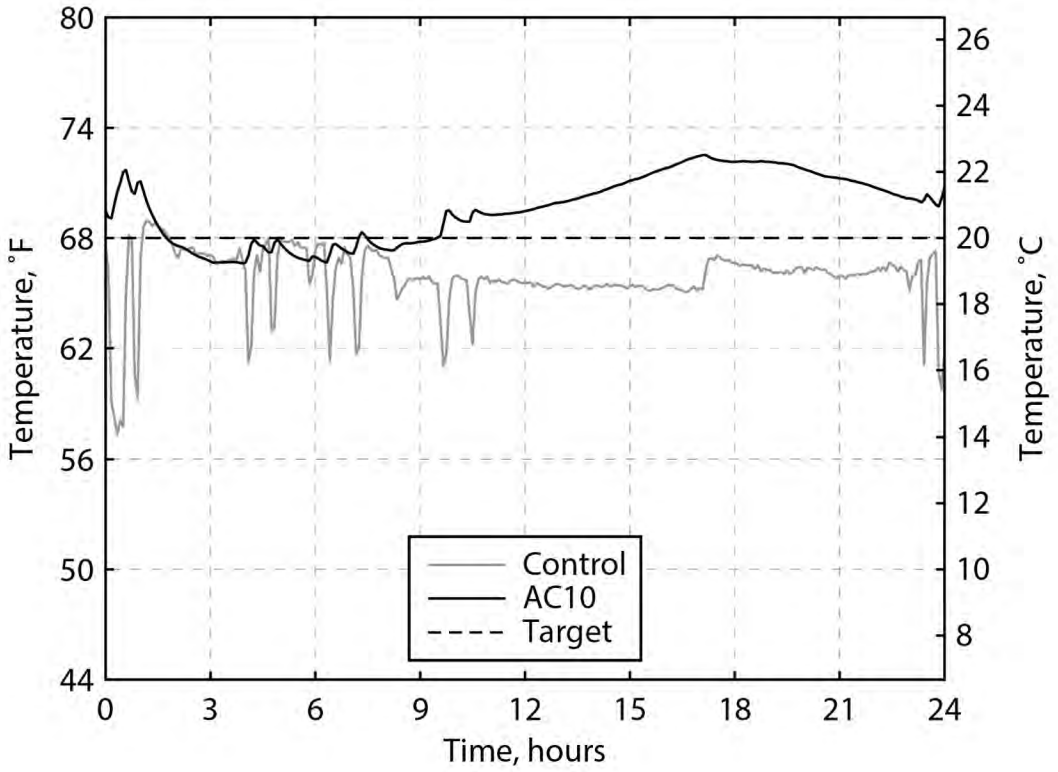


Figure 4.20: Core temperatures for batch AC10 during initial 24 hours after casting.

Curing temperatures throughout the 7-day ambient curing regimen for each batch are provided in Figure 4.21 through Figure 4.24. The specimens used for core temperatures of the ambient cured batches presented here could not be placed in the wet room with the remaining batch specimens but were instead submerged in a water bath and left at ambient laboratory conditions. This was due to the lack of a second datalogger at the time of data collection (collection of heat cured data was conducted simultaneously), proper weatherproof housing for a datalogger, and necessary battery or charging power. However, the time during which the core temperature specimen is placed in the water bath can be clearly recognized due the reduction in temperature fluctuations. During this time, between days one to four, the recorded control temperature remained nearly identical to the core temperature, protected by the water bath from the greater fluctuations of the external laboratory temperature that were present before and after this period. This effect was absent in Figure 4.24, as the representative curing specimen for batch AC10 was accidently not placed in the water bath for moisture treatment.

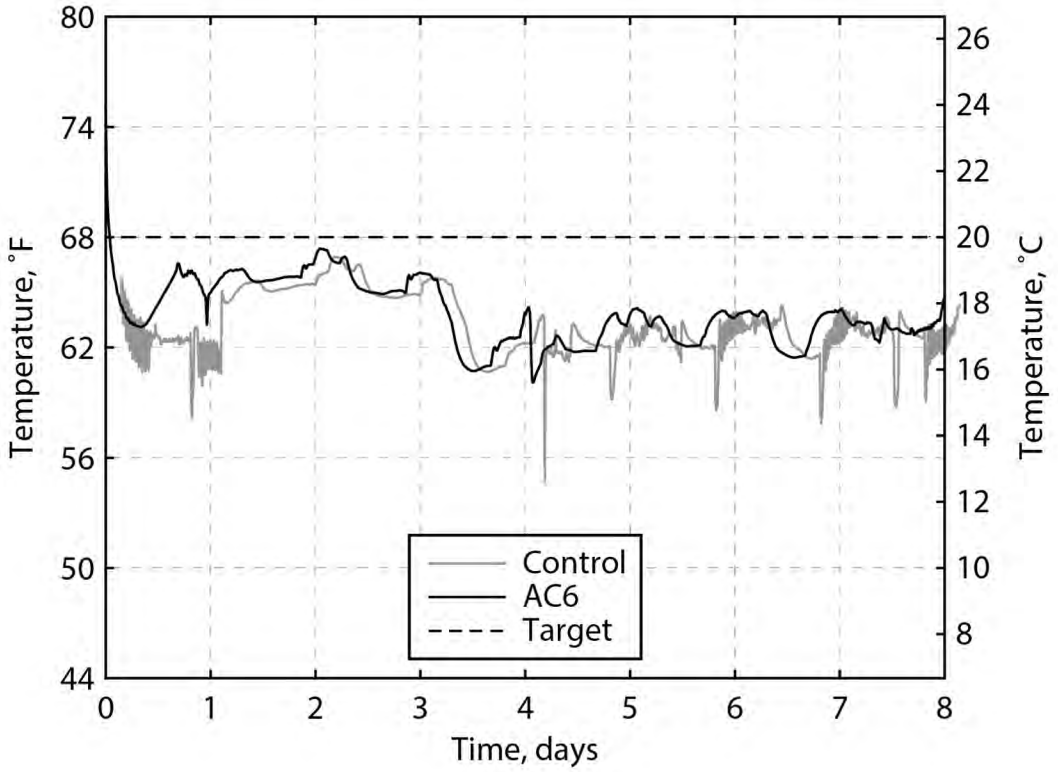


Figure 4.21: Core temperatures for batch AC6 during 7-day ambient curing regimen.

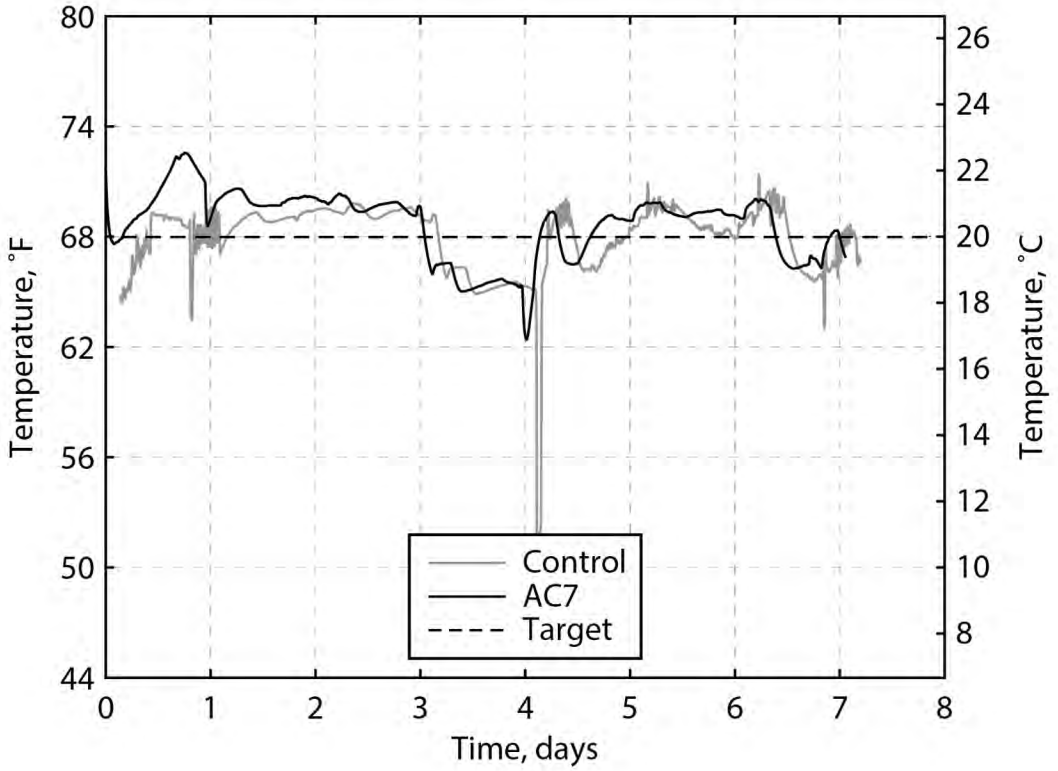


Figure 4.22: Core temperatures for batch AC8 during 7-day ambient curing regimen.

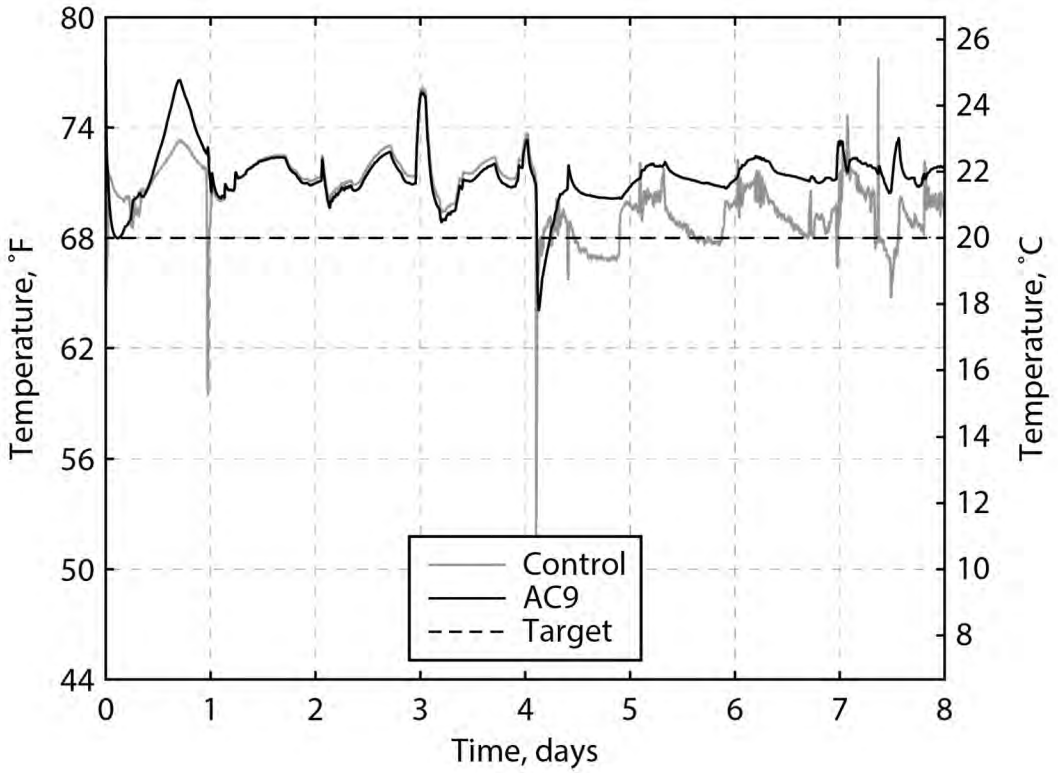


Figure 4.23: Core temperatures for batch AC9 during 7-day ambient curing regimen.

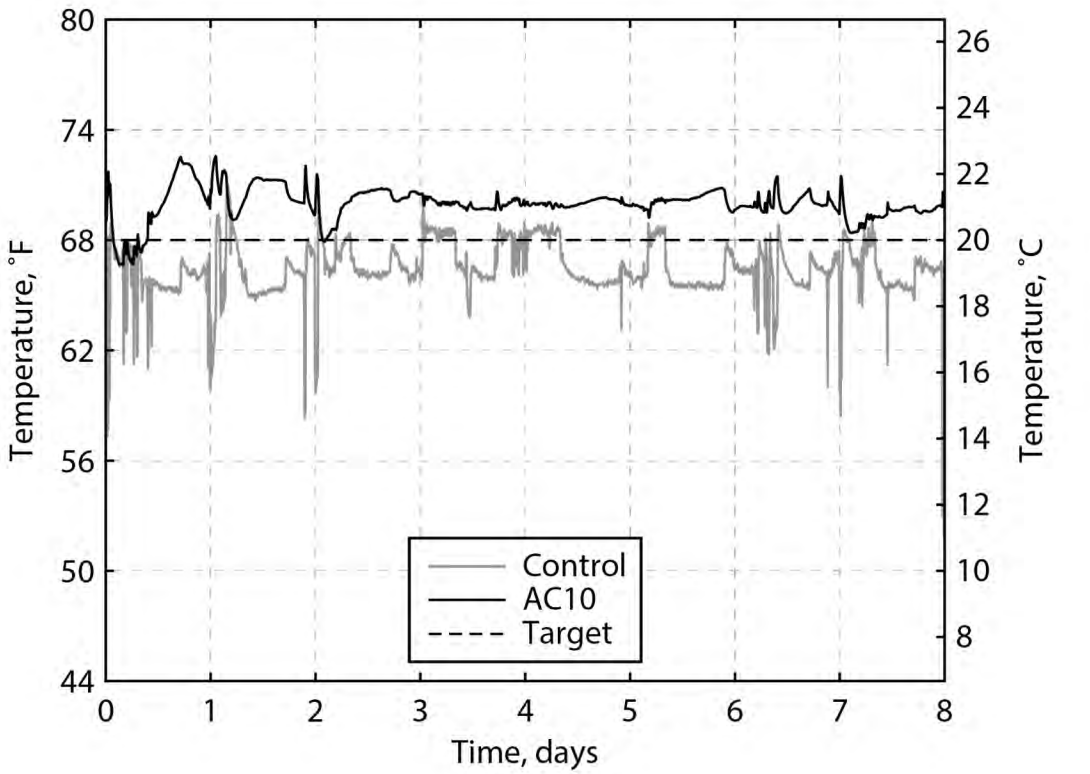


Figure 4.24: Core temperatures for batch AC10 during 7-day ambient curing regimen.

4.2.5.3 Compressive Strength

The results of previous studies on early-age compressive strength gain for thermally cured cube specimens had previously identified initial set to occur at approximately 14 hours after casting for the mixture proportions used in this study (Giesler 2014). Results of thermally cured specimens from the current study indicated approximately 90% of 7-day compressive strength was developed by 48 hours after casting (see Section 4.2.4.3). Based on these results, the testing program of ambient cured specimens was modified to begin at three days after casting, operating under the assumption that strength gain would occur less rapidly for the ambient curing regimen. Thus, early-age strength gain was investigated by testing specimens as outlined in Section i.i at 24-hour intervals during the seven-day curing period beginning three days after casting (Figure 4.25). Beginning at seven days after casting, long-term strength gain was monitored by testing specimens at 7-, 14-, or 28-day intervals. Compressive strength (f_c) results for UHPC produced with ambient curing are summarized based on specimen age at testing in Table 4.63, and data up to 365 days after casting are presented in Figure 4.26.

In Figure 4.25, compressive strengths average 14.2 ksi (98.2 MPa) at three days after casting and steadily increased to an overall average 7-day compressive strength of 16.1 ksi (111 MPa). In Figure 4.26, compressive strengths continued to steadily increase, averaging 19.1 ksi (131 MPa) at 28 days. From this point forward, the average compressive strength was remained relatively consistent over the long-term (Figure 4.26). Outliers in the dataset can most likely be attributed to imperfections in cube specimens. The compressive strength results for each batch produced using the thermal curing regimen are presented in Section 4.2.5.7.

Table 4.63: Summary of Compressive Strength Results for UHPC Produced Using Ambient Curing

Age days	Specimen Count	$f_{c,avg}$ ksi (MPa)	Std. Dev. ksi (MPa)
3	4	14.2 (98.2)	1.00 (6.89)
4	4	14.5 (100)	0.37 (2.57)
5	6	14.0 (96.5)	2.29 (15.8)
6	6	15.0 (104)	2.07 (14.2)
7	20	16.1 (111)	1.71 (11.8)
14	6	16.7 (115)	0.84 (5.77)
21	6	18.0 (124)	0.63 (4.36)
28	6	19.1 (131)	0.55 (3.82)
42	2	20.3 (140)	0.89 (6.15)
56	6	19.1 (132)	0.77 (5.31)
84	6	19.4 (134)	1.04 (7.16)
112	2	20.1 (139)	0.43 (2.96)
164	2	20.5 (141)	0.32 (2.20)
182	2	19.7 (136)	0.07 (0.47)
365	5	20.9 (144)	1.29 (8.88)

NOTE: Results based on 4.0 in. (100 mm) cube specimens.

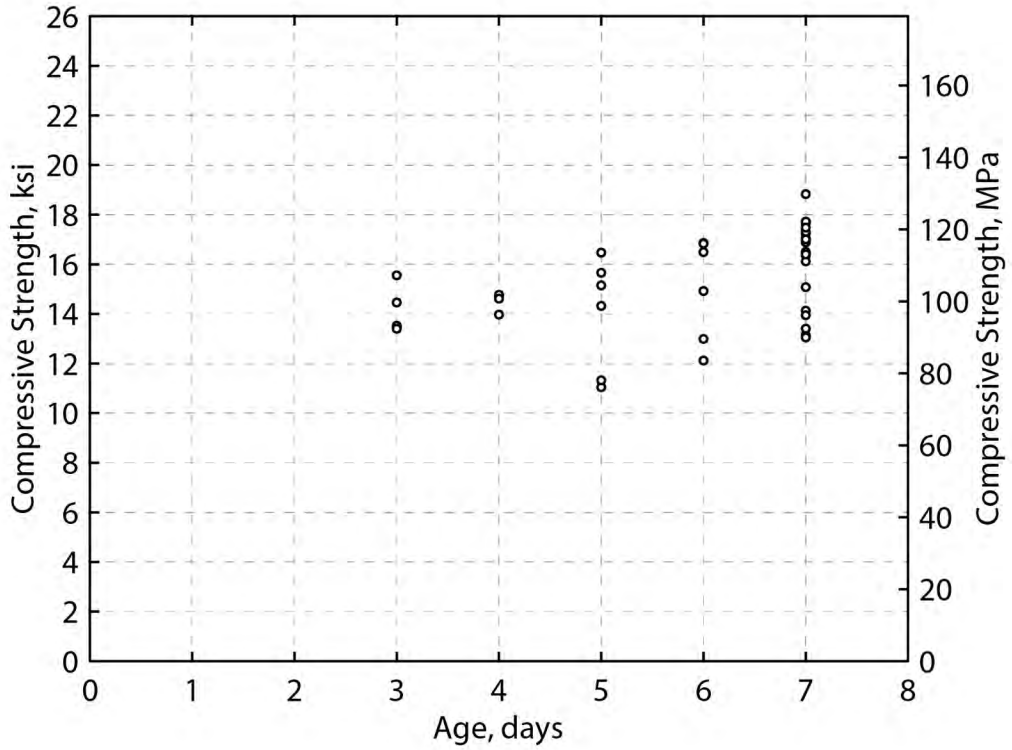


Figure 4.25: Compressive strength gain of 4.0 in (100 mm) UHPC cube specimens produced using the ambient curing regimen during the first seven days after casting.

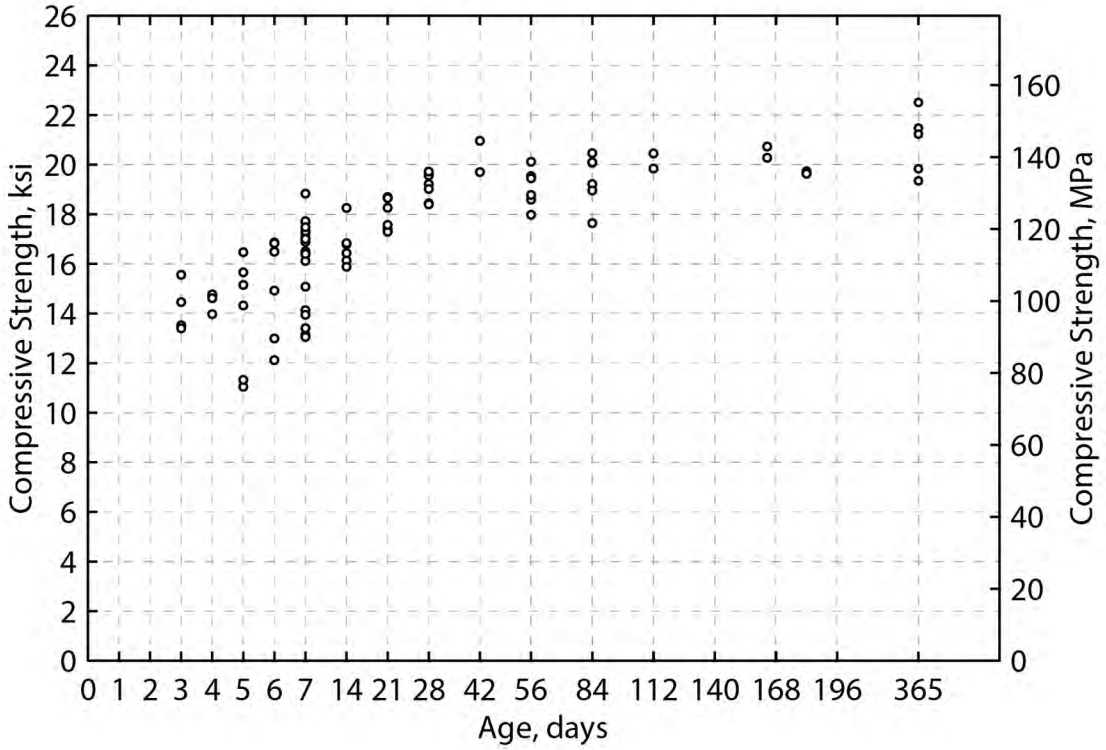


Figure 4.26: Compressive strengths of 4.0 in (100 mm) UHPC cube specimens produced using the ambient curing regimen up to 365 days after casting.

4.2.5.4 Unit Weight

The 4.0 in. (100 mm) cube specimens produced for evaluation of compressive strength were additionally used to determine the unit weight (w_c) of UHPC as outlined in Section i.ii. Specimens were weighed immediately prior to testing, and the average unit weight for all batches produced using the ambient curing regimen was 150.1 lb/ft^3 (2405 kg/m^3). The unit weight results for UHPC produced using the ambient curing regimen are summarized based on specimen age at testing in Table 4.64 below and presented for each batch in Section 4.2.5.7.

Table 4.64: Summary of Unit Weight Results for UHPC Produced Using Ambient Curing

Age days	Specimen Count	$w_{c,avg}$ lb/ft^3 (kg/m^3)	Std. Dev. lb/ft^3 (kg/m^3)
3	4	149.8 (2399)	1.05 (16.8)
4	4	151.7 (2430)	1.40 (22.5)
5	6	149.6 (2397)	1.63 (26.0)
6	6	150.6 (2412)	1.13 (18.1)
7	20	150.4 (2409)	1.76 (28.2)
14	6	150.0 (2403)	1.28 (20.5)
21	6	150.0 (2403)	0.74 (11.9)
28	6	150.8 (2416)	1.50 (24.1)
42	2	150.3 (2408)	0.52 (8.34)
56	6	150.0 (2403)	1.36 (21.8)
84	6	149.9 (2402)	1.46 (23.4)
112	2	150.4 (2409)	0.64 (10.3)
168	2	150.4 (2409)	0.64 (10.3)
182	2	148.8 (2384)	1.68 (26.9)
365	5	149.3 (2391)	1.27 (20.3)

NOTE: Results based on 4.0 in. (100 mm) cube specimens.

4.2.5.5 Modulus of Rupture

The results of early-age modulus of rupture strength gain for thermally cured prism specimens had previously indicated the modulus of rupture was fully developed within approximately two to four days after concrete placement (see Section 4.2.4.5). Thus, under the assumption that strength gain would occur less rapidly for ambient cured specimens, the modulus of rupture (defined here as the flexural stress corresponding to first cracking of the specimen) was evaluated by testing prism specimens (as outlined in Section i.iii) produced using the ambient curing regimen at 24-hour intervals during the seven day curing period beginning three days after casting (Figure 4.27). The modulus of rupture (f_r) results for UHPC produced using the ambient curing regimen are summarized based on specimen age at testing in Table 4.65, and data up to 365 days after casting are presented in Figure 4.28.

Analysis of LVDT data to determine the occurrence of first cracking indicated the modulus of rupture for ambient cured specimens required six days after casting to develop at least 90% of the 7-day average modulus of rupture strength, which for all batches was approximately 656 psi (4.52 MPa). Similar to the compressive strength results for ambient cured specimens, the long-term modulus of rupture continued to increase in strength as seen in Figure 4.28. Average modulus of rupture strength at 28 days was 725 psi (5.0 MPa) and continued to increase to an average strength of 905 psi (6.24 MPa) at an age of one year. The modulus of rupture strength results for each batch produced using the ambient curing regimen are presented for each batch in Section 4.2.5.7.

Table 4.65: Summary of Modulus of Rupture Results for UHPC Produced Using Ambient Curing

Age days	Specimen Count	$f_{r,avg}$ psi (MPa)	Std. Dev. psi (MPa)
3	4	453.0 (3.12)	108.1 (0.75)
4	4	594.4 (4.10)	38.1 (0.26)
5	6	543.9 (3.75)	71.6 (0.49)
6	6	632.7 (4.36)	49.2 (0.34)
7	16	655.6 (4.52)	69.9 (0.48)
14	4	709.1 (4.89)	114.7 (0.79)
21	4	709.2 (4.89)	89.7 (0.62)
28	4	725.3 (5.00)	111.8 (0.77)
56	4	832.8 (5.74)	142.0 (0.98)
84	4	816.7 (5.63)	92.2 (0.64)
182	2	941.3 (6.49)	124.6 (0.86)
365	2	904.7 (6.24)	232.0 (1.60)

NOTE: Results based on 16.0 x 3.0 x 4.0 in. (406 x 76 x 102 mm) beam specimens.

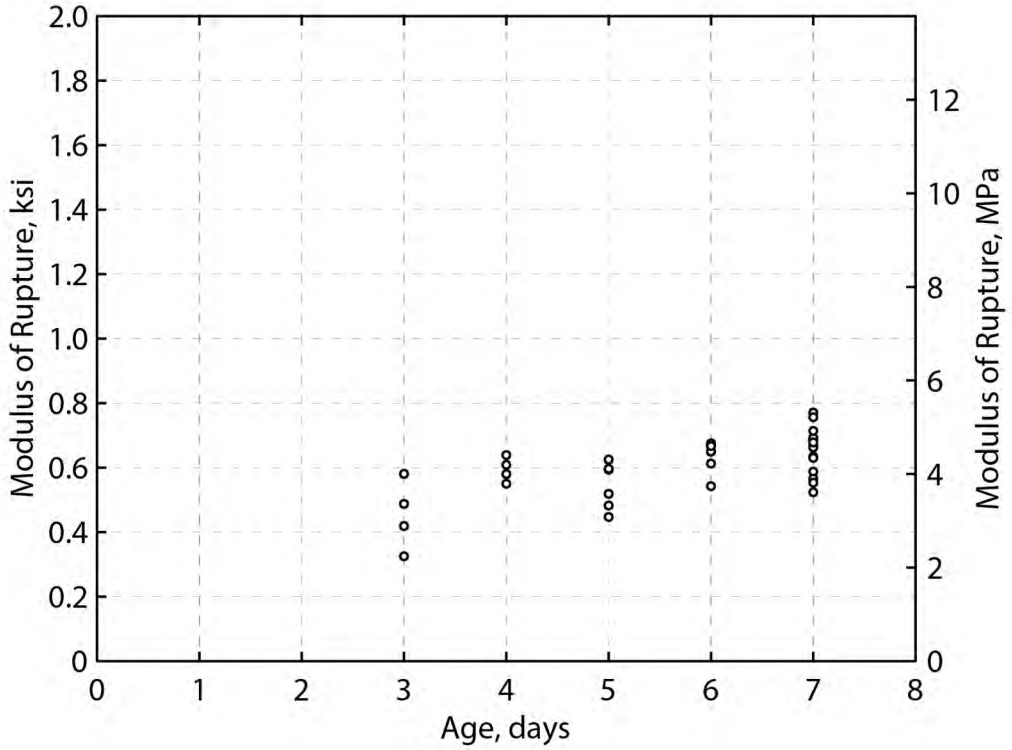


Figure 4.27: Modulus of rupture strength gain of UHPC prism specimens produced using the ambient curing regimen during the first seven days after casting.

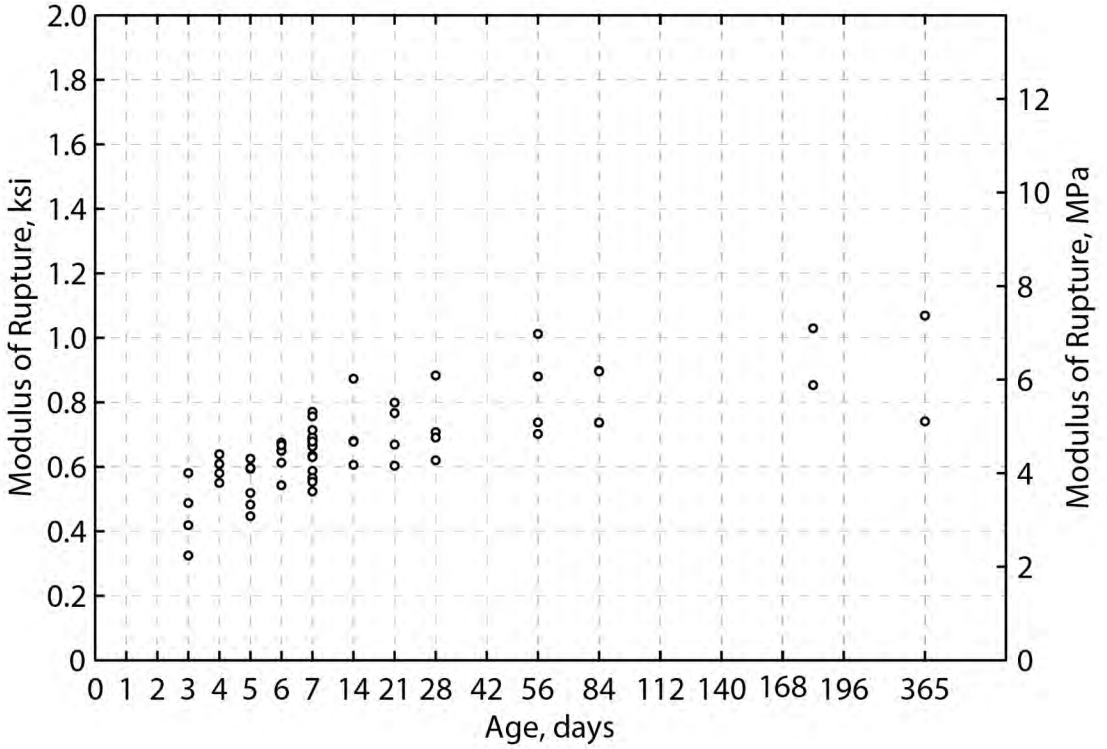


Figure 4.28: Modulus of rupture strengths of UHPC prism specimens produced using ambient curing up to 365 days after casting.

4.2.5.6 Modulus of Elasticity

The long-term modulus of elasticity (E_c) of UHPC produced with ambient curing was mapped by testing 4.0 in. x 8.0 in. (102 mm x 203 mm) cylinder specimens at 7-, 14-, or 28-day intervals as outlined in Section i.iv. Results of testing are summarized in Table 4.66 and presented in Figure 4.29 up to 365 days after casting. Initial specimens were tested at the end of the seven-day thermal curing regimen, with an average value of 5382 ksi (37.1 GPa), and subsequent values remained relatively constant as the concrete ages. Some variance in the results is expected due to the non-homogenous nature of concrete and can also be the result of imperfections in the specimen geometry or batch/specimen strength. The modulus of elasticity results for UHPC produced using the ambient curing regimen are summarized based on specimen age at testing in Table 4.66 below and presented for each batch in Section 4.2.5.7.

Table 4.66: Summary of Modulus of Elasticity Results for UHPC Produced Using Ambient Curing

Age days	Specimen Count	$E_{c,avg}$ ksi (GPa)	Std. Dev. ksi (GPa)
7	4	5382 (37.1)	364 (2.51)
14	2	5176 (35.7)	253 (1.75)
21	2	5492 (37.9)	1.91 (0.01)
28	2	6175 (42.6)	871 (6.00)
42	2	6318 (43.6)	103 (0.71)
56	2	5952 (41.0)	144 (0.99)
84	2	6548 (45.1)	860 (5.93)
112	2	6782 (46.8)	959 (6.61)
164	2	5834 (40.2)	289 (2.00)
365	4	6100 (42.1)	235 (1.62)

NOTE: Results based on 4.0 x 8.0 in. (102 x 203 mm) cylinder specimens.

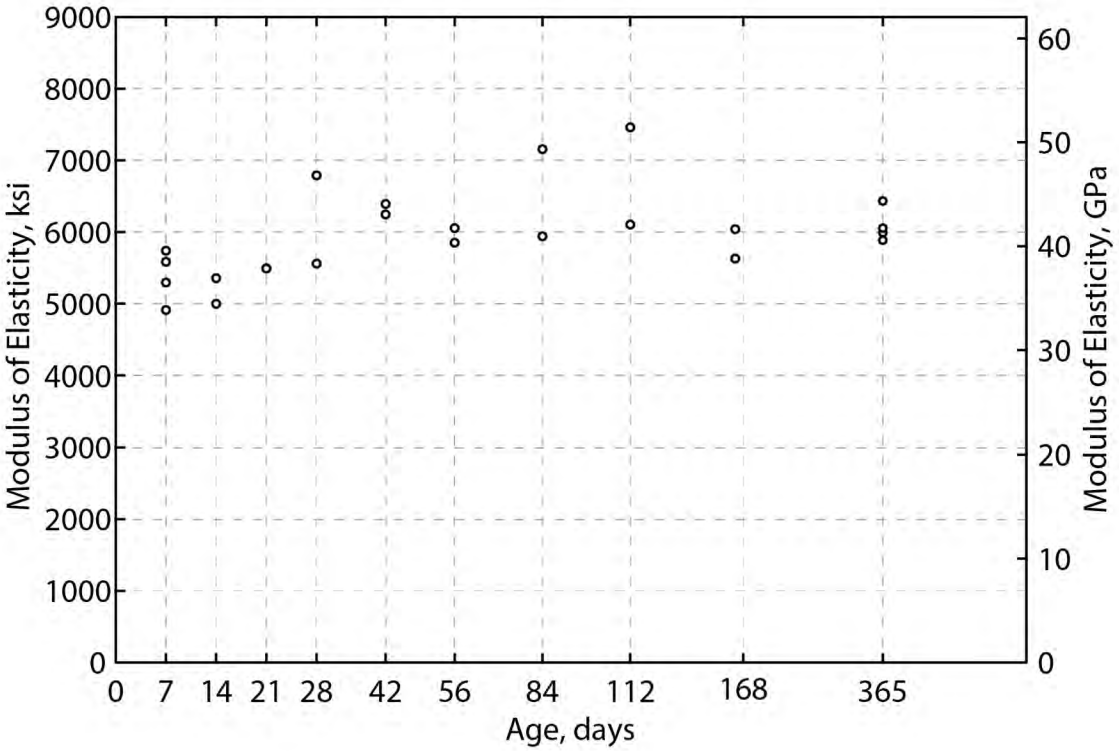


Figure 4.29: Modulus of elasticity strengths of UHPC cylinder specimens for the ambient curing regimen up to 365 days after casting.

4.2.5.7 Batch Results for UHPC Using Ambient Curing Regimen

Data is presented in the following sections for each batch of UHPC produced using the ambient curing regimen.

4.2.5.7.1 Batch AC1

Table 4.67: Unit Weight Results for Batch AC1

Specimen No.	Age days	Weight lb (kg)	w_c lb/ft^3 (kg/m^3)	Average lb/ft^3 (kg/m^3)	Std. Dev. lb/ft^3 (kg/m^3)
1	7	5.12 (2.32)	145.0 (2323)		
2	7	5.27 (2.39)	149.3 (2391)	147.2 (2357)	3.00 (48.1)
3	182	5.21 (2.37)	147.6 (2365)		
4	182	5.30 (2.40)	150.0 (2403)	148.8 (2384)	1.68 (26.9)
5	362	5.21 (2.36)	147.4 (2361)		
6	--	--	--	147.4 (2361)	--
	Average	5.22 (2.37)	147.9 (2369)		
	Std. Dev.	0.068 (0.031)	1.93 (30.9)		

NOTE: Results based on 4.0 in. (100 mm) cube specimens.
(--) no data/not applicable

Table 4.68: Compressive Strength Results for Batch AC1

Specimen No.	Age days	f_c ksi (MPa)	Average ksi (MPa)	Std. Dev. ksi (MPa)
1	7	13.4 (92.4)		
2	7	13.9 (96.2)	13.7 (94)	0.382 (2.63)
3	182	19.7 (136)		
4	182	19.6 (135)	19.7 (136)	0.068 (0.47)
5	362	19.4 (133)		
6	--	--	19.4 (133)	--
	Average	17.2 (119)		
	Std. Dev.	3.24 (22.33)		

NOTE: Results based on 4.0 in. (100 mm) cube specimens.
(--) no data/not applicable

Table 4.69: Modulus of Rupture Results for Batch AC1

Specimen No.	Age days	f_r psi (MPa)	Average psi (MPa)	Std. Dev. psi (MPa)
1	7	553 (3.81)		
2	7	678 (4.68)	616 (4.24)	88.4 (0.609)
3	182	1029 (7.10)		
4	182	853 (5.88)	941 (6.49)	125 (0.859)
5	362	741 (5.11)		
6	362	1069 (7.37)	905 (6.24)	232.0 (1.600)
	Average	821 (5.66)		
	Std. Dev.	202 (1.39)		

NOTE: Results based on 4.0 x 8.0 in. (102 x 203 mm) cylinder specimens.

4.2.5.7.2 Batch AC2

Table 4.70: Unit Weight Results for Batch AC2

Specimen No.	Age days	Weight lb (kg)	w_c lb/ft^3 (kg/m^3)	Average lb/ft^3 (kg/m^3)	Std. Dev. lb/ft^3 (kg/m^3)
1	5	5.22 (2.37)	147.8 (2368)		
2	5	5.21 (2.36)	147.4 (2361)	147.6 (2364)	0.300 (4.81)
3	6	5.33 (2.42)	150.8 (2416)		
4	6	5.25 (2.38)	148.6 (2380)	149.7 (2398)	1.56 (25.0)
5	7	5.30 (2.40)	150.1 (2404)		
6	7	5.31 (2.41)	150.2 (2407)	150.2 (2405)	0.120 (1.92)
	Average	5.27 (2.39)	149.2 (2389)		
	Std. Dev.	0.050 (0.023)	1.42 (22.7)		

NOTE: Results based on 4.0 in. (100 mm) cube specimens.

Table 4.71: Compressive Strength Results for Batch AC2

Specimen No.	Age days	f_c ksi (MPa)	Average ksi (MPa)	Std. Dev. ksi (MPa)
1	5	11.0 (76.2)		
2	5	11.3 (78.1)	11.2 (77)	0.197 (1.36)
3	6	13.0 (89.6)		
4	6	12.1 (83.6)	12.6 (87)	0.617 (4.25)
5	7	13.1 (90.6)		
6	7	13.1 (0.0)	13.1 (91)	0.059 (0.405)
	Average	12.3 (84.7)		
	Std. Dev.	0.93 (6.39)		

NOTE: Results based on 4.0 in. (100 mm) cube specimens.

Table 4.72: Modulus of Rupture Results for Batch AC2

Specimen No.	Age days	f_r psi (MPa)	Average psi (MPa)	Std. Dev. psi (MPa)
1	5	483 (3.33)		
2	5	447 (3.08)	465 (3.20)	25.2 (0.174)
3	6	543 (3.74)		
4	6	613 (4.22)	578 (3.98)	49.5 (0.341)
5	7	566 (3.90)		
6	7	630 (4.34)	598 (4.12)	45.5 (0.314)
	Average	547 (3.77)		
	Std. Dev.	71.7 (0.495)		

NOTE: Results based on 4.0 x 8.0 in. (102 x 203 mm) cylinder specimens.

4.2.5.7.3 Batch AC3

Table 4.73: Unit Weight Results for Batch AC3

Specimen No.	Age days	Weight lb (kg)	w_c lb/ft^3 (kg/m^3)	Average lb/ft^3 (kg/m^3)	Std. Dev. lb/ft^3 (kg/m^3)
1	7	5.28 (2.40)	149.6 (2397)		
2	7	5.36 (2.43)	151.9 (2433)	150.8 (2415)	1.60 (25.7)
3	28	5.34 (2.42)	151.3 (2424)		
4	28	5.39 (2.44)	152.6 (2445)	152.0 (2434)	0.921 (14.8)
5	56	5.31 (2.41)	150.3 (2408)		
6	56	5.39 (2.44)	152.6 (2444)	151.4 (2426)	1.60 (25.7)
7	84	5.32 (2.41)	150.8 (2415)		
8	84	5.38 (2.44)	152.3 (2440)	151.6 (2428)	1.12 (18.0)
	Average	5.35 (2.43)	151.4 (2426)		
	Std. Dev.	0.040 (0.018)	1.12 (17.9)		

NOTE: Results based on 4.0 in. (100 mm) cube specimens.

Table 4.74: Compressive Strength Results for Batch AC3

Specimen No.	Age days	f_c ksi (MPa)	Average ksi (MPa)	Std. Dev. ksi (MPa)
1	7	16.4 (113)		
2	7	17.5 (121)	16.9 (117)	0.764 (5.27)
3	28	18.4 (127)		
4	28	19.0 (131)	18.7 (129)	0.438 (3.02)
5	56	19.4 (134)		
6	56	20.1 (139)	19.8 (136)	0.471 (3.25)
7	84	19.0 (131)		
8	84	20.1 (139)	19.5 (135)	0.805 (5.55)
	Average	18.7 (129)		
	Std. Dev.	1.28 (8.85)		

NOTE: Results based on 4.0 in. (100 mm) cube specimens.

Table 4.75: Modulus of Rupture Results for Batch AC3

Specimen No.	Age days	f_r psi (MPa)	Average psi (MPa)	Std. Dev. psi (MPa)
1	7	714 (4.92)		
2	7	524 (3.61)	619 (4.27)	134.5 (0.928)
3	28	620 (4.27)		
4	28	691 (4.76)	655 (4.52)	49.9 (0.344)
5	56	738 (5.08)		
6	56	702 (4.84)	720 (4.96)	25.2 (0.174)
7	84	666 (4.59)		
8	84	631 (4.35)	648 (4.47)	25.2 (0.174)
	Average	661 (4.55)		
	Std. Dev.	68.4 (0.471)		

NOTE: Results based on 4.0 x 8.0 in. (102 x 203 mm) cylinder specimens.

4.2.5.7.4 Batch AC4

Table 4.76: Unit Weight Results for Batch AC4

Specimen No.	Age days	Weight lb (kg)	w_c lb/ft^3 (kg/m^3)	Average lb/ft^3 (kg/m^3)	Std. Dev. lb/ft^3 (kg/m^3)
1	3	5.24 (2.38)	148.3 (2376)		
2	3	5.30 (2.40)	150.1 (2405)	149.2 (2390)	1.28 (20.5)
3	7	5.25 (2.38)	148.7 (2382)		
4	7	5.30 (2.40)	150.0 (2403)	149.4 (2393)	0.921 (14.8)
5	28	5.25 (2.38)	148.7 (2381)		
6	28	5.29 (2.40)	149.7 (2399)	149.2 (2390)	0.761 (12.2)
7	56	5.27 (2.39)	149.2 (2390)		
8	56	5.26 (2.38)	148.8 (2384)	149.0 (2387)	0.240 (3.85)
	Average	5.27 (2.39)	149.2 (2390)		
	Std. Dev.	0.024 (0.011)	0.683 (10.9)		

NOTE: Results based on 4.0 in. (100 mm) cube specimens.

Table 4.77: Compressive Strength Results for Batch AC4

Specimen No.	Age days	f_c ksi (MPa)	Average ksi (MPa)	Std. Dev. ksi (MPa)
1	3	13.4 (92.4)		
2	3	14.5 (100)	13.9 (96)	0.747 (5.15)
3	7	15.1 (104)		
4	7	16.1 (111)	15.6 (108)	0.735 (5.07)
5	28	19.2 (132)		
6	28	18.4 (127)	18.8 (130)	0.549 (3.78)
7	56	19.5 (135)		
8	56	18.8 (129)	19.2 (132)	0.538 (3.71)
	Average	16.9 (116)		
	Std. Dev.	2.40 (16.55)		

NOTE: Results based on 4.0 in. (100 mm) cube specimens.

Table 4.78: Modulus of Rupture Results for Batch AC4

Specimen No.	Age days	f_r psi (MPa)	Average psi (MPa)	Std. Dev. psi (MPa)
1	3	419 (2.89)		
2	3	325 (2.24)	372 (2.56)	66.3 (0.457)
3	7	771 (5.31)		
4	7	756 (5.21)	763 (5.26)	10.2 (0.070)
5	28	883 (6.09)		
6	28	708 (4.88)	795 (5.48)	124 (0.856)
7	56	880 (6.07)		
8	56	1012 (6.98)	946 (6.52)	93.2 (0.643)
	Average	719 (4.96)		
	Std. Dev.	235 (1.62)		

NOTE: Results based on 4.0 x 8.0 in. (102 x 203 mm) cylinder specimens.
(--) no data/not applicable

4.2.5.7.5 Batch AC5

Table 4.79: Unit Weight Results for Batch AC5

Specimen No.	Age days	Weight lb (kg)	w_c lb/ft^3 (kg/m^3)	Average lb/ft^3 (kg/m^3)	Std. Dev. lb/ft^3 (kg/m^3)
1	3	5.29 (2.40)	149.7 (2399)		
2	3	5.33 (2.42)	150.8 (2416)	150.3 (2407)	0.761 (12.19)
3	7	5.31 (2.41)	150.2 (2407)		
4	7	5.40 (2.45)	152.8 (2448)	151.5 (2427)	1.80 (28.9)
5	14	5.29 (2.40)	149.7 (2399)		
6	14	5.31 (2.41)	150.2 (2407)	150.0 (2403)	0.360 (5.8)
7	21	5.27 (2.39)	149.3 (2392)		
8	21	5.30 (2.40)	150.1 (2405)	149.7 (2399)	0.561 (8.98)
	Average	5.31 (2.41)	150.4 (2409)		
	Std. Dev.	0.038 (0.017)	1.07 (17.2)		

NOTE: Results based on 4.0 in. (100 mm) cube specimens.

Table 4.80: Compressive Strength Results for Batch AC5

Specimen No.	Age days	f_c ksi (MPa)	Average ksi (MPa)	Std. Dev. ksi (MPa)
1	3	13.5 (93.2)		
2	3	15.6 (107)	14.5 (100)	1.44 (9.91)
3	7	16.4 (113)		
4	7	17.0 (117)	16.7 (115)	0.453 (3.12)
5	14	16.4 (113)		
6	14	16.8 (116)	16.6 (115)	0.284 (1.96)
7	21	17.3 (119)		
8	21	17.6 (121)	17.4 (120)	0.197 (1.36)
	Average	16.3 (113)		
	Std. Dev.	1.29 (8.90)		

NOTE: Results based on 4.0 in. (100 mm) cube specimens.

Table 4.81: Modulus of Rupture Results for Batch AC5

Specimen No.	Age days	f_r psi (MPa)	Average psi (MPa)	Std. Dev. psi (MPa)
1	3	488 (3.36)		
2	3	581 (4.00)	534 (3.68)	65.8 (0.454)
3	7	663 (4.57)		
4	7	588 (4.05)	625 (4.31)	53.0 (0.366)
5	14	606 (4.18)		
6	14	873 (6.02)	739 (5.10)	189 (1.30)
7	21	766 (5.28)		
8	21	799 (5.51)	783 (5.40)	23.0 (0.158)
	Average	670 (4.62)		
	Std. Dev.	131 (0.900)		

NOTE: Results based on 4.0 x 8.0 in. (102 x 203 mm) cylinder specimens.

4.2.5.7.6 Batch AC6

Table 4.82: Unit Weight Results for Batch AC6

Specimen No.	Age days	Weight lb (kg)	w_c lb/ft^3 (kg/m^3)	Average lb/ft^3 (kg/m^3)	Std. Dev. lb/ft^3 (kg/m^3)
1	7	5.30 (2.40)	150.1 (2404)		
2	7	5.35 (2.43)	151.5 (2427)	150.8 (2415)	1.00 (16.0)
3	14	5.25 (2.38)	148.8 (2383)		
4	14	5.25 (2.38)	148.7 (2382)	148.7 (2383)	0.040 (0.641)
5	21	5.29 (2.40)	149.7 (2398)		
6	21	5.28 (2.39)	149.5 (2394)	149.6 (2396)	0.160 (2.57)
7	84	5.24 (2.38)	148.3 (2376)		
8	84	5.28 (2.39)	149.5 (2394)	148.9 (2385)	0.801 (12.8)
	Average	5.28 (2.39)	149.5 (2395)		
	Std. Dev.	0.035 (0.016)	0.991 (15.9)		

NOTE: Results based on 4.0 in. (100 mm) cube specimens.

Table 4.83: Compressive Strength Results for Batch AC6

Specimen No.	Age days	f_c ksi (MPa)	Average ksi (MPa)	Std. Dev. ksi (MPa)
1	7	14.1 (97.4)		
2	7	16.5 (114)	15.3 (106)	1.68 (11.6)
3	14	16.1 (111)		
4	14	15.9 (109)	16.0 (110)	0.180 (1.24)
5	21	17.4 (120)		
6	21	18.6 (129)	18.0 (124)	0.878 (6.06)
7	84	17.6 (122)		
8	84	20.1 (138)	18.9 (130)	1.72 (11.8)
	Average	17.1 (118)		
	Std. Dev.	1.82 (12.55)		

NOTE: Results based on 4.0 in. (100 mm) cube specimens.

Table 4.84: Modulus of Rupture Results for Batch AC6

Specimen No.	Age days	f_r psi (MPa)	Average psi (MPa)	Std. Dev. psi (MPa)
1	7	668 (4.60)		
2	7	692 (4.77)	680 (4.69)	17.2 (0.119)
3	14	680 (4.69)		
4	14	678 (4.67)	679 (4.68)	1.77 (0.012)
5	21	669 (4.61)		
6	21	603 (4.16)	636 (4.38)	46.4 (0.320)
7	84	898 (6.19)		
8	84	896 (6.18)	897 (6.18)	1.33 (0.009)
	Average	723 (4.98)		
	Std. Dev.	111 (0.762)		

NOTE: Results based on 4.0 x 8.0 in. (102 x 203 mm) cylinder specimens.

4.2.5.7.7 Batch AC7

Table 4.85: Unit Weight Results for Batch AC7

Specimen No.	Age days	Weight lb (kg)	w_c lb/ft^3 (kg/m^3)	Average lb/ft^3 (kg/m^3)	Std. Dev. lb/ft^3 (kg/m^3)
1	4	5.32 (2.41)	150.7 (2414)		
2	4	5.31 (2.41)	150.3 (2408)	150.5 (2411)	0.280 (4.49)
3	5	5.33 (2.42)	150.8 (2416)		
4	5	5.34 (2.42)	151.1 (2420)	151.0 (2418)	0.200 (3.21)
5	6	5.34 (2.42)	151.3 (2424)		
6	6	5.36 (2.43)	151.8 (2431)	151.6 (2428)	0.320 (5.13)
7	7	5.34 (2.42)	151.1 (2420)		
8	7	5.38 (2.44)	152.5 (2442)	151.8 (2431)	0.961 (15.4)
	Average	5.34 (2.42)	151.2 (2422)		
	Std. Dev.	0.024 (0.011)	0.671 (10.7)		

NOTE: Results based on 4.0 in. (100 mm) cube specimens.

Table 4.86: Compressive Strength Results for Batch AC7

Specimen No.	Age days	f_c ksi (MPa)	Average ksi (MPa)	Std. Dev. ksi (MPa)
1	4	14.0 (96.3)		
2	4	14.6 (101)	14.3 (99)	0.455 (3.14)
3	5	15.7 (108)		
4	5	14.3 (98.8)	15.0 (103)	0.945 (6.51)
5	6	14.9 (103)		
6	6	16.8 (116)	15.9 (109)	1.35 (9.30)
7	7	16.9 (116)		
8	7	17.3 (119)	17.1 (118)	0.301 (2.08)
	Average	15.6 (107)		
	Std. Dev.	1.30 (8.95)		

NOTE: Results based on 4.0 in. (100 mm) cube specimens.

Table 4.87: Modulus of Rupture Results for Batch AC7

Specimen No.	Age days	f_r psi (MPa)	Average psi (MPa)	Std. Dev. psi (MPa)
1	4	580 (4.00)		
2	4	609 (4.20)	594 (4.10)	20.3 (0.140)
3	5	596 (4.11)		
4	5	625 (4.31)	611 (4.21)	20.3 (0.140)
5	6	650 (4.48)		
6	6	667 (4.60)	658 (4.54)	11.9 (0.082)
7	7	684 (4.72)		
8	7	634 (4.37)	659 (4.55)	35.4 (0.244)
	Average	631 (4.35)		
	Std. Dev.	35.6 (0.245)		

NOTE: Results based on 4.0 x 8.0 in. (102 x 203 mm) cylinder specimens.

4.2.5.7.8 Batch AC8

Table 4.88: Unit Weight Results for Batch AC8

Specimen No.	Age days	Weight lb (kg)	w_c lb/ft^3 (kg/m^3)	Average lb/ft^3 (kg/m^3)	Std. Dev. lb/ft^3 (kg/m^3)
1	4	5.40 (2.45)	153.0 (2451)		
2	4	5.40 (2.45)	152.8 (2448)	152.9 (2449)	0.160 (2.57)
3	5	5.29 (2.40)	149.9 (2400)		
4	5	5.32 (2.41)	150.8 (2415)	150.3 (2408)	0.641 (10.3)
5	6	5.30 (2.40)	150.0 (2402)		
6	6	5.33 (2.42)	150.8 (2416)	150.4 (2409)	0.601 (9.62)
7	7	5.27 (2.39)	149.3 (2392)		
8	7	5.31 (2.41)	150.4 (2409)	149.9 (2401)	0.761 (12.2)
	Average	5.33 (2.42)	150.9 (2417)		
	Std. Dev.	0.048 (0.022)	1.35 (21.6)		

NOTE: Results based on 4.0 in. (100 mm) cube specimens.

Table 4.89: Compressive Strength Results for Batch AC8

Specimen No.	Age days	f_c ksi (MPa)	Average ksi (MPa)	Std. Dev. ksi (MPa)
1	4	14.7 (102)		
2	4	14.8 (102)	14.8 (102)	0.026 (0.180)
3	5	15.2 (104)		
4	5	16.5 (114)	15.8 (109)	0.933 (6.44)
5	6	16.5 (114)		
6	6	16.9 (116)	16.7 (115)	0.262 (1.80)
7	7	18.8 (130)		
8	7	17.3 (119)	18.0 (124)	1.12 (7.70)
	Average	16.3 (113)		
	Std. Dev.	1.40 (9.68)		

NOTE: Results based on 4.0 in. (100 mm) cube specimens.

Table 4.90: Modulus of Rupture Results for Batch AC8

Specimen No.	Age days	f_r psi (MPa)	Average psi (MPa)	Std. Dev. psi (MPa)
1	4	550 (3.79)		
2	4	639 (4.40)	594 (4.10)	62.8 (0.433)
3	5	519 (3.58)		
4	5	594 (4.09)	556 (3.84)	53.0 (0.366)
5	6	675 (4.65)		
6	6	649 (4.48)	662 (4.57)	18.1 (0.125)
7	7	681 (4.70)		
8	7	690 (4.76)	686 (4.73)	6.19 (0.043)
	Average	625 (4.31)		
	Std. Dev.	63.9 (0.440)		

NOTE: Results based on 4.0 x 8.0 in. (102 x 203 mm) cylinder specimens.

4.2.5.7.9 Batch AC9

Table 4.91: Unit Weight Results for Batch AC9

Specimen No.	Age days	Weight lb (kg)	w_c lb/ft^3 (kg/m^3)	Average lb/ft^3 (kg/m^3)	Std. Dev. lb/ft^3 (kg/m^3)
1	7	5.39 (2.44)	152.6 (2445)		
2	7	5.36 (2.43)	151.8 (2432)	152.2 (2439)	0.561 (8.98)
3	42	5.30 (2.40)	150.0 (2402)		
4	42	5.32 (2.41)	150.7 (2414)	150.3 (2408)	0.521 (8.34)
5	84	5.30 (2.40)	150.0 (2402)		
6	84	5.25 (2.38)	148.8 (2383)	149.4 (2393)	0.841 (13.5)
7	112	5.30 (2.40)	150.0 (2402)		
8	112	5.33 (2.42)	150.9 (2417)	150.4 (2409)	0.641 (10.3)
9	168	5.33 (2.42)	150.8 (2416)		
10	168	5.29 (2.40)	149.9 (2401)	150.4 (2409)	0.641 (10.3)
11	365	5.25 (2.38)	148.7 (2381)		
12	365	5.28 (2.40)	149.6 (2397)	149.1 (2389)	0.681 (10.9)
	Average	5.31 (2.41)	150.3 (2408)		
	Std. Dev.	0.041 (0.018)	1.15 (18.4)		

NOTE: Results based on 4.0 in. (100 mm) cube specimens.

Table 4.92: Compressive Strength Results for Batch AC9

Specimen No.	Age days	f_c ksi (MPa)	Average ksi (MPa)	Std. Dev. ksi (MPa)
1	7	17.1 (118)		
2	7	17.7 (122)	17.4 (120)	0.467 (3.22)
3	42	19.7 (136)		
4	42	21.0 (145)	20.3 (140)	0.892 (6.15)
5	84	20.5 (141)		
6	84	19.2 (132)	19.8 (137)	0.882 (6.08)
7	112	20.5 (141)		
8	112	19.8 (137)	20.1 (139)	0.430 (2.96)
9	168	20.3 (140)		
10	168	20.7 (143)	20.5 (141)	0.319 (2.20)
11	365	19.8 (137)		
12	365	21.2 (146)	20.5 (141)	0.991 (6.84)
	Average	19.8 (136)		
	Std. Dev.	1.26 (8.69)		

NOTE: Results based on 4.0 in. (100 mm) cube specimens.

Table 4.93: Modulus of Elasticity Results for Batch AC9

Specimen No.	Age days	E_c ksi (GPa)	Average ksi (GPa)	Std. Dev. ksi (GPa)
1	7	5584 (39)		
2	7	5295 (37)	5440 (37.5)	205 (1.41)
3	42	6391 (44)		
4	42	6245 (43)	6318 (43.6)	103 (0.709)
5	84	7156 (49)		
6	84	5940 (41)	6548 (45.1)	860 (5.93)
7	112	7460 (51)		
8	112	6104 (42)	6782 (46.8)	959 (6.61)
9	168	5629 (39)		
10	168	6039 (42)	5834 (40.2)	289 (2.00)
11	365	5994 (41)		
12	365	6056 (42)	6025 (41.5)	44 (0.30)
	Average	6158 (42)		
	Std. Dev.	619 (4.27)		

NOTE: Results based on 4.0 x 8.0 in. (102 x 203 mm) cylinder specimens.

4.2.5.7.10 Batch AC10

Table 4.94: Unit Weight Results for Batch AC10

Specimen No.	Age days	Weight lb (kg)	w_c lb/ft^3 (kg/m^3)	Average lb/ft^3 (kg/m^3)	Std. Dev. lb/ft^3 (kg/m^3)
1	7	5.36 (2.43)	151.7 (2429)		
2	7	5.27 (2.39)	149.2 (2390)	150.4 (2410)	1.72 (27.6)
3	14	5.37 (2.44)	152.2 (2438)		
4	14	5.31 (2.41)	150.5 (2410)	151.3 (2424)	1.20 (19.2)
5	21	5.30 (2.40)	150.0 (2403)		
6	21	5.35 (2.42)	151.4 (2425)	150.7 (2414)	0.961 (15.4)
7	28	5.31 (2.41)	150.5 (2410)		
8	28	5.37 (2.44)	152.2 (2438)	151.3 (2424)	1.20 (19.2)
9	56	5.30 (2.40)	150.0 (2402)		
10	56	5.27 (2.39)	149.3 (2391)	149.6 (2397)	0.481 (7.70)
11	365	5.32 (2.41)	150.6 (2412)		
12	365	5.30 (2.40)	150.1 (2405)	150.4 (2409)	0.320 (5.13)
	Average	5.32 (2.41)	150.6 (2413)		
	Std. Dev.	0.036 (0.016)	1.01 (16.2)		

NOTE: Results based on 4.0 in. (100 mm) cube specimens.

Table 4.95: Compressive Strength Results for Batch AC10

Specimen No.	Age days	f_c ksi (MPa)	Average ksi (MPa)	Std. Dev. ksi (MPa)
1	7	16.9 (117)		
2	7	17.7 (122)	17.3 (119)	0.552 (3.80)
3	14	18.3 (126)		
4	14	16.8 (116)	17.5 (121)	1.03 (7.12)
5	21	18.3 (126)		
6	21	18.7 (129)	18.5 (127)	0.308 (2.12)
7	28	19.6 (135)		
8	28	19.7 (136)	19.6 (135)	0.113 (0.780)
9	56	18.6 (128)		
10	56	18.0 (124)	18.3 (126)	0.431 (2.97)
11	365	22.5 (155)		
12	365	21.5 (148)	22.0 (152)	0.719 (4.96)
	Average	18.9 (130)		
	Std. Dev.	1.72 (11.9)		

NOTE: Results based on 4.0 in. (100 mm) cube specimens.

Table 4.96: Modulus of Elasticity Results for Batch AC10

Specimen No.	Age days	E_c ksi (GPa)	Average ksi (GPa)	Std. Dev. ksi (GPa)
1	7	5739 (40)		
2	7	4911 (34)	5325 (36.7)	585 (4.04)
3	14	4997 (34)		
4	14	5355 (37)	5176 (35.7)	253 (1.75)
5	21	5493 (38)		
6	21	5490 (38)	5492 (37.9)	1.91 (0.013)
7	28	5559 (38)		
8	28	6790 (47)	6175 (42.6)	871 (6.00)
9	56	5850 (40)		
10	56	6054 (42)	5952 (41.0)	144 (0.995)
11	365	5909 (41)		
12	365	6441 (44)	6175 (42.6)	376 (2.59)
	Average	5716 (39)		
	Std. Dev.	545 (3.76)		

NOTE: Results based on 4.0 x 8.0 in. (102 x 203 mm) cylinder specimens.

4.2.6 Comparison of Results and Property Interactions

The following subsections present comparisons of the results for thermal (TC) and ambient (AC) curing regimens, analysis of the interactions between compressive strength and the other measured material properties, and evaluation of the curing regimens.

4.2.6.1 Compressive Strength

Time-dependent compressive strength (f_c) data for TC and AC regimens are compared in Figure 4.30 and Figure 4.31. All samples tested are represented by a single circular marker in Figure 4.30, with TC specimens indicated in black, and AC specimens indicated in gray. In Figure 4.31, the average compressive strength for each test day (based on specimen age at testing) is presented and includes error bars representing the standard deviation of the data. It should be noted that samples were tested for all batches at the 7-day reference age, and sample sizes tends to decrease with age [see Table 4.14 (Section 4.2.4.3) and Table 4.63 (Section 4.2.5.3)].

Results indicate TC specimens typically developed approximately 90% of their 7-day strength within the first 48 hours after casting, after only 24 hours of elevated thermal curing. Achieving a 7-day average compressive strength of 20.8 ksi (143 MPa), compressive strengths for TC specimens remained relatively constant with increasing age. In contrast, strength gain for AC specimens was much more gradual. Producing an average 7-day compressive strength of 16.1 ksi (111 MPa), strengths continued to increase through the first month and up to the first year after casting. For all specimens tested at a minimum age of 28 days, the average compressive strength for AC specimens was 19.7 ksi (136 MPa), approximately 94% of the comparative average for thermal cured specimens of 21.0 ksi (145 MPa).

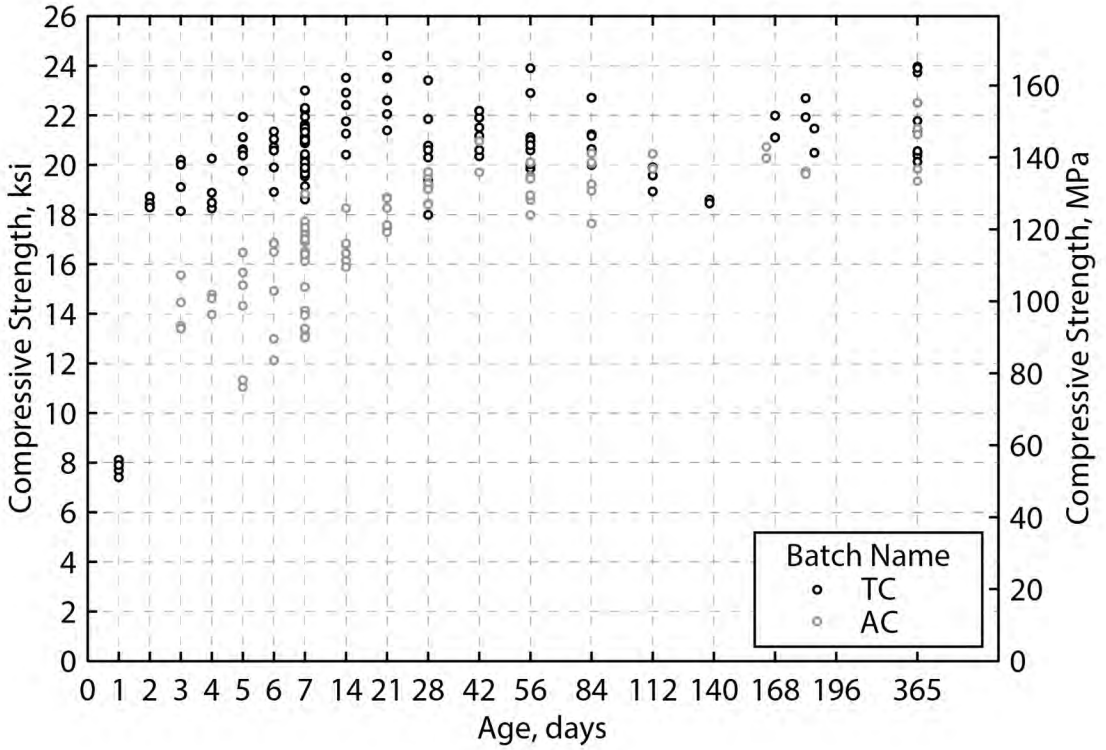


Figure 4.30: Comparison of compressive strength results from 4.0 in (100 mm) UHPC cube specimens for thermal and ambient curing regimens.

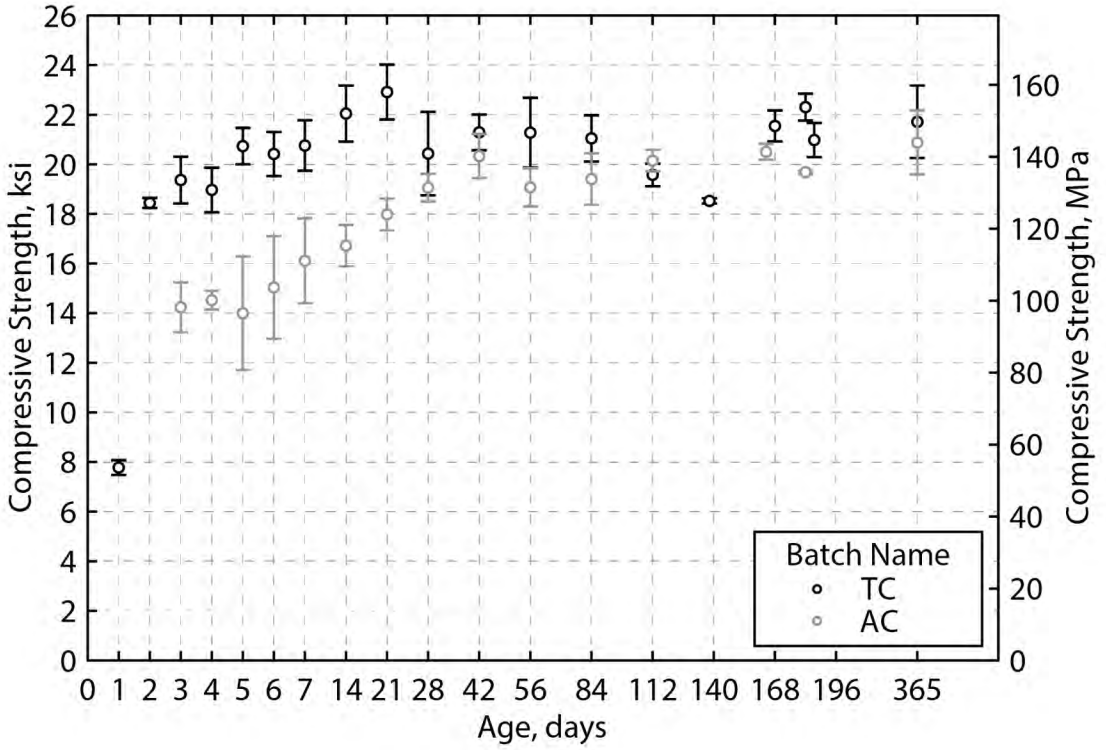


Figure 4.31: Average compressive strengths from 4.0 in (100 mm) UHPC cube specimens for thermal and ambient curing regimens.

4.2.6.1.1 Initial Set Data

Because the effects of high HRWRA content for UHPC mixture proportions are known to retard initial setting times, a previous study by Giesler (2014) was conducted using nearly identical mixture proportions to those presented in Table 4.13 (Section 4.2.1) and the thermal curing regimen shown in Figure 4.4 (Section 4.2.4.1), the results of which are provided in Figure 4.32 and Figure 4.33.

Cubes were demolded beginning a few hours after casting, though specimens readily bulged and did not remain intact until after approximately 13 hours. Initial set of the UHPC specimens was identified to consistently occur at approximately 14 hours following casting (Giesler, 2014). Two specimens were tested every hour from 14 to 24 hours after casting to capture the rapid initial strength gain before initiation of thermal treatment. As seen in Figure 4.32, a linear trend was quickly developed, and compressive strength gains followed this progression through approximately the first 40 hours (Giesler, 2014). After beginning thermal treatment, two specimens were tested at 24-hour increments through the remainder of the 7-day curing regimen.

Comparing results from the current study for specimens produced with the thermal curing regimen exhibited development of early-age compressive strength consistent with the results of Giesler (2014). The results of both studies are provided for the 7-day thermal curing regimen in Figure 4.34, with the results from Giesler (2014) presented in gray as batch IS, and the results of thermal curing specimens tested for this research (see also Figure 4.11) shown as a single dataset in black as batch TC. For the 7-day reference age strength, average compressive strength for all initial set batches was 21.6 ksi (149 MPa) (Giesler, 2014), which compares well to the 7-day average compressive strength of 20.8 ksi (143 MPa) for TC batches (see Table 4.14). Combining the results of the two studies increases the early-age compressive strength gain dataset for the unique UHPC mixture proportions, helps to fill gaps in the strength gain development curve, and increases confidence in the results for thermal cured specimens.

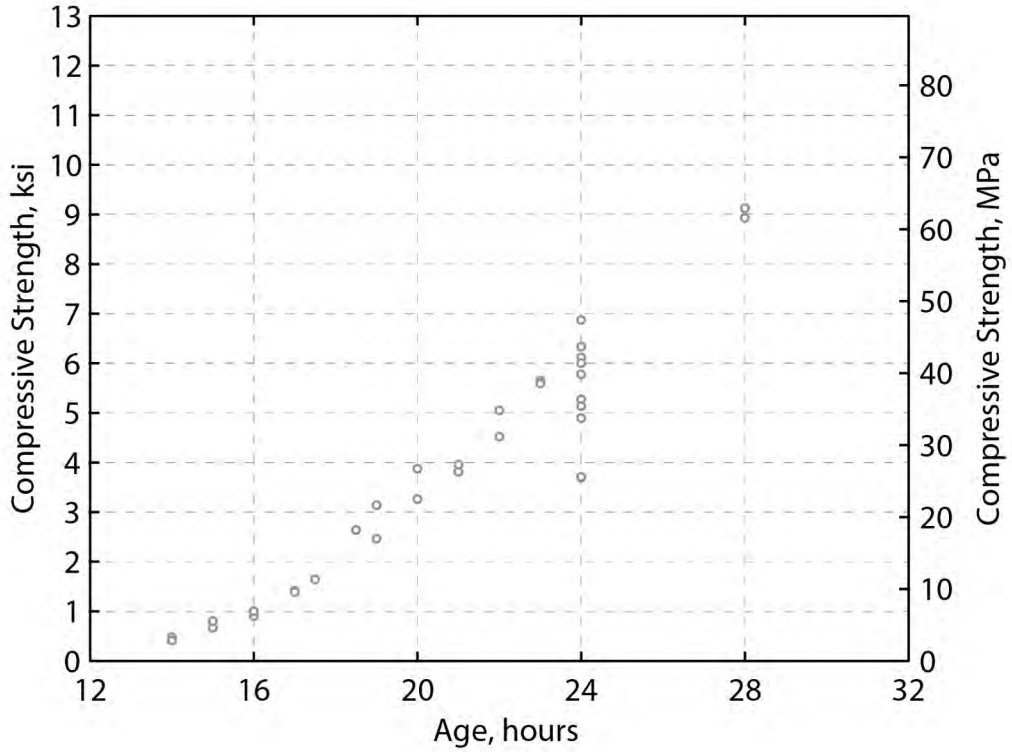


Figure 4.32: Compressive strength gain of thermal cured 4.0 in (100 mm) UHPC cube specimens during initial 24 hours after casting from Giesler (2014) initial set study.

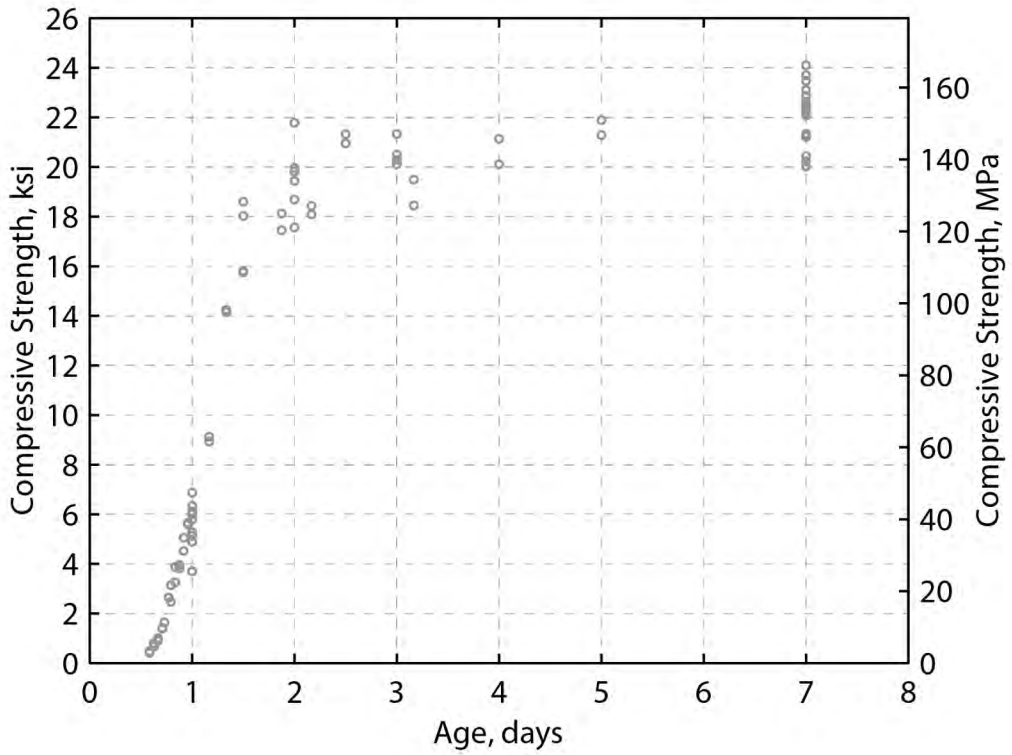


Figure 4.33: Compressive strength gain of thermal cured 4.0 in (100 mm) UHPC cube specimens during the 7-day thermal curing regimen from Giesler (2014) initial set study.

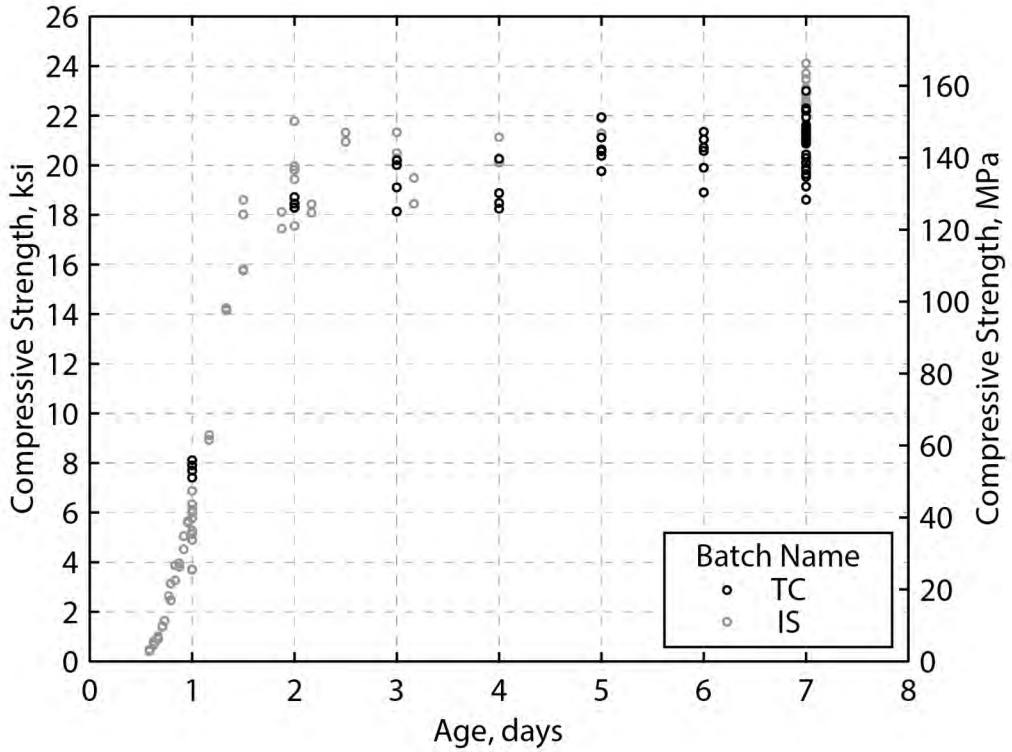


Figure 4.34: Combined results for compressive strength gain of 4.0 in (100 mm) UHPC cube specimens from Giesler (2014) initial set study and TC specimens.

4.2.6.2 Unit Weight

In reference to Table 4.15 (Section 4.2.4.4) and Table 4.64 (Section 4.2.5.4), results for unit weight (w_c) as evaluated by 4.0 in. (100 mm) cube specimens were relatively similar for both TC and AC specimens. The results show that the unit weight of this UHPC ranged between approximately 145 lb/ft^3 (2323 kg/m^3) to 153 lb/ft^3 (2453 kg/m^3), regardless of specimen age at testing or curing regimen used for production. The average unit weight for all batches produced using the thermal and ambient curing regimens were nearly equal at 149.8 lb/ft^3 (2399 kg/m^3) and 150.1 lb/ft^3 (2405 kg/m^3), respectively. Additionally, the interaction between compressive strength and unit weight, plotted for all TC and AC specimens in Figure 4.35, which includes Equation 4.1 representing the AASHTO equation for unit weight previously discussed in Section 4.2.3.2. The general trend of exhibits consistent behavior across the combined results. The data seems to slightly increase in unit weight with increasing compressive strength, though samples tested at 24 hours with strengths below 10.0 ksi (69.0 MPa) fall almost directly in the middle of this range. With respect to Equation 4.1, valid for compressive strengths between 5.0 ksi (34.5 MPa) and 15.0 ksi (103.4 MPa), the unit weight of this UHPC consistently falls below the predicted value for strengths above the applicable range. Based on the results, it would be reasonable to estimate the unit weight of this UHPC as 155 lb/ft^3 (2483 kg/m^3), regardless of concrete age or curing regimen, and conservatively increased to 160 lb/ft^3 (2563 kg/m^3) when accounting for steel reinforcement.

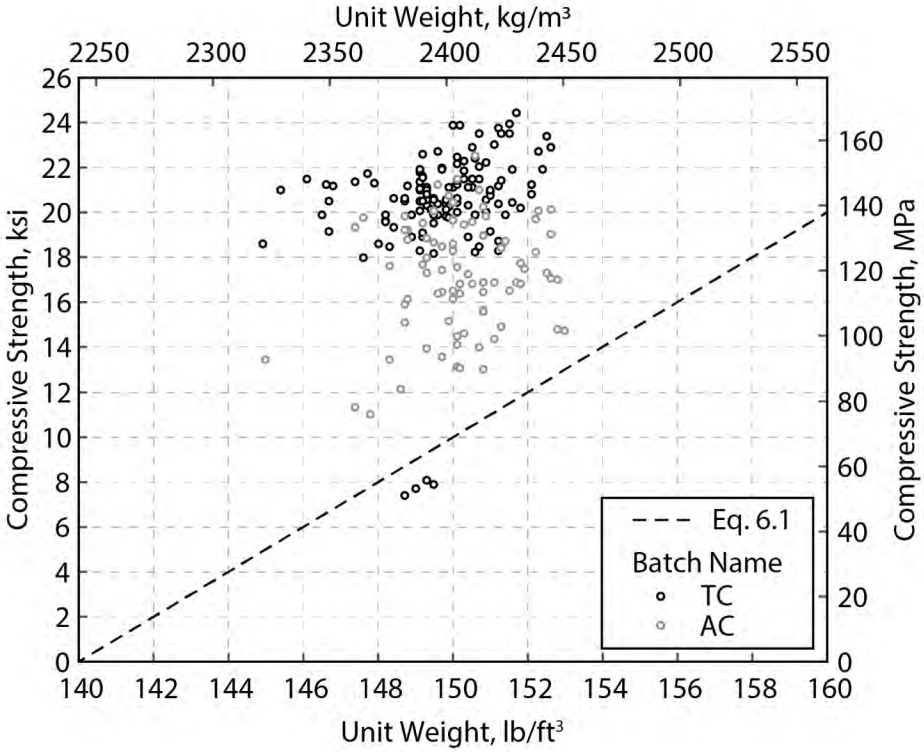


Figure 4.35: Compressive strength versus unit weight for 4.0 in. (100 mm) UHPC cube specimens for thermal and ambient curing regimens.

4.2.6.3 Modulus of Rupture

Time-dependent modulus of rupture (f_r) data for TC and AC regimens are compared in Figure 4.36 and Figure 4.37. All samples tested are represented by a single circular marker in Figure 4.36, with TC specimens indicated in black, and AC specimens indicated in gray. In Figure 4.37, the average modulus of rupture for each test day (based on specimen age at testing) is presented and includes error bars representing the standard deviation of the data. It should be noted that specimens were tested for all batches at the 7-day reference age, and sample sizes tends to decrease with age [see Table 4.16 (Section 4.2.4.5) and Table 4.65 (Section 4.2.5.5)].

Results provide average 7-day modulus of rupture strengths of 1203 psi (8.30 MPa) for TC specimens and 656 psi (4.52 MPa) for AC specimens, and observed trends are similar to those for compressive strength. Modulus of rupture developed quickly after initiation of elevated thermal curing for TC specimens, achieving approximately 90% of 7-day strength after 48 to 72 hours after casting then remaining relatively constant with increasing age. Observed strengths for AC specimens were significantly lower than strengths for TC specimens and strength gain was much more gradual and continued to increase with age up to a year after casting, with average modulus of rupture strengths surpassing 900 psi (6.21 MPa).

Figure 4.38 illustrates the interaction between modulus of rupture and compressive strength. TC and AC datasets are plotted and compared to Equation 4.2 and Equation 4.3 that calculate modulus of rupture as a function of compressive strength. Discussed in Section i.iii, Equation 4.2 (AASHTO, 2017) is valid for compressive strengths between 5.0 ksi (34.5 MPa) and 15.0 ksi (103.4 MPa), and Equation 4.3 was developed based on extensive testing of a commercial UHPC (Graybeal, 2006b) and is displayed using the linear multiplier, x, equal to 7.8 for thermally treated UHPC and 6.7 for untreated UHPC.

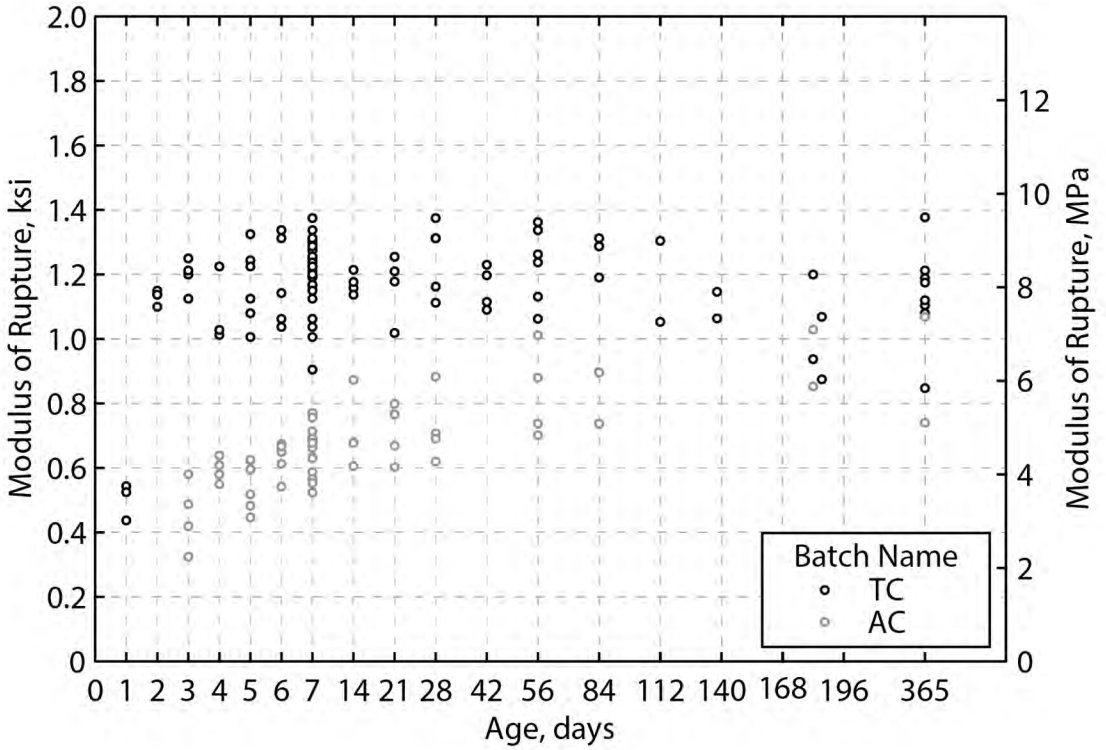


Figure 4.36: Comparison of modulus of rupture strength gain of UHPC prism specimens for thermal and ambient curing regimens.

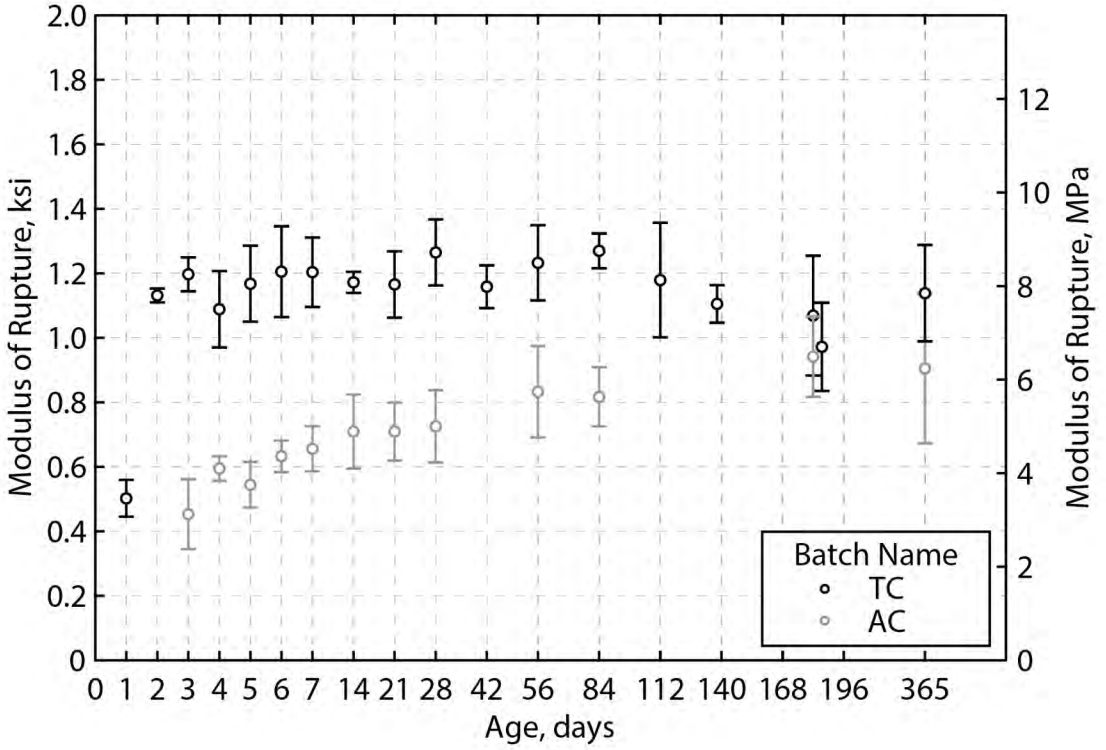


Figure 4.37: Average modulus of rupture strength of UHPC prism specimens for thermal and ambient curing regimens.

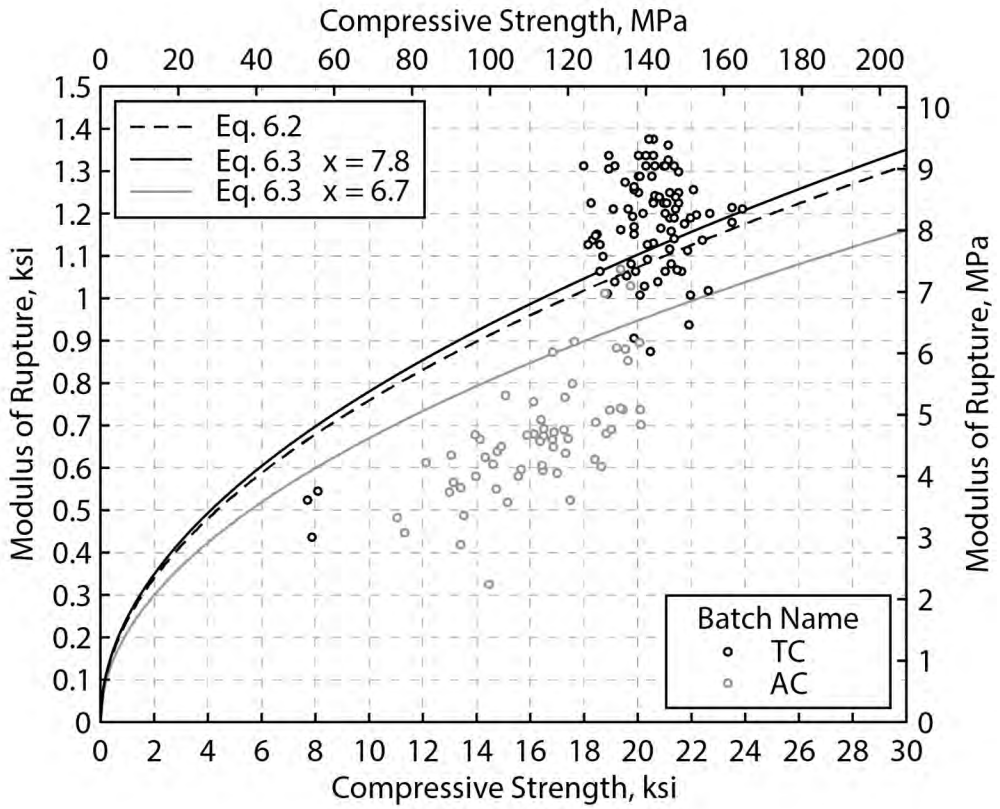


Figure 4.38: UHPC modulus of rupture versus compressive strength for thermal and ambient curing regimens.

Although no definite trend is apparent for TC specimens, both equations provide a reasonable prediction of modulus of rupture for compressive strengths above 17 ksi (120 MPa), but overestimate modulus of rupture for compressive strengths below this threshold. Additional early-age testing of specimens at lower compressive strength would be required to further evaluate the accuracy of the equations, though it is noted that TC specimens only fell in this range within the first 48 hours after casting. In contrast, results for AC specimens exhibited a definite trend of increasing modulus of rupture with increasing compressive strength, and values consistently fell below the curves provided by Equation 4.2 and Equation 4.3 with x = 6.7 for untreated UHPC.

4.2.6.4 Modulus of Elasticity

Time-dependent modulus of elasticity data for TC and AC regimens are compared in Figure 4.39 and Figure 4.40. All samples tested are represented by a single circular marker in Figure 4.39, with TC specimens indicated in black, and AC specimens indicated in gray. In Figure 4.40, the average modulus of elasticity for each test day (based on specimen age at testing) is presented and includes error bars representing the standard deviation of the data. It should be noted that samples were tested for all batches at the 7-day reference age, and sample sizes tends to decrease with age [see Table 4.17 (Section 4.2.4.6) and Table 4.66 (Section 4.2.5.6)].

Noting that sample set sizes were very small, results show the modulus of elasticity remains consistent for TC specimens with only small increases in strength with increasing age. At 168 days after casting, average modulus of elasticity for TC specimens is within 10% of the 7-day strength. As with the other measured properties, strength gain of AC specimens was gradual, and strengths continued to increase until approximately 28 days after casting. Unlike the other properties, modulus of elasticity did not significantly differ between TC and AC specimens. At seven days, average modulus of elasticity for AC specimens was approximately 90% of the TC average. Moreover, the overall average modulus of elasticity for TC specimens of 5995 ksi (41.3 GPa) as nearly identical to the AC overall average of 5936 ksi (40.9 GPa). These results indicate that elevated thermal curing is not critical to development of early-age modulus of elasticity, though a much larger sample size is necessary to qualify any conclusions.

Figure 4.41 illustrates the interaction between modulus of elasticity and compressive strength. TC and AC datasets are plotted and compared to Equation 4.4 through Equation 4.8 that calculate modulus of elasticity as a function of compressive strength and were developed based on NSCs, HSCs, and commercial UHPC (see discussion in Section 4.2.3.4).

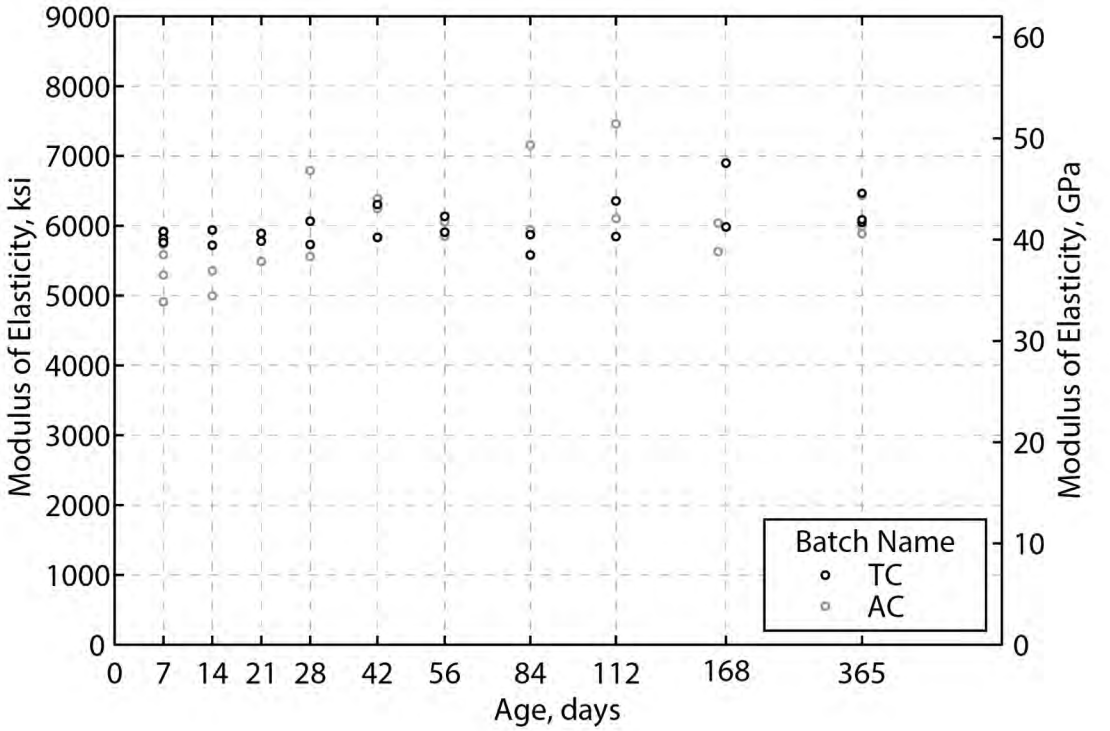


Figure 4.39: Comparison of modulus of elasticity strength gain of UHPC cylinder specimens for thermal and ambient curing regimens.

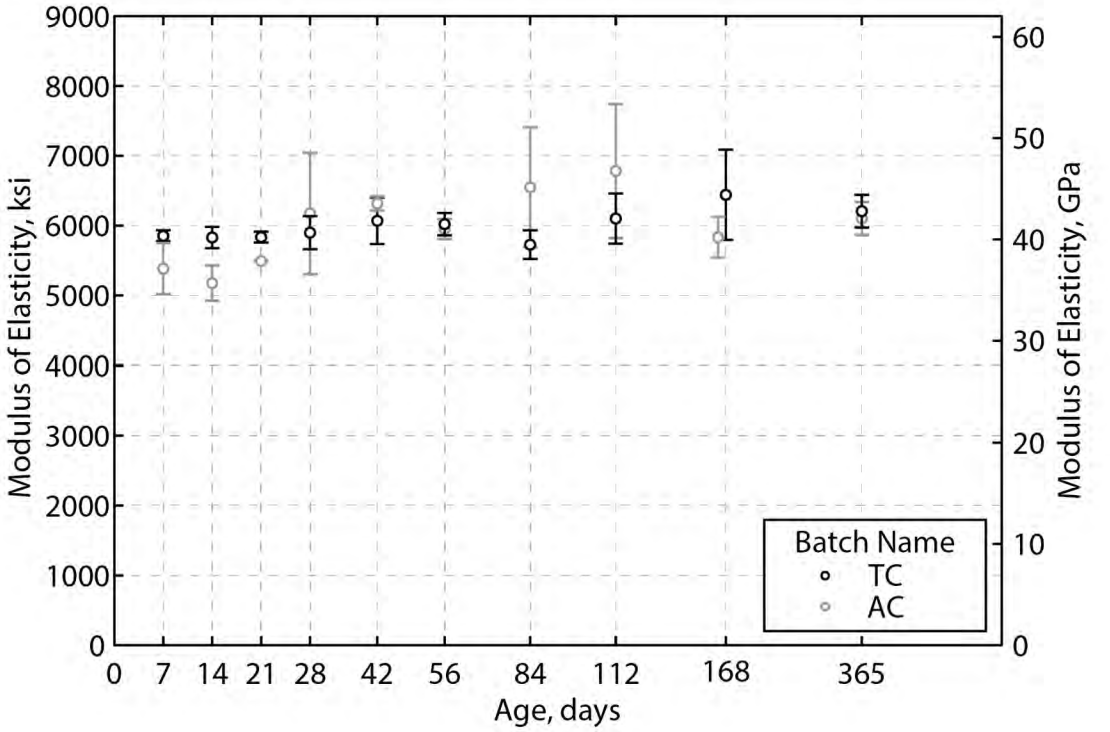


Figure 4.40: Average modulus of elasticity strength of UHPC cylinder specimens for thermal and ambient curing regimens.

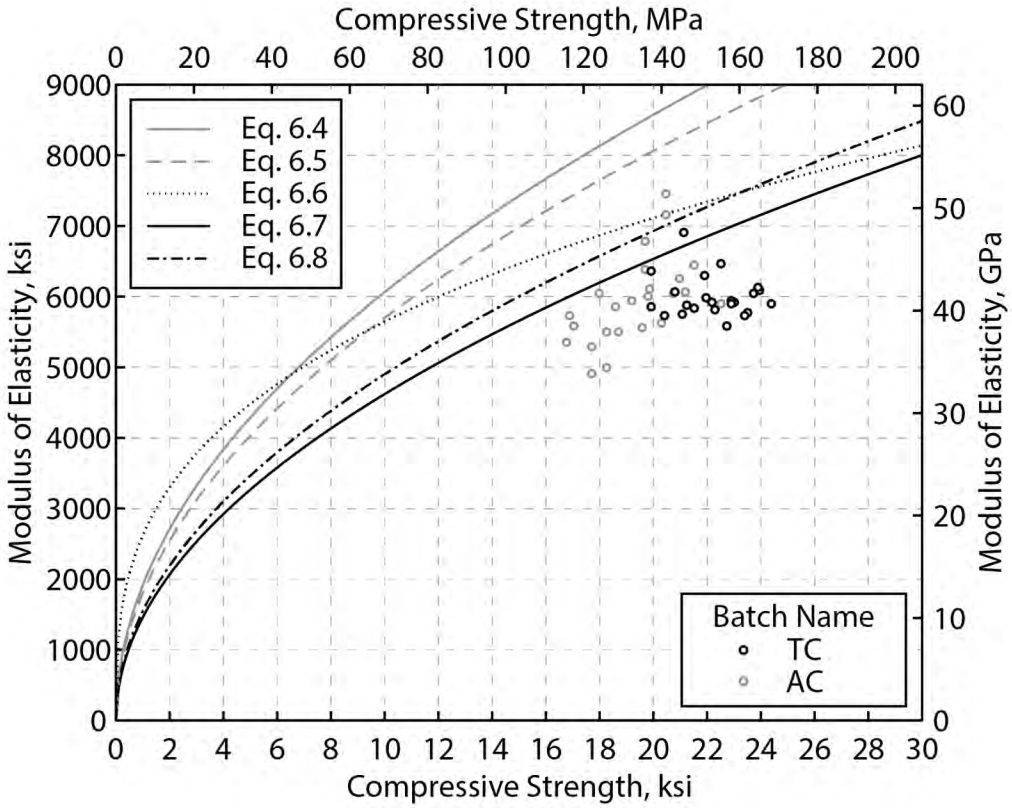
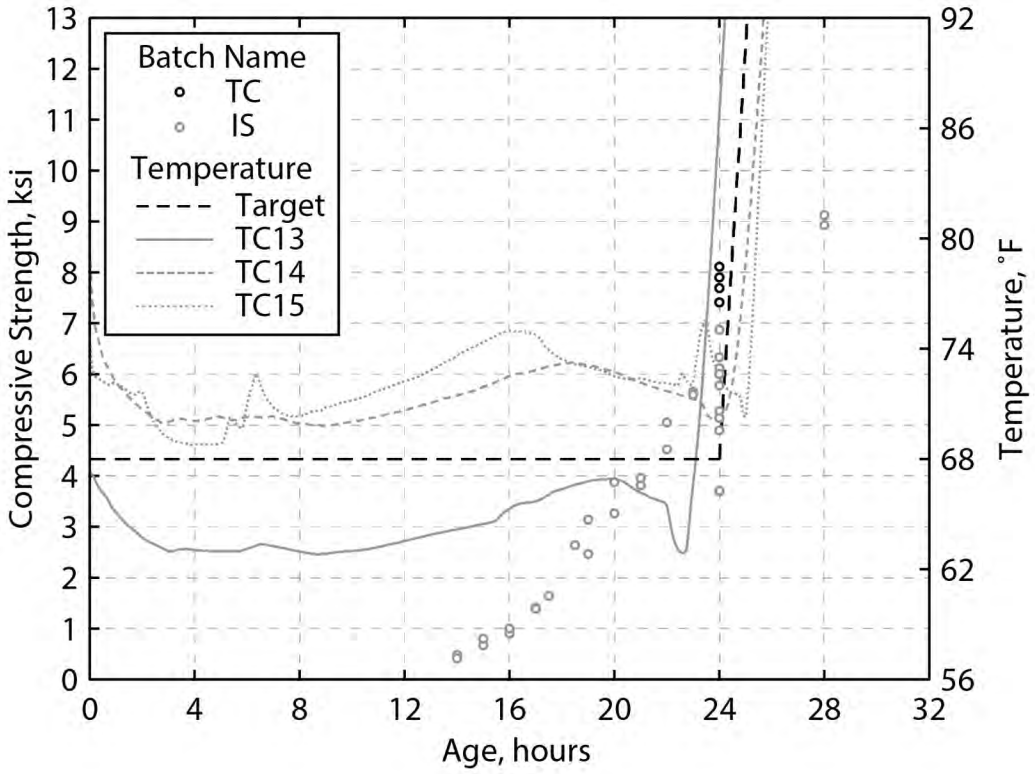


Figure 4.41: UHPC modulus of elasticity versus compressive strength for thermal and ambient curing regimens.

Like the interaction between modulus of rupture and compressive strength (Figure 4.38), the data in Figure 4.41 indicates a trend of increasing modulus of elasticity corresponding to increasing compressive strength for AC specimens, while no discernable trend is identified for TC specimens. The equations from literature clearly overestimate the modulus of elasticity for the UHPC developed with local materials for both thermal and ambient curing, which is likely due to varying constituent materials, not least of which the type and content of fiber reinforcement. The closest approximation is provided by Equation **Error! Reference source not found.** (Graybeal, 2006b), though additional data and analysis is required to determine a more accurate representation of this behavior and, if necessary, to develop a new equation for this unique UHPC.

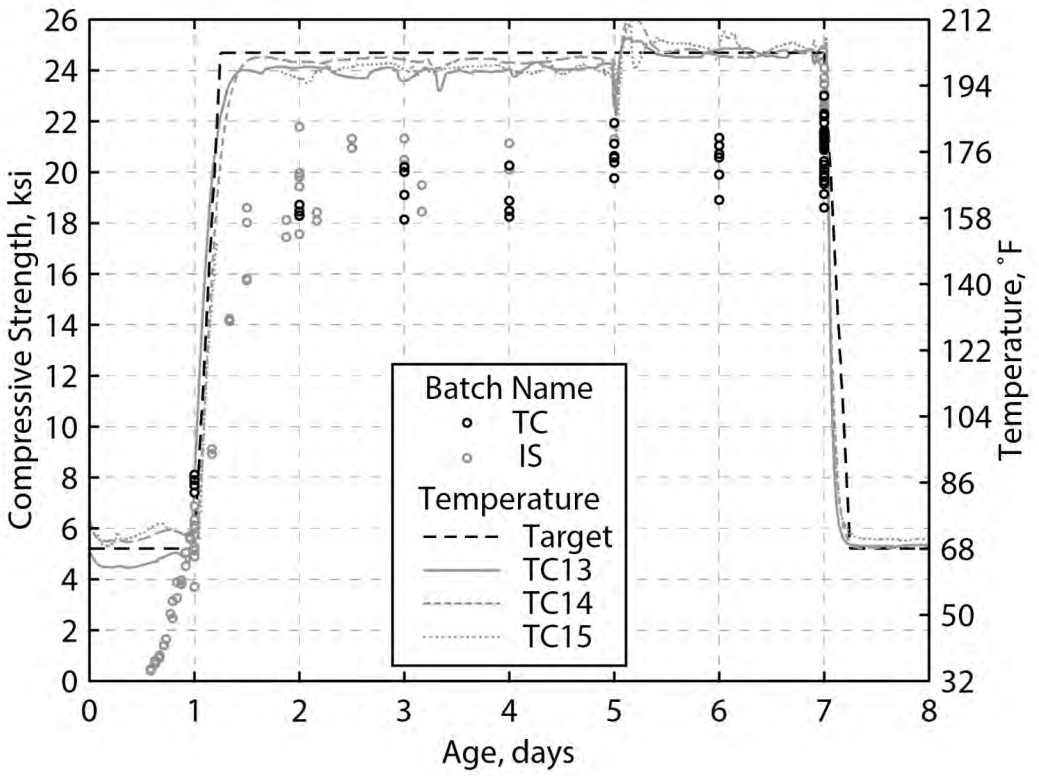
4.2.6.5 Evaluation of Curing Regimens

The results of early-age compressive strength development can be used to evaluate the curing regimens used for this study. The combined results of the initial set study conducted by Giesler (2014) and results of thermal cured specimens are plotted during the initial 24 hours after casting (Figure 4.42) and the full 7-day thermal curing regimen (Figure 4.43) overlaying the curing temperatures captured by thermocouples embedded in cube specimens (see also Section 4.2.4.2). Compressive strengths for AC specimens are similarly plotted overlaying the curing temperatures captured by thermocouples embedded in cube specimens (see also Section 4.2.5.2) during the 7-day ambient curing regimen (Figure 4.44).



1.0 ksi = 6.895 MPa $\qquad$ T(°C) = [T(°F) – 32] ÷ 1.8

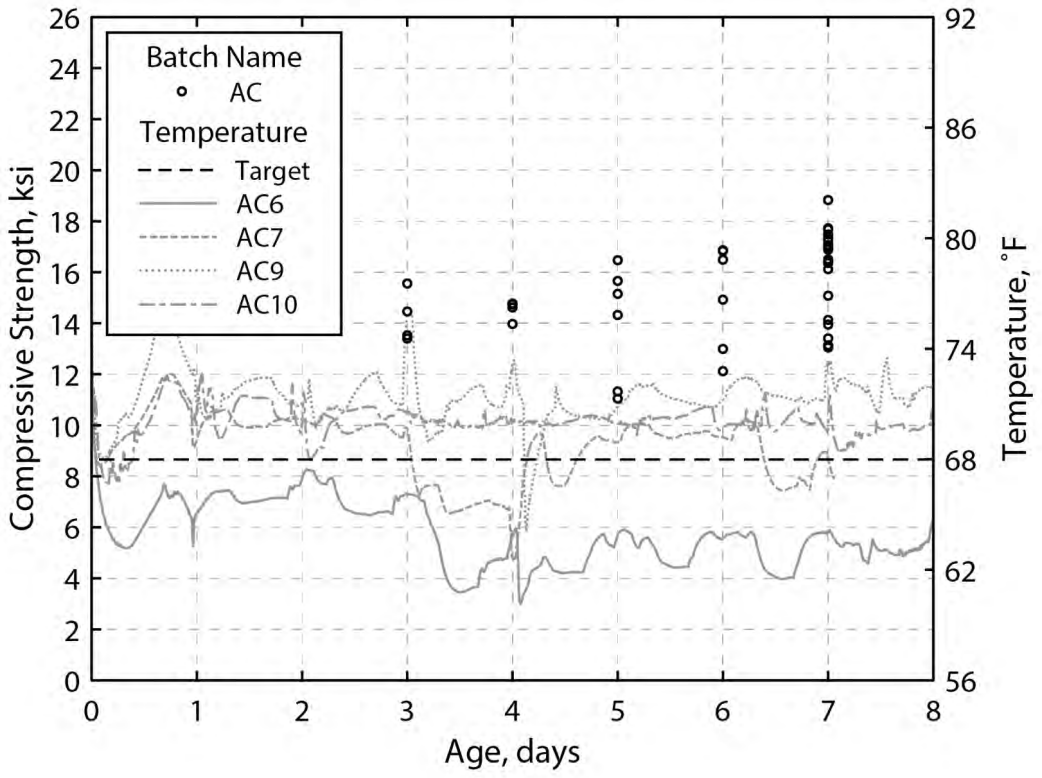
Figure 4.42: Combined results for compressive strength gain of 4.0 in (100 mm) UHPC cube specimens from Giesler (2014) initial set study and TC specimens versus core temperatures during initial 24 hours after casting.



1.0 ksi = 6.895 MPa $T(°C) = [T(°F) - 32] \div 1.8$

Figure 4.43: Combined results for compressive strength gain of 4.0 in (100 mm) UHPC cube specimens from Giesler (2014) initial set study and TC specimens versus core temperatures during 7-day thermal curing regimen.

It is clear from the combined results in Figure 4.42 that initial set identified by Giesler (2014) at approximately 14 hours after casting followed initiation of the internal hydration reaction that consistently began between 8 to 10 hours after casting, evident by the rising core temperatures of each specimen monitored. Rapid early-age strength gain was then exhibited with initiation of elevated thermal curing at 24 hours after casting. Strength gain then slows as maximum curing temperatures are achieved and increases steadily through the remainder of the 7-day regimen. In the absence of elevated temperatures, early-age strength gain for AC specimens was more gradual and resulting in lower 7-day compressive strengths, but strengths continued to increase with age. However, these results are particularly important when evaluating the thermal curing regimen.



1.0 ksi = 6.895 MPa $\qquad$ T(°C) = [T(°F) – 32] ÷ 1.8

Figure 4.44: Compressive strength gain of 4.0 in (100 mm) UHPC cube specimens versus core temperatures during 7-day ambient curing regimen.

To further illustrate the effects of thermal curing on strength gain, the average compressive strength ($f_{c,avg}$) and modulus of rupture ($f_{r,avg}$) results for TC and AC specimens are plotted in Figure 4.45. In this figure, all results have been normalized to the 7-day average strengths for TC specimens, or approximately 21.0 ksi (145 MPa) for compressive strength and 1200 psi (8.30 MPa) for modulus of rupture. First, results show that for TC specimens, $f_{c,avg}$ (solid black line) and $f_{r,avg}$ (dashed black line) developed approximately 90% (or greater) of 7-day strengths by two days after casting and only 24 hours of elevated thermal curing. In contrast, $f_{c,avg}$ for AC specimens (solid gray line) required 28 days to develop 90% of 7-day TC strength, and $f_{r,avg}$ for AC specimens (dashed gray line) only manages to develop 75–80% of 7-day TC strength after more than six months after casting.

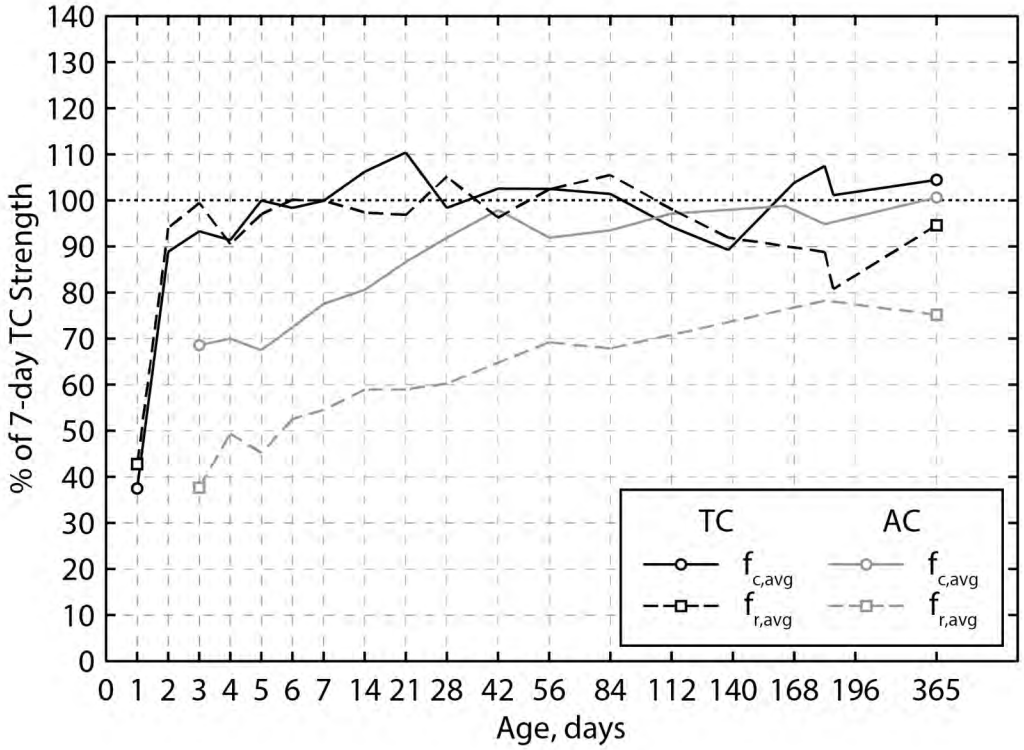


Figure 4.45: Average compressive strength and modulus of rupture results for TC and AC specimens normalized to 7-day target strengths.

The effects of thermal curing are clearly significant, both in terms of achieving high early strength gain, and for development of modulus of rupture in general. However, the significance of long-term strength gain of AC specimens and the fact that the target compressive strength for thermal cured specimens using these mixture proportion of 20 ksi (138 MPa) can be nearly achieved with ambient curing should not be understated. Coupled with the results of TC specimens, a case can be made for significant reduction of the thermal curing regimen. The combined results indicate that the thermal curing regimen may be reduced from four days of wet heat curing and two additional days of dry heat curing (see Figure 4.4) to as few as two or three days of wet heat curing. This would reduce the thermal curing regimen to a total length of three or four days from the time of casting.

Additional consideration for the thermal curing can be made based on the results of testing. With respect to Figure 4.42 and the consistent drop in core temperatures exhibited at approximately 20 hours after casting, it may be beneficial to initiate elevated thermal curing earlier than 24 hours. It should also be noted that TC specimens were generally placed in room temperature water to begin thermal curing at 24 hours. Pre-heating the water to maximum hydration temperatures [approximately 75°F (24°C) as presented in Figure 4.42] or greater and applying thermal treatment as soon as possible after initial set, perhaps at 16 or 18 hours after casting, would avoid the decrease in core temperatures during initial hydration, aid rapid early strength gain, and possibly facilitate further reduction of the curing regimen.

4.3 Chemical Analysis of UHPC

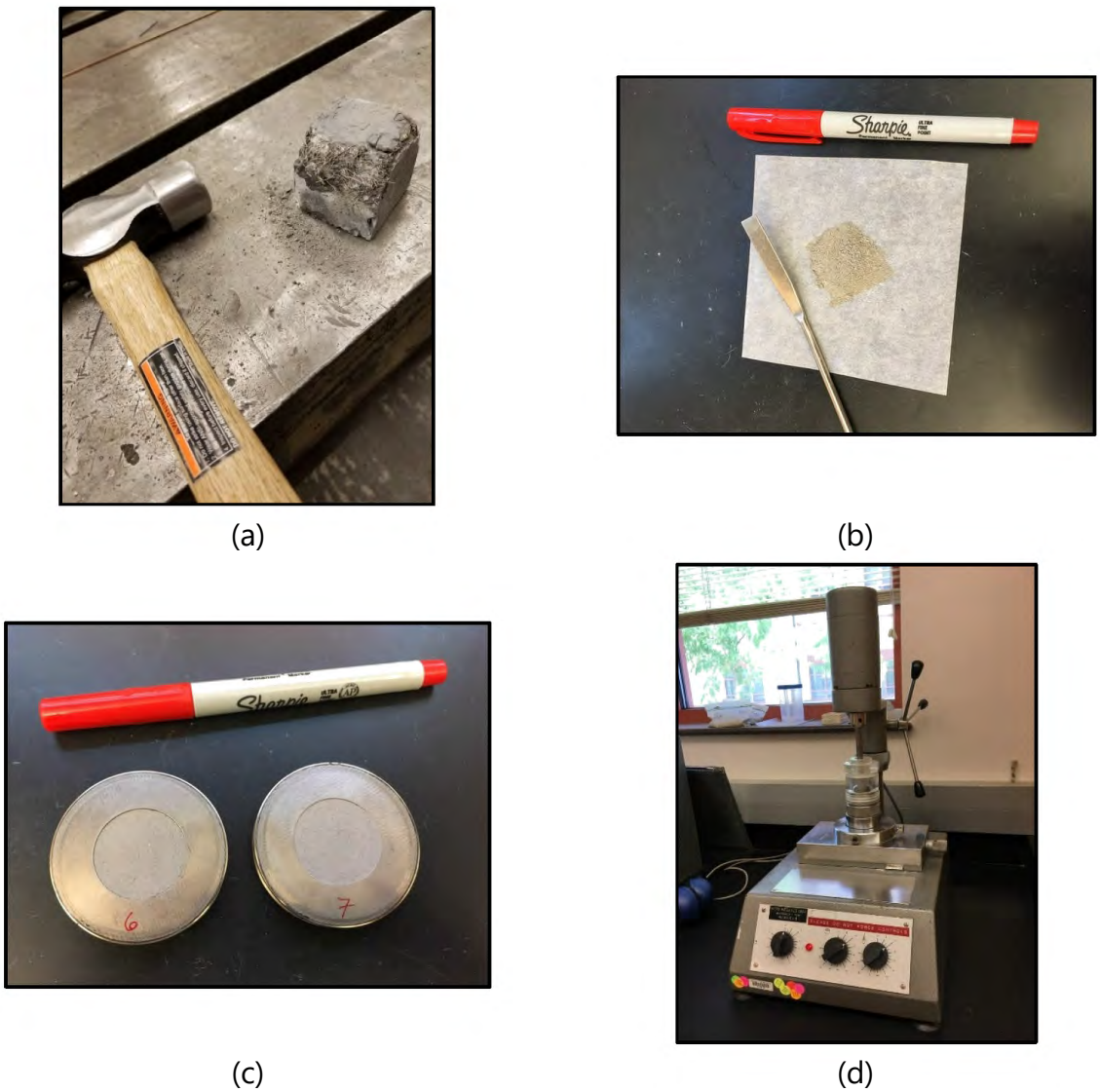
4.3.1 X-Ray Diffraction (XRD)

X-Ray Diffraction (XRD) has been considered a reliable method in detecting the amount of ettringite that may exist in a concrete sample. This testing was performed in cooperation with the New Mexico Bureau of Geology and Mineral Resources located in Socorro, New Mexico. XRD gives an analysis of solid materials and provides a qualitative and quantitative analyses of crystalline and mineral structures present in the sample. X-Rays are directed at the sample, and depending on the atomic structure of the sample, will diffract the rays in different directions. The
angles and strength of the beam's diffraction correlate directly to a specific substance.

To conduct the test, the sample must be ground into a talcum-powder like consistency. Typically, a hand grinder with a ceramic grinding wheel is used to grind NMSU developed UHPC, however for this test this method was considered too risky and inefficient to gather the test sample. For one, the grinding wheel degrades with use, and as the wheel slowly breaks apart on the grinding surface, some of the wheel may become present in the sample being collected. Additionally, the grinding wheel does allow for very finely ground samples, however most of the sample is typically lost to the surrounding air or blown out of the container used to collect the sample by the fans inside the grinder. To address these issues, the samples were instead hand ground using a hammer and steel roller. Two 2 in. (50 mm) cubes, 1 heat treated and 1 untreated, were selected. Table 7 shows the masses of the cubes before and after grinding, and the percent retained. 14.85 g (0.03 lb.) of the heat-treated sample and 14.43 g (0.03 lb.) of the untreated sample were used for BET testing, and the rest of the sample kept in a sealed plastic container.

Another important consideration with XRD is the steel fibers present in the ground samples. The fibers themselves were intact, having not been affected by the hand grinding. However, since the XRD's purpose is to identify possible ettringite crystals in the concrete and cement, thus the steel fibers were not necessary to be present, and,

according to the New Mexico Bureau of Geology and Mineral Resources, would show up in the results. The fibers were not necessarily detrimental but would serve as an unnecessary complexity to the testing. To simplify the results, a magnet was used to remove the majority of steel fibers from the sample. Finally, the sealed containers wrapped in bubble wrap and sent in a sealed package to the Bureau for processing and testing. Figure 4.46 shows the XRD test preparation steps.



(a) (b)

(c) (d)

Figure 4.46: XRD test preparation – (a) crushing and griding; (b) powder collection; (c) electronic mortal and pastel; (d) sample containment.

4.3.2 Brunauer, Emmett and Teller Testing Procedure

The Brunauer, Emmett and Teller (BET) testing theory utilizes gas adsorption to discern specific surface area, pore size, and pore volume of solids. These are critical pieces of information for this study considering the general notion that the more porous and permeable a concrete is, the more susceptible it is to sulfate attack and DEF. The BET theory is tested using an extended adsorption analyzer, model ASAP 2050 made by Micromeritics. The basic principle behind the extended adsorption analysis begins with a solid, in this case the ground UHPC sample, placed inside a test tube, in which a pure gas at a cryogenic temperature, in this case liquid nitrogen, is essentially pumped into. The gas is dosed from a low to a high pressure against the solid, and after each dosage the gas is allowed to stabilize. As the pressure increases with each dose, the nitrogen is adsorbed by the ground UHPC surface, pores and all. Using the changes in pressure after stabilization of each dose, and with the knowledge of the gas's ideal and non-ideal behavior, solid weight, and dimensions of the gas molecules, a surface area can be derived. This is a simplified procedure but helps the reader understand conceptually how the BET test allows surface area to be calculated in this method. A more specific procedure entails the following.

The sample solid itself, as stated above, is prepared the same as for the XRD test, except that the steel fibers are left in the UHPC sample. The reasoning behind this is that when considering the porosity of a completed concrete structure, all constituents must be considered. The first important value that must be found is the weight of the sample to be put through the ASAP 2050. A test tube is massed, then UHPC is added to the same test tube and then massed again. Next, a degassing procedure must take place. Degassing basically makes sure that any impurities, usually moisture and atmospheric gases, bound to the surface of the UHPC can be removed, and this is done by applying an inert gas, in this case helium, while at the same time elevating the temperature of the tube. This process can take varying amounts of time depending on the solid. The ASAP 2050 allows

for two samples to be degassed at once. Tubes for both heat treated and untreated UHPC were prepped for degassing. In total, the degassing procedure took roughly one week to complete. The cause of this isn't directly known but was thought to be attributed to the MasterGlenium 3030, since it has unknown constituents that could have caused the degassing to take longer than anticipated. After degassing, the heat treated UHPC sample was selected for analysis first. 4 L (0.3 gallons) of liquid nitrogen are placed in a container which raises via a s elevated platform so that the test tube is immersed in the liquid nitrogen. The gas is then dosed against the UHPC as explained above, so that the gas is slowly adsorbed by the UHPC. Then, after desorption of the gas takes place and the test concluded, the mass of the tube is taken again. The tube now has no gas present in it, and the new mass allows the amount of gas removed from the sample to be calculated, along with the true mass of the solid to be found as well. This mass of the solid is then plugged into the ASAP 2050's program, which then returns a variety ofresults**.** This entire procedure is then repeated for the untreated UHPC sample. Thus, at the end of the test, surface area, pore size, and pore volume are discerned. Figure 4.47 shows a flow chart of the nitrogen being adsorbed onto the surface of the particle, and the progression of layers of particles that form on the surface as the test progresses. As the test begins, the surface begins to slowly adsorb gas molecules at lower pressures. As the pressure increases, this sporadic coverage of adsorbed particles becomes larger and larger, until a complete monolayer or layer one-molecule thick is formed across the entire surface of the particle, pores included, and a surface area can be calculated. As the test progresses, the pores will fill more and more, forming more layers as the test progresses, beginning in the smaller pores of the particle and onward to larger particles. Finally, as the gas pressure continues to increase past that point, the entire sample and pores will be filled with nitrogen, and calculations can be used to find items like pore distribution, pore volume, and pore diameter. The value of the monolayer is found by manipulation of the isotherm curves formed by the testing. Once this monolayer value is found, along with other pertinent

criteria, the instrumentation and software can return desired values for items like surface area, pore characteristics, and more (Gas Sorption Analysis Brochure 2001). Figure 4.48 shows the BET testing procedure.

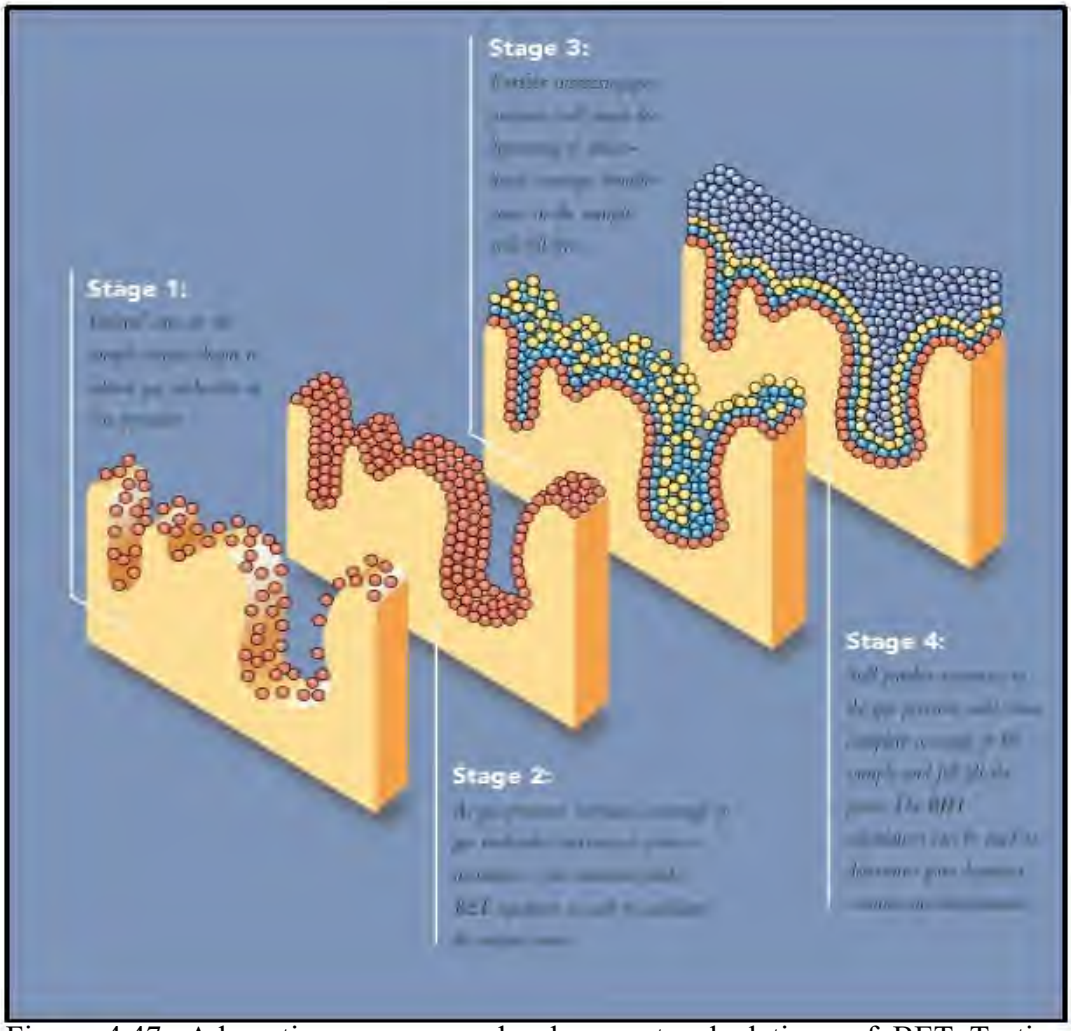
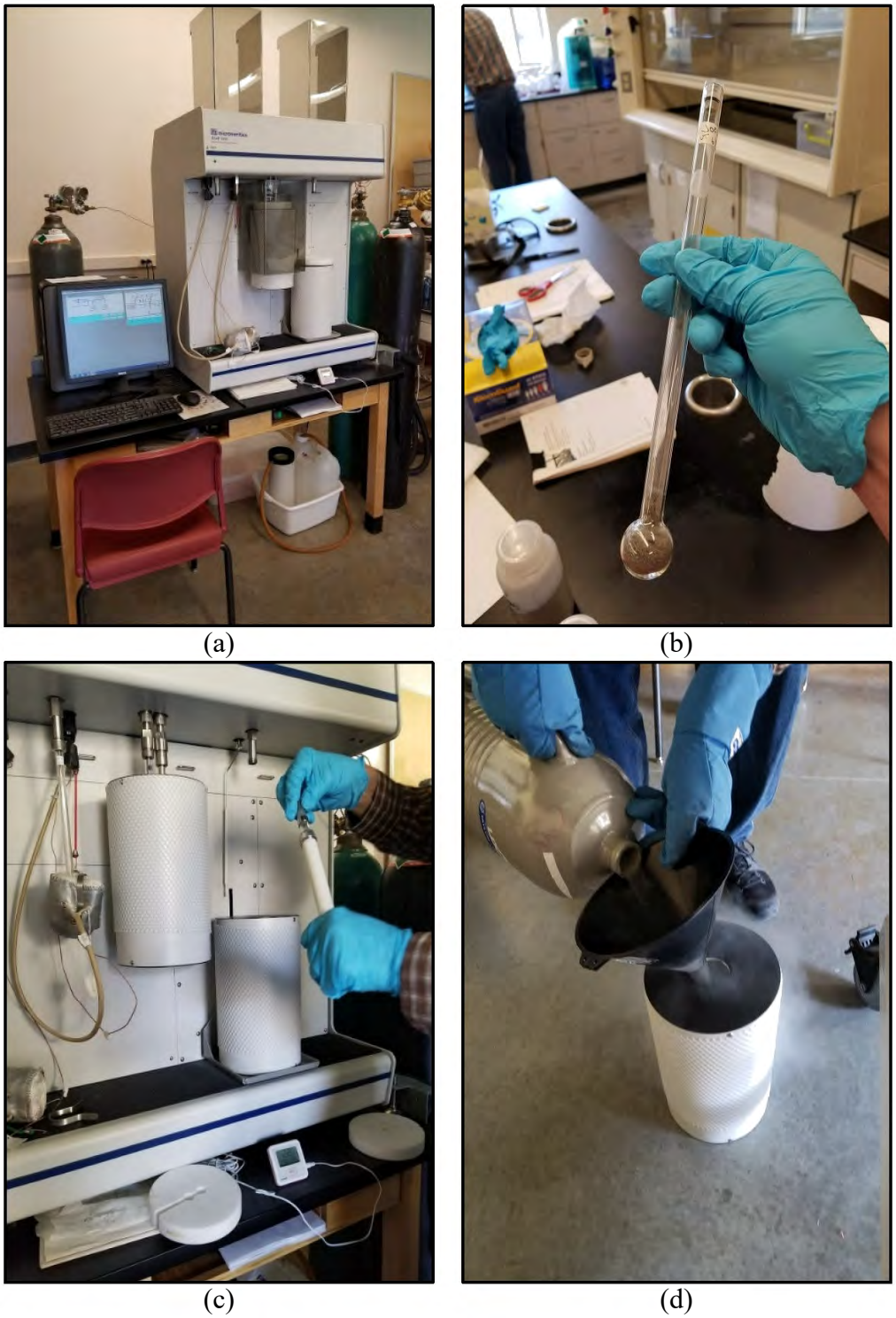


Figure 4.47: Adsorption process and subsequent calculations of BET Testing (Gas Absorption Analysis Brochure, 2001).



(a) (b)

(c) (d)

Figure 4.48: BET Testing - (a) ASAP 2050; (b) test tube filled with sample; (c) liquid nitrogen basin; (d) sample placement following degassing.

4.3.3 Scanning Electron Microscope Testing Procedure

The Scanning Electron Microscope (SEM) is a common tool used in the observance of DEF, as it allows for the crystalline structure to be directly observed under certain conditions. The SEM requires samples to be a maximum of 2 cm (0.39 in.) in length and width.

Two 2 in. (50 mm) UHPC cubes, one having been cured using heat treated methods and one having been cured in ambient air, were prepared for the SEM. The ceramic chop saw located in the NMSU Structural Systems and Material Testing Lab (SSMTL) is an effective means to cut the 2 in. (50 mm) cubes as it allows a constant jet of water to be applied to the operating saw to cut cleanly and quickly through solid materials like UHPC. The 2 in. (50 mm) cubes were measured so that two-2 cm cubes could be obtained from each 2 in. (50 mm) cube. The measurements took the blade of the saw into account to make sure the cubes were not too small. The cubes are then takento the NMSU Microscopy Imaging Suite in Skeen Hall. A height measurement is first taken of the 2 cm (0.79 in.) cube, before an adhesive tape is applied to the opposite side of what side is to be observed by the SEM. Careful consideration is also taken to make sure that the side being observed was an internal part of the 2 in. (50 mm) cube exposed by the cutting to optimize the visibility of hydration products. Next, the sample is placed on a pedestal inside a chamber in the SEM which removes air and eliminates the possibility of outside interference once the SEM testing begins. Once vacuum conditions have been achieved, the pedestal is raised closer to the lens of the SEM itself. The S-3400N II's programs and control panels allow for both coarse and fine focusing wheels along with a magnification wheel that allow easy magnification and focusing. A spherical control allows the microscope to move freely over the surface of the sample. From here, pictures are obtained once a desired structure has been identified. However, because concrete has a higher surface area with many pores, the surface can accumulate a high quantity of electrons. These electrons then cause a shaky, blurry image on the SEM, and higher

magnifications are not able to produce clear images of the hydration product structures. Instead, Au/Pd film is typically applied to the surface of the concrete, which limits the number of electrons accumulating on the surface and produces a clearer image. However, even with the Au/Pd film, structures can take a long period of time to locate, and due to the tight budget of this study excessive time could not be taken to locate specific hydration structures considering the hourly cost of use of the SEM. Thus, images were taken of different clearly visible parts of both heat treated and untreated samples. Following the capturing of the images, air is allowed back into the chamber before the pedestal is lowered and the sample can be removed from the SEM to conclude the test.

4.4 Direct Tension Tests

4.4.1 Objective

This study investigates the effects of mixture proportions, curing process, and curing time on the direct tensile behavior of locally developed ultra high performance concrete (UHPC). Due to the difficulty of performing tests, tensile tests are uncommon resulting in little to no standardized testing methods. This allows for variation in testing parameters such as specimen shape, specimen dimensions, loading rate, etc. Multiple tests are being performed using several mixture proportions, as well as several different specimen dimensions beginning with the mixture proportions shown in Table 4.97 and specimens shown in Figure 4.49.

Table 4.97: Preliminary UHPC Mix Proportions (Yields 1 ft^3)

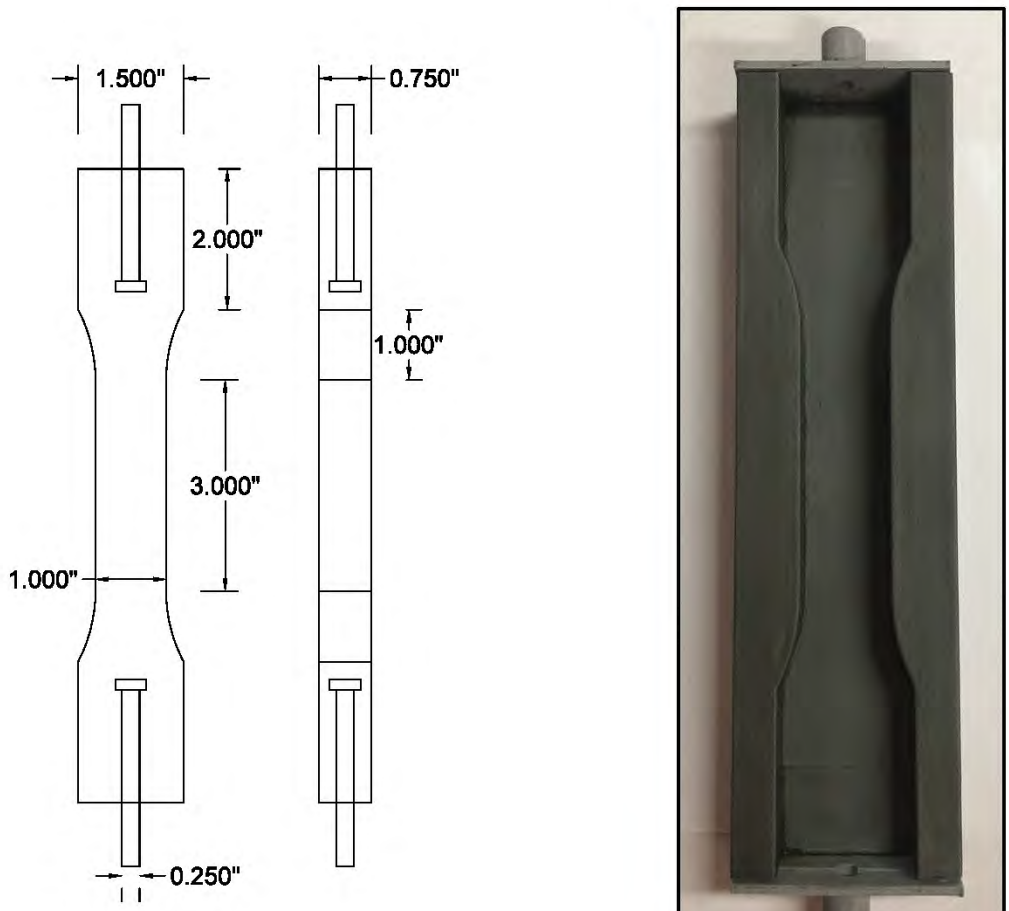
Constituent	Quantity
Cement	50.9 lb
Silica Fume	6.4 lb
Fly Ash	6.4 lb
Sand	62.3 lb
Steel Fibers	7.4 lb
HRWRA	1/3 gal
Water	10.2 lb



Figure 4.49: Direct tension specimens.

4.4.2 Specimen Design

To create a mold that was both precise and durable while keeping costs at a minimum, 3D printing was utilized. The dog bone specimen design consists of an upper grip region 1.5 in. (38 mm) wide by 2 in. (50 mm) long, a reduced region 1 in. wide by 3 in. long, and a transition region. The specimen is 9 in. (229 mm) in total length and is 0.75 in. (19 mm) thick. Once the forms were designed, they were printed out of polylactic acid or PLA plastic. PLA is a biodegradable and renewable plastic commonly used for 3D printing due to its ease of use as well as its durability. The original design sketch as well as the formwork can be seen in Figure 4.50.



(a) (b)

Figure 4.50: Direct tension dog-bone specimen – (a) dimensions; (b) mold.

4.4.3 Test Setup and Instrumentation

Preliminary tests have been performed on specimens cured in a wet room for seven days with the intention of varying both the curing process as well as age of testing. These tests are performed on an Instron 5882 electromechanical testing system as seen in Figure 4.51. This system, along with several accessories, loads the dog-bone shaped specimens in direct tension. To adequately grip the specimens, while also limiting the risk of crushing the concrete in the grip section, a 0.25 in. (6.35 mm) Grade 5 bolt is embedded into the specimen. During testing, the specimens are setup with an Instron static axial clip-on extensometer at the middle of the gauge length of the reduced region to measure strain. The extensometer has a 2 in. (50 mm) gauge length and a +100/-10% max strain which provides adequate travel distance while also fitting within the gauge length of the reduced region. This data along with tensile forces gathered by the system, allow tensile strengths to be calculated.



Figure 4.51: Direct tension specimen being loaded (with extensometer).

4.4.4 Preliminary direct tension results

Table 4.98: Preliminary Direct Tension Results

Mix Design	Mix date	Test date	Specimen Number	Cross Sectional Area at failure (in^2)	Maximum Tensile Force (lb)	Tensile Strength (psi)	Failure Region	Mix date	Test date	Specimen Number	Compressive Stregnth (psi)
1700	12/10/18	1/10/19	1	.75	550.5	734.00	Gage Length (O)	12/10/18	1/10/19	1	1874
	12/10/18	1/10/19	2	1.125	836.1	743.20	Grip	12/10/18	1/10/19	2	1807
	12/10/18	1/10/19	3	1.125	731.5	650.22	Grip	12/10/18	1/10/19	3	1869
	12/11/18	1/10/19	4	1.125	Unavailable	Unavailable	Grip	12/10/18	1/10/19	4	1908
	12/11/18	1/10/19	5	1.125	849.9	755.47	Grip	12/10/18	1/10/19	5	1873
	12/11/18	1/10/19	6	1.125	997.9	887.02	Grip	12/11/18	1/10/19	6	1998
								12/11/18	1/10/19	7	1976
								12/11/18	1/10/19	8	1987
								12/11/18	1/10/19	9	1890
								12/11/18	1/10/19	10	2020
								12/11/18	1/10/19	11	1947
1700	1/22/19	1/29/19	1	1.125	770.1	684.53	Grip	1/22/19	1/29/19	1	1403
	1/22/19	1/29/19	2	.9375	773.2	824.75	Transition	1/22/19	1/29/19	2	1501
	1/22/19	1/29/19	3	.75	754.4	1005.87	Gage Length (I)	1/22/19	1/29/19	3	1502
	1/22/19	1/29/19	4	.75	728.3	971.07	Gage Length (I)				
	1/22/19	1/29/19	5	.75	675.9	901.20	Gage Length (I)				
	1/22/19	1/29/19	6	1.125	799.1	710.31	Grip				
	1/22/19	1/29/19	7	.75	809	1078.67	Gage Length (O)				
1700	2/1/19	2/8/19	1	.9375	900	960.00	Transition	2/1/19	2/8/19	1	1690
	2/1/19	2/8/19	2	.75	1004.8	1339.73	Gage Length (I)	2/1/19	2/8/19	2	1625
	2/1/19	2/8/19	3	.75	938.6	1251.47	Gage Length (O)	2/1/19	2/8/19	3	1631
	2/1/19	2/8/19	4	.75	914.8	1219.73	Gage Length (O)	2/1/19	2/28/19	4	1799
	2/1/19	2/8/19	5	.75	514.7	686.27	Gage Length (I)	2/1/19	2/28/19	5	1555
	2/1/19	2/8/19	6	.75	602.6	803.47	Gage Length (O)	2/1/19	2/28/19	6	1549
	2/1/19	2/8/19	7	.75	831	1108.00	Gage Length (I)				
1700	2/15/19	2/22/19	1	.75	1202.1	1602.80	Gage Length (I)	2/15/19	2/22/19	1	1571
	2/15/19	2/22/19	2	.75	475	633.33	Gage Length (I)	2/15/19	2/22/19	2	1576
	2/15/19	2/22/19	3	1.125	869.1	772.53	Grip	2/15/19	2/22/19	3	1601
	2/15/19	2/22/19	4	1.125	697.3	619.82	Grip	2/15/19	2/22/19	4	1527
	2/15/19	2/22/19	5	.75	906.5	1208.67	Gage Length (I)	2/15/19	3/15/19	5	1706
	2/15/19	2/22/19	6	.75	701.8	935.73	Gage Length (O)	2/15/19	3/15/19	6	1553
	2/15/19	2/22/19	7	1.125	823.2	731.73	Grip	2/15/19	3/15/19	7	1774
	2/15/19	2/22/19	8	.75	1180.1	1573.47	Gage Length (I)	2/15/19	3/15/19	8	1515
	2/15/19	2/22/19	9	.9375	960.7	1024.75	Transition	2/15/19	3/15/19	9	1738
	2/15/19	2/22/19	10	.9375	884.7	943.68	Transition				

1. Cross sectional area when failure occurred in the grip region calculated using gross dimensions
2. Cross sectional area when failure occurred in the transition area calculated using the average of the gross dimensions in the grip region and the reduced region

THIS PAGE INTETIONALLY LEFT BLANK

Task 5: Identify Potential Additional Uses of UHPC

TASK 5: IDENTIFY POTENTIAL ADDITIONAL USES OF UHPC

Further research programs were initiated and conducted at NMSU to examine potential uses of nonproprietary UHPC. Following a thorough review of current literature, several applications were identified and investigated including closure joints, shear keys, and bridge deck overlays. The following sections present the experimental methodology and findings of these investigations.

5.1 Joint Applications

Adjacent box beam bridges are constructed by placing box beams next to one another, grouting a joint, applying a transverse post-tensioning force, and then placing a thin wearing surface or structural deck on top (FWHA 2015). These bridge superstructures are attractive because of their relatively shallow superstructure depth and ease of construction. The National Cooperative Highway Research Program (NCHRP) Synthesis 393 reported a wide variety of practices used by state highway agencies for the connection details between adjacent box beams. These practices include partial depth or full depth joints, joints grouted before or after transverse post-tensioning, prepackaged or non-prepackaged grout materials, post-tensioned or non-tensioned transverse ties, a wide range of applied transverse post-tensioning forces, and cast-in-place concrete decks or no decks. Cracking in post-tensioned concrete box girders generally results, in a broad sense, for the following reasons: inadequate flexural and shear capacity, no consideration of thermal stresses, insufficient attention to stresses developed by curvature of tendons, improper or inappropriate construction techniques, lack of quality workmanship to meet the tolerances necessary for problem free structures, and understrength materials (Podolny 1985). These problems are not limited to those of prestressed box girder bridges but may occur in other types of structures with similar conditions and details. All cracks are not avoidable in post-tensioned concrete box girder bridges, since not all portions of the structure are precompressed in three directions and local concrete shrinkage is not always controllable. Certain cracks may not be structurally serious, while others are. In segmental box girders, flexure cracks will generally occur in or near the segment joints. As the cracks propagate up to the top flange, they will become fine microcracks. A few states reported that their methods had reduced the longitudinal cracking, whereas others had not been successful using similar methods. Research being conducted to evaluate those practices at the design and construction phases could lead to connection details that prevent cracking and leakage at the joints and extend the service life of adjacent box beam bridges.

To investigate the behavior of non-proprietary UHPC joints, a box girder – joint system was selected for the basis of the design of the scaled specimens. The cross sections of the box girders top flange were re-designed and use to construct the slab-joint-slab specimens. The system was loaded on one side of the specimen, forcing the load to be transferred through the joint, and the load / deflection of the system was measured. Additionally, the gap opening / closing was measured along the length of the joint. These measurements enabled the behavior of the joint to

be investigated. The research utilized the non-proprietary UHPC developed at NMSU for the joint and conventional normal weight concrete (NWC) typical of bridge construction in NM for the box girders top flange. The specimens were instrumented with numerous sensors to measure the behavior of the system under load. The experimental results were used to analyze the behavior of the UHPC joint as the NWC slabs were loaded and the load was transferred through the joint. Specimens were subjected to load – unload cycles, as well as, at the completion of the cyclic loading, a continuously increasing load at a set rate till the system failed. The test was designed to provide a better understanding of the joint's behavior with typical vehicular loads. Additional tests were completed using non-shrink grout typically used by the NMDOT for joint applications. The results of these tests were compared to the results of the UHPC joint tests to demonstrate the differences in behavior.

The testing of the UHPC joints and NWC slab system served to further verify and improve the use of UHPC in structural applications. With approximately 50 percent of bridges in New Mexico using prestressed concrete, implementing UHPC in design has the potential to have a significant impact on the cost and performance of bridges in New Mexico (Weldon et al. 2012). By investigating the use of non-proprietary UHPC for joint applications, this work provides additional information to accelerate the utilization of UHPC in the state of New Mexico and the surrounding region. The research conducted will assist in future consideration of UHPC applications to increase the longevity of our infrastructures.

5.1.1 Design of Test Specimens

Bridges constructed with adjacent precast prestressed concrete box beams have been in service for many years and provide an economical solution for short and medium span bridges. A recurring problem with this type of bridge is the cracking in the longitudinal joints between adjacent beams, resulting in reflective cracks forming in the asphalt wearing surface or concrete deck. The cracking appears to be due to early-age shrinkage, temperature gradients, and traffic loads. As cracks appear, water can penetrate the cracks and cause corrosion of the reinforcement and prestressing strands. In the United States, there are three typically used generic partial depth joint geometries Types I, II and III joints and one full depth joint geometry Type IV shown in Figure 5.1. El-Remaily et al. (1996), Lall et al. (1998) and Sang (2010) reported that longitudinal cracking was seldom found in adjacent box beam bridges with the Type V joint.

Liu and Phares (2018) conducted multiple levels of material tests and developed a finite element modeling approach which is capable of simulating early-age joint behavior to select the best material associated with various joint geometries that can resists early-age joint cracking. Four materials including epoxy grout, cement-based construction grout, fiber reinforced concrete and shrinkage compensated concrete were evaluated using a combination of modeling and material test results. The results indicated that the Type V joint filled with shrinkage concrete is expected to perform superior to the Type IV joint filled with epoxy. It was also found that the Type V joint filled with shrinkage concrete still induces tensile stress near the exterior of the interface, and that the placement of reinforcement near the edge will have sufficient capacity to resist the debonding at the interface during the early-age period when initial cracking has been found to occur.

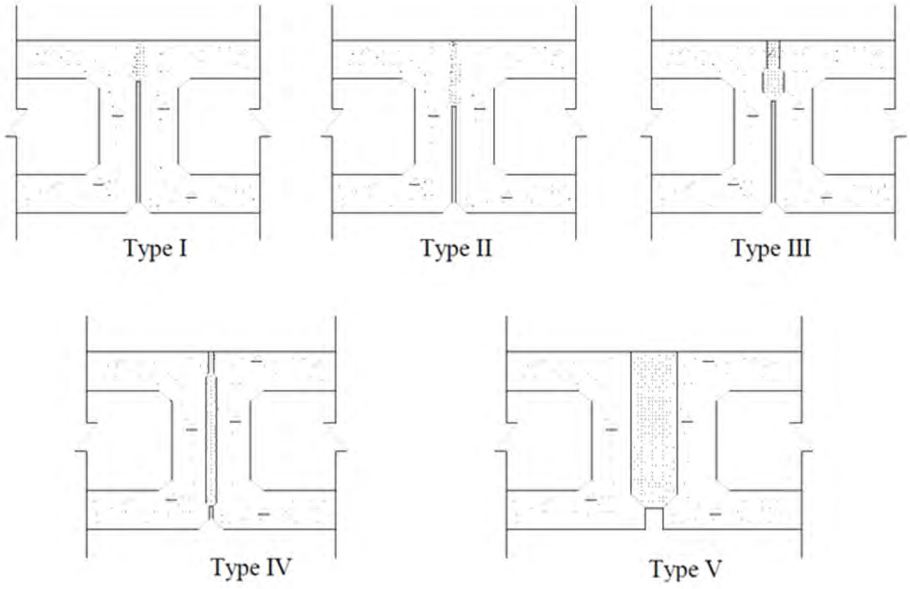


Figure 5.1 Basic joint geometries.

This research consisted of casting several joints with varying parameters to investigate the mechanical behavior of using UHPC in lieu of conventional grout. The box girders utilized in this work were designed based upon standard NMDOT (2018) shapes and only minor changes were made to facilitate the geometric features of the joint. The initial test focused on replicating the rebar spacing, size of rebar and top slab thickness used for box girders per NMDOT standards as shown in Figure 5.2 through Figure 5.5. Two 4.5 ft (1.37 m) long box girders flanges were constructed with No. 6 (No.19) longitudinal non-prestressed bar reinforced at 8 in. (203.2 mm) on center as shown in Figure 5.6. Typical NMDOT high performance concrete was selected as the material for the box girder top flanges. The box beam – joint interface was left smooth from the form work used to produce the joints opening (i.e., no surface roughening was conducted), creating a worse-case scenario for the bond between the HPC and UHPC. To enhance the load transfer capabilities of the UHPC joint, as well as to provide resistance to shrinkage induced early age cracking, reinforcing steel was detailed and included per NMDOT standards. The transverse interface-crossed reinforcing steel in-and-out of the box beam were lapped by each other in a staggered configuration. Figure 5.6 shows the box girder with the transverse steel in the joint. The longitudinal reinforcing steel was used to enhance the strength and serviceability of the specimen and force the failure location to occur at the joint. The compressive strength of the box beam concrete was tested in accordance to ASTM C39 for the box girder concrete at 28 days. Time dependent tests were conducted on the joint material, for the compressive strength following ASTM C39 and for the flexural tensile strength test following ASTM C78 at 7 days, 14 days, and 28 days. The material test results are discussed later in this chapter. After investigating the initial design shown in Figure 5.6 that was modified based on NMDOT standards shown in shown in Figure 5.2 and Figure 5.5, the rebar was varied to investigate an additional potential economic benefit of reducing the cross-sectional area of steel required compared to conventional grouted joints.

The following presents the different parameters used for specimens 1 through 6:

- Specimen 1 joint reinforcement utilized NMDOT joint lab splice configuration which was No. 4 (No.13) rebar at lap splice spacing of 6” with a lap length of 4.5in. (114.3 mm).
- Specimen 2 joint reinforcement utilized the same NMDOT top slab reinforcement, but the joint lab splice spacing configuration was increased to 12 in. (304.8 mm) but keeping the No. 4 (No.13) rebar and lap length of 4.5in. (114.3 mm) the same as test specimen 1.
- Specimen 3 joint reinforcement was the same as specimen 1. The 6 in. (152.4 mm)lap splice spacing configuration and 4.5 in. (114.3 mm) rebar lap length was kept the same, but the rebar size was decreased to No. 3 (No.10) rebar.
- Specimen 4 joint reinforcement utilized the same joint lab splice spacing configuration of 12 inches (305 mm) as specimen 2, but the No. 4 (No.13) rebar was changed to No. 3 (No.10) rebar. The lap length of 4.5 inches (114.3 mm) for rebar at the joint stayed constant.

- Specimen 5 joint reinforcement was identical to specimen 1 in order to replicate and compare the UHPC to the non-shrink grout joint data.
- Specimen 6 joint reinforcement utilized the same top slab reinforcement as test specimen 2 to compare the UHPC to the non-shrink grout joint data.

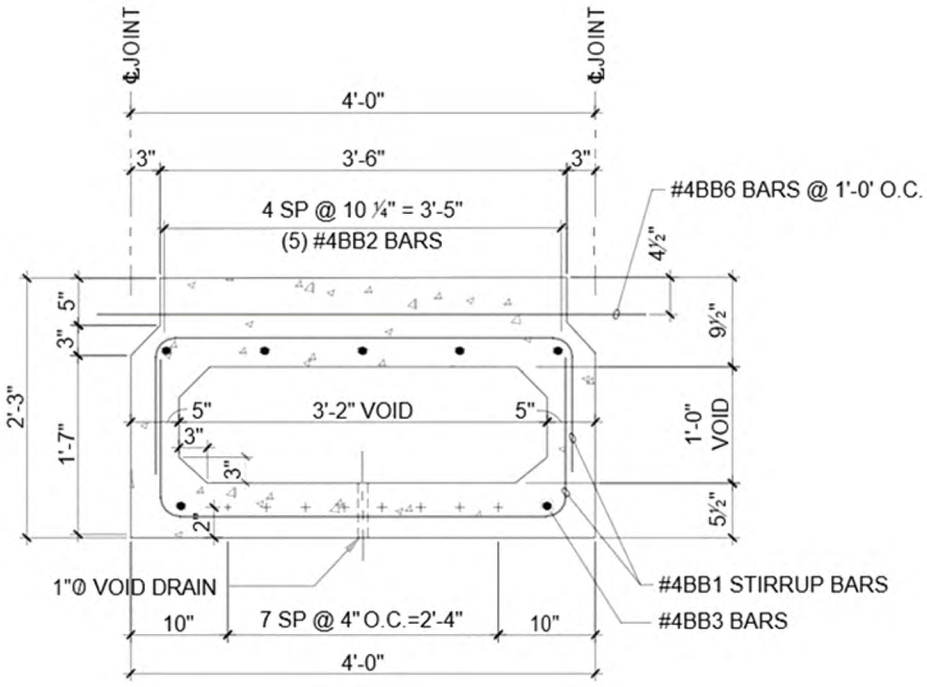


Figure 5.2 Typical NMDOT box girder cross-section.

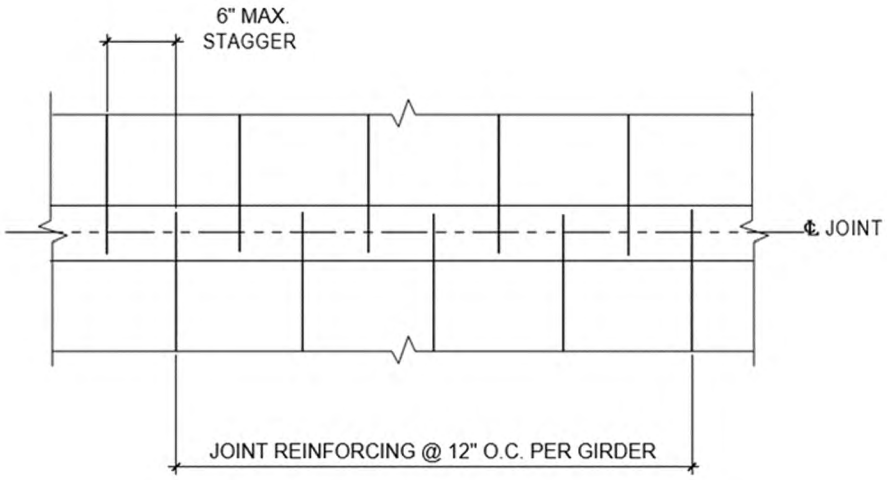


Figure 5.3 Typical NMDOT staggered bar lap detail.

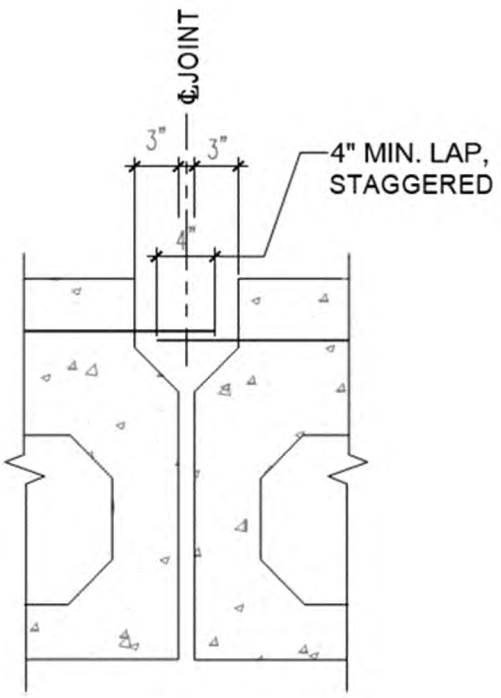
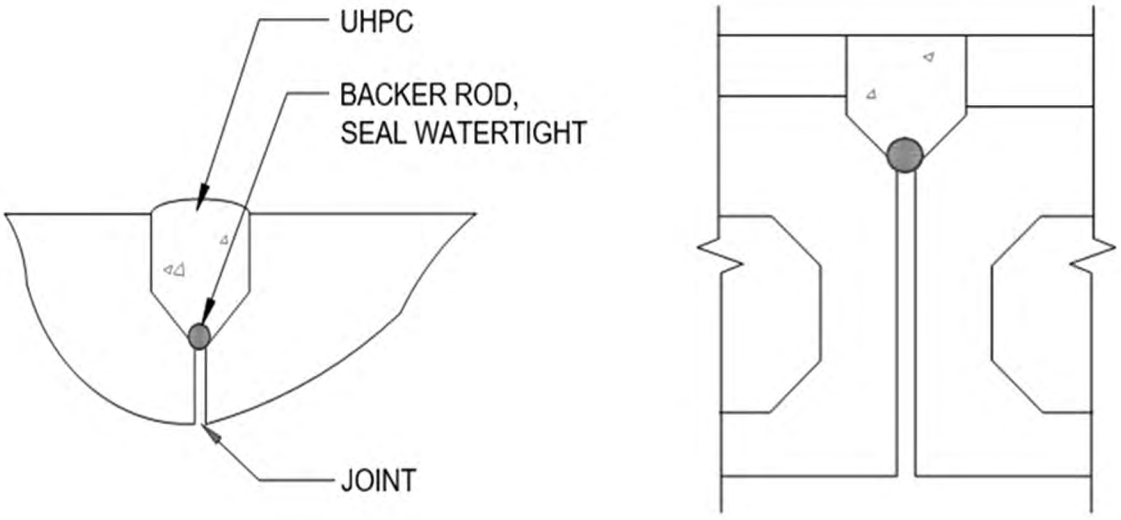


Figure 5.4 NMDOT box girder joint lap splice cross section.



(a) (b)

Figure 5.5 NMDOT box girder joint cross-sections with UHPC (a) before joint grinded flat, (b) after joint grinded down smooth.

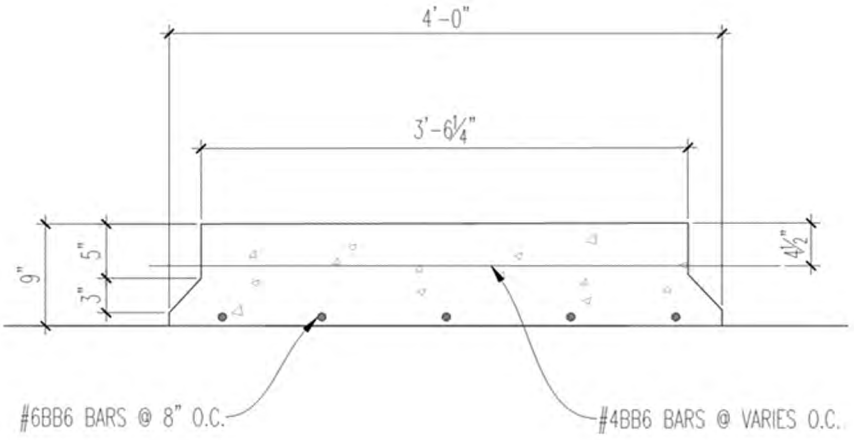


Figure 5.6 Modified top flange of NMDOT box girder cross-section.

5.1.2 Test Set-up and Instrumentation

Flexural testing of the UHPC joint presented used several forms of instrumentation to capture specimen behavior. The external instrumentation used include load cells, linear displacement transducers (LVDTs), string potentiometers, and tiltmeters. The real-time behavior the full-scale UHPC specimen during flexural testing was monitored using LabView software connected to an NI data acquisition system. Figure 5.7 though Figure 5.9 show the instrumentation used on the testing system. Figure 5.9 shows LVDT locations for determining transverse deflection behavior in the jointing region. The string potentiometers shown in Figure 5.9 were used to monitor and measure the vertical deflected shape of the system. Figure 5.7 shows the electronic tiltmeters utilized to capture beam rotation in the longitudinal orientation.

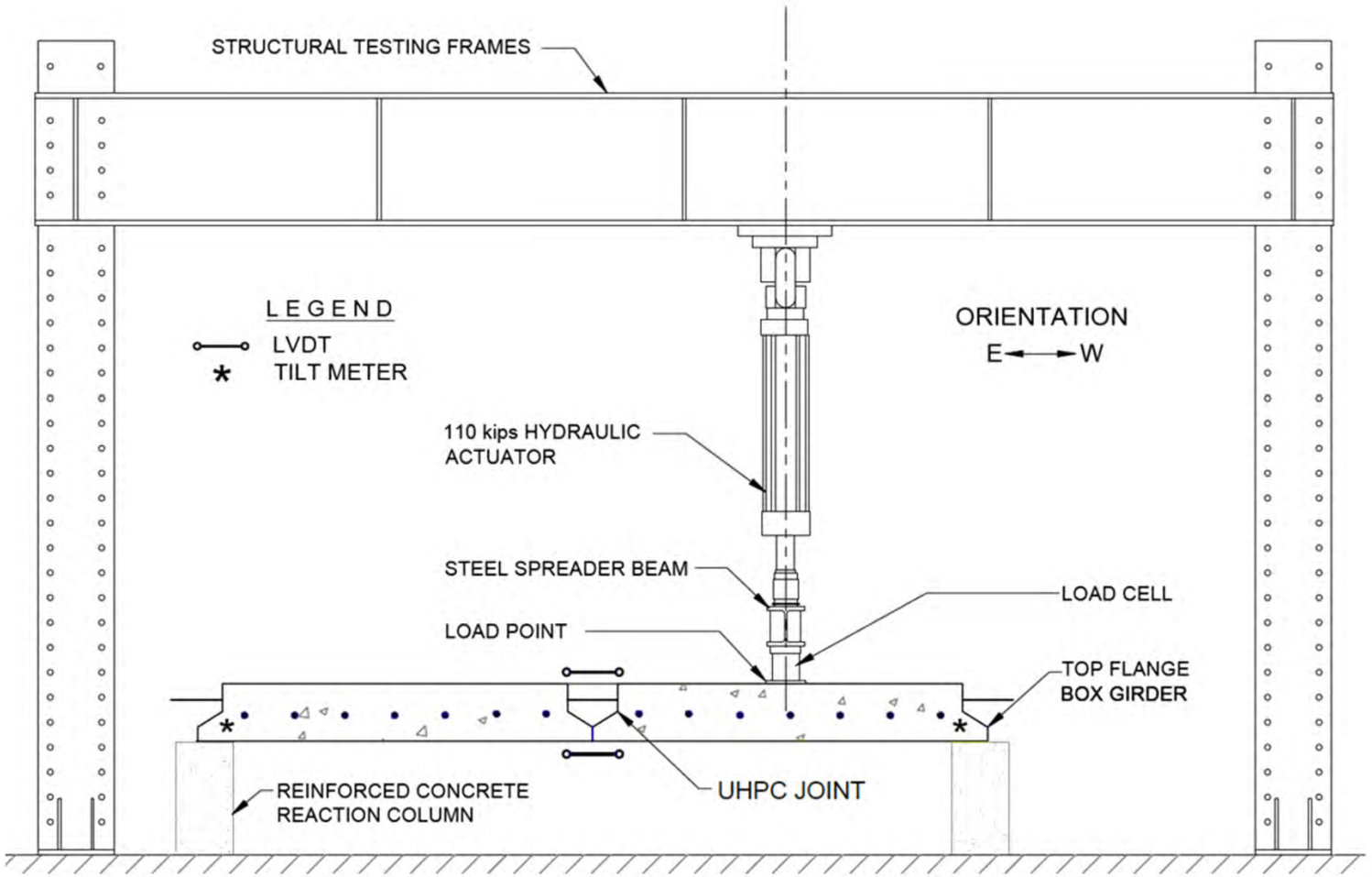


Figure 5.7: North view of test setup.

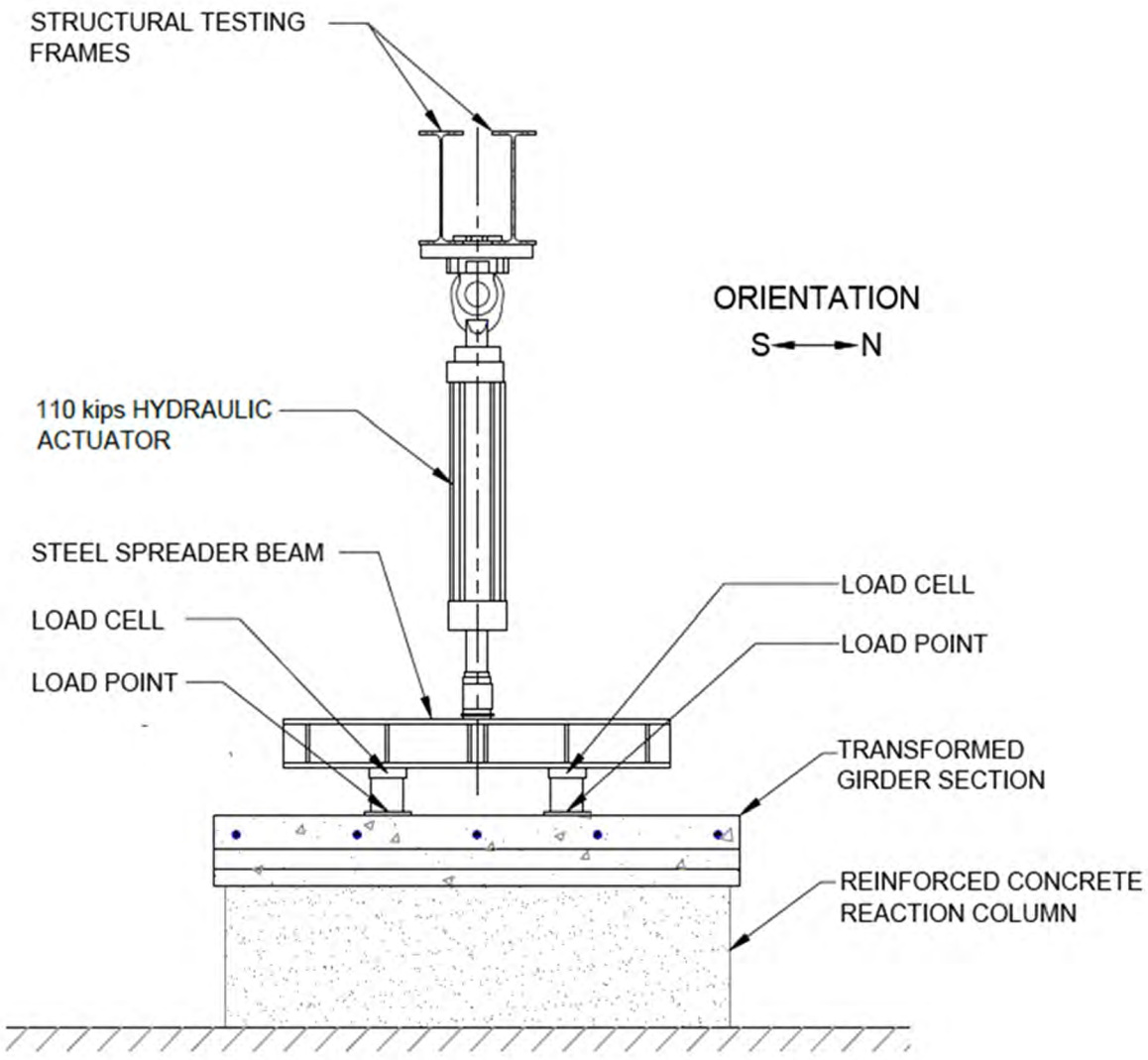
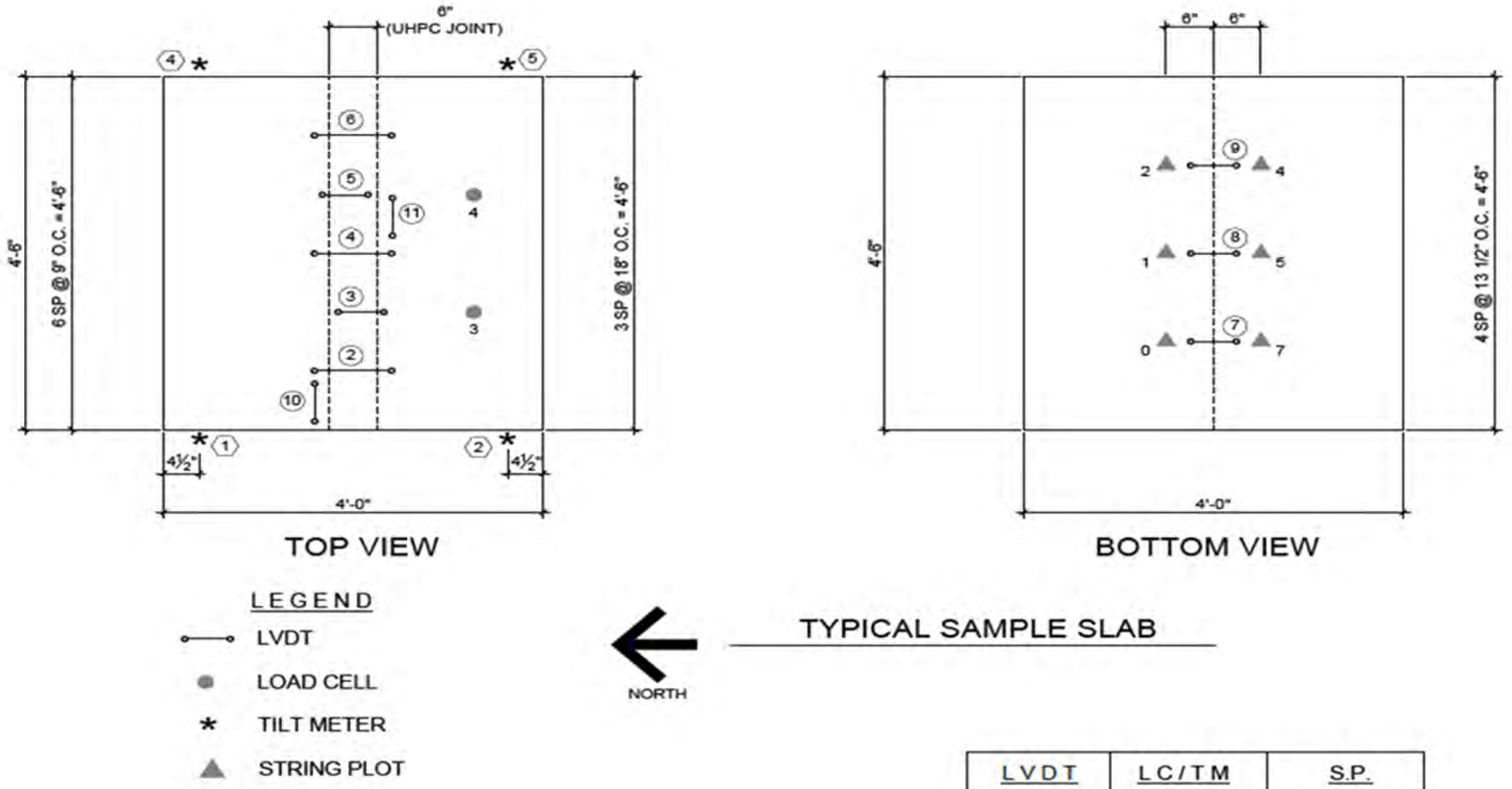


Figure 5.8: East view of test setup.



LVDT	LC / TM	S.P.
2 LVDT	3 LC	0 SP
3 LVDT	4 LC	1 SP
4 LVDT	1 TM	2 SP
5 LVDT	2 TM	4 SP
6 LVDT	4 TM	5 SP
7 LVDT	5 TM	7 SP
8 LVDT		
9 LVDT		
10 LVDT		
11 LVDT		

Figure 5.9: Top and bottom view of test setup.

5.1.3 Material

To promote locally developed, non-proprietary UHPC, sand with a specific gravity of 2.63 from Socorro, New Mexico was used for the fine aggregate. All sand was oven dried at 105 ± 5°C (221 ± 9°F) to remove all moisture prior to mixing. Commercially available Rio Grande Type I/II Portland cement, class F fly ash, and Rheomac SF 100 silica fume were used as cementitious materials in the mixture proportions and commercially available water reducer MasterGlenium 3030 NS were used in the mixture. The chemical and physical properties of the cement, fly ash, and silica fume are presented in Table 3.1. The same fine sand and cementitious materials were used throughout this research and did not vary between joints. 1.5% by volume of 0.5 in. (13 mm) straight steel fibers with an aspect ratio of 65 and a tensile strength of 400 ksi (2660 MPa) were used. Compressive and flexural tests were performed on sample specimens under ambient and heat curing conditions with results showing a relative increase in strength as mixtures increased in steel fiber percentage (Alvarez, 2019). Alvarez (2019) concluded that flexural strength is directly increased at higher steel fiber contents, as they provide more ductility; however, compressive strength was also slightly increased until a certain content of steel fibers, with a couple of exceptions that can be attributed to the random orientation of steel fibers and dissimilar confinement of fiber reinforcement.

Table 5.1: Chemical and Physical Properties of Cementitious Material (Alvarez, 2019).

Chemical Compound	Cement	Fly Ash	Silica Fume
	Chemical Composition Percentage (%)		
SiO2	20.3	61.83	96.9
Al2O3	4.6	24.54	0.2
Fe2O3	3.4	4.22	0.2
CaO	63.9	1.45	0.3
K2O	-	1.32	0.3
Na2O	-	1.41	0.2
MgO	1.91	0.74	0.2
SO3	2.86	0.18	0.1
Loss on ignition	2.24	0.36	2.17
Insoluble residue	0.38	-	-
pH	-	10-11	7.65
Physical Properties			
Relative Density	3.15	1.96	2.24
Specific Surface Area	335 m^2/kg	2500 m^2/kg	26810 m^2/kg
Autoclave Expansion	0.05%	-0.03%	-
Moisture Content	-	0.09%	0.04%

5.1.4 Mixture Proportions

Starting with the previous UHPC mixture proportions developed by Lyell (2011) as a bases of the mix design. The cementitious materials are comprised of 80% portland cement and 20% SCMs split equally between silica fume and fly ash. As seen in Table 3.2, the mixture used 20% of the total cementitious materials was comprised of silica fume and fly ash 50% fly ash and 50% silica fume and nominal sand contents of 1700 lb/yd3 (1009 kg/m3). The w/cm ratio used was 0.15 with the addition to HRWRA MasterGlenium 3030 NS to provide workability. High strength, 0.5-in. (13 mm) straight steel fibers with a tensile strength of 380 ksi (2600 MPa) were added at 1.5% by volume.

Table 5.2: UHPC Mixture Proportions

Cement, lb/yd^3 [kg/m3]	Silica Fume, lb/yd^3 [kg/m^3]	Fly Ash, lb/yd^3 [kg/m^3]	Fine Sand, lb/yd^3 [kg/m^3]	Steel Fibers, lb/yd^3 [kg/m^3]	Water, lb/yd^3 [kg/m^3]	HRWRA, gal/yd^3 [L/m^3]
1374 [815]	172 [102]	172 [102]	1700 [1010]	200 [119]	258 [153]	9.31 [46.1]

5.1.5 Preparation of Test Compressive Strength Specimens

Compressive strength specimens consisted of 4.0 in. (100 mm) cubes cast in steel molds. All steel molds were oiled lightly prior to the placement of concrete to facilitate demolding of the UHPC. Casting included setting the steel molds on a vibrating table while the UHPC was placed inside the molds to improve consolidation. The time and intensity of vibration depended on the consistency of each mixture. If a mixture was stiff, rodding was performed to ensure good consolidation. After the specimens were cast, a plastic sheet was placed over all samples to avoid moisture loss. Specimens remained covered at ambient conditions for 24 hours, and then demolded prior to being cured as outlined in Section 5.1.7.

5.1.6 Preparation of Box Girder Top Slab

Box girder sections can be constructed in stages, beginning with the bottom slab, webs and finally the top slab. The bottom slab is typically cast first, web reinforcing and longitudinal ducts for post-tensioning tendons are then tied and portions of the webs would be cast. Supports for top slab forming are then placed in the portion where webs are complete and finally cast. Many bridges combine the casting of the bottom slab and webs into one stage. As shown in the following Figure 5.10 through Figure 5.14, the process to create the testing set-up began with the form work to create the top slab of the box girders to test the joint between each slab.

Twelve molds, shown in Figure 5.10, in total were built using custom form work and had holes drilled in them with varied rebar spacing to produce different designs. The test results were compared to investigate the strength, vertical deflection and transverse deflection in the system. Eight of the slabs were used to cast the UHPC joints, the other four molds were used for the control specimens using typical non-shrink grout. The strongest configurations from the UHPC test were used in the control specimen tests to utilize best comparable results.



Figure 5.10: Slab formwork.

After all the form work was built and reinforcement was placed, the forms were filled with NWC having 4,500 psi (31.0 MPa) compressive strength and cured for 7 days wet and 14 days at ambient condition for a total of 28 days of curing (Figure 5.11). The concrete was vibrated with a Makita XRV01T cordless 4 ft (1.2 m) concrete vibrator during casting to ensure consolidation of the concrete was achieved. Without some form of consolidation, the concrete could possibly have honeycombing creating weak points in the specimens. Utilizing past research work, previously built supports were placed and leveled to the ground with grout. The grout also acted as a footing for the supports to help prevent tipping and/or sliding during the tests. Figure 5.12 shows the slabs for Specimen 1 placed on the supports with an additional temporary support in the middle prior to casting and curing the joint.

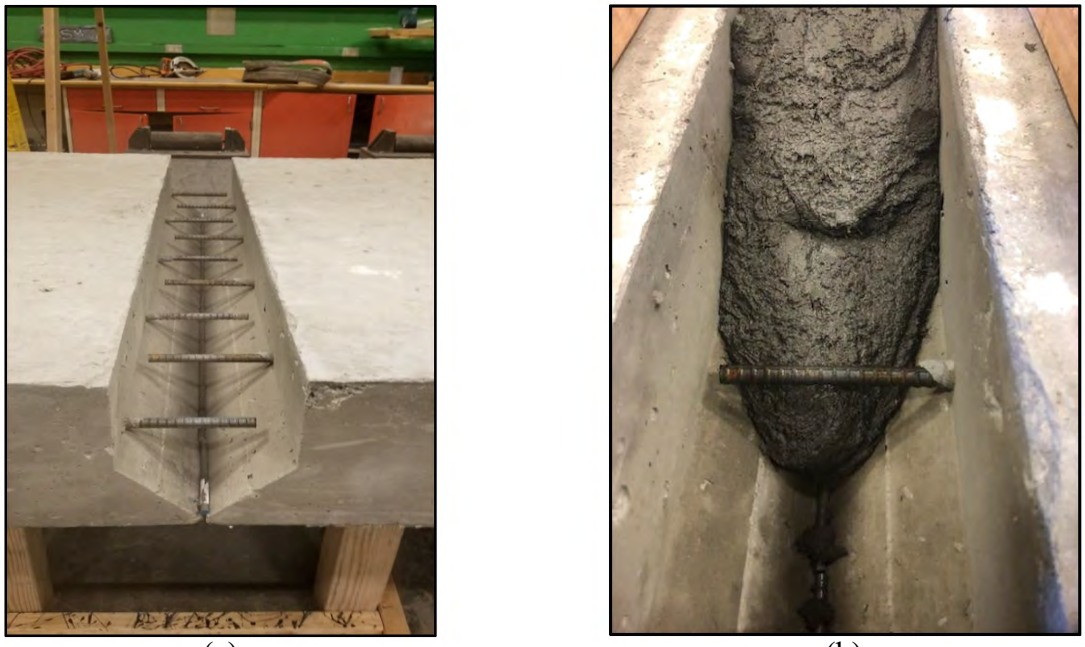


Figure 5.11: Casting of the slabs.



Figure 5.12: Specimen No. 1 slab prior to casting and curing of the joint.

Reinforcement extended out of the mold to allow lap slicing in the joint. Reinforcement costs, difficulties in fabrication, and challenges with field assembly are all factors that can be positively addressed by specifying field-cast, lap-splice connections with UHPC. Yuan et al. (2018) test results showed when a direct tensile force was applied to the UHPC connections, the box beam concrete cracked rather than the connection interface or the UHPC itself. This indicates that the interface bond between the UHPC and the box beam with an exposed aggregate (EA) surface preparation and rebar in a non-contact lap splice is of similar or greater tensile strength as compared to the tensile strength of the box beam concrete. This was also observed in a study by De la Varga et al. (2016) where interface bond between different grout materials and concrete was investigated. They found that, for connections with UHPC and EA, the failure primarily occurs in the concrete rather than at the interface or within UHPC itself. This is not true for conventional grout connections, as the interface often fails under the same conditions. Yuan et al. (2018) notes that the discrete steel reinforcement that is distributed along the length of the UHPC connections provides further advantages in terms of increasing local shear and tensile strengths and limiting the crack width if any cracks should develop at the interface. Connections between precast box girders are one example of a field-cast connection that takes advantage of UHPC. Rebar from one side overlaps with the rebar from an adjacent side, and the void between them is filled with UHPC. The connection transfers moment, shear, and tensile forces across the joint using short, straight rebar spaced at intervals typical to conventional deck design. The width of the connection is based on the rebar development and lap-splice lengths plus construction tolerance. Figure 5.13 shows the typical lap spacing of the joints. UHPC was then placed in the joint and cured for 14-days and tested.



(a) (b)

Figure 5.13: View of experimental joint (a) prior to casting and (b) during casting.

Lastly, all equipment was added two days prior testing to ensure correct configuration and that all the equipment was working properly as shown in Figure 5.7 through Figure 5.9. The loading beam was then added with two loading cells in order to mimic live load tires of a vehicle passing over a bridge. The loading cells were place at third points in both directions in order to ensure the most balanced loading condition can be met and that no unequal loading scenarios will occur such as the south face of the slab will see higher stresses than the north face. This could cause a zippering effect when a crack or separations in the joint starts and continues from one end to the other in the joints bond between the UHPC and NWC in which induces a weaker path for the load to cause failure.



Figure 5.14: Specimen No. 1 testing setup.

5.1.7 Curing Regimen

All specimens were cured at room temperature (20 °C [68 °F]) for the first 24 hours prior to being demolded. The curing regimen consisted of wetting the specimens for the first 7 days of curing while leaving wetted burlap covering all specimens to keep them in contact with water as long as possible before reapplying water every 12 hours. After the 7-day wet curing stage, the specimens were left at room temperature until the tests were conducted. After this curing process was completed, 14-day compressive and flexural strengths were measured.

5.1.8 Compressive Strength Test

Cube compressive strength samples were tested (as outlined in Section i.i) for each pour day for the scaled specimen, UHPC joint, and non-shrink grout joint. Table 3.3, 3.4, and 3.5 summarizes the 14-day/testing day averages for each batch correlating to the test day. The sample sizes were 4.0 in. (100 mm) cubes, so only strength from these samples are compared in this section. NWC average compressive strengths were consistent and ranged the same strength from each cast. Cast 1 refers to slab specimens No.1 and 2 and Cast 2 refers to slab specimens No. 3 through 6.

Table 5.3: Comparison of Average Compressive Strengths for Full-Scale Specimens (NWC)

4.0 in. (100 mm) Cube Specimen	Average Compressive Strength, ksi (MPa)		Test Day Age
	14-Day	Test Day	
Cast 1-Batch 1 Cast 1-Batch 2	4.2 (28.9) 3.9 (26.9)	4.7 (32.4)	135
Cast 2-Batch 1 Cast 2-Batch 2	3.7 (25.5) 4.1 (28.2)	4.6 (31.7)	138

Table 5.4: Comparison of Average Compressive Strengths for Joint Specimens (UHPC)

4.0 in. (100 mm) Cube Specimen	Average Compressive Strength, ksi (MPa)		Test Day Age
	14-Day	Test Day	
Specimen 1-Batch 1 Specimen 1-Batch 2	13.8 (95.1) 13.1 (90.5)	14.9 (102.7)	16
Specimen 2-Batch 1 Specimen 2-Batch 2	15.2 (104.8) 15.3 (105.5)	17.3 (119.3)	24
Specimen 3-Batch 1 Specimen 3-Batch 2	17.1 (117.9) 16.5 (113.76)	18.3 (126.17)	24
Specimen 4-Batch 1 Specimen 4-Batch 2	15.9 (109.6) 16.0 (110.3)	16.2 (111.7)	15

UHPC cube specimens had compressive strengths less than anticipated but were acceptable due to the average strengths for the test specimens were considered to be consistently close to the minimum compressive strength [17,000 psi (117.2 MPa)] required for UHPC according to ASTM C1856 (2017). Several factors may have contributed to the lower compressive strengths in UHPC samples, such as poor consolidation, numerous individuals preparing and casting concrete, and overuse of form release. Compressive strength of UHPC is governed primarily by the density of the material microstructure. The greater the particle packing of constituents, the greater the density and resulting compressive strength increases. The second factor that is shown to govern UHPC strengths is the curing regimen. The effects of various curing regimens and their contributions to compressive strength development are well documented, though results are more dependent on the particular mixture proportions under investigation.

The grout cube specimens did not yield favorable average strengths for specimen 5, although the average for were considered to be consistently close. When comparing to specimen 6, the grout strength difference was due to the addition of pea gravel. The addition of pea gravel was used per manufacture recommendation when the joint size thickness is larger than 3 inches (76.2 mm). This showed a minimal average strength increase of about 1.0 ksi, but seen in later results, specimen 5 joint strength was drastically different with the addition of pea gravel.

Table 5.5: Comparison of Average Compressive Strengths for Joint Specimens (Non-Shrink Grout)

4.0 in. (100 mm) Cube Specimen	Average Compressive Strength, ksi (MPa)		Test Day Age
	14-Day	Test Day	
Specimen 5-Batch 1	3.8 (26.1)	4.5 (31.)	23
Specimen 5-Batch 2	4.2 (28.9)		
Specimen 6-Batch 1	5.5 (37.9)	4.6 (31.7)	21
Specimen 6-Batch 2	4.8 (33.1)		

5.1.9 Flexural Strength Test

To assess the flexural strength of the UHPC, flexural testing was conducted according to ASTM C1609 (2012) and were tested (as outlined in Section i.iii) after curing for 28 days at ambient conditions. The results of flexural testing are presented in Table 3.6.

Table 5.6: Flexural Strengths for Joint Specimens (UHPC)

Specimen Prismatic 3x4x16 in. (76x102x406 mm)	MOR Strength, ksi (MPa) 14-day/Test-Day
Specimen 1	11.7 (52.1)
Specimen 2	10.2 (45.4)
Specimen 3	12.1 (53.8)
Specimen 4	12.1 (53.8)



Figure 5.15: UHPC prism at failure under flexural test.

5.1.10 Experimental Results

During the tests, load and displacement were measured by several types of sensors: load cells, linear variable displacement transducers, string potentiometers, and tiltmeters. In total, 22 sensors were used and placed symmetrically on both slabs to compare the loaded slab and non-loaded slab behavior. The slab-joint system was tested with simple support boundary conditions. The load was applied by a single actuator on one slab, so the load was transferred across the joint to the second slab. The load was distributed by a spreader beam to two load points. The specimen was not restrained on the supports and was stable due to friction between the specimen and the supports. The results of the specimen tests were used to analyze the behavior of the UHPC joint as the NWC slabs were loaded. Some specimens were subjected to load-unload cycles. After the cyclic loading the specimens were loaded at a set rate till the system failed. Cyclic load test was performed after a minimum of 14 days of curing of the UHPC joint or non-shrink grouted joint. The cyclic loading was applied at a frequency of 2 to 4 cycles per minute (cpm) for up to 400 cycles. The maximum load at failure varied for each specimen depending on the reinforcement spacing, size, and joint material.

The LVDTs were placed at the top and bottom of the specimens along the length of the specimens joint. LVDTs collected displacement data during each test and are provided for Specimens 1 through 6. As the specimens were loaded, the LVDTs measured the compression of the joint material at the top and gap opening at the bottom.

String potentiometers were attached to the bottom of the specimens on each slab to measure vertical deflections during loading. Although the application of the load was additionally monitored at each load point through the use of the in-house fabricated load cells, the load-deflection behavior presented was based off of the total load applied to the specimens, measured by the hydraulic actuator load cell. The total load (y-axis) recorded by the actuator load cells was plotted versus the vertical deflection (x-axis) captured.

When tiltmeter data was available, the data provided additional data on the rotation behavior exhibited by the specimen. Data recorded by tiltmeters (x-axis) is plotted versus total actuator load (y-axis) for the specimens with this data available. Note that data recorded at NE and SE locations are represented as negative rotation, and NW and SW rotations as positive.

5.1.10.1 Specimen 1

The reinforcement in the joint for Specimen 1 utilized the typical NMDOT joint lap splice configuration, No. 4 (No. 13) bars at spacing of 6 in. (152.4 mm) with a lap length of 4.5 in. (114.3 mm). Figure 5.16 through Figure 5.21 show load versus vertical deflection and Figure 5.22 through Figure 5.29 showed the load versus transverse deflection behavior of Specimen 1 under cyclic loading. Approximately 200 cycles were applied at a constant rate of 2 cpm. During the load-unload cycles, the specimen was loaded to between 19,000 lb (86.7 kN) to 21,000 lb (93.4 kN). As can be seen in Figure 5.16, small residual deformations occurred after each cycle, indicating that the system had some damage occurring such as debonding and or cracking. This can be seen in Figure 5.36 as initial cracking occurred. Figure 5.22 shows the specimen softening at the approximate 19,500 lb (93.4 kN). LVTD data in. Loss of bond and cracking can be seen as the load was unloaded; permanent deformation in the joint of the system was observed. This can be contributed to the fact that gap opening at the slab-joint interface at the bottom of the joint was observed. Figure 5.27 through Figure 5.29, indicate that separation at the joint and slab specimen continued at each cycle, but also show that the gap opening did not increase at the peak of loading. This can be closely related to the fact that the failure of the testing specimen occurred at the application of load on the slab. As the load increased during loading the bond between the UHPC and NWC was lost, but as the load increased the crack on the east slab would open and during each cycle. As a result, the LVDTs the gap at the joint did not continue to open, therefore do not correlate to the large vertical deflections as shown in Figure 5.16 through Figure 5.21. This can relate to the increase of cross-sectional reinforcement creating a relatively stiff structure. It can be seen in Figure 5.30 through Figure 5.33, as the specimens were loaded on the east slab, an increase of rotation on that east slab (tiltmeter 2 and 5) was the result of the slab cracking on the same side and corelated to the larger deflection as well.

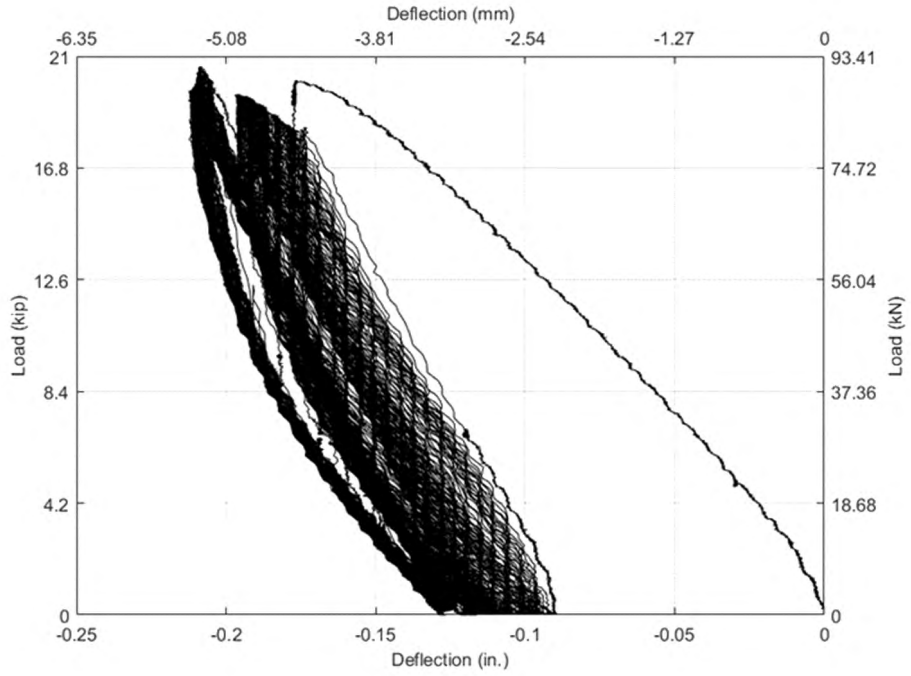


Figure 5.16: Specimen No. 1- cyclic test load versus vertical deflection (SP 0).

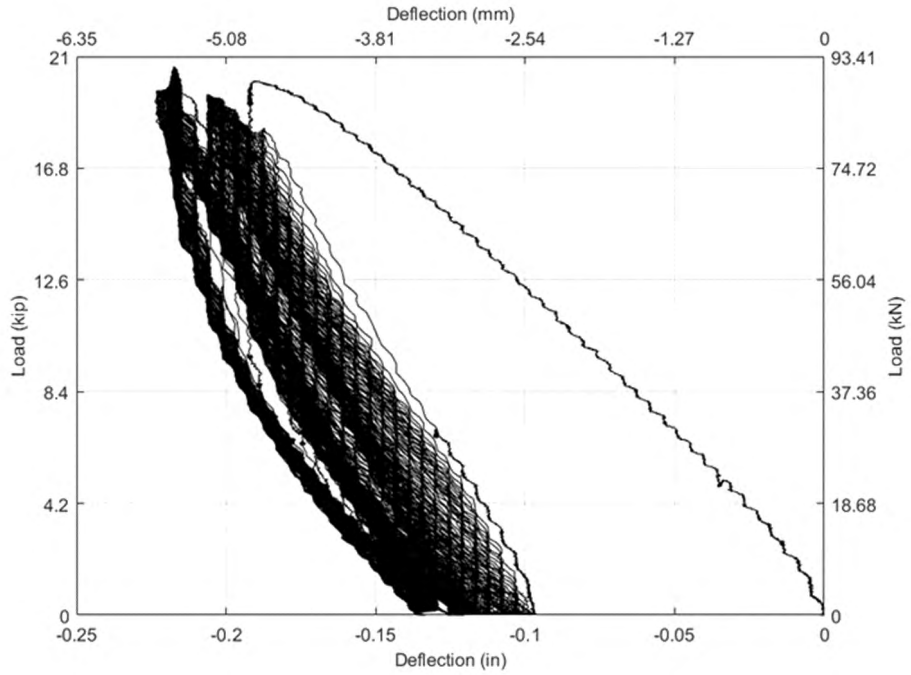


Figure 5.17: Specimen No. 1- cyclic test load versus vertical deflection (SP 1).

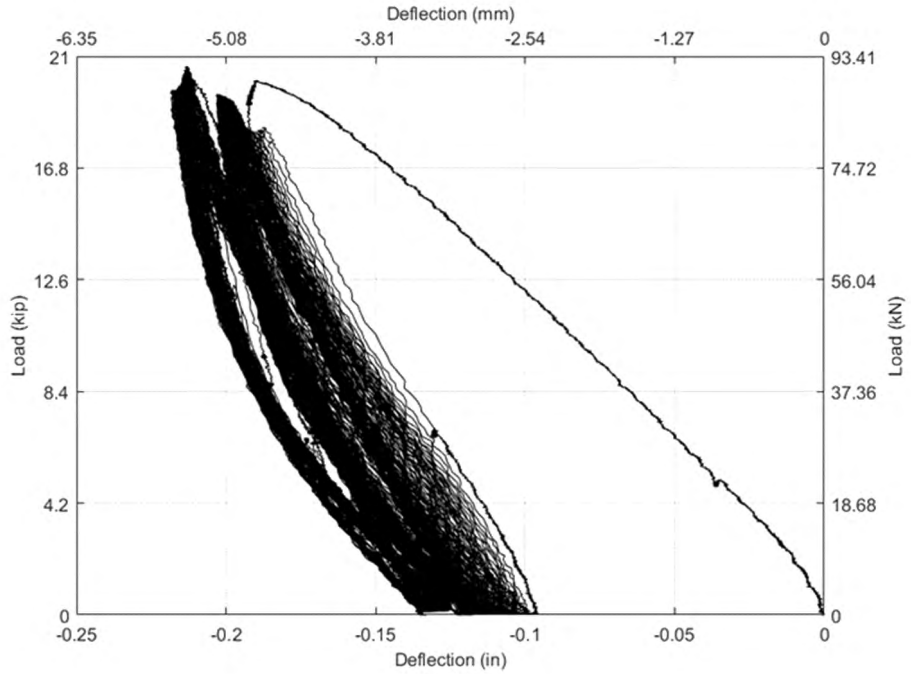


Figure 5.18: Specimen No. 1- cyclic test load versus vertical deflection (SP 2).

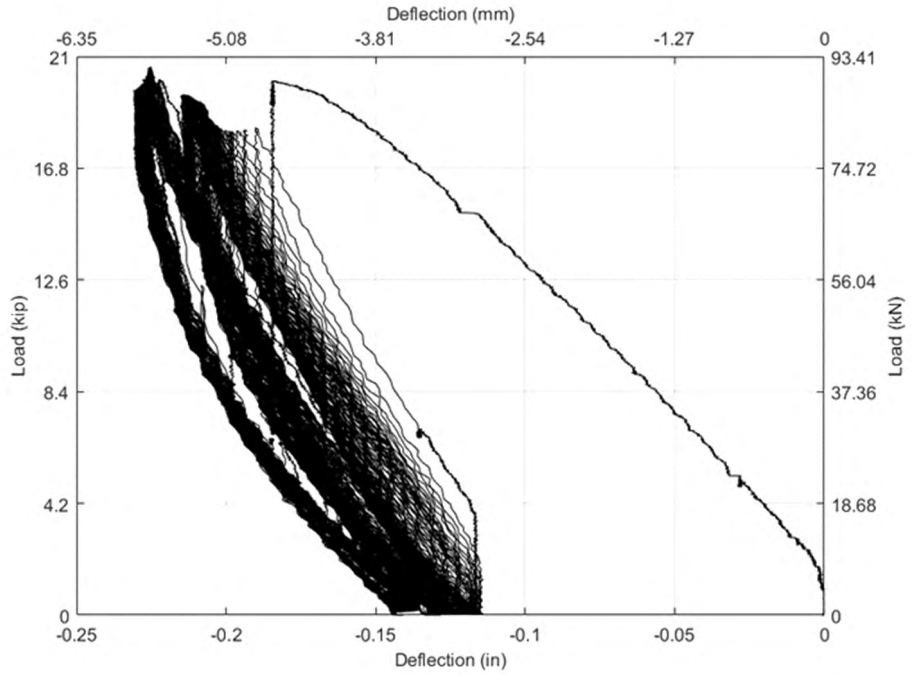


Figure 5.19: Specimen No. 1- cyclic test load versus vertical deflection (SP 4).

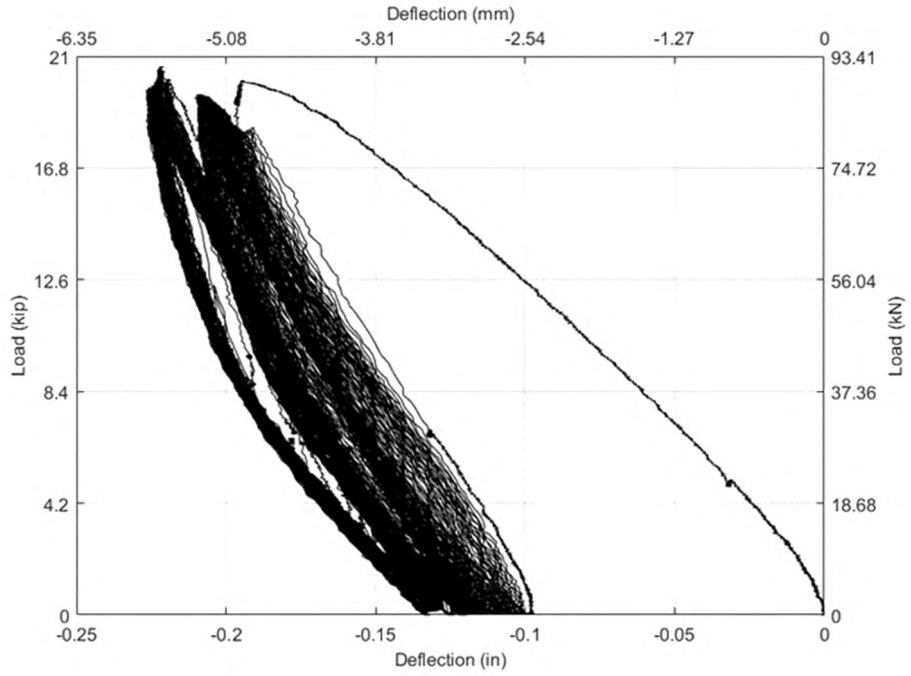


Figure 5.20: Specimen No. 1- cyclic test load versus vertical deflection (SP 5).

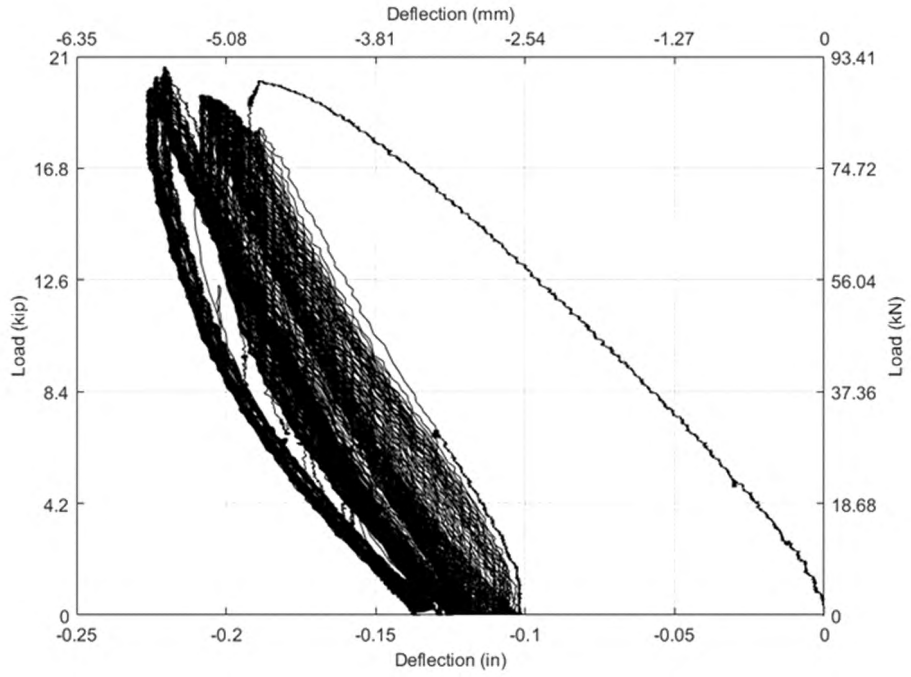


Figure 5.21: Specimen No. 1- cyclic test load versus vertical deflection (SP 7).

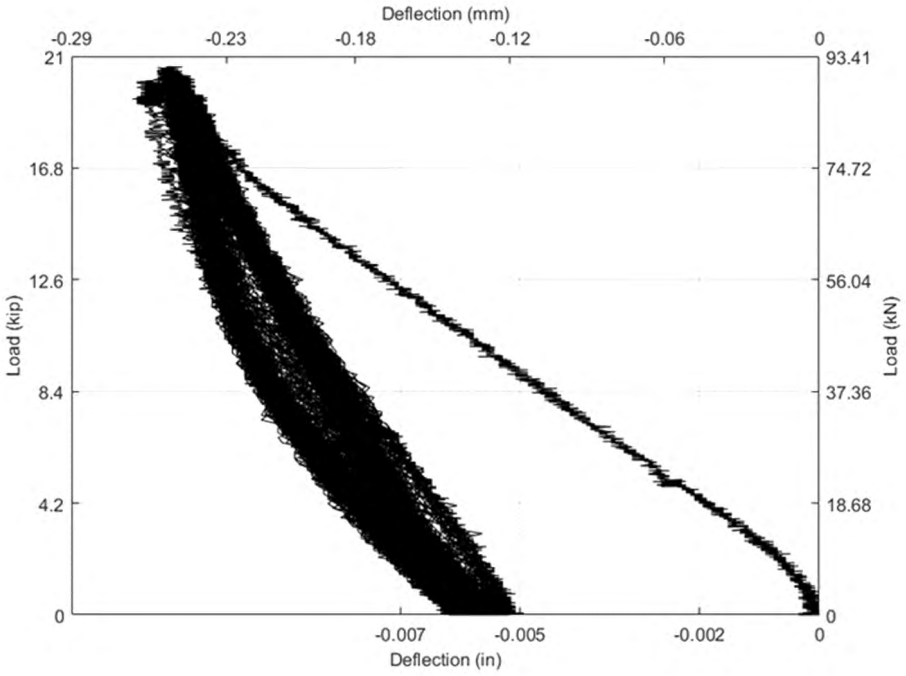


Figure 5.22: Specimen No. 1- cyclic test load versus transverse deflection (LVDT 2).

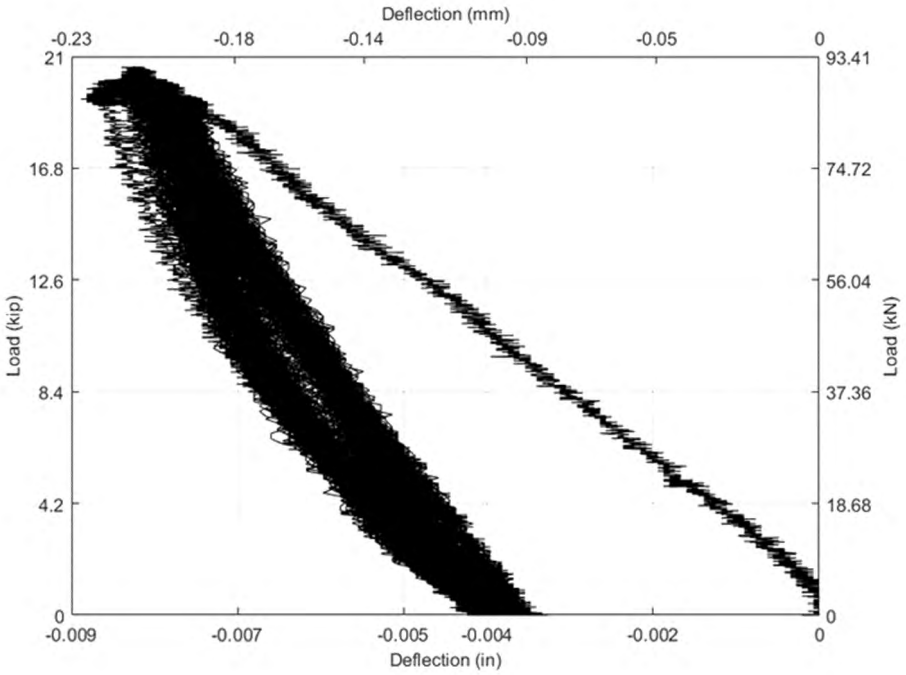


Figure 5.23: Specimen No. 1- cyclic test load versus transverse deflection (LVDT 3).

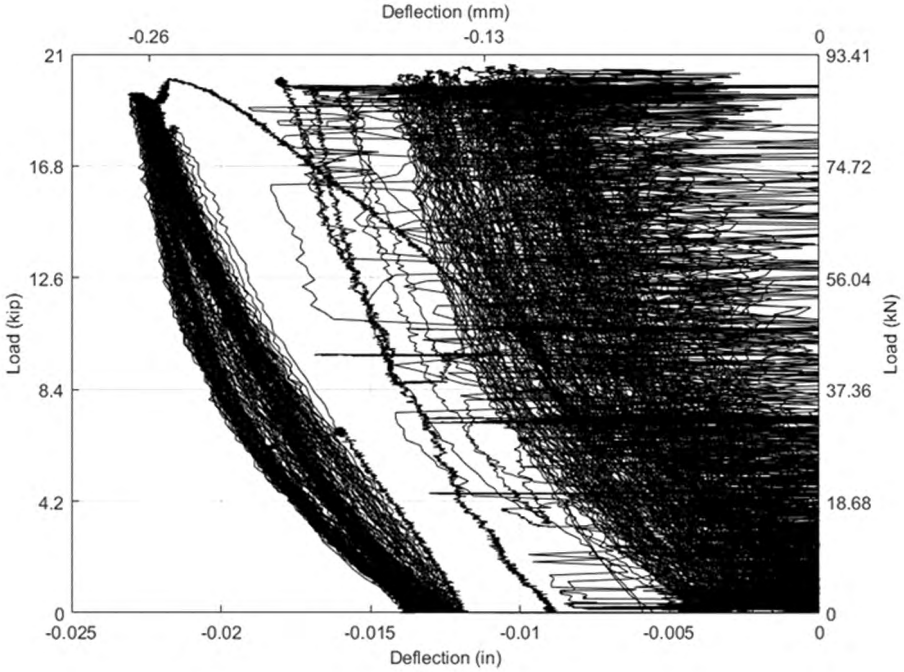


Figure 5.24: Specimen No. 1- cyclic test load versus transverse deflection (LVDT 4).

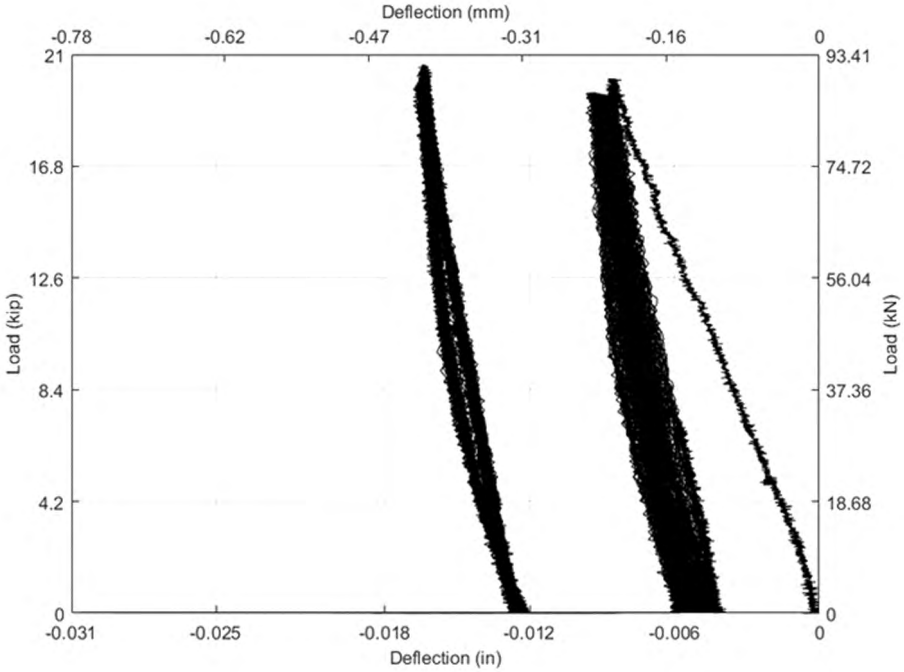


Figure 5.25: Specimen No. 1- cyclic test load versus transverse deflection (LVDT 5).

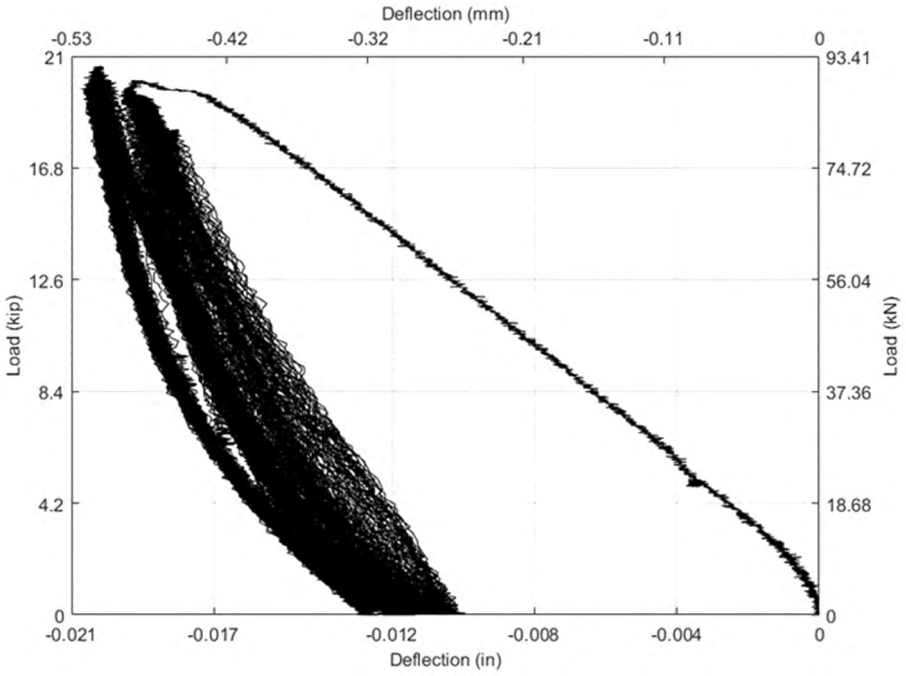


Figure 5.26: Specimen No. 1- cyclic test load versus transverse deflection (LVDT 6).

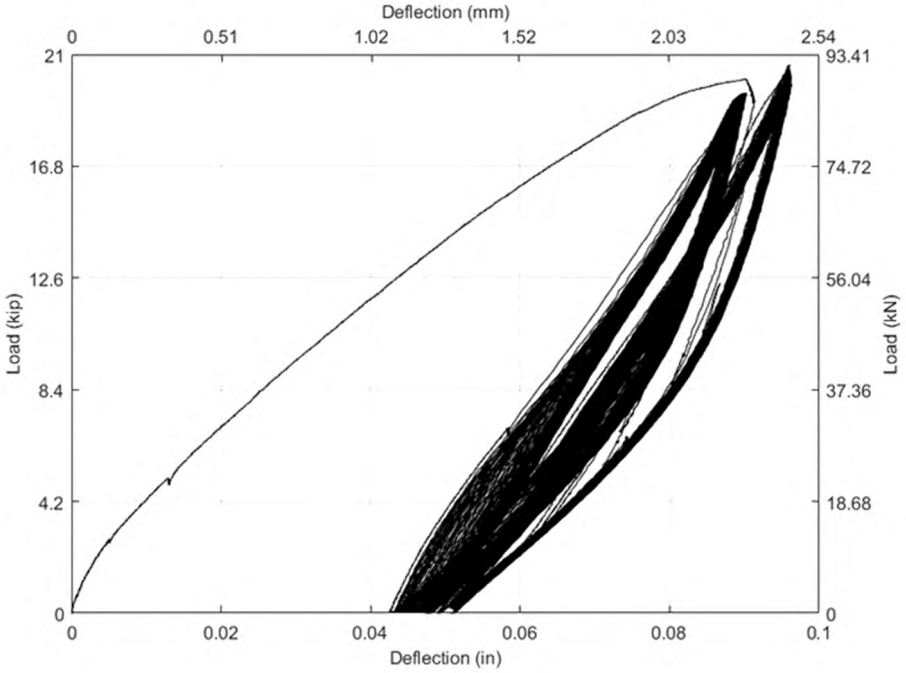


Figure 5.27: Specimen No. 1- cyclic test load versus transverse deflection (LVDT 7).

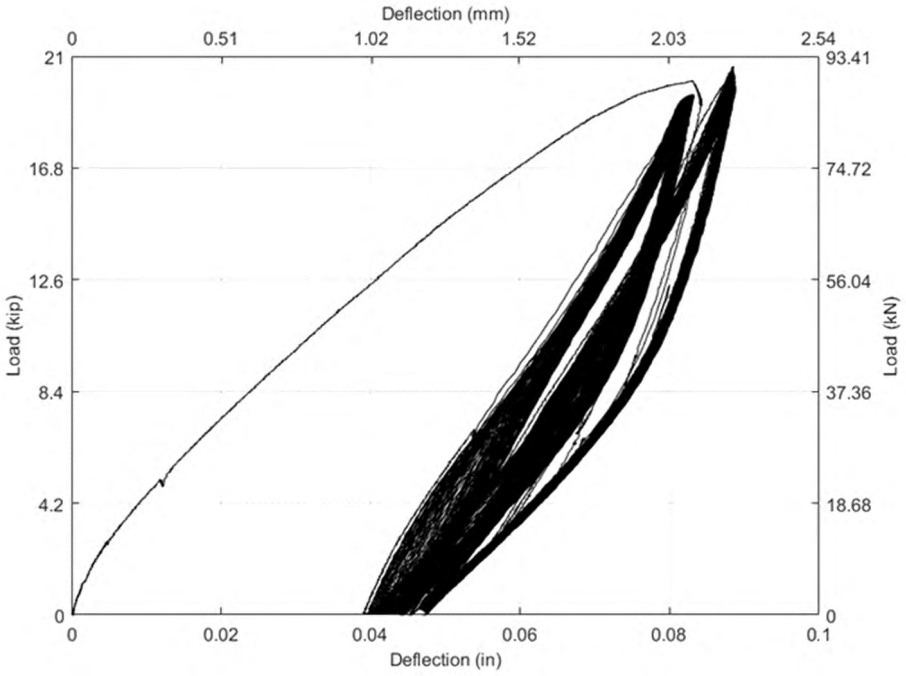


Figure 5.28: Specimen No. 1- cyclic test load versus transverse deflection (LVDT 8).

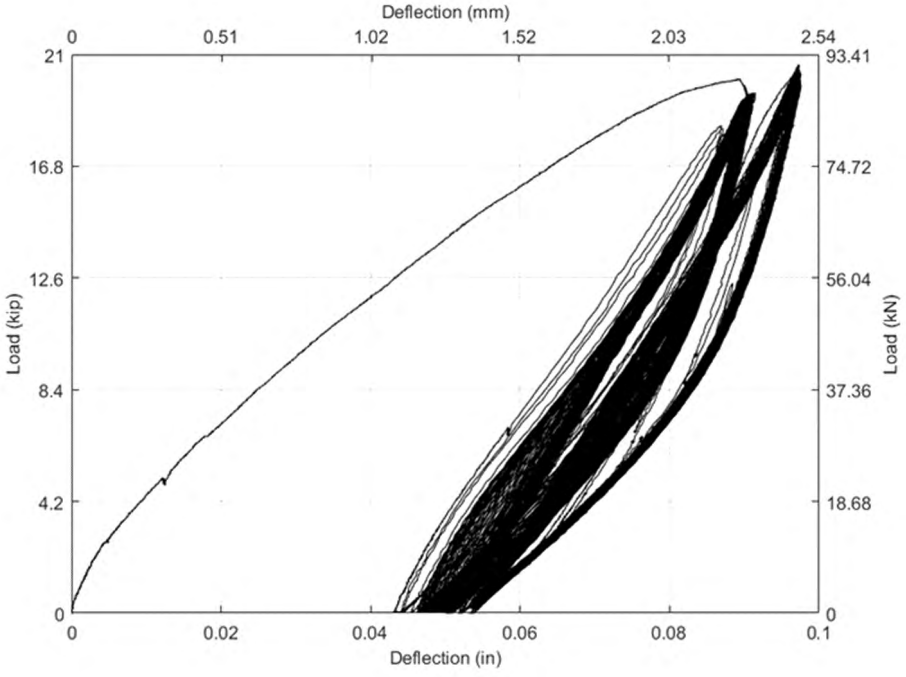


Figure 5.29: Specimen No. 1- cyclic test load versus transverse deflection (LVDT 9).

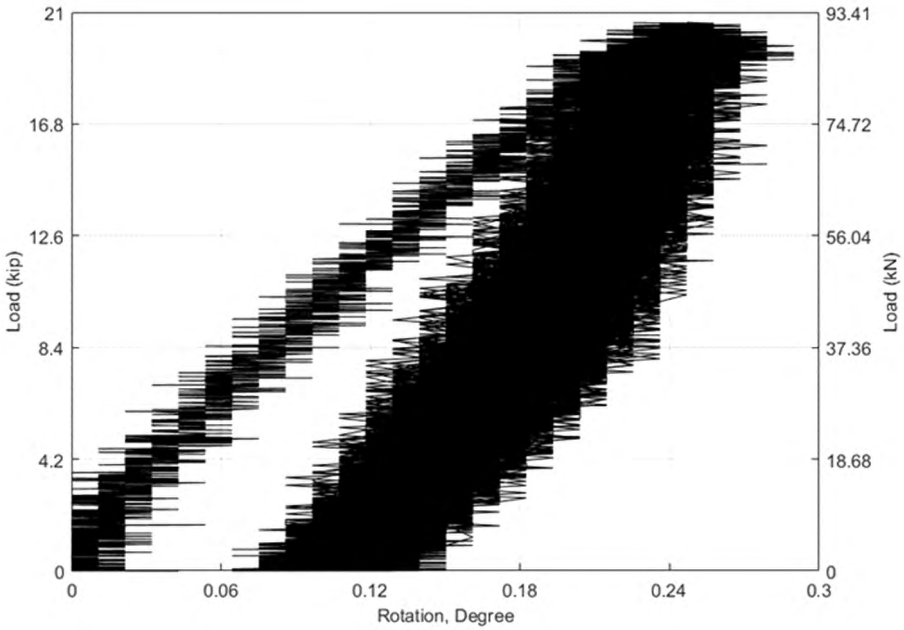


Figure 5.30: Specimen No. 1- cyclic test load versus rotation (Tiltmeter 1).

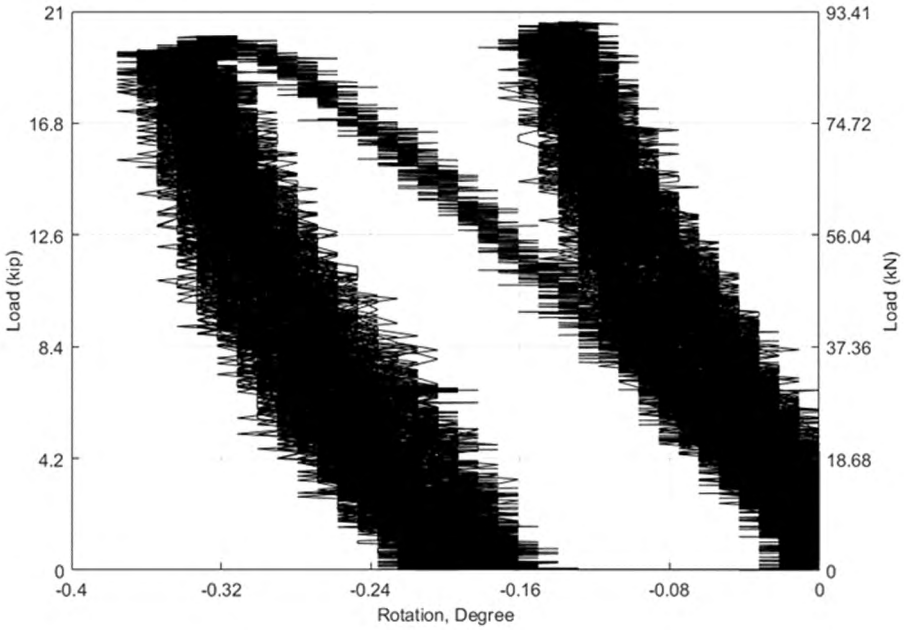


Figure 5.31: Specimen No. 1- cyclic test load versus rotation (Tiltmeter 2).

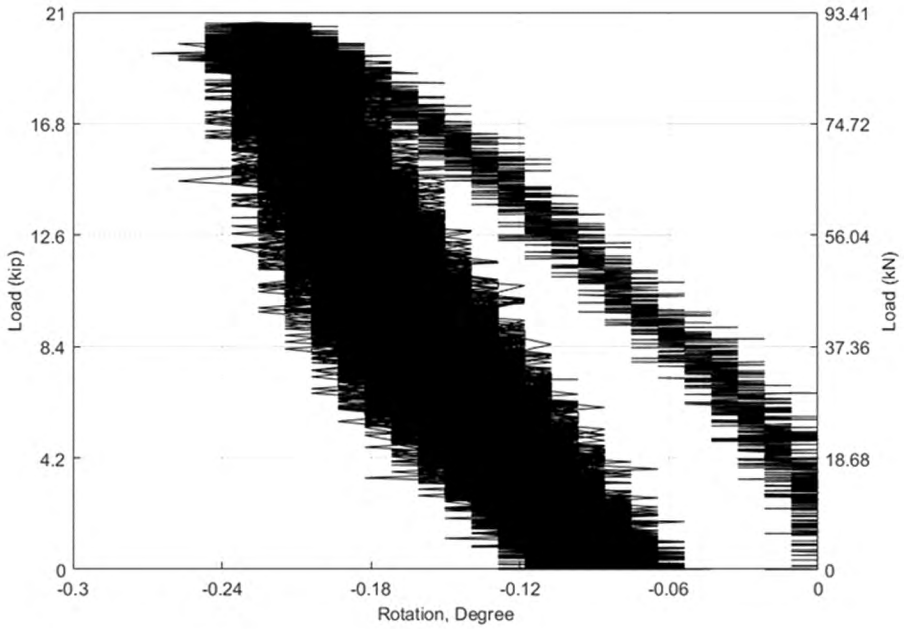


Figure 5.32: Specimen No. 1- cyclic test load versus rotation (Tiltmeter 4).

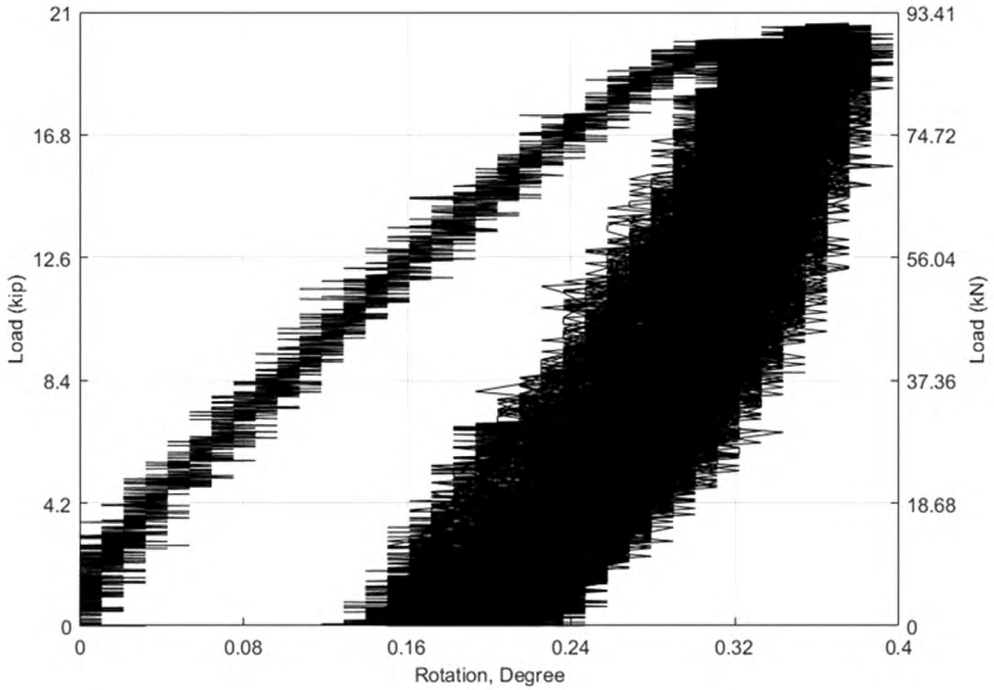


Figure 5.33: Specimen No. 1- cyclic test load versus rotation (Tiltmeter 5).

After the cyclic test was complete, the slab was unloaded and then loaded at a rate of 0.025 in./minute (0.64 mm/minute) to failure. While the system was being loaded, a crack formed approximately 1.5 ft (0.45 m) away from the joint directly under the point of application of the load, as can be seen in Figure 4.22. Figure 4.19 shows the specimen failure occurred at approximately 26,000 lb (115.7 kN). Figure 5.37 and Figure 5.38 show the specimen at failure. Failure occurred as the cracks at the point of application of the load propagated and continued in the longitudinal direction along the reinforcement in the slab to the other side of the system (Figure 5.38). Figure 5.34 shows the vertical deflection comparison between each side of the testing specimens joint. SPs 0, 1 and 2 did not deflect as much as SP4, 5 and 7. This is because SPs 4, 5, and 7 were on the loaded side of the specimen, as well as where the separation of the joint and cracking of the slab occurred. It can be seen in Figure 5.34, as the load increased to approximately 22 kips (98 kN); the vertical deflection recorded by SPs 0 through 7 deflected the same on both sides of the joint. When initial cracking occurred in the slab, a loss of strength can be observed as a "drop" in the data, as the crack propagated towards the flexural reinforcement. Once the reinforcement was engaged, the specimen had an increase in strength until yielding of the reinforcement occurred. Then, the specimen started to deflect more with little additional load.

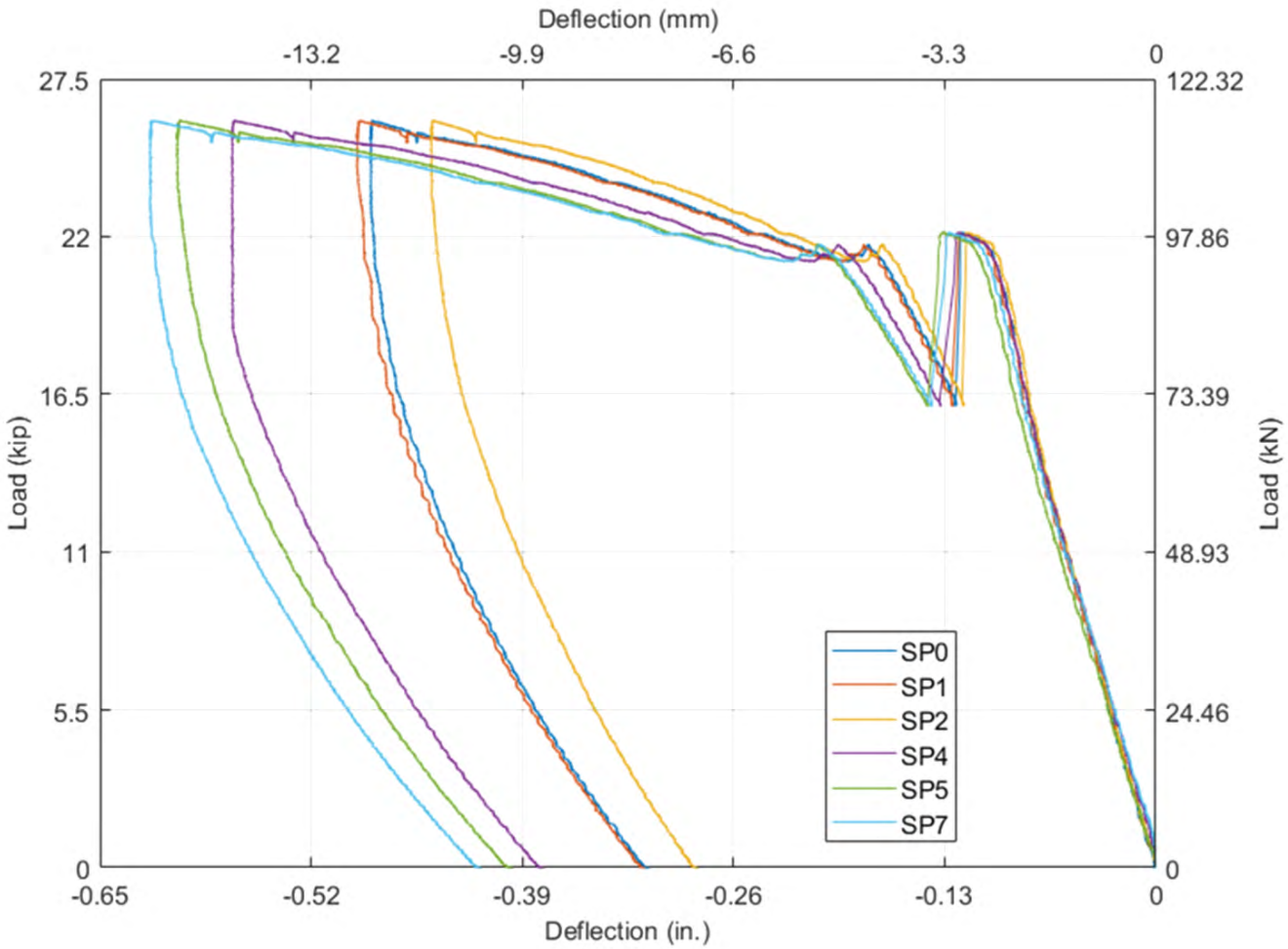


Figure 5.34: Specimen No. 1- failure test load versus vertical deflection.

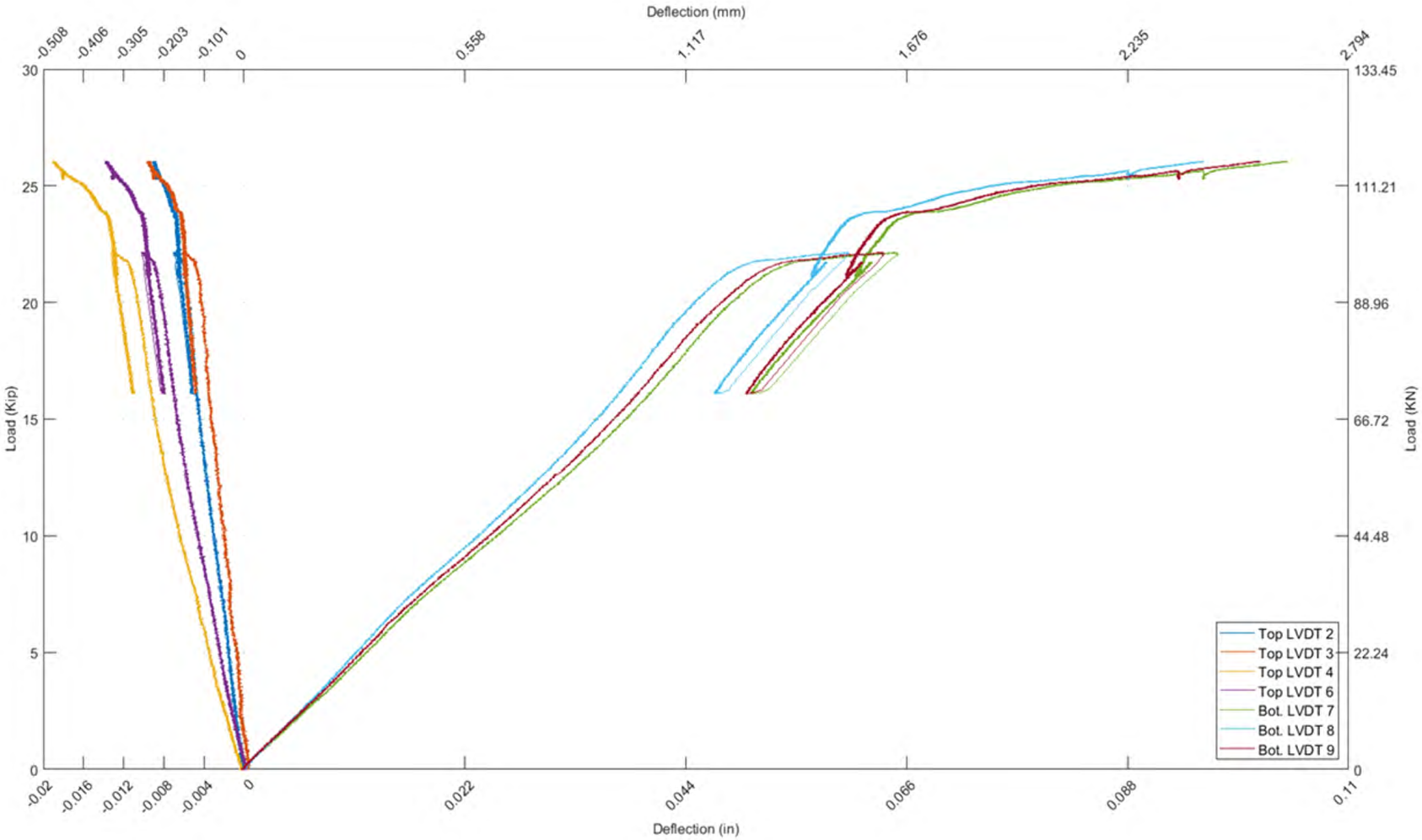


Figure 5.35: Specimen No. 1- failure test load versus transverse deflection.

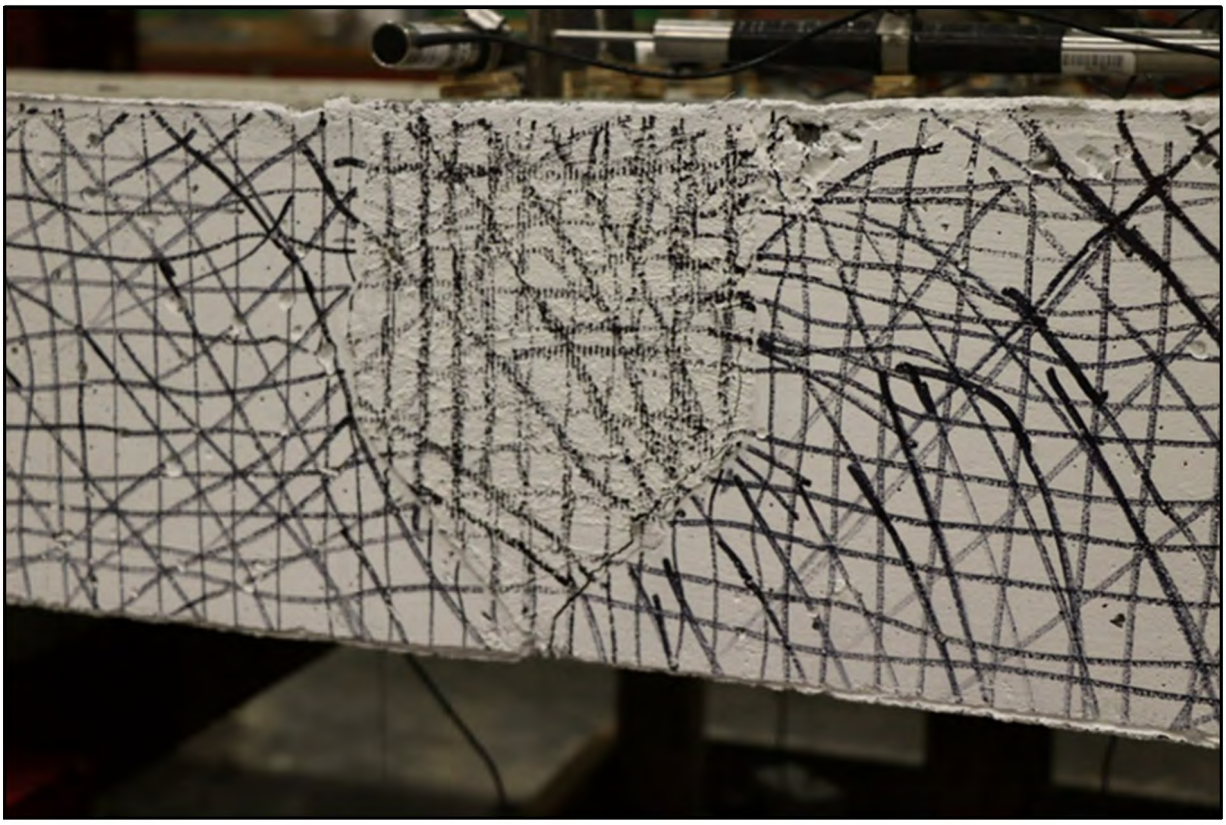


Figure 5.36: Specimen No. 1- initial separation at bond of joint.



Figure 5.37: Specimen No. 1- failure at south face.

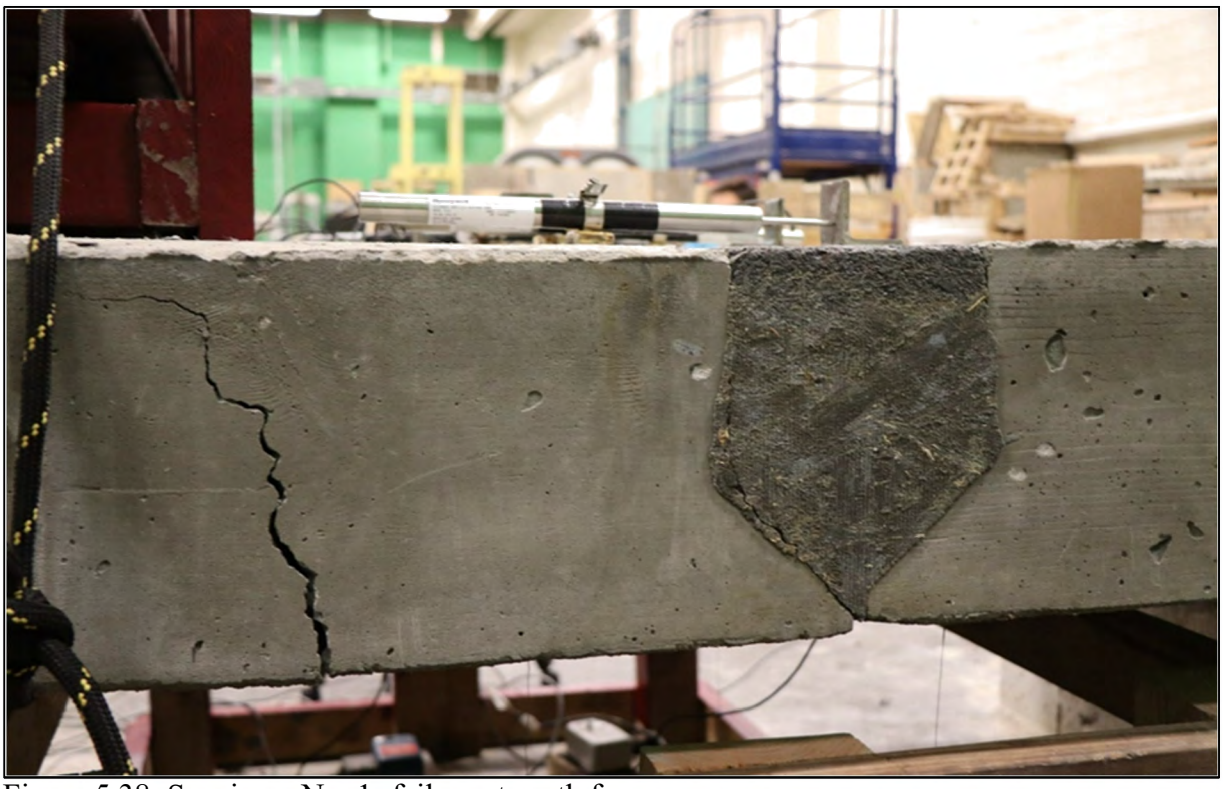


Figure 5.38: Specimen No. 1- failure at north face.

5.1.10.2 Specimen 2

Specimen 2 joint reinforcement utilized the same NMDOT top slab reinforcement but the joint lab splice configuration which was increased to a spacing of 12 in. (304.8 mm) but keeping the No. 4 (No.13) rebar and lap length of 4.5 in. (114.3 mm) the same as test Specimen 1. Figure 5.39 through Figure 5.44 shows the load-deflection behavior of Specimen 2 during the cyclic test. The test took roughly 3 hours to complete 400 cycles. The cycle loading was at 2 cpm fore 200 cycles and then increased to 4 cpm for the remainder of the test. The specimens load was maintained around 10,000 lb (44.5 kN) during the first 200 cycles and then changed to a just under 12,000 lb (53.4 kN) for the last 200 cycles. As can be seen in Figure 5.39, residual displacements occurred after each cycle. Therefore, the system had some minor damage occurring. Initial cracking can be seen in Figure 5.39. The specimen carried approximately 11,200 lb (49.8 kN), prior to opening a crack at the joint. LVTD data, shown in Figures 4.30 through 4.38, indicate that the concrete at the top of the joint and specimen deflected more as each cycle occurred more so than Specimen 1. The larger deflections measured in Specimen 2, when compared to Specimen 1, can be attributed to the decrease in cross section area of reinforcement (greater spacing). Permanent deformation was recorded. This can be contributed to the fact that partial separation at the bottom of the joint was observed, increasing the amount of vertical deflection which induced larger compressive stresses at the top of the joint. Figure 5.45 through Figure 5.47, indicate that separation at the joint and slab specimen continued at each cycle, but also show that the gap opening increased at the peak of loading. This can be closely related to the fact that the failure of the testing specimen was at the joint of the specimen. As the load increased during the cyclic test, the bond separated more during each cycle. Due to the weak point in the system on the west side of the specimens joint, LVDT 5 (Figure 5.48) showed larger compressive deformations than LVDT 3 (Figure 5.46). Figure 5.39 through Figure 5.44 indicate a smaller initial stiffness in the specimens compared to Specimen 1, due to the decrease in cross sectional area of reinforcement. It can be seen in Figure 5.53 through Figure 5.56, an increase of rotation (tiltmeter 1 and 4) furthest from the load was the result of the slab and joint material separating on the same side of the tiltmeters and correlated to the larger deflections as well shown in SPs 0 and 1 (Figure 5.39 and Figure 5.40).

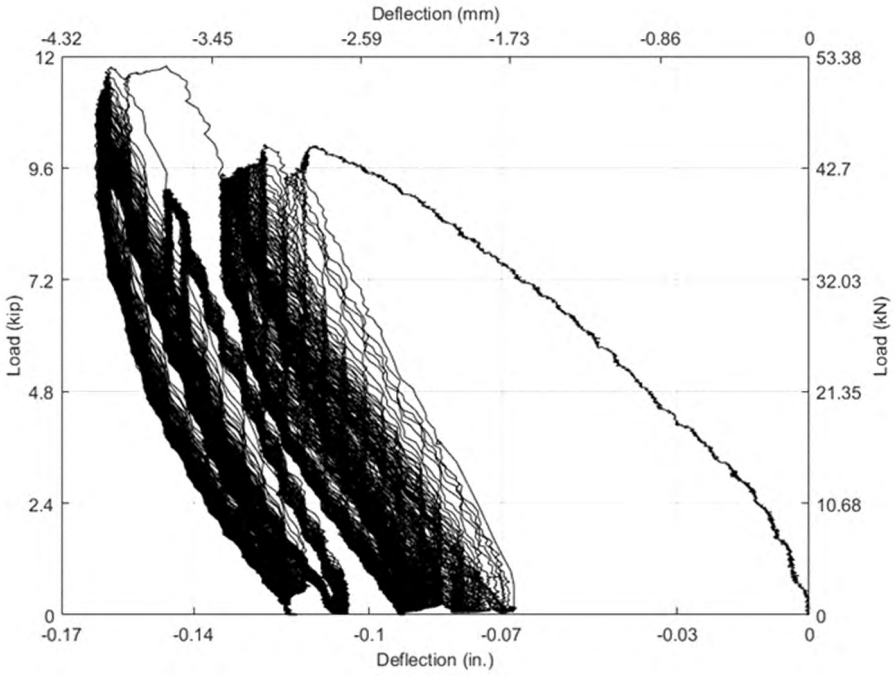


Figure 5.39: Specimen No. 2- cyclic test load versus vertical deflection (SP 0).

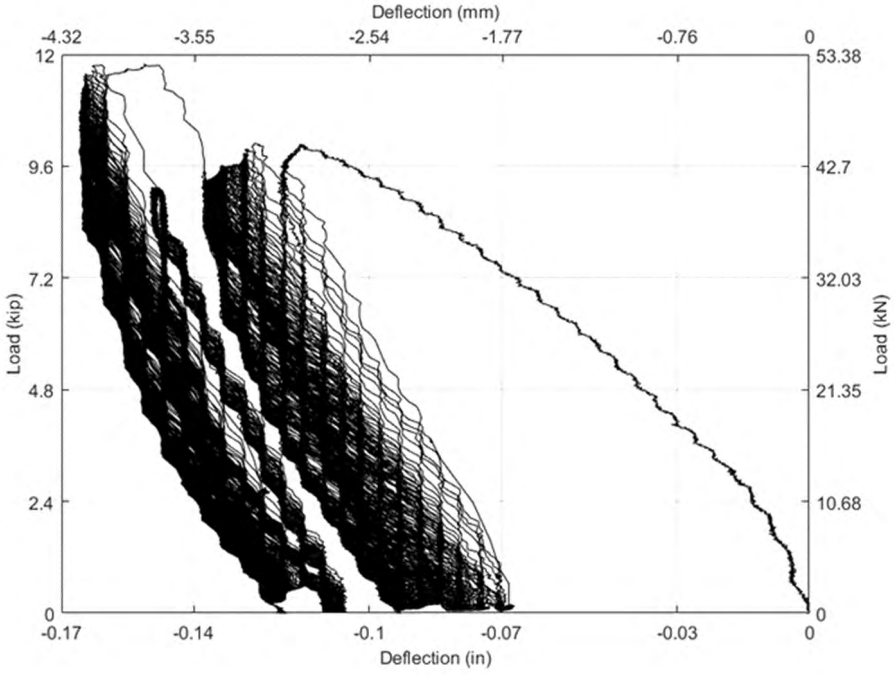


Figure 5.40: Specimen No. 2- cyclic test load versus vertical deflection (SP 1).

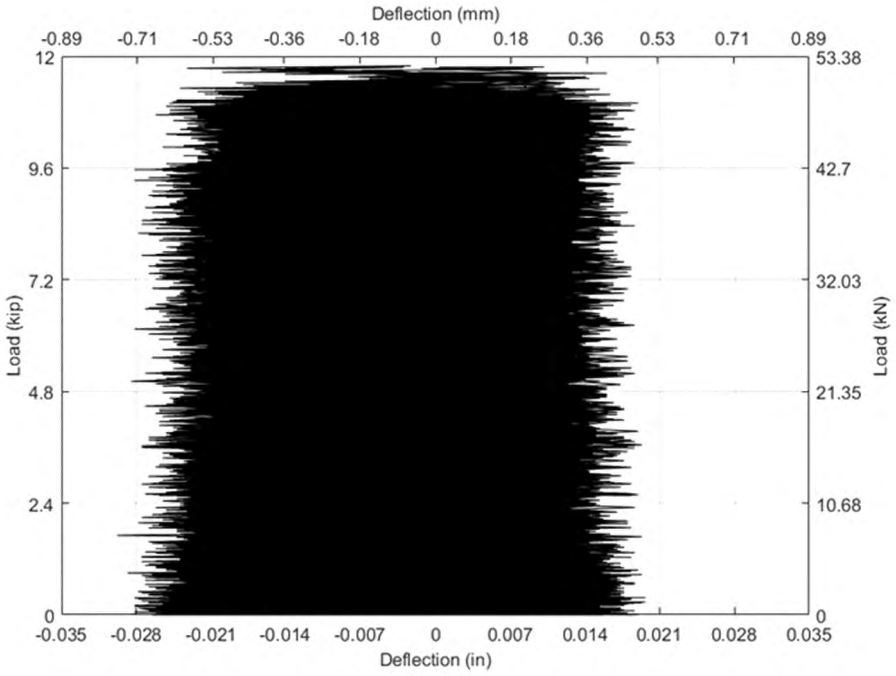


Figure 5.41: Specimen No. 2- cyclic test load versus vertical deflection (SP 2).

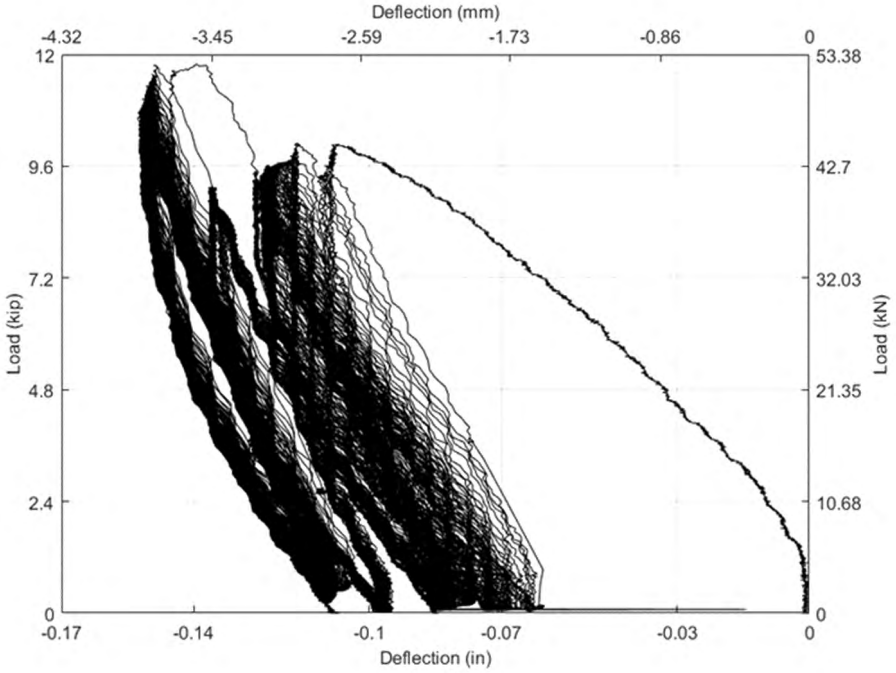


Figure 5.42: Specimen No. 2- cyclic test load versus vertical deflection (SP 4).

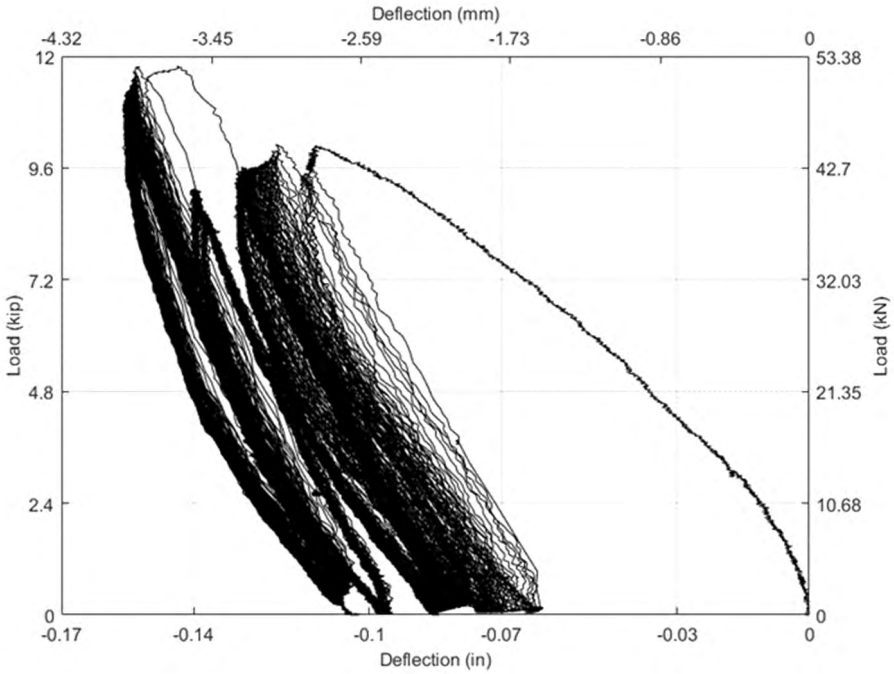


Figure 5.43: Specimen No. 2- cyclic test load versus vertical deflection (SP 5).

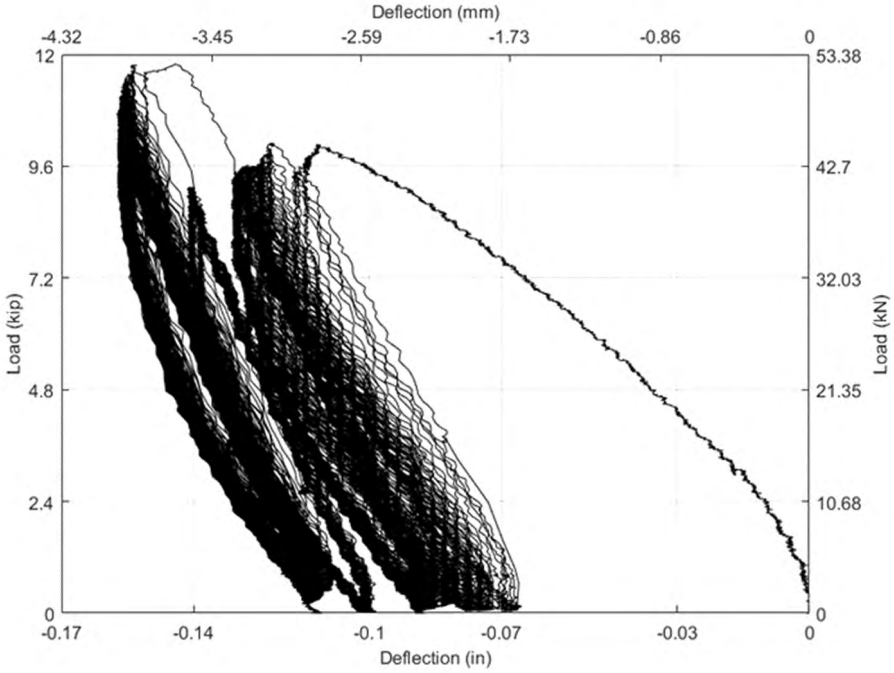


Figure 5.44: Specimen No. 2- cyclic test load versus vertical deflection (SP 7).

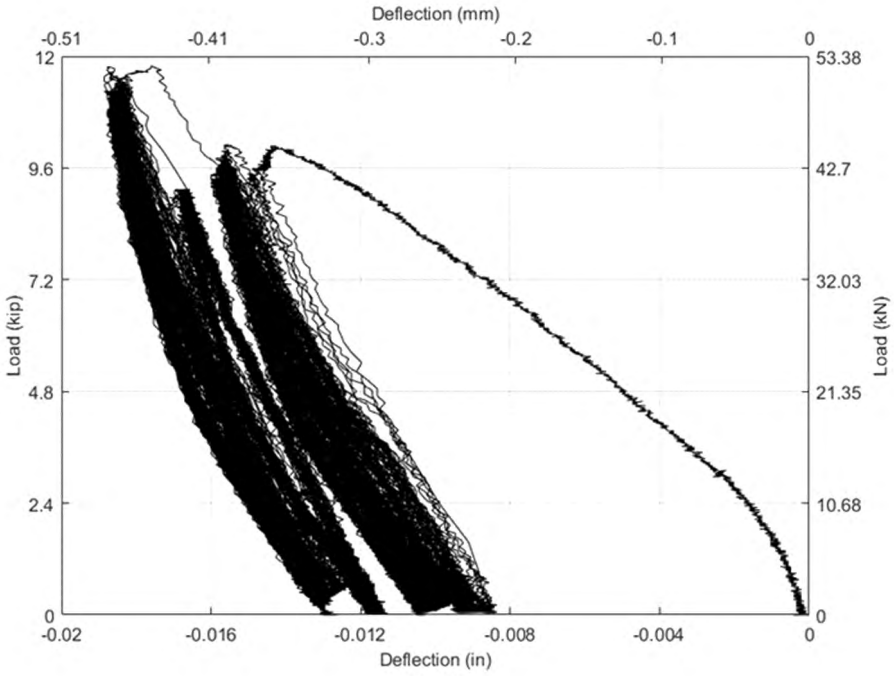


Figure 5.45: Specimen No. 2- cyclic test load versus transverse deflection (LVDT 2).

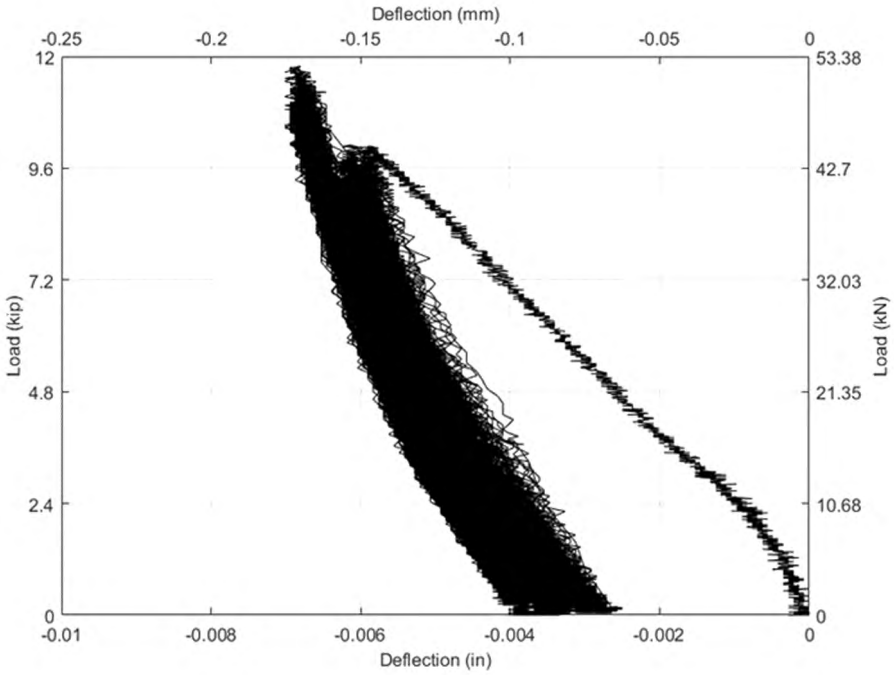


Figure 5.46: Specimen No. 2- cyclic test load versus transverse deflection (LVDT 3).

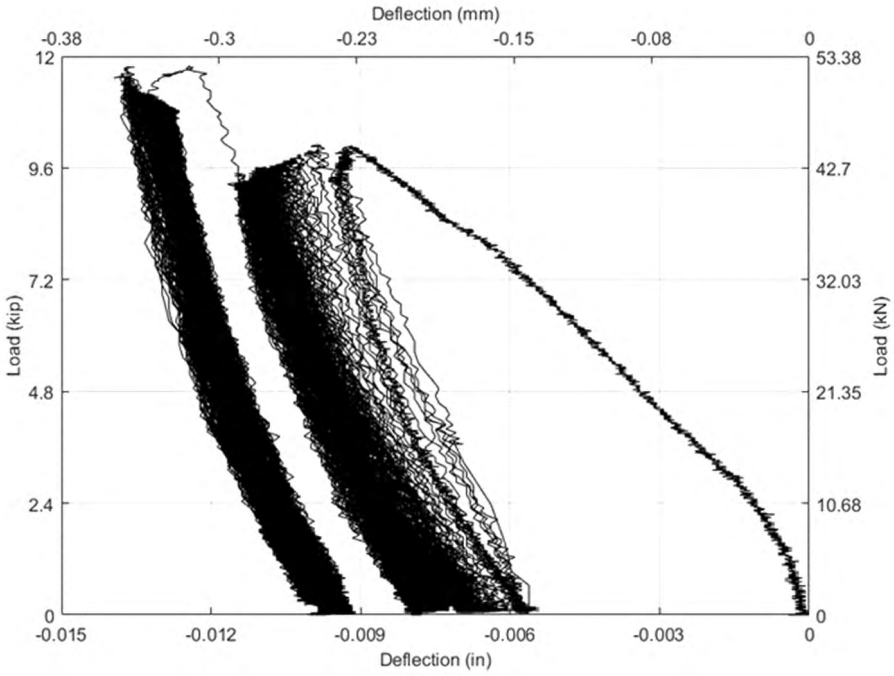


Figure 5.47: Specimen No. 2- cyclic test load versus transverse deflection (LVDT 4).

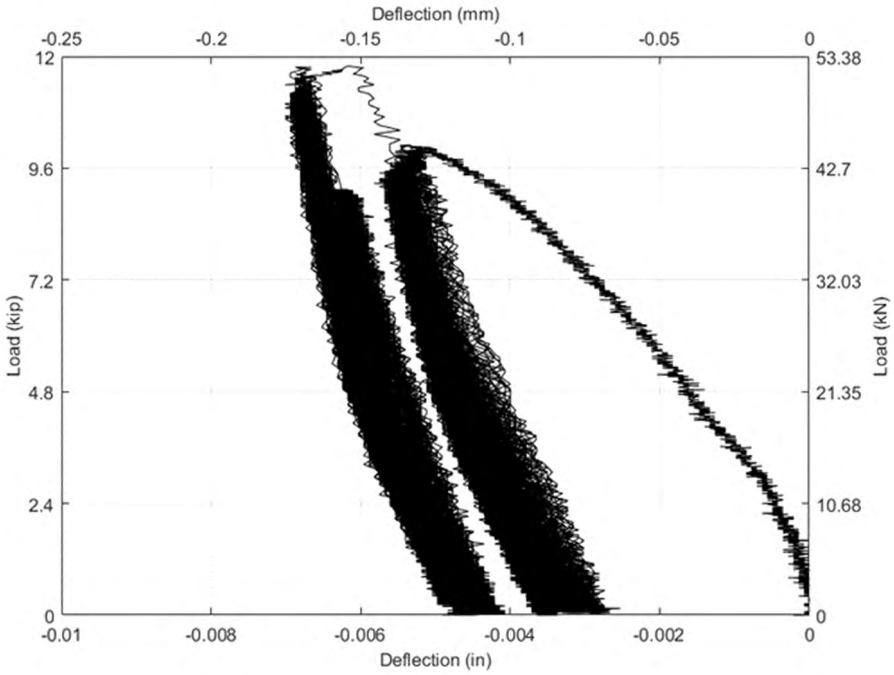


Figure 5.48: Specimen No. 2- cyclic test load versus transverse deflection (LVDT 5).

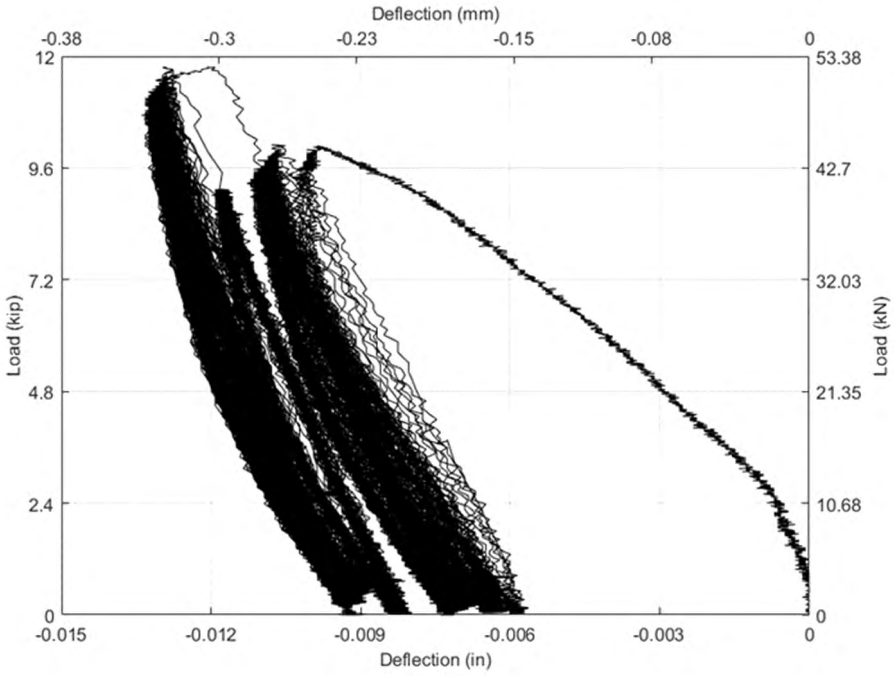


Figure 5.49: Specimen No. 2- cyclic test load versus transverse deflection (LVDT 6).

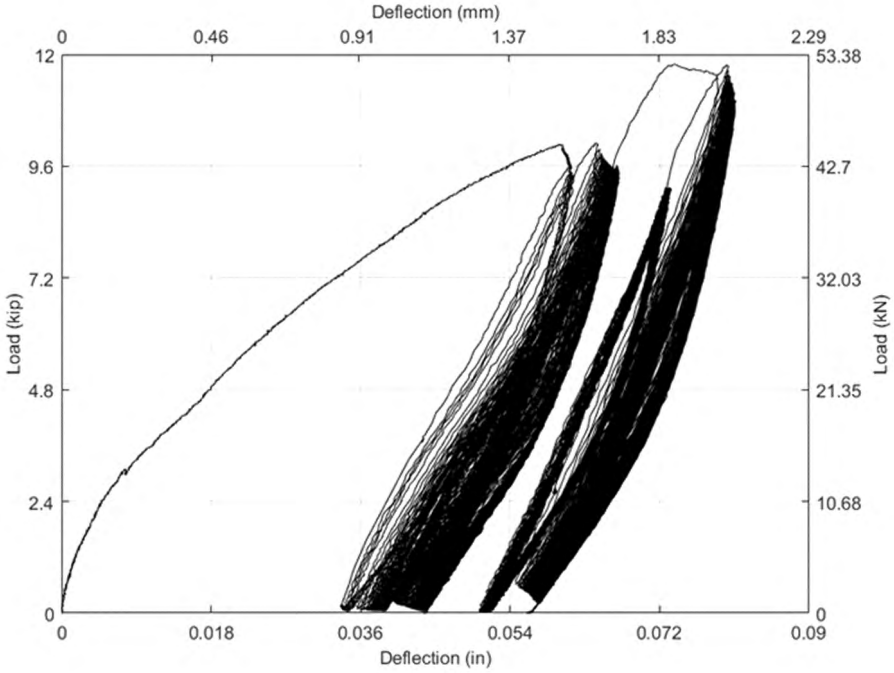


Figure 5.50: Specimen No. 2- cyclic test load versus transverse deflection (LVDT 7).

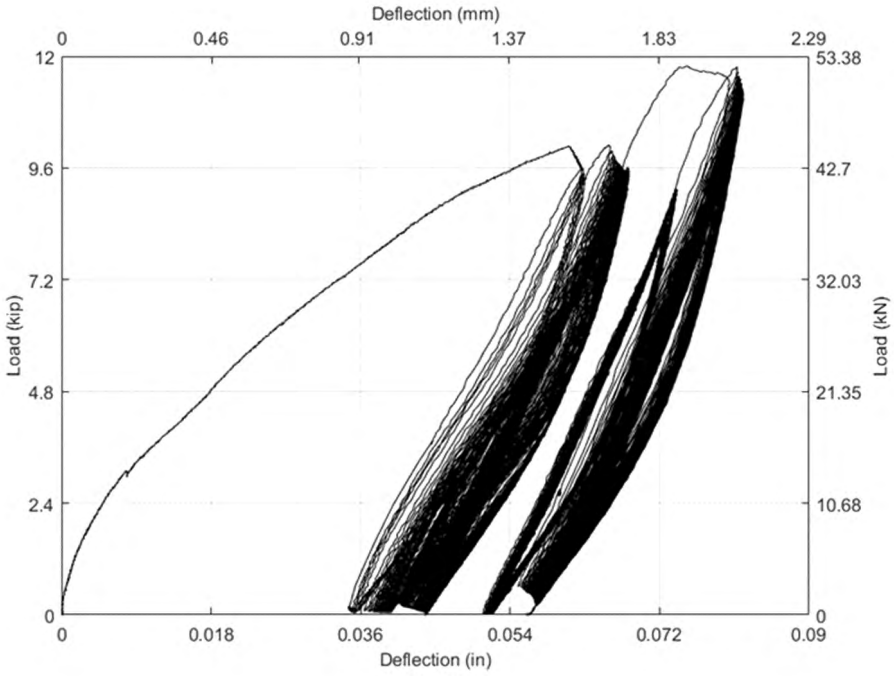


Figure 5.51: Specimen No. 2- cyclic test load versus transverse deflection (LVDT 8).

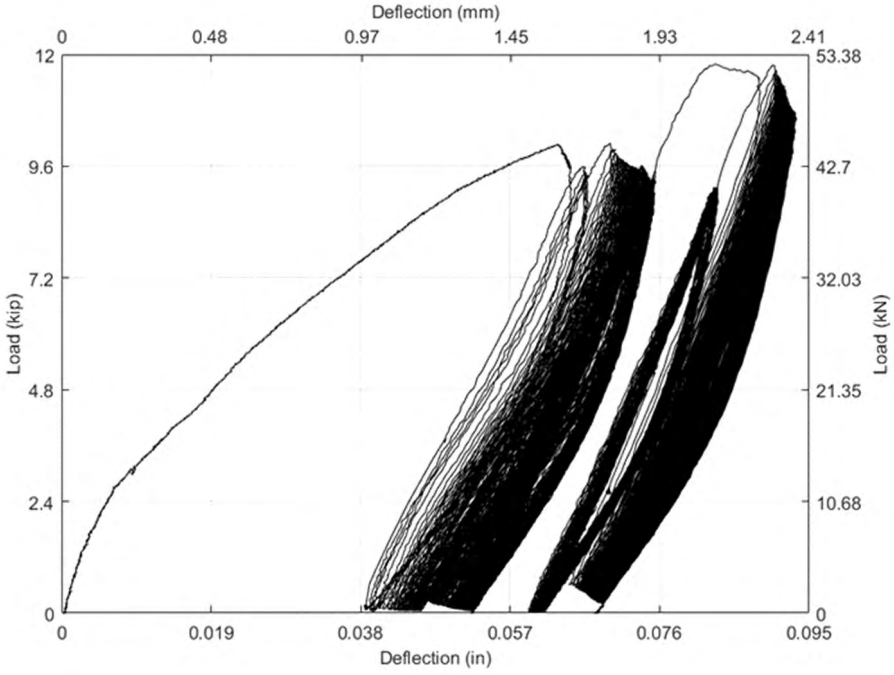


Figure 5.52: Specimen No. 2- cyclic test load versus transverse deflection (LVDT 9).

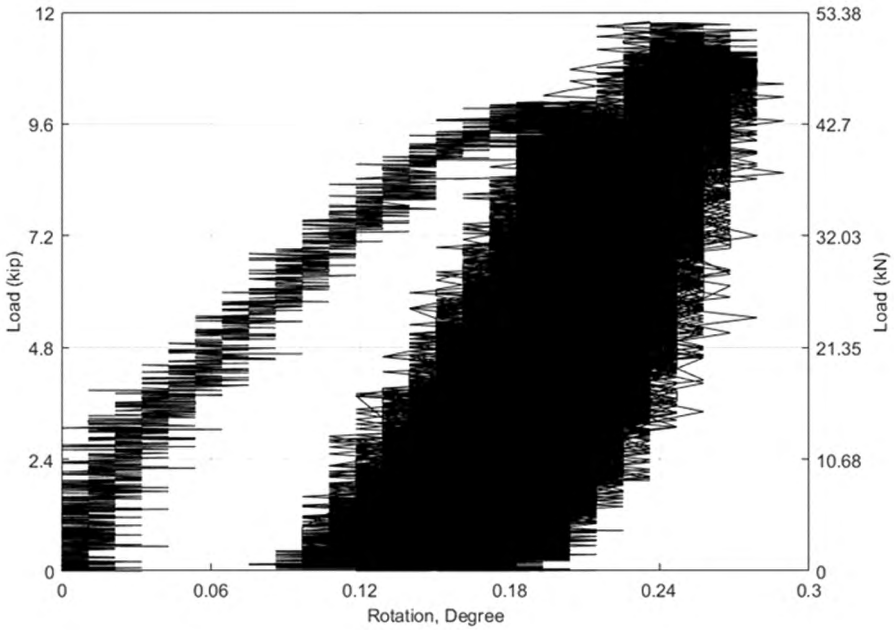


Figure 5.53: Specimen No. 1- cyclic test load versus rotation (Tiltmeter 1).

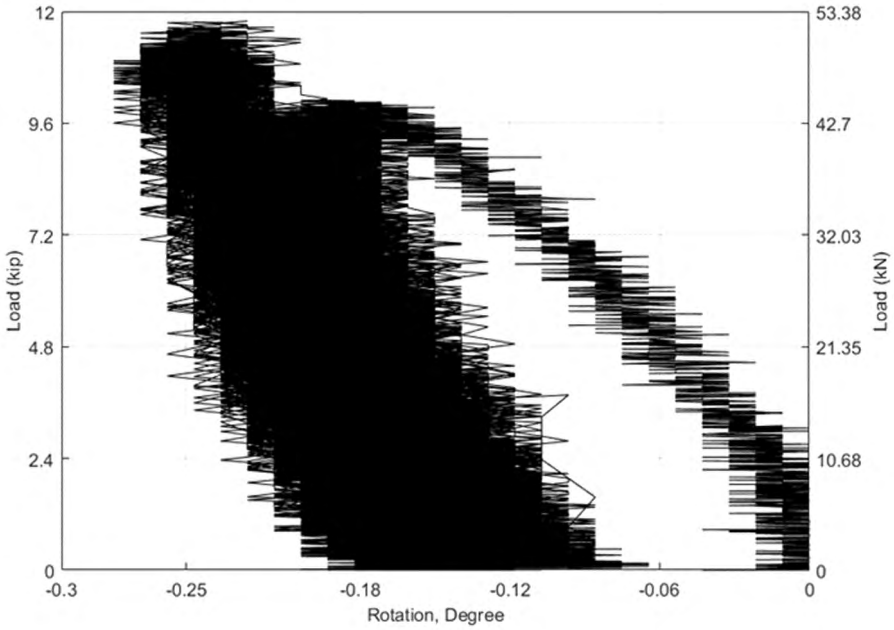


Figure 5.54: Specimen No. 1- cyclic test load versus rotation (Tiltmeter 2).

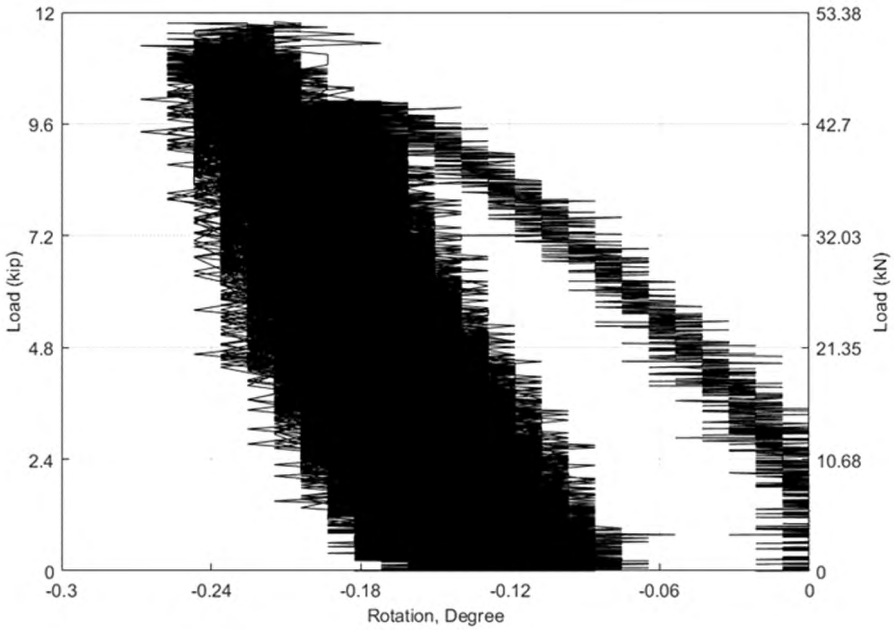


Figure 5.55: Specimen No. 1- cyclic test load versus rotation (Tiltmeter 4).

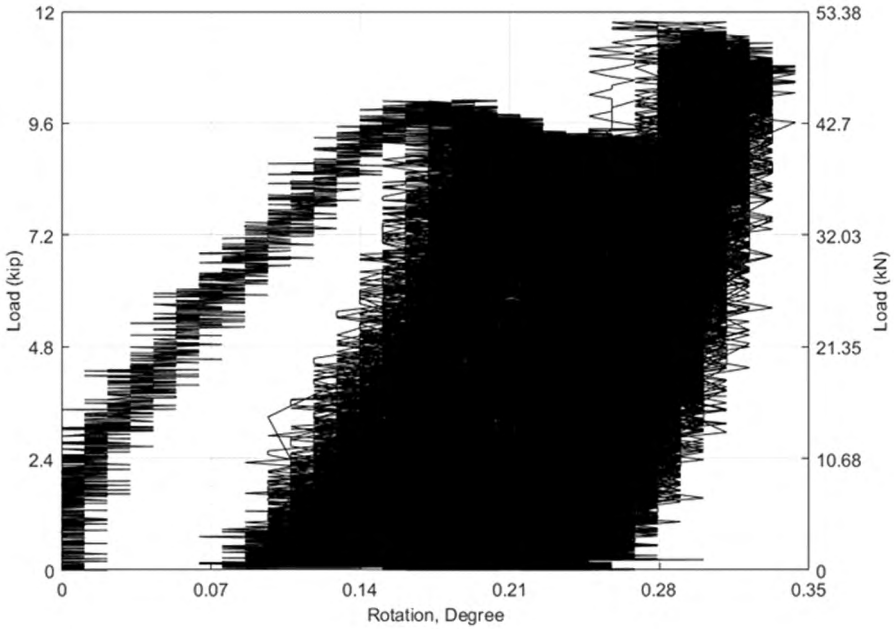


Figure 5.56: Specimen No. 1- cyclic test load versus rotation (Tiltmeter 5).

After the cyclic test was complete, the slab was fully unloaded which allowed for re-alignment of the load actuator and then the specimen was loaded at a rate of 0.025 in./minute to failure. While the system was continuously being loaded, the bond interface between the NWC and UHPC joint started to separate and can be seen in Figure 5.59. Figure 5.60 shows the specimen failure point occurring around 16,500 lb (73.4 kN). Figure 5.61 shows the failure of the specimen with the joint and slab separating on the west side all the way through to the other side. Figure 5.57 show the vertical deflection comparison between each side of the test specimen's joint. SPs 0 and 1 deflected more than SPs 4, 5 and 7. Even though SPs 4, 5, and 7 were on the loaded (east) side of the specimen, separation of the joint material and the slab specimen occurred on the opposite (west) side. It can be seen in the Figure 5.57 as the load increased to around 12 kips (50 kN); the vertical deflection recorded by SPs 0 through 7 deflected the same on both sides of the joint. When initial separation occurred at the joint material and slab, the flexural reinforcement in the joint engaged and the specimen strength started to increase. As load continued to be applied, yielding of the reinforcement in the joint occurred. Then, the specimen started to deflect more with little additional load in which can be correlated to the gap opening increasing over time, which lead to the difference of the vertical data produced from each side of the joint. Figure 5.58 showed LVDT 5 had larger deflections than LVDT 3. This was most likely due to the gap opening occurred on that same side of the joint that can be seen in Figure 5.60.

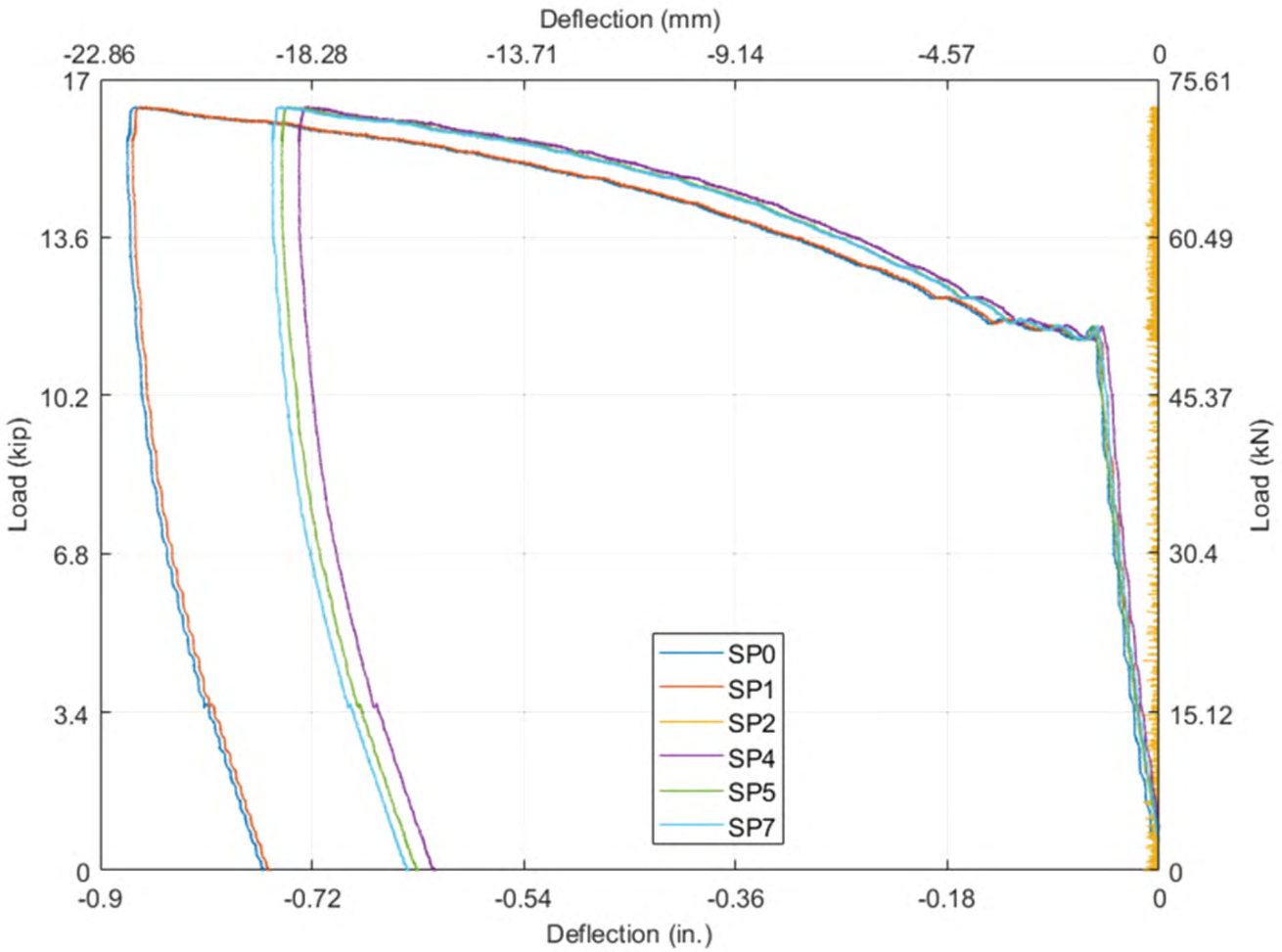


Figure 5.57: Specimen No. 2- failure test load versus vertical deflection.

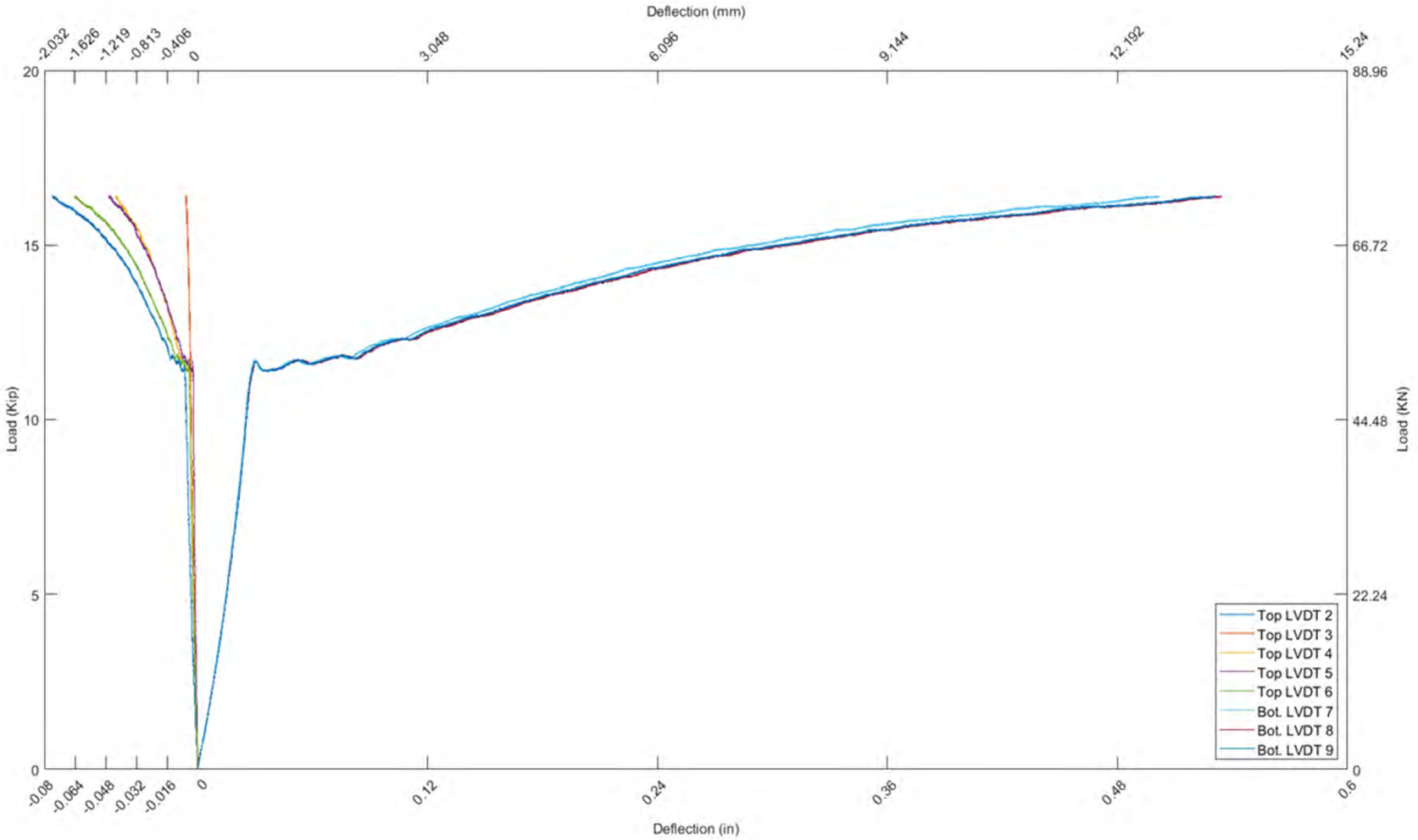


Figure 5.58: Specimen No. 2- failure test load versus transverse deflection.



Figure 5.59: Specimen No. 2- initial separation at bond of joint



Figure 5.60: Specimen No. 2- failure at south face.

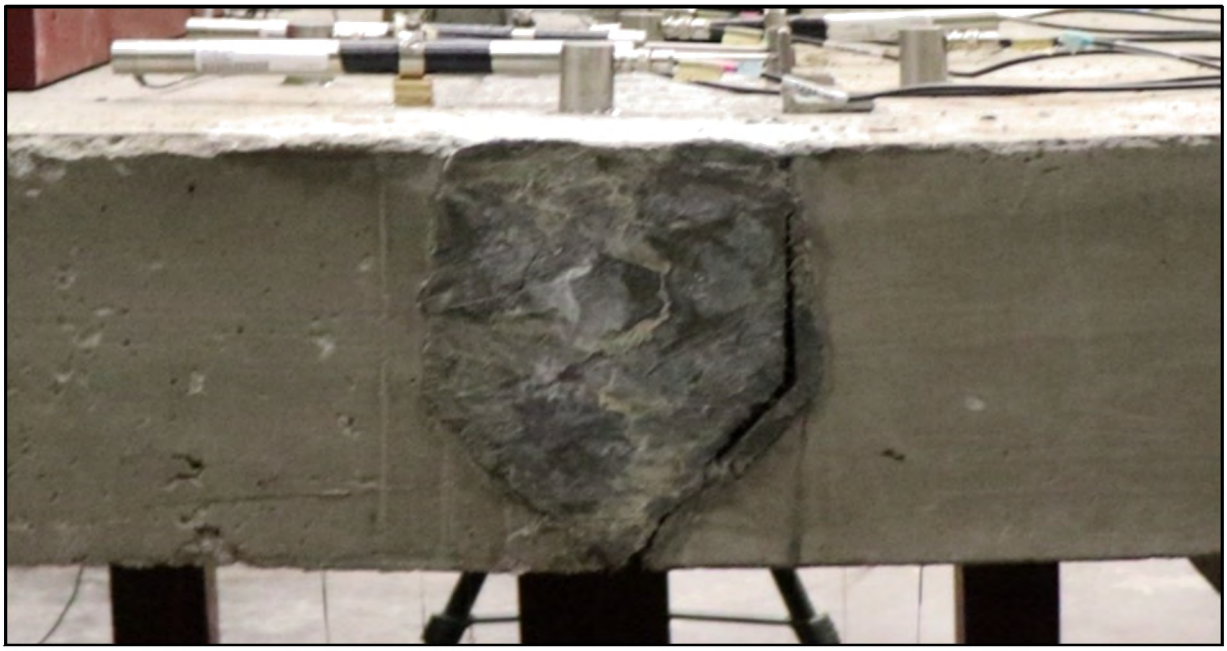


Figure 5.61: Specimen No. 2- failure at north face.

5.1.10.3 Specimen 3

Specimen 3 joint reinforcement was modified from the NMDOT top slab reinforcement shown previously in Section 5.1.1. The 6 in. (25.4 mm) joint lab splice configuration and 4.5 in. (114.3 mm) rebar lap length was kept the same, but the rebar size was decreased to No. 3 (No.10) rebar. Figure 5.62 shows the load-deflection behavior of Specimen 3 during a pre-loading and failure test. It was intended to pre-load the specimen to 15,000 lb (66.7 kN) before beginning the cyclic test, but the load drastically dropped before this could be achieved. Figure 5.62 shows this initial drop before unloading the specimen. The joint had shown a small gap between the UHPC and slab, suggesting this was the initial cracking location during the test and can be seen in Figure 5.64 and Figure 5.65.

After the load was removed, the slab was then loaded at a rate of 0.05 in./minute (1.27 mm/minute) to failure. While the system was continuously being loaded, the bond interface between the NWC and UHPC joint started to separate, including a propagating crack under the load, similar to Specimen 1. Figure 5.64 and Figure 5.65 shows the joint separation and the start of the crack developing in the NWC slab. As the specimen load already softened, permanent deformation can be seen in Figure 5.62. Figure 5.66 and Figure 5.67 show the larger cracking occurring in the slab. It was decided to stop the loading around 18,000 lb (80.1 kN) because the slab specimen had failed and only the No. 3 (No.10) rebars were holding everything together. Figure 5.62 show the vertical deflection comparison between each side of the test specimen's joint. SPs 0, 1 and 2 did not deflect as much as SPs 4 and 7. This is due to the fact SPs 4 and 7 were on the loaded side of the specimen as well as where the separation of the joint and cracking of the slab occurred. This is comparable to test Specimen 1 failure in the slab and not at the joint. It can be seen in the Figure 5.62, as the load increased to around 14.5 kips (60 kN) the vertical deflection already started to separate from each other on both sides of the joint. Due to a sudden drop of strength, the specimen was fully unloaded to visually inspect the test setup to ensure the test could be continued safely. When the specimen was loaded again, cracking occurred on the slab a loss of strength increase was observed. Small drops of strength can be seen in Figure 5.62 as the crack propagated towards the flexural reinforcement. Once the reinforcement started to engage, the specimen strength increased until yielding of the reinforcement occurred and ultimately the test was stopped.

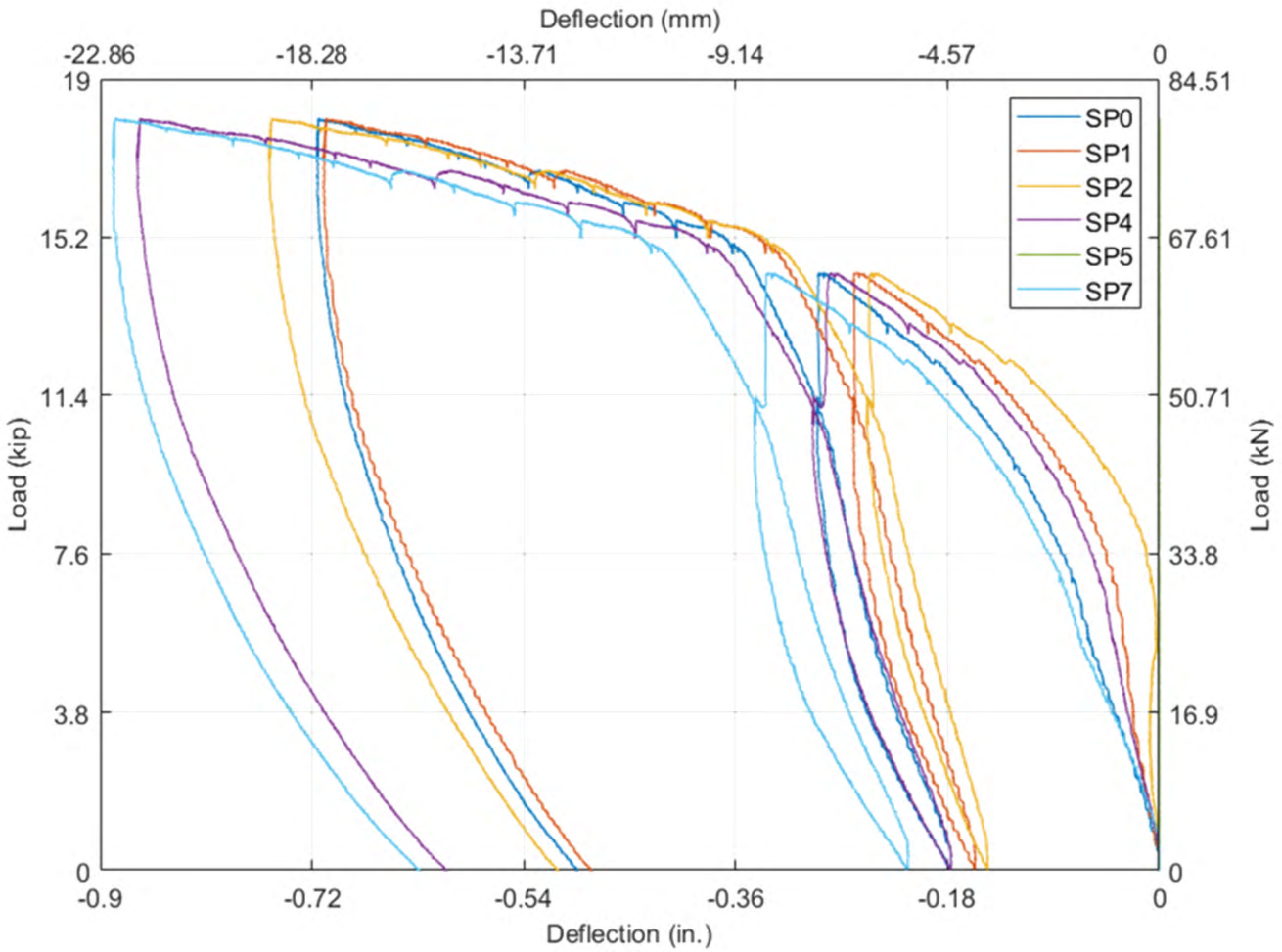


Figure 5.62: Specimen No. 3- failure test load versus vertical deflection.

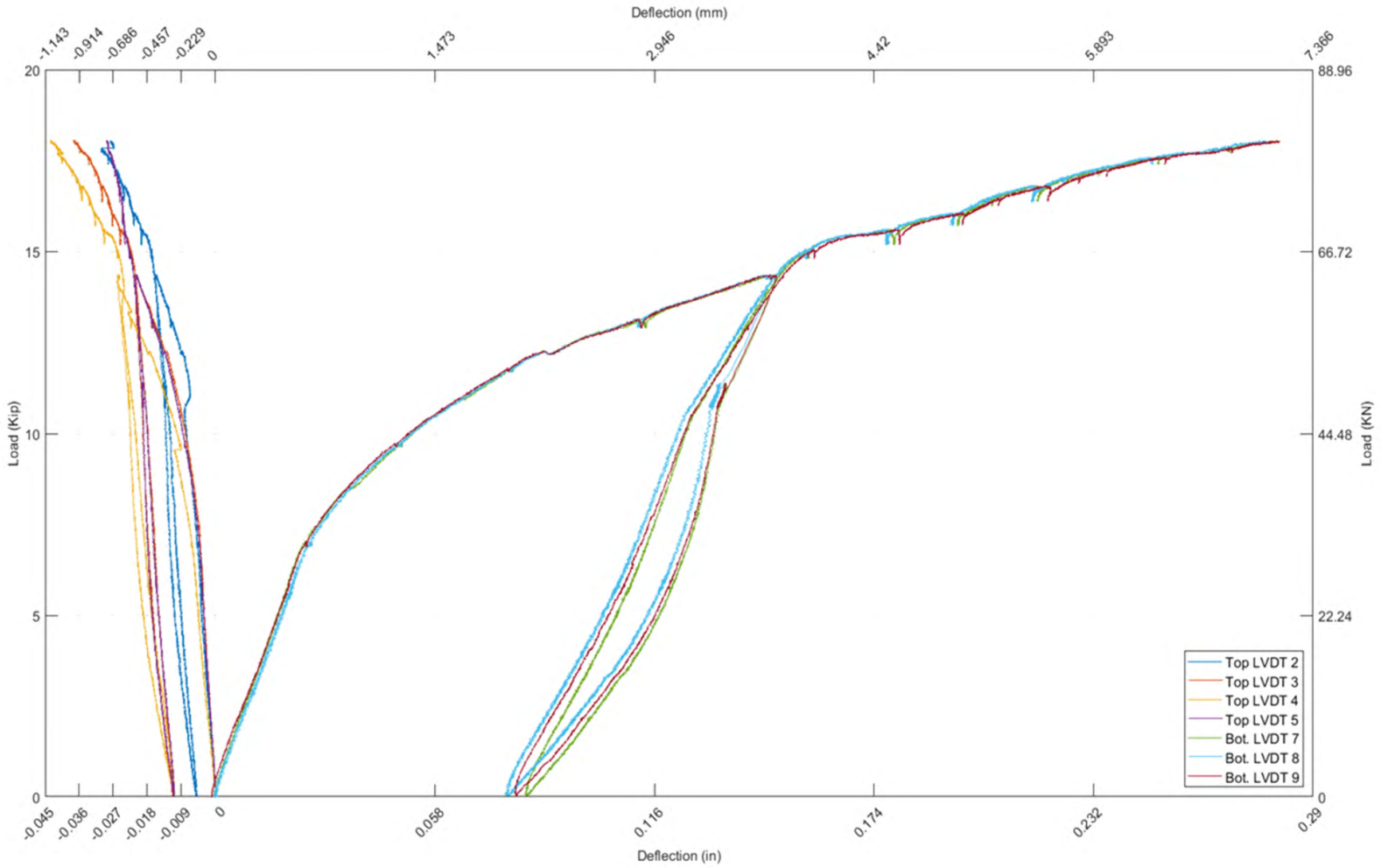


Figure 5.63: Specimen No. 3- failure test load versus transverse deflection.



Figure 5.64: Specimen No. 3- initial separation at south face bond of joint.



Figure 5.65: Specimen No. 3- initial separation at top side bond of joint.

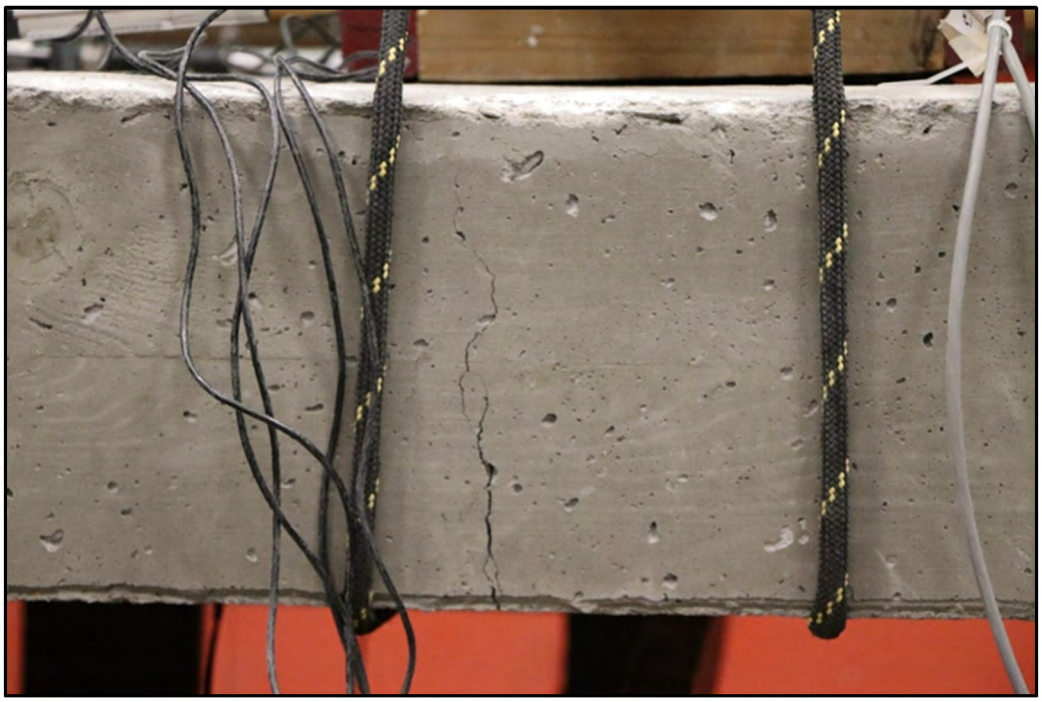


Figure 5.66: Specimen No. 3- initial cracking of the slab specimen.

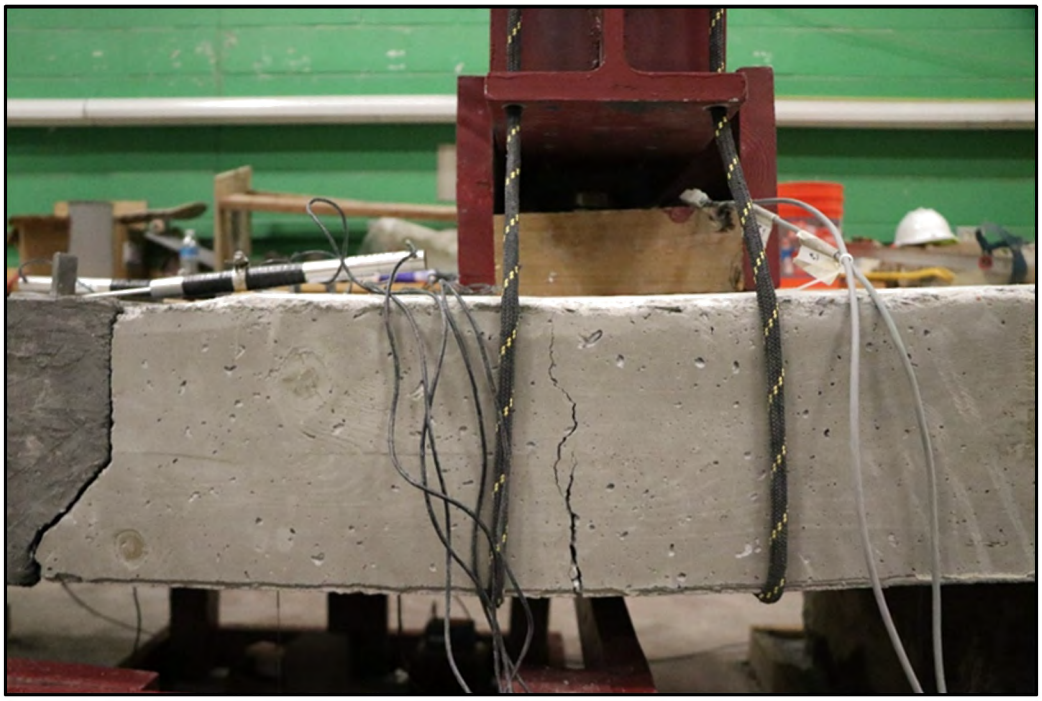


Figure 5.67: Specimen No.3- failure at south face.



Figure 5.68: Specimen No. 3- failure at north face.

5.1.10.4 Specimen 4

Specimen 4 joint reinforcement utilized the same NMDOT top slab reinforcement, but the joint lab splice configuration was increased to a spacing of 12 in. (304.8 mm) and the No. 4 (No. 13) rebar was changed to No. 3 (No.10) rebar. The lap length of 4.5 in. (114.3 mm) for rebar at the joint remained constant. Figure 5.69 through Figure 5.81 shows the load-deflection behavior of Specimen 4 during the cyclic test. The test took roughly 2 hours to complete 200 cycles, conducted at 2 cpm. The specimens load was maintained around 4,000 lb (17.8 kN) during the 200 cycles. The 4,000 lb (17.8 kN) load was taken conservatively because the reinforcement spacing was increased from Specimen 3 and to avoid reaching nonlinear behavior of the specimen. As can be seen in Figure 5.69, residual displacements occurred after each cycle. Therefore, showing that damage was occurring in the system. Figure 5.84 shows initial cracking of the specimen. The specimen carried approximately 3,800 lb (16.9 kN), prior to opening a crack at the joint. Permanent deformation was recorded by the LVTD data in Figure 5.74 through Figure 5.81. This can be contributed to the fact that large separation at the bottom of the joint was observed, increasing the amount of vertical deflection which induced higher compressive stresses at the top of the joint. Figure 5.79 through Figure 5.81, indicate that separation at the joint and slab specimen continued at each cycle and show that the gap open increased as well. As the load increase during the cyclic test, the bond separates even more over time. Due to the joint separation on both sides of the specimen's joint, the SPs 0 through 7 (Figure 5.69 through Figure 5.73) showed the similar amounts of deformations. Figure 5.69 through Figure 5.73 show that Specimen 4 had an even smaller initial stiffness compared to Specimens 1 through 3 due to the decrease in cross sectional area of reinforcement (reduction in flexural reinforcement size from and an increase in spacing).

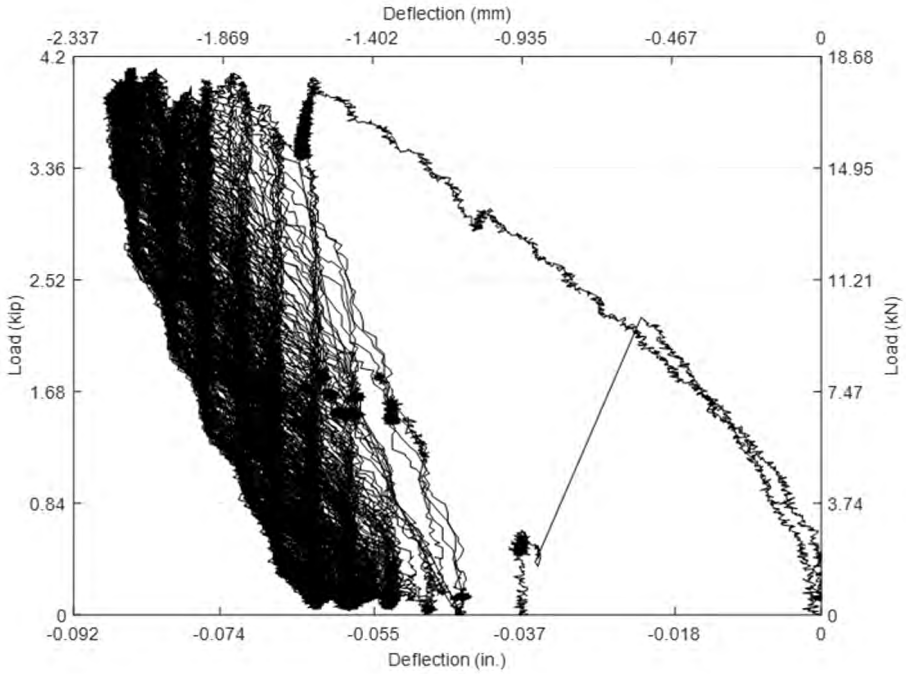


Figure 5.69: Specimen No. 4- cyclic test load versus vertical deflection (SP 0).

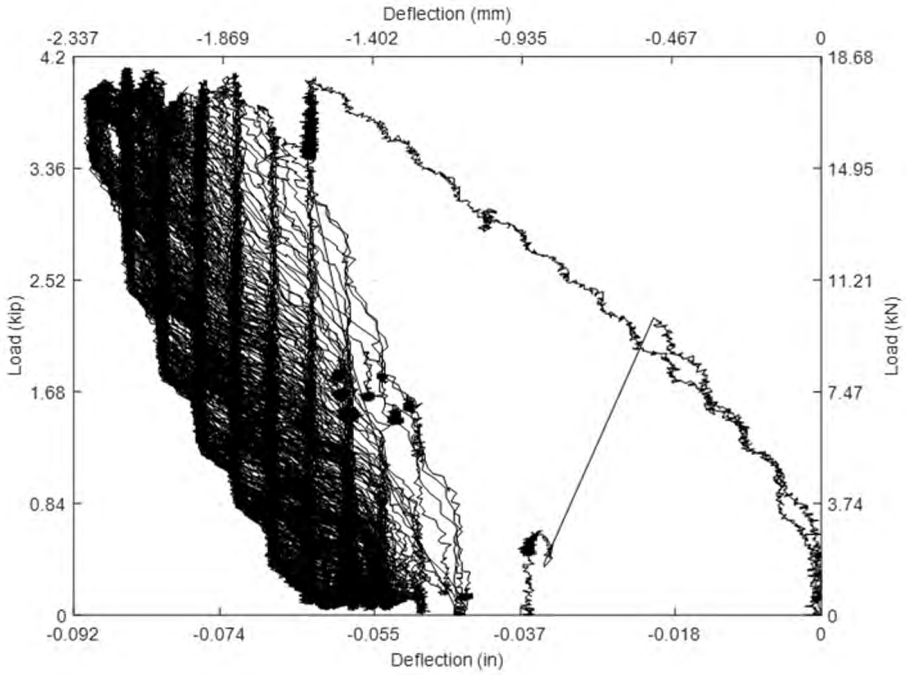


Figure 5.70: Specimen No. 4- cyclic test load versus vertical deflection (SP 1).

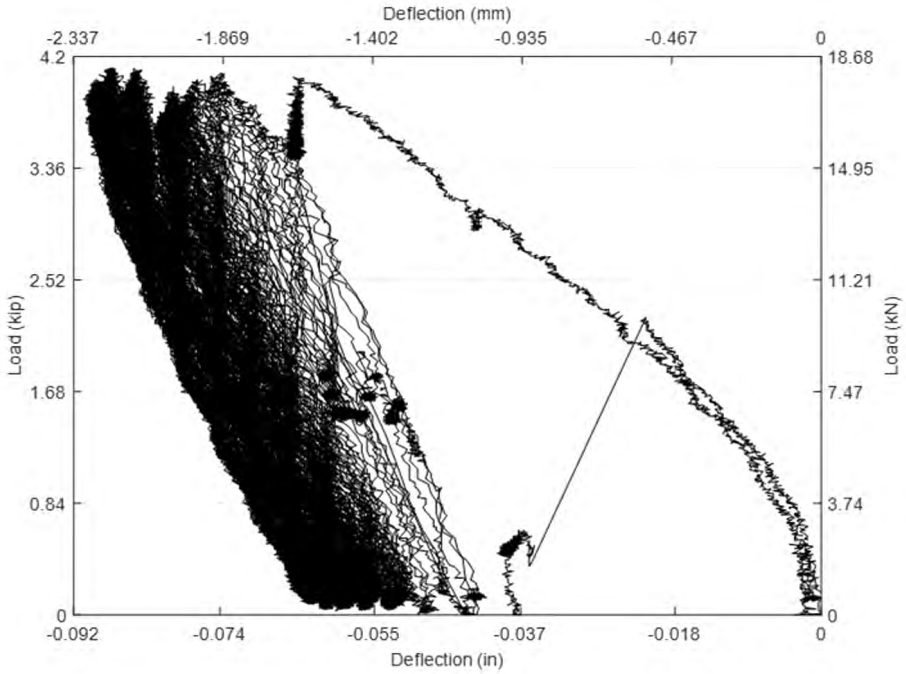


Figure 5.71: Specimen No. 4- cyclic test load versus vertical deflection (SP 2).

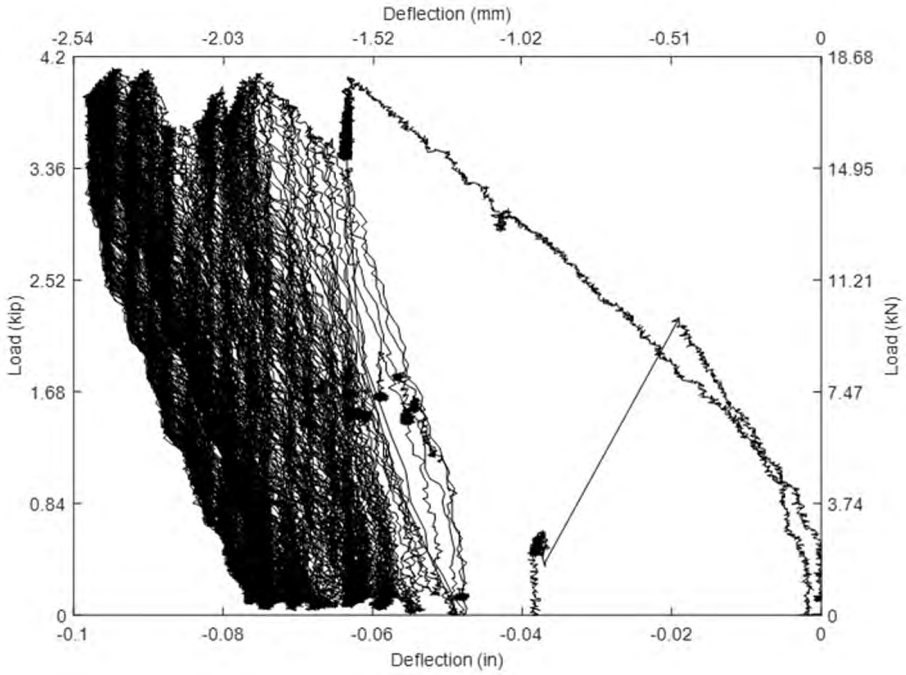


Figure 5.72: Specimen No. 4- cyclic test load versus vertical deflection (SP 4).

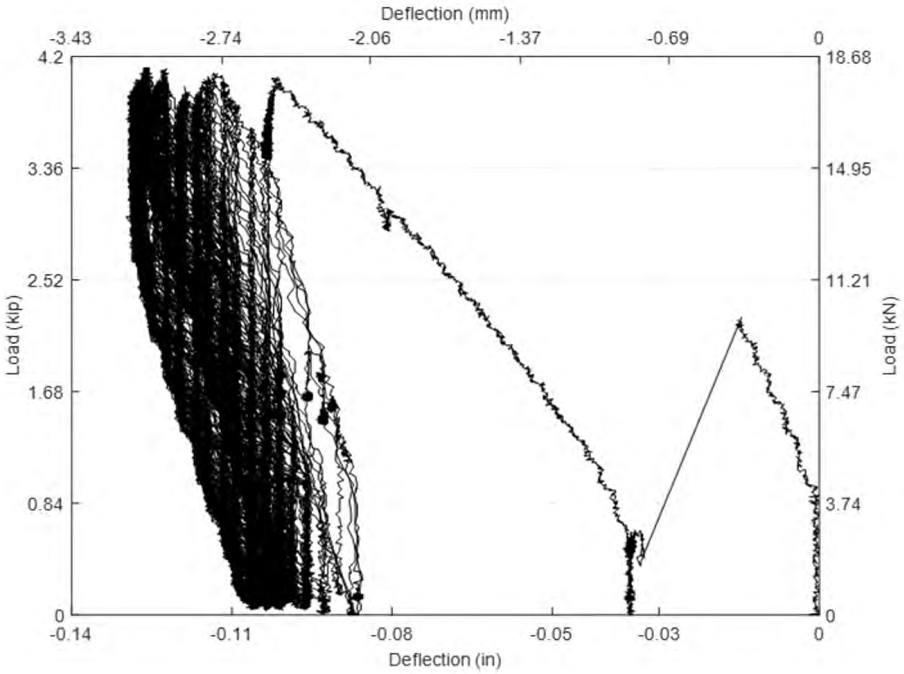


Figure 5.73: Specimen No. 4- cyclic test load versus vertical deflection (SP 7).

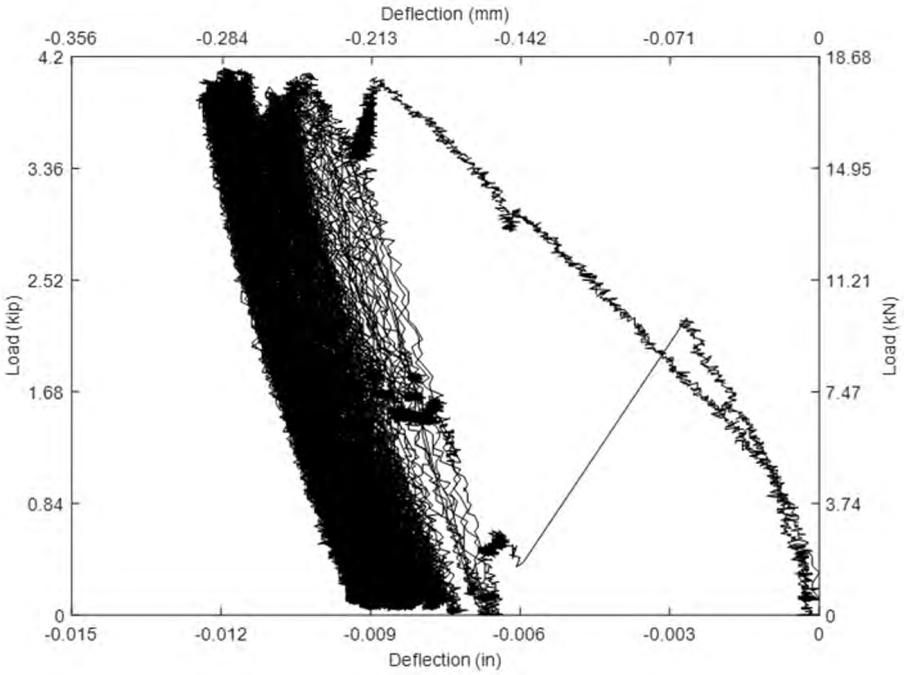


Figure 5.74: Specimen No. 4- cyclic test load versus transverse deflection (LVDT 2).

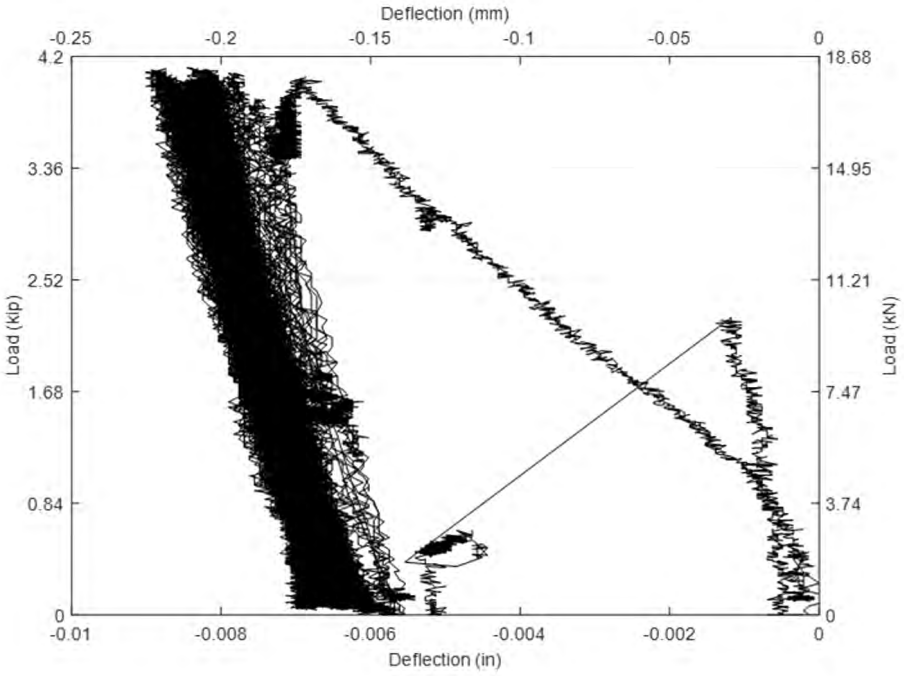


Figure 5.75: Specimen No. 4- cyclic test load versus transverse deflection (LVDT 3).

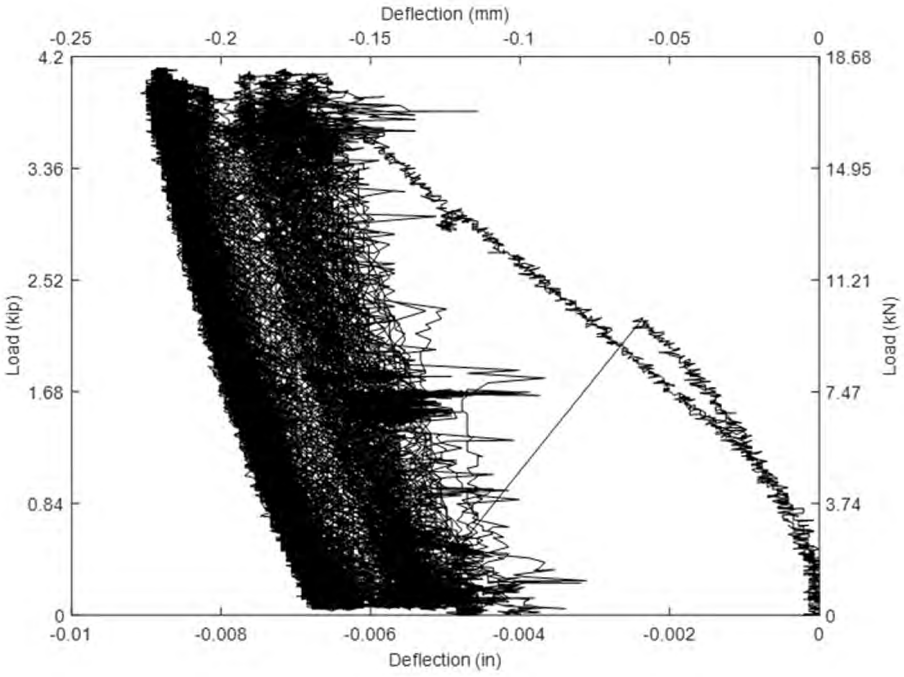


Figure 5.76: Specimen No. 4- cyclic test load versus transverse deflection (LVDT 4).

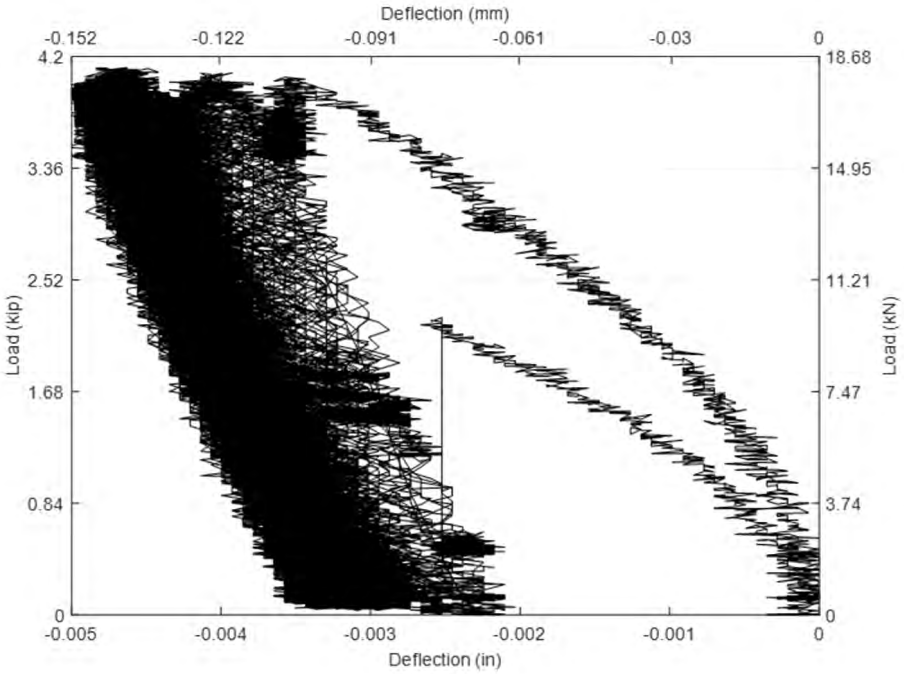


Figure 5.77: Specimen No. 4- cyclic test load versus transverse deflection (LVDT 5).

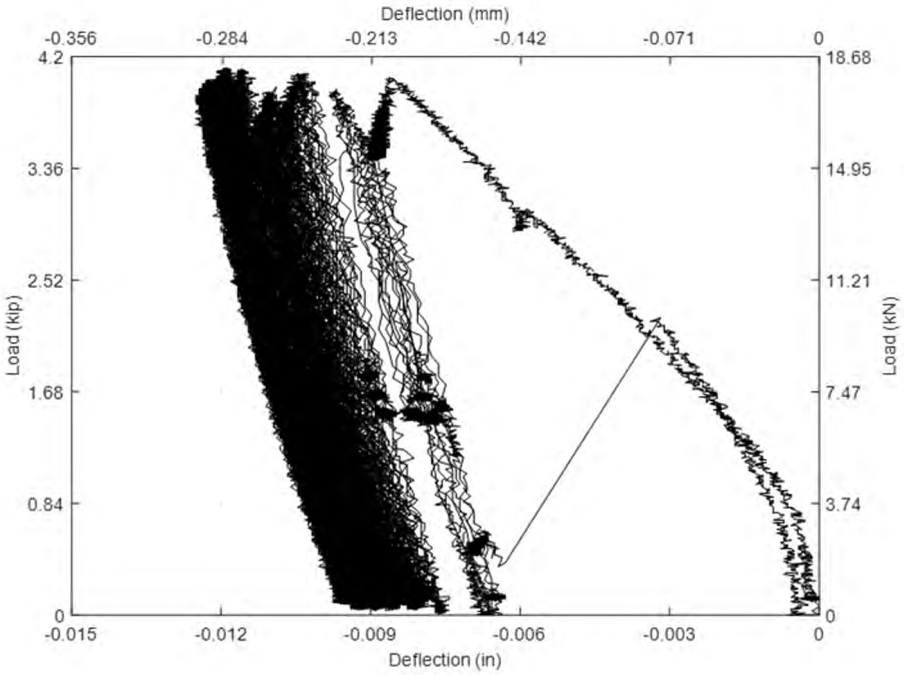


Figure 5.78: Specimen No. 4- cyclic test load versus transverse deflection (LVDT 6).

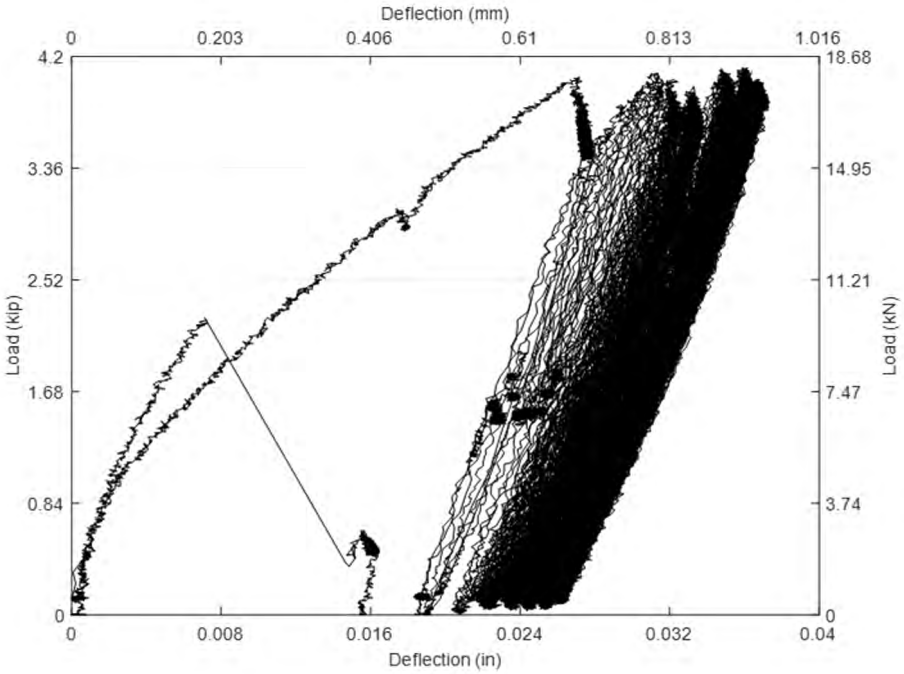


Figure 5.79: Specimen No. 4- cyclic test load versus transverse deflection (LVDT 7).

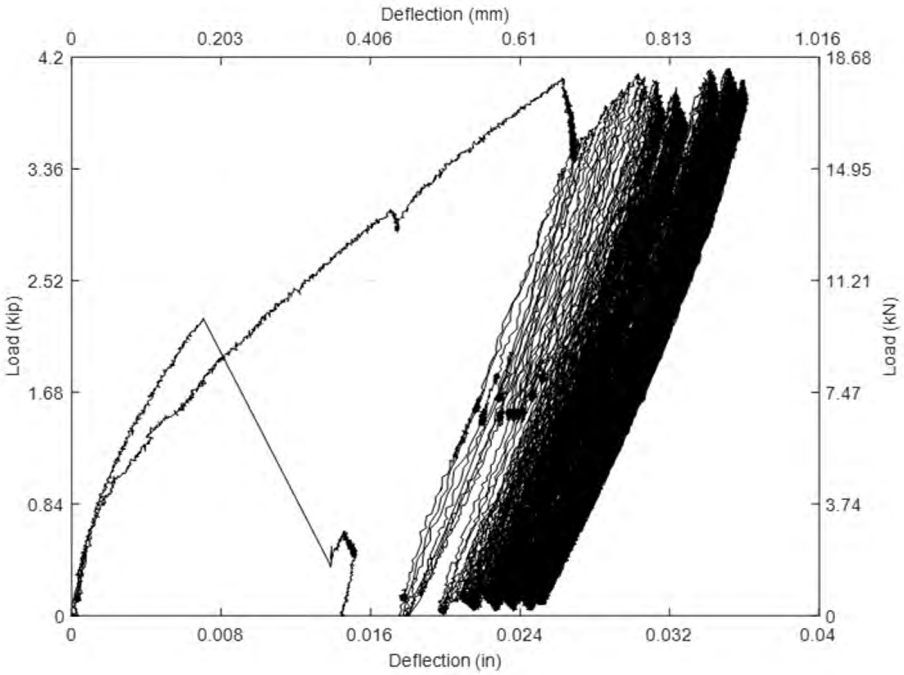


Figure 5.80: Specimen No. 4- cyclic test load versus transverse deflection (LVDT 8).

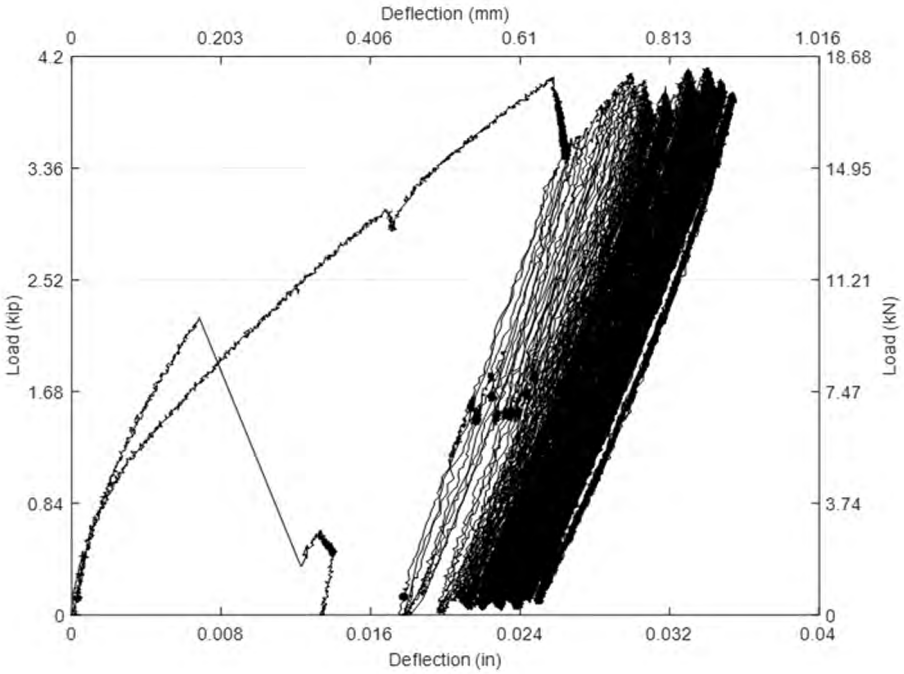


Figure 5.81: Specimen No. 4- cyclic test load versus transverse deflection (LVDT 9).

After the cyclic test was complete, the slab was unloaded and then loaded at a rate of 0.01 in./minute (0.25 mm/minute) till 8,800 lb (39.1 kN) and then increased to 0.05 in./minute (1.27 mm/minute) until failure. While the system was continuously being loaded, the bond interface between the NWC and UHPC joint started to separate and can be seen in Figure 5.84. As the specimen softened, permanent deformation stated to occur as the test continued. Figure 5.74 shows the specimen failure point occurring around 11,500 lb (51.2 kN) and Figure 5.85 and Figure 5.86 correlates this failure load with the joint and slab separating on the left side all the way through to the other side (Figure 5.87). Figure 5.82 show the vertical deflection comparison between each side of the testing specimens joint. The graph shows SPs 0, 1 and 2 deflected relatively similar to SPs 4 and 7. This is due to the fact the specimen joint material separated from the slabs on both sides of the joint. It can be seen in the Figure 5.82 as the load increased to around 12.5 kips (50 kN); the vertical deflection recorded by SPs 0 through 7 deflected parallel to each other on both sides of the joint. When initial cracking occurred around 5.5 kips (27 kN), a loss of strength was observed but the strength started to increase again throughout the test. It was concluded that micro cracking and joint separations showed in Figure 5.82 was the cause of each drop of strength and continued to occur as the load increased. Once the reinforcement started to engage due to the separation of the joint on both sides of the joint, the specimen strength started to increase, and the reinforcement was yielded and was the only element holding the specimen together. The specimen started to deflect more with little additional load and a large vertical displacement.

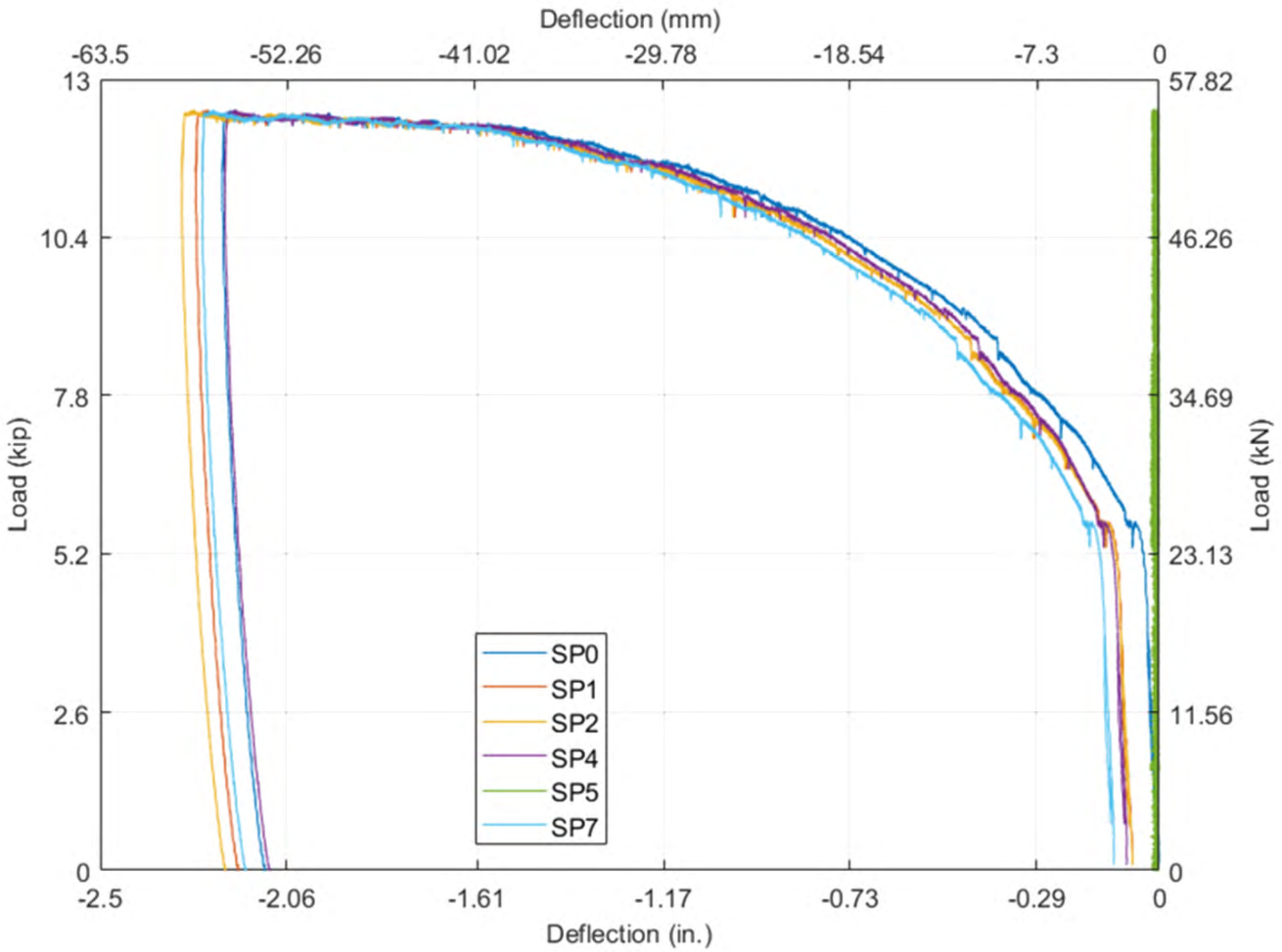


Figure 5.82: Specimen No. 4- failure test load versus vertical deflection.

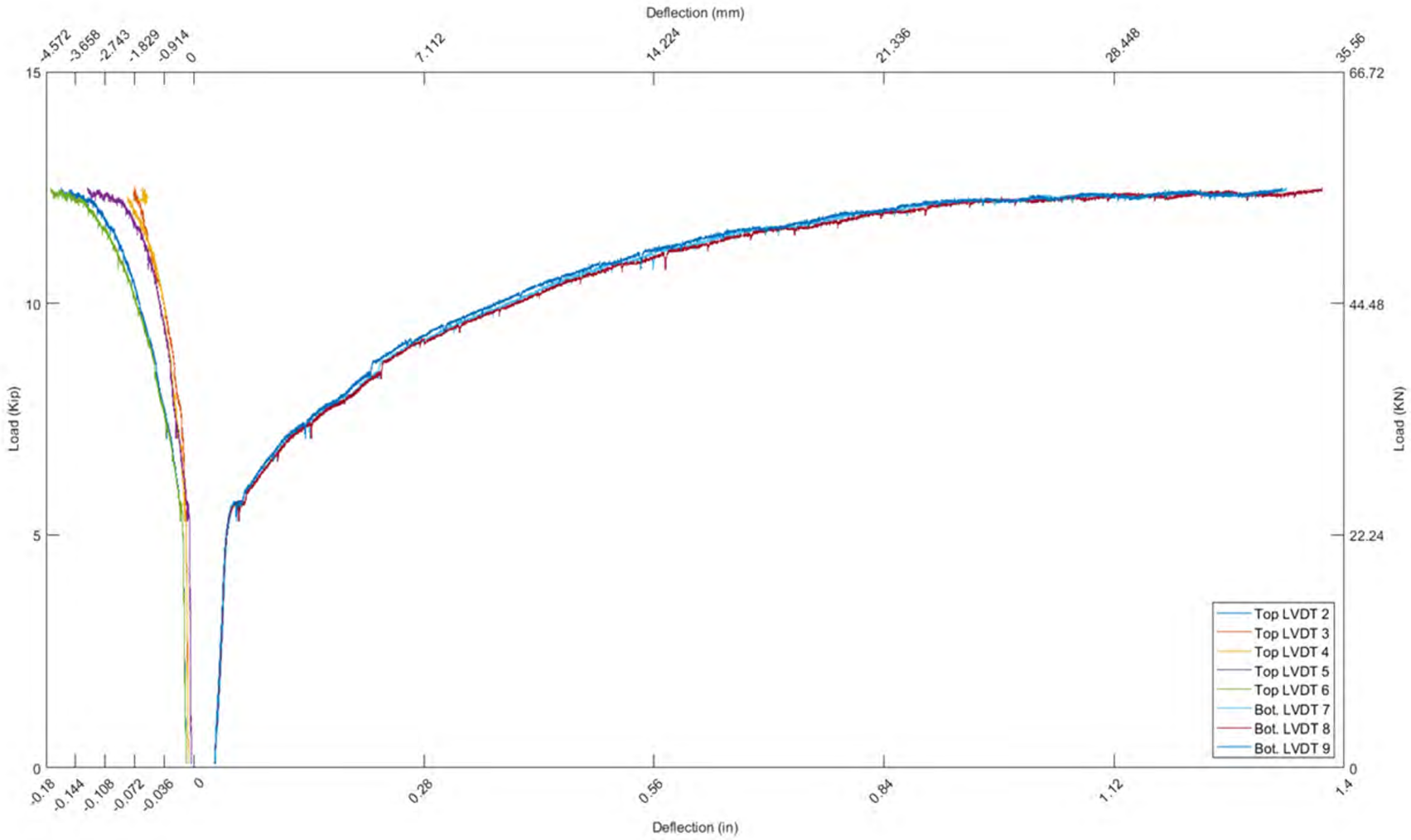


Figure 5.83: Specimen No. 4- failure test load versus transverse deflection



Figure 5.84: Specimen No. 4- initial separation at bond of joint.

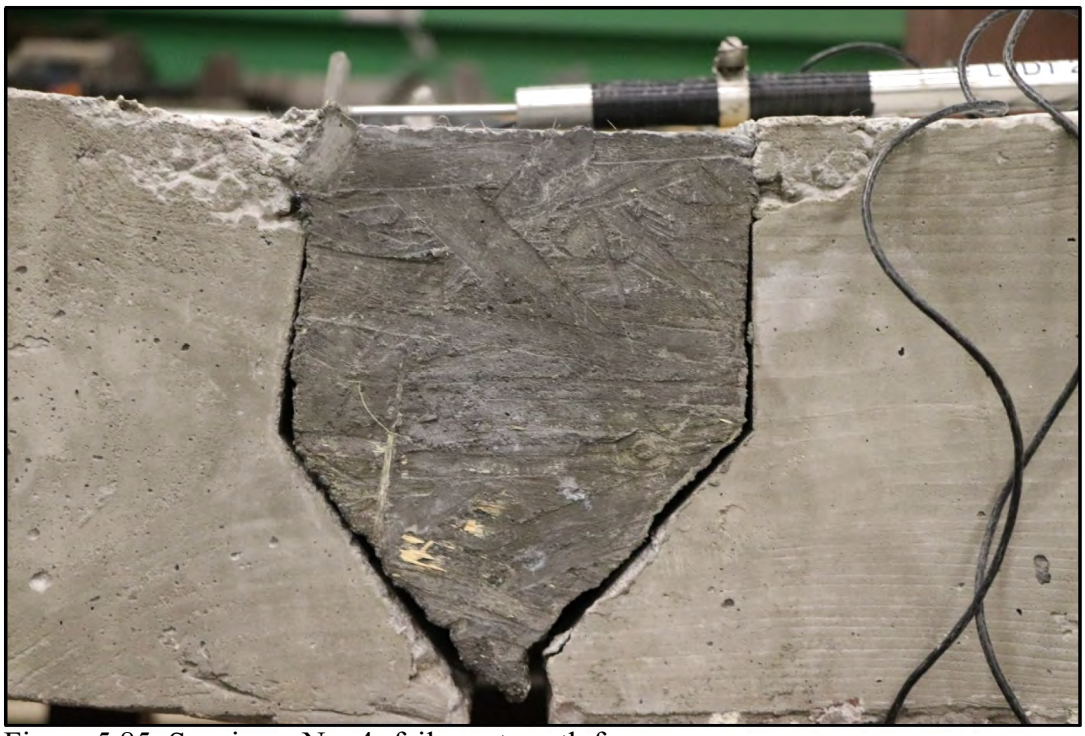


Figure 5.85: Specimen No. 4- failure at south face.

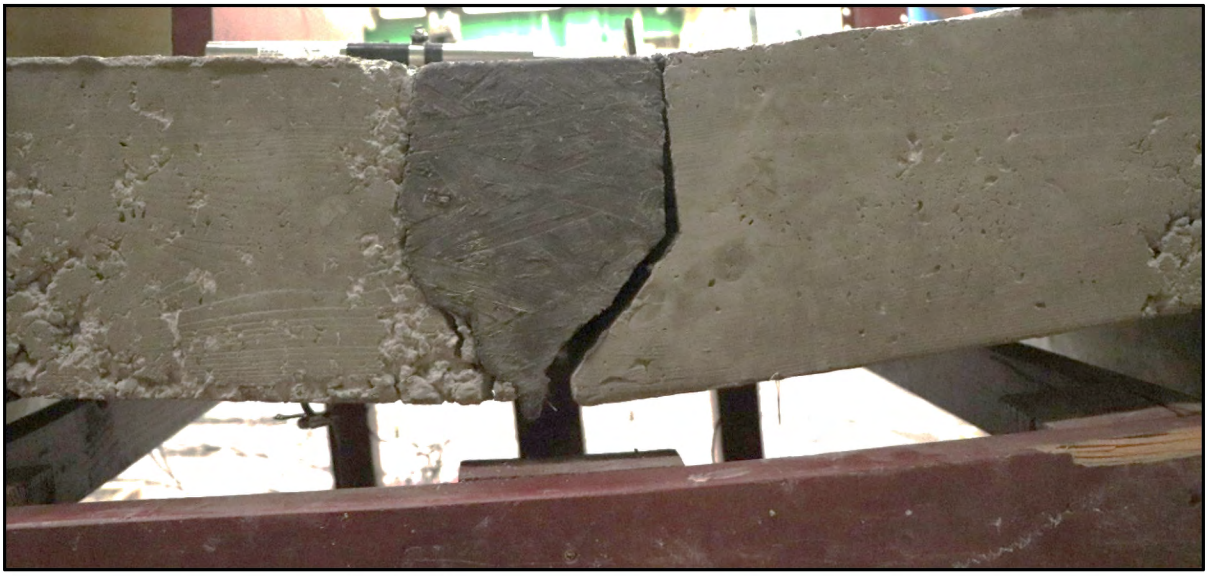


Figure 5.86: Specimen No. 4- failure at north face.

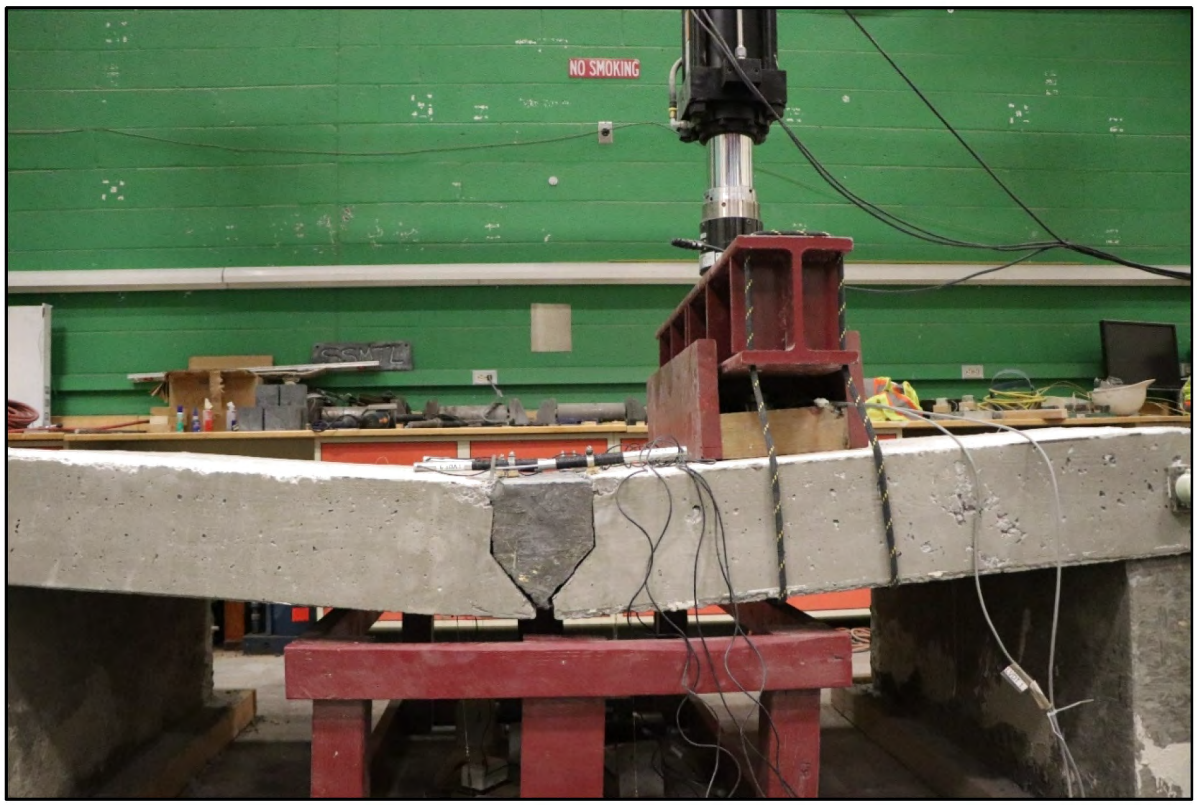


Figure 5.87: Specimen No. 4- failure of overall system.

5.1.10.5 Specimen 5

Specimen 5 joint reinforcement was identical to Specimen 1 to replicate and compare the UHPC and non-shrink grout data. Figure 5.88 shows the load-deflection behavior of Specimen 5. It was intended to conduct a cyclic test, but due to strength of the grout a brittle failure in the joint happen. The load drastically dropped before any significant load could be achieved. Figure 5.88 shows strength lost before even reaching 400 lb (1.8 kN) of force on the specimen. The joint had shown cracking due to self-weight already large gap between the grout and slab, suggesting the joint was going to fail early on and can be seen in Figure 5.86 and Figure 5.90. Figure 5.91 and Figure 5.92 shows the brittle failure of the grout in the joint as the load reached around 350 lb (350 kN) of force.

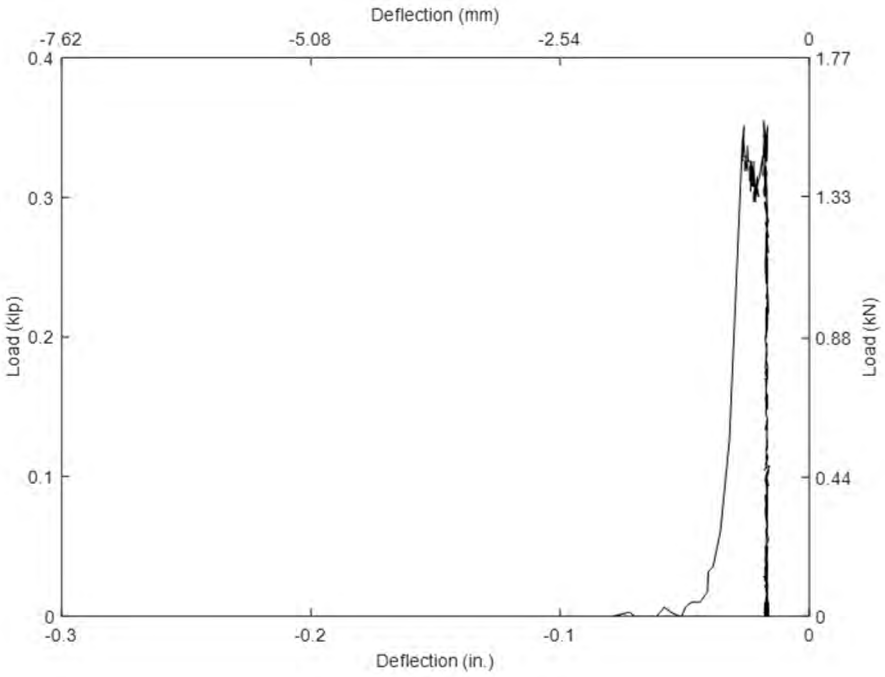


Figure 5.88: Specimen No. 5- failure test load versus vertical deflection (SP 1).

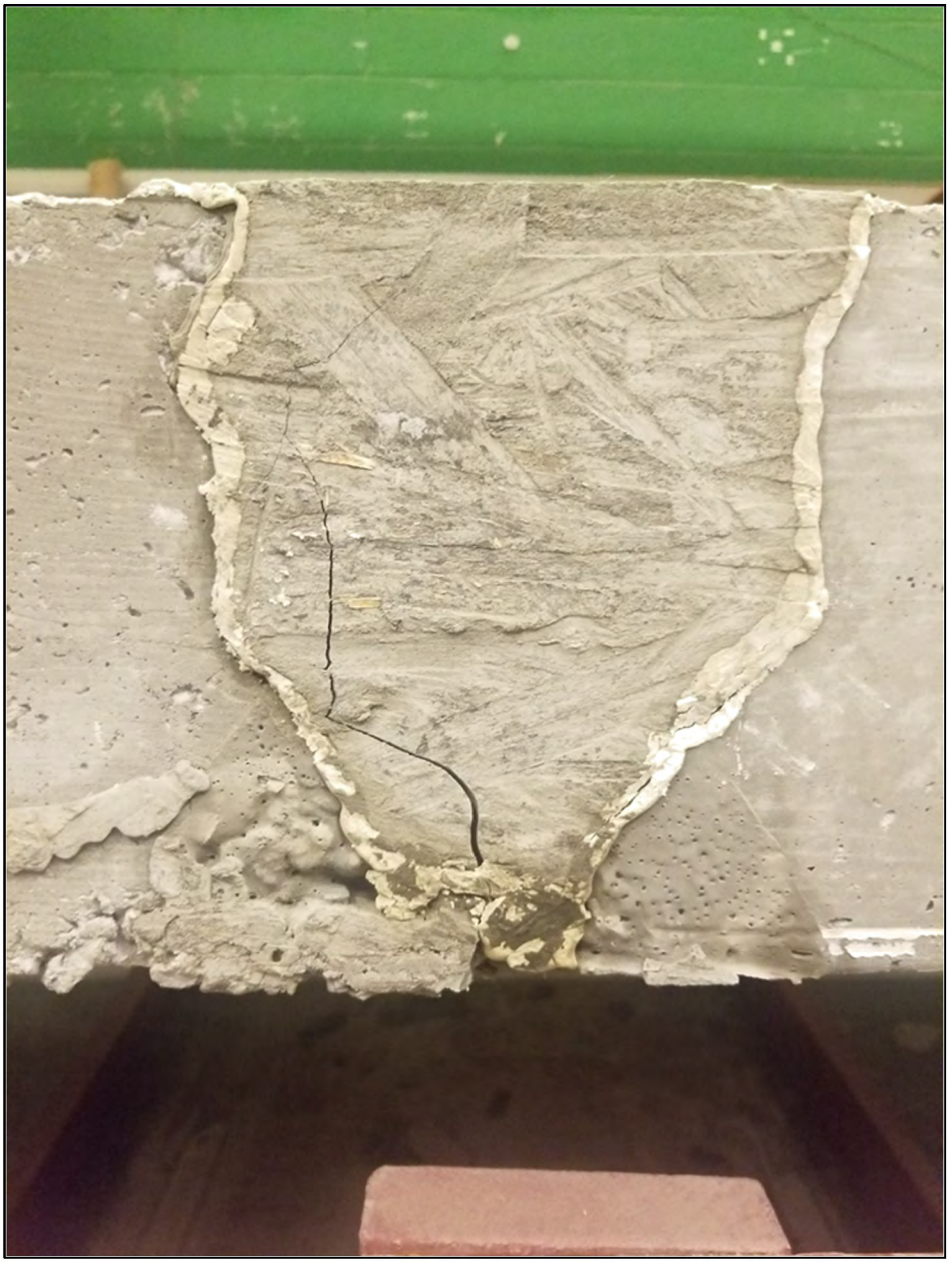


Figure 5.89: Specimen No. 5- self weight cracking at south face.

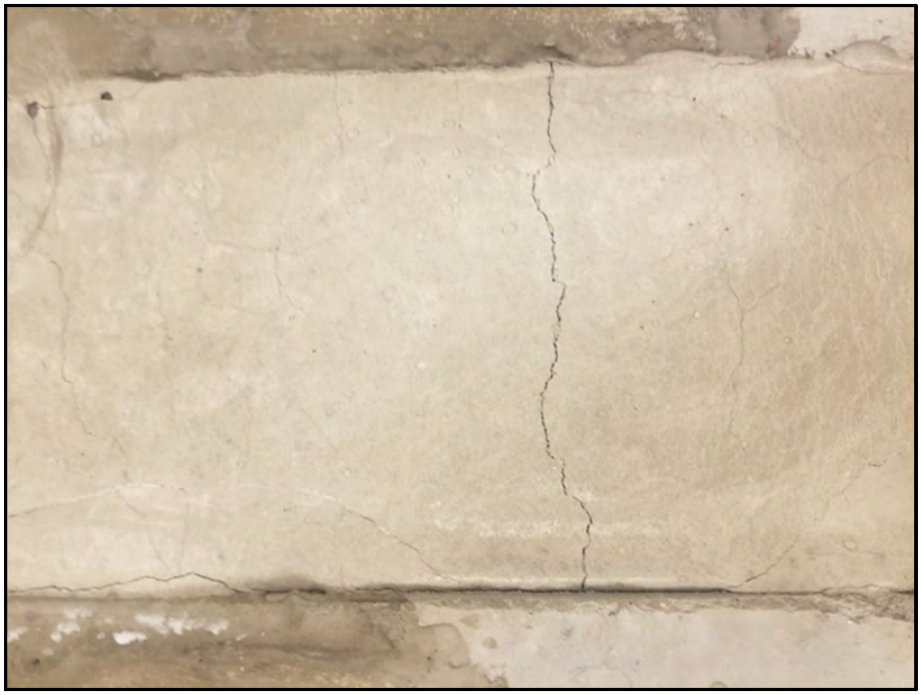


Figure 5.90: Specimen No. 5- self weight cracking at top side.



Figure 5.91: Specimen No. 5- failure at south face.



Figure 5.92: Specimen No. 5- failure of overall system.

5.1.10.6 Specimen 6

Specimen 6 joint reinforcement utilized the same top slab reinforcement as Specimen 2 to compare the behavior of the UHPC and non-shrink grouted joints. Figure 5.93 through Figure 5.105 shows the load-deflection behavior of Specimen 6 during a cyclic test. The test took roughly 3 hours to complete 400 cycles. The cycle loading was at 2 cpm fore 200 cycles and then changed to 4 cpm for the remainder of the test. The specimens load was maintained around 5,750 lb (25.6 kN) for all 400 cycles. As can be seen in Figure 5.93, residual displacements occurred after each cycle. Therefore, the system had some damage occurring such as debonding, cracking, or settling of the system may be plausible as well. Figure 5.108 shows cracking of the specimen. The specimen carried approximately 4,500 lb (49.8 kN), prior to a visual observation of a crack at the joint material. LVTD data in Figures 4.83 through 4.90 indicate that the concrete at the top of the join and specimen crushed a little as each cycle occurred. Permanent deformation was recorded by the LVTD data in Figure 5.98 through Figure 5.105. This can be contributed to the fact that the joint material compressive strength or the overall stiffness that was relatively low compared to Specimen 2 by 22 percent and can be seen in Figure 5.93. Figure 5.103 through Figure 5.105, indicate that little separation at the joint and slab specimen occurred at each cycle, but also show that the gap open did experience permanent deformation that could not be physically seen. This can be closely related to the fact that the failure of the testing specimen was the joint. As the load increase during the cyclic test and started to reach its peak, the joint material crack opened and propagated more during each cycle. As the joint material stresses increased and cracks formed in the material, the rebar was assumed to have separated from the grout and pull out of the joint. This ultimately was the failure mechanism for this specimen due to the bond strength could not overcome the tensile forces due to the loads. Due to a new weak point in the system, the LVDT did not pick up any rebar pull out that occurred during the test. Figure 5.93 through Figure 5.97 show a lower initial stiffness of Specimen 6 compared to Specimen 2. This can be related to the decrease in strength of the material compared to UHPC.

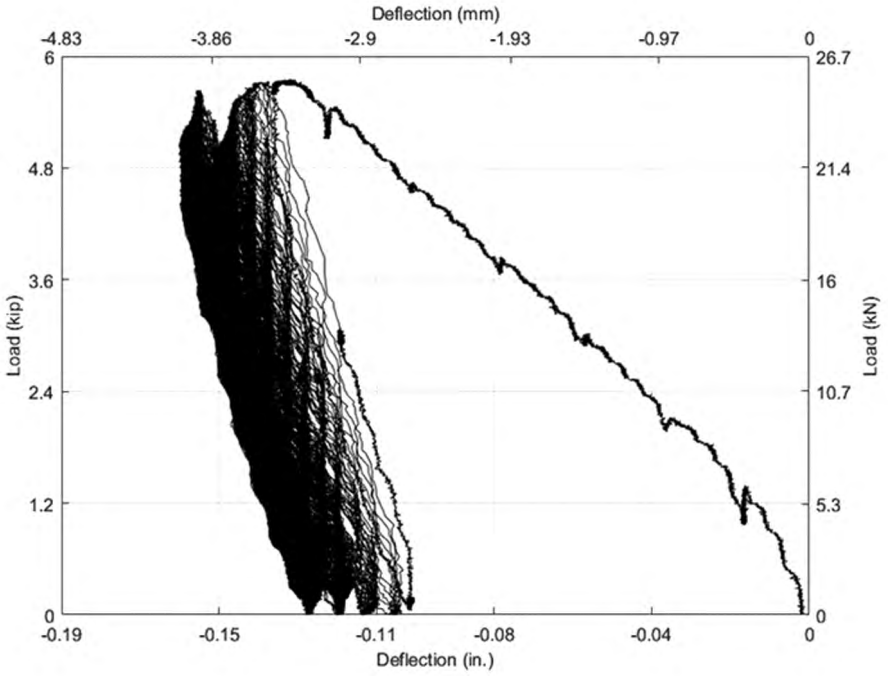


Figure 5.93: Specimen No. 6- cyclic test load versus vertical deflection (SP 0).

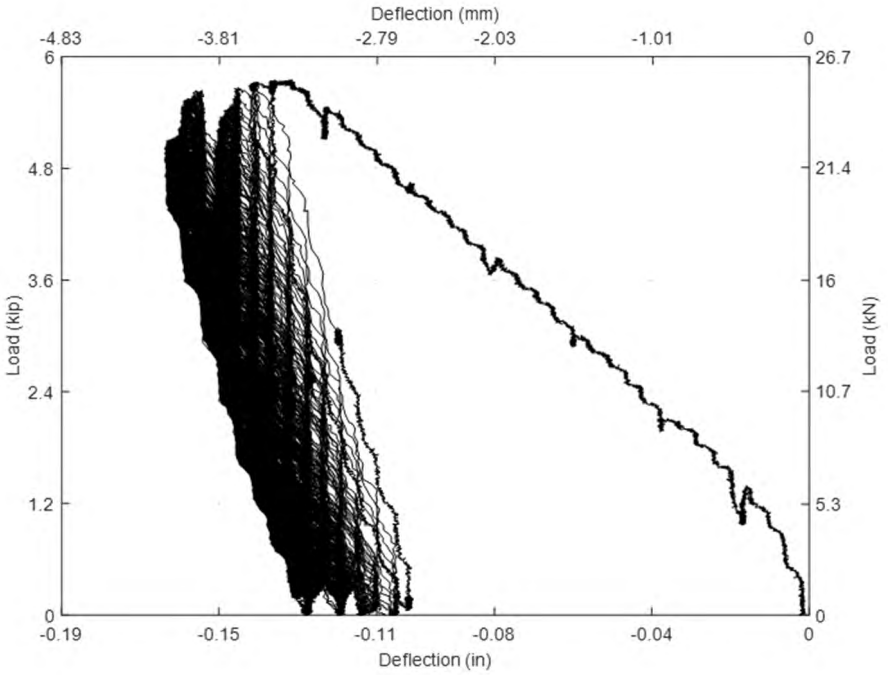


Figure 5.94: Specimen No. 6- cyclic test load versus vertical deflection (SP 1).

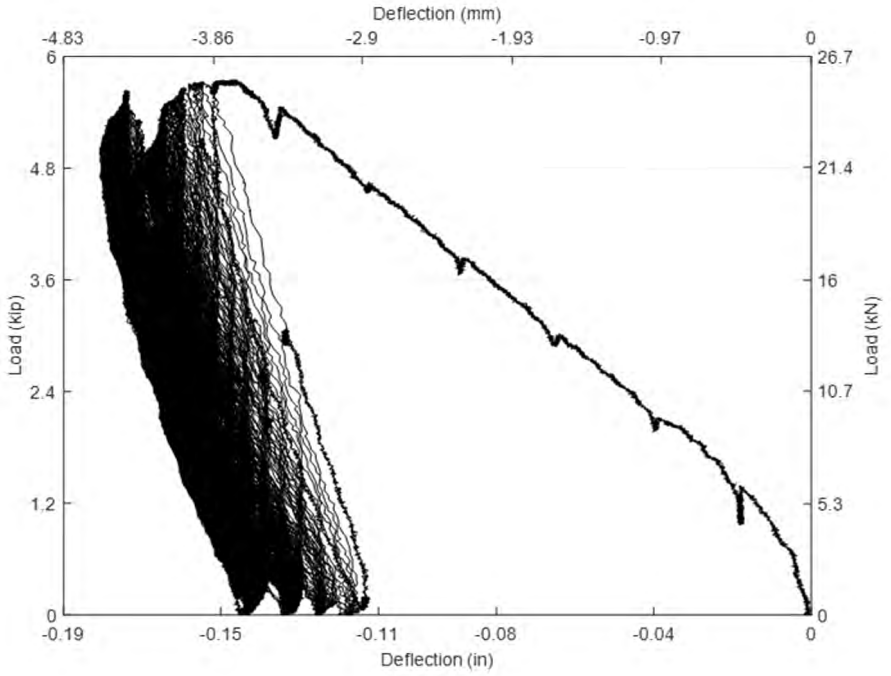


Figure 5.95: Specimen No. 6- cyclic test load versus vertical deflection (SP 2).

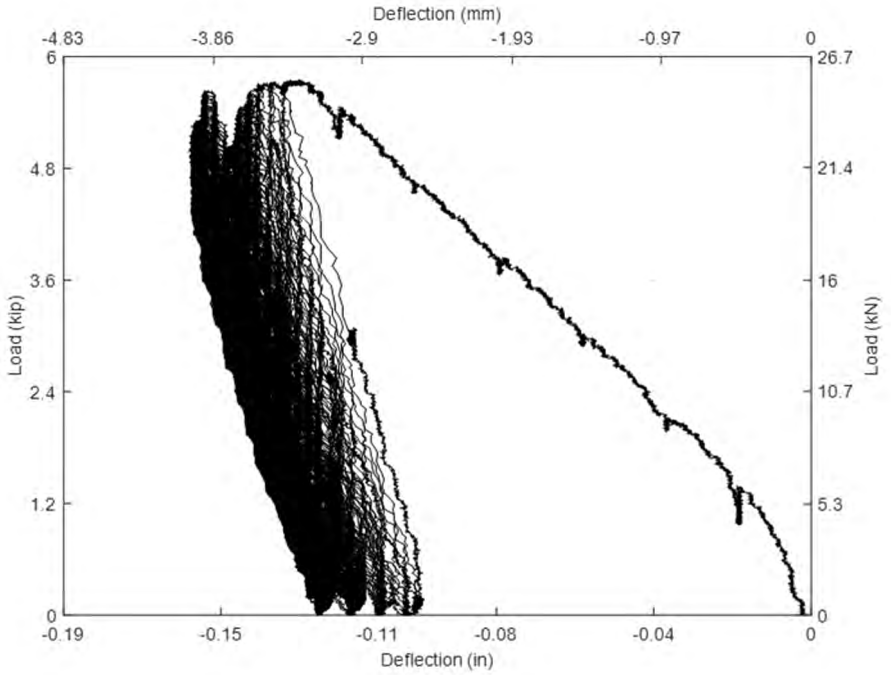


Figure 5.96: Specimen No. 6- cyclic test load versus vertical deflection (SP 4).

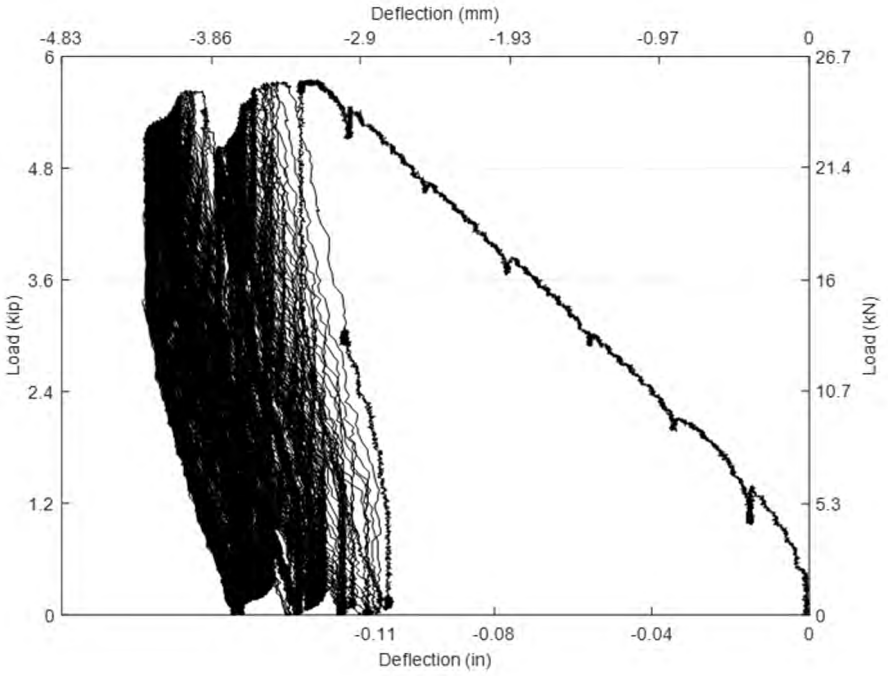


Figure 5.97: Specimen No. 6- cyclic test load versus vertical deflection (SP 7).

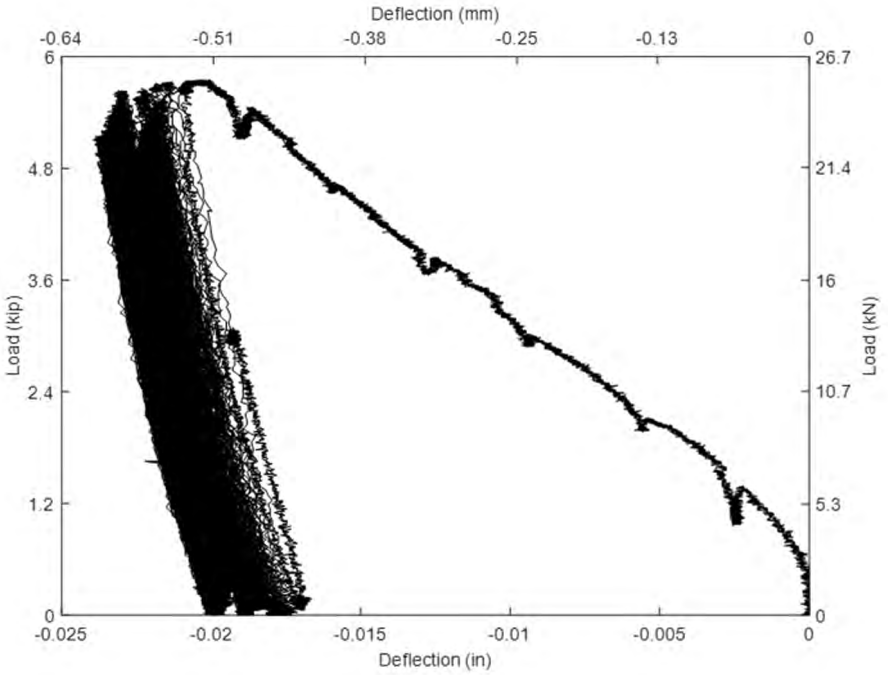


Figure 5.98: Specimen No. 6 - cyclic test load versus transverse deflection (LVDT 2).

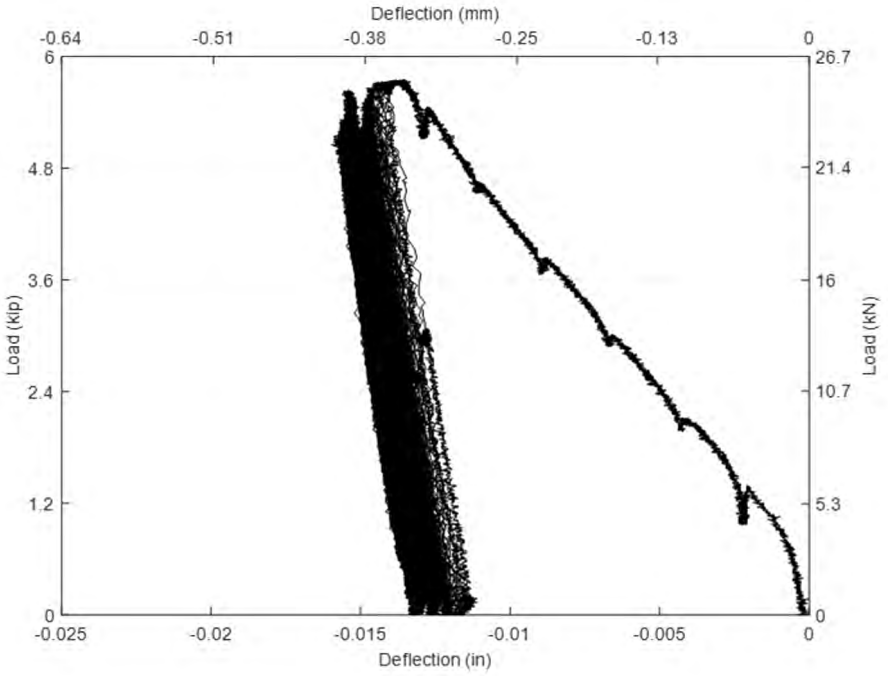


Figure 5.99: Specimen No. 6 - cyclic test load versus transverse deflection (LVDT 3).

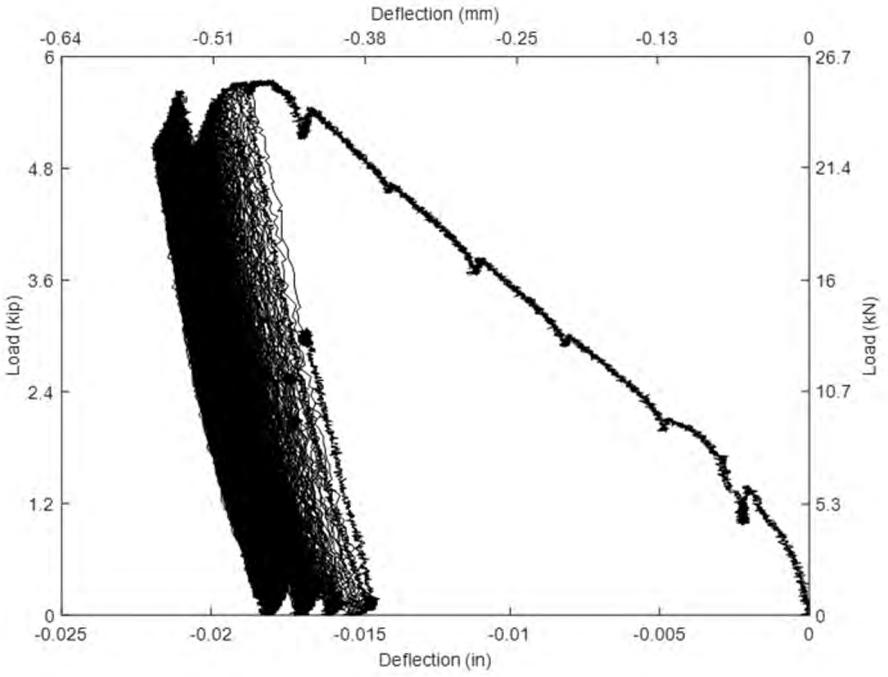


Figure 5.100: Specimen No. 6 - cyclic test load versus transverse deflection (LVDT 4).

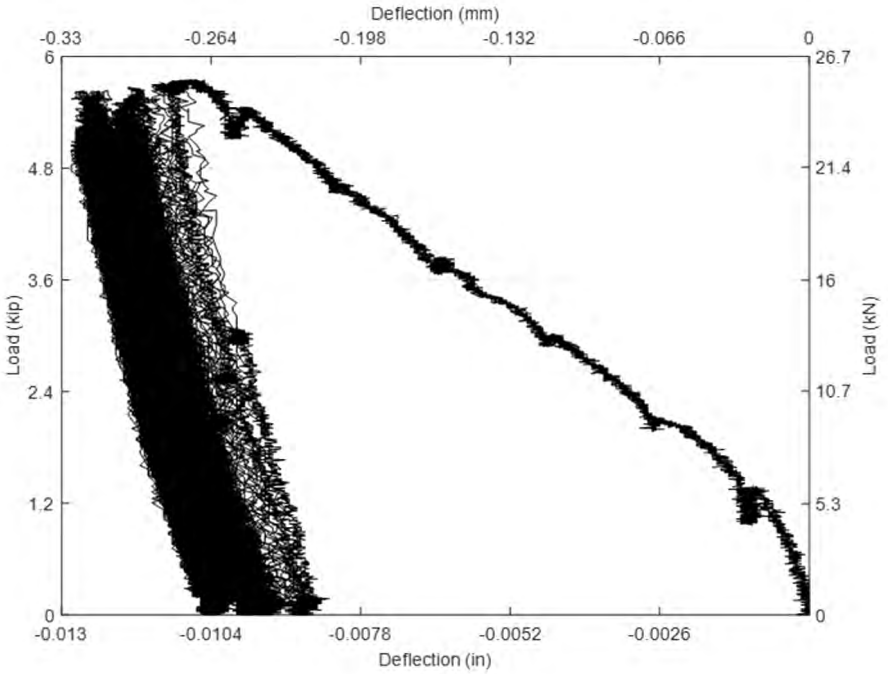


Figure 5.101: Specimen No. 6 - cyclic test load versus transverse deflection (LVDT 5).

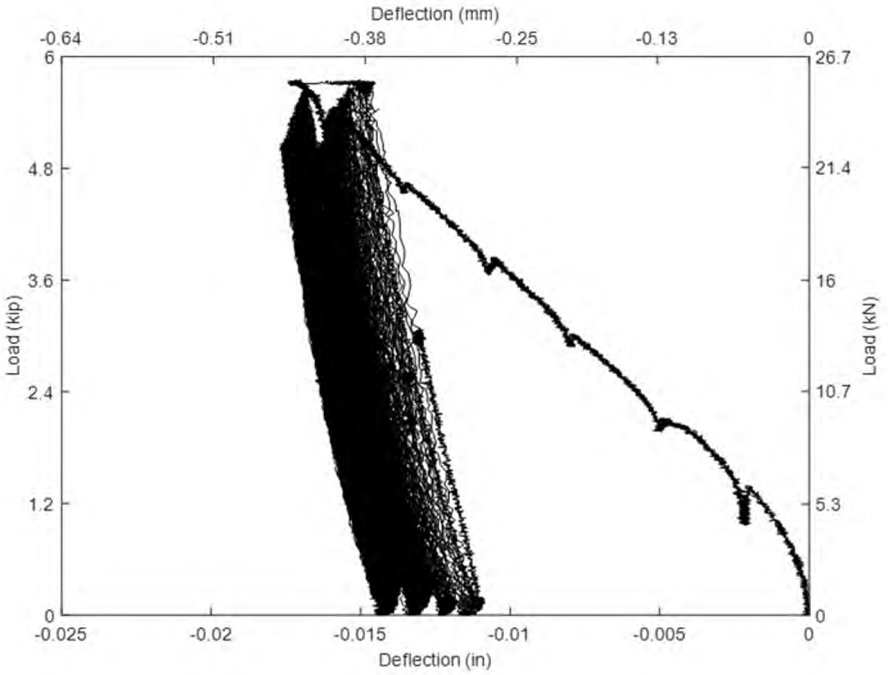


Figure 5.102: Specimen No. 6 - cyclic test load versus transverse deflection (LVDT 6).

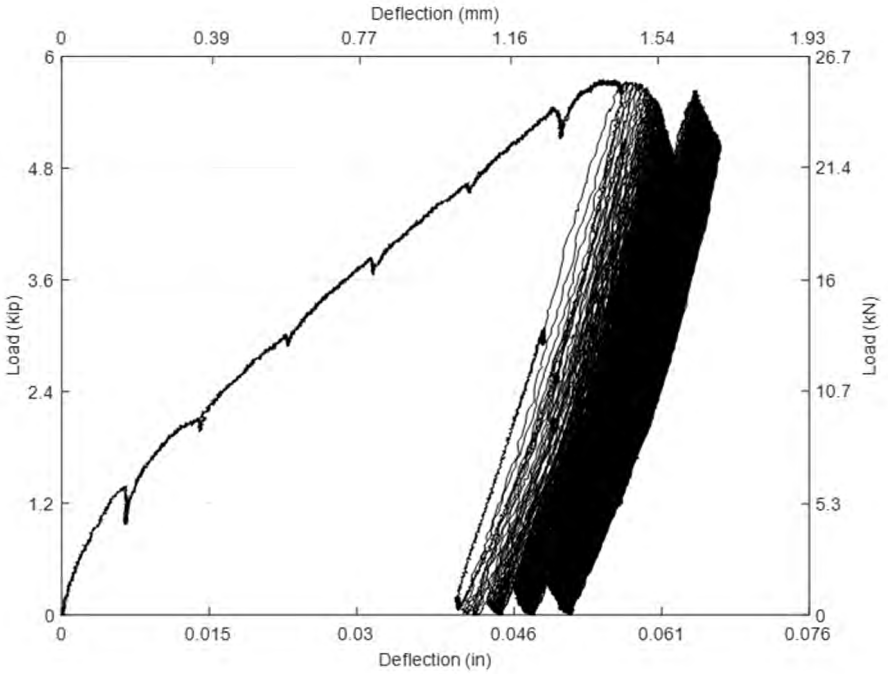


Figure 5.103: Specimen No. 6 - cyclic test load versus transverse deflection (LVDT 7).

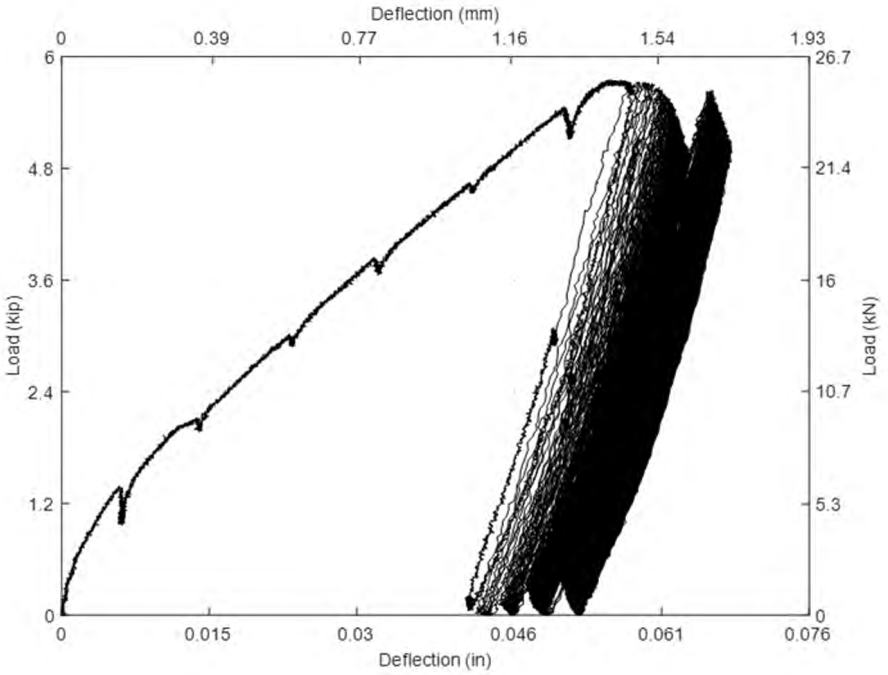


Figure 5.104: Specimen No. 6 - cyclic test load versus transverse deflection (LVDT 8).

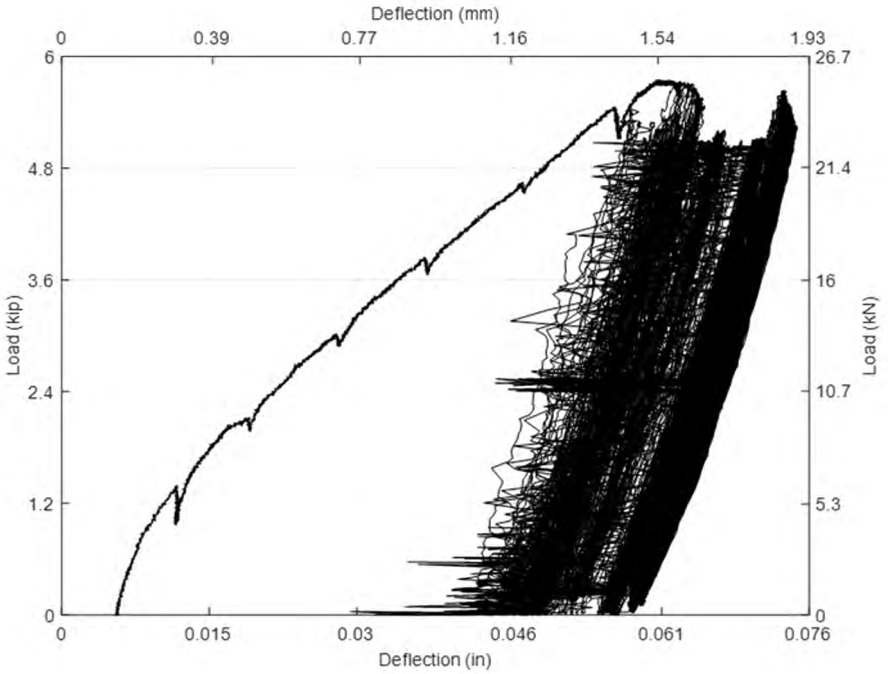


Figure 5.105: Specimen No. 6 - cyclic test load versus transverse deflection (LVDT 9).

After the cyclic test was complete, the slab was unloaded and then loaded at a rate of 0.05 in./minute to failure. While the system was continuously being loaded, no visual gap opening at the joint could be seen. It is noted that the ultimate load of 7,500 lb (33.3kN) is significantly lower than that of the UHPC therefore showing the bonding force of the grout in the joint was weaker. As the specimen softened, permanent deformation was recorded. Figure 5.99 shows the specimen failure point occurring around 7,500 lb (33.3kN) correlating Figure 4.93, showing the failure as the joint cracked at the front face of the specimen. Figure 5.106 show the vertical deflection comparison between each side of the testing specimen's joint and shows SPs 0 through 7 all had different deflections throughout the test. This can be due to the fact micro cracking and separation occurred internally in the joint material of the specimen. It can also be seen in the Figure 5.106 as the load increased to around 8 kips (32 kN); the vertical deflection data stayed relatively parallel to each other until initial cracking occurred on the slab. A loss of strength was recorded most likely due to the crack in the joint material as it propagated towards the flexural reinforcement. Once the reinforcement engaged, the specimen strength started to increase until the separation of the reinforcement and joint material occurred. Then, the specimen started to deflect more with little additional load, ultimately leading to failure of the testing Specimen 6.

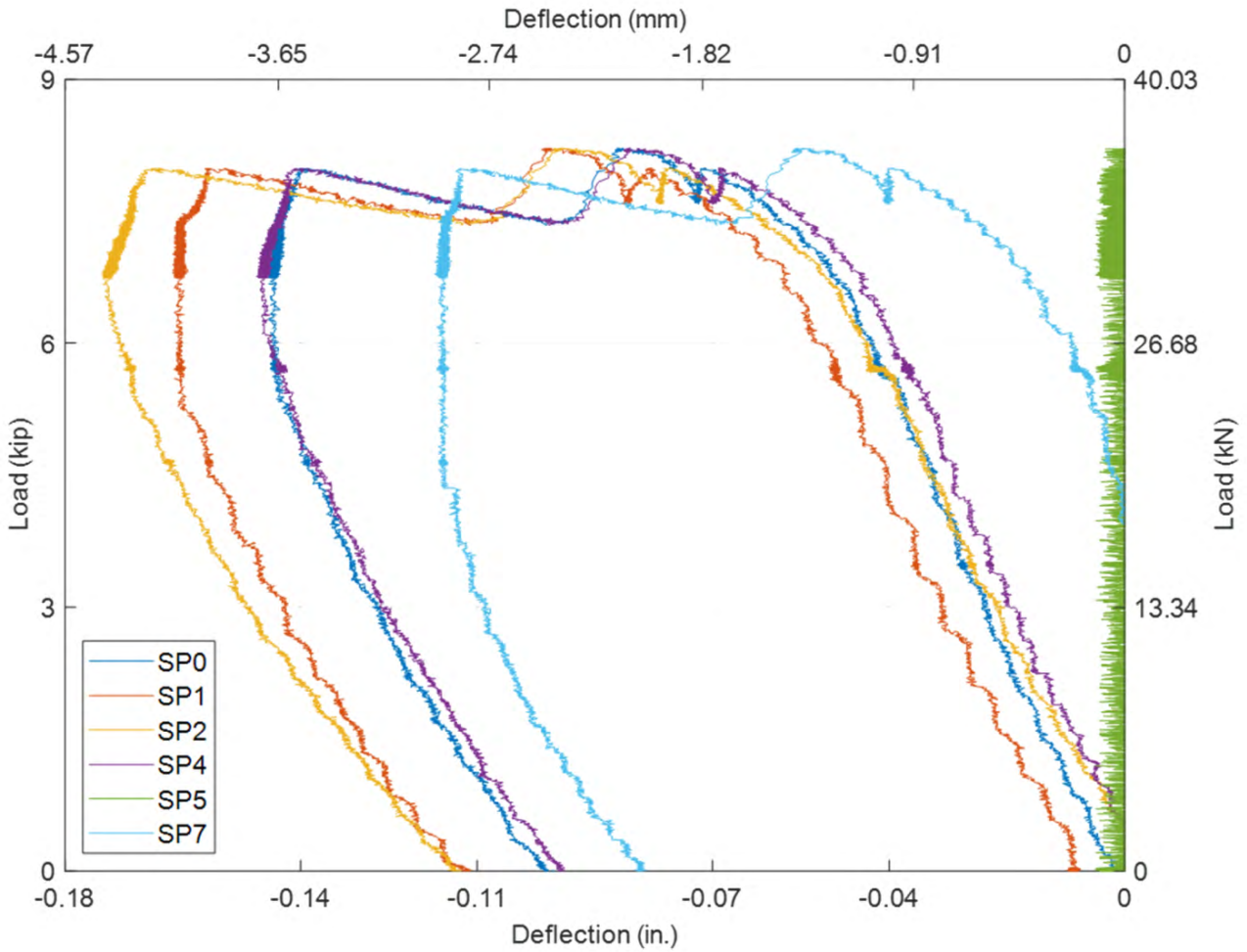


Figure 5.106: Specimen No. 6- failure test load versus vertical deflection.

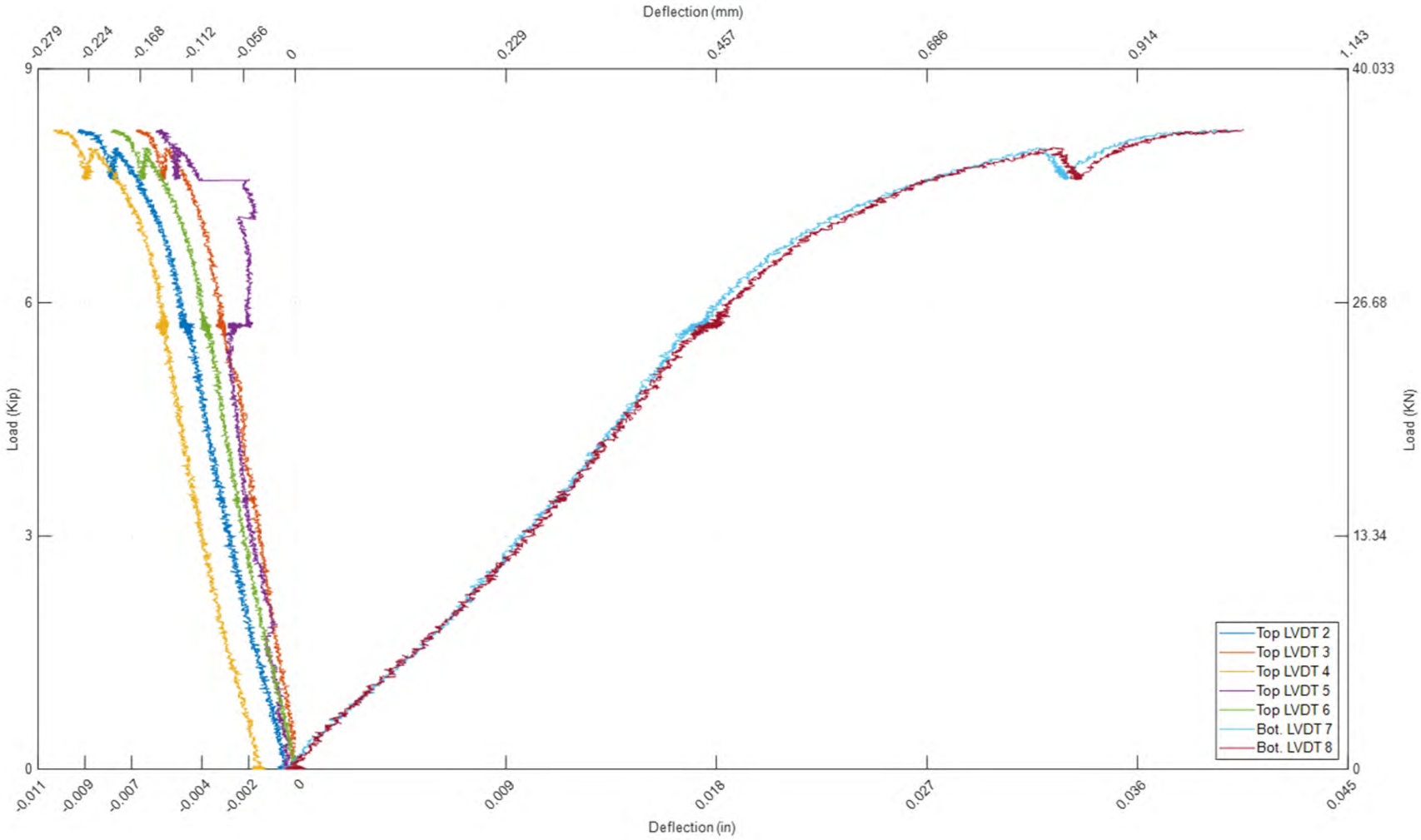


Figure 5.107: Specimen No. 6- failure test load versus transverse deflection.



Figure 5.108: Specimen No. 6- failure at south face

5.1.10.7 Cyclic Test Comparison

Table 4.1 shows a summary of the cyclic loading for each test. Specimens 1, 2, 4, and 6 were loaded to a maximum load of 20 kips (88.96 kN), 11.8 kips (52.49 kN), NA, 4.1 kips (18.23 kN), NA, and 5.7 kips (25.34 kN), respectively. Each specimen had approximately 400 cycles applied. The vertical displacement data at mid span during the cyclic loads were measured. While only the east slab was loaded, the measured displacements from both slabs were similar, indicating that the joint transferring the load from one slab to the other and maintained its integrity throughout testing. The displacement remained nearly constant throughout the cycles with no significant increase in displacement. However, some residual displacements were observed during each cycle, indicating that some minor degradation in the system was occurring such as minor cracking and debonding of the joint material. The joint however, continued to transfer load throughout the cyclic loading.

The displacement data from string potentiometers 1 and 5, which are located at the center of each slab, were used to identify the maximum vertical deflection. The results show that Specimens 1 had the largest vertical displacements. This can be attributed to the increase of the cyclic load compared to the other test. Ultimately this was expected to occur as reducing the overall load also reduces the amount of stress at the joint in which decreases the overall deflections. This expectation was assumed to occur with the introduction of the non-shrink grout mix on Specimen 6. The expectation was not met due to the fact the grout joint cyclic test was lower, but the vertical displacement and gap opening was higher than specimen two which had the same amount of joint reinforcement. Results suggest that test during the cyclic test, the separation between the joint material and slab was minimal for Specimens 1, 2, and 4. Therefore, held the slab system together allowing for more increase in load and less deflection. The grouted test specimen 6 did not show visually a separation between the joint material and slab, but initial cracks were observed in the same path of the joints lapped rebar. The bond between the rebar and the joint material appeared to separate and correlated with the fact the joints gap opening increased and so did vertical displacement. It did not seem as if the rebar was yielding in the system but crushing at the top of the joint was visible.

Table 5.7: Cyclic Test Measured Data Summary.

Specimen	Load, kips (kN)	Vertical Displacement, in. (mm)	Gap Opening, in. (mm)	Initial Stiffness, kip/in.(kN/mm)	Variations
1	20 (88.96)	0.23 (5.3)	0.09 (2.3)	106.6 (18.6)	UHPC, #4 at 12" O.C
2	11.8 (52.49)	0.16 (4.06)	0.07 (1.8)	60.5 (10.6)	UHPC, #4 at 24" O.C
3	NA	NA	NA	NA	UHPC, #3 at 12" O.C
4	4.1 (18.23)	0.12 (3.1)	0.03 (0.8)	48.1 (8.4)	UHPC, #3 at 24" O.C
5	NA	NA	NA	NA	Grout, #4 at 12" O.C
6	5.7 (25.36)	0.18 (4.5)	0.075 (1.9)	38.4 (6.7)	Grout, #4 at 24" O.C

5.1.10.8 Failure Test Comparison

Table 4.2 shows a summary of the failure loading for each test. Specimens 1 – 6 had a maximum load of 26 kips (115.6 kN), 16.4 kips (72.95 kN), 18.1 kips (80.51 kN), 12.5 kips (55.60 kN), 0.35 kips (1.55 kN), and 8.2 kips (36.47 kN), respectively. The loading rate for the failure tests was approximately 0.5 in./min. The vertical displacement data at mid span during the tests were measured as well. This could not be observed in specimen 5 due to failing the specimen at a low load before the tests could be conducted.

The displacement data from string plots 1 and 5, which are at the center of each beam, was used to identify the maximum vertical deflection and LVDT 4 and 8 was used to identify the maximum gap and crushing displacements. The results show that Specimens 1, 2, and3, 4 (UHPC Joints) vertical displacements increased as the load increase. Specimen 1 and 3 shared the same amount of rebar only varying in size from a No. 4 (No.13) to a No. 3. It was expected for the strength to decrease as the cross-section reinforcement decreased as well. Additionally, with the decrease in the joints rebar cross section, the stiffness of the whole system decrees and can be seen in the over vertical deflection. As rebars lap spacing was increased from 6 inches to 12 inches the loads were expected to decrease as well increase in deflection. This expectation was assumed to occur with the introduction of the non-shrink grout mix as well. The expectation was met due to the fact the grouted joint specimen 6 failure load was lower in compared to joints two by a factor of 2, but the vertical displacement and gap opening was lower than specimen two which had the same amount of joint reinforcement. Results suggest that during the failure test, the separation between the joint material and slab was minimal for specimen 1 and 3 due to the overall failure of the systems was in the slab and not the joint. Therefore, held the slab system together allowing for more increase in load and less deflection. Specimen 2 and 4 decreased the rebar spacing which led to a decrease in load capacity as well as an increase in overall deflection. Stiffness in the slabs joint reinforcements shows to have played a key part in strength and strain of the system. The grouted test specimen 6 did not show any separation in the joint material and slab, therefore created a more rigid joint connection. But due to the rigidity increase of the joint, the joint became more brittle and gave a reduction in load capacity overall. When comparing the grouted specimen 6 and UHPC joint specimen 1, UHPC show to yield roughly the same amount of gap opening but both differ in vertical displacement and strength. The UHPC was more ductile and had greater strength capacity than the gout material as shown in Table 4.2.

Table 5.8: Failure Test Measured Data Summary.

Specimen	Load, kips (kN)	Vertical Displacement, in. (mm)	Gap Opening, in. (mm)	Variations
1	26 (115.6)	0.62 (15.7)	0.10 (2.5)	UHPC, #4 at 12” O.C
2	16.4 (72.95)	0.87 (22.1)	0.53 (13.5)	UHPC, #4 at 24” O.C
3	18.1 (80.51)	0.83 (21.1)	0.28 (7.1)	UHPC, #3 at 12” O.C
4	12.5 (55.60)	1.11 (28.2)	0.62 (15.7)	UHPC, #3 at 24” O.C
5	0.35 (1.55)	NA	NA	Grout, #4 at 12” O.C
6	8.2 (36.47)	0.17 (4.3)	0.09 (2.3)	Grout, #4 at 24” O.C

5.1.11 Conclusions and Limitations

The following conclusion show valuable findings in this research and are as follow:

- The steel fibers in the UHPC joint interface can potentially start to carry the tensile self-weight load before the joint material gains its full strength, thereby reducing early constructions cracks that may occur before the system is in its final designed condition.
- The bond at the interface between the slabs and joint was visually observed to separate during each test of the UHPC and then rebar bar started to yield which can be seen in experimental data results produced.
- Three different failure modes were observed during testing. The first failure mode was due to the separation of the joint material and slab specimens, the second failure mode was due to the strength of jointed material, and the third failure mode due to the strength of the NWC concrete slabs.
    i. The first type of failure mode occurred at the interface between the joint material and the concrete slabs. This failure mode occurs by wide horizontal and/or vertical gap opening between the joint's material and NMC slabs before cracking at the joint was visible. This failure was observed in all test specimens and can be seen in Figure 5.18, Figure 5.25, Figure 5.29, Figure 5.37, Figure 5.43, and Figure 5.50.
    ii. One specimen failed by the second type of failure mode that occurs was due to crushing of the weak material due to the flexural stresses induced on the specimen 5 joint. This failure mode is shown in Figure 5.44 and was assumed to have been avoided in specimen 6 by the addition of pea gravel to the non-shrink grout.
    iii. Specimen 1 and 3 specimens failed due to the third failure mode. The failure occurred by diagonal cracking in the middle (loaded) concrete slab. It is believed that the failure was at the rebar along the same path of the load and caused a weak point in the slab. Due to the joint rebar spacing and size being the same for both tests the strength of the joint was stronger than that of the slab. This lead the load being induced on the slab to find the next weak point and can be seen in Figure 5.20 and Figure 5.32. This would most likely would not be the case in a box girder due to the increase in the moment of inertia but could potentially be problem if used in slabs.
- The first specimen had a failure at the point of load application location of the slab, telling us that joint was stronger than the slab itself. The specimen had a total of nine rebar of No. 4 (No.13) bars at the joint, creating a stronger joint. The failure was also along a rebar location, showing the load path to the weakest cross sectional area.
- Specimen two had five rebar of No. 4 (No.13) at the joint and the specimen failure at the joint. The failure was at the interface between the UHPC joint and NWC slab. This showed that the bond failed, but ultimately after the bond failed the joint continued to transfer load across it until the reinforcement yielded.

- Specimen three had nine rebar of No. 3 (No.10) bars lapped in the joint and the failure was at the point of application of the load on the East slab. The failure location was the same as test specimen one indicating that the nine rebar created a more rigid connection than the slab itself even after the rebar size was decreased one size. The failure was also along a rebar location, showing the load path to the weakest cross sectional area.
- Specimen four had five rebar of No. 3 (No.10) at the center joint and a failure at the joint occurred. The failure was at the interface between the UHPC joint and NWC slab as seen in test specimen two. This showed that the bond failed, but ultimately after the bond failed the joint continued to transfer load across it until the reinforcement yielded.
- Specimen five had nine rebar of No. 4 (No.13) bars in the joint. During testing the load drastically dropped before any test could be achieved. The joint failed before even reaching 400 lb (1.8 kN) of force on the specimen. The grout is high flow, non-aggregate, non-shrink grout and does not require anything additional other than water when the joint size is less than 3in. (76.2 mm). this is vital because anything larger than that size requires that the grout must be extended 30% by weight powder with 3/4 in. (1cm) pea gravel. The joint had shown cracking due to self-weight already large gap between the grout and slab, suggesting the joint was going to fail early on and a failure at the joint occurred while the system was being preloaded loaded. As shown in specimen six, the addition of the pea gravel had a vast impact on the joints system strength and should be pointed out the importance of making sure that the correct procedures are used in the field.
- Specimen six had five rebar of No. 4 (No.13) bars crossing the joint and failure occurred at the joint occurred. It is seen that the specimen carried approximately 11,200 lb (49.8 kN), prior to opening a crack at the joint. As the specimen load passed the yield point, permanent deformation stated to occur as the test continued and finally failure of the system and can be seen with the joint cracking at the front face of the specimen.
- The results show that specimens one, two, and four (UHPC Joints) vertical displacements increased as the cyclic load was higher. This is to be expected as the only change in the system was the rebar size and spacing therefore reducing the overall load, the amount of stress at the joint was also decreased.
- During the cyclic test, the separation between the joint material and slab was minimal for specimen one, two, and four. Therefore, held the slab system together allowing for more increase in load and less deflection.
- The results show that specimens one, two, and three, four (UHPC Joints) vertical displacements increased as the load increase. Specimen one and three shared the same number of bars crossing the joint but varied in the size of bar. Specimen one had No. 4 (No.13), whereas specimen three had a No. 3 (No. 10) which was a 58% decrease in cross section steel. It was expected for the strength to decrease as the cross section reinforcement decreased as well. Additionally, with the decrease in the joints rebar cross section, the stiffness of the whole system decrees and can be observed when comparing the vertical deflections. As rebar lap spacing was increased from 6 in. (152 mm) in specimens three

and four to 12 in. (304 mm), the loads capacity of the joint system was expected to decrease as well increase in the overall vertical deflections.

- When comparing the grout specimen six and UHPC joint specimen one, UHPC show to yield roughly the same amount of gap opening but both differ in vertical displacement and strength. As stated earlier, the UHPC had a greater load capacity than the grout material by a 68.8% difference.
- Typical the information to be produced from the cyclic loading is to observe the structural joint degradation of the material and ultimately leading to fatigue. Fatigue is appropriately defined as the progressive and localized damage of a material's molecular structure, which occurs when the material is subject to cyclic loading, eventually weakening the material. The repeated stress, strain, force and tensile load acting in such a situation is one of the reasons why the load needed for fatigue failure is far less than the ultimate tensile strength of the material. Though cycling test were conducted, most information was produced by the failure test as the cycling was not productive in the amount of time used. At one point only 200 cycles were conducted in a 4 hr. span, ideally a significant amount of cycles to achieve results would have been desired. What was observed during the cyclic tests was that for every specimen, permanent deformation occurred at each cycle through the test and that even though the joints were separated from the slabs, the load was still being transferred.
- Specimen 5 results could not be used as a direct comparison which impacted the over results in the test due to being one of only two controlled grout tests to compare with the UHPC joints. What can be extracted was that the us of pea gravel in the grout when a joint is larger than 3 inches (76.2 mm) greatly increased the strength of the material and this can be seen in joint specimen 6 as the load capacity of the system increased from 350 lb (1.5 kN) to 8,000 lb (35.6 kN).
- The connections can be smaller and to outperform the connected elements thus eliminating the connections as a weak link in the structure. You can effectively use UHPC in place of grout in the joint allowing you to take advantage of the mechanical properties for field-cast connections and provide you the ability to take control of the design by varying the amount (size, spacing) of the reinforcement that crosses the joint.

5.2 UHPC Shear Keys in Concrete Bridges

The objective of this study was to analyze the load-deflection behavior of a shear key system utilizing the non-proprietary UHPC. The results of a UHPC shear key were compared to a non-shrink grout (typical of bridge design in New Mexico) shear key. The bond of the two materials was compared to determine if UHPC provided a more effective bond with the precast concrete girder and increased the tensile strength of the shear key, inhibiting cracking caused by thermal fluctuations and shear loading. The steel fibers within the UHPC also aid in bridging micro-cracks that cannot be prevented, making the shear key more durable and sustainable.

To assess the behavior of the shear keys and the two different grouting materials, six tests were performed on full-scale 25-foot-long (7.62 m) reinforced concrete channel girders. The tests varied based on the use of UHPC or non-shrink grout as the grouting material. Four flexural tests were performed on the jointed girders with a four-point loading orientation placed at the mid-span of the eastern girder. Two shear tests were performed with four-point loading of the eastern girder located approximately 12 in. (304.8 mm) from the edge of the girder support. By applying load to only the eastern girder the load transfer through the shear key was better observed. Flexural testing of the girders consisted of 1,000 load-unload cycles to an estimated service-load deflection of 0.40 in. (10.2 mm). This deflection was estimated based on current standards. To have a more comprehensive understanding of the UHPC's performance it was tested with varying grouting methods that would affect the bond. The two grouting scenarios chosen modified the surface preparation of the precast concrete girder with the aim of understanding the impact of bond strength on overall shear key performance. Cyclic tests were also performed on a single girder with no grouted shear key. This test assisted in calculating the moment transfer through the shear key. Shear testing of the girders was done by subjecting the girders to 1,000 load-unload cycles at a maximum load of 20,000 lbs (88.96 kN). This loading was calculated based on the concrete shear capacity of the girders. A single girder was also tested under shear loading to aid in the determination of the shear distribution factor of the shear key. Material property samples were taken of the grout material for each test and were tested to determine the compressive strength and modulus of elasticity of the grouting material.

Through comparative analysis of shear key behavior with the different grouting materials the efficacy of a non-proprietary UHPC shear key was determined. The use of non-proprietary UHPC can be implemented in current infrastructure to repair and prolong the in-service life of structures. Although UHPC has been determined to be too high of an economic cost, the results of this project demonstrate that using UHPC as a joint material can maintain and improve durability without using large quantities of UHPC. Moreover, using a UHPC design which utilizes locally sourced materials will positively affect the economic impact of construction without sacrificing the superior performance of the material.

5.2.1 Full-Scale Experimental Methods

The channel girders used for the testing were recovered from a two simple span bridge located in Anthony, New Mexico. The original bridge, identified as Bridge 5296, was an in-service bridge located 0.7 miles East of NM-28 junction. Built in 1959, Bridge 5296 was structurally deficient and was recently replaced with Bridge 9706, the first UHPC bridge in New Mexico. The channel shaped reinforced concrete girders harvested from Bridge 5296 are 3 feet wide with a span length of 25 feet and had a concrete design strength of 3,000 psi; the girder cross-section is shown in Figure 5.109a. Along the longitudinal length of each girder is a trapezoidal recess that, when joined with the adjacent girder member, forms the shear key as seen in Figure 5.109b. Although the recovered girders did have minor damage, including a slight residual deflection, they were deemed adequate for the scope of this test. The flexural tests were completed using the same girders. The shear tests used a different pair of girders due to the damage sustained in the ultimate flexural load tests. For all flexural tests, the shear key material was removed and replaced at the completion of each test. The first and third flexural tests used UHPC as the grouting material. The variation in these two tests was the preparation of the girder surface to facilitate o inhibit bond with the UHPC grouting material. In the first test no surface roughening or wetting was done prior to placing the UHPC in the keyway; this test, referred to as CL1, was done to observe the behavior of a shear key with minimal bond to the precast girders. The second test, referred to as CL2, used US Spec NA non-shrink grout, an approved non-shrink grouting material by the New Mexico Department of Transportation (NMDOT). The third test performed on the two-girder system (CL4) used UHPC as the grouting material. This test varied from CL1 in that the walls of the shear key were wetted prior to casting to aid in the bond formation between girder and grouting material. All three tests were subjected to a cyclic loading of 1,000 load-unload cycles at the service condition deflection. An individual girder (CL3) was then subjected to 3 load-unload cycles at the same service condition deflection to quantify the load-deflection behavior of an isolated girder. The final flexural test completed investigated the overload, or post-yield, behavior of the shear key girder system when UHPC was used as the grouting material. Two shear tests were also performed. First, a single girder was subjected to multiple load-unload cycles to aid in the calculation and analysis of shear transfer across the girder system; this test is referred to as CL5. The second test, CL6, used a two-girder system jointed by a UHPC shear key and was subjected to 1,000 load-unload cycles. The following sections of this chapter discusses the test set-up and instrumentation, grouting materials, grouting methods, and loading criteria.

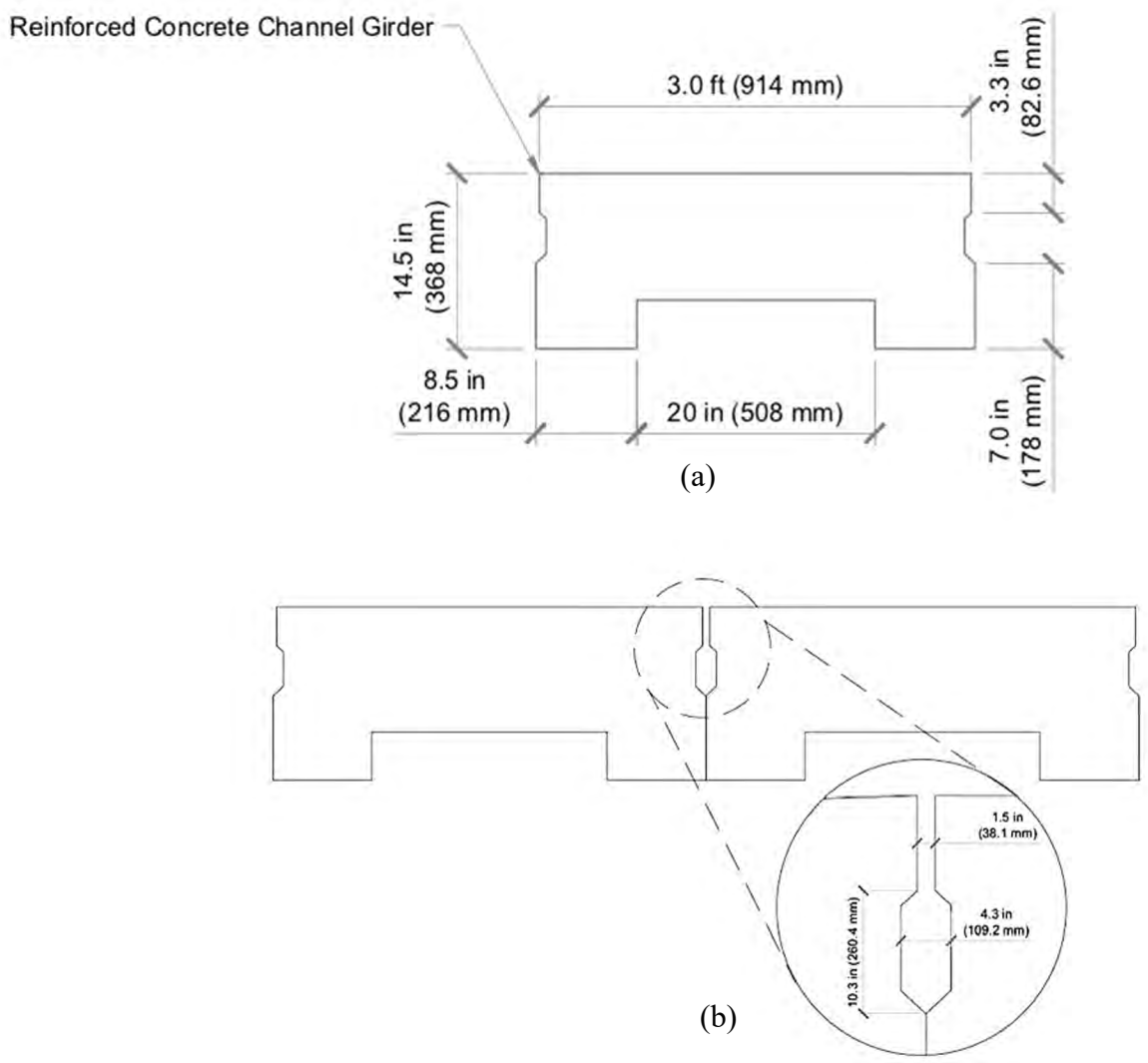


Figure 5.109: Bridge 5296 girder cross-section (a) reinforced concrete channel girder cross-section (b) shear key detail.

5.2.1.1 Flexural Test Set-Up and Instrumentation

Longitudinal four-point flexural tests were completed on two adjacent girders connected by a grouted shear key in the Structural Systems and Materials Testing Laboratory (SSMTL) at NMSU. The two-girder system flexural tests used the structural set-up shown in Figure 5.110. The girders were placed adjacent to one another on six concrete support columns. A steel reinforced elastomeric bearing was placed at all six bearing locations to support lateral movement and rotation and properly imitate current NMDOT practices. The elastomeric bearings had dimensions of 10 in. (254 mm) wide by 20 in. (500 mm) long by 1-7/8 in. (47 mm) thick. Each elastomeric pad had 3 laminations of 1/8 in. (3.2 mm) A36 steel with a 1/4 in. (6.4 mm) cover. Each bearing was designed in accordance with the 2017 AASHTO LRFD Specifications in section 14.7.5. The girders were placed within a structural testing frame beneath two, 110-kip (490-kN) capacity hydraulic actuators. The hydraulic actuators were placed 24 in. (610 mm) apart, each 12 in. (305 mm) from mid-span, resulting in a pure moment region. The actuators were placed only above the east girder to cause maximum load transfer between the girders at mid-span. The load transfer between girders was determined by testing a single girder and calculating the difference of the load carrying capacity between the single girder and the two-girder system. The load was applied by controlling the displacement of the hydraulic actuators through the use of a computer software. While adjusting the displacement of the actuator heads, the load applied to the girder was measured by internal load cells in the actuators. The load was distributed from the actuator heads into four-point loading through the use of steel spreader beams, shown in Figure 5.110. The steel spreader beams distributed the load to 3 in. (75 mm) diameter semi-circular load points centered over each stem of the east girder. The load at all four points was measured with additional load cells to capture the load distribution.

The girders were instrumented with multiple sensors to capture the behavioral response resulting from the applied loading and to determine the efficiency of shear and moment transfer across the shear key. The position of the sensors is shown in Figure 5.111. Electronic clinometers, also known as tiltmeters, were placed at mid-depth of the exterior face of each girder at the support locations to measure rotations at the girder ends and measure the symmetry of the applied loads. String potentiometers were attached to the bottom of the interior stems at quarter points and at mid-span to measure vertical deflections of the girder. Two additional string potentiometers were placed at mid-span on the bottom of the east exterior stem. LVDT's were used to measure axial displacements in the girders near mid-span, which were then used to calculate the curvature of the girders. To accomplish this, three LVDT's were placed at different elevations on the exposed longitudinal face of each girder at mid-span as shown in the oval detail provided in Figure 5.110. To measure any gap openings in the shear key, LVDT's were also placed across both the top and bottom of the shear key joint at one quarter point and at mid-span, shown in Figure 5.111.

When testing the single girder in flexure, the same longitudinal four-point loading was used, as shown in Figure 5.112. The single girder was also instrumented as similar to the two-girder system as possible to ensure comparability of the results. The instrumentation used on the single girder tested in flexure can be seen in Figure 5.113. Testing of the single girder also utilized

the 10 in. by 20 in. (254 mm by 500 mm) elastomeric bearings used in the two-girder system tests. All sensors were connected to a data acquisition system, facilitating real time monitoring and data collection throughout testing.

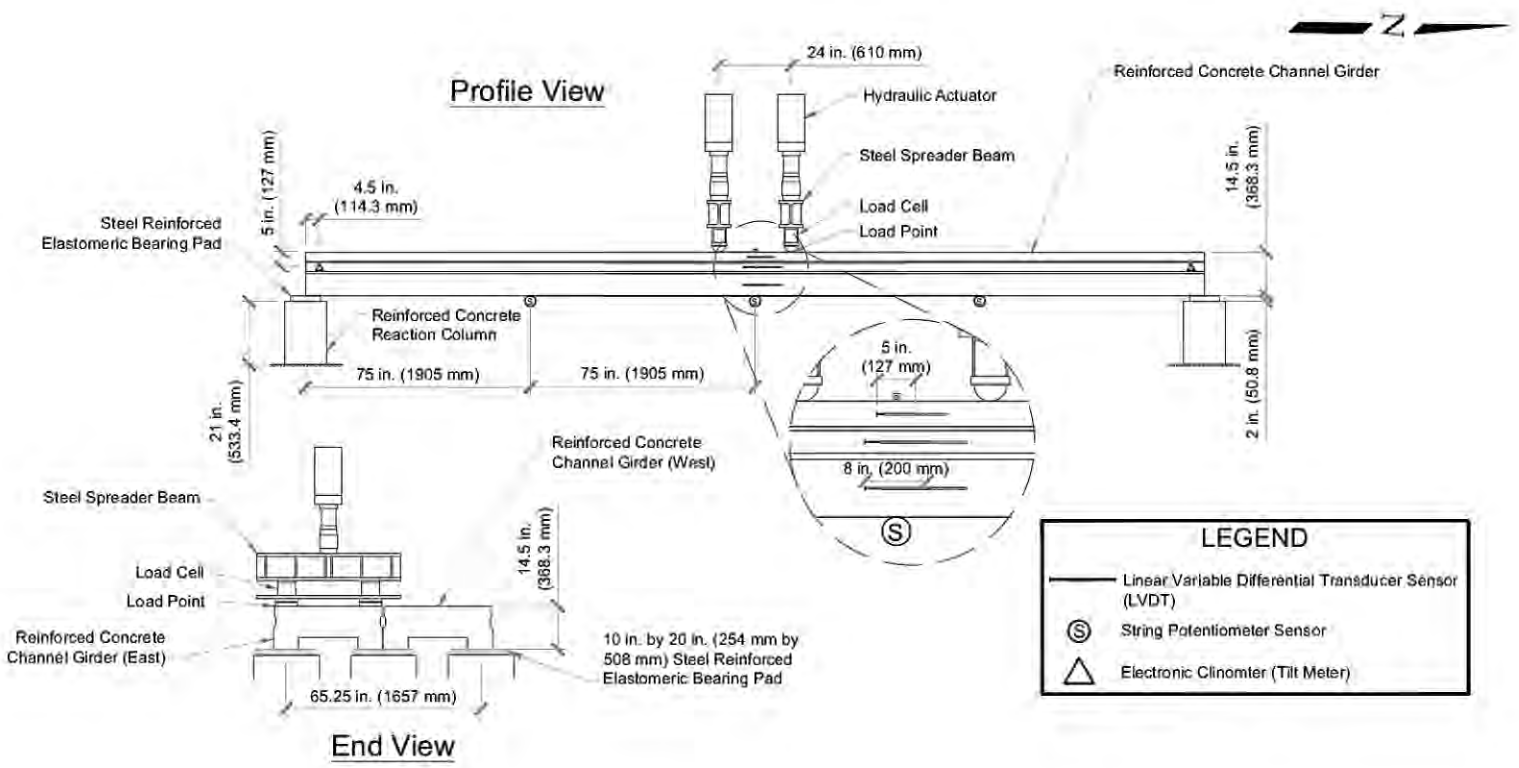


Figure 5.110: Profile view of two-girder system flexural test set-up and instrumentation.

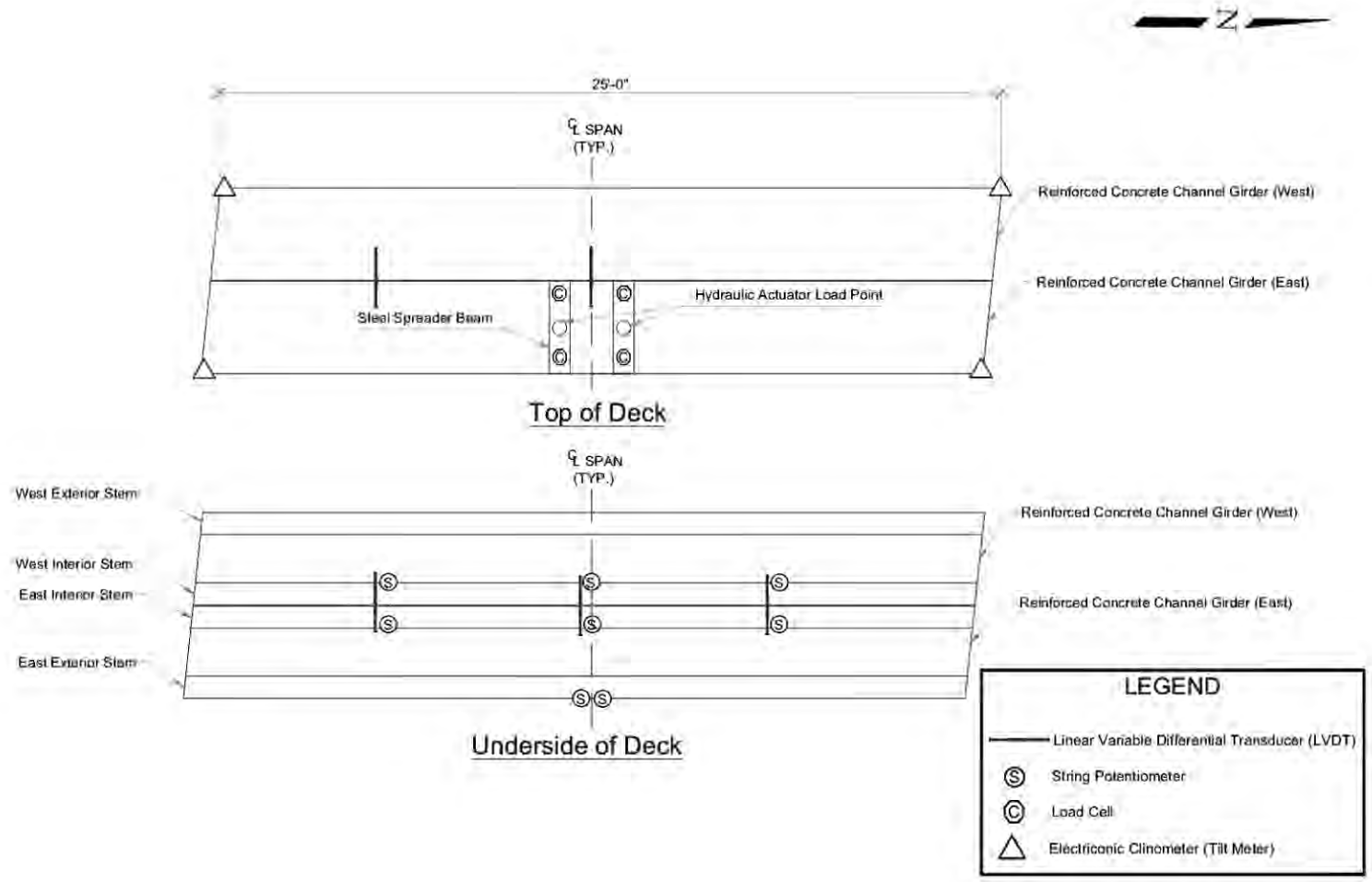


Figure 5.111: Plan view of two-girder system flexural test set-up and instrumentation.

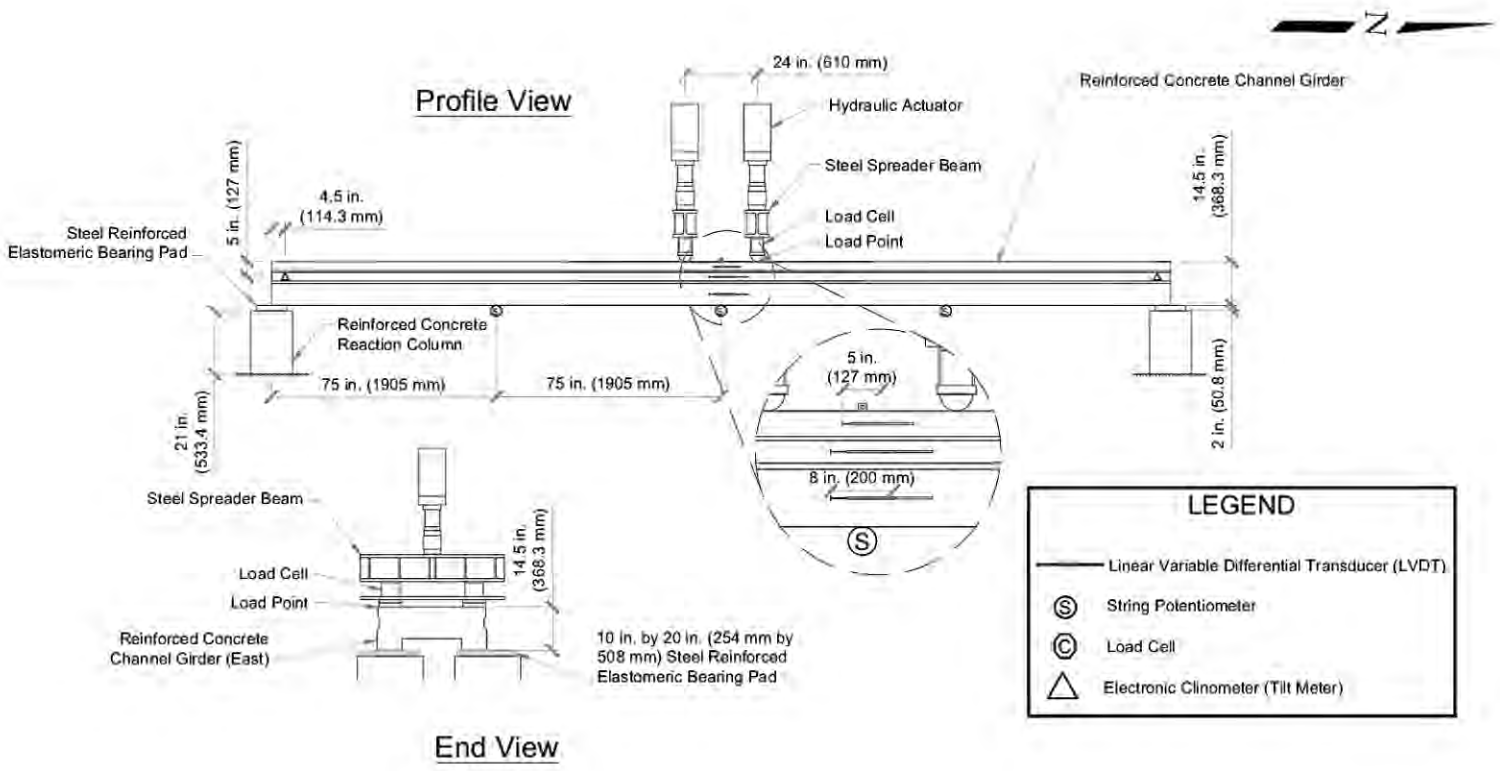


Figure 5.112: Profile view of single girder system flexural test set-up and instrumentation.

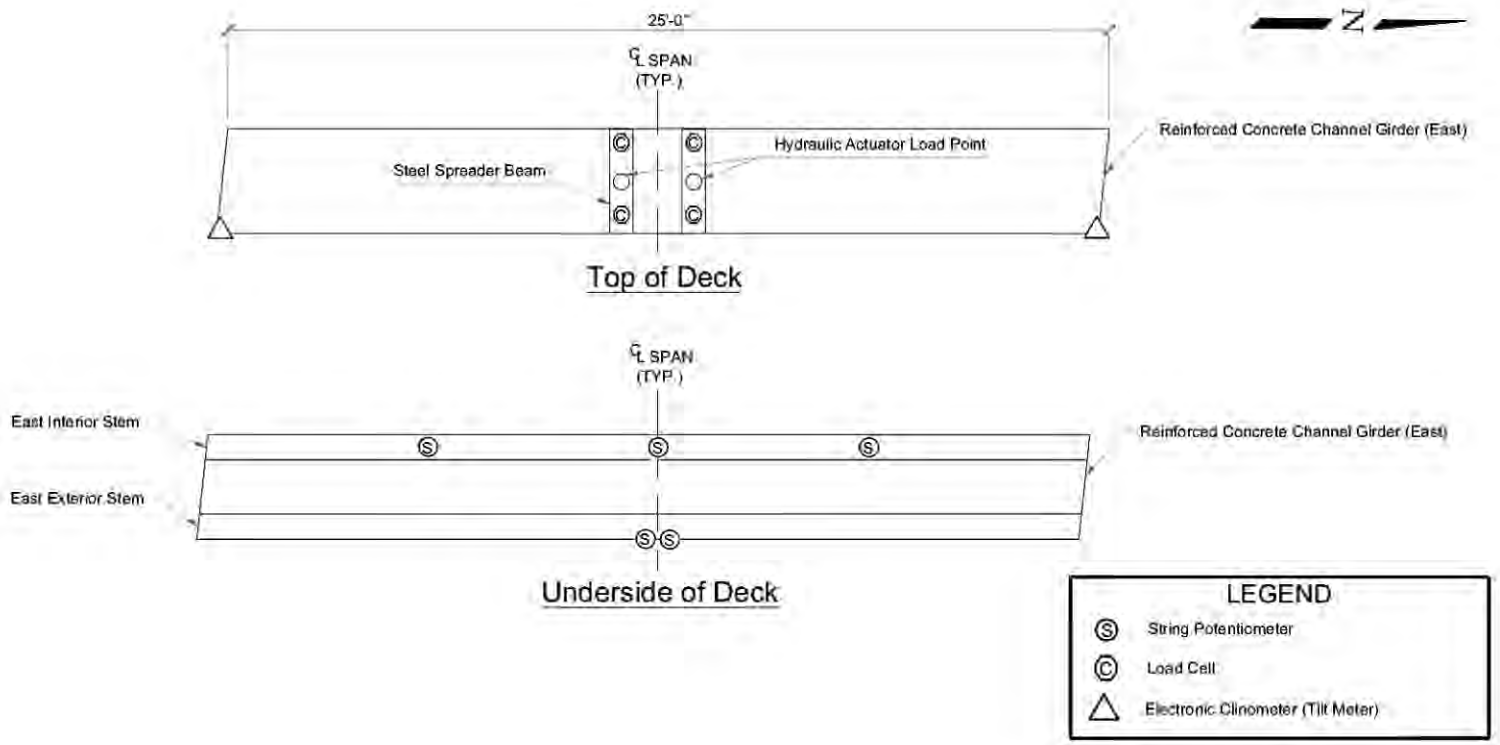


Figure 5.113: Plan view of single girder system flexural test set-up and instrumentation.

5.2.1.2 Shear Testing Set-Up and Instrumentation

Shear testing of two adjacent girders connected by a grouted shear key was performed using longitudinal four-point loading. The structural frame and actuators used in these tests was located at the SSMTL at NMSU. The two girders were placed adjacently on six concrete supporting columns. Each bearing point of the concrete channel girders was supported by a 10 in. by 20 in. (254 mm by 500 mm) steel reinforced elastomeric bearing with a thickness of 1-7/8 in. (47 mm). The specifications of these bearings are detailed in Section 3.1. The actuators were placed 24 in. (610 mm) apart, with the north actuator positioned 12 in. (305 mm) from the edge of the support. Each concrete channel girder was found to have an effective reinforcement depth of 10-5/8 in. (270 mm) resulting in a critical shear region at 10-5/8 in. (270 mm) from edge of the support. The north most actuator was placed at a distance of 12 in. (305 mm) from edge of the support to mitigate possible punching shear that could occur due to high loading conditions. Two steel spreader beams were then placed on the girder directly under each actuator. Two load cells were placed at each end of the steel spreader beams providing capture of the four-point loading. Load was then applied to the girders through 3 in. (76.2 mm) semi-circular contact points placed under the load cells at each end of the steel spreader beams. Positioning of the loading points and actuators can be seen in Figure 5.114. Loading of the girder system was accomplished by controlling the displacements of the hydraulic actuators through computer software. The girders were loaded both monotonically and cyclically. Loads applied were recorded through internal load cells within the hydraulic actuators, along with the four external load cells placed beneath the steel spreader beams.

The girders were also instrumented with various string potentiometers, linear variable differential transducers (LVDT) and electronic clinometers to fully perceive the behavior of the shear key under the loading conditions. The position of all sensors used are detailed in Figure 5.114 and Figure 5.115. The electronic clinometers, also known as tiltmeters, were placed at mid-depth of the exterior face of each girder over each support to measure rotations at the girder ends. String potentiometers were attached to the bottom of the interior stems at quarter points and at mid-span to measure vertical deflections of the girder. Two additional string potentiometers were placed on the underside of the exterior stem of both girders at mid-span to measure the deflection across the entire system. Curvature and axial displacement of the girders was measured by three LVDT's placed at different elevations on the exposed longitudinal face of each girder at mid-span, shown in the oval detail provided in Figure 5.114. To measure any gap openings in the shear key, LVDT's were also placed across both the top and bottom of the shear key joint at both quarter points, mid-span and at the center point of the four-point loading, shown in Figure 5.115.

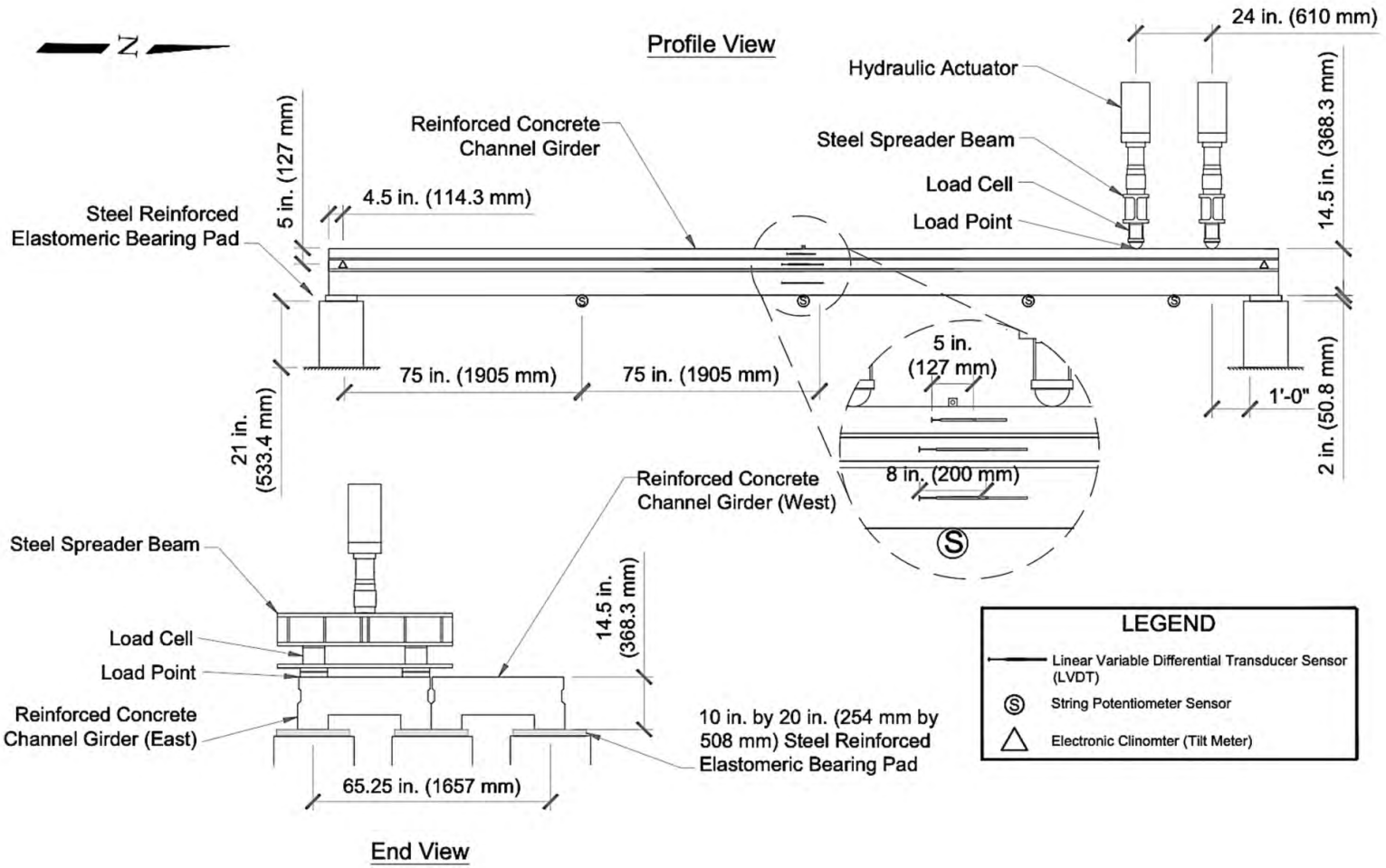


Figure 5.114: Profile view of two- girder system shear test set-up and instrumentation.

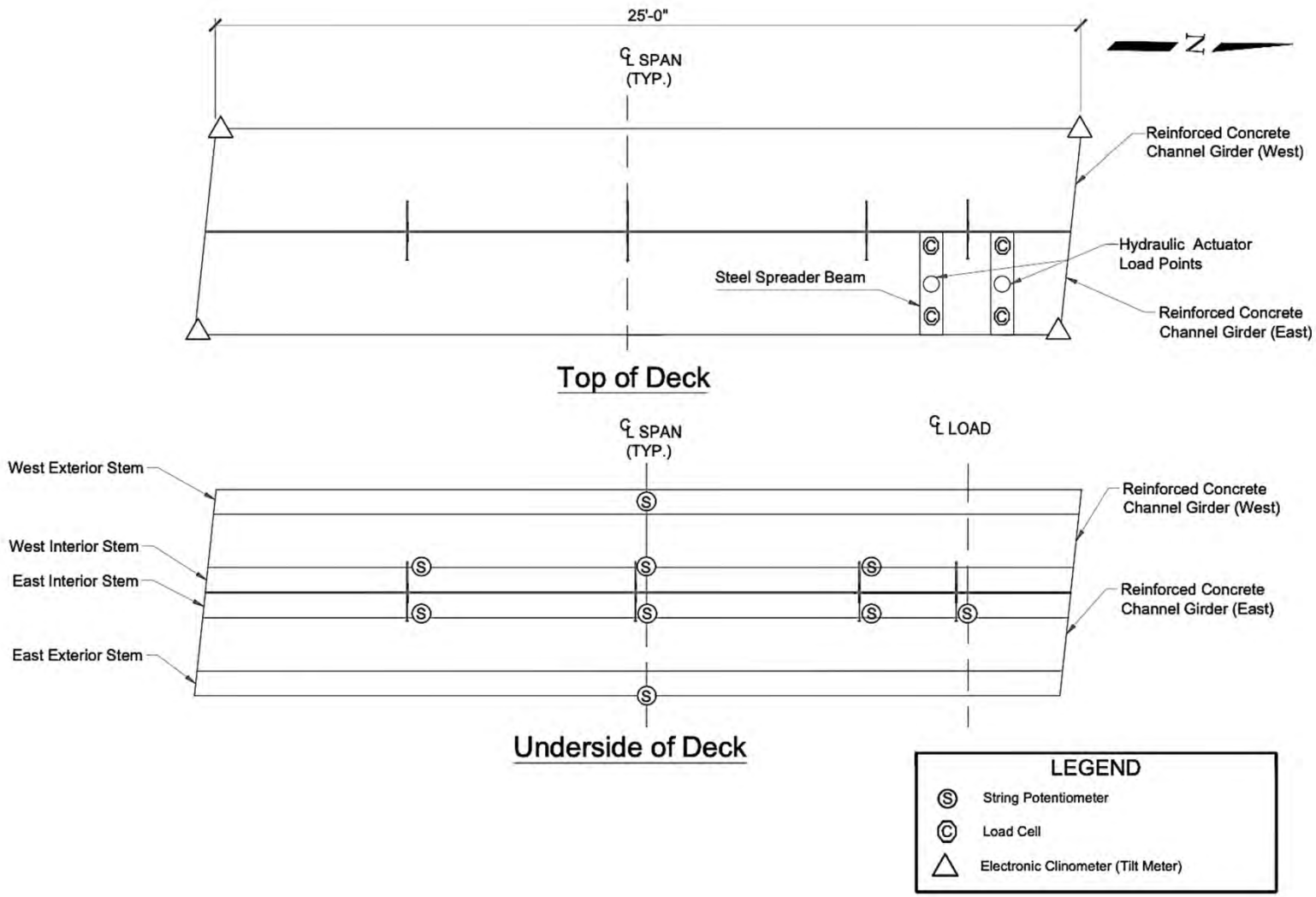


Figure 5.115: Plan view of two-girder system shear test set-up and instrumentation.

A single girder was also tested with the objective of observing shear load effects. This test was used to determine the shear transfer achieved during the two-girder system shear test. The same four-point loading was used in the single girder test that was utilized in the two-girder system test. Figure 5.116 and Figure 5.117 presents the hydraulic actuator location and instrumentation of the single girder shear test. Placement of the instrumentation was kept as similar as possible to ensure the results were comparable. The single girder test set-up maintained the use of concrete column supports and steel reinforced elastomeric bearings positioned at each bearing location, shown in Figure 5.116. All sensors were connected to a data acquisition system, facilitating real time monitoring and data collection throughout testing.

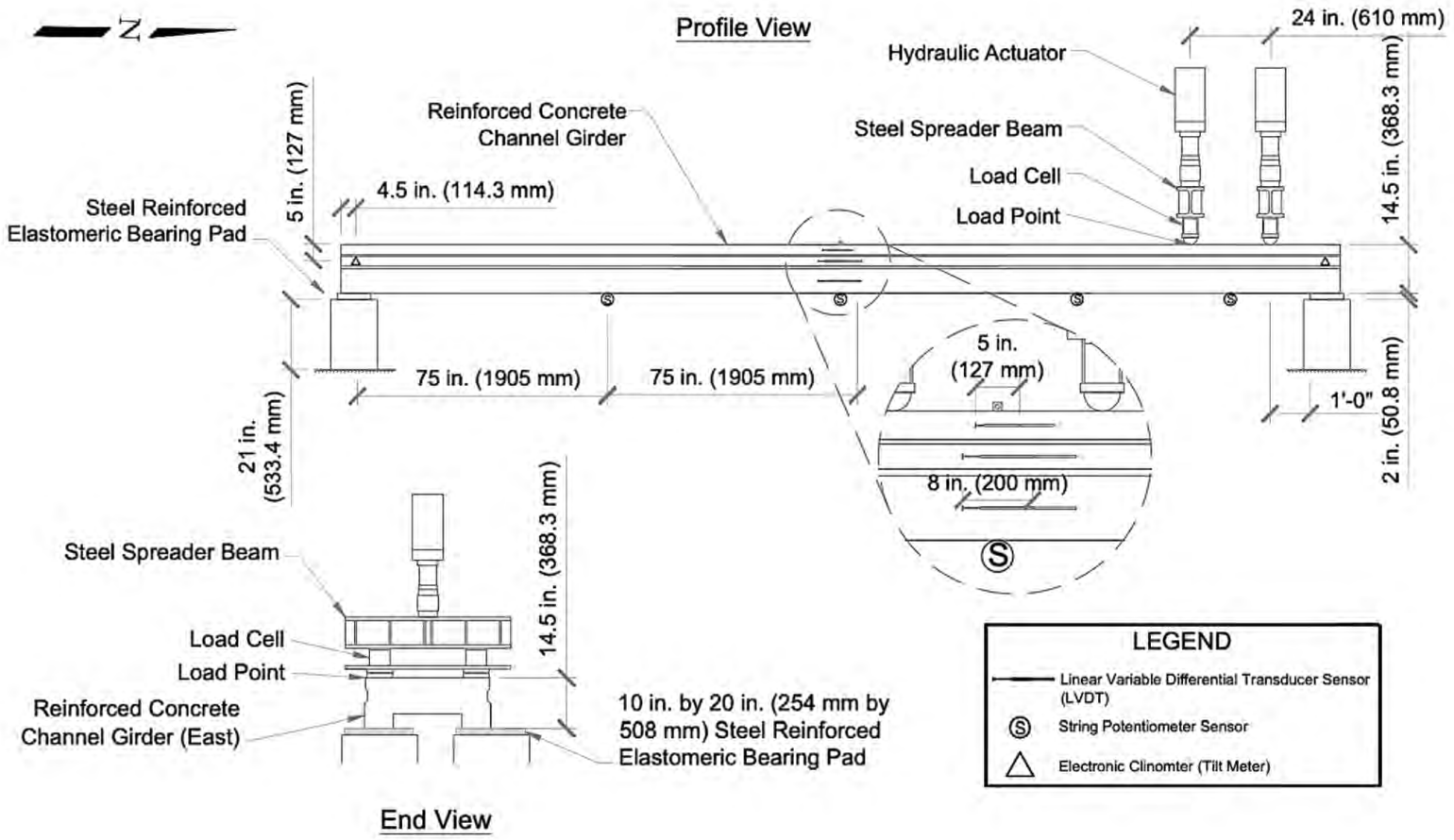


Figure 5.116: Profile view of single girder system shear test set-up and instrumentation.

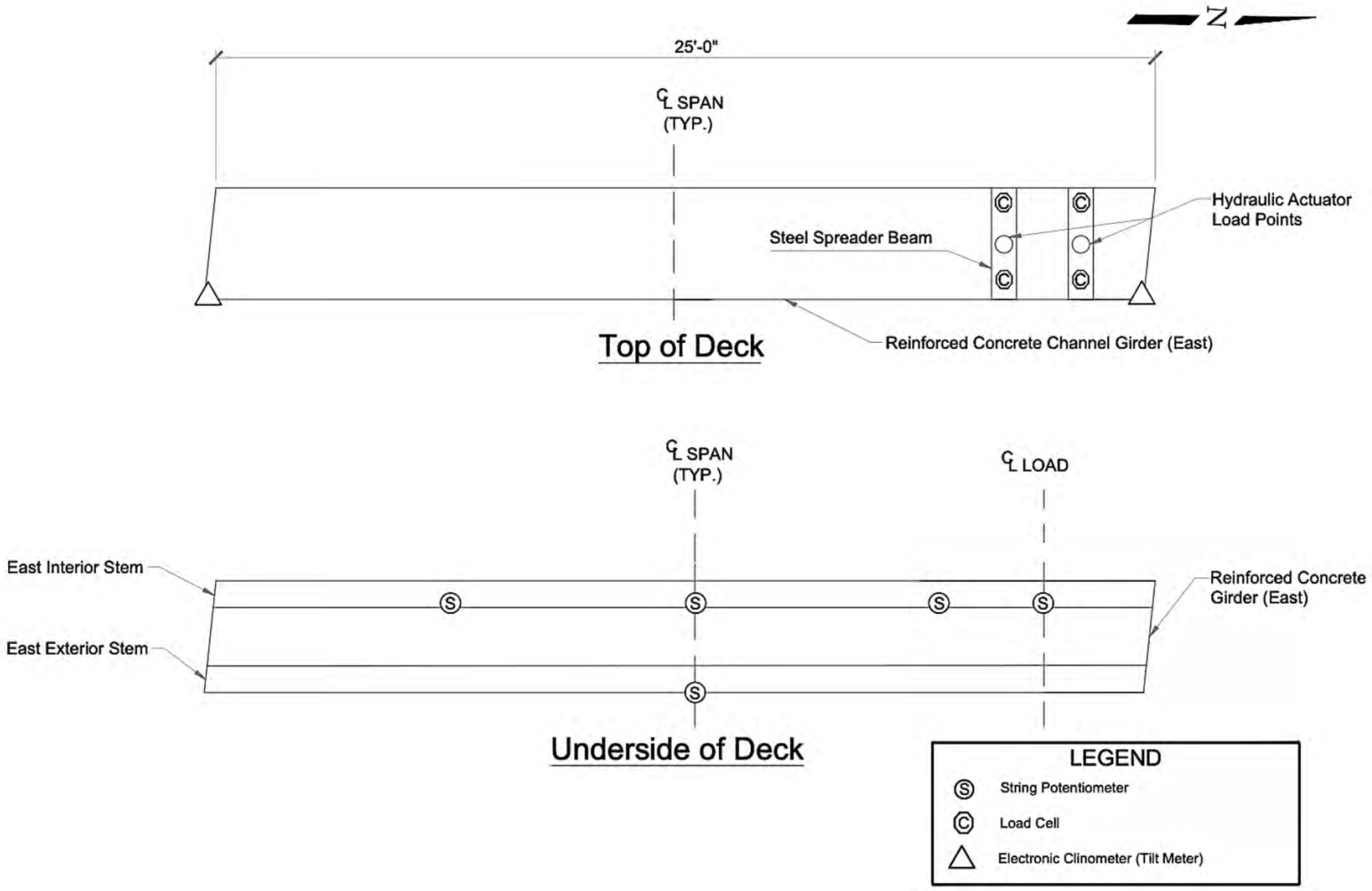


Figure 5.117: Plan view of single girder system flexural test set-up and instrumentation.

5.2.1.3 Grouting Materials

UHPC and US Spec NA non-shrink grouts were used as the grouting materials for this study. The UHPC mix design used was developed in previous studies at NMSU. The mix design, detailed in Table 5.9, used sand, cement and class F fly ash acquired from local sources. Class F fly ash was used to reduce the cost of the UHPC and improve economy. The sand used in the mix design had an aggregate top size that passed through a No. 4 sieve [0.187 in. (4.76 mm) nominal opening]. Silica fume, HRWRA, and steel fibers were also used in the UHPC mix and were sourced from regional suppliers. The HRWRA used was MasterGlenium 3030 and was added to increase workability of the material while maintaining a water to cement ratio of 0.15. Steel fibers used were Dramix® OL 13/0.2, produced by Bakaert, and had a length of 0.51 in. (13 mm) and tensile strength of 399 ksi (2750 MPa). The steel fibers were straight and had no coating, as seen in Figure 5.118.

Table 5.9: Nonproprietary UHPC Mix Design

Material	Cement	Silica Fume	Class F Fly Ash	Sand	HRWRA gal/yd^3 (L/m^3)	Water	Steel Fibers
lb/yd^3 (kg/m^3)	1377 (817)	172 (102)	172 (102)	1700 (1009)	9.0 (45)	258 (153)	200 (119)

The mixture design of the US Spec NA non-shrink grout is detailed in Table 5.10. The US Spec NA non-shrink grout is a NMDOT approved product. During mixing of the non-shrink grout, it was found that the manufacturer's maximum recommended water content was higher than needed. Adequate workability of the material was achieved using 9.2% less water volume than the maximum recommendation. The water content that was used during mixing is stated in Table 5.10.

Table 5.10: US Spec NA non-shrink grout mixture proportions

Materials	Cement	Silica Fume	Fly Ash	Crystalline Silica	Water (9.2% less than recommended)
%	40-80	5-20	5-20	>0.1	-
lb/yd^3 (kg/m^3)	1020-2040 (608-1217)	128-510 (76-304)	128-510 (76-304)	>2.55 (1.52)	750 (448)

5.2.1.4 Grouting Methods

After the girders were placed together on the six support columns with elastomeric bearing pads the underside of the shear key was caulked with DAP concrete waterproof filler and sealant caulk. While the underside of the girders were in direct contact, the underside shear key was caulked to decrease the potential for moisture loss. The caulk also assisted to contain the grout placed within the shear key. A wood block was placed at the ends of the shear key joint above the supporting columns to prevent leakage of the grouting material. The first test completed, referred to as CL1, used UHPC as the grouting material and was cast with the intention of minimizing the bond between the grout and concrete girder. A poor bond was achieved by neither saturating nor roughening the shear key surface. By not properly preparing the shear key walls, it provided a worst-case scenario, and it was expected that the UHPC would neither effectively bond with the precast concrete nor transfer loads effectively between the girders. On the other tests (CL2, CL4, ultimate flexural loading, CL6, and ultimate shear loading), an effective bond between the grouting material and precast concrete girder was desired. To accomplish this, the shear key recess on the precast concrete girder was wetted to saturated surface dry (SSD) conditions prior to the casting of the grouting material. By wetting the surface of the concrete, it was expected to create a better bond with the grouting material by eliminating moisture loss during the hydration process.

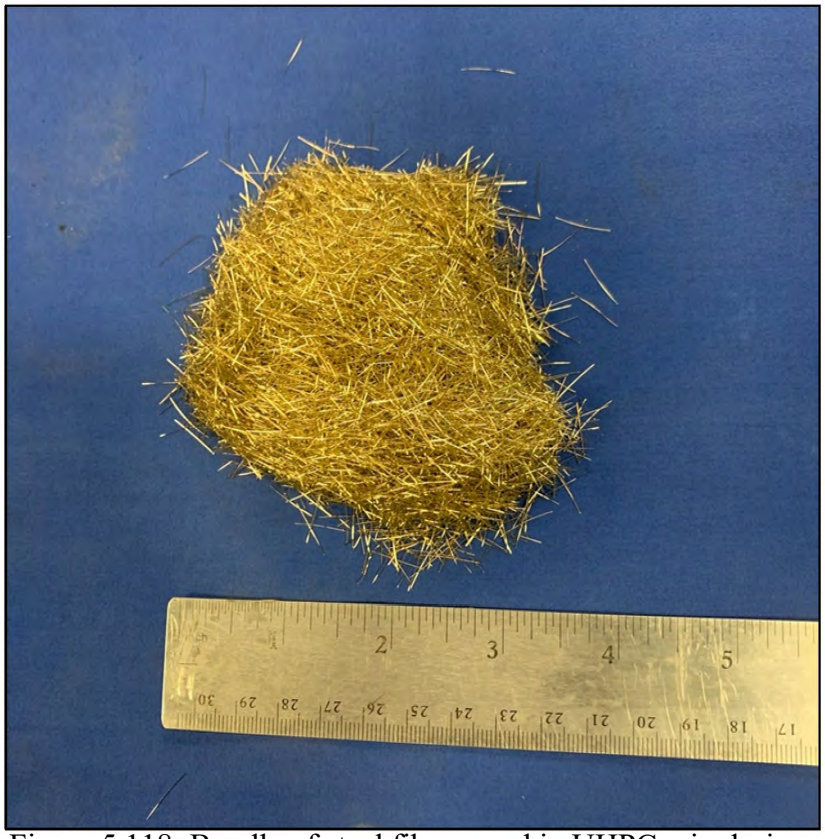


Figure 5.118: Bundle of steel fibers used in UHPC mix design.

When casting, the grouting material was placed within the shear key through the 3/4 in. (19.1 mm) upper opening of the joint. The methods of placing and consolidating varied between the two grouting materials used due to the difference in each materials workability. UHPC being less fluid was cast by placing the material on a tray, or hawk, and was then troweled into the opening, as shown in Figure 5.119a. This process began at mid-span of the joint, moving towards the ends, until the shear key joint was entirely filled. During placement the UHPC was vibrated with a 1/4 in. (6.35 mm) pencil vibrator to ensure consolidation and prevent honeycombing, as seen in Figure 5.119b. On the other hand, the US Spec NA non-shrink grout had a fluid consistency allowing for easier casting. The material was poured into the shear key through the 3/4 in. (19.1 mm) opening starting at mid-span until the entire shear key was filled. Due to the material's fluidity, it was not necessary to vibrate the grouting material. With the underside of the shear key caulked there was no leakage of the grouting material during casting.

After casting, the shear key joint was covered in plastic for 24-hours to decrease moisture loss. After 24 hours the plastic was removed, and the shear key was covered with moistened burlap to continue aiding the strength gain of the grouting material. The wooden blocks placed at the end of the shear key joint were also removed at this point. The burlap was wetted daily to ensure the material was provided a wet cure environment. Before testing the burlap was removed and the girders were instrumented as described in Section 3.1 and 3.2.

(a)

(b)

Figure 5.119: Grouting of shear key with UHPC (a) use of trowel to place UHPC in top opening of shear key, (b) pencil vibrator being used to consolidate UHPC within shear keyway

5.2.1.5 Flexural Loading

All flexural tests were subjected to cyclic loading to analyze the deflection behavior of the grouted shear key. The loading criteria for the cyclic loading was chosen based on deflection limits specified in AASHTO LRFD Bridge Design Specifications. The criteria used is summarized in Table 5.11. These deflection limits include:

1. The AASHTO 2.5.2.6.2 criterion states that the allowable deflection limit for general vehicular loads on a concrete bridge is equal to the Span/800. The girders had a span of 288 in. (7315 mm), therefore the allowable deflection limit was calculated as 0.360 in. (9.14 mm).
2. Application of the design truck shown in Figure 5.120 was also used according to AASHTO 3.6.1.2.2. The girders had a width of 36 in. (0.91 m) causing only a single wheel load from each axle of the 72 in. (1.83 m) transverse wheel spacing to be present at any one time. Therefore, a distribution factor of one (DF=1.0) was conservatively assumed for the following two configurations:
    a. To produce the most extreme force effect, the 32.0-kip (142-kN) axles were assumed to be spaced at 14.0 ft (4.27 m), with one 16.0-kip (71.2-kN) wheel load from each of the two axles placed on the girder equidistant from mid-span. The mid-span deflection due to this configuration was calculated to be 0.228 in. (5.80 mm).
    b. The total force of a single 32.0-kip (142-kN) axle was assumed to act as a point load at mid-span. The mid-span deflection due to this configuration was calculated to be 0.388 in. (9.85 mm).

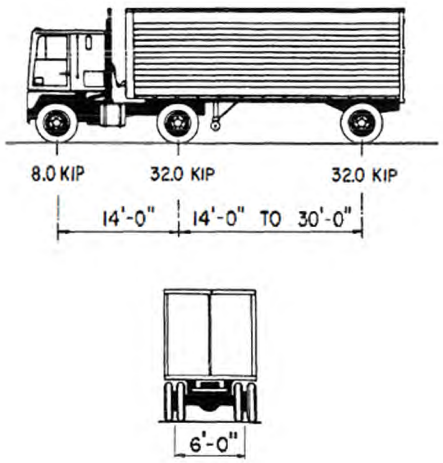


Figure 5.120 (AASHTO 2012): Characteristics of HS20 design truck.

Table 5.11: Summary of Deflection Criteria for Cyclic Loading

Case	Load	Criterion	Description	Deflection in. (mm)
1	Span/800	AASHTO 2.5.2.6.2	Girder clear span of 288 in. (7315 mm)	0.36 (9.14)
2a	Design Truck	AASHTO 3.6.1.2.2	16.0-kip (71.2-kN) axles spaced 14.0 ft. (4.27 m) and positioned equidistant from girder midspan	0.23 (5.79)
2b	Design Truck	AASHTO 3.6.1.2.2	32.0-kip (142-kN) point load at girder midspan	0.39 (9.86)
			Cyclic Loading Target Deflection	0.40 (10.16)

The first full scale test utilizing poorly bonded UHPC as the shear key material was designated as Cyclic Loading 1 (CL1). Using the loading configuration shown in Figure 5.110, the girder was loaded at a constant rate of 0.05 in./min (1.27 mm/min) until a mid-span deflection of 0.40 in. (10.2 mm) was achieved. At this point the girder was then unloaded and this loading process was repeated. In total the girder was subjected to 1,000 load-unload cycles, maintaining a mid-span deflection of 0.40 in. (10.2 mm). For the first 50 cycles the girders were loaded at a rate of 2 cycles/min. The remaining 950 cycles were completed at a rate of 4 cycles/min.

At the completion of CL1 the girders were separated and the poorly bonded UHPC was removed using a chisel. The girders were repositioned and prepared for the second test which used properly bonded US Spec NA non-shrink grout. The same loading process and deflection was completed for the second test, referred to as Cyclic Loading 2 (CL2). Maintaining the testing set-up and loading process allowed for more accurate comparisons of the load deflection behavior. At the completion of CL2, the girders were once again separated, and the grouting material was removed from the concrete girder. A baseline to determine the load transfer effects of the shear key was developed by subjecting a single girder to cyclic loading. This test, referred to as Cyclic Loading 3 (CL3), measured the behavior when no load transfer to an adjacent girder was possible. Test set-up and instrumentation for CL3 is detailed in Figure 5.112. Remaining consistent, the girder was loaded at a constant rate of 0.05 in./min (1.27 mm/min) to the desired deflection of 0.40 in. (10.2 mm) and then unloaded. This process was repeated for a total of three load-unload cycles. The number of cycles completed were limited to three because there was no degradation of the shear key to be observed. Therefore, the simple load deflection of a single girder could be accomplished in just three cycles.

The final full-scale test used both girders positioned and instrumented in the same manner as CL1 and CL2. This test, regarded as Cyclic Loading 4 (CL4), used UHPC that was properly

bonded as the grouting material. The girder was loaded at a constant rate of 0.05 in./min (1.27 mm/min) to the desired deflection of 0.40 in. (10.2 mm) and then unloaded. The girder was cycled with respect to the desired deflection for 100 load-unload cycles at a rate of 2 cycles/min. At the completion of 100 cycles, the girder deflection was increased to observe the behavior up to ultimate loading.

The ultimate loading was used to analyze the overload behavior of the shear key. This ultimate loading was performed with the same longitudinal four-point bending as cyclic loading, shown in Figure 5.110. The girder was loaded to the cyclic loading target deflection of 0.40 in. (10.2 mm) and then the deflection was increased to 0.80 in. (20.3 mm). At this time the girder was unloaded to 0.40 in. (10.2 mm) of deflection, shown in Figure 5.121. This process continued, increasing the maximum deflection reached by increments of 0.40 in. (10.2 mm) after every unload cycle. A final deflection of 2.0 in. (50.8 mm) was reached. The girders were then cycled between a deflection of 0.40 in. (10.2 mm) and 2.0 in. (50.8 mm) for three cycles at a rate of 0.1 in./min (2.54 mm/min). Once cycling was complete the girder was fully unloaded and the residual deflection was recorded. Finally, the girders were again loaded to 0.40 in. (10.2) of deflection, accounting for residual effects, and cycled for another 100 load-unload cycles at a rate of 4 cycles/min.

Figure 5.121: Load versus deflection of east and west girders during ultimate loading.

5.2.1.6 Shear Loading

Cyclic loading was performed on both shear tests to measure the deflection and rotational behavior of the girders. At the completion of CL6 an ultimate test was performed on the two-girder system to emulate an overload behavior that could occur in the field. Loading criteria for the cyclic loading was based on a load limit calculated using ACI 318-14 specifications. To remain conservative Equations 3.1 and 3.2 were used to determine maximum loading based on the shear capacity of the concrete alone. Concrete strength used for calculating shear capacity was 3,000 psi (20.68 MPa). The results of the concrete channel girder shear capacity is shown in Table 5.12. To remain conservative and prevent cracking of the girder, two-thirds of the total concrete shear capacity was chosen as the target load.

$$V_c = 1.9\sqrt{f_c'} + 2500\rho\frac{Vd}{M} \leq 3.5\sqrt{f_c'}b_w d \quad 3.1$$

Where,
f'_c = the concrete strength in psi,
ρ = the reinforcement ratio,
V = the shear force due to dead load,
d = the effective beam depth,
M = the moment due to dead load, and
b_w = the width of the beam.

$$V_c = 2\lambda\sqrt{f_c'}b_w d \quad 3.2$$

Where,
f'_c = the concrete strength in psi,
λ = modification factor for lightweight concrete (taken as 1.0 for normal weight concrete),
b_w = the width of the beam, and

d = the effective beam depth.

Table 5.12: Load criteria for shear testing

Equation	Criterion	Shear Capacity (V_c), lb (kN)
3.1	ACI Table 22.5.5.1	30,700 (136.6)
3.2	ACI Equation 22.5.5.1	30,101 (133.9)
Cyclic Loading Target Load		20,000 (89.96)

The first shear test performed was on single girder and was designated as Cyclic Loading 5 (CL5). Using the loading configuration shown in Figure 5.116, the girder was loaded at a constant rate of 0.05 in./min (1.27 mm/min) until a total load of 20,000 lb (89.96 kN) was reached. At this point the girder was then unloaded and this loading process was repeated. In total the girder was subjected to three load-unload cycles, maintaining a total applied load of 20,000 lb (89.96 kN).

The second full-scale shear test used both girders positioned and instrumented as shown in Figure 5.114 and Figure 5.115. This test, regarded as Cyclic Loading 6 (CL6), used adequately bonded UHPC as the grouting material. The girder was loaded at a constant rate of 0.05 in./min (1.27 mm/min) to the target load of 20,000 lb (89,96 kN) and then unloaded. The girder was cycled with respect to the desired load for 100 load-unload cycles at a rate of 2 cycles/min. At the completion of 100 cycles, the cycle rate was increased to 4 cycles/min for 900 cycles, reaching a total of 1,000 load-unload cycles. At the completion of the 1,000 cycles the load was increased to observe the behavior up to ultimate loading.

5.2.1.7 Casting and Curing

All specimens were formed using the following steel molds: 4 in. (101.6 mm) cubes, 4 in. by 8 in. (101.6 mm by 203.2 mm) cylinders, and 6 in. by 12 in. (152.4 mm by 304.8 mm) cylinders. In preparation for casting, the steel molds used were coated in a bond release oil to prevent damage of the specimen. When placing the UHPC in the molds a vibration table was used to ensure consolidation of the material. This method of consolidation was chosen to simulate the consolidation of the grout within the shear key, which was vibrated using a 1/4 in. (6.35 mm) pencil vibrator. The use of a vibration table was not necessary in the case of the US Spec NA non-shrink grout because of the fluid behavior of the material. During casting of the full-size shear key, the pencil vibrator was also deemed unnecessary. Once casting was complete the samples were covered in plastic sheeting to limit moisture evaporation. The samples remained covered for 24 hours in a room temperature environment, 70°F (20°C) and 30% relative humidity. At the end of the 24-hour period the specimens were removed from the steel molds and placed in a moist cure environment (73°F [23°C] and 98% relative humidity) for a duration of 7 or 28 days. The samples were removed from the wet cure environment immediately before testing for the 7- and 28-day strength of each specimen.

5.2.2 Material Property Test Results

The compressive strengths for the UHPC and US Spec NA non-shrink grout used for the large-scale shear key tests are provided in Table 5.13. The development of compressive strength was evaluated for the materials of these investigations using 4.0 in. (100 mm) UHPC cube specimens as outlined in Section i.i. Following casting, the specimens were cured at ambient temperatures [68°F (20°C) and 30% relative humidity] for 24-hours. After 24-hours, the specimens were cured at 73°F (23°C) with a relative humidity of 98% until an age of 28 days was reached. At 28-days, between four and six specimens were tested. Several specimens were also tested on the same day that full-scale tests were performed. Both grouting material specimens used the same curing regimen. The average measured strengths are provided in Table 5.14. According to ASTM C1856 the minimum required 28-day strength of UHPC is 17,000 psi (120 MPa), and as can be observed, the UHPC used in this research met this requirement.

Table 5.13: Compressive strength results for UHPC and US Spec NA

Day Tested	CL1 UHPC ksi (MPa)	CL2 US Spec NA ksi (MPa)	CL4 and Ultimate Flexural Loading UHPC ksi (MPa)	CL6 and Ultimate Shear Loading UHPC ksi (MPa)
7-day	-	3.72 (25.6) 6.26 (43.2) 6.70 (46.2) 5.77 (39.8)	14.9 (103) 13.3 (91.7) 13.8 (95.1) 14.4 (92.4) 13.2 (91.0)	12.8 (88.3) 15.4 (106) 15.2 (105) 15.4 (106) 10.5 (72.5) 15.2 (105)
28-day	17.7 (122) 18.0 (124) 19.0 (131) 17.6 (121) 18.4 (127) 18.6 (128) 19.0 (131) 18.3 (126) 17.2 (118) 19.9 (137) 17.8 (123) 18.5 (128)	5.26 (36.3) 6.26 (43.2) 6.85 (47.2) 5.01 (34.5)	17.2 (119) 17.3 (119) 16.1 (111) 17.7 (122) 15.9 (110) 17.5 (121)	17.1 (118) 15.9 (109) 15.1 (104) 16.9 (117) 16.7 (115) 15.9 (109) 18.4 (127) 14.4 (99.1) 17.8 (123) 16.0 (111)

Table 5.14: Average compressive strengths of UHPC and US Spec NA

		CL1 UHPC ksi (MPa)	CL2 US Spec NA ksi (MPa)	CL4 and Ultimate Flexural Loading UHPC ksi (MPa)	CL6 and Ultimate Shear Loading UHPC ksi (MPa)
7-day Strength	ksi (MPa)	-	5.61 (38.7)	13.9 (96.1)	14.1 (97.2)
	Std. Dev., σ	-	1.14	0.63	1.84
28-day Strength	ksi (MPa)	18.2 (126)	5.85 (40.3)	16.9 (117)	16.4 (113)
	Std. Dev., σ	0.74	0.75	0.70	1.14

Table 5.15 presents the modulus of elasticity results found through testing of the 4 in. by 8 in. (101.6 mm by 203.2 mm) and 6 in. by 12 in. (152.4 mm by 304.8 mm) cylinders. These specimens were cured with the same regimen used for the cube specimens. These tests were performed on the same day that full-scale testing was performed; the testing age for each cylindrical specimen is specified in Table 5.15. One 4 in. by 8 in. (101.6 mm by 203.2 mm) cylinder and one 6 in. by 12 in. (152.4 mm by 304.8 mm) cylinder was used to test the modulus of elasticity for each grouting material.

Table 5.15: Modulus of elasticity results of UHPC and US Spec NA

Specimen Size		CL1 UHPC	CL2 US Spec NA	CL4 and Ultimate Flexure UHPC	CL6 and Ultimate Shear UHPC
4 in. by 8 in. (101.6 mm by 203.2 mm)	ksi (MPa)	4,234 (29,192)	3,093 (21,326)	6,545 (45,126)	5,776 (39,824)
6 in. by 12 in. (152.4 mm by 304.8 mm)	ksi (MPa)	5,211 (35,929)	2,635 (18,168)	5,081 (35,023)	6,207 (42,795)
Testing Age		46 days	9 days	7 days	7 days

5.2.3 Cyclic Testing

Full-scale tests were performed on two 25 ft (7.62 m) long adjacent reinforced concrete girders with a longitudinal shear key joint. These tests were used to determine the load-deflection behavior, moment distribution, and shear distribution of the two-girder system. The girders were tested in flexure using the set-up shown in Figure 5.110, and Figure 5.112. Shear tests were performed using the testing configuration shown in Figure 5.114 through Figure 5.116. Two actuators and spreader beams were used to apply the four-point loading to one girder (the eastern girder) while the deflections of both girders were measured. The girder deflections were used to determine the load transfer across the shear key to the second girder (the western girder). Loads and deflections were measured using internal load cells within the hydraulic actuators and string potentiometers placed along the length of the girders, as can be seen in Figure 5.110 through Figure 5.117.

Four cyclic tests were performed using varying grouting materials and grouting methods: CL1, UHPC grout with a poor interface bond; CL2, US Spec NA non-shrink grout with proper bond; CL3, single girder with no grouted shear key; CL4, UHPC grout with proper bond. The grouting method used in CL1 caused a poor bond at the interface between the grout and precast girder because no surface preparation was performed. This lack of preparation caused moisture loss at the interface resulting in a weaker bond. Tests CL2 and CL4 had a more effective bond because the walls of the shear key were prepared by pre-wetting the surface 24-hours before casting of the shear key. CL3 was performed in order to determine the moment distribution through the shear key in tests CL1, CL2 and CL4. CL1 and CL2 were subjected to 1,000 load-unload cycles with the maximum deflection reaching 0.40 in. (10.2 mm). Being that CL3 was a single girder, with no grouted shear key, it was determined that 3 load-unload cycles provided the necessary measurements needed for analysis. Only 100 load-unload cycles were completed during CL4 because it was concluded that no additional information would be gained considering that 1,000 cycles had already been performed on a UHPC shear key during CL1. The fifth test performed was an ultimate loading of the girders to analyze the overload behavior of the system. This was performed immediately after CL4 was concluded.

The load-deflection results of these tests were analyzed by plotting the load versus the vertical mid-span deflection that was measured during testing. The load quantities used in this analysis are the sum of both actuator loads applied during testing. These internal load cells have an accuracy of ±15.0 lb (66.7 N).

5.2.3.1 Cyclic Loading 1

5.2.3.1.1 Vertical Deflection Behavior

The first test performed, CL1, used poorly bonded UHPC as the grouting material. A poor bond was created between the grout and precast girder by eliminating any preparation of the shear key walls prior to casting. The shear key system shown in Figure 5.110 was implemented and the east girder was loaded at a constant mid-span deflection rate of 0.05 in/min (1.27 mm/min) until a mid-span vertical deflection of 0.40 in. (10.2 mm) was reached. The girder was then unloaded. This load-unload cycle was repeated for 1,000 cycles. For the first 100 cycles the girder was loaded at 2 cycles per minute, after which the loading rate was increased to 4 cycles per minute.

To analyze the results of the CL1 test the applied load was plotted versus the vertical deflections at the various string potentiometer locations shown in Figure 5.111. In Figure 5.122 and Figure 5.123 the load-deflection behavior of the east girder is compared with that of the west girder. The location that displayed the greatest difference in deflection between the adjacent girders is at the mid-span location. The greatest average difference in deflection of the girders at mid-span was found to be 0.084 in. (2.13 mm) when comparing the exterior stem of the eastern girder and the interior stem of the west girder, presented in Figure 5.122a. Comparing the interior stems of both girders at mid-span gives an average deflection difference of 0.017 in. (0.43 mm), shown in Figure 5.122b. It is expected that the exterior stem of the east girder would have a higher average deflection during loading due to the lack of support, while the interior stem of the east girder resisted loading more effectively due to the shear key joint. This suggests that the girders were deflecting approximately equally throughout the cyclic loading and therefore the shear key was adequately transferring the load. Figure 5.123 shows the approximate deflection of both east girder stems and the west girder interior stem as the girders were loaded. The deflection points shown (increasing downward) were found at 1,000 lb (4.45 kN) load increments until the maximum average load was reached. As seen in Figure 5.123 the interior stems of the girders deflected similarly while the exterior stem of the east girder reached the greatest deflection. The average peak load and mid-span deflection during CL1 was calculated as 13.9 kips (61.9 kN) and 0.40 in. (10.2 mm), respectively. Throughout the duration of the testing the girder remained linear elastic.

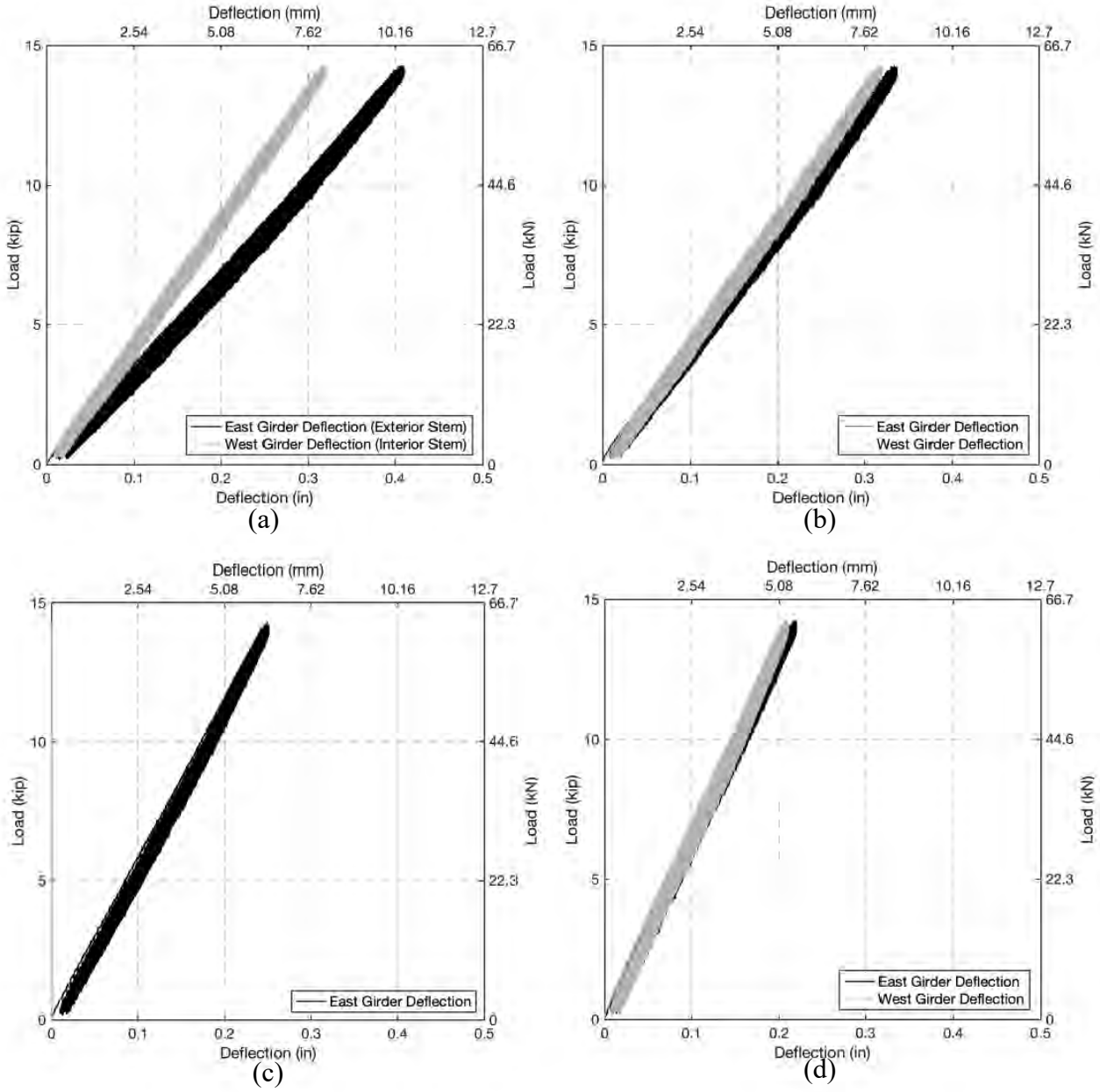


Figure 5.122:Load versus vertical deflection of east and west adjacent girders for CL1 for (a) exterior stem of the east girder and interior stem of the west girder at mid-span, (b) interior stem of each girder at mid-span, (c) interior stem of each girder at the first quarter point of span, and (c) interior stem of each girder at third quarter point of span.

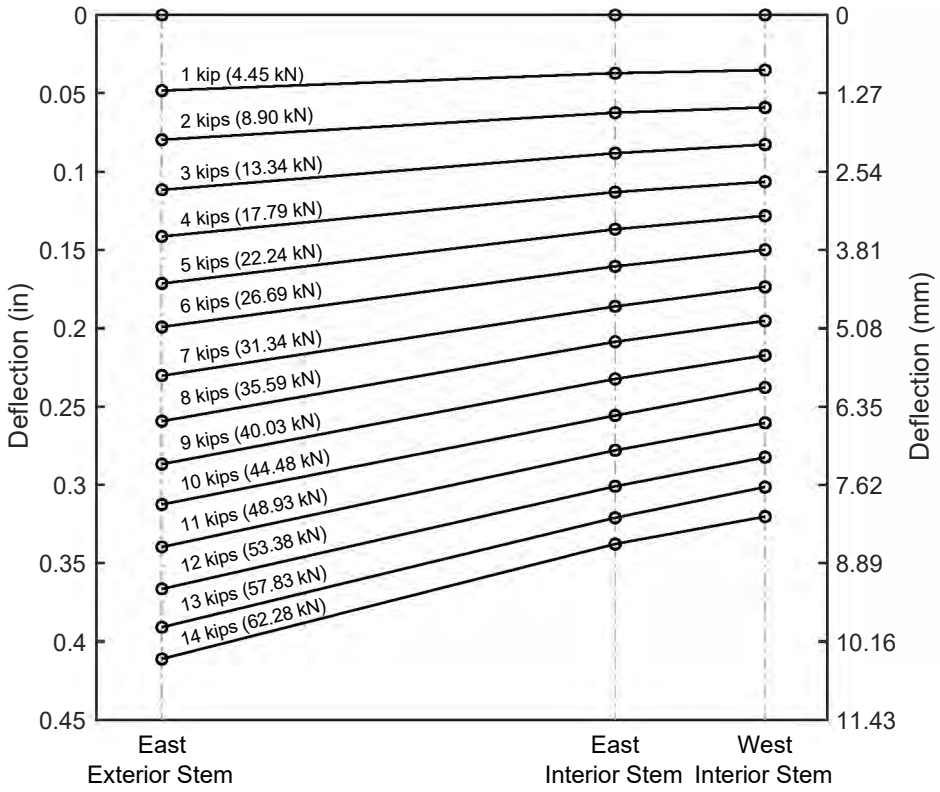


Figure 5.123: Transverse view of vertical deflection of adjacent girders during CL1 at 1.0 kip (4.45 kN) intervals.

5.2.3.1.2 Transverse Deflection Behavior

During CL1, multiple LVDT's were placed perpendicular to the shear key joint on both the top and bottom of the joint, as shown in Figure 5.111. Results from these LVDT's show the deformations (i.e., opening and/or closing) of the shear key in the transverse direction, seen in Figure 5.124. The largest deflection found during CL1 was a 0.0015 in. (0.038 mm) opening below the shear key at the third quarter point of the span, shown in Figure 5.124c. This opening indicates that the bottom of the shear key joint was in tension, which remained consistent across the span of the beam. Figure 5.124 also indicates that the top of the shear key joint was deflecting due to compression, closing the joint. These results suggest that, while minimal, the entire span of the girders was rotating about the shear key. This is a similar result to what Miller et al. (1999) concluded in his study on shear keys. This suggest that the applied load along with the thermal variations may cause higher rotations about the shear key.

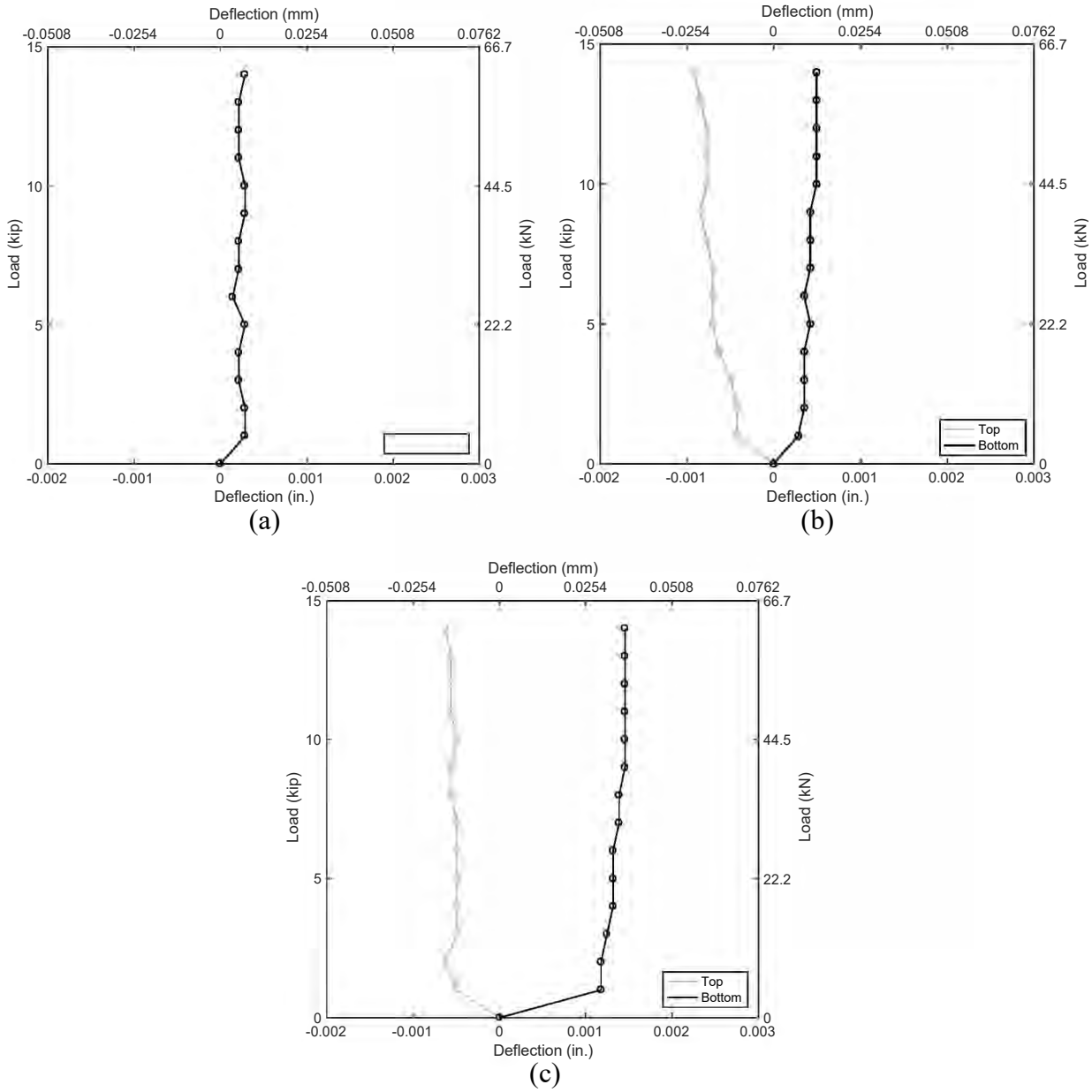


Figure 5.124: Load versus transverse deflection of shear key joint during CL1 at (a) first quarter point of span, (b) mid-span, and (c) third quarter point of span.

5.2.3.2 Cyclic Loading 2

5.2.3.2.1 Vertical Deflection Behavior

The second test completed utilized US Spec NA non-shrink grout as the shear key grouting material. Before casting of the shear key, the walls of the shear key formed by the precast concrete girders was wetted for a 24-hour period. The wetted surface allowed for a more effective bond between the non-shrink grout and precast girder. Once casting and curing was complete, as described in Section 3.2, the girders were instrumented and loaded as shown in Figure 5.110 and Figure 5.111. The test set-up and instrumentation of this test, referred to as CL2, was performed with the same methodology as CL1 to facilitate the comparison of results. The test began with the loading the east girder at a rate of 0.05 in/min (1.27 mm/min) until a vertical mid-span deflection of 0.40 in. (10.2 mm) was reached. The girder was then unloaded and the cyclic load-unload cycles began. The girders were subjected to 1,000 load-unload cycles beginning at a rate of 2 cycles/minute for the first 100 cycles; the loading rate was then increased to 4 cycles/minute for the 900 remaining cycles.

The load-deflection behavior of the girders at the different string potentiometer locations is shown in Figure 5.125. The greatest average deflection was found at the mid-span location. An average deflection difference of the east girder (exterior stem) and west girder (interior stem) was observed to be 0.081 in. (2.06 mm), shown in Figure 5.125a. Similar to CL1, this difference in deflection is greater than that of the interior stems of both girders at mid-span, which was found to be 0.015 in. (0.381 mm), seen in Figure 5.125b. This can once again be attributed to the lack of support on the exterior side of the girder. The minimal difference in deflection between the interior stems also indicates that the shear key was transferring the load effectively resulting in the girders behaving with nearly equal deflections, shown in Figure 5.126. During CL2 the average peak load and average mid-span deflection was found to be 13.4 kips (59.6 kN) and 0.40 in. (10.2 mm), respectively.

When comparing the results between CL1 and CL2, it was calculated that the differential deflection of the girders was approximately 0.003 in. (0.08 mm) greater in CL1 than in CL2. Having a slightly lower deflection difference shows that the load transferred through the shear key in CL2 was marginally better than in CL1. This improvement in load transfer is attributed to the improved bond strength of the non-shrink grout, which was created by the preparation of the shear key surface. CL1 also resulted in a larger deflection of the exterior side of the east girder compared to CL2. This is also a result of the successful load transfer of the shear key that occurred during CL2.

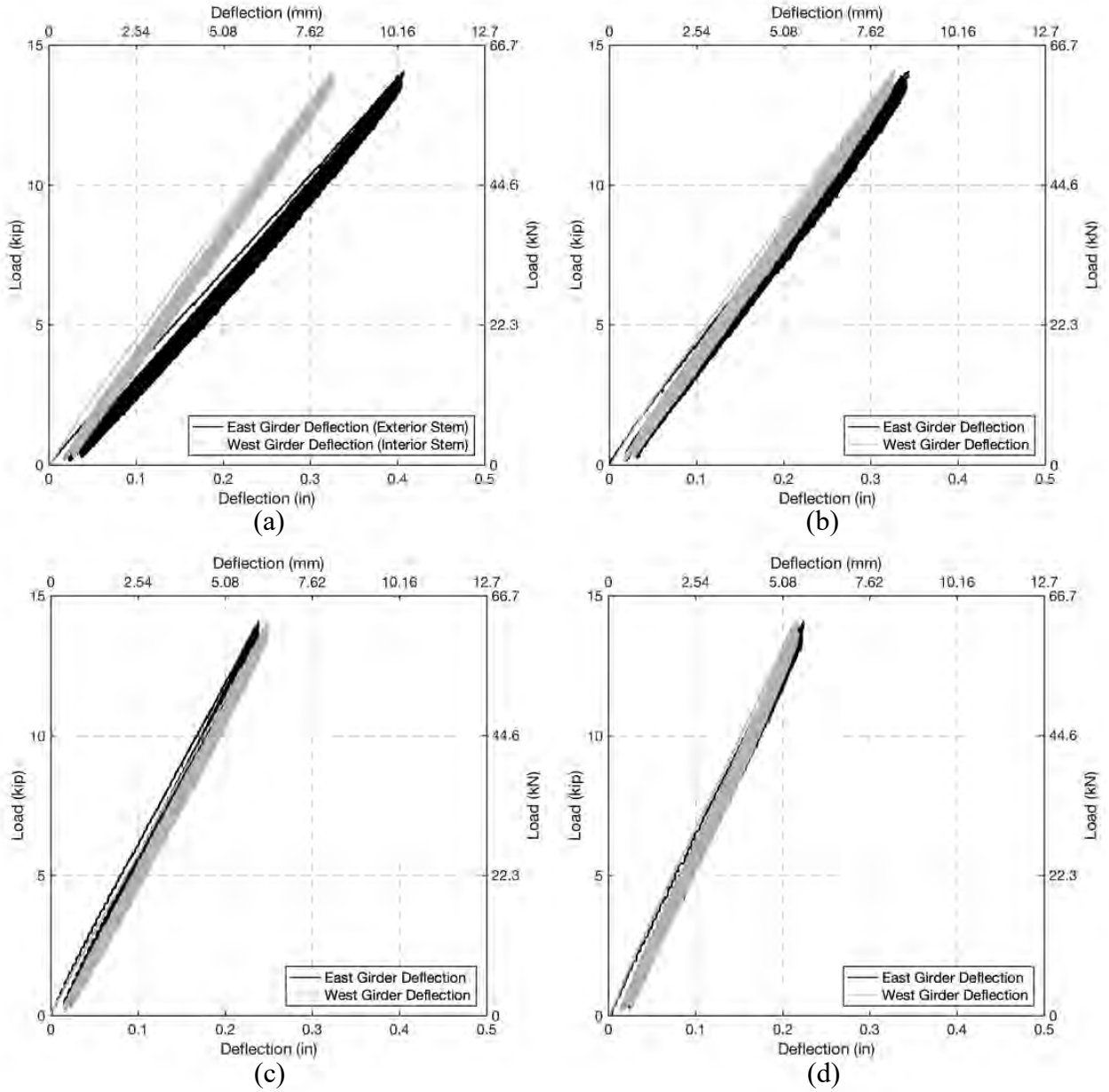


Figure 5.125: Load versus vertical deflection of east and west adjacent girders for CL2 for (a) exterior stem of the east girder and interior stem of the west girder at mid-span, (b) interior stem of each girder at mid-span, (c) interior stem of each girder at the first quarter point of span, and (c) interior stem of each girder at third quarter point of span.

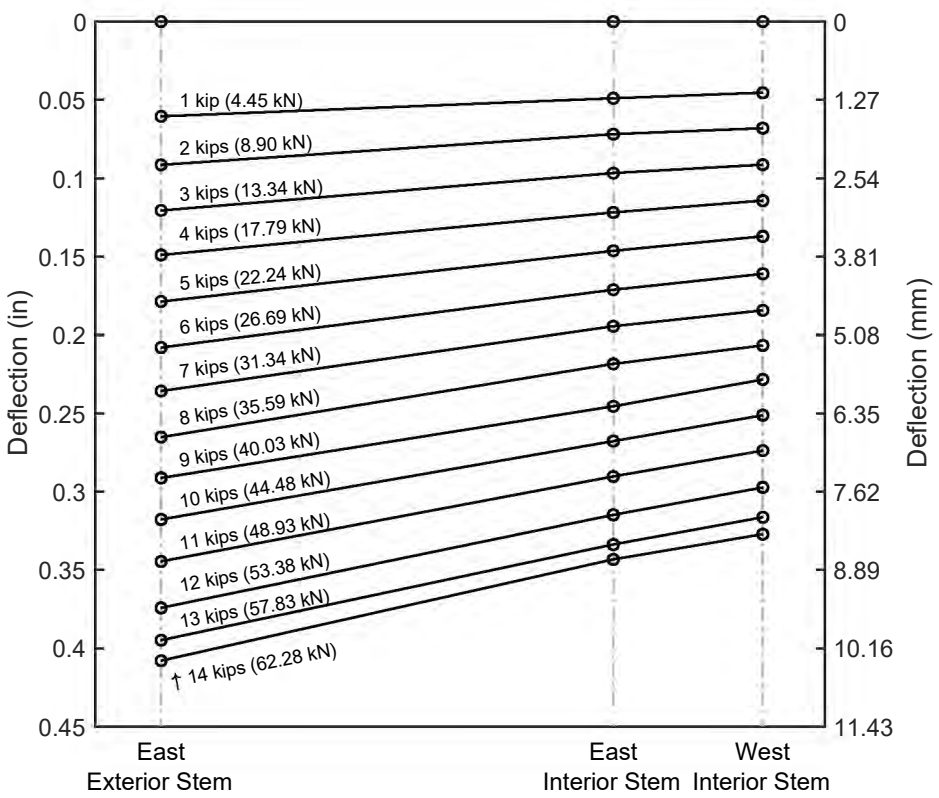


Figure 5.126: Transverse view of vertical deflection of adjacent girders during CL2 at every 1.0 kip (4.45 kN).

5.2.3.2.2 Transverse Deflection Behavior

As shown in Figure 5.111, multiple LVDT's were placed perpendicular to the shear key joint during CL2 to measure any transverse gap opening of the joint. Results from these measurements are presented in Figure 5.127. The largest transverse deflection found during CL2 was an opening of 0.0024 in. (0.061 mm) across the top of the girders at the third quarter point of span, shown in Figure 5.127c. This opening indicates that the top of the girder was in tension at the third quarter point.

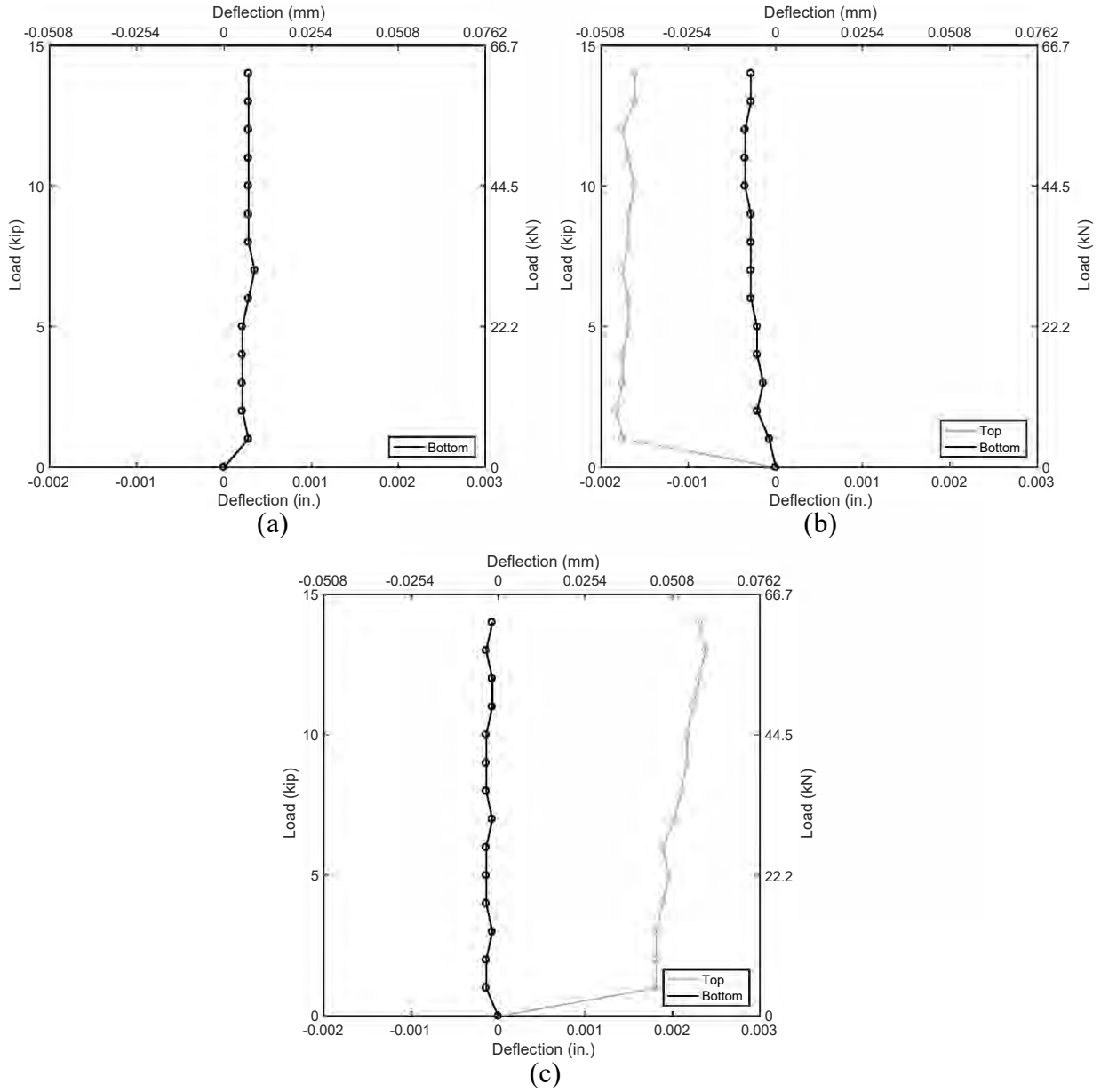


Figure 5.127: Load versus transverse deflection of shear key joint during CL2 for (a) first quarter point of span, (b) mid-span, and (c) third quarter point of span.

5.2.3.3 Cyclic Loading 3

5.2.3.3.1 Vertical Deflection Behavior

The next cyclic test completed, CL3, was performed on a single girder with no grouted shear key. Figure 5.112 and Figure 5.113 show the test set-up and instrumentation that was used to test the east girder. Loading began at a rate of 0.05 in/min until a mid-span vertical deflection of 0.40 in. (10.2 mm) was reached. The girder was then subjected to three load-unload cycles, all reaching a mid-span deflection of 0.40 in. (10.2 mm). This test was performed to provide measurements of the load-deflection behavior of a single girder with no resistance from a shear key.

In Figure 5.128 the load-deflection behavior of the girder measured during CL3 is presented. The results from CL3 show that an average load of 7.40 kips (32.9 kN) was required to achieve the desired mid-span deflection. This average load was approximately half of the load measured in both CL1 and CL2. With this information the moment distribution factor of each test was determined. During CL3 the girder continued to remain linear elastic and no damage was observed.

(a) (b)

(c)

Figure 5.128: Load versus vertical deflection of single girder for CL3 at (a) mid-span, (b) first quarter point of span, and (c) third quarter point of span.

5.2.3.4 Cyclic Loading 4

5.2.3.4.1 Vertical Deflection Behavior

The final cyclic flexural test completed used UHPC as the shear key grouting material. In this test the shear key wall surface was prepared by pre-wetting for 24 hours prior to casting. This surface preparation was done with the intention of creating a strong interface bond between the UHPC grout and the precast concrete girder. This cyclic test, referred to as CL4, was performed with the same four-point loading test set-up and instrumentation as those used in CL1 and CL2, seen in Figure 5.110 and Figure 5.111. Testing began by loading the east girder at a rate of 0.05 in/min (1.27 mm/min) until a mid-span deflection of 0.40 in. (10.2 mm) was reached. The girder was then unloaded and subjected to 1,000 load unload cycles. The first 100 cycles completed were loaded at a rate of 2 cycles/minute; the remaining 900 cycles were loaded at a rate of 4 cycles/min. After the completion of the 1,000 cycles the ultimate loading of the girder began.

The load-deflection results of CL4 are shown in Figure 5.129. A maximum difference in deflection between the adjacent girders was found at mid-span. The exterior stem of the east girder and interior stem of the west girder were found to have a differential deflection of 0.14 in. (3.57 mm), shown in Figure 5.129a. When comparing the interior stems of both girders the difference in deflection was calculated to be 0.04 in. (1.02 mm), presented in Figure 5.129b. These differential deflections are an increase from those calculated during CL1 and CL2. Figure 5.130 presents the vertical deflection of both stems of the east girder and the interior stem of the west girder at every 1,000 lb (4.45 kN) of load applied. The differential deflection between the interior stems is also higher in Figure 5.130 than that of CL1 and CL2. The slope of the deflection line increased compared to that of CL1 and CL2, shown in Figure 5.123 and Figure 5.126. The peak load and average mid-span deflection recorded during CL4 was 13.2 kips (58.7 kN) and 0.40 in. (10.2 mm), respectively.

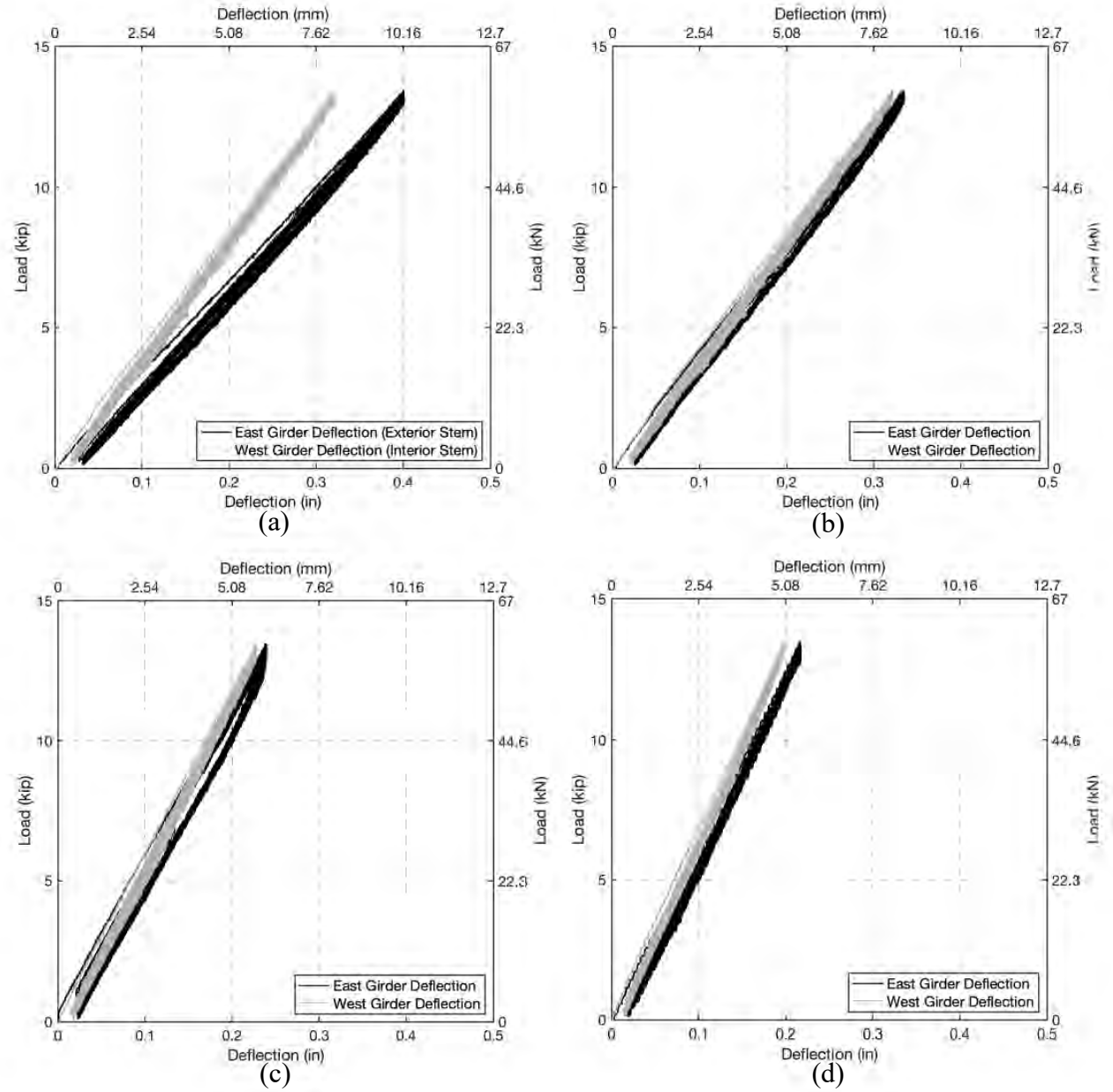


Figure 5.129: Load versus vertical deflection of east and west adjacent girders for CL4 for (a) exterior stem of the east girder and interior stem of the west girder at mid-span, (b) interior stem of each girder at mid-span, (c) interior stem of each girder at the first quarter point of span, and (c) interior stem of each girder at third quarter point of span.

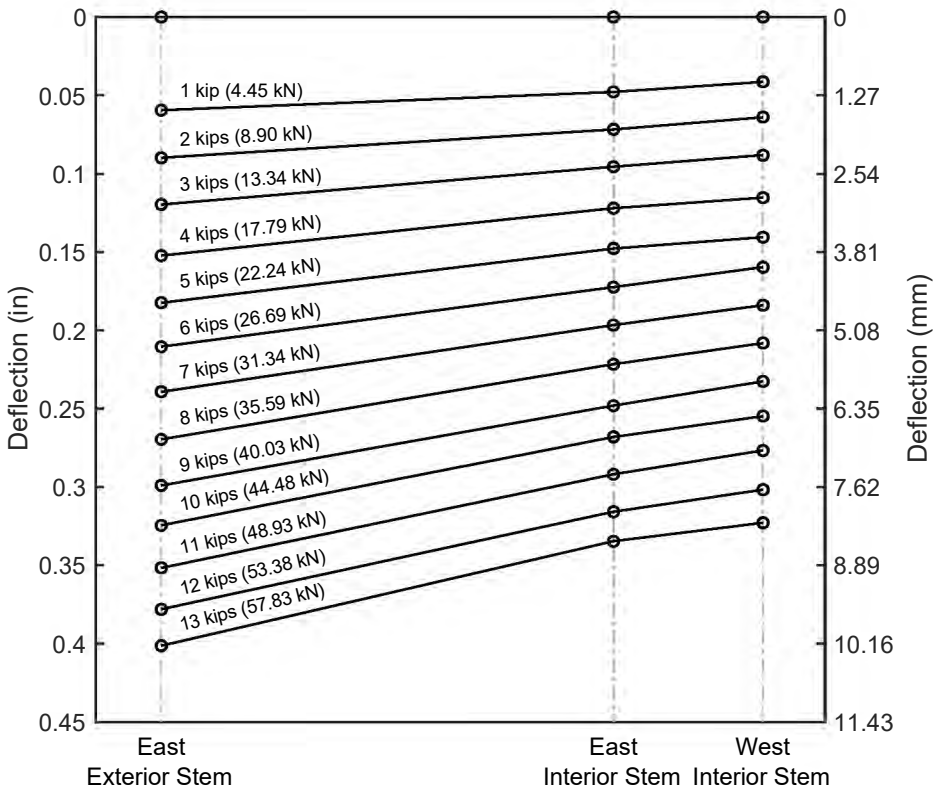


Figure 5.130: Transverse view of vertical deflection of adjacent girders during CL4 at every 1.0 kip (4.45 kN).

5.2.3.4.2 Transverse Deflection Behavior

To maintain consistency LVDT's were placed perpendicular to the shear key joint during CL4 as shown in Figure 5.111, similar to CL1 and CL2. These LVDT's measured the transverse deflection, or gap opening, of the shear key joint as shown in Figure 5.131. Across the span of the adjacent girders the transverse deflection was found to behave with compression along the top of the joint and tension along the bottom. This implies that the girders were rotating about the shear key, similar to CL1. However, the girders began to rotate in the opposite direction as the load was increased. Figure 5.131b and Figure 5.131c show that as the load increased the top of the shear key joint began to expand while the bottom began to contract. The largest transverse deflection found was found to be 0.0014 in. (0.036 mm) closing of the bottom of the shear key joint at mid-span.

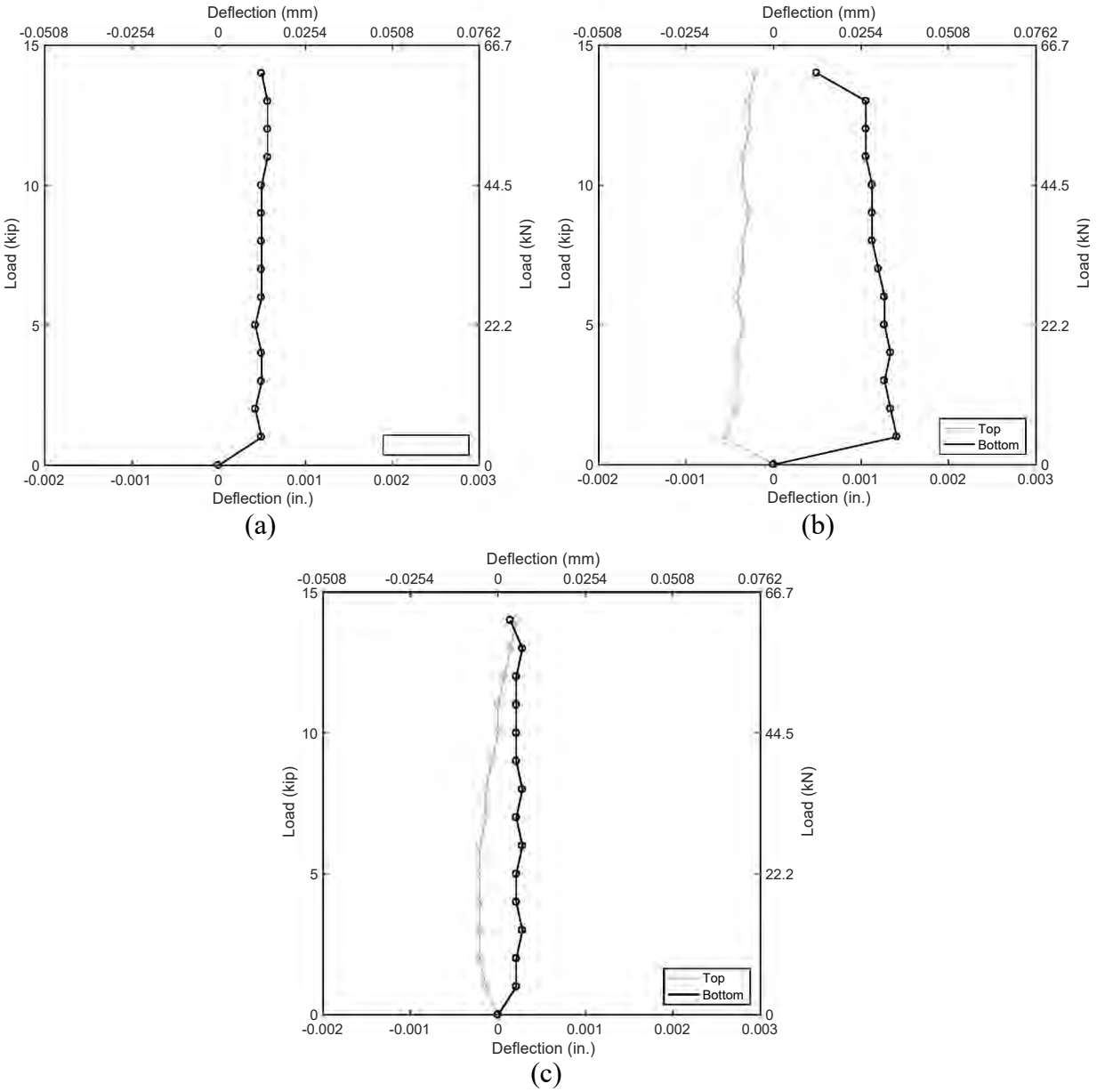


Figure 5.131: Load versus transverse deflection of shear key joint during CL4 at (a) first quarter point of span, (b) mid-span, and (c) third quarter point of span.

5.2.3.5 Comparison of Flexural Cyclic Loading

5.2.3.5.1 Vertical Deflection Behavior

To better understand the behavior of each shear key grouting material the load-deflection behavior was compared across all four tests. Figure 5.132 presents the load-deflection response of the vertical mid-span deflection locations of each cyclic test. As seen in Figure 5.132 the stiffness (slope of the load-deflection) of the girder system decreased slightly over the entire testing period with CL1 being stiffest and CL4 the least stiff. Figure 5.133 also shows the increase in deflection for each test with CL4 reaching maximum deflection at approximately 13 kips (57.83 kN). The loss in stiffness appears to have occurred between tests, while the systems behaved linear elastically during their individual testing. This could be a result of the girders being previously in-service and accumulating minor damage during the individual tests. However, the difference is so slight that it is difficult to place any significance on the observation. As shown in Figure 5.132, each stem decreased by approximately the same load capacity indicating that it was the girders or test setup losing stiffness and therefore not indicative of the shear key performance. The more important observation is that each grouting material behaved similarly, and each two-girder system nearly doubled the load carrying capacity of a single girder. This result implies that there is little mechanical difference between the three shear key designs.

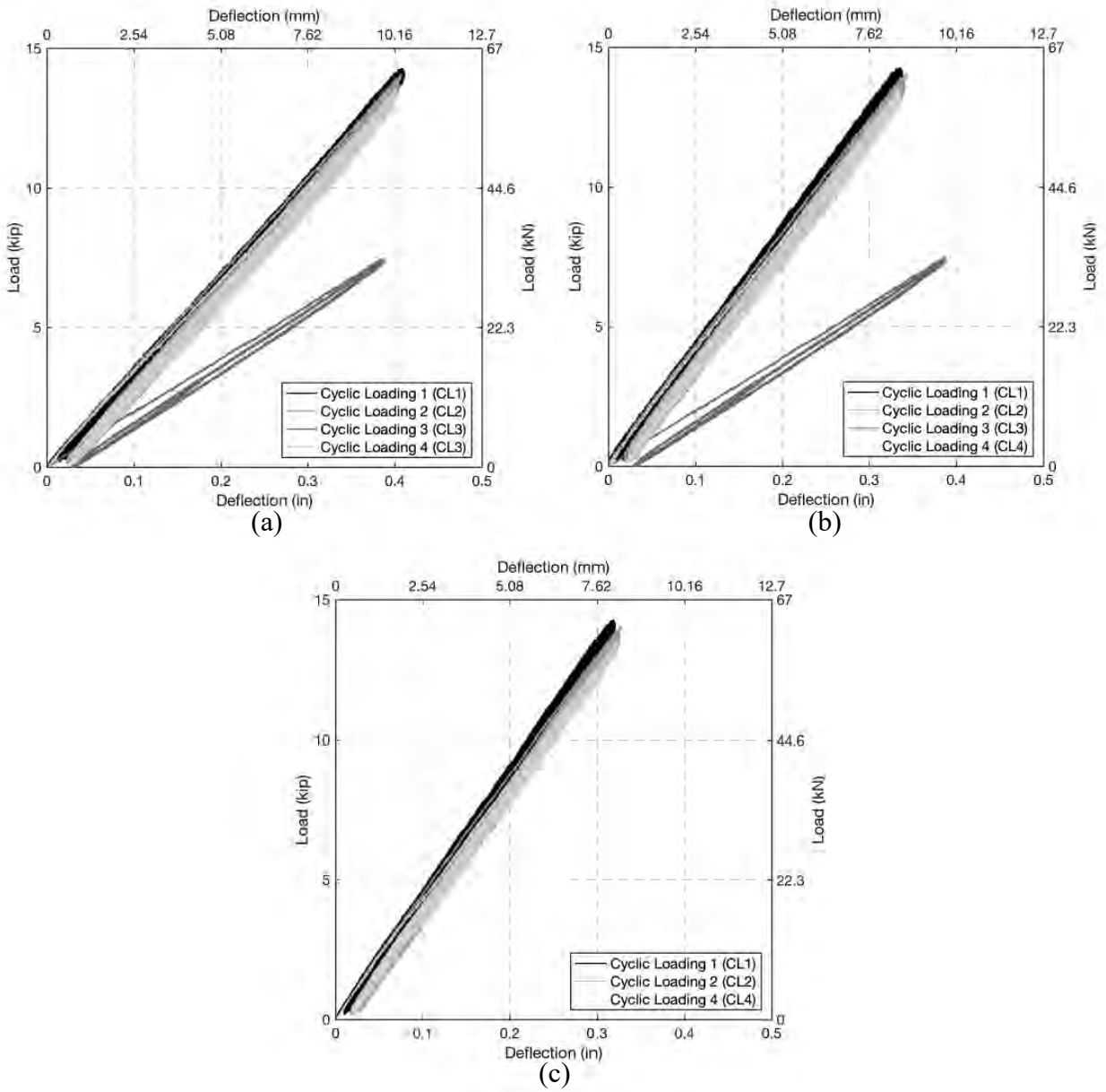


Figure 5.132: Comparison of load versus vertical mid-span deflection of adjacent girders for (a) exterior stem of east girder, (b) interior stem of east girder at mid-span, and (c) interior stem of west girder.

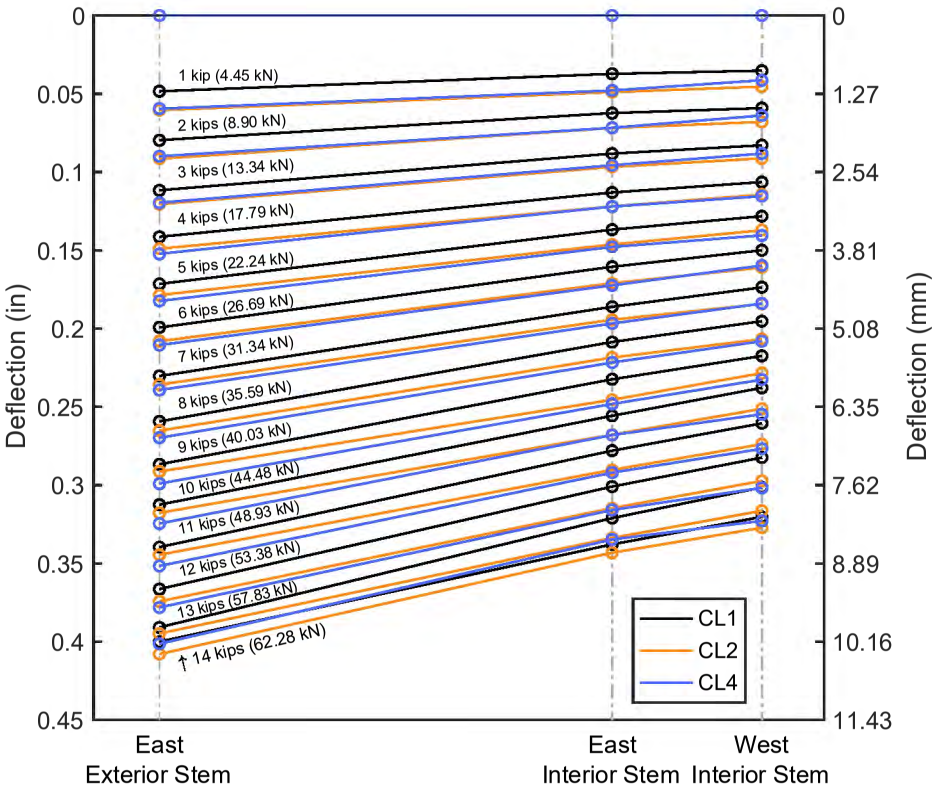


Figure 5.133: Transverse view comparison of vertical deflection of adjacent girders during cyclic loading at every 1.0 kip (4.47 kN).

5.2.3.5.2 Transverse Deflection Behavior

The load-deflection behavior of the transverse deflections across the shear key are compared in Figure 5.134. As seen in Figure 5.134 all girder systems had minimal gap opening of the shear key joint. This observation is significant when considering that no transverse post-tensioning was applied to the systems tested. With no transverse support the grouting materials were still able to maintain bond between the precast concrete girders, successfully transferring the applied load across the system.

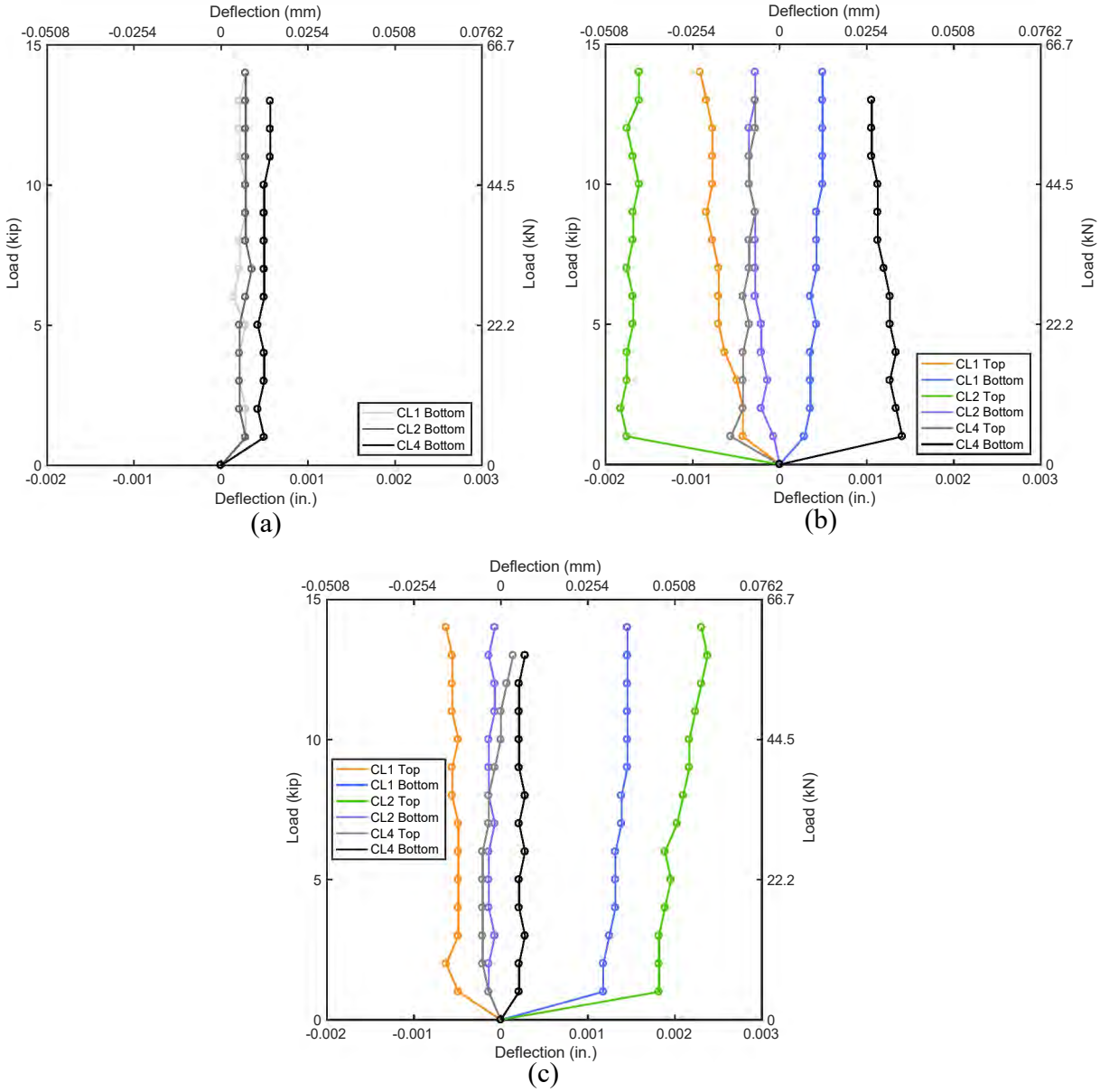


Figure 5.134: Comparison of load versus transverse deflection of the shear key during cyclic loading at (a) first quarter point of span, (b) mid-span, and (c) third quarter point of span.

5.2.3.6 Cyclic Loading 5

5.2.3.6.1 Vertical Deflection Behavior

The fifth cyclic test completed, CL5, tested a single girder under a shear loading. The test set-up and instrumentation of the girder can be seen in Figure 5.116 and Figure 5.117. The girder was loaded at a rate of 0.05 in/min (1.27 mm/min) until an applied load of 20 kips (88.96 kN) was reached. At this point the girder was fully unloaded. This process continued until three load-unload cycles were completed.

The load-deflection behavior of a single girder under shear loading can be seen in Figure 5.135. The results of CL5 found that the maximum deflection occurred at midspan and that a peak load of 20 kips (88.96) caused a midspan deflection of 0.295 in. (7.49 mm). This peak deflection occurred at the interior stem which is a result of the bridge skew causing the four-point loading to be further from the support at the interior stem compared to the exterior stem. Results from CL5 were used to calculate the shear distribution factor of the grouted shear key system tested during CL6.

(a) (b)

(c)

Figure 5.135: Load versus vertical deflection of single girder for CL5 at (a) first quarter point of span, (b) midspan and (c) third quarter point of span.

5.2.3.6.2 Rotation

During CL5 the rotation of the girder ends was captured to better understand the girder behavior under the high shear loading. The rotations measured is presented in Figure 5.136. Rotations were found to be larger on the north end of the girder where load was being applied. The maximum rotation at the north end was found to be -0.23 degrees while the south end rotated to 0.15 degrees.

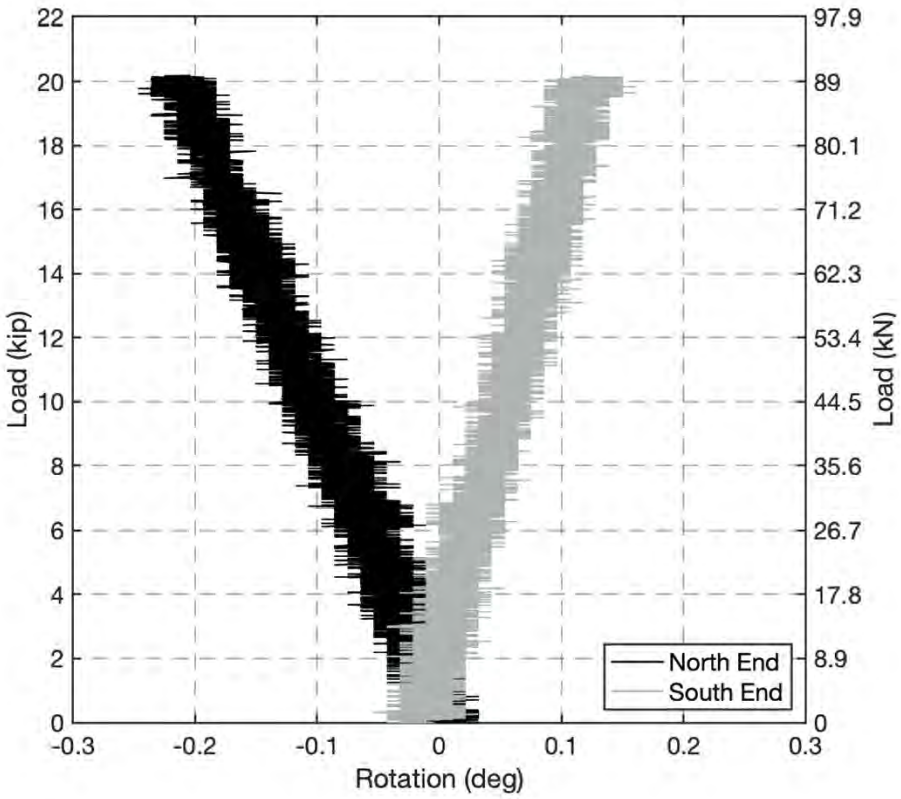


Figure 5.136: Load versus rotation of single girder during CL5.

5.2.3.7 Cyclic Loading 6

5.2.3.7.1.1 Vertical Deflection Behavior

The final full-scale tests conducted used a two-girder system set-up as shown in Figure 5.114. This shear tests had a grouted shear key of adequately bonded UHPC and was instrumented as shown in Figure 5.115. Cyclic loading 6, CL6, began by loading the east girder at a rate of 0.05 in/min (1.27 mm/min) until a maximum load of 20 kips (88.96 kN) was reached. The girder was then fully unloaded. This process continued until 1,000 load-unload cycles were completed. The first 100 cycles were conducted at 2 cycles/min, after which the rate was increased to 4 cycles/min for the remaining 900 cycles. At the competition of cyclic testing, the ultimate shear test was performed.

The maximum differential deflection that occurred across the system during CL6 occurred at midspan between the exterior stem of each girder and was measured as 0.026 in. (0.66 mm), as seen in Figure 5.137b. The maximum differential deflection between the interior stems was found to be 0.014 in. (0.30 mm). The maximum differential displacement occurred at approximately 19 kips (84.52), as seen in Figure 5.139. Throughout the testing of CL6 an average peak load of 19.9 kips (88.5 kN) and average peak deflection of 0.14 in. (3.56 mm) was reached. Analysis of the adjacent girder deflection at the midspan cross-section shows that the east girder's interior stem deflected more than its exterior stem, as seen in Figure 5.139. This is a result of the rectangular four-point loading applied to the girder which has approximately an 18º skew. This caused the two load points above the interior stem to be a small distance closer to midspan. The minimum deflection measured during CL6 occurred at the center of the four-point loading, as seen in Figure 5.138, which is a result of the minimal distance between the support and the four-point loading.

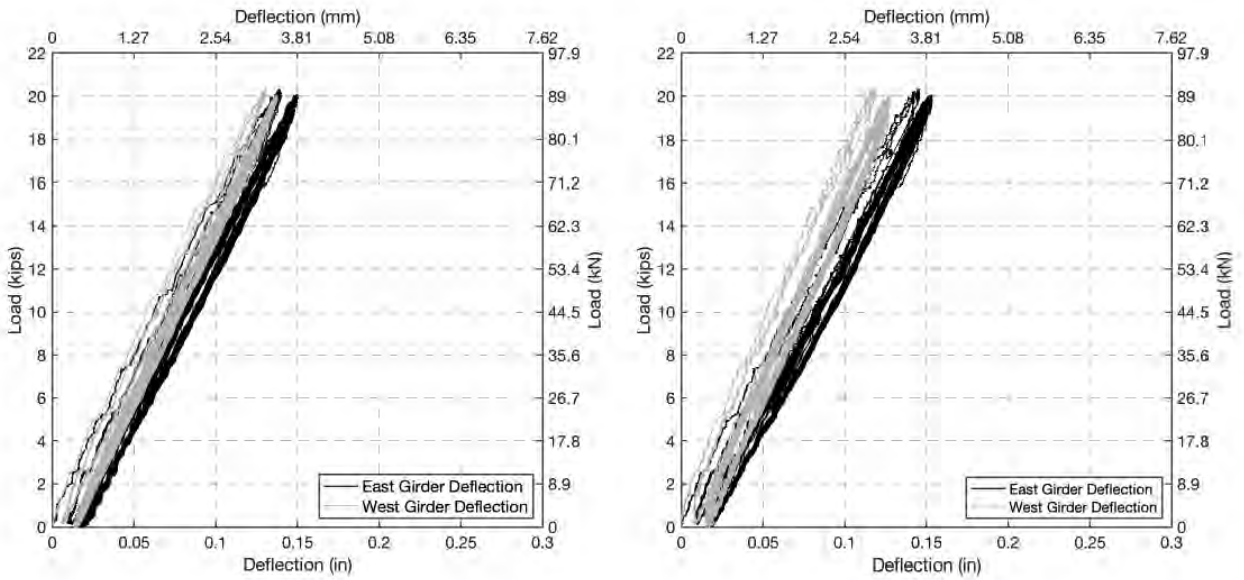


Figure 5.137: Load versus deflection of adjacent girders for CL6 for (a) interior stem of each girder at midspan, and (b) exterior stem of each girder at midspan.

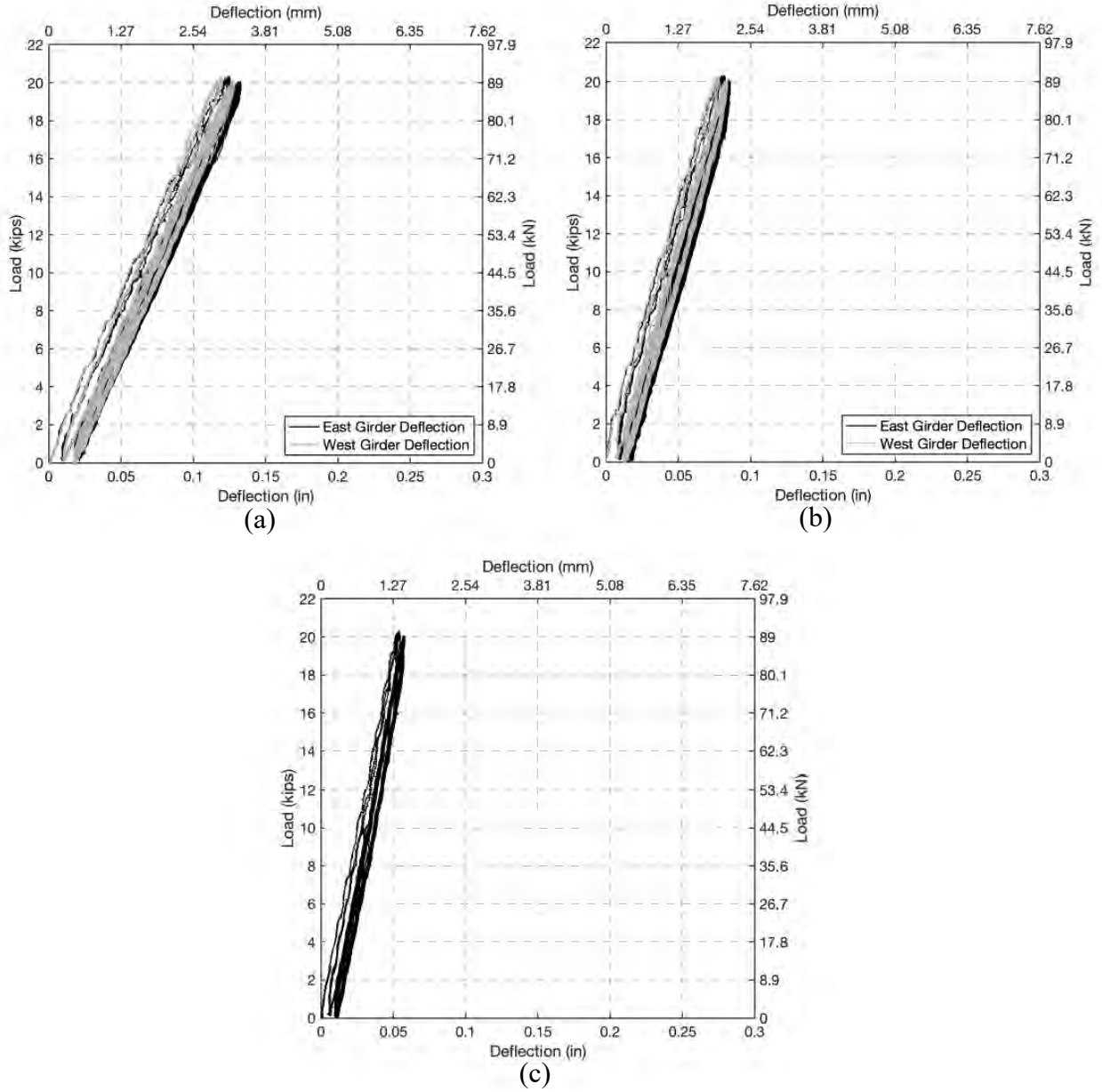


Figure 5.138: Load versus deflection of adjacent girders for CL6 at (a) interior stem of each girder at first quarter-point of span, and (b) interior stem of each girder at third quarter point of span, and (c) centerline of four-point loading.

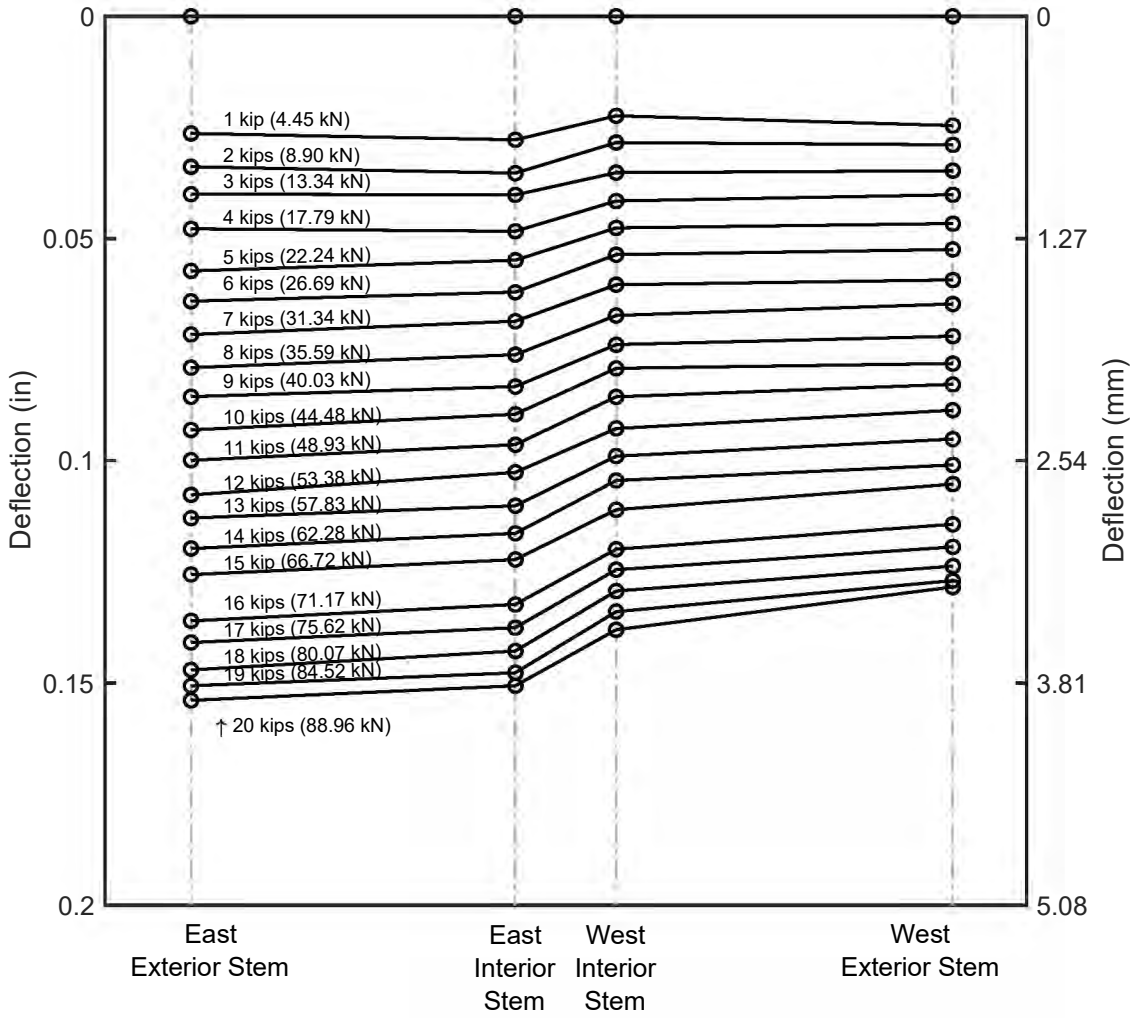


Figure 5.139: Transverse view of vertical deflection of adjacent girders during CL6 at every 1.0 kip (4.45 kN).

5.2.3.7.1.2 Transverse Deflection Behavior

Multiple LVDT's were placed perpendicular to the shear key joint during CL6, as shown in Figure 5.115. These LVDT's measured the transverse deformations (i.e., opening and/or closing) of the shear key and results of these measurements can be seen in Figure 5.140. During testing the shear key remained in compression on both the top and bottom of the beam. Because of this, there was no opening of the joint and the UHPC was able to maintain a bond with the precast concrete girders. The maximum compression measured during CL6 was found to be 0.00042 in. (0.0107 mm).

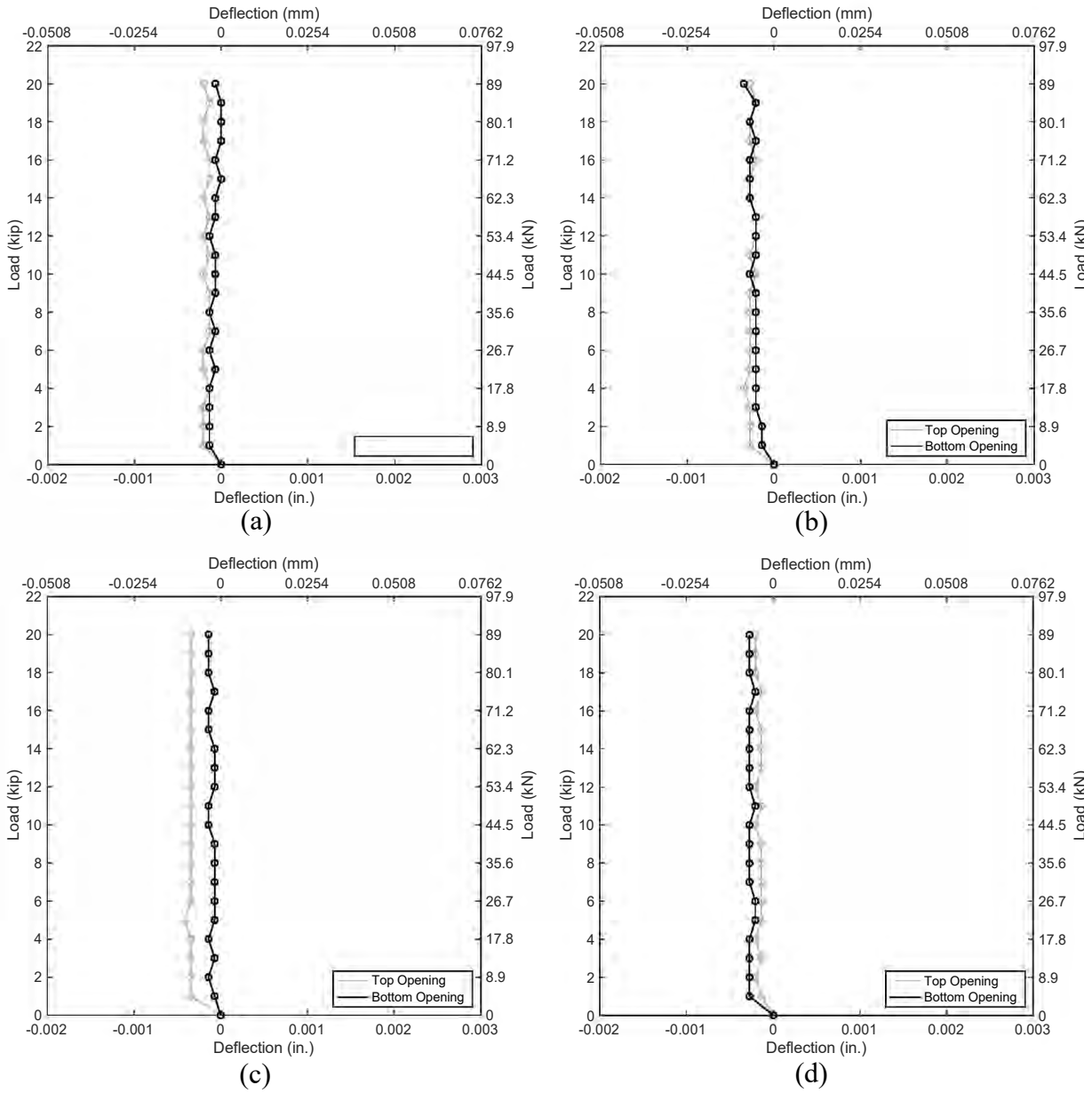


Figure 5.140: Load versus transverse deflection of shear key joint during CL6 at (a) first quarter point of span, (b) mid-span, (c) third quarter point of span, and (d) centerline of four-point loading.

5.2.3.8 Comparison of Shear Cyclic Loading

5.2.3.8.1 Vertical Deflection Behavior

Comparative analysis of the load-deflection behavior of CL5 and CL6 tests was performed to better understand the performance of the UHPC shear key. The load-deflection behavior of the east girder from each test is shown in Figure 5.141. The addition of the shear key did decrease the deflection of the east girder by approximately half at each deflection point measured. This indicates that the UHPC shear key remained bonded during the cyclic loading and successfully transferred the shear load across the system.

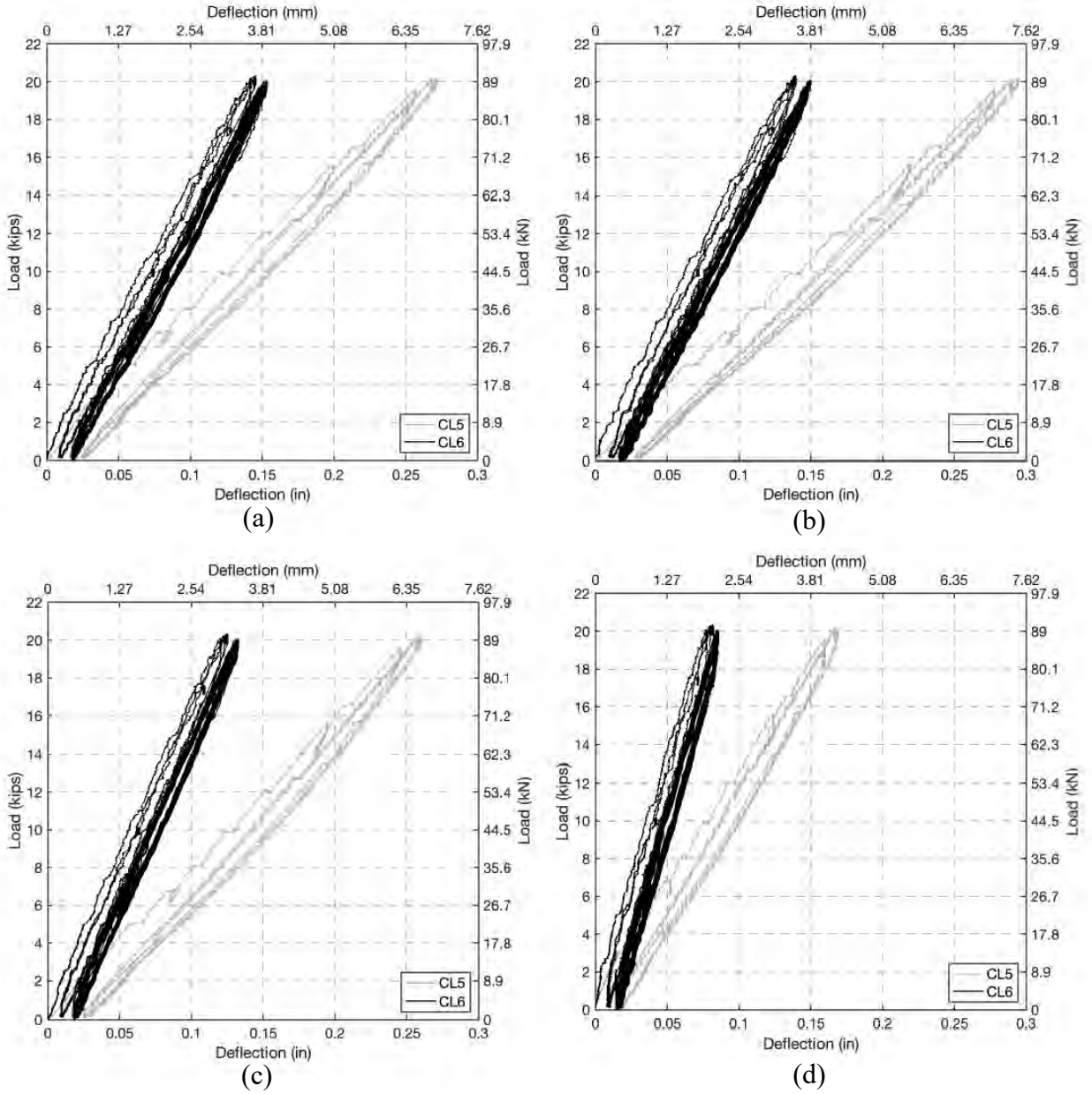


Figure 5.141: Comparison of load versus vertical deflection of CL5 and CL6 at (a) exterior stem of east girder at midspan, (b) interior stem of east girder at mid-span, (c) interior stem of east girder at first quarter point of span, and (d) interior stem of east girder at third quarter point of span.

5.2.4 Ultimate Loading

5.2.4.1 Flexural Testing Results

5.2.4.1.1 Vertical Deflection Behavior

After completion of CL4 an ultimate loading of the fully bonded UHPC shear key system was performed. This test was completed with the intention of emulating an overload behavior. Ultimate loading of the channel girders was performed with longitudinal four-point bending as shown in Figure 5.110. Loading began at an initial deflection of 0.40 in. (10.2 mm) and was increased to a deflection of 0.80 in. (20.3 mm). The girder was then unloaded to the previous 0.40 in. (10.2 mm) of deflection. This process continued with an increase in peak deflection of 0.40 in. (10.2 mm) after every unload cycle until a maximum deflection of 2.0 in. (50.8 mm) was reached. The maximum deflection of 2.0 in. (50.8 mm) reached (five times the service displacement) exceeded the AASHTO deflection criteria sufficiently to represent the desired overload behavior. At this point, the girders were cycled between 0.40 in. (10.2 mm) and 2.0 in. (50.8 mm) of deflection for three cycles at a constant rate of 0.1 in/min (2.54 mm/min). After completion of these cycles, the girders were unloaded, and the residual deflection was measured at 0.30 in. (7.62 mm). To complete the test, the girders were once again loaded to 0.40 in. (10.2 mm) of deflection at a rate of 0.1 in/min (2.54 mm/min). The residual deflection was taken into account, which put the total displacement at 0.7 in. (17.8 mm) from the beginning of the ultimate load test. The girder was cycled up to the new 0.40 in. (10.2 mm) deflection point for 100 load-unload cycles at a rate of 4 cycles/min. These last 100 cycles were completed to mimic the behavior of a bridge structure that remains in-service after an overload event.

Vertical deflection results of the overload test are presented in Figure 5.142 and Figure 5.143. The average peak load applied during the ultimate loading was 57.2 kips (254 kN) and an average peak deflection of 1.99 in. (50.5 mm) was reached. Figure 5.142 shows that the girders began to yield at approximately 1.2 in. (30.5 mm) of deflection. During testing, yielding was also seen visually as cracks appeared and propagated at mid-span. The vertical deflection of the east girder stems and west girder interior stem at every 5,000 lb (22.24 kN) of load applied can be seen in Figure 5.143. During this test the exterior stem of the east girder and interior stem of the west girder were found to have a differential deflection of approximately 0.43 in. (10.80 mm), as seen in Figure 5.142b and Figure 5.143; the maximum differential deflection occurred as a maximum vertical deflection of 2.0 in. (50.8 mm) was reached.

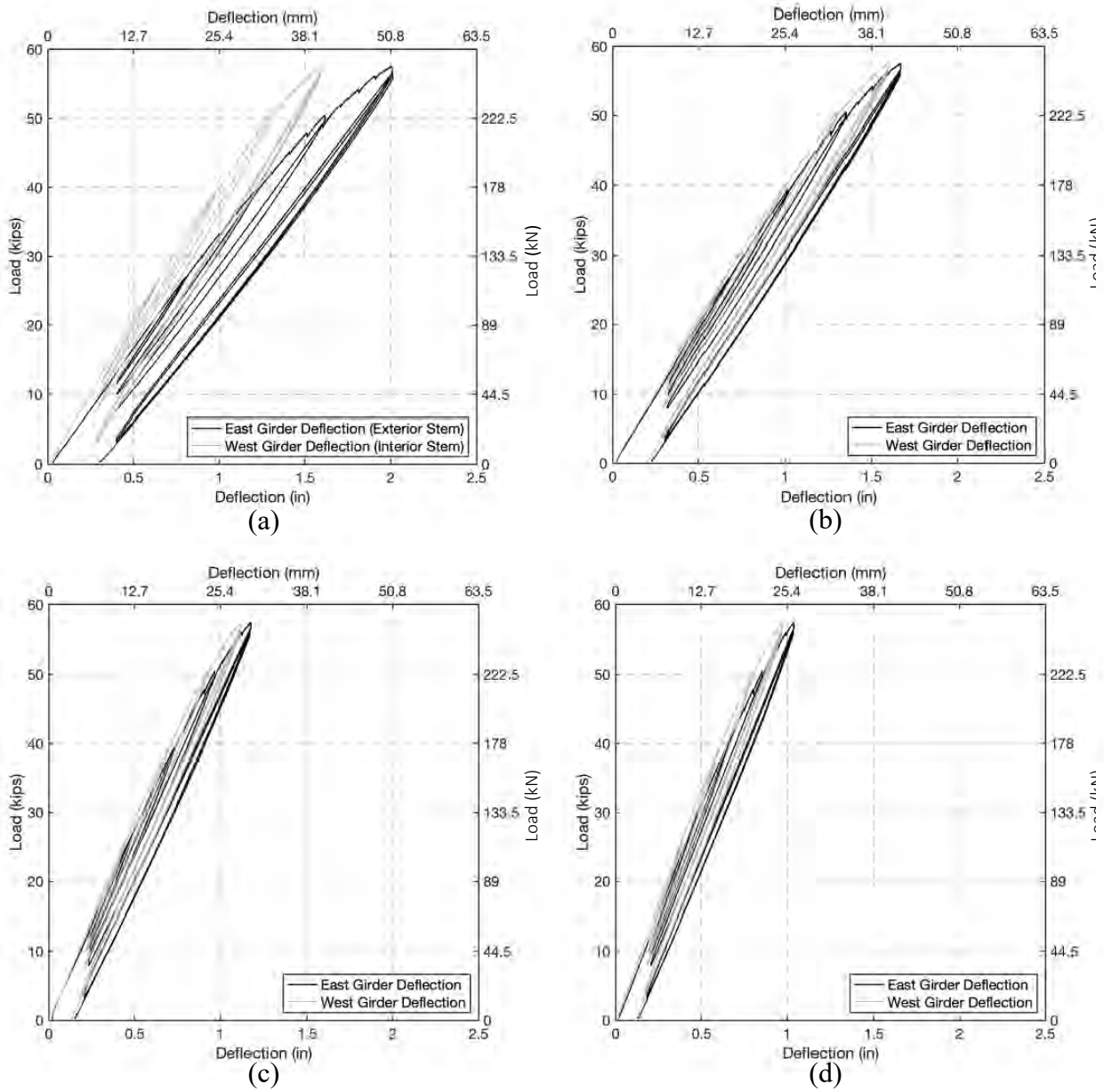


Figure 5.142: Load versus vertical deflection of east and west adjacent girders for ultimate loading for (a) exterior stem of the east girder and interior stem of the west girder at mid-span, (b) interior stem of each girder at mid-span, (c) interior stem of each girder at the first quarter point of span, and (c) interior stem of each girder at third quarter point of span.

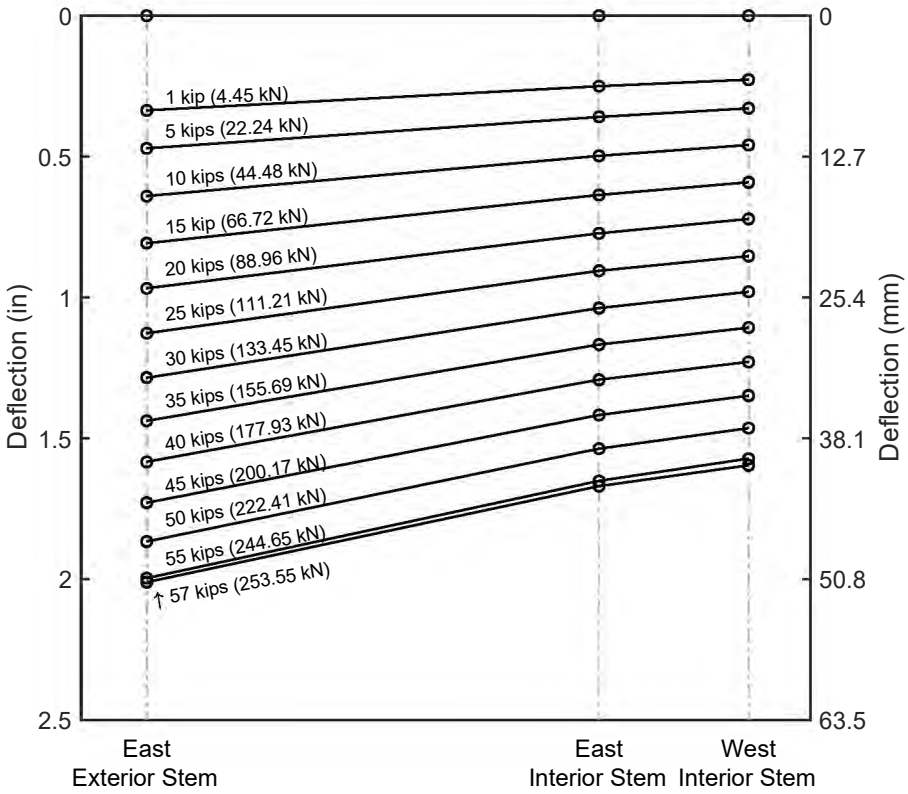


Figure 5.143: Transverse view of vertical deflection of adjacent girders during ultimate loading at 5.0 kip (4.45 kN) intervals.

The load-deflection behavior of the girders during the final 100 cycles is shown in Figure 5.144 and Figure 5.145. An average peak load of 13.7 kips (60.9 kN) was observed during the final 100 cycles. This load caused an average peak deflection of 0.68 in. (12.3 mm), including residual deflections. At the completion of the test, it was observed that flexural cracks had propagated at regular intervals across the mid-span of both the east and west girders. By comparing Figure 5.144 with the results of CL4, presented in Figure 5.129, it was found that while the vertical displacement had increased, the girders still required approximately the same load to reach the 0.40 in. (10.2 mm) deflection beyond the permanent 0.3 in. (7.62 mm) deflection. However, the differential deflection that occurred between the exterior stem of the east girder and interior stem of the west girder was found to be larger for the final 100 cycles, seen in Figure 5.144a, than that of CL4, seen in Figure 5.129a. This suggest that the 57.2 kip (254 kN) loading caused bond damage to the shear key, decreasing the load transfer between girders and causing the east girder to carry a more substantial amount of the load. The loss of load transfer can also be seen in Figure 5.145 as the slope of deflection between the stems increases compared to earlier testing.

(a) (b)

(c) (d)

Figure 5.144: Load versus vertical deflection of east and west adjacent girders during final 100 cycles for (a) exterior stem of the east girder and interior stem of the west girder at mid-span, (b) interior stem of each girder at mid-span, (c) interior stem of each girder at the first quarter point of span, and (c) interior stem of each girder at third quarter point of span.

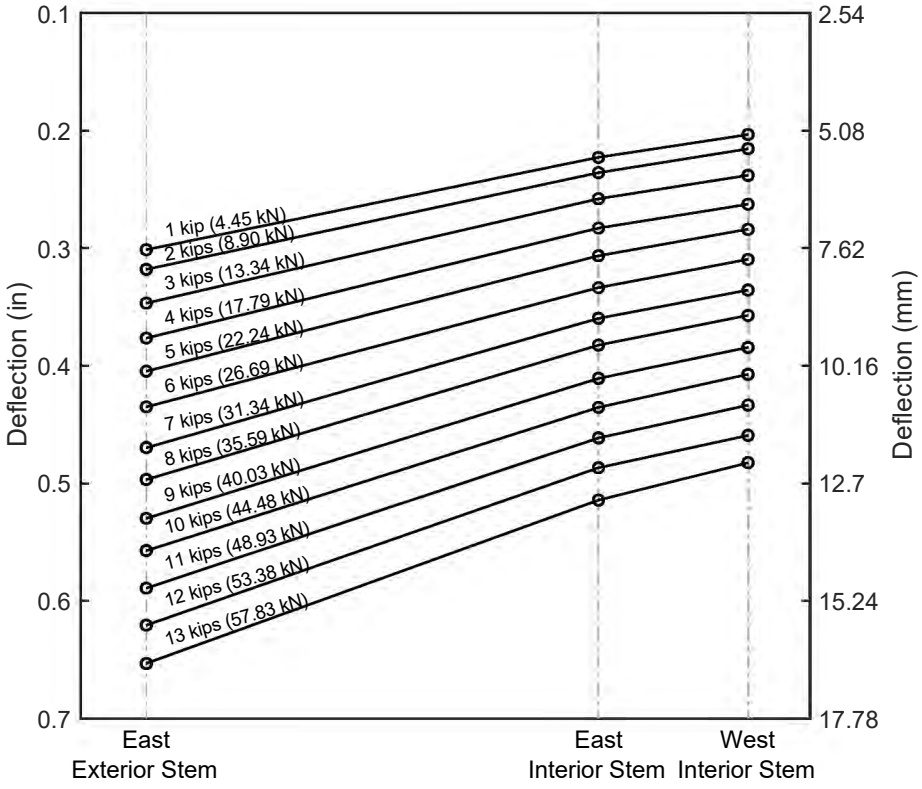


Figure 5.145: Transverse view of vertical deflection of adjacent girders during final 100 cycles at every 1.0 kip (4.45 kN).

5.2.4.1.2 Transverse Deflection Behavior

During overload testing LVDT's were placed perpendicular to the shear key joint, as shown in Figure 5.111. These measurements were taken to understand the transverse deflection behavior of the shear key with no transverse post-tensioning reinforcement during an overload situation. Results from the LVDT's are presented in Figure 5.146. The maximum transverse deflection that occurred was a 0.0006 in. (0.015 mm) deflection in compression occurring along the bottom of the joint at the third quarter point of span. For the duration of the overload test the bottom of the shear key joint remained in compression and the top of the joint behaved in tension. This suggests that the girders were rotating about the shear key and that the change in rotation that occurred as load increased, seen in Figure 5.131, continued as the overload test was performed.

The transverse deflection results of the final 100 cycles are presented in Figure 5.147. The results of this test remain consistent with the previous overload test as the bottom of the shear key behaves in compression and the top behaves in tension. The maximum deflection found during the final 100 cycles was 0.0009 in. (0.023 mm) in tension, which occurred along the top of the shear key at mid-span.

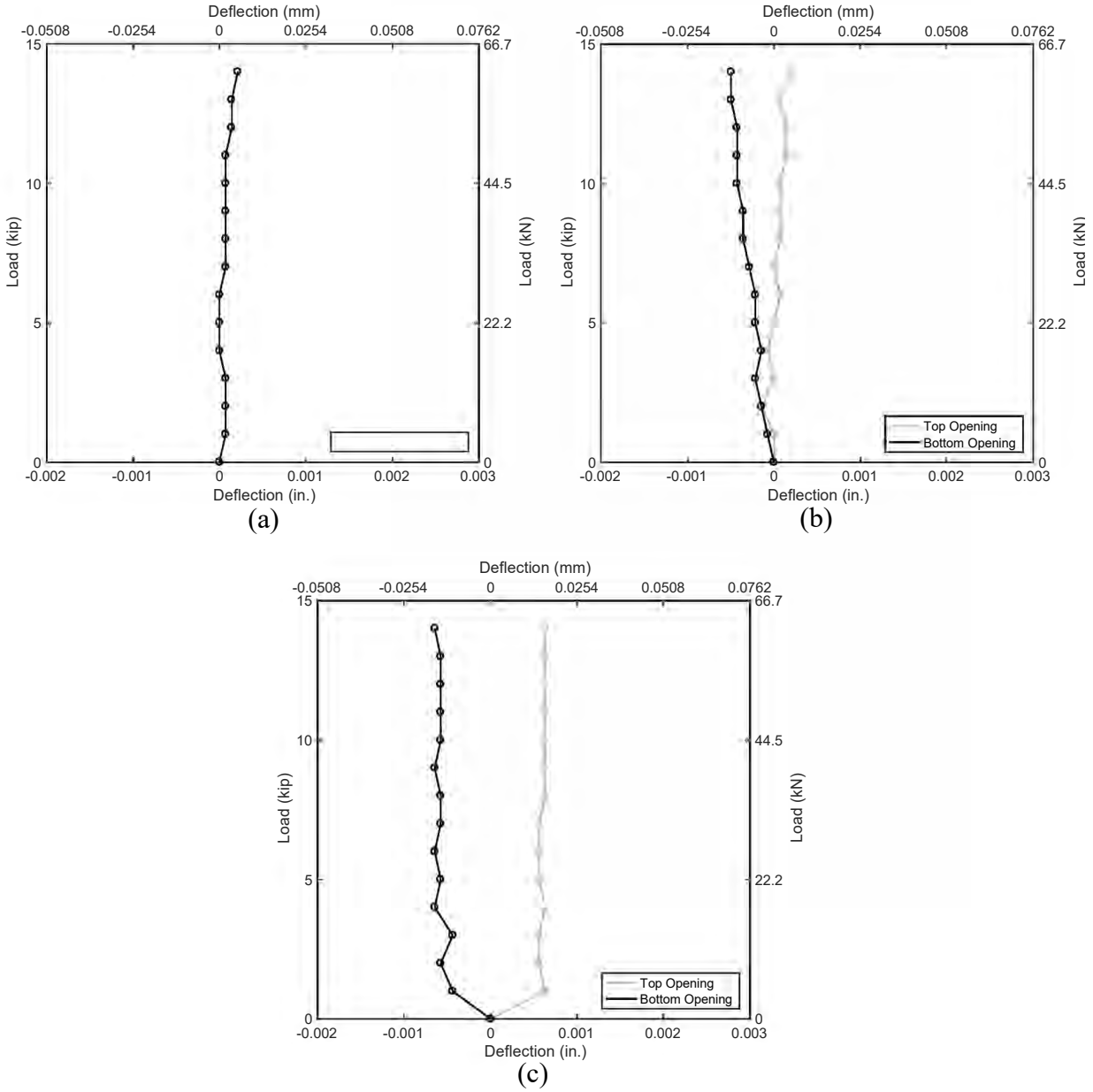


Figure 5.146: Load versus transverse deflection of shear key joint during ultimate loading at (a) first quarter point of span, (b) mid-span, and (c) third quarter point of span.

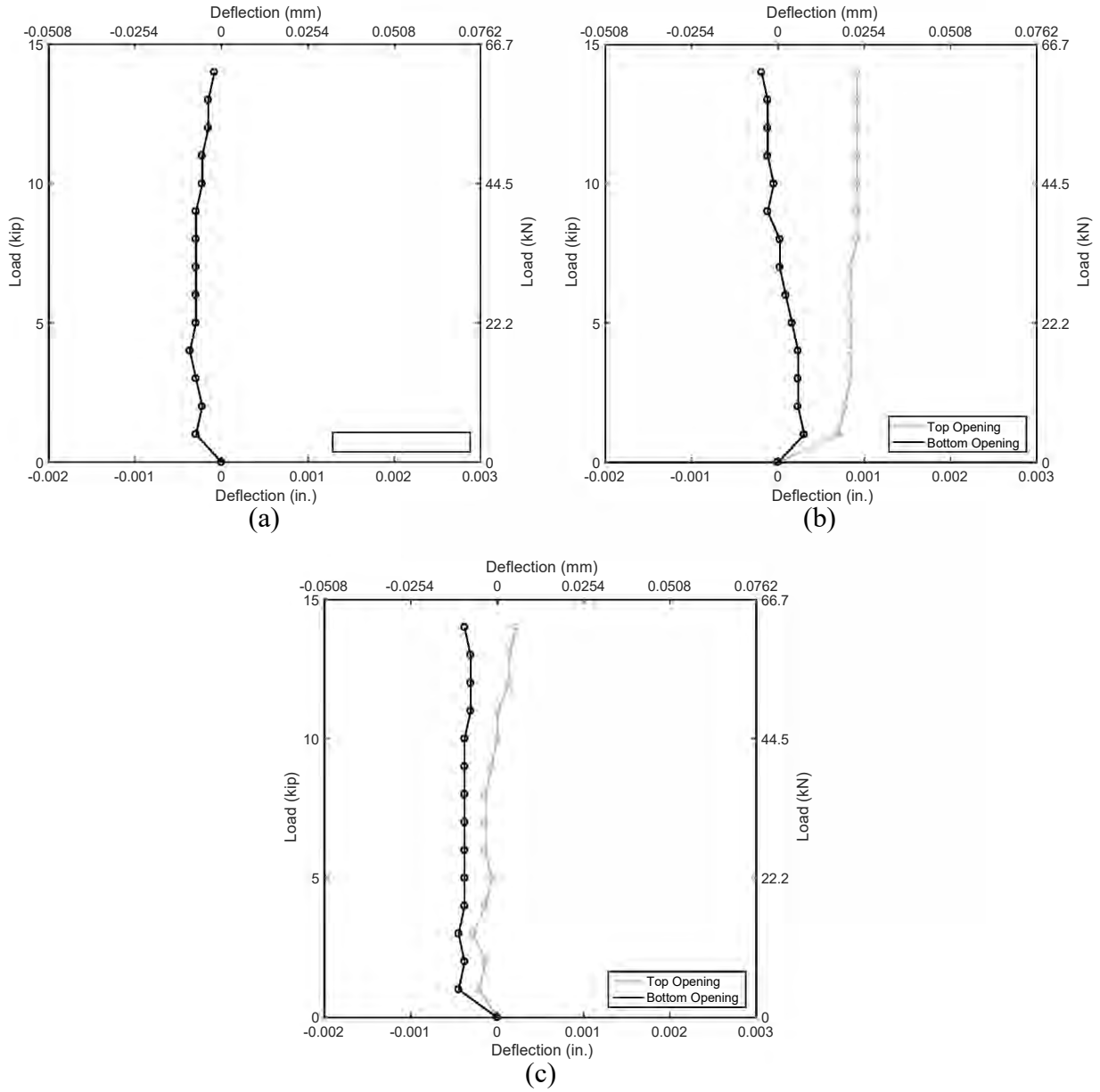


Figure 5.147: Load versus transverse deflection of shear key joint during final 100 cycle at (a) first quarter point of span, (b) mid-span, and (c) third quarter point of span.

5.2.4.2 Shear Testing Results

5.2.4.2.1 Vertical Deflection Behavior

At the completion of CL6 the adjacent girder system the applied load was increased until an ultimate load was reached. This test was performed to measure the overload behavior of the shear key and determine the shear transfer across the system. The girders were loaded at a rate of 0.05 in./min (1.27 mm/min) until a load of 40 kips (177.93 kN) was reached. At this point the girders were unloaded back to 20 kips (88.96 kN). This process continued, increasing the load reached by 20 kips (88.96 kN) each cycle, until a load of 80 kips (355.86 kN) was reached. At this point loading was slowed to an increase of 10 kips (44.48 kN) per cycle, to ensure that a catastrophic failure did not occur. The girders were loaded up to a maximum load of 110 kips (489.30 kN). The girders were then fully unloaded.

The load-deflection behavior of the ultimate shear loading can be seen in Figure 5.148, Figure 5.149, and Figure 5.150. A maximum deflection of 0.93 in. (23.7 mm) and peak load of 110.48 kips (491.4 kN) was reached during testing. The maximum differential deflection was found between the exterior stems of each girder and was measured at 0.24 in. (6.10 mm), as seen in Figure 5.148. Similar to CL6, the minimum deflection occurred at the centerline of the four-point loading due to the proximity of loading to the concrete support column, as seen in Figure 5.149c. Results presented in Figure 5.150 show the vertical deflection of both interior and exterior stems of each girder at load increments of 10,000 lb (44.48 kN). Through analysis of Figure 5.150 it was found that the differential deflection between the interior stems of the adjacent girders began to increase at approximately 50 kips (222.4 kN). This indicates that some bond damage to the shear key occurred causing a decrease in the load transfer across the system.

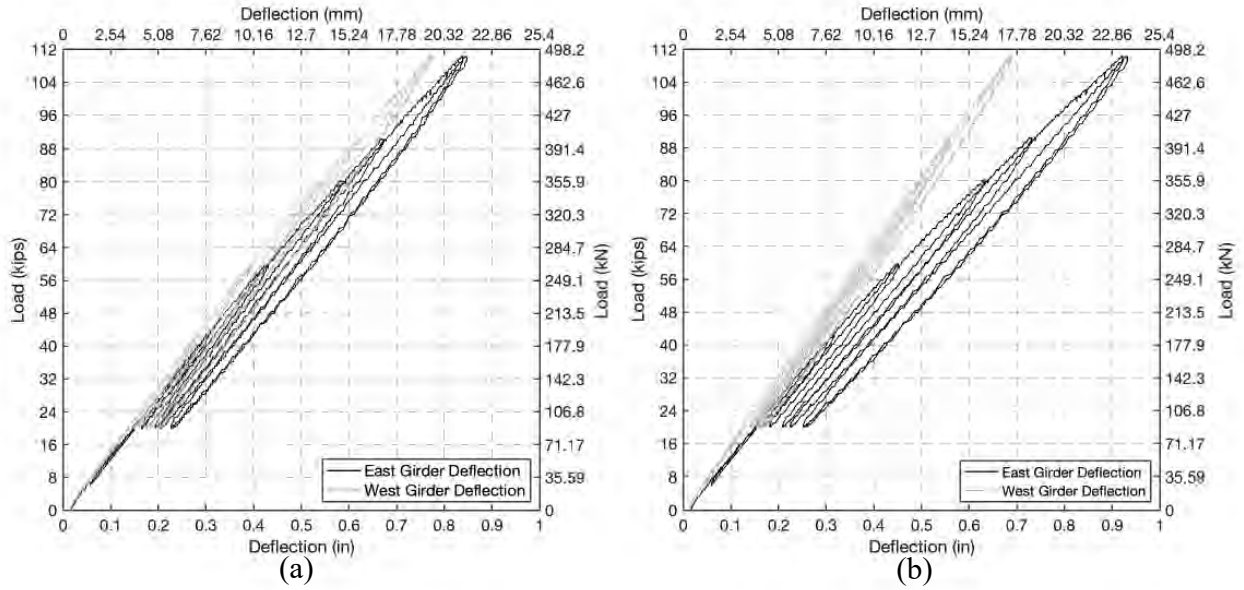


Figure 5.148: Load versus vertical deflection of east and west adjacent girders for ultimate shear loading at (a) interior stem of each girder at midspan and (b) exterior stem of each girder at midspan.

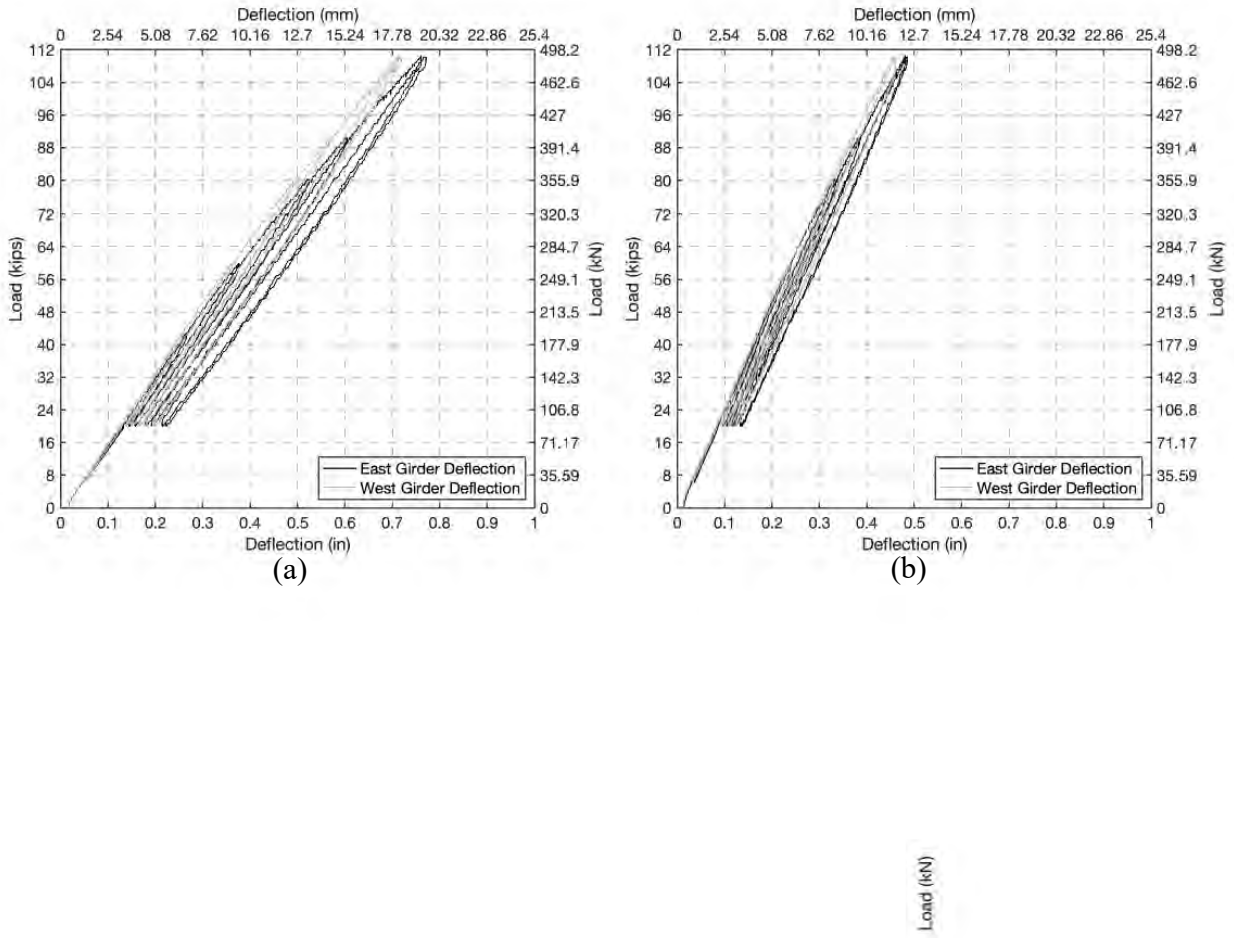


Figure 5.149:Load versus deflection behavior of adjacent girders for ultimate shear loading for (a) interior stem of each girder at the first quarter point of span, and (b) interior stem of each girder at third quarter point of span, and (c) centerline of four-point loading.

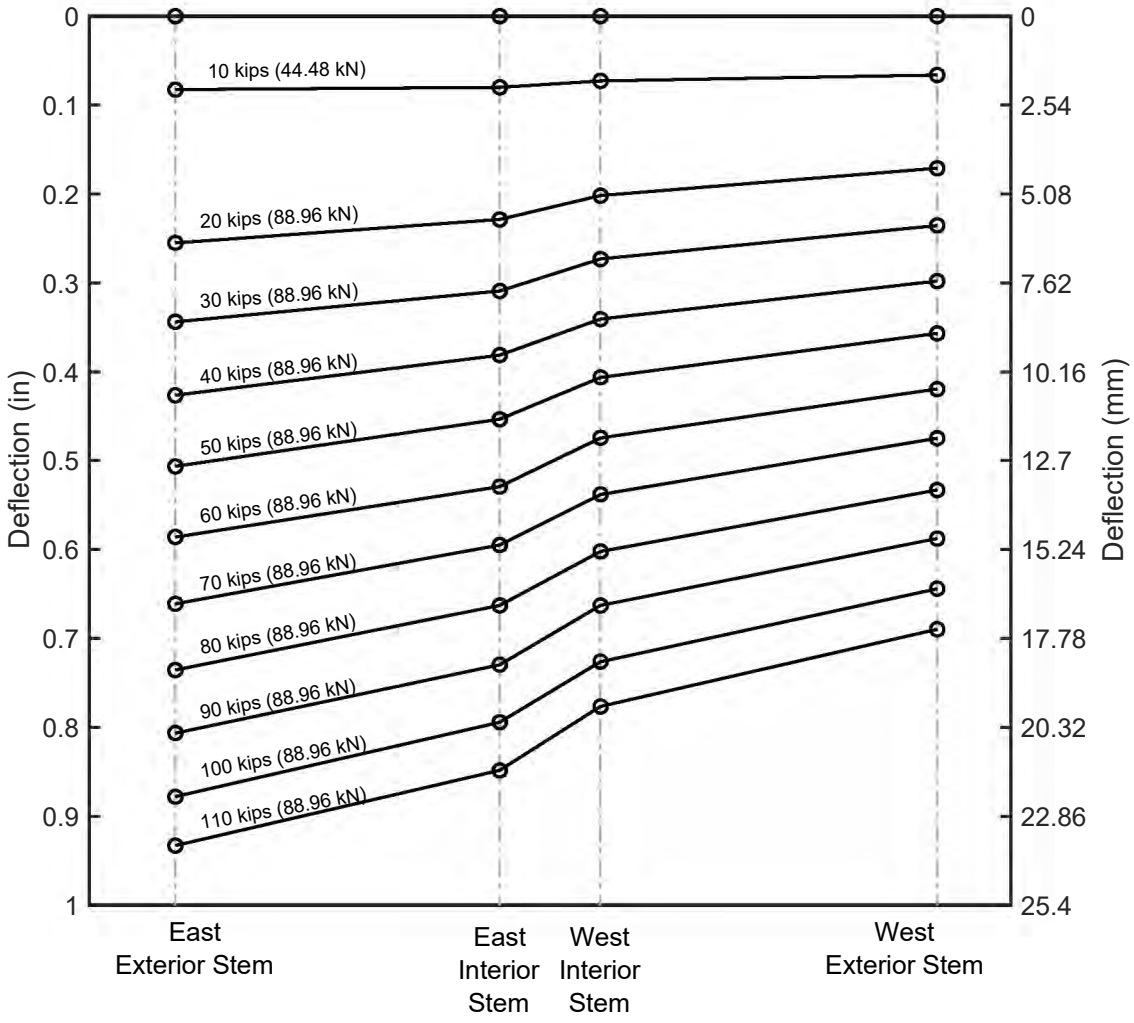


Figure 5.150: Transverse view of vertical deflection of adjacent girders during CL6 at every 10.0 kip (44.5 kN).

5.2.4.2.2 Transverse Deflection Behavior

To fully analyze the load-deflection behavior of the two-girder system, LVDT's were placed perpendicular to the shear key joint on both the top and bottom of the beams to measure any tension and/or compression occurring about the shear key. The girders were instrumented with the LVDT's as presented in Figure 5.115 and the measurements captured are presented in Figure 5.151. There were approximately zero deformations measured across the shear key until an applied load of approximately 50 kips (222.4 kN) was reached. At this point it appears that the bond between the UHPC and precast concrete began to deteriorate causing the top of the shear key to deform in tension (open). A maximum opening of the shear key occurred beneath the shear key joint underneath the centerline of loading, as seen in Figure 5.151d. This maximum opening of the shear key was measured as 0.0396 in. (1.0 mm).

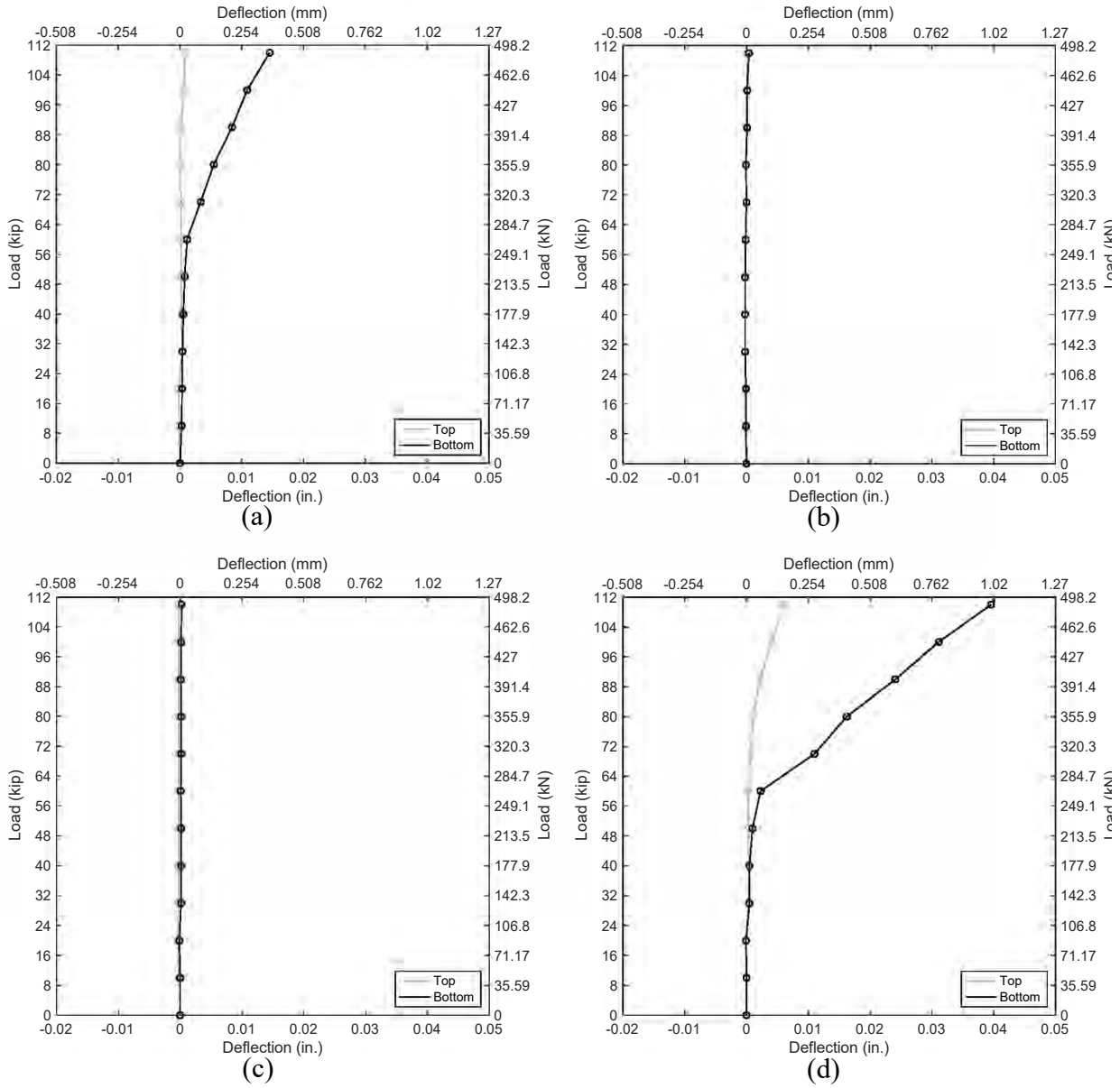


Figure 5.151: Load versus transverse deflection of shear key joint during ultimate shear loading at (a) first quarter point of span, (b) mid-span, (c) third quarter point of span, and (d) centerline of four-point loading.

5.2.5 Moment Distribution Factors

To better understand the load transfer during flexural testing, and its effect on the load-deflection behavior of each cyclic test, the moment distribution factors were calculated. This was accomplished by attaining the difference between the moment in the east girder at different cycles for the grouted shear key tests (CL1, CL2 and CL4) and the mean moment from the single girder test (CL3). Equation 5.1 was used to find the moment distribution factors.

$$DF = \frac{M_2 - M_1}{M_2} \quad 5.1$$

Where,
M_1 = the average moment obtained for the single girder test (CL3)
M_2 = the average of the moments found at cycle 1, cycle 500, and cycle 1000 for the east girder in the CL1, CL2, and CL3 tests.

The moment distribution factors that were found through these calculations are presented in Table 5.16. These results suggest that the moment distribution was influenced by the slight decrease in girder stiffness. By analyzing the change in the moment distribution factor between cycles 1 and 100 for CL1, CL2 and CL4, it was found that the non-shrink grout (CL2) was deteriorating more quickly than either of the UHPC shear keys. As seen in Table, the moment distribution of the non-shrink gout decreased by 0.003 more than the adequately bonded UHPC during the same span of cyclic loads.

Table 5.16: Moment Distribution Factors of CL1, CL2, and CL4

Loading Scenario	Moment Distribution Factor (DF)
CL1	0.498
CL2	0.440
CL4	0.436

Table 5.17: Change In Moment Distribution Factors for CL1, CL2 and CL4 Between Cycle 1 and Cycle 100

Loading Scenario	Change in Moment Distribution Factor (DF)
CL1	0.007
CL2	0.008
CL4	0.005

5.2.6 Shear Distribution Factor

To fully analyze the behavior of the UHPC shear key tested under four-point shear loading the shear distribution factors were calculated. This calculation was done through comparison of the load-deflection behavior of the single girder tested in CL5 and the two-girder system tested in CL6. Equation 5.2 was used to estimate the shear distribution across the across the system. Because the same target shear load was used during both CL5 and CL6, the amount of achieved deflection from each test was used to calculate the shear distribution factor.

$$\mathrm{DF} = \frac{\delta_1 - \delta_2}{\delta_2} \qquad 5.2$$

Where,
δ_1 = the average deflection obtained for the single girder test (CL5), and
δ_2 = the average of the deflection obtained for the east girder during CL6.
Using Equation 5.2, the shear distribution factor for CL6 was calculated to be 0.547. This shear distribution factor indicates that the UHPC was able to adequately transfer the shear force across the system.

5.2.7 Summary

Table 5.18 provides a summary of the load-defection behavior for the cyclic and ultimate loading tests performed.

Table 5.18: Summary of Maximum Load-Deflection Behavior for Adjacent Girders

Loading Scenario	Average Load kips (kN)	Average Vertical Deflection in. (mm)	Maximum Transverse Deflection in. (mm)
CL1	13.9 (61.9)	0.40 (10.2)	0.0015 (0.038)
CL2	13.4 (59.6)	0.40 (10.2)	0.0024 (0.061)
CL3	7.40 (32.9)	0.40 (10.2)	-
CL4	13.2 (58.7)	0.40 (10.2)	0.0014 (0.036)
Ultimate Flexural Loading	55.9 (249)	2.00 (50.8)	0.0006 (0.015)
CL5	20 (89.0)	0.30 (7.49)	-
CL6	19.9 (88.5)	0.14 (3.56)	0.0004 (0.011)
Ultimate Shear Loading	110 (491)	0.24 (6.10)	0.0396 (1.006)

5.2.8 Conclusions

The following sections provide the conclusions found through the analysis of the full-scale flexural and shear testing.

5.2.8.1 Flexural Testing

Three cyclic tests and an ultimate loading test was completed on a two-girder system with a grouted shear key loaded under four-point bending applied at the midspan of one girder causing a flexural loading of the systems. The three cyclic tests performed used poorly bonded UHPC grout, US Spec NA non-shrink grout, and adequately bonded UHPC grout, respectively. A fourth test was performed on a single girder with no grouted shear key loaded in four-point bending at midspan. The following conclusions were found through comparative analysis of the test results:

- Two full-scale flexural cyclic tests of a two-girder system with a UHPC grouted shear key demonstrated that the UHPC was able to bond successfully with the precast concrete girders to withstand the maximum in-service design deflection for an equivalent bridge. This was true for both the poorly bonded UHPC grout (not pre-wetted) and adequately bonded UHPC grout (pre-wetted).
- The bond and load transfer observed between the UHPC grout and precast concrete girders occurred with no transverse post-tensioning or other lateral restraint. This suggests that UHPC does not require the additional lateral compression to carry the applied stresses.
- During the three full-scale flexural cyclic tests performed, two with UHPC grout and one with US Spec NA non-shrink grout, the girder stiffness had a slight decrease between test set-ups. Since the same two girders were used for all flexural tests, it appears some damage was sustained during testing causing a decrease in stiffness and is not representative of the shear key behavior.
- Rotation about the shear key was observed during the full-scale flexural tests. This was similar to the observation by Miller et al. (1999) that the shear key acts as a hinge between the precast concrete girder members.
- Flexural tests using UHPC, poorly bonded and adequately bonded, were found to have lower transverse deformation of the shear key (i.e., opening and/or closing) compared to the US Spec NA non-shrink grout. This indicates that the bond strength of UHPC was greater than the non-shrink grout, regardless of a pre-wetted surface preparation.
- The differential deflection of the interior stems was less during CL4 (adequately bonded UHPC) compared to the other two tests. This indicates that the bond between UHPC and the precast concrete girders was more effective when the girder surface was prepared by pre-wetting and was thus able to transfer the applied loads effectively across the two-girder system.
- The differential deflection of the interior stem of each girder during CL2, the second full-scale test using US Spec NA non-shrink grout, increased as the load applied was increased.

This indicates that the non-shrink grout was deteriorating as load was applied, minimizing the load transfer across the system.

- While the maximum load reached during CL4 (adequately bonded UHPC) was less than that reached during CL1 (poorly bonded UHPC) and CL2 (US Spec NA non-shrink grout), the differential deflection between the interior stems of each girder was the lowest of all three cyclic tests, indicating that UHPC did outperform non-shrink grout when the surface is prepared adequately.
- The change in the moment distribution factor between cycles 1 and 100 was found to be greatest for the non-shrink grout (CL2). This suggests that the non-shrink deteriorates more quickly than UHPC (CL1 and CL4) and therefore a UHPC shear key was able to transfer load more effectively.
- After the ultimate flexural loading test, the adequately bonded UHPC was tested under cyclic loading. Results of this test showed that the UHPC was able to remain effective beyond the linear load-deflection behavior.
-

5.2.8.2 Shear Testing

Two tests were performed using a four-point shear loading. The tests included the cyclic loading of a single girder, as well as the cyclic and ultimate loading of a two-girder system with an adequately bonded UHPC shear key. The following conclusions were found through analysis comparative analysis of the two tests:

- One full-scale two-girder system test was performed with a four-point shear loading positioned 12 in. (304.8 mm) from the edge of the north support. Throughout the duration of the shear cyclic loading the shear key had no opening of the joint suggesting that the UHPC grout bonded successfully to the precast concrete girder and transferred the shear loads effectiviely.
- With no lateral compression or transverse post-tensioning, the UHPC shear key successfully transferred the shear loads across the system further indicating that the UHCP had a strong bond with the adjacent girders.
- The differential deflection of the interior stems of each girder was lower than those found during all three cyclic flexural tests. This indicates that the UHPC was better able to transfer the shear loads across the system compared to the flexural loads.
- During the ultimate loading of the UHPC shear key, the UHPC was able to maintain an effective bond up to approximately 50 kips (222.4 kN). The differential deflection of the interior stem of each girder began to increase at this suggesting that the bond between girder and UHPC was becoming less efficient.
- Transverse deformation of the shear key during ultimate shear loading also showed that the shear key began to open when an applied load of approximately 50 kips (222.4 kN) indicating the bond of the UHPC was becoming less effective.

5.3 UHPC and NSC Composite Beams

This study aims to investigate the effects that ultra high performance concrete (UHPC) has on the behavior of unreinforced and reinforced beams when used in conjunction with normal strength concrete (NSC). The behavioral properties being evaluated include cracking behavior, ultimate load, maximum deflection, load-deflection relationship, and moment-curvature relationship. These properties are being analyzed for several parameter variations in the beam design. Ultimately, these variations will include either a single or multiple layer of UHPC with NSC making up the remaining cross section. These parameters include the presence of UHPC in several portions of the beams including single or multiple layers throughout the cross section and may also include UHPC making up the shear region of the beams with NSC making up the remainder of the beam.

5.3.1 Mixture Proportions

Table 5.19 and Table 5.20 present the mixture proportions for the UHPC and NSC used in the composite beams.

Table 5.19 Ultra High Performance Concrete Mixture Proportions

Constituent	Quantity, /1 yd^3	Quantity, /1 m^3
Cement	1374 lb	815 kg
Silica Fume	173 lb	103 kg
Fly Ash	173 lb	103 kg
Sand	1682 lb	998 kg
Steel Fibers	200 lb	119 kg
HRWRA	9 gal	44.6 l
Water	276 lb	164 kg

Table 5.20 Normal Strength Concrete Mixture Proportions

Constituent	Quantity, /1 yd^3	Quantity, /1 m^3
Water	354 lb	210 kg
Cement	851 lb	505 kg
Coarse Aggregate	1661 lb	985 kg
Fine Aggregate	1021 lb	606 kg

5.3.2 Preliminary Specimen Design

Preliminary tests were performed on beams with cross sections of 6 inches by 6 inches and lengths of 24 and 30 inches. Additionally, lengths are currently being prepared for testing. During each test three specimens were tested, 1 beam with a normal concrete cross section and 2 beams with composite cross sections. Both concretes were mixed and cast at the same time with several steps taken to ensure proper bond between the two mixes. These steps included rodding the interface between the UHPC and NSC layers 0.5 inches deep as well as using a vibrating table. With the extra steps taken, no debonding between the two different concretes was observed during testing.

The first test (040919) and the fourth test (062719) consisted of composite beams with cross sections consisting of 1 inch of UHPC at the bottom and 5 inches of NSC on top. The second test (051719) and the third test (062619) consisted of composite beams with cross sections consisting of 1 inch of UHPC on bottom and 1 inch of UHPC on top with 4 inches of NSC in between. The first four sets of tests were performed on 24-inch-long beams. The fifth test (080519) and the ninth test (102419) consisted of composite beams with 1 inch of UHPC at the bottom and 5 inches of NSC on top with two #3 bars near the UHPC-NSC interface. The sixth test (081219) and the eighth test (101719) consisted of composite beams with 1 inch of UHPC at the bottom of the entire beam with UHPC also making up the shear regions of the beam, 6 inches from each end of the beam. NSC made up the rest of the beam. The seventh test (082219) consisted of composite beams with 1 inch of UHPC at the bottom of the entire beam with UHPC also making up the shear regions of the beam, 6 inches from each end of the beam. NSC made up the rest of the beam with two No. 3 bars near the UHPC-NSC interface. The fifth through the ninth tests were performed on 30 in. long beams. UHPC and NSC mixes have followed the mix designs provided above. Figure 5.152 through Figure 5.159 show the beam specimens tested. Other parameter variations to be tested include reinforcement size and beam length to ensure realistic flexural behavior.

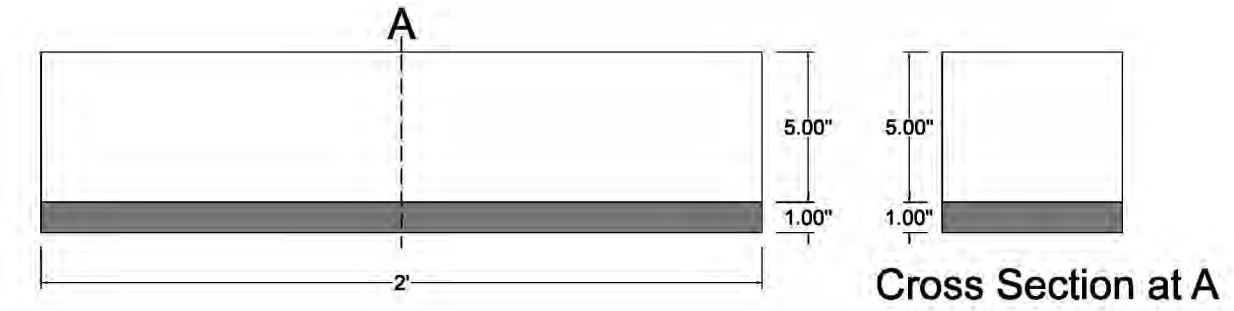


Figure 5.152: Composite beam design for tests (040919) and (062719).

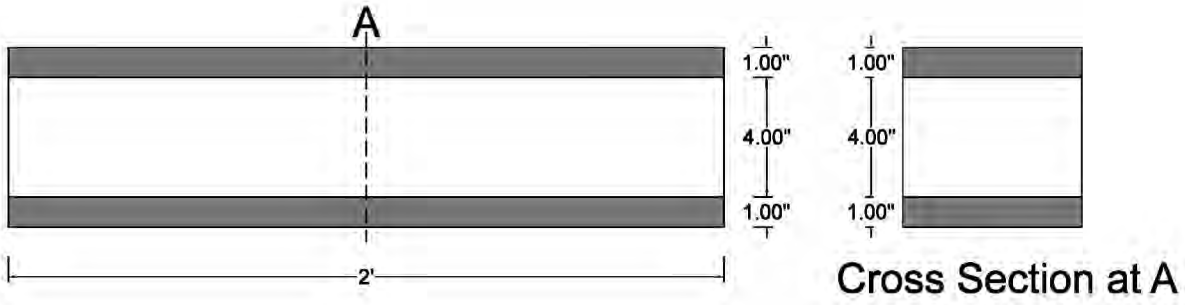


Figure 5.153: Composite beam design for tests (040919) and (062719).

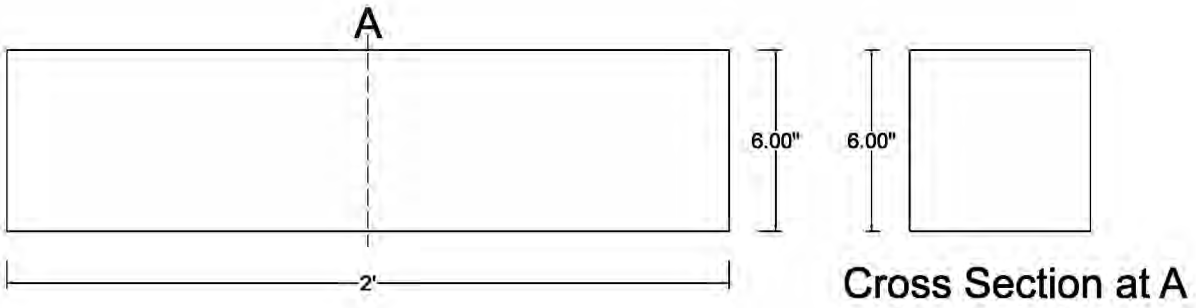


Figure 5.154: NSC beam design tested with 24 in. composite beams.

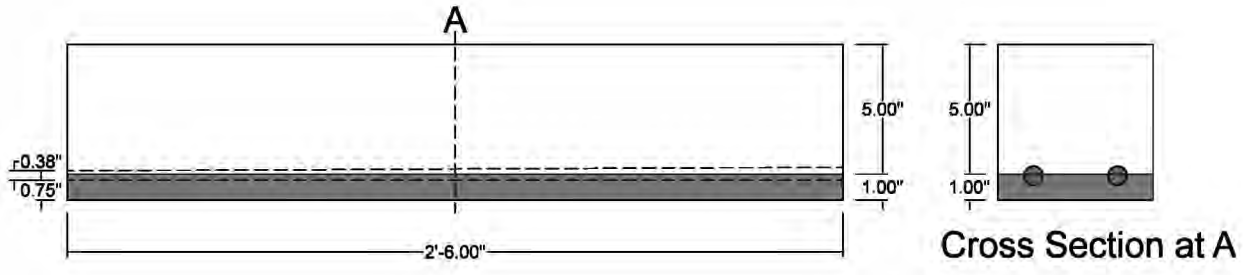


Figure 5.155: Composite beam design for tests (080519) and (102419).

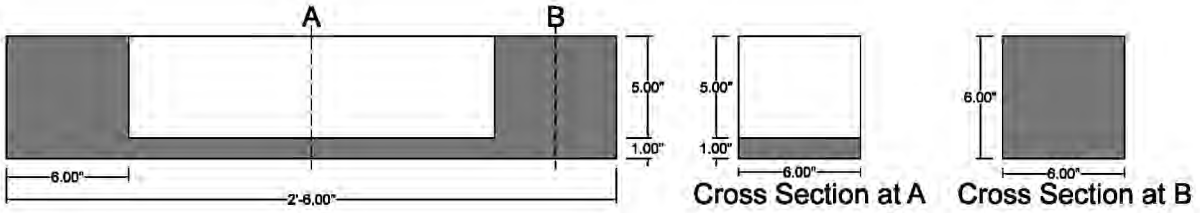


Figure 5.156: Composite beam design for tests (081219) and (101719).

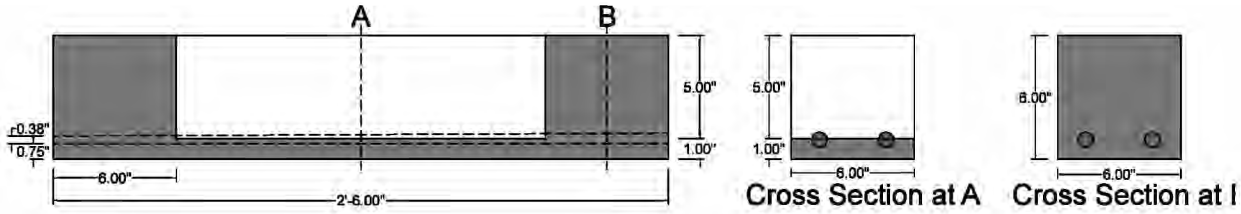


Figure 5.157: Composite beam design for test (082219).

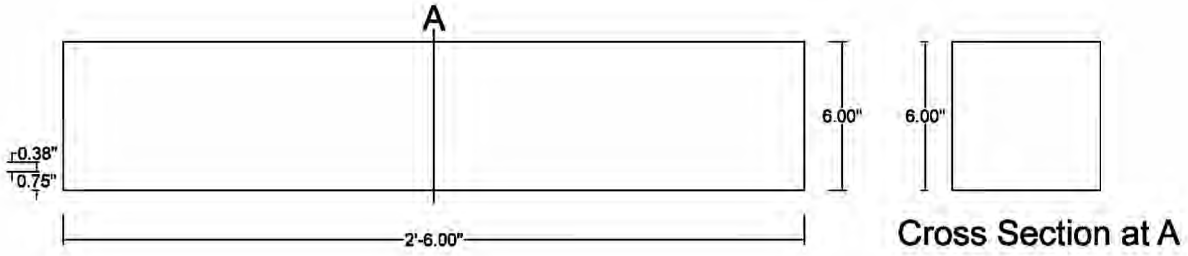


Figure 5.158: NSC beam design tested with 30 in. unreinforced composite beams.

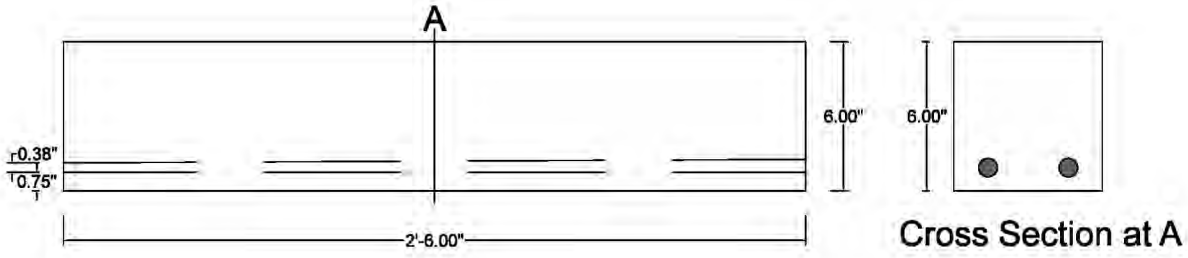


Figure 5.159: NSC beam design tested with 30 in. reinforced composite beams.

5.3.3 Test Setup and Instrumentation

The test specimens were cured in a wet room for 28 days following casting. After curing, specimens are placed on the specimens at predetermined locations. These sensors included up to four linear variable differential transducers (LVDT's), two string potentiometers, and two load cells. LVDT's are affixed at locations on each beam to obtain the behavior of the different materials. These locations vary between beams depending on the layout of the cross section; however, the general basis of the LVDT placement is to place them at the midpoints of each respective material, or as close as space allows, and near the UHPC and NSC interfaces. This allows for recording of the linear displacement at those locations which can later be used for calculations such as neutral axis depth or can be converted to strain values to be used in the analysis of strain profiles at different loads throughout the test. The test set-ups are shown in Figure 5.160, Figure 5.161, and Figure 5.162. String potentiometers are placed at midspan both at the top of the beam and at the bottom. Load cells are placed centered below both supports. Along with these sensors, LabView computer software was used to record data in real time allowing observation of the behavior during the tests while also recording the data for future analysis. Figure 5.163, Figure 5.164, and Figure 5.165 show the test set-ups for the NSC and composite beams.

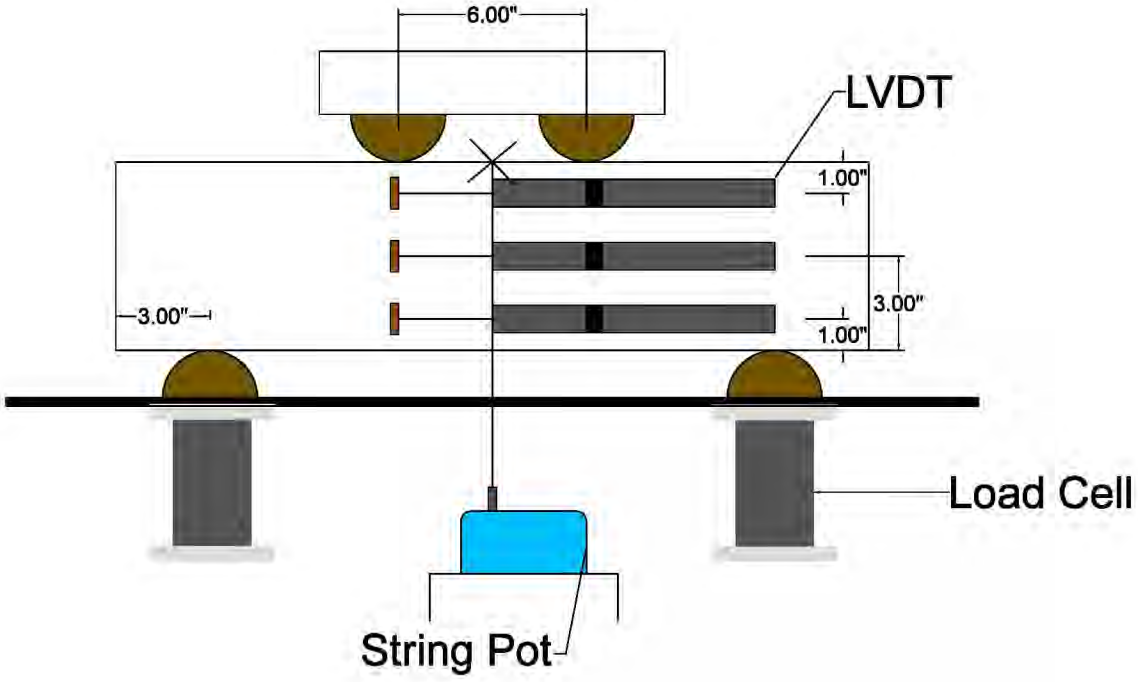


Figure 5.160: Instrumentation set up for NSC beams.

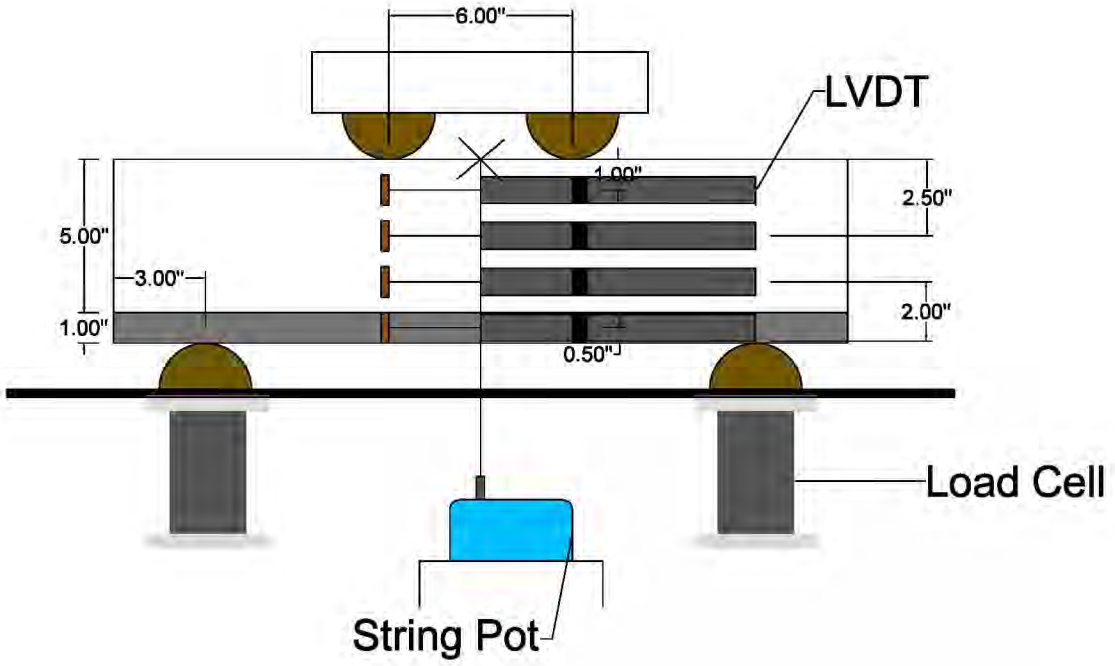


Figure 5.161: Instrumentation set up for beams with 1 in. of UHPC at the bottom.

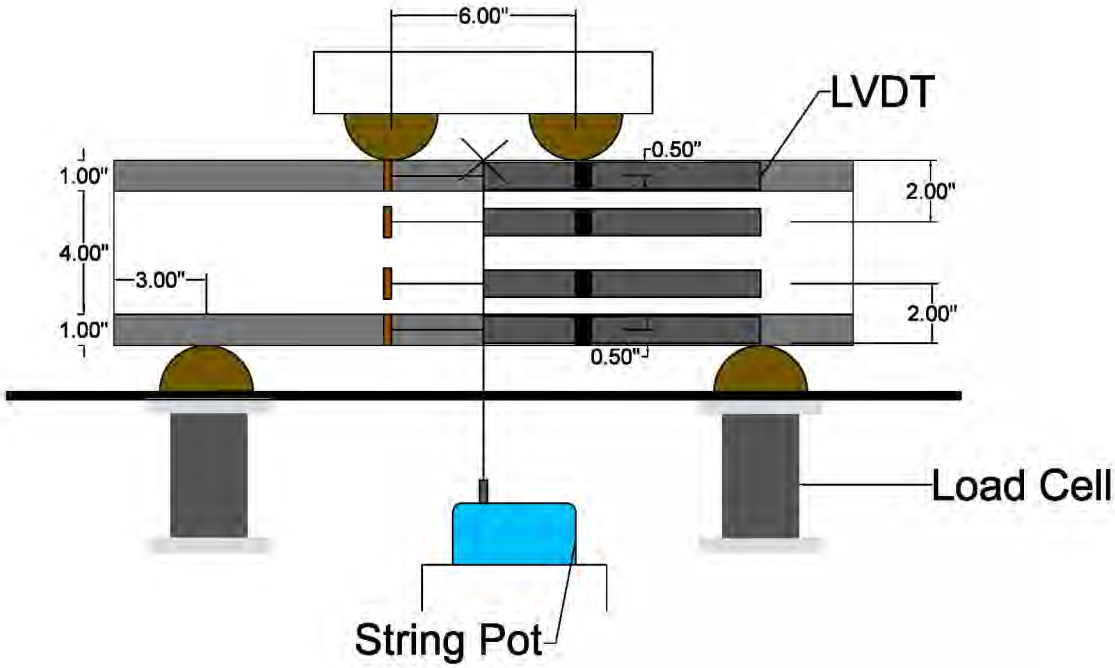


Figure 5.162: Instrumentation set up for beams with 1 in. of UHPC at the bottom and at the top.

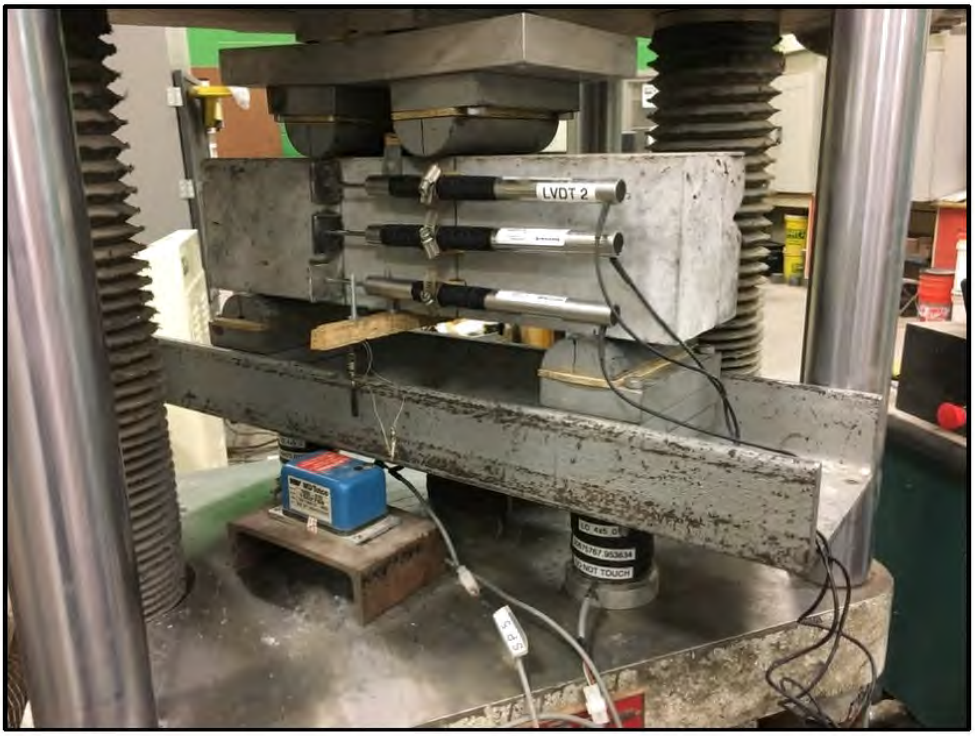


Figure 5.163: Test set-up for NSC beams.



Figure 5.164: Test set-up for beams with 1in. of UHPC at the bottom.



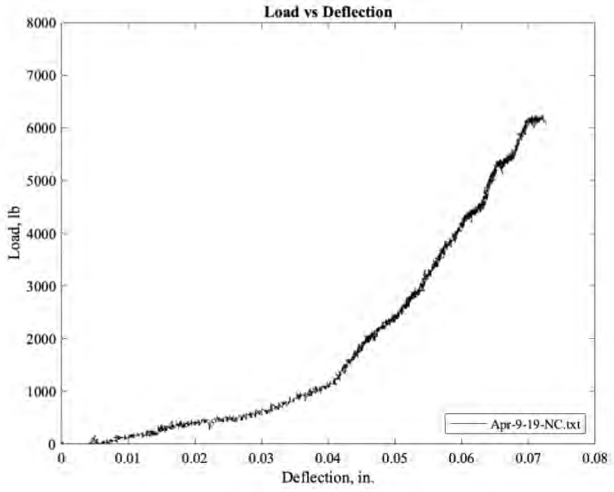
Figure 5.165: Test set-up for beams with 1 in. of UHPC at the bottom and at the top.

5.3.4 Preliminary Results

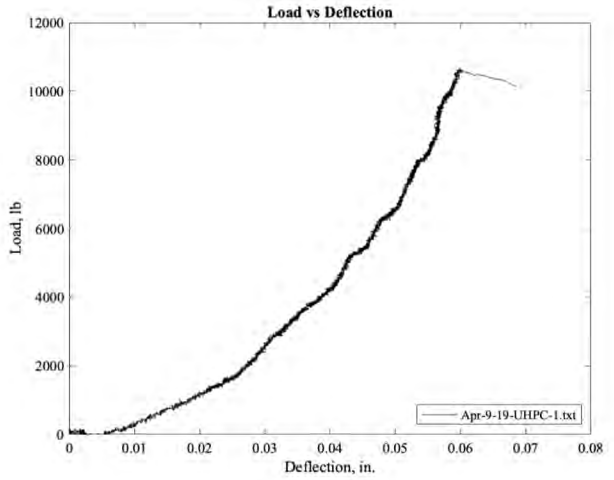
The presence of UHPC in the cross section of the beam directly effects the load deflection relationship. When comparing the beams, from test (040919), with UHPC to the purely NSC beam, much larger ultimate load can be achieved. The NSC beam reached a maximum load of just over 6000 lb. The cross section made up NSC with 1 inch of UHPC at the bottom, a maximum load of just over 11000 lb was achieved before failure. This increase in strength became even more apparent with test (051719) which shows ultimate loads reaching nearly 15000 lb when the second layer of UHPC is added to the cross section at the compression face. Similar results were obtained from tests (062619) and (062719) with ultimate strengths of the composite beams being slightly higher than those of their NSC counterparts. It should be noted however, that the presence of UHPC in the cross section led to, in most cases, a significant decrease in maximum deflection before failure. These observations can be seen in Figures 6.24 – 6.30.

The results obtained from the initial tests on unreinforced beams provided adequate enough results to continue investigating the effects of UHPC on beam behavior. Figures 21-25 show load versus deflection results from the tests performed on the 30-inch-long beams. These results showed similar behaviors to the shorter beams with the composite beams from each test always reaching higher ultimate strengths than the NSC beam tested. However, when comparing these effects in unreinforced and reinforced concrete beams, it can be seen that the increase in strength was more drastic in unreinforced beams.

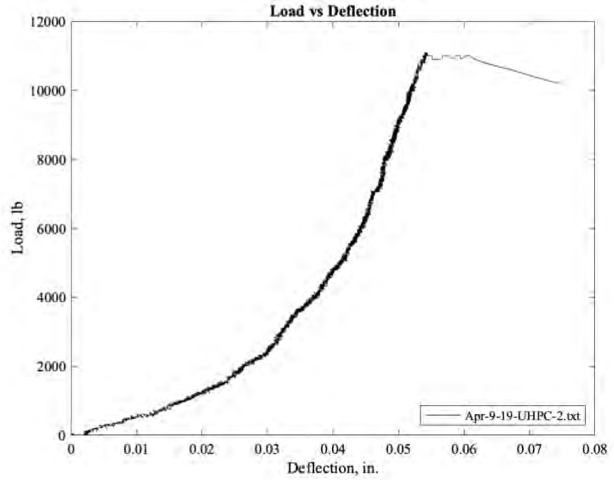
Further analysis is currently underway on the data gathered from each test to provide moment curvature relationships, deflection versus time relationships, neutral axis versus load relationships, as well as strain profiles.



(a)

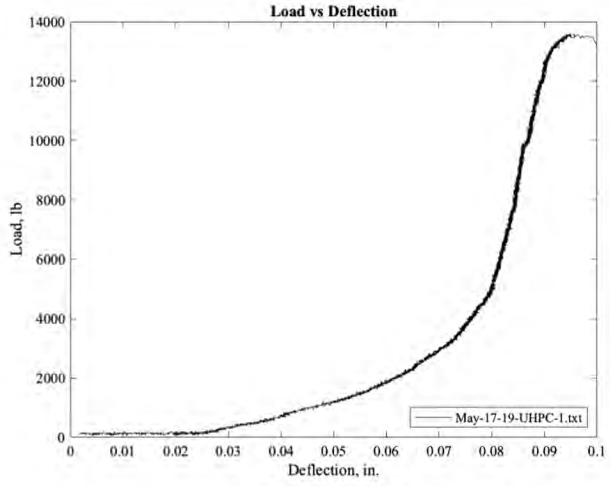


(b)

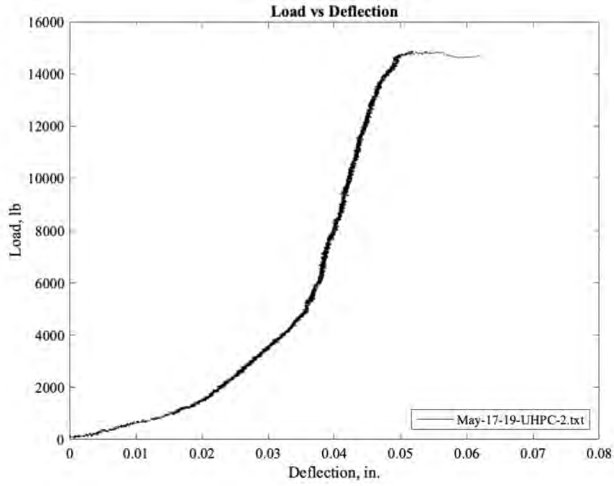


(c)

Figure 5.166: Load vs deflection for plot for tests (040919) – (a) NSC beam, (b) First composite beam, (c) Second composite beam.

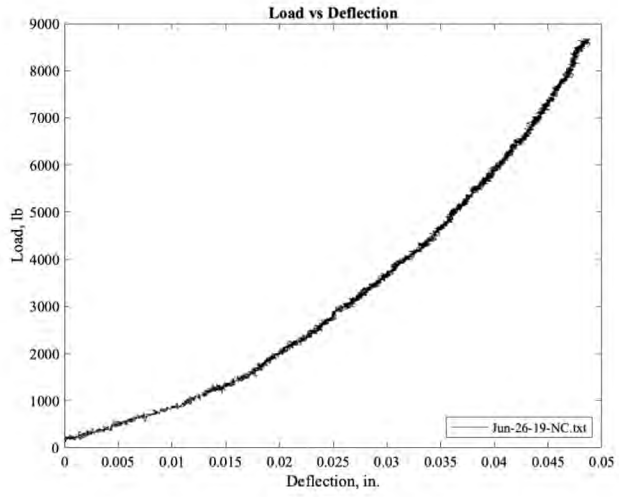


(a)

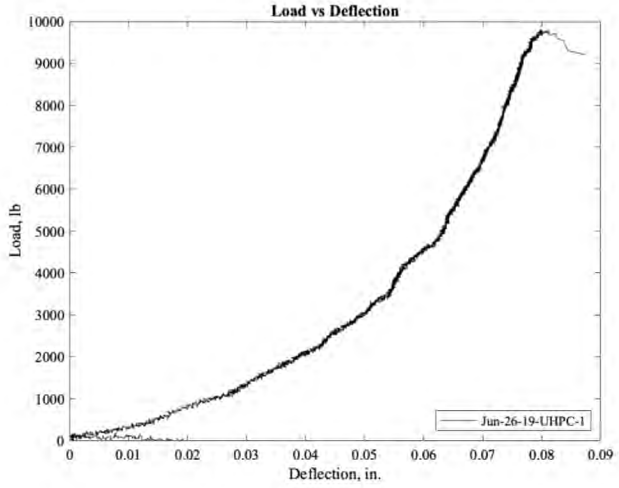


(b)

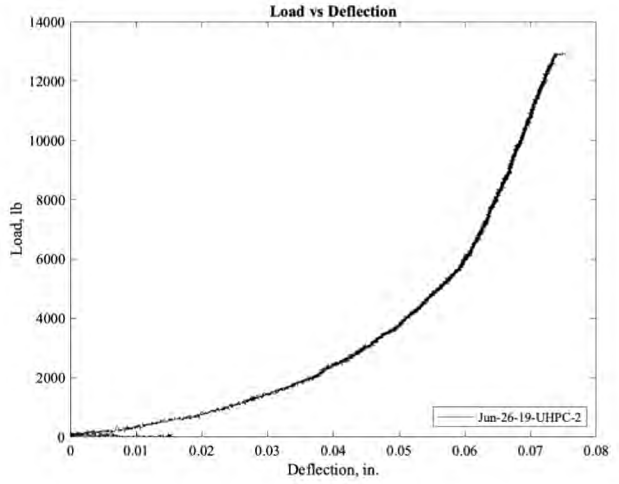
Figure 5.167: Load vs deflection for plot for tests (051719) – (a) First composite beam, (b) Second composite beam.



(a)

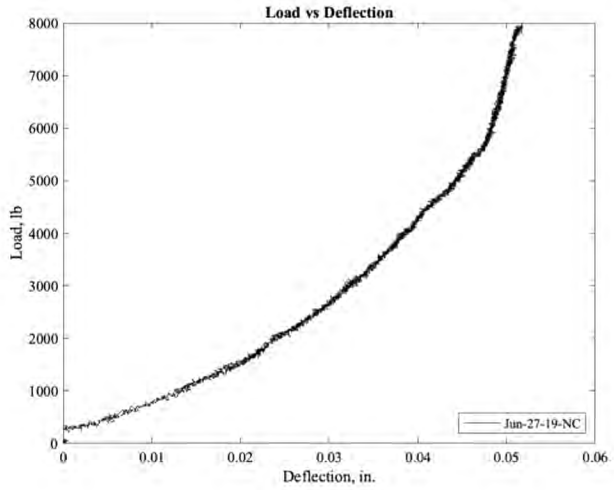


(b)

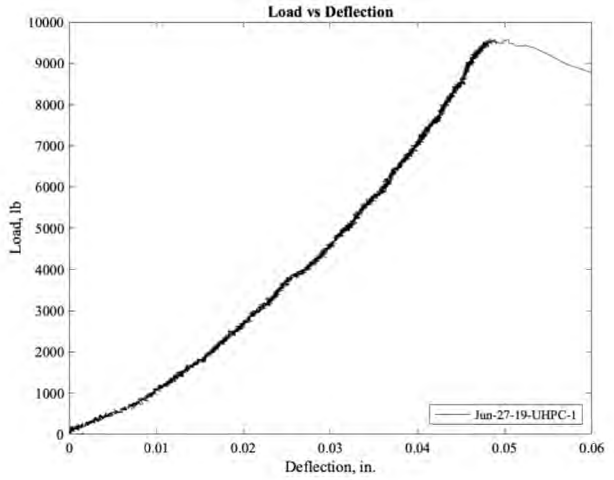


(c)

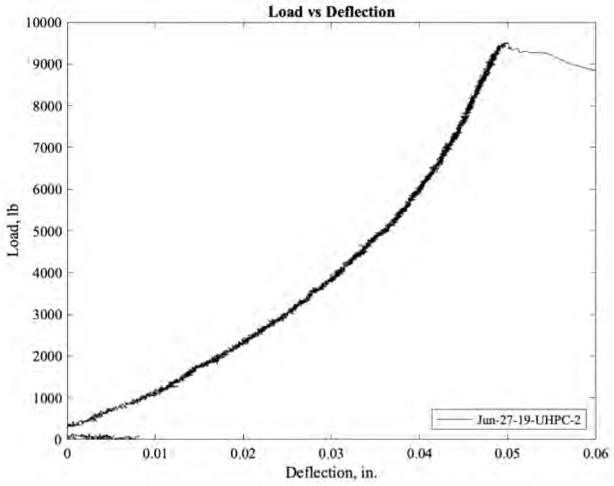
Figure 5.168: Load vs deflection for plot for tests (062619) – (a) NSC beam, (b) First composite beam, (c) Second composite beam.



(a)

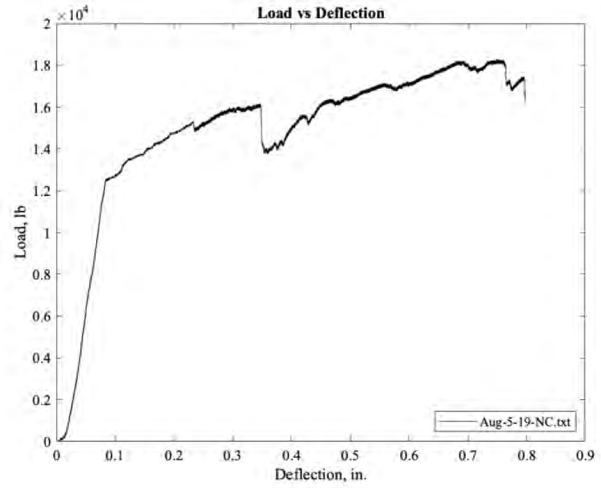


(b)

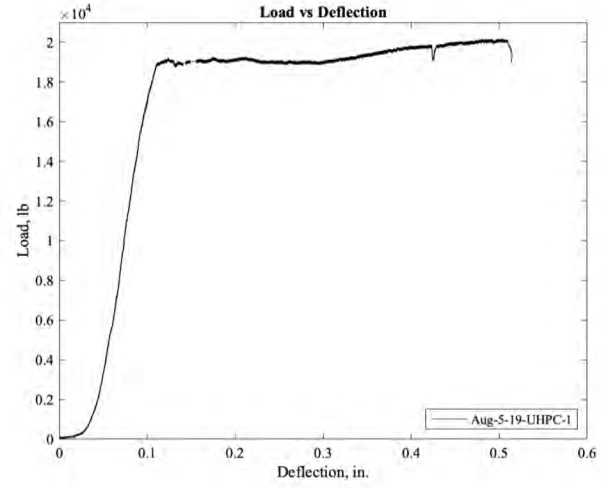


(c)

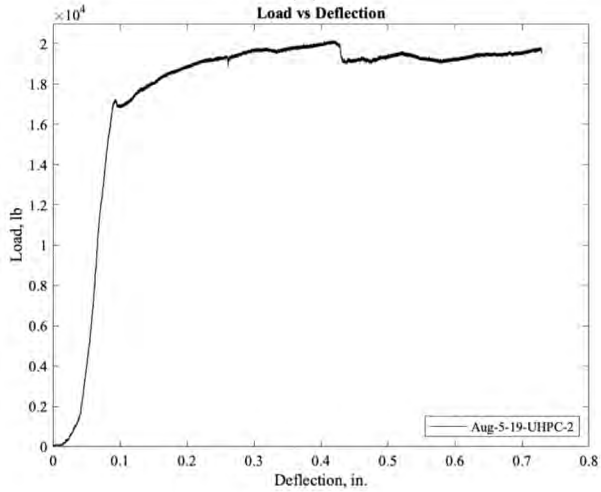
Figure 5.169: Load vs deflection for plot for tests (062719) – (a) NSC beam, (b) First composite beam, (c) Second composite beam.



(a)

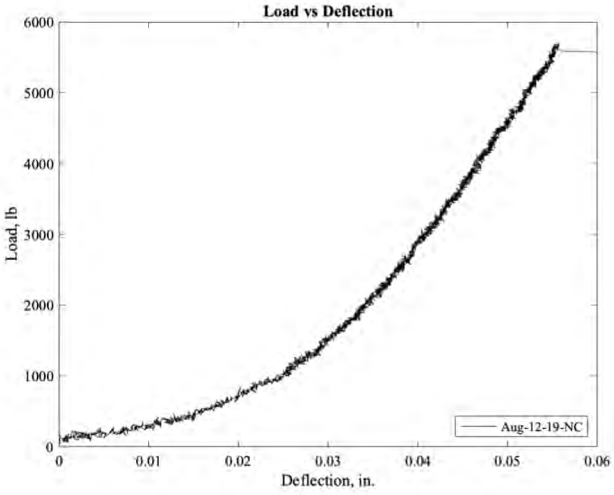


(b)

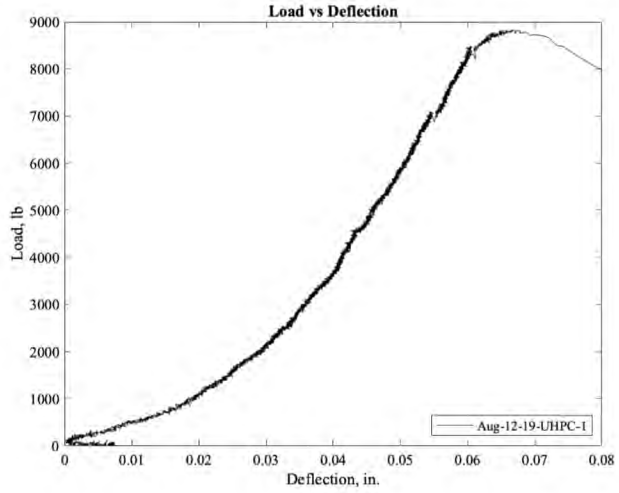


(c)

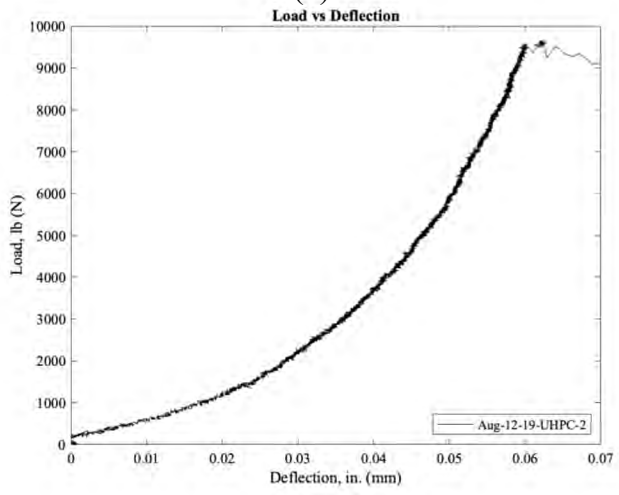
Figure 5.170: Load vs deflection plot for tests (080519) – (a) NSC beam, (b) First composite beam, (c) Second composite beam.



(a)

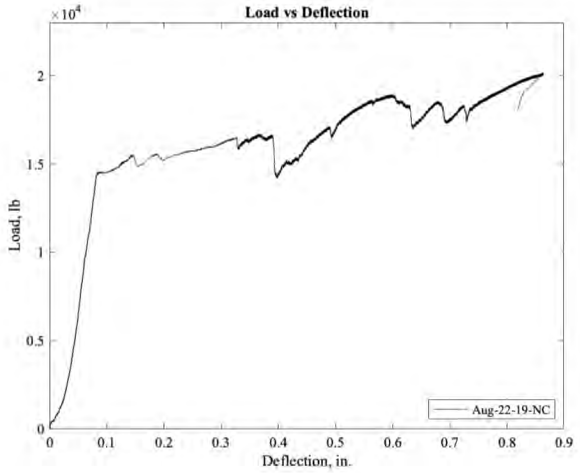


(b)

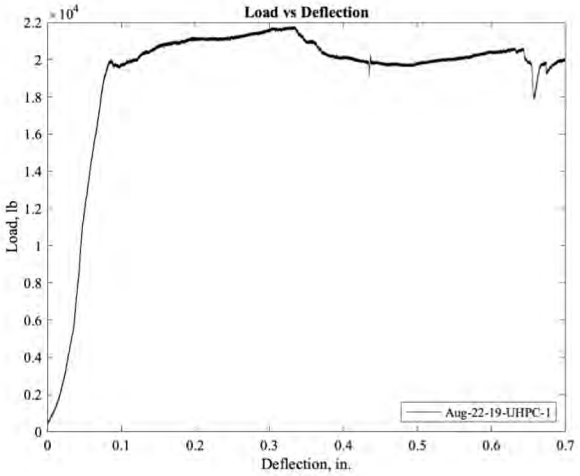


(c)

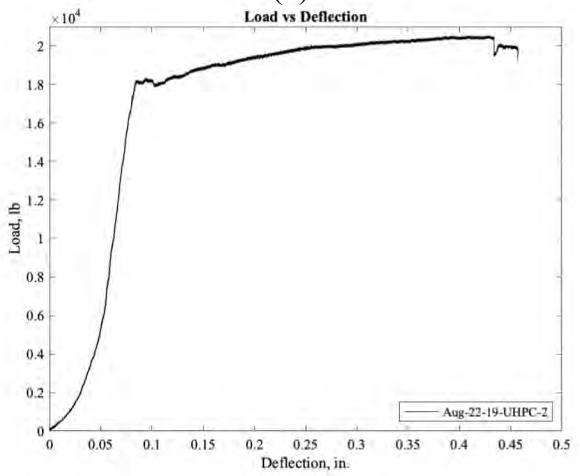
Figure 5.171: Load vs deflection for plot for tests (081219) – (a) NSC beam, (b) First composite beam, (c) Second composite beam.



(a)

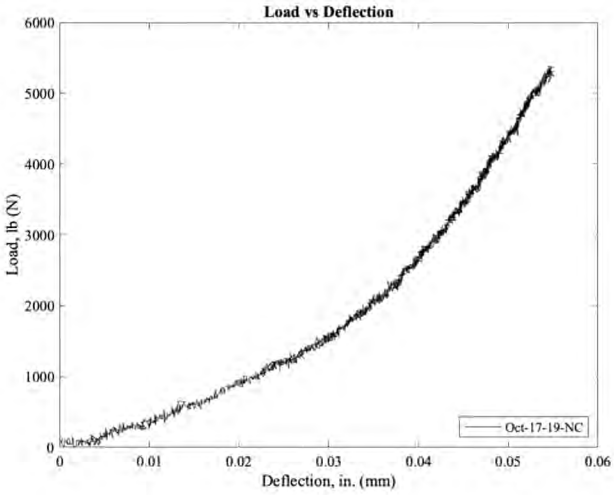


(b)

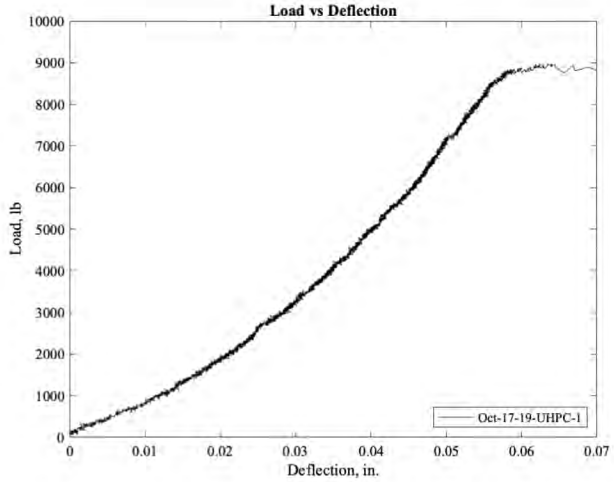


(c)

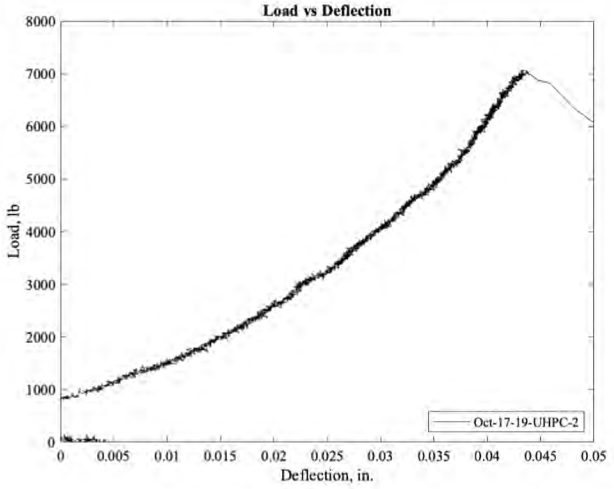
Figure 5.172: Load vs deflection for plot for tests (082219) – (a) NSC beam, (b) First composite beam, (c) Second composite beam.



(a)

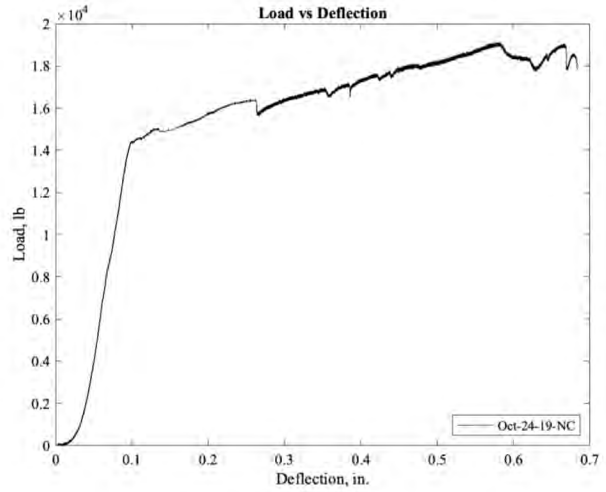


(b)

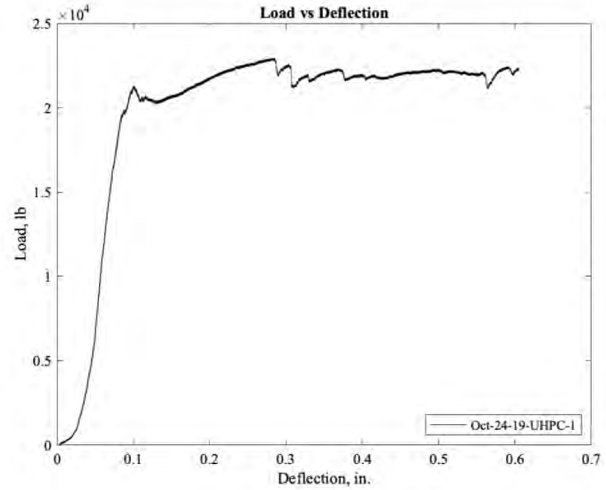


(c)

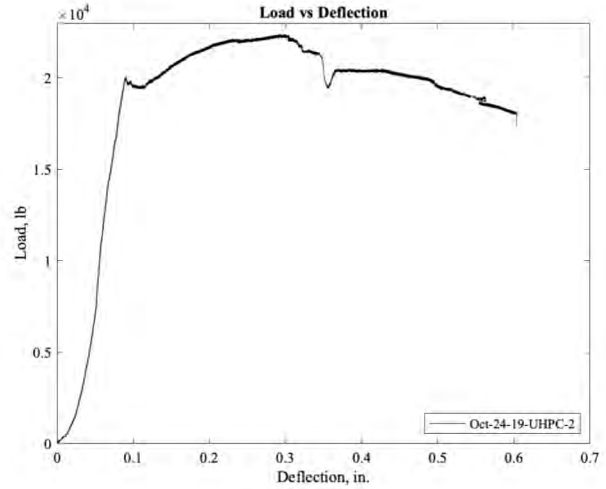
Figure 5.173: Load vs deflection plot for tests (101719) – (a) NSC beam, (b) First composite beam, (c) Second composite beam.



(a)



(b)



(c)

Figure 5.174: Load vs deflection for plot for tests (102419) – (a) NSC beam, (b) First composite beam, (c) Second composite beam.

5.4 UHPC As an Overlay Material

Shrinkage behavior of UHPC overlays on NSC slabs was investigated through analysis of nine slabs with a single parameter variation in either the slab or the overlay. parameter variations analyzed where selected based on which elements were influencing the most the in the structural capacity of the slabs and included the thickness of the NSC substrate, reinforcement steel area in the slab, use of overlay or without overlay, thickness of overlay, percentage by volume of fibers in UHPC mixture, and exposure conditions. The strain in each slab was measured and monitored with gauges embedded in the substrate over the course of one year to understand the influence that UHPC overlay had on the NSC substrates. Additionally, the stress developed at the interface between UHPC and NSC was investigated to identify methods to control shrinkage and reduce cracking.

5.4.1 Mixture Proportions

This research investigated NSC substrates with UHPC overlays; therefore, each material had different mixture proportions and constituents. The components for the NSC slabs included coarse aggregates, sand, cement, class F fly ash, and water. The UHPC had some of the basic components of NSC including cement, sand, class F fly ash, and water, but did not include coarse aggregate. Additional constituents of UHPC include silica fume, a superplasticizer, and steel fibers. Each of these mixtures and their properties are provided in the following sections.

5.4.2 UHPC

The UHPC mixture used in this research is a nonproprietary mixture developed at NMSU (Allena, 2010; Lyell, 2011; Weldon et al., 2012). This UHPC mixture is characterized by using components available regionally such as sand, cement, and fly ash.

The fine aggregate was locally available sand that passed a No. 4 sieve that has a nominal opening of 0.187 in. (4.76 mm). The cementitious materials included Type I/II cement, silica fume, and class F fly ash. Cement constituted 80% of the total cementitious materials and the remaining of 20% was silica fume and class F fly ash at a ratio of 50% silica fume and 50% fly ash. A water-to-cementitious materials (w/cm) ratio of 0.15 was used for the UHPC mixture. To improve workability, a high range water reducing admixture (HRWRA), BASF MasterGlenium 3030 NS, was used. The final component of the UHPC mixture was Dramix® micro steel fibers, 0.5 in. (13 mm) in length with a 0.008 in. (0.20 mm) diameter and a minimum tensile strength of 290 ksi (2000 MPa).

Within the UHPC mixtures, three different percentages by volume of steel fibers were used, 1.5, 2.0, and 3.0%. To compensate for the increase in the volume of fibers, the amount of sand was reduced to maintain the same percentage of the other components. The 1.5% steel fiber content was selected because it was the optimized fiber percentage selected by previous work at NMSU (Weldon et al., 2012). To explore the effect of fibers, a 3.0% steel fiber content was chosen based on an UHPC overlay using a 3.25% volume of steel fibers recently placed on Mud Creek Bridge, Iowa, USA. The 2.0% steel fiber content was selected as a mid-point was between the other two values to explore trends in the behavior. Table 5.21 through Table 5.23 present the typical material proportions of the UHPC mixtures used in this research.

Table 5.21 Mixture Proportions of UHPC with 1.5% of Steel Fibers

Material	Unit	Amount/yd^3 (Amount /m^3)
Cement	lb (kg)	1,377 (625)
Silica Fume	lb (kg)	172 (78)
Fly ash	lb (kg)	172 (78)
Sand	lb (kg)	1,688 (765.7)
Steel fibers	lb (kg)	200 (90.7)
HRWRA	gal (L)	9 (34)
Water	lb (kg)	270 (122.5)

Table 5.22 Mixture Proportions of UHPC with 2.0% of Steel Fibers

Material	Unit	Amount/yd^3 (Amount /m^3)
Cement	lb (kg)	1,377 (625)
Silica Fume	lb (kg)	172 (78)
Fly ash	lb (kg)	172 (78)
Sand	lb (kg)	1,666 (755.7)
Steel fibers	lb (kg)	267 (121.1)
HRWRA	gal (L)	9 (34)
Water	lb (kg)	270 (122.5)

Table 5.23 Mixture Proportions of UHPC with 3.0% of Steel Fibers

Material	Unit	Amount/yd^3 (Amount /m^3)
Cement	lb (kg)	1,377 (625)
Silica Fume	lb (kg)	172 (78)
Fly ash	lb (kg)	172 (78)
Sand	lb (kg)	1,621 (735.3)
Steel fibers	lb (kg)	400 (181.44)
HRWRA	gal (L)	9 (34)
Water	lb (kg)	270 (122.5)

5.4.3 NSC

The substrate used for all the specimens was a NSC mixture provided by a local ready-mixture company. The mixture proportions included fine and coarse aggregates with a 1.0 in. (25.4 mm) aggregate top size, Type I/II cement, class F fly ash, and water. The mixture had a water-to-cementitious (w/cm) ratio of 0.39, a slump of approximately 4.0 in. (101.6 mm), a unit weight of 142.96 lb/ft^3 (2290 kg/m^3), and a design strength of 4500 psi (31 MPa). The mixture proportions for the NSC are provided in Table 5.24.

Table 5.24 Mixture Proportions of NSC

Material	Amount lb (kg)
Cement	508 (230.4)
Fly Ash	127 (57.6)
Fine Aggregate	1225 (555.7)
Coarse Aggregate	1750 (793.8)
Water	250 (113.4)
Total	3860 (1750.9)

5.4.4 Measured Material Properties

Material property tests were conducted to characterize the nonproprietary UHPC, the NSC, and the mild steel reinforcement. The properties measured include compressive strength, modulus of elasticity, and modulus of rupture for UHPC and NSC. Also, to understand the shrinkage behavior of the UHPC overlay, a long-term shrinkage test was performed on UHPC prisms. The mild steel reinforcement was tested to obtain the yield stress, ultimate stress, and the stress-strain behavior. The following sections describe the measured material properties as well as the test procedures used based on establish standards.

5.4.4.1 Compressive Strength

To verify the compressive strength of the concrete, tests were conducted on companion specimens of each mixture that was cast for the project. Table 5.25 presents the compressive strength results for the UHPC and NSC specimens tested. The NSC had an average compressive strength of 5.35 ksi (37.0 MPa) with a sample standard deviation of 0.07 ksi (0.35 MPa). The UHPC had an average compressive of 17.7 ksi (122 MPa) with a sample standard deviation of 1.03 ksi (7.06 MPa).

Table 5.25 Compressive Strengths of NSC and UHPC Specimens

		Compressive Strength (28 days)			
		(ksi)	(MPa)	(ksi)	(MPa)
NSC	Specimen 1	5.3	36.7	7.3	50.3
	Specimen 2	5.4	37.2	7.3	50.3
	Average	5.35	37.0	7.3	50.3
	Standard Deviation	0.07	0.35	0.0	0.0
UHPC	Slab 1	15.8	109	19.2	132
	Slab 3	17.9	123	18.8	130
	Slab 4	17.4	120	-	-
	Slab 5	18.4	127	19.3	133
	Slab 6	18.7	129	21.2	146
	Slab 7	16.8	116	19.0	131
	Slab 8	17.8	123	-	-
	Slab 9	18.9	130	19.5	134
	Average	17.7	122	19.5	134
	Standard Deviation	1.03	7.1	0.87	5.89

5.4.4.2 Modulus of Elasticity

The long-term modulus of elasticity was evaluated for this investigation using 6.0 in. x 12.0 in. (152 mm x 305 mm) cylinder specimens for NSC and UHPC at 28 days as outlined in Section i.iv. Due to small batching sizes, the large cylinder size, and the need for other types of test specimens, modulus of elasticity specimens were not produced for each batch of UHPC. However, because Slabs 1-5, 7, and 8 were produced using the same mixture proportions, it was assumed the concrete for those batches would exhibit similar behavior. Therefore, modulus of elasticity tests were performed for just three batches of UHPC and for the NSC mixture as shown in Table 5.26. The average modulus of elasticity of UHPC was 6,275 ksi (43,262 MPa) with a sample standard deviation of 111.6 ksi (769.8 MPa).

Table 5.26 Modulus of Elasticity for NSC and UHPC Specimens

		Modulus of Elasticity	
		(ksi)	(MPa)
NSC	Specimen 1	3,686	25,414
UHPC	Slab 1 (1.5% fibers)	-	-
	Slab 3 (1.5% fibers)	-	-
	Slab 4 (1.5% fibers)	-	-
	Slab 5 (1.5% fibers)	-	-
	Slab 6 (2.0% fibers)	6,354	43,809
	Slab 7 (1.5% fibers)	6,147	42,382
	Slab 8 (1.5% fibers)	-	-
	Slab 9 (3.0% fibers)	6,323	43,596
	Average	6,275	43,262
	Standard Deviation	111.6	769.8

5.4.4.3 Modulus of Rupture

Modulus of rupture strength, defined herein as the flexural stress corresponding to first cracking, was evaluated for this investigation using 16.0 x 3.0 x 4.0 in. (406 x 76 x 102 mm) beam specimens as outlined in Section i.iii. Specimens were tested at 28 days for the three different UHPC mixtures and for the NSC mixture. Results from the tests are shown in Table 5.27.

Table 5.27 Flexural performance and modulus of rupture for NSC and UHPC specimens

		Flexural Performance				Modulus of Rupture	
		Ultimate Load		First Peak Load			
		(lb)	(N)	(lb)	(N)	(psi)	(MPa)
NSC	Specimen 1	3,270	14,546	3,270	14,546	1090	7.52
	Specimen 2	2,970	13,211	2,970	13,211	990	6.83
	Average	3,120	13,879	3,120	13,879	1,040	7.17
	Standard Deviation	212	944	212	944	71	0.50
UHPC	Slab 1 (1.5% fibers)	8,990	39,990	7,636	33,967	2,545	17.55
	Slab 3 (1.5% fibers)	-	-	-	-	-	-
	Slab 4 (1.5% fibers)	-	-	-	-	-	-
	Slab 5 (1.5% fibers)	-	-	-	-	-	-
	Slab 6 (2.0% fibers)	10,570	47018	6,981	31,053	2,327	16.04
	Slab 7 (1.5% fibers)	-	-	-	-	-	-
	Slab 8 (1.5% fibers)	8,970	39,901	7,706	34,278	2,569	17.71
	Slab 9 (3.0% fibers)	9,760	43,415	6,960	30,960	2,320	16.00
	Average	9,573	42,581	7,321	32,565	2,440	16.83
	Standard Deviation	760	3,380	406	1,804	135	0.93

5.4.4.4 Longer-Term Shrinkage

The characterization of UHPC long term shrinkage was necessary due to contribution of shear stresses at the bond interface between the NSC substrate and the UHPC overlay. Therefore, a test was performed on 3 x 4 x 16 in. (76 x 102 x 406 mm) UHPC prisms with embedded gage studs at the center of transverse face at the end of the prisms according to the ASTM C157 (2017) standard. The length of the specimens were measured at different ages (1, 2, 3, 5, 7, 14, 28 days), with the first measurement taken at 24 hours after casting the specimens and the last at 28 days. After the first measurement was taken, the specimens were placed in a wet room for curing. After 7 days the specimens were cured in ambient conditions until the last measurement at the age of 28 days. To conduct the test a comparator and a reference bar were used to obtain the change in length of the specimens. The specimen was placed in the comparator to obtain the dial measurement as shown in Figure 5.175.

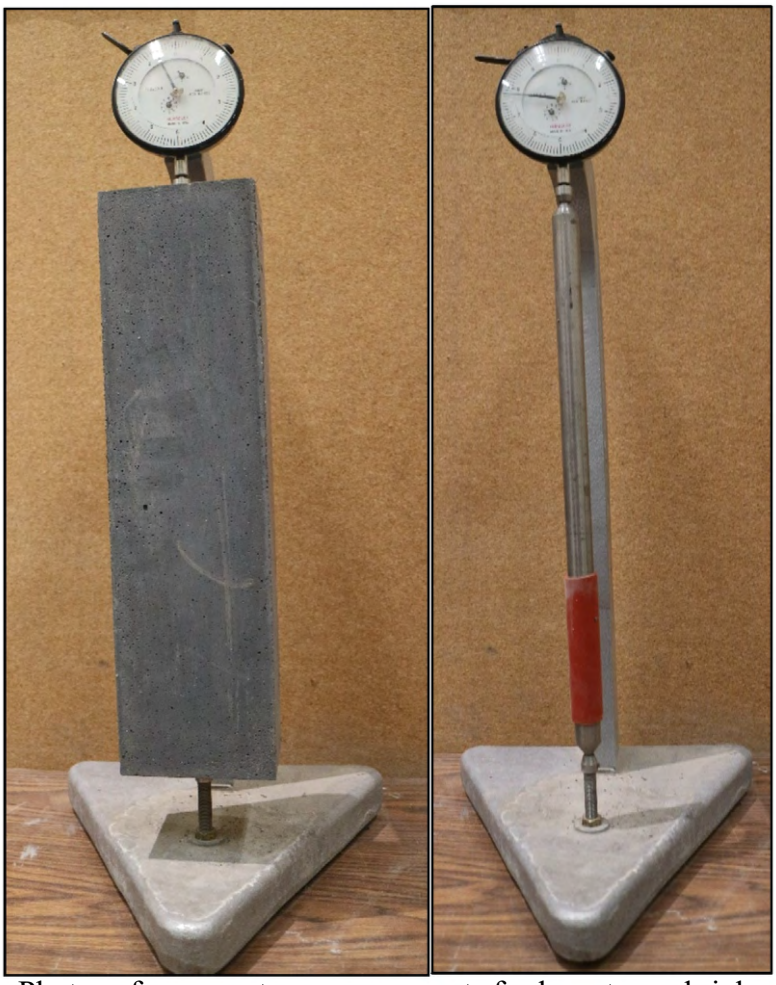


Figure 5.175: Photos of comparator measurements for long-term shrinkage procedure.

The measurements for each specimen were collected as well as the reading of the reference bar every day of the test ages. Once the measurements were collected, the change in length of the specimens was calculated using Equation 5.1 as follows:

$$\Delta L_x = \frac{\text{CRD} - \text{initial CRD}}{G} \text{ x } 100 \qquad 5.1$$

where:
ΔL_x = length change of specimen at any age (%)
CRD = difference between specimen and reference bar the comparator readings at any age
G = gage length [10 in. (250 mm)]

The results are shown in Figure 5.176 which include the values obtained at different ages of the specimens. As seen in the figure, shrinkage generally exhibited had less drastic changes after day 7 when the slabs were placed in ambient conditions. In the last measurement at the age of 28 μm and Slab 9 with 250 μm. Furthermore, the results shown that shrinkage is being reduced in UHPC mixtures with higher percentage of fibers as it was expected.

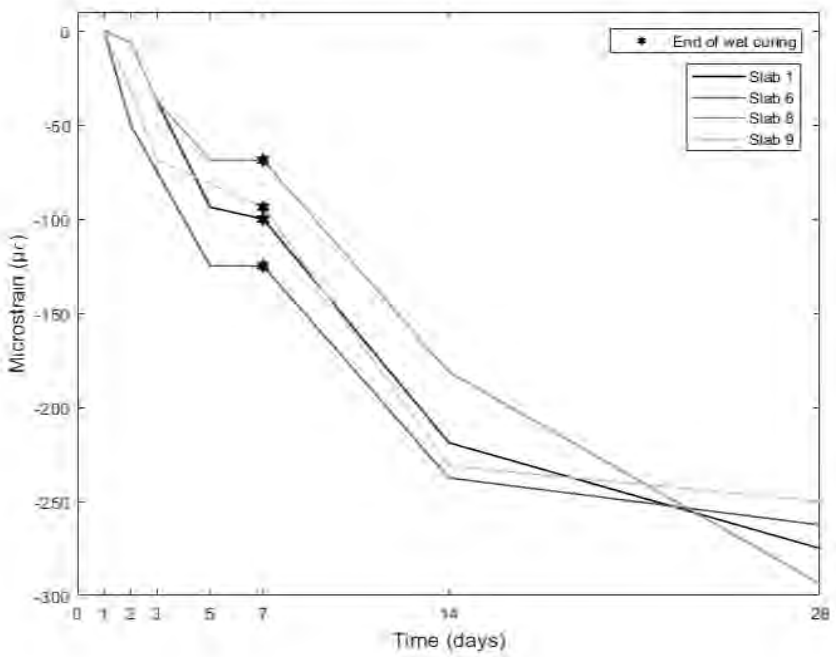


Figure 5.176: UHPC longer term shrinkage data.

5.4.4.5 Tensile Test of Mild Reinforcement

Tension tests of mild steel reinforcement provide information on the strain-stress behavior of the material. In this test, steel reinforcement was subjected to an axial tension force until failure is reached following ASTM A370 (2018). For this research, No. 3 (No. 10) Grade 40 and No. 4 (No. 13) Grade 60 steel reinforcing bars were used for the slab reinforcement. Based on the standard specifications three 8 in. (20.3 cm) long specimens of each size of steel reinforcement were tested in a tension testing machine having a 60,000 lb (267 kN) capacity with controlled deflection of 0.1 in./min (2.54 mm/min). An extensometer with a gauge length of 2.0 in. (50 mm) was attached to the reinforcement specimens to measure elongation and obtained the strain as shown in Figure 5.177.



Figure 5.177: Steel tension test on a No. 3 (No. 10) rebar.

The stress-strain behavior of both sizes of reinforcement are presented in Figure 5.178 and Figure 5.179in which yield point, ultimate stress and fracture are presented. Table 5.28 presents the characteristics of each specimen tested.

Table 5.28 Stress-strain behavior steel reinforcement

Size	Specimen	Yield		Ultimate		Rupture	
		Stress, ksi (MPa)	Strain, in./in. (mm/mm)	Stress, ksi (MPa)	Strain, in./in. (mm/mm)	Stress, ksi (MPa)	Strain, in./in. (mm/mm)
No. 3 (No. 10)	1	49.30 (340)	0.0015	71.06 (490)	0.2012	51.70 (357)	0.3709
	2	49.95 (344)	0.0019	70.86 (489)	0.1980	53.46 (369)	0.3423
	3	48.07 (331)	0.0017	70.91 (489)	0.0823	50.88 (351)	0.3034
	Average	49.10 (338)	0.0017	70.94 (489)	0.1605	52.01 (359)	0.3389
	Standard Deviation	0.96 (6.66)	0.0002	0.10 (0.58)	0.068	1.32 (9.17)	0.034
No. 4 (No. 13)	1	66.49 (458)	0.0022	100.26 (691)	0.1202	84.40 (582)	0.2040
	2	65.49 (458)	0.0023	101.17 (698)	0.1176	85.53 (590)	0.2310
	3	66.53 (459)	0.0023	100.37 (692)	0.1167	83.50 (576)	0.1880
	Average	66.2 (458)	0.0023	100.6 (694)	0.118	84.5 (583)	0.208
	Standard Deviation	0.59 (0.58)	0.000058	0.50 (3.79)	0.0018	1.02 (7.02)	0.0217

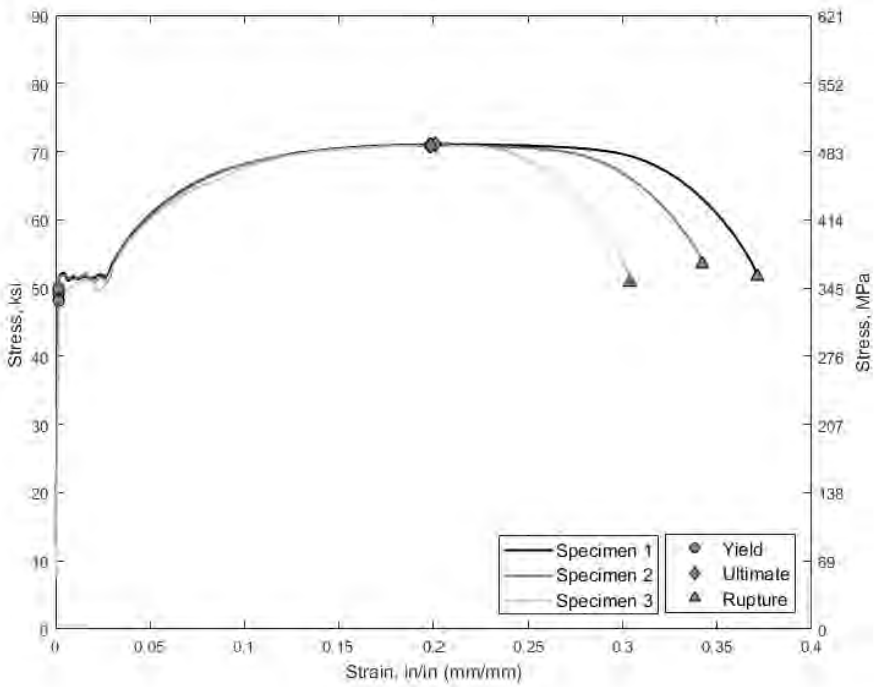


Figure 5.178: Stress-strain behavior No. 3 (No. 10) rebar.

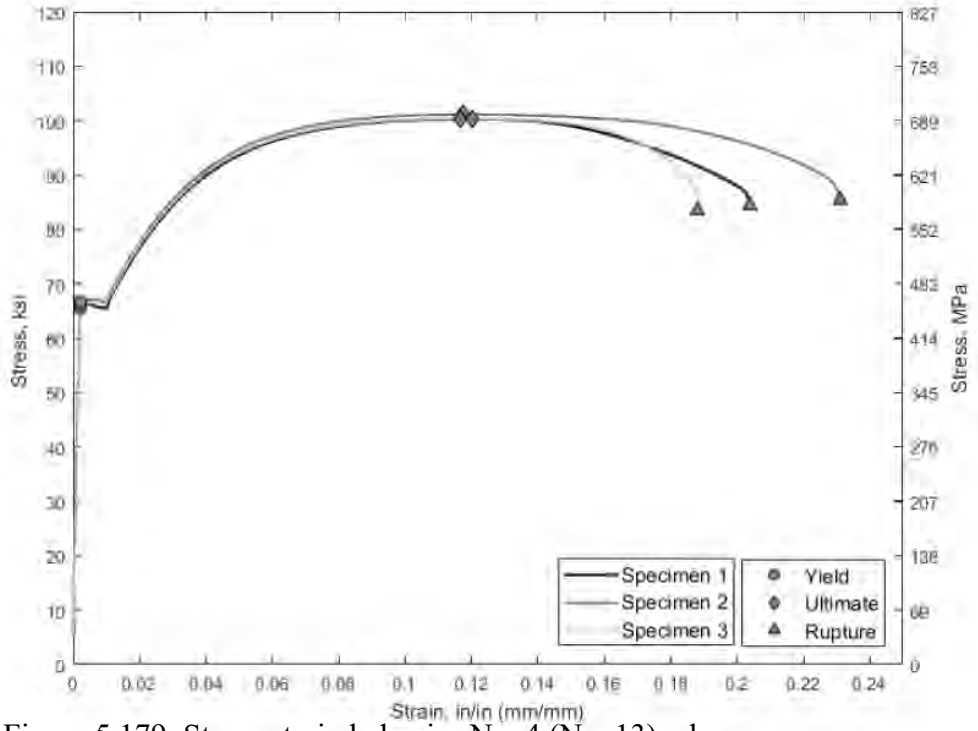


Figure 5.179: Stress-strain behavior No. 4 (No. 13) rebar.

5.4.5 Design Selection

The research investigated the behavior of UHPC overlays on NSC substrates; therefore, it was necessary to represent a typical bridge deck using small scale specimens to place the overlay. Thus, different parameters were analyzed to determine how they affect the ultimate moment capacity; as a result, the parameters that were expected to influence the behavior most were selected to investigate and included the thickness of NSC slab, reinforcement bar size, volume of fibers in the UHPC, and thickness of the overlay. Nine NSC reinforced slabs with dimensions of 3 x 3 ft (91.4 x 91.4 cm) with varied thickness were used for the substrate (i.e., bridge deck). Each slab had varied reinforcement sizes consisting of six bars, three in each direction with a cover of 2.0 in (51 mm) from bottom of the slab to the bottom layer of the steel reinforcement. Additionally, the specimens had varied parameters including exposure conditions, application of overlay, the slope of slab during application of the UHPC overlay, and composition of the UHPC overlay. The specific characteristics of each slab are shown in Table 5.29 and were selected in a way in which at least two slabs can be compared with a single parameter variation per pair of slabs.

Table 5.29 Characteristics of Specimens

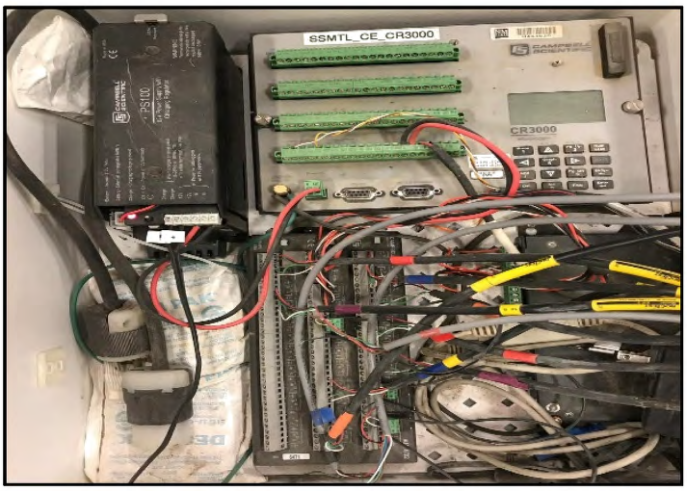
Slab No.	Exposure Condition	NSC Substrate thickness in. (cm) (cm)	Bar size	Overlay	Slope (%)	Type of UHPC (Fiber %)	UHPC Overlay thickness (in.)	(cm)
1	Controlled	4.0 (10.2)	No. 3 (No. 10)	Yes	0	1.5 %	1.0	2.54
2	Controlled	4.0 (10.2)	No. 3 (No. 10)	No	-	-	-	-
3	Environmental	4.0 (10.2)	No. 4 (No. 13)	Yes	0	1.5 %	1.0	2.54
4	Environmental	4.0 (10.2)	No. 3 (No. 10)	Yes	7	1.5 %	1.0	2.54
5	Environmental	4.5 (11.4)	No. 3 (No. 10)	Yes	0	1.5 %	2.0	5.08
6	Environmental	4.5 (11.4)	No. 3 (No. 10)	Yes	0	2.0 %	1.0	2.54
7	Environmental	6.0 (15.2) 15.2	No. 4 (No. 13)	Yes	0	1.5 %	1.0	2.54
8	Environmental	4.0 (10.2)	No. 3 (No. 10)	Yes	0	1.5 %	1.0	2.54
9	Environmental	4.5 (11.4)	No. 3 (No. 10)	Yes	0	3.0 %	1.0	2.54

5.4.6 Instrumentation for Data Acquisition

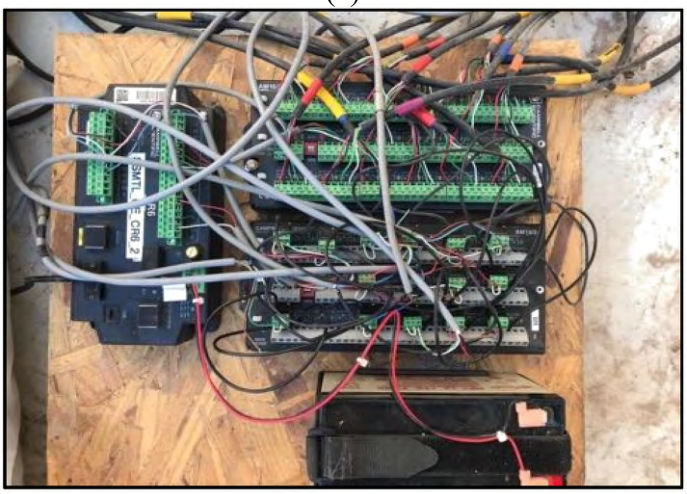
Instrumentation and a data acquisition system was necessary to understand the shrinkage behavior of the specimens. The strain experienced in the substrate was measured by itself and with UHPC overlay. To continuously measure the changes in the strain, each slab was had eight strain sensors placed in strategic locations. Two types of sensors were used, Strain Gauges (SG) attached to steel reinforcement, and Vibrating Wire Strain Gauges (VWSGs) embedded in the NSC substrate. To determine the changes in strain, VWSG and SG were connected to a datalogger that saved all sensor frequency measurements that were later used to determine the strain in the substrate. In the following sections the working mechanisms of the different instrumentation is described with more detail as well as the location of each sensor and the placing procedure.

5.4.6.1 Dataloggers

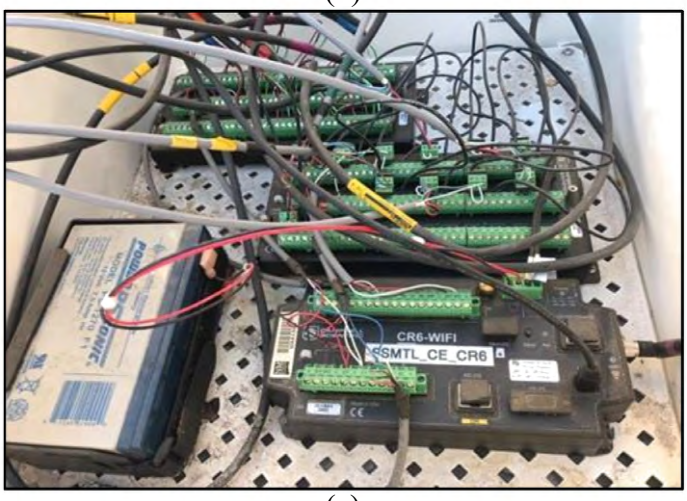
A datalogger is a device that can store data that is recorded by the sensors for a period of time. For this research three dataloggers from Campbell® Scientific, Inc., were used. The dataloggers used are a CR3000 Micrologger®, a CR6, and a CR6-WIFI, each of them was connected to two AM16/32B relay multiplexer to increase the number of terminals. Therefore, each datalogger had a capacity of connecting 32 sensors, being able to collect data for four slabs per datalogger. The acquisition system works with any sensor that has an electrical response; thus, the dataloggers were able to detect the differential voltage-based strain measurements of the SG and VWSG and store the data in the internal memory of the system. A software LoggerNet was used to connect the datalogger to a computer and extract all the stored data. The sensors connected to the dataloggers monitored the specimens 24 hours for about 13 months, starting the day of production until testing day. The change in voltage of these sensors was recorded at 10-minute intervals, which was the average of the change in voltage measured every two minutes within the 10-minute period. The average change in voltage was used to determine the strain in the substrate. Figure 5.180 shows the dataloggers that were used.



(a)



(b)



(c)

Figure 5.180: Dataloggers – (a) CR3000 Micrologger®, (b) CR6, and (c) CR6-WIFI.

5.4.6.2 Strain Gauges

There are different types of strain gauges, but the ones that were used in this research were electrical resistance strain gauges. These type of strain gauges are characterized by being a small rectangular strip of foil with maze-like wiring patterns on them which are connected to electrical cables. Electrical resistance strain gauges measure the changes in resistance when the wires are elongated or shortened due to change in strain. These sensors are attached to the material and are sensitive to small changes in strain, even those due to changes in temperature. A 120.4 Ω Strain Gauges (SG) with a length of 0.08 in. (2 mm) were attached to the outer steel reinforcement in longitudinal and transverse direction as shown in Figure 5.181. A total of four sensors were used in each slab with the purpose of measuring the strain the steel reinforcement experienced in both directions. The procedure followed to attach the strain gauges to the reinforcement was initiated with the preparation of a smooth plane surface in the middle of the reinforcement, then the sensors were adhered to the reinforcement with the use of glue and catalyst and finalized by securing the sensors with electric tape to prevent any damage. Once the sensors were attached to the reinforcement a final check before placing them in the reinforcement mesh was done to ensure that the resistance was between the limits of ±0.5 Ω.

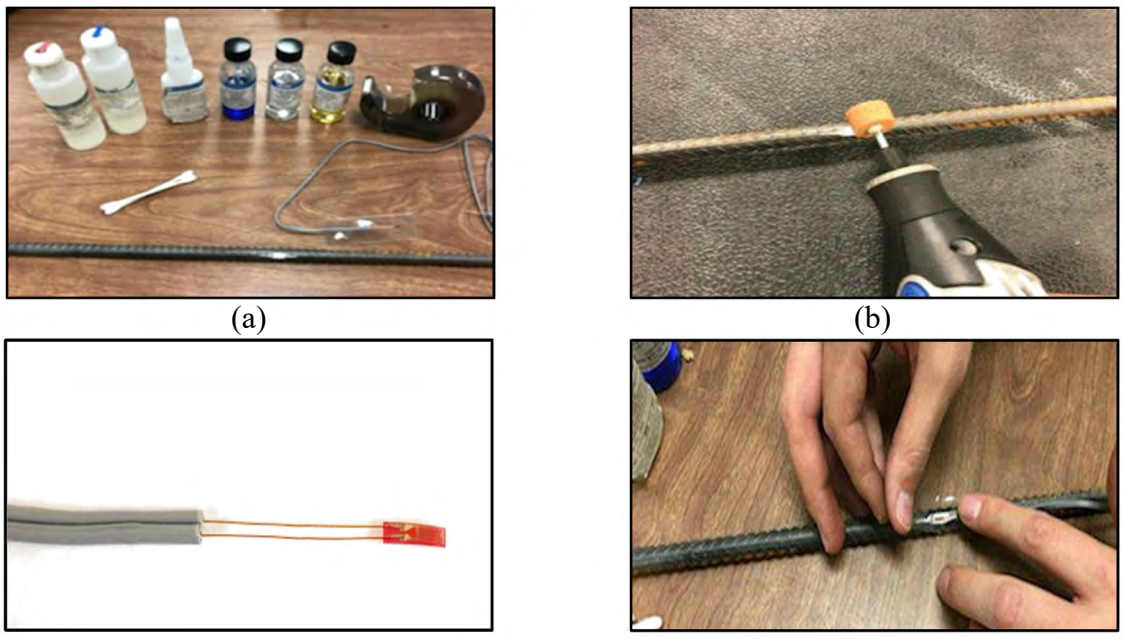


Figure 5.181: Types of sensors – (a) materials used to attached strain gauges; (b) surface preparation of rebar; (c) strain gauge; (d) placing of strain gauges on reinforcement.

5.4.6.3 Vibrating Wire Strain Gauges (VWSG)

Vibrating Wire Strain Gauges (VWSGs) were embedded in the concrete substrate to measure internal strains in the specimen. VWSGs consist of a sensor that has two flanges at each end of a stainless-steel tube in which a high-strength steel wire is inside the tube and fasten to the end of each flange. An electromagnet is located at the center of the tube coated in epoxy resin which vibrates and measure the vibration frequency of the wire; thus, when the VWSGs are connected to a datalogger these measurements are recorded. The EM-5 RocTest VWSGs with a length of 6.74 in. (171.4 mm) were placed on top and bottom of the reinforcement at the midspan of the slab as shown in Figure 5.182. The VWSGs were tied with steel wire from the middle of the sensors and then tied to the steel bar leaving a space of approximately 1.75 in. (44.45 mm) between the two gauges. This allows strain measurements at top and bottom of the slab (tension/compression zones).



(a) (b)

Figure 5.182: Vibrating Wire Strain Gauges – (a) VWSGs attached to the rebar before reinforcement mesh production: and (b) location of VWSGs at midspan of slab on top and bottom of the rebar.

5.4.7 Specimen Production

In the next sections, a detail description of the procedures followed to construct the nine slabs and overlays is presented. The production of the specimens took approximately one month from the installation of the sensors to the placement of the overlay. The production methods used in the laboratory were used to simulate the field work and to have similar results and behavior between small- and full-scale specimens.

5.4.7.1 NSC Slabs

The preparation of the slabs started with the placement of the sensors. The strain gauges were placed at the middle of the length of the steel bars located at the edges of the slabs, and the VWSG where place on top and bottom of the rebar as mentioned before. After the sensors were installed, the reinforcement mesh was constructed with six steel bars for each slab. The steel bars with both VWSGs and the SG were placed in the two parallel edges of the slabs and the two steel bars with just the SG were placed at the other two edges. The two steel bars without sensors were placed in the middle in each direction as shown in Figure 5.183. Once the reinforcement mesh was ready, the formwork was built. The formwork was organized in a way that nine slabs were cast at the same time and consisted of six plywood sheets of 4 by 8 ft (1.22 by 2.44 m), four C12X20.7 steel channels, and 2x8 lumber pieces. The plywood sheets were placed on top of concrete prisms; these prisms were positioned at all edges of each slab as well as in the middle of each slab to have more stability. These prisms were required to give an elevation to the slabs to have access to the sensors cords that needed to pass through the wood to be connected to the dataloggers. Then, the plywood sheets were tied together and were sealed with silicone. After the silicone dried, an aluminum foil tape was place on top of it to help preventing leakage of the concrete. After this, the steel channels were bolted together to form an outer box and the lumber pieces was used as dividers to build each individual slabs.

When the formwork was ready, holes in each corner of the slabs were drilled so the cords of the VWSGs could pass through the wood. After the formwork preparation was completed and the release agent that was applied to surface, 2.0 in. (50.8 mm) chairs were used to place the reinforcement mesh and prevent the contact of the steel bars with the release agent.

The final step was casting the NSC for the substrate. The nine slabs were cast at the same time with the same NSC batch. One slab was cast at a time, and a vibrator was used to ensure good consolidation. When the desired thickness was met, the surface of each slab was trowel finished. Once casting was complete, the slabs were cover with plastic. After 24 hours, the slabs were wet twice a day for three days to maintain the surface moisture. Six days after casting the formwork was removed. Some images of this process can be seen in Figure 5.184.

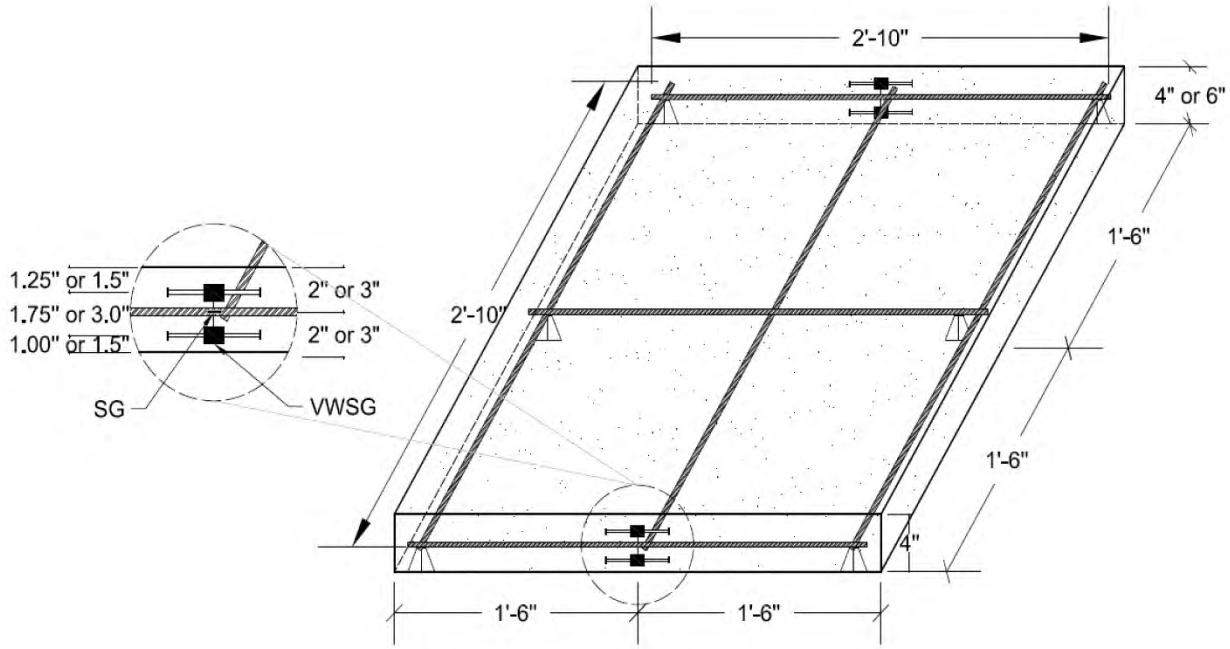
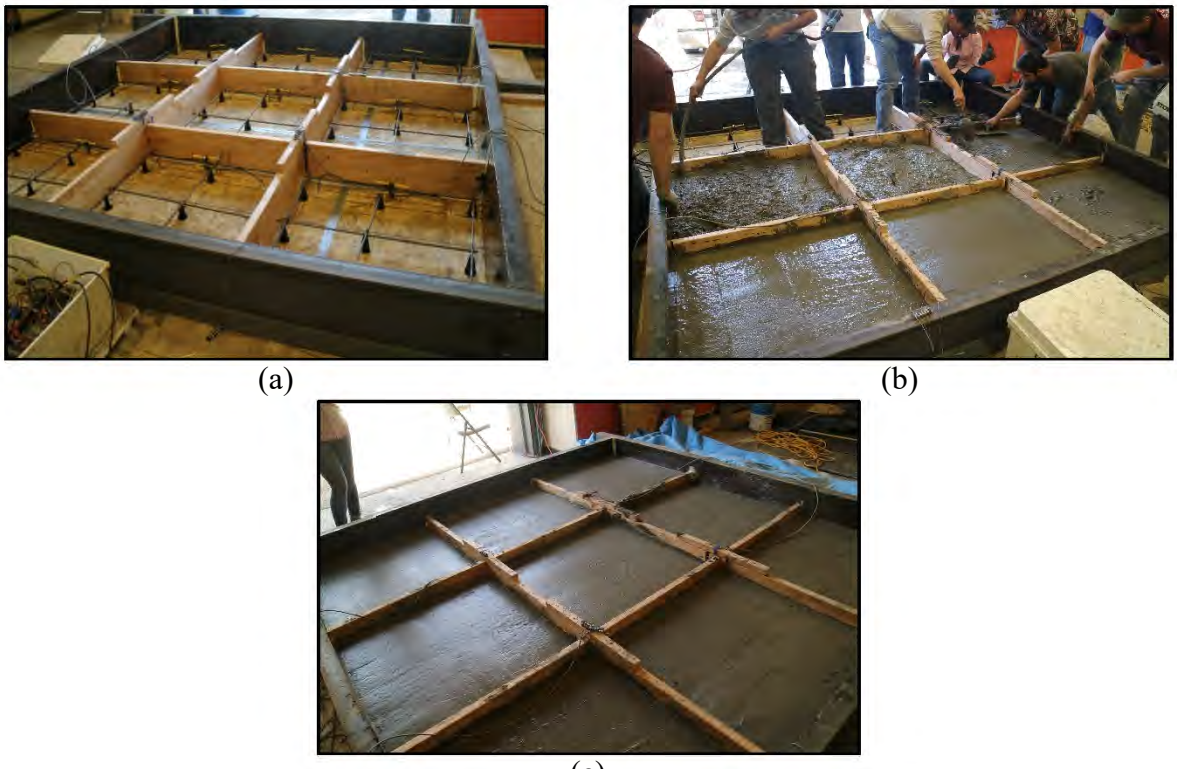


Figure 5.183: Slab design and location of sensors (VWSG and SG).



(a) (b)

(c)

Figure 5.184: Preparation of slabs – (a) formwork and sensors; (b) placement of NSC substrate; (c) final view of slabs after surface finished.

5.4.7.2 UHPC Overlays

At 30 days of age, the surface preparation of the NSC slabs was completed to ensure a good bond between the overlay and the substrate. The surface was prepared using air hammers to create a rough surface in the center of the slabs and hand grinding at the edges until the aggregates were exposed as shown in Figure 5.185.



(a) (b)

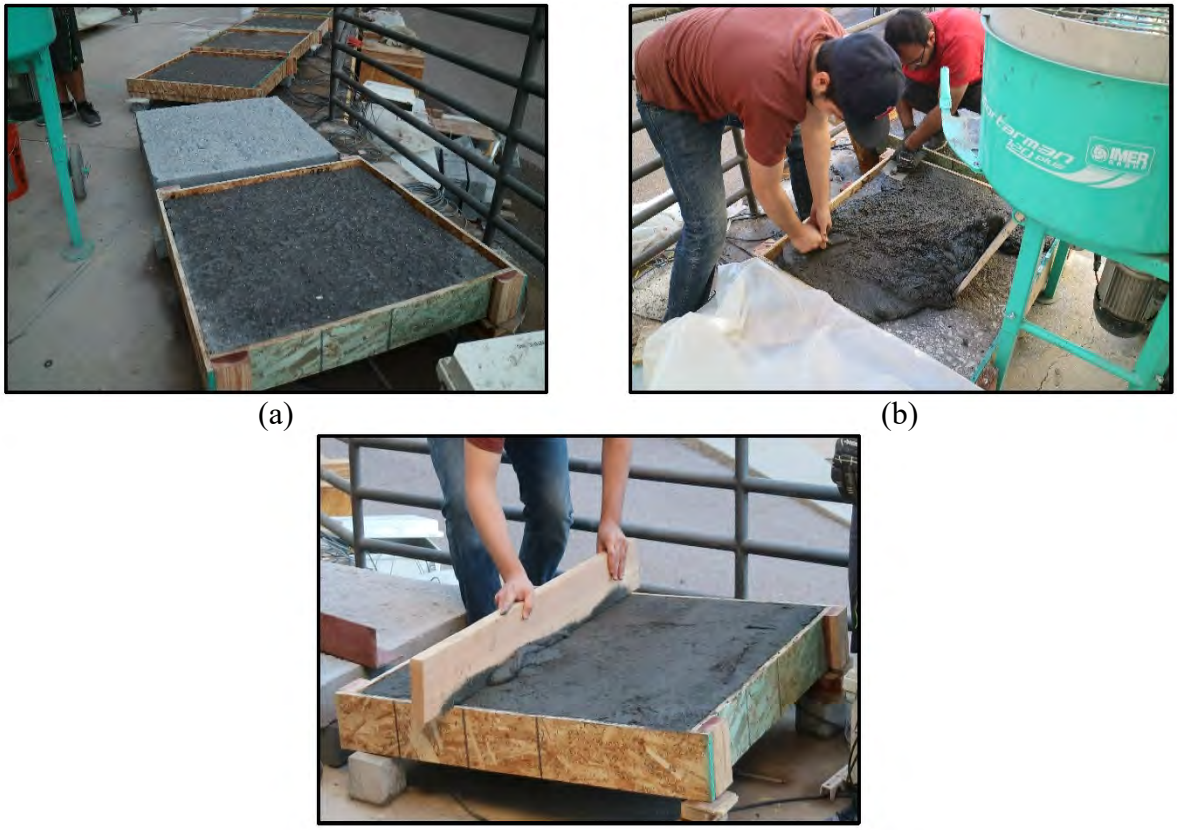
Figure 5.185: Texturizing slabs surface – (a) Procedure used with air hammers and (b) final texturized surface.

Following surface roughening, the surfaces were cleaned with pressurized air to eliminate all dust and remaining particles. Then the ASTM E965 (2015) procedure was followed to measure the texture depth of each slab. The procedure consisted of spreading 0.85 oz (25 ml) of glass spheres on the clean surface using a flat hard square plate in a circular patch. The spheres covered the voids of the texturized surface and the diameter of the circular area covered by the spheres was measured in four equally spaced locations of the circumference and the average diameter was used to calculate the texture depth. This test was executed in each quadrant of the slabs and the texture depth obtained for each slab is provided in Table 5.30. The average texture depth was 0.084 in. (2.143 mm) which is greater than the minimum texture depth of 0.08 in. (2 mm) that is adequate to create bond strength between UHPC and NSC based on Newtson et al. (2018).

Table 5.30 Results of Macrotexture Depth Using Volumetric Technique

Specimen	Depth I		Depth II		Depth III		Depth IV	
	(in.)	(mm)	(in.)	(mm)	(in.)	(mm)	(in.)	(mm)
Slab 1	0.089	2.28	0.064	1.63	0.096	2.44	0.107	2.73
Slab 2	0.086	2.19	0.069	1.75	0.086	2.19	0.086	2.19
Slab 3	0.072	1.83	0.054	1.37	0.060	1.53	0.061	1.56
Slab 4	0.074	1.88	0.106	2.58	0.077	1.95	0.046	1.17
Slab 5	0.076	1.93	0.089	2.25	0.096	2.43	0.084	2.13
Slab 7	0.117	2.99	0.153	3.89	0.125	3.18	0.102	2.58
Slab 8	0.111	2.81	0.089	2.25	0.072	1.83	0.080	2.02
Slab 9	0.082	2.08	0.093	2.37	0..070	1.79	0.067	1.71
Avg.	0.088	2.25	0.090	2.26	0.087	2.17	0.079	2.011
Std. Dev.	0.017	0.43	0.031	0.78	0.021	0.52	0.021	0.519

After the substrate was textured, plywood formwork was built around each slab for the application of the UHPC deck overlay. Then, the surface was saturated for 24 hours prior the placement of UHPC. Once the surface and the formwork were ready, a 4.25 ft^3 (0.120 m^3) portable mixer was used to prepare the UHPC. Due to limitations in the volume capacity of the mixer, the UHPC for the overlay was mixed one batch per slab providing 9 ft^2 (0.84 m^2) of area. This mixing procedure was executed next to each slab to facilitate the application. Once the UHPC mixture was ready and workable, the mixture was placed on the NSC slabs. The surface was then trowel finished using the same procedure as the one used for the substrate slabs. The only variation was that the wood and the trowels used for this procedure were saturated continuously due to the high speed in which the UHPC dries. As a result, a smooth UHPC surface was acquired, and then the overlays were covered with plastic to reduce moisture loss and prevent cracking. Figure 5.186 shows some of the steps during the placement of the overlay. After 12 hours of casting the overlays, wet burlap was placed on top of the UHPC, and it was re-wet every 12 hours for seven days.



(a) (b)

(c)

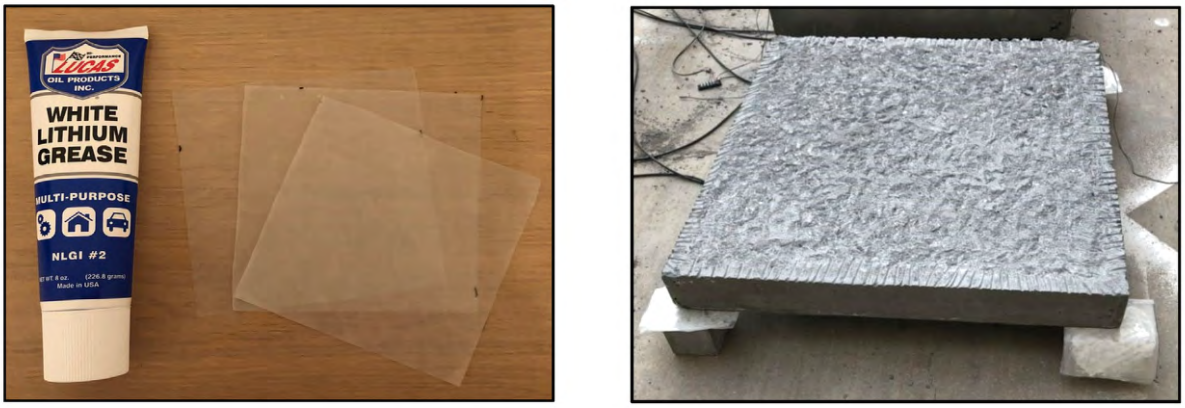
Figure 5.186: Construction of UHPC overlay – (a) saturated surface with exposed aggregates before UHPC application; (b) application of UHPC with workable consistency; (c) surface finished for UHPC deck overlay.

5.4.8 Tests Setup and Instrumentation

There were two different tests that were conducted on the specimens. The first was the measurement of the shrinkage in slabs following casting until the second test was conducted. The second test was a cyclic flexural test. The following subsections present the test setups, procedures followed, and the materials used for the tests.

5.4.8.1 Strain Measurement

The strain measurement test in the slabs started at the time of the casting of the NCS slabs. After the substrate specimens were taken out of their form works, the specimens were paced over four, 4.0 in. (102 mm) cube supports, one at each corner. To minimize friction between the supports and the slabs, three square layers of plastic, approximately 6 in. (152 mm) long, with grease between each layer were used. The greased plastic at the supports allowed the slabs to be able to shrink or expand freely and minimize lateral support restraint. Figure 5.187 shows the materials and setup of the test for every specimen.



(a) (b)

Figure 5.187: Strain setup test – (a) materials that were used for the test setup (b) colocation of plastic with grease between the slab and the cubes.

5.4.8.2 Flexural Test

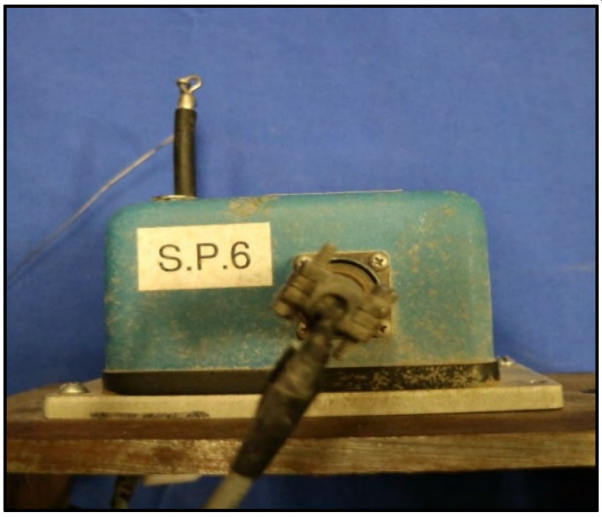
The slabs were subjected to a flexural test in which two different types of loading were used, cyclic and ultimate loading. The test setup and the instrumentation that was used for these tests as well as the description of each type of loadings will be presented in this section. All slabs were subjected to the cyclic loading; however, only select specimens were tested to ultimate failure.

Each slab was placed on top of six 1 x 1.75 x 2 ft (30.5 x 53.3 x 61 cm) reinforced concrete supports, three supports on each side of the slab. The three supports continuous had a length long enough so the whole length of the slab had complete contact with the supports on each side. Between the supports and the slab, neoprene bearing pad of 2.0 x 10 x 20 in. (5.1 x 25.4 x 50.8 cm) dimensions were used to have a low-friction sliding surface during flexural test. The span length of the slabs between supports was 2.5 ft (76.2 cm), having 3 in. (7.62 cm) on each side contact with the supports. The 4 ft (122 cm) long steel spreader beam was placed at midspan of the slab perpendicular to the frame, and the actuator, with a capacity of 110 kip (490 kN), was positioned in the middle of the spreader beam. The actuator was attached to the steel frame and to a computer to control the load that is applied to the specimen.

The instrumentation that was used in the test included LVDTs, string potentiometer, tiltmeters, and strain gauges (Figure 5.188). These were positioned in strategic places to understand the behavior of the slabs under cyclic and ultimate loading. A total of nine LVDTs were used in the slabs with overlays and seven LVDTs in the slab without an overlay, these were used to record the deformation of the specimen at midspan on two faces. Three LVDTs were used on the bottom face of the slab at midspan and at 4 in. (10.16 cm) from the edge of the slab in the longitudinal direction and two more were placed in the top face of the overlay at 8 in. (20.32 cm) from each edge. Two LVDTs were placed on each vertical transverse face of the slab (North and South faces) at mid-height of the NSC substrate, and at mid-height of the UHPC overlay. Five string potentiometers in the longitudinal and transverse direction were used to collect the deflections of the specimen as the load was applied. Four of them were placed at 4 in. (10.16 cm) from the edge at midspan of the four sides of the slab and one more at the center of the slab. The tiltmeters were used to record the inclination that the specimen experienced and were positioned at each corner of the slab on the North and South faces. Figure 5.189 shows the test setup and Figure 5.190 the location of each of the sensors.



(a)



(b)



(c)

Figure 5.188: Construction of UHPC overlay – (a) saturated surface with exposed aggregates before UHPC application; (b) application of UHPC with workable consistency; (c) surface finished for UHPC deck overlay.



Figure 5.189: Flexural test setup.

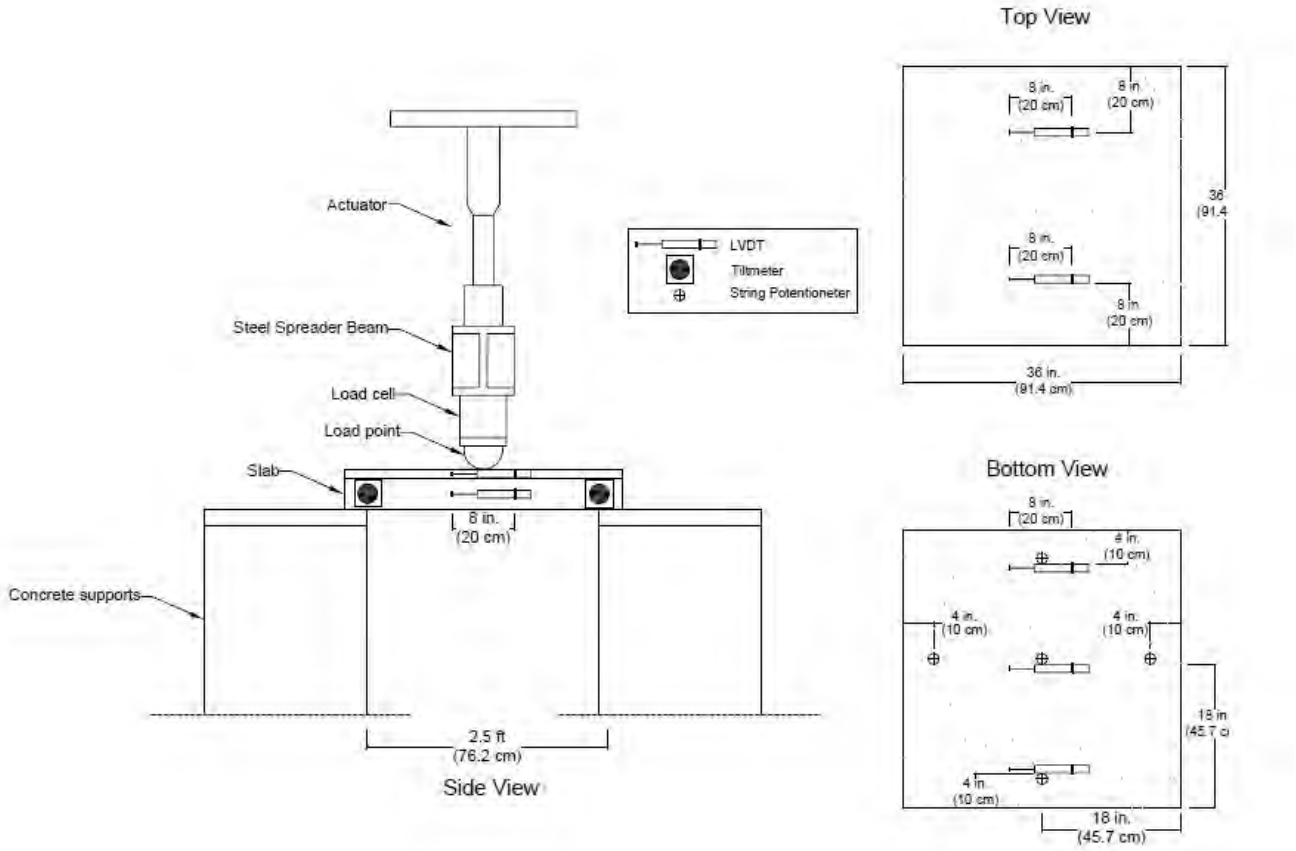


Figure 5.190: Flexural test instrumentation plan.

All sensors were connected to a data acquisition system, and real time monitoring was performed using the LabView software. The sensors communicated with the software that was programmed to output the load deflection curves to monitor the behavior of the slab and know when the slabs passed through the different phases such as linear elastic, yield, strain hardening, ultimate load, necking and failure.

The cyclic load applied to the slabs started from zero to half of their nominal capacity completing four cycles per minute. This load was calculated for each slab using equilibrium. The components considered for equilibrium were the compression force of UHPC and NSC, and the tension force of the reinforced steel. Once the nominal moment was known the nominal load was calculated.

Some slabs were loaded to failure to learn more about the behavior of the UHPC overlay. For Slab 1, the procedure consisted in loading until half of its capacity and then a cycle loading was performed by loading and unloading. The slab was cycled three times from zero to half of its capacity. Then three more cycles were performed by from zero to calculated maximum capacity. After these cycles, the slab was loaded at a rate of 0.05 in/min (1.27 mm/min) with a controlled deflection of 0.05 in (1.27 mm) until failure was shown in the load-deflection curve presented in

the LabView software. This curve was plotted using the deflection measurements recorded by the string potentiometers and the load recorded by the load cells. For Slab 2 to Slab 9 a similar procedure was followed in which the slabs were subjected to five cycles reaching their half capacity. Then after those cycles were performed, the slabs were tested to failure by applying the same loading parameters as Slab 1 which were a loading rate of 0.05 in/min (1.27 mm/min) with a controlled deflection of 0.05 in (1.27 mm).

5.4.8.3 Digital Image Correlation

Digital Image Correlation (DIC) was used to monitor the behavior of Slab 1 during flexural testing. This technique was able to measure displacement, strains, deflections, and crack propagation developed during the test. The method was applied in two locations of the slab: location 1 was the right vertical face of the slab, and location 2 was half of the top west surface of the overlay as shown in Figure 5.191 and Figure 5.192, respectively. For location 1 the cameras were placed approximately 7 ft (2.1 m) apart from the analyzed surface, and for location 2 the cameras were placed on top of the slab at approximately 7ft (2.1 m) height looking down. To capture the deformation during the test two cameras for each location monitored were used. The two cameras were used to take images of the slab at different stages (i.e., loads) during loading, and with the use of an advanced software the surface movement of the slab was tracked. To prepare the surface of the slab, the areas were first painted white, then small drops of black paint were sprayed on the surface to create a stochastic pattern, which is necessary to have thousands of points that can be correlated and be easily identified in the image to track deformations. This movement is measured by tracking pixels or facets within the pattern painted on the specimen.



Figure 5.191: Location 1 of application of DIC (right side of the slab).


Figure 5.192: Location 2 of application of DIC (top face west side).

5.4.9 RESULTS

This chapter presents the results obtained during the different tests conducted in this research. Results include measurements from sensors embedded in the slabs during the thirteen-month period to investigate the interaction of the overlay and substrate. The analysis of the data acquired by VGSGs includes the comparison of temperature recorded by the sensors with the temperature recorded by the National Weather Service, and the strain and shrinkage behavior of the slabs before and after the application of the UHPC overlay. The measured data was also used to analyze the behavior of the shear interface between the UHPC overlay and the NSC substrate. Additionally, the measured results the flexural test performed on each specimen are provided. These results include load-deflection and moment-curvature behaviors of each of the nine specimens.

5.4.9.1 Vibrating Wire Strain Gauges

The internal temperature experienced by the slabs was measured by the VWSGs and compared with the temperature recorded by the National Weather Service in Las Cruces, New Mexico. The temperature measured from both sources was similar, with slightly higher temperatures measured in the slabs during summer season approximately from day 50 until day 200. This difference can be attributed to the slabs being placed in a location with minimal shade throughout the day. Therefore, the slabs had complete exposure to sunlight during peak temperature periods. Figure 5.193 shows the changes in temperature of Las Cruces, New Mexico and Figure 5.194 through Figure 5.202 show the temperatures measured in Slabs 1-9, respectively. Each slab had four embedded VWSGs. The naming convention used is: VSTS - Vibrating Wire Strain Gauge in the Top South, VSBS - Bottom South, VSTN - Top North and VSBN - Bottom North. It is noted that north and south was defined at the time of casting. Figure 5.194, Figure 5.195, and Figure 5.197 (Slab 1, 2 and 4) have a gap in data due to a loss of power to the datalogger. The temperature measured by Slab 1 and 2 (Figure 5.194 and Figure 5.195) show less fluctuation in temperature after day 52 when the slabs were moved inside the laboratory with controlled conditions where the temperature stayed in a range between 60 to 75 °F (16 to 24°F). Figure 5.196 to Figure 5.202 (Slabs 3-9) show similarities in temperature measurements, as expected with only slight variations due to differences in thicknesses of the slabs. The thinner slabs experienced higher temperatures.

The temperatures in Las Cruces, New Mexico during the period of time from March 2018 to March 2019 had average temperatures varying from 30 to 90 °F (-1 °C to 32 °C), with a maximum temperature of approximately 105 °F (41°C) and a minimum temperature of 18 °F (-8 °C). These temperatures are similar to the internal measurements from the VWSGs in the slabs, having average temperatures ranging from 24 to 142 °F (-4 to 61 °C). The maximum internal measured temperature was 146 °F (63 °C) and a minimum temperature of approximately 24 °F (-4 °C) in the slabs exposed to environmental conditions.

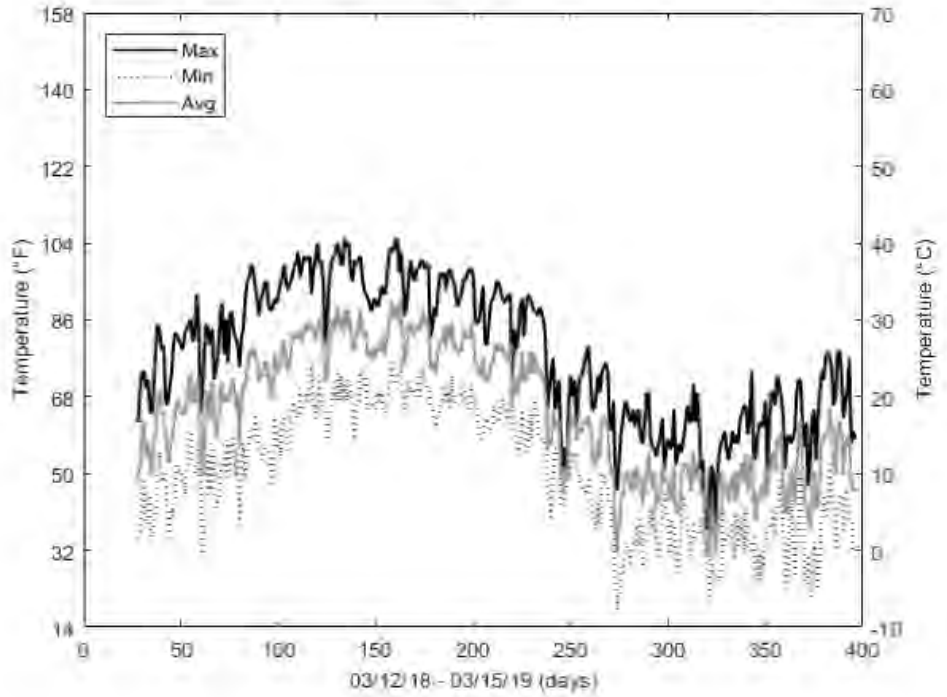


Figure 5.193: Temperature in Las Cruces, NM.

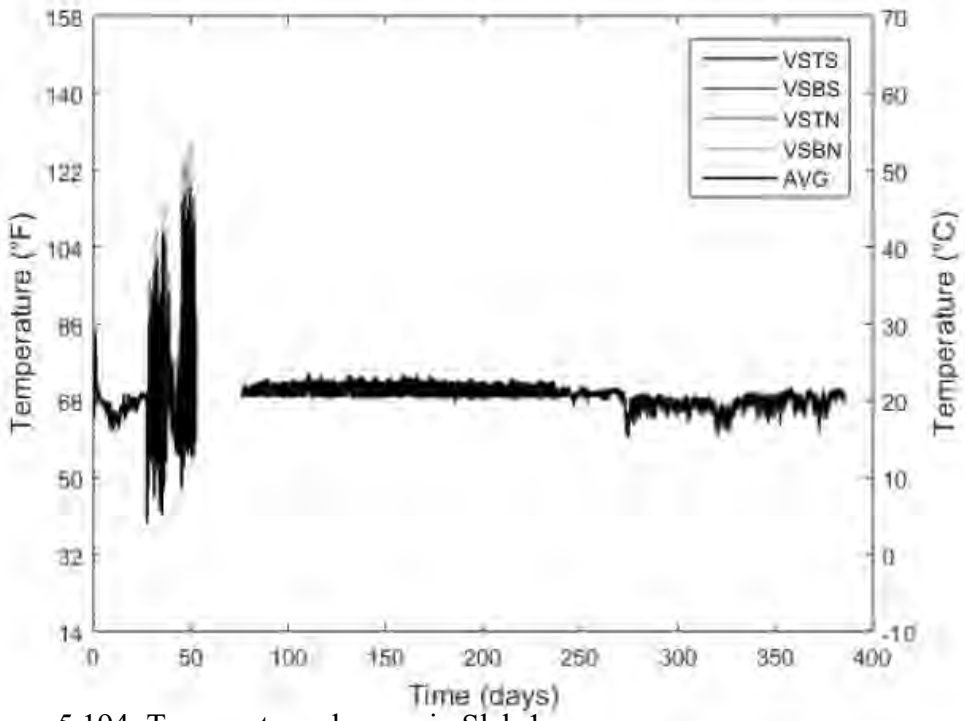


Figure 5.194: Temperature changes in Slab 1.

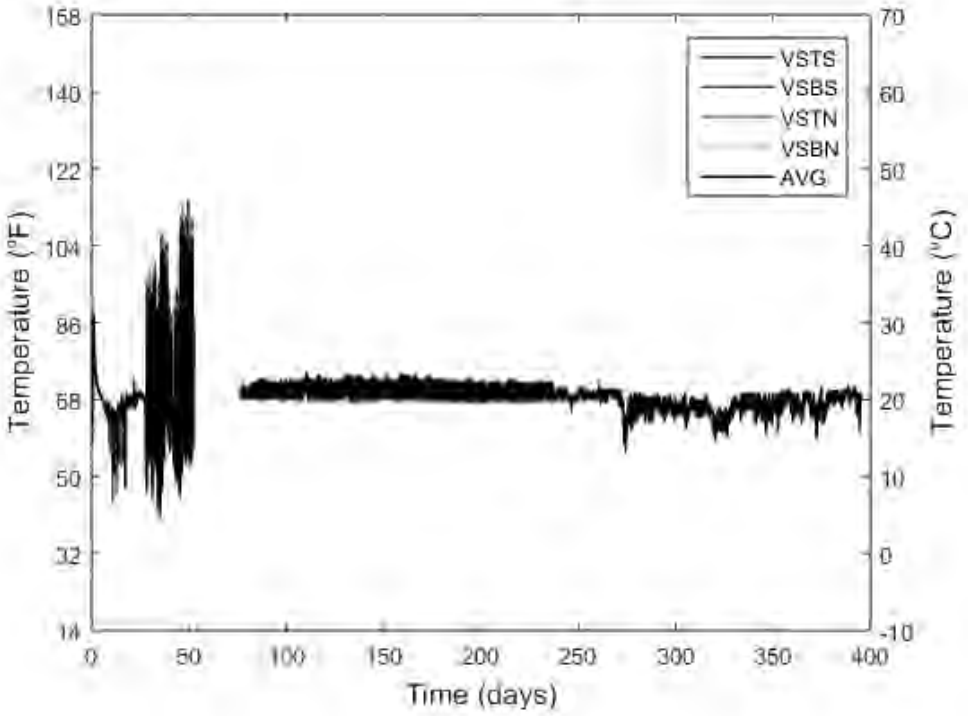


Figure 5.195: Temperature changes in Slab 2.

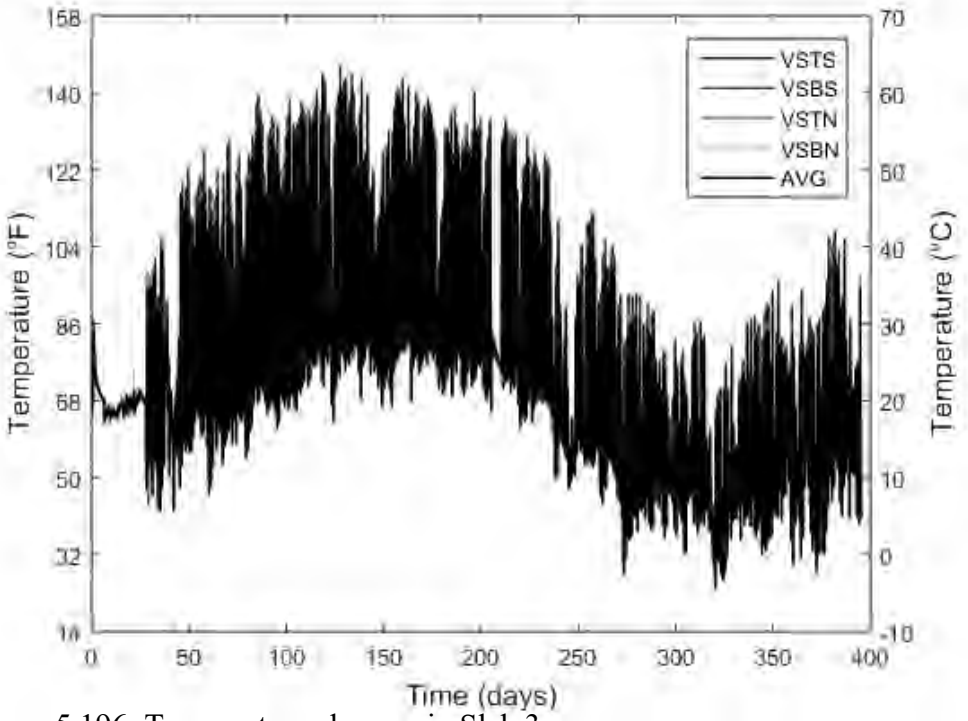


Figure 5.196: Temperature changes in Slab 3.

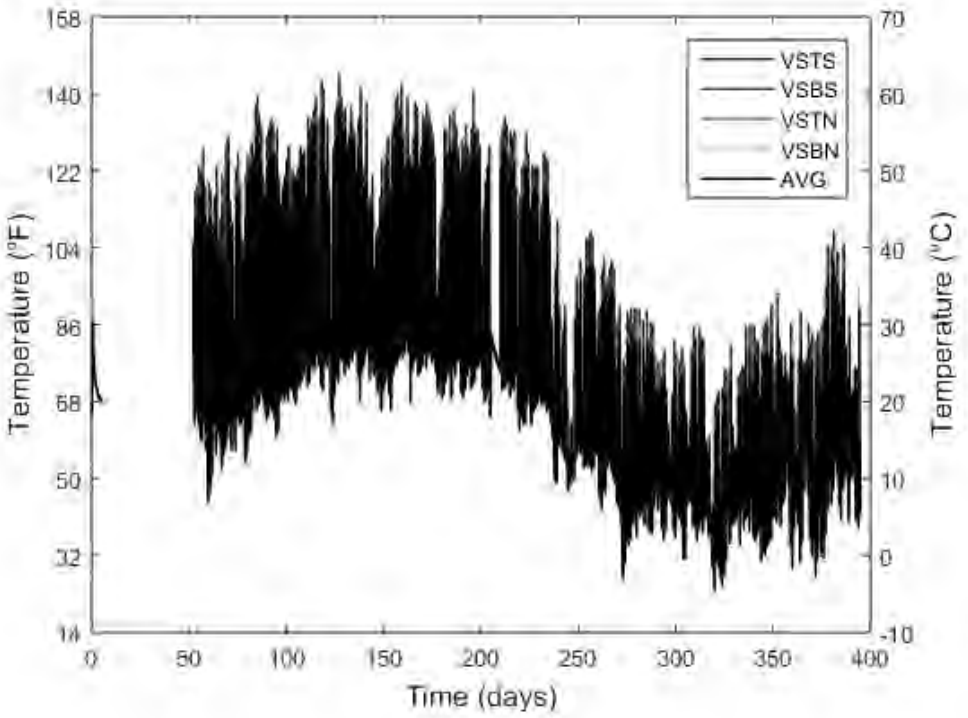


Figure 5.197: Temperature changes in Slab 4.

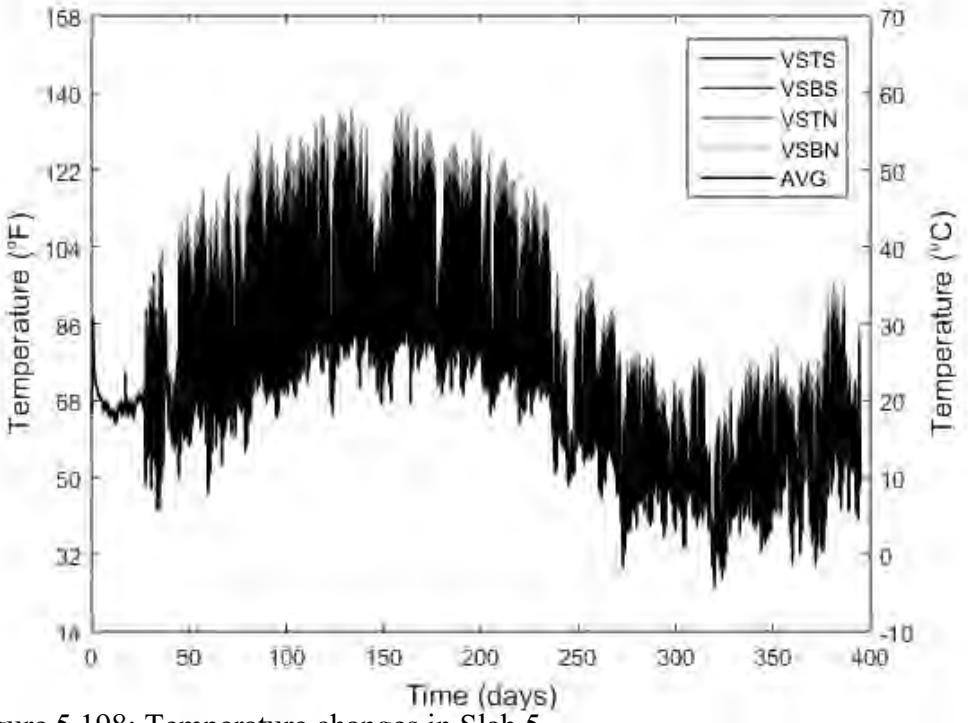


Figure 5.198: Temperature changes in Slab 5.

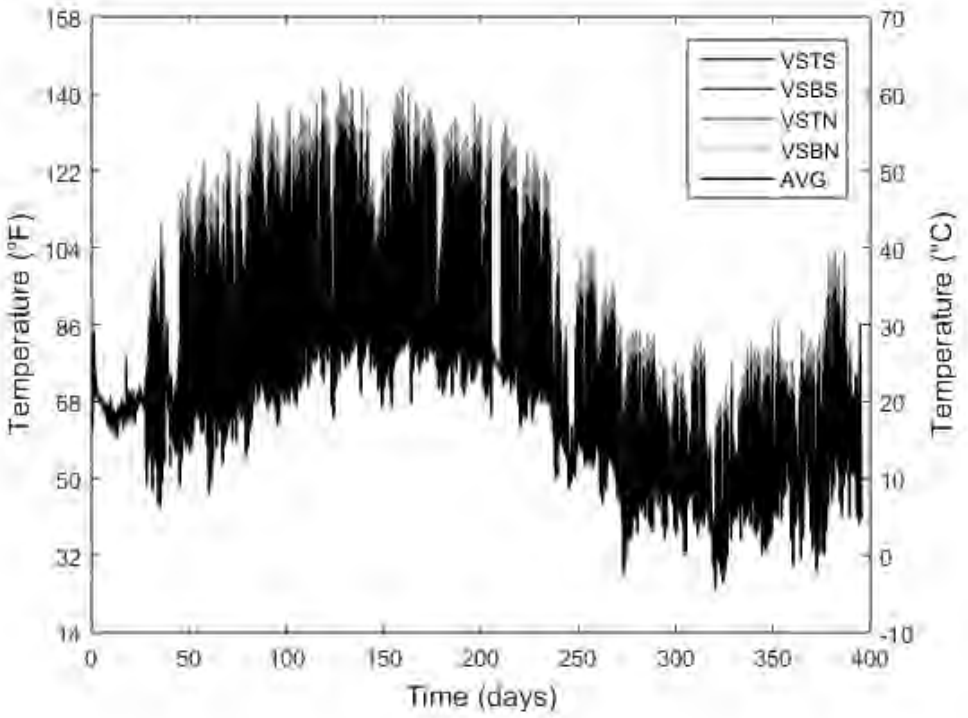


Figure 5.199: Temperature changes in Slab 6.

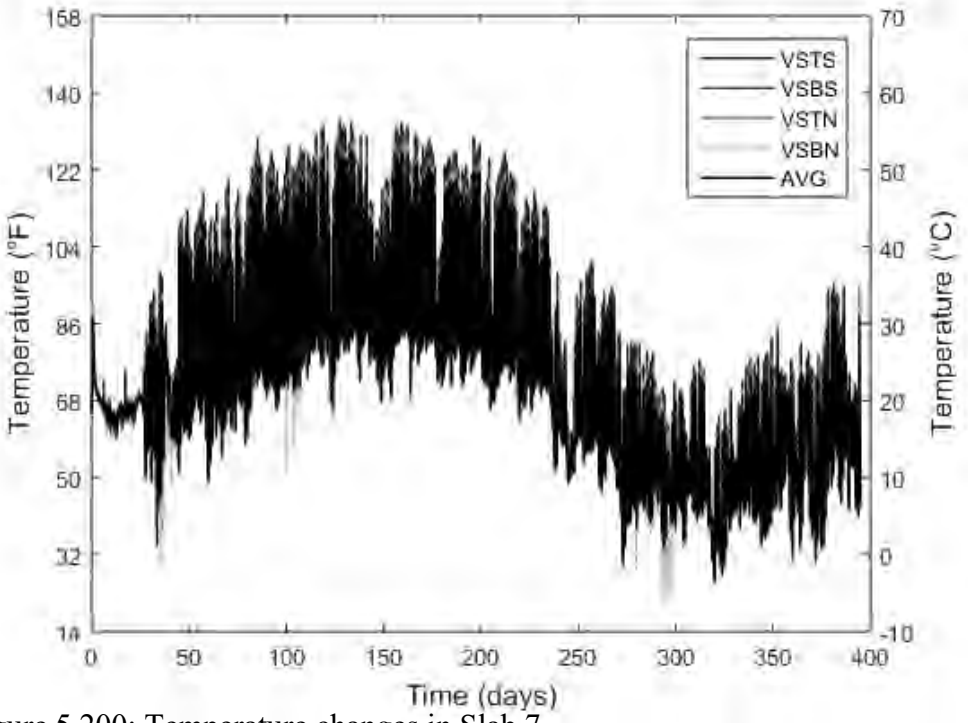


Figure 5.200: Temperature changes in Slab 7

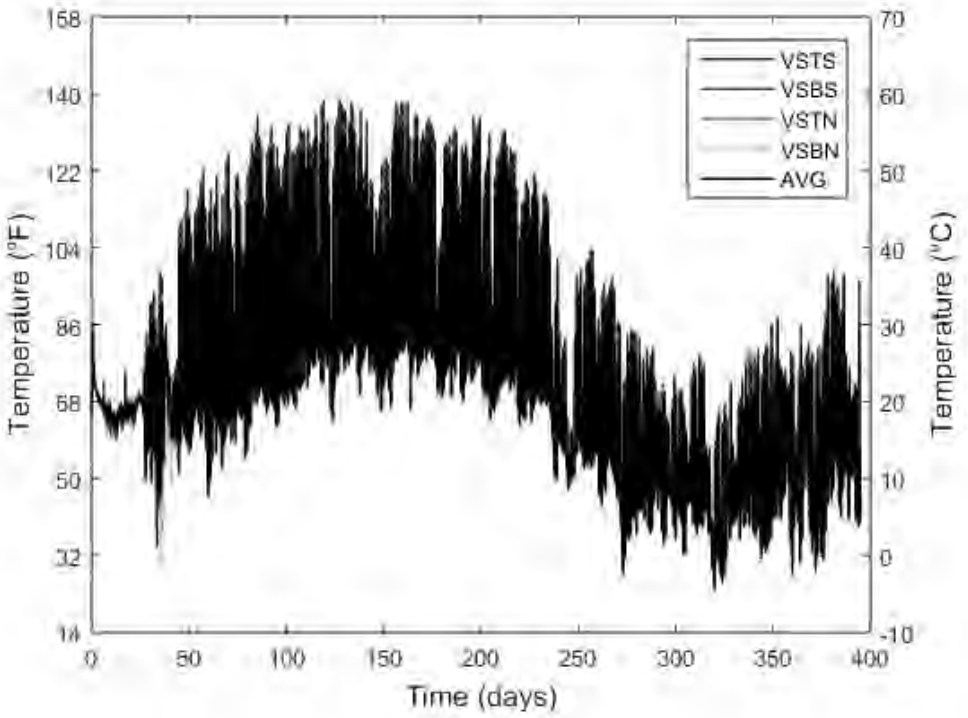


Figure 5.201: Temperature changes in Slab 8

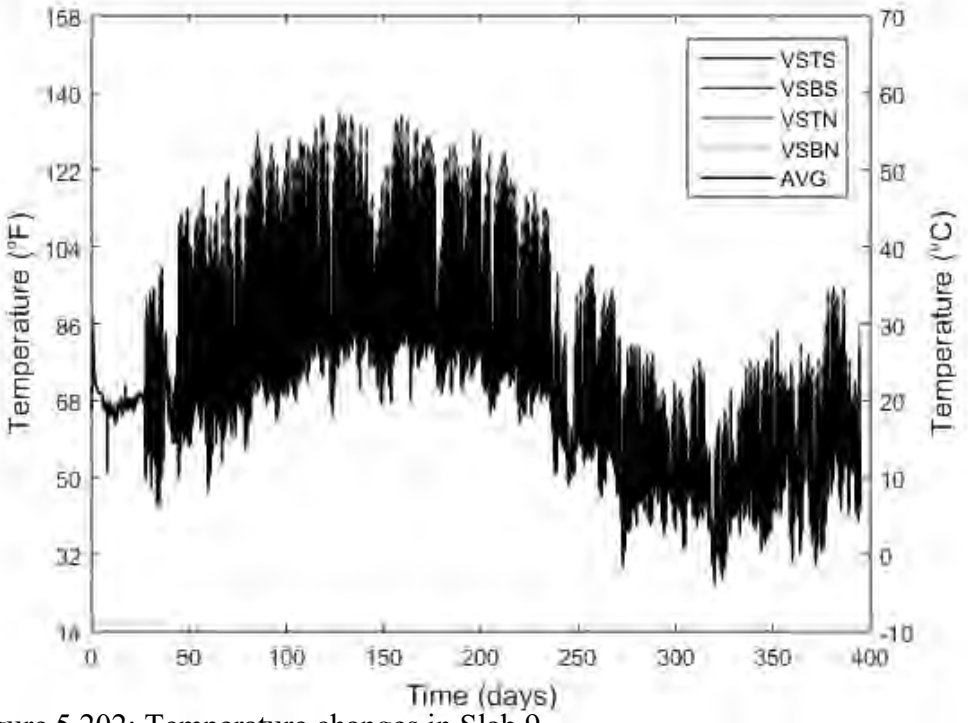


Figure 5.202: Temperature changes in Slab 9

Figure 5.203 through Figure 5.211 show the strain versus time plots for Slab 1-9, respectively. Annotations of the principal events that the slabs experienced from casting day until the last day of recorded data are noted on the figures. A jump in strain at day seven was caused when the formwork was removed. At day 27 the slabs were exposed to environmental conditions (moved from inside the laboratory to outside) for placement of the overlay, and the strain started to have larger fluctuation due to larger changes in temperature. At day 37 when the overlay was placed, the sensors near the top of the slabs started having smaller strain values around -200 με, and the sensors at the bottom had larger values around -350 με. This behavior was due to wetting the top surface in preparation for placement of the overlay. The top sensors had less strain due to the proximity to the wet surface which induced expansion of the material. The bottom sensors were influenced less by the moisture, thus had larger strains. The last event that Slabs 1 and 2 were subjected to, was the controlled exposure (these slabs were moved back into the laboratory at day 52) once the overlay was placed. Due to the controlled temperature in the laboratory, the fluctuation in the strains in these specimens was less.

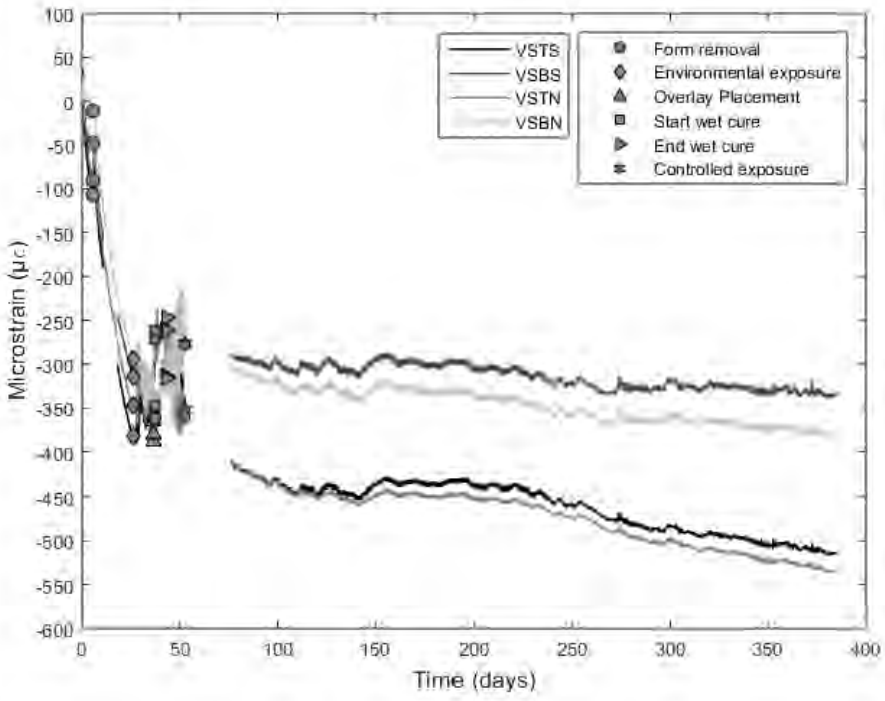


Figure 5.203: Strain versus time in Slab 1.

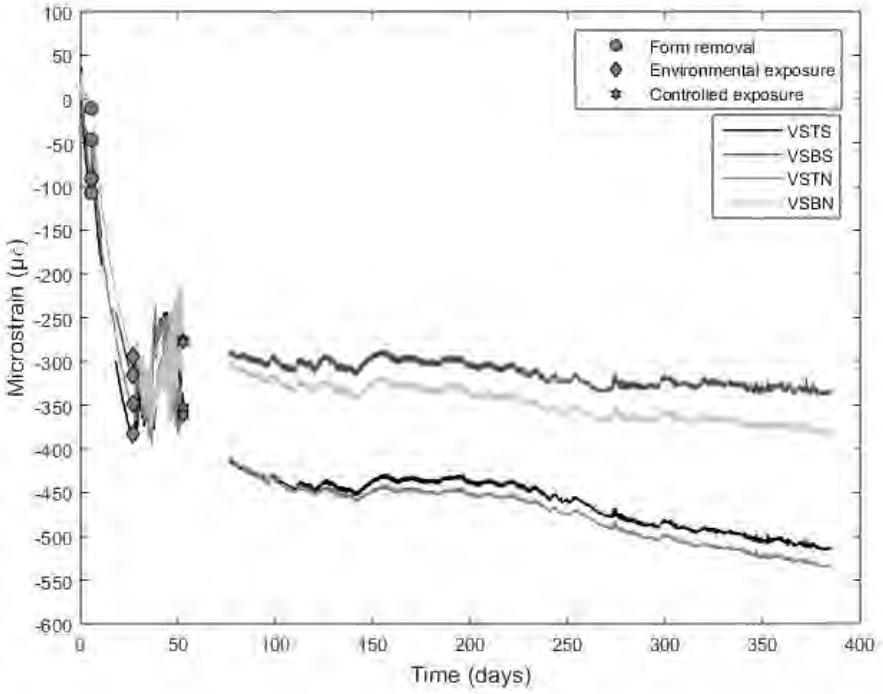


Figure 5.204: Strain versus time in Slab 2.

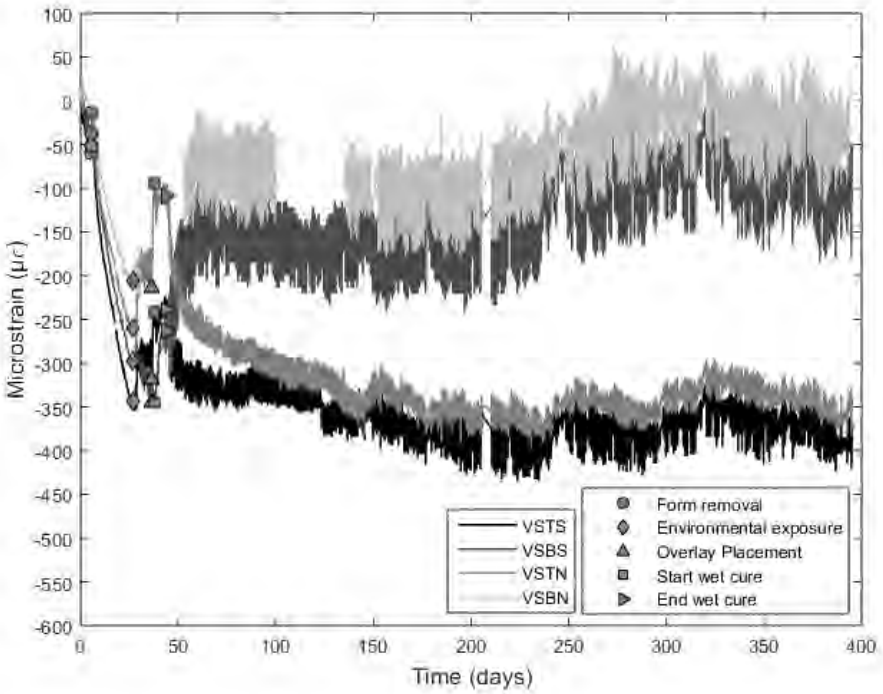


Figure 5.205: Strain versus time in Slab 3.

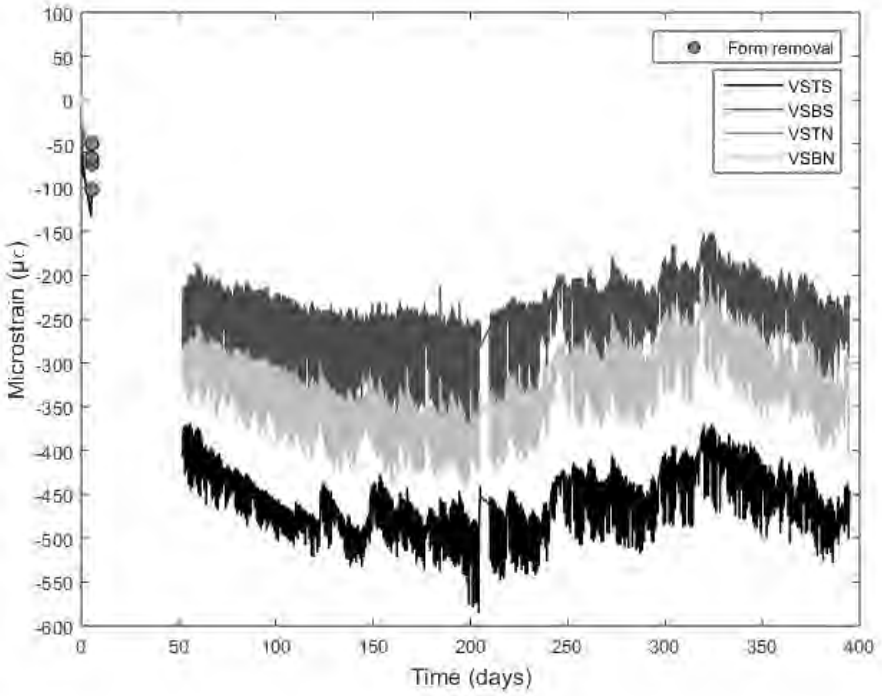


Figure 5.206: Strain versus time in Slab 4.

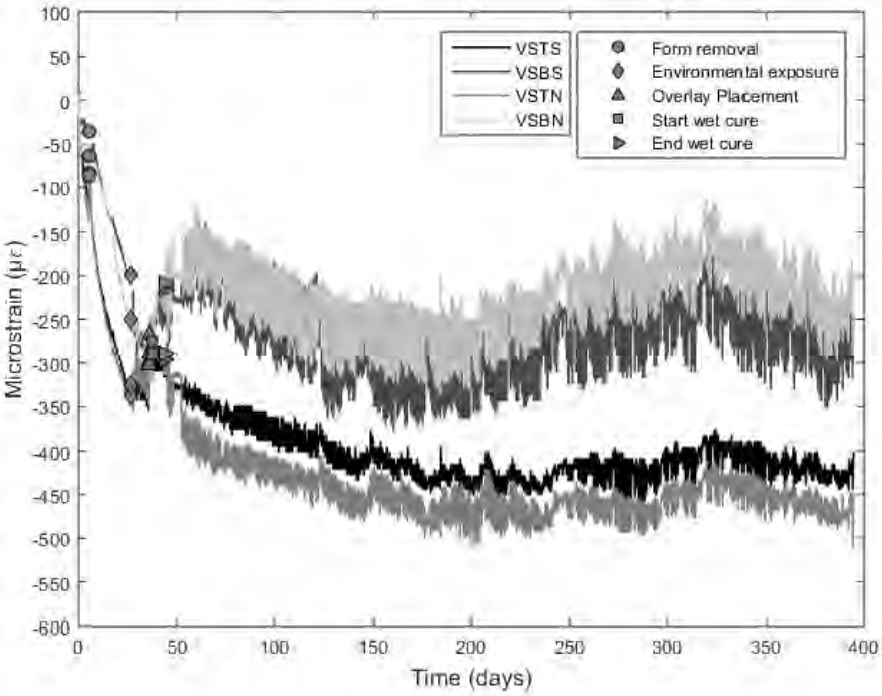


Figure 5.207: Strain versus time in Slab 5.

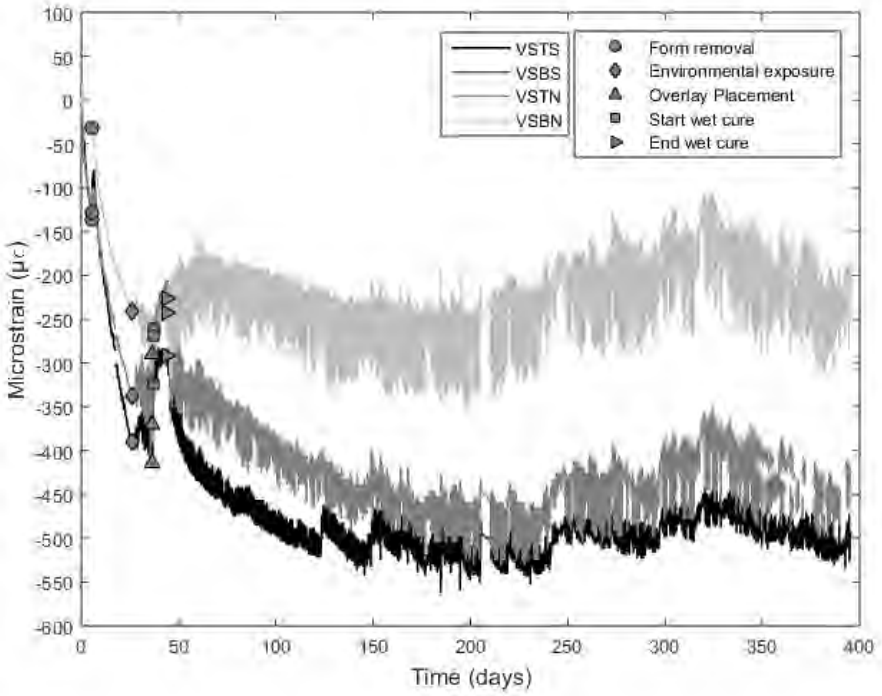


Figure 5.208: Strain versus time in Slab 6.

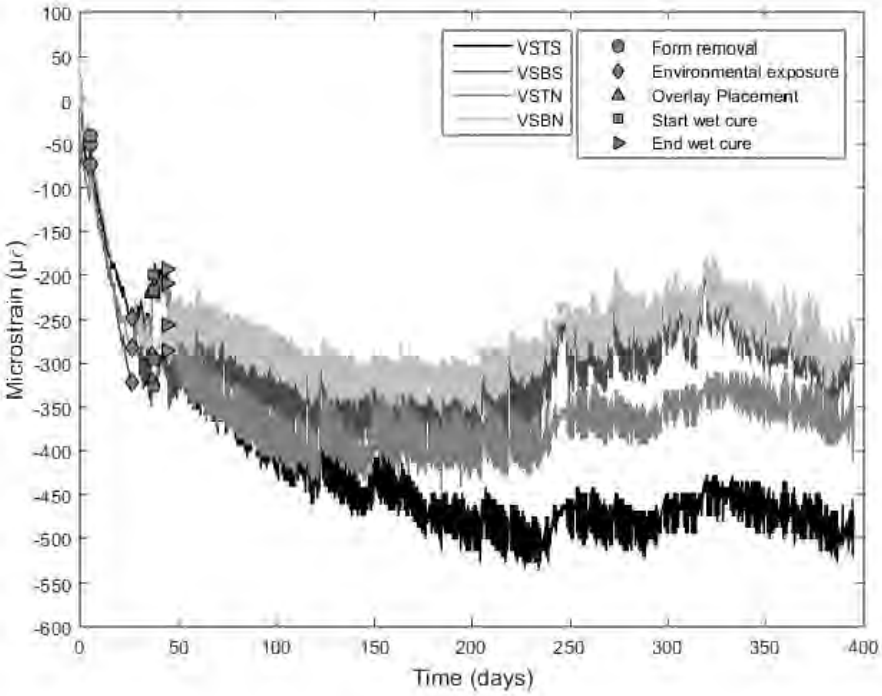


Figure 5.209: Strain versus time in Slab 7.

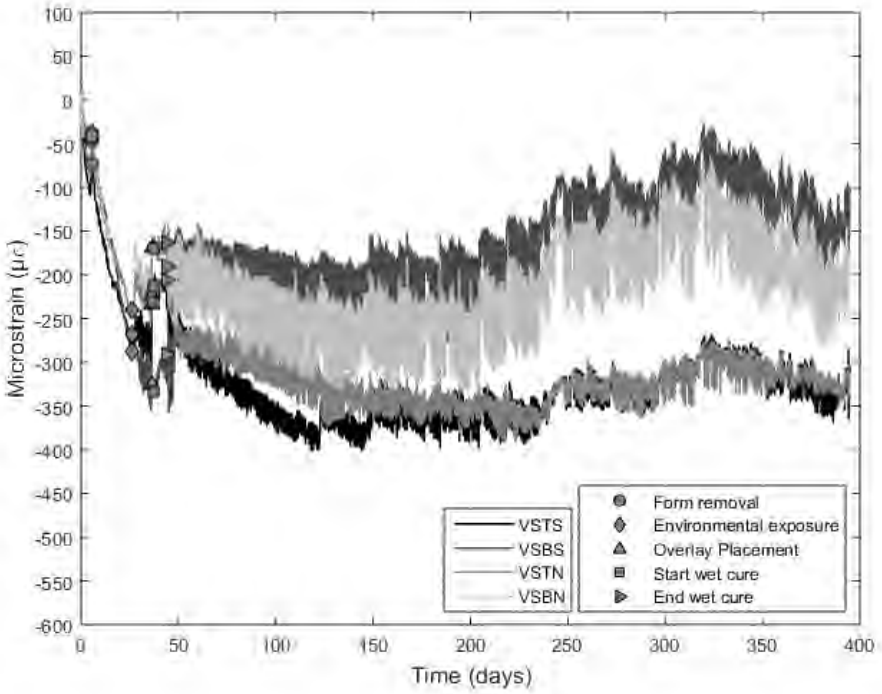


Figure 5.210: Strain versus time in Slab 8.

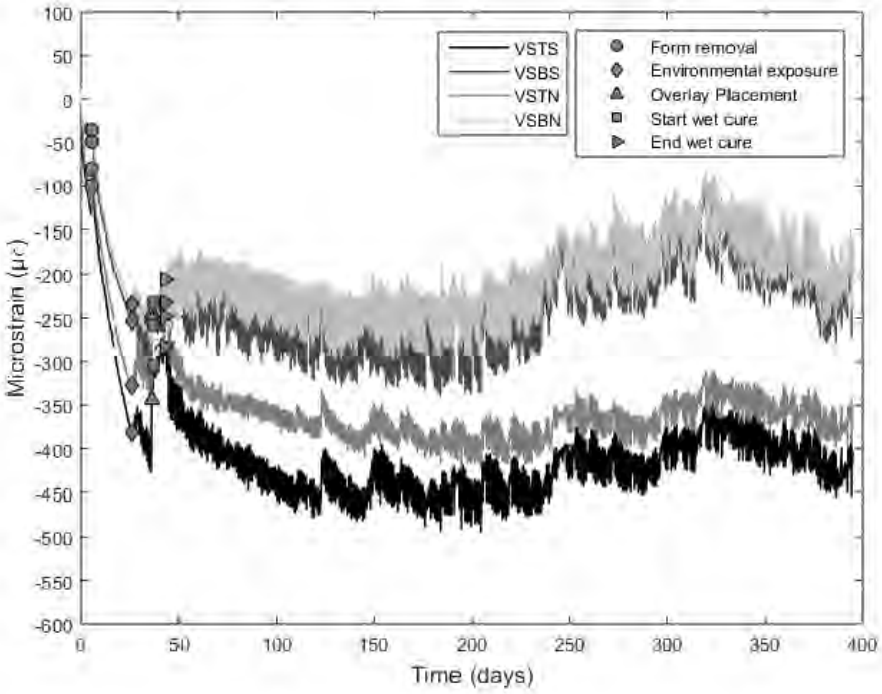


Figure 5.211: Strain versus time in Slab 9.

The first pair of slabs compared are Slab 1 and Slab 2. Both slabs have a NSC substrate thickness of 4 in. (102 mm), a reinforcement mesh of No. 3 (No. 10) bars, and were kept in controlled conditions. The difference between the two specimens is that Slab 1 has an UHPC overlay deck and Slab 2 does not. In general, the strains measured in the two slabs followed the same trend up to the placement of the overlay on Slab 1. At this point, the average strains were -373.4 με and -317 με for Slab 1 and 2 respectively, with the top and bottom gauges measuring similar values. After the placement of the UHPC overlay, the strain gauges (VSTL and VSTR), near the top of the slab reduced in value due to the compressive force induced by the shrinkage of the overlay. The strain gauges (VSBL and VSBR) near the bottom of the slab had an increased rate of tensile strain due to the bending effect of the eccentric load produced by the shrinkage of the UHPC overlay. This is in contrast to the trends observed in Slab 2 (no overlay). The strains measured in Slab 2 continued to increase more uniformly with the top and bottom gauges measuring similar strains. It is noted that the strains measured during the wet cure period (day 37 to day 43) were influenced by the curing. During this period, the changes in strain remained smaller, particularly near the top of the slabs where moisture was applied.

The next pair of specimens compared is Slab 3 (Figure 5.205) and Slab 7 (Figure 5.209). These slabs have a reinforcement mesh made of No. 4 bars (No. 13), a 1.0 in. (25 mm) thick UHPC overlay and were exposed to environmental conditions. The parameter varied between these slabs was the thickness of the NSC substrate. Slab 3 has a thickness of 4 in. (102 mm) and Slab 7 has a thickness of 6 in. (152 mm). As shown in Figure 5.209 (Slab 7) the strain had an approximate 25% increase in the measured strain in Figure 5.205 (Figure 4.13), and the strains on Slab 7 measured on top and bottom have a smaller range of values than the measured in Slab 3. Furthermore, it is observed that the influence of the overlay on the thicker substrate (Slab 7) was reduced.

Comparing Slab 3 (Figure 5.205) and Slab 8 (Figure 5.210), both slabs have a 4 in. (102 mm) thick NSC substrate, a 1 in. (25 mm) thick UHPC overlay and were exposed to environmental conditions. The difference in this pair of slabs is that Slab 3 has a mesh of No. 4 (No. 13) bars and Slab 8 has a mesh of No. 3 (No. 10) bars. The strain changes in Slab 8 (Figure 5.210) tend to be more similar in the top and bottom sensors than the measured strains in Slab 3 (Figure 5.205) indicating that Slab 8 had less influence of the overlay than Slab 3. However, the measured strains in the bottom are larger in the substrate with the smaller reinforcement ratio (Slab 8) which means that a higher reinforcement ratio can help to reduce the total shrinkage on the slab. Thus, even though the overlay had less influence in Slab 8, the strain measured by the sensors in Slab 3 had smaller values.

The next pair, Slab 1 (Figure 5.203) and Slab 8 (Figure 5.210), had a 4 in. (102 mm) thick NSC substrate, a 1 in. (25 mm) thick UHPC overlay, and reinforcement mesh consisting of No. 4 (No.13) bars. The difference in these two slabs is that Slab 1 was exposed to controlled conditions and Slab 8 was exposed to environmental conditions. As expected, the measured strain in Slab 1 became more uniform after being placed in controlled conditions, having less fluctuation in the strain and temperature measurements. Slab 1 shows strains in the rage of -300 με to -500 με, compared to Slab 8 that has recording strains values between -50 με to -400 με.

Slab 5 (Figure 5.207) and Slab 8 (Figure 5.210) were also compared. Both slabs had a No. 3 (No. 10) reinforcement mesh and were exposed to environmental conditions. The difference in these two slabs was that Slab 8 has a thickness of 4 in. (102 mm) and 1 in. (25 mm) of overlay, and Slab 5 has a thickness of 4.5 in. (114 mm) substrate and a 2 in. (50 mm) overlay. As shown in Figure 5.210, the strain measured in Slab 8 by the top and bottom sensors had a smaller gap between the values than the strains of top and bottom sensors of Slab 5 indicating that the thickness of the overlay was not a factor that can reduce the influence that the UHPC overlay had on the NSC slab. The strain values measured by the bottom sensors in Slab 8 had values ranging between -50 με to -300 με and the top sensors had a range of -280 με to -400 με, while the strain measurements in Slab 5 that had values in bottom sensors between -150 με to -350 με and top sensors ranging between -300 με to -450 με. This shows that the strain measured in both top and bottom VWSGs in Slab 5 had higher values than Slab 5. These can be due to VWSG subjected to higher compressive strains due to thicker overlay causing more shrinkage.

The behaviors of Slab 6 (Figure 5.208), Slab 8 (Figure 5.210), and Slab 9 (Figure 5.211) were also compared. The three specimens had a reinforcement mesh of No. 3 (No. 10) rebar, 1 in. (25 mm) of overlay, and were exposed to environmental conditions. The parameter variation in these slabs is the percentage of fibers in the UHPC overlay. Slab 8 had 1.5%, Slab 6 had 2% of fibers, and Slab 9 had 3% fibers by volume of the mixture proportions. Among these three slabs, Slab 8 experienced less shrinkage, having strain values up to -400 με, followed by Slab 9 with maximum strain values of approximately -500 με, and Slab 6 with values up to -550 με. Also, strain measured by the top and bottom VWSGs in Slab 8 were closer to each other compared with Slab 6 and Slab 9 indicating that the UHPC overlay used in Slab 8 had less influence in the NSC substrate. Based on this data, the percentage of fibers did not make a substantial impact on reducing the shrinkage experienced by the slab but did reduce the shrinkage of the UHPC overlay.

Finally, the behaviors of Slab 4 (Figure 5.206) and Slab 8 (Figure 5.210) were compared. These slabs had the same thickness of 4 in. (10.2 cm), mesh reinforcement of No. 3 (No. 10) rebar and 1 in. (2.5 cm) overlay with 1.5% fiber percentage. The parameter varied in this pair of slabs was the inclination of Slab 4 which had a 7% slope during the observation period and Slab 8 remained level (0% slope). Even though the material components of these slabs were the same, the strains measured in Slab 4 were larger than Slab 8. This behavior can be attributed to different arrangement of steel fibers due to position of NSC substrate at the application of UHPC.

Figure 5.212 shows the average shrinkage of each slab measured by the four VWSGs embedded in the NSC substrate. Comparing the average strains of all the specimens, Slab 1 is experienced the largest shrinkage, approximately -0.07 in. (1.78 mm) Slab 1 and Slab 2 experienced similar shrinkage and less fluctuation due to the controlled exposure. The slabs with the least amount of shrinkage are Slab 3 and Slab 8 with a highest value of approximately -0.04 in. (-1.02 mm).

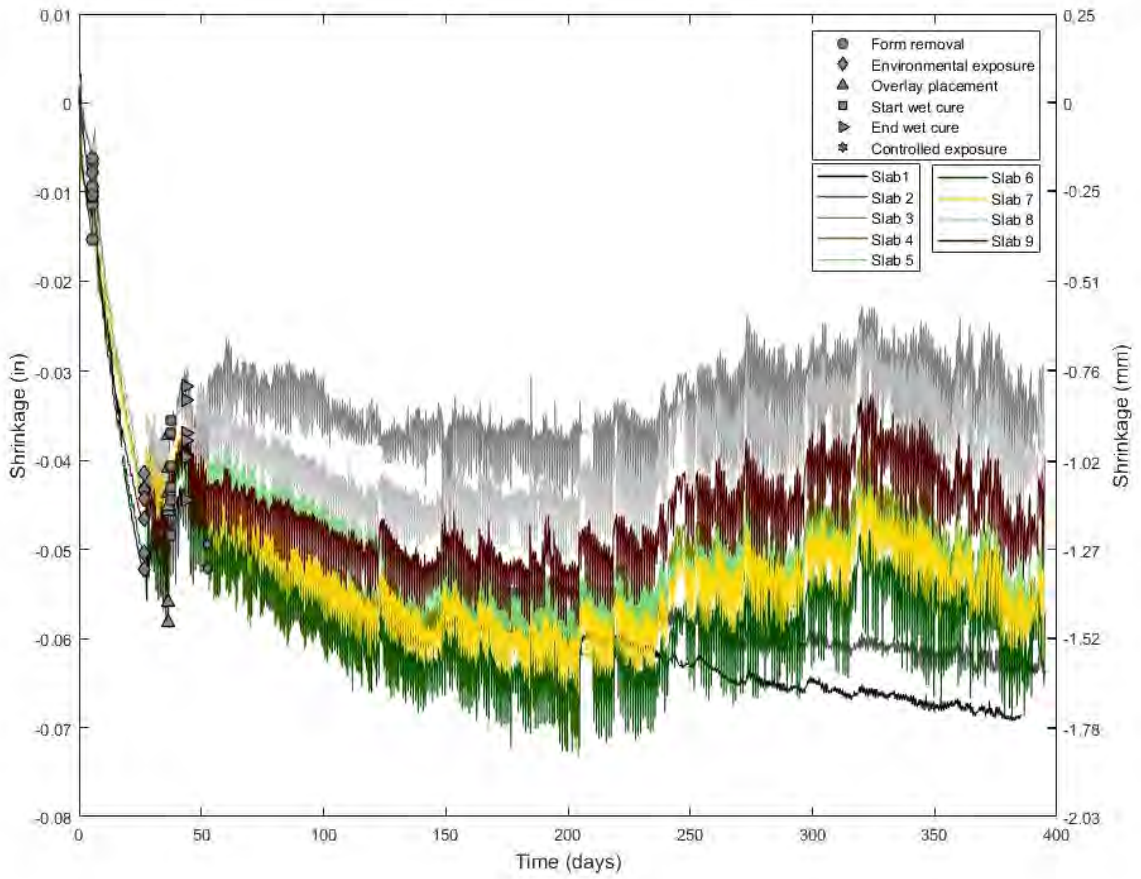


Figure 5.212: Average shrinkage versus time for all slabs.

In Figure 5.213, the strain due to UHPC deck overlay was isolated from the total strain measured in the slabs to compare the impact that the UHPC overlay deck had in the NSC substrates. As can be seen in Figure 5.213, Slab 3 had less shrinkage due to UHPC overlay. This can be attributed to the increased reinforcement in the substrate. This can be an important factor to control the shrinkage in the slabs.

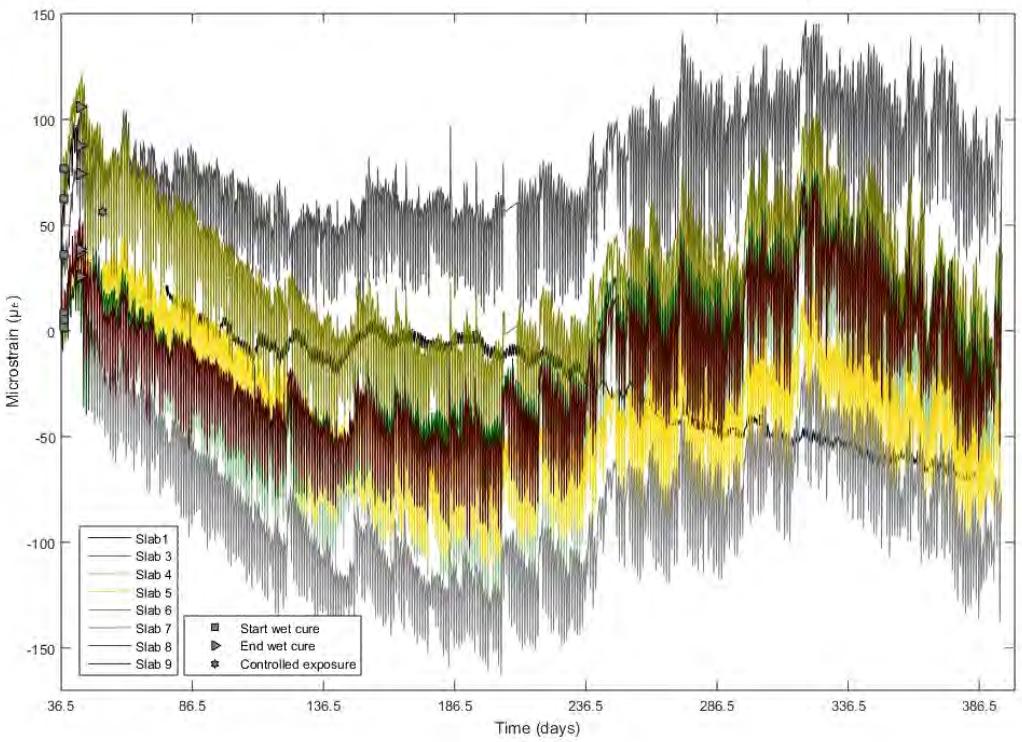


Figure 5.213: Strain versus time due to UHPC deck overlay.

To explore the effect of the shrinkage of the UHPC overlay on the substrate, the strain caused by the overlay was isolated. To isolate the strain caused by the overlay, the average shrinkage strain of the substrate at day 36.5 (immediately prior to the application of the overlay) was subtracted from the total strain. Figure 5.214 through Figure 5.221 show the strains from day 36.5 until tested in flexure, with the average strain developed in the substrate subtracted from the total strain. This strain, however, includes strain due to the shrinkage of the overlay plus any shrinkage strains developed in the substrate. Therefore, to eliminate the strain developed from the shrinkage of the substrate, the average strain developed in each slab by day 36.5 was also subtracted from the total strain. The strain developed in the substrate due to the shrinkage of the UHPC overlay was used to calculate the neutral axis height. The neutral axis demonstrates the effect of the different design parameters had on the overall behavior of the slab-overlay system.

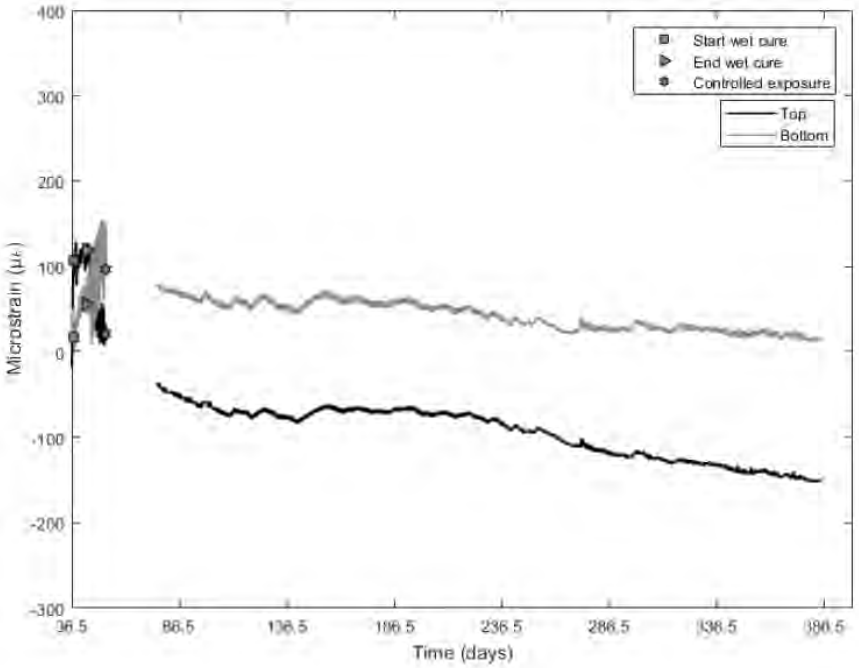


Figure 5.214: Strain versus time due to UHPC only in Slab 1.

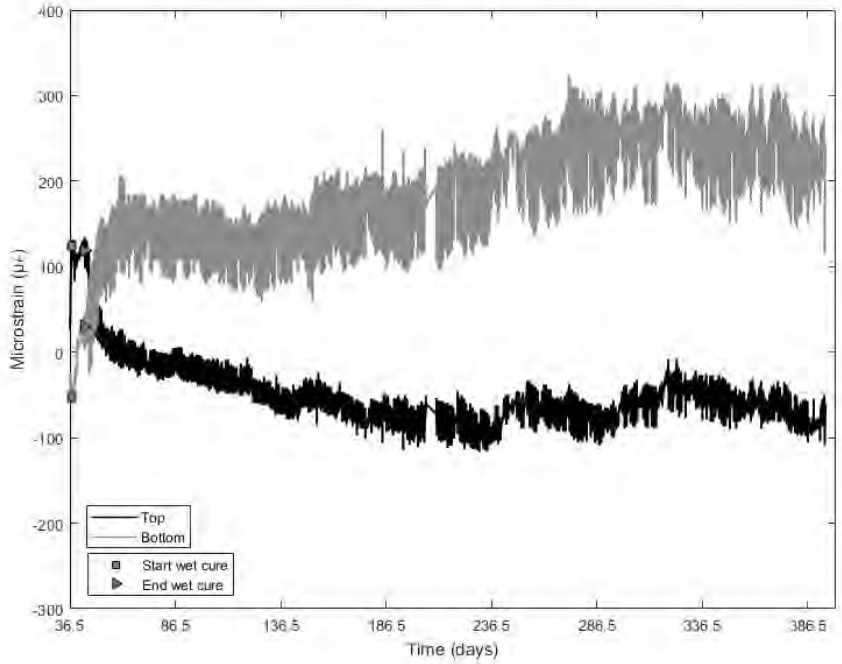


Figure 5.215: Strain versus time due to UHPC only in Slab 3.

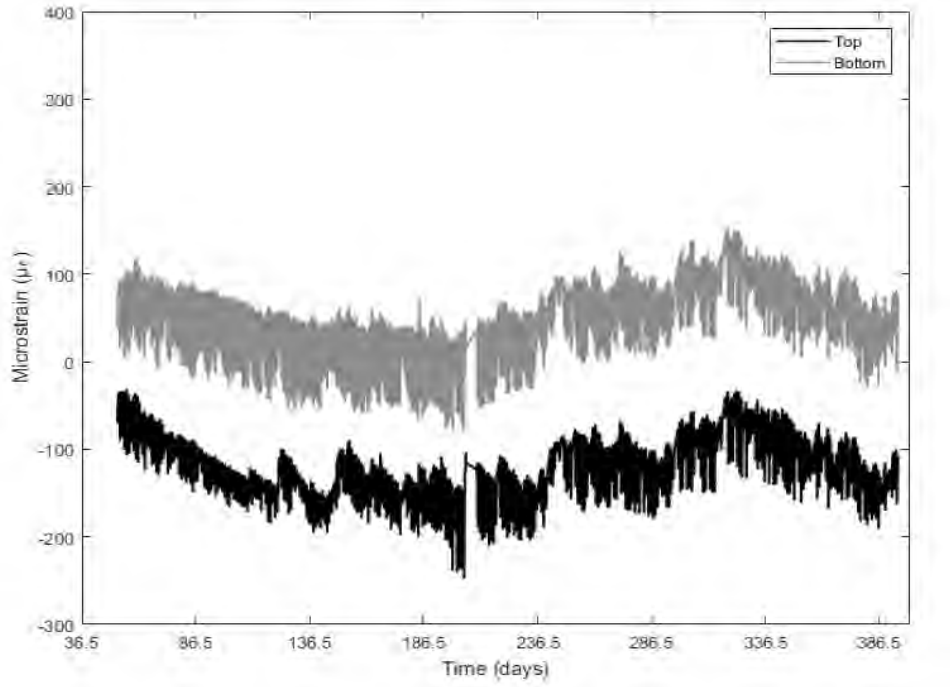


Figure 5.216: Strain versus time due to UHPC only in Slab 4.

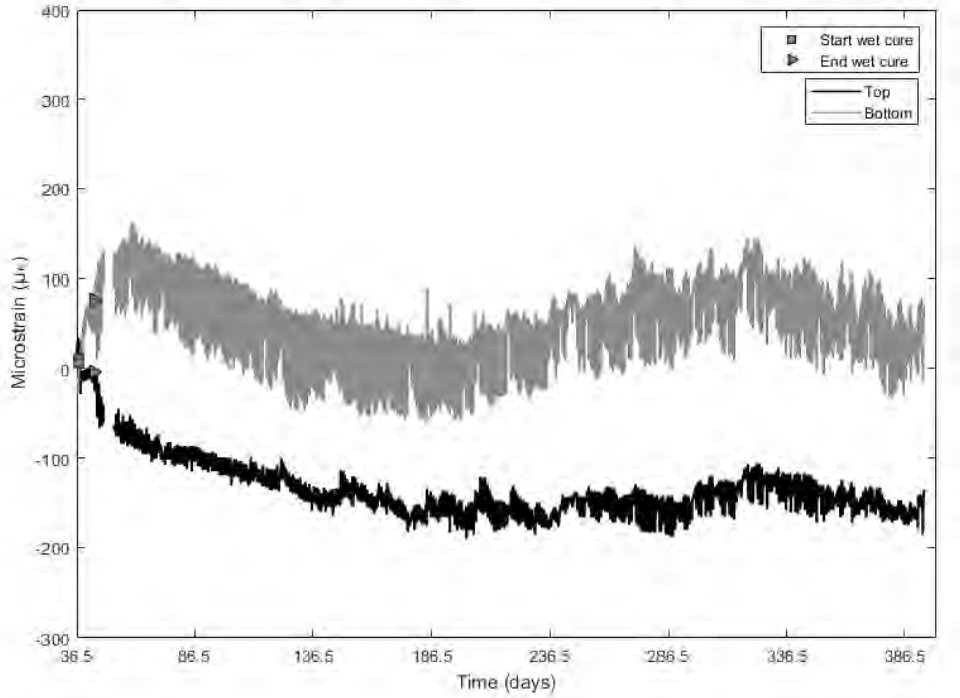


Figure 5.217: Strain versus time due to UHPC only in Slab 5.

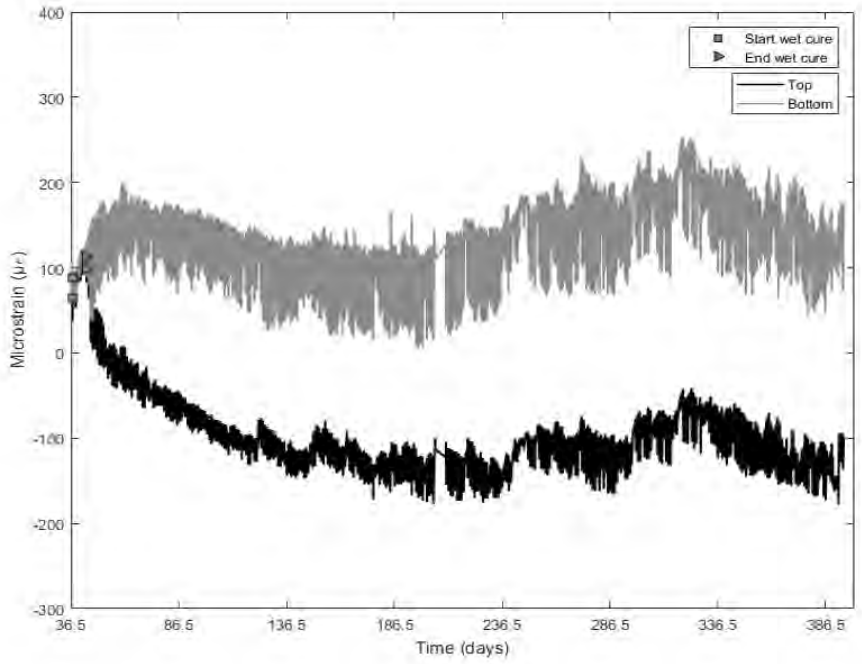


Figure 5.218: Strain versus time due to UHPC only in Slab 6.

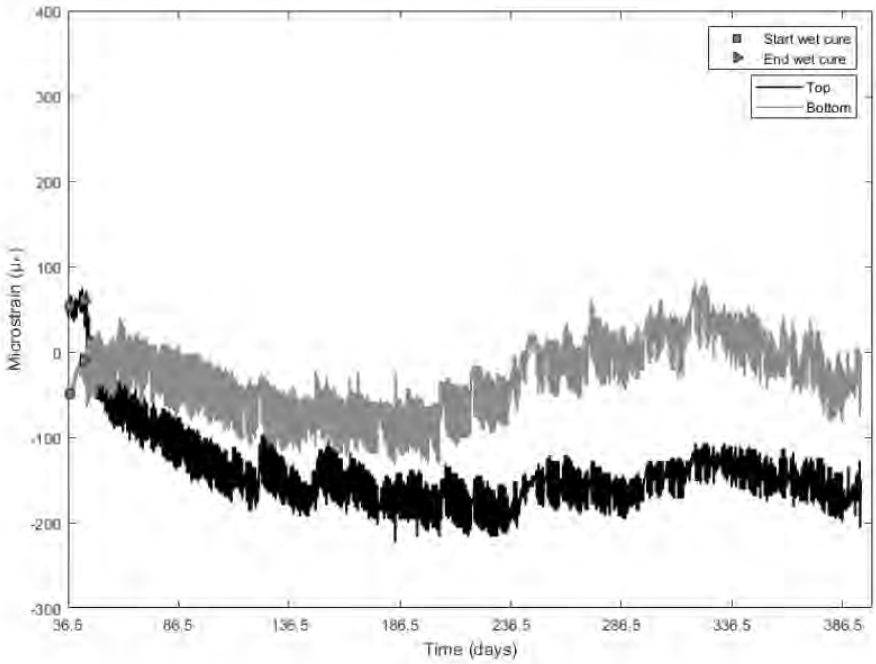


Figure 5.219: Strain versus time due to UHPC only in Slab 7.

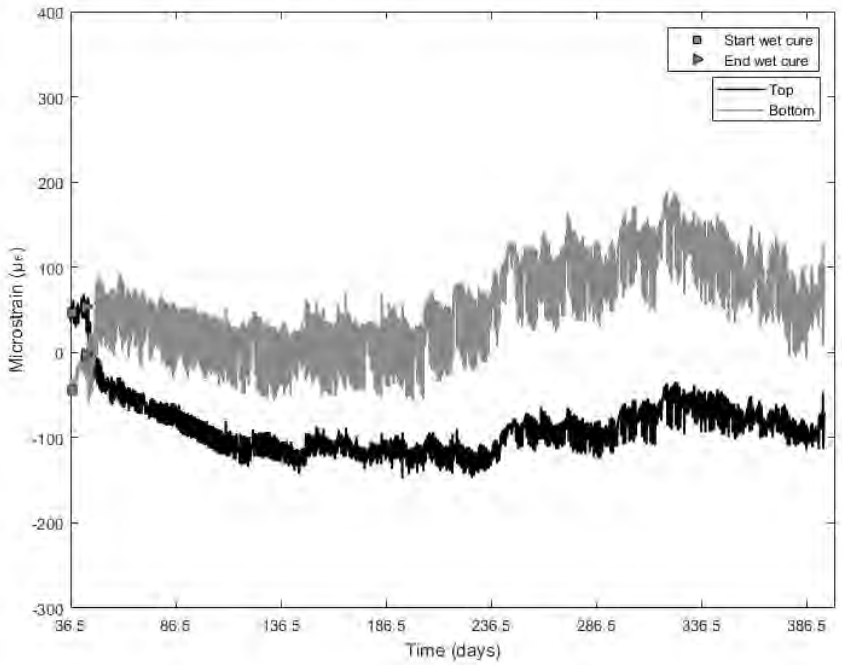


Figure 5.220: Strain versus time due to UHPC only in Slab 8.

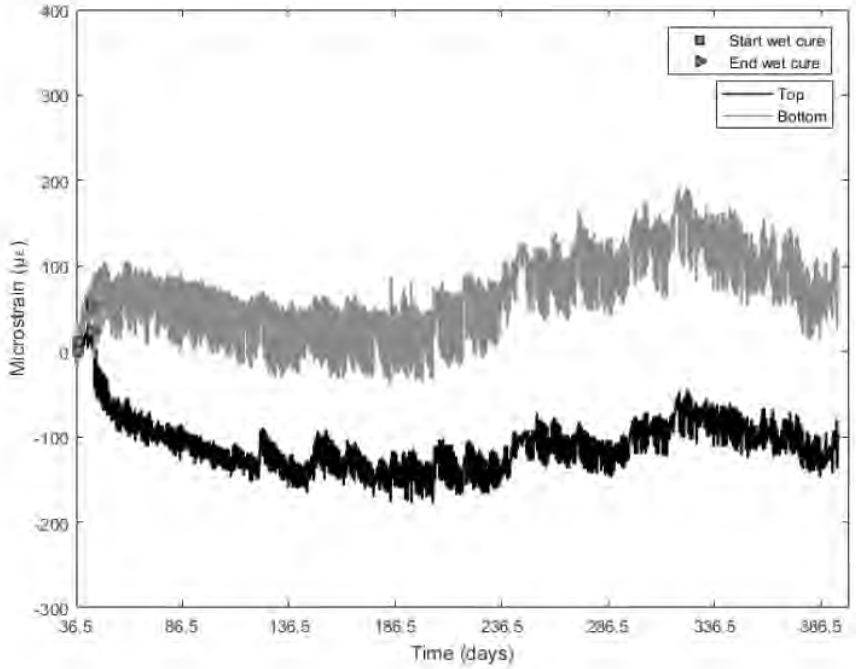


Figure 5.221: Strain versus time due to UHPC only in Slab 9.

The strain developed in the substrate due to the effect of the shrinkage of the UHPC overlay was used to calculate the neutral axis height. The neutral axis demonstrates the effect of the different design parameters had on the overall behavior of the slab-overlay system. The neutral axis was determined using Equation 5.2 below and the results for each slab are plotted in Figure 5.222 through Figure 5.229.

$$NA = \frac{x\,\epsilon_t}{\epsilon_t - \epsilon_b} + y \qquad 5.2$$

Where,
NA = neutral axis height
ϵ_t = average strain of top VWSGs
ϵ_b= average strain of bottom VWSGs
x = distance from bottom VWSGs to top VWSGs
y = distance from the bottom of the slab to the bottom VWSGs

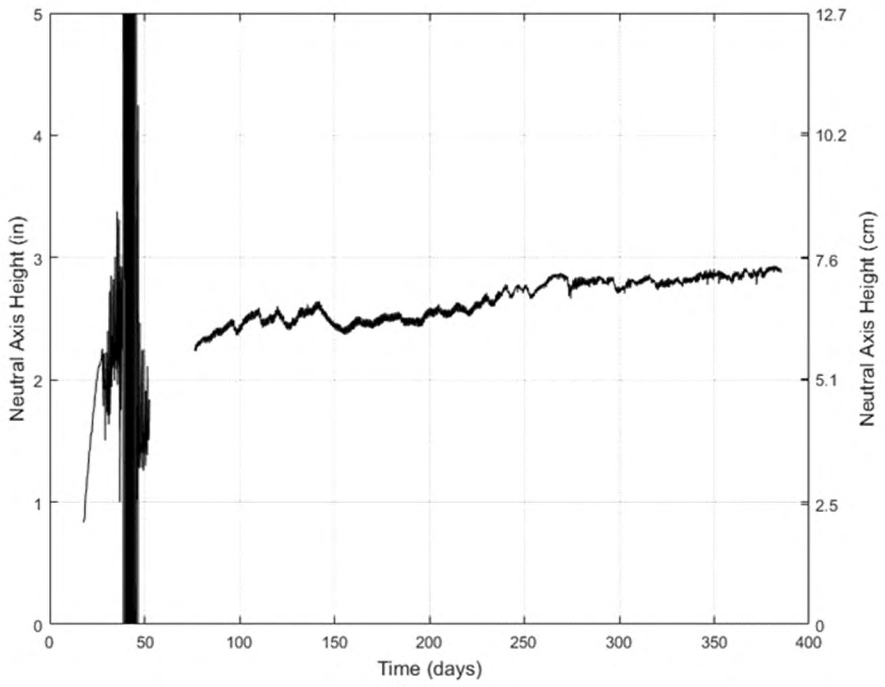


Figure 5.222: Neutral axis height Slab 1.

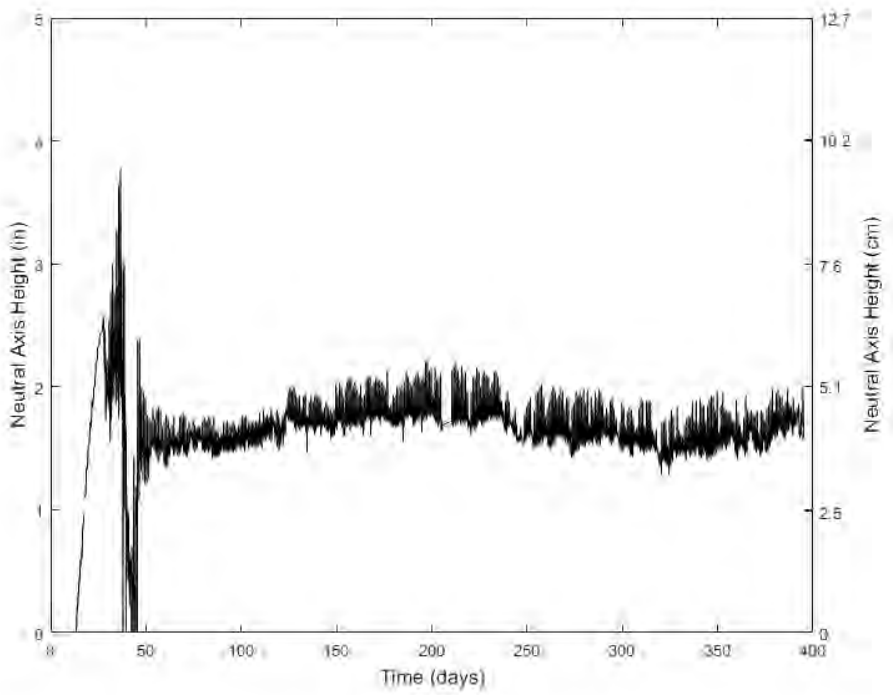


Figure 5.223: Neutral axis height Slab 3.

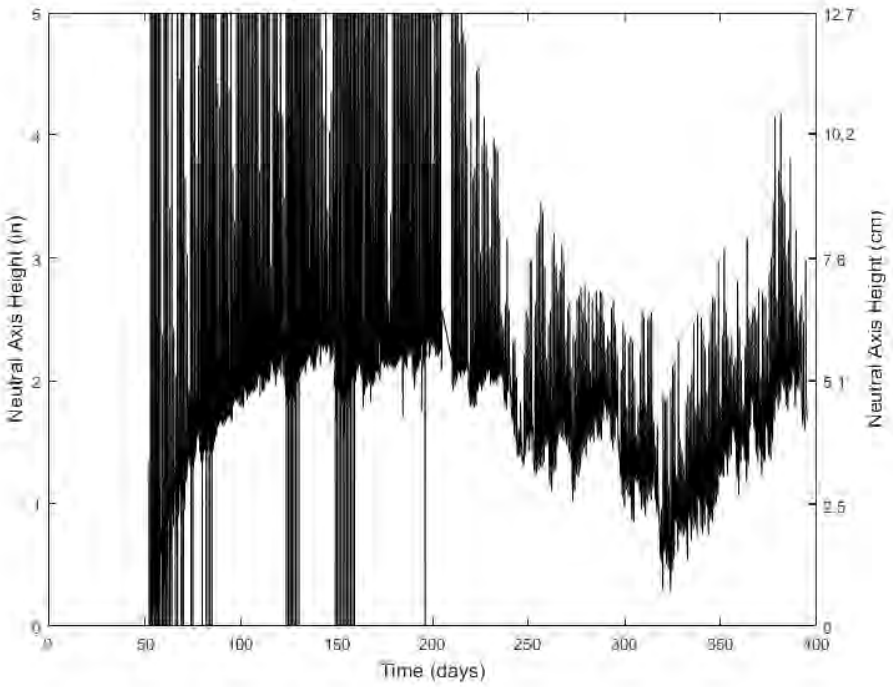


Figure 5.224: Neutral axis height Slab 4.

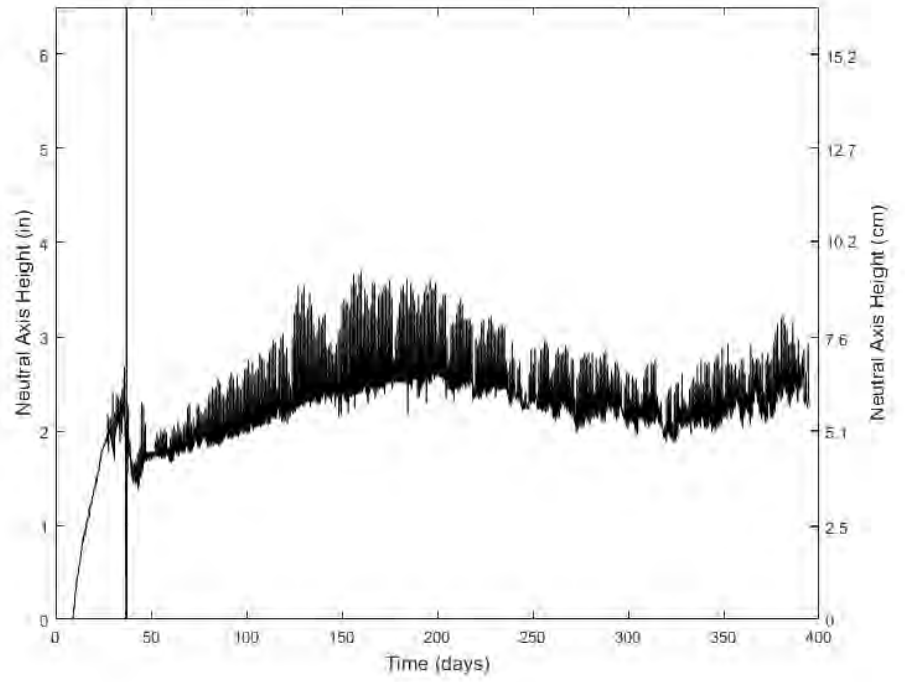


Figure 5.225: Neutral axis height Slab 5.

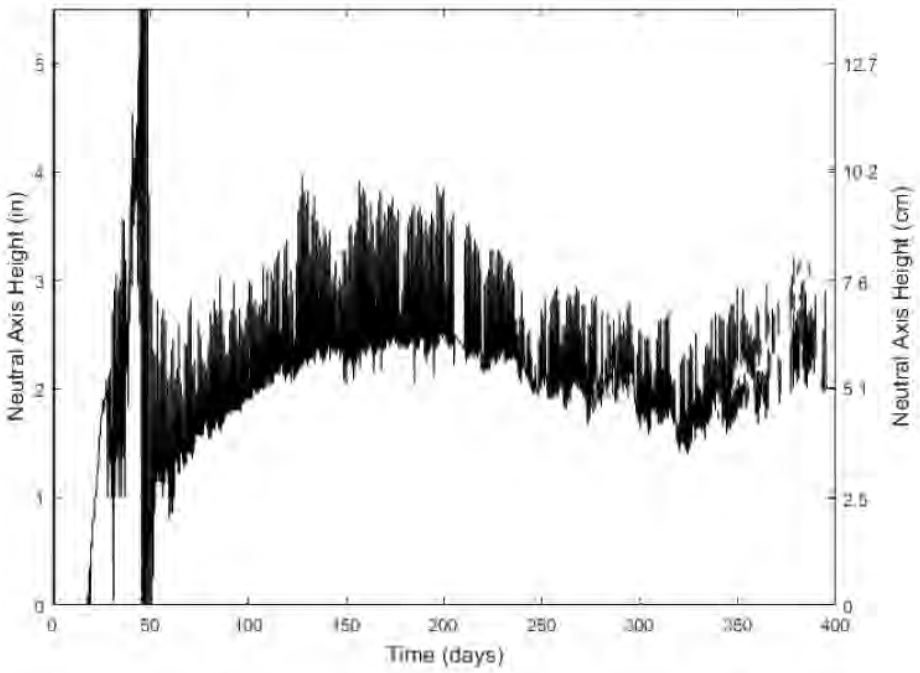


Figure 5.226: Neutral axis height Slab 6.

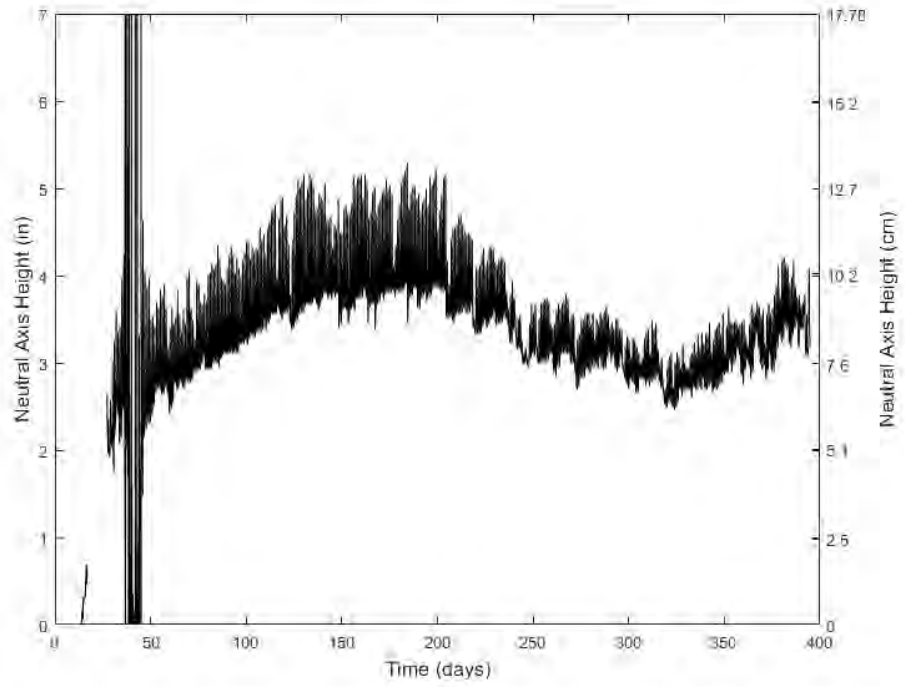


Figure 5.227: Neutral axis height Slab 7.

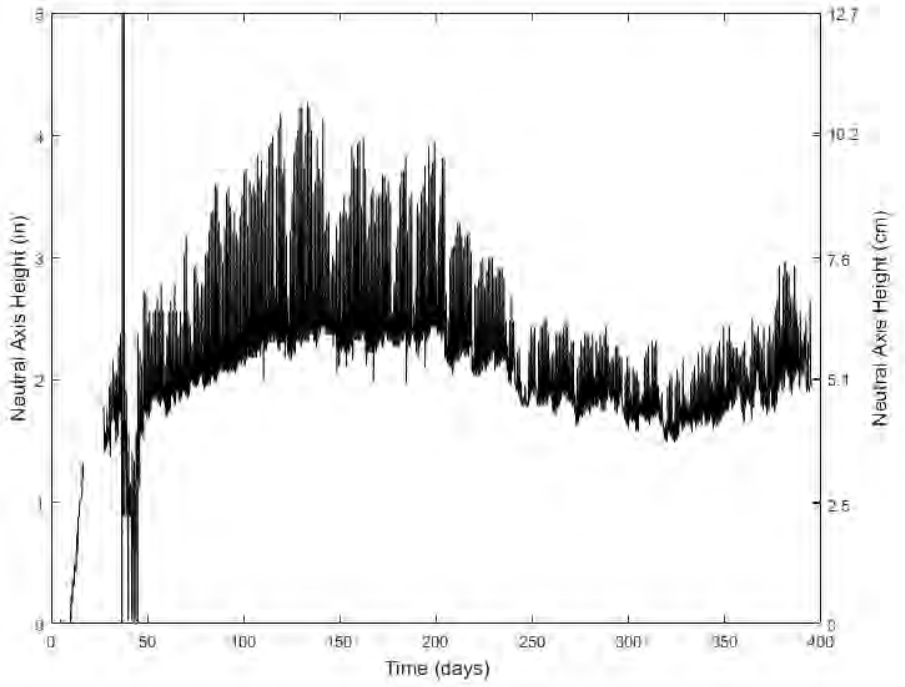


Figure 5.228: Neutral axis height Slab 8.

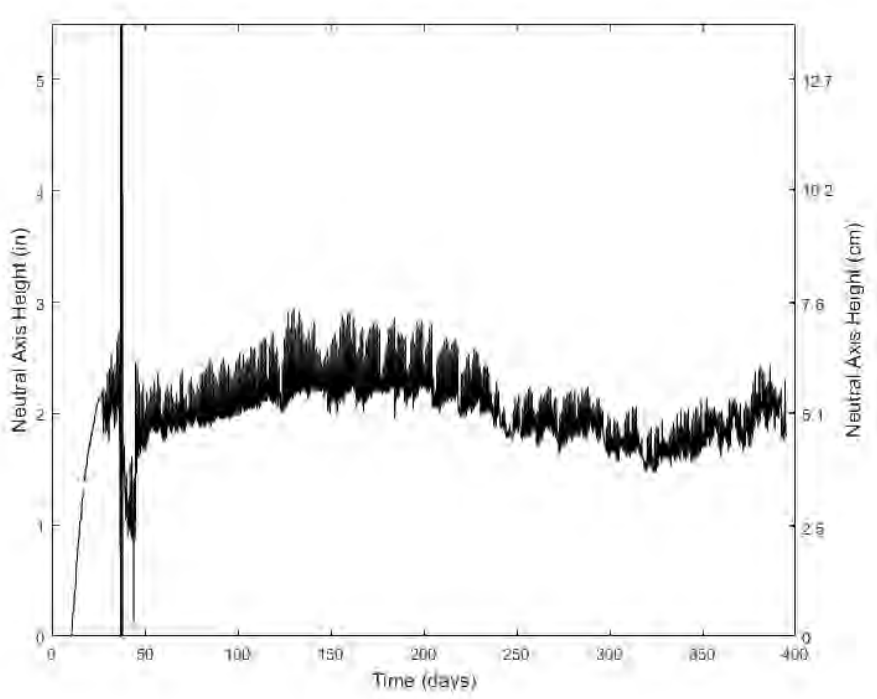


Figure 5.229: Neutral axis height Slab 9.

As shown in Figure 5.222 through Figure 5.229, the neutral axis in all slabs increased from almost the mid-height of the slab as the UHPC continued to shrink following the placement of the overlay. This indicates that the bond between the substrate and the overlay was adequate for the two materials to act compositely. The changes in NA height also show the impact that the UHPC overlay had on the substrate material. Comparing the increased in height of the NA after the application of UHPC overlay, Slab 9 had the least increase in height, which can be attributed to the lightest percentage of fibers in the overlay. The next slab show lees effect on then NA due to UHPC was Slab 3, followed by Slab 1 and Slab 8; therefore, demonstrating that the overlay had a smaller effect on the substrate. Due to the increased fiber percentage and reinforcement ratio of Slabs 9 and 3 respectively, it is evident that these parameters have a significant influence on the behavior of the system.

The VWSG data was also used to calculation the shear stress at the interface between the NSC substrate and the UHPC overlay. For this analysis, the shear force was calculated using Equations 5.3 and 5.4 as follows:

$$\epsilon \cdot E = -\frac{P}{A} + \frac{P \cdot e \cdot y}{I_c} \qquad 5.3$$

$$P = \frac{\in \cdot E \cdot A \cdot I_C}{-I_C + A \cdot e \cdot y} \quad 5.4$$

Where,
$\in =$ strain measured by each VWSGs
A = area of NSC that is in contact with UHPC
I_c = moment of inertia of the composite section
E = modulus of elasticity of NSC
e = eccentricity of shear force, measured from neutral axis to the top of NSC slab
y = distance from NA to the VGSG

Once the shear force was determined, the shear stress was calculated using Equation 5.5 and tabulated in Table 5.31.

$$\tau = \frac{P}{(l/2) \cdot w} \quad 5.5$$

where:
P = shear force at interface
l = length of the slab
w = width of the slab

Table 5.31 Shear Stress Range at Interface

	Shear stress, psi (kPa)	
	Lowest	Highest
Slab 1	-70.0 (483)	5.0 (35)
Slab 3	1.0 (7.0)	11 (76)
Slab 4	-50.0 (345)	0.0 (0.0)
Slab 5	5.0 (35)	20 (138)
Slab 6	-15.0 (103)	6.0 (41)
Slab 7	-70 (483)	-30 (207)
Slab 8	-5.0 (35)	15 (103)
Slab 9	5.0 (35)	16 (110)

Based on the range of shear stress that each slab experienced at the interface with the UHPC overlay, Slab 3 and Slab 9 experienced less shear stress at interface. As mention before, the reinforcement ratio and the percentage of fibers in UHPC overlay does have a significant impact in reducing the shear developed at the interface between NSC and UHPC overlay.

5.4.10 Flexural Testing Results

For this test, different sensors were used for data acquisition such as LVDTs, string potentiometers, tiltmeters, and strain gauges. To have a better understanding of the flexural test results load-deflection and moment-curvature plots are provided for the slabs from the cyclic loading and ultimate loading tests. For load-deflection plots, the load was the applied by the hydraulic actuator and was measured by the internal load cell, and the deflection was the measured at midspan in both directions by string potentiometers. For the moment-curvature plots, the midspan deformations measured by the LVDTs in the normal strength concrete and the UHPC was converted to strain by dividing the reading of the LVDT by the gage length between the anchor location and the LVDT. With the strain measurement the height from the LVDT placed at half thickness of the NSC slab to neutral axis location was calculated using Equation 4.5. Then curvature was calculated using Equation 5.6.

$$x = \frac{\epsilon_2 \cdot (\frac{t_s}{2} + \frac{t_o}{2})}{\epsilon_2 - \epsilon_1} \qquad 5.6$$

where:
x = distance from LVDT placed at half thickness of the NSC slab to neutral axis location
ϵ_1 = Strain measured by LVDT placed at half thickness of the UHPC overlay
ϵ_2 = Strain measured by LVDT placed at half thickness of the NSC slab
t_s = thickness of the NSC slab
t_o = thickness of the UHPC overlay
Once the neutral axis depth was known, the curvature was calculated using Equation 5.7

$$\emptyset = \frac{\epsilon_2}{x} \qquad 5.7$$

5.4.10.1 Cyclic Load Testing

Cyclic load tests were performed on eight of the nine slabs in which the slabs underwent 1000 cycle at half of their nominal section capacity ($0.5M_n$). The load versus deflection behavior for Slabs 2 through 9 are provide in Figure 5.230 through Figure 5.238, followed by the load versus deformation behavior in Figure 5.239 through Figure 5.247, which are then followed by the moment curvature behavior in Figure 5.248 through Figure 5.255. For load versus vertical deflections analysis, the data measured in each slab by the string potentiometers was plotted. Deflection of the slab was recorded at five points: the center of the slab (S.P.C.), midspan at the north edge (S.P.MN.), midspan at the south edge (S.P.MS.), and at midspan in the perpendicular direction of the applied load in the east and west (S.P.E. and S.P.W.). For the load versus horizontal deformation analysis, the deformation measurements of the LVDTs were used. Similar to string potentiometers the data was obtained in five different positions including top and bottom: the center of the slab in the bottom face (LVDT CB), midspan at the north edge in the bottom face (LVDT MNB.), midspan at the south edge in the bottom face (LVDT MSB), midspan at the north edge in the top face (LVDT MNT.), and midspan at the south edge in the top face (LVDT MST). Finally, for the moment-curvature behavior the deformation measured by the LVDTS that were placed in the vertical sides of the slabs at mid-height of the UHPC and midheight of NSC in the north and south faces. String potentiometers and LVDTs measured deflections and deformations during the 1000 load-unload cycles performed on the slabs. During these tests, no visual damage or debonding of the overlay were observed in the slabs.

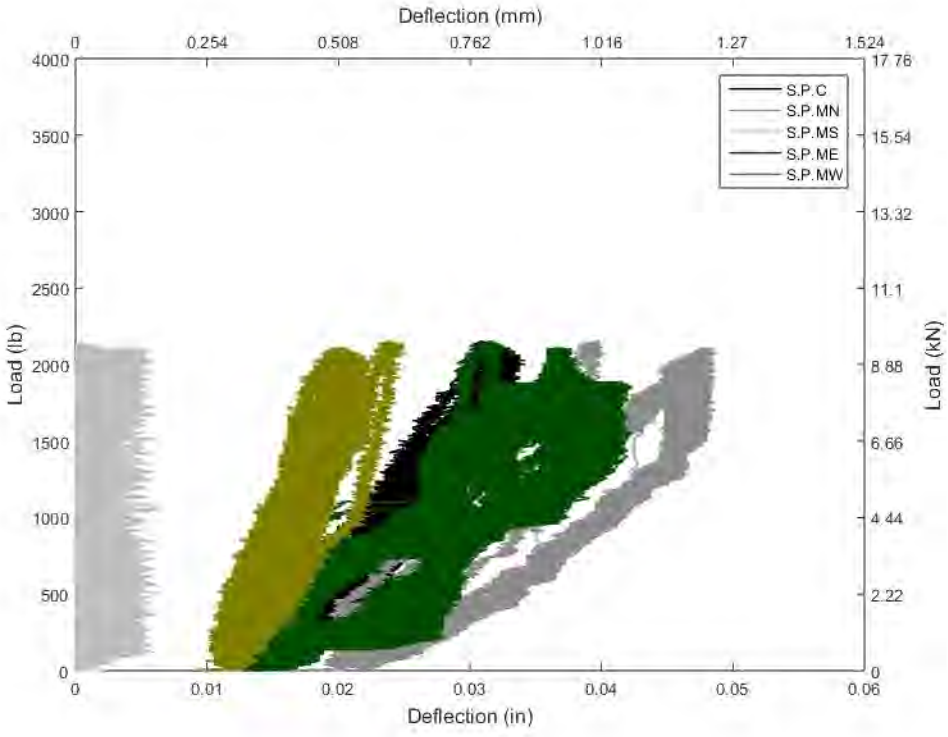


Figure 5.230: Load versus deflection Slab 2.

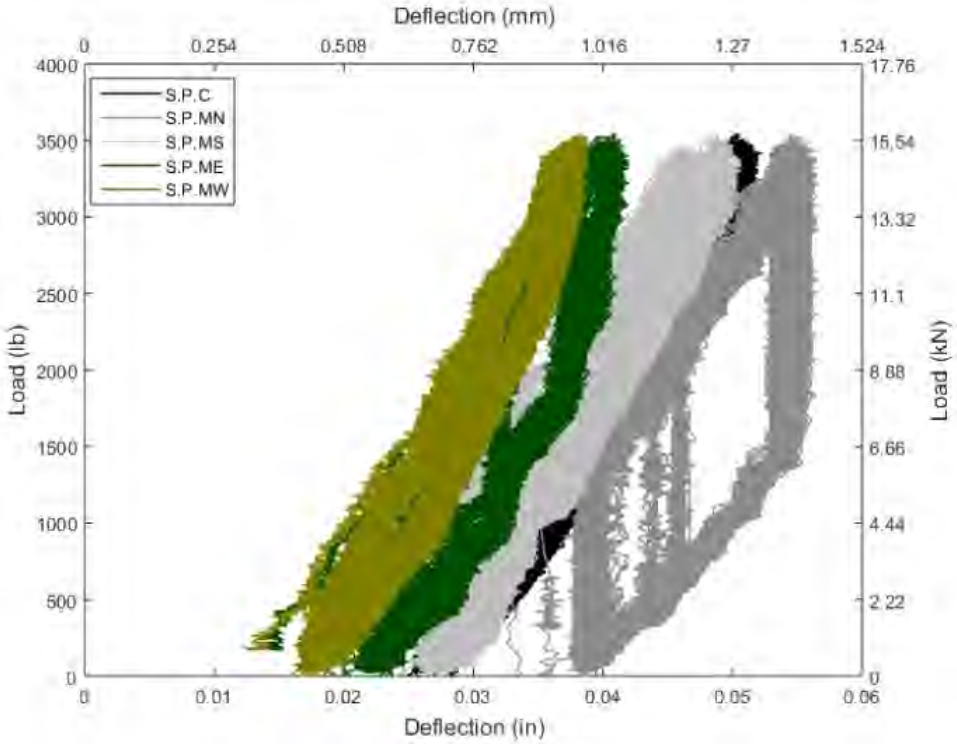


Figure 5.231: Load versus deflection Slab 3.

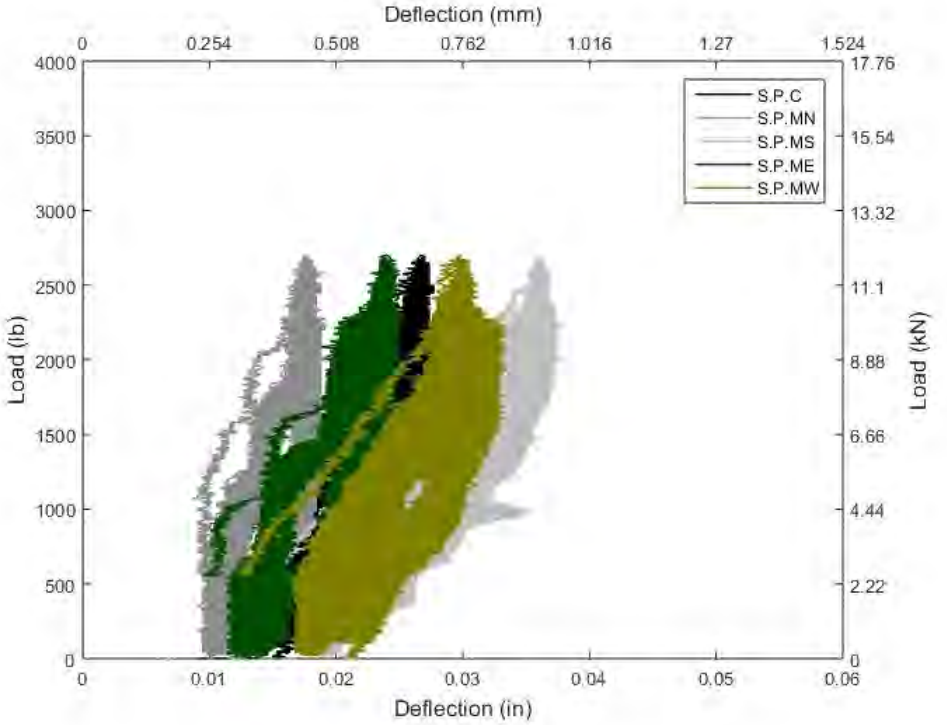


Figure 5.232: Load versus deflection Slab 4 (load applied perpendicular to direction of slope during casting of UHPC).

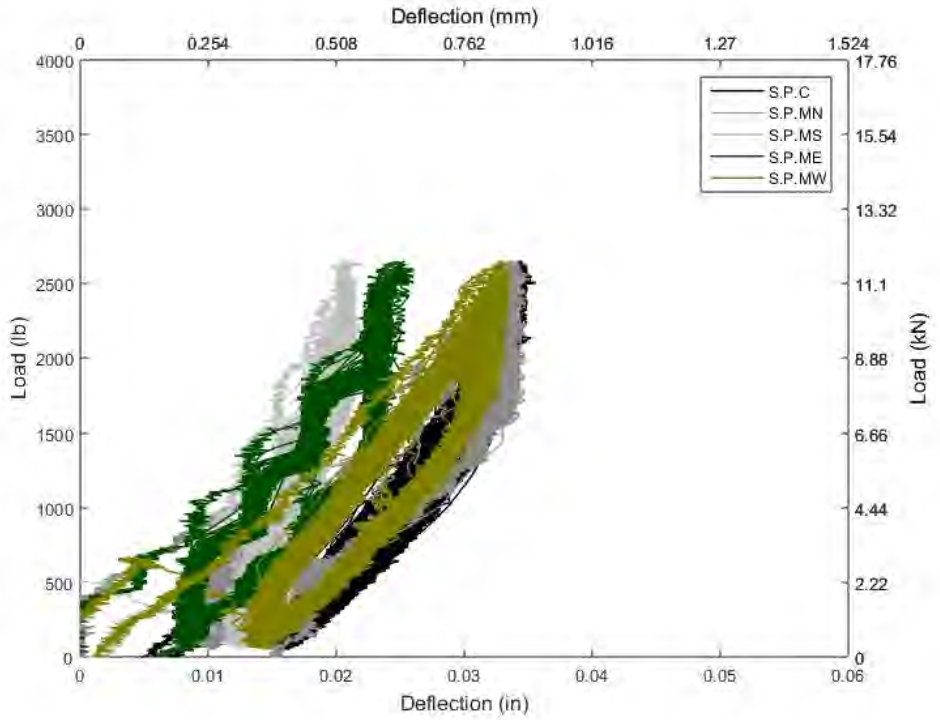


Figure 5.233: Load versus deflection Slab 4 (load applied parallel to direction of slope during casting UHPC).

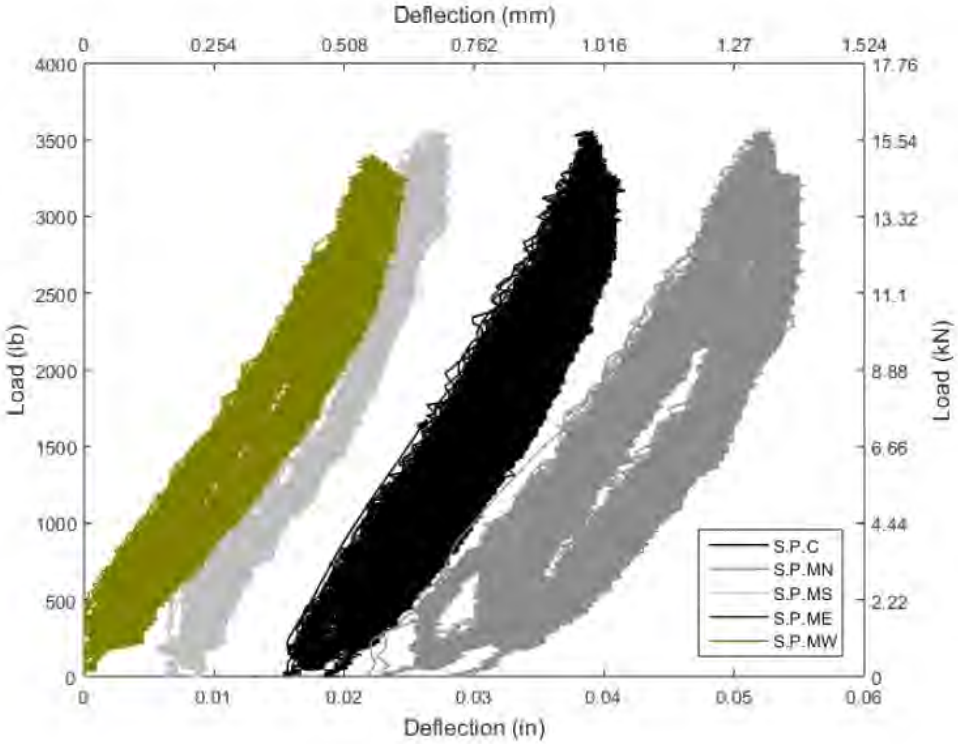


Figure 5.234: Load versus deflection Slab 5.

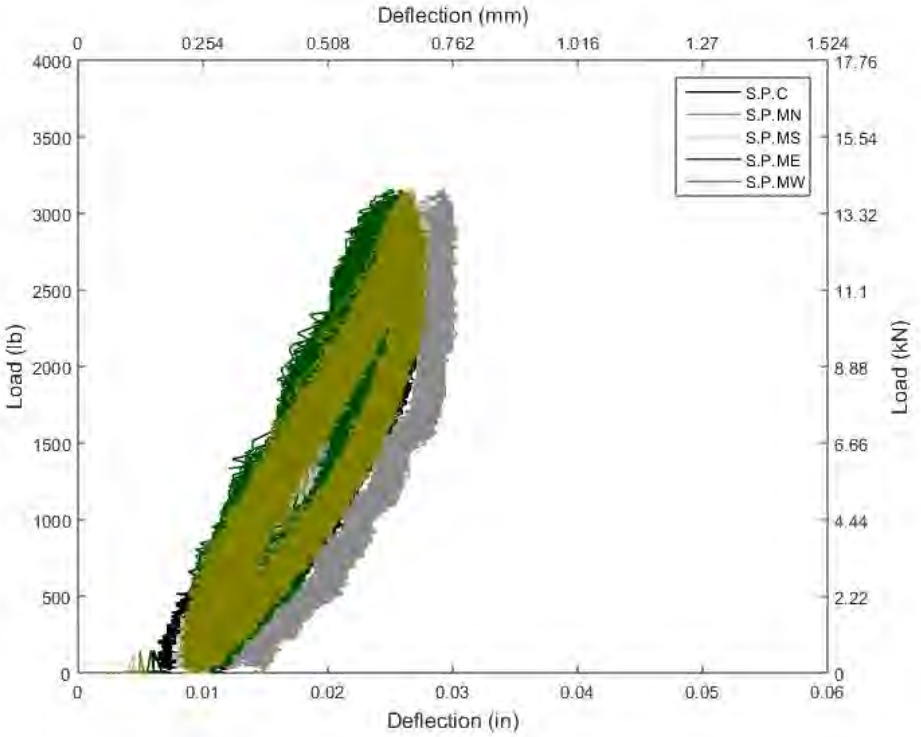


Figure 5.235: Load versus deflection Slab 6.

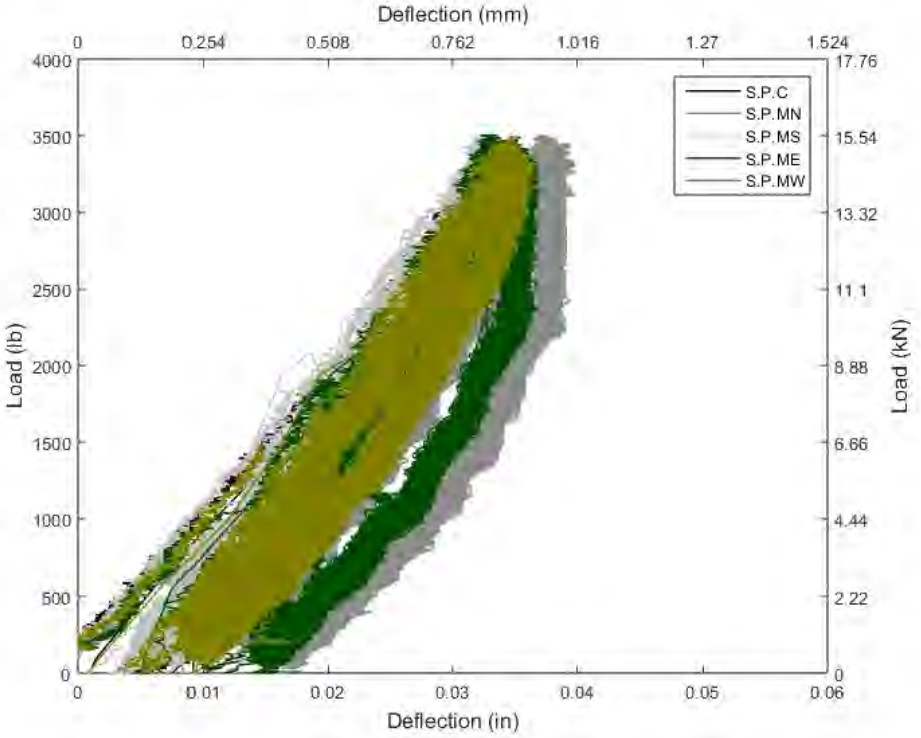


Figure 5.236: Load versus deflection Slab 7.

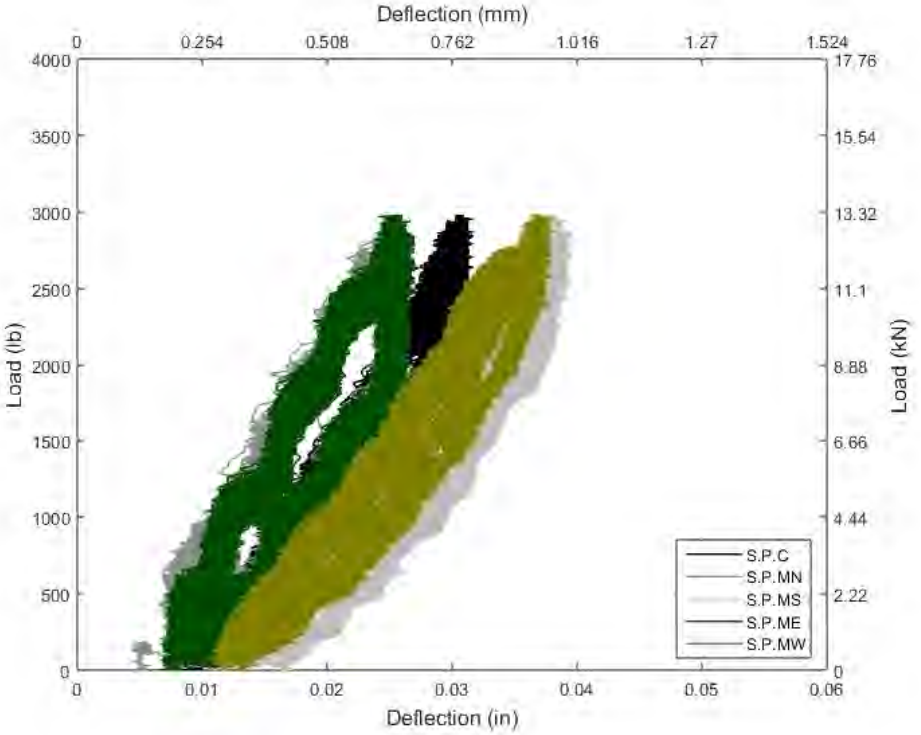


Figure 5.237: Load versus deflection Slab 8.

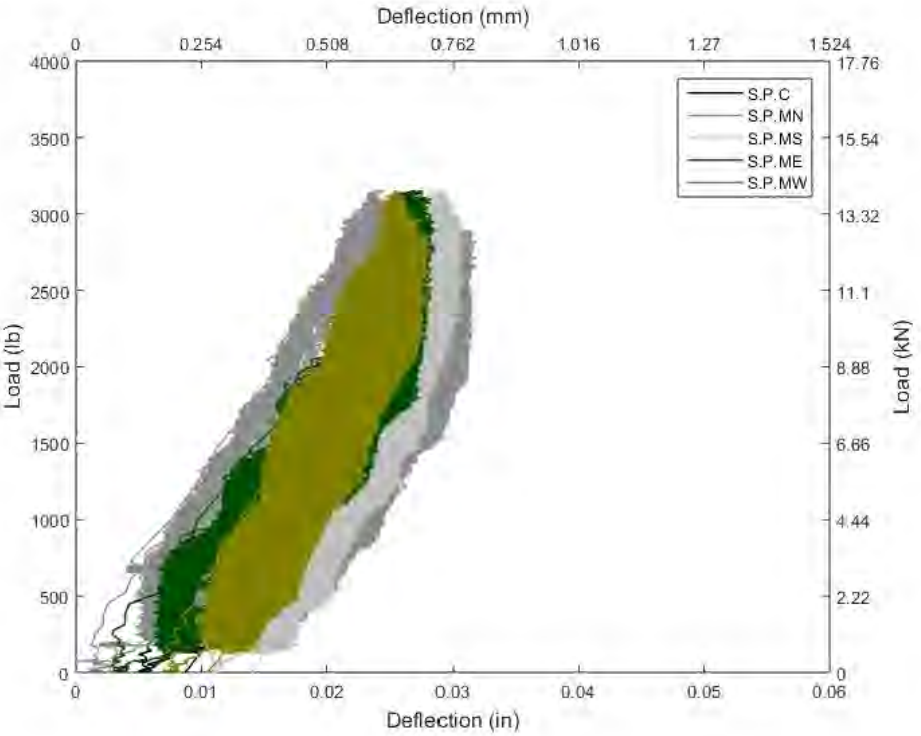


Figure 5.238: Load versus deflection Slab 9.

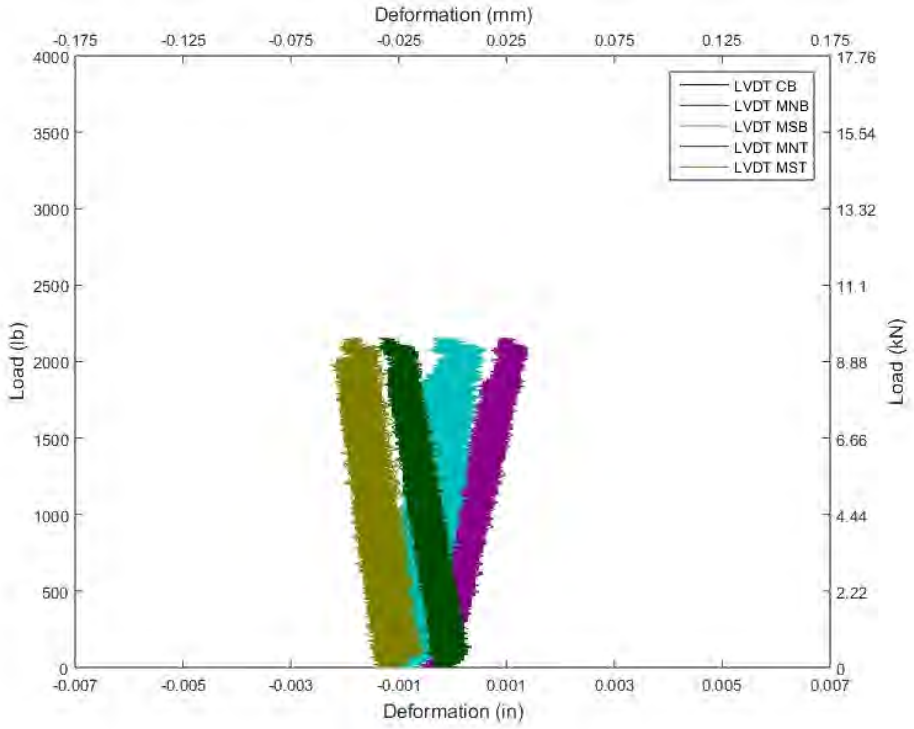


Figure 5.239: Load versus deformation Slab 2.

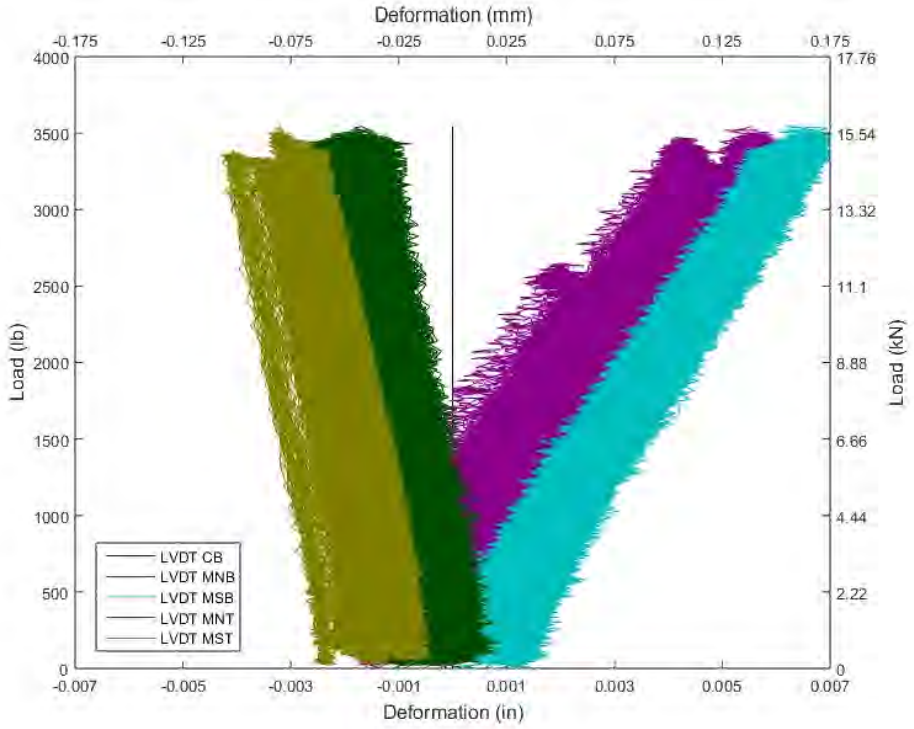


Figure 5.240: Load versus deformation Slab 3.

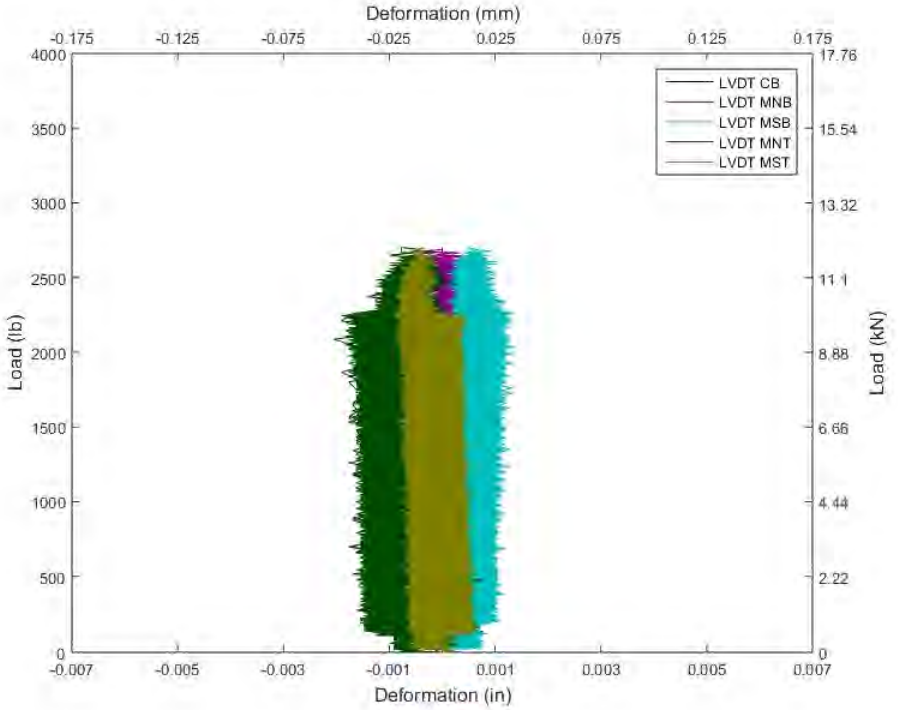


Figure 5.241: Load versus deformation Slab 4 (load applied perpendicular to direction of slope during casting of UHPC).

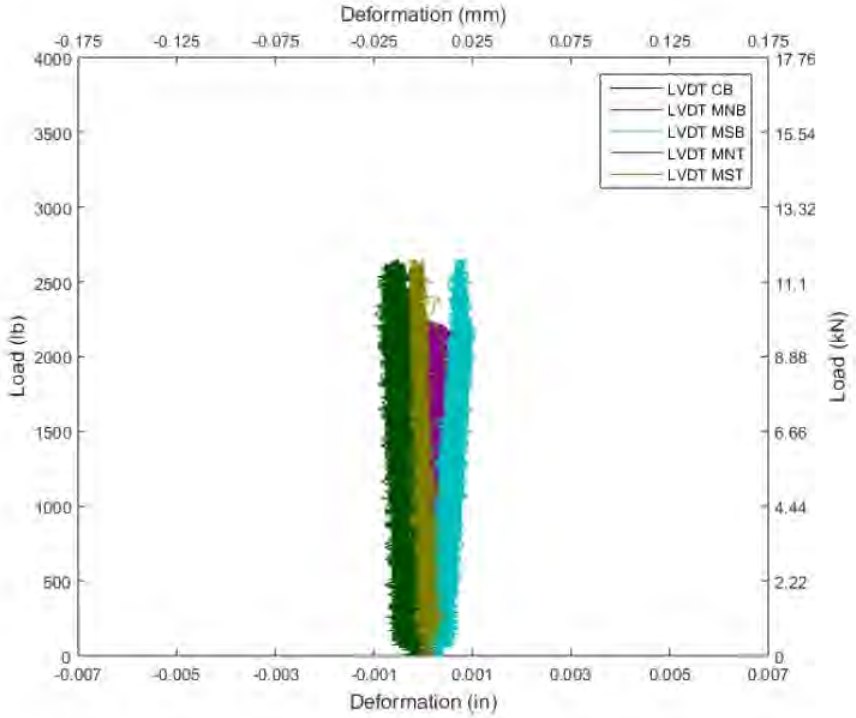


Figure 5.242: Load versus deformation Slab 4 (load applied parallel to direction of slope during casting of UHPC).

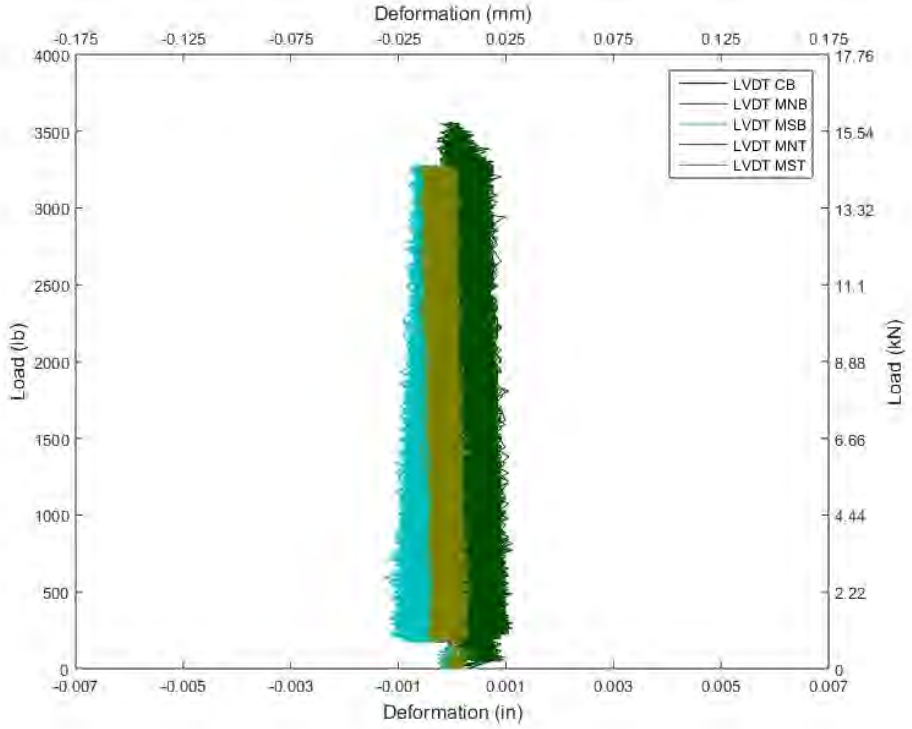


Figure 5.243: Load versus deformation Slab 5.

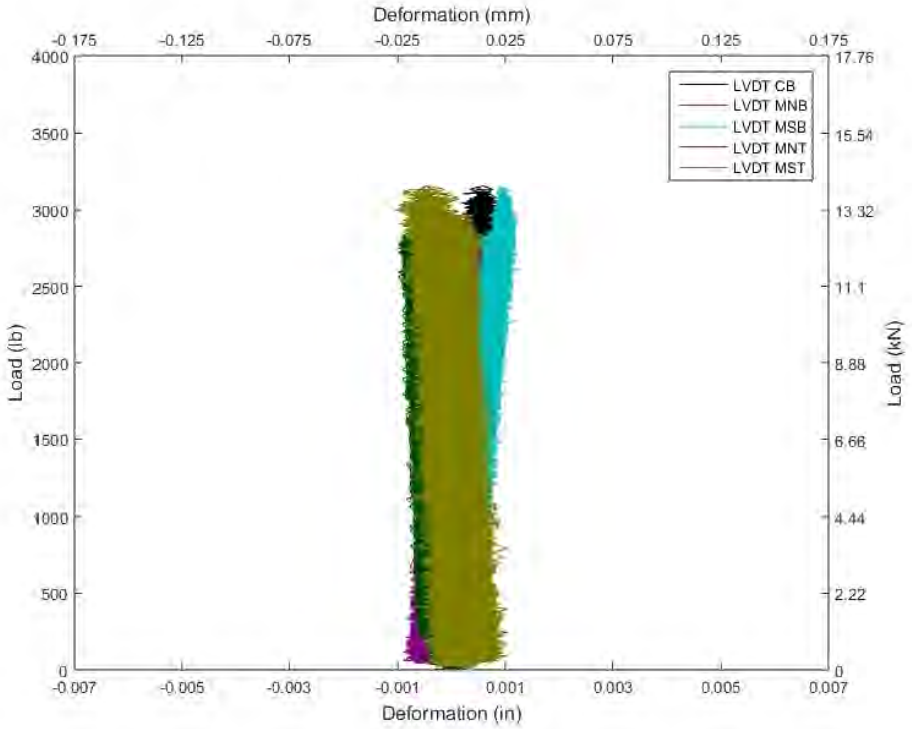


Figure 5.244: Load versus deformation Slab 6.

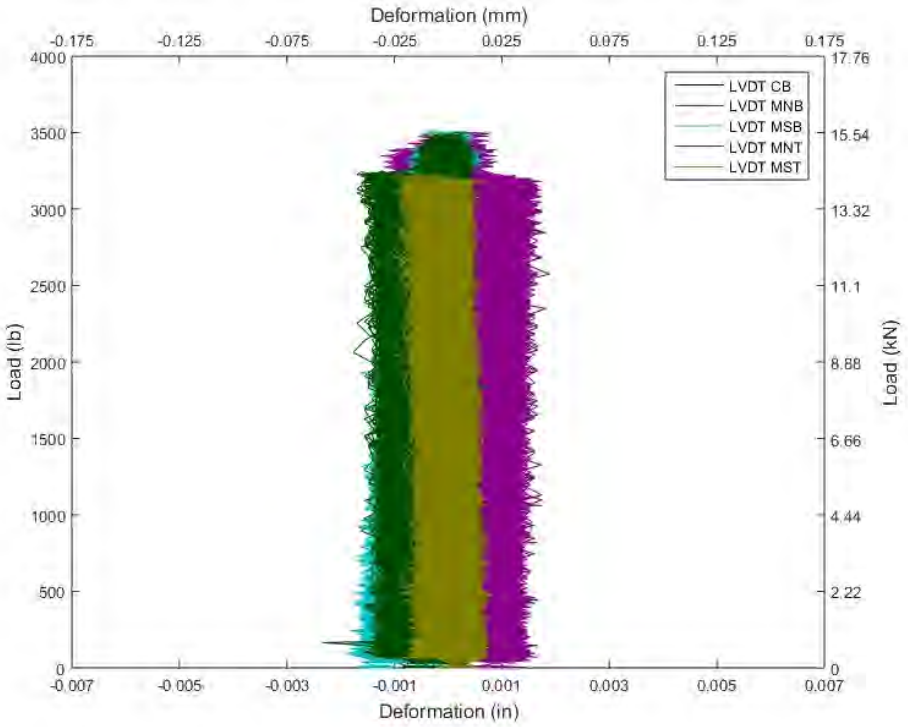


Figure 5.245: Load versus deformation Slab 7.

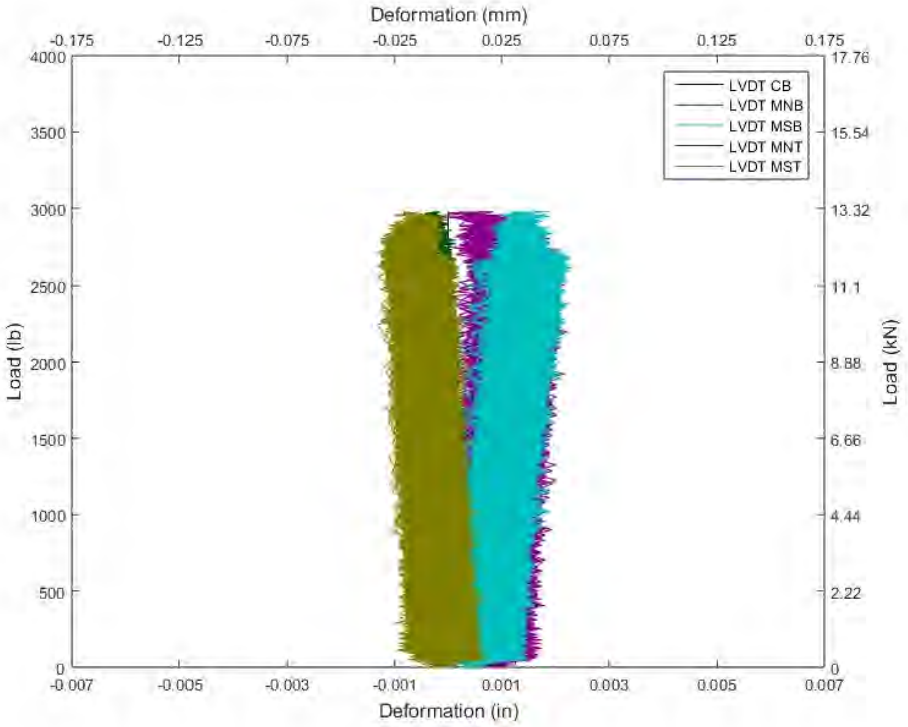


Figure 5.246: Load versus deformation Slab 8.

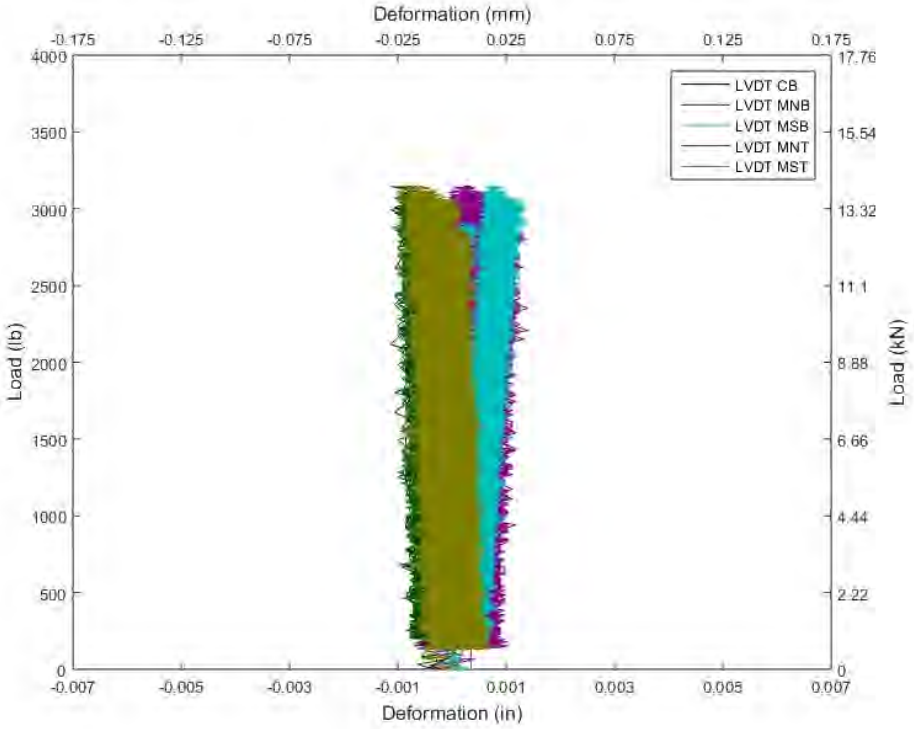


Figure 5.247: Load versus deformation Slab 9.

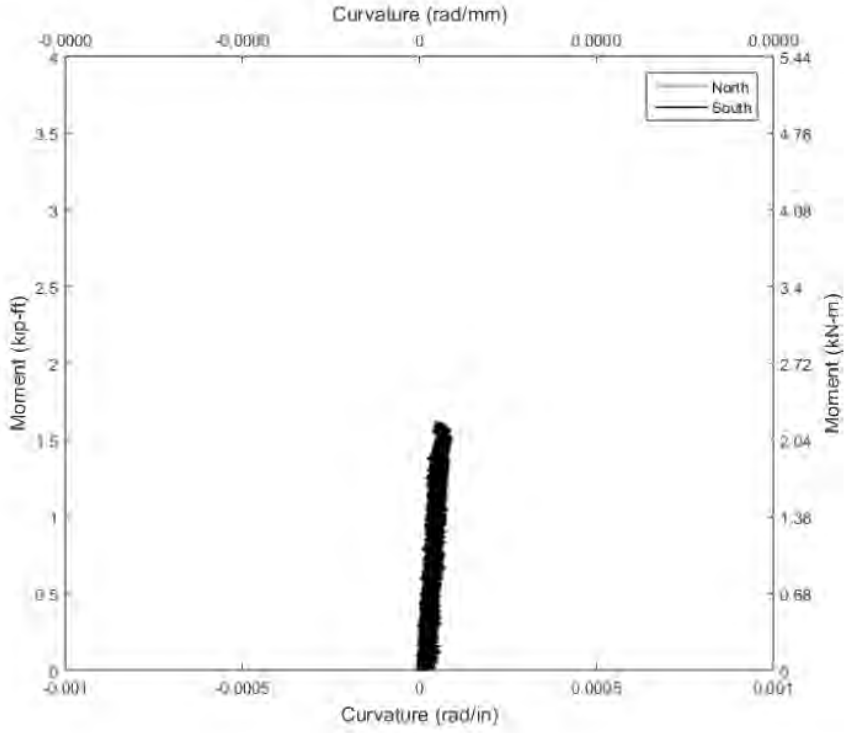


Figure 5.248: Moment curvature behavior Slab 2.

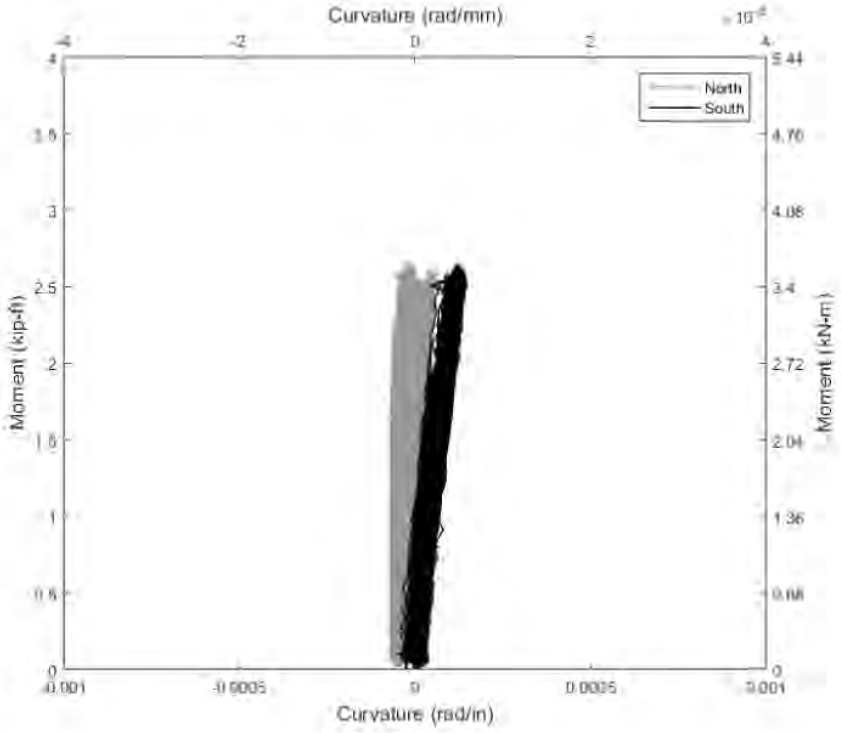


Figure 5.249: Moment curvature behavior Slab 3.

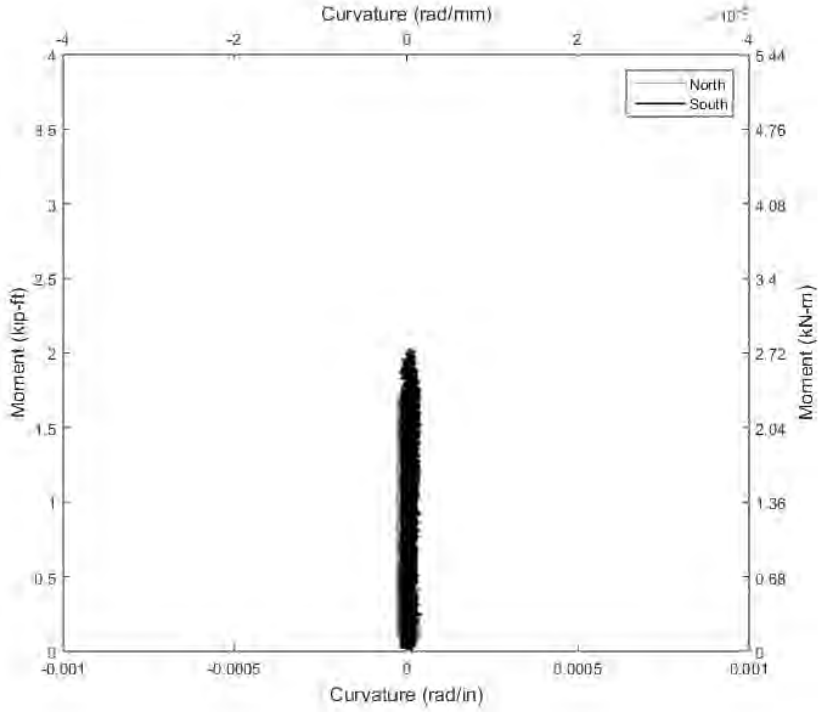


Figure 5.250: Moment curvature behavior Slab 4 (load applied perpendicular to direction of slope during casting of UHPC).

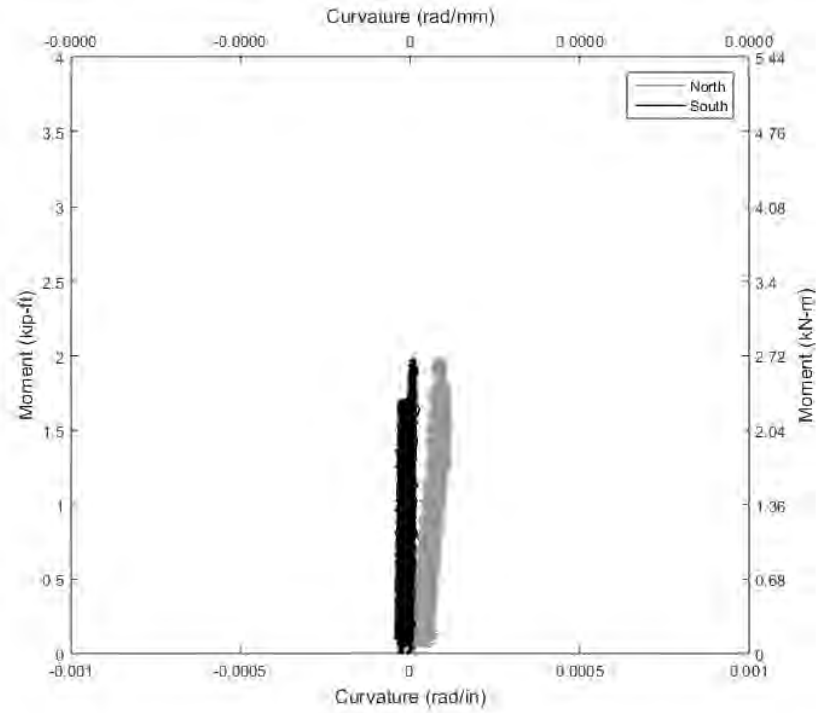


Figure 5.251: Moment curvature behavior Slab 4 (load applied parallel to direction of slope during casting of UHPC).

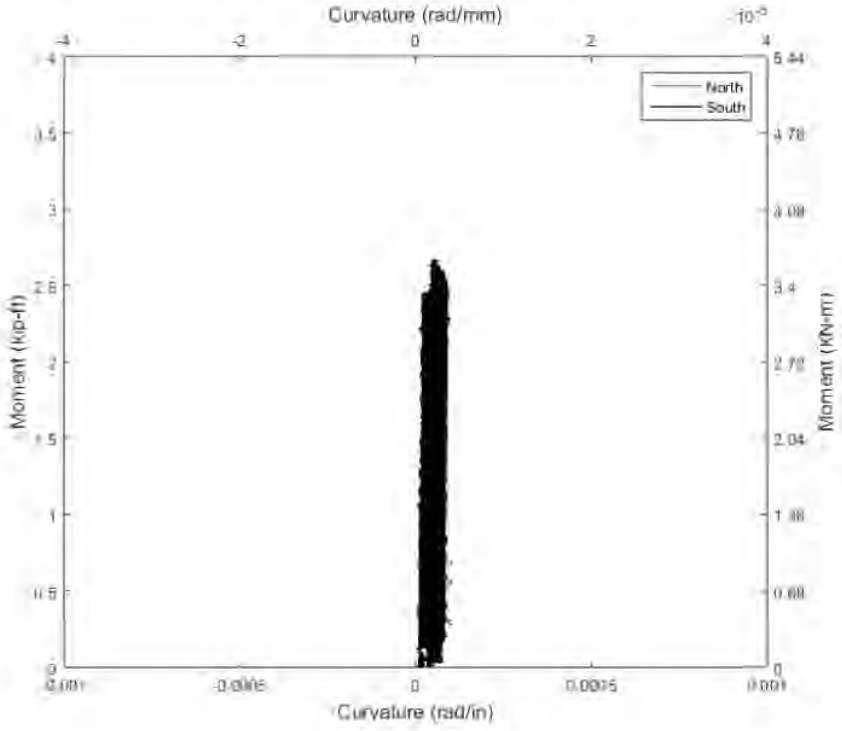


Figure 5.252: Moment curvature behavior Slab 5.

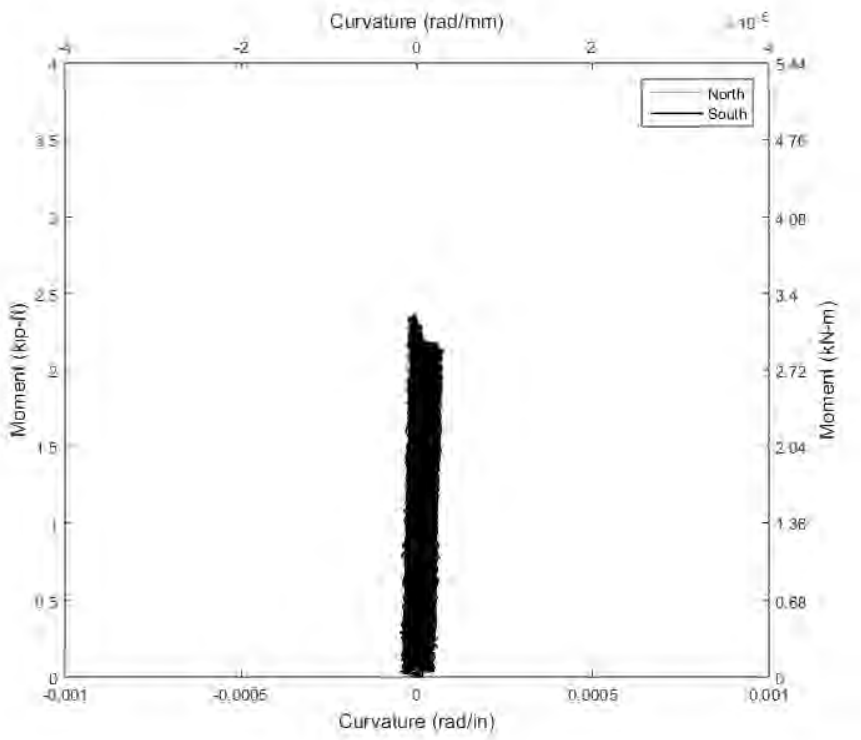


Figure 5.253: Moment curvature behavior Slab 6.

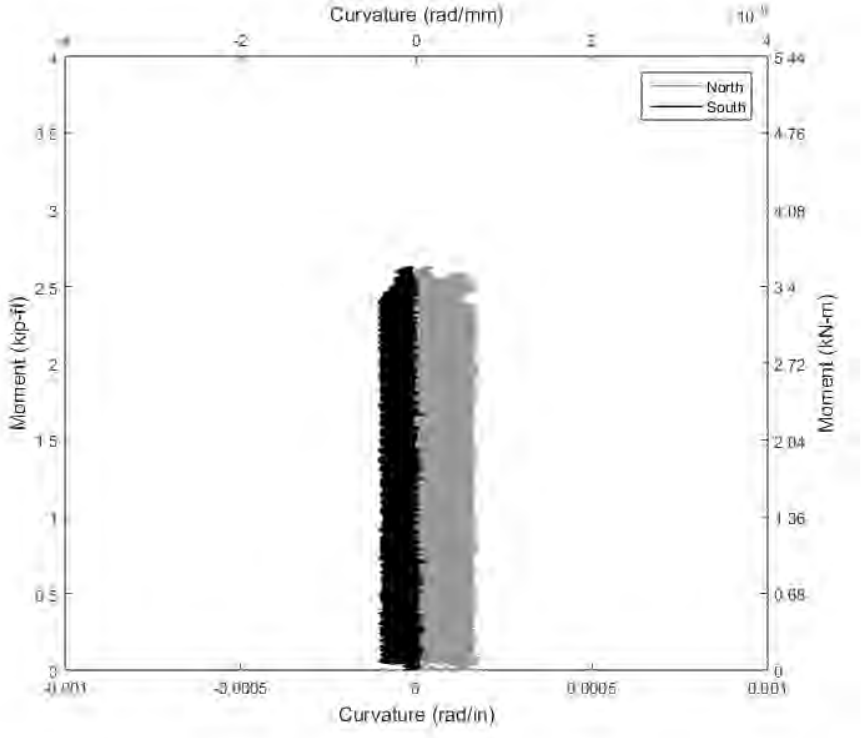


Figure 5.254: Moment curvature behavior Slab 7.

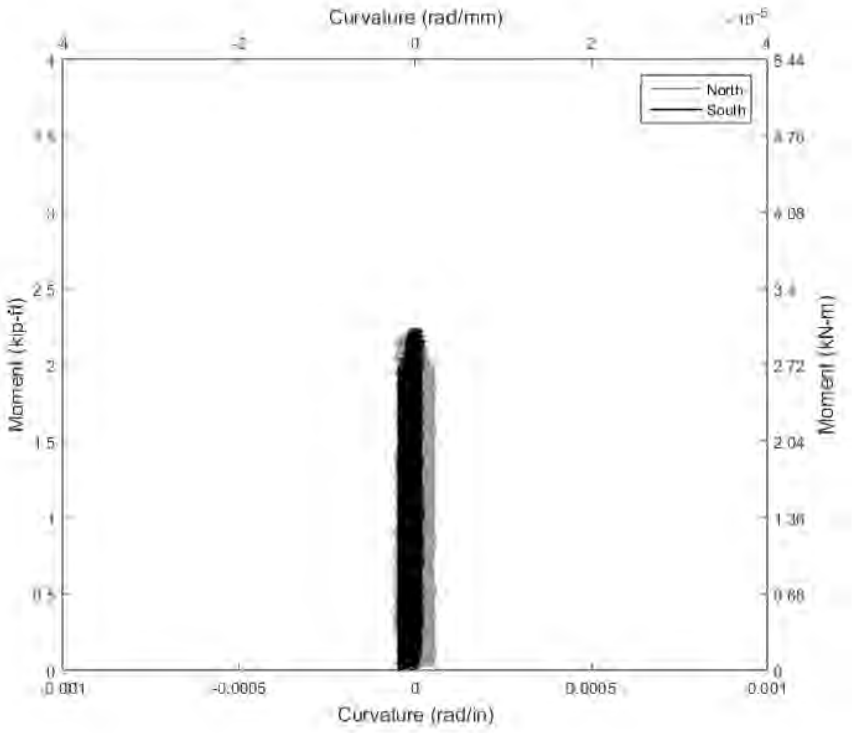


Figure 5.255: Moment curvature behavior Slab 8.

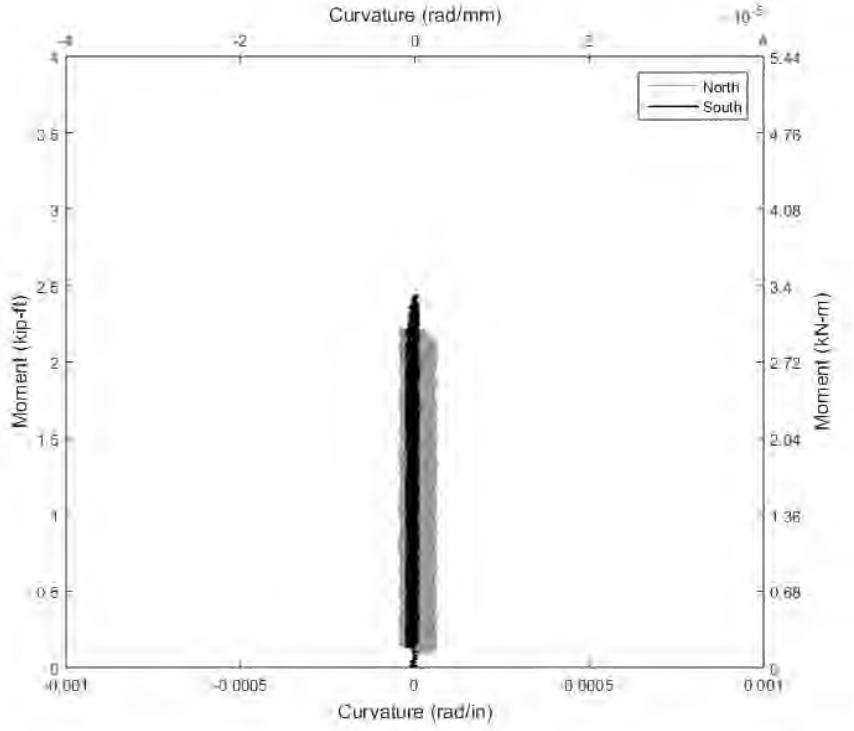


Figure 4.1: Moment curvature behavior Slab 9.

As shown in Figure 5.230 through Figure 5.238, the slabs experienced cracking during the first cycle, as expected, and experienced a small drop in the load-deflection curve. However, the specimen remained in the cracked-linear elastic range of reinforced concrete behavior. The initial crack happened in the substrate NSC. The load applied to the slabs was half of their nominal strength, considering composite behavior between the UHPC overlay and NSC substrate. Considering the composite behavior, this capacity was up to approximately 8.5 times the capacity of the NSC substrate.

Comparing the deflection between Slab 2 (without overlay) and Slab 8 (with overlay) the stiffness of the slab increased approximately 63% due to the application of the UHPC overlay. This indicates that the overlay increased the strength and the stiffness of the member and acts together with the substrate to resist deformation, in addition to reducing the deterioration of the substrate.

Comparing the deflection that the slabs experienced due the load application, it can be observed that the percentage of fibers as well as the thickness of the overlay increased the stiffness of the composite section substantially. Slab 9 (3% fibers) had the smallest deflection, followed by Slab 6 (2% fibers) and Slab 4 (7% slope, 1.5%). The deflection measured for these Slabs 4 and 6 were similar, and a 5% decrease in deflections compared to Slab 9. Therefore, the fiber percentage influenced the stiffness of the composite. Slab 4 (7% slope) had an increase of about 38% stiffness compared with Slab 8 (0 % slope) when Slab 4 was tested perpendicular to the direction of the casting of the slope. The increase may be due to a more favorable orientation of the fibers within the UHPC due to the placement of the overlay at a slope. This can be sustained comparing the results obtained by test Slab 4 in the other orientation (parallel to the direction of load) in which Slab 4 shows a more similar behavior to the other slabs with 1.5% percentage of fibers in UHPC. Slab 9 (3% fibers) had an increase in stiffness of approximately 38% when compared to Slab 8 (1.5% fibers).

The deflections for Slab 7 (6 in. (152 mm) NSC thickness, with No. 4 (No. 13) rebar) had an increase of approximately 7% when compared to Slab 3 (4 in. (102 mm) NSC thickness, and No. 4 (No. 13) rebar). This indicates that the thickness of the substrate is a parameter that can also influence the behavior.

5.4.10.2 Ultimate Load Testing

Ultimate flexural load testing was performed on all the slabs. For Slab 1 of 4 in. (102 mm) NSC substrate, No. 3 (No. 10) reinforcement, and 1 in. (254 mm) UHPC overlay of 1.5% fibers, DIC was used to provide additional information on the behavior of the composite section. The Slab 1 was cycled three times from zero to half of its capacity. Then three additional cycles were performed at its estimated maximum capacity. After the cycles, the slab was loaded to failure. For the other slabs, only five cycles to half of their capacity were performed prior to take them to failure. For this test, an analysis of the load-deflection, load-deformation, and moment-curvature behavior was conducted. For these analyses, load versus the vertical deflection of the slab were plotted using the data of string potentiometers (using the same notation as the cyclic load test). For load versus deformation, the LVDTs horizontal deformation positioned at the same spots as the cyclic load test were used. For the third analysis, the moment was determined from the load measured by the internal load cell and the curvature was calculated using the deformation measured by the LVDTs from the south and north side of the slab. Curvature was only calculated on the south side in Slab 1 because the DIC was on the north side.

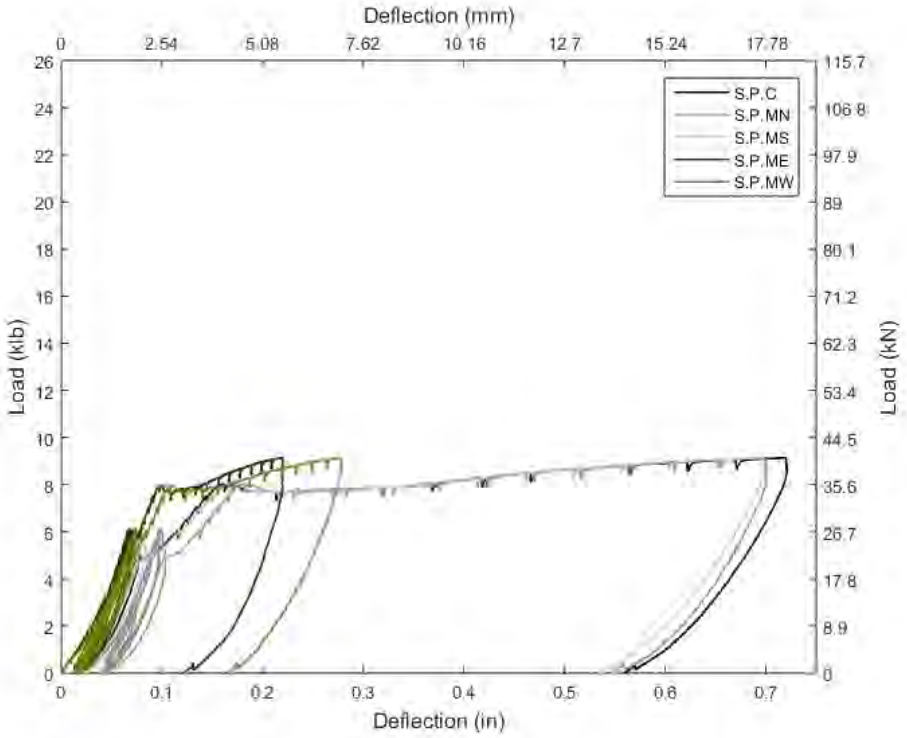


Figure 5.256: Load versus deflection Slab 1.

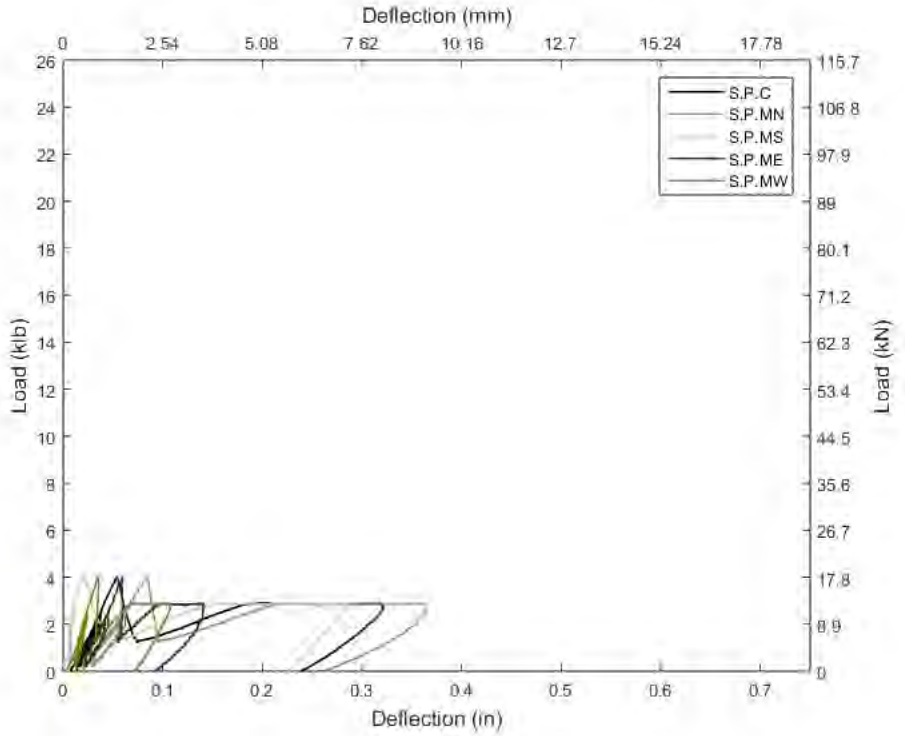


Figure 5.257: Load versus deflection Slab 2.

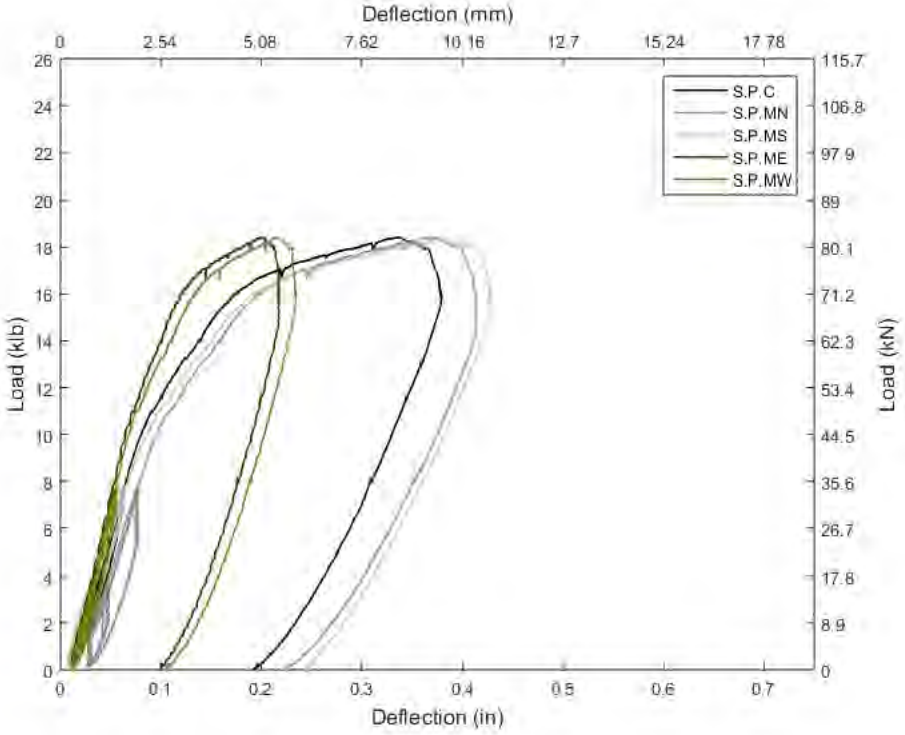


Figure 5.258: Load versus deflection Slab 3.

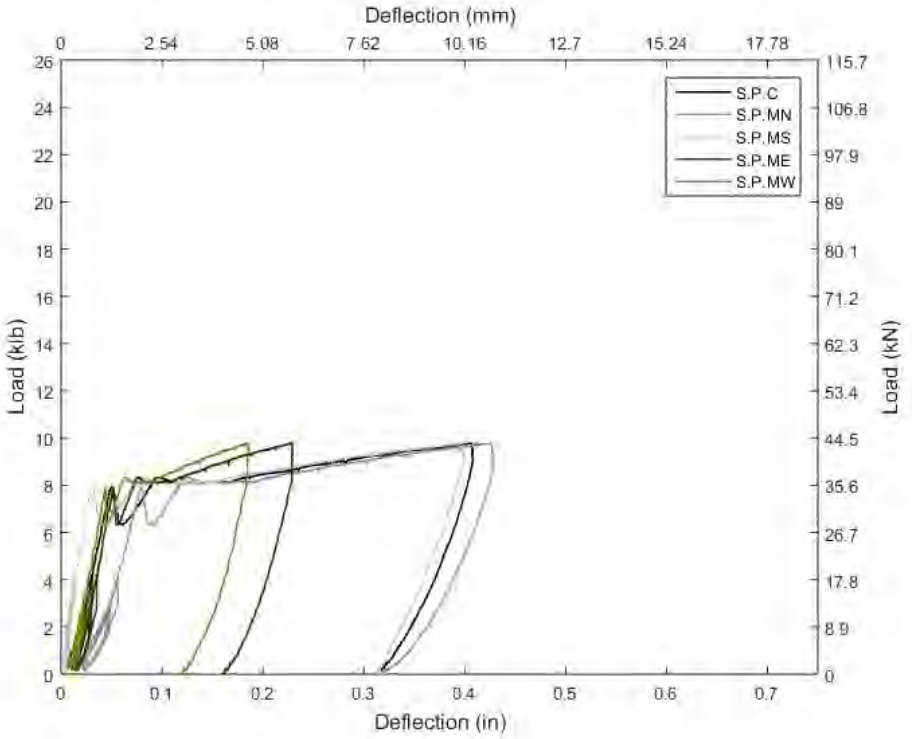


Figure 5.259: Load versus deflection Slab 4.

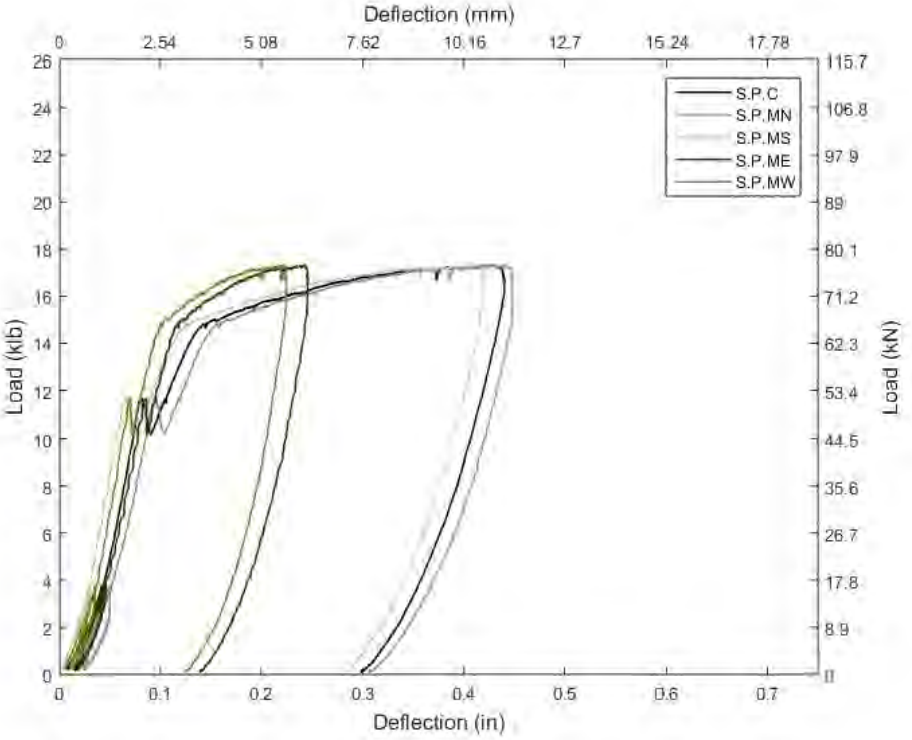


Figure 5.260: Load versus deflection Slab 5.

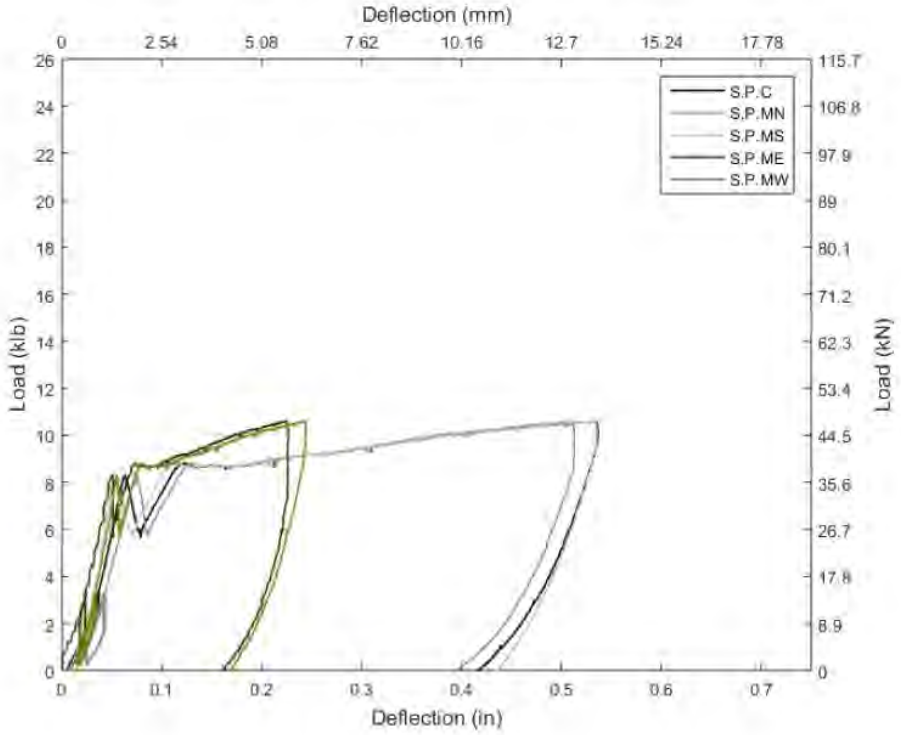


Figure 5.261: Load versus deflection Slab 6.

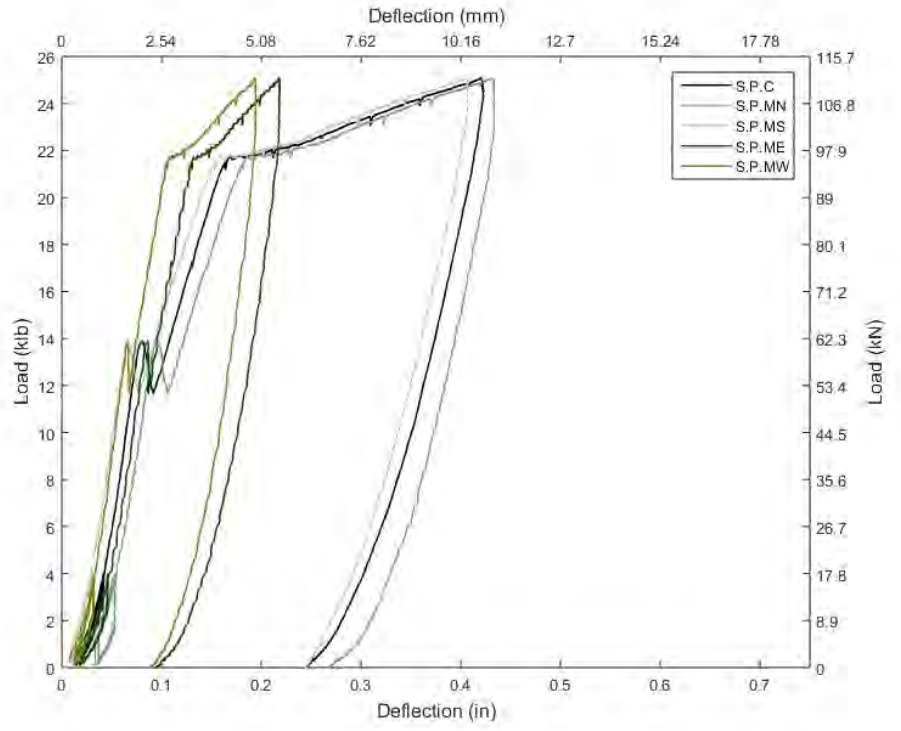


Figure 5.262: Load versus deflection Slab 7.

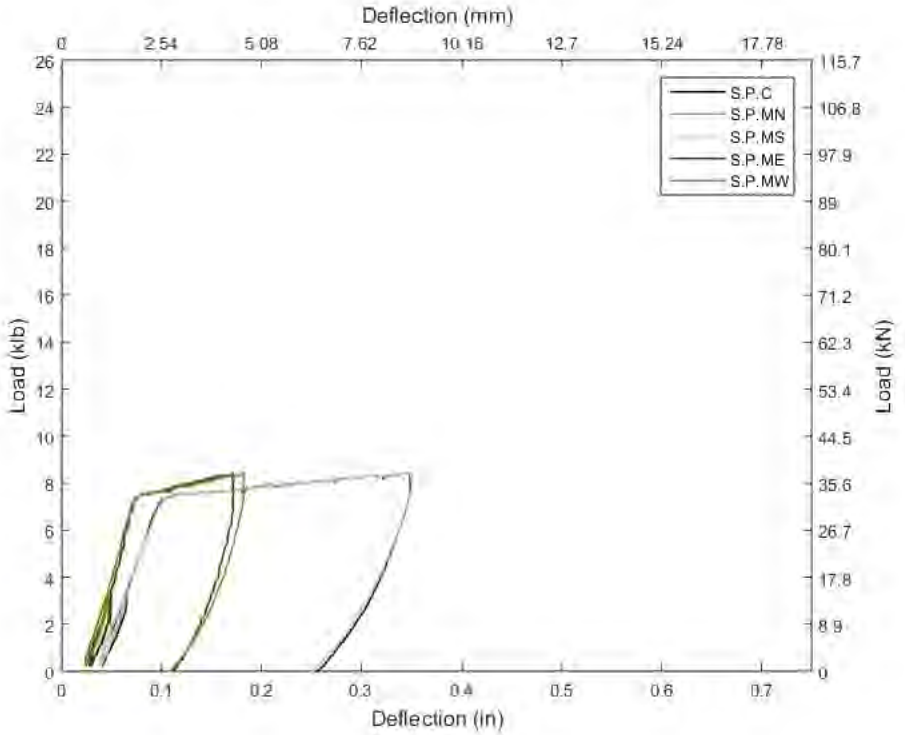


Figure 5.263: Load versus deflection Slab 8.

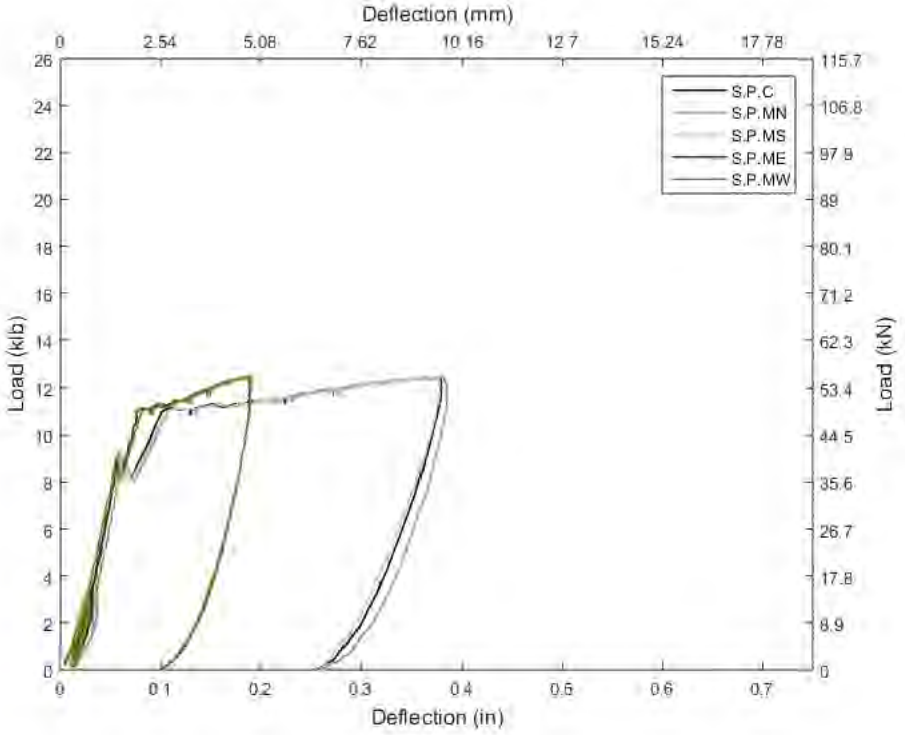


Figure 5.264: Load versus deflection Slab 9.

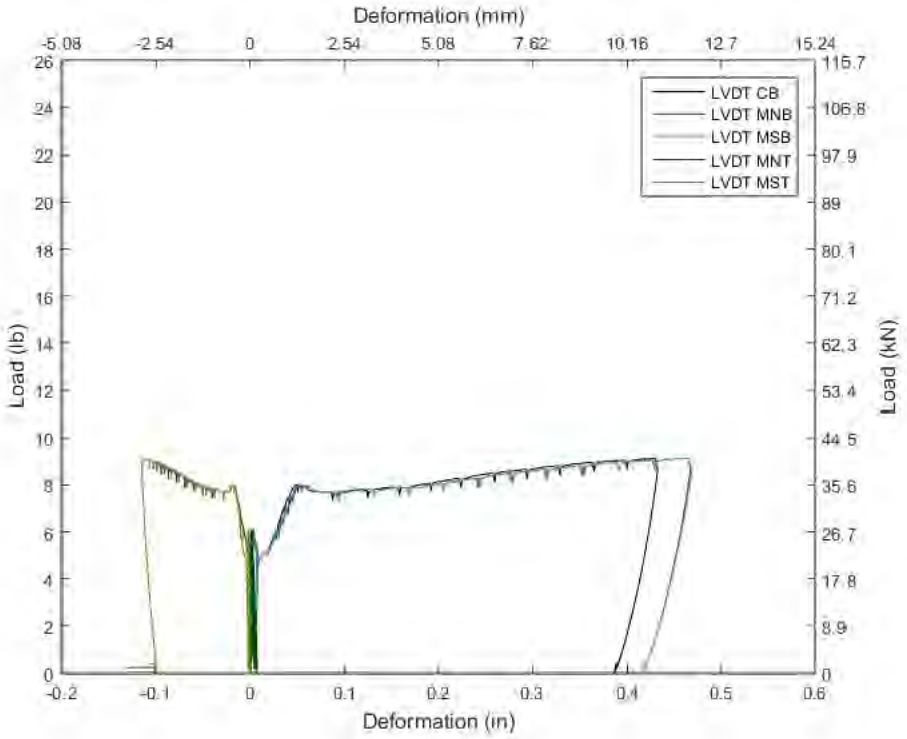


Figure 5.265: Load versus deformation Slab 1.

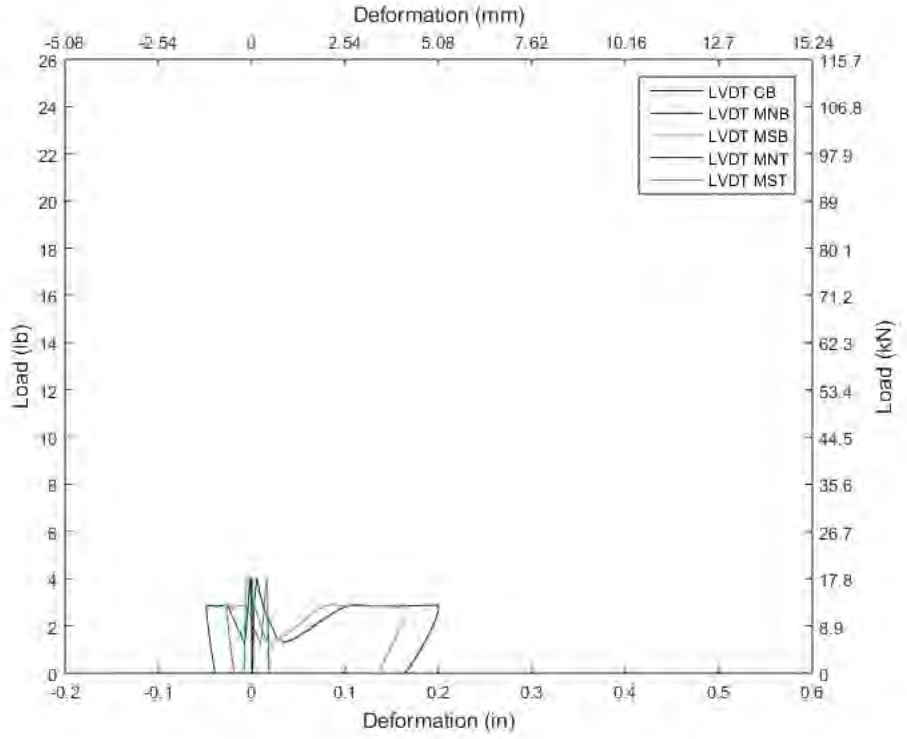


Figure 5.266: Load versus deformation Slab 2.

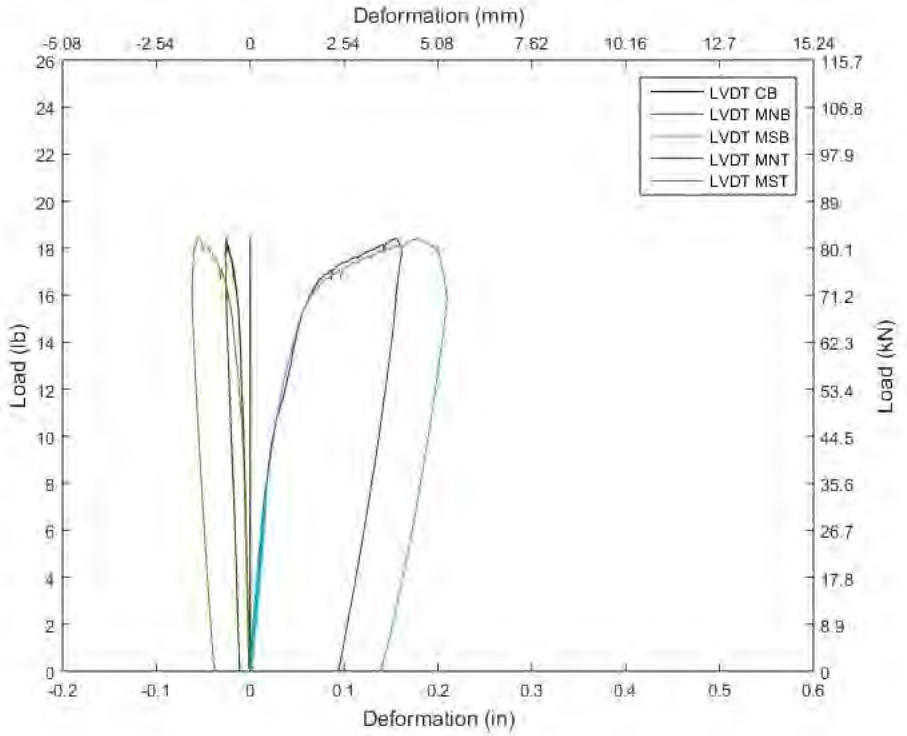


Figure 5.267: Load versus deformation Slab 3.

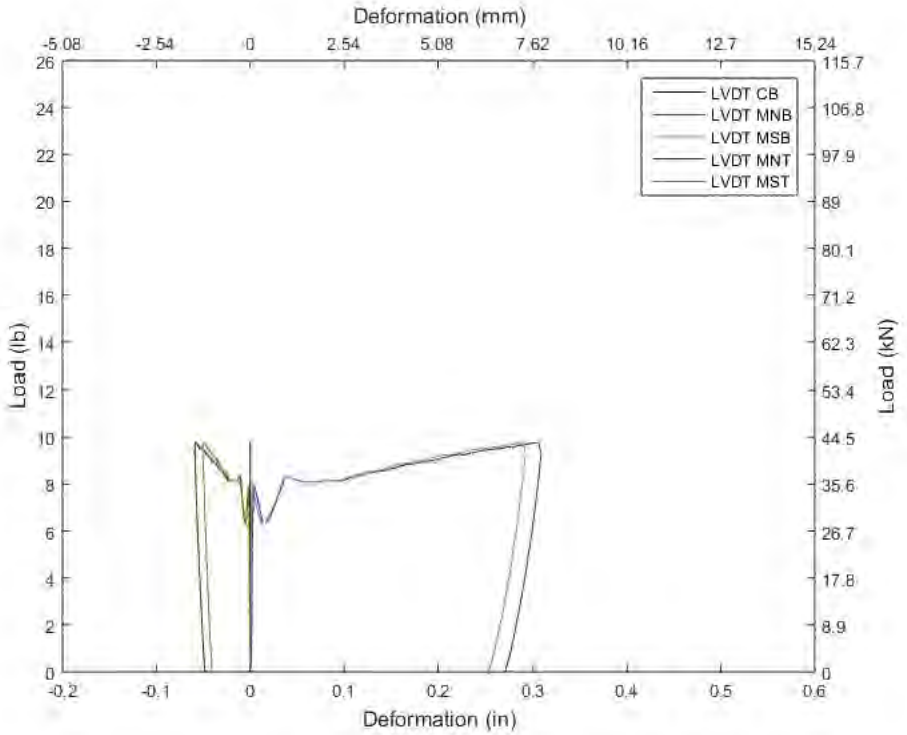


Figure 5.268: Load versus deformation Slab 4.

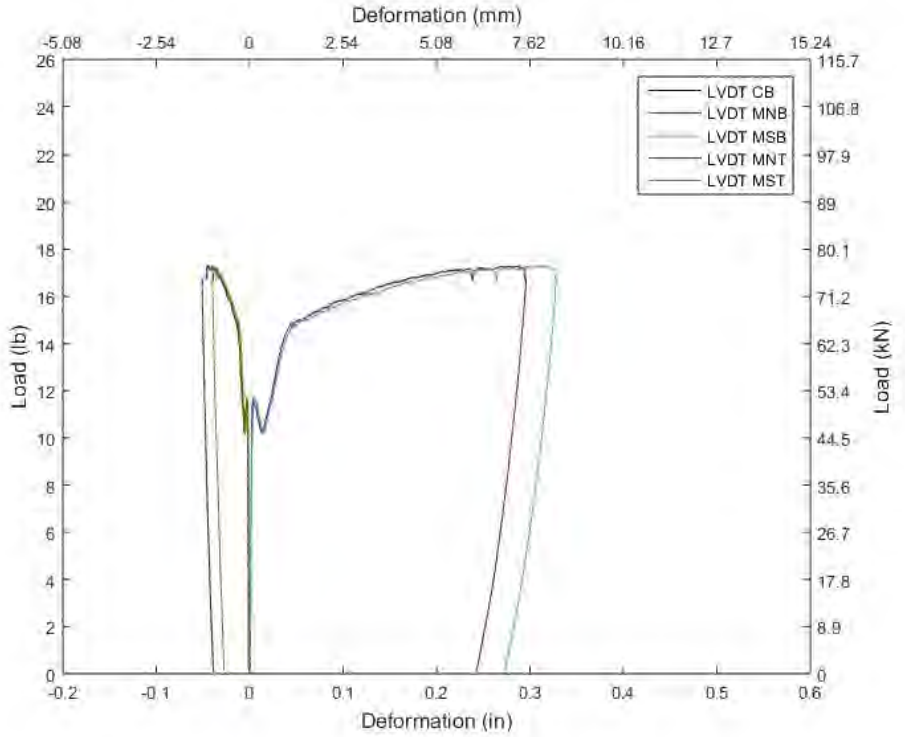


Figure 5.269: Load versus deformation Slab 5.

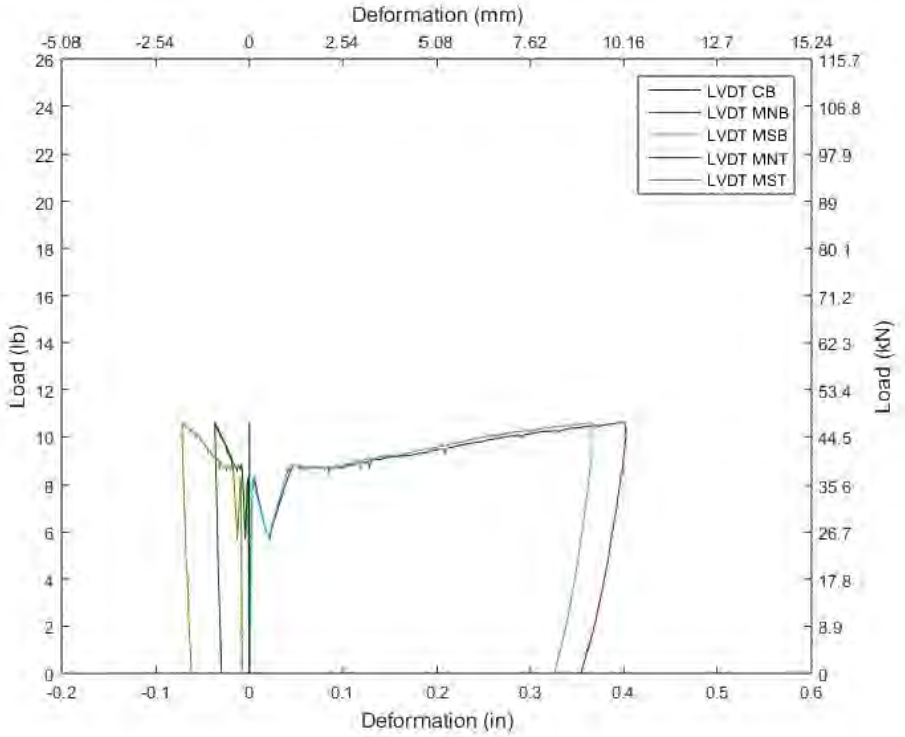


Figure 5.270: Load versus deformation Slab 6.

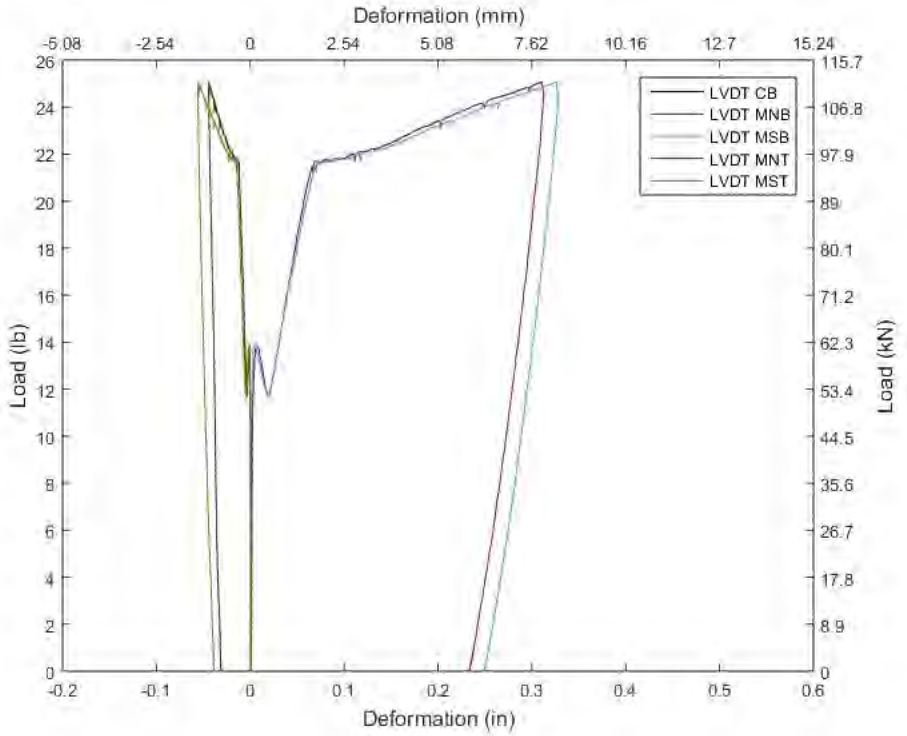


Figure 5.271: Load versus deformation Slab 7.

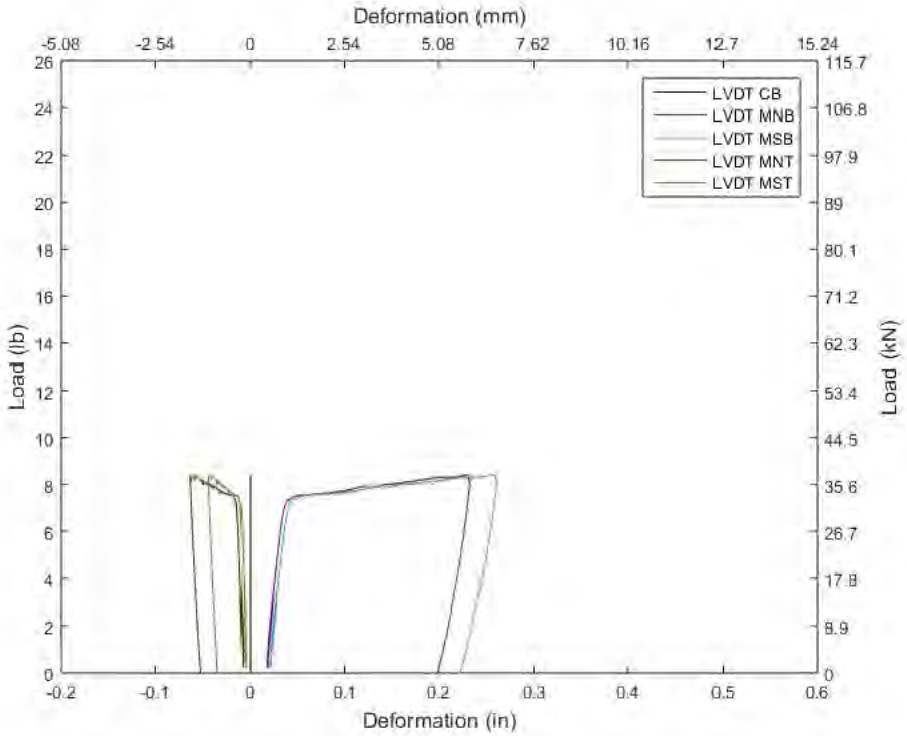


Figure 5.272: Load versus deformation Slab 8.

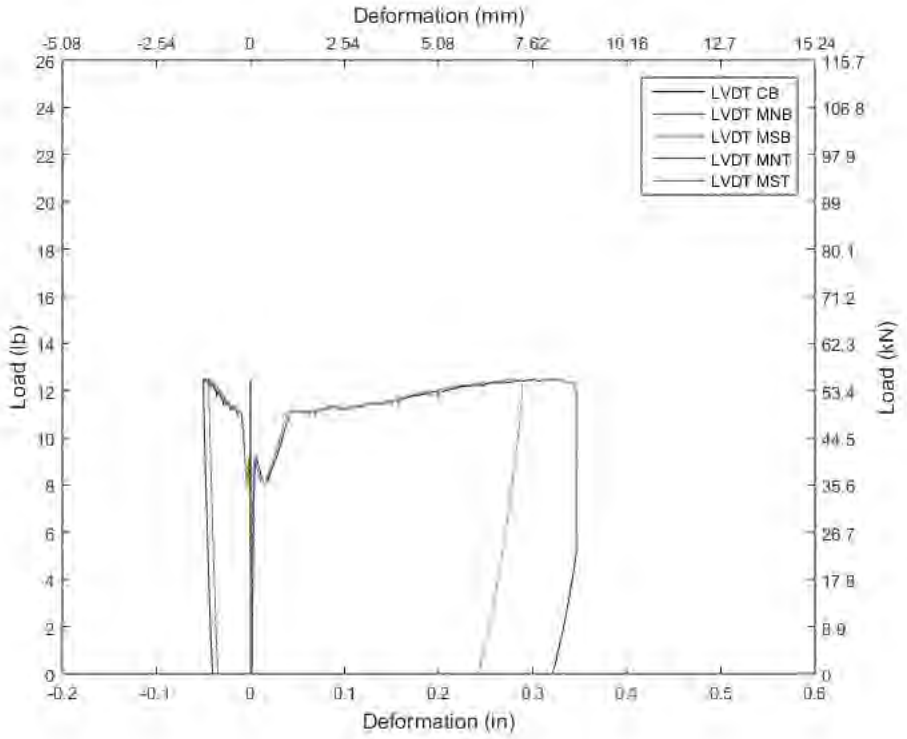


Figure 5.273: Load versus deformation Slab 9.

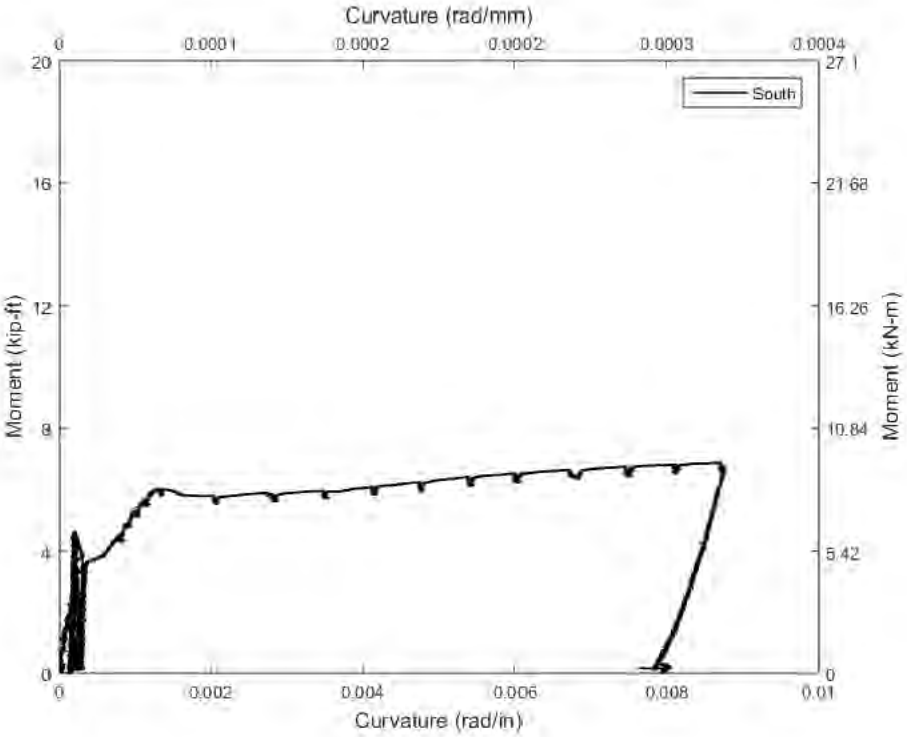


Figure 5.274: Moment curvature behavior Slab 1.

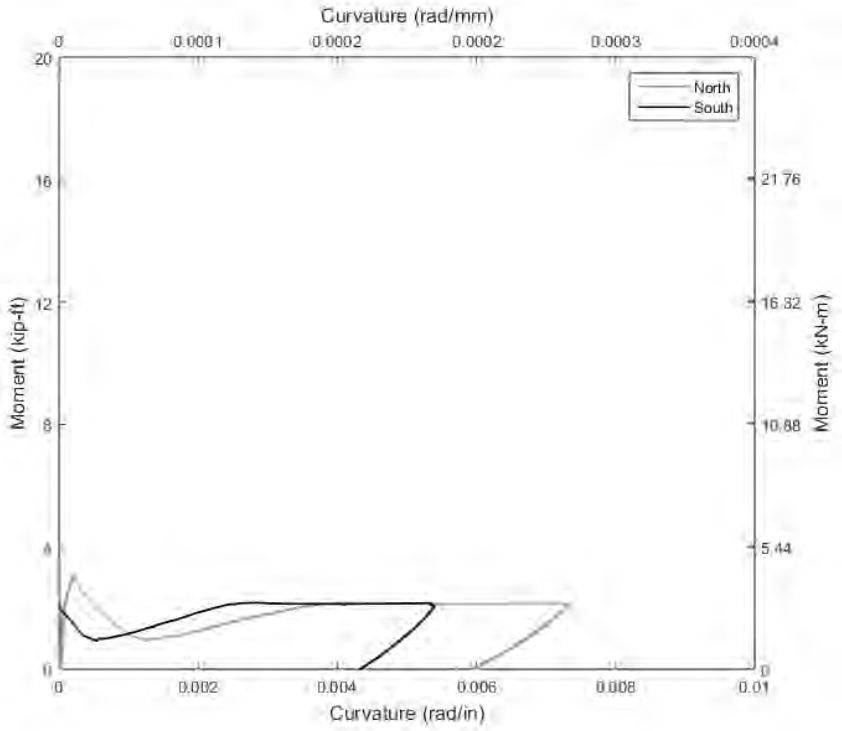


Figure 5.275: Moment curvature behavior Slab 2.

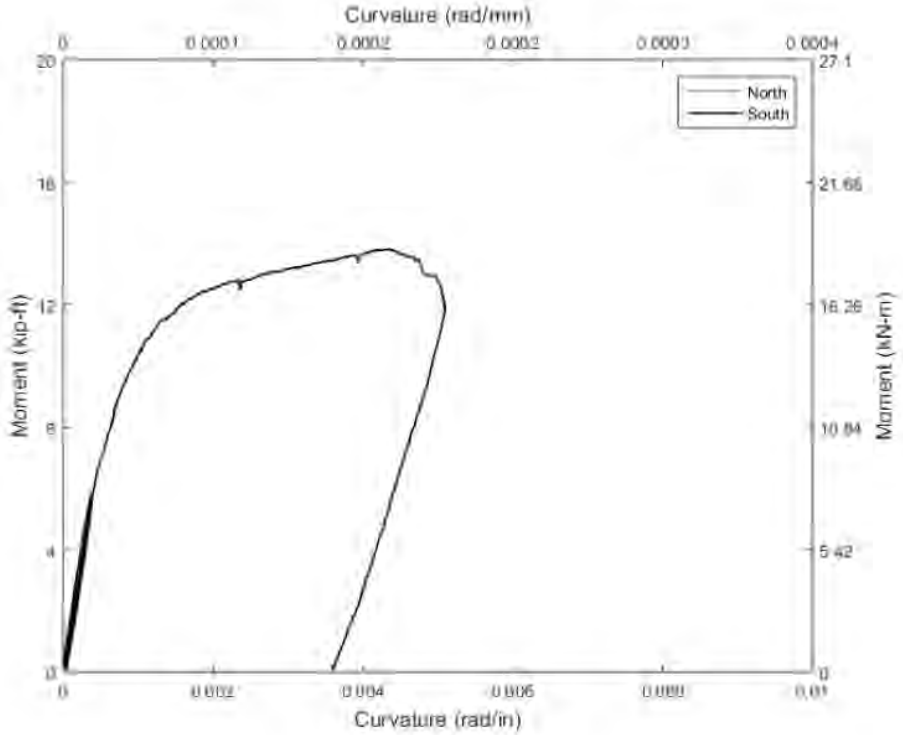


Figure 5.276: Moment curvature behavior Slab 3.

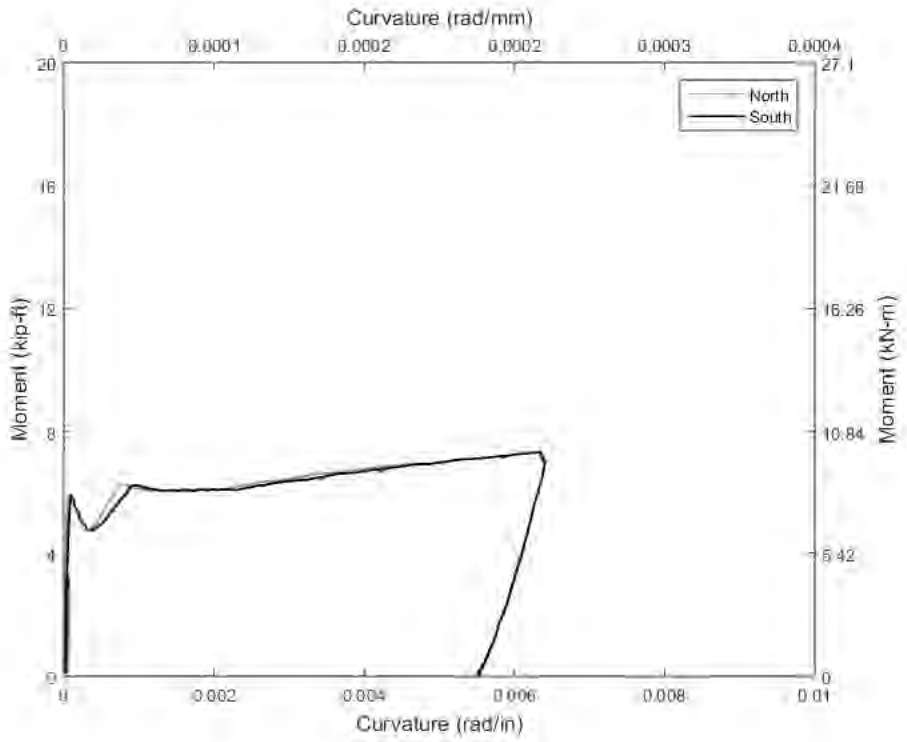


Figure 5.277: Moment curvature behavior Slab 4.

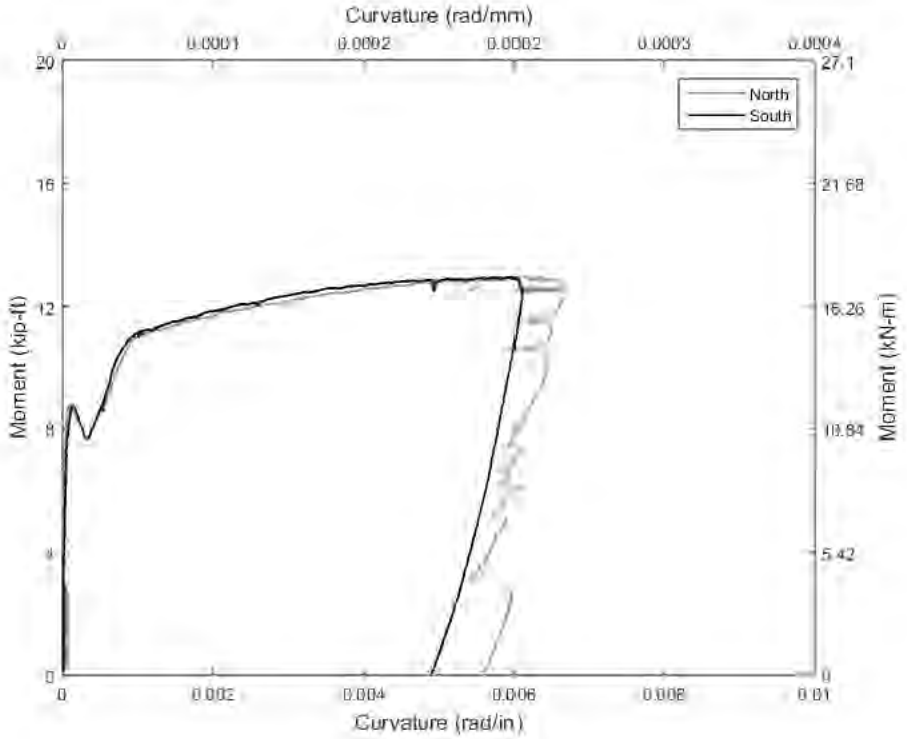


Figure 5.278: Moment curvature behavior Slab 5.

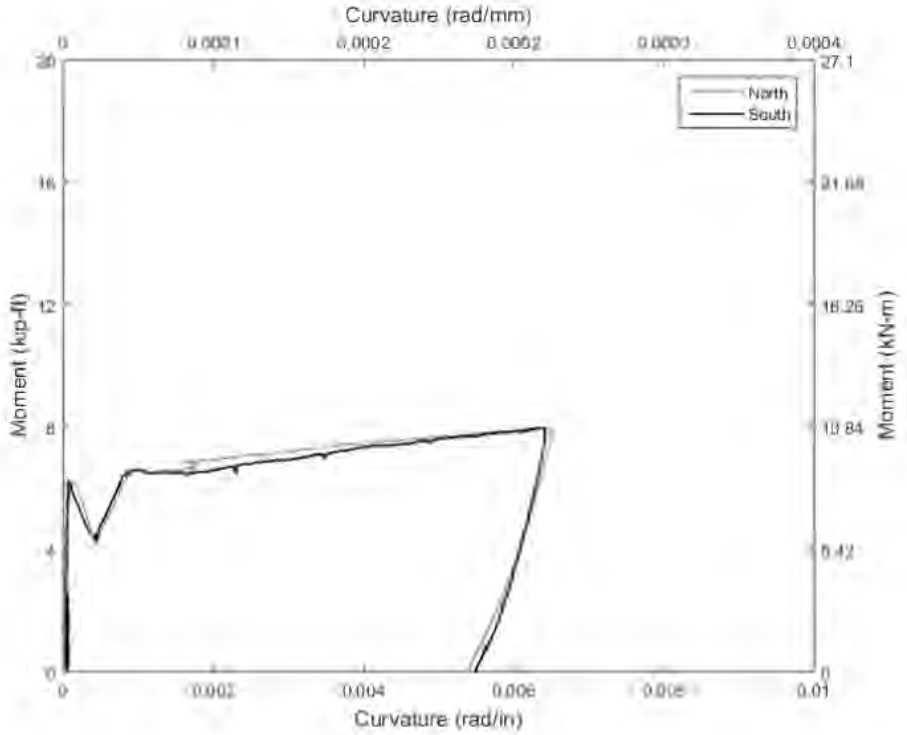


Figure 5.279: Moment curvature behavior Slab 6.

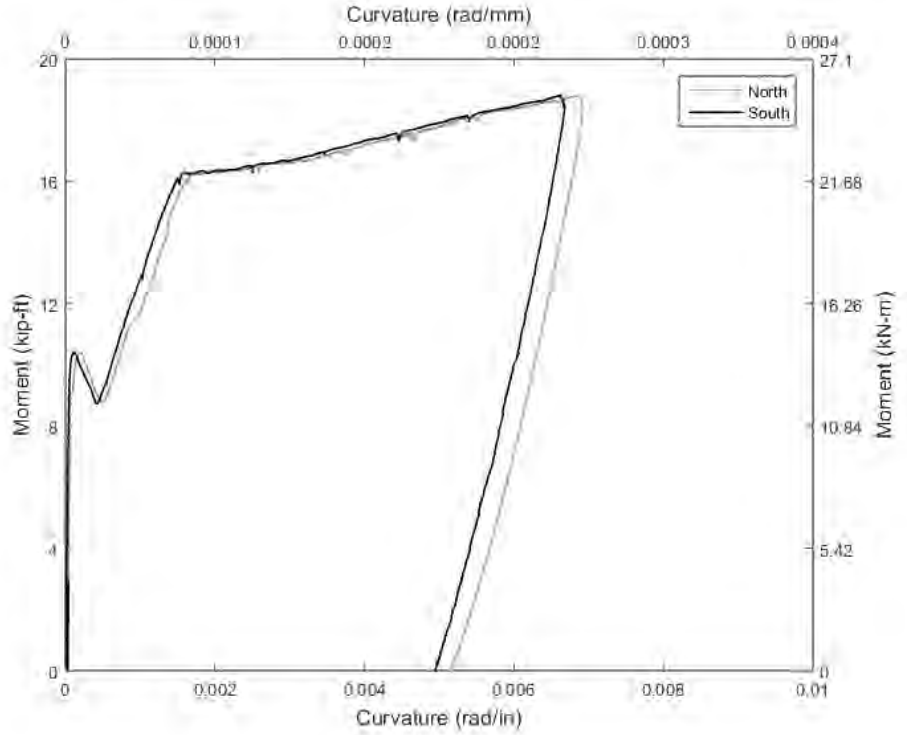


Figure 5.280: Moment curvature behavior Slab 7.

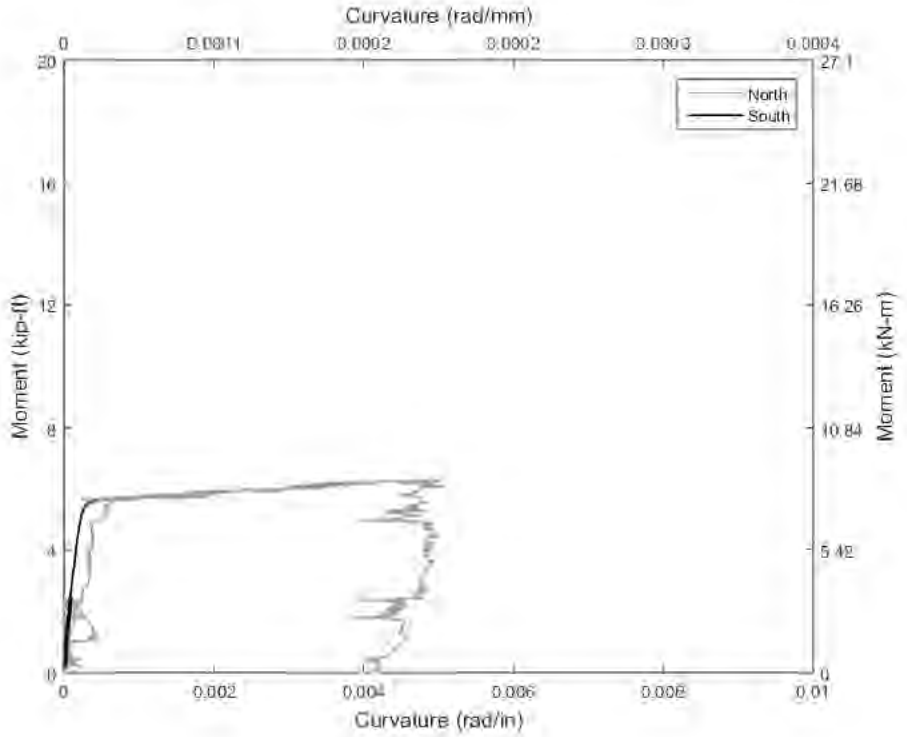


Figure 5.281: Moment curvature behavior Slab 8.

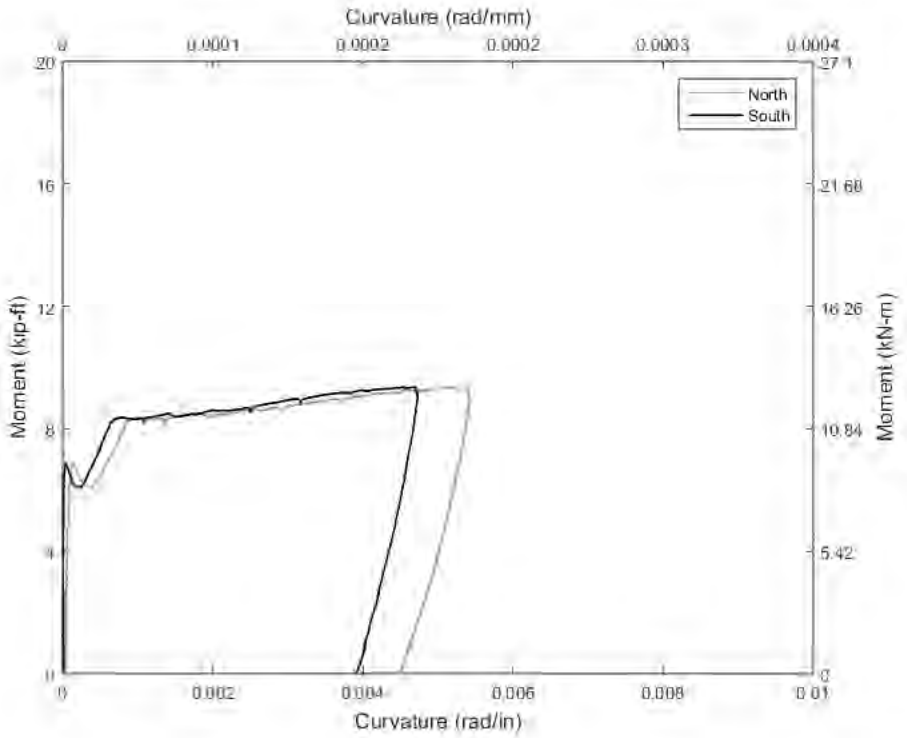


Figure 5.282: Moment curvature behavior Slab 9.

As shown in Figure 5.256, the failure load for Slab 1 was 9100 lb (40.5 kN) with a maximum deflection of 0.72 in. (18.3 mm) measured at the center of the slab. The deflections measured by the three string potentiometers at midspan along the same line in which the load was applied was greater than the recorded by the potentiometers that were closer to the supports. This indicates that the slab was experiencing a one-way deflection. In Figure 5.265, the deformation in the LVDTs that were placed at the top of the overlay measured negative, or compressive, deformations. The LVDTs near the bottom measured positive, or tensile, deformations due to flexure. At approximately at 5000 lb (22.2 kN), the system began to soften and go into the non-linear elastic region. At this point, the deformations start growing more rapidly as the load continued to be applied measuring a maximum deflection at 0.46 in. (11.7 mm) at the final load of 9100 lb (40.5 kN). Figure 5.274 shows the moment-curvature relationship, which is similar to the load-deflection behavior. The maximum measured curvature was 0.012 rad/in. (0.0005 rad/mm) at a maximum moment of 6.8 kips-ft (9.2 kN-m).

Comparing the results obtained from all the Slabs, Slab 7 is the one that sustained more load and staying at similar maximum deformation compare with Slab 3, 4, 5 having a maximum deflection of about 0.42 in. (10.67 mm). As shown in Figures 4.65 to 4.91, the slabs have a sudden failure before continuing sustaining more load. This sudden failure occurs when the crack at midspan in the Slabs started to show in the vertical face in north and south sides. By the values obtained in this test, the UHPC overlay provides an increase in the load capacity of the slabs and reducing the deformation of the specimen. Comparing results from Slab 2 (without overlay) and Slab 3 (with overlay), the deformation of these two were similar of about 10% of difference, but the load that was applied in Slab 3 was about 4.5 times more than the load applied in Slab 2.

The final deformation of Slab 1 with overlay and Slab 2 without overlay are shown in Figure 5.283 and Figure 5.284 respectively. In this figure the crack started growing at midspan throw the whole length of the slab, and in the case of Slab 1 the crack was propagated to the UHPC due to transfer to stresses to the overlay. Similar behavior to Slab 1 was found in all the other slabs. The data obtained by DIC consisted of deflection and strain measurements at different load stages. This method was used during the ultimate load flexural test performed on Slab 1. The failure load recorded for Slab 1 was 9100 lb (40.5 kN), when this load was applied the total deflection recorded at the top of the slab was approximately 0.55 in. (14 mm). Figure 5.285 show the vertical displacement recorded by DIC in which the bottom of the figure is the midspan of the slab. The displacement closer to midspan (bottom of the figure) was not captured due to obscured area created by distribution beam used in the flexural test. The displacement of the slab in Figure 5.286 shown that was deflecting uniformly across its width, which means that the slab was deflecting in one-way action. This is also confirmed by the strain measured by DIC (Figure 5.287 and Figure 5.288 when the actuator was applying 8900 lb (39.6 kN) load, were the strains showed higher values at the center of the slab in the range of 2000 με.

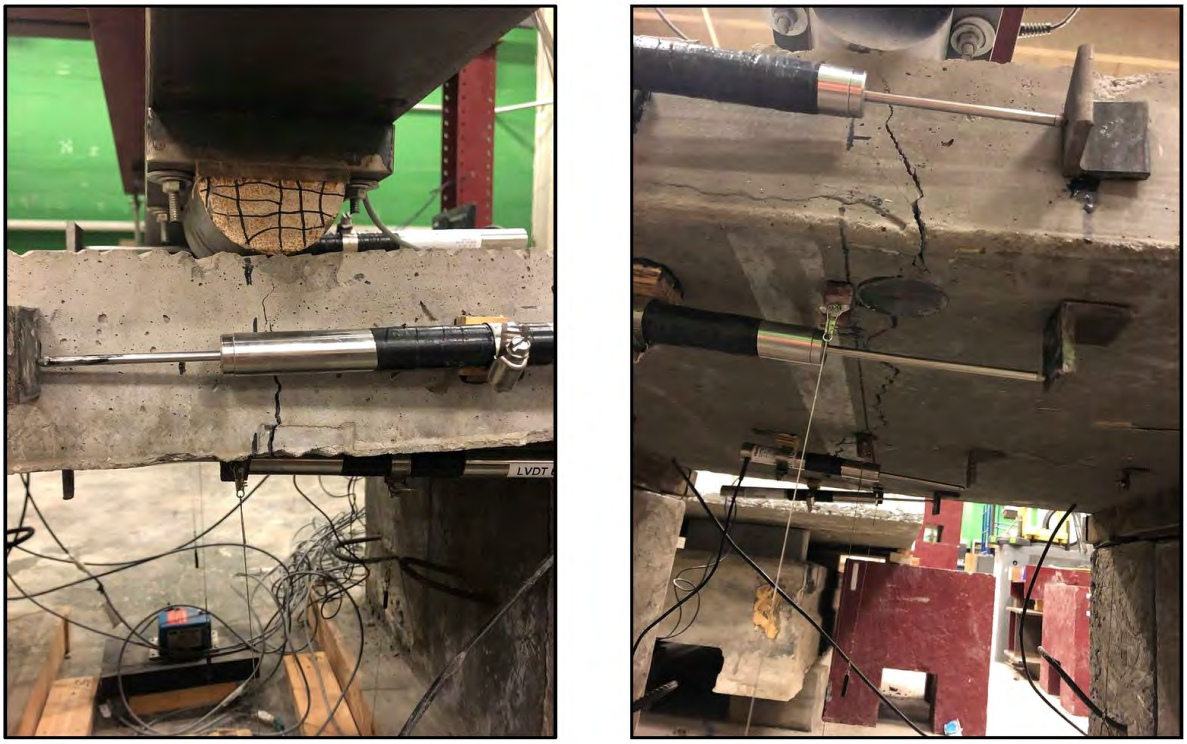


(a)



(b)

Figure 5.283: Final deformation of Slab 1 – (a) South side view and (b) bottom view.



(a) (b)

Figure 5.284: Final deformation of Slab 2 – (a) South side view and (b) bottom view.

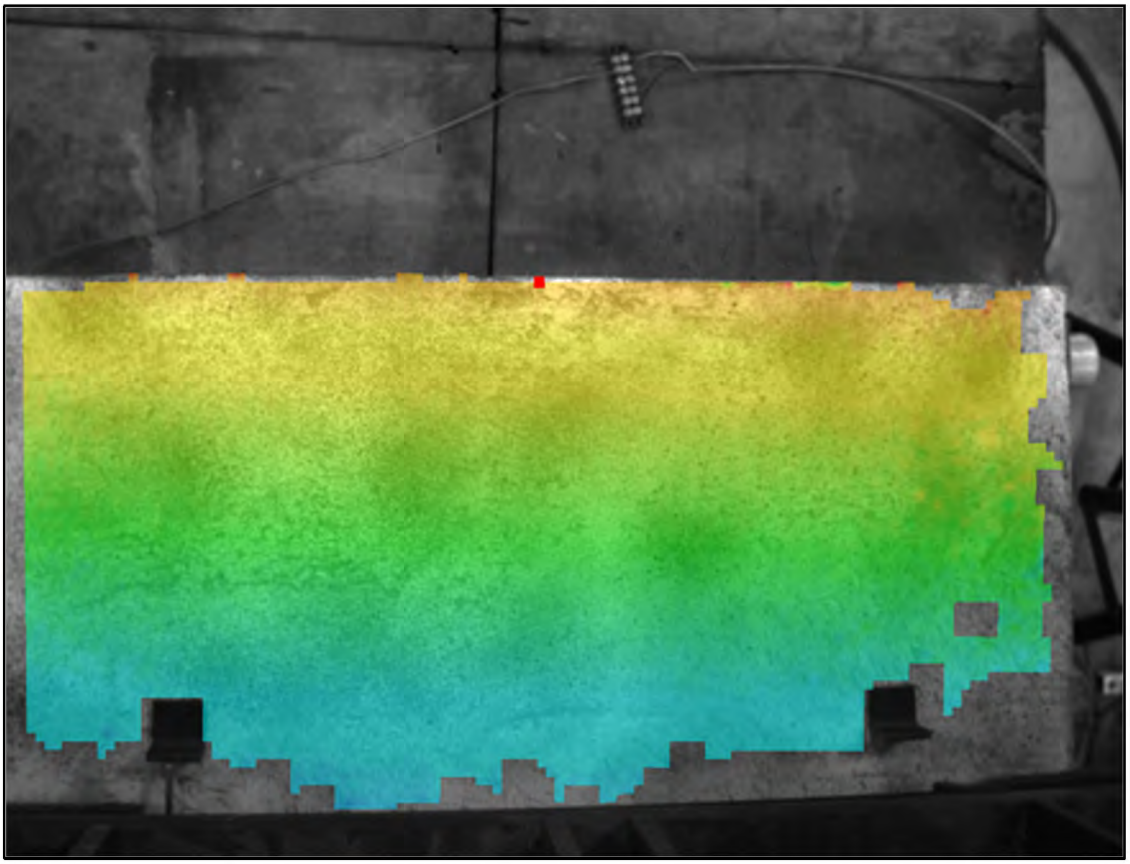


Figure 5.285: Vertical displacements of the top of the slab (9100 lb [40.5 kN]).

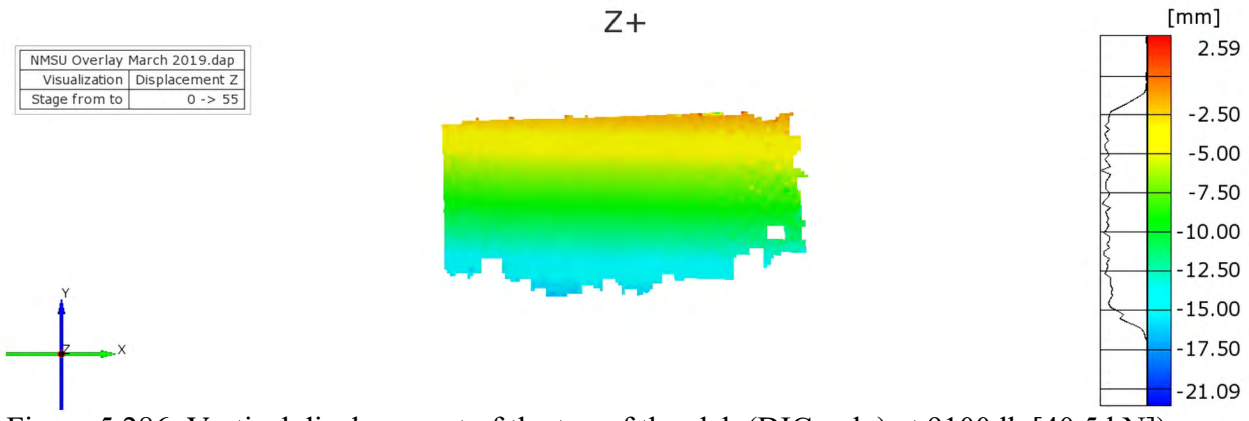


Figure 5.286: Vertical displacement of the top of the slab (DIC only) at 9100 lb [40.5 kN]).

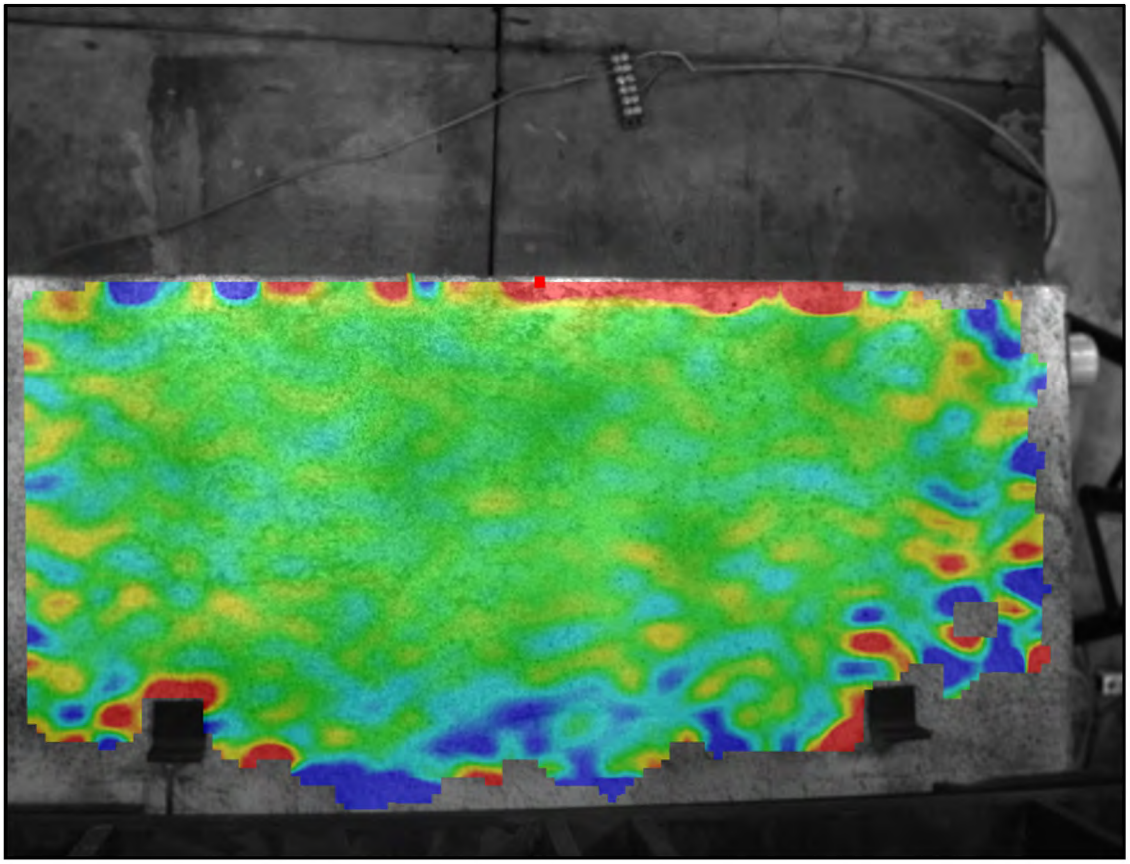


Figure 5.287: Bending strains at top of the slab (8900 lb [39.6 kN]).

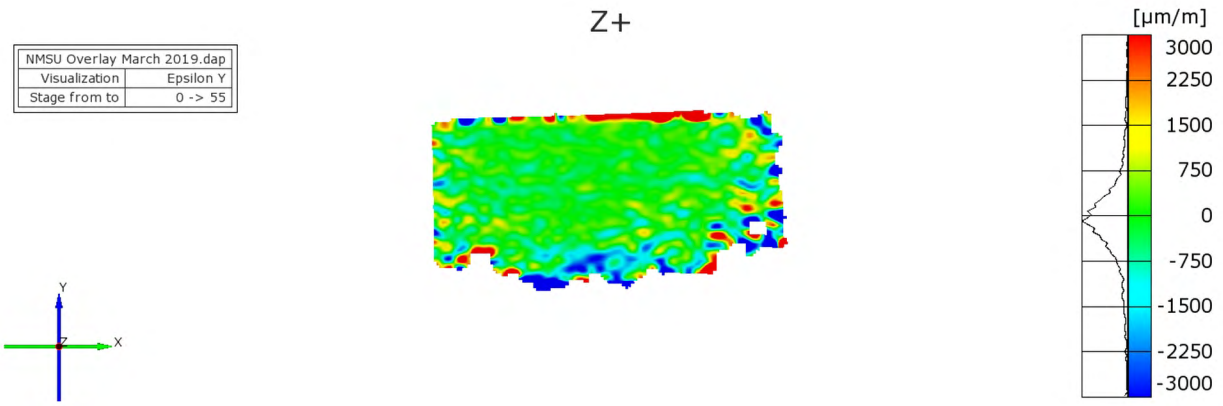


Figure 5.288: Bending strains at top of the slab (8900 lb [39.6 kN]).

DIC was also used in the side face of the slab in which vertical displacements were measured obtaining the highest displacement at midspan, as expected. The load when the first crack start to developed was able identified at 4500 lb (20 kN). Then during the three cycles performed from 0 to 6000 lb (0 to 26.7 kN) the cracked had a stable growth, and when the load was increasing to failure at the fourth time the slab was loaded to 6000 lb (26.7 kN) the cracked started growing significantly (Figure 4.53). The strain measurements in Figure 4.53 goes from +2000 με (red) to -2000 με (blue). Figure 5.289 and Figure 5.290 show the discontinuity presented in the displacements of the contour plot which made evident the development of the crack at the fourth time loading at 6000 lb (26.7 kN).

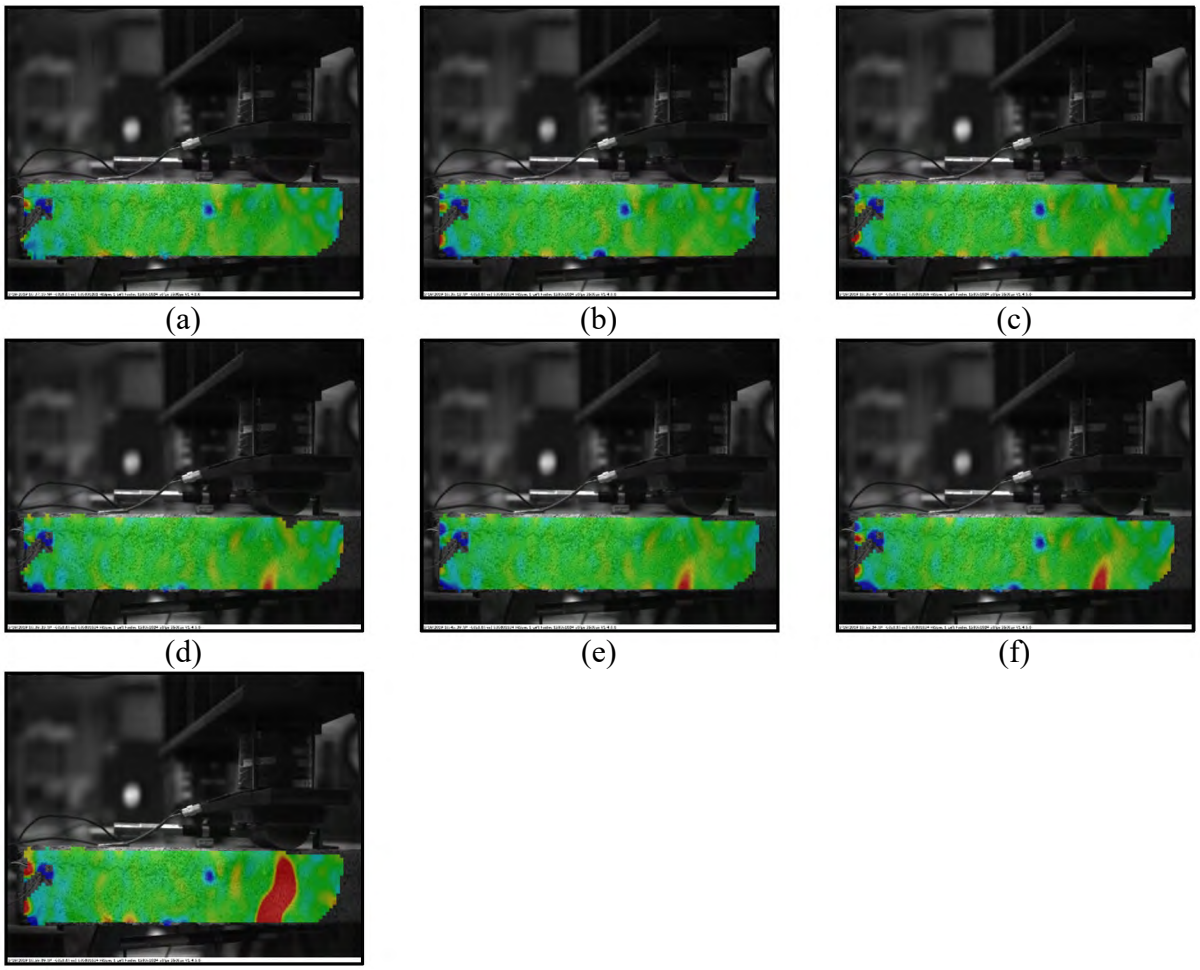


Figure 5.289: Bending Strains in Slab – (a) at 4500 lb (20 kN), (b) at 5000 lb (22 kN), (c) at 5500 lb (24.5 kN), (d) at 6000 lb (26.7 kN) in cycle 1, (e) at 6000 lb (26.7 kN) in cycle 2, (f) at 6000 lb (26.7 kN) in cycle 3, (g) at 6000 lb (26.7 kN) going to failure.

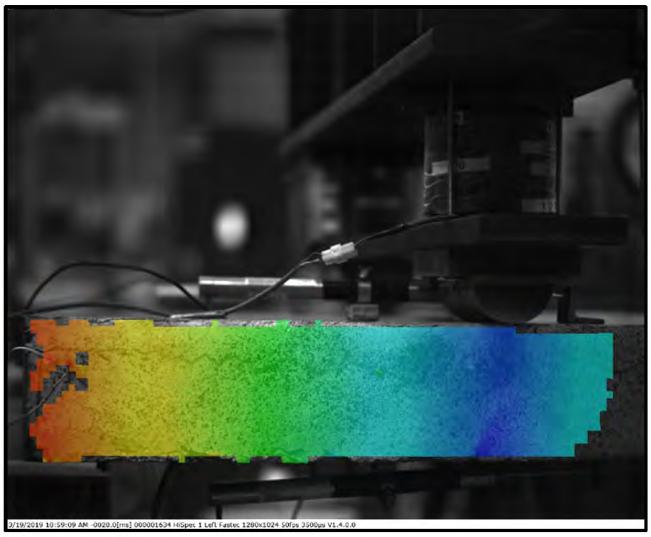


Figure 5.290: Vertical displacement on side of the slab.



Figure 5.291: Vertical displacement on side of the slab (DIC only).

Other images were captured to determine if delamination occurred between the UHPC overlay and the NSC substrate. Figure 5.292 shows the longitudinal strains at the slab edge at 8900 lb (39.6 kN). No discontinuity was present in the strains to the left of the crack. This means that delamination did not occur at this stage of the test, nor at the end of the test. The gradually transition of the strains from compression in the bottom to tension in the top provides evidence to ensure that delamination not occur.

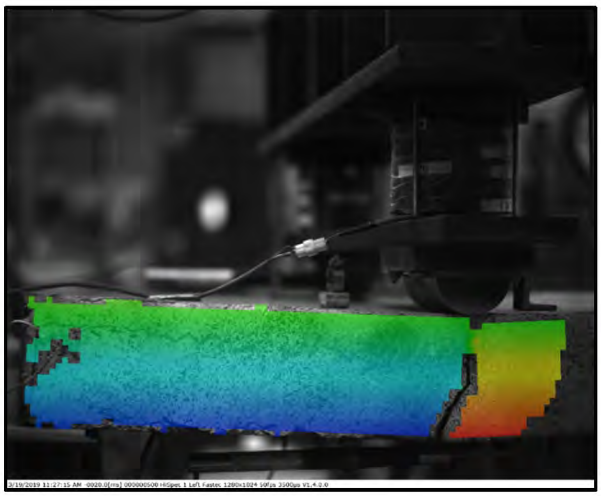


Figure 5.292: Longitudinal strains on side of slab.

More evidence that delamination did not occur in the slab is the plot of length versus displacement shown in Figure 5.293. The displacement experienced in different sections of the vertical side of the slab approximately 1.97 in. (50 mm) from midspan to the edge of the slab were monitored at the stage of loading of 8900 lb (39.6 kN). This plot does not show any discontinuity along the horizontal axis which means that no delamination was developed for the entirety of the slab test.

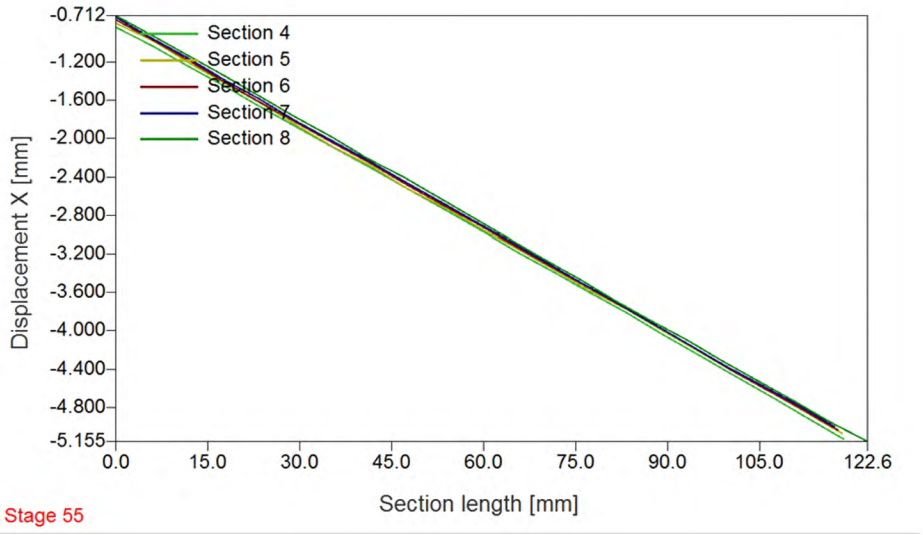


Figure 5.293: Displacement of sections along slab edge.

5.4.11 Conclusions

UHPC is an enhanced concrete material that can be used to improve infrastructure by reducing deterioration and increasing the service life of the structure. UHPC has many advantages when used as an overlay material to protect bridge decks or to increase its capacity. The results obtained from this research demonstrate that locally produced UHPC has the potential to serve as an overlay material and that proper bond between the UHPC overlay and a substrate material can be achieved with proper surface preparation.

Different parameters were analyzed in this research such as the surface preparation and texture depth, application of UHPC overlay, shrinkage of the overlay and normal strength concrete and UHPC, shear stress at the overlay-substrate interface, and the flexural behavior of the composite section. To evaluate how different parameters influenced the behavior of the UHPC overlay-NSC substrate slab specimens, VWSGs were used to measure the changes in strain in the slabs over an extended period of time. The strain changes included shrinkage, application of the UHPC overlay, and thermal deformations. With this data, the influence the UHPC overlay had on the NSC substrate was investigated and the shear stress developed at the bond interface between the two materials was estimated, which is important to understand to prevent cracking and delamination. After the monitoring period was over, flexural tests were conducted on the composite specimens. The sensors used to measure the behavior during flexural testing included VWSGs, SGs, LVDTs, string potentiometers, and tiltmeters.

Some of the parameters that significantly influenced the behavior of the slab specimens overlay was the steel reinforcement in the substrate, the thickness of the substrate material, and the fiber content in the overlay. As expected, the reinforcement used in the slabs is relevant for shrinkage and thermal deformations. Results shown that slabs with higher reinforcement ratios of 0.008 compared to slabs with a reinforcement ratio of 0.005 experienced smaller changes in strain. The thickness of the substrate was also an important factor for the strain. Based on the analysis of strain results, the thicker slabs with thickness of 7 in. (17.8 cm) or 6.5 in. (16.5 cm) experienced greater shrinkage than thinner slabs, thus larger strains. Based on this research reinforcement ratio is more important than reinforcement area since similar slabs contained the same amount of steel area. Results also show that the percentage of fibers influence the shrinkage of the UHPC overlay. Higher percentages of fibers in the mixture reduced the amount of the strain measured after the application of the UHPC overlay.

As expected, the slabs exposed to laboratory conditions experienced shrinkage and the changes in stain were more uniform than the slab that was exposed to environmental conditions. The slabs that were exposed to environmental conditions were exposed to drastic changes in temperature and multiple freeze-thaw cycles, however, these extreme conditions did not affect the bond between the UHPC overlay and the NSC substrate. After being tested under 1000 cycles to a load approximately equal to 50% of the nominal strength of each slab, and (for some specimens) ultimate flexural loading, the UHPC and NSC acted as a composite section, and at the end of the testing, no debonding was observed.

To achieve the bond between the substrate and the overlay, the NSC surfaces were prepared using a chipping method with an air hammer. After the surface was textured, it was cleaned and saturated for a minimum of 24 hours prior to UHPC application. This method achieved an effective bond between the NSC and UHPC overlay, even at failure during flexural test in which the cracks propagated into the UHPC overlay. This method of surface preparation is not ideal for large applications as it is an exhaustive and time-consuming procedure. Therefore, hydro-demolition or shot-blasting are other types of surface preparation methods that are recommended. However, it is recommended to have a clean, saturated surface when the overlay is applied.

The workability of the UHPC is an important factor when placing the overlay. Wood and steel screeds were found as useful tools to have a better distribution of the UHPC in the substrate surface. A smooth surface was hard to achieve due to the low w/cm ratio of the UHPC and the faster drying of the UHPC. For this reason, is recommended to immediately cover the finish the surface and cover the UHPC with plastic to help reduce the loss of moisture.

Based on the results of this research, it has been demonstrated that locally developed UHPC can effectively be used as an overlay material. The UHPC bonded with the substrate material effectively, and after being exposed to environmental conditions (including freezing and thawing) and loaded to failure, no debonding was observed. The estimated shear stress at the interface of the two materials had a maximum range of -700 με to 5 με.

Some of the recommendations for UHPC overlay applications for future work is to further investigate full scale decks under cyclic and ultimate loading to have a better understanding of the performance of UHPC as an overlay. Also, it is recommended to perform flexural test on specimens at early ages to reduce the curing period of the UHPC overlay to ensure adequate bond at lower strengths. It is also recommended to study the shear stress at the overlay-substrate interface on larger UHPC overlay applications. This can provide additional information regarding its performance in regard to resistance to cracking. Finally, further investigation of the behavior of UHPC overlays with mild reinforcement or different percentages and types of fibers is recommended. These parameters can further improve the resistance to cracking, provide additional strength to the bridge, and/or increase the durability of the system.

THIS PAGE INTETIONALLY LEFT BLANK

REFERENCES

AASHTO (American Association of State Highway and Transportation Officials). (2011). *Manual for bridge evaluation, with 2011, 2013, 2014, and 2015 interim revisions* (2nd ed.). Washington, DC: AASHTO.

AASHTO (American Association of State Highway and Transportation Officials). (2012). *AASHTO LRFD bridge design specifications, customary U.S. units*, (6th ed.). Washington, DC: AASHTO.

AASHTO (American Association of State Highway and Transportation Officials). (2016). *AASHTO M 203M/M 203-12 (2016)*. Washington, DC: AASHTO.

AASHTO (American Association of State Highway and Transportation Officials). (2017). *AASHTO LRFD bridge design specifications, customary U.S. units*, (6th ed.). Washington, DC: AASHTO.

ACI (American Concrete Institute). (2014). *Building code requirements for structural concrete and commentary*. ACI 318-14. Farmington Hills, MI: ACI.

ACI (American Concrete Institute). (2018). *Ultra-high-performance concrete: An emerging technology report*. ACI 239R-18. Farmington Hills, MI: ACI.

ACI (American Concrete Institute). (2019). *Building code requirements for structural concrete and commentary*. ACI 239R-19. Farmington Hills, MI: ACI.

AFGC-SETRA (Association Française de Génie Civil-Service d'Études Techniques des Routes et Autoroutes). (2002). *Ultra-high performance fibre-reinforced concretes—Interim recommendations*. Paris: AFGC-SETRA.

Aguilar, C. V., Jáuregui, D. V., Newtson, C. M., Weldon, B. D., and Cortez, T. M. (2015). Load rating a prestressed concrete double T-beam bridge without plans by field testing. *Transportation Research Record,* 2522(9), 90–99. https://doi.org/10.3141/2522-09.

Aguilar, C. V., Jáuregui, D. V., Weldon, B. D., and Newtson, C. M. (2018). Rating of prestressed concrete adjacent beam bridges without plans. Special Publication, 323, 5.1–5.20. FarmingtonHills, MI: ACI.

Ahlborn, T. M., Harris, D. K., Misson, D. L., and Peuse, E. J. (2011). Characterization of strength and durability of ultra-high performance concrete under variable curing conditions. *Transportation Research Record,* 2251, 68–75. https://doi.org/10.3141/2251-07.

Alahmari, T. S., Kennedy, C. S., Cuaron, A. M., Weldon, B. D., and Jáuregui, D. V. (2019). Field testing of a prestressed concrete bridge with high performance and locally developed ultra-high performance concrete girders. *Frontiers in Built Environment*, 5(114). https://doi.org/10.3389/fbuil.2019.00114.

Alampalli, S., and Kunin, J. (2003). Load testing of an FRP bridge deck on a truss bridge. *Applied Composite Materials*, 10(2), 85–102. https://doi.org/10.1023/A:1022885728627.

Alampalli, S., and Lund, R. (2006). Estimating fatigue life of bridge components using measured strains. *Journal of Bridge Engineering*, 11(6), 725–736. https://doi.org/10.1061/(ASCE)1084-0702(2006)11:6(725).

Alampalli, S., Frangopol, D. M., Grimson, J., Kosnik, D., Halling, M., Lantsoght, E. O., Weidner, J. S., Yang, D. Y., and Zhou, Y. E. (2019). Primer on bridge load testing. *Transportation Research Circular*, (E-C257).
Allena, S. (2010). *Ultra high strength concrete using local materials*. PhD dissertation. Las Cruces, NM: New Mexico State University.
Allena, S., and Newtson, C. M. (2011). Ultra-high strength concrete mixtures using local materials. *Journal of Civil Engineering and Architecture*, 5(4) (Serial No. 41), 322–330.
ASTM. (2007). ASTM C1260: Standard test method for potential alkali reactivity of aggregates (mortar-bar method). West Conshohocken, PA: ASTM International.
ASTM. (2008). ASTM C666: Standard test method for resistance of concrete to rapid freezing and thawing. West Conshohocken, PA: ASTM International.
ASTM. (2010). ASTM A615: Standard specification for deformed and plain carbon-steel for concrete reinforcement. West Conshohocken, PA: ASTM International.
ASTM. (2013). ASTM C882: Standard test method for bond strength of epoxy-resin systems used with concrete by slant shear. West Conshohocken, PA: ASTM International.
ASTM. (2014). ASTM A1064: Standard specification for carbon-steel wire and welded wire reinforcement, plain and deformed, for concrete. West Conshohocken, PA: ASTM International.
ASTM. (2014). ASTM C469: Standard test method for static modulus of elasticity and poisson's ratio of concrete in compression. West Conshohocken, PA: ASTM International.
ASTM. (2015). ASTM A370: Standard test methods and definitions for mechanical testing of steel products. West Conshohocken, PA: ASTM International.
ASTM. (2015). ASTM C617: Standard practice for capping cylindrical concrete specimens. West Conshohocken, PA: ASTM International.
ASTM. (2015). ASTM C1231: Standard practice for use of unbonded caps in determination of compressive strength of hardened cylindrical concrete specimens. West Conshohocken, PA: ASTM International.
ASTM. (2015). ASTM E965: Standard test method for measuring pavement macrotexture depth using a volumetric technique. West Conshohocken, PA: ASTM International.
ASTM. (2016). ASTM A416: Standard specification for low-relaxation, seven-wire steel strand for prestressed concrete. West Conshohocken, PA: ASTM International.
ASTM. (2016). ASTM A820: Standard specification for steel fibers for fiber-reinforced concrete. West Conshohocken, PA: ASTM International.
ASTM. (2017). ASTM C1202: Standard test method for electrical indication of concrete's ability to resist chloride ion penetration. West Conshohocken, PA: ASTM International.
ASTM. (2017). ASTM C1856: Standard practice for fabricating and testing specimens of ultra-high performance concrete. West Conshohocken, PA: ASTM International.
ASTM. (2018). ASTM C39: Standard test method for compressive strength of cylindrical concrete specimens. West Conshohocken, PA: ASTM International.
ASTM. (2019). ASTM C1609: Standard test method for flexural performance of fiber-reinforced concrete (using beam with third-point loading). West Conshohocken, PA: ASTM International.

Bache, H. H. (1988). The new strong cements: Their use in structures. *Physics in Technology*, 19(2), 43–50.
Beer, F., Johnston, E. R., DeWolf, T., and Mazurek, D. F. (2012). *Mechanics of materials*, (7th edition). New York, USA: McGraw-Hill Education.
Bentley Systems, Inc. (2012). LEAP CONSPAN® precast/prestressed bridge beam analysis, design and load rating v12.01.00.00 (US) volume I – user manual. Exton, PA: Bentley Systems, Inc.
Bierwagen, D., and McDonald, N. (2005). Ultra High Performance Concrete Highway Bridge. *Proc., 2005 Mid-Continent Transportation Research Symposium,* 1–14.
BSI (British Standards Institution). (1983). *Method for determination of compressive strength of concrete cubes*. BS 1881 Part 116. London: BSI.
Cai, H., Abudayyeh, O., Abdel-Qader, I., Attanayake, U., Barbera, J., and Almaita, E. (2012). Bridge deck load testing using sensors and optical survey equipment. *Advances in Civil Engineering*, 2012:493983. https://doi.org/10.1155/2012/ 493983.
Carbonell Muñoz, M. A., Harris, D. K., Ahlborn, T. M., and Froster, D. C. (2014). Bond performance between ultrahigh-performance concrete and normal-strength concrete. *Journal of Materials in Civil Engineering*, 26(8). https://doi.org/10.1061/(ASCE)MT.1943-5533.0000890.
CSI (Campbell Scientific, Inc). (2020). *CR6–Measurement and Control Datalogger*. Logan, UT: CSI. Retrieved from https://www.campbellsci.com/cr6.
Cuaron, A. M., Jáuregui, D. V., and Weldon, B. D. (2017). Invited student paper—A procedure for load rating reinforced concrete slab bridges without plans. *TRB 96th Annual Meeting compendium of papers* (No. 17–01754). Washington, DC: Transportation Research Board.
Dili, A. S., and Santhanam, M. (2004). Investigations on reactive powder concrete: A developing ultra high strength technology. *The Indian Concrete Journal*, 78(4), 33–38.
Eppers, S. and Müller, C. (2008). Autogenous shrinkage strain of ultra-high performance concrete (UHPC). *Proc., 2nd International Symposium on Ultra High Performance Concrete*, 433–441. Kassel, Germany: Kassel University Press.
Fehling, E., Leutbecher, T., and Bunje, K. (2004). Design relevant properties of hardened ultra high performance concrete. *Proc., International Symposium on Ultra High Performance Concrete*, 39–48. Kassel, Germany: Kassel University Press.
Fliestra, J., Ahlborn, T. M., Harris, D. K., and de Melo e Silva, H. (2012). Creep behaviour of UHPC under compressive loading with varying curing regimes. *Proc., Hipermat 2012 3rd International Symposium on UHPC and Nanotechnology for High Performance Construction Materials*, 333–340. Kassel, Germany: Kassel University Press.
Giesler, A. J. (2014). The flexural behavior and analysis of prestressed ultra high performance concrete beams made from locally available materials. MS thesis. Las Cruces, NM: New Mexico State University.
Giesler, A. J., Applegate, S. B., and Weldon, B. D. (2016). Implementing nonproprietary, ultra-high-performance concrete in a precasting plant. *PCI Journal*, 61(6): 68–80.

Giesler, A. J., McGinnis, M. J. and Weldon, B. D. (2018). Flexural behavior and analysis of prestressed ultra-high-performance concrete beams made from locally available materials. *PCI Journal*, 63(6), 66–80.
Graybeal, B. A. (2006a). *Structural behavior of ultra high performance concrete prestressed I-girders*. Rep. No. FHWA-HRT-06-115. McLean, VA: Federal Highway Administration.
Graybeal, B. A. (2006b). *Material property characterization of ultra-high performance concrete*. Rep. No. FHWA-HRT-06-103. McLean, VA: Federal Highway Administration.
Graybeal, B. A. (2015). Compression testing of ultra-high performance concrete. *Advances in Civil Engineering Materials*, 4(2), 102–112. https://doi.org/10.1520/ACEM20140027.
Graybeal, B. A, and Stone, B. (2012). *Compression response of a rapid-strengthening ultra-high performance concrete formulation*. Rep. No. FHWA-HRT-12-064, National Technical Information Service Accession No. PB2012-112545. McLean, VA: Federal Highway Administration.
Guaderrama, L. R., and Weldon, B. D. (2013). Compressive stress-strain behavior of ultra high performance concrete using local materials. *Proc., 92nd Annual Meeting of the Transportation Research Board*, No. 13-3339, Washington DC.
Haber, Z. B., De la Varga, I., Graybeal, B. A., Nakashoji, B., and El-Helou, R. (2018). *Properties and behavior of UHPC-class materials*. Rep. No. FHWA-HRT -18-036. McLean, VA: Federal Highway Administration.
Haber, Z. B., Munoz, J. F., De la Varga, I., and Graybeal, B. A. (2018). Bond characterization of UHPC overlays for concrete bridge decks: Laboratory and field testing. *Construction and Building Materials*, 190, 1056–1068. https://doi.org/10.1016/j.conbuildmat.2018.09.167.
Haber, Z. B., Munoz, J. F., and Graybeal, B. A. (2017). *Field testing of an ultra-high performance concrete overlay*. Rep. No. FHWA-HRT-17-096. McLean, VA: Federal Highway Administration.
Hag-Elsafi, O., Alampalli, S., and Kunin, J. (2004). In-service evaluation of a reinforced concrete T- beam bridge FRP strengthening system. *Composite Structures*, 64(2), 179–188. https://doi.org/10.1016/j.compstruct.2003. 08.002
Harris, D. K., Carbonell Muñoz, M. A., Gheitasi, A., Ahlborn, T. M., and Rush, S. V. (2015). The challenges related to interface bond characterization of ultra-high-performance concrete with implications for bridge rehabilitation practices. *Advances in Civil Engineering Materials*, 4(2), 75–101. https://doi.org/10.1520/ACEM20140034.
Hou, T. C., and Lynch, J. P. (2006). Rapid-to-deploy wireless monitoring systems for static and dynamic load testing of bridges: validation on the Grove Street Bridge. *Proc., Nonintrusive Inspection, Structures Monitoring, and Smart Systems for Homeland Security*, 61780D. San Diego, CA: International Society for Optics and Photonics.
Jauregui, D. V., Weldon, B. D., and Aguilar, C. V. (2019). Load rating of prestressed concrete bridges without design plans by nondestructive field testing. In E.O.L Lantsoght (Ed.), *Load Testing of Bridges: Proof Load Testing and the Future of Load Testing* (pp. 27–65). CRC Press. https://doi.org/10.1201/9780429265969.

John, E. E., Ruiz, E. D., Floyd, R. W., and Hale, W. M. (2011). Transfer and development lengths and prestress losses in ultra-high performance concrete beams. *Transportation Research Record,* 2251, 76–81. https://doi.org/10.3141/2251-08.
Kennedy, C. S. (2018). Diagnostic and proof load testing of NM Bridge 9706 using high performance and locally developed ultra high performance concrete. MS thesis. Las Cruces, NM: New Mexico State University.
Kleinhans, D. D., Myers, J. J., and Nanni, A. (2007). Assessment of load transfer and load distribution in bridges utilizing FRP panels. *Journal of Composites for Construction*, 11(5), 545–552. https://doi.org/10.1061/(ASCE)1090-0268(2007)11:5(545).
Leet, K. M., Uang, C., and Gilbert, A. M. (2008). *Fundamentals of structural analysis*. New York, NY: McGraw Hill Companies
Lyell, E. K. (2011). Optimization of ultra high performance concrete mixture proportions using locally available materials. MS thesis. Las Cruces, NM: New Mexico State University.
Manning, M. P. (2015). Design and comparative flexural analyses of prestressed bridge girders using high performance and locally developed ultra-high performance concretes. MS thesis. Las Cruces, NM: New Mexico State University.
Manning, M. P., Weldon, B. D., McGinnis, M. J., Jáuregui, D. V., and Newtson, C. M. (2016). Behavior comparison of prestressed channel girders from high-performance and ultrahigh-performance concrete. *Transportation Research Record*, 2577(8): 60-68. https://doi.org/10.3141/2577-08.
McGinnis, M. J., Barbachyn, S., and Kurama, Y. C. (2014). Application of multiple digital image correlation sensors in earthquake engineering. *Proc., 10th National Conference in Earthquake Engineering*, Earthquake Engineering Research Institute, Anchorage, AK, 2014.
Muro-Villanueva, J. (2015). Mixture proportioning and freezing and thawing durability of ultra high performance concrete mixtures using local materials. PhD dissertation. Las Cruces, NM: New Mexico State University.
Muro-Villanueva J., Newtson C. M., Weldon, B. D., Jauregui, D. V., and Allena, S. (2013). Freezing and thawing durability of ultra high strength concrete. *Journal of Civil Engineering and Architecture*, 7(8), 907–915. https://doi.org/10.17265/1934-7359/2013.08.001.
Naaman, A. E. (2011a). Half a century of progress leading to ultra-high performance fiber reinforced concrete: Part 1-Overall review. *Proc., 2nd International RILEM Conference on Strain Hardening Cementitious Composites*, 17–26. RILEM Publications SARL.
Naaman, A. E. (2011b). Half a century of progress leading to ultra-high performance fiber reinforced concrete: Part 2-Tensile stress-strain response. *Proc., 2nd International RILEM Conference on Strain Hardening Cementitious Composites*, 27–23. RILEM Publications SARL.
Naaman, A. E., and Reinhardt, H. W. (2006). Proposed Classification of HRFRC Composites Based on their Tensile Response. *Materials and Structures*, 39(5), 547–555.
Naaman, A. E., and Wille, K. (2012). The path to ultra-high performance fiber reinforced concrete (UHP-FRC): Five Decades of Progress. *Proc., Hipermat 2012 3rd International Symposium on*

UHPC and Nanotechnology for High Performance Construction Materials, 3–13. Kassel, Germany: Kassel University Press.
Newtson, C. M., Weldon, B. D., Al-Basha, A. J., Manning, M. P., Toledo, W. K., and Davila, L. D. (2018). *Bridge deck overlays using ultra-high performance concrete*. Final Report Project No. 17CNMS01. Transportation Consortium of South-Central States (Tran-SET).
NI (National Instruments Corporation). (2006). *SCXI Chassis User Manual*. Austin, TX: NI. Retrieved from https://www.ni.com/pdf/manuals/374423l.pdf.
NI (National Instruments Corporation). (2009). *SCXI-1520 user manual*. Austin, TX: NI. Retrieved from https://www.ni.com/pdf/manuals/372583e.pdf.
NI (National Instruments Corporation). (2012). *SCXI-1540 user manual*. Austin, TX: NI Corporation. Retrieved from http://www.ni.com/pdf/manuals/372581c.pdf.
NMDOT (New Mexico Dept. of Transportation). (2013). *Bridge procedures and design guide*. Santa Fe, NM: NMDOT.
NMDOT (New Mexico Dept. of Transportation). (2018). *Bridge procedures and design guide*. Santa Fe, NM: NMDOT.
Omega (Omega Engineering Inc.). (2018a). *Thermocouples*. Norwalk, CT: Omega. Retrieved from https://www.omega.com/en-us/resources/thermocouples.
Omega (Omega Engineering Inc.). (2018b). *What is a thermistor and how does it work?* Norwalk, CT: Omega. Retrieved from https://www.omega.com/en-us/resources/thermistor.
Omega (Omega Engineering Inc.). (2018c). *What is a linear variable differential transformer?* Norwalk, CT: Omega. Retrieved from https://www.omega.com/en-us/resources/lvdt-sensors.
Omega (Omega Engineering Inc.). (2019). *Strain Gauge*. Norwalk, CT: Omega. Retrieved from https://www.omega.com/en-us/resources/strain-microstrain.
Phares, B. M., Wipf, T. J., Greimann, L. F., and Lee, Y. S. (2005). Health monitoring of bridge structures and components using smart structure technology volume II. *WisDOT Rep. No. 0092-04-14*. Wisconsin Highway Research Program. Wisconsin Dept. of Transportation.
Piérard, J., Dooms, B., and Cauberg, N. (2012). Evaluation of durability parameters of UHPC using accelerated lab tests. *Proc., Hipermat 2012 3rd International Symposium on UHPC and Nanotechnology for High Performance Construction Materials*, 371–376. Kassel, Germany: Kassel University Press.
Randl, N., Steiner, T., Ofner, S., Baumgartner, E., and Mészöly, T. (2014). Development of UHPC mixtures from an ecological point of view. *Construction and Building Materials*, 67, 373–378. https://doi.org/10.1016/j.conbuildmat.2013.12.102.
Regalado, A., Carpenter, B. A., Jáuregui, D. V., and Weldon, B. D. (2017). Performance evaluation of a reinforced concrete slab bridge retrofitted with carbon fiber reinforcement polymer laminate system. *Transportation Research Record,* 2642, 68–76. https://doi.org/10.3141/2642-09.
Richard, P., and Cheyrezy, M. (1995). Composition of reactive powder concretes. *Cement and Concrete Research*, 25(7), 1501–1511.

Roctest Ltd. (2017a). *EM Series Embedded Vibrating Wire Strain Gauge*. Saint-Lambert: Roctest Limited. Retrieved from https://roctest.com/en/product/em-series-embedded-vibrating-wire-strain-gauge/.
Roctest Ltd. (2017b). *SM-5 Series Surface Mount Vibrating Wire Strain Gauge*. Saint-Lambert: Roctest Limited. Retrieved from https://roctest.com/en/product/sm-5-series-surface-mount-vibrating-wire-strain-gauge-2/.
Roctest Ltd. (2017c). *RT-MUX 16/32–Signal Multiplexer*. Saint-Lambert: Roctest Limited. Retrieved from https://roctest.com/en/product/rt-mux-1632-signal-multiplexer/.
Rossi, P. (2000). Ultra-high performance fibre reinforced concretes (UHPFRC): An overview. *Proc., 5th International RILEM Symposium on Fibre Reinforced Concrete (FRC)*, 87–100. RILEM Publications SARL.
Russell, H. R., and Graybeal, B. A. (2013). *Ultra-high performance concrete: A state-of-the-art report for the bridge community*. Rep. No. FHWA-HRT-13-060. McLean, VA: Federal Highway Administration.
Simon, A., Courtois, A., Clauzon, T., Coustabeau, E., and Vinit, S. (2015). Long-term measurement of strain in concrete: durability and accuracy of embedded vibrating wire strain gauges. *Proc., SMAR 2015–3rd Conference on Smart Monitoring, Assessment and Rehabilitation of Civil Structures*.
Smith, B. J., Kurama, Y. C., and McGinnis, M. J. (2011). Design and measured behavior of a hybrid precast concrete wall specimen for seismic regions. *Journal of Structural Engineering*, 137(10), 1052–1062.
Sorelli, L., Constantinides, G., Ulm, F. J., and Toutlemonde, F. (2008). The nano-mechanical properties of ultra high performance fibre reinforced concrete. *Proc., BEFIB 2008: 7th RILEM International Symposium on Fibre Reinforced Concrete*, 39–49. RILEM Publications SARL.
Sritharan, S., Doiron, G., Bierwagen, D., Keierleber, B., and Abu-Hawash, A. (2018). First application of UHPC bridge deck overlay in North America. *Transportation Research Record*, 2672, 40–47. https://doi.org/10.1177/0361198118755665.
Steinhart, J. S., and Hart, S. R. (1968). Calibration curves for thermistors. *Deep Sea Research and Oceanographic Abstracts*, 15(4), 497–503. Elsevier.
Taylor, C. W. (2010). Feasibility analysis of ultra high performance concrete in prestressed concrete bridge applications. MS thesis. Las Cruces, NM: New Mexico State University.
Taylor, C. W., Weldon, B. D., Jáuregui, D. V., and Newtson, C. M. (2013). Case studies using ultrahigh-performance concrete for prestressed bridge design. *Practice Periodical on Structural Design and Construction*, 18(4), 261–267. https://doi.org/10.1061/(ASCE)SC.1943-5576.0000167.
TE Connectivity. (2017a). *What is a string pot?* Retrieved from https://www.te.com/usa-en/products/sensors/position-sensors/potentiometric-sensors/cable-actuated-position-sensors/what-is-a-string-pot.html.
TE Connectivity. (2017b). *Accustar® electronic clinometer*. Retrieved from https://www.te.com/sensorsolutions.

Thomas, M. D. A., Shehata, M. H., Shashiprakash, S. G., Hopkins, D. S., and Cail, K. (1999). "Use of ternary cementitious systems containing silica fume and fly ash in concrete." *Cement and Concrete Research*, 29(8), 1207–1214.
Tuthill, L. H. (1982). Alkali silica reaction–40 years later. *Concrete International*, 32–35.
TXDOT. (2011). Test procedure for determining the coefficient of thermal expansion of concrete. Tex-428-A. Texas Dept. of Transportation.
Ulm, F. J. (2004). *Bending and Shear Design of Iowa DOT Sample Bridge—Update*. Department of Civil and Environmental Engineering, Massachusetts Institute of Technology, Cambridge, MA.
Visage, E. T. (2013). Experimental analysis of the flexural behavior of ultra-high performance concrete beams using local materials. MS thesis. Las Cruces, NM: New Mexico State University.
Visage, E. T., Weldon, B. D., Jauregui, D. V., and Newtson, C. M. (2019). Flexural performance of ultrahigh-performance concrete developed using local materials. *Journal of Materials in Civil Engineering*, 31(5). https://doi.org/10.1061/(ASCE)MT.1943-5533.0002683.
Weldon, B. D., Jáuregui, D. V., Newtson, C. M., Taylor, C. W., Montoya, K. F., and Allena, S. (2010). *Feasibility analysis of ultra high performance concrete for prestressed concrete bridge applications—Final report*. NMDOT Rep. No. NM09MSC-01. Santa Fe, NM: New Mexico Dept. of Transportation.
Weldon, B. D., Jáuregui, D. V., Newtson, C. M., Taylor, C. W., Montoya, K. F., Allena, S., Muro-Villanueva, J., Tahat, M., Lyell, E., and Visage, E.T. (2012). *Feasibility analysis of ultra high performance concrete for prestressed concrete bridge applications, phase ii—Final report*. NMDOT Rep. No. NM09MSC-01. Santa Fe, NM: New Mexico Dept. of Transportation.
Wille, K., Kim, D. J., and Naaman, A. E. (2011). Strain-hardening UHP-FRC with low fiber contents. *Materials and Structures*, 44(3), 583–598.
Wipf, T. J., Phares, B. M., Sritharan, S., Degen, B. E., and Giesmann, M. T. (2009). Design and evaluation of a single-span bridge using ultra-high performance concrete. *Rep. No. IHRB Project TR-529,* Highway Research Board, Iowa Dept. of Transportation.
WRI (Wire Reinforcement Institute). (2016). *Manual of standard practice–structural welded wire reinforcement*. WWR–500–R–16 (9th ed.). Hartford, CT: WRI.